

# **RIKEN Accelerator Progress Report**

2001

vol. **35**

理化学研究所  
*RIKEN (The Institute of Physical and Chemical Research)*

**RIKEN Accelerator Progress Report** 2001  
**January-December**

vol. **35**

理化学研究所  
**RIKEN (The Institute of Physical and Chemical Research)**  
**Wako, Saitama, 351-0198 JAPAN**

Chairperson of the Editorial Committee  
K. Asahi

Editorial Committee

T. Abe	T. Ichihara
K. Ishida	T. Kambara
O. Kamigaito	Y. Kobayashi
A. Kohama	A. Ozawa
I. Shimamura	K. Yazaki

All rights reserved. This report or any part thereof may not be reproduced in any form (including photostatic or microfilm form) without written permission from the publisher.

All reports are written on authors' responsibility and thus the editors are not liable for the contents of the report.

# CONTENTS

	Page
<b>I. PREFACE</b> .....	1
<b>II. OPERATION OF ACCELERATORS</b>	
RILAC operation .....	3
RRC and AVF operation .....	5
Operation of the tandem accelerator .....	7
<b>III. RESEARCH ACTIVITIES</b>	
<b>1. Nuclear Physics</b>	
Triaxially deformed states in the Monte-Carlo Shell Model .....	9
Extreme location of the fluorine drip line .....	10
Magic numbers of exotic nuclei .....	11
A Search for a unified effective interaction for Monte-Carlo Shell-Model calculations (III) .....	12
Relativistic mean field theory with pion for finite nuclei .....	13
Parity-violating mean field theory with the pion .....	14
Cranked relativistic mean-field study of chiral doublet bands .....	15
Three-dimensional TDHF calculation on reactions of unstable nuclei .....	16
Resonance and continuum states in weakly bound systems .....	17
Triaxial deformation in $^{10}\text{Be}$ .....	18
Equilateral-triangular shape in $^{14}\text{C}$ .....	19
Description of the Gamow-Teller resonance within the phonon damping model .....	20
Phonon damping model using random-phase-approximation operators .....	21
Improved treatment of ground-state correlations: Modified random-phase approximation .....	22
Determination of the matter surface distribution of unstable nuclei .....	23
Observation of new neutron and proton magic numbers .....	24
Possibility of an enlarged core structure of $N = 15$ neutron-rich nuclei .....	25
Fission-barrier heights estimated by a nuclear mass formula .....	26
Estimation of alpha-decay half-lives with phenomenological formulas .....	27
A software supporting experimental plan for new elements synthesis .....	28
A two-step model for fusion and synthesis of superheavy elements .....	29
$^{44}\text{Ti}$ : Its initial abundance in Cassiopeia A and its detection possibility in SN 1987A with INTEGRAL .....	30
Formation of nuclear “pasta” in cold neutron star matter .....	31

Recent developments in an experiment to measure nuclear half-lives relevant to the astrophysical r-process .....	32
r-process in prompt supernova explosions .....	33
r-process nucleosynthesis in the type-II supernova model with a neutron star mass of $\sim 1.4M_{\odot}$ .....	34
Neutrinos from supernova explosions and protoneutron stars .....	35
Shell-Model calculations for ${}_{\Lambda}^{17}\text{O}$ and ${}_{\Lambda}^{16}\text{O}$ with microscopic $\Lambda\text{N}$ and $\Sigma\text{N}$ effective interactions .....	36
Nuclear $\bar{K}$ bound states in proton-rich systems to be formed by $(\text{K}^-, \pi^-)$ reactions through $\Lambda^*$ as a doorway .....	37
Coulomb logarithm in the electron-cooling process .....	38
Measurement of the effect of a non-equilibrium liquid $D_2+T_2$ mixture in muon-catalyzed $dt$ fusion .....	39
Electron-RI collider at MUSES: A possible electron spectrometer .....	40
High-spin isomeric beam line .....	41
NaI(Tl) response for radioactive isotope beams .....	42
Absolute detection efficiency measurement of large plastic scintillators for neutrons at 100 MeV .....	43
Polarization transfer measurement for $d$ - $p$ elastic scattering .....	44
Measurement of the analyzing powers for the $\vec{d}d \rightarrow {}^3\text{He}p$ and $\vec{d}d \rightarrow {}^3\text{He}n$ reactions at 270 MeV .....	45
Measurement of the tensor analyzing power ( $T_{20}$ ) in the $dd \rightarrow {}^3\text{He}p$ and $dd \rightarrow {}^3\text{He}n$ reactions at $0^\circ$ .....	46
Measurement of single and double spin-flip probabilities in inelastic deuteron scattering on ${}^{12}\text{C}$ at 270 MeV .....	48
Measurement of Doppler-shift attenuated $\gamma$ rays from the ${}^{18}\text{O}(2_1^+)$ state .....	49
Projectile excitation in ${}^{16}\text{O}+{}^{208}\text{Pb}, {}^{nat}\text{C}$ at $E({}^{16}\text{O}) = 100\text{A MeV}$ : Preliminary results ..	50
Indirect measurement of the solar-neutrino production reaction ${}^7\text{Be}(p,\gamma){}^8\text{B}$ .....	51
Determination of the astrophysical S factor of the ${}^8\text{B}(p,\gamma){}^9\text{C}$ capture reaction from the ${}^8\text{B}(d,n){}^9\text{C}$ reaction .....	52
Inelastic scattering of ${}^{12}\text{Be}$ with ${}^4\text{He}$ .....	53
Isomeric $0^+$ state in ${}^{12}\text{Be}$ .....	54
Molecular states in ${}^{12}\text{Be}$ and ${}^{14}\text{Be}$ .....	55
Isobaric analog state of ${}^{14}\text{Be}$ .....	56
Two-neutron breakup experiments on ${}^{11}\text{Li}$ , ${}^{14}\text{Be}$ and ${}^{17}\text{B}$ .....	57
${}^{11}\text{C}(p,\gamma){}^{12}\text{N}$ reaction studied by the Coulomb dissociation method .....	58
Low-energy E1 strength in ${}^{13}\text{O}$ .....	59
Study of proton resonance states in ${}^{13}\text{O}$ and ${}^{12}\text{N}$ using elastic resonance scattering ....	60

Projectile fragmentation of $^{14}\text{O}$ at 60 A MeV on $^4\text{He}$ .....	61
Coulomb dissociation of $^{13}\text{N}$ and $^{14}\text{O}$ .....	62
E1 strength of the subthreshold $3/2^+$ state in $^{15}\text{O}$ and its influence on the CNO reaction $^{14}\text{N}(p,\gamma)^{15}\text{O}$ .....	63
Measurements of the reaction cross sections of C isotopes at intermediate energy .....	64
Study of the spin polarization of $^{19}\text{C}$ for a $g$ -factor measurement .....	65
Search for $^{21}\text{B}$ .....	66
Measurement of the Longitudinal Momentum Distribution of $^{22}\text{O}$ .....	67
First experimental evidence of core modification in a near drip-line nucleus, $^{23}\text{O}$ .....	68
Study of the $^{22}\text{Mg}(p,\gamma)^{23}\text{Al}$ reaction by the Coulomb-dissociation method .....	69
Coulomb excitation of $^{24}\text{Si}$ .....	70
Study of the first excited state in a very neutron-rich nucleus, $^{30}\text{Ne}$ .....	71
Proton inelastic scattering by $^{32}\text{Mg}$ .....	72
Large collectivity of $^{34}\text{Mg}$ .....	73
Spectroscopy of $^{34}\text{Si}$ with inelastic deuteron scattering .....	74
Production cross sections of neutron rich $N = 50$ nuclei in 66 A MeV $^{86}\text{Kr}$ -induced reactions .....	75
Coulomb excitation of $^{84}\text{Se}$ .....	76
$g$ -Factor of a high-spin isomer in $^{149}\text{Dy}$ .....	77
Study of PHENIX Electron Trigger .....	78
Measurement of the $^8\text{Li}(\alpha,n)^{11}\text{B}$ reaction cross section with $^8\text{Li}$ beams below 1.5 MeV/n energy .....	80
Indication of a reduced chiral order parameter from the $1s \pi^-$ states in $^{205}\text{Pb}$ and light nuclei .....	82
<b>2. Atomic and Solid-State Physics</b>	
Bound states of a positron with molecules .....	83
Diabatic ionization model for capture of antiprotons by atoms .....	84
Tunneling effect in the single ionization of Ne by an intense laser field .....	85
Theoretical intensity distributions of K X-ray satellite spectra emitted from Al .....	86
Studies on electron degradation and thermalization in $\text{H}_2$ and $\text{D}_2$ gases .....	87
Elastic-wave source characterization for 95 MeV/u Ar-ion irradiation on solids .....	88
Anomalous shift of the Curie temperature in Fe-Ni Invar alloys irradiated with high-energy ions .....	89
Final lattice sites and atomic motion of $^{57}\text{Fe}$ atoms in Si immediately after GeV-ion implantation .....	90
On-line TDPAC studies using the $^{19}\text{O}$ beam .....	91

Stopping power measurement of $^{84}\text{Kr}$ in a laser-produced plasma .....	92
TOF spectral profile of fullerene-like fragment ions in $\text{C}^{6+}-\text{C}_{60}$ collisions .....	93
Lattice location of hydrogen in Nb-Mo alloys .....	94
High-resolution soft X-ray measurements in 2.3 keV/u $\text{N}^{7+}$ ions transmitted through an Au microcapillary target .....	95
Visible light emission from slow highly charged ions transmitted through a Ni microcapillary .....	96
Improvement of experimental setup for Ion-atom crossed-beam measurements at energy range below 100 eV/q .....	97
Current status of a cooling system for MCI using positron plasma .....	98
Precision spectroscopy of the Zeeman splittings of the $^9\text{Be}^+ 2^2\text{S}_{1/2}$ hyperfine structure levels .....	99
A cryogenic ion trap for improving the trapping lifetime of $\text{Be}^+$ ions .....	100
Optical detection of atoms and ions in superfluid helium .....	101
Study of $\text{BaF}_2$ crystal by a positron annihilation technique .....	102
Temperature dependence of the Compton profile for $\text{BaF}_2$ crystal .....	103
$\mu\text{SR}$ study of the Cu-spin dynamics in $\text{La}_{2-x}\text{Sr}_x\text{Cu}_{1-y}\text{Zn}_y\text{O}_4$ .....	104
Isomer effect on charge transfer from $\text{C}_3\text{H}_4$ molecules (allene and propyne) at keV energies .....	105
Microwave resonances in the hyperfine structure of antiprotonic helium and deduction of the antiprotonic orbital magnetic moment .....	106

### 3. Radiochemistry and Nuclear Chemistry

In-beam Mössbauer study on valence states of $^{57}\text{Fe}$ decaying from $^{57}\text{Mn}$ implanted into $\text{KMnO}_4$ (II) .....	107
Stimulation of transferrin-dependent $^{59}\text{Fe}$ and $^{48}\text{V}$ uptake in rat isolated adipocytes by insulin or vanadyl treatment .....	108
Abnormal metabolism of trace elements in mouse caused by Zn-deficiency during the growth period .....	109
Brain regional uptake of trace elements in normal mice during development .....	110
Brain regional tracer uptake and elemental concentration in mice fed Zn-deficient and -excessive diets .....	111
Subcellular distribution of trace elements in mouse brain regions using the multitracer technique .....	112
Lateral and sexual differences in concentrations of trace elements in cerebral cortex of normal mice .....	113
Trace-element transfer from pregnant mice to the fetuses .....	114
Influence of sodium iron ethylenediaminetetraacetic acid and ferrous sulfate on the transport of trace elements in everted intestinal segments of rats .....	115

Metabolic studies on multitracer-injected rats and plants using a prototype multitracer gamma-ray emission imaging system (MT-GREI): A proposal .....	116
Alleviation of Cadmium cytotoxicity by manganese (II) .....	117
Measurement of the binding affinity of multitracer to an apoplast protein extracted from soybean root .....	118
Influence of samarium on the uptake of trace elements by marigold .....	119
The effect of EDTA complexation on diffusion of various ions in granitic rock .....	121
Molecular design of organic ligands highly selective for lanthanide metal ions .....	122
New multitracer production: Development of a gas-jet coupled multitarget system and an automated rapid chemistry apparatus .....	123
<b>4. Radiation Chemistry and Radiation Biology</b>	
Ultrafast plasma luminescence of heavy-ion tracks in insulators .....	125
Enhancement of $^{137}\text{Cs}$ accumulation by phytochelatin synthetase expression in rhizofungus <i>Fusarium oxysporum</i> .....	127
Effective plant-mutation method using heavy-ion beams (VI) .....	128
Isolation of sterile mutants of <i>Verbena hybrida</i> using heavy-ion beam irradiation .....	129
Isolation of variegated mutants of <i>Petunia hybrida</i> using heavy-ion beam irradiation ..	130
Induction of mutation in <i>Sandersonia aurantiaca</i> Hook. by heavy-ion beam irradiation .....	131
Mutation induction in human cells after low-dose exposure to heavy ions .....	132
Delayed cell-cycle progression following exposure to heavy ions .....	133
<b>5. Instrumentation</b>	
Development of the in-flight separator CRIB .....	135
Test of low-energy RI beam production with CRIB .....	137
The first observation of slow muon beam at the RIKEN-RAL Muon Facility .....	138
Design of a spin polarized positron beam and a spin rotator .....	140
On-line collection of $^8\text{Li}$ ions from the projectile fragment separator using an rf-ion guide system .....	141
Development of RI atomic beam device with a Laval-type nozzle .....	143
Development of a detector system for transient magnetic field experiments .....	145
Gas cell RI beam stopper with electric transportation system .....	146
RF deflector system for proton-rich RI beams (II) .....	147
Liquid hydrogen target for SMART experiments .....	148
Development of polarized proton target for RI beam experiment .....	149
Continuous spin precession of noble gas nuclei with active feedback system .....	151
Rotating target system for the Big-RIPS separator .....	152

Performance of a new gas-filled recoil separator GARIS at RILAC facility measured using $^{208}\text{Pb}$ and $^{209}\text{Bi}$ recoils .....	154
Installation of a high-resolution magnetic spectrograph PA .....	156
Development of a multiple-reflection TOF mass spectrometer .....	157
Improving neutron detection efficiency by using passive converters .....	159
High-efficiency positron moderator using electropolished tungsten meshes .....	160
Development of a time-of-flight detector with streak camera II .....	161
Study of scintillator radiation hardness .....	162
Development of fast timing beam line scintillator for RIPS with PMTs operated in vacuum .....	164
Development of plastic scintillators as possible energy detectors for proton scattering at RIBF .....	165
Development of segmented Ge array .....	167
A hybrid array for charged-particle and $\gamma$ detection .....	169
Development of reaction-suppressed total-energy detector .....	171
Development of a beam loss monitor .....	173
Absolute calibration of deuteron beam polarization at intermediate energies via $^{12}\text{C}(\vec{d}, \alpha)^{10}\text{B}^*[2^+]$ reaction .....	174
Advanced network for RIKEN Accelerator Research Facility .....	176
RIPS control system with EPICS .....	177
Trial of RTLinux for embedded control and measuring system .....	178
Simulation of imaging using Compton camera .....	179
<b>6. Material Analysis</b>	
Mechanical properties of polyimide films implanted with metals .....	181
Development of a highly sensitive high-resolution in-air particle-induced X-ray emission (PIXE) system: II .....	182
<b>7. RIKEN-BNL Collaboration on Spin Physics Program</b>	
Polarized gluon distribution for light hadron pair productions in semi-inclusive pol-DIS .....	185
Polarized $s$ -Quark distribution in charmed hadron production .....	186
Charmed hadron production and polarized gluon distribution .....	187
Uncertainty of polarized gluon distribution at RHIC .....	188
Single-spin asymmetries and soft-gluon poles .....	189
Partons and QCD in high-energy $pp$ collisions .....	190
Gluon saturation from small- $x$ evolution equation .....	191
Structural change of Cooper pairs in color superconductivity .....	192

Light Goldstone boson and domain walls in the $K^0$ -condensed phase of high density quark matter .....	193
Non-perturbative renormalization of pion exchange .....	194
The flow of colored glass in heavy ion collisions .....	195
Soft gluon dynamics at non-zero baryon density .....	196
Neutrino cross sections and future observations of ultrahigh-energy cosmic rays .....	197
Scaling relations for the transverse mass spectra and the color glass condensate .....	198
Hadronic signals of QGP .....	199
Kaon condensation in QCD .....	200
Novel phenomena in high-density QCD .....	201
Hydrodynamic analysis of elliptic flow at RHIC .....	202
Initial coherent gluon production from the color glass condensate in relativistic nuclear collisions .....	203
Probing the QGP equation of state with two-particle interferometry .....	204
Hadron spectrum for quenched domain-wall fermions with an improved gauge action ..	205
Calculation of $K \rightarrow \pi\pi$ decay in quenched domain-wall QCD .....	206
CP violation in K decay from lattice QCD .....	207
Chirality and localisation of domain wall fermion eigenvectors .....	208
QCDOC project .....	209
QCD phase structure with many flavors .....	210
Nucleon axial charge on the lattice .....	211
Gauge actions and chiral symmetry of domain wall fermions .....	212
Scalar glueball mass reduction at finite temperature in SU(3) anisotropic lattice QCD .....	213
Calorons and localization of Dirac eigenvectors in lattice QCD .....	215
Overview of RIKEN/RBRC activities for RHIC spin physics 2001 .....	216
Measurement of neutral pion transverse momentum distributions at $\sqrt{s_{NN}} = 130$ GeV Au+Au collisions .....	218
Measurement of the transverse energy distributions in Au+Au collisions at $\sqrt{s_{NN}} = 130$ GeV .....	219
Spin monitoring for first polarized proton collisions .....	220
Final result of analyzing power measurement of proton-carbon elastic scattering in CNI region at 22 GeV/c .....	221
Asymmetry measurement of charged hadrons at PHENIX .....	222
Parity violation at RHIC in jet production .....	223
Operation of the PHENIX muon identifier .....	224

Performance of the PHENIX muon identifier .....	225
RHIC pC CNI polarimeter readout .....	226
Results from RHIC polarimeter commissioning run 2000 .....	228
PHENIX muon tracker: Construction, year-2 operation and preliminary data analysis .....	229
Geometry alignment of PHENIX Muon tracker .....	231
First commissioning of the PHENIX south muon tracker: The gas system and the optical alignment system .....	232
Analytical field calculation of helical magnets with an axially symmetric iron yoke ....	234
Computing center in Japan for RHIC physics (CC-J) .....	236
Operation of Objectivity/DB system at CCJ .....	238
Data Carousel/ORNL batch system for HPSS at CCJ .....	240
Measurement of electron and photon at RHIC-PHENIX .....	241
Performance of PHENIX RICH for RHIC first year run .....	242
Performance of the PHENIX EMC calorimeter .....	243
Hadron measurement at RHIC/PHENIX .....	244
Analysis of experiment KEK PS-E325, for the measurement of $\omega/\phi$ meson decays in nuclear matter .....	245
<b>8. Miscellaneous</b>	
Development of new analytical system using the electron cyclotron resonance ion source and heavy ion linear accelerator .....	247
<b>IV. NUCLEAR DATA</b>	
New method for calculating aggregate fission-product decay heat with full use of macroscopic-measurement data .....	249
<b>V. DEVELOPMENT OF ACCELERATOR FACILITIES</b>	
Effect of plasma electrode position on the beam intensity of heavy ions from RIKEN 18 GHz ECRIS .....	251
Effect of plasma chamber surface on production of highly charged ions from ECRIS ...	253
Liquid-He-free SC-ECRIS at RIKEN .....	254
Development of ECR ion sources for high-intensity heavy ion beams .....	256
Laser plasma for direct plasma injection to RFQ Linac on RIKEN laser ion source ....	258
Carbon beam acceleration using direct injection method .....	260
Development of long-lived carbon foil for charge stripper in RILAC .....	262
Low-energy beam test of liquid film charge stripper .....	264
Control system for RRC, AVF and RILAC .....	266
Measurement of an open-loop transfer function of a feedback control system of cavity voltage .....	268

Development of multi-injection system for the AVF cyclotron .....	270
Construction of the flat-top acceleration system in the RIKEN AVF Cyclotron .....	272
AVF-PA beam transport system .....	274
Beam transport line from AVF to CRIB-F0 target .....	275
Conceptual design of the fixed-frequency ring cyclotron .....	277
Magnetic field measurement of the IRC sector magnets .....	279
Electric field measurement of the acceleration resonator for the Intermediate-stage Ring Cyclotron (IRC) .....	281
Design study on beam transport system from IRC to RARF .....	283
Status of the SRC for the RIKEN RI Beam Factory .....	285
Effect of $\nu_r + \nu_z = 2$ resonance in the SRC .....	287
Superconducting bending magnet for the injection system of the RIKEN SRC .....	289
Superconducting sector magnet for the RIKEN SRC .....	291
Design of the extraction bending magnet for the RIKEN SRC .....	293
Quench protection of RIKEN Superconducting Ring Cyclotron .....	295
Design study of beam transport lines from SRC to Big RIPS .....	297
Design study of quadrupole magnets for the beam-transport line and BigRIPS separator .....	299
Projectile fragment separator BigRIPS for the RI-Beam Factory project .....	301
Superconducting quadrupole magnet with small refrigerators .....	303
Design study of 2 Tesla dipole magnet by three-dimensional calculation .....	305
Studies on MUSES control system using RT-CORBA .....	307
Update of MUSES ACR lattice design .....	308
Design of MUSES electron cooler at RIKEN .....	310
Instability during electron-cooling bunching, predicted from a simulation .....	312
Design of highly-sensitive current monitor with HTS SQUID and HTS magnetic shield .....	314
Development of the kicker magnet for MUSES (II) .....	316
<b>VI. RADIATION MONITORING</b> .....	
Routine work for radiation safety in the Ring Cyclotron Facility .....	319
Shielding calculation for the CSM installation at RILAC .....	321
Improvement of radiation safety system for RIKEN Ring Cyclotron .....	323
<b>VII. LIST OF PUBLICATIONS</b> .....	325
<b>VIII. LIST OF PREPRINTS</b> .....	333

<b>IX. PAPERS PRESENTED AT MEETINGS</b>	336
<b>X. LIST OF SYMPOSIA</b> .....	351
<b>XI. LIST OF SEMINARS</b> .....	353
<b>XII. LIST OF PERSONNEL</b> .....	357

**AUTHOR INDEX**

## I. PREFACE

This issue of RIKEN Accelerator Progress Report reports research activities of the RIKEN Accelerator Research Facility (RARF) during the calendar year of 2001. The research programs have been coordinated in the framework of the project entitled Multidisciplinary Researches on Heavy-Ion Science. The project involves a variety of fields such as: nuclear physics, nuclear astrophysics, atomic physics, nuclear chemistry, radiation biology, condensed matter physics in terms of accelerator or radiation application, plants mutation, material characterization, application to space science, accelerator physics and engineering, laser technology, and computational technology.

These activities involved ten laboratories, five Centers involving seven divisions, the RIKEN-RAL Center, and the RBRC (RIKEN BNL Research Center), and more than 350 researchers from domestic and foreign institutions. Thirty-six universities and institutes from within Japan and 33 institutes from 10 countries are included.

Major research activities of the RARF are based on the heavy-ion accelerator complex consisting of the  $K = 540$  MeV RIKEN Ring Cyclotron (RRC), the energy-variable heavy-ion linear accelerator (RILAC), and the  $K = 70$  MeV azimuthally varying field cyclotron (AVF), which have altogether provided a beam time (on the target) of more than 4000 hours through the year. This number is slightly shorter than those of previous years because of the planned shutdown due to the construction-program of the RI Beam Factory. The three accelerators deliver heavy-ion beams of a variety of elements with energies ranging from a few  $A$  MeV to  $135 A$  MeV. The two-injector machines (AVF and RILAC) are equipped with ECR heavy-ion sources. The AVF is additionally equipped with a polarized ion source for vector and tensor polarized deuterons. The three accelerators have been used in various configurations. The RRC operates either with the AVF or the RILAC as the injector. The AVF has been providing beams of ions of mass number up to 60. The energy booster for the RILAC has been installed so that the maximum beam energy from the RILAC has been raised to  $6 A$  MeV. High-intensity beams of intermediate-mass ions will be able to be delivered in early 2002. That also will enable to deliver high-intensity beams of intermediate-mass elements such as Ni and Kr up to  $85 A$  MeV from RRC. In addition, the AVF and the RILAC are used separately, when they are not used as the injector, for low-energy applications. In particular, the use of high-intensity RILAC beams is expected to provide great opportunities for

superheavy element researches. Two thirds of the RRC research beam time ( $\sim 3300$  hours in total) is used for nuclear physics and nuclear astrophysics and one third is used by atomic physics, material science, nuclear chemistry, radiation biology and others. While, the AVF beam time were also used for fields other than nuclear physics. The research beam time at the AVF is 2100 hours and 800 hours at the RILAC.

The RARF carries many international collaborations. Among them are large-size two international-collaboration programs using overseas accelerator facilities: one is the muon science project at ISIS in collaboration with the Rutherford-Appleton Laboratory (RAL), and the other is the spin physics program at RHIC in collaboration with the Brookhaven National Laboratory (BNL). The pulsed muon-beam facility at ISIS has been operating steadily. At the RHIC facility, the first heavy-ion beam and the first polarized proton beams have been successfully accelerated. The first collision of polarized protons in the collider was observed in December 2001. Other smaller collaborations using foreign facilities are going on at Lanzhou (China), Dubna (Russia), CERN, GSI (Germany), and TRIUMF (Canada).

The use of RI beams is the main focus of the activities at the RRC. Major subjects pursued are: (1) exotic nuclear structure and new dynamics of extremely neutron-rich nuclei (such as those with a neutron halo or skin), (2) nuclear astrophysics involving unstable-nucleus reactions, (3) synthesis of new unstable isotopes far from the valley of stability, (4) extensive measurements of nuclear moments. Characteristic features of intermediate-energy direct reactions are often exploited for such studies.

We have collaborated with the CNS of the University of Tokyo for installing the new low-energy RI beam separator (CRIB) to use the low-energy beam from the AVF. High-quality low-energy RI beams are now available as a CNS/RIKEN facility.

Highlights of the year include: (1) The discovery of  ${}^5\text{H}$  nucleus. (2) A continuation of discovery of new magic numbers to  $Z = 16$ ,  $N = 32$  and  $34$ . These studies show that the magic numbers are radically changing off the stability line. (3) Observation of isobaric analog states of halo nuclei. (4) Continuous developments in Coulomb excitation and Coulomb dissociation of neutron rich nuclei. (5) Detailed study of three-body interactions with polarized deuteron beam. (6) The delivery of the first slow muon beam at the RAL facility. (7) The development of an on-line polarimeter for the RHIC spin project.

In theory, outstanding results have been obtained and continue to emerge from Monte-Carlo Shell model calculations. Many properties of nuclei far from the stability lines have been correctly predicted using the Alphleet parallel computer in RARF. The  $N = 16$  magic number in oxygen isotopes has been understood by an inclusion of the spin-isospin interactions. Also, the study of molecular states with alpha clusters and loosely bound neutrons under covalent bonds is of special interest in the theory group. New Relativistic Mean Field model of nuclei are under development including the pion field. This new model is expected to open new base for nuclear structure.

Intermediate-energy heavy ions from the RRC have found their own applicability. A strikingly efficient mutagenic effect has been observed when the embryo of a Tobacco plant is shot by heavy ions. High-energy heavy ions were irradiated to the plants placed in the

air for desirable amount of LET. It has opened a method to produce mutants that is efficient and well controlled. The method is so efficient that it is expected to offer new possibilities of bioscience research through comparison between normal and mutagenic samples. The first flowers developed by this method are now available commercially.

The RI Beam Factory project is progressing well. The building for the cyclotrons and the separators are under construction. The sector magnets of the IRC has been completed. The first experiment is expected to start in 2005.

I. Tanihata

*Director, Experimental System Group  
RIKEN Accelerator Research Facility*

## **II. OPERATION OF ACCELERATORS**



## RILAC operation

E. Ikezawa, M. Kase, S. Kohara, O. Kamigaito, M. Fujimaki, T. Nakagawa, M. Kidera, N. Fukunishi, M. Nagase, M. Kobayashi-Komiyama, I. Yokoyama, T. Aihara,\* T. Ohki,\* H. Hasebe,\* H. Yamauchi,\* A. Uchiyama,\* A. Goto, and Y. Yano

RILAC has been upgraded using accelerators of the charge-state multiplier (CSM). Six cavities of the CSM were installed just after the installation of the final cavity of RILAC as a booster in the summer of 2000, as shown in Figs. 1 and 2.<sup>1)</sup> The maximum beam energy, boosted by the CSM, became 5.8 MeV/nucleon. High-power tests of the new cavities have been under way since September 2000,<sup>2)</sup> and a beam test was started in May 2001.<sup>3)</sup> The  $^{40}\text{Ar}^{11+}$  beam was successfully accelerated up to 5.8 MeV/nucleon with an intensity of  $4.8\text{ p}\mu\text{A}$ . The beam energy was determined by the analyzer magnet BM90 in which a NMR probe measured the magnetic flux density precisely. The transmission efficiency through the CSM was 98% for the  $\text{Ar}^{11+}$  beam. However, the maximum transmission efficiency from the ion source to the end of the CSM was 62% in this case, because the typical transmission efficiency from the ion source to the end of RILAC is 50 to 70%.

To utilize the beams accelerated by RILAC or the RILAC + CSM for various experiments, the beam transport system was replaced with a new one, as shown in Fig. 2.<sup>4)</sup> It has one main transport line to the RIKEN Ring Cyclotron (RRC) and six branches (beam lines e1–e6). The e2, e3, e5 and e6 beam lines are used for radiation chemistry, for the search for super-heavy elements with a gas-filled recoil isotope separator (GARIS), for the development of a new charge stripper system and for the accelerator mass spectrometer, respectively. The e4 beam line is exclusively used by the CNS of University of Tokyo.

One of the most important experiments proposed here is the search for super-heavy elements via a sub-barrier fusion reaction with the GARIS. The maximum energy was selected for this research. It has been decided that for the next two years, until the RIBF is ready to start, a stand-alone use of RILAC using the CSM will be mainly used for this experiment.

We tested the beam delivery to RRC and the new experiment course with the conventional beam energies of RILAC. We also carried out a preliminary beam test for the GARIS experiment with the maximum beam energy. We did not detect a sizable beam loss in either case. Since May, RILAC has been in steady operation and has supplied various kinds of ion beams for an acceleration test and test experiments.

We experienced the following machine problems during this reporting period.

- (1) Two quadrupole magnets in the drift tubes (DT1-1 and DT2-17) of the No. 1 and No. 2

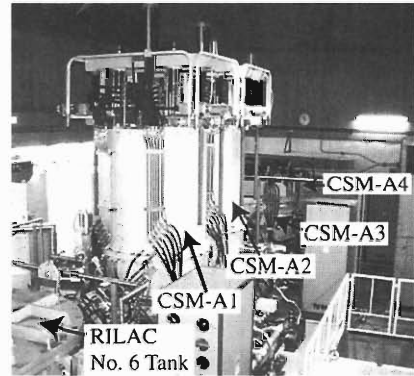


Fig. 1. Photograph of the CSM A1–A4 cavities.

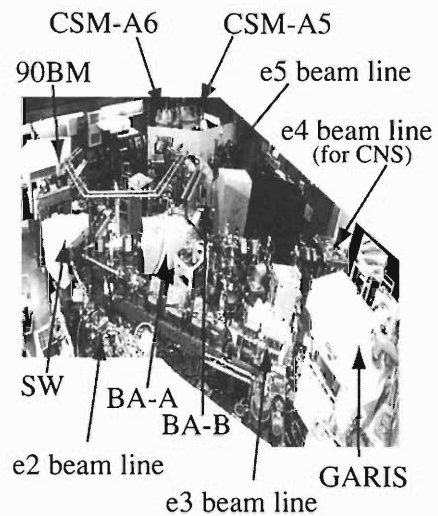


Fig. 2. Photograph of the CSM A5–A6 cavities, the beam lines e1–e5 and the GARIS in the No. 1 target room.

RILAC cavities suffered insulation failure in their tape coils and the beam was accelerated without these magnets being excited during the operation. The magnets and the drift tubes were replaced with new ones in April 2001.

- (2) An rf feeder for the No. 5 RILAC cavity had a vacuum leak at the cone-shaped alumina insulator. The insulator was replaced with a new one.
- (3) A contact finger in a coaxial line supplying radio frequency power from the No. 5 main amplifier to the feeder melted due to rf currents being too high.
- (4) A serious water leak has been detected in the

\* SHI Accelerator Service, Ltd.

CSM A4 cavity at the top of the outer conductor of the power feeder. The reason is that the brazing around the water channel was incomplete. Since the brazing was made in the same way in the CSM A3, A5, and A6 cavities, we replaced the outer conductor in all of these cavities.

- (5) An 18 GHz ECR ion source suffered insulation failure between the plasma chamber and the solenoid coil. The surface of the insulator was cleaned and was reused.
- (6) All water pumps were inspected. As a result, a water pump of the deionized water circuit for RILAC was overhauled because of a deteriora-

tion of the mechanical seals, and a cooling tower pump for the RFQ injector was found to be worn out, and thus we replaced it with a new one.

#### References

- 1) E. Ikezawa et al.: RIKEN Accel. Prog. Rep. **34**, 3 (2001).
- 2) O. Kamigaito et al.: Proc. 13th Symp. on Accelerator Science and Technology, Osaka, 2001-10 (2001), p. 229.
- 3) E. Ikezawa et al.: Proc. 13th Symp. on Accelerator Science and Technology, Osaka, 2001-10 (2001), p. 169.
- 4) N. Fukunishi et al.: RIKEN Accel. Prog. Rep. **34**, 327 (2001).

## RRC and AVF operation

M. Kase, T. Kageyama, M. Nagase, S. Kohara, T. Nakagawa, E. Ikezawa, M. Fujimaki, N. Fukunishi, S. Numata, O. Kamigaito, M. Kidera, A. Yoneda, M. Kobayashi-Komiyama, I. Yokoyama, H. Isshiki,\* H. Akagi,\* R. Abe,\* N. Tsukiori,\* K. Takahashi,\* T. Maie,\* R. Ohta,\* K. Kobayashi,\* M. Nishida,\* A. Goto, and Y. Yano

The statistics of operation of the RIKEN Ring Cyclotron (RRC) in 2001 is shown in Table 1. The RRC together with the AVF and the RILAC have routinely provided a beam time of more than 4000 hours throughout the year 2001. This value is smallest among these ten years. The RRC operation was interrupted frequently in 2001 due to the installation of AVF beam transport and also improvements of the AVF. The RILAC-RRC operation has been limited since 2000, because the RILAC had been shut down due to the upgrade program.

More than fifty kinds of ion beams were prepared in 2001. These beams were used in experiments in a variety of fields, such as nuclear physics, atom and solid-state physics, radiochemistry, nuclear chemistry, and radiation biology.

With the framework of the collaboration between RIKEN and CNS of Tokyo University, the following projects have been carried out and almost all of these projects were completed this year.

- (1) The 14 GHz ECR ion source was installed in the ion source room of AVF.
- (2) The two 45-deg dipole magnets between the horizontal beam line from the ion source and the vertical injection line of AVF was replaced by a new horizontally rotationable 90-deg dipole magnet. As the result, the switching of more than one ECR ion source in a short time became possible, keeping the vertical injection line for the polarized ion source as before.
- (3) A flat top rf system was added to cavities of the AVF. Efficient extraction of a high-quality beam is expected at the AVF.<sup>1)</sup>
- (4) A new beam transport line from the AVF to the present beam line of the RRC was designed and

was partially completed in summer 2001. It will be connected to the beam line to the E2 target room, where the PA appearing in the next item is installed.

- (5) Two large-scale apparatuses of the nuclear physics experiment, CRIB and PA, were installed in the target rooms E6 and E2. An experiment involving the CRIB has been carried out since summer 2001.
- (6) The maximum energy of the RILAC was upgraded from 4 to 6 MeV/nucleon. Four linac cavities were added to the first unit of the CSM which was completed in 1999.

With the completion of the CSM, a new configuration of the RILAC-CSM-RRC operation became possible. It was found that it is very useful for improving the beam intensity of some beams. The RRC was designed to operate using a harmonic number of 9 in the case of the RILAC-RRC. Due to the energy variability of the RILAC, the RRC has been operated using higher harmonic numbers such as 10, 11, and 12 as well as the designed one. In the new scheme of the RILAC-CSM-RRC, the RRC can be operated using harmonic numbers of 8, 7 or 6. Some beams, which had been available only in the AVF-RRC, can be obtained with a much more intensity in this scheme, because lower-charge-state ions are acceptable for RILAC and also because the transmission efficiency of the RILAC is better than that of the AVF. Such beams, some of which are very important for nuclear physics experiments, are listed in Table 2 and shown in Fig. 1. To realize these accelerations, however, a more powerful re-buncher is necessary for the injection of the RRC.

A test of the RILAC-CSM-RRC with  $h = 8$  was carried out in October 2001. A beam of 64 MeV/nucleon  $^{84}\text{Kr}$  was accelerated with a beam intensity of 60 pA which is fifty times that obtained in the AVF-RRC so far. Half of the beam was lost in the RRC, because the rf power of rebuncher before the RRC was insufficient.

A superconducting ECR ion source has been developed and its beam test is now in progress.<sup>2)</sup> As the method of inserting a solid element into the ECR plasma, a micro-oven system was installed in the 18 GHz ECR at RILAC. The beam intensity of some solid ions is expected to increase.

Charge stripping of ions after the RILAC will be a very essential matter for the RIBF. Recently a long-lived carbon foil has been successfully produced,<sup>3)</sup> and also, a liquid-type stripper has been developed.<sup>4)</sup>

Table 1. Statistics of RRC operation in 2001.

Operation time of RRC	6258 hr
Beam Service Time	4084 hr
Nuclear Physics Experiment	92%
Non-Nuclear Physics Experiment	8%
RILAC-RRC Operation	8%
AVF-RRC Operation	92%

\* SHI Accelerator Service, Ltd.

Table 2. Upgrade of beam intensities with CSM.

Ion	(Present Data)					(Expected Data)						
	AVF → RRC					RILAC → CSM → RRC						
	$E_{RRC}$ ( $h_{RRC}$ ) (MeV/n)	$Q_i$	$Q_f$	$E_{AVF}$ (MeV/n)	effi. (%)	Beam intens. (pA)	$E_{RRC}$ ( $h_{RRC}$ ) (MeV/n)	$Q_i$	$Q_f$	$E_{CSM}$ (MeV/n)	effi. (%)	Beam intens. (pA)
$^{28}\text{Si}$	135 (5)	10+	→ 14+	7.0	50	50	124 (6)	6+	→ 14+	6.5	40	1000
RILAC(37.8MHz)+A1+A2+A3+A4+A5+A6+RRC												
$^{18}\text{O}$	100 (5)	6+	→ 8+	5.5	90	250	86 (7)	4+	→ 8+	4.8	85	>1000
RILAC(37.8MHz)+A1+A2+A3+A4+RRC												
$^{40}\text{Ar}$	95 (5)	11+	→ 17+	5.2	42	90	86 (7)	9+	→ 17+	5.7	45	>1000
RILAC(37.8MHz)+A1+A2+A3+A4+A5+(A6)+D1+RRC												
$^{48}\text{Ca}$	70 (5)	11+	→ 18+	4.0	33	4	64 (8)	9+	→ 17+	3.6	36	500
RILAC(37.8MHz)+A1+A2+D1+RRC												
$^{86}\text{Kr}$	70 (5)	20+	→ 31+	4.0	8	1	64 (8)	16+	→ 30+	3.6	12	60
RILAC(37.8MHz)+A1+A2+D1+RRC												
$^{84}\text{Kr}$							64 (8)	16+	→ 30+	3.6	12	60
							Already tested RILAC(37.8MHz)+A1+A2+RRC					

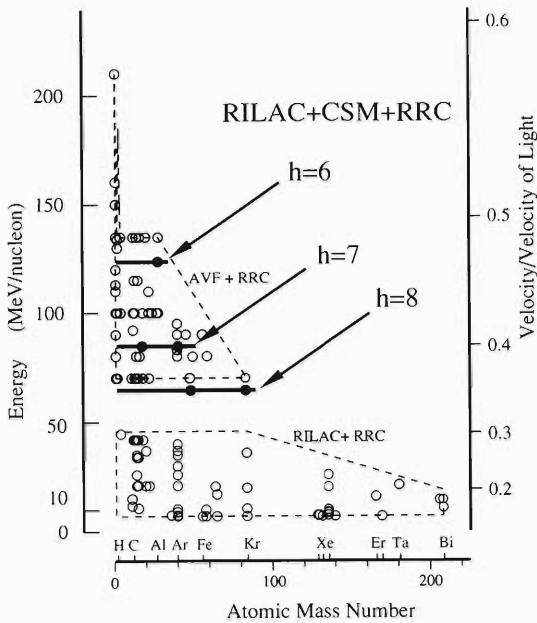


Fig. 1. Performance of RRC. The two regions surrounded by dashed lines are the conventional acceptances for the AVF+RRC and RILAC+RRC. The open circles denotes the beams accelerated previously. The three solid lines shows the beams obtained with the new scheme of RILAC+CSM+RRC and the solid circles are beams shown in Table 1.

A previous control system has been replaced by a new one using EPICS.<sup>5)</sup> The low-level interfaces (CAMAC-CIM-DIM, GPIB) were kept as before. The new control system covers not only the entire accelerator but also experimental apparatuses such as RIPS and SMART. A new interface, which had been developed for power supplies in RIBF, is also included in the new system and tested in a routine operation.

#### References

- 1) S. Kohara et al.: Proc. 13th Symp. on Accelerator Science and Their Applications, Suita, Oct. (2001), p. 235.
- 2) T. Nakagawa, T. Kurita, M. Kidera, M. Imanaka, Y. Higurashi, M. Tsukada, S. M. Lee, M. Kase, and Y. Yano: Rev. Sci. Instrum. **73**, 513 (2002).
- 3) H. Hasebe et al.: Proc. 13th Symp. on Accelerator Science and Their Applications, Suita, Oct. (2001), p. 369.
- 4) H. Akiyoshi et al.: Proc. 13th Symp. on Accelerator Science and Their Applications, Suita, Oct. (2001), p. 331.
- 5) M. Komiyama et al.: Proc. 13th Symp. on Accelerator Science and Their Applications, Suita, Oct. (2001), p. 411.

## Operation of the tandem accelerator

K. Ogiwara, T. Urai, and T. Kobayashi

The 1.7 MeV tandem accelerator was operated for a total of 141 days for experiments, except for the time taken for machine inspection and a beam test, during the annual reporting period from Nov. 1, 2000 to Oct. 31, 2001.

Experimental studies on the following subjects were performed, and some are still in progress.

- (1) Rutherford backscattering spectroscopy (RBS)
  - (a) Channeling analysis of dopants in semiconducting materials
  - (b) RBS analysis of polystyrene surfaces and glassy carbon films modified by ion implantation

- (2) Nuclear reaction analysis (NRA)
  - (a) Lattice location of hydrogen in niobium alloys by means of the channeling method
- (3) Particle-induced X-ray emission (PIXE)
  - (a) Trace element analysis of biological and environmental samples using energy-dispersive X-ray spectrometry
  - (b) Development of a highly sensitive high-resolution in-air PIXE system for chemical state analysis
  - (c) Characterization of the II-VI ternary semiconducting crystals



### **III. RESEARCH ACTIVITIES**



# 1. Nuclear Physics



# Triaxially deformed states in the Monte-Carlo Shell Model

N. Shimizu, T. Otsuka,\*<sup>1</sup> T. Mizusaki,\*<sup>2</sup> and M. Honma\*<sup>3</sup>

[Nuclear Structure, Shell Model, Collective Motion]

For over half a century, typical collective motions and the transitional states between them were investigated and related to the dynamical symmetries, which the Hamiltonian originally has. In order to investigate these states microscopically in terms of the nuclear shell model, the Monte-Carlo Shell Model (MCSM) was developed.<sup>1)</sup>

In the Xe-Ba region, where the mass number is around 130, the nuclei are well known to exhibit the quadrupole collective properties of a triaxial deformation. They are called  $\gamma$ -unstable nuclei, because their potential-energy surfaces appear to be flat in the direction of  $\gamma$ , which represents the degree of freedom of triaxial deformation. Their microscopic investigation using the nuclear shell model, which was made possible by the development of the MCSM, is especially important in the transitional region. On the other hand, the existence of a new dynamical E(5) symmetry was proposed at the transitional nucleus between the spherical and triaxially deformed nuclei.<sup>2)</sup> The microscopic study also enables us to discuss its validity.

In order to discuss the properties of an intrinsic state schematically, we generated a triaxially deformed wave function using BCS theory in the external quadrupole field, the strengths of which corresponded to the deformation parameters,  $(\beta, \gamma)$ . By combining this wave function and the nuclear-shell-model Hamiltonian, which was obtained through a study using the MCSM, we obtained a potential-energy surface parametrized by  $\beta$  and  $\gamma$ . The Hamiltonian comprised a single-particle potential, pairing, quadrupole-pairing, and quadrupole-quadrupole interactions. Figure 1 represents the surfaces of Ba isotopes without angular-momentum projection (upper part) and those with projection (lower part).

The even-even nuclei,  $^{136,134,132}\text{Ba}$ , span a transitional region from a nucleus having the feature of a spherical vibrator ( $^{136}\text{Ba}$ ) to one having a triaxial deformation ( $^{132}\text{Ba}$ ). The upper-left part of Fig. 1 shows a feature of spherical shape, because its minimal point is located at  $\beta = 0$ . On the other hand, the upper-right part shows the characteristics of a deformed rotor. We can see that  $^{134}\text{Ba}$  is a transitional nucleus, and that its surface appears to be flat in the region  $0 < \beta < 0.1$ .

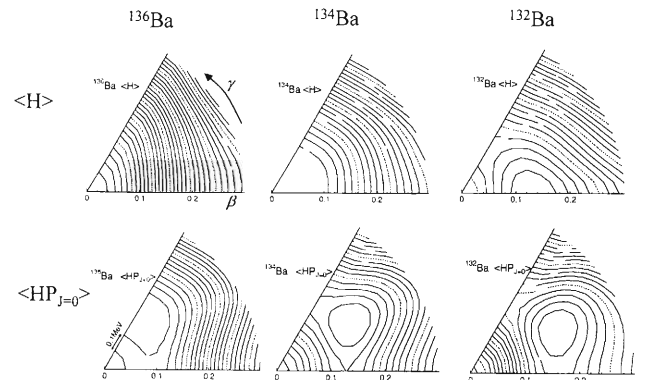


Fig. 1. Potential-energy surfaces of Ba isotopes. The upper figures show the surfaces of the intrinsic states, and the lower ones correspond to the  $J = 0^+$  states. The solid (dashed) contour line separations are 100 keV (500 keV).

This characteristic is consistent with the assumption of E(5) symmetry.

When we turn our eyes to surfaces with angular-momentum projection, the situation changes drastically. The minima occur in the direction of  $\gamma \simeq 30^\circ$  in the surfaces of  $^{134}\text{Ba}$  and  $^{132}\text{Ba}$ , although they still appear to be flat in the direction of  $\gamma$ , or  $\gamma$ -unstable. This suggests that the restoration of rotational symmetry plays an important role in obtaining the triaxial state. This phenomenon was also studied and discussed by Hayashi *et al.* in theoretical work concerning  $^{188}\text{Os}$ .<sup>3)</sup> We have investigated the structures of Ba isotopes more microscopically, the results of which are being prepared for publication.

## References

- 1) T. Otsuka, M. Honma, T. Mizusaki, N. Shimizu, and Y. Utsuno: Prog. Part. Nucl. Phys. **47**, 319 (2001), and references therein.
- 2) F. Iachello: Phys. Rev. Lett. **85**, 3580 (2000); R. F. Casten and N. V. Zamfir: Phys. Rev. Lett. **85**, 3584 (2000).
- 3) A. Hayashi, K. Hara, and P. Ring: Phys. Rev. Lett. **53**, 337 (1984).

\*1 Department of Physics, University of Tokyo

\*2 Institute of Natural Science, Senshu University

\*3 Center for Mathematical Sciences, University of Aizu

# Extreme location of the fluorine drip line<sup>†</sup>

Y. Utsuno,<sup>\*1</sup> T. Otsuka,<sup>\*2</sup> T. Mizusaki,<sup>\*3</sup> and M. Honma<sup>\*4</sup>

[NUCLEAR STRUCTURE shell model, unstable nuclei]

In neutron-rich nuclei, the magic number can shift from that of stable nuclei to another. For instance, the  $N = 20$  magic number disappears at around  $Z = 12$ , and a new  $N = 16$  one appears near oxygen.<sup>1)</sup> The location of the drip line sensitively reflects the magic structure. In this direction, the drip line of fluorine isotopes with  $Z = 9$  attracts much interest: the drip line is located at  $N = 16$  for  $Z = 6, 7,$  and  $8,$  while it extends farther to  $N = 22$  or more for  $Z = 9.$ <sup>2)</sup> In this study, we investigated how the drip line suddenly extends in fluorine isotopes based on large-scale shell-model calculations using the Monte Carlo shell model (MCSM).<sup>3)</sup> Because the model space and the effective interaction are the same as those used in a study of the yrast properties of O, Ne, Mg, and Si isotopes,<sup>4)</sup> the present study gives a unified picture of this region in going from stable to unstable nuclei. Note that this effective interaction reproduces the O drip line.

The two-neutron separation energies of  $N = 20$  isotones were calculated from  $Z = 9$  to  $14,$  as shown in Fig. 1(a). For  $Z = 10$  to  $14,$  the agreement between the experiment and the calculations with full configurations is excellent. By comparing the full calculations with those in which the configuration is truncated within the 0-particle 0-hole excitation ( $0p0h$ ) from the  $N = 20$  core, the importance of the excited configurations is clearly seen, as shown in the ground-state probabilities in Fig. 1(b). To be more interesting, the  $4p4h$  configurations rather increase for smaller  $Z.$  The  $N = 20$  nucleus,  $^{29}\text{F},$  is not bound against two-neutron emission unless the  $4p4h$  configurations are taken into account. This binding mechanism of  $^{29}\text{F},$  *i.e.,* large  $4p4h$  contribution to the ground state, which is small for  $N \neq 20$  nuclei, is in sharp contrast to the previous picture of the so-called “island of inversion.”<sup>5)</sup> The “island of inversion” picture results in the ground state of  $^{29}\text{F}$  having the  $0p0h$  configurations, and fails to reproduce unbound  $^{26}\text{O}$  and bound  $^{29}\text{F}$  simultaneously.<sup>5,6)</sup> In the present picture,  $^{29}\text{F}$  gains correlation energy through mixing among the  $0p0h,$   $2p2h,$  and  $4p4h$  configurations, and becomes a bound nucleus in a natural way. By the mixing of the  $4p4h,$  the deformation is not so enhanced, but the pairing correlation plays a significant role.

Large  $4p4h$  mixing occurs due to the narrowing

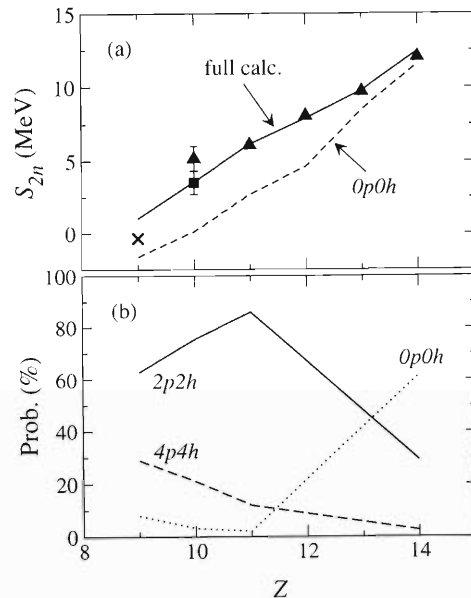


Fig. 1. (a) Two-neutron separation energies of  $N = 20$  isotones from F to Si compared between experiments (the triangles and the square) and shell-model calculations with various truncation schemes. The cross in  $^{29}\text{F}$  represents the  $0p0h + 2p2h$  calculation. (b) Probabilities of the  $npnh$  ( $n = 0, 2, 4$ ) configurations in their ground states.

$N = 20$  shell gap, which is defined by the difference in the *effective single-particle energies*<sup>4)</sup> between the *sd* shell and the *pf* shell, for smaller  $Z.$  The narrowing shell gap is caused by a sharp lowering of the neutron  $0d_{3/2}$  orbit as protons occupy the  $0d_{5/2}$  orbit, being essential in both the disappearance of the  $N = 20$  magic number and the appearance of the  $N = 16$  one. Direct evidence about the narrowing shell gap, such as the negative-parity energy levels, has not yet been observed experimentally. However, it seems that the extreme location of fluorine isotopes indicates this narrowing, because, provided that it is absent, the bound fluorine must stop at  $N = 18.$

## References

- 1) A. Ozawa et al.: Phys. Rev. Lett. **84**, 5493 (2000).
- 2) H. Sakurai et al.: Phys. Lett. B **448**, 180 (1999).
- 3) T. Otsuka et al.: Prog. Part. Nucl. Phys. **47**, 319 (2001).
- 4) Y. Utsuno et al.: Phys. Rev. C **60**, 054315 (1999).
- 5) E. K. Warburton et al.: Phys. Rev. C **41**, 1147 (1990).
- 6) E. Caurier et al.: Phys. Rev. C **58**, 2033 (1998).

<sup>†</sup> Condensed from the article in Phys. Rev. C **64**, 011301 (R) (2001)

<sup>\*1</sup> Japan Atomic Energy Research Institute

<sup>\*2</sup> Department of Physics, University of Tokyo

<sup>\*3</sup> Institute of Natural Sciences, Senshu University

<sup>\*4</sup> Center for Mathematical Sciences, University of Aizu

## Magic numbers of exotic nuclei<sup>†</sup>

T. Otsuka,<sup>\*1</sup> R. Fujimoto,<sup>\*1</sup> Y. Utsuno,<sup>\*2</sup> B. A. Brown,<sup>\*3</sup> M. Honma,<sup>\*4</sup> and T. Mizusaki<sup>\*5</sup>

[NUCLEAR STRUCTURE shell model, unstable nuclei]

The magic numbers in exotic nuclei can be different from those of stable nuclei due to a spin-isospin dependent part of the nucleon-nucleon interaction. In particular, the spin-flip isospin-flip process due to this interaction produces significant monopole shifts of energies of single-particle states of exotic nuclei, and hence can change their shell structure drastically.

In order to understand underlying single-particle properties of a nucleus, we can make use of *effective (spherical) single-particle energies (ESPE's)*, which represent mean effects from the other nucleons on a nucleon in a specified single-particle orbit.

Figure 1 shows neutron ESPE's for  $^{30}\text{Si}$  and  $^{24}\text{O}$ , both of which have  $N = 16$ . The Hamiltonian and the single-particle model space are the same as those used in Ref. 1, where the structure of exotic nuclei with  $N \sim 20$  has been successfully described within a single framework. The valence orbits are then  $0d_{5/2,3/2}$ ,  $1s_{1/2}$ ,  $0f_{7/2}$  and  $1p_{3/2}$ .

The nucleus  $^{30}\text{Si}$  has six valence protons in the  $sd$  shell and is a stable nucleus, while  $^{24}\text{O}$  has no valence proton and is a neutron-rich exotic nucleus. For  $^{30}\text{Si}$ , the neutron  $0d_{3/2}$  and  $1s_{1/2}$  are rather close to each other (see Fig. 1 (a)). For  $^{24}\text{O}$ , as shown in Fig. 1 (b), the  $0d_{3/2}$  is lying much higher and is quite close to the  $pf$  shell, giving rise to a large gap ( $\sim 6$  MeV) between  $0d_{3/2}$  and  $1s_{1/2}$ . This large gap was pointed out in Ref. 2. On the other hand, for the stable nucleus  $^{30}\text{Si}$ , a considerable gap ( $\sim 4$  MeV) is created between the  $0d_{3/2}$  and the  $pf$  shell (See Fig. 1 (a)). Thus, the  $N = 20$  magic structure is evident for  $^{30}\text{Si}$ , whereas the  $N = 16$  magic number arises in  $^{24}\text{O}$ . In  $^{24}\text{O}$ , the  $0d_{3/2}$  is lying higher reflecting the large spin-orbit splitting which is basically the same as that for  $^{17}\text{O}$ . Although this high-lying  $0d_{3/2}$  orbit is not so relevant to the ground state of lighter O isotopes, it should affect binding energies of nuclei around  $^{24}\text{O}$ . Such an anomaly was pointed out by Ozawa *et al.*<sup>3)</sup> in observed binding energy systematics.

The dramatic change of ESPE's from  $^{24}\text{O}$  to  $^{30}\text{Si}$  is primarily due to the strongly attractive interaction between a proton in  $0d_{5/2}$  and a neutron in  $0d_{3/2}$ . A schematic picture on this point is shown in Fig. 1 (c) for the general cases comprised of a pair of orbits

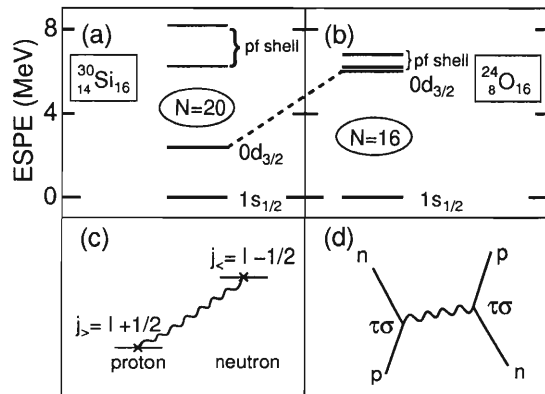


Fig. 1. ESPE's for (a)  $^{30}\text{Si}$  and (b)  $^{24}\text{O}$ , relative to  $0d_{5/2}$ . (c) The major interaction producing the basic change between (a) and (b). (d) The process relevant to the interaction in (c).

$j_> = l + 1/2$  and  $j_< = l - 1/2$  with  $l$  being the orbital angular momentum. Note that  $j_>$  and  $j_<$  are nothing but spin-orbit coupling partners. The present case corresponds to  $l = 2$ . As one moves from  $^{24}\text{O}$  to  $^{30}\text{Si}$ , six valence protons are put into the  $0d_{5/2}$  orbit. Consequently, due to the strong attraction shown in Fig. 1 (c), a neutron in  $0d_{3/2}$  is more bound in  $^{30}\text{Si}$ , and its neutron  $0d_{3/2}$  ESPE becomes so low as compared to that in  $^{24}\text{O}$  where such attraction is absent.

The process illustrated in Fig. 1 (d) produces the attractive interaction in Fig. 1 (c). The nucleon-nucleon interaction in this process is written as

$$V_{\tau\sigma} = \tau \cdot \tau \sigma \cdot \sigma f_{\tau\sigma}(r). \quad (1)$$

The interaction  $V_{\tau\sigma}$  produces large matrix elements for the spin-flip isospin-flip processes: proton in  $j_> \rightarrow$  neutron in  $j_<$  and vice versa. This gives rise to the interaction in Fig. 1 (c) with a strongly attractive monopole term for the appropriate sign of  $V_{\tau\sigma}$ .

In neutron-rich exotic nuclei, due to this mechanism, magic numbers such as  $N = 8, 20, 38/40$ , *etc.* can disappear, while  $N = 6, 16, 34$ , *etc.* may arise, producing a variety of interesting structures and effects. Mean field theories should be developed so as to incorporate fully the above-mentioned monopole shifts.

### References

- 1) Y. Utsuno *et al.*: Phys. Rev. C **60**, 054315 (1999).
- 2) B. A. Brown: Revista Mexicana de Fisica **39**, Suppl. 2, 21 (1983).
- 3) A. Ozawa *et al.*: Phys. Rev. Lett. **84**, 5493 (2000).

<sup>†</sup> Condensed from the article in Phys. Rev. Lett. **87**, 082502 (2001)

<sup>\*1</sup> Department of Physics, University of Tokyo

<sup>\*2</sup> Japan Atomic Energy Research Institute

<sup>\*3</sup> NSCL, Michigan State University, USA

<sup>\*4</sup> Center for Mathematical Sciences, University of Aizu

<sup>\*5</sup> Institute of Natural Sciences, Senshu University

# A Search for a unified effective interaction for Monte-Carlo Shell-Model calculations (III)

M. Honma,\*<sup>1</sup> T. Otsuka,\*<sup>2</sup> B. A. Brown,\*<sup>3</sup> and T. Mizusaki\*<sup>4</sup>

[Shell model, Effective interaction]

An effective interaction is a key ingredient of the nuclear shell model. For light nuclei, there are several “standard” effective interactions, such as the Cohen-Kurath<sup>1)</sup> and the USD<sup>2)</sup> interactions for the  $p$  and  $sd$  shells, respectively. In the next major shell, *i.e.*, in the  $pf$ -shell, such an effective interaction has not been available, mainly because the conventional shell-model calculation has been difficult due to the huge dimension of the Hamiltonian matrix. However, the Monte Carlo Shell Model (MCSM)<sup>3)</sup> has removed this difficulty. Thus, it is a quite challenging problem to construct a *unified* effective interaction which is successful throughout the  $pf$ -shell, including both the beginning and the middle of the shell.

We have approached this problem by a “model-independent” method, in which 195 two-body matrix elements and 4 single-particle energies are treated as parameters, and are determined by a least-squares fit to the experimental energy data. We carried out several series of iterative fitting calculations,<sup>4)</sup> and have presented the GF40A interaction.<sup>5)</sup> In this report we introduce a much improved interaction, which is called GXPF1, as described below.

The fitting procedure was the same as that of the GF40A interaction, except that the data selection was slightly changed and the number of varied linear combinations of parameters was increased from 40 to 70. Starting from the realistic G-matrix interaction with core-polarization corrections based on the Bonn-C potential,<sup>6)</sup> the GXPF1 interaction was obtained with a rms error of 168 keV within FDA\* (few-dimensional basis approximation with empirical corrections).

The GXPF1 interaction was examined from various viewpoints and was found to be quite successful over a wide mass range. As an example, in Fig. 1, various properties of the first  $2^+$  states are shown for even-even  $N$  or  $Z = 28$  nuclei. In the present calculations, constant effective charges of  $e_p = 1.23$  and  $e_n = 0.54$  are used for all nuclei. It can be seen that the overall systematics is reproduced reasonably well. Recently, new experimental data have been published for the  $B(E2)$  of  $^{58-64}\text{Ni}$  by Kenn *et al.*,<sup>9)</sup> which are also shown in Fig. 1(B) by open squares. The present results for  $^{58}\text{Ni}$ ,  $^{60}\text{Ni}$ , and  $^{64}\text{Ni}$  are much closer to these new data. It is worth noting that the present results successfully

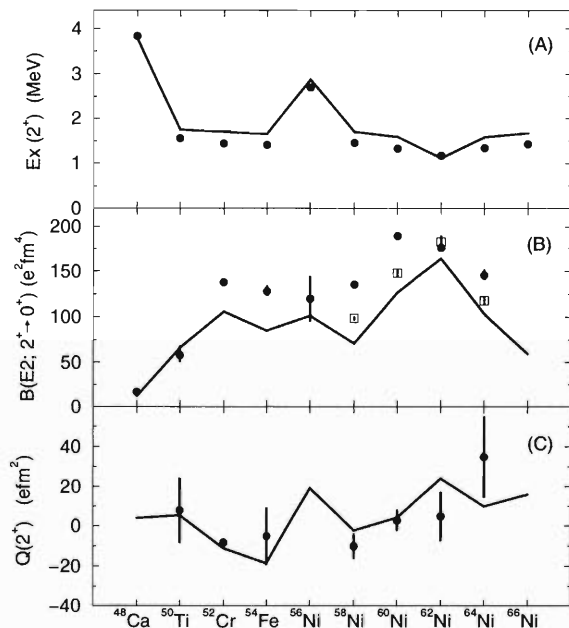


Fig. 1. Various systematics of the first  $2^+$  states of  $N$  or  $Z = 28$  semi-magic nuclei: (A) excitation energies, (B)  $B(E2)$  values to the ground state, and (C) electric quadrupole moments. The filled circles and open squares show the experimental data.<sup>7-9)</sup> Theoretical values obtained by the FDA\* are shown by the solid lines.

reproduce the experimental systematics over the  $N$  or  $Z = 28$  shell gap including the doubly-magic nucleus  $^{56}\text{Ni}$ .

Applications to unexplored regimes of large neutron numbers or high excitation energy are of great interest.

## References

- 1) S. Cohen and D. Kurath: Nucl. Phys. **73**, 1 (1965).
- 2) B. A. Brown and B. H. Wildenthal: Ann. Rev. Nucl. Part. Sci. **38**, 29 (1988).
- 3) T. Otsuka *et al.*: Phys. Rev. Lett. **81**, 1588 (1998).
- 4) M. Honma *et al.*: RIKEN Accel. Prog. Rep. **33**, 16 (2000); RIKEN Accel. Prog. Rep. **34**, 15 (2001).
- 5) M. Honma *et al.*: to be published in Nucl. Phys. A.
- 6) M. Hjorth-Jensen *et al.*: Phys. Rep. **261**, 125 (1995).
- 7) R. B. Firestone *et al.*: *Table of Isotopes* (Wiley, New York, 1996).
- 8) G. Kraus *et al.*: Phys. Rev. Lett. **73**, 1773 (1994).
- 9) O. Kenn *et al.*: Phys. Rev. C **63**, 021302 (R) (2000).

\*<sup>1</sup> Center for Mathematical Sciences, University of Aizu

\*<sup>2</sup> Department of Physics, University of Tokyo

\*<sup>3</sup> Michigan State University, USA

\*<sup>4</sup> Department of Law, Senshu University

# Relativistic mean field theory with pion for finite nuclei

S. Sugimoto,\* H. Toki,\* and K. Ikeda

[NUCLEAR STRUCTURE, relativistic mean field model, pion]

We have developed a mean-field model that incorporates the pion. It is based on the relativistic mean field (RMF) theory. We applied the new model to various  $N=Z$  nuclei and found that the pion has a large effect on the nuclear mean field.

Recently, mean-field models, relativistic or non-relativistic, are widely used to study nuclear structure. They can reproduce the saturation property of nuclei and the properly large spin-orbit splittings, and therefore give results that agree with the experimental data, especially bulk data. In these models the tensor force from the pion exchange is usually missing. However, we know that the tensor force plays an important role in nuclear structure based on many studies. Therefore, it is interesting to study nuclear structure in a relativistic mean-field framework with the pion.

In the relativistic mean field theory, we make the mean field approximation (the Hartree approximation). In this approximation, because the pion is a pseudoscalar meson, the expectation value of the pion field should be zero if we assume parity symmetry of single-particle states in a mean field. This is the reason why we did not include the pion in the RMF theory. However, if we imagine that single-particle states in the mean field are not good parity states, namely, mixed-parity states, the situation drastically changes. In this case, the pion can be exchanged by those states because there exist parity partners in themselves. As a result, the expectation value of the pion field becomes finite. The total wave function made by the mixed-parity states is not a good parity state, and therefore we need to project out the good parity state from it. In this way, we can obtain a wave function that includes the correlation caused by the pion.

The Lagrangian which we use is

$$\begin{aligned}
 L = & \bar{\psi} \left( i\gamma_\mu \partial^\mu - M - g_\sigma \sigma - g_\omega \gamma_\mu \omega^\mu \right. \\
 & \left. - \frac{f_\pi}{m_\pi} \gamma^5 \gamma_\mu \tau^a \partial^\mu \pi^a \right) \psi \\
 & + \frac{1}{2} \partial_\mu \sigma \partial^\mu \sigma - \frac{1}{2} m_\sigma^2 \sigma^2 - \frac{1}{4} W_{\mu\nu} W^{\mu\nu} \\
 & + \frac{1}{2} m_\omega^2 \omega_\mu \omega^\mu + \frac{1}{2} \partial_\mu \pi^a \partial^\mu \pi^a - \frac{1}{2} m_\pi^2 \pi^a \pi^a.
 \end{aligned}$$

In the above equation, only linear terms are written, but in the actual calculation the non-linear terms of the sigma and omega mesons are included. For the coupling constants and masses for mesons, except for

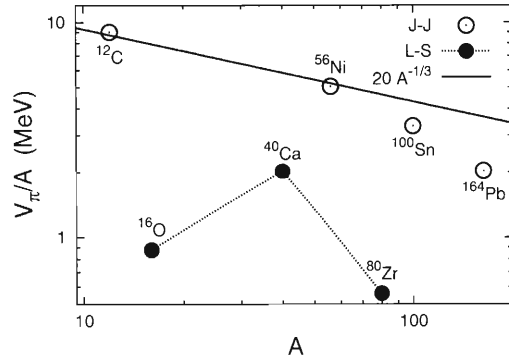


Fig. 1. Pion energy per nucleon as a function of the mass number in a log-log plot.<sup>3)</sup> There are two groups: one is for the jj-closed shell nuclei, denoted by the open circles, the other is for the LS-closed shell nuclei, denoted by the solid circles. The pion energy per nucleon for the jj-closed shell nuclei decreases monotonically and follows a steeper curve than  $A^{-1/3}$ , which is shown by the solid line.

the pion, we use the TM1 parameter set.<sup>1)</sup> For the pion-nucleon coupling we adopt the pseudovector type and set the value to  $f_\pi \approx 1$ , which is taken from the Bonn A potential.<sup>2)</sup> Because the TM1 parameter set is determined in the absence of the pion, the effect of the pion is included in the other mesons. Therefore, we should refit the parameters in the presence of the pion. This is our next task.

In Fig. 1 we show the potential energy of the pion normalized by mass numbers.<sup>3)</sup> From this figure we can see that the pion energies do not behave volume-like and make a large contribution to the binding energies (about 5 MeV per nucleon for  $^{56}\text{Ni}$ ).

We have just started a study of the pion in a relativistic mean-field model. Thus, our result is not very quantitative. We need to significantly modify our model. However, we believe that through this study we can obtain a new understanding of how the pion behaves in nuclei.

## References

- 1) Y. Sugahara and H. Toki: Nucl. Phys. A **579**, 557 (1994).
- 2) R. Brockmann and R. Machleidt: Phys. Rev. C **42**, 1965 (1990).
- 3) H. Toki, S. Sugimoto, and K. Ikeda: nucl-th/0110017.

\* Research Center for Nuclear Physics, Osaka University

# Parity-violating mean field theory with the pion

K. Ikeda, S. Sugimoto,\* and H. Toki\*

[NUCLEAR STRUCTURE, pion, parity-mixing mean field]

Since the establishment of the shell model, we usually solve nuclear many-body problems in model space, where the single-particle states have good parities. On the other hand, the parity of a nucleon changes when it absorbs or emits a pion. As for the importance of the pion, we remind ourselves of the findings involving few-body systems.<sup>1)</sup> The calculated results demonstrate a dominant role of the tensor force in a few-body system. Almost half of the attraction is caused by the tensor force. Recent variational calculations of the Argonne group up to the  $A = 8$  system also demonstrate the dominant role of the pion.<sup>2)</sup> These facts suggest that we look into the possibility of a finite pion mean field in nuclear systems.

In doing this, we have to break the parity and isospin symmetries once the pion mean field becomes finite. Starting with the relativistic meson-nucleon Lagrangian density, which includes the pion term, we can obtain the equations of motion for the nucleon and mesons.<sup>3)</sup> For simplicity, we write only the equations for the nucleon, sigma and pion using only the linear terms:

$$(i\gamma^\mu \partial_\mu - M - g_\sigma \sigma - g_\omega \gamma^\mu \omega_\mu - g_\pi \gamma_5 \gamma^\mu \partial_\mu \pi^a \tau^a) \psi = 0, \quad (1)$$

$$(-\Delta + m_\sigma^2) \sigma = -g_\sigma \langle \bar{\psi} \psi \rangle. \quad (2)$$

$$(-\Delta + m_\pi^2) \pi^a = g_\pi \partial_i \langle \bar{\psi} \gamma_5 \gamma^i \tau^a \psi \rangle. \quad (3)$$

Here, the brackets  $\langle \dots \rangle$  denote the ground state expectation value. The pion field is generally finite when the source term breaks the parity. When the pion field is finite in Eq. (3), the nucleon single-particle state breaks the parity in Eq. (1), which again makes the pion source term finite. The self-consistency solution for the coupled equations provides a converged solution.

We consider the  $N=Z$  closed-shell nuclei. Since we assume spherical symmetry for the intrinsic state, the single-particle state can be expressed as

$$\psi_{njm}(x) = \sum_{\kappa} W_{\kappa}^n \phi_{\kappa jm}(x), \quad (4)$$

where the summation over  $\kappa$  means parity mixing.

Since we are especially interested in the occurrence of a finite pion mean field, we take the TM1 parameter set of the  $(\sigma, \omega, \rho)$  model, which guarantees the saturation property, and take the value of the Bonn A potential for the pion-nucleon coupling. Our study

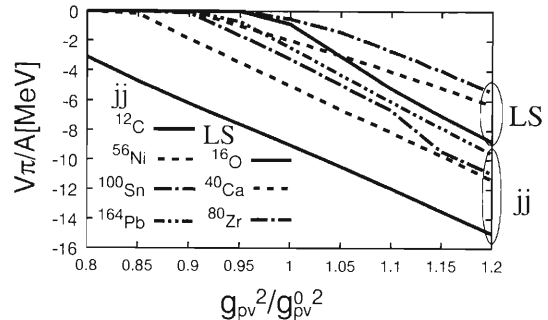


Fig. 1. Pion potential energies for different values of the coupling constant ( $\alpha g_\pi^2$ ), within a range  $0.8 \leq \alpha \leq 1.2$ .

on the pion potential energies of the self-consistent solutions have provided results for the following  $N=Z$  closed-shell nuclei:  $^{12}\text{C}$ ,  $^{16}\text{O}$ ,  $^{40}\text{Ca}$ ,  $^{56}\text{Ni}$ ,  $^{80}\text{Zr}$ ,  $^{100}\text{Sn}$ , and  $^{164}\text{Pb}$ . The results of our study along with detailed discussions are presented in Ref. 4. In Fig. 1, we additionally show the results of the pion potential energies of the self-consistent solutions for different values of the coupling constant. The critical value of the coupling constant ( $g_{\pi(\text{cr.})}^2$ ) is defined such that it leads to an infinitesimal pion potential energy. We have shown that  $g_{\pi(\text{cr.})}^2$  for  $^{12}\text{C}$  is smaller than  $0.80g_\pi^2$  and for other nuclei is between  $0.80g_\pi^2$  and  $0.95g_\pi^2$ . The critical values increase gradually with an increase of the mass number, although there is an appreciable difference in the critical values between two groups of the jj- and LS closed-shell nuclei.

In future work we must fix the parameters of the Lagrangian, which include the effects of the pion mean field and the rho meson tensor term, and also take into account the Fock term in the coupled channel equations of the nucleon and mesons.

## References

- 1) Y. Akaishi: in *Few-Body System in Realistic Interaction in Cluster Models and Other Topics* (World Scientific, Singapore, 1986), p. 259.
- 2) R. B. Wiringa, S. C. Pieper, J. Carlson, and V. R. Pandharipande: *Phys. Rev. C* **62**, 014001 (2001).
- 3) B. D. Serot and J. D. Walecka: *Advances in Nuclear Physics*, Vol. 16 (Plenum Press, New York, 1986).
- 4) H. Toki, S. Sugimoto, and K. Ikeda: nucl-th/0110017 (to be submitted in *Phys. Rev. Lett.*) and the references therein.

\* Research Center for Nuclear Physics, Osaka University

# Cranked relativistic mean-field study of chiral doublet bands

H. Madokoro and M. Matsuzaki\*

[NUCLEAR STRUCTURE, Tilted axis cranking]

Recently, much experimental data have been obtained which show the evidence of a tilted axis rotation. There are two topics concerning this phenomenon: one is *shears bands*;<sup>1)</sup> the other is *chiral doublet bands*.<sup>2)</sup> Theoretically, mean-field models have turned out to be very powerful tools for studying these tilted axis rotations. So far, all mean-field calculations were, however, based on a simple pairing + QQ interaction, or a phenomenological core + particle picture. Fully microscopic and self-consistent calculation with more sophisticated effective interactions was strongly desired.

In our previous work,<sup>3)</sup> we for the first time extended the relativistic mean field (RMF) model, which has succeeded to reproduce many properties of finite nuclei, to a description of tilted axis rotation. Our result for the shears bands in <sup>84</sup>Rb was satisfactory. We are now paying much attention to another interesting topic, that is, the chiral doublet bands. As discussed in Ref. 2, this pair of bands appears in triaxially deformed nuclei as the result of a breaking of the so-called ‘chiral symmetry’ in the intrinsic frame. The rotational axis would then deviate from any of the principal axes. Therefore, we must perform a three-dimensionally tilted calculation in the full  $\theta - \phi$  plane, where  $\theta$  and  $\phi$  represent the tilt angles. This is contrary to the shears bands in which a description assuming the two-dimensional rotation is adequate.

In this work, we show a preliminary result of the RMF model applied to the observed tilted bands in <sup>134</sup>Pr. Although we have just finished an improvement of the code so as to include pairing correlations, we concentrate here on an investigation without pairing. The configuration is assumed to be that a proton particle and a neutron hole exist in the  $1h_{11/2}$  high- $j$  orbital. The valence particle and hole are essential for the appearance of a tilted rotating state.

Figure 1 shows the calculated and experimental kinematical moments of inertia. The result is shown from  $\Omega = 0.1$  MeV up to  $\Omega = 0.4$  MeV. Above this frequency, the minimum suddenly moves towards the 1-axis, and we can no longer obtain any tilted rotating states. This is consistent with the experimental observation where a band crossing occurs at a higher frequency, as has been seen. Up to  $\Omega = 0.4$  MeV, we find relatively good agreement with the experimental values.

Table 1 shows how the position of the minima in the  $\theta - \phi$  plane changes as the rotational frequency in-

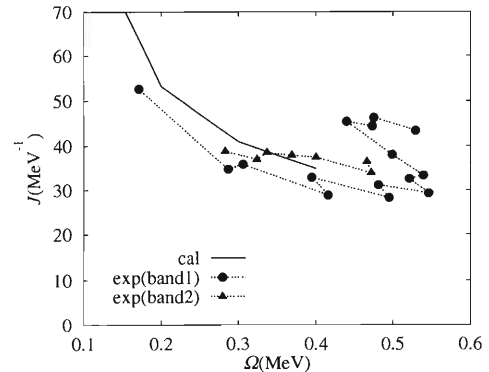


Fig. 1. Calculated and experimental kinematical moments of inertia in <sup>134</sup>Pr as functions of the rotational frequency.

Table 1. Calculated tilt angles,  $\theta$  and  $\phi$ .

$\Omega$ (MeV)	$\theta$	$\phi$
0.1	53°	0°
0.2	55°	0°
0.3	58°	0°
0.4	60°	0°

creases. As can be seen from the table, we obtained two-dimensionally tilted rotating states, but no three-dimensional minimum appears (that is,  $\theta$  is deviated from either 0° or 90°, but  $\phi$  is always 0°). This is inconsistent with the experimental observation where chiral doublet bands are observed. The discrepancy can be attributed to the fact that we neglected the pairing correlations. In order for the three-dimensionally tilted state to appear, the angular momentum of the ‘core’ part should be in the direction of the 2-axis, while neglecting the pairing would make the core rigid-like and, therefore, a rotation around the shortest axis (1-axis) would be favored. Including the pairing may make the core irrotational-flow-like and the moment of inertia around the 2-axis becomes the largest, resulting in the core angular momentum directed in this axis. Such a calculation with pairing is now in progress.

## References

- 1) G. Baldisiefen et al.: Nucl. Phys. A **574**, 521 (1994).
- 2) S. Frauendorf and J. Meng: Nucl. Phys. A **617**, 131 (1997).
- 3) H. Madokoro, J. Meng, M. Matsuzaki, and S. Yamaji: Phys. Rev. C **62**, 61301 (R) (2000).

\* Fukuoka University of Education

## Three-dimensional TDHF calculation on reactions of unstable nuclei<sup>†</sup>

K.-H. Kim, T. Otsuka,<sup>\*1</sup> and P. Bonche<sup>\*2</sup>

[NUCLEAR REACTION, Unstable nuclei]

Recent developments in experiments with radioactive nuclear beams have opened a new field in nuclear physics, the study of nuclei far from the  $\beta$ -stability line (*i.e.* unstable nuclei). Much experimental information on the structure of such nuclei has been reported and has exhibited several interesting phenomena, such as a neutron halo and neutron skin, which have not been seen in stable nuclei. Such characteristic features of the structure of unstable nuclei have attracted much interest not only in themselves, but also in their effects on reactions. However, studies of the reactions of unstable nuclei with neutron skin have been limited both experimentally and theoretically. We consider here the reactions of unstable nuclei with neutron skin.

We have applied here the time-dependent Hartree-Fock (TDHF) method<sup>1)</sup> in three dimensions with the full Skyrme interaction<sup>2)</sup> to study unstable nuclei. Since we completely remove symmetry constraints imposed on the wavefunction, except for the one with respect to the reaction plane, the numerical calculations have become much larger and more difficult to perform. We mention that, at present, the TDHF is probably the only possible and practical means for describing massive transfer and fusion of nuclei with neutron skin where the density, mean potential and shape of the nuclei may change much more drastically compared to stable nuclei and the core part of halo nuclei in an unexpected way.

We discuss here the reactions of  $^{28}\text{O}$  and  $^{60}\text{Ca}$  as examples of unstable nuclei with neutron skin. In the case of the  $^{28}\text{O}+^{16}\text{O}$  and  $^{28}\text{O}+^{40}\text{Ca}$  reactions, an enhancement of the fusion cross section is not seen compared to the reactions between stable nuclei, such as  $^{16}\text{O}+^{16}\text{O}$  and  $^{16}\text{O}+^{40}\text{Ca}$ . These results are consistent with the results of two-dimensional calculations.<sup>3)</sup>

Since in the case of light nuclei, such as  $^{28}\text{O}$ , the number of neutrons in the neutron skin is not large, for example it is four in  $^{28}\text{O}$ , and they are all loosely bound, neutron transfer can easily occur compared to the case with stable nuclei, although the separation of these neutrons from the core can easily occur compared with the situation in stable nuclei. Therefore, neutron transfer does not enhance the fusion cross section directly, and massive nucleon transfers are seen.

The situation is different in the case of reactions of  $^{60}\text{Ca}$ . Similarly to the reactions of  $^{28}\text{O}$ , a significant difference in the fusion cross section between the  $^{60}\text{Ca}+^{40}\text{Ca}$  and  $^{40}\text{Ca}+^{40}\text{Ca}$  reactions is not seen. In the case of the  $^{60}\text{Ca}+^{16}\text{O}$  reaction, on the other hand, the fusion cross section becomes larger compared with the  $^{40}\text{Ca}+^{16}\text{O}$  reaction. We can also see that the cross section of the neutron transfer of this reaction is not as large as that of the  $^{60}\text{Ca}+^{40}\text{Ca}$  reaction. In this case, neutron flow can still easily occur due to the difference in the neutron Fermi energies between  $^{60}\text{Ca}$  and  $^{16}\text{O}$ , similar to the  $^{60}\text{Ca}+^{40}\text{Ca}$  reaction, although the channels of the neutron transfer are not so favoured energetically. The relation between neutron transfer and fusion of these reactions is interesting. We are now studying the mechanism of these reactions and the reactions of heavier neutron-rich nuclei in detail.

### References

- 1) K.-H. Kim, T. Otsuka, and P. Bonche: *J. Phys. G* **23**, 1267 (1997).
- 2) E. Chabanat, P. Bonche, P. Hansel, J. Meyer, and R. Schaeffer: *Phys. Scr. T* **56**, 31 (1995).
- 3) K.-H. Kim, T. Otsuka, and M. Tohyama: *Phys. Rev. C* **50**, R566 (1994).

---

<sup>\*1</sup> Department of Physics, University of Tokyo

<sup>\*2</sup> Service de Physique Théorique, CE Saclay, France

# Resonance and continuum states in weakly bound systems

T. Nakatsukasa\*<sup>1</sup> and K. Yabana\*<sup>2</sup>

[Hartree-Fock and random phase approximation]

Recent developments in radioactive beam techniques enable us to access nuclei near drip-lines. The drip-line nuclei are weakly bound finite fermion systems. One would naturally expect that the continuum should be taken into account explicitly in any description of their structures and reactions.

Bound solutions of the Schrödinger equation for the Hamiltonian,  $H = T + V$ , can be formally written as

$$\Psi = \frac{1}{E - T} V \Psi. \quad (1)$$

Here, a Green's function,  $(E - T)^{-1}$ , can be uniquely defined, since the operator,  $E - T$ , is negative-definite. Bound states are characterized by discrete spectra,  $E_n$  ( $n = 0, 1, 2, \dots$ ).

On the other hand, for continuum states, since  $E - T$  has zero eigenvalues, we need to modify Eq. (1) into the Lippmann-Schwinger equation. First, we need to add a zero-eigenvalue solution of the  $E - T$ ,  $\Phi_0$ . Furthermore, in order to uniquely define the Green's function,  $(E - T)^{-1}$ , it is necessary to specify a boundary condition. For usual physical situations, it is natural to adopt an outgoing boundary condition (OBC) for scattering waves,

$$\Psi = \Phi_0 + \frac{1}{E - T + i\eta} V \Psi. \quad (2)$$

For two-body systems, one may easily separate the relative coordinates from those of the center of mass. Then, the OBC becomes rather trivial because this is essentially a problem involving a single degree of freedom. For many-body systems, however, it can be very complicated to settle the OBC for many degrees of freedom.

We present a method to simulate the OBC, which we call the "absorbing boundary condition" (ABC).<sup>1)</sup> The Green's function with the OBC is written as Eq. (2), where  $+i\eta$  is an infinitesimal imaginary quantity ( $\eta > 0$ ). Now, we allow this imaginary part to depend on the coordinate and to be finite,  $+iW(\mathbf{r})$ .  $W(\mathbf{r})$  is taken to be positive far outside the system (at large  $r$ ) and zero elsewhere. This means that, for  $E > 0$ , the wave number,  $k$ , has a positive imaginary part,  $+i\gamma(\mathbf{r})$ , at large  $r$ . The outgoing wave defines its asymptotic behavior as

$$\psi^{(+)} \sim f(\Omega) \frac{e^{ikr}}{r}, \quad \text{at } r \rightarrow \infty. \quad (3)$$

Thus, with a complex potential of  $-iW(\mathbf{r})$ , the outgoing wave dampens as

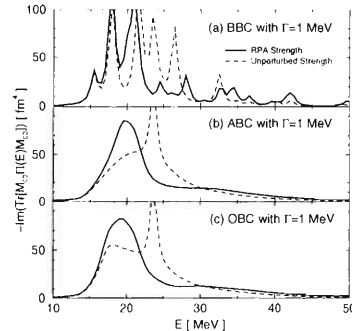


Fig. 1. Monopole response in  $^{12}\text{C}$  calculated with the BKN interaction. Different boundary conditions are adopted; (a) BBC (Box boundary condition), (b) ABC, and (c) OBC.

$$\psi^{(+)} \sim f(\Omega) \frac{e^{ikr - \gamma r}}{r}, \quad \text{at } r \rightarrow \infty, \quad (4)$$

while the incoming wave diverges. Therefore, if we impose the vanishing boundary condition at large  $r$ , only outgoing waves are allowed. Since the complex potential takes care of the boundary condition, we can solve Eq. (2) with  $\Psi|_{\text{boundary}} = 0$ , instead of constructing the OBC.

An advantage of the ABC is simplicity of its numerical calculation. We may solve scattering problems in the same way as we do for bound states. Another advantage is that the ABC easily implements a real-time calculation.<sup>2)</sup> Instead of taking an energy representation, we may calculate the time evolution of the quantum states directly. We have demonstrated that the real-time method with the ABC can properly take account of the continuum in linear-response calculations.<sup>2)</sup> In real-time calculations, it is very difficult to handle the OBC explicitly. The disadvantage is that the ABC cannot properly handle low-energy escaping particles and a long-range Coulomb potential.

We have studied the continuum response of deformed nuclei with the OBC and ABC.<sup>3)</sup> The monopole response in  $^{12}\text{C}$  is shown in Fig. 1 as an example. The results demonstrate that the ABC is able to reproduce the same results as the OBC, except in the vicinity of the threshold energy. See Refs. 2 and 3 for details.

## References

- 1) R. Kosloff and D. Kosloff: J. Comput. Phys. **63**, 363 (1986).
- 2) T. Nakatsukasa and K. Yabana: J. Chem. Phys. **114**, 2550 (2001).
- 3) T. Nakatsukasa and K. Yabana: RIKEN Rev., No. 39, 96 (2001).

\*<sup>1</sup> Physics Department, Tohoku University

\*<sup>2</sup> Institute of Physics, University of Tsukuba

# Triaxial deformation in $^{10}\text{Be}$

N. Itagaki,<sup>\*1</sup> S. Hirose,<sup>\*1</sup> T. Otsuka,<sup>\*1</sup> S. Okabe,<sup>\*2</sup> and K. Ikeda

[Cluster structure, Neutron-rich nuclei, Triaxial deformation]

The nucleus  $^{10}\text{Be}$  has been known to have a strong  $\beta$  deformation due to the  $\alpha$ - $\alpha$  core. However, triaxial deformation is also possible as a result of the dynamics of the two valence neutrons. This has been theoretically discussed based on the deformed oscillator model,<sup>1)</sup> in which a  $\gamma$  distortion of  $34.8^\circ$  has been predicted.

In our previous study of  $^{10}\text{Be}$ ,<sup>2)</sup> all of the observed low-lying positive- and negative-parity states could be explained as combinations of three basic orbits ( $K^\pi = 3/2^-, 1/2^+$ , and  $1/2^-$ ) of two valence neutrons around the two  $\alpha$ -clusters. Here, the  $z$ -axis is taken to be the axis connecting two  $\alpha$ -clusters. If we adopt  $K^\pi = 3/2^-$  or  $1/2^-$  orbits for the two valence neutrons, there appear two rotational bands in low energy; one is dominated by the  $K = 0$  intrinsic structure and the other by  $K = 2$ . The calculated two  $2^+$  states of these bands can be related to the observed first  $2^+$  state at 3.358 MeV and the second  $2^+$  state at 5.958 MeV. It is therefore important to show how the triaxial intrinsic configuration emerges in these states, and how the orbits of the valence neutrons deviate from axial symmetry. Here, we discuss our calculation of the electro-magnetic transition between these  $K = 0$  and  $K = 2$  bands ( $B(E2: K = 2 \rightarrow K = 0)$ ) as a signal of a triaxial deformation. This transition is suppressed when the orbitals are of pure axial symmetry. However, the orbitals may deviate from axial symmetry, when the valence neutrons are mutually more correlated and form a localized di-neutron pair due to the neutron-neutron interaction. The recoil effect of the valence neutrons with respect to the  $\alpha$ - $\alpha$  core then plays a role to break the axial symmetry of the charge distribution.

The total wave function is fully antisymmetrized and expressed as a superposition of Slater determinants with various configurations of the valence neutrons. The Slater determinants are also superposed with respect to different relative distances between the two  $\alpha$  clusters. Projection to the eigen states of the angular momentum ( $J$ ) is numerically performed. All nucleons are described by Gaussians with a common oscillator parameter,  $s = \frac{1}{\sqrt{2\nu}}$ , set equal to 1.46 fm.

We estimate the degree of the triaxiality as a function of the  $\gamma$  angle. The ratio  $\frac{B(E2: 2_2^+ \rightarrow 2_1^+)}{B(E2: 2_1^+ \rightarrow 0_1^+)}$  becomes 0.34 in our calculation, which agrees with the

Davydov-Filippov model<sup>3)</sup> at around  $\gamma = 19^\circ$ . Also,  $\frac{B(E2: 2_2^+ \rightarrow 0_1^+)}{B(E2: 2_1^+ \rightarrow 0_1^+)}$  calculated with the Davidov-Filippov model crosses with our result of 0.059 at around  $\gamma = 17^\circ$  and  $22^\circ$ . These results strongly suggest that  $^{10}\text{Be}$  has a triaxial deformation of  $\gamma = 15^\circ$ - $20^\circ$ . Although the  $\alpha$ - $\alpha$  core is of axial symmetry and electric charge exists only in the  $\alpha$ 's, the recoil effect gives rise to a change from axial symmetry to the triaxial shape.

We can show triaxial deformation by artificially weakening the spin-orbit interaction. With decreasing spin-orbit interaction, the orbits of the valence neutrons deviate from the  $jj$ -coupling limit, and the di-neutron configuration becomes important. Here, the system becomes 3 body-like and the  $B(E2: 2_2^+ \rightarrow 2_1^+)$  value drastically increases.

A similar di-neutron component has been discussed in weakly bound systems with the so-called halo structure. For example, in  $^6\text{He}$ , in addition to the shell model-like space, the model space of di-neutron+ $^4\text{He}$  has been shown to be important. This means that a locally-correlated di-neutron wave function is important for describing the valence neutrons with small binding energy and a spatially extended distribution. This is consistent with our discussion on the effect of varying the strength of the spin-orbit interaction. Namely, when the valence neutrons with low-binding energies have a halo structure, the contribution of the spin-orbit interaction between the core and the valence neutrons becomes weak. Here, the valence neutrons construct a di-neutron pair with spin singlet, by which they can increase the spatial overlap between them and the contribution of the attractive interaction. Therefore, it is very challenging to explore the triaxial deformations in  $^{12}\text{Be}$  and  $^{14}\text{Be}$ , which have weakly bound neutrons as well as deformed cores.

## References

- 1) M. Harvey and F. C. Khanna: in *Nuclear Spectroscopy and Reactions, Part D, Models of Light Nuclei*, edited by J. Cerny (Academic Press, New York, 1975), p. 69.
- 2) N. Itagaki and S. Okabe: Phys. Rev. C **61**, 044306 (2000).
- 3) A. S. Davydov and G. F. Filippov: Nucl. Phys. **8**, 237 (1958).

<sup>\*1</sup> Department of Physics, University of Tokyo

<sup>\*2</sup> Center for Information and Multimedia Studies, Hokkaido University

## Equilateral-triangular shape in $^{14}\text{C}$

N. Itagaki,<sup>\*1</sup> T. Otsuka,<sup>\*1</sup> S. Okabe,<sup>\*2</sup> and K. Ikeda

[Cluster structure, Neutron-rich nuclei, Inversion doublet]

Recently, discussions of molecular states have been extended to neutron-rich C isotopes. In our previous study,<sup>1)</sup> we applied our approach introduced for Be isotopes to C isotopes, and the possibility of an  $\alpha$ - $\alpha$ - $\alpha$  linear-chain configuration was pointed out. In the present work, we investigate another kind of cluster structure in  $^{14}\text{C}$ , that is an equilateral-triangular shape of the  $3\alpha$  core. A state with this symmetry is expected to appear at a much lower in energy than that in the linear-chain case. According to group theory, when the system has an equilateral-triangular configuration of  $3\alpha$ , a rotational band structure with  $K^\pi = 3^-$  appears. In  $^{12}\text{C}$ , the  $3^-$  state has been observed at  $E_x = 9.6$  MeV. From the theoretical side, it has been analyzed based on many models that this state corresponds to the band head of the  $K^\pi = 3^-$  rotational band, and the triangular-symmetry of the  $3\alpha$ -cluster is reflected in this band.<sup>2)</sup> However, the presence of an equilateral-triangular shape of  $3\alpha$  is not fully established for  $^{12}\text{C}$ , since the  $4^-$  and  $5^-$  states, which are members of a rotational band starting from  $3^-$ , have not been observed. Here, the  $3^-$  state is already above the  $3\alpha$  threshold by about 2 MeV; therefore, large resonance widths are expected for the  $4^-$  and  $5^-$  states, which makes any observation difficult. On the contrary, we investigate neutron-rich C isotopes and show that this band structure is much more stabilized in energy due to the attractive interaction among the valence neutrons around the  $3\alpha$  core.

A microscopic  $\alpha+\alpha+\alpha+n+n$  model is introduced, and the total wave function is fully antisymmetrized and expressed by a superposition of basis states with different relative distances between the  $\alpha$ -clusters and various configurations of the valence neutrons around the  $\alpha$ -clusters. In  $^{14}\text{C}$ , two valence neutrons rotate around the  $3\alpha$ -core symmetrically, just like covalent electrons in molecules. To describe such a density distribution, we introduce two kinds of basis states: shell-model-like and molecular-orbital basis states. In the shell-model-like basis state, the valence neutrons are described as shell-model orbits around the center of  $3\alpha$ . This basis state describes the neutron-density around the center, and is valid for the describing the yrast states with relatively small  $\alpha$ - $\alpha$  distances. The lowest shell-model orbit of neutrons around  $3\alpha$  localized on the  $xy$ -plane is  $p_z$  ( $\Phi(SM(p_z)^2)$ ). However, the two

valence neutrons are not only localized around the center of the  $3\alpha$ -triangle, but they also rotate around each  $\alpha$ - $\alpha$  pair. Therefore, we introduce another kind of the basis state, the molecular-orbital basis state ( $\Phi(MO)$ ), where the orbit of the valence neutrons is described as a linear combination of orbits around each two- $\alpha$  pair. This basis state is important when the  $\alpha$ - $\alpha$  distance becomes larger. The model space is  $\alpha+^{10}\text{Be}(\alpha+\alpha+2n)$ .

Due to mixing of the  $\Phi(SM(p_z)^2)$  and  $\Phi(MO)$  configurations, there appear two  $3^-$  states in the low energy region. From the second  $3^-$  state, a rotational band structure comprised of the  $3_2^-, 4_1^-,$  and  $5_1^-$  states is calculated just around the  $^{10}\text{Be}+\alpha$  threshold. Furthermore, it is significant that the corresponding states are experimentally observed in  $-2.21$  MeV ( $3^-$ ) and  $-0.34$  MeV ( $4^-$ ) with respect to the  $^{10}\text{Be}+\alpha$  threshold energy. This situation is very different from that of  $^{12}\text{C}$ .

The calculation shows that the ground  $0^+$  state, the yrast  $2^+$  state, and the  $4^+$  state states ( $0_2^+, 2_2^+, 4_2^+$ ) around the  $^{10}\text{Be}+\alpha$  threshold energy fit into the  $J(J+1)$  rule. In this energy region, corresponding states are also experimentally observed. The calculated electro-magnetic transition probabilities prove that these states are members of a rotational band. The  $B(E2: 2_2^+ \rightarrow 4_2^+)$  and the  $B(E2: 0_2^+ \rightarrow 2_2^+)$  values are calculated to be  $16.4 e^2\text{fm}^4$  and  $38.1 e^2\text{fm}^4$ , respectively, and this ratio of 0.46 almost agrees with the well-known value of 0.51 for a rigid-rotor. This result suggests that a positive-parity rotational band with the cluster structure also appears around the  $^{10}\text{Be}+\alpha$  threshold energy.

We have shown that both of the positive-parity (band head is  $0^+$ ) and the negative-parity (band head is  $3^-$ ) rotational bands appear around the  $^{10}\text{Be}+\alpha$  threshold energy. Although the neutron configurations are slightly different, these two rotational bands are considered to comprise an inversion doublet structure.

### References

- 1) N. Itagaki, S. Okabe, K. Ikeda, and I. Tanihata: Phys. Rev. C **64**, 014301 (2001).
- 2) Y. Fujiwara, H. Horiuchi, K. Ikeda, M. Kamimura, K. Katō, Y. Suzuki, and E. Uegaki: Prog. Theor. Phys. Suppl. No. 68, 60 (1980).

<sup>\*1</sup> Department of Physics, University of Tokyo

<sup>\*2</sup> Center for Information and Multimedia Studies, Hokkaido University

## Description of the Gamow-Teller resonance within the phonon damping model<sup>†</sup>

N. Dinh Dang, T. Suzuki,\* and A. Arima

[NUCLEAR STRUCTURE, phonon damping model, Gamow-Teller resonance]

The phonon damping model (PDM)<sup>1)</sup> has been extended to describe the damping of charge-exchange resonances. The formalism was applied to calculate the strength distribution of the Gamow-Teller resonance in <sup>90</sup>Nb. The obtained results in two versions PDM-1 and PDM-2 of the model, shown as the solid and dashed lines in Fig. 1, respectively, are found to be in reason-

able agreement with the recent experimental data (full circles with error bars)<sup>2)</sup> and with those of a previous study with explicit microscopic coupling to  $2p2h$  configurations using a realistic interaction (dotted line).<sup>3)</sup>

### References

- 1) N. Dinh Dang and A. Arima: Phys. Rev. Lett. **80**, 4145 (1998); Nucl. Phys. A **636**, 427 (1998); N. Dinh Dang, K. Tanabe, and A. Arima: Phys. Rev. C **58**, 3374 (1998).
- 2) T. Wakasa et al.: Phys. Rev. C **55**, 2909 (1997).
- 3) N. Dinh Dang, A. Arima, T. Suzuki, and Y. Yamaji: Nucl. Phys. A **621**, 719 (1997).

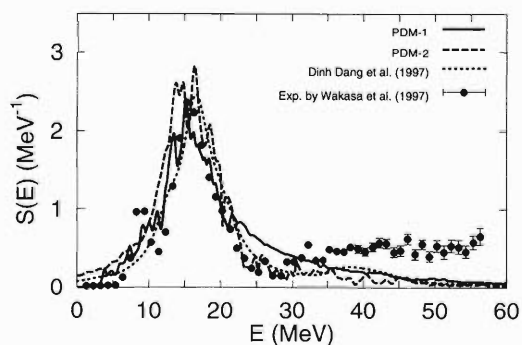


Fig. 1. Strength functions of the GTR in <sup>90</sup>Nb. See text for the notation.

<sup>†</sup> Condensed from the article in Phys. Rev. C **64**, 027303 (2001)

\* Department of Physics, College of Humanities and Sciences, Nihon University

# Phonon damping model using random-phase-approximation operators<sup>†</sup>

N. Dinh Dang and A. Arima

[phonon damping model, random-phase approximation]

A fully microscopic interpretation of the phonon damping model (PDM) is proposed. The phonon operator, which generates collective excitations, such as the giant dipole resonance (GDR), is constructed from coherent particle-hole pairs. The phonon energy is determined as the solution of a dispersion equation within the random-phase approximation (RPA). The phonon structure is found in terms of the RPA  $X$  and  $Y$  amplitudes. The formalism has been illustrated by numer-

ical calculations within a schematic model. The results of the calculations, shown in Fig. 1, demonstrate the same feature of GDR as a function of temperature obtained previously within PDM-1,<sup>1)</sup> which employs structureless phonons.

## References

- 1) N. Dinh Dang and A. Arima: Phys. Rev. Lett. **80**, 4145 (1998); Nucl. Phys. A **636**, 427 (1998).

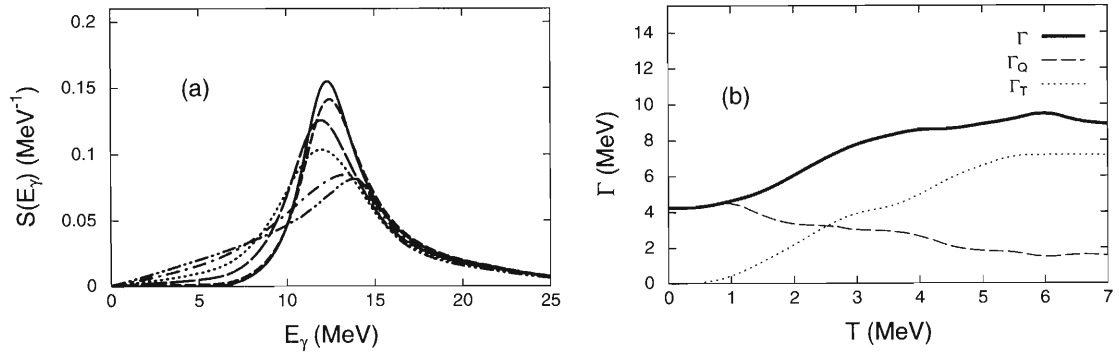


Fig. 1. Temperature dependence of the strength functions (a) and width (b) of GDR. In (a): the solid, short dashed, long dashed, dotted, dash-dotted and dash-double dotted lines are results at  $T = 0, 1, 1.5, 2, 3,$  and  $5$  MeV, respectively. In (b): The thick solid, dashed, and dotted lines are the total width  $\Gamma$ , the quantal width  $\Gamma_Q$ , and the thermal width  $\Gamma_T$ , respectively, as described in the text.

<sup>†</sup> Condensed from the article in Phys. Rev. C **64**, 024302 (2001)

# Improved treatment of ground-state correlations: Modified random-phase approximation<sup>†</sup>

N. Dinh Dang and V. Zelevinsky\*

[ground-state correlations, random-phase approximation, superconducting pairing gap]

A method is proposed to improve the treatment of the ground-state correlations in a finite Fermi system compared to the standard random-phase approximation (RPA) or earlier suggested renormalized RPA.<sup>1-5)</sup> The correlations lead to nonzero quasiparticle occupancies in the ground state. The method employs modified quasiparticles obtained by a canonical transformation of the usual quasiparticles explicitly involving the quasiparticle occupation numbers. A set of equations is derived, which allows one to determine these occupation numbers along with the RPA modes. The formalism is illustrated with the Lipkin-Meshkov-Glick model, and a model for superconducting pairing at finite temperature. With the new approach, the ground-state correlations are significantly reduced, the energy of the first excited state becomes closer

to the exact solution around the region where the RPA collapses, and the superconducting gap decreases monotonously instead of having a sharp phase transition. We discuss the effective equivalence of the interaction effects and the variation of temperature for the ground-state correlations.

## References

- 1) K. Hara: *Prog. Theor. Phys.* **32**, 88 (1964).
- 2) D. J. Rowe: *Phys. Rev.* **175**, 1293 (1968).
- 3) P. Schuck and S. Ethofer: *Nucl. Phys. A* **212**, 269 (1973).
- 4) F. Catara, N. Dinh Dang, and M. Sambataro: *Nucl. Phys. A* **579**, 1 (1994).
- 5) N. Dinh Dang and A. Arima: *Phys. Rev. C* **62**, 024303 (2000).

---

<sup>†</sup> Condensed from the article in *Phys. Rev. C* **64**, 064319 (2001)

\* Department of Physics and Astronomy, Michigan State University, USA

# Determination of the matter surface distribution of unstable nuclei

A. Kohama, R. Seki,\* A. Arima, and S. Yamaji

[NUCLEAR REACTION: matter density distribution of nuclei, least-square fitting, proton-  
nucleus elastic scattering]

Experimental facilities for unstable nuclei have been receiving much attention in the recent years. RI-Beam Factory (RIBF) is under construction at RIKEN in Japan, and the Rare Isotope Accelerator (RIA) facility is being proposed in the U.S. Such facilities will provide much data for the physics of unstable nuclei. Among various aspects of unstable nuclei, one of interest is the one-body matter density distribution,  $\rho(\mathbf{r})$ . The distribution is a fundamental quantity of nuclei, and will serve as an important measure to test how well we understand nuclear structure. It is perhaps an appropriate time to make a close investigation as to how well one could determine the one-body matter density distributions from the various kinds of data that are expected to emerge from the facilities.

As a concrete example, we have examined the types of experiments that are under consideration at RIBF. Unstable nuclei are often characterized as those with a large surface region generated by loosely bound valance nucleons.<sup>1)</sup> Of course, we must treat the entire region of the distribution, but will pay particular attention to determining the surface region, which is our main interest.

To this end, we have demonstrated that the surface region of the matter-density distribution can be determined well, even by the relatively low-intensity beams expected to be available at the upcoming radioactive beam facilities.<sup>2)</sup> The density distribution is determined in a model-independent way<sup>3,4)</sup> by generating pseudo data and by carefully applying a statistical and systematic error analysis. We have illustrated how the determination deteriorates in the central region of the density, as the quality of data decreases.<sup>2)</sup>

We have applied our analysis to the determination of the matter density distribution of a neutron-rich nucleus (Fig. 1), in which some of the parameters in the basis functions are fixed to those of the neighboring stable nucleus. This would allow a practical procedure in which one can apply the information of the density distribution of a stable nucleus to an analysis of its unstable isotopes.<sup>2)</sup>

## References

- 1) I. Tanihata et al.: Phys. Rev. Lett. **55**, 2676 (1985).
- 2) A. Kohama, R. Seki, A. Arima, and S. Yamaji: RIKEN Rev. No. 39, 155 (2001).

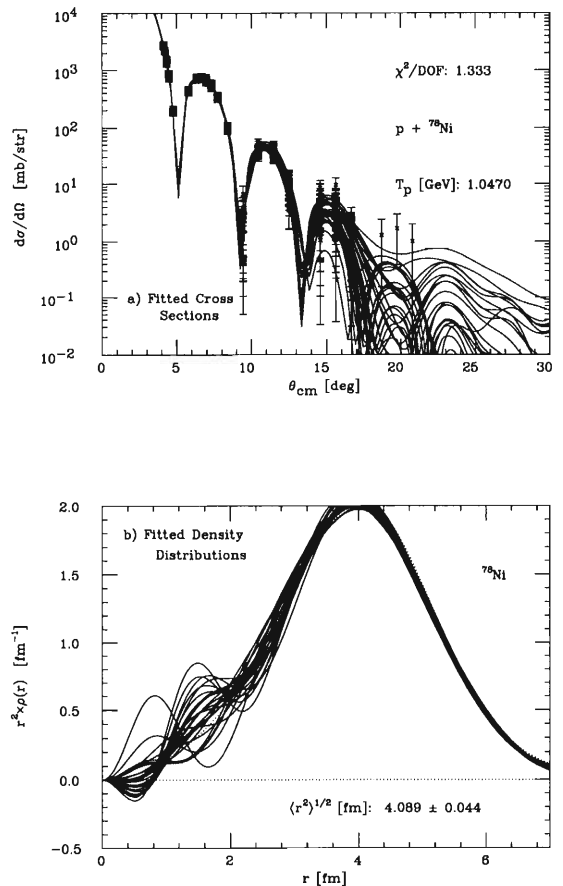


Fig. 1. Results of the least-square fitting for the pseudo-data set group C of  $^{78}\text{Ni}$ , which corresponds to a nuclear beam intensity of  $10 [\text{s}^{-1}]$  at RIBF.  $R (= 10 [\text{fm}])$  is the maximum distance to probe nuclei by the experiment, and  $M (= 10)$  is the number of basis functions. We use here the Gaussian basis function.<sup>5)</sup> a) 25 fitted cross sections (solid curve) and all of the pseudo-data (cross with bar). b) 25 fitted density distributions (solid curve), and the original distribution (dotted curve). The density distributions are drawn in the form of  $r^2 \rho(r)$ .

- 3) J. L. Friar and J. W. Negele: Adv. Nucl. Phys. **8**, 219 (1975).
- 4) A. Kohama, S. Yamaji, R. Seki, and A. Arima: RIKEN Accel. Prog. Rep. **34**, 19 (2000).
- 5) M. Kamimura: Phys. Rev. A **38**, 621 (1988).

\* Department of Physics and Astronomy, California State University, Northridge, and W. K. Kellogg Radiation Laboratory, California Institute of Technology, USA

# Observation of new neutron and proton magic numbers<sup>†</sup>

R. Kanungo, I. Tanihata, and A. Ozawa

[Magic number, separation energy, beta decay Q value, excitation energy]

Our concept of a nucleus as having a shell structure is born out of the existence of magic nucleon numbers where nuclei exhibit extra stability. So far, the observation of these magic numbers, has been based mostly on the study of nuclei on and near the stability line, and were found to be  $N = 2, 8, 20, 50, 82, 126$ , and likewise for  $Z$ .

Over the past decade, however, our knowledge about nuclei has vastly expanded with the scope of studying unstable nuclei. This reveals a considerable modification of the shell structure when one moves to a neutron-rich region. Recently, Ozawa *et al.* have shown the presence of a new neutron magic number,  $N = 16$ ,<sup>1)</sup> based on a systematic study of the single-neutron separation energy in neutron-rich nuclei. These observations suggest the possibility of a change of shell closures in a wide range of neutron-rich nuclei.

A magic number can be observed as sharp discontinuities in certain observables, such as the Q value of beta decay ( $Q_{\beta^-}$ ), the single-neutron separation energy ( $S_n$ ), and the excitation energies of the first excited state ( $E_{ex}^{1st}$ ) of even-even nuclei.

Breaks in the systematics of these three quantities show the existence of new magic numbers at  $Z = 16$  and  $N = 30$  in neutron-rich regions of the nuclear chart. Shell closure at  $N = 32$  is also observed. The recently reported new magic number,  $N = 16$ ,<sup>1)</sup> was also reconfirmed in this analysis from new view points. After extending such systematic studies to the proton-rich region of the nuclear chart, we observe breaks in the systematics at  $N = 16$ ,  $Z = 16$ , and  $N = 6$ .

A summary of the new neutron and proton magic numbers and their relevant positions in the nuclear chart is presented in Fig. 1. It can be observed that the

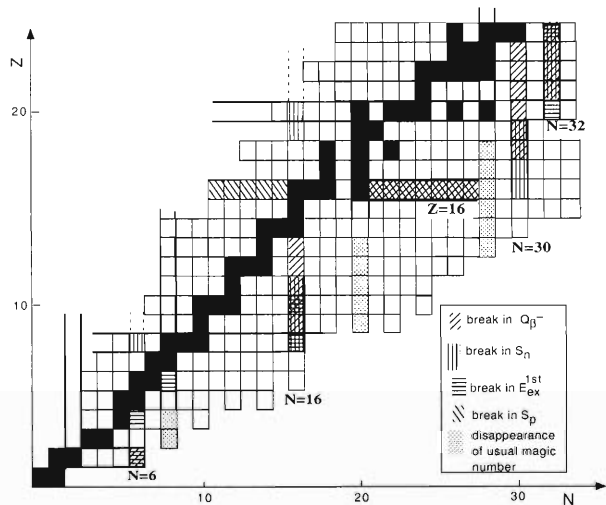


Fig. 1. Summary of new magic numbers and their locations in the nuclear chart.

magic numbers on either side of the stability line are quite identical and only differ for stable nuclei. Such a symmetrical situation is indicative of the importance of the isospin-dependent nucleon-nucleon interaction. It has recently been pointed out by Otsuka *et al.*<sup>2)</sup> that the spin-isospin part of the nucleon-nucleon interaction is important for explaining the  $N = 16$  magic number. The present observations over a wide range are in conformity with such a possibility.

## References

- 1) A. Ozawa *et al.*: Phys. Rev. Lett. **84**, 5493 (2000).
- 2) T. Otsuka *et al.*: Phys. Rev. Lett. **87**, 082502 (2001).

<sup>†</sup> Condensed from the article in Phys. Lett. B **528**, 58 (2002)

## Possibility of an enlarged core structure of $N = 15$ neutron-rich nuclei<sup>†</sup>

R. Kanungo, I. Tanihata, and A. Ozawa

[Halo, Glauber model, interaction cross-section]

The recently measured interaction cross-section data for  $^{22}\text{N}$ ,  $^{23}\text{O}$ , and  $^{24}\text{F}$  in a  $^{12}\text{C}$  target at relativistic energies have been analysed in a few-body Glauber model approach. The conventional fixed core-plus-neutron model for halo nuclei is unable to explain the observed enhanced cross section for these nuclei by any selection of the neutron orbitals. Microscopic calculations,

like those in the many-body Monte-Carlo shell model, relativistic mean field theory and cluster model, are also shown to fail to describe the large difference in the interaction cross section between  $^{22}\text{O}$  and  $^{23}\text{O}$ . A possibility of core enlargement is suggested in these nuclei.

---

<sup>†</sup> Condensed from the article in Phys. Lett. B **512**, 261 (2001)

# Fission-barrier heights estimated by a nuclear mass formula

H. Koura\*

[Spontaneous fission, Binding energies and masses]

Our group recently constructed a nuclear mass formula<sup>1,2)</sup>, which we refer to as the KUTY formula, composed of a gross part and a shell part. For the shell part, we first calculate the proton and neutron spherical shell energies using modified Woods-Saxon type potentials.<sup>3)</sup> The shell energy of a deformed nucleus is expressed as the minimum sum of an appropriate mixture of the above-mentioned spherical shell energies and an average deformation energy with respect to the deformation parameters. This mass formula gives ground-state masses and shapes for nuclei ranging from  ${}^4\text{He}$  to superheavies. The standard deviation of the calculated masses from the experimental masses of the 1995 Mass Evaluation<sup>4)</sup> is about 680 keV.

Although our mass formula is constructed by considering only the equilibrium nuclear shapes, the potential energy surface for spontaneous fission can be calculated by the same method as that used for obtaining the shell energies. The fission-barrier height is defined as the highest saddle point from the ground-state shell energy towards the prolate shapes. In this report we limit the nuclear shape to the  $\alpha_2$ ,  $\alpha_4$ ,  $\alpha_6$  deformations in the range  $-0.2 < \alpha_2 < 0.5$ .

We show the energy surfaces against the nuclear deformation for some superheavy nuclei in Figs. 1 and 2.

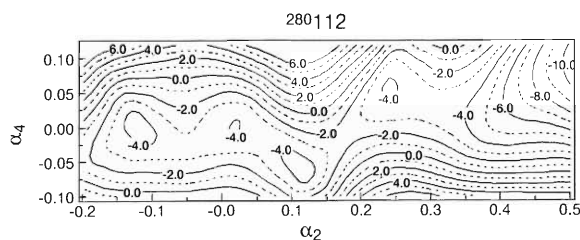


Fig. 1. Calculated energy surface of  ${}^{280}_{112}$ . The ground-state shape of this nucleus is at about  $\alpha_2 = 0.11$  and  $\alpha_4 = -0.06$ .

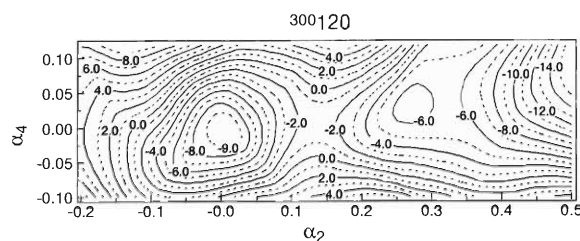


Fig. 2. Calculated energy surface of  ${}^{300}_{120}$ . The ground-state shape of this nucleus is at about  $\alpha_2 = \alpha_4 = 0.0$ .

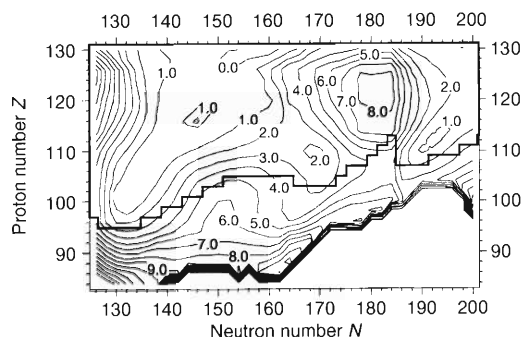


Fig. 3. Fission-barrier heights for even-even nuclei. The neutron-rich nuclei located below the solid line may have a higher saddle point in the region  $\alpha_2 > 0.5$ .

For the nucleus  ${}^{280}_{112}$ , the height of the fission barrier is only about 2 MeV and its width is relatively narrow. The spontaneous-fission half-life is consequently expected to be rather short for this nucleus. On the contrary, for the nucleus  ${}^{300}_{120}$ , the fission-barrier height is about 8 MeV, and this width is fairly wide. Therefore, the spontaneous fission of this nucleus is expected to have a very long partial half-life, much longer than the  $\alpha$ -decay half-life.

We show the fission-barrier heights in Fig. 3 for even-even nuclei in the  $84 \leq Z \leq 130$  and  $126 \leq N \leq 200$  ranges. The nuclei located below the solid line in Fig. 3 may have a higher saddle point in the region  $\alpha_2 > 0.5$  because we limited the range in the present calculation. In this figure, the “hill” of the barrier heights of the nuclei near  ${}^{304}_{122}$  is seen. The heights of these nuclei are about 8 MeV or more. On the contrary, the “basin” of the barrier heights of the nuclei near  ${}^{278}_{110}$  is also seen. These heights are about 2 MeV. There are also other neutron-deficient nuclei having relatively low fission-barrier heights.

## References

- 1) H. Koura et al.: Nucl. Phys. A **674**, 44 (2000).
- 2) H. Koura et al.: RIKEN-AF-NP-394 (2001).
- 3) H. Koura and M. Yamada: Nucl. Phys. A **671**, 96 (2000).
- 4) G. Audi and A. H. Wapstra: Nucl. Phys. A **595**, 409 (1995).

\* Advanced Research Institute for Science and Engineering, Waseda University

## Estimation of alpha-decay half-lives with phenomenological formulas

H. Koura,\* T. Tachibana,\* and M. Yamada\*

[Alpha decay, Binding energies and masses]

We estimate alpha-decay half-lives  $T_\alpha$  (s) from experimental  $Q_\alpha$ -values (MeV) with a phenomenological formula. The parameter values in the formula are adjusted for the experimental  $T_\alpha$  and  $Q_\alpha$  of the Evaluated Nuclear Structure Data File (ENSDF), 2000 version.<sup>1)</sup>

The alpha-decay half-life is written as

$$T_\alpha = \log_e 2 / (N_{\text{coll}} \times P), \quad (1)$$

where  $N_{\text{coll}}$  is the collision frequency of an  $\alpha$  particle to a potential wall and  $P$  is the penetration probability.

Here, we consider two phenomenological formulas. One is the Viola-Seaborg formula<sup>2)</sup> with an even-odd hindrance term  $h$ ,

$$\log_{10} T_\alpha = (aZ + b) / \sqrt{Q_\alpha} + (cZ - d) + h, \quad (2)$$

where  $a$ ,  $b$ ,  $c$ ,  $d$  are adjustable parameters.

Another formula is derived from the penetration probability of an  $\alpha$  particle for a spherical Coulomb potential, while neglecting such higher order terms as

$$\begin{aligned} \log_{10} T_\alpha = & 1.7195 \sqrt{\frac{A-4}{A}} Z_D / \sqrt{Q_\alpha} \\ & - 1.2901 \sqrt{\frac{A-4}{A}} \sqrt{RZ_D} \\ & + 0.07466 \sqrt{\frac{A-4}{A}} R^{3/2} / Z_D^{1/2} \cdot Q_\alpha \\ & - \log_{10} N_{\text{coll}} - 1.59175 + h, \end{aligned} \quad (3)$$

where

$$R = r_0 A_D^{1/3} + d_0, \quad r_0 = 1.08 \text{ fm}, \quad (4)$$

subscript D indicates a daughter nucleus, and  $N_{\text{coll}}$  and  $d_0$  are adjustable parameters.

As for  $h$ , we adopt a simple expression,

$$h = h_0 \delta_{\text{eo}}, \quad (5)$$

with

$$\delta_{\text{eo}} = \begin{cases} 0 & \text{for even-even nuclei,} \\ 1 & \text{for odd-}A \text{ nuclei,} \\ 2 & \text{for odd-odd nuclei.} \end{cases} \quad (6)$$

Here,  $h_0$  is an adjustable parameter.

The values of the fitted parameters for Eq. (2) are  $a = 1.55261$ ,  $b = 0.73247$ ,  $c = -0.21669$ ,  $d = 31.9949$ , and  $h_0 = 0.56718$  for  $Q_\alpha$  and  $T_\alpha$  in MeV and second, respectively. The root-mean square (RMS) deviation of  $\log T_\alpha$  from the experimental ones is 0.3625 for

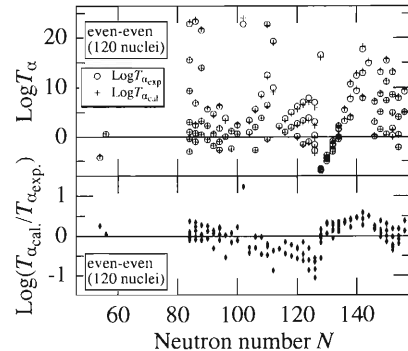


Fig. 1. Experimental and estimated  $\log T_\alpha$  using Eq. (3) (upper). Differences between the above two  $\log T_\alpha$  (lower). All data are for even-even nuclei.

120 even-even nuclei. The RMS deviation is 0.7708 for 151 odd- $A$  nuclei and is 0.9845 for 63 odd-odd nuclei. Because  $10^d$  roughly corresponds to the collision frequency  $N_{\text{coll}}$  of the  $\alpha$  particle, which should be about  $10^{20-22}$  Hz, the value of  $d$  is too large.

The values of the fitted parameters for Eqs. (3) and (4) are  $N_{\text{coll}} = 10^{20.05}$  Hz,  $d_0 = 2.0$  fm, and  $h_0 = 0.61410$ . The values of  $N_{\text{coll}}$  and  $d_0$  are reasonable. The RMS deviations for even-even nuclei, for odd- $A$  nuclei and for odd-odd nuclei are 0.3512, 0.7500 and 0.9802, respectively. Figure 1 shows the differences between the experimental and estimated  $T_\alpha$  of Eqs. (3) and (4) for even-even nuclei. This figure shows a distinct discontinuity at  $N = 126$  because of the magicity. At  $N = 102$  ( $^{174}\text{Hf}_{102}$ ) a large discrepancy is seen. This nucleus is isolated from the other even-even nuclei, and has a relatively larger deformation than the others.

By using these formulas we can estimate the  $T_\alpha$  for unknown nuclei with estimated  $Q_\alpha$  from a mass formula. In Ref. 3 we predict the unmeasured  $T_\alpha$  using Eq. (2) with  $Q_\alpha$  from the mass formula.<sup>4)</sup>

### References

- 1) Evaluated Nuclear Structure Data File (ENSDF), 2000 August version, communicated through Nuclear Data Center, Japan Atomic Energy Research Institute.
- 2) V. E. Viola and G. T. Seaborg, Jr.: *J. Inorg. Nucl. Chem.* **28**, 741 (1966).
- 3) T. Horiguchi et al.: *Chart of the nuclides 2000* (Japan Atomic Energy Research Institute, Tokai-mura, 2001).
- 4) H. Koura et al.: *Nucl. Phys. A* **674**, 44 (2000); RIKEN-AF-NP-394 (2001).

\* Advanced Research Institute for Science and Engineering, Waseda University

## A software supporting experimental plan for new elements synthesis

K. Hashizume,<sup>\*1</sup> Y. Aritomo,<sup>\*2,\*3</sup> and M. Ohta<sup>\*1</sup>

[Superheavy element, Synthesis index]

In estimating the evaporation residue cross section for producing superheavy nuclei, there are many ambiguities. A theoretical prediction can inevitably have an error of one order of magnitude or more.

According to knowledge obtained from our recent systematic analyses,<sup>1-5)</sup> the essential part which controls the absolute value of the evaporation residue cross section is decomposed and classified into several components. Their sum is defined as a Synthesis Index (SI). An investigation of each term of SI gives an explanation of why a certain projectile-target mass combination is favorable or not for producing a superheavy element among various candidates of the entrance channel. SI is composed of the following terms.<sup>2,5)</sup> Each term is expressed as an exponent of 10. Therefore, for example, in term (3), if the shell correction energy changes by 1 MeV, the evaporation residue cross section changes by one order of magnitude.

In an actual calculation, when we treat a reaction in the over-barrier energy, it is assumed that the maximum cross section is realized just above the energy of the Bass barrier, *i.e.*,  $E_B^* + \Delta E$ , where  $\Delta E (> 0)$  is typically about several MeV.

(1) The index for the formation probability is given by

$$\log_{10} P_{for} = \frac{3.2 + (1/\sqrt{\Delta E + 5} + 0.085)(Z - 100)}{1 + \exp((\alpha - 0.5)/0.075)},$$

which is valid for  $Z \geq 102$ . For  $Z < 102$ , the effect of the liquid-drop part of the fission barrier becomes more important and the above formula should be modified.

(2) Since an increase in the shell correction energy by one MeV results in a one order enhancement of the survival probability, the contribution to the index is  $-\delta_{shell}$ , where  $\delta_{shell}$  is the ground-state shell correction energy.

(3) The rotational enhancement factor as a function of ground-state deformation ( $\beta_2^{gr}$ ) is expressed by  $2.0\{1 + \exp((0.15 - \beta_2^{gr})/0.015)\}^{-1}$ , where the factor 2.0 means the maximum contribution when the ground-state of the compound nucleus is strongly deformed.

(4) The contribution to the cross section depends on the neutron number of the compound nucleus ( $N$ ). The index for the neutron number dependence is  $(N - N_o)/6$ , where  $N_o$  is an arbitrary reference number. The factor 6 appearing in the denominator is derived

from the result that a six-unit increase of the neutron number in a compound nucleus enhances the survival probability by one order of magnitude. This is because, when the neutron number of compound nucleus increases, the neutron separation energy decreases and, as a result, the survival probability increases in competition with the fission process.

(5) The energy dependence of the survival probability is derived from a systematic analysis. The index for excitation energy ( $E_B^* + \Delta E$ ) is  $-0.3(E_B^* + \Delta E - E_o)$ , where  $E_o$  is also an arbitrary reference energy.

The factor 0.3 means that, in the superheavy mass region, when the excitation energy of a compound nucleus increases by 3–4 MeV, the survival probability decreases by one order of magnitude due to the chance of another multiplication of  $\Gamma_n/\Gamma_{tot}$ . That is to say, when the excitation energy increases, the number of evaporation steps also increases. Since the survival probability is proportional to  $\prod_{i=1}^m (\Gamma_n^{(i)}/\Gamma_{tot}^{(i)})$ , it decreases along with the increase of  $m$ , where  $m$  is the number of evaporation steps.

(6) When  $\Delta E$  is negative, *i.e.*, when the incident energy is under a barrier, the barrier penetrability ( $T_B$ ) should be taken into account.  $T_B$  is usually calculated by using an inverse parabola with strength  $\hbar\omega$ .

The index for the penetrability is  $\log_{10} T_B$ ,  $T_B = \{1 + \exp(-2\pi\Delta E/\hbar\omega)\}^{-1}$ . Summing up these terms, we define the Synthesis Index for  $\Delta E > 0$  (the case of over barrier energy) as follows:

$$\begin{aligned} \text{SI} = & \log_{10} P_{for}(Z, N, \alpha, E_B^* + \Delta E) \\ & - \delta_{shell} + 2.0\{1 + \exp((0.15 - \beta_2^{gr})/0.015)\}^{-1} \\ & + (N - N_o)/6 - 0.3(E_B^* + \Delta E - E_o). \end{aligned}$$

The calculation of SI will be available on the Internet home page of RIKEN from December, 2001.

### References

- 1) M. Ohta: Proc. Workshop Fusion Dynamics at the Ex-treams, Dubna, 2000-5 (World Scientific, 2001), p. 110.
- 2) M. Ohta, Y. Aritomo, V. Zagrebaev, and E. Cherepanov: Proc. Int. Conf. on Exotic Nuclei (EXON2001), Irkutsk, Russia, 2001-7, published from World Scientific.
- 3) Y. Aritomo and M. Ohta: submitted to Phys. Rev. C.
- 4) V. I. Zagrebaev, Y. Aritomo, M. G. Itkis, Yu. Ts. Oganessian, and M. Ohta: Phys. Rev. C **65**, 014607 (2001).
- 5) M. Ohta: invited talk in ND2001, Tsukuba, Oct. (2001).

<sup>\*1</sup> Department of Physics, Konan University

<sup>\*2</sup> Department of Physics, University of Tokyo

<sup>\*3</sup> Flerov Laboratory of Nuclear Reactions, JINR, Russia

# A two-step model for fusion and synthesis of superheavy elements

C. W. Shen,<sup>\*1</sup> G. Kosenko,<sup>\*2</sup> and Y. Abe<sup>\*3</sup>

[superheavy element]

We propose a theoretical framework describing the whole reaction process of synthesizing superheavy elements, starting from the encounter of a projectile and a target up to residues of the elements, through the formation of compound nuclei.<sup>1,2)</sup> Since cooling processes of compound systems are well known and established, though there are ambiguities in the parameters in statistical codes, an essentially unknown part is the formation process of compound nuclei. In lighter systems it is rather simple and just passing over the Coulomb barrier, or quantum-mechanical barrier penetration; however, in massive systems it is not the end of the process, because there is a so-called conditional saddle point or a ridgeline standing outside of the spherical ground state and inside of the Coulomb barrier. Therefore, we have two steps: firstly, over-barrier up to the contact of two nuclear surfaces and, secondly, the evolution of a pear-shape formed by contact of the projectile and the target into the spherical shape, overcoming the conditional saddle point.

The first step is treated by the classical trajectory model extended so as to include the fluctuation associated with friction. If we employ the surface friction model proposed by Gross and Kalinowski, we obtain a fully damped state at the contact point, *i.e.*, the incident energy is completely dissipated into the internal energy. In other words, the momentum is in the Boltzmann distribution. The orbital angular momentum is also dissipated to form a sticking limit. A solution of the first step, thus provides a sticking probability of the projectile and the target.

The second step is the shape evolution of di-nucleus complexes, which is again to be described by a stochastic equation, *i.e.*, a Langevin equation for shape degrees of freedom. In the framework of the two-center parameterization, at least two parameters are necessary: the distance between the two centers and the mass asymmetry. By solving the Langevin equation with the so-called one-body wall-and-window formula as friction, we obtain the formation probability of the spherical shape for various incident momenta. The obtained formation probabilities are folded with the Boltzmann distribution of the initial momentum to give rise to the final fusion probability.

Combining the statistical decay calculations with the code HIVAP, we obtain the residue cross sections of superheavy elements.  $^{48}\text{Ca}+^{244}\text{Pu}$  system is taken

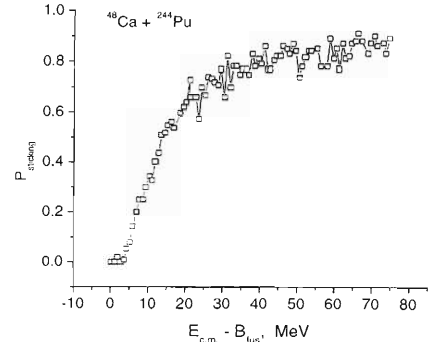


Fig. 1. Sticking probability shown as a function of the incident c.m. energy relative to the barrier.

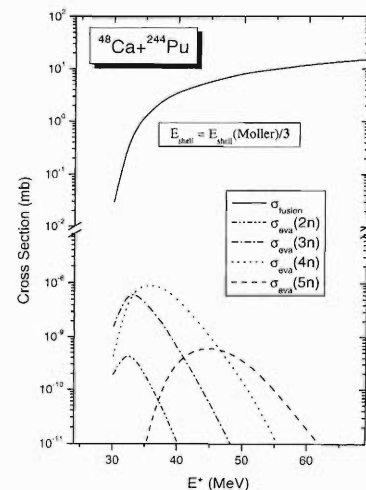


Fig. 2. Shell correction energy of 1/3 of Møller's prediction used to reproduce the order of magnitude of the experimental cross section.

as an example. Figure 1 shows the sticking probability at the contact point after the first step. Figure 2 shows the residue cross sections for  $xn$  reactions as well as the fusion excitation function. The experimental cross section to be compared is 1 – a few *pb* of the 4n channel at  $E^* \simeq 35$  MeV, which is apparently in good agreement with the calculated results shown in Fig. 2.

## References

- 1) Y. Abe, C. W. Shen, and G. Kosenko: AIP Conf. Proc. **597**, 209 (2001).
- 2) Y. Abe, C. W. Shen, and G. Kosenko: Proc. 5th Int. Conf. on Dynamical Aspects of Nuclear Fission, Casta-Papiernicka, Slovak Republic, 2001-10, to be published.

<sup>\*1</sup> Department of Nuclear Physics, China Institute of Atomic Energy, China

<sup>\*2</sup> Department of Physics, Omsk University, Russia

<sup>\*3</sup> Yukawa Institute for Theoretical Physics, Kyoto University

# $^{44}\text{Ti}$ : Its initial abundance in Cassiopeia A and its detection possibility in SN 1987A with INTEGRAL†

Y. Mochizuki

[electron-capture decay, supernovae,  $\gamma$ -ray line astrophysics]

$^{44}\text{Ti}$  is a pure orbital-electron capture decay isotope; in laboratories its half-life is measured for *neutral* atoms. Thus, the laboratory half-life value may not be directly applied to astrophysical environments where  $^{44}\text{Ti}$  is possibly in ionized states.

Mochizuki, Takahashi, Janka, Hillebrandt, and Diehl<sup>1)</sup> have argued that the electron-capture rate of  $^{44}\text{Ti}$  could be significantly reduced from its laboratory value because a high degree of ionization may be caused by reverse shock in a young supernova remnant. For the supernova remnant Cassiopeia A (hereafter, Cas A), they concluded that retardation of the decay increases the current  $^{44}\text{Ti}$ -activity by a factor of 1.5–2.5, which yields a better compatibility between the COMPTEL observation of the 1.16 MeV line activity associated with the  $^{44}\text{Ti}$  decay of this remnant and the supernova model predictions of the initial  $^{44}\text{Ti}$  abundance. However, they pointed out that the above possibility is strongly subject to the radial distribution of  $^{44}\text{Ti}$  in the ejecta.

Recently, Hughes *et al.*<sup>2)</sup> and Hwang *et al.*<sup>3)</sup> reported map of the X-ray emitting ejecta in Cas A, which includes Fe and Ca. Since  $^{44}\text{Ti}$  is considered to exist along with Fe and it ultimately decays to  $^{44}\text{Ca}$ , the distributions of Fe and Ca may be referred to as indicators of the position of  $^{44}\text{Ti}$  in the ejecta. In the present paper I reexamined the ionization effect of  $^{44}\text{Ti}$  on its initial abundance in Cas A, discussed in the paper,<sup>1)</sup> with newly obtained observational information.

It is shown that under certain conditions the ionization of  $^{44}\text{Ti}$  increases its current activity and accordingly removes any apparent discrepancies between  $^{44}\text{Ti}$  production in the supernova explosion as inferred from COMPTEL  $\gamma$ -line measurements and theoretical expectations from the current supernova nucleosynthesis models (see Fig. 1).

On the other hand, detection of the  $^{44}\text{Ti}$   $\gamma$ -line from the supernova remnant SN 1987A is the one of prime targets for the INTEGRAL mission, a gamma-ray astronomy satellite planned to be launched in 2002. The ionization effects of  $^{44}\text{Ti}$  in SN 1987A are also briefly discussed here.

If we assume no reduction of the  $\beta$ -decay rate, the  $^{44}\text{Ti}$  amounts of  $\sim 1.5 \times 10^{-4} M_{\odot}$  ( $M_{\odot}$  shows the solar mass), suggested from the fitting of the late lightcurve of SN 1987A, would produce on Earth a  $\gamma$ -ray flux of  $\sim 3 \times 10^{-6} \text{ cm}^{-2} \text{ s}^{-1}$ . This is close to the sensitivity limit of INTEGRAL.

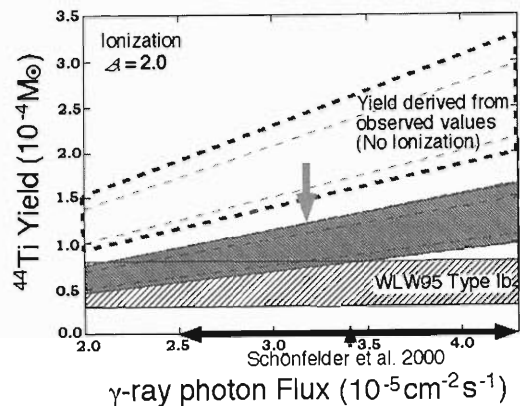


Fig. 1. Initial yield of  $^{44}\text{Ti}$  at the time of the explosion of Cas A as a function of the  $\gamma$ -ray photon flux, by which the observed result from the COMPTEL experiment<sup>5)</sup> is indicated by the arrow. WLW95 indicates a theoretical result<sup>6)</sup> of the initial  $^{44}\text{Ti}$  yield predicted for the type of supernova explosion like Cas A. The apparent discrepancies are reduced by taking the history of the  $^{44}\text{Ti}$  ionization into account. Details are found in an article of Nucl. Phys. A **688**, 58c (2001).

Contrary to the Cas A case, a simple linear analysis shows that the retardation of  $^{44}\text{Ti}$  decay *decreases* its activity for a supernova remnant that is younger than the lifetime of  $^{44}\text{Ti}$ , *i.e.*  $\sim 100$  yr. This arises from the linear dependence of the activity on the decay rate.

Recently, helium-like and hydrogen-like ions of O, Ne, Mg, and Si have been observed in SN 1987A with the Chandra X-ray observatory.<sup>4)</sup> If  $^{44}\text{Ti}$  is in the hydrogen-like ionization state, it is expected from a linear analysis that the activity is reduced by  $\sim 50\%$  in the case that assumes no retardation of the decay rate. This means that the expected flux from SN 1987A may lie below the detection limit of INTEGRAL.

## References

- 1) Y. Mochizuki et al.: Astron. Astrophys. **346**, 831 (1999).
- 2) J. P. Hughes et al.: Astrophys. J. **528**, L109 (2000).
- 3) U. Hwang et al.: Astrophys. J. **537**, L119 (2000).
- 4) D. N. Burrows et al.: Astroph/0009265.
- 5) V. Schönfelder et al.: Astron. Astrophys. Suppl. **143**, 145 (2000).
- 6) S. E. Woosley et al.: Astrophys. J. **448**, 315 (1995).

† Extracted from the article of Nucl. Phys. A **688**, 58c (2001)

# Formation of nuclear “pasta” in cold neutron star matter<sup>†</sup>

K. Iida, G. Watanabe,\* and K. Sato\*

[Dense matter, Fission instability, Proton clustering, Neutron stars]

Nuclear matter exhibits the coexistence of a liquid phase with a gas phase at subnuclear densities, due to the attractive force responsible for nuclear binding. Such a coexistence is believed to be present in the outer part of a neutron star.<sup>1)</sup> Since gravitational coupling is far smaller than Coulomb coupling, the star’s gravitational stability requires nuclear matter to be neutralized by electrons. The resulting electrically neutral matter is usually referred to as neutron star matter. At sufficiently low temperatures, relevant to neutron star interiors, long-range Coulomb interactions force the system to separate periodically into liquid and gas segments of macroscopic size, adding a crystalline property to the liquid-gas coexistence. As the electron chemical potential increases with increasing pressure, a system in  $\beta$  equilibrium has the liquid phase neutron-enriched and leaves the gas phase almost free of protons.

At zero temperature, it is believed that the energetically favorable configuration of the mixed phase possesses interesting spatial structures;<sup>1)</sup> the liquid (gas) phase is divided into periodically arranged parts of roughly spherical, rod-like, or slab-like shape, embedded in the gas (liquid) phase and in a roughly uniform electron gas. Hereafter, we refer to these parts composed of the liquid and gas phases as ‘nuclei’ and ‘bubbles,’ respectively. Recent calculations, performed within the Wigner-Seitz approximation using specific nuclear models, indicate that at a density of about  $10^{14} \text{ g cm}^{-3}$ , which is rather small compared with the saturation density of symmetric nuclear matter,  $\rho_s \simeq 2.7 \times 10^{14} \text{ g cm}^{-3}$ , the spatial structure changes from a bcc Coulomb lattice of roughly spherical nuclei to a two-dimensional triangular lattice of rod-like nuclei. With the density increased further, it is transformed into a layered structure composed of slab-like nuclei and bubbles. Next, a two-dimensional triangular lattice of rod-like bubbles and a bcc Coulomb lattice of roughly spherical bubbles appear in turn. Finally, at a density of about  $\rho_s/2$ , the system dissolves into uniform nuclear matter. These changes of the spatial structure, accompanied by a reduction of the total surface area, are governed by competition between the electrostatic and surface energies. Since slabs and rods look something like lasagna and spaghetti, the phases with positional order of one and two dimensions are often referred to as nuclear “pasta.”

In a separate study,<sup>2)</sup> we more extensively calculated

the corresponding equilibrium phase diagrams for zero-temperature neutron star matter at subnuclear densities. From a typical compressible liquid-drop model for nuclei, we predicted that the phases with rod-like nuclei and with slab-like nuclei are energetically favored in the density regime just below  $\rho_s$  and at zero temperature; it is thus important to consider how these nuclei are formed. Such formation requires the simultaneous migration of an infinite number of nucleons, in contrast to the case of ordinary chemical reactions. This prevents the nuclear system from crossing the energy barrier formed between the initial and final states in configuration space via quantum tunneling. Instead, “pasta” formation can be driven by instabilities with respect to fluctuations around the initial state.

In this work, we examined the kinds of instabilities that are involved in the formation and decay of rod-like and slab-like nuclei at zero temperature. As such, we first note an instability with respect to quadrupolar deformation of spherical nuclei, as originally investigated in the context of nuclear fission by Bohr and Wheeler. We also consider an instability with respect to proton clustering in uniform matter. This clustering is induced by the isospin symmetry energy. At an instability point that the system reaches during decompression, the gain due to this energy compensates for the gradient and Coulomb energies produced by the resulting inhomogeneities, and hence a phase with nuclei of some form appears.

We extend these considerations to other changes in nuclear shapes. The possible instability with respect to proton clustering in planar and cylindrical nuclei tends to divide each nucleus into nuclei of lower dimension, while the possible fission-like instability of slab-like and rod-like nuclei tends to lead to the formation of uniform matter and slab-like nuclei, respectively. Using a typical nuclear model, we find that planar and cylindrical nuclei are stable with respect to deformation-induced fission and proton clustering. This suggests the possibilities that such nuclei persist beyond the equilibrium transition points, and that the size of the stellar region containing them exceeds the equilibrium prediction.

## References

- 1) C. J. Pethick and D. G. Ravenhall: *Annu. Rev. Nucl. Part. Sci.* **45**, 429 (1995).
- 2) G. Watanabe, K. Iida, and K. Sato: *Nucl. Phys. A* **676**, 455 (2000).

<sup>†</sup> Condensed from the article in *Prog. Theor. Phys.* **106**, 551 (2001)

\* Department of Physics, University of Tokyo

## Recent developments in an experiment to measure nuclear half-lives relevant to the astrophysical r-process

M. A. Famiano, S. Nishimura, Y. Nishi, R. N. Boyd,\* and I. Tanihata

[r-process,  $\beta$ -decay, Nucleosynthesis]

Many nuclei of astrophysical interest and their significant reactions have yet to be studied experimentally. In particular, astrophysical processes which produce nuclei heavier than iron are postulated to include reactions of nuclei far from stability. In the r-process, the rate at which nuclei progress from low mass to higher mass, and (to a lesser extent) the nuclei through which they progress (the r-process path) depend on the  $\beta$ -decay rates of those nuclei. These rates are expected to be much more than  $1\text{ s}^{-1}$ .<sup>1)</sup> An experiment has been constructed to measure fast  $\beta$ -decay rates, allowing one to study nuclei further from stability, and to hopefully push the frontier of knowledge closer towards the r-process path. Because of the low production yields of the nuclei of interest, it is useful to simultaneously produce and measure as many of these nuclei as possible.

The current detector system, shown in Fig. 1, consists of five implantation target layers, each containing 11 targets. Nuclei are implanted into any one of the target layers (used to facilitate charge separation). The targets are rotated out of the beam line into layers of position-sensitive detector arrays. Each array is constructed of two orthogonal layers of plastic scintillator fiber arrays and a NaI scintillator for detecting coincident gamma rays. A correlation will be made between the position of the detected  $\beta$  particle and the beam implantation position in the target. The target wheel can be rotated to an accuracy of  $0.05^\circ$ , corresponding to a position accuracy of about 0.2 mm, much less than the position resolution of the fiber detector arrays. The time difference between production and detection is the decay time of the implanted ion. The rotation of the target wheel also serves the pur-

pose of reducing the buildup of long-lived nuclei. Since the target wheel has 11 positions, then the sequence of implantation — followed by a rotation — must occur 11 times before a target returns to its original position and is implanted again. For example, for a lifetime of 200 ms, any given target is implanted only once every 4.4 s ( $200\text{ ms} \times 11\text{ rotations} \times 2\text{ steps per rotation}$ ). The minimum lifetime that can be measured, limited by the rotation speed of the wheel, is on the order of 100 ms for rotation between the beam and the detector array.

The fiber arrays (Fig. 1) must maximize the efficiency, while minimizing the cross-talk between adjacent pixels. For this reason, multi-clad scintillating fibers were chosen. Also, the flexibility allows for ease of installation and manipulation, because the resulting system requires at least 20 such fiber arrays in close proximity. Each layer is divided into 16 channels. The overlap between an X channel and a Y channel creates a pixel, each of which is 4 mm square. One layer has an absolute efficiency for  $\beta$  detection of about 50%, resulting in a total efficiency of 25%. Cross-talk and position sensitivity tests were conducted using a collimated  $^{90}\text{Sr}$  source. Any cross-talk between adjacent fibers would result in events in adjacent fibers. It was found that the cross-talk between adjacent pixels is negligible, while most of it appears to be on the glass surface of the photo-multiplier tubes to which the array is coupled, and comprises only a very small percentage of the single count rate, and is thus not expected to be a problem. The position resolution of these detectors is a single pixel, enabling the location of the detected particle to be known with little uncertainty.

Using various simulation packages, the target configuration can be optimized to stop isotopes of interest and their neighboring isotopes. Likewise, particle identification is also done using the time-of-flight of the secondary particles.

The second stage of this experiment is planned for early 2002 with a heavier primary beam. An initial data analysis, followed by improvements to the detection system, will allow measurements of new half-lives. The possibility for determining the level structure, in addition to the half-lives of proton-rich nuclei, exists as well, permitting a large growth in our knowledge of astrophysically interesting nuclei.

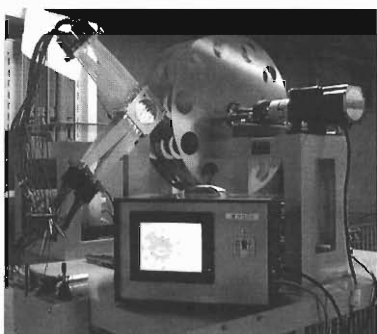


Fig. 1. Target wheel apparatus and detector array (exposed for clarity).

\* Physics Department, Ohio State University, USA

### References

- 1) G. Wallerstein et al.: Rev. Mod. Phys. **69**, 995 (1997).

## *r*-process in prompt supernova explosions

K. Sumiyoshi,<sup>\*1</sup> M. Terasawa,<sup>\*2,\*3</sup> G. Mathews,<sup>\*4</sup> T. Kajino,<sup>\*2,\*3</sup> S. Yamada,<sup>\*5</sup> and H. Suzuki<sup>\*6</sup>

[Nucleosynthesis, *r*-process, Unstable nuclei, Supernova]

A recent increase of experimental data of unstable nuclei towards the *r*-process path gives strong motivations to study the nature of *r*-process nucleosynthesis. It is now crucial to discuss the impact of the structure and reaction of unstable nuclei around the *r*-process path on nucleosynthesis in the astrophysical environment of the *r*-process.

Meanwhile, the findings of *r*-process elements in extremely metal-poor stars by astronomical observations provide important clues to pin down astrophysical sites for the *r*-process.<sup>1)</sup> Those data of very old stars strongly indicate supernova explosions of massive stars as a unique origin of the *r*-process. A recent analysis further suggests more than one kind of supernova origin, which might be linked with the mass range of presupernova stars. The abundance pattern of the *r*-process may be different depending on the supernova mechanism: a delayed explosion and a prompt explosion, corresponding to massive and less massive stars, respectively. For massive stars, the *r*-process in a neutrino-driven wind has already been studied.<sup>2)</sup>

To pursue whether less-massive stars contribute to the *r*-process, we have studied *r*-process nucleosynthesis in neutron-rich ejecta from a prompt supernova explosion of a low-mass ( $11 M_{\odot}$ ) progenitor.<sup>3)</sup> A prompt explosion can occur for low-mass supernova progenitors with small iron core masses and small rates of electron capture. To model a prompt explosion, we have performed a general relativistic hydrodynamic simulation of adiabatic collapse and bounce<sup>4)</sup> using a relativistic nuclear-matter equation of state.<sup>5)</sup> The electron fraction ( $Y_e$ ) during the collapse was fixed at the initial-model value. The size of the inner collapsing core was then large enough to enable a prompt explosion to occur in the hydrodynamical calculation.

While adopting the calculated trajectories of promptly ejected material, we explicitly computed the burst of neutronization due to electron captures on free protons in the photodissociated ejecta after passage of the shock. The thermal and compositional evolution of the neutron-rich material ejected from near the surface of nascent neutron star was obtained. These were used in nuclear reaction network calculations to evaluate the products of *r*-process nucleosynthesis. We have solved the nuclear reaction network<sup>6)</sup> including about

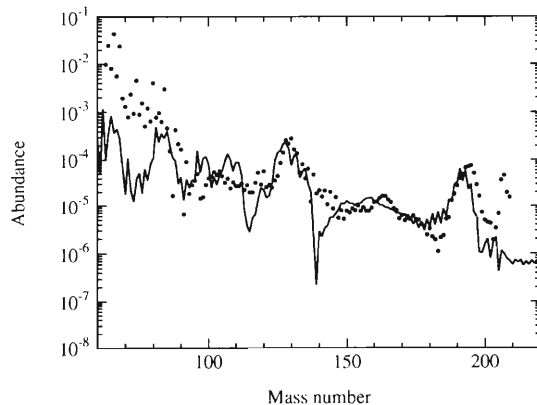


Fig. 1. Calculated final abundance of *r*-process elements ejected from a prompt supernova explosion of an  $11 M_{\odot}$  star (line) compared with the solar abundance (dots).

3000 nuclei up to the neutron drip line to follow the abundance of the nucleosynthesis products. We sum up the products from ejected materials to evaluate the total amount of *r*-process elements and their pattern. Figure 1 shows the total abundance of the *r*-process elements produced in the ejected material from a prompt explosion.

We find that, unlike in earlier studies of nucleosynthesis in prompt supernovae, the amount of *r*-process material ejected per supernova is quite consistent with observed galactic *r*-process abundances. Furthermore, the computed *r*-process abundances are in good agreement with the solar abundances of the *r*-process elements for  $A > 100$ . This suggests that prompt supernovae are promising *r*-process sites. Such events may be responsible for the abundances of the heaviest *r*-process nuclei.

### References

- 1) C. Sneden et al.: *Astrophys. J.* **533**, L139 (2000).
- 2) K. Sumiyoshi, H. Suzuki, K. Otsuki, M. Terasawa, and S. Yamada: *Pub. Astron. Soc. Jpn.* **52**, 601 (2000).
- 3) K. Sumiyoshi, M. Terasawa, G. J. Mathews, T. Kajino, S. Yamada, and H. Suzuki: *Astrophys. J.* **562**, 880 (2001).
- 4) K. Sumiyoshi, H. Suzuki, S. Yamada, and H. Toki: submitted to *Nucl. Phys.* (2001).
- 5) H. Shen, H. Toki, K. Oyamatsu, and K. Sumiyoshi: *Prog. Theor. Phys.* **100**, 1013 (1998).
- 6) M. Terasawa, K. Sumiyoshi, T. Kajino, G. J. Mathews, and I. Tanihata: *Astrophys. J.* **562**, 470 (2001).

<sup>\*1</sup> Numazu College of Technology

<sup>\*2</sup> Department of Astronomy, University of Tokyo

<sup>\*3</sup> National Astronomical Observatory

<sup>\*4</sup> Department of Physics, University of Notre Dame, USA

<sup>\*5</sup> Institute of Laser Engineering, Osaka University

<sup>\*6</sup> Department of Physics, Tokyo University of Science

## r-process nucleosynthesis in the type-II supernova model with a neutron star mass of $\sim 1.4M_{\odot}$

M. Terasawa,<sup>\*1,\*2</sup> K. Sumiyoshi,<sup>\*3</sup> T. Kajino,<sup>\*2</sup> and G. Mathews<sup>\*4</sup>

[r-process, supernova, neutron star, neutron capture]

It is generally believed that the r-process occurs under explosive conditions at very high neutron density, high temperature, and high entropy. It has been discussed that core-collapse supernovae could provide the most likely environment for the r-process. It is now commonly accepted that a massive Fe core explodes with the help of neutrino heating in a supernova explosion of, at least, a massive star.<sup>1)</sup> Because of the conversions of neutrons to protons, this strong neutrino flux, however, hinders the r-process, and the r-process cannot occur in even a supernova model with very high entropy,  $\sim 400$  (in units of the Boltzmann constant,  $k_B$ ).<sup>1,2)</sup> Therefore, it is necessary that the dynamical timescale of the explosion is much shorter than the timescale of the neutrino interactions not to disturb the r-process. So far, some authors showed that the successful r-process can occur in the fast neutrino-driven wind model, even with relatively low entropy,  $\sim 200$ .<sup>3)</sup> However these models assumed the neutron star mass,  $M_{NS} \sim 2.0M_{\odot}$  ( $M_{\odot}$  is the solar mass), although the typical  $M_{NS}$  is considered to be  $\sim 1.4M_{\odot}$  based on observations.

The timescale of the explosion model that shows a successful r-process pattern is under 10 msec.<sup>3)</sup> On the other hand, the timescale of the r-process is about a few seconds. Therefore the r-process is considered to occur in the outer boundary region just behind the shock wave.<sup>4)</sup> We should study more about the outer boundary condition, which is given by the outer boundary pressure ( $P_{out}$ ) in simulations. Thus, we simulate the neutrino-driven wind with the typical neutron star,  $M_{NS} = 1.4M_{\odot}$ , and investigate the dependence of the abundance pattern on  $P_{out}$ .

We summarize the key quantities in Table 1. Here,  $T_{out}$ ,  $Y_{\alpha,out}$  and  $Y_{seed,out}$  stand for the temperature (in the unit of  $10^9$  K) and the abundances of alpha particles and seed nuclei at the outer boundary, respectively. In each model, the dynamical timescale of the explosion is almost the same and sufficiently short, a few 10 msec. The r-process nuclei are synthesized by the  $\alpha$ -process and the r-process. At first, neutron-rich seed nuclei with mass number  $\sim 100$  are made by the  $\alpha$ -process. After that, the r-process starts from these seed nuclei and makes heavy r-process elements.

From Table 1,  $T_{out}$  becomes lower as  $P_{out}$  becomes

Table 1. Summary of parameters and key quantities.

$P_{out}$ [dyn/cm <sup>2</sup> ]	$T_{out}$	$Y_{\alpha,out}$	$Y_{seed,out}$
$10^{22}$	1.3	0.177	$2.1 \times 10^{-3}$
$10^{21}$	0.7	0.198	$1.2 \times 10^{-3}$
$10^{20}$	0.3	0.202	$3.7 \times 10^{-4}$

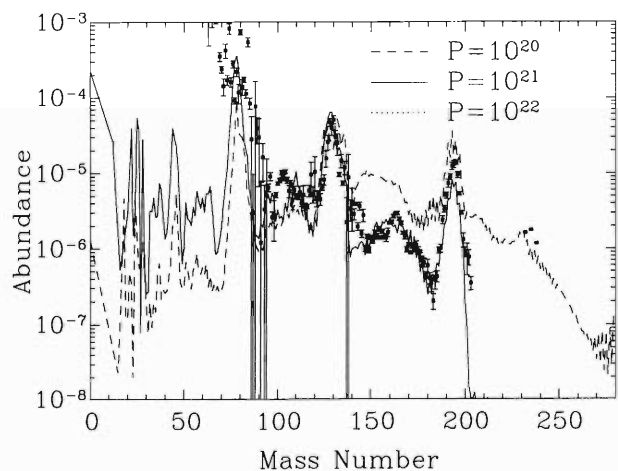


Fig. 1. Final abundance pattern.

lower, because the matter flows farther from the neutron star. When  $T_{out}$  is high,  $Y_{\alpha,out}$  is small and  $Y_{seed,out}$  is large. This is because the  $\alpha$ -capture reactions are sensitive to the temperature and proceed rapidly because of the high temperature. The large value of  $Y_{seed,out}$  means a decrease in the number of neutrons per one seed. As a result, it becomes difficult to synthesize heavy elements by the r-process for a large  $P_{out}$  value. In Fig. 1, we show the result of nucleosynthesis calculations and the solar r-process abundance pattern. From these reasons, we find that the heavier nuclei are synthesized with decreasing the  $P_{out}$  value. By the comparison with the solar abundance, the solid line is most likely in the case of  $1.4M_{\odot}$ .

### References

- 1) S. E. Woosley, J. R. Wilson, G. J. Mathews, R. D. Hoffman, and B. S. Meyer: *Astrophys. J.* **433**, 229 (1994).
- 2) B. S. Meyer: *Astrophys. J. Lett.* **449**, 55 (1995).
- 3) K. Sumiyoshi, H. Suzuki, K. Otsuki, M. Terasawa, and S. Yamada: *Publ. Astron. Soc. Jpn.* **52**, 601 (2000).
- 4) M. Terasawa, K. Sumiyoshi, T. Kajino, I. Tanihata, and G. Mathews: *Astrophys. J.* **562**, 470 (2001).

<sup>\*1</sup> Department of Astrophysics, University of Tokyo

<sup>\*2</sup> National Astronomical Observatory

<sup>\*3</sup> Numazu College of Technology

<sup>\*4</sup> Department of Physics, The University of Notre Dame, USA

# Neutrinos from supernova explosions and protoneutron stars

H. Suzuki,\*<sup>1</sup> K. Sumiyoshi,\*<sup>2</sup> S. Yamada,\*<sup>3</sup> and H. Toki\*<sup>4</sup>

[supernova, neutrinos, protoneutron star]

Using a new numerical EOS (equation of state) table calculated by Shen *et al.*,<sup>1)</sup> we performed numerical simulations of supernova explosions and protoneutron star cooling. The EOS is based on the relativistic mean field theory, and the parameters in its Lagrangian have been chosen to reproduce the experimental properties of both stable and unstable nuclei. Furthermore, the numerical table covers such a wide range of thermodynamical quantities (temperature, 0–100 MeV; electron fraction, 0–0.56; density,  $10^{5.1}$ – $10^{15.4}$  g/cc) that it is very useful for supernova simulations.

As a first step towards full simulations of core collapse and the subsequent explosion in massive stars, we have studied the adiabatic collapse of stellar cores. The initial core structures were taken from numerical stellar models of Woosley's group and Nomoto's group. The succeeding dynamics of the cores was calculated with a spherically symmetric, general-relativistic hydrodynamical code developed by Yamada.<sup>2)</sup> In order to explore the characteristics of Shen's EOS simply, we neglected electron capture and neutrino transport in the cores. This approximation could be used to estimate the upper limit of the core mass, which explodes promptly. As a result, we found, in precollapse cores, compositional differences between our models and those with popular Lattimer & Swesty's EOS: nuclei with neutron number greater than 40 are more abundant and free protons are less abundant in the cores with Shen's EOS. This might result in a reduction of the electron-capture rates during the core collapse, and would be preferable for successful prompt explosions. Hydrodynamical simulations without electron capture and neutrino transport for various initial cores show that light cores ( $\leq 1.4M_{\odot}$ ) explode promptly with bounce shock, while massive cores can not explode. We thus confirmed that even with Shen's new EOS the bounce shock wave alone cannot explode massive cores.

Another implication of our numerical simulations is r-process nucleosynthesis. If the core explodes promptly, neutron-rich material would be ejected and r-process nucleosynthesis might occur in the ejecta. Although this possibility was investigated formerly by Hillebrandt *et al.*, they used an artificial distribution

of electron fraction and concluded that too many r-process nuclei are synthesised to reproduce the observational data. On the other hand, we evaluated numerically the electron fraction of each shell of ejecta while considering the electron capture on free protons after the passage of shock. In collaboration<sup>3)</sup> with Terasawa, nucleosynthesis in each shell was studied using the calculated trajectory in the density-temperature plane and the electron fraction of each shell. The resultant relative abundance of heavy nuclei up to  $A \sim 200$  has good agreement with the observational data. In addition, our estimation of the total abundance of r-process nuclei ejected from past prompt supernovae indicates that there is no inconsistency between the observation and our numerical results. We point out a new interesting idea that relatively light r-process elements are formed in delayed supernovae, while heavy nuclei are synthesised in prompt supernovae.

We also investigated the quasistatic evolution of protoneutron stars with a numerical code including neutrino transfer (MGFLD scheme). Using the new EOS table<sup>1)</sup> covering a very wide thermodynamic regime, time evolution for even 50 seconds could be studied. Compared with simulations using Wolff's old EOS, the central temperature of the protoneutron star and the average energy of emitted neutrinos become somewhat lower, but the qualitative feature does not change. A lepton-rich initial model and a hot initial model were also studied, and we obtained the result that the average energy of non-electron-type neutrinos is not much higher than that of electron-type antineutrinos at the late stage of a supernova neutrino burst. This fact might affect the implication of SN1987A data on the neutrino oscillation parameters. More comprehensive studies including the collapse/explosion phase and convection/accretion effects are required.

## References

- 1) H. Shen, H. Toki, K. Oyamatsu, and K. Sumiyoshi: Nucl. Phys. A **637**, 435 (1998).
- 2) S. Yamada: Astrophys. J. **475**, 720 (1997).
- 3) K. Sumiyoshi, M. Terasawa, G. J. Mathews, T. Kajino, S. Yamada, and H. Suzuki: Astrophys. J. **562**, 880 (2001).

\*<sup>1</sup> Tokyo University of Science

\*<sup>2</sup> Numazu College of Technology

\*<sup>3</sup> Institute of Laser Engineering, Osaka University

\*<sup>4</sup> Research Center for Nuclear Physics, Osaka University

# Shell-Model calculations for ${}_{\Lambda}^{17}\text{O}$ and ${}_{\Lambda}^{16}\text{O}$ with microscopic $\Lambda\text{N}$ and $\Sigma\text{N}$ effective interactions

S. Fujii, R. Okamoto,\* and K. Suzuki\*

[Hypernuclei, Shell model, Effective interaction]

One of the challenging problems in theoretical studies of  $\Lambda$  hypernuclei is to describe their properties, starting from hyperon-nucleon (YN) and nucleon-nucleon (NN) interactions given in free space. The nuclear shell-model approach would be one of the promising methods for this problem over a wide range of mass numbers of  $\Lambda$  hypernuclei. In shell-model calculations, however, we need to introduce an effective interaction because of a limited model space. The microscopic derivation of an effective interaction for nuclear shell-model calculations is a fundamental problem for a microscopic understanding of nuclei.

We have proposed a method for a microscopic description of  $\Lambda$  hypernuclei within the framework of the unitary-model-operator approach (UMOA).<sup>1,2)</sup> UMOA is a many-body theory that leads to an energy-independent and Hermitian effective interaction with the property of decoupling. We have applied UMOA to calculations of  $\Lambda$  single-particle energies in  ${}_{\Lambda}^{17}\text{O}$  and  ${}_{\Lambda}^{41}\text{Ca}$ , using various YN interactions given by the Nijmegen and the Jülich groups. Some reasonable results have been obtained, such as small spin-orbit splittings of  $\Lambda$  compared with those in nuclei, though the results depend considerably on the YN interactions employed.

Lately, we have been making shell-model calculations for  ${}_{\Lambda}^{16}\text{O}$  in addition to  ${}_{\Lambda}^{17}\text{O}$ , using the effective interaction derived in previous works. Furthermore, we are trying to introduce a  $\Sigma\text{N}$  effective interaction into the shell-model calculation. In the shell-model calculations of  $\Lambda$  hypernuclei made so far, the effects of the  $\Sigma\text{N}$  channel have been treated as renormalization into a  $\Lambda\text{N}$  effective interaction in many cases. The degrees of freedom of  $\Sigma$  have not been treated explicitly in the shell-model calculations. Therefore, it is interesting to derive an effective YN interaction which includes not only the  $\Lambda\text{N}$  channel, but also the  $\Sigma\text{N}$  one, and to apply such an effective interaction to shell-model calculations for  $\Lambda$  hypernuclei.

As the first step, we have examined the effect of the  $\Sigma\text{N}$  channel on  $\Lambda$  single-particle energies in  ${}_{\Lambda}^{17}\text{O}$ . Figure 1 shows the dependence of the  $\Lambda$  single-particle energies for the Nijmegen soft-core (NSC) 89 and the NSC97f YN potentials on the the model-space size of the  $\Sigma\text{N}$  channel. The number  $\rho_Y$  for  $Y = \Lambda, \Sigma$  in Fig. 1 is defined as

$$\rho_Y = 2n_Y + l_Y + 2n_N + l_N, \quad (1)$$

with the harmonic-oscillator quantum numbers,

\* Department of Physics, Kyushu Institute of Technology

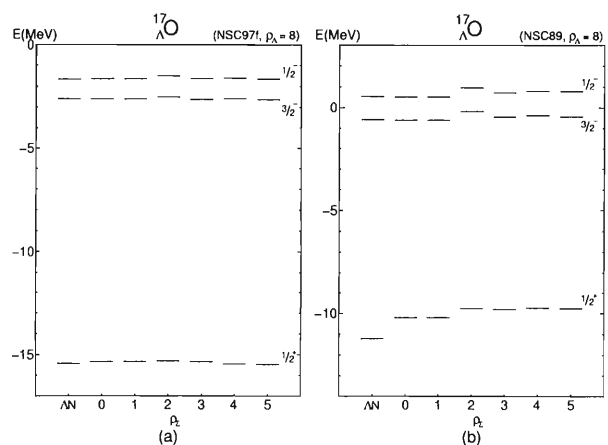


Fig. 1. Calculated energy levels in  ${}_{\Lambda}^{17}\text{O}$  for the NSC97f (a) and the NSC89 (b) potentials as a function of  $\rho_{\Sigma}$ . The energy levels with “AN” are the results without the  $\Sigma\text{N}$  channel in the model space.

$\{n_Y, l_Y\}$  and  $\{n_N, l_N\}$ , of the hyperon and the nucleon, respectively. As for the value of  $\rho_{\Lambda}$ , we fix it as  $\rho_{\Lambda} = 8$  which is a sufficiently large number to see the  $\rho_{\Sigma}$ -dependence. We can see that the results for the NSC97f (the left-hand side of Fig. 1) are almost stable for the values of  $\rho_{\Sigma}$ . This suggests that the renormalization of the effects of the  $\Sigma\text{N}$  channel into the  $\Lambda\text{N}$  effective interaction is very good. On the other hand, the results for the NSC89 (the right-hand side of Fig. 1) imply that we should take a number larger than 3 as  $\rho_{\Sigma}$  to obtain convergent results. This is mainly because of the strong  $\Sigma\text{N}$ - $\Lambda\text{N}$  coupling effect of the NSC89 potential.

A high-resolution gamma-ray spectroscopy experiment for  ${}_{\Lambda}^{16}\text{O}$  is in progress at BNL. Fine structures reflecting the properties of the underlying YN interactions should be obtained. Therefore, it is of great importance to investigate the origin of the fine structure from a microscopic point of view. We are now performing a shell-model calculation for  ${}_{\Lambda}^{16}\text{O}$ , using not only the  $\Lambda\text{N}$  effective interaction, but also the  $\Sigma\text{N}$  one. The calculation result for  ${}_{\Lambda}^{16}\text{O}$  will be reported elsewhere in the near future.

## References

- 1) S. Fujii, R. Okamoto, and K. Suzuki: Nucl. Phys. A **651**, 411 (1999); Nucl. Phys. A **676**, 475 (2000).
- 2) S. Fujii, R. Okamoto, and K. Suzuki: Prog. Theor. Phys. **104**, 123 (2000).

# Nuclear $\bar{K}$ bound states in proton-rich systems to be formed by $(K^-, \pi^-)$ reactions through $\Lambda^*$ as a doorway

T. Yamazaki and Y. Akaishi\*

[kaon, strangeness few-body systems]

We propose to form very exotic nuclear  $\bar{K}$  bound states in proton-rich systems using  $(K^-, \pi^-)$  reactions. The structure of  $K^-pp$ ,  $K^-ppp$  and  $K^-pppn$  was predicted to be deeply bound by variational calculations based on  $\bar{K}N$  interactions, which we derived previously to predict deeply bound  $K^-ppn$  and  $K^-ppnn$ .<sup>1)</sup> Figure 1 shows the calculated  $\bar{K}N$  and  $\bar{K}$ -nucleus potentials and the bound levels in  $\Lambda(1405)$ ,  ${}^2_{\bar{K}}\text{H}$  and  ${}^3_{\bar{K}}\text{H}$  for the  $K^-p$ ,  $K^-pp$  and  $K^-ppn$  systems, respectively.

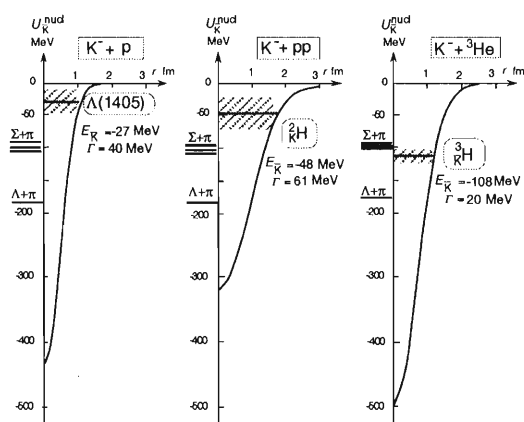


Fig. 1. Calculated  $\bar{K}N$  and  $\bar{K}$ -nucleus potentials and bound levels:  $\Lambda(1405)$ ,  ${}^2_{\bar{K}}\text{H}$  and  ${}^3_{\bar{K}}\text{H}$  for  $K^-p$ ,  $K^-pp$  and  $K^-ppn$  systems, respectively. The nuclear contraction effect is taken into account. The shaded zones indicate the widths. The  $\Sigma\pi$  and  $\Lambda\pi$  emission thresholds are also shown.

Table 1.  $\bar{K}$  nuclei produced by  $(K^-, \pi^-)$ .

Target	$\bar{K}$ nucleus	$[B, \Gamma]$
d	${}^2_{\bar{K}}\text{H} = K^-pp$	[38,51]
${}^3\text{He}$	${}^3_{\bar{K}}\text{He} = K^-ppp$	
${}^4\text{He}$	${}^4_{\bar{K}}\text{He} = K^-pppn$	
${}^9\text{Be}$	${}^9_{\bar{K}}\text{Be} = K^-p\alpha\alpha$	

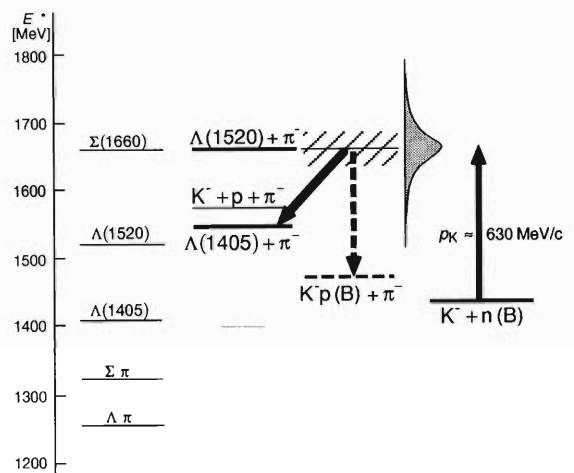


Fig. 2. Energy diagram relevant to the formation of  $\bar{K}$  bound states in  $(K^-, \pi^-)$  reactions through  $\Lambda(1520) + \pi^-$  resonance as a doorway.

The reason for this deep binding is due to a strong attraction between  $K^-$  and p, which helps to contract the nucleus (unbound without  $K^-$ ) to which  $K^-$  is bound.

A possible formation process for  $\bar{K}$  bound states in the  $(K^-, \pi^-)$  reactions was proposed; that is, the elementary production of  $\Lambda(1405)$  and  $\Lambda(1520)$  in  $n(K^-, \pi^-)\Lambda^*$  propagates in the nucleus and serves as a doorway for the formation of  $\bar{K}$  bound states (see Fig. 2).

Table 1 shows light target nuclei and  $\bar{K}$  bound states to be formed through  $\Lambda$  doorways by the  $(K^-, \pi^-)$  reaction, as well as for the calculated binding energies ( $B$  in MeV) and widths ( $\Gamma$  in MeV) with nuclear contraction.

## References

- 1) Y. Akaishi and T. Yamazaki: Nucl. Phys. A **684**, 409c (2000).
- 2) Y. Akaishi and T. Yamazaki: Phys. Rev. C, in press.

\* Institute of Particle and Nuclear Studies, High Energy Accelerator Research Organization (KEK)

# Coulomb logarithm in the electron-cooling process

H. Amemiya, T. Tanabe, and T. Katayama

[Electron cooling, Coulomb collision, Coulomb logarithm, Ion beam]

In the conventional theory<sup>1,2)</sup> of electron cooling, the Coulomb logarithm is assumed to be a constant. It is considered to be only weakly dependent on the relative velocity between an ion and electrons. However, this assumption is not always accurate for ions with a velocity comparable to, or less than, the electron thermal velocity where the most efficient cooling is expected. In the present work, the cooling rate is calculated more precisely by taking the Coulomb logarithm as a variable.

The loss rate of the momentum  $\mathbf{P}$  of an ion travelling with a velocity  $\mathbf{V}$  in electrons with a velocity distribution  $f(\mathbf{v})$  is

$$\frac{d\mathbf{P}}{dt} = -\frac{4\pi Q}{m} \int L_c \frac{\mathbf{V}}{U} \cdot \frac{f(\mathbf{v})}{U^2} d\mathbf{v}; \quad \frac{\mathbf{V}}{U} = \frac{\partial U}{\partial \mathbf{V}}, \quad (1)$$

where  $Q = N_e Z^2 e^4 / (4\pi\epsilon_0)^2$ ,  $N_e$  is the electron density,  $Z$  is the charge of ion,  $U = (V^2 + v^2 - 2Vv \cos\theta)^{1/2}$ ,  $L_c = \ln(\lambda/\rho)$  is the Coulomb logarithm,  $\lambda$  is the Debye length,  $\rho$  is the minimum access distance given by  $\rho = Ze^2 / (4\pi\epsilon_0 m V^2)$ ,  $m$  is the reduced mass given by  $m^{-1} = m_e^{-1} + M^{-1}$ ,  $M$  is the ion mass, and  $e$ ,  $m_e$  are the electron charge and mass, respectively.

We seek a potential  $\Phi$  which satisfies

$$-\frac{\partial \Phi}{\partial V} = -\frac{4\pi Q}{m} \int L_c \frac{\mathbf{V}}{U} \cdot \frac{1}{U^2} f(\mathbf{v}) d\mathbf{v}. \quad (2)$$

Using the fact that  $L_c$  consists of constant and variable parts as

$$L_c = L_o + \ln\left(\frac{U}{s}\right)^2; \quad L_o \equiv \ln(6N_D/Z), \quad (3)$$

where  $N_D = (4\pi/3)N_e\lambda^3$ ,  $s = (2\kappa T_e/m)^{1/2}$ , we find

$$\Phi(V) = -\frac{4\pi Q}{m} \int \frac{(L_o + 2) + \ln(U/s)^2}{U} f(\mathbf{v}) d\mathbf{v}. \quad (4)$$

Thus, the rate of energy cooling becomes

$$\frac{dE_{\parallel}}{dt} = \mathbf{V} \cdot \frac{d\mathbf{P}}{dt} = -\mathbf{V} \cdot \nabla_V \Phi(V). \quad (5)$$

The rate of energy broadening is given by integrating  $\nabla \cdot (\nabla U)$  over  $f(\mathbf{v})$  as

$$\frac{dE_{\perp}}{dt} = \frac{1}{2} \frac{4\pi Q}{M} \int L_c (\Delta_V U) f(\mathbf{v}) d\mathbf{v}, \quad (6)$$

where  $\Delta_V$  is the Laplacian.

Defining another potential,

$$\Psi(V) = -\frac{1}{2} \frac{4\pi Q}{m} \int L_c U f(\mathbf{v}) d\mathbf{v}, \quad (7)$$

we can express

$$\frac{dE_{\perp}}{dt} = -\frac{m}{M} \left[ \Delta_V \Psi(V) + 3 \cdot \frac{4\pi Q}{m} \int \frac{f(\mathbf{v})}{U} d\mathbf{v} \right], \quad (8)$$

$$\Delta_V \Psi(V) = \Phi(V) - \frac{4\pi Q}{m} \int \frac{1}{U} f(\mathbf{v}) d\mathbf{v}. \quad (9)$$

We also define dimensionless functions of  $\alpha = V/s$ ,  $\phi_1$  and  $\phi_2$ , as

$$\phi_1(\alpha) = -\int \frac{1}{(U/s)} f(\mathbf{v}) d\mathbf{v}, \quad (10)$$

$$\phi_2(\alpha) = -\int \frac{\ln(U/s)^2}{(U/s)} f(\mathbf{v}) d\mathbf{v}. \quad (11)$$

While  $\phi_1$  is a conventional function,<sup>1,2)</sup>  $\phi_2$  is a function for a modification. The relations similar to the electrostatics<sup>3)</sup> for the case of constant  $L_c$ ,  $\Delta_V \Psi = \Phi$  and  $\Delta_{\alpha} \phi = f(\mathbf{v})$ , are modified by Eq. (9) and  $\Delta_{\alpha} \phi_1 = f(\mathbf{v})$ ,  $\Delta_{\alpha} \phi_2 = \ln(\alpha^2) f(\mathbf{v})$  respectively, for the case of variable  $L_c$ .

Then, (5) and (8) become

$$\frac{dE_{\parallel}}{dt} = -C\alpha \{ (L_o + 2) \nabla_{\alpha} \phi_1(\alpha) + \nabla_{\alpha} \phi_2(\alpha) \}, \quad (12)$$

$$\frac{dE_{\perp}}{dt} = -C \frac{m}{M} \{ L_o \phi_1(\alpha) + \phi_2(\alpha) \}, \quad (13)$$

where  $C = 4\pi Q/ms$ . Note that these relations hold for any forms of  $f(\mathbf{v})$ . If Eqs. (12) and (13) are integrated for the ion velocity distribution  $F(\mathbf{V})$ , we obtain the cooling and broadening rates of an ion beam. In this case, it is sufficient to calculate  $\phi_1$  and  $\phi_2$ , since  $\nabla_{\alpha} \phi_1$  and  $\nabla_{\alpha} \phi_2$  disappear by partial integration.

As typical cases of  $f(\mathbf{v})$ , an isotropic Maxwellian distribution (non magnetic case) and a two-temperature distribution (frozen case) have been dealt with, where besides the elliptic function  $K(k)$  a logarithmic-elliptic function  $L(k)$  is introduced, *i.e.*

$$L(k) = \int_0^{\pi/2} \frac{\ln(1 - k^2 \sin^2 \theta) d\theta}{\sqrt{1 - k^2 \sin^2 \theta}}. \quad (14)$$

It has been found that the cooling rate of the previous theory<sup>1,2)</sup> is overestimated for ions with velocities larger than  $(2\kappa T_e/m)^{1/2}$  while the energy broadening rate is underestimated for all ion velocities. More details on cooling and energy broadening rates using  $\phi_1$  and  $\phi_2$  are forthcoming.

## References

- 1) H. Poth: Phys. Rep. **196**, 135 (1990).
- 2) I. N. Meshkov: Phys. Part. Nucl. **25**, 631 (1994).
- 3) B. A. Trubnikov: in *Reviews of Plasma Physics*, Vol. 1, edited by M. A. Leontovich (Consultants Bureau, New York, 1966), p. 105.

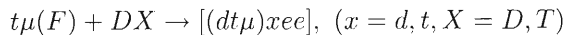
## Measurement of the effect of a non-equilibrium liquid $D_2+T_2$ mixture in muon-catalyzed $dt$ fusion

K. Ishida, K. Nagamine, T. Matsuzaki, N. Kawamura,\*<sup>1</sup> S. N. Nakamura,\*<sup>2</sup> Y. Matsuda, M. Kato,\*<sup>3</sup> H. Sugai,\*<sup>3</sup> M. Tanase,\*<sup>3</sup> K. Kudo,\*<sup>4</sup> N. Takeda,\*<sup>4</sup> and G. H. Eaton\*<sup>5</sup>

[Muon catalyzed fusion, tritium, fusion neutron]

One of the critical steps in the muon catalysis fusion cycle ( $\mu$ CF) is the formation of muonic molecular ions. The  $dt\mu$ -formation rate ( $\lambda_{dt\mu}$ ) has to be much faster than the muon decay rate ( $\lambda_0 = 0.45 \times 10^6 \text{ s}^{-1}$ ) for the  $\mu$ CF to catalyze many  $dt$ -fusions. Concerning  $dt\mu$  formation by a collision of  $t\mu$  with  $D_2$  or  $DT$ , a resonant formation mechanism has been proposed to explain an unexpectedly large formation rate.<sup>1)</sup> In this process, the  $dt\mu$ -molecular binding energy resonantly goes to the vibrational and rotational energy of the final compound molecule ( $[(dt\mu)dee]^*$  etc.) and any small energy difference between the initial and final states is compensated by the kinetic energies of the participating atoms and molecules.

In contrast to the nonresonant (Auger) process, the resonant process depends on the temperature as well as the states of the participating atoms and molecules. Among various  $dt\mu$  molecular formation rates,  $\lambda_{dt\mu-x}^F$ ,



where  $F$  is the hyperfine state,  $\lambda_{dt\mu-d}^0$  for a singlet  $t\mu$  colliding with  $D_2$  molecule was calculated to make a dominant contribution at low temperature. However, so far, the temperature dependence of the  $dt\mu$  formation rate, which was measured mostly on equilibrated targets, is not fully explained by the calculation. Thus, an experiment which can measure the contributions of  $D_2$  and  $DT$  molecules separately is essential to understand the resonant mechanism correctly, and would give us a key to improving the catalysis efficiency.

When we mix  $D_2$  and  $T_2$ , an equilibrium state is reached due to the reaction  $D_2 + T_2 \rightleftharpoons 2DT$ . It is known that this reaction is rapid (order of 10 minutes) in the room-temperature gas phase, while it is slow (a few days) in the low-temperature liquid. Thus, if we mix  $D_2$  and  $T_2$  in the liquid phase and observe how the  $\mu$ CF neutron yield is affected as the equilibrium is gradually reached, we can separate the contributions of  $D_2$  and  $DT$  molecules to  $dt\mu$ -molecule formation.

The experiment was performed at the RIKEN-RAL Muon Facility.  $D_2$  gas and  $T_2$  gas were separately prepared and solidified at 15 K one after another in the target chamber. The target was then warmed up to

20 K to become the liquid state. Figure 1 shows the measured neutron disappearance rate ( $\lambda_n$ ), neutron yield per muon ( $Y_n$ ),  $\mu$ CF cycling rate ( $\lambda_c = \lambda_n Y_n / \phi$ ) and the muon loss per cycle ( $W = (\lambda_n - \lambda_0) / \phi \lambda_c$ ) as a function of time after  $D_2+T_2$  mixing. Data were taken for the liquid state (open circles in Fig. 1) up to 110 hours after  $D_2+T_2$  mixing. The target gas was then warmed up to room temperature so that the equilibration would proceed completely. The gas was liquefied again to obtain data for a fully equilibrated target (filled circles in Fig. 1).

It can be seen that the cycling rate was enhanced by 30% in the non-equilibrium state just after  $D_2+T_2$  mixing, while the muon loss probability was almost constant. These results are well explained by taking into account the resonant mechanism and the equilibration process with a time constant of 56 hours. A preliminary analysis shows that  $\lambda_{dt\mu-d}^0 \sim 4\lambda_{dt\mu-t}^0$ , which is consistent with the theory, at least qualitatively. A detailed analysis is in progress.

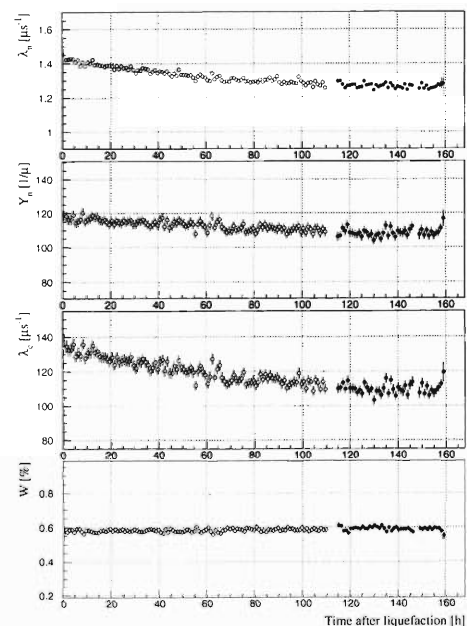


Fig. 1. Measured neutron disappearance rate ( $\lambda_n$ ), neutron yield ( $Y_n$ ), cycling rate ( $\lambda_c$ ) and muon loss per cycle ( $W$ ) as a function of time after  $D_2$  and  $T_2$  mixing.

\*<sup>1</sup> High Energy Accelerator Research Organization (KEK)

\*<sup>2</sup> Tohoku University

\*<sup>3</sup> Japan Atom Energy Research Institute

\*<sup>4</sup> National Institute of Advanced Industrial Science and Technology

\*<sup>5</sup> Rutherford Appleton Laboratory, UK

### References

- 1) E. A. Vesman: Zh. Eks. Theo. Fiz. Pis. **5**, 50 (1967). (Sov. Phys. JETP Lett. **5**, 91 (1967).)

## Electron-RI collider at MUSES: A possible electron spectrometer

T. Suda, S. Kato,<sup>\*1</sup> K. Maruyama,<sup>\*2</sup> and I. Tanihata

[Electron-RI collider, charge distribution, high resolution spectrometer]

A collider of electrons and radioactive ion beams, the eRI collider, planned for the second phase of the RIKEN RI Beam Factory project, aims to explore the not-yet-determined charge distribution of many unstable nuclei by elastic electron scattering, and at providing one of the most fundamental observables to investigate exotic nuclear structures of unstable nuclei far from the stability line.

As we have previously reported,<sup>1-3)</sup> the feasibility of the eRI collider has been demonstrated and the accessible nuclei at the collider have been identified under the expected luminosities. In addition to this study, the requirements for an electron spectrometer to measure the elastic scattering cross section has already been clarified.

Since the elastic-scattering cross section of unstable nuclei is to be measured, the excitation-energy resolution at the Nucleus-Rest (NR) frame of  $\Delta\omega_{NR} \sim 0.1$  MeV will be indispensable. This requirement is equivalent to the momentum resolution of  $10^{-4}$  for electron detection in the Collider (COL) frame, which requires a high-resolution spectrometer instead of a medium-resolution large-acceptance spectrometer, such as CLAS at JLAB.

In this report, we present a possible electron spectrometer for the collider experiments currently under discussion. As shown in Fig. 1, it is a QD-type spectrometer, whose Q magnet is one of the optical elements of the collider. The collision takes place inside the Q magnet, and scattered electrons appear from the side of the magnet. The pole shape of the Q magnet at the exit of both sides is designed to provide a dipole field in order to give a further kick to the scattered electrons. The design of this special Q magnet is also underway with this spectrometer design.

The advantage of this ‘beam-line’ spectrometer is the ability to cover a very forward scattering angle, such as a few degrees, without any serious interference with the collider, where the Mott cross section rapidly becomes large. Another advantage is to have a wide scattering angular range which covers a wide range of the momentum transfer,  $q_{NR}$ , at a time.

This spectrometer has a scattering-angle coverage of 200 mrad in the horizontal plane. The gap of the dipole is 25 cm, corresponding to a vertical angular acceptance of 100 mrad. In addition, the expected finite interaction region in the longitudinal direction ( $\sim$

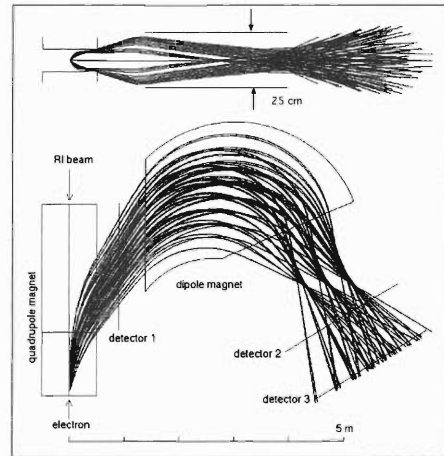


Fig. 1. Proposed electron spectrometer for the eRI collider of MUSES.

10 cm) is well covered by its acceptance. By adjusting the collision point in the longitudinal direction, this spectrometer can cover a different scattering angular range from 100 to 700 mrad. The first-order momentum resolution is  $1/7200$ , which is very close to the requirements mentioned above.

At electron scattering facilities, such as MAMI and JLAB, a vertical-bending spectrometer is often employed. This is not only because one can rotate the spectrometer to a very backward angle, but also because measurements of the momentum and scattering angle are decoupled, at least in the first-order optics.

We, however, employ a spectrometer which bends scattered electrons horizontally, in order to realize a large scattering-angle coverage. This configuration requires the insertion of a position detector (“detector 1”) between the Q and D magnets in addition to the focal-plane detectors (“detector 2” and “detector 3”) for determining of the momentum and scattering angle. To avoid multiple-scattering effects in the inserted detector, which distort the scattering-angle information, the detector must have a sufficiently small material thickness.

### References

- 1) T. Suda, K. Maruyama, and I. Tanihata: RIKEN Accel. Prog. Rep. **33**, 52 (2000).
- 2) T. Suda, K. Maruyama, and I. Tanihata: RIKEN Accel. Prog. Rep. **34**, 49 (2001).
- 3) T. Suda: A proposal for RIKEN RI Beam Factory, F01-23 (<http://rarfaxp.riken.go.jp/~suda/eRI/proposal.pdf>, 2001).

<sup>\*1</sup> Yamagata University

<sup>\*2</sup> Kitasato University

## High-spin isomeric beam line

T. Kishida, H. Watanabe, E. Ideguchi, T. Kubo, Y. Yang, M. Ishihara, S. Yamamoto, Y. Gono,<sup>\*1</sup>  
 T. Morikawa,<sup>\*1</sup> T. Tsutsumi,<sup>\*1</sup> T. Fukuchi,<sup>\*1</sup> S. Motomura,<sup>\*1</sup> H. Tsuchida,<sup>\*1</sup> O. Kashiyama,<sup>\*1</sup> K. Saitoh,<sup>\*1</sup>  
 M. Shibata,<sup>\*1</sup> A. Odahara,<sup>\*2</sup> Y. Zhang,<sup>\*3</sup> X. Zhou,<sup>\*3</sup> B. Cederwall,<sup>\*4</sup> T. Bäck,<sup>\*4</sup> and D. Bucurescu<sup>\*5</sup>

[NUCLEAR REACTIONS,  $^{16}\text{O}(^{136}\text{Xe},7n)^{145m}\text{Sm}$ ,  $^{13}\text{C}(^{145m}\text{Sm},xn)$ , Radioactive beams, Isomer]

A high spin isomeric beam line has been constructed at RIKEN utilizing the inverse kinematics of fusion-evaporation reactions. The secondary beams of fusion reaction residues produced in a gas target are collected with a superconducting solenoid and transported to the secondary target position through the RIPS. The principle of separation between the secondary beams and the primary beam is based on the magnetic rigidity and the charge state distributions. For better separation, a charge stripper section is placed between the superconducting solenoid and the RIPS. Rectangular slits of variable widths and positions have been placed at the dispersive focal plane F1, in order to reduce the intensity of the primary beam transported to F3.

In a recent experiment, a high spin isomeric beam of  $^{145m}\text{Sm}$  with a spin of  $49/2\hbar$  and a half-life of  $0.96\ \mu\text{s}$  was used, which was produced via the reaction  $^{16}\text{O}(^{136}\text{Xe}, 7n)^{145m}\text{Sm}$ . The energy and intensity of the projectile were  $7.6\ \text{A MeV}$  and  $3 \times 10^{11}$  ions/s, respectively. The thickness of the target material ( $\text{CO}_2$  gas) was  $0.91\ \text{mg}/\text{cm}^2$ . The stripper foil was a  $0.8\ \mu\text{m}$ -thick Al foil, and the solenoid was operated under the condition that the beam optics was a point-to-parallel setting. The obtained intensity of the  $^{145m}\text{Sm}$  high spin isomeric beam was  $1\text{--}2 \times 10^5$  pps with a kinematic energy of  $5.53 \pm 0.11\ \text{A MeV}$ . The main impurities were due to contamination of the primary beam. The ratios of all the components in the charged particles at the experimental focal point were 10% for the  $^{145m}\text{Sm}$  isomer, 10% for the  $^{145}\text{Sm}$  ground state, 50% for the other reaction products and 30% for both direct and indirect (scattered) contaminations of the  $^{136}\text{Xe}$  primary beam.

However, when the first experiment concerning the secondary fusion reaction  $^{13}\text{C}(^{145m}\text{Sm}, xn)^{158-x}\text{Er}$  was performed, the purity of the high spin isomeric beam became much worse due to a change in the primary beam condition. A careful analysis of the time structure of neutron evaporation events revealed the fraction of each background component. Fig. 1 A-C indicate the variations of the  $\gamma$ -ray intensities in Nd isotopes as a function of the time difference between the

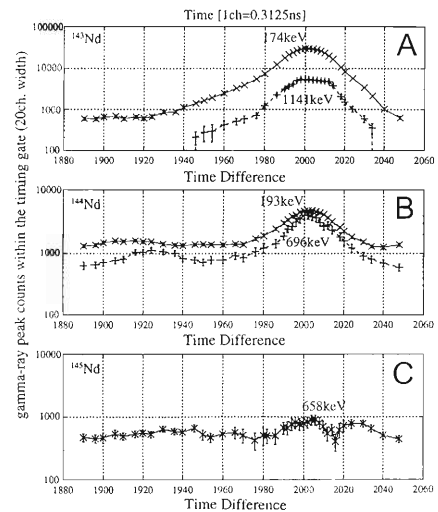


Fig. 1. Time structures of the  $\gamma$ -ray intensities in Nd's.

RF signals and the neutron counter signals. A prominent ridge around channel number 2000 in the figures was formed by the fusion products with direct contamination by  $^{136}\text{Xe}$ . From these spectra, the intensity of each component can be roughly estimated: 0.34% for the  $^{145m}\text{Sm}$  isomer, 0.34% for the  $^{145}\text{Sm}$  ground state, 1.7% for the other reaction products, more than 85% for direct  $^{136}\text{Xe}$  and more than 12% for indirect  $^{136}\text{Xe}$ . Even under such a bad condition, four peaks corresponding to the transitions in the yrast band of  $^{154}\text{Er}$  were identified.

Improvements were recently made in the gas target and primary beam handling system in order to reduce both the direct and indirect components of  $^{136}\text{Xe}$ . To improve the gas target, the thickness of the apertures was made thinner; 14 mm-thick brass apertures of the gas cell were replaced by  $100\ \mu\text{m}$ -thick tantalum, and the 10 mm-thick aluminum apertures of the outer chambers by  $100\ \mu\text{m}$ -thick tantalum. This improvement reduced the indirect component. For improving the primary beam handling system, a movable collimating slit was placed on the beam axis before the gas target system in order to limit the emittance of the primary beam and to make the downstream beam more stable and more insensitive to the operating condition of the accelerator. This improvement reduced the indirect component by preventing irradiation of the target cell. It also made the beam spot more stable at F1, thus reducing the direct component.

<sup>\*1</sup> Department of Physics, Kyushu University

<sup>\*2</sup> Nishinippon Institute of Technology

<sup>\*3</sup> Institute of Modern Physics, China

<sup>\*4</sup> Royal Institute of Technology, Sweden

<sup>\*5</sup> Horia Hulubei National Institute of Physics and Nuclear Engineering, Romania

## NaI(Tl) response for radioactive isotope beams

T. Suda, M. Chiba, T. Izumikawa,\* R. Kanungo, T. Kato, A. Ozawa, T. Suzuki,\* I. Tanihata, T. Yamaguchi, and T. Zheng

[Total energy detector, nuclear reaction rate, response functions]

A NaI(Tl) detector has been demonstrated to be a good total-energy detector for particle identification in a heavy-ion involved reaction. For instance, an energy resolution of 0.7% (FWHM) was obtained for a 110A-MeV  $^{22}\text{Ne}$  beam. In spite of its excellent energy resolution, the nuclear reaction contribution inside the total energy detector is not negligible, which introduces a serious background for particle identification. In the case of the 110A-MeV  $^{22}\text{Ne}$  beam, about 7% of the total events is found to suffer nuclear reactions.

Since the nuclear reaction rate must depend on the reaction cross section of the incident nucleus, the NaI(Tl) response to exotic nuclei, such as a halo nucleus, is expected to differ from the others. In order to develop a total-energy detector, which has a good energy resolution and a smaller nuclear reaction contribution, it is important to understand the nuclear reaction contribution inside a total-energy detector.

The NaI(Tl) response functions have been measured for several radioactive isotopes, whose  $A/Z$  is close to 3 at the RIPS beam line using a  $^{22}\text{Ne}$  beam of 110A MeV. No degrader has been placed at F1, and the fragments have been transported to a NaI(Tl) detector placed at F3. The size of the NaI(Tl) crystal is  $3''\phi \times 6$  cm, and the position of the fragments on the NaI(Tl) crystal have been monitored by two PPACs placed at F3. Particle identification was performed based on the standard  $B\rho\text{-}\Delta E\text{-TOF}$  method.

Figure 1 shows the response functions for isotopes of  $Z = 3, 4, 5$  and 6. In Table 1, the kinetic energy of the fragments, their range in the crystal and the nuclear rate experimentally determined are shown. The width of the full-energy peaks shown in Fig. 1 is about 1.2% (FWHM), which is consistent with the width of the momentum slit at F1.

The nuclear reaction rate of the fragments (11–28%) are larger compared with that for the primary  $^{22}\text{Ne}$  beam (7%). Especially, it reaches nearly 30% for  $^{11}\text{Be}$ , which is known to be a halo nucleus.

How can we understand this? We correct the reaction rate due to a range difference by a simulation. A longer range for smaller  $Z$  fragments may introduce a larger nuclear reaction rate. The simulation program is coded to estimate the nuclear reaction rate in the NaI(Tl) crystal by using the reaction cross section calculated by a phenomenological formula proposed by Kox *et al.*<sup>1)</sup> The energy dependence of the reaction cross section is taken into account above

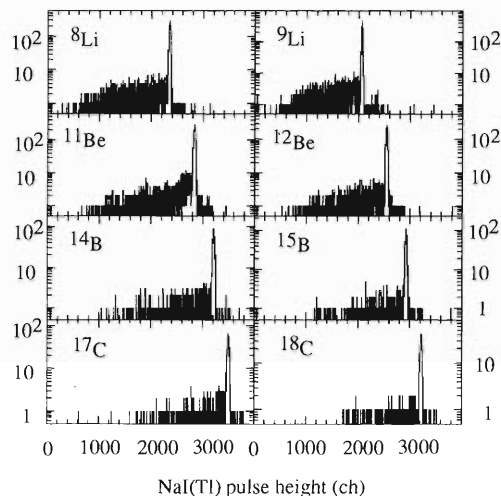


Fig. 1. Pulse height spectra of the NaI(Tl) detector for radioactive isotope beams.

Table 1. Nuclear reaction rate in the NaI(Tl) detector with the results of a simulation.

	energy (MeV/u)	range (g/cm <sup>2</sup> )	reaction rate (%)	simulation (%)
$^{22}\text{Ne}$	110	3.5	7	6.8
$^8\text{Li}$	108	13.9	$28 \pm 0.6$	18
$^9\text{Li}$	87	10.6	$25 \pm 0.4$	15
$^{11}\text{Be}$	102	9.5	$27 \pm 0.5$	15
$^{12}\text{Be}$	85	7.7	$17 \pm 0.4$	12
$^{14}\text{B}$	97	7.3	$22 \pm 0.8$	12
$^{15}\text{B}$	83	5.9	$13 \pm 0.6$	10
$^{17}\text{C}$	93	5.5	$15 \pm 0.6$	10
$^{18}\text{C}$	82	4.7	$11 \pm 0.9$	9

10 MeV/nucleon, where the formula is believed to work reasonably well.

The results of the simulation, presented together in the table, account for the larger fraction of the nuclear reaction contribution for lower  $Z$ , which comes from the longer range compared with  $^{22}\text{Ne}$  and larger  $Z$  isotopes.

The simulation is found to give a good estimate of the nuclear reaction rate for  $^{22}\text{Ne}$ , but underestimates the rate for radioactive splices. It also underestimates by a factor of almost two for a halo nucleus,  $^{11}\text{Be}$ , which may indicate that the reaction cross section of  $^{11}\text{Be}$  is much larger than the Kox's prediction.

### References

- 1) S. Kox *et al.*: Phys. Rev. C **35**, 1678 (1987).

\* Niigata University

## Absolute detection efficiency measurement of large plastic scintillators for neutrons at 100 MeV

S. Okada,<sup>\*1</sup> T. Hayashi,<sup>\*1</sup> K. Hirai,<sup>\*1</sup> H. Ikeda,<sup>\*1</sup> K. Itahashi,<sup>\*1</sup> M. Iwasaki,<sup>\*1</sup> T. Katayama,<sup>\*1</sup> M. Miura,<sup>\*1</sup>  
A. Miyajima,<sup>\*1</sup> T. Nakamura,<sup>\*1</sup> M. Sato,<sup>\*1</sup> T. Sugimoto,<sup>\*1</sup> D. Tomono,<sup>\*1</sup> T. Yoneyama,<sup>\*1</sup> T. Nagae,<sup>\*2</sup>  
H. Outa,<sup>\*2</sup> H. C. Bhang,<sup>\*3</sup> B. H. Kang,<sup>\*3</sup> J. H. Kim,<sup>\*3</sup> H. J. Lim,<sup>\*3</sup> T. Suzuki,<sup>\*4</sup> H. Baba,<sup>\*5</sup> and N. Fukuda

[Detection efficiency, Plastic scintillators]

In our recent nuclear experiments<sup>1,2)</sup> at KEK-PS, many large plastic scintillation counters (1–2 [m]) have been used for detecting neutrons of 10–200 MeV so as to achieve both a large solid angle and a sufficient TOF length. It is indispensable to measure the absolute detection efficiency for neutrons within 10% error. We performed a test experiment (MS108) to measure the neutron detection efficiency for our two large plastic counters whose sizes are  $100 \times 20 \times 5$  [cm] ( $\times (3 \times 2)$  counters) and  $200 \times 30 \times 3$  [cm] ( $\times 2$  counters), respectively. Since the cross section of the  ${}^7\text{Li}(p, n_0, 1){}^7\text{Be}$  (g.s.+0.43 MeV) reaction was measured with less than a 6%<sup>3)</sup> error, the quasi-monoenergetic neutrons produced via this reaction were used as a neutron source.  $n_0$  and  $n_1$  denote the neutrons produced from a reaction in which the residual nuclide  ${}^7\text{Be}$  is produced in the ground and first excited states, respectively. Although these two states cannot be distinguished due to the limit of the TOF resolution, they have sufficient ability to be employed as a monoenergetic neutron source. The  $\text{H}_2^+$  beam from the RIPS beamline was used as an incident proton beam at 100 MeV.

These neutron counters were located at a distance of 5 meters from a  ${}^7\text{Li}$  production target, which had  $0.2\text{g}/\text{cm}^2$  thickness. The configuration of these counters was arranged so as to be close in the real setup of our KEK experiments; we piled and layered these neutron counters. The same charged-particle veto counters as that of our experiments were installed in front of the neutron counters. The number of incident protons was counted by a small counter located in front of the production target. This counter had a thickness of 1 mm. Thus, the neutrons produced by the reactions at this small counter was one of the main neutron background sources. The protons scattered at the production target were prevented from hitting the neutron counters by using a sweep magnet (13 kG). However, because a beam dump was located at a distance of about 4 meters from the neutron counters, the neutrons caused by dumped protons could be a background source. Therefore, we made empty target runs for estimating of these backgrounds.

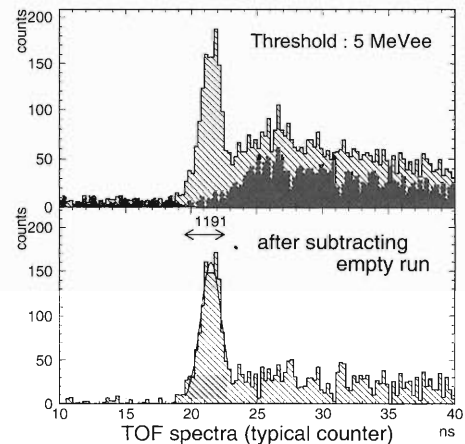


Fig. 1. TOF spectra for a typical counter at 5 MeV threshold.

The TOF spectrum for a typical counter at a 5 MeV electron-equivalent threshold is shown in the top of Fig. 1. The dashed line shows the spectrum for an empty run. We could clearly observe a sharp peak coming from ground and the first excited state (g.s.+0.43 MeV). Because any accidental background can be evaluated from the yield at the faster components than this peak, this background was evaluated to be less than 6%. The spectrum after subtracting the empty run is shown at the bottom. By gating this peak, the number of events from ground and the first excited state could be accurately counted.

Now a detailed analysis of the detection efficiency is in progress. Comparing the results of this analysis with those of Monte-Carlo simulation codes for the neutron detection efficiencies, CECIL<sup>4)</sup> and SCINFUL,<sup>5)</sup> we will certify the accuracy of the absolute detection efficiency and its dependencies on the threshold. Detecting neutrons by large plastic scintillators has recently been a key point in the field of nuclear experiments. The results of this experiment will offer data for this study.

### References

- 1) H. Outa et al.: KEK-PS E462 proposal (2000).
- 2) M. Iwasaki et al.: Nucl. Instrum. Methods Phys. Res. A **473**, 286 (2001).
- 3) T. N. Taddeucci et al.: Phys. Rev. C **41**, 2548 (1990).
- 4) R. A. Cecil, B. D. Anderson, and R. Madey: Nucl. Instrum. Methods **161**, 439 (1979).
- 5) J. K. Dickens: ORNL-6436, Oak Ridge National Laboratory (1988).

<sup>\*1</sup> Department of Physics, Tokyo Institute of Technology

<sup>\*2</sup> Institute of Particle and Nuclear Studies, High Energy Accelerator Research Organization (KEK)

<sup>\*3</sup> Department of Physics, Seoul National University, Korea

<sup>\*4</sup> Department of Physics, University of Tokyo

<sup>\*5</sup> Department of Physics, Rikkyo University

## Polarization transfer measurement for $d$ - $p$ elastic scattering

K. Sekiguchi,<sup>\*1</sup> H. Sakai,<sup>\*1</sup> A. Tamii,<sup>\*1</sup> K. Yako,<sup>\*1</sup> S. Sakoda,<sup>\*1</sup> H. Kato,<sup>\*1</sup> Y. Maeda,<sup>\*1</sup> M. Hatano,<sup>\*1</sup> T. Saito,<sup>\*1</sup> N. Uchigashima,<sup>\*1</sup> H. Okamura,<sup>\*2</sup> T. Uesaka,<sup>\*2</sup> K. Suda,<sup>\*2</sup> J. Nishikawa,<sup>\*2</sup> N. Sakamoto,<sup>\*</sup> T. Ohnishi, Y. Satou,<sup>\*3</sup> T. Wakasa,<sup>\*4</sup> N. K. Nayestanaki,<sup>\*5</sup> and K. Ermisch<sup>\*5</sup>

[NUCLEAR REACTIONS,  ${}^1\text{H}(\vec{d}, p){}^2\text{H}$ ,  $E_d = 270$  MeV measured:  $K_y^{y'}$ ,  $K_{yy}^{y'}$ ,  $K_{xx}^{y'}$ ,  $K_{xz}^{y'}$ ]

We have reported precise measurements of cross sections and all deuteron analyzing powers at  $E_d = 140$ , 200, and 270 MeV, and compared the obtained data with the Faddeev calculations with and without the Tucson-Melbourne (TM) 3NF model.<sup>1,2)</sup> For the cross section and the vector analyzing power ( $A_y^d$ ), including the 3NF model brings a good agreement of the data, while for the tensor analyzing power the agreement is deteriorated when the 3NF model is included. In order to further assess the 3NF effects, we extended the measurement to new observables, namely polarization transfer measurement for the  $\vec{d} + p \rightarrow \vec{p} + d$  elastic scattering.

The experiment was performed at the RIKEN Accelerator Research Facility using tensor and vector polarized deuteron beams of 270 MeV. A liquid hydrogen (19.8 mg/cm<sup>2</sup>) or CH<sub>2</sub> (93.4 mg/cm<sup>2</sup>) target was bombarded and scattered protons were momentum analyzed by the magnetic spectrograph SMART. The polarization of the scattered protons was measured with the focal-plane polarimeter DPOL. The measured observables were the deuteron to proton polarization transfer coefficients ( $K_y^{y'}$ ,  $K_{xx}^{y'}$ ,  $K_{yy}^{y'}$ , and  $K_{xz}^{y'}$ ) in the angular range of  $\theta_{c.m.} = 90^\circ - 180^\circ$ . This measurement also yielded an induced polarization ( $P^{y'}$ ) of the outgoing protons. The relation between the polarizations and the observables is expressed as

$$p_{y'} \left( \frac{d\sigma}{d\Omega} \right) = \left( \frac{d\sigma_0}{d\Omega} \right) \left( P^{y'} + \frac{3}{2} K_y^{y'} p_y + \frac{2}{3} K_{xx}^{y'} + \frac{1}{3} K_{xx}^{y'} + \frac{1}{3} K_{yy}^{y'} + \frac{1}{3} K_{zz}^{y'} \right),$$

where  $x$ ,  $y$ , and  $z$  are the coordinates of the incident deuterons;  $x'$ ,  $y'$ , and  $z'$  are those of the emitted protons; and  $\left( \frac{d\sigma_0}{d\Omega} \right)$  denotes the cross section with unpolarized beams.

Figure 1 shows the experimental results with open squares. The errors are only statistical. The open squares are our previous data in a test measurement.<sup>1)</sup> The two measurement data provide a good agreement, except for  $K_{xx}^{y'} - K_{yy}^{y'}$  at  $\theta_{c.m.} = 150^\circ$ . The dark and light shaded bands in Fig. 1 are the calculated results

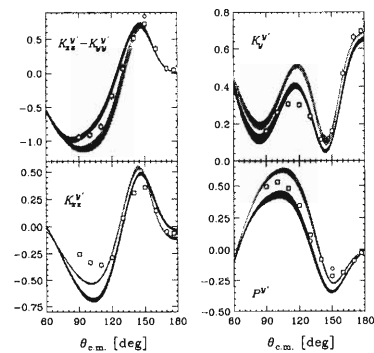


Fig. 1.  $K_{xx}^{y'} - K_{yy}^{y'}$ ,  $K_y^{y'}$ ,  $K_{xz}^{y'}$ , and  $P^{y'}$  for  $d$ - $p$  elastic scattering at  $E_d^{lab} = 270$  MeV. The dark and light shaded bands in Fig. 1 are the calculated results with and without TM 3NF, respectively. The CDBonn, AV18, Nijmegen I,II and 93 potentials are considered as  $NN$  forces. The Coulomb force is not included. The horizontal axis ( $\theta_{c.m.}$ ) is defined as the angle between the incident and outgoing deuterons in the center-of-mass system.

with and without TM 3NF by the Bochum-Cracow group,<sup>1,3)</sup> respectively. The CDBonn, AV18, Nijmegen I,II and 93<sup>4)</sup> potentials are taken as two nucleon ( $NN$ ) interactions. Note that the Coulomb interaction is not included. The horizontal axis ( $\theta_{c.m.}$ ) is defined as the angle between the incident and outgoing deuterons in the center-of-mass system. For  $K_{xx}^{y'} - K_{yy}^{y'}$ , the data support the 3N force calculations, while for the other observables ( $K_y^{y'}$ ,  $K_{xz}^{y'}$ ,  $P^{y'}$ ) large differences between the data and the  $NN$  force predictions are not reproduced by including the 3NF model.

The results of the comparison for the polarization transfer coefficients reveal that the TM 3NF model has deficiencies in its spin parts and that these observables are useful to clarify the spin dependence of 3NF effects.

### References

- 1) H. Sakai, K. Sekiguchi, H. Witala et al.: Phys. Rev. Lett. **84**, 5288 (2000).
- 2) K. Sekiguchi et al.: RIKEN Accel. Prog. Rep. **34**, 50 (2001); K. Sekiguchi et al.: Nucl. Phys. A **684**, 574c (2001).
- 3) H. Witala et al.: Phys. Rev. C **63**, 024007 (2001).
- 4) R. Machleidt: Phys. Rev. C **63**, 024001 (2001); R. B. Wiringa et al.: Phys. Rev. C **51**, 38 (1995); V. G. J. Stoks et al.: Phys. Rev. C **49**, 2950 (1994).

<sup>\*1</sup> School of Science, University of Tokyo

<sup>\*2</sup> Department of Physics, Saitama University

<sup>\*3</sup> Center for Nuclear Study, University of Tokyo

<sup>\*4</sup> Research Center for Nuclear Physics, Osaka University

<sup>\*5</sup> KVI, The Netherlands

# Measurement of the analyzing powers for the $\vec{d}d \rightarrow {}^3\text{Hp}$ and $\vec{d}d \rightarrow {}^3\text{He}$ reactions at 270 MeV

T. Saito,<sup>\*1</sup> V. P. Ladygin,<sup>\*2</sup> T. Uesaka,<sup>\*3</sup> H. Sakai,<sup>\*1</sup> H. Okamura,<sup>\*3</sup> A. I. Malakhov,<sup>\*2</sup> S. G. Reznikov,<sup>\*2</sup>  
 A. Y. Isupov,<sup>\*2</sup> N. B. Ladygina,<sup>\*2</sup> N. Sakamoto, T. Ohnishi, A. Tamii,<sup>\*1</sup> K. Sekiguchi,<sup>\*1</sup> K. Yako,<sup>\*1</sup>  
 S. Sakoda,<sup>\*1</sup> K. Suda,<sup>\*3</sup> H. Kato,<sup>\*1</sup> Y. Maeda,<sup>\*1</sup> M. Hatano,<sup>\*1</sup> J. Nishikawa,<sup>\*3</sup> N. Uchigashima,<sup>\*1</sup>  
 H. Kumasaka,<sup>\*3</sup> R. Suzuki,<sup>\*3</sup> and Y. Satou,<sup>\*4</sup>

[ $\vec{d}d \rightarrow {}^3\text{Hp}$  ( ${}^3\text{He}$ ) reaction,  $E_d = 270$  MeV, Analyzing powers]

The structure of  ${}^3\text{H}$  and  ${}^3\text{He}$  nuclei in the high internal momentum region has not been clearly understood. The tensor analyzing powers for the  $\vec{d}d \rightarrow {}^3\text{Hp}$  and  $\vec{d}d \rightarrow {}^3\text{He}$  reactions are appropriate probes to study the ratio of the S- and D-state wave functions of  ${}^3\text{H}$ ( ${}^3\text{He}$ ) nuclei in the high-momentum region. Calculations with the One Nucleon Exchange (ONE) approximation<sup>1)</sup> show that the angular distributions of the tensor analyzing powers for these reactions are sensitive to the structure of the  ${}^3\text{H}$ ( ${}^3\text{He}$ ) if  ${}^3\text{H}$ ( ${}^3\text{He}$ ) is emitted in the forward hemisphere in the center-of-mass frame. On the other hand, they depend mainly on the structure of the deuteron in the case of backward emission. Measurements of these observables with a 270 MeV deuteron beam at  $\theta_{\text{cm}}({}^3\text{H}$  or  ${}^3\text{He}) \leq 90^\circ$  provide information about the  ${}^3\text{H}$ ( ${}^3\text{He}$ ) spin structure up to a relative momentum of a  $dN$  pair of  $\sim 600$  MeV/c. Since  ${}^3\text{H}$  and  ${}^3\text{He}$  are mirror nuclei of each other, the nature of charge symmetry breaking can also be studied by measuring the analyzing powers for both the  $\vec{d}d \rightarrow {}^3\text{Hp}$  and  $\vec{d}d \rightarrow {}^3\text{He}$  reactions.

We measured the tensor and vector analyzing powers ( $A_{yy}$ ,  $A_{xx}$ ,  $A_{xz}$ , and  $A_y$ ) for the  $\vec{d}d \rightarrow {}^3\text{Hp}$  and  $\vec{d}d \rightarrow {}^3\text{He}$  reactions at  $E_d = 270$  MeV over almost the full angular range. A  $\text{CD}_2$  target was bombarded by polarized deuteron beams. Scattered particles were momentum-analyzed by the SMART spectrograph. In the case of the  ${}^3\text{He}$  channel, we detected  ${}^3\text{He}$ . In the case of the  ${}^3\text{Hp}$  channel,  ${}^3\text{H}$  (protons) were detected if  ${}^3\text{H}$  were emitted in the forward (backward) angles in the center-of-mass frame. We also measured the energy spectra with a carbon target in order to subtract the contributions from carbon nuclei in the  $\text{CD}_2$  target. Beam polarizations were monitored with the beam-line polarimeters based on the  $dp$  elastic scattering.

The preliminary results of the analyzing powers are presented in Fig. 1. The results of the  ${}^3\text{Hp}$  and  ${}^3\text{He}$  channels are plotted by filled and open circles, respectively. The solid, dot-dashed, and dashed lines are the results of ONE calculations with different  ${}^3\text{He}$  wave functions from Refs. 2, 3, and 4, respectively. The Paris deuteron wave function was used in these cal-

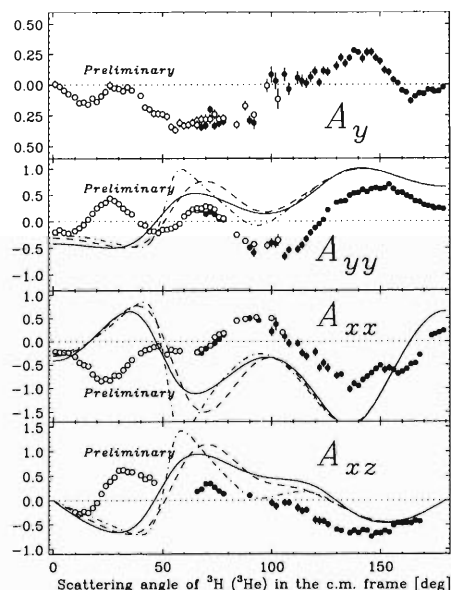


Fig. 1. Preliminary results of the analyzing powers for the  $\vec{d}d \rightarrow {}^3\text{Hp}$  and  $\vec{d}d \rightarrow {}^3\text{He}$  reactions at  $E_d = 270$  MeV. The filled and open circles are for the  ${}^3\text{Hp}$  and  ${}^3\text{He}$  channels, respectively. Explanations for the curves are given in the text.

culations. The general features of the angular distributions of the analyzing powers were reproduced by ONE calculations at the backward emission angles of  ${}^3\text{H}$ , while great discrepancies were found between the ONE predictions and the experimental results at forward angles. These results indicate that there might be some problems in the wave function of the three-body system used in the ONE calculations. Since the results of the  ${}^3\text{Hp}$  and  ${}^3\text{He}$  channels are in agreement, the effects of charge symmetry breaking have not been observed within the experimental uncertainty.

## References

- 1) V. P. Ladygin, N. B. Ladygina, H. Sakai, and T. Uesaka: Part. Nucl. Lett. **3(100)**-2000, 74 (2000).
- 2) J. M. Laget, J. F. Lecomte, and F. Lefebvres: Nucl. Phys. A **370**, 479 (1981).
- 3) F. D. Santos, A. M. Eiro, and A. Barosso: Phys. Rev. C **19**, 238 (1979).
- 4) R. Schiavilla, V. R. Pandharipande, and R. B. Wiringa: Nucl. Phys. A **449**, 219 (1986).

\*1 Department of Physics, University of Tokyo

\*2 LHE-JINR, Russia

\*3 Department of Physics, Saitama University

\*4 Center for Nuclear Study, University of Tokyo

## Measurement of the tensor analyzing power ( $T_{20}$ ) in the $dd \rightarrow {}^3\text{Hp}$ and $dd \rightarrow {}^3\text{Hen}$ reactions at $0^\circ$

V. P. Ladygin,<sup>\*1</sup> T. Uesaka,<sup>\*1</sup> T. Saito,<sup>\*2</sup> M. Hatano,<sup>\*2</sup> A. Yu. Isupov,<sup>\*3</sup> H. Kato,<sup>\*2</sup> H. Kumasaka,<sup>\*1</sup>  
 N. B. Ladygina,<sup>\*3</sup> Y. Maeda,<sup>\*2</sup> A. I. Malakhov,<sup>\*3</sup> J. Nishikawa,<sup>\*1</sup> T. Ohnishi, H. Okamura,<sup>\*1</sup>  
 S. G. Reznikov,<sup>\*3</sup> H. Sakai,<sup>\*2</sup> N. Sakamoto, S. Sakoda,<sup>\*2</sup> Y. Satou,<sup>\*4</sup> K. Sekiguchi,<sup>\*2</sup>  
 K. Suda,<sup>\*1</sup> R. Suzuki,<sup>\*1</sup> A. Tamii,<sup>\*2</sup> N. Uchigashima,<sup>\*2</sup> and K. Yako<sup>\*2</sup>

[Three-nucleon Structure, polarized deuteron]

For the last decade, the tensor analyzing power ( $T_{20}$ ) for one-nucleon transfer reactions, like  $dp$  and  $d^3\text{He}$  backward elastic scattering, or  $d^3\text{He} \rightarrow p^4\text{He}$ , at intermediate energies in collinear geometry has been intensively studied as an important source of information about the spin structure of light nuclei at short distances.

The tensor analyzing power ( $T_{20}$ ) in the  $dd \rightarrow {}^3\text{Hp}$  and  $dd \rightarrow {}^3\text{Hen}$  reactions at 140, 200 and 270 MeV of the deuteron kinetic energy and in collinear geometry has been measured at RARF using the SMART spectrograph.<sup>1)</sup> The beam polarization has been measured with a polarimeter based on  $dp$  elastic scattering. It was continuously monitored during a run. The momentum of the secondary particles was reconstructed using the information from the drift chambers placed at the focal plane of the SMART spectrograph.<sup>1)</sup> The identification of the  $p$ ,  $d$ ,  ${}^3\text{H}$  and  ${}^3\text{He}$  was done using the pulse-height and timing information from three plastic scintillators. The  $CD_2 - C$  subtraction was made for each setting of the spectrograph to obtain the contribution from deuterium.

The obtained data are shown in Fig. 1 versus the initial deuteron momentum. The open triangles and squares are the  $T_{20}$  data in the  $dd \rightarrow {}^3\text{Hp}$  reaction with  ${}^3\text{H}$  emission at  $0^\circ$  and  $180^\circ$  in the c.m., respectively, while the solid circles represent the data in the  $dd \rightarrow {}^3\text{Hen}$  channel at  $0^\circ$ . The solid and dashed curves represent the calculations<sup>2)</sup> performed within a one-nucleon exchange (ONE) approximation for the forward and backward kinematics, respectively. In this model the tensor analyzing power ( $T_{20}$ ) in collinear geometry has the following form:

$$T_{20} = \frac{2\sqrt{2}r - r^2}{\sqrt{2}(1 + r^2)}, \quad (1)$$

where  $r$  is the  $D/S$ -waves ratio in  ${}^3\text{H}({}^3\text{He})$  or in the deuteron at the corresponding internal momentum for the forward and backward kinematics, respectively. Equation (1) is also valid for  $T_{20}$  in  $d^3\text{He}$  and  $dp$  backward elastic scatterings and in the  $d^3\text{He} \rightarrow p^4\text{He}$  reaction. Therefore, the dependence of  $T_{20}$  for these reac-

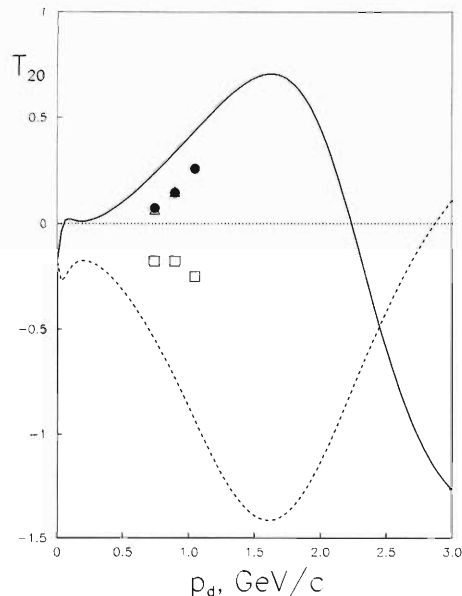


Fig. 1.  $T_{20}(0^\circ)$  in the  $dd \rightarrow {}^3\text{Hp}$  and  $dd \rightarrow {}^3\text{Hen}$  reaction as a function of  $p_d$ . The solid and broken lines represent the ONE calculations<sup>2)</sup> with the  ${}^3\text{He}$  wave function of Ref. 3.

tions versus the internal momentum must be the same if ONE is valid.

One can see that the data obtained for both channels,  $dd \rightarrow {}^3\text{He}(0^\circ)n$  (solid circles) and  $dd \rightarrow {}^3\text{H}(0^\circ)p$  (open triangles), within the achieved experimental accuracy are in good agreement. The sign of  $T_{20}$  in the  $dd \rightarrow {}^3\text{Hp}({}^3\text{Hen})$  reaction is opposite when  ${}^3\text{H}({}^3\text{He})$  is emitted in the forward or backward direction in the center-of-mass system. The sign of the  $T_{20}$  data at  $0^\circ$  in the center-of-mass system is positive and agrees with that obtained in the  $d^3\text{He} \rightarrow {}^3\text{Hed}$  reaction.<sup>3)</sup> For the backward kinematics, the sign of the  $T_{20}$  data is negative in accordance with the signs of  $T_{20}$  in  $dp$  backward elastic scattering<sup>4)</sup> and in the  $d^3\text{He} \rightarrow p^4\text{He}$  reaction.<sup>5)</sup> This fact is attributed to the sensitivity of the data to the  $D/S$ -ratio in the  ${}^3\text{H}({}^3\text{He})$  and deuteron.

Although the global feature that  $T_{20}$  is negative and its magnitude increases with the projectile momentum is consistent with the prediction of the ONE approximation, the absolute magnitude of  $T_{20}$  deviates dra-

<sup>\*1</sup> Saitama University

<sup>\*2</sup> University of Tokyo

<sup>\*3</sup> LHE-JINR, Russia

<sup>\*4</sup> Center for Nuclear Study, University of Tokyo

matically from the calculations at the backward angles. In addition, the magnitudes are even different among the dp backward elastic scattering, the  $d^3\text{He} \rightarrow p^4\text{He}$ , and the  $dd \rightarrow {}^3\text{H}(180^\circ)p$  reactions. Therefore, one can conclude that a mechanism beyond ONE is necessary for a better description of the data, and that the mechanism gives different effects depending on the reactions. One possible theoretical approach to the problem is to use 3N Faddeev amplitudes instead of the ONE amplitudes. Measurements of additional polarization observables will also help us to understand

the mechanism more clearly.

#### References

- 1) T. Ichihara et al.: Nucl. Phys. A **569**, 287c (1994).
- 2) V. P. Ladygin, N. B. Ladygina, H. Sakai, and T. Uesaka: Part. Nucl. Lett. **3(100)**, 74 (2000).
- 3) M. Tanifuji et al.: Phys. Rev. C **61**, 024602 (1999).
- 4) V. Punjabi et al.: Phys. Lett. B **350**, 178 (1995).
- 5) T. Uesaka et al.: Phys. Lett. B **467**, 199 (1999); Few-Body Systems Suppl. **12**, 497 (2000).

## Measurement of single and double spin-flip probabilities in inelastic deuteron scattering on $^{12}\text{C}$ at 270 MeV<sup>†</sup>

Y. Satou,<sup>\*1</sup> S. Ishida,<sup>\*2</sup> H. Sakai,<sup>\*1,\*3</sup> H. Okamura,<sup>\*4</sup> H. Otsu,<sup>\*5</sup> N. Sakamoto, T. Uesaka,<sup>\*4</sup> T. Wakasa,<sup>\*6</sup> T. Ohnishi, K. Sekiguchi,<sup>\*3</sup> K. Yako,<sup>\*3</sup> T. Ichihara, T. Niizeki,<sup>\*7</sup> K. S. Itoh,<sup>\*5</sup> and N. Nishimori<sup>\*8</sup>

[[ $(d, d')$  reaction, spin-flip probability]

A polarization transfer measurement in inelastic deuteron scattering is one of the essential probes of isoscalar spin excitations. The reaction is selective of isoscalar transitions, while the spin  $S = 1$  nature of the deuteron allows spin transfer to the target. The measurement of deuteron SFPs should provide a means to disentangle between spin and non-spin excitations. The single and double SFPs,  $S_1$  and  $S_2$ , are expressed in terms of polarization observables by the following relations:

$$S_1 = \frac{1}{9}(4 - P^{y'y'} - A_{yy} - 2K_{yy}^{y'y'}), \quad (1)$$

$$S_2 = \frac{1}{18}(4 + 2P^{y'y'} + 2A_{yy} - 9K_y^{y'} + K_{yy}^{y'y'}). \quad (2)$$

The quantities  $A$ ,  $P$  and  $K$  refer to the analyzing power, polarizing power and polarization transfer coefficient, one (two) index stands for the vector (tensor) polarization, and the lower (upper) one for the incident (outgoing) beam. The determination of  $S_1$  and  $S_2$  thus requires vector and tensor polarized beams and vector and tensor polarimeters.

We have succeeded to measure the single and double spin-flip probabilities through a direct observation of polarization transfer, thus by measuring all of the coefficients in Eqs. (1) and (2) in inelastic deuteron scattering on  $^{12}\text{C}$  at  $E_d = 270$  MeV. The experiment was

performed using vector and tensor polarized deuteron beams from the RIKEN Ring Cyclotron, the magnetic spectrometer SMART and a focal-plane deuteron polarimeter, DPOL. DPOL utilized  $\vec{d} + \text{C}$  elastic scattering for vector polarization measurements, and the  $^1\text{H}(\vec{d}, 2p)$  charge exchange reaction for tensor polarization measurements. It allowed all of the polarization components of the scattered deuterons to be measured simultaneously over a wide excitation energy range (4 and 24 MeV). The observed  $S_1$  value is large for the spin-flip  $1^+$  (12.71 MeV) state, while it is close to zero for other non-spin-flip states, such as the first  $2^+$  (4.44 MeV) state. The  $S_2$  values are consistent with zero for all of the measured excitation energy range, and no clear indication of the  $\Delta S = 2$  states has been obtained from the present measurement. The overall trends of the SFP angular distributions for the  $1^+$  and  $2^+$  states are well described by the microscopic DWIA calculations. The demonstrated feasibility of measuring the deuteron SFPs as well as the capability of the DWIA theory to reproduce the data will add a new alternative probe of nuclear structure. Further experiments are planned in a search for the  $\Delta S = 1$  and 2 transitions in a higher excitation energy region in  $^{12}\text{C}$  and in other nuclei.

<sup>†</sup> Condensed from the article in Phys. Lett. B **521**, 153 (2001)

<sup>\*1</sup> Center for Nuclear Study, University of Tokyo

<sup>\*2</sup> Soei Corporation

<sup>\*3</sup> Department of Physics, University of Tokyo

<sup>\*4</sup> Department of Physics, Saitama University

<sup>\*5</sup> Department of Physics, Tohoku University

<sup>\*6</sup> Research Center for Nuclear Physics, Osaka University

<sup>\*7</sup> Tokyo Kasei University

<sup>\*8</sup> Japan Atomic Energy Research Institute

## Measurement of Doppler-shift attenuated $\gamma$ rays from the $^{18}\text{O}(2_1^+)$ state

N. Imai,<sup>\*1</sup> N. Aoi,<sup>\*1</sup> H. Sakurai,<sup>\*1</sup> K. Demichi,<sup>\*2</sup> H. Kawasaki,<sup>\*2</sup> H. Baba,<sup>\*2</sup> Zs. Dombrádi,<sup>\*3</sup> Z. Elekes,<sup>\*3</sup> N. Fukuda, Zs. Fülöp,<sup>\*3</sup> A. Gelberg,<sup>\*4</sup> T. Gomi,<sup>\*2</sup> H. Hasegawa,<sup>\*2</sup> H. Iwasaki,<sup>\*5</sup> E. Kaneko,<sup>\*2</sup> S. Kanno,<sup>\*2</sup> T. Kishida, Y. Kondo,<sup>\*6</sup> T. Kubo, S. Michimasa,<sup>\*5</sup> T. Minemura, M. Miura,<sup>\*6</sup> T. Motobayashi,<sup>\*2</sup> T. Nakamura,<sup>\*6</sup> M. Notani,<sup>\*3</sup> T. Ohnishi,<sup>\*1</sup> H. J. Ong,<sup>\*1</sup> A. Saito,<sup>\*2</sup> S. Shimoura,<sup>\*5</sup> T. Sugimoto,<sup>\*6</sup> S. Takeuchi,<sup>\*2</sup> K. Yoneda, H. Watanabe, and M. Ishihara

[NUCLEAR REACTIONS:  $^{197}\text{Au}(^{18}\text{O}, ^{18}\text{O}^*)^{197}\text{Au}$   $E = 48.2$  MeV/u; DSA]

The  $B(E2; 0_{g.s.}^+ \rightarrow 2_1^+)$  values in even-even neutron-rich nuclei have been successfully measured at intermediate energies by using the Coulomb excitation method.<sup>1,2)</sup> However, this technique is not suitable for a nucleus with  $Z < 8$ , since the nuclear excitation competes with the Coulomb excitation for low- $Z$  projectiles. As an alternative, we propose a mean-life measurement of the  $2_1^+ \rightarrow 0_{g.s.}^+$  transition using the Doppler-shift attenuation method at intermediate energy. Here, we report on the first attempt to apply this method to fast ( $\beta \simeq 0.3$ ) projectiles.

In this experiment, we used a thick target and the projectile velocity was degraded in the target. Accordingly, the Doppler shifted  $\gamma$ -ray energy was spread over a certain region. The energy of the  $\gamma$  ray emitted inside the target was distributed continuously, while that emitted outside the target was constant since the projectile did not change its velocity any more. The latter component became larger when the mean-life was longer. Therefore, when we properly chose the target thickness and the projectile energy so that the time for the projectile to pass through the target would be comparable with the mean-life of its excited state, the mean-life can be determined from the shape of the energy spectrum of 500  $\gamma$ -ray events with  $\pm 10\%$  uncertainty.

As a test, we applied this method to the  $^{18}\text{O}(2_1^+)$  state, whose mean-life is precisely known to be  $2.79 \pm 0.07$  ps.<sup>3)</sup> The experiment was performed at RIKEN. The energy of the  $^{18}\text{O}$  primary beam of 100 MeV/u was degraded by a  $^9\text{Be}$  target of 463 mg/cm<sup>2</sup> and an aluminum degrader of 1358 mg/cm<sup>2</sup>. Figure 1 shows a schematic view of the experimental setup. At the final focal plane of RIPS,<sup>4)</sup> an energy of 48.2 MeV/u was obtained. The  $^{18}\text{O}$  beam hit a 580 mg/cm<sup>2</sup> thick  $^{197}\text{Au}$  target. In this case, the time needed to pass through the target was 3.5 ps. The de-excitation  $\gamma$  rays from the inelastically excited  $^{18}\text{O}$  nuclei were detected by four clover Ge detectors (Clovers). Each Clover was

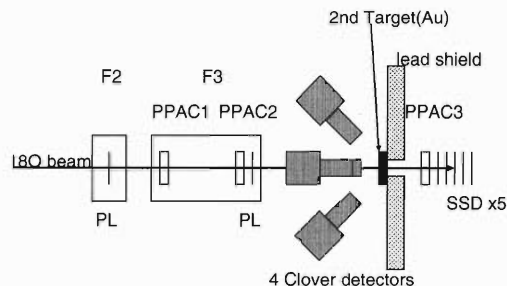


Fig. 1. The layout of the detection system. See text for details.

located 30 cm upstream from the target at 150 degrees with respect to the beam direction.

The observed Doppler-shifted  $\gamma$ -ray energy was spread due to the finite angular acceptance and the change in the velocity. The spread due to the angular acceptance was about 25 keV, while the energy spread by the velocity change was 100 keV. We would thus distinguish between a  $\gamma$  ray from outside the target and that from inside. The scattering angle was measured by three parallel plate avalanche counters, two of which were located upstream and the third one downstream of the target. Particle identification of the scattered particle was carried out with a silicon telescope using the  $\Delta E$ - $E$  method. A silicon telescope was placed 30 cm downstream from the target, covering an angular acceptance of  $\pm 9.6$  degrees. It consisted of five layers of silicon detectors with thicknesses of 0.5, 1.0, 0.5, 1.0, and 0.5 mm, respectively. Each layer was composed of four silicon detectors. In order to prevent the background  $\gamma$  rays from the silicon detectors, we put a 5 cm thick lead shield between the Clovers and the silicon telescope (See Fig. 1). Data analysis is in progress.

### References

- 1) T. Motobayashi et al.: Phys. Lett. B **346**, 9 (1995).
- 2) T. Glasmacher: Ann. Rev. Nucl. Part. Sci. **48**, 1 (1998).
- 3) G. C. Ball et al.: Nucl. Phys. A **377**, 268 (1982).
- 4) T. Kubo et al.: Nucl. Instrum. Methods Phys. Res. B **70**, 309 (1992).

\*1 University of Tokyo

\*2 Rikkyo University

\*3 ATOMKI, Hungary

\*4 University of Koeln, Germany

\*5 Center for Nuclear Study, University of Tokyo

\*6 Tokyo Institute of Technology

# Projectile excitation in $^{16}\text{O}+^{208}\text{Pb},^{nat}\text{C}$ at $E(^{16}\text{O}) = 100\text{A MeV}$ : Preliminary results

S. Kumar,\* V. M. Datar,\* D. R. Chakrabarty,\* E. T. Mirgule,\* R. Kanungo, K. Kusaka, K. Morimoto, A. Ozawa, I. Tanihata, F. Tokunai, and K. Yoshida

[NUCLEAR REACTION  $^{16}\text{O}+^{208}\text{Pb},^{nat}\text{C}$  at  $E(^{16}\text{O}) = 100\text{A MeV}$ ; Coulomb excitation]

The giant resonance (GR) strength function in exotic nuclei is a topic of current interest. This can be measured from the Coulomb excitation (CEX) of high-energy exotic nuclei by a high-Z target. With a motivation to conduct such studies with radioactive ion beams from the RIPS facility, a test run was undertaken using a stable  $^{16}\text{O}$  beam. The results of a partial analysis of the data are presented in this report.

Targets of  $^{208}\text{Pb}$  ( $351\text{ mg/cm}^2$ ) and  $^{nat}\text{C}$  ( $180\text{ mg/cm}^2$ ) were bombarded with an  $^{16}\text{O}$  beam ( $1600\text{ MeV}$ ,  $\sim 10^5\text{ pps}$ ) in the RIPS beam line. The projectile-like residues (PR) were detected in two detector stacks ( $2^\circ$  to  $9^\circ$  on either side of the beam) consisting of a pair of X and Y Si-strip detectors ( $450\ \mu\text{m}$ , 10 strips), two Si-PIN diodes ( $450\ \mu\text{m}$ ), three Si(Li)s ( $2\text{ mm}$ ) and two plastics ( $12$  and  $8\text{ mm}$ ). The light particles ( $n$ ,  $p$  and  $\alpha$ ) were detected in three multi-layer plastic walls at distances of between 3 and 5 m from the target and covering  $\sim 2^\circ$  to  $20^\circ$ . The layers consisted of plastic bars of cross-section  $6\text{ cm} \times 6\text{ cm}$ , having PMTs at both ends. Thin plastic layers ( $5$  to  $10\text{ mm}$ ) were kept in front of two walls. The front layer was used for identifying the light particles whose energy was derived from the time of flight. An array of 125  $\text{BaF}_2$  detectors ( $\epsilon \sim 75\%$ ) was used to detect  $\gamma$  rays from the excited PRs. The target and detectors were kept in air. The beam was monitored by a PPAC, which also generated a fast reference time output.

In the present analysis, one PR-stack, one plastic wall and only decay by light charged particles (LCP),  $p$  and  $\alpha$ , are considered. The  $\gamma$  decay of the PR is ignored. The analysis included only those events which correspond to the detection of one PR in the stack detector and the corresponding LCP in those parts of the wall shadowed by the stack detectors and in the shadow-free central zone. The energies of the LCPs and PRs were corrected for the energy loss in air and the stack material. From the measured energy and the direction of the PR and the associated LCP, the excitation energy ( $E_X$ ) of  $^{16}\text{O}$  was calculated. The contribution from air in the beam path, measured with a blank target, was significant (Fig. 1) and subtracted. A comparison of the subtracted Pb and C spectra, normalized to the number of target atoms, showed that the nuclear excitation (NEX) is significant at this beam energy. These normalized C spectra are scaled up by

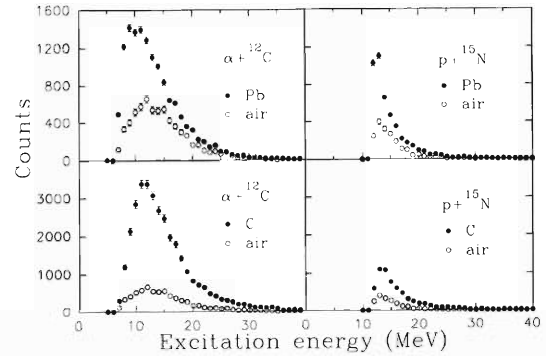


Fig. 1.  $E_X$ -spectra in  $^{16}\text{O}$  in two decay channels for  $^{208}\text{Pb}$  and C targets. The contribution from air is also shown.

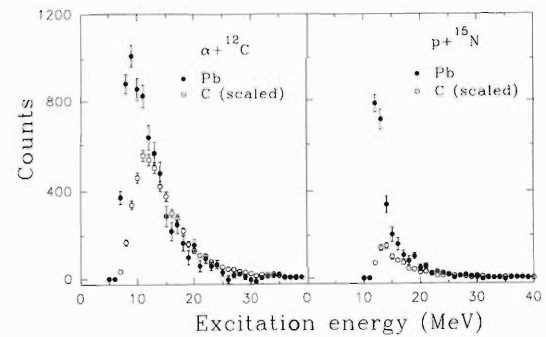


Fig. 2.  $E_X$ -spectra in  $^{16}\text{O}$  after subtracting air contribution. The C spectra are scaled for estimating the nuclear contribution in the Pb spectra.

a factor of 1.76 (ratio of the interaction radii in the two systems) and are compared with the Pb spectra in Fig. 2. This shows that the CEX exceeds NEX for  $E_X$  below  $\sim 12\text{ MeV}$ . Thus, the extraction of the GR strength can be made from CEX at this beam energy if a significant fraction of the sum-rule strength lies well below this  $E_X$ . This may be true for very exotic nuclei. The neglect of PR  $\gamma$ -rays in the analysis implies that the actual  $E_X$  spectra are somewhat different from those shown. The cross section at lower  $E_X$  will be depleted with a corresponding increase at higher  $E_X$ . However, the conclusions regarding the relative importance of CEX and NEX is not expected to change.

\* Nuclear Physics Division, Bhabha Atomic Research Centre, India



## Determination of the astrophysical S factor of the ${}^8\text{B}(p, \gamma){}^9\text{C}$ capture reaction from the ${}^8\text{B}(d, n){}^9\text{C}$ reaction

D. Beaumel,<sup>\*1</sup> T. Kubo, T. Teranishi,<sup>\*2</sup> H. Sakurai,<sup>\*3</sup> S. Fortier,<sup>\*1</sup> A. Mengoni,<sup>\*4</sup> N. Aoi,<sup>\*3</sup> N. Fukuda, M. Hirai,<sup>\*5</sup> N. Imai,<sup>\*3</sup> H. Iwasaki,<sup>\*2</sup> H. Kumagai, H. Laurent,<sup>\*1</sup> S. M. Lukyanov,<sup>\*6</sup> J. M. Maison,<sup>\*1</sup> T. Motobayashi,<sup>\*7</sup> T. Nakamura,<sup>\*8</sup> H. Ohmura,<sup>\*9</sup> S. Pita,<sup>\*1</sup> K. Yoneda, and M. Ishihara

[Transfer reaction, Nucleosynthesis]

Radiative capture reactions play a crucial role in astrophysics, since they are involved in most basic processes, such as hydrogen burning. In the case of the capture of charged particles, a direct measurement of the cross sections is especially difficult due to the low incident energies at astrophysical sites (compared to the Coulomb barrier). Indirect methods, for which the capture cross section is deduced from another reaction, provide alternative approaches, particularly appropriate when radioactive nuclei are involved. Transfer reactions are a long-standing tool in this respect. The determination of spectroscopic factors allows one to deduce the direct radiative cross section by using two-body potential models. When the reaction is peripheral, recent studies<sup>1)</sup> have shown that, instead of spectroscopic factors, the relevant quantities to be extracted from transfer reactions are asymptotic normalization coefficients (ANC), which define the asymptotic part of the nuclear overlap function between the initial and final nuclei. These coefficients are determined in a similar way as spectroscopic factors (*i.e.* by normalizing a calculated DWBA cross section to the data), but are much less dependent on the DWBA parameters.

In our study, we determined the ANC's corresponding to the overlap ( ${}^9\text{C}|{}^8\text{B}, p$ ) via the  ${}^8\text{B}(d, n){}^9\text{C}$  transfer cross section. From these ANC's the cross section (or equivalently, the S factor) of the capture reaction,  ${}^8\text{B}(p, \gamma){}^9\text{C}$ , can be deduced. Because the  ${}^8\text{B}$  nucleus has a short half-life (0.77 s), this reaction cannot play

a role in stars like the sun, but it may become<sup>2)</sup> a link between light nuclei of the proton-proton chain and CNO nuclei (the hot p-p chain) in a very hot and dense medium. Due to the short half-life, a direct measurement of  ${}^8\text{B}(p, \gamma){}^9\text{C}$  is impossible at the moment.

At the RIKEN facility, we have measured the cross section of the  ${}^8\text{B}(d, n){}^9\text{C}$  reaction at 14.4 MeV/u in inverse kinematics. A radioactive  ${}^8\text{B}$  beam was produced using the RIPS device. The  ${}^8\text{B}$  yield was roughly  $10^4$  pps. The  ${}^9\text{C}$  ejectiles were detected in coincidence with the neutrons, allowing us to separate good events from the background, despite a very low count rate.

The deduced value for the S factor of the  ${}^8\text{B}(p, \gamma){}^9\text{C}$  reaction is

$$S_{18} = 45 \pm 13 \text{ eV}\cdot\text{b.}^{3)}$$

This result is roughly a factor of two lower than the calculated value already reported,<sup>4)</sup> where a microscopic cluster model was used. It is in stronger disagreement (factor 4) with the calculation of another reference.<sup>2)</sup>

### References

- 1) A. M. Mukhamedzhanov et al.: Phys. Rev C **51**, 3472 (1995).
- 2) M. Wiescher et al.: Astrophys. J. **343**, 352 (1989).
- 3) D. Beaumel et al.: Phys. Lett. B **514**, 226 (2001).
- 4) P. Descouvemont: Nucl. Phys. A **646**, 26 (1999).

<sup>\*1</sup> Institut de Physique Nucléaire, France

<sup>\*2</sup> Center for Nuclear Study, University of Tokyo

<sup>\*3</sup> Department of Physics, University of Tokyo

<sup>\*4</sup> Ente per le Nuove Tecnologie, l'Energia e l'Ambiente, Italy

<sup>\*5</sup> National Institute of Radiological Science

<sup>\*6</sup> Joint Institute for Nuclear Research, Russia

<sup>\*7</sup> Rikkyo University

<sup>\*8</sup> Tokyo Institute of Technology

<sup>\*9</sup> Chiba Institute of Technology

## Inelastic scattering of $^{12}\text{Be}$ with $^4\text{He}$

Y. U. Matsuyama,<sup>\*1</sup> T. Motobayashi,<sup>\*1</sup> S. Shinoura,<sup>\*2</sup> T. Minemura, A. Saito,<sup>\*1</sup> H. Baba,<sup>\*1</sup> H. Akiyoshi, N. Aoi,<sup>\*3</sup> Y. Ando,<sup>\*1</sup> T. Gomi,<sup>\*1</sup> Y. Higurashi,<sup>\*1</sup> K. Ieki,<sup>\*1</sup> N. Inai,<sup>\*3</sup> N. Iwasa,<sup>\*4</sup> H. Iwasaki,<sup>\*2</sup> S. Kanno,<sup>\*1</sup> S. Kubono,<sup>\*2</sup> M. Kunibu,<sup>\*1</sup> S. Michimasa,<sup>\*2</sup> H. Murakami,<sup>\*1</sup> T. Nakamura,<sup>\*5</sup> H. Sakurai,<sup>\*3</sup> M. Serata,<sup>\*1</sup> E. Takeshita,<sup>\*1</sup> S. Takeuchi,<sup>\*1</sup> T. Teramishi,<sup>\*2</sup> K. Ue,<sup>\*2</sup> K. Yamada,<sup>\*1</sup> and Y. Yanagisawa

[NUCLEAR REACTION:  $^4\text{He}(^{12}\text{Be}, ^{12}\text{Be}^*)$ , Inelastic Scattering, Liquid helium]

We studied inelastic  $\alpha + ^{12}\text{Be}$  scattering by measuring the  $\gamma$ -decay of  $^{12}\text{Be}$  in its excited states. This was the first experiment with RI beams using a liquid-He target developed earlier.<sup>1)</sup>

The experiment was carried out with RIPS. A primary  $^{16}\text{O}$  beam of 135 MeV/nucleon bombarded a  $^9\text{Be}$  production target with 1480 mg/cm<sup>2</sup> thickness to obtain a radioactive beam of  $^{12}\text{Be}$ . The  $^{12}\text{Be}$  nuclei in the beam were separated event by event from contaminants using time-of-flight (TOF) information between two plastic 0.5 mm thick scintillators separated by 5.3 m from each other. The energy of the beam was approximately 60 MeV/nucleon, the purity of the  $^{12}\text{Be}$  beam was more than 90% and the intensity was around  $3 \times 10^4 \text{ s}^{-1}$ .

A liquid-He target of 250 mg/cm<sup>2</sup> was placed at the focal plane of RIPS. Liquid helium was confined within a cell with a Havar foil window of 24 mm diameter. The direction and position of a beam particle at the target were measured by two sets of parallel plate avalanche counters (PPAC's) installed upstream from the target.

Outgoing particles were detected and identified by a plastic scintillator array hodoscope located 4 m downstream from the target. The array consisted of three layers ( $\Delta E$ , E1, and E2) of 5 mm, 60 mm, and 60 mm thickness, respectively. The energies and scattered angles of the particles were determined by the TOF's and hit positions in the hodoscope, respectively. Each particle was identified by using the TOF- $\Delta E$  and TOF-E methods.

Sixty-eight NaI(Tl) scintillators surrounded the target to detect  $\gamma$  rays emitted from excited  $^{12}\text{Be}$  nuclei. Each scintillator crystal was of rectangular shape with a size of  $6 \times 6 \times 12 \text{ cm}^3$  coupled with a 5.1 cm  $\phi$  photomultiplier tube. The segmentation of the array allowed us to correct for Doppler shifts from moving reaction products.

Figure 1 shows the  $\gamma$ -ray energy spectrum associated with  $^{12}\text{Be}$  identified in the hodoscope. It was obtained as a sum of each Doppler-corrected spectrum of all the NaI(Tl) scintillators. As one can see in Fig. 1, two full-energy peaks were observed. The energies were

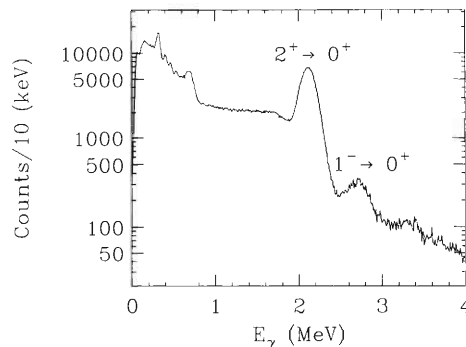


Fig. 1. Doppler-corrected  $\gamma$ -ray spectrum measured in coincidence with  $^{12}\text{Be}$ .

determined to be 2.10 MeV and 2.68 MeV. The first peak is assigned to the  $2_1^+ \rightarrow 0_{g.s.}^+$  transition, whereas the second one might correspond to the  $1^- \rightarrow 0_{g.s.}^+$  transition, which has been observed in the Coulomb excitation experiment.<sup>2)</sup>

Figure 2 shows the experimental differential cross section for inelastic scattering exciting the  $2_1^+$  state and the  $1^-$  state in  $^{12}\text{Be}$ . A clear difference is seen between the  $2_1^+$  and  $1^-$  distributions suggesting the usefulness of  $\alpha$ -inelastic scattering for nuclear-structure studies.

Data analyses are now in progress.

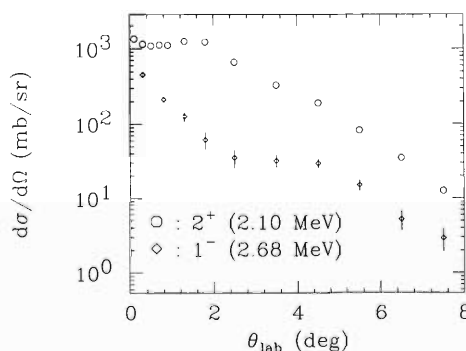


Fig. 2. Observed differential cross section for inelastic scattering exciting the  $2_1^+$  state and the  $1^-$  state on  $^{12}\text{Be}$ .

<sup>\*1</sup> Department of Physics, Rikkyo University  
<sup>\*2</sup> Center for Nuclear Study, University of Tokyo  
<sup>\*3</sup> Department of Physics, University of Tokyo  
<sup>\*4</sup> Department of Physics, Tohoku University  
<sup>\*5</sup> Department of Physics, Tokyo Institute of Technology

### References

- 1) H. Akiyoshi et al.: RIKEN Accel. Prog. Rep. **34**, 193 (2001).
- 2) H. Iwasaki et al.: Phys. Lett. B **491**, 8 (2000).

## Isomeric $0^+$ state in $^{12}\text{Be}$

S. Shimoura,<sup>\*1</sup> A. Saito,<sup>\*2</sup> T. Minemura, Y. U. Matsuyama,<sup>\*2</sup> H. Baba,<sup>\*2</sup> H. Akiyoshi, N. Aoi,<sup>\*3</sup> T. Gomi,<sup>\*2</sup> Y. Higurashi,<sup>\*2</sup> K. Ieki,<sup>\*2</sup> N. Imai,<sup>\*3</sup> N. Iwasa,<sup>\*4</sup> H. Iwasaki,<sup>\*1</sup> S. Kanno,<sup>\*2</sup> S. Kubono,<sup>\*1</sup> M. Kumibu,<sup>\*2</sup> S. Michimasa,<sup>\*1</sup> T. Motobayashi,<sup>\*2</sup> T. Nakamura,<sup>\*5</sup> H. Sakurai,<sup>\*3</sup> M. Serata,<sup>\*2</sup> E. Takeshita,<sup>\*2</sup> S. Takeuchi,<sup>\*2</sup> T. Teranishi,<sup>\*1</sup> K. Ue,<sup>\*1</sup> K. Yamada,<sup>\*2</sup> Y. Yanagisawa, and M. Ishihara

[Isomeric state,  $\gamma$ - $\gamma$  correlation, Radioactive beam experiment]

An isomeric  $0^+$  state in  $^{12}\text{Be}$  was searched by using the projectile fragmentation of  $^{18}\text{O}$  on a Be target. The doppler-shift corrected energy spectra for  $\gamma$ -rays and the  $\gamma$ - $\gamma$  angular correlation were analyzed for determining the excitation energy and for confirming the spin, respectively.

The experiment was performed at the RIKEN Accelerator Research Facility. A primary beam of  $^{18}\text{O}$  projectiles at 100 A MeV bombarded on a 2-g/cm<sup>2</sup> thick Be target. The  $^{12}\text{Be}^{(*)}$  nuclides at 60 A MeV were selected by the RIKEN Projectile Fragment Separator (RIPS).<sup>1)</sup> The typical intensity and the purity of the  $^{12}\text{Be}$  beam were  $2 \times 10^4$  pps and more than 85%, respectively. Two plastic scintillators at the second (F2) and at third (F3) focal points of the RIPS were used for identifying the  $^{12}\text{Be}$  event by event by using the time-of-flight (TOF) between the two scintillators and the pulse heights. Here, the TOF between the production target and F3 was about 250 ns. Gamma rays were detected by an array of 68 NaI(Tl) scintillators (DALI) about 70 cm downstream of the F3 scintillator. Each NaI(Tl) had an active volume of 12 cm (horizontal)  $\times$  6 cm (vertical)  $\times$  6 cm (along beam line). The array was divided into 6 layers consisting of 8, 12, 14, 14, 12, and 8 NaI(Tl) scintillators, each of which surrounded the beam axis. Timing signals of NaI(Tl) were used to discriminate the true coincidence from the accidental one, and to evaluate the vertex point from which the  $\gamma$ -ray was emitted. The vertex point was used for Doppler-shift corrections event-by-event. The  $^{12}\text{Be}$  nucleus after decay was detected by a plastic scintillator hodoscope with a  $1 \times 1$  m<sup>2</sup> active area located 4 m downstream of DALI. The hodoscope consisted of a 5-mm thick  $\Delta E$  plane and a 60-mm thick  $E$  plane. The  $\Delta E$  plane was divided horizontally into 13 slats and the  $E$  plane consisted of 16 horizontal bars. Particle identification was performed by using  $\Delta E$ -TOF and  $E$ -TOF information.

We analyzed events where two NaI(Tl) scintillators made signals from in-flight  $^{12}\text{Be}$  particles, where  $E_{\text{high}}$  and  $E_{\text{low}}$  denote the energies of the higher and lower pulse heights of the two NaI(Tl), respectively. A broad

bump was found at around  $E_{\text{high}} = 2$  MeV and  $E_{\text{low}} = 0.15$  MeV. This peak became sharp after a correction for the Doppler effect, the energies of the two  $\gamma$ -rays in the rest frame were determined to be 2.1 and 0.14 MeV, respectively. Since the former energy corresponds to the excitation energy of the  $2^+$  state, a new state at about 0.14 MeV above the  $2^+$ , *i.e.* an isomeric state at  $E_x = 2.24$  MeV, is indicated. It is noted that a small peak with the same excitation energy seen in the spectrum of  $^{10}\text{Be}(t,p)$  reaction<sup>2)</sup> may correspond to the present isomeric state.

In order to determine the spin of the new state, we have examined an azimuthal angular correlation of these two  $\gamma$ 's with respect to the direction of the  $^{12}\text{Be}$  momentum. Figure 1 shows the observed angular correlation together with a theoretical prediction assuming a cascade decay of  $0_2^+ \rightarrow 2_1^+ \rightarrow 0_1^+$ . We conclude that the isomeric state has spin  $0^+$  based on the excellent fit.

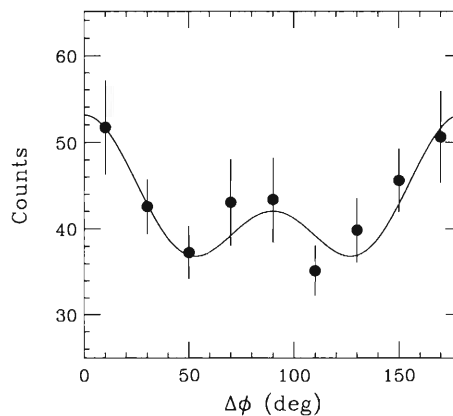


Fig. 1. Azimuthal angular correlation pattern of 2.1-MeV and 0.14-MeV gamma rays. The solid line denotes the theoretical prediction assuming the  $0^+ \rightarrow 2^+ \rightarrow 0^+$  transition.

### References

- 1) T. Kubo et al.: Nucl. Instrum. Methods Phys. Res. B **70**, 309 (1992).
- 2) H. T. Fortune et al.: Phys. Rev. C **50**, 1355 (1994).

<sup>\*1</sup> Center for Nuclear Study, University of Tokyo

<sup>\*2</sup> Department of Physics, Rikkyo University

<sup>\*3</sup> Department of Physics, University of Tokyo

<sup>\*4</sup> Faculty of Science, Tohoku University

<sup>\*5</sup> Department of Applied Physics, Tokyo Institute of Technology

Molecular states in  $^{12}\text{Be}$  and  $^{14}\text{Be}$ 

A. Saito,<sup>\*1</sup> S. Shimoura,<sup>\*2</sup> S. Takeuchi,<sup>\*1</sup> T. Motobayashi,<sup>\*1</sup> H. Akiyoshi, Y. Ando,<sup>\*1</sup> N. Aoi,<sup>\*3</sup> Zs. Fülöp,<sup>\*4</sup>  
 T. Gomi,<sup>\*1</sup> Y. Higurashi,<sup>\*1</sup> M. Hirai,<sup>\*5</sup> N. Iwasa,<sup>\*6</sup> H. Iwasaki,<sup>\*2</sup> Y. Iwata,<sup>\*5</sup> H. Kobayashi,<sup>\*1</sup>  
 M. Kurokawa,<sup>\*2</sup> Z. Liu,<sup>\*7</sup> T. Minemura, S. Ozawa, H. Sakurai,<sup>\*3</sup> M. Serata,<sup>\*1</sup>  
 T. Teranishi,<sup>\*2</sup> K. Yamada,<sup>\*1</sup> Y. Yanagisawa, and M. Ishihara

[NUCLEAR REACTIONS:  $^{14}\text{Be}(^{12}\text{C},\text{X})^{12,14}\text{Be} \rightarrow ^6\text{He}+^6\text{He}, ^6\text{He}+^8\text{He}$ , 75 A MeV]

Excited states in  $^{12}\text{Be}$  and  $^{14}\text{Be}$  were studied by measuring the  $^6\text{He}+^6\text{He}$  and  $^6\text{He}+^8\text{He}$  breakup channels in the two-neutron removal and the inelastic scattering of an exotic  $^{14}\text{Be}$  beam, respectively.

The experiment was carried out at RIPS in the RIKEN Accelerator Research Facility. Excited states in  $^{12}\text{Be}$  and  $^{14}\text{Be}$  were populated in the final state of the  $^{14}\text{Be}+^{12}\text{C}$  interaction at an incident energy of 75 A MeV. The reaction products were measured and identified by a hodoscope of a plastic scintillator array with an active area of  $1 \times 1 \text{ m}^2$  located 4.9 m downstream of the target. The decay energies for  $^{12}\text{Be} \rightarrow ^6\text{He}+^6\text{He}$  and  $^{14}\text{Be} \rightarrow ^6\text{He}+^8\text{He}$  were extracted by the invariant-mass method.

Figure 1 shows the decay-energy spectra for the breakup channels of (a)  $^{12}\text{Be}$  and (b)  $^{14}\text{Be}$ . The peak at 1.7 MeV in Fig. 1 (a) is a new excited state at 11.8 MeV in  $^{12}\text{Be}$ , and the others correspond to the peaks reported in Ref. 1. Three new levels in  $^{14}\text{Be}$  were found at 10.8 MeV, 11.6 MeV, and 15.5 MeV.

Angular-correlation data of decay particles were analyzed to determine the spins of these observed states. Figure 2 shows the result for the peak at 1.7 MeV for  $^{12}\text{Be}$  in Fig. 1 (a).  $\psi$  is the angle of the relative velocity of the decay particles with respect to the beam direction.<sup>2)</sup> The solid, dashed, and dotted curves show

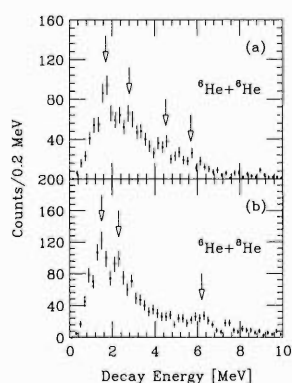


Fig. 1. Decay-energy spectra of (a)  $^{12}\text{Be}^* \rightarrow ^6\text{He}+^6\text{He}$  and (b)  $^{14}\text{Be}^* \rightarrow ^6\text{He}+^8\text{He}$ .

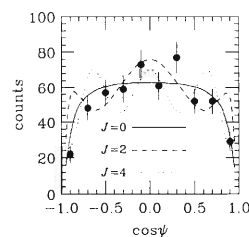


Fig. 2. Angular correlation for the peak at 1.7 MeV in Fig. 1 (a).

the results of Monte-Carlo simulations assuming the spins of the states to be  $J = 0$ ,  $J = 2$ , and  $J = 4$ , respectively. The geometrical acceptance of the experimental setup was taken into account. For  $J = 2$  and  $J = 4$ , isotropic backgrounds were assumed in addition to a resonance contribution. Their relative magnitude was fixed to be 2:1. The spin of the state was assigned to be 0 by comparing the  $\chi^2$  values ( $\chi^2_{J=0} = 1.4$ ,  $\chi^2_{J=2} = 2.9$ ,  $\chi^2_{J=4} = 2.4$ ). In the same way, the angular correlations for the peaks in Fig. 1 (b) were also analyzed. However we were not able to fix the spins of these states because of large  $\chi^2$  values.

Figure 3 shows the energy-spin systematics of the levels in  $^{12}\text{Be}$ . The open squares correspond to the data of Ref. 1. The solid line is the best fit to the open squares. The solid circle represents the new excited state observed in the present study. According to the energy-spin systematics, the new level may be a member of the rotational band with the  $^6\text{He}-^6\text{He}$  cluster structure in  $^{12}\text{Be}$  proposed by Freer *et al.*<sup>1)</sup>

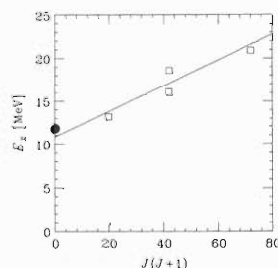


Fig. 3. Energy-spin systematics of levels in  $^{12}\text{Be}$ .

<sup>\*1</sup> Department of Physics, Rikkyo University  
<sup>\*2</sup> Center for Nuclear Study, University of Tokyo  
<sup>\*3</sup> Department of Physics, University of Tokyo  
<sup>\*4</sup> ATOMKI, Hungary  
<sup>\*5</sup> National Institute of Radiological Science  
<sup>\*6</sup> Department of Physics, Tohoku University  
<sup>\*7</sup> Institute of Modern Physics, China

## References

- 1) M. Freer *et al.*: Phys. Rev. Lett. **82**, 1383 (1999); M. Freer *et al.*: Phys. Rev. C **63**, 034301 (2001).
- 2) M. Freer: Nucl. Instrum. Methods Phys. Res. A **383**, 463 (1996).

Isobaric analog state of  $^{14}\text{Be}^\dagger$ 

S. Takuchi,<sup>\*1</sup> S. Shimoura,<sup>\*2</sup> T. Motobayashi,<sup>\*1</sup> H. Akiyoshi, Y. Ando,<sup>\*1</sup> N. Aoi,<sup>\*3</sup> Zs. Fülöp,<sup>\*4</sup>  
 T. Gomi,<sup>\*1</sup> Y. Higurashi,<sup>\*1</sup> M. Hirai,<sup>\*5</sup> N. Iwasa,<sup>\*6</sup> H. Iwasaki,<sup>\*2</sup> Y. Iwata,<sup>\*5</sup> H. Kobayashi,<sup>\*1</sup>  
 M. Kurokawa,<sup>\*2</sup> Z. Liu,<sup>\*7</sup> T. Minemura, S. Ozawa, H. Sakurai,<sup>\*3</sup> M. Serata,<sup>\*1</sup> T. Teranishi,<sup>\*2</sup>  
 K. Yamada,<sup>\*1</sup> Y. Yanagisawa, and M. Ishihara

[NUCLEAR REACTIONS:  $^1\text{H}(^{14}\text{Be}, ^{14}\text{B}^*)$ , 74 A MeV; Isobaric analog state; Charge exchange reaction; Radioactive beam experiment; Coulomb displacement energy; Halo structure]

The halo structure of the neutron-dripline nucleus  $^{14}\text{Be}$  has been investigated by various approaches, such as the interaction cross section measurement, dissociation reaction and  $^{14}\text{Be}$  fragmentation.<sup>1-4)</sup> In the recent plausible view, the mixing of *s* and *d*-wave components in the halo wave function has been suggested. Another aspect of the structure of  $^{14}\text{Be}$  may be explored by studying its Isobaric Analog State (IAS). Since the wave function of the IAS is essentially the same as that of its isobaric partner, possible exotic natures of  $^{14}\text{Be}$  may be traced in properties of the IAS such as the Coulomb displacement energy ( $\Delta E_C$ ) and the width of the IAS. In the present study, we have measured the  $^{14}\text{Be}(p,n)^{14}\text{B}^*$  reaction in inverse kinematics at  $E_{\text{in}} = 74$  A MeV.

The experiment was performed at the RIKEN Accelerator Research Facility. A secondary beam of  $^{14}\text{Be}$  was produced by using the projectile fragmentation of a 100 A MeV  $^{18}\text{O}$  beam on a 1110 mg/cm<sup>2</sup> thick  $^9\text{Be}$  target, and selected by the RIPS.<sup>5)</sup> Energy of the incident  $^{14}\text{Be}$  beam was  $74 \pm 4$  A MeV in the middle of a secondary target, and a typical intensity was  $10^4$  cps with a purity of around 80%. After traversing through the plastic-scintillator detectors, the  $^{14}\text{Be}$  beam was focused on a hydrogen or deuterium target with the thicknesses of 187 and 204 mg/cm<sup>2</sup>, respectively.

The decay particles from  $^{14}\text{B}^*$  were detected in coincidence by a  $\Delta E$ - $E$  plastic scintillator hodoscope with a  $1 \times 1$  m<sup>2</sup> active area, which was located at 4.9 m downstream from the target. Information on the particle hit position was obtained by the segmentation and time difference between signals from two photomultipliers attached to the both ends of each scintillator bar. Velocities of the decay particles were determined by the TOF over the 4.9 m flight path between the target and the hodoscope. Charged particles were identified by using the  $\Delta E$  - TOF and  $E$  - TOF methods. For neutron detection, the  $\Delta E$  plane served as a charged-

particle veto. The momentum vectors of the decay particles were determined by combining their velocities and hit positions on the hodoscope, and were used to reconstruct the decay energy of  $^{12}\text{Be}+p+n$  system.

A prominent peak was observed in the decay energy spectrum of  $^{12}\text{Be}+p+n$  channel on a hydrogen target, while no peak was observed in the (d, 2n) reaction, indicating the  $\Delta S = 0$  nature. The peak observed in the (p, n) reaction was assigned to the IAS of  $^{14}\text{Be}$  because of the characteristics of  $\Delta S = 0$ ,  $\Delta L = 0$  derived from the angular distribution of  $^{14}\text{B}^*$ . The excitation energy and the width of the observed IAS were determined to be  $17.06 \pm 0.03$  MeV and  $0.11 \pm 0.05$  MeV (FWHM), respectively.

Coulomb displacement energy of  $1.62 \pm 0.11$  MeV was deduced between the ground state of  $^{14}\text{Be}$  and its IAS. This is smaller than the  $\Delta E_C$  value of 1.97 MeV for  $^{10}\text{Be}$  and 1.83 MeV for  $^{12}\text{Be}$ . This small  $\Delta E_C$  value suggests spatial extension of the wave function of the exchanged proton in the IAS, indicating the halo structure of the  $^{14}\text{Be}$  nucleus.

A relatively large width of  $\Gamma = 0.11 \pm 0.05$  MeV was obtained for the IAS. Assuming that  $^{14}\text{B}^*$  (IAS) decays to the  $^{13}\text{Be}+p$  system, the particle-decay widths were calculated to be  $\Gamma^0 = 0.24$  MeV and  $\Gamma^0 = 0.001$  MeV for pure *s* and *d*-wave, respectively. The *s*-wave spectroscopic factor of  $45 \pm 20\%$  is extracted from the observed width.

These results suggest a considerable contribution of the  $2s_{1/2}$  orbital in the ground state of  $^{14}\text{Be}$ .

## References

- 1) I. Tanihata et al.: Phys. Lett. B **206**, 592 (1988).
- 2) T. Suzuki et al.: Nucl. Phys. A **658**, 313 (1999).
- 3) M. Labiche et al.: Phys. Rev. Lett. **86**, 600 (2001).
- 4) M. Zahar et al.: Phys. Rev. C **48**, R1484 (1993).
- 5) T. Kubo et al.: Nucl. Instrum. Methods Phys. Res. B **70**, 309 (1992).

<sup>†</sup> Condensed from the article in Phys. Lett. B **515**, 255 (2001)

<sup>\*1</sup> Rikkyo University

<sup>\*2</sup> Center for Nuclear Study, University of Tokyo

<sup>\*3</sup> University of Tokyo

<sup>\*4</sup> ATOMKI, Hungary

<sup>\*5</sup> National Institute of Radiological Sciences

<sup>\*6</sup> Tohoku University

<sup>\*7</sup> Institute of Modern Physics, China

## Two-neutron breakup experiments on $^{11}\text{Li}$ , $^{14}\text{Be}$ and $^{17}\text{B}$

T. Nakamura,<sup>\*1</sup> T. Sugimoto,<sup>\*1</sup> N. Fukuda, N. Aoi,<sup>\*2</sup> H. Baba,<sup>\*3</sup> D. Bazin,<sup>\*4</sup> T. Gomi,<sup>\*3</sup> N. Imai,<sup>\*2</sup> K. Hasegawa,<sup>\*3</sup> M. Ishihara, T. Kobayashi,<sup>\*5</sup> Y. Kondo,<sup>\*1</sup> T. Kubo, M. Miura,<sup>\*1</sup> T. Motobayashi,<sup>\*3</sup> A. Saito,<sup>\*3</sup> H. Sakurai,<sup>\*2</sup> T. Yakushiji,<sup>\*5</sup> Y. Yanagisawa, K. Yoneda, K. Watanabe,<sup>\*5</sup> and Y. X. Watanabe

[Neutron Halo, Coulomb dissociation, Nuclear breakup]

We have studied Coulomb and nuclear dissociations of two-neutron halo nuclei  $^{11}\text{Li}$ ,  $^{14}\text{Be}$ , and  $^{17}\text{B}$  by a kinematically complete measurement on Pb and C targets. The momentum vectors of the outgoing core fragment and two neutrons were measured in coincidence to reconstruct the invariant mass of the excited states of these nuclei. The aim of the experiment is to study low-lying E1 excitation in the Coulomb dissociation<sup>1-5)</sup> and other multipole excitations in the nuclear dissociation<sup>5)</sup> in terms of the halo property. In addition, the semi-exclusive spectrum, one neutron plus the core fragment, was included in the data to extract the structure of the unbound resonances of  $^{10}\text{Li}$ ,  $^{13}\text{Be}$ , and  $^{16}\text{B}$ . These structures are important for understanding the single-particle levels of neutron halo nuclei as well as the binding mechanism of the three-body Borromean structure. Inclusive breakup cross sections were also measured to study the reaction mechanism concerning the three-body breakup of halo nuclei.

The experiment was performed at the radioactive beam line RIPS. An  $^{18}\text{O}$  beam at 100 MeV/u was used to produce  $^{11}\text{Li}$  and  $^{14}\text{Be}$  secondary beams, and  $^{22}\text{Ne}$  at 110 MeV/u was used to produce a  $^{17}\text{B}$  beam. The typical intensities of the secondary beams were 40 k cps, 6 k cps, and 700 cps for  $^{11}\text{Li}$ ,  $^{14}\text{Be}$  and  $^{17}\text{B}$ , respectively. The energy of the secondary beams was adjusted to be about 70 MeV/u on the target.

The experimental setup is shown in Fig. 1. The momentum of the beam ion was obtained by tracing the trajectory by the two PPAC's, and by measuring the time of flight (TOF) between a thin plastic scintillator located about 5 m upstream of the target and the PPAC close to the target. The outgoing charged fragment was bent by the dipole magnet, and tracked by the two drift chambers (FDC1, FDC3) at the entrance and exit of the magnet. The time of flight measured by the hodoscope was combined with the tracking information to extract the momentum of the fragment.

Neutrons were measured by 54 rods of plastic scintillators, each having dimensions of 214 (W)  $\times$  6 (H)  $\times$  6 (D) cm<sup>3</sup>. These rods were arranged into two walls, as

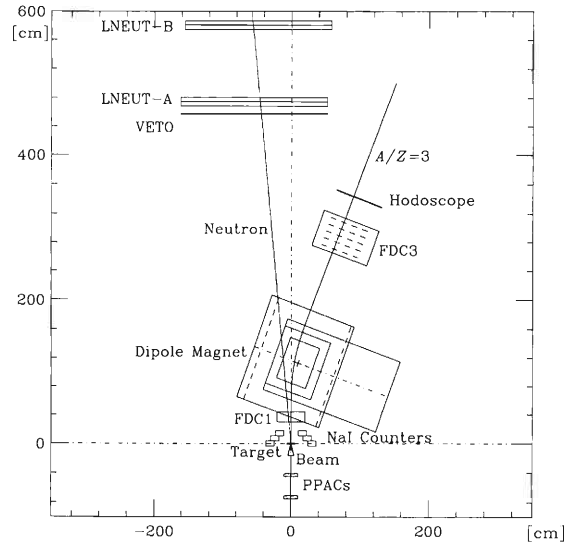


Fig. 1. Experimental setup of breakup experiments on  $^{11}\text{Li}$ ,  $^{14}\text{Be}$  and  $^{17}\text{B}$ .

shown in the figure (labeled LNEUT-A and LNEUT-B). The TOF and hit position of the outgoing neutron were measured to reconstruct the momentum. The efficiency of the neutron detector was studied by a separate experiment using the  $^7\text{Li}(p,n)^7\text{Be}$  reaction with a  $\text{H}_2^+$  molecule beam at 70 MeV/u.

Thirty-six pieces of NaI(Tl) surrounding the target were used to detect the de-excitation  $\gamma$  rays from the core fragment. The  $\gamma$ -ray information can be used to estimate the core excitation of the parent nucleus in the breakup reactions.

An analysis of the data is now in progress.

### References

- 1) T. Nakamura et al.: Phys. Rev. Lett. **83**, 1112 (1999).
- 2) K. Ieki et al.: Phys. Rev. Lett. **70**, 730 (1993).
- 3) S. Shimoura et al.: Phys. Lett. B **348**, 29 (1995).
- 4) M. Zinser et al.: Nucl. Phys. A **619**, 151 (1997).
- 5) T. Aumann et al.: Phys. Rev. C **59**, 1252 (1999).

\*1 Tokyo Institute of Technology

\*2 University of Tokyo

\*3 Rikkyo University

\*4 National Superconducting Cyclotron Laboratory, Michigan State University, USA

\*5 Tohoku University

## $^{11}\text{C}(\text{p},\gamma)^{12}\text{N}$ reaction studied by the Coulomb dissociation method

T. Minemura, T. Motobayashi,<sup>\*1</sup> S. Shimoura,<sup>\*2</sup> H. Murakami,<sup>\*1</sup> Y. Ando,<sup>\*1</sup> Y. Yanagisawa, Y. Iwata,<sup>\*3</sup>  
S. Ozawa, S. Takeuchi,<sup>\*1</sup> Y. Higurashi,<sup>\*1</sup> K. Yamada,<sup>\*1</sup> T. Gomi,<sup>\*1</sup> M. Serata,<sup>\*1</sup> H. Kobayashi,<sup>\*1</sup>  
T. Teranishi,<sup>\*2</sup> N. Aoi,<sup>\*4</sup> M. Hirai,<sup>\*3</sup> H. Iwasaki,<sup>\*2</sup> N. Imai,<sup>\*4</sup> N. Iwasa,<sup>\*5</sup> M. Kurokawa,<sup>\*2</sup> H. Akiyoshi,  
Zs. Fülöp,<sup>\*6</sup> H. Sakurai,<sup>\*4</sup> K. Yoshida, Z. Liu, and M. Ishihara

[NUCLEAR REACTIONS:  $^{208}\text{Pb}(^{12}\text{N}, ^{11}\text{C})^{208}\text{Pb}$ , Coulomb dissociation]

The importance of the radiative capture reaction,  $^{11}\text{C}(\text{p},\gamma)^{12}\text{N}$ , at low energies has been discussed in connection with an astrophysical nuclear burning process, called hot pp chain.<sup>1)</sup> Hence, the cross section of  $^{11}\text{C}(\text{p},\gamma)^{12}\text{N}$  determines the critical condition for the production of  $^{12}\text{C}$  in very massive stars through  $\beta^+$  decay<sup>2)</sup> or for the synthesis of  $^{11}\text{B}$  in nova.<sup>3)</sup>

In the region of astrophysical interest, there are two resonant states in  $^{12}\text{N}$ : the first excited state with  $J^\pi = 2^+$  at  $E_{\text{ex}} = 0.960$  MeV, and the second one with  $2^-$  at 1.19 MeV. These energies correspond to the center-of-mass energies ( $E_{\text{cm}}$ ) for the capture reaction or the  $\text{p}-^{11}\text{C}$  relative energies ( $E_{\text{rel}}$ ) in breakup measurements of 0.359 MeV and 0.589 MeV, respectively. Concerning astrophysical implications, the most important property is the radiative width ( $\Gamma_\gamma$ ) of the 1.19 MeV state.

Experiments have been performed at RIKEN using the secondary beam line, RIPS. A 77.0 MeV/nucleon  $^{12}\text{N}$  radioactive beam was produced through a fragmentation reaction of a primary 135 MeV/nucleon  $^{16}\text{O}$  beam. A 30 mg/cm<sup>2</sup>  $^{208}\text{Pb}$  target was bombarded by a secondary  $^{12}\text{N}$  beam. Protons and  $^{11}\text{C}$  produced in the  $^{12}\text{N}$  dissociation were detected by a plastic-scintillator hodoscope with an active area of  $1 \times 1$  m<sup>2</sup> located 5.1 m downstream of the target. The hodoscope was set in a vacuum chamber, and consisted of two types of layers: thirteen 5 mm thick  $\Delta E$  layers and sixteen 60 mm thick  $E$  layers. The energy-loss signal from the  $\Delta E$  plane was combined with the time-of-flight (TOF) to identify the atomic number ( $Z$ ) of each fragment. The mass ( $A$ ) was determined from a correlation between the TOF and the energy deposit in the  $E$  layer. The energy of the fragment was determined by its measured mass and the velocity obtained from the TOF. The complete kinematics of the reaction products, the total energy and relative momentum vector of the  $\text{p}+^{11}\text{C}$  system, were thus fully determined. To measure  $\gamma$  rays emitted from excited states of  $^{11}\text{C}$  in the channel of  $^{12}\text{N} \rightarrow \text{p}+^{11}\text{C}^*$ , a  $\gamma$ -ray detector system, called DALI (Detector Assembly for Low Intensity radiation), consist-

ing of sixty-four NaI(Tl) scintillators, was set around the target.

The experimental relative-energy spectrum is shown in Fig. 1. The closed circles represent the data obtained in the present work. The solid curve shows the result of a Monte-Carlo simulation assuming three contributions, two resonances at  $E_{\text{cm}} = 0.359$  MeV and 0.589 MeV, and direct proton capture, whose magnitudes were treated as fitting parameters. The bump observed at around 0.6 MeV is mainly due to the E1 excitation of  $^{12}\text{N}$  from the  $1^+$  ground state to the  $2^-$  state at  $E_{\text{ex}} = 1.19$  MeV. The radiative width,  $\Gamma_\gamma = 13.0 \pm 0.5$  meV, was extracted by comparing the yield of the resonance and the result of a distorted-wave calculation with corrections due to the detector response. This is in between the two different predictions by Wiescher *et al.*<sup>4)</sup> (2 meV) and Descouvemont and Baraffe<sup>5)</sup> (140 meV). The present result is consistent with that of the Coulomb dissociation experiment at GANIL<sup>2)</sup> ( $6_{-3.5}^{+7}$  meV), but the accuracy is greatly improved.

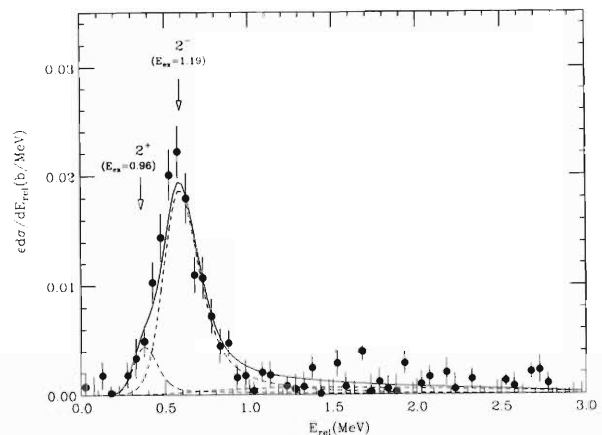


Fig. 1. Relative energy spectrum obtained for the  $^{208}\text{Pb}(^{12}\text{N}, ^{11}\text{C})^{208}\text{Pb}$  reaction. The solid curve represents the results of a Monte-Carlo simulation, comprising the three components shown by the dashed curves.

### References

- 1) A. Jorissen *et al.*: *Astron. Astrophys.* **221**, 161 (1989).
- 2) P. Descouvemont *et al.*: *Nucl. Phys. A* **514**, 66 (1990).
- 3) M. Arnould *et al.*: *Astron. Astrophys.* **42**, 55 (1975).
- 4) M. Wiescher *et al.*: *Astrophys. J.* **343**, 352 (1989).
- 5) A. Lefebvre *et al.*: *Nucl. Phys. A* **592**, 69 (1995).

<sup>\*1</sup> Rikkyo University

<sup>\*2</sup> Center for Nuclear Study, University of Tokyo

<sup>\*3</sup> National Institute of Radiological Sciences

<sup>\*4</sup> University of Tokyo

<sup>\*5</sup> Tohoku University

<sup>\*6</sup> ATOMKI, Hungary

## Low-energy E1 strength in $^{13}\text{O}$

T. Minemura, T. Motobayashi,<sup>\*1</sup> S. Shimoura,<sup>\*2</sup> H. Murakami,<sup>\*1</sup> Y. Ando,<sup>\*1</sup> Y. Yanagisawa, Y. Iwata,<sup>\*3</sup> S. Ozawa, S. Takeuchi,<sup>\*1</sup> Y. Higurashi,<sup>\*1</sup> K. Yamada,<sup>\*1</sup> T. Gomi,<sup>\*1</sup> M. Serata,<sup>\*1</sup> H. Kobayashi,<sup>\*1</sup> T. Teranishi,<sup>\*2</sup> N. Aoi,<sup>\*4</sup> M. Hirai,<sup>\*3</sup> H. Iwasaki,<sup>\*2</sup> N. Imai,<sup>\*4</sup> N. Iwasa,<sup>\*5</sup> M. Kurokawa,<sup>\*2</sup> H. Akiyoshi, Zs. Fülöp,<sup>\*6</sup> H. Sakurai,<sup>\*4</sup> K. Yoshida, Z. Liu, and M. Ishihara

[NUCLEAR REACTIONS:  $^{208}\text{Pb}(^{13}\text{O}, ^{12}\text{N} p)^{208}\text{Pb}$ , Coulomb dissociation]

We studied the low-energy E1 strength in  $^{13}\text{O}$  by a Coulomb dissociation measurement. The process  $^{13}\text{O} \rightarrow ^{12}\text{N} + p$  in the field of  $^{208}\text{Pb}$  was measured using radioactive  $^{13}\text{O}$  beams with 83.5 MeV/nucleon incident energy.

Only a few levels are known for  $^{13}\text{O}$ , based on the pion charge-exchange reaction data,<sup>1)</sup> which has a limited the energy resolution for precise spectroscopic studies. The nuclear structure of  $^{13}\text{O}$  is also important for evaluating the astrophysical reaction rate of the radiative capture process,  $^{12}\text{N}(p, \gamma)^{13}\text{O}$ . This reaction is expected to play a role in the hot p-p mode nuclear burning in hydrogen-rich massive objects.<sup>2)</sup>

A theoretical estimate was made for the  $^{12}\text{N}(p, \gamma)^{13}\text{O}$  reaction rate by Wiescher *et al.*<sup>2)</sup> in their network calculation for the hot p-p mode. The quoted resonance corresponds to the state observed in the  $^{13}\text{C}(\pi^+, \pi^-)^{13}\text{O}$  reaction.<sup>1)</sup>

Experiments have been performed at RIKEN using the secondary beam line, RIPS. A 83.5 MeV/nucleon  $^{13}\text{O}$  radioactive beam was produced through a fragmentation reaction of a primary 135 MeV/nucleon  $^{16}\text{O}$  beam. A 55 mg/cm<sup>2</sup>  $^{208}\text{Pb}$  target was bombarded by the secondary  $^{13}\text{O}$  beam. The breakup fragments,  $^{12}\text{N}$  and proton, were detected in coincidence after traveling through a 5.1 m flight-path by a plastic scintillator hodoscope. From the fragments' velocities, measured by their time-of-flight and their hit positions in the hodoscope, we could reconstruct the p- $^{12}\text{N}$  relative energy.

Figure 1 shows the E1 strength function for  $^{13}\text{O}$  extracted from the Coulomb dissociation yield. The dashed curve represent the line shape expected for an s-wave E1 resonances assuming the full single-particle strength calculated by the R-matrix theory.<sup>3)</sup> The contribution from quadrupole excitation was estimated from data taken with a carbon target in the same setup, and was subtracted. The sum of the  $B(E1)$  strength in the range  $0.5 \text{ MeV} < E_{\text{rel}} < 2.0 \text{ MeV}$  is  $0.079 \pm 0.003 \text{ e}^2\text{fm}^2$ . This is close to a prediction by Sagawa *et al.*<sup>4)</sup> Their large-scale shell-model calculation

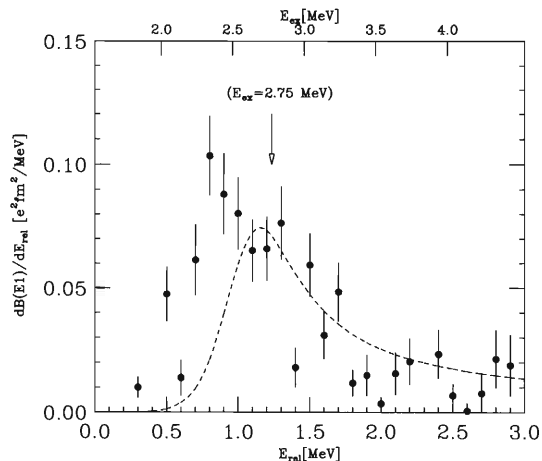


Fig. 1. Dipole strength function for  $^{13}\text{O}$  obtained from the Coulomb dissociation yield. The dashed curve show the line shape assuming an s-wave resonance fitted to the data around 1.2 MeV.

results in a large  $B(E1; \uparrow)$  of  $0.056 \text{ e}^2\text{fm}^2$  at around 2.9 MeV excitation energy. This large E1 amplitude at low excitation energies is remarkable, because the lowest E1 states in other  $Z = 8$  nuclei are located at higher energies of 5.17 MeV ( $^{14}\text{O}$ ), 5.18 MeV ( $^{15}\text{O}$ ) and 7.12 MeV ( $^{16}\text{O}$ ). The observed large E1 strength should considerably increase the reaction rate of the  $^{12}\text{N}(p, \gamma)^{13}\text{O}$  reaction compared with that predicted by Wiescher *et al.*<sup>2)</sup> because their predicted strength ( $\Gamma_\gamma = 24 \text{ meV}$ ) corresponds to a lower  $B(E1)$  of  $0.001 \text{ e}^2\text{fm}^2$ .

### References

- 1) P. A. Seidl *et al.*: Phys. Rev. C **30**, 1076 (1984).
- 2) M. Wiescher *et al.*: Astrophys. J. **343**, 352 (1989).
- 3) F. C. Barker and P. B. Treacy: Nucl. Phys. **38**, 33 (1962).
- 4) H. Sagawa, T. Suzuki, H. Iwasaki, and M. Ishihara: Phys. Rev. C **63**, 034310 (2001).

<sup>\*1</sup> Department of Physics, Rikkyo University  
<sup>\*2</sup> Center for Nuclear Study, University of Tokyo  
<sup>\*3</sup> National Institute of Radiological Sciences  
<sup>\*4</sup> Department of Physics, University of Tokyo  
<sup>\*5</sup> Faculty of Science, Tohoku University  
<sup>\*6</sup> ATOMKI, Hungary

# Study of proton resonance states in $^{13}\text{O}$ and $^{12}\text{N}$ using elastic resonance scattering

T. Teranishi,\*<sup>1</sup> S. Kubono,\*<sup>1</sup> S. Shimoura,\*<sup>1</sup> M. Notani,\*<sup>1</sup> Y. Yanagisawa, S. Michimasa,\*<sup>1</sup> K. Ue,\*<sup>1</sup>  
H. Iwasaki,\*<sup>1</sup> M. Kurokawa,\*<sup>1</sup> Y. Sato,\*<sup>1</sup> T. Morikawa,\*<sup>2</sup> A. Saito,\*<sup>3</sup> and Zs. Fülöp\*<sup>4</sup>

[Unstable nuclei, Nuclear astrophysics]

We have developed an in-flight low-energy RI beam separator, CRIB,<sup>1)</sup> under the RIKEN-CNS joint-research program. One of the applications of low-energy RI beams ( $< 10$  MeV/nucleon) is a study of resonance states in unstable nuclei, which are of great interest for nuclear structure and nuclear astrophysics. This report describes the first experimental result obtained at CRIB. The experiment aimed at studying resonance states in unstable nuclei,  $^{13}\text{O}$  and  $^{12}\text{N}$ , via elastic scattering  $^{12}\text{N}+p$  and  $^{11}\text{C}+p$ , respectively. Data of these resonances is important to understand a hydrogen burning process at high temperature in metal-deficient stars.

The elastic scattering was measured in inverse kinematics with RI beams,  $^{12}\text{N}$  and  $^{11}\text{C}$ , and a proton target. In this situation, the center-of-mass energy and angle can be determined by measuring the energy and angle of the recoil proton at better resolution than by measuring those of the heavy ejectile. It is useful to apply the thick-target method,<sup>2,3)</sup> where the target thickness is chosen to be comparable to the range of the beam in the target. Due to a large energy loss of the beam, a wide range of the excitation function,  $d\sigma/d\Omega(E)$ , of elastic scattering can be measured at the same time. Protons were detected at forward angles in the laboratory frame. At a fixed angle, the proton energy spectrum has roughly the same shape as the excitation function. In the excitation function, a resonance can be identified as an interference pattern of potential scattering and resonance scattering.

Secondary beams,  $^{12}\text{N}$  and  $^{11}\text{C}$ , were produced by the  $^3\text{He}(^{10}\text{B},^{12}\text{N})n$  and  $^3\text{He}(^{10}\text{B},^{11}\text{C}+p)n$  reactions, respectively. A primary beam of  $^{10}\text{B}$  at 7.8 MeV/nucleon from the AVF cyclotron has an intensity of 200 pA. The production target was a cell containing  $^3\text{He}$  gas with a thickness of 0.25 mg/cm<sup>2</sup>. The secondary beams were separated by CRIB with an energy degrader of 10- $\mu\text{m}$  mylar foil at the dispersive focal plane. The beam obtained was a mixture of  $^{12}\text{N}$  (3%) at 3.9 MeV/nucleon and  $^{11}\text{C}$  (15%) at 3.4 MeV/nucleon. The total secondary-beam intensity was about  $10^5$  particles/sec. The experimental setup was installed at the dispersive focal plane of CRIB. The setup consisted of two PPACs for beam tagging,

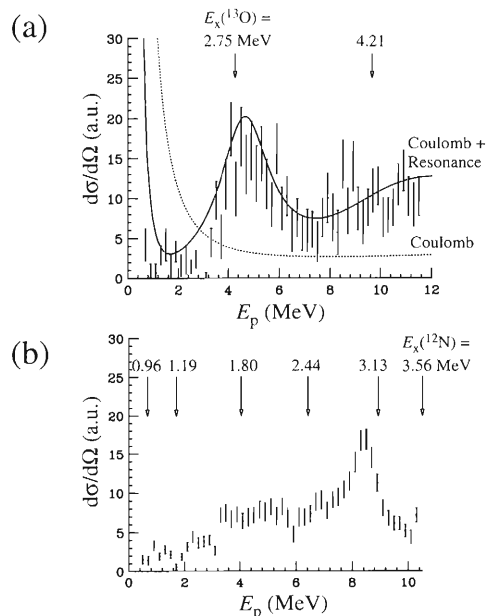


Fig. 1. Preliminary experimental results of the proton spectra for (a)  $^{12}\text{N}+p$  and (b)  $^{11}\text{C}+p$  elastic resonance scattering.

a  $\text{CH}_2$  target of 90  $\mu\text{m}$  and a set of  $\Delta E$ - $E$  silicon detectors, which covered scattering angles of 0–5° for the recoil protons.

Figure 1 (a) and (b) show preliminary results of the proton energy spectra for  $^{12}\text{N}+p$  and  $^{11}\text{C}+p$ , respectively. In the spectra, many resonance states in  $^{13}\text{O}$  and  $^{12}\text{N}$  were identified. The analysis of the spectra using resonance formulae is now in progress. The values of the width, spin and parity will be newly determined for the resonance states at  $E_x = 2.75$  and 4.21 MeV in  $^{13}\text{O}$  and  $E_x = 3.13$  MeV in  $^{12}\text{N}$ .

## References

- 1) Y. Yanagisawa et al.: RIKEN Accel. Prog. Rep. **34**, 183 (2001).
- 2) K. P. Artemov et al.: Sov. J. Nucl. Phys. **52**, 408 (1990).
- 3) S. Kubono: Nucl. Phys. A **693**, 221 (2001), and references therein.

\*<sup>1</sup> Center for Nuclear Study, University of Tokyo

\*<sup>2</sup> Department of Physics, Kyushu University

\*<sup>3</sup> Department of Physics, Rikkyo University

\*<sup>4</sup> ATOMKI, Hungary

## Projectile fragmentation of $^{14}\text{O}$ at 60 A MeV on $^4\text{He}$

H. Baba,<sup>\*1</sup> S. Shimoura,<sup>\*2</sup> T. Minemura, Y. U. Matsuyama,<sup>\*1</sup> A. Saito,<sup>\*1</sup> H. Akiyoshi, N. Aoi,<sup>\*3</sup> T. Gomi,<sup>\*1</sup> Y. Higurashi,<sup>\*1</sup> K. Ieki,<sup>\*1</sup> N. Imai,<sup>\*3</sup> N. Iwasa,<sup>\*4</sup> H. Iwasaki,<sup>\*3</sup> S. Kanno,<sup>\*1</sup> S. Kubono,<sup>\*2</sup> M. Kunibu,<sup>\*1</sup> S. Michimasa,<sup>\*2</sup> T. Motobayashi,<sup>\*1</sup> T. Nakamura,<sup>\*5</sup> H. Sakurai,<sup>\*3</sup> M. Serata,<sup>\*1</sup> E. Takeshita,<sup>\*1</sup> S. Takeuchi,<sup>\*1</sup> T. Teranishi,<sup>\*2</sup> K. Ue,<sup>\*2</sup> K. Yamada,<sup>\*1</sup> and Y. Yanagisawa

[NUCLEAR REACTIONS:  $^4\text{He}(^{14}\text{O}, X)$ , 60 A MeV; Projectile fragmentation]

We have studied the systematics of the production cross sections of light isotopes for the projectile fragmentation of  $^{14}\text{O}$  at 60 A MeV on a liquid-helium target. The experiment was performed at the RIPS (RIKEN projectile-fragment separator) beam line. A beam of  $^{14}\text{O}$  was produced by the fragmentation of an  $^{16}\text{O}$  beam at 135 A MeV on a  $^9\text{Be}$  target with a thickness of 1295 mg/cm<sup>2</sup>. The  $^{14}\text{O}$  nucleus and contaminants were identified using time-of-flight (TOF) information obtained from two 0.5 mm thick plastic scintillators separated by 5.3 m from each other. The  $^{14}\text{O}$  beam bombarded a 100 mg/cm<sup>2</sup> liquid-helium target. Reaction products were identified using a  $\Delta E$ - $E$  plastic hodoscope<sup>1)</sup> 4 m downstream from the target. The scattered angles of the particles were determined by hit positions in the hodoscope. The hodoscope consisted of  $\Delta E$  and  $E$  plastic scintillators of 5 and 60 mm thicknesses.

The production cross sections from the reaction of  $^4\text{He}(^{14}\text{O}, X)$  at 60 A MeV were measured, and compared with a calculation using an empirical parameterization code, EPAX.<sup>2)</sup> The observed cross sections were determined by identified particle counts in the hodoscope at the target-in run and the target-out run. The particle acceptances of the hodoscope were derived based on information of the angular distribution. These results are shown in Fig. 1. The closed circles indicate the measured production cross sections. Some nuclei have not been observed due to the too-short lifetimes or too-small cross sections. The solid histogram represents the EPAX calculations. The dotted histogram represents the EPAX calculations, including decay products from unbound nuclei, such as  $^5\text{He} \rightarrow ^4\text{He} + n$ ,  $^4\text{Li} \rightarrow ^3\text{He} + p$ ,  $^5\text{Li} \rightarrow ^4\text{He} + p$ ,  $^6\text{Be} \rightarrow ^4\text{He} + p + p$ ,  $^8\text{Be} \rightarrow ^4\text{He} + ^4\text{He}$ ,  $^9\text{B} \rightarrow ^4\text{He} + ^4\text{He} + p$ .

EPAX reproduced the global tendency of the cross sections obtained in the present measurement, although considerable differences in the absolute value was found for  $^8\text{Li}$ ,  $^{10}\text{Be}$  and carbon isotopes. For neutron-rich fragments of  $^8\text{Li}$  and  $^{10}\text{Be}$ , the cross sections were much smaller than EPAX. Fragments of

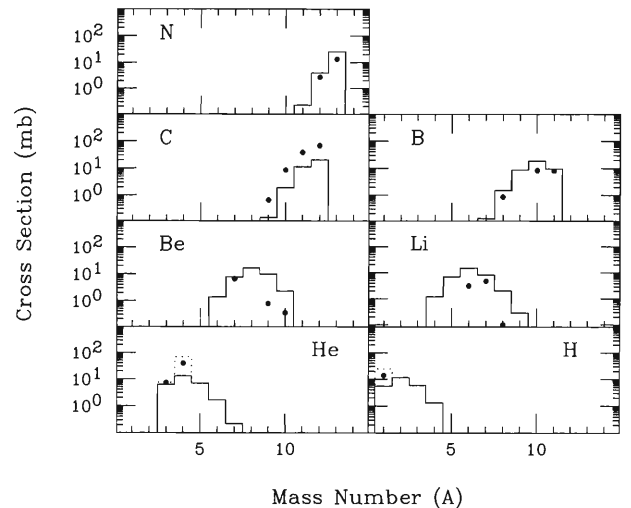


Fig. 1. Cross sections from the reaction  $^4\text{He}(^{14}\text{O}, X)$  at 60 A MeV. The closed circles indicate the measured production cross sections. The histograms represent the EPAX calculations. The statistical error is generally smaller than the size of the data points.

$^6\text{He}$ ,  $^8\text{He}$  and  $^9\text{Li}$  were not observed. This indicates that fragments located on the opposite side of the  $\beta$  stable line to the projectile are difficult to produce in the fragmentation reactions.

For all carbon isotopes, the cross sections are ten-times larger than those found by EPAX calculations. This discrepancy is possibly due to the sizeable effect of the inelastic excitation to the states above the particle emission threshold. An analysis including such inelastic scattering is in progress.

### References

- 1) I. Hisanaga et al.: RIKEN Accel. Prog. Rep. **31**, 162 (1998).
- 2) K. Sümmerer and B. Blank: Phys. Rev. C **61**, 034607 (2000).

<sup>\*1</sup> Department of Physics, Rikkyo University

<sup>\*2</sup> Center for Nuclear Study, University of Tokyo

<sup>\*3</sup> Department of Physics, University of Tokyo

<sup>\*4</sup> Faculty of Science, Tohoku University

<sup>\*5</sup> Department of Applied Physics, Tokyo Institute of Technology

Coulomb dissociation of  $^{13}\text{N}$  and  $^{14}\text{O}$ 

M. Serata,<sup>\*1</sup> T. Motobayashi,<sup>\*1</sup> S. Shimoura,<sup>\*2</sup> H. Akiyoshi, Y. Ando,<sup>\*1</sup> N. Aoi,<sup>\*2</sup> Zs. Fülöp,<sup>\*3</sup> T. Gomi,<sup>\*1</sup> Y. Higurashi,<sup>\*1</sup> M. Hirai,<sup>\*4</sup> K. Ieki,<sup>\*1</sup> N. Imai,<sup>\*2</sup> N. Iwasa,<sup>\*5</sup> H. Iwasaki,<sup>\*2</sup> Y. Iwata,<sup>\*4</sup> H. Kobayashi,<sup>\*1</sup> M. Kurokawa,<sup>\*2</sup> T. Minemura, H. Murakami,<sup>\*1</sup> S. Ozawa, H. Sakurai,<sup>\*2</sup> S. Takeuchi,<sup>\*1</sup> T. Teranishi,<sup>\*2</sup> K. Yamada,<sup>\*1</sup> Y. Yanagisawa, K. Yoshida, Z. Liu, and M. Ishihara

[NUCLEAR REACTIONS:  $^{208}\text{Pb}(^{13}\text{N},\text{p})^{12}\text{C}$ ) $^{208}\text{Pb}$ , 76 A MeV;  $^{208}\text{Pb}(^{14}\text{O},\text{p})^{13}\text{N}$ ) $^{208}\text{Pb}$ , 85 A MeV; Coulomb dissociation

In order to test the Coulomb dissociation method<sup>1)</sup> in extracting radiative-capture cross sections of astrophysical interest, we studied the processes  $^{13}\text{N} \rightarrow ^{12}\text{C} + \text{p}$  and  $^{14}\text{O} \rightarrow ^{13}\text{N} + \text{p}$  in the field of  $^{208}\text{Pb}$  via the lowest E1 resonances in  $^{13}\text{N}$  ( $1/2^+$ ;  $E_{\text{ex}} = 2.37$  MeV) and  $^{14}\text{O}$  ( $1^-$ ;  $E_{\text{ex}} = 5.17$  MeV), respectively. The earlier results of the  $^{14}\text{O}$  dissociation at RIKEN<sup>2)</sup> and GANIL<sup>3)</sup> agreed with a direct measurement performed at Louvain-La-Neuve.<sup>4)</sup> The RIKEN experiment<sup>2)</sup> also measured the  $^{13}\text{N}$  dissociation, and the extracted E1 strength was consistent with that obtained from direct measurements of the  $^{12}\text{C}(\text{p},\gamma)^{13}\text{N}$  reaction. However, these agreements were confirmed at accuracies of around 30%. The present experiment was aimed at improving the experimental accuracy.

Radioactive beams of  $^{13}\text{N}$  and  $^{14}\text{O}$  were provided by using the projectile fragmentation of a 135 A MeV  $^{16}\text{O}$  beam with a 1.4 g/cm<sup>2</sup> Be target. The  $^{13}\text{N}$  and  $^{14}\text{O}$  beams were separated by the RIPS facility,<sup>5)</sup> and bombarded a Pb target with a thickness of 55 mg/cm<sup>2</sup>. The averaged energies were 76 A MeV and 85 A MeV, respectively, for  $^{13}\text{N}$  and  $^{14}\text{O}$  at the middle of the target. Outgoing charged particles were detected in coincidence by a  $\Delta E$ - $E$  hodoscope,<sup>6)</sup> and their velocities were measured by the time-of-flight. The relative energies of the breakup fragments were calculated from their velocities and relative angle. An array of 64 NaI(Tl) scintillators was placed around the target to detect  $\gamma$ -rays with the process  $^{13}\text{N} \rightarrow ^{12}\text{C}^*(2^+; 4.44 \text{ MeV}) + \text{p}$ , which can not be separated from the  $^{12}\text{C}(0^+; \text{g.s.}) + \text{p}$  dissociation by only measuring the fragments.

Figure 1 shows the angular distributions of the experimental yield together with theoretical predictions normalized to the data. The energy resolution and the coincidence efficiency were taken into account in a theoretical calculation based on the distorted-wave theory, assuming pure E1 Coulomb excitation. As seen in the figures, the experimental distributions can be fairly well reproduced by the calculations, especially for the  $^{13}\text{N}$  dissociation. The normalization factors

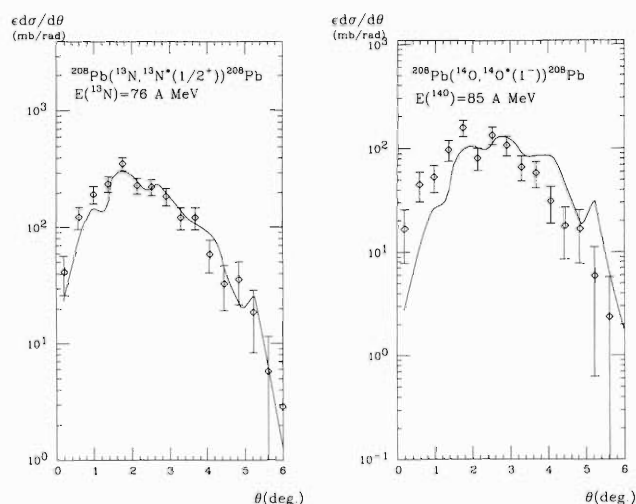


Fig. 1. Experimental and calculated angular distributions for the reactions  $^{208}\text{Pb}(^{13}\text{N}, \text{p})^{12}\text{C}$ ) $^{208}\text{Pb}$  (left part) and  $^{208}\text{Pb}(^{14}\text{O}, \text{p})^{13}\text{N}$ ) $^{208}\text{Pb}$  (right part).

lead to radiative widths of  $0.52 \pm 0.04$  eV ( $^{13}\text{N}$ ) and  $2.8 \pm 0.2$  eV ( $^{14}\text{O}$ ). The former is in very good agreement with the adopted value,  $0.50 \pm 0.04$  eV, based on direct  $^{12}\text{C}(\text{p},\gamma)^{13}\text{N}$  measurements. Thus, the reliability of the Coulomb dissociation method has been tested to an accuracy of the order of 10% in this case.

The extracted width for  $^{14}\text{O}$  agrees within the errors with the results by the previous Coulomb dissociation experiments,  $3.1 \pm 0.6$  eV<sup>2)</sup> and  $2.4 \pm 0.9$  eV,<sup>3)</sup> and that by the direct capture measurement,  $3.8 \pm 1.2$  eV.<sup>4)</sup>

## References

- 1) G. Baur et al.: Nucl. Phys. A **458**, 188 (1986).
- 2) T. Motobayashi et al.: Phys. Lett. B **264**, 259 (1991).
- 3) J. Kiener et al.: Nucl. Phys. A **552**, 66 (1993).
- 4) P. Decroock et al.: Phys. Rev. Lett. **67**, 808 (1991).
- 5) T. Kubo et al.: Nucl. Instrum. Methods Phys. Res. B **70**, 309 (1992).
- 6) I. Hisanaga et al.: RIKEN Accel. Prog. Rep. **31**, 162 (1998).

\*1 Rikkyo University

\*2 University of Tokyo

\*3 ATOMKI, Hungary

\*4 National Institute of Radiological Sciences

\*5 Tohoku University

# E1 strength of the subthreshold $3/2^+$ state in $^{15}\text{O}$ and its influence on the CNO reaction $^{14}\text{N}(p,\gamma)^{15}\text{O}$

K. Yamada,<sup>\*1</sup> T. Motobayashi,<sup>\*1</sup> H. Akiyoshi, N. Aoi,<sup>\*2</sup> Zs. Fülöp,<sup>\*3</sup> T. Gomi,<sup>\*1</sup> Y. Higurashi,<sup>\*1</sup> N. Imai,<sup>\*2</sup> N. Iwasa,<sup>\*4</sup> H. Iwasaki,<sup>\*5</sup> Y. Iwata,<sup>\*6</sup> H. Kobayashi,<sup>\*1</sup> M. Kurokawa,<sup>\*5</sup> Z. Liu,<sup>\*7</sup> T. Minemura, S. Ozawa, H. Sakurai,<sup>\*2</sup> M. Serata,<sup>\*1</sup> S. Shimoura,<sup>\*5</sup> S. Takeuchi,<sup>\*1</sup> T. Teranishi,<sup>\*5</sup> Y. Yanagisawa, K. Yoshida, and M. Ishihara

[NUCLEAR REACTIONS:  $\text{Pb}(^{15}\text{O},^{15}\text{O}\gamma)$ , 100 A MeV; Coulomb excitation, Nuclear astrophysics]

The Coulomb excitation of  $^{15}\text{O}$  was studied to determine the radiative width ( $\Gamma_\gamma$ ) of the  $3/2^+$  state in  $^{15}\text{O}$ . The higher tail of the state may affect the low-energy behavior of the reaction, which is important for the astrophysical rate of the CNO reaction  $^{14}\text{N}(p,\gamma)^{15}\text{O}$ .

The experiment was performed at RIPS<sup>1)</sup> at the RIKEN Accelerator Research Facility. A secondary  $^{15}\text{O}$  beam with an energy of 100 A MeV was focused on a lead target and excited by the Coulomb force. The de-excitation  $\gamma$ -ray was detected by a NaI(Tl)-scintillator array with 64 crystals. The scattered particles were detected by a plastic scintillator hodoscope<sup>2)</sup> consisting of a 5 mm thick  $\Delta E$  plane and a 60 mm thick  $E$  plane. Details of the setup are described in Ref. 3.

Figure 1 shows the Doppler-corrected  $\gamma$ -ray energy spectrum measured in coincidence with inelastically scattered  $^{15}\text{O}$  detected by detectors at the angle  $\theta = 63^\circ$ . The peak observed at 3.6 MeV is due to background photons originating from the target excitation, which corresponds to the  $2^+$  state at 4.1 MeV in  $^{208}\text{Pb}$ . No distinct peak can be seen at 6.79 MeV, where the yield due to the  $3/2^+ \rightarrow \text{g.s.}$  transition is expected. We fitted the experimental spectrum by five components: three ground-state transitions from the 5.24, 6.18 and 6.79 MeV states in  $^{15}\text{O}$ , the  $\gamma$ -ray spectrum due to the target excitation, and an exponential background. The line shapes for the transitions were obtained by a simulation which took into account the detector response. The spectrum for the target excitation was evaluated by data taken by detectors at a backward angle, where photons from  $^{15}\text{O}$  are greatly reduced due to the Doppler shift. The solid curve in the figure shows the result of the fit. The peak at 5.2 MeV is due mainly to direct excitation of the  $1/2^+$  and  $5/2^+$  states at 5.183 MeV and 5.241 MeV, respectively, and also the feeding of the  $5/2^+$  state from the higher  $5/2^+$  state at 6.859 MeV and the  $7/2^+$  state at 7.276 MeV. The dotted curve indicates the evaluated spectrum for the target excitation, and the straight

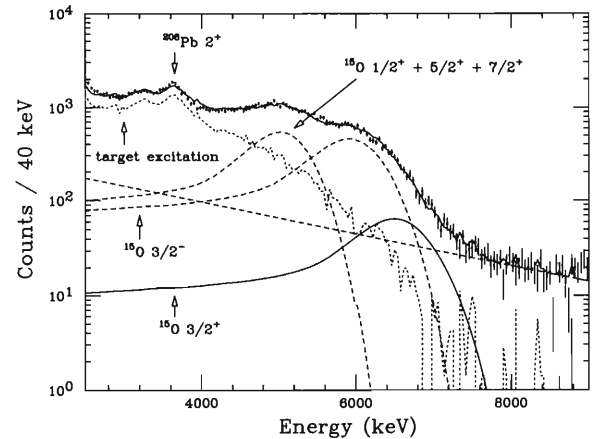


Fig. 1. Doppler-corrected  $\gamma$ -ray spectrum measured in coincidence with  $^{15}\text{O}$  and fitted by five components.

dashed line is the exponential background. The result of the fit for the component of the  $3/2^+$  state at 6.793 MeV is shown by the solid curve.

The radiative width,  $\Gamma_\gamma = 1.44^{+0.13}_{-0.42}$  eV, for the  $3/2^+$  state is extracted by comparing the measured cross section and the DWBA calculation assuming E1 Coulomb excitation. Considering the possible contribution from minor gamma transitions from other states, a fair estimate of the  $1\sigma$  upper limit of the radiative width is 1.6 eV. This result is consistent with a recent lifetime measurement by the Doppler-shift attenuation method.<sup>4)</sup> Their result corresponds to the width  $\Gamma_\gamma = 0.41^{+0.34}_{-0.13}$  eV. Thus only a minor effect of the  $3/2^+$  state is expected for the low-energy  $^{14}\text{N}(p,\gamma)^{15}\text{O}$  cross section.

## References

- 1) T. Kubo et al.: Nucl. Instrum. Methods Phys. Res. B **70**, 309 (1992).
- 2) I. Hisanaga et al.: RIKEN Accel. Prog. Rep. **31**, 162 (1998).
- 3) K. Yamada et al.: RIKEN Accel. Prog. Rep. **33**, 67 (2000).
- 4) P. F. Bertone et al.: Phys. Rev. Lett. **87**, 152501 (2001).

<sup>\*1</sup> Department of Physics, Rikkyo University

<sup>\*2</sup> Department of Physics, University of Tokyo

<sup>\*3</sup> ATOMKI, Hungary

<sup>\*4</sup> Department of Physics, Tohoku University

<sup>\*5</sup> Center for Nuclear Study, University of Tokyo

<sup>\*6</sup> National Institute of Radiological Science

<sup>\*7</sup> Institute of Modern Physics, China

## Measurements of the reaction cross sections of C isotopes at intermediate energy

T. Yamaguchi, T. Zheng,<sup>\*1,\*2</sup> A. Ozawa, M. Chiba,<sup>\*3</sup> R. Kanungo, T. Kato, K. Katori, K. Morimoto, T. Ohnishi, T. Suda, I. Tanihata, Y. Yamaguchi,<sup>\*4</sup> A. Yoshida, and K. Yoshida

[NUCLEAR REACTION: Be(<sup>22</sup>Ne, <sup>16</sup>C):  $E = 110A$  MeV; Measured reaction cross sections]

The interaction and reaction cross sections of unstable nuclei have been measured so far all over the world to investigate their radii and density distributions. Recently, interaction cross sections of carbon isotopes were measured at high energy,  $\sim 960A$  MeV at GSI.<sup>1)</sup> The interaction cross section can be related to the interaction radius. For stable nuclei, the interaction radii were found to follow  $r_I \propto A^{1/3}$ ,<sup>1)</sup> where  $A$  is the mass number. After applying this relation to neutron-rich carbon isotopes, however, it was found that the cross section at  $A = 16$  greatly deviates from this property. This might suggest the anomaly of nuclear structures near <sup>16</sup>C. Based on this result, the reaction cross sections for <sup>12,14-16</sup>C were measured at intermediate energies (50A and 80A MeV) to study the density distributions of these carbon isotopes.

According to Glauber theory,<sup>2)</sup> the reaction cross section is given by the product of the nucleon densities of the projectile and the target, multiplied by the nucleon-nucleon cross sections. Because the nucleon-nucleon cross sections become larger at lower energy, the reaction cross sections at lower energy become more sensitive to the outer part of the density. Thus, in principle, the density distributions of the projectiles can be studied based on the energy dependence of the cross sections. The reaction cross sections at both intermediate and high energy<sup>1)</sup> are analyzed to determine the density distributions.

In the present experiment we applied a new technique to the transmission method to measure the reaction cross sections. A schematic drawing of the experimental setup is shown in Fig. 1.

The experiment was performed using the RIKEN Projectile fragment Separator (RIPS). C beams were produced by bombarding a <sup>22</sup>Ne beam with 110A MeV on a Be target, which was located at F0, and transported to the dispersive focus, F1. After  $B\rho$  selection and an energy-loss analysis by a wedge degrader, they arrived at the F2 focus achromatically, where the reaction target C (20mm) was placed. Then, the projectiles as well as the reaction products were transported and focused by the quadrupole triplet to the final focus, F3, which was  $\sim 6$ m downstream, as shown in Fig. 1.

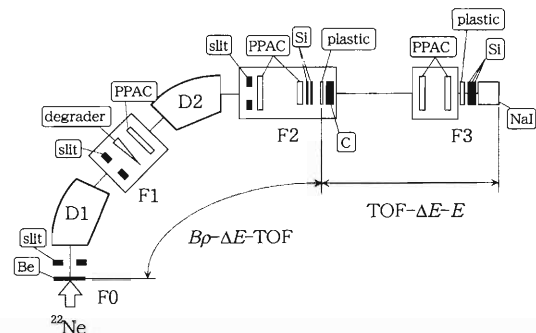


Fig. 1. Schematic depiction of the experimental setup.

Particle identification before the reaction target was done by means of  $B\rho$ - $\Delta E$ -TOF method. The detector system commonly used at RIPS was applied to count and identify the incident particles. One more parallel plate avalanche counter (PPAC) was installed to define the beam emittance at F2.

After the reaction target, the TOF- $\Delta E$ - $E$  method was applied to identify the outgoing particles. This method provides good mass separation due to good time and energy resolutions for time-of-flight (TOF) and  $E$  counters. Thin plastic scintillation counters were used to measure the TOF between F2 and F3, and a NaI ( $3'' \phi$ , 60 mm) counter was applied to  $E$  measurements. For  $Z$  identification, three silicon detectors ( $50 \times 50 \text{ mm}^2$ ,  $150 \mu\text{m}$ ) were placed in front of the NaI counter.

In this experiment, transmission from F2 to F3 is important to determine the cross sections precisely. For <sup>12</sup>C, transmission of more than 98% was obtained without the reaction target when the emittance cut was applied at F2 before the reaction target. The result of the cross section of <sup>12</sup>C is consistent with a phenomenological parameterization of the reaction cross sections given by Kox *et al.*<sup>3)</sup> For <sup>16</sup>C, a larger enhancement of the cross section at intermediate energy has been observed compared with that of high energy relative to the calculation. Further analysis is ongoing.

### References

- 1) A. Ozawa *et al.*: Nucl. Phys. A **693**, 32 (2001) and references therein.
- 2) R. J. Glauber: in *Lectures in Theoretical Physics*, Vol. 1 (1959), p. 315.
- 3) S. Kox *et al.*: Phys. Rev. C **35**, 1678 (1987).

\*1 Peking University, China

\*2 Tokyo University of Science

\*3 Tohoku University

\*4 Niigata University

# Study of the spin polarization of $^{19}\text{C}$ for a $g$ -factor measurement

D. Kameda,<sup>\*1</sup> H. Ueno, K. Asahi, H. Miyoshi,<sup>\*1</sup> A. Yoshimi, W. Sato, H. Watanabe, N. Imai,<sup>\*2</sup> J. Murata, K. Shimada,<sup>\*1</sup> J. Kaihara,<sup>\*1</sup> K. Yoneda, T. Koike,<sup>\*1</sup> Y. Kobayashi, and H. Ogawa<sup>\*3</sup>

[NUCLEAR STRUCTURE,  $^{19}\text{C}$ , Spin polarization,  $\beta$ -NMR method]

Based on the  $\beta$ -NMR method for spin-polarized radioactive-isotope beams, the  $g$  factor of the ground state of light unstable nuclei has been measured.<sup>1)</sup> For measuring  $g$  factors, it is important to produce spin-polarization in the projectile fragmentation reaction. In the present work, magnitude of the spin polarization of  $^{19}\text{C}$  was studied. In the case of  $^{19}\text{C}$ , the ground-state  $g$  factor is extremely sensitive to whether the spin-parity is  $J^\pi = 1/2^+, 3/2^+, 5/2^+$ , which are possible candidates for the ground state; the corresponding Schmidt value are  $g_{s_{1/2}} = -3.83$ ,  $g_{d_{3/2}} = +0.77$ , and  $g_{d_{5/2}} = -0.77$ . Similar observations are gained in more realistic shell-mode calculations.<sup>2)</sup> Owing to the large difference, the spin-parity can be assigned by measuring the  $g$  factor as a different approach using nuclear-reaction studies.<sup>3)</sup>

A beam of  $^{19}\text{C}$  was obtained from the fragmentation of  $^{22}\text{Ne}$  projectiles at an energy of 110 MeV/nucleon on a  $^9\text{Be}$  target of 736 mg/cm<sup>2</sup> thickness. In order to produce spin polarization, the  $^{19}\text{C}$  fragments were accepted by RIPS at emission angle of  $\theta_L = 0.8^\circ - 6.2^\circ$  and a momentum of  $p_F = 7.95 - 8.44$  GeV/c. The  $^{19}\text{C}$  fragments were then isotope-separated and implanted in a stopper material to which a magnetic field of  $B_0 = 40.07$  mT was applied. For measuring the spin polarization ( $P$ ), appropriate stopper materials should be chosen so that they can provide a sufficiently long relaxation time compared with the  $\beta$ -decay lifetime of  $^{19}\text{C}$  ( $\tau = 65.6$  ms). In the case of  $J^\pi(^{19}\text{C}_{\text{g.s.}}) = 1/2^+$ , graphite can be used for this purpose.<sup>1)</sup> This material, however, might not be applicable for the cases of  $J^\pi(^{19}\text{C}_{\text{g.s.}}) = 3/2^+$  and  $5/2^+$  because of the effect of  $^{19}\text{C}$  quadrupole relaxation. For these cases, Pt is known to be applicable by studying the  $^{17}\text{C}$   $g$ -factor measurement.<sup>1)</sup> Conversely, Pt cannot be used for the  $J^\pi(^{19}\text{C}_{\text{g.s.}}) = 1/2^+$  case because of the short relaxation time expected from its large  $g$  factor.

The value of  $A_\beta P(^{19}\text{C}_{\text{g.s.}})$  were measured by means of the adiabatic field rotation method using a similar experimental setup, described in Ref. 1, where  $A_\beta$  is the  $\beta$ -ray asymmetry factor. Based on this technique, the value of  $A_\beta P(^{19}\text{C}_{\text{g.s.}})$  can be determined without any information concerning the  $g$  factor. In measurements with graphite and Pt stoppers,  $A_\beta P(^{19}\text{C}_{\text{g.s.}}) = -0.29 \pm 0.17\%$  and  $-0.18 \pm 0.26\%$  were

observed, respectively.

Although the obtained statistics do not permit detailed discussions, it can be said that the spin polarization is very small in all cases of  $J^\pi(^{19}\text{C}_{\text{g.s.}})$ . Three possibilities can be considered for the observed small polarization. Firstly, the polarization appears to be diminished because of the large background. Figure 1 shows a decay curve accumulated in the  $^{19}\text{C}$   $\beta$  decay. The large background is due to the daughter nuclei after  $^{19}\text{C}$   $\beta$  decay. Secondly, non-vanishing angular momentum due to the Fermi motion in a group of nucleons in the projectile that is removed through the fragmentation process, which is essential mechanism of the spin polarization,<sup>1)</sup> can not be expected if the spin-parity of the ground state is  $1/2^+$ . Finally, it is known from our previous studies that fragments can not be spin-polarized using a Be target in some cases, although it has an advantage concerning the yield. An experiment with another target, such as  $^{93}\text{Nb}$ , is under consideration.

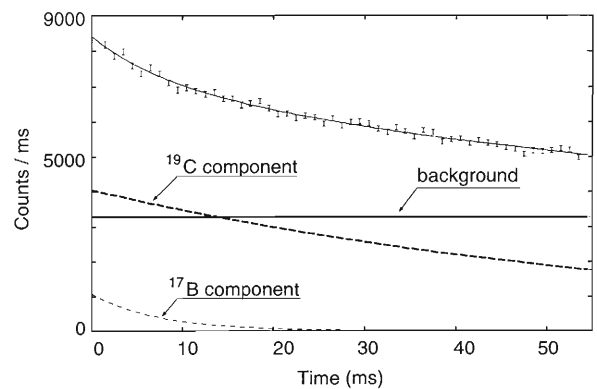


Fig. 1.  $\beta$ -decay curve accumulated in the present measurement. The two main components obtained from the fitting analysis are shown together with that of  $^{19}\text{C}$  (thick dotted curve). The thick line and the thin dotted curve show a constant background due to the long-lived daughter nuclei and  $^{17}\text{B}$  implanted as a beam contamination, respectively.

## References

- 1) K. Asahi et al.: RIKEN Rev., No. 39, 142 (2001).
- 2) B. A. Brown et al: OXBASH, MSU Cycl. Lab. Rep., No. 524, 1 (1986).
- 3) R. Kanungo et al.: Nucl. Phys. A **677**, 171 (2000).

<sup>\*1</sup> Department of Physics, Tokyo Institute of Technology

<sup>\*2</sup> Department of Physics, University of Tokyo

<sup>\*3</sup> National Institute of Advanced Industrial Science and Technology

## Search for $^{21}\text{B}$

A. Ozawa, Y. Yamaguchi,<sup>\*1</sup> T. Izumikawa,<sup>\*1</sup> R. Kanungo, T. Kato,<sup>\*1</sup> Y. Kawamura,<sup>\*1</sup> K. Kimura,<sup>\*2</sup> S. Momota,<sup>\*3</sup> T. Onishi, T. Suda, T. Suzuki,<sup>\*1</sup> I. Tanihata, T. Yamaguchi, K. Yoshida, and T. Zheng<sup>\*4</sup>

[NUCLEAR REACTIONS:  ${}^9\text{Be}({}^{40}\text{Ar},\text{X})$ ,  $E({}^{40}\text{Ar}) = 94 \text{ A MeV}$ ]

A very neutron-rich nucleus,  $^{21}\text{B}$ , has been searched based on motivation concerning the  $N = 16$  magic number.<sup>1)</sup> In a previous report,<sup>2)</sup> the motivation for this experiment and the experimental setup for the first attempt were described in detail. In this report, we describe the experimental setup for the second attempt and the results of a search.

The experimental setup at RIPS for the second attempt is almost similar to the previous one. The main differences are the installation of a plastic scintillator at F1 (thickness = 0.5 mm), which provides timing and analog signals, and the use of a Ta production target instead of a Be target, as in the previous experiment. The  ${}^{40}\text{Ar}$  beam was accelerated at the AVF and RIKEN Ring Cyclotron up to 94 A MeV and reacted with a 681 mg/cm<sup>2</sup> thick Ta target. The typical primary beam intensity was 41 pA. The magnetic rigidity of the first half of RIPS was set at 5.616 Tm in order to optimize the yield of the  $^{21}\text{B}$  isotopes. To reduce the relative rates of light isotopes, a thin aluminum wedge with a mean thickness of 223 mg/cm<sup>2</sup> was used at F1. The magnetic rigidity of the second part of the RIPS spectrometer was thereby adjusted to 5.530 Tm.

Particle identification was performed by a standard method based on the energy loss ( $\Delta E$ ), time-of-flight (TOF) and magnetic rigidity ( $B\rho$ ) measured for each fragment. The TOF of each fragment was determined from the F2-P1 timing and the F1-P1 timing. Two SSD detectors at F2 provided independent energy-loss values ( $\Delta E$ ). Additional energy-loss values were obtained from F1-P1. The magnetic fields at the two dipoles were monitored by NMR probes.

The Ta production target was irradiated for 121.5 hours in total. Particle identification for the  $^{21}\text{B}$  setting showed 16 events of the candidate. However, the identification suffered from serious background due to scattered light particles, mainly  $^{11}\text{Li}$ . In order to confirm  $Z = 5$  as candidates, we checked the energy-loss value from F1-P1. The energy-loss values of all  $^{21}\text{B}$  candidates coincided with those in  $^{11}\text{Li}$ . Thus, we conclude that those candidates were scattered particles of  $^{11}\text{Li}$ , and no event for  $^{21}\text{B}$  was observed in this measurement.

To show the particle instability of  $^{21}\text{B}$ , we measured the production cross sections for B-isotopes with the

same experimental setup using Be and Ta targets. To deduce the production cross sections, we need to know the transmission efficiency from F0 to F2 in RIPS. We used MOCADI simulations<sup>3)</sup> to obtain the transmission. The present cross sections are shown in Fig. 1. Previously, Momota *et al.* measured the production cross section for a reaction of  ${}^{40}\text{Ar} + \text{Be}$  with 90 A MeV.<sup>4)</sup> For  $^{15}\text{B}$ , our present data is consistent with this value, which shows the validity of the MOCADI simulations.

The present results of the  $^{21}\text{B}$  search only gave an upper limit of the production cross sections of  $^{21}\text{B}$ , as shown in Fig. 1. The upper limit is much smaller (factor of 12) than the production cross sections extrapolated by EPAX,<sup>5)</sup> which were normalized to our experimental cross sections. Thus, this large discrepancy shows the particle instability of  $^{21}\text{B}$ .

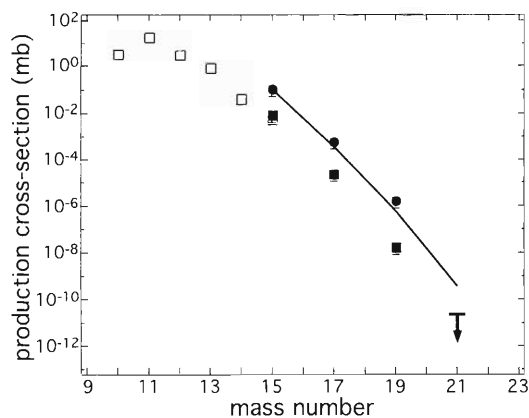


Fig. 1. Experimental production cross section for B isotopes produced with an  ${}^{40}\text{Ar}$  primary beam at 94 A MeV on Be (squares) and Ta (circles) targets. The closed marks show the present data. The open squares show the previous data.<sup>4)</sup> The upper limit of the production cross section of  $^{21}\text{B}$  is shown by the arrow. The curve shows the extrapolation of the experimental data using EPAX parameterization.<sup>5)</sup>

### References

- 1) A. Ozawa et al.: Phys. Rev. Lett. **84**, 5493 (2000).
- 2) A. Ozawa et al.: RIKEN Accel. Prog. Rep. **34**, 72 (2001).
- 3) N. Iwasa et al.: Nucl. Instrum. Methods Phys. Res. B **126**, 284 (1997).
- 4) S. Momota et al.: Nucl. Phys. A, in press.
- 5) K. Sümmerer et al.: Phys. Rev. C **61**, 034607 (2000).

<sup>\*1</sup> Niigata University

<sup>\*2</sup> Nagasaki Institute of Applied Science

<sup>\*3</sup> Kochi University of Technology

<sup>\*4</sup> Tokyo University of Science

# Measurement of the longitudinal momentum distribution of $^{22}\text{O}$

M. Chiba,\*<sup>1</sup> R. Kamungo, N. Iwasa,\*<sup>1</sup> S. Nishimura, A. Ozawa, C. Samanta,\*<sup>2</sup>  
T. Suda, T. Suzuki,\*<sup>3</sup> T. Yamaguchi, T. Zheng, and I. Tanihata

[NUCLEAR STRUCTURE;  $^{22}\text{O}$ , Momentum distribution, TOF]

We measured the longitudinal momentum distribution of  $^{22}\text{O}$  via a break-up reaction. Measuring the longitudinal momentum distribution of neutron-rich nuclei enables us to investigate nuclear structures. The shape of the longitudinal momentum distribution of valence neutrons provides information about the orbits occupied by them.

Usually, the momentum distribution is measured with a magnetic spectrometer. The present measurement was based on a time-of-flight (TOF) technique with nearly full acceptance. This helped to reduce complexities arising due to a finite spectrometer acceptance.

The experiment was performed using the RIKEN projectile fragment separator (RIPS). The experimental setup is shown in Fig. 1. A primary  $^{40}\text{Ar}$  beam at 93.7 A MeV was impinged on a 280 mg/cm<sup>2</sup> Be target to produce an  $^{22}\text{O}$  secondary beam. The RIPS was operated in an achromatic mode with a 425 mg/cm<sup>2</sup> aluminum wedge degrader and a momentum acceptance of 0.8%. We installed a 0.5 mm thick plastic scintillator at the dispersive focus, F1. The typical count rate of the plastic detector at F1 was  $\sim 10^6$  Hz.

The  $^{22}\text{O}$  beam was bombarded onto a 450 mg/cm<sup>2</sup> carbon target installed at the first achromatic focus F2. After the carbon target, we installed a 0.5 mm thick plastic scintillator at F2. Another 1.5 mm thick scintillator was located 5.5 m downstream at the final achromatic focus, F3. To monitor the beam size we installed parallel plate avalanche counters (PPAC) at

all foci.

Particle identification (PID) before the carbon target was performed by the magnet rigidity ( $B\rho$ )- $\Delta E$ -TOF method.  $B\rho$  information was obtained from position information of a PPAC in F1.  $\Delta E$  and TOF information were obtained from a 350  $\mu\text{m}$  Si detector at F2 and two plastic detectors at F1 and F2, respectively.

After the carbon target, reaction products were identified by the  $\Delta E$ -TOF-E method.  $\Delta E$  information was obtained from a stack of 17 Si detectors. TOF information was obtained from two plastic detectors at F2 and F3. The total energy information was obtained from a  $3^\circ\phi \times 6\text{ cm}$  NaI(Tl) detector positioned at the end of beam line. The typical energy resolution of the NaI(Tl) detector was  $\sim 1\%$  in FWHM for 65 A MeV  $^{21}\text{O}$ .

A typical TOF-E plot is shown in Fig. 2. We could identify the one neutron removal fragment,  $^{21}\text{O}$ , and the unreacted  $^{22}\text{O}$ . The population ratio of  $^{21}\text{O}$  to  $^{22}\text{O}$  was  $\sim 1.0 \times 10^{-3}$ . In addition, a few of the two-neutron removal fragment  $^{20}\text{O}$  were observed.

The main source of the background was nuclear reaction events which occurred in the NaI(Tl) detector, because the shape of the background in the TOF spectrum was the same as that of unreacted  $^{22}\text{O}$ .

To reduce the background, we are now developing a nuclear reaction-suppressed total-energy detector system. The data analysis is still in progress.

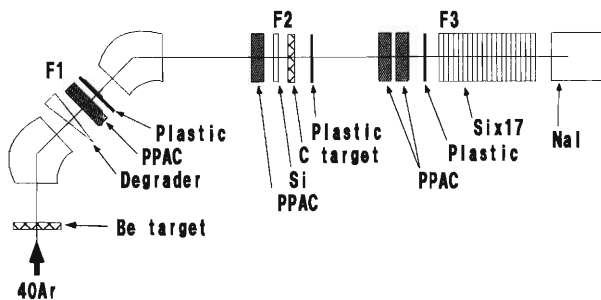


Fig. 1. Experimental setup.

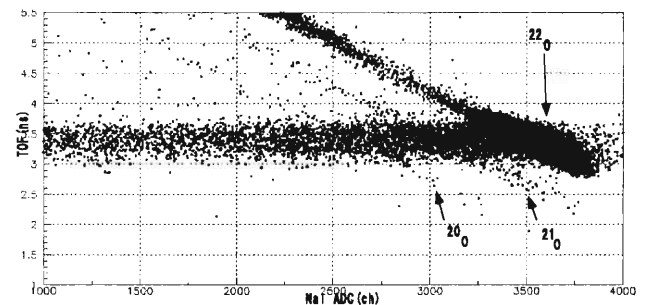


Fig. 2. Particle identification spectrum for fragments of  $^{22}\text{O}$  at the final achromatic focus, F3.

\*1 Tohoku University

\*2 Saha Institute of Nuclear Physics, India

\*3 Niigata University

## First experimental evidence of core modification in a near drip-line nucleus, $^{23}\text{O}$

R. Kanungo, M. Chiba, N. Iwasa,<sup>\*1</sup> S. Nishimura, A. Ozawa, C. Samanta,<sup>\*2,\*3</sup> T. Suda,  
T. Suzuki,<sup>\*4</sup> T. Yamaguchi, T. Zheng, and I. Tanihata

[Momentum distribution, Halo, time-of-flight]

The measured interaction cross sections<sup>1)</sup> of neutron-rich N, O, F isotopes indicate an abrupt rise in the cross section the  $N = 15$  isotopes. This is expected to be a signature of halo formation. However, an anomaly arises in understanding the observed enhancement of the cross-sections within the usual core-plus-neutron halo model. Namely, in such an approach, a consideration of the neutron occupying the  $2s_{1/2}$  orbital is insufficient to explain the amount of enhancement. This has led to the proposition of new form of core-modified structure for these isotopes.<sup>2)</sup> It should be mentioned here that the usual halo model considers the core to have same size and properties as a free nucleus. The usual halo model has successfully described the known halo nuclei in the p-shell region. We conducted a further experimental investigation to probe the cause for such a structure through a measurement of the longitudinal momentum distribution of  $^{23}\text{O}$ .

The experimental technique adopted for this purpose was a new one based on the time-of-flight principle. The salient feature of this technique in comparison to the usually adopted spectrometer technique is that the breakup fragments are transported to the final focus after the reaction target without passing through any dipole magnet. This has helped us to obtain a nearly full acceptance. The advantage of this feature is not only that the extraction of the momentum distribution becomes relatively simple, covering a large momentum range, but also that the measurements can be made at the same time for multi-nucleon removal, proton knock out and pickup reactions. Furthermore, it allows measurements of the interaction cross sections with the same experimental setup. The details on of the setup are discussed in Ref. 3.

In the present experiment, the longitudinal momentum distributions of fragments from the two-neutron removal as well as one-neutron removal from  $^{23}\text{O}$  in a reaction with a C-target at 72 A MeV were measured. The unexpectedly narrow width of  $^{21}\text{O}$  ( $115 \pm 34$  MeV/c in FWHM) from fragmentation of  $^{23}\text{O}$  is the first direct evidence of a change in the structure of  $^{22}\text{O}$

inside  $^{23}\text{O}$  compared to the bare  $^{22}\text{O}$  nucleus. A theoretical interpretation of the present data considering neutron correlation is an involved study, no formalism of which yet exists. Therefore, at present we interpret the data by folding the momentum distributions of  $^{23}\text{O} \rightarrow ^{22}\text{O}$  and  $^{22}\text{O} \rightarrow ^{21}\text{O}$ , which also considers the simultaneous emission of the two neutrons. Taking into account all possibilities of two-neutron removal through the ground as well as excited states of  $^{22}\text{O}$ , in a normal shell model configuration (*i.e.*  $J^\pi = 1/2^+$  for  $^{23}\text{O}$ ), we obtained a distribution which is wider than the observed one. On the other, hand if we assume the possibility of two neutrons in  $^{23}\text{O}$  to be emitted from the  $2s_{1/2}$  orbital (which would mean one of the neutrons in the so-called  $^{22}\text{O}$  core is in the  $2s_{1/2}$  orbital), we obtain a consistent description of the two-neutron removal distribution. It should be mentioned here that both the interaction cross section and the momentum distribution analysis of free  $^{22}\text{O}$  indicate that the valence neutron is in the  $1d_{5/2}$  orbital.

This observation indicates a strong modification of the core structure for neutron halo-like *sd* shell nuclei near the drip-line. The probability of two neutrons occupying the *s*-orbital in  $^{23}\text{O}$  may suggest the lowering of the *s*-orbital, thus providing a reason for the  $N = 16$  magic number. This also introduces a new two-fold definition of a valence nucleon, one which determines the spin of the nucleus, and the other which participates with greater probability in the reaction. The  $^{22}\text{O}$  momentum distribution from  $^{23}\text{O}$  fragmentation shows a width of  $73 \pm 15$  MeV/c in FWHM. In the same experiment we also measured the longitudinal momentum distribution of one-neutron removal from  $^{22}\text{O}$ . This is reported in Ref. 3.

### References

- 1) A. Ozawa et al.: Nucl. Phys. A **691**, 599 (2001).
- 2) R. Kanungo et al.: Phys. Lett. B **512**, 261 (2001).
- 3) M. Chiba et al.: RIKEN Accel. Prog. Rep. **35**, 67 (2002).

<sup>\*1</sup> Department of Physics, Tohoku University

<sup>\*2</sup> Present address: Physics Department, Virginia Commonwealth University, USA

<sup>\*3</sup> Permanent address: Saha Institute of Nuclear Physics, India

<sup>\*4</sup> Department of Physics, Niigata University

## Study of the $^{22}\text{Mg}(p,\gamma)^{23}\text{Al}$ reaction by the Coulomb-dissociation method

T. Gomi,<sup>\*1</sup> T. Motobayashi,<sup>\*1</sup> K. Yoneda, S. Kanno,<sup>\*1</sup> N. Aoi,<sup>\*2</sup> Y. Ando,<sup>\*1</sup> H. Baba,<sup>\*1</sup> K. Demichi,<sup>\*1</sup> Zs. Fülöp,<sup>\*3</sup> U. Futakami,<sup>\*1</sup> H. Hasegawa,<sup>\*1</sup> Y. Higurashi,<sup>\*1</sup> K. Ieki,<sup>\*1</sup> N. Imai,<sup>\*2</sup> N. Iwasa,<sup>\*4</sup> H. Iwasaki,<sup>\*5</sup> T. Kubo, S. Kubono,<sup>\*5</sup> M. Kunibu,<sup>\*1</sup> Y. U. Matsuyama,<sup>\*1</sup> S. Michimasa,<sup>\*5</sup> T. Minemura, H. Murakami,<sup>\*1</sup> T. Nakamura,<sup>\*6</sup> A. Saito,<sup>\*1</sup> H. Sakurai,<sup>\*2</sup> M. Serata,<sup>\*1</sup> S. Shimoura,<sup>\*5</sup> T. Sugimoto,<sup>\*6</sup> E. Takeshita,<sup>\*1</sup> S. Takeuchi,<sup>\*1</sup> K. Ue,<sup>\*5</sup> K. Yamada,<sup>\*1</sup> Y. Yanagisawa, A. Yoshida, and M. Ishihara

[NUCLEAR REACTIONS:  $^{208}\text{Pb}(^{23}\text{Al},p)^{22}\text{Mg}^{208}\text{Pb}$ , 50 AMeV; Coulomb dissociation]

We performed an experimental study of the stellar  $^{22}\text{Mg}(p,\gamma)^{23}\text{Al}$  reaction using the Coulomb-dissociation method. This reaction is relevant to the nucleosynthesis of  $^{22}\text{Na}$  in Ne-rich novae.<sup>1-3)</sup> The first excited state of  $^{23}\text{Al}$ , lying at 405 keV above the proton threshold,<sup>3)</sup> is located near the Gamow energy for novae. Therefore, the  $^{22}\text{Mg}(p,\gamma)^{23}\text{Al}$  reaction in the rp-process could be dominated by resonant capture through the first excited state. In the present study we aimed at making a determination of the radiation width ( $\Gamma_\gamma$ ) of the first excited state in  $^{23}\text{Al}$ .

The experiment was performed at the RIPS beam line. A radioactive beam of  $^{23}\text{Al}$  was produced by the projectile fragmentation reaction of a  $^{28}\text{Si}$  beam on a  $^9\text{Be}$  target. A beam of  $^{23}\text{Al}$  at 50 MeV/nucleon bombarded a 88 mg/cm<sup>2</sup>  $^{208}\text{Pb}$  target. The products of the breakup reaction,  $^{22}\text{Mg}$  and a proton, were detected, respectively, by a silicon telescope and a plastic scintillator hodoscope located 56 cm and 4 m downstream of the target. A stack of sixty-eight NaI(Tl) scintillators was placed around the target to measure deexcitation  $\gamma$ -rays when  $^{22}\text{Mg}$  is excited to a bound state. The details can be found in Ref. 4.

To select the breakup events through the first excited state in  $^{23}\text{Al}$ , and also to reduce the contributions of higher excited states, we analyzed the data under the condition that the opening angle between  $^{22}\text{Mg}$  and a proton is smaller than  $9^\circ$ . Under this coincidence condition, the time-of-flight (TOF) distribution of the breakup protons is shown in Fig. 1. The observed peaks gave a trace of the resonant-state excitation. Figure 2 shows a Doppler-corrected  $\gamma$ -ray spectrum obtained under the same condition. As shown in this figure, we observed deexcitation  $\gamma$ -rays corresponding to the  $2^+ \rightarrow 0^+$  transition of  $^{22}\text{Mg}$ . This indicates a considerable contribution of the process  $^{23}\text{Al} \rightarrow ^{23}\text{Al}^*(E_x \approx 2 \text{ MeV}) \rightarrow p + ^{22}\text{Mg}^*(2^+; E_x = 1.246 \text{ MeV})$ , which should be subtracted to extract the breakup cross section of interest.

From the TOF distribution of protons, we obtained

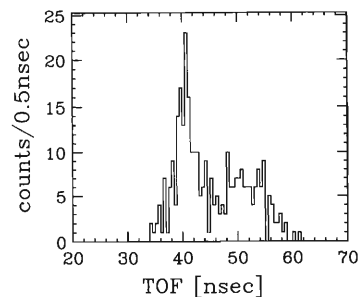


Fig. 1. TOF distribution of the breakup protons obtained under the condition that the opening angle between  $^{22}\text{Mg}$  and a proton is smaller than  $9^\circ$ . When the p- $^{22}\text{Mg}$  relative energy is 405 keV, it is estimated that the TOF of protons ranges from 38 to 48 nsec.

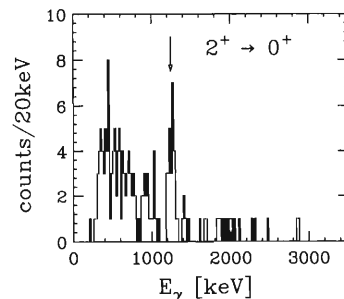


Fig. 2. Doppler-corrected  $\gamma$ -ray spectrum in coincidence with breakup events. The  $2^+ \rightarrow 0^+$  transition of  $^{22}\text{Mg}$  can be seen.

a rough estimate of the cross section of the Coulomb-dissociation reaction through the first excited state of  $^{23}\text{Al}$  to be 4 mb. Supposing that the spin and parity of  $^{23}\text{Al}$  is  $5/2^+$  for the ground state and  $1/2^+$  for the first excited state, the cross section corresponds to  $\Gamma_\gamma \simeq 6 \times 10^{-7} \text{ eV}$ , which is compatible with the value predicted by J. A. Caggiano *et al.*<sup>3)</sup>

### References

- 1) H. Herndl *et al.*: Phys. Rev. C **52**, 1078 (1995).
- 2) H. Schatz *et al.*: Phys. Rev. Lett. **79**, 3845 (1997).
- 3) J. A. Caggiano *et al.*: Phys. Rev. C **64**, 025802 (2001).
- 4) T. Gomi *et al.*: RIKEN Accel. Prog. Rep. **34**, 73 (2001).

<sup>\*1</sup> Rikkyo University  
<sup>\*2</sup> University of Tokyo  
<sup>\*3</sup> ATOMKI, Hungary  
<sup>\*4</sup> Tohoku University  
<sup>\*5</sup> Center for Nuclear Study, University of Tokyo  
<sup>\*6</sup> Tokyo Institute of Technology

Coulomb excitation of  $^{24}\text{Si}$ 

S. Kanno,<sup>\*1</sup> T. Gomi,<sup>\*1</sup> T. Motobayashi,<sup>\*1</sup> K. Yoneda, N. Aoi,<sup>\*2</sup> Y. Ando,<sup>\*1</sup> H. Baba,<sup>\*1</sup> K. Demichi,<sup>\*1</sup> Zs. Fülöp,<sup>\*3</sup> U. Futakami,<sup>\*1</sup> H. Hasegawa,<sup>\*1</sup> Y. Higurashi,<sup>\*1</sup> K. Ieki,<sup>\*1</sup> N. Imai,<sup>\*2</sup> N. Iwasa,<sup>\*4</sup> H. Iwasaki,<sup>\*5</sup> T. Kubo, S. Kubono,<sup>\*5</sup> M. Kunibu,<sup>\*1</sup> Y.U. Matsuyama,<sup>\*1</sup> S. Michimasa,<sup>\*5</sup> T. Minemura, H. Murakami,<sup>\*1</sup> T. Nakamura,<sup>\*6</sup> A. Saito,<sup>\*1</sup> H. Sakurai,<sup>\*2</sup> M. Serata,<sup>\*1</sup> S. Shimoura,<sup>\*5</sup> T. Sugimoto,<sup>\*6</sup> E. Takeshita,<sup>\*1</sup> S. Takeuchi,<sup>\*1</sup> K. Ue,<sup>\*5</sup> K. Yamada,<sup>\*1</sup> Y. Yanagisawa, A. Yoshida, and M. Ishihara

[ $^{208}\text{Pb}(^{24}\text{Si}, ^{24}\text{Si}\gamma)^{208}\text{Pb}$ , Coulomb excitation]

The coulomb excitation of a very proton-rich nucleus,  $^{24}\text{Si}$ , to its  $2^+$  state was studied using a radioactive beam of  $^{24}\text{Si}$  at 57.9 MeV/nucleon bombarding a  $^{208}\text{Pb}$  target. The nucleus,  $^{24}\text{Si}$ , was produced by using projectile fragmentation of a  $^{28}\text{Si}$  primary beam on a  $^9\text{Be}$  production target. The fragments were collected and analyzed by RIPS. The extracted  $^{24}\text{Si}$  intensity was typically  $3.2 \times 10^3 \text{ s}^{-1}$ . Particle identification of the secondary beam was carried out event-by-event using the time-of-flight (TOF) information between the cyclotron RF and a plastic scintillator with  $500 \mu\text{m}$  thickness set at the second focal point of RIPS. A  $^{208}\text{Pb}$  target of  $56.8 \text{ mg/cm}^2$  thickness was placed at the focal point of RIPS, and used to excite the projectiles. The position and incident angles of the beam at the target were measured by two sets of parallel-plate avalanche counters (PPAC) placed at third focal point (F3).

Scattered  $^{24}\text{Si}$  nuclei were detected by a counter telescope placed 60 cm from the target in a vacuum. The telescope consisted of four layers of eight ion-implanted silicon detectors of  $50 \times 50 \text{ cm}^2$  effective area and  $500 \mu\text{m}$  thickness. The particles of interest were mostly stopped in the last layer. An isotopic identification of scattered particles was achieved by the  $\Delta E - E$  method. A good resolving power of the detector telescope enabled us to distinguish  $^{24}\text{Si}$  from other reaction products with  $Z = 8 - 14$ .

Sixty-eight NaI(Tl) scintillators surrounded the target to detect  $\gamma$ -rays. Each scintillator crystal was of rectangular shape with a size  $6 \times 6 \times 12 \text{ cm}^3$ . The energy and efficiency calibration of each NaI(Tl) crystal was made by using standard  $^{22}\text{Na}$ ,  $^{60}\text{Co}$ ,  $^{88}\text{Y}$ ,  $^{137}\text{Cs}$  sources. The high granularity of the setup allowed us to measure the angle of the  $\gamma$ -ray emission, which was useful in correcting large Doppler shifts of the  $\gamma$  rays from the excited  $^{24}\text{Si}$ , that was moving with  $v/c \approx 0.3$ .

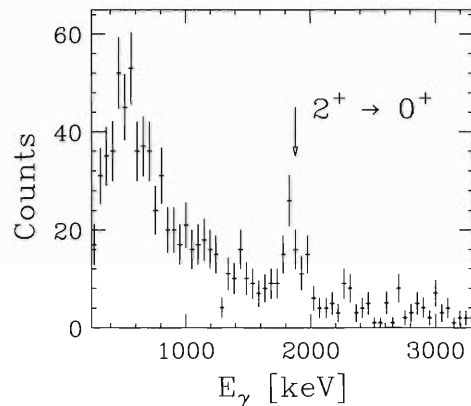


Fig. 1. The de-excitation  $\gamma$  ray.

Excitation to the  $2^+$  state was identified by measuring the  $\gamma$ -ray de-excitation of the  $2^+$  state in coincidence with the scattered  $^{24}\text{Si}$  ions. Figure 1 shows the  $\gamma$ -ray energy spectrum associated with the  $^{24}\text{Si} + ^{208}\text{Pb}$  inelastic scattering. It was obtained by summing the spectra for all of the NaI(Tl) scintillators after a Doppler-shift correction. The accidental coincidence yield was subtracted from the energy spectrum by using data obtained by setting a gate at the region beside the true-coincidence peak in the  $^{24}\text{Si}$ - $\gamma$  time-difference spectrum. As can be clearly seen in the figure, only one full-energy peak was observed at  $1.89 \text{ MeV}^{(1)}$  corresponding to the  $2^+ \rightarrow 0^+$  transition. Further analysis to extract the  $B(E2)$  value is now in progress.

## References

- 1) H. Schatz et al.: Phys. Rev. Lett. **20**, 79 (1997).

\*1 Rikkyo University

\*2 University of Tokyo

\*3 ATOMKI, Hungary

\*4 Tohoku University

\*5 Center for Nuclear Study, University of Tokyo

\*6 Tokyo Institute of Technology

## Study of the first excited state in a very neutron-rich nucleus, $^{30}\text{Ne}$

Y. Yanagisawa, M. Notani,<sup>\*1</sup> H. Sakurai,<sup>\*2</sup> S. Shimoura,<sup>\*1</sup> H. Iwasaki,<sup>\*1</sup> S. Michimasa,<sup>\*1</sup> K. Ue,<sup>\*1</sup>  
M. Kurokawa,<sup>\*1</sup> N. Iwasa,<sup>\*3</sup> M. Kunibu,<sup>\*4</sup> H. Baba,<sup>\*4</sup> T. Gomi,<sup>\*4</sup> A. Saito,<sup>\*4</sup> T. Minemura,  
Y. U. Matsuyama,<sup>\*4</sup> H. Higurashi,<sup>\*4</sup> S. Kanno,<sup>\*4</sup> M. Serata,<sup>\*4</sup> E. Takeshita,<sup>\*4</sup> S. Takeuchi,<sup>\*4</sup>  
K. Yamada,<sup>\*4</sup> K. Demichi,<sup>\*4</sup> H. Hasegawa,<sup>\*4</sup> H. Akiyoshi, N. Fukuda, K. Yoneda, N. Aoi,<sup>\*2</sup>  
N. Imai,<sup>\*2</sup> T. Sugimoto,<sup>\*5</sup> T. Nakamura,<sup>\*5</sup> and T. Motobayashi<sup>\*4</sup>

[NUCLEAR REACTIONS:  $p(^{30}\text{Ne}, ^{30}\text{Ne}\gamma)p$ ,  $p(^{29}\text{Ne}, ^{29}\text{Ne}\gamma)p$ ]

An interesting aspect of the region around  $N = 20$  nuclei is the transition from spherical to deformed shapes in the so-called ‘island of inversion.’<sup>1)</sup> We report on the first energy measurement of the  $2_1^+$  excited state in a very neutron-rich nucleus,  $^{30}\text{Ne}$ , with  $N = 20$ .

In-beam  $\gamma$  spectroscopy using radioactive beams has been carried out by some methods in recent years. We have performed proton inelastic scattering with a liquid-hydrogen target by detecting de-excitation  $\gamma$ -rays in coincidence with scattered particles. This method takes advantage of its high experimental efficiency, because the useful target thickness of liquid hydrogen is one or two orders thicker than that of other methods. The method can be now applied to very neutron-rich nuclei even with a beam intensity on the order of 0.1 counts per second.

An experiment was performed at RIPS. A primary  $^{40}\text{Ar}$  beam of 94 MeV/nucleon with a typical intensity of 60 pA bombarded a  $^{nat}\text{Ta}$  target with a thickness of 666 mg/cm<sup>2</sup>. To maximize the beam intensity of  $^{30}\text{Ne}$ , the experiment was operated with a full-momentum acceptance of 6%. Particle identification of the secondary beam was performed by a standard method based on the energy loss ( $\Delta E$ ), time-of-flight (TOF) and magnetic rigidity ( $B\rho$ )<sup>2)</sup> for separating  $^{29}\text{Ne}$  and  $^{30}\text{Ne}$  beams. The positions of the fragments at the momentum-dispersive focal plane (F1) were recoded using a parallel-plate avalanche counter (PPAC) in order to determine the  $B\rho$  values. The TOF of each fragment was measured from timing signals of a plastic scintillator placed at F2 and RF signals of the cyclotron. Two silicon detectors were located in front of the final focal plane (F3) for measuring the energy loss. The  $^{30}\text{Ne}$  beam was obtained to be 0.2 cps with a contamination of  $^{29}\text{Ne}$ ,  $^{31}\text{Na}$  and  $^{32}\text{Na}$  beams.

The  $^{30}\text{Ne}$  beams impinged on a liquid-hydrogen target<sup>3)</sup> with a thickness of 180 mg/cm<sup>2</sup>, which was placed at F3 to excite the projectiles. Scattered particles were detected and identified by a PPAC and a silicon tele-

scope located about 50 cm downstream of the target. The identification of  $Z$  was obtained by the TOF- $\Delta E$  method. DALI with sixty-eight NaI(Tl) scintillators was placed around the target to detect the de-excited  $\gamma$  rays emitted from excited fragments.

Figure 1 (a) and (b) show a preliminary result of the energy spectra of  $\gamma$  rays with a doppler-shift correction. They were obtained by  $^{29}\text{Ne}$  and  $^{30}\text{Ne}$  beams in coincidence with the fragments of Ne isotopes, respectively. In Fig. 1 (a),  $\gamma$  lines at around 440, 600, and 1300 keV can be observed, whereas the  $\gamma$  line at 790 keV can clearly be observed in Fig. 1 (b), except for the  $\gamma$  line in Fig. 1 (a). Note that the spectra show the  $\gamma$  ray from  $^{28}\text{Ne}$ , 1320 keV. Compared to both spectra, the  $\gamma$  rays at 790(30) keV were assigned to be the  $2^+ \rightarrow 0^+$  transition associated with  $^{30}\text{Ne} + p$  inelastic scattering. Also, the remaining two peaks in Fig. 1 (a) may be from the fragments of  $^{29}\text{Ne}$ . A further analysis is now in progress.

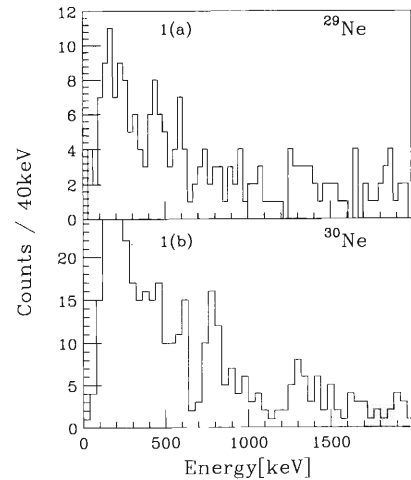


Fig. 1. Doppler-corrected energy spectra of  $\gamma$ -rays obtained in coincidence with  $^{29}\text{Ne}$ (1(a)) and  $^{30}\text{Ne}$ (1(b)) beams and fragments of Ne isotopes.

### References

- 1) E. K. Warburton et al.: Phys. Rev. C **41**, 1147 (1990).
- 2) H. Sakurai et al.: Phys. Lett. B **448**, 180 (1999).
- 3) H. Akiyoshi et al.: RIKEN. Accel. Prog. Rep. **32**, 167 (1999).

<sup>\*1</sup> Center for Nuclear Study, University of Tokyo

<sup>\*2</sup> University of Tokyo

<sup>\*3</sup> Tohoku University

<sup>\*4</sup> Rikkyo University

<sup>\*5</sup> Tokyo Institute Technology

## Proton inelastic scattering by $^{32}\text{Mg}$

H. Hasegawa,<sup>\*1</sup> T. Motobayashi,<sup>\*1</sup> M. Kunibu,<sup>\*1</sup> Y. Yanagisawa, T. Nakamura,<sup>\*2</sup> M. Notani,<sup>\*3</sup> T. Gomi,<sup>\*1</sup> T. Sugimoto,<sup>\*2</sup> H. Baba,<sup>\*1</sup> A. Saito,<sup>\*1</sup> Y. Mizoi, S. Kanno,<sup>\*1</sup> H. Iwasaki,<sup>\*3</sup> E. Takeshita,<sup>\*1</sup> K. Demichi,<sup>\*1</sup> S. Michimasa,<sup>\*3</sup> K. Ue,<sup>\*3</sup> N. Fukuda, N. Iwasa,<sup>\*4</sup> M. Kurokawa,<sup>\*3</sup> S. Shimoura,<sup>\*3</sup> H. Sakurai,<sup>\*4</sup> and M. Ishihara

[Proton inelastic scattering, nuclear deformation]

A sudden disappearance of the  $N = 20$  shell closure was suggested for the very neutron-rich nucleus  $^{32}\text{Mg}$  based on the low excitation energy (885 keV) of its first  $2^+$  state,<sup>1,2)</sup> and an enhanced  $B(E2)$  of  $454 \pm 78 e^2\text{fm}^4$  was obtained in the  $0^+ \rightarrow 2^+$  Coulomb excitation.<sup>3)</sup> The present study is aimed at investigating a possible difference between the amounts of proton- and neutron-deformations for  $^{32}\text{Mg}$  by measuring the proton inelastic scattering, hoping that more detailed information would become possible on the nuclear structure.

The experiment was carried out at RIPS. Primary beams of  $^{40}\text{Ar}$  with a energy of 93.6 MeV/nucleon bombarded a 641 mg/cm<sup>2</sup> thick  $^{181}\text{Ta}$  target. Radioactive  $^{32}\text{Mg}$  beams with a energy of 59.6 MeV/nucleon were extracted by the RIPS. The secondary beams contained 3% of  $^{34}\text{Al}$ , 28% of  $^{30}\text{Na}$  and small amounts of other nuclides as well as  $^{32}\text{Mg}$  with a fraction of 68%. The beams bombarded a liquid-hydrogen target<sup>4)</sup> with a thickness of 180 mg/cm<sup>2</sup>, contained in a cooled cell with windows made of 6.6  $\mu\text{m}$  havar foils. The overall beam-target luminosity was obtained by measuring event-by-event the hit position of the beam on the target using position information provided from two sets of parallel-plate avalanche counters (PPACs) set upstream of the target. The averaged energy of  $^{32}\text{Mg}$  in the middle of the target was 49.5 MeV/nucleon. The reaction products were measured by a counter telescope placed 48 cm from the target. The telescope consisted of three identical ion-implanted silicon detectors of  $50 \times 50 \text{ mm}^2$  effective area and 500  $\mu\text{m}$  thickness. The particles reaching the third detector were rejected in the analysis. The scattering angle was measured by a parallel-plate avalanche counter (PPAC) placed in front of the silicon detectors. The  $\gamma$ -ray deexcitation was measured in coincidence with the inelastically scattered  $^{32}\text{Mg}$  ions. A DALI setup consisting of fifty-four identical NaI(Tl) scintillators was positioned around the target for  $\gamma$ -ray detection. The typical energy resolution of each 12-cm-length and  $6 \times 6\text{-cm}^2$ -area scintillator was 9.1% for the 662 keV  $\gamma$ -ray. The Doppler shift was corrected for by the detector angle with respect to the beam direction.

Particle identification for magnesium ions was performed by the function  $a\Delta E(E + k\Delta E)^b$ , which was

proposed by Stokes, Northrop and Boyer<sup>5)</sup> using signals from the first and second silicon detectors. Parameters  $k$  and  $b$  were adjusted so as to achieve the best isotope separation, whereas  $a$  is an arbitrary constant. The resultant width, 0.8 (FWHM), is a measure of the mass resolution of the present measurement. Figure 1 shows the Doppler-corrected spectra of  $\gamma$ -rays measured in coincidence with  $^{32}\text{Mg}$ . In the spectrum two peaks have been identified. One at 0.9 MeV is due to the transition from the first excited  $2^+$  state at 895 keV to the ground state in  $^{32}\text{Mg}$ . Considering the present isotopic resolution, a peak seen at around 1.5 MeV is attributed to a transition in  $^{32}\text{Mg}$ . This energy may coincide with that of the peak (1430 keV) observed in the fragmentation experiments at GANIL<sup>6)</sup> and RIKEN,<sup>7)</sup> where  $\gamma$ - $\gamma$  correlation data indicate that the peak corresponds to a transition to the  $2^+$  state from a higher state, the spin of which is not established. An analysis is now in progress.

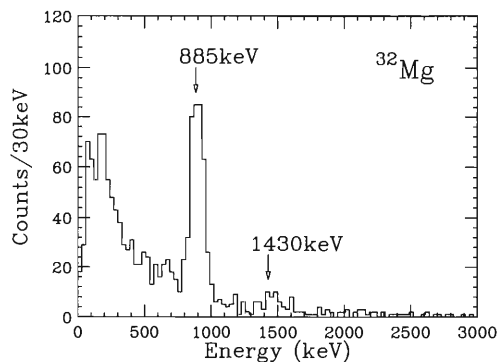


Fig. 1. Doppler-corrected spectrum of  $\gamma$ -rays in coincidence with  $^{32}\text{Mg}$ , produced by proton inelastic scattering by  $^{32}\text{Mg}$ .

### References

- 1) C. Détraz et al.: Phys. Rev. C **19**, 164 (1979).
- 2) D. Guillemaud-Müller et al.: Nucl. Phys. A **426**, 37 (1984).
- 3) T. Motobayashi et al.: Phys. Lett. B **346**, 9 (1995).
- 4) H. Akiyoshi et al.: RIKEN Accel. Prog. Rep. **32**, 167 (1999).
- 5) R. H. Stokes, J. A. Northrop, and K. Boyer: Rev. Sci. Instr. **29**, 61 (1958).
- 6) F. Azaiez et al.: AIP Conf. Proc. **481**, 243 (1998).
- 7) K. Yoneda et al.: Phys. Lett. B **499**, 233 (2001).

<sup>\*1</sup> Rikkyo University

<sup>\*2</sup> Tokyo Institute of Technology

<sup>\*3</sup> Center for Nuclear Study, University of Tokyo

<sup>\*4</sup> University of Tokyo

## Large collectivity of $^{34}\text{Mg}^\dagger$

H. Iwasaki,<sup>\*1</sup> T. Motobayashi,<sup>\*2</sup> H. Sakurai,<sup>\*3</sup> K. Yoneda, T. Gomi,<sup>\*2</sup> N. Aoi,<sup>\*3</sup> N. Fukuda, Z. Fülöp,<sup>\*4</sup> U. Futakami,<sup>\*2</sup> Z. Gacsi,<sup>\*4</sup> Y. Higurashi,<sup>\*2</sup> N. Imai,<sup>\*3</sup> N. Iwasa,<sup>\*5</sup> T. Kubo, M. Kumibu,<sup>\*2</sup> M. Kurokawa,<sup>\*1</sup> Z. Liu,<sup>\*6</sup> T. Minemura, A. Saito,<sup>\*2</sup> M. Scrata,<sup>\*2</sup> S. Shimoura,<sup>\*1</sup> S. Takeuchi,<sup>\*2</sup> Y. X. Watanabe, K. Yamada,<sup>\*2</sup> Y. Yanagisawa, and M. Ishihara

[NUCLEAR REACTIONS: Pb, C( $^{34}\text{Mg}$ ,  $^{34}\text{Mg}\gamma$ ), 44.9 MeV/nucleon, Coulomb excitation, Deduced  $B(E2)$ ]

Experimental evidence for deformed nuclei in the so-called ‘island of inversion,’<sup>1)</sup> centered at  $Z \sim 11$  and  $N \sim 21$ , was first obtained by a mass measurement,<sup>2)</sup> which revealed that the neutron-rich  $^{31,32}\text{Na}$  isotopes are more tightly bound than predicted theoretically. In this region, the most convincing evidence for an anomalous deformation has been obtained in the  $N = 20$  nucleus  $^{32}\text{Mg}$  from the low  $E(2_1^+)$  of 886 keV<sup>3)</sup> and the large  $B(E2)$ <sup>4)</sup> of 454(78)  $\text{e}^2\text{fm}^4$  as well as an enhancement of the binding energy.<sup>5)</sup> Currently, great interest is focused on investigating more neutron-rich nuclei beyond  $N = 20$  to elucidate how the anomaly evolves across the region of the island.

Here, we report on the first measurement of  $B(E2; 0_{\text{g.s.}}^+ \rightarrow 2_1^+)$  for the very neutron-rich nucleus  $^{34}\text{Mg}$  with  $N = 22$ , which was performed with the intermediate-energy Coulomb excitation method.<sup>6)</sup> A very large value of the measured  $B(E2)$ , together with the low  $E(2_1^+)$ ,<sup>7)</sup> indicates that the deformation of  $^{34}\text{Mg}$  is even larger than in the classical case of  $^{32}\text{Mg}$ .

The experiment was performed at the RIPS facility<sup>8)</sup> in RIKEN. A secondary  $^{34}\text{Mg}$  beam at 44.9 MeV/nucleon bombarded a 693 mg/cm<sup>2</sup>-thick Pb target. The typical intensity of the  $^{34}\text{Mg}$  beam was 4 counts per second. Scattered particles were detected and identified by an array of silicon detectors. By using a granular array of 66 NaI(Tl) detectors, we measured de-excitation  $\gamma$  rays in coincidence with the scattered particles. Angle-integrated cross sections were obtained from the observed  $\gamma$ -ray yields. Data were also taken with a 339 mg/cm<sup>2</sup>-thick C target to evaluate nuclear excitation contributions. The details of the experimental arrangement are described elsewhere.<sup>9)</sup>

Figure 1 shows the Doppler-corrected  $\gamma$ -ray energy spectrum obtained from  $^{34}\text{Mg} + \text{Pb}$  scattering. In the spectrum, a single dominant peak stands out at 656(7) keV. Since the intermediate-energy Coulomb excitation selectively excites the  $2_1^+$  state of an even-even nucleus, we conclude that the  $\gamma$  transition corresponds to de-excitation of the first excited  $2_1^+$  state of

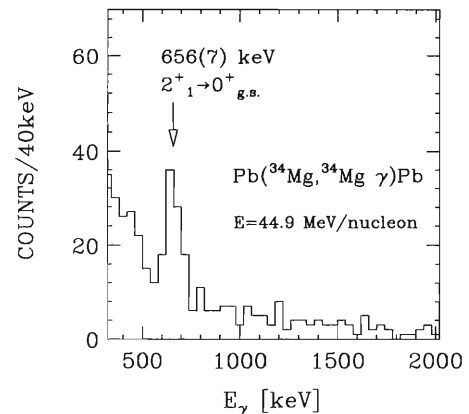


Fig. 1. Doppler-corrected  $\gamma$ -ray energy spectrum obtained in the inelastic scattering of  $^{34}\text{Mg}$  at 44.9 MeV/nucleon with a Pb target.

$^{34}\text{Mg}$  located at 656(7) keV.

An experimental deformation parameter ( $\beta_2$ ) of 0.58(6) was deduced through an ECIS calculation by searching for the  $\beta_2$  value which best reproduces the measured cross section of 286(52) mb. The error in  $\beta_2$  includes both experimental uncertainties and theoretical ambiguities regarding the choice of optical potentials and the nuclear contribution. We then obtain  $B(E2; 0_{\text{g.s.}}^+ \rightarrow 2_1^+) = 631(126) \text{e}^2\text{fm}^4$ , which is the largest among the E2 strengths observed for nuclei in the vicinity of the island of inversion. The very large  $B(E2)$  value, corresponding to a quadrupole deformation parameter of  $\beta_2 \approx 0.6$ , strongly indicates that  $^{34}\text{Mg}$  is a well-deformed nucleus.

### References

- 1) E. K. Warburton et al.: Phys. Rev. C **41**, 1147 (1990).
- 2) C. Thibault et al.: Phys. Rev. C **12**, 644 (1975).
- 3) C. Détraz et al.: Phys. Rev. C **19**, 164 (1979); D. Guillemaud-Mueller et al.: Nucl. Phys. A **426**, 37 (1984).
- 4) T. Motobayashi et al.: Phys. Lett. B **346**, 9 (1995).
- 5) C. Détraz et al.: Nucl. Phys. A **394**, 378 (1983).
- 6) T. Glasmacher: Ann. Rev. Nucl. Part. Sci. **48**, 1 (1998).
- 7) K. Yoneda et al.: Phys. Lett. B **499**, 233 (2001).
- 8) T. Kubo et al.: Nucl. Instrum. Methods Phys. Res. B **70**, 309 (1992).
- 9) H. Iwasaki et al.: Phys. Lett. B **522**, 227 (2001).

<sup>†</sup> Condensed from the article in Phys. Lett. B **522**, 227 (2001)

<sup>\*1</sup> Center for Nuclear Study, University of Tokyo

<sup>\*2</sup> Rikkyo University

<sup>\*3</sup> University of Tokyo

<sup>\*4</sup> ATOMKI, Hungary

<sup>\*5</sup> Tohoku University

<sup>\*6</sup> Institute of Modern Physics, China

Spectroscopy of  $^{34}\text{Si}$  with inelastic deuteron scattering

N. Iwasa,<sup>\*1</sup> T. Motobayashi,<sup>\*2</sup> H. Sakurai,<sup>\*3</sup> H. Akiyoshi, Y. Ando,<sup>\*2</sup> N. Aoi,<sup>\*3</sup> H. Baba,<sup>\*1</sup> N. Fukuda,<sup>\*3</sup>  
 Zs. Fülöp,<sup>\*4</sup> U. Futakami,<sup>\*2</sup> T. Gomi,<sup>\*2</sup> Y. Higurashi, K. Ieki,<sup>\*2</sup> H. Iwasaki,<sup>\*3</sup> T. Kubo, S. Kubono,<sup>\*5</sup>  
 H. Kinugawa,<sup>\*2</sup> H. Kumagai, M. Kunibu,<sup>\*2</sup> S. Michimasa,<sup>\*5</sup> T. Minemura,<sup>\*2</sup> H. Murakami,<sup>\*2</sup>  
 A. Saito,<sup>\*2</sup> S. Shimoura,<sup>\*5</sup> S. Takeuchi,<sup>\*2</sup> Y. Yanagisawa, K. Yoneda, and M. Ishihara

[NUCLEAR REACTIONS:  $^2\text{H}(^{34}\text{Si}, ^{34}\text{Si} \gamma)$ ]

Excited states in  $^{34}\text{Si}$  were studied by measuring de-excitation  $\gamma$  rays in coincidence with  $^{34}\text{Si}$  ion produced by deuteron inelastic scattering in reversed kinematics.

A radioactive ion beam of  $^{34}\text{Si}$  produced in the fragmentation reaction of a primary  $^{40}\text{Ar}$  beam in a beryllium target and separated by the RIKEN projectile fragment separator (RIPS) bombarded a liquid-deuterium target. The reaction products were analyzed by four silicon counter telescopes arranged in a  $2 \times 2$  matrix. The de-excitation  $\gamma$ -rays were detected by a NaI(Tl) array consisting of 68 NaI(Tl) crystals surrounding the target from 40 to 138 degrees in coincidence with  $^{34}\text{Si}$  detected by the silicon telescopes. A lead shield with a thickness of 5 cm surrounded the NaI(Tl) array for background reduction.

Figure 1 (a) and (b) show the de-excitation  $\gamma$  spectra for the  $^2\text{H}(^{34}\text{Si}, ^{34}\text{Si} \gamma)$  reaction in the projectile and laboratory frames, respectively. Nine  $\gamma$  lines at 591, 930, 1010, 1193, 1435, 1715, 1941, 2696 and 3328 keV were observed in the projectile frame, whereas a 511-keV line was observed in the laboratory frame. The lines at 1010 and 1941 keV are known to be from  $^{33}\text{Si}$  and  $^{32}\text{Si}$ , respectively, and the lines at 930 and 3328 keV are from  $^{34}\text{Si}$ .<sup>1)</sup> Recently, Nummela *et al.* discovered lines at 591, 1193, 1715 and 2696 keV by their  $\beta$ -delayed  $\gamma$  measurements, but they were not placed in the decay schemes, except for the 591-keV line.<sup>2)</sup> The solid curve in Fig. 1 (a) represents a fit with these gamma lines. The line shape (dashed curve) of each transition was calculated by Monte-Carlo simulations. An additional  $\gamma$  line at 2300 keV and an exponential background (dotted curve) were necessary to fit the spectrum.

The above assignments of the gamma lines have been confirmed by a careful analysis using particle identification from the silicon telescope obtained by the  $\Delta E$ - $E$  method. Exceptions are the 1435 and 2300 keV lines. The 2300-keV line was not reported in previous papers.<sup>1-3)</sup> The 1435-keV line was tentatively assigned as a  $(\frac{7}{2}^-) \rightarrow (\frac{3}{2}^+)$  transition of  $^{33}\text{Si}$  by Fornal *et al.*,<sup>3)</sup> however, our analysis favors assigning the line to be

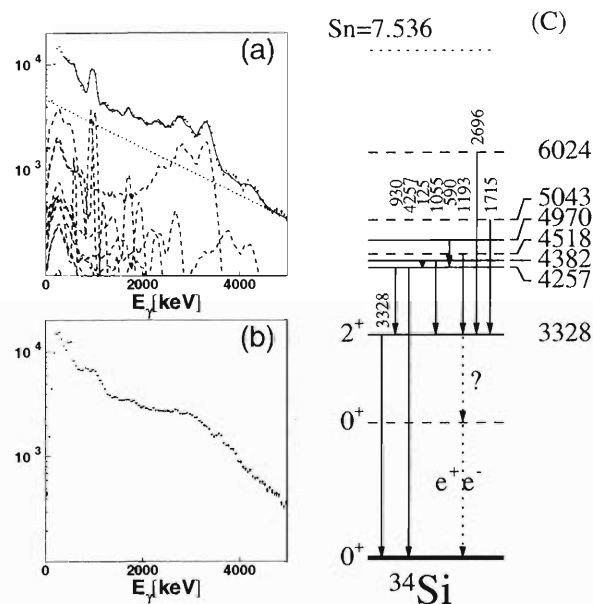


Fig. 1.  $\gamma$  spectra in (a) the projectile frame and (b) the laboratory frame in coincidence with  $^{34}\text{Si}$  detected by the silicon counter telescope. (c) Decay scheme of  $^{34}\text{Si}$ .

from  $^{34}\text{Si}$ .

In order to construct a decay scheme,  $\gamma$ - $\gamma$  coincidence data were analyzed. The lines at 591, 930, 1193, 1715 and 2696 keV were observed in coincidence with that at 3328 keV. The 930-keV line was not observed with the 1193-, 1715- and 2696-keV  $\gamma$  lines. From these facts, the 1193-, 1715- and 2696-keV lines are tentatively assigned to the transitions from states at 4518 keV, 5043 keV and 6024 keV to the  $2^+$  state, as indicated by the dashed lines in Fig. 1 (c).

## References

- 1) R. B. Firestone *et al.*: *Table of Isotopes*, 8th ed., (A Wiley-Interscience Publication, New York, 1998).
- 2) S. Nummela *et al.*: *Phys. Rev. C* **63**, 044316 (2001).
- 3) B. Fornal *et al.*: *Phys. Rev. C* **49**, 2413 (1994).

\*1 Tohoku University

\*2 Rikkyo University

\*3 University of Tokyo

\*4 ATOMKI, Hungary

\*5 Center for Nuclear Study, University of Tokyo

## Production cross sections of neutron rich $N = 50$ nuclei in $66 A$ MeV $^{86}\text{Kr}$ -induced reactions

N. Aoi,<sup>\*1</sup> A. Kobayakawa,<sup>\*1</sup> T. Matsuura,<sup>\*1</sup> H. Sakurai,<sup>\*1</sup> N. Imai,<sup>\*1</sup> Y. Ando,<sup>\*2</sup> H. Baba,<sup>\*2</sup> K. Demichi,<sup>\*2</sup> U. Futakami,<sup>\*2</sup> T. Gomi,<sup>\*2</sup> H. Hasegawa,<sup>\*2</sup> Y. Higurashi,<sup>\*2</sup> K. Ieki,<sup>\*2</sup> H. Ikeda,<sup>\*3</sup> N. Iwasa,<sup>\*4</sup> H. Iwasaki,<sup>\*1</sup> S. Kanno,<sup>\*2</sup> T. Kubo, M. Kunibu,<sup>\*2</sup> M. Kurokawa,<sup>\*3</sup> Z. Liu,<sup>\*5</sup> Y. U. Matsuyama,<sup>\*2</sup> S. Michimasa,<sup>\*6</sup> T. Minemura,<sup>\*2</sup> M. Miura,<sup>\*3</sup> T. Motobayashi,<sup>\*2</sup> H. Murakami,<sup>\*2</sup> T. Nakamura,<sup>\*3</sup> M. Notani,<sup>\*6</sup> Q. Pan,<sup>\*5</sup> A. Saito,<sup>\*2</sup> M. Serata,<sup>\*2</sup> S. Shimoura,<sup>\*6</sup> T. Sugimoto,<sup>\*3</sup> E. Takeshita,<sup>\*2</sup> S. Takeuchi,<sup>\*2</sup> K. Ue,<sup>\*6</sup> K. Yamada,<sup>\*2</sup> Y. Yanagisawa, K. Yoneda, X. Zhou,<sup>\*5</sup> and M. Ishihara

[NUCLEAR REACTIONS:  $^9\text{Be}(^{86}\text{Kr}, X)$ ,  $E(^{86}\text{Kr}) = 66 A$  MeV; Measured production cross sections of  $^{80}\text{Zn}$ ,  $^{81}\text{Ga}$ ,  $^{82}\text{Ge}$ , and  $^{83}\text{As}$

The fragmentation reaction of  $^{86}\text{Kr}$  is profitable in the production of neutron-rich nuclei lying along the neutron magic number 50 towards the doubly magic nucleus,  $^{78}\text{Ni}$ . In this work, we measured the production cross sections of neutron-rich  $N = 50$  nuclei in the fragmentation of  $66 A$  MeV  $^{86}\text{Kr}$ , which allowed us to make a reliable estimation of the secondary-beam intensities available with RIPS. The obtained results were compared with the cross sections of the same reactions at higher energy ( $500 A$  MeV)<sup>1</sup> as well as the production cross sections in the in-flight fission reaction.<sup>2)</sup>

A primary beam of  $^{86}\text{Kr}$  was accelerated by the AVF and RING Cyclotrons and bombarded a  $97 \text{ mg/cm}^2$  thick Be target at  $66 A$  MeV. The typical beam intensity was  $0.5 \text{ pA}$ . Projectile-like fragments were collected and analyzed by RIPS. The angular acceptance of RIPS was set at the maximum value of  $5 \text{ msr}$ . The momentum acceptance was defined using a slit at F1 and was set at  $0.5\%$ .

The fragments were transported to the final focal plane (F3) and detected by a parallel-plate avalanche counter (PPAC) and four layers of Si detectors ( $0.5 \text{ mm}$  thick) located behind the PPAC. The PPAC provided detection timing and the positions of fragments. The time-of-flight (TOF) between the production target and F3 was determined from the time difference between the PPAC and the RF signal of the accelerator.

Particle identification was made by measuring the magnetic rigidity ( $B\rho$ ), time-of-flight (TOF), and energy deposit in the second and third Si detectors ( $\Delta E$  and  $E$ ). The atomic number was determined from the correlation between the TOF and  $\Delta E$ .  $E$  information was incorporated for the determination of  $A$ .

Differential cross sections were measured with eight  $B\rho$  settings ranging from  $2.74 Tm$  to  $2.83 Tm$ . The cross sections were determined from a fit of the

observed momentum distribution to an asymmetric Gaussian. The collection efficiency was corrected for based on the angular acceptance calculated by the INTENSITY code.

The obtained production cross sections are shown in Fig. 1 together with the results concerning the fragmentation of  $^{86}\text{Kr}$  at  $500 A$  MeV<sup>1</sup> and that of the in-flight fission of uranium.<sup>2)</sup> The present result agrees well with that at  $500 A$  MeV, while they are about two orders of magnitude smaller than the in-flight fission reaction cross sections. The prediction by EPAX2<sup>3)</sup> (solid line) gives almost consistent values in this region, but the slope is less steep than the observed value. A simple exponential extrapolation (dashed line) gives  $\sim 10^{-12}$  barn for the production cross section of  $^{78}\text{Ni}$ .

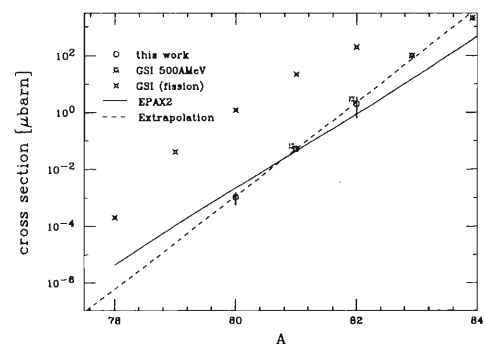


Fig. 1. Production cross sections of  $N = 50$  isotones as a function of the atomic numbers.

### References

- 1) M. Weber et al.: Nucl. Phys. A **578**, 659 (1994).
- 2) M. Bernas: AIP Conf. Proc. **455**, 664 (1998).
- 3) K. Sümmerer et al.: Phys. Rev. C **61**, 034607 (2000).

\*1 University of Tokyo  
 \*2 Rikkyo University  
 \*3 Tokyo Institute of Technology  
 \*4 Tohoku University  
 \*5 Institute of Modern Physics, China  
 \*6 Center for Nuclear Study, University of Tokyo

Coulomb excitation of  $^{84}\text{Se}$ 

N. Aoi,<sup>\*1</sup> N. Imai,<sup>\*1</sup> Y. Ando,<sup>\*2</sup> H. Baba,<sup>\*2</sup> K. Demichi,<sup>\*2</sup> U. Futakani,<sup>\*2</sup> T. Gomi,<sup>\*2</sup> H. Hasegawa,<sup>\*2</sup> Y. Higurashi,<sup>\*2</sup> K. Ieki,<sup>\*2</sup> H. Ikeda,<sup>\*3</sup> N. Iwasa,<sup>\*4</sup> H. Iwasaki,<sup>\*1</sup> S. Kamuo,<sup>\*2</sup> A. Kobayakawa,<sup>\*1</sup> T. Kubo,<sup>\*</sup> M. Kumibu,<sup>\*2</sup> M. Kurokawa,<sup>\*3</sup> Z. Liu,<sup>\*5</sup> T. Matsuura,<sup>\*1</sup> Y. U. Matsuyama,<sup>\*2</sup> S. Michinasa,<sup>\*6</sup> T. Minemura,<sup>\*2</sup> M. Miura,<sup>\*3</sup> T. Motobayashi,<sup>\*2</sup> H. Murakami,<sup>\*2</sup> T. Nakamura,<sup>\*3</sup> M. Notani,<sup>\*6</sup> Q. Pan,<sup>\*5</sup> A. Saito,<sup>\*2</sup> H. Sakurai,<sup>\*1</sup> M. Serata,<sup>\*2</sup> S. Shinoura,<sup>\*6</sup> T. Sugimoto,<sup>\*3</sup> E. Takeshita,<sup>\*2</sup> S. Takeuchi,<sup>\*2</sup> K. Ue,<sup>\*6</sup> K. Yamada,<sup>\*2</sup> Y. Yanagisawa, K. Yoneda, X. Zhou,<sup>\*5</sup> and M. Ishihara

[NUCLEAR REACTION:  $\text{Pb}(^{84}\text{Se}, ^{84}\text{Se}\gamma)$ , Coulomb excitation]

Unstable nuclei around the  $N = 50$  neutron magic number have drawn our interest from the point of view of both nuclear structure and nucleosynthesis. However, experimental information was limited, mainly due to difficulties in the secondary-beam production. In this work, a neutron-rich  $N = 50$  nucleus,  $^{84}\text{Se}$ , was studied through a Coulomb excitation measurement.

The  $^{84}\text{Se}$  beam was produced at RIPS<sup>1)</sup> using the projectile fragmentation reaction of  $^{86}\text{Kr}$ . The primary beam of  $^{86}\text{Kr}$  was accelerated by the AVF and RING Cyclotrons and bombarded a  $97\text{ mg/cm}^2$  thick Be target at  $66\text{ A MeV}$ . The typical beam intensity was  $0.5\text{ pA}$ . The width of the momentum slit at F1 was set at 1%. A flat Al plate (instead of a wedge-shaped one) was used for the energy degrader at F1, and a reasonably small beam spot size of  $12\text{ mm}$  (FWHM) was obtained at F3 thanks to the narrow momentum acceptance. An isotope purity of 83% was achieved with an intensity of about 5 keps.

The  $^{84}\text{Se}$  beam irradiated a  $226\text{ mg/cm}^2$  thick Pb target. The energy of the  $^{84}\text{Se}$  beam was  $38.6\text{ A MeV}$  at the middle of the target. The position and incident angle of the secondary beam was measured with two sets of parallel-plate avalanche counters (PPAC's) located upstream of the secondary target. Scattered particles were detected by a PPAC and a Si telescope located about  $50\text{ cm}$  downstream from the secondary target covering a scattering angle of up to about 6 degrees in the laboratory frame. This PPAC was used for determining the scattering angle of the outgoing particles. The Si telescope consisted of two layers, each of which had four Si detectors placed in a two-by-two matrix. The size of each detector was  $5\text{ cm} \times 5\text{ cm} \times 325\text{ }\mu\text{m}$ . The Si telescope provided  $\Delta E$ - $E$  information, which was used to identify the atomic number ( $Z$ ) of the outgoing particle.

The de-excitation  $\gamma$ -rays were detected with DALI, which consisted of 68 NaI(Tl) scintillators. The energy of the observed  $\gamma$ -ray was corrected for the Doppler shift based on the position of the scintillator which

detected the  $\gamma$ -ray.

Figure 1 shows the Doppler shift-corrected  $\gamma$ -ray spectrum observed in coincidence with the outgoing selenium ( $Z = 34$ ) isotopes. The  $\gamma$ -ray peaks at  $1455\text{ keV}$  and  $667\text{ keV}$  are ascribed to the transitions between known states in  $^{84}\text{Se}$ <sup>2)</sup>: the transition from the first excited state ( $J^\pi = 2^+$ ,  $E_x = 1455\text{ keV}$ ) to the ground state and that from the  $2122\text{ keV}$  state (tentatively  $1^-$ ) to the first excited state. Besides these  $\gamma$ -ray lines, several peaks are seen in the spectrum, such as those around  $1\text{ MeV}$ ,  $1.3\text{ MeV}$  and  $1.8\text{ MeV}$ . Assignments of the transitions to these lines were not made. Further analysis, including a determination of the transition strength and establishment of the transition assignments, is in progress.

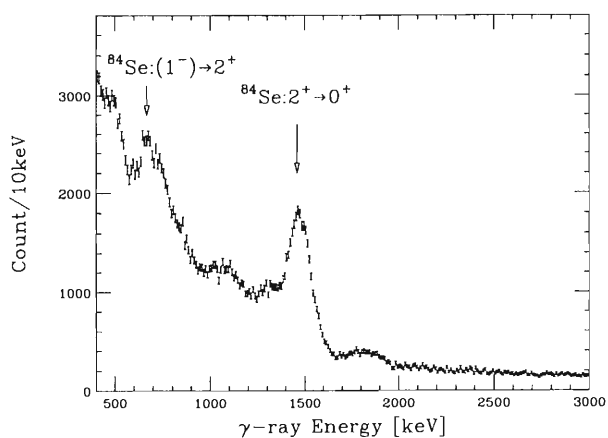


Fig. 1. Doppler shift-corrected  $\gamma$ -ray spectrum observed in coincidence with the outgoing selenium.

## References

- 1) T. Kubo et al.: Nucl. Instrum. Methods Phys. Res. B **70**, 309 (1992).
- 2) R. B. Firestone et al.: *Tables of Isotopes* (Wiley, New York, 1996), p. 491.

\*1 University of Tokyo

\*2 Rikkyo University

\*3 Tokyo Institute of Technology

\*4 Tohoku University

\*5 Institute of Modern Physics, China

\*6 Center for Nuclear Study, University of Tokyo

## g-Factor of a high-spin isomer in $^{149}\text{Dy}$

H. Watanabe, H. Ueno, W. Sato, A. Yoshimi, D. Kameda,\*<sup>1</sup> T. Kishida, Y. Kobayashi, H. Miyoshi,\*<sup>1</sup>  
A. Odahara,\*<sup>2</sup> Y. Gono,\*<sup>3</sup> and K. Asahi

[NUCLEAR REACTION  $^{24}\text{Mg}(^{132}\text{Xe},7n)^{149m}\text{Dy}$ ,  $E = 7\text{ MeV/nucleon}$ ; measured  $\gamma(\theta, B, t)$ ]

Many isomeric states have been observed in nuclei near the semi-doubly magic nucleus  $^{146}\text{Gd}$  ( $Z = 64$ ,  $N = 82$ ). These isomers are mainly produced when the valence particles around the  $^{146}\text{Gd}$  core align on the symmetry axis. Such a feature is most likely maintained even at a higher spin state. That is why high-spin isomers could be observed in  $N = 83$  isotones with atomic numbers from 60 to 68. The excitation energies and half-lives of these high-spin isomers were systematically studied in detail.<sup>1)</sup> However, the g-factor and quadrupole moment have been measured only in the high-spin isomer of  $^{147}\text{Gd}$  so far. The configuration and deformation parameter ( $\beta$ ) of this isomer were deduced from these experimental quantities to be  $[\nu(f_{7/2}h_{9/2}i_{13/2})\pi(h_{11/2}^2)_{49/2}^+]$  and  $-0.19$ ,<sup>3)</sup> respectively. A deformed independent particle model (DIPM)<sup>4)</sup> well reproduces the characteristics of a high-spin isomer in  $^{147}\text{Gd}$ . According to this calculation, high-spin isomer in  $^{149}\text{Dy}$ , whose excitation energy and half-life are 8.52 MeV and 28 ns,<sup>5)</sup> respectively, is expected to have the same configuration and deformation as that in  $^{147}\text{Gd}$ . In this work, therefore, we attempted to measure the g-factor of the high-spin isomer in  $^{149}\text{Dy}$  in order to check the validity of this calculation.

Figure 1 shows a schematic diagram of the experimental setup. The high-spin isomer in  $^{149}\text{Dy}$  was produced and aligned via an inverse kinematic fusion re-

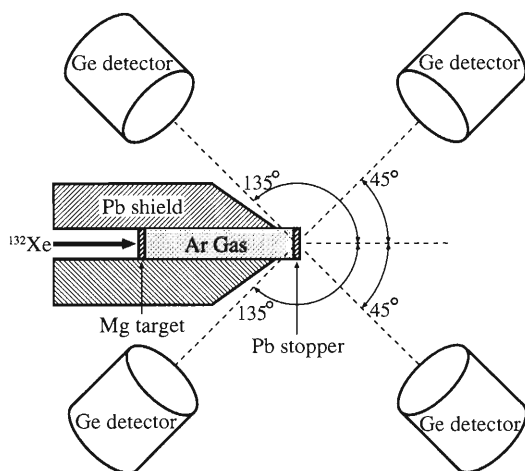


Fig. 1. Schematic drawing of the experimental setup.

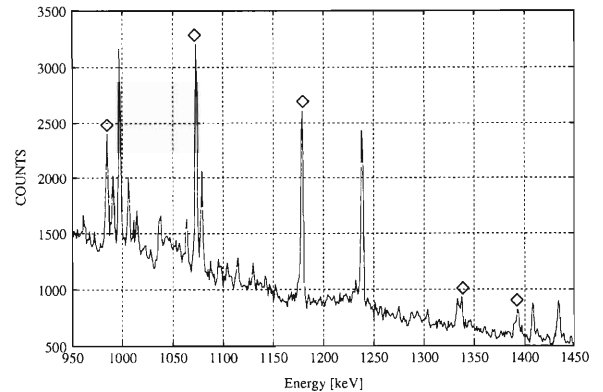


Fig. 2.  $\gamma$ -ray singles spectrum measured by a Ge detector. Gamma rays emitted from  $^{149m}\text{Dy}$  are indicated by the diamonds.

action,  $^{24}\text{Mg}(^{132}\text{Xe},7n)^{149m}\text{Dy}$ , with a pulsed beam of  $^{132}\text{Xe}$  accelerated up to an energy of 7 MeV/nucleon by the RIKEN Ring Cyclotron. The beam repetition time was selected to be  $1\ \mu\text{s}$ . The recoil nuclei were stopped on a lead foil placed 7 cm downstream from a magnesium target. An external magnetic field of 1.5 T was applied to the stopper perpendicularly to both the beam axis and the detection plane. The space between the target and the stopper was filled with Ar gas to retain alignment of the recoil nuclei during the flight. It took about 4 ns to pass through the Ar gas region. This recoil-into-gas technique allows us to measure only  $\gamma$  rays emitted via an isomeric state ( $t_{1/2} \geq 1\ \text{ns}$ ) by enclosing a production target with lead shields. Gamma rays from the stopper position were measured with four Ge detectors located at  $\pm 45^\circ$ ,  $\pm 135^\circ$ . A  $\gamma$ -ray singles spectrum obtained in this experiment is shown in Fig. 2. The g-factor is extracted from the ratio of the  $\gamma$ -ray intensities,  $R(t) = [I(\theta, t) - I(-\theta, t)] / [I(\theta, t) + I(-\theta, t)]$ , where  $I(\theta, t)$  indicates the normalized and background-corrected yield of  $\gamma$  ray decaying the isomeric state. An analysis of the experimental data is now in progress.

### References

- 1) A. Odahara et al.: Nucl. Phys. A **620**, 363 (1997), and references therein.
- 2) O. Häusser et al.: Phys. Rev. Lett. **42**, 1451 (1979).
- 3) O. Häusser et al.: Nucl. Phys. A **443**, 135 (1985).
- 4) T. Dossing et al.: Phys. Scr. **24**, 258 (1981).
- 5) T. Fukuchi: Master Thesis. Kyushu University (1999).

\*<sup>1</sup> Tokyo Institute of Technology

\*<sup>2</sup> Nishinippon Institute of Technology

\*<sup>3</sup> Department of Physics, Kyushu University

## Study of PHENIX Electron Trigger

T. Matsumoto,<sup>\*1</sup> H. Hamagaki,<sup>\*1</sup> K. Oyama,<sup>\*1</sup> K. Ozawa,<sup>\*1</sup> T. Sakaguchi,<sup>\*1</sup> S. Kametani,<sup>\*2</sup>  
J. Kikuchi,<sup>\*2</sup> M. Tamai,<sup>\*1</sup> and Y. Tanaka,<sup>\*3</sup>

[Quark Gluon Plasma, High Energy Heavy Ion Collisions, PHENIX, RHIC]

One of the major goals of the PHENIX experiment is to investigate the property of new states of matter through electron and electron-pair measurements.<sup>1,2)</sup> The Electron Trigger using a Ring Imaging Cherenkov (RICH) detector and an ElectroMagnetic Calorimeter (EMCal) is dedicated to this purpose. At RHIC, the designed luminosity is  $1.4 \times 10^{31} \text{ cm}^{-2} \text{ sec}^{-1}$  in p + p at  $\sqrt{s} = 500 \text{ GeV}$  and  $6.0 \times 10^{26} \text{ cm}^{-2} \text{ sec}^{-1}$  in Au + Au at  $\sqrt{s_{NN}} = 200 \text{ GeV}$ . The reaction rate with these luminosities is 12 MHz in p+p and 1.2 kHz in Au + Au. Since the Data Collection Module (DCM) has a maximum bandwidth of 25 kHz, a rejection factor of approximately 500 (12 MHz/25 kHz) is needed in the extreme case of p + p collisions.

As a first level hardware trigger, the PHENIX LVL-1 trigger system decides whether to accept the data or not from the detector subsystem's LVL-1 signals within 40 Bunch Crossing (BC) after an event. The Electron Trigger is constructed from the RICH and EMCal LVL-1 signals.

The PHENIX detector complex has two central arms and two muon arms. Both RICH and EMCal are located in the central arms. The RICH is one of the major devices for electron identification. The Cherenkov photons generated by electrons, positrons, and high momentum hadrons are reflected by spherical mirrors and detected by 5120 PMT arrays. The RICH LVL-1 signal is generated when the analog sum of 20 PMT's ( $4(\phi) \times 5(z)$ ) output exceeds a trigger threshold. The primary information from EMCal is the energy and spatial position of photons and electrons. One arm comprises four sectors of lead-scintillator (PbSc) modules, the other has two sectors of PbSc and two of lead-glass (PbGl). The EMCal LVL-1 signal is generated when the deposited energy in 4 towers exceeds a threshold value. The Electron Trigger uses the matrix coincidence between 256 bits of RICH LVL-1 signal and 172 bits of EMCal LVL-1 signal.

The study of an Electron Trigger consisted of two stages. First, the trigger algorithm, efficiency and rejection power were studied by simulations. The 60 k single  $J/\psi \rightarrow e^+e^-$  events, 54 k single  $\phi \rightarrow e^+e^-$  events and 200 k minimum-bias events of p + p, Si + Si,

Ag + Ag and Au + Au were used. The results were described briefly in the CNS annual report 1999.<sup>3)</sup> Main conclusion was that the RICH threshold should be 3 photo-electrons per trigger-tile under the condition of CO<sub>2</sub> radiator gas, and the EMCal energy threshold should be 0.9 GeV for the  $J/\psi$  trigger and 0.3 GeV for the  $\phi$  trigger. The RICH LVL-1 hardware was developed based on this study.<sup>4)</sup> The trigger algorithm was then applied to real data and trigger performance was evaluated. This is the main topic described in this report.

From the obtained data, 593000 events of Au + Au full-field data at  $\sqrt{s_{NN}} = 130 \text{ GeV}$  were used in this study. The electrons from the collision points, which were off center by 30 cm in the  $z$  direction, didn't reach the EMCal surface because of the pole pieces of the central magnet. Thus the absolute value of the  $z$ -vertex reconstructed by Beam-Beam Counters (BBC) within 30 cm was required in these event samples.

Table 1 gives the centrality class and corresponding number of binary collisions as well as the number of participants in a event.

Events were sorted into 6 centrality classes, as listed in the table. These classes were derived from the combination of Zero Degree Calorimeters (ZDC) and BBC. The number of participants was calculated using a Glauber model. The number of participants in most peripheral events was around 5. These event samples are useful to evaluate the electron trigger performance for a p + p run.

Figure 1 shows the single electron trigger efficiency for RICH as a function of the trigger threshold, which has units of photo-electron in a trigger-tile.

This simulation result shows that the trigger efficiency is almost 100% when the threshold level is below 3 photo-electrons, and declines with an increase in the threshold level. The RICH threshold was fixed to

Table 1. Centrality classes of a Au + Au event.

Centrality	Binary Collisions	Participants
0 - 5%	$945 \pm 141$	$347 \pm 52$
5 - 15%	$673 \pm 100$	$271 \pm 41$
15 - 30%	$383 \pm 57$	$178 \pm 27$
30 - 60%	$123 \pm 18$	$76 \pm 11$
60 - 80%	$19 \pm 11$	$19 \pm 11$
80 - 92%	$3.7 \pm 2.2$	$5 \pm 3$

<sup>\*1</sup> Center for Nuclear Study, Graduate School of Science, University of Tokyo

<sup>\*2</sup> Advanced Research Institute for Science and Engineering, Waseda University

<sup>\*3</sup> Nagasaki Institute of Applied Science

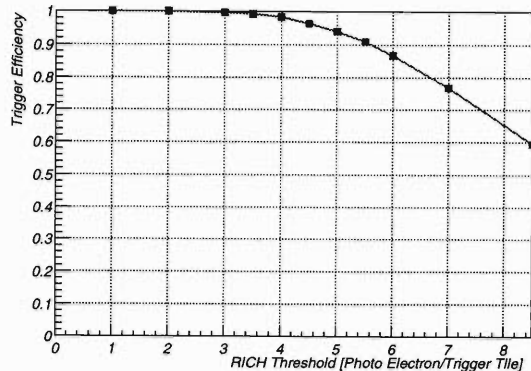


Fig. 1. Simulated trigger efficiency as a function of number of photo-electrons in a trigger tile.

3 photo-electrons from the simulation result.

Table 2 shows the summary of trigger rate under the various conditions for the last Au + Au run. Rejection powers of around 3 (0.3 GeV) and around 8 (0.9 GeV) were achieved. Here, the rejection power is defined by the number of total events divided by the number of triggered events.

Figure 2 shows the rejection power as a function of the centrality classes, which are described in Table 1. The closed circles are for the case when the EM-Cal energy threshold was set to 0 GeV (corresponds to RICH only trigger), the open square shows the  $\phi$  trigger (0.3 GeV) and the closed square shows the  $J/\psi$  trigger (0.9 GeV), respectively. Since matrix coincidence hardware will not be ready, complete look-up (256 bits + 172 bits) can not be done in an upcoming run. Because a feasible way is half sector matching (16 bits + 16 bits), this matching was used as the coincidence method in this study.

The rejection power clearly moves upward as the centrality goes down in Au + Au collision. In the most

Table 2. Survival rate under various trigger conditions.

Trigger	Count	Ratio
Total Event	593000	
RICH Hit (3 photo-electron)	376418	63%
EMCal Hit (0.3 GeV)	310725	52%
EMCal Hit (0.9 GeV)	142288	24%
RICH and EMCal (0.3 GeV)	160132	27%
RICH and EMCal (0.9 GeV)	74428	13%

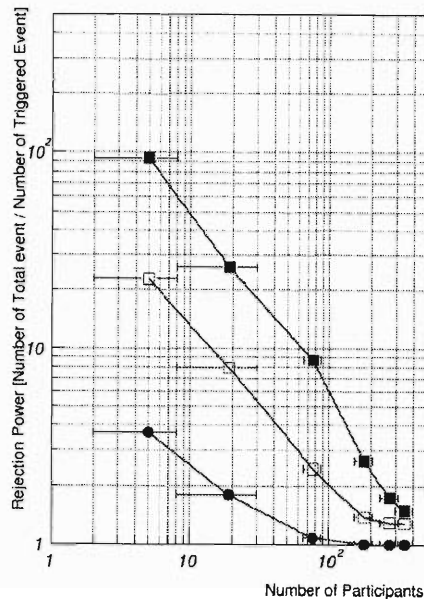


Fig. 2. The rejection power as a function of centrality.

The closed circle shows RICH only trigger, open square shows  $\phi$  trigger (EMCal threshold = 0.3 GeV) and closed square shows  $J/\psi$  trigger (EMCal threshold = 0.9 GeV).

central case, the rejection power is approximately 1.5. At 80-92% centrality, rejections of 23( $\phi$  trigger) and 95 ( $J/\psi$  trigger) were achieved. Although these results are not directly applicable to the coming p + p events, simple extrapolation to the p + p case (number of participants = 2) provides a rejection factor larger than 200 in the  $J/\psi$  trigger case.

An Electron trigger algorithm has been developed and applied to PHENIX real data. It is expected that a good rejection power to reduce the trigger rate down to the level of DAQ capability will be achieved in an upcoming p + p run.

#### References

- 1) PHENIX Conceptual Design Report, BNL (1993) (unpublished).
- 2) PHENIX Collaboration: Nucl. Phys. A **638**, 565c (1998).
- 3) T. Matsumoto et al.: CNS-REP-25, July (2000), p. 23.
- 4) T. Matsumoto et al.: CNS-REP-25, Oct. (1998), p. 25.

## Measurement of the ${}^8\text{Li}(\alpha, n){}^{11}\text{B}$ reaction cross section with ${}^8\text{Li}$ beams below 1.5 MeV/n energy

M. Kurata-Nishimura, S. Nishimura, Y. Nishi, M. A. Famiano, I. Tanihata, P. Walden,<sup>\*1</sup> P. Amaudruz,<sup>\*1</sup> R. Poutissou,<sup>\*1</sup> J. M. Poutissou,<sup>\*1</sup> L. Buchmann,<sup>\*1</sup> R. N. Boyd,<sup>\*2</sup> L. Sahin,<sup>\*3</sup> A. Murphy,<sup>\*2</sup> and B. Fulton<sup>\*4</sup>

[Nucleosynthesis, Inhomogeneous Big Bang models]

We have performed measurements of the cross section for the  ${}^8\text{Li}(\alpha, n){}^{11}\text{B}$  reaction with a  ${}^8\text{Li}$  beam with 0.6 MeV/n energy at the TRIUMF cyclotron of the ISAC facility. This reaction is considered to be crucial to predict the light-element abundances from big-bang nucleosynthesis.<sup>1)</sup>

Although some previous experiments were made to determine this reaction cross section,<sup>2-4)</sup> they were not even in qualitative agreement with each other. Measurements of the low-energy cross section, below 1 MeV/n, which are important for predicting the abundances of light elements by inhomogeneous big-bang models of nucleosynthesis (IBBN), have not been measured yet due to difficulty of handling low-energy beams.

The Isotope Separator and Accelerator (ISAC) which was constructed at TRIUMF (Canada) recently, consists of two systems. One is a target assembly where many different isotopes can be produced by bombarding various elements with 500 MeV protons beam from the TRIUMF cyclotron. The other device, a Radio Frequency Quadrupole (RFQ), is used as the first step for increasing the energy of the isotopes extracted from the target. By using this facility, singly charged ion beams consisting of isotopes whose mass is less than 30 atomic mass units can be accelerated. Moreover, the ISAC facility at TRIUMF is designed to provide the world's most intense beams of accelerated radioactive isotopes for a wide range of experimental programs. ISAC employs the ISOL (Isotope Separation On-Line) technique, where short-lived isotopes are continuously produced, ionized and transported as a focused beam. Hence, the most important reactions involved in the chains of nuclear reactions occurring in explosive astrophysical sites become available for study.

For determining the  ${}^8\text{Li}(\alpha, n){}^{11}\text{B}$  reaction cross section, the neutron production rate is measured. Neutrons are emitted from 0 degree to 180 degrees in the laboratory system. The identification of neutrons can be done by measuring the energy and emission polar angle, since the incident energy of a  ${}^8\text{Li}$  beam is well fixed and momentum of the  ${}^4\text{He}$  gas is negligible. Because of the high beam intensity (more than  $1 \times 10^7$  particles per sec.), any kind of beam counter is not use-

ful to be operated under such a high-current condition.

We have installed 3 neutron counter walls which consist of 16 plastic scintillator slats with 2 PMT's in the ISAC experimental hall. The neutron counter has dimensions of  $6 \times 6 \times 108 \text{ cm}^3$  and two PMT's (Hamamatsu H6410) are attached to the ends of the plastic scintillator. The neutron walls are placed at 1.6 m away from the center of a He gas target by taking into account the time-of-flight separation of neutrons emitted from the ground state of  ${}^{11}\text{B}$  and ones emitted from the first excited state of  ${}^{11}\text{B}$ . The neutron walls cover the polar angle from 21 degrees to 140 degrees with around a 6% geometrical acceptance.

The signal from the PMT's is divided into two lines: one is used for a timing measurement after discrimination; the other is used for a charge measurement. The hit position on the counter is determined by the time difference between both side PMT's and also the ratio of the integrated charge from them. The energy of a neutron is determined by the time-of-flight method by measuring the time difference between the neutron counter signal as a start and the cyclotron-RF clock timing as a common stop.

Sixteen signal lines from 8 counters are fed into one discriminator module (CAMAC 3412), where the threshold and width are adjusted to 50 mV and 80 ns, respectively. The sum output from this discriminator is reshaped at the level indicating 2 of any 16 PMT's firing, and is then used in the trigger logic.

In order to trigger events indicating that  ${}^{11}\text{B}$  or any charged particles scattered in a target, a target cell which includes 5 small pieces of plastic scintillators read by a multi-anode PMT (HAMAMATSU R5900L16) is installed in the vacuum chamber. The entrance and exit windows of the target cell are closed with Ni foil less than 250 nm in thickness to allow  ${}^8\text{Li}$  beams to pass through it.  ${}^4\text{He}$  gas is filled in the cell at pressures of 20 to 25 torr.

Three trigger settings are employed in this experiment. The first one, called the single trigger, requires one of the neutron counters to fire. The second one, called the double trigger, requires two of the neutron counters to fire within a 200 ns interval, covering slow neutrons. This double trigger makes it possible to require adjacent hits of scattered neutrons in the counter. The third one requires a single trigger OR double trigger AND that the target cell counter fires.

The beam spot was well-tuned at the target entrance

<sup>\*1</sup> TRIUMF Cyclotron Laboratory, Canada

<sup>\*2</sup> Ohio State University, USA

<sup>\*3</sup> Oak Ridge National Laboratory, USA

<sup>\*4</sup> University of York, USA

window with a size of less than  $3\text{ mm}\phi$ . Although an intensity of  $1.8 \times 10^7$  particles per sec was achieved with a beam energy of  $0.6\text{ MeV/n}$ , it was 1 order of magnitude less than what we expected.

The analysis is still progressing. At this moment, no clear neutron peak has been observed in any trigger settings. The reason is due to a considerable amount of gamma-ray background from the target area. As long as we survey the radiation around the target, almost 70% of the beam seems to be stopped at the exit window area. This value is much worse than we estimated in a simulation. We believe that the main component

of background is gamma rays related to the beta decay of  $^8\text{Li}$  stopped at the target window area, and that the rest is the room background. Surely the separation of gamma signals from the neutron signal is essential. This result will be used to improve the experimental setup for the next run.

#### References

- 1) M. J. Balbes et al.: Phys. Rev. Lett. **71**, 3931 (1993).
- 2) X. Gu et al.: Phys. Lett. B **343**, 31 (1995).
- 3) R. N. Boyd et al.: Phys. Rev. Lett. **68**, 1283 (1992).
- 4) Y. Mizoi et al.: Phys. Rev. C **62**, 065801 (2000).

# Indication of a reduced chiral order parameter from the $1s \pi^-$ states in $^{205}\text{Pb}$ and light nuclei

H. Geissel,<sup>\*1</sup> H. Gilg,<sup>\*2</sup> A. Gillitzer,<sup>\*3</sup> R. S. Hayano,<sup>\*4</sup> S. Hirenzaki,<sup>\*5</sup> K. Itahashi,<sup>\*6</sup> M. Iwasaki,<sup>\*6</sup> P. Kienle,<sup>\*2</sup> M. Münch,<sup>\*2</sup> G. Münzenberg,<sup>\*1</sup> W. Schott,<sup>\*2</sup> K. Suzuki,<sup>\*4</sup> D. Tomono,<sup>\*6</sup> H. Weick,<sup>\*1</sup> T. Yamazaki, and T. Yoneyama<sup>\*6</sup>

[pion, pionic states, chiral symmetry]

It is of great importance to study the s-wave (local) part of the pion-nucleus interaction, as emphasized recently,<sup>1,2)</sup> since not only the s-wave strength as a whole

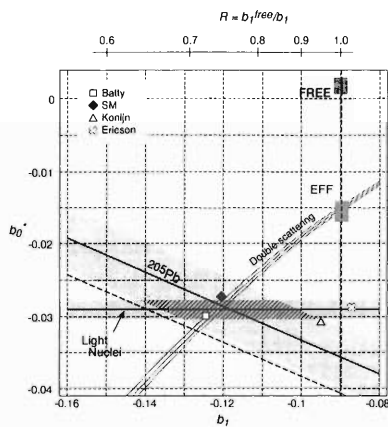


Fig. 1. Presentation of the isoscalar ( $b_0^*$ ) and the isovector ( $b_1$ ) parameters in units of  $m_\pi^{-1}$ . The  $1s$  states of light symmetric pionic atoms give a shaded horizontal band. The  $b_0^* - b_1$  constraint by the  $1s$  state of  $^{205}\text{Pb}$  with a neutron skin effect is shown by another shaded band with  $1\sigma$  error lines. The  $b_0^* - b_1$  constraint without a neutron skin effect is shown by the broken line. The double-scattering effect,<sup>5)</sup> when  $b_1$  is modified in the nuclear medium, is shown by three dotted curves corresponding to different nuclear densities of  $0.155$ ,  $0.165$  and  $0.175 \text{ fm}^{-3}$ . The free- $\pi\text{N}$  values (“FREE”) and their effective values (“EFF”) after the double scattering corrections are also indicated. The scale for the reduction of the squared chiral order parameter,  $R = b_1^{\text{free}}/b_1 \approx f_\pi^{*2}/f_\pi^2$ , is indicated in the upper part. Various potential parameters obtained from the global fitting of pionic atom data are also shown.

translates into a pion mass excess in a nuclear medium, but also its isovector parameter ( $b_1$ ) is related to the pion decay constant ( $f_\pi$ ). The isoscalar  $b_0^*$  (including the density-quadratic term) and isovector  $b_1$  parameters of the s-wave pion-nucleus interaction in the Ericson-Ericson potential were deduced to be

$$b_0^* = -0.029 \pm 0.0013 m_\pi^{-1},$$

$$b_1 = -0.116 \pm 0.018 m_\pi^{-1},$$

by using the binding energies and widths of the  $1s \pi^-$  states in both light pionic atoms and the deeply bound  $\pi^-$  state in  $^{205}\text{Pb}$ ,<sup>3)</sup> in which a neutron skin effect<sup>4)</sup> is taken into account (see Fig. 1). The enhanced isovector strength,  $|b_1|$ , over the free- $\pi\text{N}$  value ( $-0.090$ ) infers that the squared chiral order parameter is reduced in the nuclear medium by

$$R = \frac{f_\pi^{*2}}{f_\pi^2} = \frac{b_1^{\text{free}}}{b_1} = 0.78^{+0.14}_{-0.12}.$$

This is in accordance with Weise’s prediction,  $R \sim 0.65$ , as an indication of a partial restoration of chiral symmetry breaking.<sup>2)</sup>

The isoscalar part is accounted for as arising from a double-scattering effect, without invoking a large  $\text{Re } B_0\rho(r)^2$  term.

## References

- 1) P. Kienle and T. Yamazaki: Phys. Lett. B **514**, 1 (2001).
- 2) W. Weise: Acta Phys. Pol. **31**, 2715 (2000).
- 3) H. Geissel et al.: Phys. Rev. Lett., in press.
- 4) A. Trzcińska et al.: Phys. Rev. Lett. **87**, 082501 (2001).
- 5) N. Kaiser and W. Weise: Phys. Lett. B **512**, 283 (2001).

<sup>\*1</sup> Gesellschaft für Schwerionenforschung, Germany  
<sup>\*2</sup> Physik-Department, Technische Universität München, Germany  
<sup>\*3</sup> Institut für Kernphysik, Forschungszentrum Jülich, Germany  
<sup>\*4</sup> Department of Physics, University of Tokyo  
<sup>\*5</sup> Department of Physics, Nara Women’s University  
<sup>\*6</sup> Department of Physics, Tokyo Institute of Technology

## 2. Atomic and Solid-State Physics



## Bound states of a positron with molecules

M. Tachikawa, I. Shimamura, R. J. Buenker,<sup>\*1</sup> and M. Kimura<sup>\*2</sup>

It is now known that in electron ( $e^-$ )-polar molecule systems, an infinite number of stable electron bound states can be formed in the Born-Oppenheimer approximation if the polar molecule has a dipole moment larger than  $D_c = 1.625$  Debye (D).<sup>1)</sup> This is a consequence of a long-range dipole interaction, behaving as  $\sim r^{-2}$  at large  $r$ , regardless of the nature of the short-range interactions. Even if the dipole moment is smaller than  $D_c$ , or there is no dipole moment at all, the formation of bound states around a molecule may still be possible, though their number should be finite. Indeed, these considerations have furnished basic knowledge about electron attachment to polar molecules, and have also been found to be useful for a systematic understanding of low-energy electron scattering by molecules.

These theoretical considerations do not depend on the sign of the dipole interaction. Therefore, we expect that a positron ( $e^+$ ) has an infinite number of bound states around a stationary polar molecule whose dipole moment exceeds  $D_c = 1.625$  D at the equilibrium nuclear position, although the spatial distribution of the positron can be expected to be opposite to that of an attached electron. These considerations have not been fully appreciated in studies of possible positron attachment to molecules.

Possible positron binding states with atoms have been studied theoretically,<sup>2)</sup> and two important mechanisms of electron binding to atoms have been proposed: (i) a positron forms a positronium within an

atom, and (ii) a positron can be trapped on the tail of a long-range polarization potential. For molecular cases, there have been some theoretical attempts<sup>3-5)</sup> to investigate a possible formation of positron bound states based on the Hartree-Fock, quantum Monte Carlo and other approaches.

We have investigated a number of different molecules from non-polar to strongly polar molecules. By using the HF method with the inclusion of higher order corrections, we have confirmed that, indeed,  $\text{OH}^-$  ions can maintain a bound state with a positron. We have found that the electron cloud on the H atom shifts toward the O atom because of the higher electronegativity of the O atom. Next, we added a positron to the  $\text{OH}^-$  ion, and found that p orbitals in the O atom stretch out toward the positron, and are significantly deformed. This is because the positron is more attracted by a negative charge centered on the O atom, and is eventually captured by it.

### References

- 1) W. R. Garrett: *J. Chem. Phys.* **73**, 5721 (1980).
- 2) G. Ryzhikh, J. Mitroy, and K. Varga: *J. Phys. B* **31**, 3965 (1998).
- 3) H. A. Kurtz and K. D. Jordan: *J. Chem. Phys.* **75**, 1876 (1981).
- 4) D. Bressanini, M. Mella, and G. Morosi: *J. Chem. Phys.* **109**, 1716 (1998).
- 5) M. Tachikawa, K. Mori, K. Suzuki, and K. Iguchi: *Int. J. Quantum. Chem.* **70**, 491 (1998).

<sup>\*1</sup> Theoretische Chemie, Bergische Universität-Gesamthochschule Wuppertal, Germany

<sup>\*2</sup> Graduate School of Science and Engineering, Yamaguchi University

# Diabatic ionization model for capture of antiprotons by atoms

Y. Teranishi and I. Shimamura

Collision processes involving an antiproton have attracted much attention recently, since the Antiproton Decelerator (AD) facility at CERN is expected to open new possibilities for related experiments.<sup>1)</sup> Even though the capture of antiprotons by atoms or molecules is one of the most important processes in analyzing these experiments, accurate theoretical calculations are available only for the simplest target, *i.e.*, the hydrogen atom.<sup>2)</sup> In the present study, we propose a simple, diabatic ionization model for the capture cross sections for atomic targets in general, and discuss its validity by comparing with other theoretical results.

In our model, we assume that the target atom (A) is ionized with unit probability when, and only when, an antiproton ( $\bar{p}$ ), following the classical trajectory, reaches a critical distance ( $R_c$ ) from the target nucleus, at which point the diabatic ionization potential becomes zero. In other words,  $R_c$  satisfies the equation

$$V^{\text{atom}}(R_c) = V^{\text{ion}}(R_c), \quad (1)$$

where  $V^{\text{atom}}(R)$  and  $V^{\text{ion}}(R)$  are diabatic potentials of the antiproton-atom system  $\bar{p}$ -A and of the antiproton-ion system  $\bar{p}$ -A<sup>+</sup>, respectively, defined by

$$V^{\text{atom}}(R) = \langle \Psi^{\text{atom}} | V_{\text{atom}-\bar{p}}(R) | \Psi^{\text{atom}} \rangle, \quad (2)$$

and

$$V^{\text{ion}}(R) = \langle \Psi^{\text{ion}} | V_{\text{ion}-\bar{p}}(R) | \Psi^{\text{ion}} \rangle. \quad (3)$$

We assume that the antiproton is captured by the atom if ionization occurs at collision energies  $E$  below the ionization threshold. The capture cross section is then given by

$$\sigma = \frac{\pi}{E}(E + \Delta E)R_c^2, \quad (4)$$

where  $\Delta E \equiv V^{\text{atom}}(R_c) - V^{\text{atom}}(\infty)$ . If we make a further assumption that the angular momentum of the emitted electron is negligible, the cross section differential in the continuous classical angular momentum  $l$  of the formed antiprotonic atom  $\bar{p}A^+$  is given by

$$\frac{d\sigma}{dl} = 2\pi \frac{l}{2\mu E}, \quad (5)$$

where  $\mu$  is the reduced mass of  $\bar{p}A^+$ . The maximum angular momentum is given by

$$l_{\text{max}} = \{2\mu(E + \Delta E)R_c\}^{1/2}. \quad (6)$$

The parameters  $R_c$  and  $\Delta E$  were calculated for various atomic targets with atomic numbers  $Z = 1-54$  using the Hartree-Fock wave functions. The total (cap-

ture + ionization) cross sections for He and Ne atoms are shown in Figs. 1 and 2 and are compared with the results of classical-trajectory Monte Carlo (CTMC) calculations.<sup>3,4)</sup> As shown in these figures, our results agree well with the CTMC results.

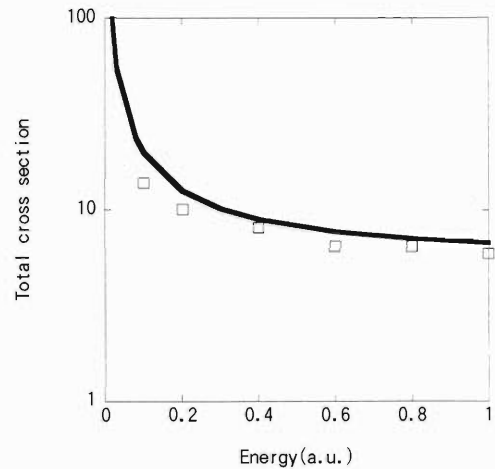


Fig. 1. Total cross sections for He. The solid line indicates the present calculation, and the open square the CTMC calculation.

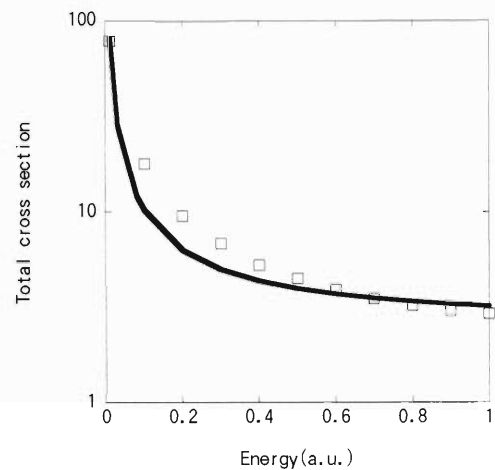


Fig. 2. Total cross sections for Ne. The solid line indicates the present calculation, and the open square CTMC calculation.

## References

- 1) Y. Yamazaki: AIP Conf. Series **498**, 48 (1999).
- 2) K. Sakimoto: Phys. Rev. A **65**, 012706 (2002).
- 3) J. S. Cohen: Phys. Rev. A **56**, 3583 (1997).
- 4) J. S. Cohen: Phys. Rev. A **59**, 1160 (1999).

## Tunneling effect in the single ionization of Ne by an intense laser field

Y. Teranishi and I. Shimamura

The study of atoms and molecules in intense laser fields has grown over the last decade. Developments in the laser technology have led to short-pulse lasers with field strengths on the order of one atomic unit. Ionization of atoms and molecules by such a strong field takes place due to tunneling ionization or over-the-barrier ionization.

Feeler and Olson<sup>1)</sup> studied the single ionization of Ne by using the classical Monte-Carlo method to obtain the momentum distribution of  $\text{Ne}^+$  after ionization by 800 nm lasers with various intensities of from  $3 \times 10^{14}$  to  $3 \times 10^{15}$  W/cm<sup>2</sup>. In this intensity regime, the Keldysh parameter ( $\gamma$ ), defined by

$$\gamma = \sqrt{\frac{2E_0\omega^2}{I}}, \quad (1)$$

where  $E_0$ ,  $\omega$ , and  $I$  are the ionization potential of the target, the frequency of the laser field, and the intensity of the laser field, respectively, is smaller than unity (0.775 to 0.245), which may imply that over-the-barrier ionization plays a dominant role, and that classical mechanics can describe the ionization process. Their calculation, however, gives a rather broad momentum distribution of  $\text{Ne}^+$  compared to the experimental results. In the present study, the momentum distribution of  $\text{Ne}^+$  was calculated by the classical Monte-Carlo method including the tunneling effect. The role of tunneling in the ionization process was considered.

In order to treat a multi-electron target in the classical mechanical framework, we considered only one active electron subjected to the model potential proposed by Garvey *et al.*<sup>2)</sup> The initial condition for the electron is given by the micro canonical ensemble. Hamilton's equations were solved by the Runge-Kutta method, and when the electron reaches the potential barrier, the tunneling probability was calculated assuming one-dimensional motion along the direction of the laser polarization, namely,

$$P = \frac{1}{1 + \exp(2\pi|\sigma|)}. \quad (2)$$

Here,  $\sigma$  is defined by

$$\sigma = \int_{x_1}^{x_2} p(x) dx, \quad (3)$$

where  $x_1$  and  $x_2$  are the turning points,  $p(x)$  is the momentum of the electron parallel to the laser polarization, and the contour of the integration is also parallel to the laser polarization. Our results for a wavelength of 800 nm and an intensity of  $I = 1.3 \times 10^{15}$  W/cm<sup>2</sup> with and without the tunneling effect, are shown in Fig. 1 along with the experimental results given in Ref. 3. Our results show that the tunneling effect plays an important role in the ionization process even when the Keldysh parameter is smaller than unity ( $\gamma = 0.245$  in this case). The tunneling effect sharpens the momentum distribution because the pulse width is so large that the ionization is completed before the intensity reaches its peak value.

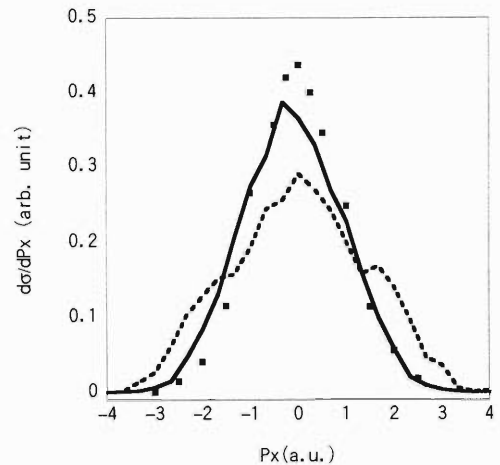


Fig. 1. Momentum distribution of the  $\text{Ne}^+$  ion after ionization by an 800 nm,  $I = 1.3 \times 10^{15}$  W/cm<sup>2</sup> laser. The solid line indicates the present calculation, and the dashed line represents CTMC without tunneling effect. The solid squares indicate the experimental values.

### References

- 1) C. R. Feeler and R. E. Olson: J. Phys. B **33**, 1997 (2000).
- 2) R. H. Garvey, C. H. Jackman, and A. E. S. Green: Phys. Rev. A **12**, 1144 (1975).
- 3) R. E. Olson, J. Pascale, and R. Hoekstra: J. Phys. B **25**, 4241 (1992).

## Theoretical intensity distributions of K X-ray satellite spectra emitted from Al

T. Yamamoto

Theoretical calculations were carried out to reproduce the fine structures of the K X-ray satellite spectra of Al induced by the impact of  $C^{3+}$  ions. These satellites are emitted from  $KL^n$  multiple ionized states, *i.e.*, excited states with one K and  $n$  L vacancies. Relative intensities of the satellites emitted from  $KL^n$  multiple ionized states are proportional to  $KL^n$  multiple ionization cross sections, if we assume that the fluorescence yields for all multiple ionized states are the same. The  $KL^n$  multiple ionization probability  $P_{KL^n}$  is expressed by a binomial equation as

$$P_{KL^n} = \sum_{a,b} \left[ \binom{2}{1} P_{1s}^1 (1 - P_{1s})^{2-1} \right] \\ \times \left[ \binom{2}{a} P_{2s}^a (1 - P_{2s})^{2-a} \right] \\ \times \left[ \binom{6}{b} P_{2p}^b (1 - P_{2p})^{6-b} \right],$$

where  $P_{1s}$ ,  $P_{2s}$  and  $P_{2p}$  are the ionization probabilities of  $1s$ ,  $2s$  and  $2p$  electrons, respectively. The Binary Encounter Approximation (BEA)<sup>1)</sup> and the Semi-Classical Approximation (SCA)<sup>2)</sup> are often employed to calculate the multiple ionization cross section, and are useful for light projectiles such as protons and alpha particles. However, large discrepancies appear between experiments and calculations for heavier projectiles carrying orbital electrons when we use these methods. Because the projectiles are treated as bare particles, *i.e.*, particles with no orbital electrons, the ionization cross section is proportional to  $Z_1^2$  in these methods, where  $Z_1$  is the atomic number of the projectile. Then, we employed the Geometrical Model,<sup>3,4)</sup> which is a modification of BEA, in order to obtain  $KL^n$  multiple ionization cross sections. This method is applicable under the condition,  $v_p \gg v_e$ , where  $v_p$  and  $v_e$  are velocities of the projectile and the L electrons, respectively, and hydrogenic wave functions are employed for the electrons in the target atom. In this method, the charge state of the projectile is assumed to be an effective charge instead of  $Z_1$ . Details of the Geometrical Model are found in the references.<sup>3)</sup> The multiple ionization cross section due to the shake process is not negligible for a target with a low- $Z$  number. The shake probabilities<sup>5)</sup> were also taken into account in these calculations. Calculated results for the K-alpha X-ray spectra of Al induced by  $C^{3+}$  ions with incident energies of 18.5, 23.6, 40.3 and 72.3 MeV are compared with experimental results<sup>6)</sup> in Fig. 1, in which theoretical intensity distributions reproduced

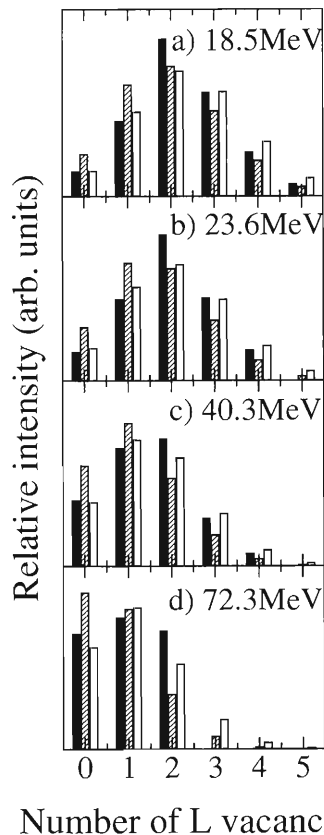


Fig. 1. Comparisons of Al K-alpha X-ray satellite distributions induced by a) 18.5, b) 23.6, c) 40.3, and d) 72.3 MeV  $C^{3+}$  ions between experiments and calculations. Solid bars represent experiments, and shaded and open bars represent calculations with and without the shake effect, respectively.

the experimental ones well. From these results, our calculation method was found to be useful for analysis of the satellite structures induced by heavy ion impacts, where conventional methods failed.

### References

- 1) J. D. Garcia: Phys. Rev. A **1**, 280 (1970).
- 2) J. M. Hansteen and O. P. Mosebekk: Nucl. Phys. A **210**, 541 (1973).
- 3) B. Sulik et al.: J. Phys. B **17**, 3239 (1984).
- 4) B. Sulik et al.: Nucl. Instrum. Methods Phys. Res. B **28**, 509 (1987).
- 5) T. Mukoyama and K. Taniguchi: Phys. Rev. A **36**, 693 (1987).
- 6) R. L. Watson et al.: Phys. Rev. A **19**, 1529 (1979).

## Studies on electron degradation and thermalization in H<sub>2</sub> and D<sub>2</sub> gases

K. Kowari\*

The relaxation of subexcitation electrons in H<sub>2</sub> gas at a temperature of 300 K and the number density of  $2.69 \times 10^{19} \text{ cm}^{-3}$  has been studied by Kowari using the Boltzmann equation.<sup>1)</sup> The Boltzmann equation, which explicitly includes elastic and inelastic collisions, is given by

$$\frac{\partial f}{\partial t} = J_{el}(f) + J_{in}(f), \quad (1)$$

where  $f = f(\mathbf{v}, t)$ , and  $\mathbf{v}$  is the velocity of an electron. In Eq. (1),  $J_{el}(f)$  and  $J_{in}(f)$  are the elastic and inelastic collision operators, respectively. The elastic collision operator is the Fokker-Planck operator, and the inelastic collision operator a difference operator. The expansion of the electron velocity distribution function in Legendre polynomials gives  $f(\mathbf{v}, t) = \sum_{l=0}^{\infty} f_l(v, t) P_l(\cos \theta)$ . We assume that the electron distribution function is spatially homogeneous and isotropic in  $\mathbf{v}$ . The electron energy distribution function is expressed as  $\rho(E, t) = 2\pi(\frac{2}{m})^{\frac{3}{2}} \sqrt{E} f(v, t)$ , where  $E = \frac{mv^2}{2}$ , and the incremental degradation spectrum as  $z(E, t) = v\rho(E, t)$ . Inserting  $\rho$  and  $z$  in Eq. (1), we obtain the equation for time evolution of  $z(E, t)$ . We solve it with an initial distribution  $\rho_0 = \delta(E - E_0)\delta(t)$ , where  $E_0$  is an electron initial energy. Once we have obtained the electron distribution function  $\rho(E, t)$ , we can calculate the electron average energy, the cumulative degradation spectrum, the cumulative net yields, and so on.

It deepens our understanding of electron degradation and thermalization in gases to carry out a study on isotope effects in D<sub>2</sub> and H<sub>2</sub> gases. We have recently carried out calculations for electron degradation and thermalization in D<sub>2</sub> gas with three different electron initial energies and complementary calculations in H<sub>2</sub>, in order to study isotope effects.<sup>2)</sup> Suppose  $n_{lm}$  is the number of collisions that excite a molecular state  $l$  to  $m$ , the net cumulative yield is calculated as

$$\tilde{n}_{lm}(t) = n_{lm}(t) - n_{ml}(t),$$

where  $m$  is greater than  $l$ . Figure 1 shows cumulative net yields for major rotational-excitation processes in H<sub>2</sub> and D<sub>2</sub>. The net yield for  $J = 1$  to 3 is the largest in H<sub>2</sub> because of the statistical weight, and that for  $J = 2$  to 4 in D<sub>2</sub>. All net yields shown in Fig. 1 seem to reach a plateau by 6 ns.

It is shown that the electron average energy in H<sub>2</sub> decreases more rapidly than that in D<sub>2</sub> until some 5.5 ns, and thereafter it decreases more slowly.<sup>2)</sup> Furthermore,

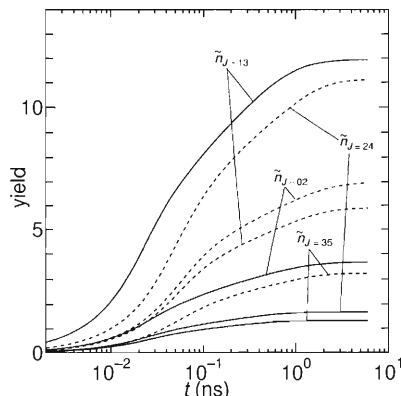


Fig. 1. The solid curves represent net yields for primary rotational excitations with an initial energy of 5 eV in H<sub>2</sub>, and the dashed curves those in D<sub>2</sub>. The symbol  $\tilde{n}_{J=02}$  indicates the net yield for  $J = 0$  to 2,  $\tilde{n}_{J=13}$  for  $J = 1$  to 3,  $\tilde{n}_{J=24}$  for  $J = 2$  to 4, and  $\tilde{n}_{J=35}$  for  $J = 3$  to 5.

the influence of collisions causing rotational excitation and deexcitation on the electron average energy after 6 ns is discussed for H<sub>2</sub> and D<sub>2</sub>.

I have given an analysis of the electron average energies in H<sub>2</sub> and D<sub>2</sub> with multi-term exponential fitting by means of a fitting algorithm I have developed.<sup>3)</sup> The paper compares the calculated exponents with experimental results by Warman and Sauer<sup>4)</sup> and by Okigaki *et al.*<sup>5)</sup>

In a series of papers<sup>1-3)</sup> electron attachment is not included, and this is considered to be justified as the cross section for electron attachment in H<sub>2</sub> is much smaller than those for the other processes involved; however, it is reported that if H<sub>2</sub> molecules are vibrationally or rotationally excited, a peak at 4 eV is strongly enhanced.<sup>6)</sup> Since the present method can include electron attachment,<sup>7)</sup> we will be able to study the negative-ion formation in H<sub>2</sub> and D<sub>2</sub> at high temperature if adequate information on the cross sections for electron attachment is given.

### References

- 1) K. Kowari: Phys. Rev. A **53**, 853 (1996).
- 2) K. Kowari: in preparation.
- 3) K. Kowari: Radiat. Phys. Chem. (2002), in press.
- 4) J. M. Warman and M. C. Sauer, Jr.: J. Chem. Phys. **62**, 1971 (1975).
- 5) S. Okigaki, E. Suzuki, K. Hayashi, K. Kurashige, and Y. Hatano: J. Chem. Phys. **96**, 8324 (1992).
- 6) H. Tawara, Y. Itikawa, H. Nishimura, and M. Yoshino: J. Phys. Chem. Ref. Data **19**, 617 (1990).
- 7) K. Kowari, Ki Leung, and B. D. Shizgal: J. Chem. Phys. **108**, 1587 (1998).

\* University of Electro-Communications

## Elastic-wave source characterization for 95 MeV/u Ar-ion irradiation on solids

T. Kambara, Y. Kanai, T. M. Kojima, Y. Nakai, Y. Yamazaki, A. Yoneda, and K. Kageyama\*

We have observed elastic waves generated by irradiation of 95 MeV/u Ar ions on various solids, and measured the propagation time of the elastic wave in the matter to determine the depth of the wave source.

The experiments were performed at the RIKEN Ring Cyclotron with a 95 MeV/u Ar beam which consisted of a single-bunch pulse with a width of 3 ns and an interval of about 60 ms. The beam preparation, monitoring and irradiation setups were similar to those for the previous experiments.<sup>1,2)</sup>

The irradiated samples were polycrystalline metals (Al and Cu), single-crystalline alkali-halides (LiF and KCl), polycrystalline  $\text{Al}_2\text{O}_3$ , fused silica ( $\text{SiO}_2$ ), and an invar alloy. The samples were square-shaped plates with similar dimensions of about  $40\text{ mm} \times 40\text{ mm} \times 10\text{ mm}$  except for the Cu plate which was  $35\text{ mm} \times 35\text{ mm} \times 10\text{ mm}$ . The beam spot size was about  $4\text{ mm} \times 4\text{ mm}$  and the beam was incident perpendicularly on the square-shaped surface (face plane). Two KCl samples were used with different surface orientations of  $\{100\}$  and  $\{111\}$ . The velocities of the longitudinal and shear waves in the samples were measured by a sing-around method.

The elastic wave was detected by piezoelectric sensors (Fuji Ceramics, M304A).<sup>3)</sup> The sensor is equipped with a head amplifier and is sensitive to oscillation perpendicular to the surface up to about 2 MHz with the highest sensitivity at about 300 kHz. Two sensors were attached to a sample: one, referred to hereafter as the side sensor, was on a side plane, and the other, referred to as the back sensor, was at the center of the back plane opposite the face plane where the beam hit.

Figure 1 shows the waveforms measured by the back sensor for various samples. The waveform is averaged over 40–50 shots to reduce the noise, and normalized to the same number (about  $9 \times 10^3$ ) of ions. The axis of the sensor was about 1.5 mm from the beam center. This distance was smaller than the diameter of the sensor and the beam spot size, therefore the shortest distance from the beam spot to the sensor was equal to the sample thickness. Since the sensor can detect the oscillations perpendicular to the surface and was positioned nearly opposite the beam spot, it detected only the longitudinal wave (compression wave).

Two of the materials, invar and fused silica, yielded much lower amplitudes than the others, as shown in Fig. 1(b). These two materials have very low coefficients of thermal expansion. The results indicate that

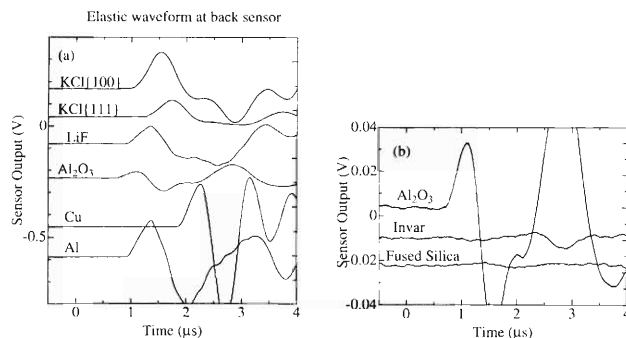


Fig. 1. Elastic waveforms captured by a sensor attached to the surface opposite the beam spot. The waveforms are normalized to the beam-bunch intensity; (b) shows those for fused silica, invar and  $\text{Al}_2\text{O}_3$  where the ordinate is expanded by a factor of 10.

the process that generates the longitudinal wave (compression wave) is influenced by the thermal expansion of the material. The results for invar and fused silica are not included in the following discussions.

We have measured the delay between the irradiation and the onset of the elastic wave. From the delay time, we have obtained the depth of the wave source from the beam spot. The depths are in accordance with, but slightly smaller than, the ranges calculated by a TRIM code<sup>4)</sup> with a relative difference of 3–10%. There is no difference between the two crystal orientations of KCl.

Both the back and side sensors detected the longitudinal wave with a positive output voltage at the onset which corresponds to an outward displacement of the surfaces. This result means that the stress at the source is compressive and propagates in all directions.

### References

- 1) T. Kambara, Y. Kanai, T. M. Kojima, Y. Nakai, A. Yoneda, K. Kageyama, and Y. Yamazaki: Nucl. Instrum. Methods Phys. Res. B **164/165**, 415 (2000).
- 2) T. Kambara, Y. Kanai, T. M. Kojima, Y. Nakai, A. Yoneda, Y. Yamazaki, and K. Kageyama: AIP Conf. Proc. **576**, 1040 (2001).
- 3) M. Shiwa, H. Inaba, and T. Kishi: J. JSNDI **39**, 374 (1990).
- 4) J. F. Ziegler, J. P. Biersack, and U. Littmark: *The Stopping and Range of Ions in Solids* (Pergamon Press, New York, 1985).

\* Department of Mechanical Engineering, Saitama University

## Anomalous shift of the Curie temperature in Fe-Ni Invar alloys irradiated with high-energy ions

F. Ono,\*<sup>1</sup> A. Iwase,\*<sup>2</sup> Y. Hamatani,\*<sup>1</sup> Y. Motoshimizu,\*<sup>1</sup> N. Ishikawa,\*<sup>2</sup>  
Y. Chimi,\*<sup>2</sup> Y. Mukumoto,\*<sup>1</sup> and T. Kambara

Fe-Ni Invar alloys are known to exhibit various anomalies in both mechanical and magnetic properties.<sup>1)</sup> Anomalies in the thermal expansion coefficient were interpreted as being due to the large positive value of the magnetovolume effect which cancels out the normal part of the thermal expansion. Anomalous decrease in the spontaneous magnetization from the Slater-Pauling curve was considered to be due to the instability of the ferromagnetic condition of the 3d-electrons.<sup>2)</sup> It is also known that Fe-Ni Invar alloys show anomalously large pressure dependence at the Curie temperature,  $T_C$ , and under the spontaneous magnetization.<sup>3-5)</sup> The Curie temperatures of Fe-Ni Invar alloys around the composition of 33.6 at%Ni were reported to decrease with pressure at a large rate of  $-36$  K/GPa. Therefore, high-energy ion irradiation is expected to introduce a large change in  $T_C$ .

The effect of high-energy ion beam irradiation on  $T_C$  of Fe-31.9 at%Ni Invar alloy was investigated using an ac-field method. To observe the Curie temperature for such a thermodynamically unstable specimen as in the case of the present study, a rapid method of observation is needed. In the present experiment we used a specially designed apparatus for instantaneous measurements of ac-susceptibility-temperature curves. By using the present method, it is possible to complete the measurement of the temperature dependence of ac-susceptibility from room temperature to 500 K within 90 sec. The irradiations were carried out at room temperature with 3.54 GeV Xe ions at fluencies of the order of  $10^{12}/\text{cm}^2$ , using the RIKEN Ring Cyclotron. The observed ac-susceptibility-temperature curves after the irradiations are shown in Fig. 1. The ac-susceptibility decreases suddenly at the Curie temperature. In this figure it is evident that  $T_C$  increases with the irradiation dose. The Curie temperatures were determined to be 410, 414 and 417 K for 1, 3 and  $5 \times 10^{12}$  ions/ $\text{cm}^2$  irradiations, respectively.

Considering the large negative pressure dependence of  $T_C$  in Fe-Ni Invar alloys, the present experimental

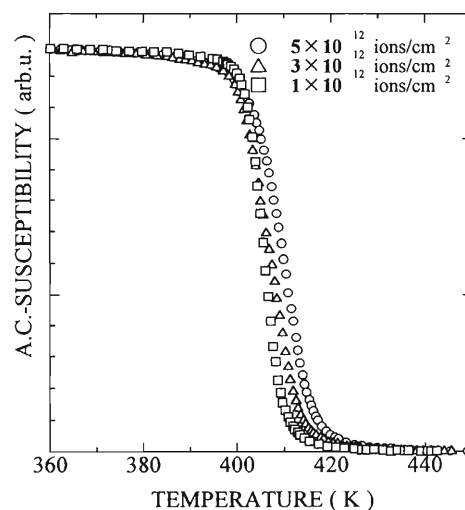


Fig. 1. Temperature dependence of ac-susceptibilities for Fe-31.9 at%Ni Invar alloys after irradiation with 3.54 GeV Xe ions to a dose up to  $5 \times 10^{12}$  ions/ $\text{cm}^2$ .

result that  $T_C$  increases with the irradiation dose implies that a negative pressure has been introduced to the specimen by the high-energy ion irradiations. Such a negative pressure may be expected to be generated along the paths of the ion beams through high-density electron excitations.

### References

- 1) For example, *The Invar Effect: A Centennial Symposium*, edited by J. Wittenauer (The Minerals, Metals & Materials Society, USA, 1997).
- 2) P. Entel, E. Hoffmann, P. Mohn, K. Schwarz, and V. L. Moruzzi: *Phys. Rev. B* **47**, 8706 (1993).
- 3) J. M. Leger, C. Loriers-Susse, and B. Vodar: *Phys. Rev. B* **6**, 4250 (1972).
- 4) F. Ono, M. Asano, R. Tanaka, S. Nakamichi, and S. Endo: *Physica B* **177**, 127 (1992).
- 5) S. Endo, M. Nishino, and F. Ono: *Sci. Technol. High Pressure* **2**, 850 (2000).

\*<sup>1</sup> Department of Physics, Okayama University

\*<sup>2</sup> Japan Atomic Energy Research Institute

## Final lattice sites and atomic motion of $^{57}\text{Fe}$ atoms in Si immediately after GeV-ion implantation

Y. Yoshida,\* S. Ogawa,\* Y. Kobayashi, and A. Yoshida

The RIKEN RI-beam factory is expected to provide a wide variety of radioisotopes, many of which are suitable for use as nuclear probes in Mössbauer spectroscopy (MS), perturbed angular distribution (PAD), and other nuclear methods. High-energy GeV-ion implantation, however, would produce serious lattice defects along the ion tracks and near the final lattice sites of the probes, making it very difficult to study the local surroundings and the atomic motion of the probes deeply implanted in a bulk material. In order to determine the damage effects in the Mössbauer spectra obtained by 2-GeV  $^{57}\text{Mn}/^{57}\text{Fe}$  implantation in Si,<sup>1)</sup> we compare the in-beam spectra with those obtained from a laboratory Mössbauer experiment on 3 nm-thick  $^{57}\text{Fe}$ -deposited CZ-Si under thermal equilibrium.

The absorption spectra were measured under a vacuum of  $10^{-6}$  Pa between 300 and 1273 K. The Fe concentration was estimated to be  $2 \times 10^{17}$  Fe/cm<sup>3</sup> from the thickness of the Fe layer, *i.e.*, at least two orders of magnitude higher than that of Fe solubility reported at 1273 K,<sup>2)</sup> and seven orders of magnitude higher than that of the in-beam experiment.<sup>1)</sup> When the specimen temperature was increased,  $\alpha$ -Fe first appeared at 300 K and subsequently different Fe-Si compounds were formed at higher temperatures. After measurement at 1273-K for one week, a singlet became the dominant component, corresponding to Fe on substitutional sites in Si. The spectra obtained at thermal equilibrium are shown in Fig. 1, which are compared with those obtained from the former in-beam experiment<sup>1)</sup> on  $^{57}\text{Mn}/^{57}\text{Fe}$  in FZ-Si (Fig. 2). In the in-beam spectra at 418 and 625 K, Fig. 2 clearly shows both interstitial and substitutional Fe components on the left- and right-hand side, respectively. In the present experiment, on the other hand, only the substitutional component is observed (Fig. 1), indicating that the Fe atoms exist mainly on the substitutional sites. Moreover, the small interstitial component with a fraction of about 5% may also be seen in the spectra measured at 573 K and 773 K. The present result, however, completely contradicts the picture generally accepted so far for the lattice sites as well as for the solubility of Fe atoms in Si.<sup>2)</sup>

Furthermore, in the in-beam experiment, both the disappearance of the interstitial component and the simultaneous relaxation effect on the centre shifts were observed at approximately 650 K, which could be interpreted to be the jumps of interstitial Fe atoms into vacancies.<sup>1)</sup> Since the substitutional component shows no line-broadening due to diffusion and is therefore quite

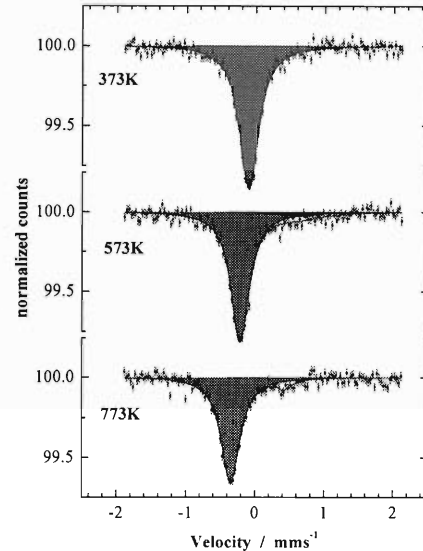


Fig. 1. Mössbauer spectra at thermal equilibrium obtained from the laboratory experiment, which shows only substitutional Fe components in Si.

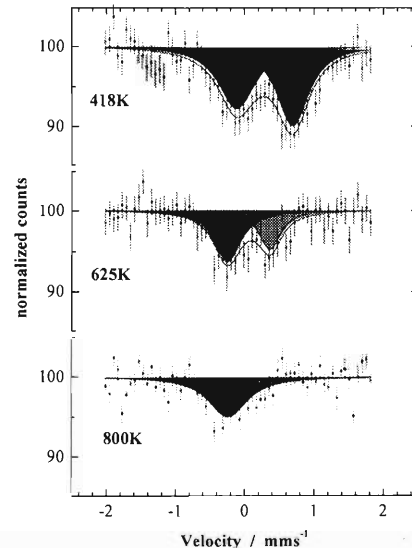


Fig. 2. In-beam Mössbauer spectra which consist of interstitial and substitutional Fe components.

stable even at 1273 K, the dynamical behavior observed in the in-beam experiment should correspond to a recovery process from a nonequilibrium to an equilibrium state around the nuclear probes.

### References

- 1) Y. Yoshida and K. Kobayashi et al.: Defect Diffus. Forum **194**, 611 (2001).
- 2) A. A. Istratov, H. Hieslmair, and E. R. Weber: Appl. Phys. A **69**, 13 (1999); A. A. Istratov, H. Hieslmair, and E. R. Weber: Appl. Phys. A **69**, 489 (2000).

\* Shizuoka Institute of Science and Technology

## On-line TDPAC studies using the $^{19}\text{O}$ beam

W. Sato, H. Ueno, H. Watanabe, H. Ogawa,<sup>\*1</sup> H. Miyoshi,<sup>\*1</sup> N. Imai,<sup>\*2</sup> A. Yoshimi,  
K. Yoneda, D. Kameda,<sup>\*1</sup> Y. Kobayashi, and K. Asahi

The time-differential perturbed angular correlation (TDPAC) method has been widely applied to research in condensed matter physics as well as nuclear physics, and it has provided valuable information on hyperfine interactions. Applicable probe nuclei are, however, limited to those having long-lived parent nuclides that allow chemical treatments for their introduction into samples of interest, and this limitation could be a cause of the restriction of investigated samples. It is hence of great importance to develop new probes that can be applied to the TDPAC method. If it is possible to produce short-lived nuclei and introduce them into samples of interest immediately after their production, those nuclei could be used as probes for the TDPAC method. In the present work, we have taken advantage of the advanced technology of particle acceleration and have developed a new short-lived probe,  $^{19}\text{F}$ , disintegrated from the parent nuclide  $^{19}\text{O}$ , for a TDPAC study of fullerene  $\text{C}_{60}$ .<sup>1)</sup>

The  $^{19}\text{O}$  beam was produced at the RIKEN Accelerator Research Facility. Ionized  $^{22}\text{Ne}$  was accelerated by two-stage acceleration with the AVF cyclotron and ring cyclotron up to 110 MeV/u at a beam intensity of 150 pA. The secondary beam  $^{19}\text{O}$  was produced using the RIKEN projectile-fragment separator.<sup>2)</sup> A well-focused pulsed  $^{19}\text{O}$  beam of 65 MeV/u was implanted in the sample, and on-line TDPAC measurements were performed on the (1357-197)-keV cascade  $\gamma$  rays emitted from  $^{19}\text{F}$  nuclei using sixteen  $\text{BaF}_2$  scintillators arranged in four independent detector planes to cover a solid angle of approximately  $2\pi$  sr.

Prior to studying polycrystalline  $\text{C}_{60}$ , the  $^{19}\text{O}$  beam was implanted in distilled water for observing the magnitude of the directional anisotropy denoted by the angular correlation coefficient  $A_{22}$ . The TDPAC spectrum of  $^{19}\text{F}$  in the distilled water is shown in Fig. 1. As generally expected for nonviscous liquid samples, the directional anisotropy of the cascade  $\gamma$  rays is negligibly perturbed. We accordingly fitted the spectrum assuming the diffusion approximation for the time-differential perturbation factor  $G_{22}(t)$ . From the fit, the angular correlation coefficient was experimentally estimated to be  $A_{22} = -0.17 \pm 0.01$ .

The TDPAC spectrum for the polycrystalline fullerene  $\text{C}_{60}$  at 73 K is plotted in Fig. 2. Since the directional anisotropy shows a slowly relaxing damped oscillatory structure, we interpreted the spectrum as having two different components: one has a static electric quadrupole interaction with the extranuclear field

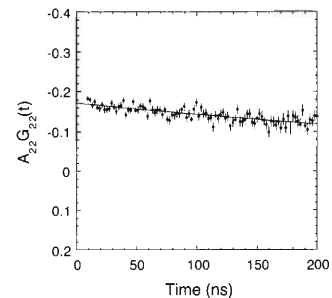


Fig. 1. TDPAC spectrum of  $^{19}\text{F}$  in distilled water at room temperature.

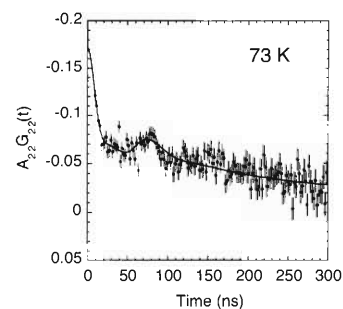


Fig. 2. TDPAC spectrum of  $^{19}\text{F}$  in polycrystalline fullerene  $\text{C}_{60}$  at 73 K.

and the other is dynamically perturbed by the field. The electric-field-gradient (EFG) value for the first component was optimized by the least-squares fit as  $|V_{zz}| = (4.4 \pm 0.8) \times 10^{18} \text{ Vcm}^{-2}$ . Taking into consideration reported values of the EFGs at the  $^{19}\text{F}$  nucleus forming a C-F bond,<sup>3)</sup> the estimated EFG value for the first component would also reflect the same type of interaction between the network carbons and fluorine atoms. In the case of the second component, it is considered that the dynamic perturbation is attributed not to the thermally activated motion but to the recoil effect triggered by the  $\beta^-$  particle emission from the  $^{19}\text{O}$  nuclei, because little, if any, temperature dependence can be observed in the TDPAC spectra. For more detailed understanding of the interaction between the  $^{19}\text{F}$  probe and  $\text{C}_{60}$  molecules, the present data should be compared with results of theoretical calculations.

### References

- 1) H. W. Kroto et al.: *Nature* **318**, 162 (1985).
- 2) T. Kubo et al.: *Nucl. Instrum. Methods Phys. Res. B* **70**, 309 (1992).
- 3) M. G. Bossenger et al.: *Hyperfine Interact.* **120/121**, 557 (1999).

<sup>\*1</sup> Department of Physics, Tokyo Institute of Technology

<sup>\*2</sup> Department of Physics, University of Tokyo

# Stopping power measurement of $^{84}\text{Kr}$ in a laser-produced plasma

A. Sakuni, T. Katayama, T. Nishimoto.\* and Y. Oguri\*

In the energy region of hundreds of keV/u, the energy dependence of the stopping power of oxygen ions in a plasma is quite different from that in cold matter.<sup>1-3)</sup> Although the experimental investigation has been conducted for a few species, the results are not sufficient to explain the physics involved in beam-plasma interaction systematically. With this background, we have experimentally investigated the dependence of the stopping power in the plasma on the atomic number of various projectiles with fixed incident energy, ranging from Kr to Bi. These projectiles are available at the CNS (Center for Nuclear Study, Univ. of Tokyo) beam line in the RILAC facility. Figure 1 shows a schematic view of the experimental setup. The energy loss of ions, which interact with the target plasma, is measured by the time-of-flight (TOF) method. In order to filter the plasma light emission, a gold foil is set in front of MCP. The laser, ion beam, and the pulser are synchronized by the digital delay generators.

A dense plasma is produced by irradiating a small lithium hydride (LiH) pellet with a Q-switched Nd-glass laser ( $\lambda = 1.054 \mu\text{m}$ , 4.5 J and 30 ns (FWHM)). The pellet diameter is approximately  $60 \mu\text{m}$ . The irradiance of the laser on the pellet is  $2 \text{ TW}/\text{cm}^2$ . The target is a plasma with a density of  $10^{18} \text{ cm}^{-3}$  and a temperature of  $\sim 15 \text{ eV}$ .

The beam consists of  $1 \text{ MeV}/u$   $^{84}\text{Kr}^{17+}$  ions, delivered with the period of 32 MHz. Figure 2 shows the signals from the bunch monitor behind the RILAC #3 cavity (a) and the stop detector (b). The beam duration of the (a) signal is about 2 ns in FWHM, while that of the (b) signal is about 5 ns in FWHM. The drift distance from the #3 cavity and the stop detector is about 50 m, and the momentum spread is 0.15%, so that the spread of beam shape is observed. For good accuracy of the experiment, we most decrease the beam spread.

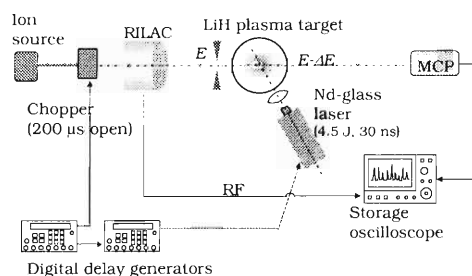


Fig. 1. Schematic view of the experimental setup.

\* Research Laboratory for Nuclear Reactor, Tokyo Institute of Technology

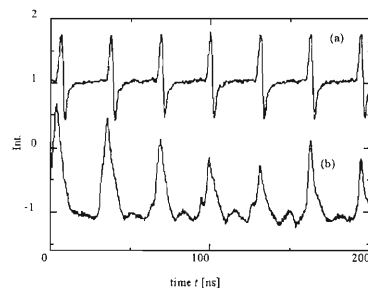


Fig. 2. Signals from the bunch monitor behind the RILAC #3 cavity (a) and the stop detector (b).

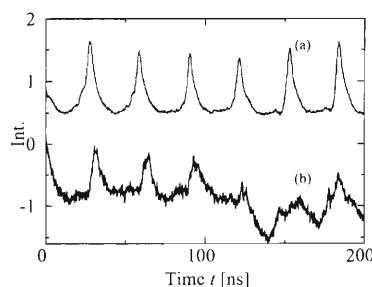


Fig. 3. Signals without (a) and with the plasma (b).

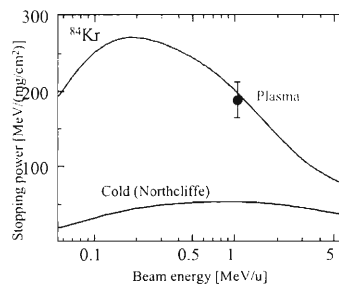


Fig. 4. Stopping power in the LiH plasma with theoretical estimation.

Figure 3 shows the signals without (a) and with the plasma (b). The energy loss was estimated by the time duration between each signal. The maximal delay was 4.1 ns at  $t = 60 \text{ ns}$  after the laser was fired and the relevant energy loss was 3 MeV. The estimated stopping power was  $190 \text{ MeV}/(\text{mg}/\text{cm}^2)$ , as shown in Fig. 4. Figure 4 also shows the stopping power calculated using the enhanced Bethe equation and the rate calculation. The experimental result agrees with the calculation.

## References

- 1) T. Katayama: J. Plasma Fusion Res. **70**, 323 (1994).
- 2) A. Sakuni et al.: Nucl. Instrum. Methods Phys. Res. A **464**, 231 (2001).
- 3) P. Nicolosi, E. Jannitti, and G. Tondello: Appl. Phys. B **26**, 117 (1981).

## TOF spectral profile of fullerene-like fragment ions in $C^{6+}-C_{60}$ collisions

Y. Nakai, T. Kambara, A. Itoh,<sup>\*1</sup> H. Tsuchida,<sup>\*2</sup> and Y. Yamazaki

A number of studies of  $C_{60}$  fragmentation have been performed with various excitation probes.<sup>1-8)</sup> In particular, production of fullerene-like fragment ions (FLFI's) has been intensively studied. The time-of-flight (TOF) peak profile for each product ion contains information on fragmentation, that is, the kinetic energy release and lifetime. We have developed a high-resolution TOF mass spectrometer to obtain information on the fragmentation mechanism. Using this spectrometer, we measured TOF peak profiles in the mass range of  $C_{50}^+$  to  $C_{58}^+$  for fragmentation by 2.5 MeV/u  $He^{2+}$  ion impact and compared them with the simulation of sequential  $C_2$  emission based on the Rice-Ramsperger-Klein-Marcus (RRKM) formalism. It was shown that the experimental results support high activation energies (9.5 eV for  $C_{60}^+$ ) and a very loose transition state.<sup>9)</sup> Here, we report TOF spectral profiles of heavy fragment ions by 2.5 MeV/u  $C^{6+}$  impact. The beam of 2.5 MeV/u  $C^{6+}$  was accelerated by the Riken-Linear-Accelerator (RILAC). The details of our experiment setup are described in Ref. 10.

Figure 1(a) shows an experimental TOF spectrum in the range of  $C_{50}^+$  to  $C_{58}^+$  by 2.5 MeV/u  $C^{6+}$  impact. Generally, the peak intensities of  $C_{60-2n}^+$  ( $n = 1$  to 5) decrease exponentially with  $n$ . These peaks have the following features: The tail of each peak of singly charged FLFI on the longer TOF side is found to curve much more gently than that on the shorter TOF side.

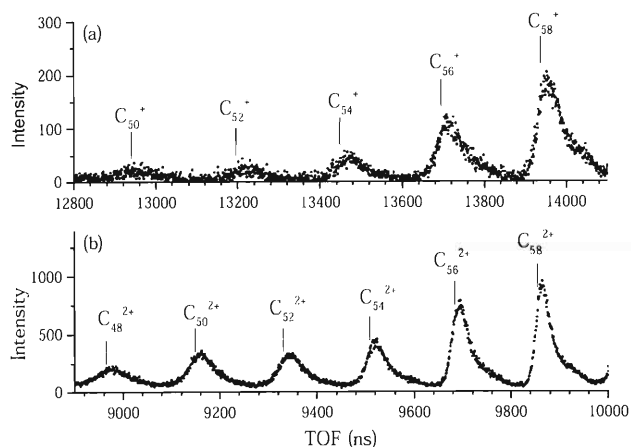


Fig. 1. (a) Experimental TOF spectrum in the range of  $C_{50}^+$  to  $C_{58}^+$  by 2.5 MeV/u  $C^{6+}$  impact. (b) Experimental TOF spectrum in the range of  $C_{48}^{2+}$  to  $C_{58}^{2+}$  by  $C^{6+}$  impact.

This asymmetry becomes less prominent with lighter fragment ions. The short vertical lines in Fig. 1(a) represent the TOF peak positions of the  $^{12}C_{60-2n}^+$  fragment ions when they are produced promptly with zero recoil energy. It is seen that all the TOF peaks are not only tailed to but are also shifted to the longer TOF side than the corresponding vertical lines. These features strongly indicate that the fragmentations take place after  $C_{60}$  is ionized by a projectile ion. The features of the TOF peak shape by  $C^{6+}$  impact are very similar to those by 2.5 MeV/u  $He^{2+}$  impact.<sup>9)</sup> This similarity indicates that the production mechanism of singly charged FLFI by 2.5 MeV/u  $C^{6+}$  impact is the same as that by 2.5 MeV/u  $He^{2+}$  impact.

Figure 1(b) shows an experimental TOF spectrum in the range of  $C_{48}^{2+}$  to  $C_{58}^{2+}$  by  $C^{6+}$  impact. The short vertical lines in Fig. 1(b) represent the TOF peak positions of the  $^{12}C_{60-2n}^{2+}$  fragment ions when they are produced promptly with zero recoil energy. The TOF spectrum of doubly charged FLFI is similar to that of singly charged FLFI. This TOF spectral similarity between singly charged FLFI and doubly charged FLFI indicates high activation energies of  $C_2$  emission from doubly charged fullerene ions as singly charged fullerene ions because the shape of the TOF peak is sensitive to the activation energy. A very recent study using a storage ring revealed that the activation energies of  $C_2$  emission from doubly charged fullerene ions are close to those from singly charged fullerene ions in the mass range of  $C_{48}$  to  $C_{70}$ .<sup>11)</sup> The similarity of the TOF spectra also implies that production mechanisms of doubly charged FLFI are the same as those of singly charged FLFI. Namely, it implies that the sequential  $C_2$  emission from excited  $C_{60}^{2+}$  ions is a dominant production mechanism of doubly charged FLFI.

### References

- 1) Y. Nakai et al.: J. Phys. B **30**, 3049 (1997).
- 2) M. Foltin et al.: J. Chem. Phys. **107**, 6246 (1997).
- 3) P. Weis et al.: J. Chem. Phys. **104**, 6246 (1996).
- 4) R. Woergoetter et al.: J. Chem. Phys. **101**, 8674 (1994).
- 5) M. Foltin et al.: J. Chem. Phys. **98**, 9624 (1993).
- 6) R. K. Yoo et al.: J. Chem. Phys. **96**, 911 (1992).
- 7) J. Laskin et al.: Chem. Phys. Lett. **242**, 249 (1995).
- 8) J. Laskin et al.: Int. J. Mass Spectrom. **177**, L9 (1998).
- 9) Y. Nakai et al.: RIKEN Accel. Prog. Rep. **34**, 102 (2001).
- 10) Y. Nakai et al.: RIKEN Accel. Prog. Rep. **33**, 79 (2000).
- 11) S. Tomita et al.: Phys. Rev. Lett. **87**, 073401 (2001).

<sup>\*1</sup> Kyoto University

<sup>\*2</sup> Nara Women's University

## Lattice location of hydrogen in Nb-Mo alloys

E. Yagi, S. Koike,<sup>\*1</sup> T. Matsumoto,<sup>\*2</sup> T. Urai, N. Tajima, and K. Ogiwara

Regarding the effect of alloying on the terminal solubility of hydrogen (TSH) in group V<sub>a</sub> metals in the periodic table (V, Nb and Ta), it has been reported that for undersized metal solutes, *e.g.*, Nb in Ta and Mo in Nb, the TSH increases rapidly with metal solute concentration up to a certain solute concentration, and for oversized solutes, *e.g.*, Ta in Nb and Nb in V, the TSH also increases with solute concentration but less rapidly.<sup>1,2)</sup> In order to understand the mechanism of this effect, the lattice location of hydrogen in such alloy systems is to be investigated. Previously we performed channelling studies to locate hydrogen in Nb-based Nb-Mo alloys with various concentrations of Mo up to 20 at.%. The result showed that, at low Mo concentrations, H atoms are trapped by Mo atoms at room temperature and are located at sites which are displaced from tetrahedral (*T*) sites by about 0.6 Å towards the nearest-neighbour lattice points (trapped sites  $T_{tr}$ ).<sup>3)</sup> At a high Mo concentration, 20 at.%Mo, H atoms are not observed at such  $T_{tr}$  sites, but a major portion of them are located at *T* sites, and 20–30% of them are at octahedral (*O*) sites at low hydrogen concentrations.<sup>4)</sup> These results indicate that the hydrogen site occupancy changes with the Mo concentration,  $C_{Mo}$ . The Nb-Mo alloy system forms a solid solution over the entire Mo concentration range. The TSH in Nb at room temperature is about 4 percent, whereas the TSH in Mo is very low. Therefore, systematic studies on the  $C_{Mo}$  dependence of hydrogen site occupancy are desired.

In the present study, the lattice location of hydrogen in an alloy with a higher Mo concentration of 26 at.% is investigated at room temperature by a channelling method utilizing a nuclear reaction  $^1\text{H}(^{11}\text{B}, \alpha)\alpha$  with a  $^{11}\text{B}$  beam of about 2 MeV, as in previous studies.<sup>5,6)</sup> For comparison, the lattice location of hydrogen in pure Nb is also investigated. Hydrogen was doped from the gas phase to a hydrogen-to-metal-atom ratio  $C_H = [\text{H}]/[\text{M}]$  of 0.023 for the Nb specimen, and three different values of  $C_H = 0.016, 0.026$  and  $0.059$  for the Nb-Mo alloy specimens. The channelling angular profiles obtained for the alloys are very similar to those of the Nb specimen. Based on the comparison of the observed angular profiles with the calculated ones, it is concluded that, irrespective of the hydrogen concentration, more than 90% of H atoms are located at *T* sites in the Nb(74 at.%)-Mo(26 at.%) alloys. Even if H atoms are located at *O* sites, the proportion is less than 10%. This is different from the result for H in Nb(80 at.%)-Mo(20 at.%) alloys, in which, at low hy-

drogen concentrations, a 20–30% *O*-site occupancy by H atoms was observed in addition to *T*-site occupancy.

The site change of hydrogen in the Nb-Mo alloys containing up to 20 at.%Mo has been explained as follows.<sup>4)</sup> At low  $C_{Mo}$ , the strain field induced by the undersized Mo atoms is localized and the internal strain is relaxed by hydrogen occupation of interstitial sites neighbouring Mo atoms; H atoms occupy well-defined  $T_{tr}$  sites near Mo atoms due to attractive elastic interaction between them. At high  $C_{Mo}$ , there will be a statistical distribution of local atomic configurations and concomitant distribution of interstitial site energy. In addition, the interference of the strain field induced by nearby Mo atoms influences the distribution of interstitial site energy. Correspondingly, trapping behaviour will become less well defined, and therefore, the number of H atoms located at  $T_{tr}$  sites per Mo atom becomes smaller. At much higher  $C_{Mo}$ , *i.e.*, 20 at.%Mo, the average separation between Mo atoms becomes even smaller, and the effect of strain fields of individual Mo atoms tends to be averaged out. It would be more appropriate to regard this alloy as a pure metal having a homogeneously reduced lattice parameter. As a result, the energy difference between *T* and *O* sites becomes smaller, and *O* sites become more easily available for occupation.

The present result for the Nb(74 at.%)-Mo(26 at.%) alloys, however, cannot be explained by such a size effect. In the Nb(74 at.%)-Mo(26 at.%) alloys, the lattice parameter is considered to be smaller than in the Nb(80 at.%)-Mo(20 at.%) alloys. Therefore, on the basis of the size effect, a larger fraction of the *O*-site occupancy would be expected in the Nb(74 at.%)-Mo(26 at.%) alloys. The experimental result is incompatible with this expectation. Therefore, other effects should be taken into account to explain the site occupancy of hydrogen in 26 at.%Mo alloys. The experiments on more concentrated alloys are now in progress.

### References

- 1) T. Matsumoto, Y. Sasaki, and M. Hihara: *J. Phys. Chem. Solids*, **36**, 215 (1975).
- 2) D. G. Westlake and J. F. Miller: *J. Less-Common Met.* **65**, 139 (1979).
- 3) E. Yagi, S. Nakamura, F. Kano, T. Kobayashi, K. Watanabe, Y. Fukai, and T. Matsumoto: *Phys. Rev. B* **39**, 57 (1989).
- 4) E. Yagi and S. Koike: *J. Phys. Soc. Jpn.* **67**, 340 (1998).
- 5) E. Yagi, T. Kobayashi, S. Nakamura, Y. Fukai, and K. Watanabe: *Phys. Rev. B* **31**, 1640 (1985).
- 6) E. Yagi, T. Kobayashi, S. Nakamura, F. Kano, K. Watanabe, Y. Fukai, and S. Koike: *Phys. Rev. B* **33**, 5121 (1986).

<sup>\*1</sup> Department of Physics, Tokyo University of Science

<sup>\*2</sup> National Institute for Materials Science

# High-resolution soft X-ray measurements in 2.3 keV/u $N^{7+}$ ions transmitted through an Au microcapillary target

Y. Iwai,<sup>\*1</sup> Y. Kanai, H. Oyama, K. Ando, H. Masuda,<sup>\*2</sup> K. Nishio,<sup>\*2</sup>  
M. Nakao,<sup>\*3</sup> T. Tamamura,<sup>\*3</sup> K. Komaki,<sup>\*1</sup> and Y. Yamazaki

X-rays emitted from 2.3 keV/u  $^{15}N^{7+}$  ions transmitted through a thin Au microcapillary foil were measured with a high-resolution soft X-ray spectrometer, to study the formation and relaxation dynamics of a hollow atom (ion)<sup>1)</sup> produced by a resonant charge transfer in ion-surface collisions.

The present study was performed using a 14.5 GHz Caprice type electron cyclotron resonance ion source in RIKEN.<sup>2)</sup> Recently, a new method of manufacturing the microcapillary foil has been developed involving a nanolithographic technique, which allows the preparation of a highly ordered microcapillary foil.<sup>3)</sup> In the present experiment, an Au microcapillary foil was used, which was  $\sim 1 \text{ mm}^2$  in area with a thickness of  $\sim 1 \mu\text{m}$ , many straight holes of  $\sim 100 \text{ nm}$  in diameter, and a honeycomb structure with a 200 nm interval, *i.e.*, the geometrical opening ratio was  $\sim 25\%$ . It was expected that efficiency would be good compared with that of a former target.<sup>4)</sup> A detailed description of the high-resolution soft X-ray spectrometer is given in Ref. 4.

Figure 1 shows an X-ray spectrum, which was taken immediately downstream of the target, for 2.3 keV/u  $^{15}N^{7+}$  ions transmitted through the microcapillary. The eight major lines are attributed to hydrogen-like and helium-like transitions, which are summarized in Table 1.<sup>5)</sup> It is expected that the relative intensity of each transition reflects the cascade transition of the hollow atom (ion). The transitions of  $np-1s$  ( $5 \leq n \leq 8$ ) were observed with the highly ordered microcapillary target for the first time and the transition from nine or more  $n$  was not observed as a peak. According to the classical over barrier model (COBm), the principal quantum number  $n_c$  in which electrons are resonantly captured from the target is given by

$$n_c(q) \sim \frac{q}{\sqrt{2W(1 + \sqrt{q/8})}},$$

where  $q$  is the charge state of the ion and  $W$  is the work function of the target (physical quantities are given in atomic units).<sup>6)</sup> The principal quantum numbers of the initially populated states can be estimated as  $n \sim q + 1 = 8$  in the present case. It is possible that the principal quantum number of the initially populated states is  $n \sim 8$ . The experimental result was consistent

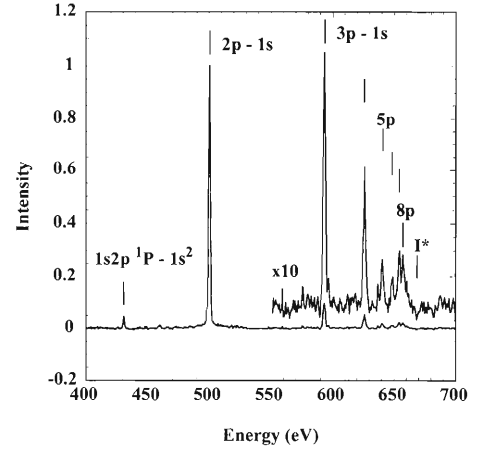


Fig. 1. Spectrum of  $K$  X-rays, measured with the spectrometer immediately downstream of the target, for 2.3 keV/u  $^{15}N^{7+}$  ions transmitted through a highly ordered Au microcapillary. Bars with transition terms show transition energies and  $I^*$  indicates  $N$  VII ionization potential energy.<sup>5)</sup>

Table 1. Observed transition energies and electronic configurations.

Experiment	Ref. data <sup>5)</sup>	Configurations	Terms
$430.4 \pm 0.4 \text{ eV}$	430.7 eV	$1s2p \rightarrow 1s^2$	$^1P_1 \rightarrow ^1S_0$
$500.3 \pm 0.5 \text{ eV}$	500.3 eV	$2p \rightarrow 1s$	$^2P_{3/2} \rightarrow ^2S_{1/2}$
	500.2 eV	$2p \rightarrow 1s$	$^2P_{1/2} \rightarrow ^2S_{1/2}$
$593.1 \pm 0.7 \text{ eV}$	592.9 eV	$3p \rightarrow 1s$	$^2P_{3/2} \rightarrow ^2S_{1/2}$
$626.1 \pm 0.7 \text{ eV}$	625.4 eV	$4p \rightarrow 1s$	$^2P_{3/2} \rightarrow ^2S_{1/2}$
$640.3 \pm 0.7 \text{ eV}$	640.4 eV	$5p \rightarrow 1s$	$^2P_{3/2} \rightarrow ^2S_{1/2}$
$648.6 \pm 0.8 \text{ eV}$	648.5 eV	$6p \rightarrow 1s$	$^2P_{3/2} \rightarrow ^2S_{1/2}$
$654.2 \pm 0.8 \text{ eV}$	653.4 eV	$7p \rightarrow 1s$	$^2P_{3/2} \rightarrow ^2S_{1/2}$
$657.1 \pm 0.8 \text{ eV}$	656.6 eV	$8p \rightarrow 1s$	$^2P_{3/2} \rightarrow ^2S_{1/2}$
Cf.	658.8 eV	$9p \rightarrow 1s$	$^2P_{3/2} \rightarrow ^2S_{1/2}$
	667.1 eV*		

\*  $N$  VII ionization potential energy

with the prediction of the COBm.

## References

- 1) S. Ninomiya et al.: Phys. Rev. Lett. **78**, 4557 (1997).
- 2) Y. Kanai et al.: RIKEN Rev., No. 31, 62 (2000).
- 3) H. Masuda, H. Yamada, M. Satoh, H. Asoh, M. Nakao, and T. Tamamura: Appl. Phys. Lett. **71**, 2770 (1997).
- 4) Y. Iwai et al.: RIKEN Rev., No. 31, 34 (2000).
- 5) R. L. Kelly: J. Phys. Chem. Ref. Data **16**, Suppl. 1 (1987).
- 6) J. Burgdoerfer, P. Lerner, and F. W. Meyer: Phys. Rev. A **44**, 5674 (1991).

<sup>\*1</sup> Institute of Physics, Graduate School of Arts and Sciences, University of Tokyo

<sup>\*2</sup> Department of Applied Chemistry, School of Engineering, Tokyo Metropolitan University

<sup>\*3</sup> NTT Corporation

## Visible light emission from slow highly charged ions transmitted through a Ni microcapillary

Y. Morishita, R. Hutton,\*<sup>1</sup> Y. Kanai, K. Ando, H. Masuda,\*<sup>2</sup> H. A. Torii,\*<sup>3</sup> K. Komaki,\*<sup>3</sup> and Y. Yamazaki

In the study of the neutralization process of a slow highly charged ion (HCI) above a metal surface, one of the most difficult and unavoidable experimental problems is that the HCI collides violently with the surface within  $\lesssim 10^{-13}$  sec due to its image charges induced on the surface. Hence, observers mainly observe the final moment, or the integrated memory of the neutralization process. A technique of using microcapillary targets made it possible to extract such ions in vacuum, which are in different stages of the neutralization above the surface.<sup>1)</sup> With the aim of observing the first electron transfer, we have constructed a beam line with a spectrometer in the visible light region, which is schematically shown in Fig. 1. HCIs, supplied by a 14.5 GHz Caprice ECRIS in RIKEN, are first impinged into a microcapillary target made of nickel which is 100 nm in diameter and 700 nm in thickness. Photons emitted from the HCIs downstream of the capillary are then collected with aluminum-coated two flat and one spherical concave mirrors, and imaged onto a slit of the spectrometer with 500 mm focal length, in which the photons are dispersed and detected with a back-illuminated CCD cooled to  $-120^\circ\text{C}$ .

Figure 2 shows a spectrum observed with 2.0 keV/u  $\text{Ar}^{7+}$  incident ions, the wavelength region of which corresponds to  $\Delta n = -1$  transitions of the exiting ions, which have captured one electron into a state with its

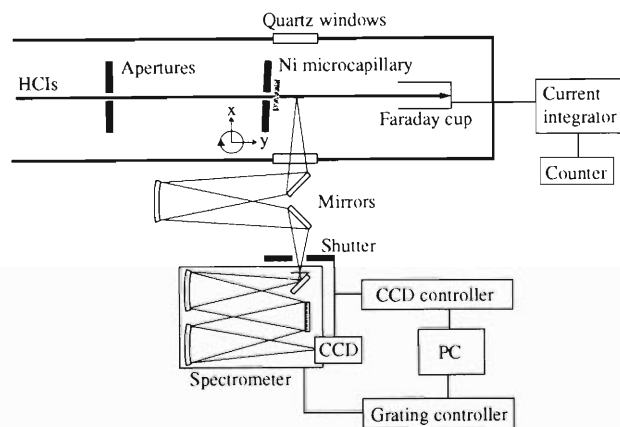


Fig. 1. Schematic drawing of the experimental setup installed in the hall for slow highly charged ions at RIKEN.

\*<sup>1</sup> Department of Physics, Lund University, Sweden

\*<sup>2</sup> Department of Industrial Chemistry, Tokyo Metropolitan University

\*<sup>3</sup> Institute of Physics, Graduate School of Arts and Sciences, University of Tokyo

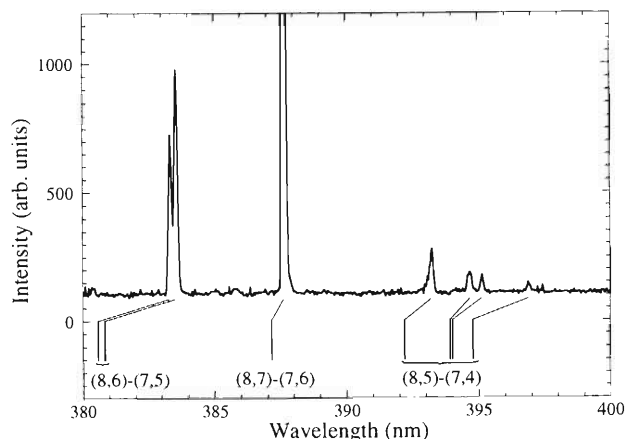


Fig. 2. A spectrum around  $n = 7-8$  transitions of  $\text{Ar}^{6+}$  ions. Transitions with  $\ell_i$  down to 5 can be observed, and lines show splittings due to fine structures for smaller  $\ell_i$  transitions.

principal quantum number of  $n_i = 8$ . The spectrum consists of seven clearly separable lines, and is thought to reflect the difference of the initial angular momentum ( $\ell_i$ ) of the captured electron.

For the identification of each line, we calculated transition wavelengths using multi-configuration Hartree-Fock codes, accounting for various wavefunctions for doubly excited states, *i.e.*,

$$3\ell_3\ell'_1, 3sn_1\ell, 3pn_2\ell, 3dn_3\ell,$$

where  $n_1 = 4-11$ ,  $n_2 = 4-6$  and  $n_3 = 4-5$ . One of the main reasons for this selection for wavefunctions is based on a fact that energy levels for singly excited states of  $\text{Ar}^{6+}$  ( $3sn\ell$ ) ions are very close to those for doubly excited  $3pn\ell'$  states because of a small gap between the  $3s$  and  $3p$  states of  $\text{Ar}^{7+}$  ions. Although transition wavelengths can not be predicted with sufficient accuracy, relative line positions make it possible to identify each line. The calculated results are shown by bars in Fig. 2. Here, (1) lines with the same  $\ell_i$  number split into some components due to fine structures of the states involved in the transitions, *i.e.*, two components for  $\ell_i = 6$  transitions and four components for  $\ell_i = 5$  transitions, and (2)  $\ell_i = 5$  transitions have longer wavelengths than  $\ell_i = 7, 6$  transitions due to the configuration interactions stated above, which is very different from a simple hydrogenic picture of an excited ion with a finite-sized core.

### References

- 1) S. Ninomiya et al.: Phys. Rev. Lett. **78**, 4557 (1997).

## Improvement of experimental setup for Ion-atom crossed-beam measurements at energy range below 100 eV/q

M. Hoshino,\* M. Kitajima,\* Y. Kanai, Y. Nakai, H. Tanaka,\* and Y. Yamazaki

Multielectron capture processes in highly charged ion (HCI) and neutral atom collisions have become one of the central topics of research in atomic collision physics. In the low-energy region, generally when the velocity is below 1 au, differential cross sections (DCSs) are very important for understanding interaction potential energy curves, which are essential in the detailed study of HCI-atom collision dynamics. Therefore, we have produced a crossed-beam experimental setup for DCS measurements of HCI-atom collisions in the energy range below 100 eV/q.<sup>1)</sup> It is known that the oscillation structure called Stückelberg oscillation appears in DCS of HCI-atom collision. This results from the interference effects between the ions scattered along different paths on the interaction potential curves. Therefore, information about the oscillation structure in DCS is very important for understanding the interaction of HCI-atom collisions. In order to observe this oscillation structure, sufficiently high angular resolution is needed, for example, less than  $\pm 0.5^\circ$  at the collision energy of 100 eV/q. However, for the DCS measurements in the  $C^{4+}$ -He collision system which we have reported,<sup>2,3)</sup> the angular resolution was not sufficiently high, so that the physical information about the interaction in these system was not obtained. Therefore, the experimental setup has been improved to enable us to monitor the size, the shape and the angular divergence of the HCI beam directly.

A collision chamber is set at the BL2 of the 14.5 GHz Caprice ECR ion source in the RIKEN Experimental Hall for slow highly charged ions.<sup>4)</sup> The collision chamber consists of a beam energy selector, an effusive nozzle and a scattered ion analyzer. Recently, we installed a beam-profile monitor in the collision chamber. The beam-profile monitor is set at the turntable with the scattered ion analyzer and can rotate from  $0^\circ$  to  $60^\circ$ . The beam-profile monitor is a multichannel plate (MCP) with a phosphor anode. Active diam-



Fig. 1. A typical beam profile of the  $N^{4+}$  ion beam at 100 eV/q obtained by the CCD camera.

eter of the MCP is 10 mm. The image of the beam on the phosphor screen is guided by two sets of plane mirrors and is monitored from outside of the collision chamber with a CCD camera. The beam-profile monitor can be moved away from the collision region to a 40 mm distance, so that the size and the angular divergence of the HCI beam can be estimated directly. The beam adjustment to obtain a high quality HCI beam can be easily carried out. A typical profile of the  $N^{4+}$  ion beam at 100 eV/q obtained by the CCD camera is shown Fig. 1. Typical beam current is about 100 pA in the collision volume at energy of 100 eV/q.  $N^{4+}$  ion beam with about 2 mm diameter and  $\pm 0.5^\circ$  angular divergence at 100 eV/q is obtained.

### References

- 1) M. Kitajima et al.: Phys. Scr. T **80**, 377 (1999).
- 2) M. Hoshino et al.: RIKEN Accel. Prog. Rep. **34**, 108 (2001).
- 3) M. Hoshino et al.: Phys. Scr. T **92**, 339 (2001).
- 4) Y. Kanai et al.: Phys. Scr. T **92**, 467 (2001).

\* Department of Physics, Sophia University

## Current status of a cooling system for MCI using positron plasma

N. Oshima, T. M. Kojima, M. Niigaki,\* A. Mohri, and Y. Yamazaki

Interaction between ultralow-energy multi-charged ions (MCIs) less than 1 eV/q and atoms/surfaces has not yet been investigated,<sup>1)</sup> since no realistic technique to produce ultraslow MCIs has been developed. In order to study this undeveloped field, a project to produce ultraslow MCIs using a positron cooling technique is under way. The principle of the positron cooling technique is the same as that of the electron cooling one, which has been successfully applied for producing low-energy antiprotons.<sup>2)</sup> Charged particles stored in a strong magnetic field lose their energies *via* cyclotron radiation, the rate of which is inversely proportional to the particle mass cubed. This fact means that if light and heavy particles are stored in a strong magnetic field simultaneously, the light particles behave as cooling agents of the heavy particles. Positrons are expected to be particularly useful because the recombination of positrons with positive ions does not take place, *i.e.*, the stored ions remain their initial charge states during the cooling. The cooling time of  $10^6$  MCIs from  $10^4$  eV to  $10^{-1}$  eV would be a few seconds when  $10^8$  positrons are stored in a trap at 5T. An ultralow-energy beam is generated if cooled MCIs are extracted slowly from the trap.

The cooling of MCIs will be practically realized in the following way<sup>3)</sup> (see Fig. 1): (1)  $10^{10}$  electrons, which are used as cooling agents for accumulating positrons, are trapped in a multi-ring electrode<sup>4)</sup> at  $B=5T$ ; (2) slow positrons are guided magnetically from a  $^{22}\text{Na}$ -based slow positron source into the trap. In the trap, the positrons are first re-moderated with a tungsten single crystal, then they are injected into the pre-loaded electron plasma. The slow positrons thus prepared are eventually trapped at the bottom of the potential valley. The positron trapping efficiency is expected to be 20–30%;<sup>5)</sup> (3) MCIs produced at an ECR ion source are injected into the trap and cooled with the positron cloud; (4) the cold MCIs (and the positrons) are extracted from the trap by ramping the potential valley. The cold MCI beam produced by such a method would be transported via an electrostatic lens system<sup>6)</sup> from the trap to a magnetic field free region for various experiments.

To date, we have constructed the following hardware: (1) the slow positron source<sup>5)</sup>; (2) the beamline which can guide both positrons and MCIs to the trap; (3) a 50-cm-long multi-ring electrode trap<sup>3,4)</sup> which consists of 23 electrodes. The slow positron source

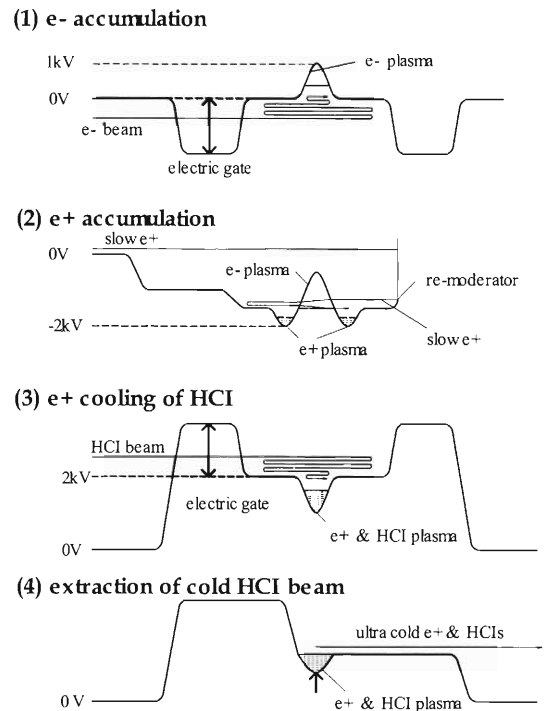


Fig. 1. Procedure of HCl cooling.

generates  $2.5 \times 10^6$  positrons/sec using a 30mCi  $^{22}\text{Na}$  radioactive source, and the beamline can transport all of the slow positrons to the trap. The multi-ring electrode trap successfully confined an electron plasma with a long lifetime of about 8 hours.

Now we are studying a technique for controlling the electron plasma precisely, particularly its charge distribution, since the positron trapping rate strongly depends on this parameter.<sup>5)</sup> We will start the positron accumulation experiment after optimizing the parameters of the electron plasma.

### References

- 1) Y. Kanai et al.: RIKEN Rev., No. 31, 62 (2000).
- 2) Y. Yamazaki et al.: Nucl. Instrum. Methods Phys. Res. B **154**, 174 (2000).
- 3) T. M. Kojima et al.: RIKEN Rev., No. 31, 70 (2000).
- 4) A. Mohri et al.: Jpn. J. Appl. Phys. **37**, 664 (1998).
- 5) N. Oshima et al.: RIKEN Rev., No. 31, 65 (2000).
- 6) M. Niigaki et al: Abst. 12th Int. Conf. Photonic, Electric and Atomic Collision, Santa Fe, New Mexico, USA, 2001-7, edited by S. Datz et al. (2001), p. 689.

\* Institute of Physics, Graduate School of Arts and Sciences, University of Tokyo

# Precision spectroscopy of the Zeeman splittings of the ${}^9\text{Be}^+ 2\ 2S_{1/2}$ hyperfine structure levels

T. Nakamura, M. Wada, K. Okada,\*<sup>1</sup> I. Katayama,\*<sup>2</sup> S. Ohtani,\*<sup>3</sup> and H. A. Schuessler\*<sup>4</sup>

To date, precision measurements of the Zeeman splittings of the ground-state hyperfine structure (HFS) of trapped ions have been performed mainly with the aim of developing frequency standards. We have proposed the application of this technique in the study of the nuclear structure of the various Be isotopes.<sup>1)</sup>

The hyperfine constant  $A$  shows a small but finite isotope dependence. The main part of this hyperfine anomaly stems from the finite distribution of the magnetism over the extended nucleus and is known as the Bohr-Weisskopf effect.<sup>2)</sup> The effect is empirically described by

$$A = A_{\text{point}}(1 + \epsilon_{\text{BW}}),$$

where  $A$  and  $A_{\text{point}}$  are the hyperfine constants for extended and point-like nuclei, respectively, and  $\epsilon_{\text{BW}}$  is the anomaly. Since  $A_{\text{point}}$  cannot be obtained experimentally, we compare the ratio of  $A$  to the nuclear  $g_I$ -factor among the isotopes. The differential anomaly

$${}^1\Delta^2 \equiv \frac{A^1/g_I^1}{A^2/g_I^2} - 1 \approx \epsilon_{\text{BW}}^1 - \epsilon_{\text{BW}}^2,$$

can then be evaluated.

We plan to investigate the neutron halo structure of the  ${}^{11}\text{Be}$  nucleus by means of the measurements of the Bohr-Weisskopf effect which is sensitive to the radial distribution of the loosely bound valence neutron. A recent theoretical estimate supports the importance of the investigation of the Bohr-Weisskopf effect in connection with the nuclear structure of  ${}^{11}\text{Be}$ .<sup>3)</sup> We have been working towards the development of exact experimental techniques for this purpose.<sup>4-6)</sup>

In order to investigate the Bohr-Weisskopf effect of  ${}^{11}\text{Be}$ , we must determine the hyperfine constant  $A$  and nuclear  $g$ -factor  $g_I$  for all of the odd Be isotopes with an accuracy of at least  $10^{-6}$ . A combined linear trap, which consists of a superconducting Helmholtz magnet and a linear rf trap, was constructed<sup>7)</sup> for testing a laser microwave multiple resonance method. Figure 1 shows typical microwave resonance spectra for the nuclear spin flip resonance and the electron spin flip resonance of  ${}^9\text{Be}^+$  under an external magnetic field of 0.47 T. We were able to determine the hyperfine constant  $A$  and the nuclear  $g_I$ -factor in units of the atomic  $g_J$ -factor from the two sets of resonance frequencies using the Breit-Rabi formula. The

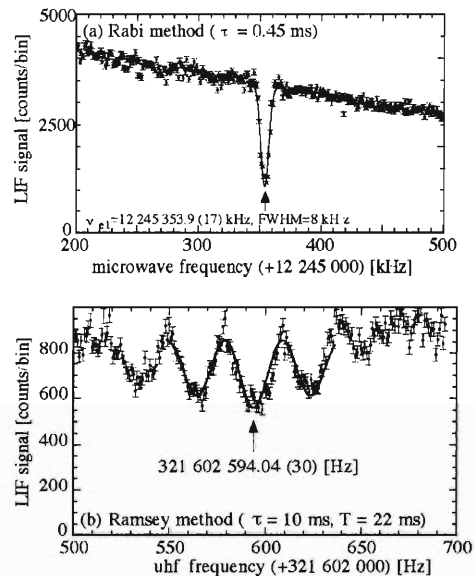


Fig. 1. Electron spin flip resonance (top) and nuclear spin flip resonance (bottom) spectra of the ground-state hyperfine structure of  ${}^9\text{Be}^+$  obtained by laser microwave multiple resonance spectroscopy under an external magnetic field.

values obtained are  $A = -625\ 008\ 835.23(75)\ \text{Hz}$  and  $g_I^1/g_J = 2.134\ 780\ 33(28) \times 10^{-4}$ .<sup>8)</sup> These values are slightly inconsistent with the NIST results by about  $2\sigma$ .<sup>9)</sup> A reason for this disagreement could be a possible quadratic dependence of the hyperfine constant  $A$  on the strength of the external magnetic field.<sup>10,11)</sup> We plan to confirm this theory in further experiments by measuring the magnetic field dependence with greater accuracy.

## References

- 1) M. Wada et al.: *Hyperfine Interact.* **81**, 161 (1993).
- 2) A. Bohr and V. F. Weisskopf: *Phys. Rev.* **77**, 94 (1950).
- 3) T. Fujita et al.: *Phys. Rev. C* **59**, 210 (1999).
- 4) M. Wada et al.: *Nucl. Phys. A* **626**, 365c (1997).
- 5) S. Fujitaka et al.: *Nucl. Instrum. Methods Phys. Res. B* **126**, 386 (1997).
- 6) K. Okada et al.: *J. Phys. Soc. Jpn.* **67**, 3073 (1998).
- 7) T. Nakamura et al.: *J. Appl. Phys.* **89**, 2922 (2001).
- 8) T. Nakamura et al.: accepted for *Opt. Commun.*
- 9) D. J. Wineland et al.: *Adv. At. Mol. Phys.* **19**, 135 (1983).
- 10) N. P. Economou et al.: *Phys. Rev. Lett.* **38**, 1394 (1977); S. J. Lipson et al.: *Phys. Rev. Lett.* **57**, 567 (1986); G. D. Fletcher et al.: *Phys. Rev. Lett.* **58**, 2535 (1987).
- 11) N. Fortson: *Phys. Rev. Lett.* **59**, 988 (1987).

\*<sup>1</sup> Department of Physics, Sophia University

\*<sup>2</sup> Institute of Particle and Nuclear Studies, High Energy Accelerator Research Organization (KEK)

\*<sup>3</sup> Institute for Laser Science, University of Electro-Communications

\*<sup>4</sup> Department of Physics, Texas A&M University, USA

# A cryogenic ion trap for improving the trapping lifetime of $\text{Be}^+$ ions

K. Okada,<sup>\*1</sup> M. Wada, I. Katayama,<sup>\*2</sup> L. Boesten,<sup>\*1</sup> T. Nakamura, and S. Ohtani<sup>\*3</sup>

Laser-microwave double resonance spectroscopy of trapped ions enables us to precisely measure the hyperfine structure splitting of alkali earth ions. We have proposed systematic measurements of the hyperfine structures of unstable Be isotopes in order to study the Bohr-Weisskopf effect.<sup>1)</sup> Normally, we have only minute amounts of unstable isotopes available to us. Thus, it is important for the laser spectroscopy of such ions to minimize the loss of the trapped ions. Moreover, buffer gas cooling is also essential for trapping such externally injected ions.<sup>2,3)</sup> The main causes of the ion loss are kinematic collisions with heavy residual background gases and chemical reactions with impurities. These problems can be solved by using a cryogenic trap whose electrodes can work as powerful cryopumps for such impurities in the trap region.<sup>4)</sup> We report the development of a cryogenic linear rf ion trap for improving the trapping lifetime of light  $\text{Be}^+$  ions.

We used an experimental setup similar to that described in our previous paper.<sup>5)</sup> The modifications are as follows. The linear rf trap was enclosed by double cryogenic cylinders. A cylindrical radiation shield in contact with a liquid helium (LHe) reservoir (1.6l) was surrounded by an outer cylinder in contact with a liquid nitrogen ( $\text{LN}_2$ ) reservoir (3.0l). The coolant injection pipes were welded to the LHe reservoir and passed through the  $\text{LN}_2$  reservoir to reduce the evaporation of LHe by thermal inflow. The residual pressure inside the vacuum chamber was approximately  $5 \times 10^{-8}$  Pa at room temperature. The pressure in the cryogenic region was estimated from the pumping speed of the cryogenic parts and from conductance calculations to be lower than  $1 \times 10^{-10}$  Pa.

We measured the storage time of He-gas-cooled  $\text{Be}^+$  ions (Fig. 1). Typically, it was of the order of 10 seconds at room temperature, but it was extended to about 15 min with LHe cooling (Fig. 1(b)). In our experiment, we showed that laser cooling assisted buffer-gas cooling even under the  $\text{LN}_2$  cooled condition (Fig. 1(c)). These results indicate that a difference in the amount of the impurities of less than  $10^{-9}$  Pa results in a considerably improved trap lifetime, *i.e.*, the lifetime of trapped light ions is very sensitive to the quality of He gas.

We also measured the trap lifetime of laser-cooled  $^9\text{Be}^+$  ions under cryogenic conditions. A lifetime of

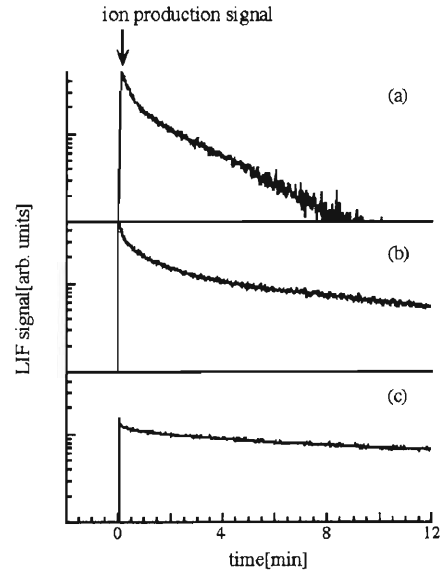


Fig. 1. Time evolution of the fluorescence signal from He-gas-cooled  $^9\text{Be}^+$  ions. Trap lifetimes  $\tau$  are 2.37(5) min for the  $\text{LN}_2$ -cooled trap (a), 14.9(1) min for the LHe-cooled trap (b), and 22.9(1) min for the  $\text{LN}_2$ -cooled trap assisted by laser cooling (c). Laser power was  $600 \mu\text{W}$  for (c), and  $40 \mu\text{W}$  for (a) and (b). The stray light level lies below the axis in all figures.  $f_{\text{rf}} = 2.457$  MHz,  $V_{\text{ac}} = 120$  V<sub>pp</sub>, He gas pressure  $p = 4 \times 10^{-3}$  Pa.

178(3) min was obtained from the dominant time constant of the fluorescence decay curve.<sup>6)</sup> This lifetime is approximately 18 times longer than the corresponding lifetime at room temperature. A laser-cooled ion crystal, which was lost within 10 minutes at room temperature, was kept for approximately 30 min without any ion loss with the cryogenic linear trap.<sup>6)</sup>

The usefulness of a cryogenic linear rf ion trap for the minimization of ion loss and for the long-term confinement of light  $\text{Be}^+$  ions was demonstrated in our experiment. Most of the ion-loss problems, particularly for buffer-gas-cooled light ions, can be solved by using a cryogenic ion trap. Such a cryogenic trap should also be useful for the accumulation of ions of an unstable isotope.

## References

- 1) M. Wada et al.: Nucl. Phys. A **626**, 365c (1997).
- 2) M. Wada et al.: RIKEN Rev., No. 31, 56 (2000).
- 3) M. Wada et al.: Nucl. Instrum. Methods Phys. Res. B **126**, 386 (1997).
- 4) M. E. Poitzsch et al.: Rev. Sci. Instrum. **67**, 129 (1996).
- 5) K. Okada et al.: J. Phys. Soc. Jpn. **67**, 3073 (1998).
- 6) K. Okada et al.: Jpn. J. Appl. Phys. **40**, 4221 (2001).

<sup>\*1</sup> Department of Physics, Sophia University

<sup>\*2</sup> Institute for Particle and Nuclear Studies, High Energy Accelerator Research Organization (KEK)

<sup>\*3</sup> Institute for Laser Science, University of Electro-Communications

# Optical detection of atoms and ions in superfluid helium

R. Saneto,\*<sup>1</sup> Y. Fukuyama, I. Tanihata, Y. Matsuo, and Q. Hui\*<sup>2</sup>

Superfluid helium (He II) is expected to be a suitable medium to study short-lived nuclei because it can instantly stop ions with high kinetic energy.<sup>1)</sup> Injected ions are trapped at a certain region of a He II chamber determined by the initial energy of ions. Then, laser spectroscopy can be applied to trapped atoms and ions to determine the structure of these nuclei. Microwave detection combined with the optical pumping method will enable us to measure hyperfine splitting of alkali and alkali-earth atoms and ions.<sup>2,3)</sup> In order to perform a laser spectroscopic study of unstable nuclei in He II, it is necessary to develop a method of detecting an optical signal. In off-line experiments, laser ablation is a useful method of implanting atoms and ions in He II. We have reported that ions produced by laser ablation were introduced into He II by applying an electric field and the mobility of ions was measured.<sup>4)</sup> In this report, we describe laser-induced fluorescence (LIF) detection of impurity atoms and ions, such as Ba, Ba<sup>+</sup>, and Sr, in He II.

The experiment was performed in a quartz container filled with He II of 1.6 K in a cryostat at saturated vapor pressure. Laser ablation with a Q-switched Nd:YAG laser (355 nm, 10 Hz, 10 mJ) was carried out above a liquid surface and produced ions were injected into He II by an electric field generated at electrodes. A detailed design of the cryostat and the electrodes is described in Ref. 4. The schematic of optical detection is illustrated in Fig. 1. For the excitation of implanted atoms and ions in He II, a pulsed dye laser pumped

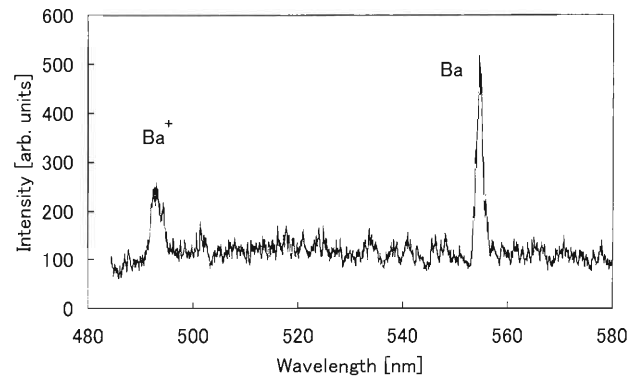


Fig. 2. Emission spectra of Ba and Ba<sup>+</sup>.

with an excimer laser was used. LIF signals were detected with a photomultiplier tube (PMT) through a monochromator. The detected signals were amplified and integrated by a boxcar averager.

Figure 2 shows the emission spectra of Ba and Ba<sup>+</sup>. The wavelength of the dye laser for excitation (446 nm) was set to the peak position of the D2 excitation line of Ba and the D1 line of Ba<sup>+</sup>, which are in the typical shape of lines in He II, were observed.<sup>5)</sup> Furthermore, we observed a number of lines of Sr and Ba.

The amount of ions injected into He II after the laser ablation is estimated to be 10<sup>8</sup> from the ion current experiment.<sup>4)</sup> Since the efficiency of our optical detection system is about 10<sup>-5</sup>, the intensity of the Ba<sup>+</sup> line in Fig. 2 corresponds to emission from 10<sup>3</sup> ions. Therefore, in order to perform optical detection of short-lived nuclei, 10<sup>5</sup> of ions would be required in the detection region.

We are now constructing a new cryostat which has a window for introducing ion beams into He II. It is necessary to determine the position of implanted ions for the efficient observation of optical signals. The new cryostat is designed to use hodoscopes that can detect the position of unstable nuclei by observing beta-ray emission.

## References

- 1) N. Takahashi et al.: *Physica B* **284/288**, 89 (2000).
- 2) T. Kinoshita et al.: *Phys. Rev. B* **49**, 3648 (1994).
- 3) T. Yabuzaki et al.: *Z. Phys. B* **98**, 367 (1995).
- 4) R. Saneto et al.: *RIKEN Accel. Prog. Rep.* **34**, 111 (2001).
- 5) B. Tabbert et al.: *J. Low Temp. Phys.* **109**, 653 (1997).

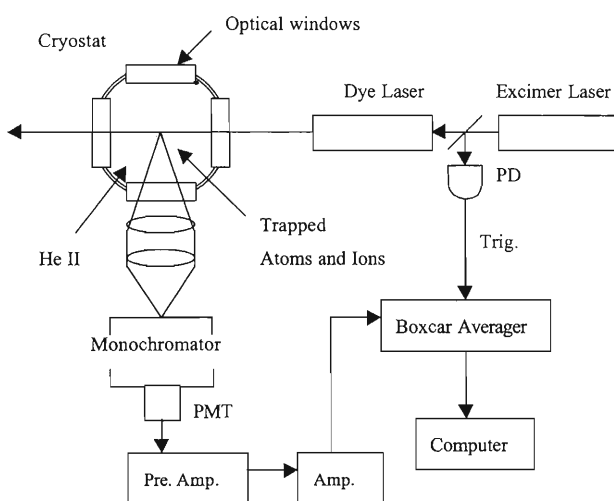


Fig. 1. Schematic of optical detection.

\*1 Keio University

\*2 University of Electro-Communications

# Study of BaF<sub>2</sub> crystal by a positron annihilation technique

K. Inoue,\* N. Suzuki, Y. Itoh, A. Goto, and T. Hyodo\*

In the last decade, BaF<sub>2</sub>, which is widely used as a material for an ultra fast  $\gamma$ -ray scintillator has attracted much interest. Its photoluminescence process is Auger-free; the radiative transition of a valence electron to a hole created in the core level stimulated by the excitation of the outermost core Ba<sup>2+</sup> 5p level.<sup>1)</sup>

In the present study, we measured the positron lifetime spectra and the doppler broadening spectra in BaF<sub>2</sub> in the temperature range of 14 K–295 K.

First, a two-component analysis of the lifetime spectra was performed. The results are shown in Fig. 1. The shorter lifetime component is attributed to the mixture of para-positronium component and the component of the positron which does not form positronium. The longer lifetime is attributed to ortho-positronium.

It is seen that in the temperature range below 90 K,  $\tau_1$ ,  $\tau_2$  and  $I_2$  are almost constant. However, in the

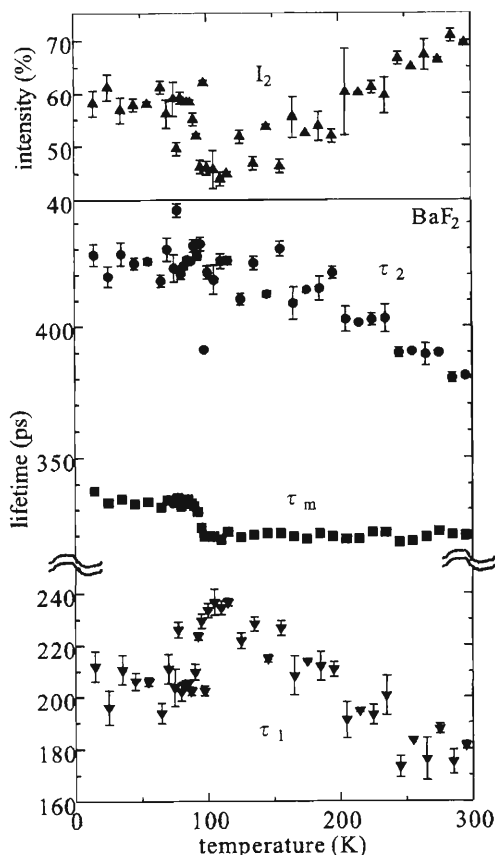


Fig. 1. Positron lifetimes and intensities for BaF<sub>2</sub>.

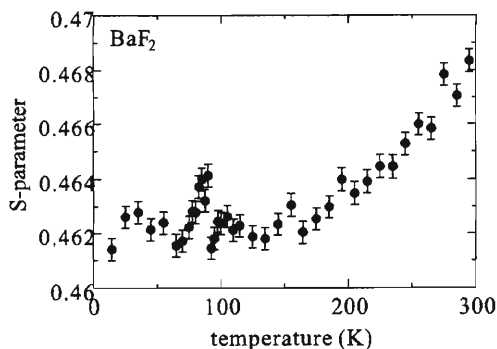


Fig. 2. S-parameter for crystalline BaF<sub>2</sub>.

range above 100 K,  $\tau_1$  and  $\tau_2$  decrease and  $I_2$  increases as temperature rises. In the temperature range between 90 K and 100 K,  $\tau_1$ ,  $I_2$  and the mean lifetime change almost step-likely, and  $\tau_2$  starts to decrease.

Figure 2 shows S-parameter, which is defined as the number of counts of the central region of the Doppler-broadened 511 keV annihilation  $\gamma$ -ray energy spectrum divided by the total number of counts. There is a sharp drop in the temperature range 90 K–100 K. This change correlates well with the result of the positron lifetime.

Such step-like changes in the positron annihilation parameters indicate the existence of a phase transition of BaF<sub>2</sub> or a change in the state of positronium.

An interesting phenomenon possibly related to our result is reported by Ejiri *et al.*<sup>1)</sup> They measured the photoluminescence spectra in BaF<sub>2</sub> and found that the photoluminescence excited at 23 K is much different from that at room temperature, and explained that the intensity of self-trapped exciton increases with cooling. They also found that the intensity of the photoluminescence of the self-trapped exciton becomes maximum at around 95 K. However, they measured the photoluminescence spectra at only five temperatures; 23 K, 54 K, 95 K, 130 K and 300 K. It is not certain that the maximum is in the range of 90 K–100 K.

It is desirable to measure the temperature dependence of various physical parameters of BaF<sub>2</sub> with small temperature steps by various experimental techniques.

## References

- 1) A. Ejiri *et al.*: J. Electron Spectrosc. Relat. Phenom. **79**, 151 (1996).

\* Graduate School of Arts and Sciences, University of Tokyo

## Temperature dependence of the Compton profile for BaF<sub>2</sub> crystal

K. Inoue,<sup>\*1</sup> N. Suzuki, N. Hiraoka,<sup>\*2</sup> M. Itou,<sup>\*2</sup> Y. Sakurai,<sup>\*2</sup> Y. Itoh, A. Goto, and T. Hyodo<sup>\*1</sup>

In the previous paper,<sup>1)</sup> we reported that the positron annihilation parameters for BaF<sub>2</sub> showed a clear step-like change in the temperature range 90 K–100 K, and that this indicated the existence of a phase transition.

Although the positron annihilation technique is highly sensitive to various phase transitions (*e.g.*, structural phase transitions, spin crossover transitions, glass transitions, and so on), it is usually difficult to identify the origin of the transition using only the positron annihilation parameters. Thus it is useful to combine this technique with other complementary techniques.

In this study, we measured the temperature dependence of the electron momentum distributions in BaF<sub>2</sub> using a high-resolution Compton scattering technique. The measurements of Compton profiles were performed at the beam line BL08W of the SPring-8 facility. A monochromatized 116 keV incident X-ray beam was scattered at an angle of 172°, dispersed by a Si[620] analyzer, and detected by a high-purity Ge detector. The momentum resolution was 0.15 atomic units (a.u.).

The results are shown in Fig. 1. The solid circles in (a) represent the Compton profile for BaF<sub>2</sub> at 85 K and the open triangles represent that at 110 K. Figure 1 (b) shows the difference between the two spectra. There is a slight difference beyond the statistical error in the central part of the spectrum (within  $\pm 2.5$  (a.u.)). This result probably corresponds to the result of the positron annihilation measurements and evidences the existence of a phase transition between 85 K and 110 K.

The difference in the Compton profiles is observed only in the central region. It suggests that this phenomenon is caused by the change of the electronic state of the valence band ( $2p$  of F<sup>-</sup>), because the momentum distribution of the valence electrons is narrow. For example, the covalency of the chemical bonding between Ba and F atoms might change between 85 K and 110 K.

The change in the Compton profiles is somewhat unclear as is apparent in the positron annihilation parameters.<sup>1)</sup> This is probably because the sensitivity to the changes of the valence electrons differs. The amplitude of the positron wave function is large in the intersti-

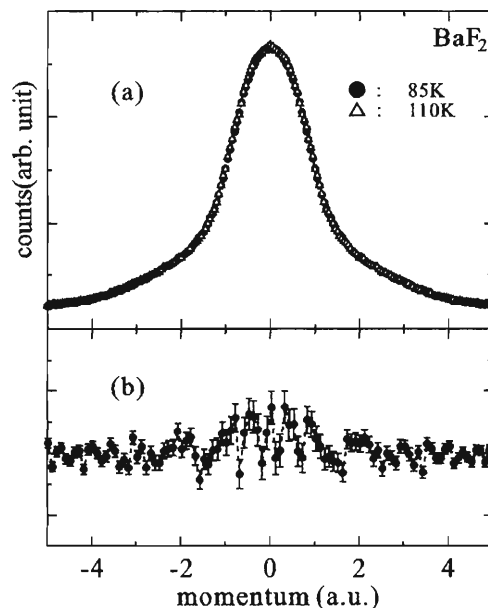


Fig. 1. (a) Compton profiles for BaF<sub>2</sub> at 85 K (solid circles) and 110 K (open triangles). (b) The difference between the above spectra.

tial region because of the repulsive force between the positron and the nuclei. Thus, positrons are sensitive to the changes of the valence electrons. The Compton profiles represent the momentum distributions of all of the electrons in a material. Thus the Compton profiles are relatively insensitive to the change of the valence electrons.

In order to clarify this point, we are also continuing to investigate the temperature dependence of BaF<sub>2</sub> by other techniques.

The measurements of Compton profiles were performed at the SPring-8 facility with the approval of the Japan Synchrotron Radiation Institute (JASRI) (Proposal No. 2001B0231-ND-1up).

### References

- 1) K. Inoue et al.: RIKEN Accel. Prog. Rep. **35**, 102 (2002).

<sup>\*1</sup> Graduate School of Arts and Sciences, University of Tokyo

<sup>\*2</sup> Japan Synchrotron Radiation Research Institute (JASRI), SPring-8

## $\mu$ SR study of the Cu-spin dynamics in $\text{La}_{2-x}\text{Sr}_x\text{Cu}_{1-y}\text{Zn}_y\text{O}_4$

I. Watanabe, T. Adachi,\* K. Takahashi,\* S. Yairi,\* Y. Koike,\* and K. Nagamine

A magnetically ordered state of Cu spins appearing at low temperatures in La-based high- $T_c$  superconductors around the hole concentration of  $\sim \frac{1}{8}$  per  $\text{Cu}^{1)}$  is now recognized to be a statically stabilized state of the dynamical stripe correlations of spins and holes. This stabilized state has been argued to lead to the suppression of superconductivity.<sup>2)</sup> Meanwhile, it has been reported by Koike *et al.*<sup>3)</sup> that the superconducting state in  $\text{La}_{2-x}\text{Sr}_x\text{Cu}_{1-y}\text{Zn}_y\text{O}_4$  (LSCZO) around  $x = 0.115$  is strongly suppressed by only 1% Zn substitution for Cu also. These results suggest that the Zn substitution affects the stabilization of the dynamical stripe correlations. Thus, in order to clarify the effect of the non-magnetic impurity, Zn, on the dynamics of the dynamical stripe correlations, muon spin relaxation measurements on the Zn-substituted LSCZO with  $x = 0.13$  were carried out at the RIKEN-RAL Muon Facility, while changing the Zn concentration from  $y = 0$  to 0.10.

Figure 1 shows the time dependence of the asymmetry parameter of the muon-spin polarization,  $A(t)$ , ( $\mu$ SR time spectrum) of LSCZO with  $y = 0, 0.01, 0.05$  and 0.10 at various temperatures. Figure 2 shows the detailed temperature dependence of the time spectrum of the Zn-substituted LSCZO with  $y = 0.01$  displayed in a short time region from 0 to 2  $\mu\text{sec}$ . In the

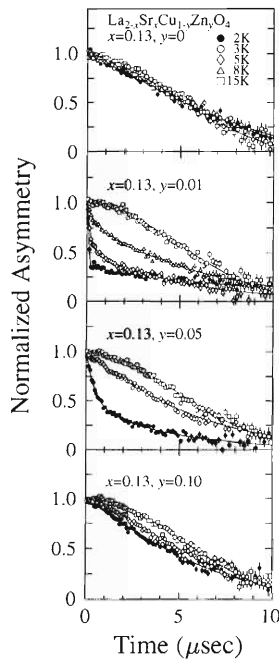


Fig. 1. Zero-field  $\mu$ SR time spectra of the Zn-substituted  $\text{La}_{2-x}\text{Sr}_x\text{Cu}_{1-y}\text{Zn}_y\text{O}_4$  with  $x = 0.13$  and  $y = 0, 0.01, 0.05$  and 0.10 obtained at various temperatures.

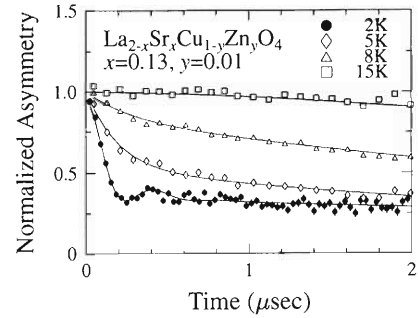


Fig. 2. Temperature dependence of the zero-field  $\mu$ SR time spectra of the Zn-substituted  $\text{La}_{2-x}\text{Sr}_x\text{Cu}_{1-y}\text{Zn}_y\text{O}_4$  with  $x = 0.13$  and  $y = 0.01$  within the early time range from 0 to 2  $\mu\text{sec}$ .

Zn-free sample, the time spectrum does not change so much, showing a Gaussian-type behavior down to 2 K, indicating no influence of the Cu moments at the muon site, that is, the Cu spins are in a paramagnetic state. In the case of the Zn-substituted LSCZO with  $y = 0.01$ , a fast depolarizing component appears at low temperatures below about 10 K and the time spectrum changes to an exponential type, and finally the muon-spin precession is observed at 2 K, as shown in Fig. 2. The muon-spin precession is no longer observed even at 2 K in the Zn-substituted LSCZO with  $y = 0.05$ . Solid lines in figures are the best-fit results obtained using the analysis function of  $A_0e^{-\lambda_0 t} + A_1e^{-\lambda_1 t} + A_2e^{-\lambda_2 t} \times \cos(\omega t + \phi)$ .

The observation of the muon-spin precession in the Zn-substituted LSCZO with  $y = 0.01$  at 2 K clearly indicates the appearance of a long-range magnetically ordered state of Cu spins. This means that the dynamically fluctuating stripe correlations are statically stabilized by only 1% substituted Zn, forming a long-range ordered state. In contrast, the disappearance of the muon-spin precession at  $y = 0.05$  means the destabilization of the statically ordered state of the stripe correlations, that is, the magnetic correlation among Cu spins tends to be destroyed by the Zn substitution for  $y > 0.01$ .

As a result, the present  $\mu$ SR study confirms that a small amount of non-magnetic impurities tends to pin and statically stabilize the dynamical stripe correlations but a large amount of non-magnetic impurities destroys the stripe correlations themselves.

### References

- 1) I. Watanabe et al.: *Hyperfine Interact.* **86**, 603 (1994).
- 2) J. M. Tranquada et al.: *Nature* **375**, 561 (1995).
- 3) Y. Koike et al.: *Solid State Commun.* **82**, 889 (1992).

\* Graduate School of Engineering, Tohoku University

## Isomer effect on charge transfer from $C_3H_4$ molecules (allene and propyne) at keV energies

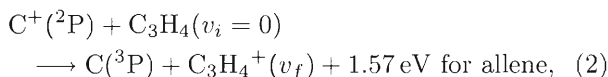
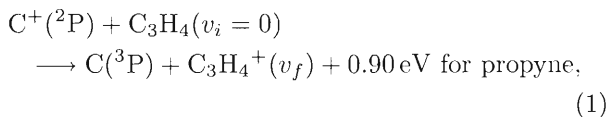
T. Kusakabe,\*<sup>1</sup> I. Shimamura, and M. Kimura\*<sup>2</sup>

Our understanding of charge transfer processes in collisions of ions and hydrocarbons above intermediate collision energies has been extremely limited due to the complexity of the target. However, it becomes increasingly important in a number of applications such as those in plasma, material, medical and astrophysical sciences.

For hydrocarbon molecules, as the number of carbon atoms increases, in general, the number of isomers increases. The  $C_3H_4$  molecule is known to possess two stable isometric molecular structures, *i.e.*, allene (propadiene;  $H_2C=C=CH_2$ ) and propyne (methylacetylene;  $HC\equiv C-CH_3$ ). It has been known that isomers always show conspicuous differences in various physical and chemical properties in stationary, or dynamical aspects in the interaction energy equivalent to the thermal energy domain. However, as a natural consensus, it has been assumed that the isomer effect rapidly disappear as the collision energy increases above, say, 50 eV regime because of a shorter interaction time, and hence, has entirely been ignored in experimental studies in the past. Therefore, it would be interesting to investigate this phenomenon to determine the degree of the effect on charge transfer depending upon the molecular structure of the isomers.

We have observed, for the first time, prominent isomer effects in charge transfer processes in collisions of  $C^+$  ions with allene and propyne even at a collision energy as high as 1000 eV.<sup>1)</sup> The present charge-transfer cross sections of allene are found to be systematically larger than those of propyne in the entire energy range studied up to 4.5 keV. In order to understand the details, we have carried out a theoretical analysis based on the DV-Xa method<sup>2)</sup> for molecular states and a semiclassical molecular orbital close coupling approach for scattering dynamics.

The specific processes we have studied are collisions of the ground-state  $C^+(^2P)$  ion with the allene and propyne ( $C_3H_4$ ) molecules:



where  $v_i$  and  $v_f$  denote the initial and final vibrational

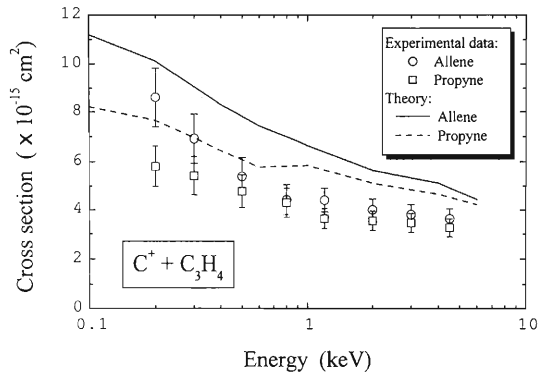


Fig. 1. Charge transfer cross sections for  $C^+-C_3H_4$  (allene and propyne) collisions.  $\circ$ ; the present data for allene,  $\square$ ; the present data for propyne. The experimental error bars denote the absolute total uncertainty. Theoretical results for allene and propyne are included in solid and dot lines, respectively.

quantum numbers, respectively, of a target molecule.

The present experimental charge-transfer cross sections are shown in Fig. 1 for allene and propyne from 0.2 to 4.5 keV along with the present theoretical results. Experimental charge-transfer cross sections of allene are consistently larger than those of propyne in the entire energy range studied, but the difference between these two sets of cross sections becomes more pronounced with the collision energy below 0.4 keV. The difference between these two sets of the cross section is 32.5% and 21.7% at 0.2 keV and 0.3 keV, respectively, and these values are much larger than the present total absolute experimental uncertainty of 14.6%. Therefore, the difference in the two sets of cross sections in the isomers is confirmed at least at the two lowest energy points. The trend of the two cross sections of calculated results, although the absolute magnitude is somewhat larger than the measured one, is found to be consistent with that of measured results, and supports our observation.

### References

- 1) T. Kusakabe et al.: Phys. Rev. A **62**, 062714 (2000).
- 2) M. Kimura and N. F. Lane: in *Advances in Atomic, Molecular and Optical Physics*, Vol. 26 (Academic Press, New York, 1989), p. 76.

\*<sup>1</sup> Department of Nuclear Engineering, Kinki University

\*<sup>2</sup> Graduate School of Science and Engineering, Yamaguchi University

# Microwave resonances in the hyperfine structure of antiprotonic helium and deduction of the antiprotonic orbital magnetic moment

E. Widmann,<sup>\*1</sup> J. Sakaguchi,<sup>\*1</sup> H. Yamaguchi,<sup>\*1</sup> T. Ishikawa,<sup>\*1</sup> R. S. Hayano,<sup>\*1</sup> J. Eades,<sup>\*2</sup> M. Hori,<sup>\*2</sup>  
H. A. Torii,<sup>\*3</sup> B. Juhász,<sup>\*4</sup> D. Horváth,<sup>\*5</sup> and T. Yamazaki

Following the discovery of a doublet splitting in the laser resonance transition  $(n, l) = (37, 35) \rightarrow (38, 34)$  in antiprotonic helium ( $\bar{p}\text{He}^+$ )<sup>1)</sup> and the theoretical study of the hyperfine structure by Bakalov and Korobov,<sup>2)</sup> an experiment to determine the quadruplet structure (see Fig. 1) using two laser pulses and one microwave was carried out during 2001 at the Antiproton Decelerator at CERN. The first laser pulse was used to induce an asymmetric population of the  $F = l \pm 1/2$  doublet whose time evolution caused by microwave transitions was detected by the second laser pulse. Two microwave resonance transitions (electron spin flipping with respect to the large orbital angular momentum ( $l = 35$ ) of  $\bar{p}$ ) were observed as predicted, as shown in Fig. 2. The observed frequencies are  $12.89624 \pm 0.00019$  and  $12.92430 \pm 0.00018$  GHz (preliminary), in excellent agreement with the predicted frequencies.<sup>2)</sup> The precision achieved in this first experiment is  $\sim 1 \times 10^{-5}$ . Since the experimental values agree with two independent theoretical calculations recently performed,<sup>3-5)</sup> they provide experimental proof

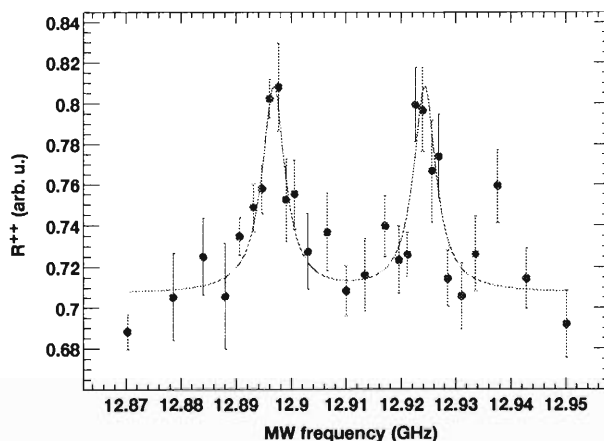


Fig. 2. Observed microwave resonance profile in the two-laser-microwave triple resonance method.

of the fundamental relation concerning the antiprotonic orbital  $g$ -factor and the anti-nuclear magneton

$$g_l(\bar{p})\mu_{\bar{N}} = -\frac{e\hbar}{2M_p c},$$

to the precision of  $\sim 1 \times 10^{-5}$ . Note that no experimental value is known for either  $g_l(p)$  or  $\mu_N$  (nuclear magneton) for the proton because no such orbiting proton exists in the matter world.

## References

- 1) E. Widmann et al.: Phys. Lett. B **404**, 15 (1997).
- 2) D. D. Bakalov and V. I. Korobov: Phys. Rev. A **57**, 1662 (1998).
- 3) V. I. Korobov and D. Bakalov: J. Phys. B **34**, L519 (2001).
- 4) N. Yamanaka, Y. Kino, H. Kudo, and M. Kamimura: Phys. Rev. A **63**, 012518 (2001).
- 5) Y. Kino, N. Yamanaka, H. Kudo, and M. Kamimura: to be published.

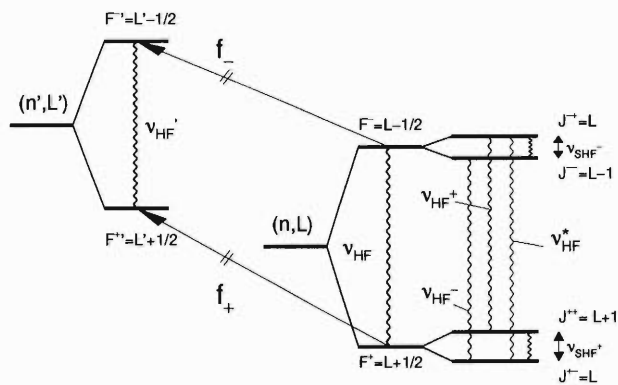


Fig. 1. Hyperfine structure of the antiprotonic helium and various transitions.

<sup>\*1</sup> Department of Physics, University of Tokyo

<sup>\*2</sup> CERN, Switzerland

<sup>\*3</sup> Institute of Physics, University of Tokyo

<sup>\*4</sup> Institute of Nuclear Research of the Hungarian Academy of Sciences, Hungary

<sup>\*5</sup> KFKI Research Institute for Particle and Nuclear Physics, Hungary

### 3. Radiochemistry and Nuclear Chemistry



## In-beam Mössbauer study on valence states of $^{57}\text{Fe}$ decaying from $^{57}\text{Mn}$ implanted into $\text{KMnO}_4$ (II)<sup>†</sup>

Y. Kobayashi, M. K. Kubo,\*<sup>1</sup> Y. Yamada,\*<sup>2</sup> T. Saito,\*<sup>2</sup> H. Ueno, H. Ogawa,\*<sup>3</sup> W. Sato, K. Yoneda, H. Watanabe, N. Imai,\*<sup>4</sup> D. Kameda,\*<sup>5</sup> H. Miyoshi, and K. Asahi

Applications of  $^{57}\text{Mn}$ , which is one of Mössbauer source nuclides for  $^{57}\text{Fe}$ , are quite rare because its half-life ( $T_{1/2} = 1.45$  min) is short. Mn occurs in various stable oxidation states up to 7+ in solids, which is not the case for Fe and Co. Therefore, Mn is considered to be one of the most attractive probes in solid-state chemistry to investigate the chemical states after nuclear transformations.

We have succeeded in obtaining well-resolved in-beam Mössbauer spectra of  $^{57}\text{Fe}$  arising from  $^{57}\text{Mn}$  implanted into  $\text{KMnO}_4$  between 11 K and 155 K.  $^{57}\text{Mn}$  particles were produced as a RI beam following the nuclear projectile fragmentation of a  $^{59}\text{Co}$  beam ( $E = 80$  A MeV) with a Be target using RIPS, and subsequently implanted into a sample of  $\text{KMnO}_4$ , in which Mn ions are in a 7+ state and form symmetric  $[\text{MnO}_4]^-$  tetrahedra. A typical  $^{57}\text{Fe}(\leftarrow ^{57}\text{Mn})$  Mössbauer spectrum of  $\text{KMnO}_4$  at 11 K is shown in Fig. 1. The obtained spectra below 90 K could be analyzed as having two components of a *doublet* and a *singlet* at least. The *doublet* was assigned to  $\text{Fe}^{2+}$  ions located interstitially or substituted for K-sites in  $\text{KMnO}_4$  from the derived Mössbauer parameters.

Suppose that the anomalous *singlet* resulted in the Fe atoms substituting for regular Mn-sites in symmetric tetrahedra. Molecular orbital calculations (DV-X $\alpha$

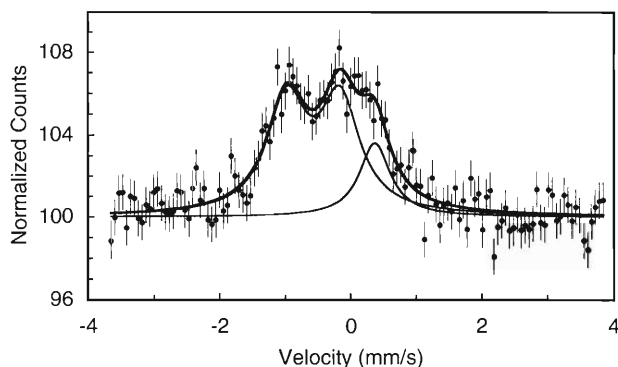


Fig. 1. A  $^{57}\text{Fe}(\leftarrow ^{57}\text{Mn})$  Mössbauer spectrum of  $\text{KMnO}_4$  at 11 K.

<sup>†</sup> Condensed from the article in J. Nucl. Radiochem. Sci., in press

\*<sup>1</sup> School of Science, University of Tokyo

\*<sup>2</sup> Department of Chemistry, Tokyo University of Science

\*<sup>3</sup> National Institute of Advanced Industrial Science and Technology (AIST)

\*<sup>4</sup> Graduate School of Science, University of Tokyo

\*<sup>5</sup> Graduate School of Science and Engineering, Tokyo Institute of Technology

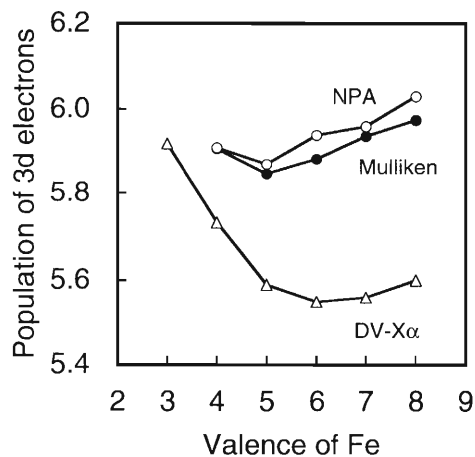


Fig. 2. Calculations for the population of 3d electrons against the valence states of Fe.

and G98) were carried out to determine the electron densities of Fe atoms in tetrahedral  $[\text{FeO}_4]^{n-}$ . The G98 calculation reveals that two species of  $[\text{FeO}_4]^{2-}$  ( $\text{Fe}^{6+}$ ) and  $[\text{FeO}_4]^0$  ( $\text{Fe}^{8+}$ ) are the most stabilized tetrahedra, and that in these species the Fe atom is located in symmetric oxygen configurations. The other  $\text{Fe}^{n+}$  atoms do not form stable tetrahedra of  $[\text{FeO}_4]^{n-}$  geometrically. The results of G98 calculation are consistent with the shape of the singlet, that is, the electric field gradient obtained in the Mössbauer spectra is zero. The nature of the Fe-O bond tends toward covalent from ionic with increasing valence state of Fe, therefore, the contribution of 3d-electrons to bonding orbitals increases, while that to antibonding orbitals decreases. Although the total population of 3d-electrons decreases as the number of antibonding electrons decreases in the region from  $\text{Fe}^{2+}$  to  $\text{Fe}^{6+}$ , the population of 3d-electrons increases because of the covalent character in the region between  $\text{Fe}^{6+}$  and  $\text{Fe}^{8+}$ , from the calculations based on the different modes (NPA, Mulliken and DV-X $\alpha$ ), as shown in Fig. 2. Therefore, the isomer shift of  $[\text{FeO}_4]^{2-}$  corresponding to  $\text{Fe}^{6+}$  appears to have a maximum value, while that of  $[\text{FeO}_4]^0$  with a higher valence state is considered to be less than the value corresponding to  $\text{Fe}^{6+}$ . On the basis of the Mössbauer parameters and the molecular orbital calculation, it is concluded that the *singlet* is assigned to the  $^{57}\text{Fe}$  atoms substituting at Mn-sites in tetrahedral  $[\text{MnO}_4]^-$  with an unusually high valence state of Fe(VIII).

## Stimulation of transferrin-dependent $^{59}\text{Fe}$ and $^{48}\text{V}$ uptake in rat isolated adipocytes by insulin or vanadyl treatment

H. Yasui,\* K. Kawabe,\* A. Nakayama,\* R. Hirunuma, S. Enomoto, and H. Sakurai\*

The biological actions of vanadium have been investigated by many researchers. Since vanadium ions, such as vanadyl ( $\text{VO}^{2+}$ ) and vanadate ( $\text{VO}_3^-$ ), have been demonstrated to normalize blood glucose levels of diabetic animals and patients, the insulin-mimetic mechanism of vanadium treatment has attracted much interest. However, a few studies on the mechanisms of biological actions in vanadium treatments have been reported.

Insulin has been demonstrated to stimulate the translocation of transferrin receptors from an intracellular compartment to the plasma membrane, and subsequently the accumulation of iron (Fe) in adipocytes, by increasing the binding and uptake of diferric transferrin.<sup>1)</sup> This insulin-dependent stimulation is based on an intracellular signaling mechanism similar to the recruitment of glucose transporters. Recently, the insulin-mimetic effect of the vanadate ion on transferrin receptors and Fe uptake in rat adipocytes was examined in order to determine its function in the translocation of glucose transporters as an acute biological response.<sup>2)</sup> Thus, we first planned to study the mechanisms of the vanadyl ion in a major oxidation state in animals, which is less toxic than the vanadate ion, as well as insulin in terms of stimulating uptake of  $^{59}\text{Fe}$  and  $^{48}\text{V}$  bound to transferrin in rat adipocytes.

A multitracer technique was used to investigate the vanadyl- or insulin-stimulated uptake of trace elements in rat isolated adipocytes. A multitracer solution containing the radioisotopes of 20 elements was prepared from a silver target irradiated by a heavy-ion beam of 135 MeV/nucleon accelerated by the RIKEN Ring Cyclotron. Male Wistar rats (200 g of body weight, 7 weeks old) were used in this study. Isolated rat adipocytes ( $2.7 \times 10^6$  cells/mL) prepared as described<sup>3)</sup> were preincubated at  $37^\circ\text{C}$  for 0.5 hr using three different concentrations ( $1$  or  $5 \times 10^{-4}$ , and  $1 \times 10^{-3}$  mM) of vanadyl sulfate or 4 nM insulin in 1 mL of KRB buffer (pH 7.4) containing 20 mg of bovine serum albumin. The multitracer solution dissolved in a physiological saline containing bovine apo-transferrin (Tf) was then added to the reaction mixture and the resulting solutions were incubated at  $37^\circ\text{C}$  for 2 hr, where a final concentration of Tf was 2 mg/mL. The reactions were terminated by soaking in ice water and the mixtures were centrifuged at 12,000 rpm for 1 min. After the solution surrounding the cells was aspirated, the radioac-

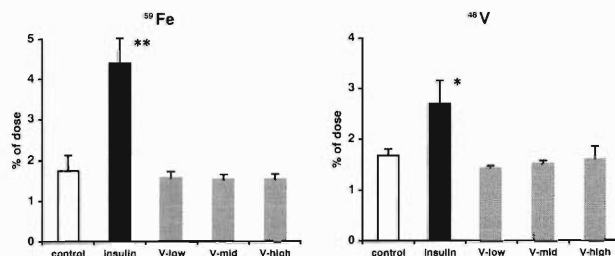


Fig. 1. Uptake ratios of  $^{59}\text{Fe}$  and  $^{48}\text{V}$  in each cell preparation at 2 hr after an addition of the multitracer solution in the cell suspension treated with insulin (4 nM) or vanadyl sulfate (V-low;  $1 \times 10^{-4}$ , V-mid;  $5 \times 10^{-4}$ , V-high;  $1 \times 10^{-3}$  mM), and in the untreated cell suspension (control group). Data are expressed as means  $\pm$ SD for 3 preparations. Significance level: \* $p < 0.05$  and \*\* $p < 0.01$  vs. control group.

tivity levels in the cells were measured by  $\gamma$ -ray spectrometry (Ortec GEM, ParkinElmer). The observed  $\gamma$ -rays were analyzed in terms of their energies and half-lives. In this study, we focused on the data of  $^{59}\text{Fe}$  and  $^{48}\text{V}$ . Their uptake rates (% dose/ $2.7 \times 10^6$  cells) were calculated.

The mean uptake ratios of  $^{59}\text{Fe}$  and  $^{48}\text{V}$ , both of which were bound to apo-transferrin, were determined in adipocytes of each group. The uptake ratios of both elements increased with the stimulation of insulin, however, the ratios were not significantly different between the control group and the vanadyl-treated group (Fig. 1).

These results indicate that the vanadyl ion treatment nearly stimulates the translocation of transferrin receptors from the cytosol to the plasma membrane in rat adipocytes as well as that of glucose transporters, suggesting the importance of roles of the vanadyl ion other than as glucose transporters in adipocytes.

### References

- 1) L. I. Tanner and G. E. Lienhard: *J. Biol. Chem.* **262**, 8975 (1987).
- 2) S. Tang, B. Lu, and I. G. Fantus: *Metabolism* **47**, 630 (1998).
- 3) M. Nakai, H. Watanabe, C. Fujiwara, H. Kakegawa, T. Satoh, J. Takada, R. Matsushita, and H. Sakurai: *Biol. Pharm. Bull.* **18**, 719 (1995).

\* Department of Analytical and Biomorganic Chemistry, Kyoto Pharmaceutical University

## Abnormal metabolism of trace elements in mouse caused by Zn-deficiency during the growth period

T. Ohyama,<sup>\*1</sup> M. Yanaga,<sup>\*1</sup> H. Maetsu,<sup>\*1</sup> M. Noguchi,<sup>\*2</sup> H. Suganuma,<sup>\*1</sup> K. Ishikawa,<sup>\*2</sup> R. Hirunuma,<sup>\*</sup> S. Enomoto, and T. Omori<sup>\*1</sup>

Zinc is a very important element in terms of health. More than 300 different enzymes in the body depend on Zn to work properly. Recently, loss of the taste in young generation caused by Zn-deficiency is increasing in Japan.

In our previous works, abnormal metabolisms of Zn and other trace elements, such as Co, Fe and Mn, in addition to various symptoms were observed in Zn-deficient mice.<sup>1)</sup> Furthermore, we also found a correlation between Zn and Co concentrations in the liver of mice fed with a Zn-deficient diet during the growth period.<sup>1)</sup> However, details of the mechanism of the change in metabolism of Zn and Co during the growth period have not been clarified yet. Therefore, in the present work, we investigated the behavior of Zn and other trace elements in mice fed with a Zn-deficient diet during the growth period after weaning using the multitracer technique. We compared the results with those for the adult mice fed with the Zn-deficient diet<sup>2,3)</sup> in order to obtain more knowledge regarding the functions and interdependencies between Zn and other trace elements in growing organisms.

Three-week old (growing mice) and 8-week old (adult mice) male mice of the ICR strain were divided into two groups; one group was fed with the Zn-deficient diet and distilled water (Zn-def. mice), and the other group was fed with the control diet and distilled water (control mice). After 3 weeks of this treatment, a multitracer solution, which was prepared from an Ag target, was orally administered or intraperitoneally injected into each mouse. Six, 24 and 72 hours after administration, various organs and tissues, such as the liver, kidney, pancreas, testis, bone, and intestine were removed and subjected to gamma-spectrometries. The oral administration method (oral) is suitable for determination of the amounts of administered trace elements absorbed through the small intestine and their distribution in the organs and tissues. On the other hand, total amounts of trace elements are absorbed when the intraperitoneal injection method (i.p.) is adopted. Therefore, results obtained using the second methods will reflect only the distribution of trace elements in the body after injection.

When the multitracer solution was orally administered to the growing or adult mice, Zn and Co uptake levels in several organs and tissues of Zn-def. mice were higher than those of control mice. This suggests that

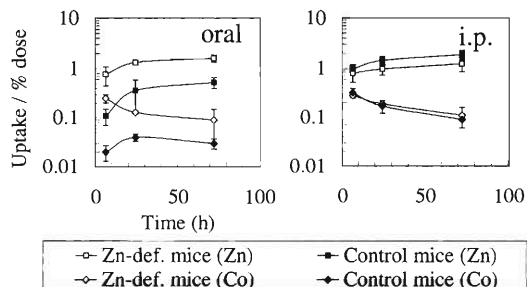


Fig. 1. Zn and Co uptake levels in bone of growing mice after oral administration and intraperitoneal injection.

Co uptake from the small intestine increased with an increase in the Zn uptake level. On the other hand, when injected intraperitoneally, such a significant enhancement of Zn and Co uptakes was not observed. On the contrary, as shown in Fig. 1, the Zn uptake levels in the bone and pancreas of Zn-def. growing mice were lower than those of control growing mice. This trend agrees with the results for INAA.<sup>1)</sup> The Zn concentrations in the bone and pancreas of Zn-def. growing mice were much lower than those of control growing mice. The INAA data indicated that Zn, which had accumulated in the bone and/or pancreas, was transported to other organs and tissues of Zn-def. growing mice which required more Zn to support their functions.

The Mn uptake levels in the liver and all the other investigated organs and tissues of growing mice were significantly higher than those of adult mice. Feure and Joel reported that the absorption levels of Mn in young animals were higher than those in adult animals, generally because of incomplete maturation of the intestine walls in young animals.<sup>4)</sup> This may be one of the reasons for the increase in Mn uptake levels in growing mice.

### References

- 1) M. Yanaga et al.: J. Radioanal. Nucl. Chem. **231**, 187 (1998); J. Radioanal. Nucl. Chem. **243**, 661 (2000); J. Radioanal. Nucl. Chem. **245**, 255 (2000).
- 2) T. Ohyama et al.: RIKEN Accel Prog. Rep. **34**, 142 (2001).
- 3) T. Ohyama et al.: J. Radioanal. Nucl. Chem. in press.
- 4) M. E. Le Feure and D. D. Joel: Life Sci. Stal. **28**, 96 (1977).

<sup>\*1</sup> Faculty of Science, Shizuoka University

<sup>\*2</sup> Department of Biology and Geosciences, Faculty of Science, Shizuoka University

## Brain regional uptake of trace elements in normal mice during development

T. Tarohda,<sup>\*1,\*2</sup> Y. Yabushita,<sup>\*3</sup> Y. Kanayama,<sup>\*3</sup> R. Amano,<sup>\*3</sup> and S. Enomoto

The knowledge of the function and metabolic behavior of trace essential elements in a variety of brain regions is of great importance. Through studying the physiological and biochemical roles of essential elements, a dramatic metabolic change can be described during the development of the brain. In the previous study, the brain uptake behavior of Mn, Zn and Se was examined. They showed that uptake rates in 1-day-old mice were higher than those in 4-, 8-, 21-, and 56-day-old mice, and the uptake of Mn was higher than that of Zn and Se for 1-day-old to 8-day-old mouse brains. In the present work we focused on the brain regional uptake of Mn, Zn and Se during the developmental stage, that is 1 day to 21 days.

Twenty normal ICR mice were used for this experiment. The mice were classified into four groups according to age (1-, 4-, 8-, and 21-day-old mice). An appropriate amount of the multitracer solution was injected intraperitoneally (*i.p.*) into each mouse (0.1 ml/5 g mouse weight). The mice were sacrificed and perfused with 0.9% NaCl solution under ether anesthesia 48 hours after the *i.p.* injection. The samples were divided into six regions; striatum (ST), cerebral cortex (CC), cerebellum (CB), hippocampus (HI), thalamus plus hypothalamus (TH) and midbrain plus pons plus medulla oblongate (MP). The uptake behavior was evaluated in terms of the regional uptake rates (% dose/g).

Figure 1 compares the regional uptake rates in the ST, CC, CB, HI, TH and MP of the brains of normal 1-, 4-, 8-, and 21-day-old mice 48 hours after the *i.p.* injection. Of all the age groups examined (1-, 4-, 8-, 21-, and 56-day-old), the regional uptake rates of Mn, Zn and Se were highest in 1-day-old mice. In comparison to the regional uptake rates of Zn and Se, the Mn regional uptake rates were higher in 1-day-old to 8-day-old mice for all brain regions, although the concentration of Mn is normally much lower than that of Zn in the brain. Mn concentration in 1-day-old mouse brains is much lower than that in 21-day-old mouse brains, and Mn concentration in the brain rapidly increased with growth in 1- to 21-day-old mice. These results suggest that Mn is crucial during the earlier stages of development. An interesting contrast is that in the all regions of the 21-day-old specimen, out of the three elements, zinc had the highest uptake rate. In the 21-day-old hippocampus, it was found that the highest trace uptake had changed from Mn to Zn (called the "turning point"), and moreover, the Zn uptake rates increased in 8-day-old to 21-day-old mice. These results suggest that the role of Zn is crucial in the later stages of development in the hippocampus. The turning point at 21 days underlines the shift in the respective roles of Mn, Zn and Se elements during development, particularly as seen in the hippocampus.

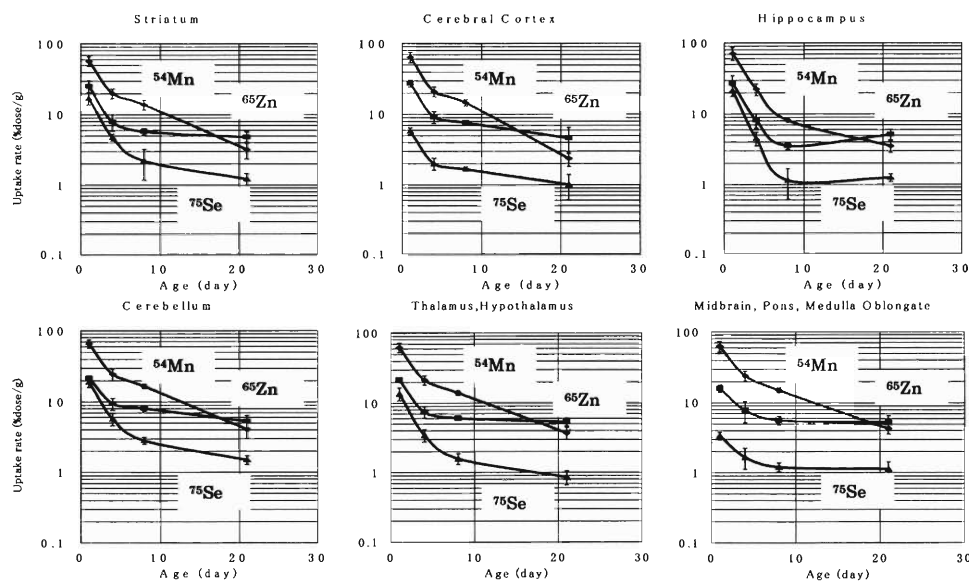


Fig. 1. Brain regions uptake rates of  $^{54}\text{Mn}$ ,  $^{65}\text{Zn}$ , and  $^{75}\text{Se}$  in normal 1-, 4-, 8-, and 21-day-old mice 48 hours after *i.p.* injection of multitracer solution. Date is expressed as means  $\pm$  S.D. ( $n = 5$ ).

<sup>\*1</sup> Graduate School of Natural Science and Technology, Kanazawa University

<sup>\*2</sup> Asanogawa General Hospital

<sup>\*3</sup> Faculty of Medicine, Kanazawa University

## Brain regional tracer uptake and elemental concentration in mice fed Zn-deficient and -excessive diets

Y. Yabushita,\*<sup>1</sup> Y. Kanayama,\*<sup>1</sup> T. Tarohda,\*<sup>2</sup> R. Amano,\*<sup>1</sup> and S. Enomoto

Zinc (Zn) is a cofactor of many proteins distributed among all enzyme classes and has diverse functions in brain homeostasis.<sup>1)</sup> Lack of Zn was shown to result in poor growth, alopecia, and anostosis,<sup>2)</sup> and its excess intake leads to toxicity. It is thought that these symptoms are caused by various element (Zn)-element (others) interrelationships rather than by the influence of the single Zn element. In this work, we examined the brain regional tracer uptake and the elemental concentration in mice fed Zn-deficient and -excessive diets in order to obtain some information about element (Zn)-element (others) interrelationships.

Dam ICR mice were fed Zn-deficient (1) (Zn concentration: 0.7 ppm), Zn-deficient (2) (3.6 ppm), Zn-adequate (36.0 ppm) or Zn-excessive (3520 ppm) diets and pure water from the 16th day of pregnancy. Natal mice pups were nurtured to three weeks and bred with their dams. Three-week-old weanling male mice ( $n = 5$ ) were used for the experiment. It was difficult for the mice to survive in the Zn-deficient (1) state; only one mouse survived. The multitracer solution was intraperitoneally (i.p.) injected into the mice. Forty-eight hours after i.p. injection, the brain was excised and dissected into eight regions. Each of the eight regions was weighed and freeze-dried immediately. The dried samples were measured using  $\gamma$ -ray spectra with a high-purity Ge detector and evaluated in terms of "brain regional uptake rate (% dose/g)." Identical

samples were analyzed using instrumental neutron activation analysis (INAA) and evaluated. As a result, the multitracer solution enabled the simultaneous tracing of  $^{46}\text{Sc}$ ,  $^{54}\text{Mn}$ ,  $^{58}\text{Co}$ ,  $^{65}\text{Zn}$ ,  $^{75}\text{Se}$ , and  $^{83}\text{Rb}$  in all brain regions. Figure 1 shows the brain regional uptake rates of  $^{65}\text{Zn}$ ,  $^{46}\text{Sc}$ ,  $^{54}\text{Mn}$ ,  $^{58}\text{Co}$ ,  $^{75}\text{Se}$ , and  $^{83}\text{Rb}$  in Zn-deficient, -adequate, and -excessive mice. The  $^{65}\text{Zn}$  uptake rates of Zn-excessive mice were significantly lower than those of Zn-adequate mice. However, all other tracers except for  $^{65}\text{Zn}$  of Zn-excessive mice were significantly higher than those of Zn-adequate mice. The  $^{83}\text{Rb}$  uptake rates of Zn-deficient (2) mice were significantly higher than those of Zn-adequate mice. Using the INAA method, the concentrations of Zn in all brain regions were determined. No significant difference in Zn concentrations in each region was observed among the four diet groups.

These findings suggest that Zn-deficient and -excessive states influence the tracer uptake rates except for  $^{65}\text{Zn}$ , however, the Zn concentration in mouse brain is not influenced by the Zn concentration of diets.

### References

- 1) J. R. Prohaska: *Physiol. Rev.* **67**, 858 (1987).
- 2) R. M. Leach et al.: in *Handbook of Nutritionally Essential Mineral Elements* (Marchel Dekker, New York, 1997), p. 185.

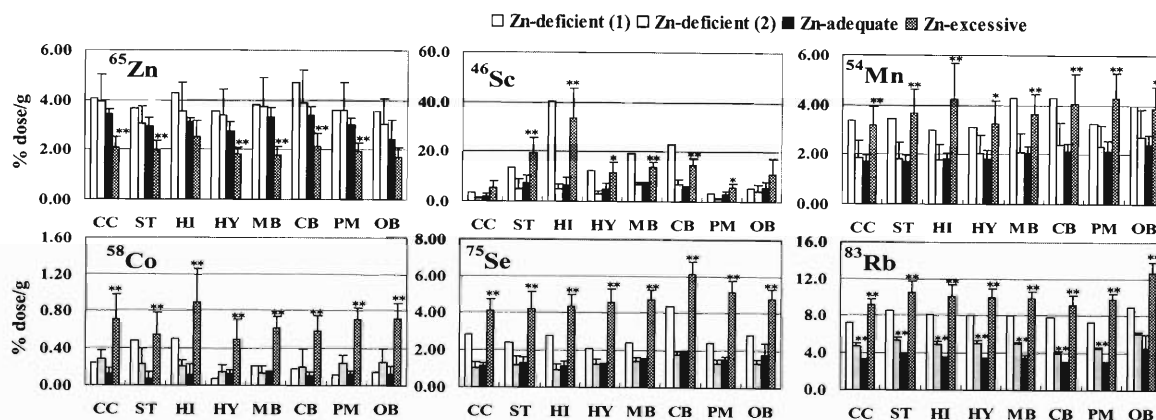


Fig. 1. Brain regional uptake rates of  $^{65}\text{Zn}$ ,  $^{46}\text{Sc}$ ,  $^{54}\text{Mn}$ ,  $^{58}\text{Co}$ ,  $^{75}\text{Se}$ , and  $^{83}\text{Rb}$  in Zn-deficient, -adequate, and -excessive mice. CC: cerebral cortex; ST: corpus striatum; HI: hippocampus; HY: thalamus and hypothalamus; MB: midbrain; CB: cerebellum; PM: pons and medulla; OB: olfactory bulb. The bar and the line represent the mean  $\pm$ S.D. for five mice. Asterisks indicate significant differences (\* $p < 0.05$ , \*\* $p < 0.01$ ) for Zn-adequate mice.

\*<sup>1</sup> Faculty of Medicine, Kanazawa University

\*<sup>2</sup> Graduate School of Natural Science and Technology, Kanazawa University

## Subcellular distribution of trace elements in mouse brain regions using the multitracer technique

Y. Kanayama,\* T. Tsuji,\* R. Amano,\* and S. Enomoto

In our previous work, we have studied the subcellular distribution of several trace elements in the brain, and then fundamental results regarding the distribution were used to determine biochemical or physiological functions of trace elements.<sup>1)</sup> To improve our experimental procedure, we divided the brain into smaller regions such as the cerebral cortex (CC), hippocampus (HI), and corpus striatum (ST). In this study, we examined the subcellular distribution of several radioactive tracers in the brain regions of normal mice, particularly in the CC, HI, and ST.

Five normal male ICR mice (6 weeks old; body weight, 31–34 g) were used in this experiment. A multitracer solution obtained from RIKEN Ring Cyclotron was prepared as a physiological saline solution. Twenty-four hours after the intraperitoneal (i.p.) injection of the multitracer solution, each mouse was perfused with a physiological saline under ether anesthesia. After excision of the brains, the CC, HI and ST were removed from the brains and weighed immediately. Subcellular fractionation was performed according to the method of Hajós.<sup>2)</sup> Each region was homogenized in 3 ml an ice-cold 0.32 M sucrose solution containing 0.01 M Tris-HCl buffer solution at pH 7.0. The nuclear fraction (NU) was obtained by centrifuging the homogenates at  $1,000 \times g$  for 10 min. The remainder was then divided into the supernatant fraction (SU) and the pellet by centrifuging at  $15,000 \times g$  for 30 min. The pellet was resuspended in 1 ml of 0.32 M sucrose solution. The suspension was carefully layered over a 0.8 M/1.2 M sucrose concentration gradient, and then ultracentrifuged at  $63,000 \times g$  for 2 hr. Finally, particles were resolved into the following fractions: the myelinated axonal fraction (MY) at the 0.32 M–0.8 M sucrose interface, the synaptosomal fraction (SY) at the 0.8 M–1.2 M sucrose interface and the mitochondrial fraction (MI) as the pellet. Each fraction was freeze-dried, and then subjected to  $\gamma$ -ray spectrometry. The uptake behavior was estimated in terms of relative subcellular fractional uptake rate (%).

As a result, the multitracer method enabled simultaneous tracing of  $^{46}\text{Sc}$ ,  $^{54}\text{Mn}$ ,  $^{58}\text{Co}$ ,  $^{65}\text{Zn}$ ,  $^{75}\text{Se}$ ,  $^{83}\text{Rb}$ ,  $^{88}\text{Zr}$ ,  $^{103}\text{Ru}$  and  $^{101}\text{Rh}$ . Figure 1 compares the rela-

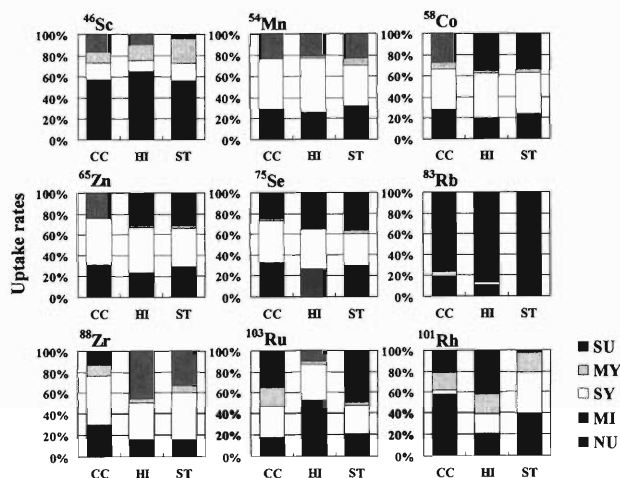


Fig. 1. Relative subcellular fractional uptake rates (%) of  $^{46}\text{Sc}$ ,  $^{54}\text{Mn}$ ,  $^{58}\text{Co}$ ,  $^{65}\text{Zn}$ ,  $^{75}\text{Se}$ ,  $^{83}\text{Rb}$ ,  $^{88}\text{Zr}$ ,  $^{103}\text{Ru}$ , and  $^{101}\text{Rh}$  in the cerebral cortex, hippocampus and corpus striatum. Abbreviations are defined as follows: SU, supernatant fraction; MY, myelinated axonal fraction; SY, synaptosomal fraction; MI, mitochondrial fraction; and NU, nuclear fraction.

tive subcellular fractional uptake rates in regions CC, HI and ST. Based on the uptake rates of  $^{54}\text{Mn}$ ,  $^{58}\text{Co}$ ,  $^{65}\text{Zn}$  and  $^{75}\text{Se}$ , it was noted that these elements are accumulated in the SY from all the brain regions.  $^{83}\text{Rb}$  is predominantly accumulated in the supernatant fraction. Based on the  $^{54}\text{Mn}$  uptake rate, the SY fractional percentage of the HI is the highest among the brain regions studied. The subcellular distribution of  $^{65}\text{Zn}$  is very similar to that of  $^{75}\text{Se}$ .

This subcellular fractionation technique described here is a useful and valuable tool for studies of chemical speciation of trace elements in the brain.

### References

- 1) R. Amano et al.: RIKEN Accel. Prog. Rep. **31**, 126 (1998).
- 2) F. Hajós: Brain Res. **93**, 485 (1975).

\* School of Health Sciences, Faculty of Medicine, Kanazawa University

## Lateral and sexual differences in concentrations of trace elements in cerebral cortex of normal mice

Y. Kanayama,\* Y. Yabushita,\* R. Amano,\* and S. Enomoto

There are few studies on the lateral and sexual differences in the behavior of trace elements in the brain. Recently, Panayi *et al.* examined the differences in trace-element concentrations between normal and Alzheimer's disease brains, and reported that there are differences between the right and left hemispheres of such brains.<sup>1)</sup> Diamond *et al.* reported that environmental enrichment induces formation of a thicker cortex in rats and sexual difference is observed as well.<sup>2)</sup> In the present work, we focused on the lateral and sexual differences in the concentrations of trace elements in the cerebral cortex by a multitracer technique and instrumental neutron activation analysis (INAA).

A multitracer was prepared from an Ag target irradiated with  $^{14}\text{N}$  beam of 135 MeV/nucleon, which was accelerated in the RIKEN Ring Cyclotron. After the chemical separation of the target, the multitracer solution for injection, which is a slightly acidic physiological saline solution (pH 2-3), was prepared.

Six male and six female normal ICR mice (4 weeks old) were used in this experiment. Forty-eight hours after intraperitoneal injection of the multitracer solution, the mice were sacrificed and perfused with physiological saline under ether anesthesia. Each brain was dissected and divided into the left and right hemispheres, and then cerebral cortical sections of each hemisphere were obtained (the obtained left and right cerebral cortical regions were in the same position). After immediate weighing and freeze-drying of the cortex samples, the radionuclides uptake behavior was evaluated in terms of brain regional uptake rates (%dose/g).

Identical cerebral cortex samples were subjected to INAA. The samples were irradiated for 2, 5, and 40 min, using a pneumatic tube system connected to the core Pn-3 site, the graphite thermal column Tc-Pn site and the core Pn-2 site of the Kyoto University Reactor. The activities ( $^{24}\text{Na}$ ,  $^{27}\text{Mg}$ ,  $^{28}\text{Al}$ ,  $^{38}\text{Cl}$ ,  $^{42}\text{K}$ ,  $^{56}\text{Mn}$ ,  $^{65}\text{Zn}$ ,  $^{82}\text{Br}$ , and  $^{86}\text{Rb}$ ) produced were measured by  $\gamma$ -ray spectrometry using detectors made of highly pure Ge, and then their concentrations were determined and expressed in  $\mu\text{g/g}$  wet weight.

The use of multitracer solution enabled simultaneous tracing of the radionuclides  $^{54}\text{Mn}$ ,  $^{65}\text{Zn}$ ,  $^{75}\text{Se}$ , and  $^{83}\text{Rb}$  in the cerebral cortex and accurate comparison of their uptake behavior. Figure 1 shows the typical results of the uptake rates of  $^{54}\text{Mn}$  and  $^{65}\text{Zn}$  in the cerebral cortices of the left and right hemispheres of the male and female mice. From these results, the uptake rates were comparable with those obtained in our previous

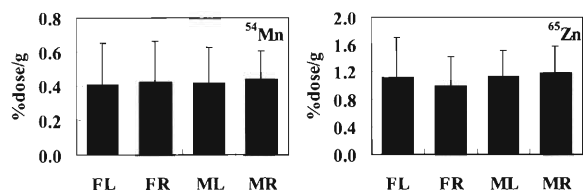


Fig. 1.  $^{54}\text{Mn}$  and  $^{65}\text{Zn}$  uptake rates in the cerebral cortices of normal mice ( $n = 6$  for each group). Abbreviations indicate as follows: FL, female-left cortex; FR, female-right cortex; ML, male-left cortex; MR, male-right cortex.

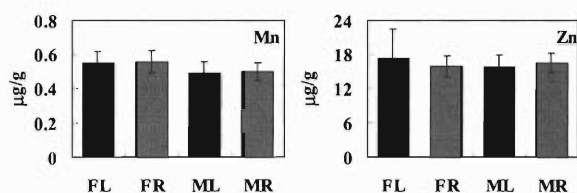


Fig. 2. Concentrations of Mn and Zn in the cerebral cortices of normal mice ( $n = 6$  for each group). Abbreviations indicate as follows: FL, female-left cortex; FR, female-right cortex; ML, male-left cortex; MR, male-right cortex.

studies.<sup>3)</sup> It was found that there was no significant difference in the cerebral cortical uptake rate of Mn and Zn between the right and left hemispheres, and/or between the male and female mice.

On the other hand, the concentrations of Na, Mg, Al, Cl, K, Mn, Zn, Br, and Rb are compared for identical samples; typical results for Mn and Zn are shown in Fig. 2. The Mn and Zn concentrations were also in agreement with our previously obtained values. Moreover, no significant difference was observed between the left and right hemispheres, and/or between the male and female mice.

In the future, studies of subjects with a neurodegenerative disease that have a notable lateralization or sexual difference, the two techniques (multitracer and INAA techniques) are potentially useful tools for determining abnormal metabolism in their brains.

### References

- 1) A. E. Panayi *et al.*: J. Radioanal. Nucl. Chem. **244**, 205 (2000).
- 2) M. C. Diamond *et al.*: Behav. Biol. **14**, 163 (1975).
- 3) Y. Yabushita *et al.*: RIKEN Rev., No. 35, 64 (2001).

\* School of Health Sciences, Faculty of Medicine, Kanazawa University

## Trace-element transfer from pregnant mice to the fetuses

T. Tsuji,\* A. Kanbara,\* R. Amano,\* E. Hirunuma, and S. Enomoto

It is interesting to study the function of the placenta as a barrier between the maternal body and the fetus, in which passage of nutrients, oxygen and waste between the maternal body and the fetus is regulated in a constant state. The fetus can accumulate and utilize essential trace elements through the placenta from the maternal body before birth. Enomoto *et al.* have studied the placenta function by a multitracer technique.<sup>1)</sup> In the present study, we also examined the quantitative uptake and retention of trace elements in the placenta, fetus, and amniotic fluid using a multitracer technique, and focused on some trace elements in the fetus immediately before birth.

A multitracer solution containing 13 radioactive isotopes (<sup>7</sup>Be, <sup>46</sup>Sc, <sup>48</sup>V, <sup>54</sup>Mn, <sup>58</sup>Co, <sup>59</sup>Fe, <sup>65</sup>Zn, <sup>75</sup>Se, <sup>83</sup>Rb, <sup>85</sup>Sr, <sup>88</sup>Zr, <sup>99</sup>Rh and <sup>103</sup>Ru) was prepared according to the method of Ambe *et al.*<sup>2)</sup> Two sixteen-day-pregnant CD-1 (ICR) dams were used for this experiment. Multitracer physiological saline (0.1 ml) was injected intravenously (i.v) into the mice via their tail. The mice were sacrificed under ether anesthesia 48 hours after i.v injection. The maternal blood, placentas and fetuses were excised and the amniotic fluids were collected; all were weighed immediately and freeze dried. The radioactivity of each dried sample was determined by  $\gamma$ -ray spectrometry using high-purity Ge detectors. The uptake behavior was evaluated in terms of uptake percentage of the injected multitracer (%).

The thirteen radioactive isotopes mentioned above were observed and evaluated in the maternal blood, placentas, fetuses and amniotic fluids in the last stage of pregnancy (18-day-pregnant dams and fetuses), as shown in Table 1. From results in Table 1, we can understand the transport, retention and excretion of these isotopes across the barrier system of the maternal blood—placentas—fetuses. Trace elements such as Be, Sc, Zr, and Ru were mainly transferred, accumulated and retained in the placentas. In particular, the Sc uptake percentage in the placentas was about 290 times that in the maternal blood and Sc hardly passed through the placental membrane into the fetuses. On the other hand, the other nine trace elements (V, Mn, Co, Fe, Zn, Se, Rb, Sr and Rh) were transferred through the placenta and mostly accumulated in the fetuses. The uptake percentage of Sr was about 130 times higher in the fetuses than in the maternal blood, and about 97 times higher in the fetuses than in the placentas. Namely, a large amount of Sr was transported and concentrated in fetuses. It can therefore be presumed that the accumulation of Sr is involved in active bone formation in fetuses and that Sr

Table 1. Uptake percentages of 13 trace elements (Be, Sc, V, Mn, Co, Fe, Zn, Se, Rb, Sr, Zr, Rh, and Ru) in the maternal blood, placentas, fetuses and amniotic fluids 48 hours after i.v injection. (unit: %)

	Maternal Blood*	Placenta**	Fetus**	Amniotic Fluid***
<sup>7</sup> Be	0.36	0.93±0.15	0.75±0.11	0.01
<sup>46</sup> Sc	0.18	52.85±4.36	N.D.	0.05
<sup>48</sup> V	0.29	3.00±0.26	9.27±0.75	0.24
<sup>54</sup> Mn	0.86	1.51±0.37	8.13±0.68	0.20
<sup>58</sup> Co	0.09	0.35±0.07	2.45±0.03	0.10
<sup>59</sup> Fe	15.57	12.12±4.91	46.78±2.82	0.07
<sup>65</sup> Zn	0.98	2.50±0.28	36.74±2.12	0.16
<sup>75</sup> Se	1.51	2.58±0.31	14.57±0.27	0.31
<sup>83</sup> Rb	2.69	2.11±0.18	14.06±0.51	0.18
<sup>85</sup> Sr	0.07	0.09±0.01	8.55±0.52	0.05
<sup>88</sup> Zr	0.33	3.54±0.66	1.07±0.11	0.06
<sup>99</sup> Rh	2.03	1.78±0.22	12.97±0.28	0.13
<sup>103</sup> Ru	0.42	0.85±0.23	0.59±0.60	0.12

\* The total blood volume calculated by multiplication of body weight by 0.07.

\*\* Each pregnant mouse had 13 placentas and fetuses on average.

\*\*\* The total volume of amniotic fluids used was 1.659 g as reported in the literature.<sup>3)</sup>

N. D. indicates "not detected"; in this case, its detection limit was estimated to be 0.03%.

is one of the bone-accumulating elements. Table 1 also shows that V, Mn, Zn, and Se, which are considered to be essential trace elements in fetuses, have similar types of uptake behavior in the maternal blood, placentas, fetuses and amniotic fluids. On the other hand, the uptake percentages of Fe and Rb in the maternal blood were equal to or slightly higher than those in the placenta. This can be explained by the fact that Fe and Rb (analogous to K) are transported into the placenta and easily pass across the maternal blood, placenta tissue and fetus.

In our laboratory, the examination of the distribution of some trace elements in the organ and tissue in fetuses immediately before birth and in pups immediately after birth is in progress. In the future, we hope to discuss on the involvement of some important elements in the final crucial stage of pregnancy and in the early stage of development.

### References

- 1) S. Enomoto et al.: RIKEN Accel. Prog. Rep. **33**, 111 (2000); **34**, 126 (2001); **34**, 127 (2001).
- 2) Ambe group had developed the multitracer method in RIKEN and reported it in: Chem. Lett. **1991**, 149; Anal. Sci. **7**, Suppl., 317 (1991); J. Radioanal. Nucl. Chem. **195**, 297 (1991).
- 3) Y. Tajima et al.: in *Biological Reference Data Book on Experiment Animals* (in Japanese) (Soft Science, Tokyo, 1989), p. 247.

\* Faculty of Medicine, Kanazawa University

## Influence of sodium iron ethylenediaminetetraacetic acid and ferrous sulfate on the transport of trace elements in everted intestinal segments of rats

K. Igarashi,\* Y. Nakanishi,\* R. Hirunuma, S. Enomoto, and S. Kimura\*

Iron deficiency in developing countries is largely due to the poor absorption of iron from their food-stuffs. The staple foods, such as grains, vegetables and legumes, contain non-heme iron, which has a low intestinal absorption efficiency compared with heme iron. Heme iron from meat and meat products is absorbed as an intact porphyrin structure by specific receptors in the brush border mucosa. On the other hand, non-heme iron must be solubilized to be absorbed from intestine. Furthermore, the staple foods also contain inhibitors of iron absorption such as phytic acid and polyphenols. The bioavailability of non-heme iron is extremely low because these inhibitors bind iron in the intestinal lumen. The absorption rate of vegetable iron is only about 1–2%.<sup>1)</sup> Iron is taken up from the lumen and retained in the mucosa, and a fraction is transferred out of the mucosa into the organism. Iron transport occurs primarily in the duodenum, jejunum and ileum, which adapt iron absorption capacity in response to changes in body iron stores. Distal parts of intestine show no regulation and are markedly less efficient in the transport of iron.

Since iron deficiency is attributed to poor absorption of dietary iron, food fortification is assumed to be an effective method for enhancing iron absorption. Food fortification has also been recommended as a long-term approach for improving iron deficiency. Therefore, iron fortification programs have been implemented to prevent iron deficiency in many developing countries.<sup>2–6)</sup>

Sodium iron ethylenediaminetetraacetic acid (NaFeEDTA), a metal chelate, is one of the fortificants used in food fortification programs. It is a flavorless, inert compound. It is reported that the bioavailability of NaFeEDTA is negligibly influenced by inhibitors of iron absorption, indicating that NaFeEDTA is a suitable food additive for iron fortification. On the other hand, it is possible that EDTA may bind to metals other than iron and influence their absorption because of its strong chelating property. In a previous study, it was shown that NaFeEDTA may possibly inhibit the incorporation of Zn and Co into rat organs because of its chelating property, although the results suggest that NaFeEDTA is not affected by tannic acid in the absorption of various elements.

Thus, to investigate the effects of NaFeEDTA and ferrous sulfate (FeSO<sub>4</sub>) on the transport of various trace elements, we determined the uptake rates of trace

Table 1. Composition of Tyrode solution.

	mmol/l
NaCl	137.00
KCl	2.70
NaH <sub>2</sub> PO <sub>4</sub>	12.00
D-glucose	15.00
NaHCO <sub>3</sub>	0.40
CaCl <sub>2</sub> ·2H <sub>2</sub> O	0.14
MgCl <sub>2</sub> ·6H <sub>2</sub> O	0.05

elements in everted intestinal segments of rats, using a multitracer technique. We further determined the effect of tannic acid on the incorporation of trace elements.

Seven-week-old male Wistar rats were purchased from Charles River Japan, Inc. and were housed in stainless steel cages. The cages were placed in an air-conditioned room with 12 h of light. They had free access to diet and drinking water.

The rats were subjected to overnight fasting and then their abdomens were opened under anesthesia. A 6-cm-long segment of each of the duodenum, jejunum and ileum was removed and everted. The segments were filled with 0.6 ml of buffer shown in Table 1 (pH 7.2), and then incubated with 10 ml of buffer containing NaFeEDTA or FeSO<sub>4</sub> and Ag-derived multitracer solution for 1 h. The perfusion was kept equilibrated with 95% O<sub>2</sub> and 5% CO<sub>2</sub> at 37°C. After incubation, the serosal solution were collected. These samples were placed in a Ge detector, and the radioactivities of the multitracers were measured.

The data on the biodistribution of samples are currently being analyzed. The experimental results obtained will indicate the mechanism of metal transport in the intestine and the effects of NaFeEDTA and FeSO<sub>4</sub> on intestinal uptake.

### References

- 1) L. Hallberg: *Ann. Rev. Nutr.* **1**, 123 (1981).
- 2) M. Olivarez, F. Pizarro, and O. Pineda: *J. Nutr.* **127**, 1407 (1997).
- 3) R. F. Florentino and M. R. A. Pedro: *Food Nutr. Bull.* **19**, 149 (1998).
- 4) V. Chavasit and K. Tontisirin: *Food Nutr. Bull.* **19**, 164 (1998).
- 5) C. Iost, J. J. Name, R. B. Jeppsen, and H. D. Ashmead: *J. Am. Coll. Nutr.* **17**, 187 (1998).
- 6) M. Layrisse, J. F. Chaves, and H. Mendez-Castellano: *Am. J. Clin. Nutr.* **64**, 903 (1996).

\* Graduate School of Human Life Sciences, Showa Women's University

## Metabolic studies on multitracer-injected rats and plants using a prototype multitracer gamma-ray emission imaging system (MT-GREI): A proposal

R. Hirunuma, S. Motomura,\*<sup>1</sup> Y. Gono,\*<sup>1</sup> R. Amano,\*<sup>2</sup> and S. Enomoto

It was proposed in multitracer research that the uptake distribution of various elements in rats and plants be examined using a new  $\gamma$ -ray detection system, multitracer  $\gamma$ -ray emission imaging (MT-GREI). A multitracer technique has been developed using the RIKEN Ring Cyclotron. The technique has been applied for the investigation of the behavior of various radioactive trace elements in chemistry, biology, pharmacology, medical sciences, and environmental science. The technique has the advantage that the behavior of various elements can be determined under strictly identical conditions. However, with the present technology, a sample has to be separated into parts and to be measured them individually. And the behavior of tracer isotopes must be confirmed. MT-GREI is proposed to identify the positions of all isotopes simultaneously. This system uses two segmented Ge detectors. A high-energy-resolution Compton camera consisting of two segmented Ge detectors was used to measure the positions of many isotopes in a sample simultaneously. Segmented Ge detectors were developed to fabricate Ge telescopes combined with large-sized Ge detectors.<sup>1)</sup> Their dimensions are  $50 \times 50 \times 20 \text{ mm}^3$ , and their cathodes are divided into 25 segments of  $10 \times 10 \text{ mm}^2$  area. The segmented Ge detector was combined with a large-sized Ge detector. They were used as a telescope and successfully corrected Doppler shifts of energies of  $\gamma$ -rays emitted from rapidly recoiling reaction products. Two segmented Ge detectors can be used for identifying the  $\gamma$ -ray source position when they are used as a telescope (a Compton camera). Monte-Carlo simulation was performed to optimize the conditions for the design of this system.<sup>2,3)</sup>

The multitracer is prepared from Ti, Ag, and Au foils irradiated with  $^{12}\text{C}$ ,  $^{14}\text{N}$ , and  $^{16}\text{O}$  beams accelerated by the RIKEN Ring Cyclotron. The first ex-

periment is to examine the uptake distribution of various elements in the organs of rats using a multitracer. The multitracer solution is administered to the rats. One to three days after administration of the multitracer, the rats are sacrificed under deep diethyl ether anesthesia, frozen immediately, fixed with ice-cold 8% carboxymethyl cellulose, frozen on the specimen stage at  $-20^\circ\text{C}$ , and sliced to  $100 \mu\text{m}$  thickness at  $-20^\circ\text{C}$  with a microtome. The distribution of radioactivity in each area of the selected slices is determined by  $\gamma$ -ray measurement using MT-GREI.

The second experiment is to examine the uptake behavior of the multitracer in various plants (for example, komatsuna, tomato, and rice). The roots of the plants are kept for several weeks in the multitracer solution. After this uptake period, the roots are washed. The roots, leaves, stems, flowers, and seeds are dried at  $30^\circ\text{C}$ , and each dried sample is determined using MT-GREI.

The distribution of radioactivity of various nuclides in each area of the selected slice samples of rats and plants was possible to detect using MT-GREI. It is believed that in medical institutions MT-GREI can be used as a substitute for autoradiography.

This system enables the measurement of a sample without separating it, which is a great advantage when used for living things. This system is primarily designed for multitracer applications. Imaging multiple nuclides simultaneously becomes possible, and its application in nuclear medicine and clinical diagnosis is expected.

### References

- 1) Y. Gono et al.: Nucl. Phys. A **588**, 241c (1995).
- 2) Y. F. Yang et al.: IEEE Trans. Nucl. Sci. **48**, 656 (2001).
- 3) S. Motomura et al.: RIKEN Rev., No. 35, 116 (2001).

\*<sup>1</sup> Department of Physics, Faculty of Science, Kyushu University

\*<sup>2</sup> School of Health Sciences, Faculty of Medicine, Kanazawa University

## Alleviation of Cadmium cytotoxicity by manganese (II)

T. Yanagiya, N. Imura,\* S. Enomoto, and S. Himeno\*

Cadmium (Cd) is a highly toxic metal that causes adverse effects in organisms, however, little is known as to how Cd enters cells. Metallothionein (MT) plays an important role in Cd detoxification. Recently, we established a Cd-resistant cell line (Cd-rB5) from immortalized MT-null mouse fibroblasts, and found that Cd-rB5 cells exhibited a marked decrease in Mn and Cd uptake.<sup>1,2)</sup> Kinetic analyses revealed that Cd traverses cells partly via a high-affinity Mn transport system, and that the suppression of this pathway is one of the determinants of the reduced susceptibility to Cd in Cd-rB5 cells.<sup>2)</sup> To clarify the role of the transport system for Mn in the cytotoxicity of Cd, we examined the modulation of cytotoxicity and accumulation of Cd by Mn, using Cd-rB5 and their parental cells.

As shown in Table 1, the simultaneous addition of MnCl<sub>2</sub> to a medium alleviated the cytotoxicity of Cd in parental cells dose dependently. In addition, the accumulation of Cd in parental cells was reduced by the addition of MnCl<sub>2</sub>. In Cd-rB5 cells, however, Mn did not modulate either the cytotoxicity or the accumulation of Cd. These results suggest that Mn may compete with Cd in entering cells, leading to a reduction of Cd cytotoxicity.

We further examined the effect of other divalent metals such as Zn, Co, Ni, Fe and Cu, on Cd-induced cytotoxicity and Cd accumulation. The cytotoxicity and accumulation of Cd in parental cells was attenuated by the addition of ZnCl<sub>2</sub>, but not by CoCl<sub>2</sub>, NiCl<sub>2</sub>, FeSO<sub>4</sub> or CuCl<sub>2</sub>, suggesting that Zn may also have an affinity to the transport system for Mn and Cd.

In this study, we demonstrated that the simultaneous addition of Mn reduced both the cytotoxicity and accumulation of Cd in parental cells, but not in Cd-rB5 cells in which the high-affinity transport system for Mn does not function. These results also suggest that the transport system for Mn may be used for the uptake of Cd. Moreover, we also demonstrated that Zn reduced the cytotoxicity and accumulation of Cd only in parental cells. Although Zn is known to be an efficient inducer of MT, a primary factor for Cd detoxification, the reduction of Cd cytotoxicity by Zn in parental cells is due not to the induction of MT, but to the inhibition of Cd accumulation. Our findings obtained from MT-null cells suggested a new role of Zn as a blocker of cellular Cd accumulation via the high-affinity Mn transport system.

Table 1. Effect of simultaneous addition of MnCl<sub>2</sub>, ZnCl<sub>2</sub>, CoCl<sub>2</sub>, NiCl<sub>2</sub>, FeSO<sub>4</sub> or CuCl<sub>2</sub> on Cd-induced cytotoxicity and Cd accumulation in Cd-rB5 and parental cells.

Metals added to the medium (μM)		Parental cells		Cd-rB5 cells	
		IC <sub>50</sub> of Cd (μM) <sup>a</sup>	<sup>109</sup> Cd uptake (% of control) <sup>b</sup>	IC <sub>50</sub> of Cd (μM) <sup>a</sup>	<sup>109</sup> Cd uptake (% of control) <sup>b</sup>
MnCl <sub>2</sub>	0	2.21	100.0 ± 3.1	22.46	100.0 ± 2.0
	1	3.86	43.9 ± 1.4 *	21.33	97.0 ± 3.0
	3	7.13	17.3 ± 1.4 *	21.51	95.8 ± 4.7
	10	21.32	9.9 ± 0.2 *	20.10	95.6 ± 2.7
	20	22.17	9.0 ± 0.8 *	16.00	101.2 ± 7.9
ZnCl <sub>2</sub>	0	2.21	100.0 ± 1.2	22.46	100.0 ± 1.3
	1	2.31	97.1 ± 1.3	22.36	101.2 ± 3.1
	3	2.33	86.1 ± 3.4 *	21.77	97.2 ± 9.4
	10	5.64	50.0 ± 4.8 *	21.96	97.6 ± 5.6
	20	8.03	38.3 ± 1.8 *	21.36	107.5 ± 4.1
CoCl <sub>2</sub>	0	2.21	100.0 ± 7.6	22.46	100.0 ± 3.9
	1	2.45	104.4 ± 2.1	22.52	102.0 ± 4.8
	3	2.51	103.1 ± 3.3	21.09	98.7 ± 1.3
	10	2.42	101.6 ± 6.2	22.66	99.1 ± 2.8
	20	2.46	92.5 ± 3.6	22.97	99.9 ± 8.6
NiCl <sub>2</sub>	0	2.21	100.0 ± 6.5	22.46	100.0 ± 0.2
	1	2.40	97.4 ± 2.8	23.27	100.5 ± 1.5
	3	2.43	102.7 ± 2.9	22.91	98.6 ± 2.4
	10	2.32	96.6 ± 3.4	21.71	100.4 ± 4.0
	20	2.38	100.1 ± 1.4	22.16	100.6 ± 3.6
FeSO <sub>4</sub>	0	2.21	100.0 ± 3.2	22.46	100.0 ± 3.1
	1	2.39	101.7 ± 6.9	22.45	103.1 ± 5.5
	3	2.57	104.9 ± 2.6	22.27	100.9 ± 4.6
	10	2.59	101.2 ± 3.2	22.68	104.0 ± 5.0
	20	2.56	92.8 ± 2.2	22.09	103.5 ± 4.3
CuCl <sub>2</sub>	0	2.21	100.0 ± 2.5	22.46	100.0 ± 3.0
	1	2.51	98.3 ± 2.0	21.96	100.8 ± 3.2
	3	2.45	98.5 ± 1.4	21.11	98.3 ± 1.7
	10	2.55	90.0 ± 2.5 *	22.44	98.0 ± 2.5
	20	2.19	84.5 ± 1.7 *	22.30	98.2 ± 2.4

<sup>a</sup> Cells were exposed to CdCl<sub>2</sub> in the absence or presence of 1, 3, 10 and 20 μM MnCl<sub>2</sub>, ZnCl<sub>2</sub>, CoCl<sub>2</sub>, NiCl<sub>2</sub>, FeSO<sub>4</sub> or CuCl<sub>2</sub> for 48 h, and then the surviving cells were determined by MTT assay. The concentration of metals required to kill 50% of the cells as calculated by MTT assay.

<sup>b</sup> Cells were exposed to 2 μM [<sup>109</sup>Cd]-CdCl<sub>2</sub> in the absence or presence of 1, 3, 10 and 20 μM MnCl<sub>2</sub>, ZnCl<sub>2</sub>, CoCl<sub>2</sub>, NiCl<sub>2</sub>, FeSO<sub>4</sub> or CuCl<sub>2</sub> for 48 h. Asterisks indicate significant differences from the value obtained in the absence of metal inhibitors by *t* test (\**P* < 0.01).

Utilization of MT-null cell lines enabled us to clarify the significant role of metal transport systems as modulators of Cd cytotoxicity. Further studies are required for the identification of Cd and Mn transporters.

### References

- 1) T. Yanagiya et al.: Life Sci. **65**, PL177 (1999).
- 2) T. Yanagiya et al.: J. Pharmacol. Exp. Therap. **292**, 1080 (2000).

\* School of Pharmaceutical Sciences, Kitasato University

## Measurement of the binding affinity of multitracer to an apoplast protein extracted from soybean root<sup>†</sup>

J. Furukawa,\* R. Hirunuma, S. Enomoto, and T. M. Nakanishi\*

More than 200 proteins were localized in plant apoplasts and the mobility of some of these proteins was thought to be affected by Al. It was also suggested that the inhibition of the protein mobility was a result of the linkage of proteins and other cell wall components mediated by Al. In this study, we compared the binding affinity of various metal elements to an apoplast protein in the presence and absence of Al by means of the multitracer technique.

Root tips of two-day-old seedlings [*Glycine max.* (L.) Merr. cv. Tsurunoko] were excised between 2 and 6 mm from the root tip, corresponding to the elongation zone. An apoplast protein was extracted from these excised roots with 50 mM MgCl<sub>2</sub> solution by means of the infiltration method. After the extraction, protein was ultrafiltered through a molecular membrane (10000 M.W., 8000 × g).

Multitracer solution was prepared from a silver foil irradiated by the RIKEN ring cyclotron. From the gamma ray spectroscopy analysis, 11 nuclides (<sup>7</sup>Be, <sup>22</sup>Na, <sup>46</sup>Sc, <sup>52</sup>Mn, <sup>59</sup>Fe, <sup>56</sup>Co, <sup>65</sup>Zn, <sup>75</sup>Se, <sup>84</sup>Rb, <sup>85</sup>Sr and <sup>87</sup>Y) were simultaneously determined.

One μg of the apoplast protein was mixed with 200 μl of 50 mM MES buffer solution (pH 5.0 and 6.0) containing the multitracer and was incubated for 30 min at 4°C and then ultrafiltered through a molecular membrane (10000 M.W., 4500 × g). The membrane was washed with the 200 μl buffer solution after ultrafiltration. To determine the effect of Al on the binding affinity of elements to the apoplast protein, buffer solutions containing AlCl<sub>3</sub> (100 μM or 1 mM) and the

multitracer were also prepared.

Table 1 shows the binding affinity of trivalent elements. The trivalent elements, Sc, Fe and Y, showed high binding affinity at both pH 5.0 and pH 6.0. The high binding affinity of trivalent elements and the low binding affinity of monovalent and divalent elements to the protein (data not shown) suggested that the binding affinity of elements to the protein increased in the following order: monovalent < divalent ≪ trivalent. At pH 5.0, the amounts of both Fe and Y binding to the protein decreased in the presence of 100 μM Al. When 1 mM of Al was added, the binding affinities of Fe and Y further decreased. The decrease in the binding affinity suggested that there was a competition between Al and either Fe or Y for binding to the apoplast protein.

We also carried out the measurement of binding affinity using the protein that was extracted from Al-treated roots (200 μM AlCl<sub>3</sub>, 2 h). After Al treatment, some proteins were not extracted. Compared with the binding affinity to the protein, the effect of Al on the binding affinity of these two elements was observed. The binding affinity of Fe decreased to 69.3% by the application of 1 mM Al. This value of binding affinity corresponded to 83.4% of that without Al treatment, whereas in the case of using protein extracted from non-Al-treated roots, the binding affinity of Fe decreased to 47.9%. A similar tendency was observed in Y. These results suggest that the proteins not extracted after Al treatment had a binding affinity competing between Al and either Fe or Y.

Table 1. Binding affinity of detected elements (% of incubated). The protein column, and Al and protein column indicate the cases with the buffer solution containing 1 μg of protein and 1 μg of protein plus Al, respectively. The numbers in brackets are the percentage of the binding affinity based on that of the protein column.

Element	pH 5.0			pH 6.0					
	Protein extracted without Al treatment			Protein extracted without Al treatment			Protein extracted after Al treatment		
	Protein	100 μM Al & Protein	1 mM Al & Protein	Protein	100 μM Al & Protein	1 mM Al & Protein	Protein	100 μM Al & Protein	1 mM Al & Protein
Sc <sup>3+</sup>	76.6±2.8 (100.0)	74.5±6.6 (97.3)	51.0±3.0 (66.6)	81.0±0.1 (100.0)	85.0±8.6 (104.8)	65.1±4.2 (80.3)	76.9±1.8 (100.0)	93.2±0.2 (121.1)	84.5±5.8 (109.8)
Fe <sup>3+</sup>	36.7±2.4 (100.0)	20.6±3.2 (56.1)	15.9±3.5 (43.3)	66.9±3.6 (100.0)	70.4±15.4 (105.2)	32.0±2.0 (47.9)	83.1±6.6 (100.0)	86.9±5.2 (104.5)	69.3±2.5 (83.4)
Y <sup>3+</sup>	93.3±2.9 (100.0)	74.5±7.3 (79.8)	17.8±5.5 (19.1)	79.4±2.9 (100.0)	65.2±9.5 (82.1)	5.9±0.7 (7.4)	94.6±6.4 (100.0)	84.6±2.0 (89.4)	40.8±8.4 (43.1)

Values are means (%) ± S.D. for at least 3 experiments.

<sup>†</sup> Condensed from the article in Anal. Sci. in press

\* Graduate School of Agricultural and Life Sciences, University of Tokyo

# Influence of samarium on the uptake of trace elements by marigold

H. Suzuki,\*<sup>1</sup> H. Kumagai,\*<sup>1</sup> F. Mori,\*<sup>2</sup> K. Sakamoto,\*<sup>2</sup> K. Inubushi,\*<sup>2</sup> and S. Enomoto

With the continual development of high-technology industries, rare-earth elements (REEs) are being used an ever widening range of materials including fluorescent substances, magnets and superconductors. With such uses, however, REEs may cause the environmental pollution. The emission of REEs into the environment would pollute soils, which in turn would affect plants. However, the influence of REEs on plants remains almost unknown, except for La, Ce, and Yb.<sup>1-3)</sup> In the previous paper,<sup>4)</sup> we revealed that La not only inhibits plant growth but also affects the uptake of trace elements such as Mn, Se, Rb, and Sc. Such effects of La may be due to the impairment of the permeability of the plasma membrane. Information on the influence of REEs on plant growth and the uptake of trace elements should be useful in revegetation or phytoremediation. Consequently, we studied the influence of Sm, which is used as a magnetic material in high-technology industries, on plant growth and the uptake of trace elements, and report our results.

Seeds of marigold plants (*Tagetes patula* L. cv. Bonanza spray) were sowed in 9-cm pots (240 mL in volume) containing 400 g of river sand with 10  $\mu\text{mol Sm kg}^{-1}$  sand (Sm treatment) or without  $\text{Sm}(\text{NO}_3)_3$ . As the elongation of the root from the marigold seed was seriously affected at Sm concentrations higher than 50  $\mu\text{mol Sm kg}^{-1}$  sand, the experiments were carried out with a Sm concentration of 10  $\mu\text{mol kg}^{-1}$  sand. Plants were grown in a biotron with a 18/6 h day/night regime, at 15,000 lux, 65% relative humidity and 25°C. The marigold seedlings were thinned to 1 plant per pot seven days after sowing. Throughout the experiment, the pots were weighed twice a day and watered to 55% of the water-holding capacity of river sand. The details of plant nutrient management have been described in our previous paper.<sup>5)</sup>

A multitracer solution was prepared from an Ag target that was irradiated with a 135 MeV/nucleon  $^{14}\text{N}$

beam accelerated by the RIKEN Ring Cyclotron. The Ag target was dissolved in  $\text{HNO}_3$  and then the Ag was precipitated with HCl as AgCl, leaving a multitracer in solution. The solution was evaporated to dryness, and dissolved in a fertilizer solution. The multitracer containing the radionuclides of  $^7\text{Be}$ ,  $^{22}\text{Na}$ ,  $^{46}\text{Sc}$ ,  $^{51}\text{Cr}$ ,  $^{54}\text{Mn}$ ,  $^{59}\text{Fe}$ ,  $^{56}\text{Co}$ ,  $^{65}\text{Zn}$ ,  $^{75}\text{Se}$ ,  $^{83}\text{Rb}$ ,  $^{85}\text{Sr}$ ,  $^{88}\text{Y}$ ,  $^{88}\text{Zr}$ , and  $^{95\text{m}}\text{Tc}$  was applied 29 days after sowing. The chemical forms of the radionuclides on administration were assumed to be  $\text{Be}^{2+}$ ,  $\text{Na}^+$ ,  $\text{Sc}^{3+}$ ,  $\text{Cr}^{3+}$ ,  $\text{Mn}^{2+}$ ,  $\text{Fe}^{3+}$ ,  $\text{Co}^{2+}$ ,  $\text{Zn}^{2+}$ ,  $\text{SeO}_3^{2-}$ ,  $\text{Rb}^+$ ,  $\text{Sr}^{2+}$ ,  $\text{Y}^{3+}$ ,  $\text{Zr}^{4+}$ , and  $\text{TcO}_4^-$ .<sup>6)</sup> The plants were sampled for analysis 21 days after the multitracer was added. The radioactivities of the plants were measured using Ge semiconductor detectors. The radioactivity applied to the pot was taken as 100% and by comparison, the radioactivity of the plant was expressed as a percentage of the uptake (relative uptake, % of DOSE).

Table 1 shows the relative uptake of radionuclides and the fresh weight of plants. The fresh weight of the aerial parts and roots of marigold decreased with Sm application. Compared to the results for La reported in the previous paper,<sup>4)</sup> the decrease in the growth of aerial parts was similar, but the decrease of the root growth was not. Consequently, Sm may have a stronger effect in inhibiting plant growth than La.

For the uptake of trace elements, Sm treatment resulted in lower uptake of  $^{22}\text{Na}$ ,  $^{54}\text{Mn}$ ,  $^{56}\text{Co}$ ,  $^{75}\text{Se}$ , and  $^{83}\text{Rb}$  than in the control. On the other hand, Sm treatment resulted in higher uptake of  $^{51}\text{Cr}$  and  $^{88}\text{Zr}$  than in the control. At the same time, the uptake of  $^7\text{Be}$ ,  $^{46}\text{Sc}$ ,  $^{59}\text{Fe}$ ,  $^{65}\text{Zn}$ ,  $^{85}\text{Sr}$ ,  $^{88}\text{Y}$ , and  $^{95\text{m}}\text{Tc}$  showed little or no difference between Sm treatment and control. In comparison with La in the previous paper,<sup>4)</sup> Sm was different in that  $^{22}\text{Na}$  and  $^{56}\text{Co}$  uptake decreased,  $^{51}\text{Cr}$  and  $^{88}\text{Zr}$  uptake increased, and  $^{46}\text{Sc}$  uptake was not affected. While REEs are considered to have characteristics similar to each other, the present results suggest

Table 1. Fresh weight of plants and relative uptake of various radionuclides by plants.<sup>a)</sup>

Treatment	Fresh weight (g plant <sup>-1</sup> )		Relative uptake (% of DOSE)													
	A.P. <sup>b)</sup>	Root	$^7\text{Be}$	$^{22}\text{Na}$	$^{46}\text{Sc}$	$^{51}\text{Cr}$	$^{54}\text{Mn}$	$^{59}\text{Fe}$	$^{56}\text{Co}$	$^{65}\text{Zn}$	$^{75}\text{Se}$	$^{83}\text{Rb}$	$^{85}\text{Sr}$	$^{88}\text{Y}$	$^{88}\text{Zr}$	$^{95\text{m}}\text{Tc}$
Control	6.42	3.29	0.1	17.1	1.6	1.2	19.4	1.5	9.8	9.3	22.4	46.9	6.5	2.4	1.2	67.2
Sm treatment	5.15	2.78	0.1	11.9	1.6	1.7	14.0	1.4	7.9	9.0	17.6	39.9	5.6	2.8	3.5	61.7
Student's <i>t</i> -test <sup>c)</sup>	**	*	n.s.	**	n.s.	*	*	n.s.	*	n.s.	*	*	n.s.	n.s.	***	n.s.

<sup>a)</sup> Each value is presented as the mean of data from four plants.

<sup>b)</sup> Aerial parts: <sup>c)</sup> n.s., not significant; \*  $P < 0.05$ ; \*\*  $P < 0.01$ ; \*\*\*  $P < 0.001$ .

\*<sup>1</sup> Radioisotope Research Center, Chiba University

\*<sup>2</sup> Faculty of Horticulture, Chiba University

that each REE itself may have unique effects on the uptake of trace elements by a plant. Further investigation is needed to elucidate which characteristics of REEs (including fine differences in their hydrolytic pH values) cause such differences.

#### References

- 1) E. Diatloff and F. W. Smith: J. Plant Nutr. **18**, 1963 (1995).
- 2) S. Ishikawa, T. Wagatsuma, and T. Ikarashi: Soil Sci. Plant Nutr. **42**, 613 (1996).
- 3) E. Diatloff, C. J. Asher, and F. W. Smith: Materials Sci. Forum **315/317**, 354 (1999).
- 4) H. Suzuki, H. Kumagai, F. Mori, K. Sakamoto, K. Inubushi, and S. Enomoto: RIKEN Accel. Prog. Rep. **34**, 145 (2001).
- 5) H. Suzuki, H. Kumagai, K. Oohashi, K. Sakamoto, K. Inubushi, S. Enomoto, and F. Ambe: Soil Sci. Plant Nutr. **46**, 283 (2000).
- 6) RIKEN Rev., No. 13, (1996).

## The effect of EDTA complexation on diffusion of various ions in granitic rock

T. Mifune,\* Y. Takahashi,\* C. Egawa,\* R. Hirunuma, and S. Enomoto

Diffusion of various ions through micropores of sediment and rocks has been studied in order to quantify their behavior in the diagenetic processes in sediment or their migration in groundwater-rock systems.<sup>1,2)</sup> The difference in diffusion behavior among various ions can be explained primarily by their diffusivity in water and also by the influence of surface diffusion, as evident for some ions which have strong affinities with mineral surfaces.<sup>2)</sup> However, their diffusion behaviors may change in the presence of complexing ligands in water such as natural organics like humic substances, and other synthetic agents. Ethylenediaminetetraacetic acid (EDTA), well-known synthetic chelating agents forming stable complexes with many cations, have been widely used in various industrial fields to date, which has resulted in high EDTA concentrations in freshwater systems ranging from 10–100  $\mu\text{g}/\text{dm}^3$ , for example, in Swiss or German rivers.<sup>3)</sup> The presence of EDTA in natural aquifers will alter the behaviors of various ions in the environment, such as their sorption and diffusion, due to the high stability of metal-EDTA complexes. In this study, we applied a multitracer technique to deduce the EDTA complexation effect on the diffusion behavior of various ions migrating through granitic rocks.

The diffusion through granitic rocks was examined by the through-diffusion method.<sup>4)</sup> Weathered granite samples from drilling cores of Toki granitic rocks, found in central Japan, were cut into 5-mm-thick and 30-mm-diameter disks. Each disk was fitted tightly between two cells filled with water (ionic strength: 0.10 mol/dm<sup>3</sup> by KCl). Three systems (A, B, and C) were studied: A, pH 4 without EDTA; B, pH 4 with 1.0 mmol/dm<sup>3</sup> EDTA; C, pH 6 with 1.0 mmol/dm<sup>3</sup> EDTA.

The radioactivity of each radioisotope in the diffusion cell increases with time, while that in the source cell apparently becomes constant after its decrease during approximately the about first 10 days, mainly due to the sorption to the rock samples. Diffusion curves selected for some cations in systems A–C are shown in Fig. 1, where the ratio of the concentration of each ion in the diffusion cell at each time,  $C_D(t)$ , to that in the source cell after reaching an apparent constant value for each ion,  $C_{S-\text{const}}$ , is plotted on the vertical axis. In the absence of EDTA (system A), each ion diffuses depending on the character of each element, regulated mainly by the charge of the ion and the hydrated ionic radius. In the presence of EDTA (systems B and C),

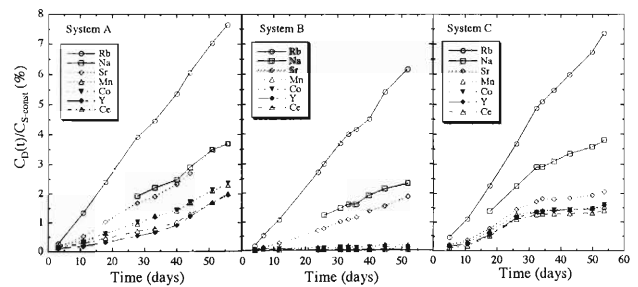


Fig. 1. Diffusion curves for systems A–C. System A: without EDTA, pH 4; System B: with EDTA (1.0 mmol/dm<sup>3</sup>), pH 4; System C: with EDTA (1.0 mmol/dm<sup>3</sup>), pH 6.

however, the behaviors of ions such as Mn(II), Co(II), Y(III), and Ce(III) that form stable complexes with EDTA are similar to one another. This must be due to the formation of the EDTA complex, where the differences among diffusion behaviors of these four ions disappear. In system B, the  $C_D(t)/C_{S-\text{const}}$  ratios for Mn(II), Co(II), Y(III), and Ce(III) were quite low during our experimental period compared with those of Rb and Na, probably due to the sorption of the EDTA complex on oxide surfaces of the weathered granite such as Fe- and Al- oxides. The negative charges on the surface increase at higher pH, which inhibits the sorption of the EDTA complex. This probably allows the diffusion of Mn(II), Co(II), Y(III), and Ce(III) as the EDTA complex at pH 6 (system C). These results indicate that in systems B and C, the diffusion of each ion is governed not by that ion's character but by the behavior of EDTA. This shows that we need to identify the species dissolved in each ion in natural aquifers in order to predict the diffusion of various ions through rocks. However, the diffusion curves of Na<sup>+</sup> and Rb<sup>+</sup> for systems B and C were similar to those for system A, since Na- and Rb- EDTA complexes do not form under this experimental condition as calculated from their stability constants. It is suggested that the diffusion behavior of Na<sup>+</sup> and Rb<sup>+</sup> is regulated by the diffusivities in water in these three systems, irrespective of the presence of EDTA.

### References

- 1) R. A. Berner: *Early Diagenesis* (Princeton University Press, Princeton, 1980).
- 2) K. Skagius and I. Neretnieks: *Water Resour. Res.* **24**, 75 (1988).
- 3) A. D. Satroutdinov et al.: *Environ. Sci. Technol.* **34**, 1715 (2000).
- 4) T. Yamaguchi and S. Nakayama: *J. Contam. Hydrol.* **35**, 55 (1998).

\* Department of Earth and Planetary Systems Science, Graduate School of Science, Hiroshima University

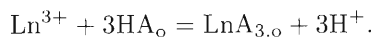
## Molecular design of organic ligands highly selective for lanthanide metal ions

S. Umetani,\*<sup>1</sup> Y. Komatsu,\*<sup>2</sup> H. Yamada,\*<sup>3</sup> and S. Enomoto

In the course of our studies on the solvent extraction of lanthanides using  $\beta$ -diketone-type acylpyrazolones and 3-phenyl-4-benzoyl-5-isoxazolone (HPBI), we have noticed that the acidity of the extractant and its separability are strongly related to the distance between the two donating oxygens. This finding has been confirmed by a systematic investigation of three series of  $\beta$ -diketones: the cyclic group (1) in which the O-O distance is governed by ring-structure geometry, the heterocyclic 4-substituted pyrazolones (2), governed by the steric effect between the 3-methyl group and bulky 4-acyl substituents,<sup>1,2)</sup> and the  $\alpha$ -substituted  $\beta$ -diketones (3), governed by the steric effect of bulky substituents at their  $\alpha$ -position. The structures of  $\beta$ -diketones in use are shown in Fig. 1.

The introduction of a methyl group to the  $\alpha$ -position in the molecular structure of benzoyltrifluoroacetone (BFA) yielded  $\alpha$ -methyl benzoyltrifluoroacetone (MBFA). Their O-O distances were estimated by the semi-empirical molecular orbital calculation, MNDO/H, to be 2.51 Å and 2.42 Å, respectively. <sup>1</sup>H NMR spectrum data clearly show that the intramolecular hydrogen bonding of MBFA is strengthened (sharp OH-peak at  $\delta = 15.8$  ppm) owing to its smaller O-O distance, compared to that of BFA (very broad OH-peak at  $\delta = 15.2$  ppm). Their dissociation constants,  $pK_a$ , were measured by the potentiometric titration method in a water-dioxane solution (25:75 v/v) to be 8.10 for BFA and 10.35 for MBFA.

The extraction of lanthanides using BFA and MBFA (denoted by HA) was performed into benzene. The overall equilibrium can be written as follows:



The validity of this equation was confirmed through the effects of pH and concentration of the extractant (HA) on the extraction of lanthanides. From this equation, the extraction constant  $K_{\text{ex}}$  and the distribution ratio D ( $D = [\text{LnA}_3]_o/[\text{Ln}^{3+}]$ ) can be deduced:

$$\begin{aligned} K_{\text{ex}} &= [\text{LnA}_3]_o[\text{H}^+]^3/[\text{Ln}^{3+}][\text{HA}]^3_o \\ &= D[\text{H}^+]^3/[\text{HA}]^3_o. \end{aligned}$$

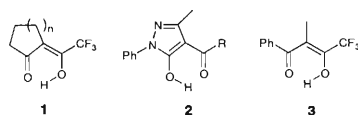


Fig. 1. Modified  $\beta$ -diketones.

Table 1. Extraction constants and  $\text{pH}_{1/2}$  values for lanthanides.

	BFA		MBFA	
	$\log K_{\text{ex}}$	SF <sup>a)</sup>	$\log K_{\text{ex}}$	SF <sup>a)</sup>
La <sup>3+</sup>	-11.70	1.38	-17.61	1.80
Pr <sup>3+</sup>	-10.32	1.32	-15.81	1.50
Eu <sup>3+</sup>	-9.00	0.66	-14.31	0.72
Ho <sup>3+</sup>	-8.34	0.64	-13.59	0.66
Yb <sup>3+</sup>	-7.80	3.90 <sup>b)</sup>	-12.93	4.68 <sup>b)</sup>

Extraction into benzene.  $[\text{BFA}]_o = [\text{MBFA}]_o = 0.1$  M.

<sup>a)</sup> SF: separation factor, defined by the difference between  $\log K_{\text{ex}}$  values of two consecutive metals. <sup>b)</sup> Separation factor for La and Yb.

$$\log K_{\text{ex}} = \log D - 3 \text{pH} - 3 \log[\text{HA}]_o.$$

Table 1 shows the extraction data of BFA and MBFA. From the data, it is clear that BFA, with its smaller  $pK_a$  and larger O-O distance, can extract lanthanides more efficiently: the  $K_{\text{ex}}$  values for BFA are in fact 105–106 times larger than those for MBFA. Otherwise, as a result of the diminution of the O-O distance, MBFA separates lanthanides more efficiently than BFA: the separation factor of La and Yb, found to be 4.68 for MBFA exceeds that for BFA which is 3.90.

It should be noted that the introduction of an  $\alpha$ -substituent in the structure of  $\beta$ -diketone is often followed by a notable decrease of the % enol tautomer of the extractant, thus hindering the solvent extraction procedure. A bromo group has been introduced to dibenzoylmethane (DBM) and BFA to obtain  $\alpha$ -BrDBM and  $\alpha$ -BrBFA with shorter O-O distances. However, due to the predomination of their keto forms, the attempt to obtain their solvent extraction data was failed. Our study is now being expanded further with a phenyl group as the  $\alpha$ -substituent for enol-rich  $\beta$ -diketone derivatives such as phenyl acetylacetone (PAA) and phenyl benzoylacetone (PBA).

### References

- 1) S. Umetani, Y. Kawase, H. Takahara, Q. T. H. Le, and M. Matsui: J. Chem. Soc., Chem. Commun. **1993**, 78.
- 2) Y. Kawase and S. Umetani: Unpublished data.

\*<sup>1</sup> Institute for Chemical Research, Kyoto University

\*<sup>2</sup> Faculty of Engineering, Kanazawa Institute of Technology

\*<sup>3</sup> Advanced Materials Laboratory, National Institute for Material Science

# New multitracer production: Development of a gas-jet coupled multitarget system and an automated rapid chemistry apparatus

H. Haba,\*<sup>1</sup> S. Enomoto, R. Hirunuma, Y. Nagame,\*<sup>1</sup> and A. Shinohara\*<sup>2</sup>

During the last ten years, the RIKEN multitracer has been successfully applied for investigations of the behavior of various elements in the fields of chemistry, biology, medicine, and geology. The multitracers were produced from metallic targets such as Ti, Ag, and Au irradiated with 135 MeV/nucleon  $^{12}\text{C}$ ,  $^{14}\text{N}$ , and  $^{16}\text{O}$  beams using the RIKEN Ring Cyclotron. After the irradiations, the multitracers were chemically separated from the target material.<sup>1)</sup> Recently, a few technical developments for the preparation of the multitracer have been reported.<sup>2,3)</sup> Takamiya *et al.*<sup>2)</sup> produced multitracers using the thermal neutron fission of  $^{235}\text{U}$  at the Kyoto University Reactor (KUR). They separated the fission products from the  $\text{UO}_2$  target using NaCl as a catcher material. Shibata *et al.*<sup>3)</sup> found that the multitracer solution was obtained quickly and easily by amalgamating the gold target irradiated with the RIKEN Ring Cyclotron.

We plan to develop a gas-jet coupled multitarget sys-

tem and an automated rapid chemistry apparatus as a novel technique for the multitracer production. A schematic of the gas-jet coupled multitarget system and the automated rapid chemistry apparatus is shown in Fig. 1. The multitracers are produced from various target materials irradiated with 135 MeV/nucleon  $^{12}\text{C}$ ,  $^{14}\text{N}$ , and  $^{16}\text{O}$  beams from the RIKEN Ring Cyclotron. The targets should be multiplied in order to collect the recoiling nuclei efficiently. The recoiling products are stopped in helium gas, attached to aerosols such as NaCl, KCl, and C, and continuously transported through a Teflon capillary tube to a chemistry room. Advantages of the gas-jet coupled multitarget system are as follows. The multitracers are separated from the target material without chemical separation and are transported to a chemistry room within a few seconds. Thus, radionuclides with short half-lives of less than 1 minute are available for experiments. In addition, targets with various chemical forms are prepared by electrodeposition or vacuum-evaporation techniques. Furthermore, the composition of the radionuclides in the multitracer is optimized by changing the target array. The radionuclides of interest are concentrated with the liquid chromatography apparatus based on ion exchange or solvent extraction. As shown in Fig. 1, the reaction products transported by the gas-jet system are deposited on the collection site of the slider. Then, the multitracers are dissolved with a desired solution and fed into the ion exchange or extraction column. We also plan to use circulating gaseous targets such as Ar, Kr, and Xe using the same experimental setup.

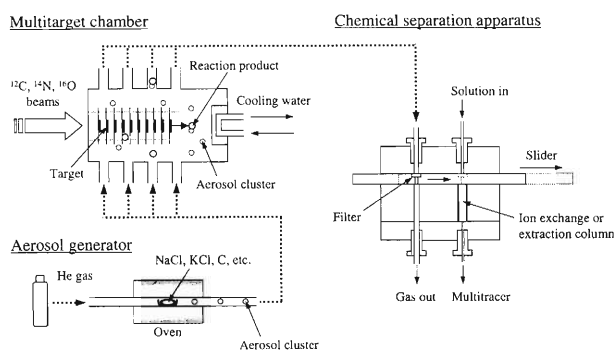


Fig. 1. Schematic of the gas-jet coupled multitarget system and the automated rapid chemistry apparatus.

## References

- 1) S. Ambe: RIKEN Rev., No. 13, 3 (1996).
- 2) K. Takamiya *et al.*: RIKEN Rev., No. 35, 107 (2001).
- 3) S. Shibata *et al.*: RIKEN Rev., No. 35, 115 (2001).

\*<sup>1</sup> Advanced Science Research Center, Japan Atomic Energy Research Institute

\*<sup>2</sup> Department of Chemistry, Graduate School of Science, Osaka University



## 4. Radiation Chemistry and Radiation Biology



# Ultrafast plasma luminescence of heavy-ion tracks in insulators

K. Kimura, T. Kambara, and M. Kase

We have developed techniques for luminescence measurements with a time resolution of 85 ps.<sup>1)</sup> Using these techniques, we observed a novel ultrafast luminescence decay component (UFLDC) from the track core in a number of wide-band-gap materials: NaF, LiF, NaCl, KCl, CsCl, KBr, KI, RbI, CsI, BaF<sub>2</sub>, MgO, and  $\alpha$ -alumina.<sup>2)</sup> The luminescence is characterized as follows. The UFLDC is a common phenomenon in wide-band-gap materials except for some types of materials such as diamond and SiO<sub>2</sub>. The lifetimes of UFLDC's are less than 100 ps and their decay curves do not have long tails. Their specific intensities increase super-linearly with increasing excitation density. Heavy-ion irradiation such as with Xe ions resulted in strong intensity whereas that with He ions did not produce the UFLDC. The specific intensities showed sample dependence, but only slight temperature dependence. The time-resolved spectra (TRS) of the UFLDC were broad bands spreading from 200 to 400 nm. These results show that the UFLDC is novel luminescence that cannot be attributed to known excited species, and moreover suggest that it arises from multiple interactions among dense electron-hole pairs. Consequently, we attribute the UFLDC to electron-hole plasmas. This is the first time that it has been confirmed that the incipient ion track can emit photons as a collective behavior. Although electron-hole plasma luminescence is known to be observed in some semiconductors by H<sup>+</sup> irradiation, this plasma arises from the diffusional recombination of free excitons with much longer lifetimes than those of the present samples but is not due to the incipient track.

However, for a detailed characterization of the electron-hole plasma, many questions remain unsolved. One of them is why the redshift from the absorption edge is so large. The second is how the luminescence takes place. Considering the analogy of electron-hole plasmas in semiconductors, it may be reasonable to suggest that the UFLDC arises from electron-hole recombination. The shift may be explained due to the displacements and bindings of holes in the incipient track. In the incipient track, ejected electrons distribute densely in a space like a sheath round a core cylinder containing holes. In the core, there is the extremely strong Coulombic repulsion among a number of excess cations, and hence binding forces in the crystal are destroyed completely and holes (halogen atoms in case of alkali halides) can move to aggregate:  $X + X^- \rightarrow X_2^-$ ,  $X + X \rightarrow X_2$ ,  $X + X + X^- \rightarrow X_3^-$ , and so forth.<sup>3)</sup> These products or intermediate states become new holes along with X, and they become the counter parts to ejected electrons when e-h plasma is relaxed. Recombination luminescence among such

holes and electrons causes the large redshift by the Stokes shift, as is well known for the self-trapped exciton, and the superposition of various shifts broadens the resultant band. If this is true, the peak and structure of the TRF should be dependent on the mass of irradiating ions and on the constituent halogen ions of the crystal.

To ascertain this and characterize the UFLDC further, it is necessary first to measure a precise TRL. To date, our TRLS have not been able to provide the correct peak maximum or the correct band structure because of the instability of ion beams and the small number of sampling wavelengths. In order to overcome these problems, we intend to develop a method for multichannel time-correlated photon counting for each ion striking, namely, a fast secondary electron detector (FASD<sup>1)</sup>) gives timing pulses of ion penetrations with a time resolution of 25 ps. Eight wavelengths of pho-

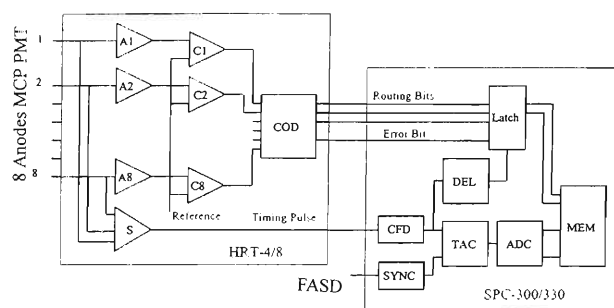


Fig. 1. System for time-correlated 8-channel photon counting for each ion striking. FASD: a fast secondary electron detector.<sup>1)</sup>

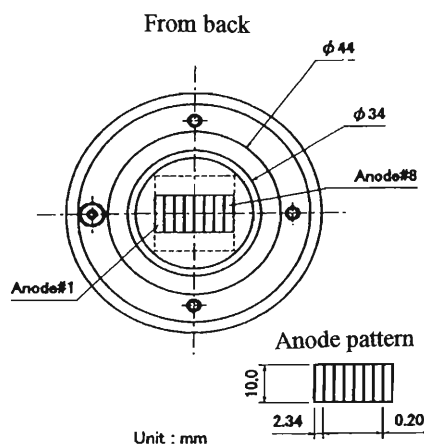


Fig. 2. A microchannel plate-mounted PMT with 8-separated anodes.

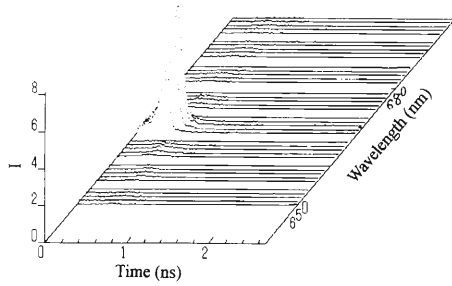


Fig. 3. Wavelength-dependent decay curves in the case that a randomly triggered diode laser is used as a light source.

ton counting are correlated with a FASD timing pulse using a time-to-amplitude converter. The 8-photon counting was performed using a microchannel-plate-mounted photomultiplier with 8 anodes and an  $\text{MgF}_2$  window (model R4110U), which was obtained from

Hamamatsu Photonics. Time-correlated counting was performed using a modified system of models SPC330 by Becker and Hickl GmbH. This system can give at least 8-wavelength data free from beam fluctuation. Figure 1 shows a part of the time-correlated counting. Figure 2 shows an 8-anode MCP-PMT. Figure 3 demonstrates wavelength-dependent decay curves in the case that a randomly triggered diode laser was used as a light source. The monochromator was a model Spectrapro-300i built by Acton Research Corporation. The figure shows that the system has sufficient resolution.

#### References

- 1) K. Kimura, J. Kaneko, S. Sharma, W. Hong, and N. Itoh: *Phys. Rev. B* **60**, 12626 (1999).
- 2) K. Kimura, S. Sharma, and A. Popov: *Radiat. Meas.* **34**, 99 (2001).
- 3) K. Kimura, S. Sharma, and A. Popov: *Nucl. Instrum. Methods Phys. Res. B*, to be published.

## Enhancement of $^{137}\text{Cs}$ accumulation by phytochelatin synthetase expression in rhizofungus *Fusarium oxysporum*

T. Soshi and I. Yamaguchi

Radionuclides released by nuclear power plants into the environment pose a potential risk to human health. Recently, significant attention has been drawn to phytoremediation as a cost-effective technology to remove pollutants from the environment. However, the rate of radionuclide removal using conventional plants is low. To improve the removal efficiency of plants, we are studying the utilization of rhizosphere microorganisms, which were known to affect plant growth and metal-ion uptake.<sup>1,2)</sup> We have shown that the non-pathogenic *Fusarium spp.* symbiotic to tomato can increase the uptake amount of radionuclides through infection.<sup>3)</sup> On the other hand, it has been suggested that metal-binding proteins or peptides can be utilized in engineering plants and microorganisms for bioremediation.<sup>4)</sup> The introduction and overexpression of metal-binding peptides, such as phytochelatins (PCs), have been exploited to increase metal accumulation by plants.<sup>5,6)</sup> We are interested in application of the transgenic technique and the rhizosphere system to phytoremediation of radionuclides. In this paper, we report that the introduction of the *Schizosaccharomyces pombe* phytochelatin synthase gene to rhizofungus *Fusarium oxysporum* is effective in increasing radionuclide accumulation.

The phytochelatin synthase (PCS) gene, SPAC3H110, was cloned by a genomic polymerase chain reaction (PCR) using PCR primers designed according to the published genomic DNA sequence data (GenBank accession number Z68144).<sup>5,6)</sup> The amplified fragment was subcloned into the expression vector, pCPXHY2, derived from pGEM4Z (Promega). In the pCPXHY2, the constitutive *Aspergillus gpd-1* gene promoter was inserted at the unique *EcoRI* site and the hygromycin B phosphotransferase gene (*hyg*) upstream of the *gpd-1* promoter for selection. The resultant plasmid pPCSHY2 was used for transformation of the non-pathogenic strain of *F. oxysporum*. Isolated transformants and a non-transformed control strain were cultured in 50 ml of potato dextrose broth at 25°C for 2 days, and then the multitracer and radioactive cesium mixture were added to these cultures. After 3 days, mycelia were collected and washed three times with 250 mM  $\text{CaCl}_2$ . Then, mycelia were harvested by filtration and dried at 50°C overnight. Radioactivity of each sample was measured by a hyperpure Ge detector (SEIKO EG&G).

Table 1 shows the radionuclide accumulation ability of transformants for  $^{51}\text{Cr}$ ,  $^{52}\text{Mn}$ ,  $^{56}\text{Co}$ ,  $^{65}\text{Zn}$ ,  $^{75}\text{Se}$ ,  $^{83}\text{Rb}$ ,  $^{88}\text{Y}$ , and  $^{137}\text{Cs}$ . The data was expressed as a

Table 1. Radionuclide accumulation ability of pPCSHY2 transformants.

Nuclide	Strain number							
	T1	T2	T4	T5	T6	T7	T8	
$^{56}\text{Co}$	0.92	0.24	0.77	0.61	0.87	0.87	0.95	
$^{51}\text{Cr}$	1.50	1.52	1.05	1.26	0.98	1.04	1.39	
$^{137}\text{Cs}$	1.48	1.35	1.35	1.24	0.60	1.47	1.42	
$^{52}\text{Mn}$	3.53	4.06	3.95	3.90	4.33	4.42	4.62	
$^{83}\text{Rb}$	0.99	1.07	1.56	1.17	0.95	1.10	1.41	
$^{75}\text{Se}$	0.55	0.60	0.59	0.61	0.61	0.68	0.66	
$^{88}\text{Y}$	1.38	1.72	1.63	1.92	1.78	1.81	1.79	
$^{65}\text{Zn}$	1.81	1.66	1.03	1.03	0.98	1.09	1.08	

ratio of activity relative to that of the control strain. PCS expression reduced the accumulation of  $^{56}\text{Co}$  and  $^{75}\text{Se}$  but it did not affect the accumulation of  $^{51}\text{Cr}$ ,  $^{83}\text{Rb}$  and  $^{65}\text{Zn}$ . A moderate increase in the accumulation of  $^{137}\text{Cs}$  and  $^{88}\text{Y}$  was observed.  $^{52}\text{Mn}$  was accumulated about four times more than the control.  $^{137}\text{Cs}$  accumulation was elevated to almost 1.5 times that of the control. The tested nuclides have not been reported to have affinity for PCs. The results suggest that PCs have affinity for at least Cs, Y and Mn ions. Alternatively, PSC expression might activate some other pathway of Cs, Y and Mn accumulation.

$^{137}\text{Cs}$  contamination has been one of a serious problem after the Chernobyl accident.<sup>7)</sup> Generally, the rate of  $^{137}\text{Cs}$  uptake by plants is very low, since Cs ions are tightly adhere to soil materials and organic compounds, thus it is difficult to remove them. The *Fusarium* strain used in this study enhances the uptake of some radionuclides including  $^{137}\text{Cs}$  by tomato through infection.<sup>1)</sup> If the PSC-expressing transformant can transfer a significant amount of Cs ions to the host plant, the removal efficiency of Cs would be increased. Further studies are needed to determine the effects of transformed *Fusarium* on the radionuclide uptake by plants.

### References

- 1) S. Gouthu et al.: RIKEN Accel. Prog. Rep. **31**, 146 (1998).
- 2) J. A. Entry: Water, Air, Soil Pollut. **88**, 167 (1996).
- 3) T. Soshi et al.: RIKEN Accel. Prog. Rep. **34**, 165 (2001).
- 4) M. Majare and L. Bulow: Trends Biotechnol. **19-2**, 67 (2001).
- 5) S.-B. Ha et al.: Plant Cell **11**, 1153 (1999).
- 6) O. K. Vatamaniuk et al.: Proc. Natl. Acad. Sci. USA **96**, 7110 (1999).
- 7) S. Dushenkov et al.: Environ. Sci. Technol. **33**, 469 (1999).

## Effective plant-mutation method using heavy-ion beams (VI)

Y. Konomi,\* T. Abe, F. Sugawara,\* and S. Yoshida

There is a difference in sensitivity to ion beams between the organs of plants.<sup>1)</sup> We found that tobacco is sensitive to irradiation with ion beams during the stage of fertilization.<sup>2)</sup> In this paper we report the effect of ion beams on various tissues of wild tobacco (*Nicotiana glutinosa*).

Dry seeds were irradiated with ion beams (N or C at 135 MeV/u) within a dose range of 20 to 800 Gy. Imbibition seeds incubated in 1/2MS agar medium for 12 to 60 hrs before irradiation, were irradiated with C-ion within a dose range of 10 to 50 Gy. After 28.7 to 101.7 hrs of pollination, intact embryos in flowers were irradiated with N-ion within a dose range of 10 and 20 Gy. One month after the irradiation, M<sub>1</sub> seeds were harvested. The M<sub>1</sub> seeds were germinated in the 1/2MS medium at 25°C under continuous light. After one month, we determined their germination percentage and survival rate (number of survival plants/number of seeds). Morphological abnormalities were observed two months after seeding.

The germination was not affected by ion-beam irradiation in the case of dry seeds. However, the germinated plants produced no leaves and died with doses higher than 600 Gy. The morphologically abnormal plants appeared with a dose of 400 Gy. The abnormality rates induced by the N- and C-ion exposures were 11.6 and 8.2%, respectively. A decrease in survival rate was observed at 50 Gy in the case of the imbibition seeds. For example, no plants survived among the irradiated seeds which were incubated over 48 hrs. In a dose range of 20 Gy, seeds with 51 hrs of incubation was the most sensitive stage to irradiation, which showed the lowest survival rate (34%) and the highest frequencies of abnormal plants (7.2%, Table 1). On the contrary, embryos showed the high frequencies of abnormal plants. The embryo stages were 28.7, 65.7 and 101.7 hrs after pollination within 10 Gy and their fre-

Table 1. Frequency of morphologically abnormal plants (MAP) induced with C-ion irradiation at various imbibition stages.

Imbibition [hrs]	Survival [%]	Frequency of MAP [%]
14	95.6 ± 0.9	0.0 ± 1.5
26	96.9 ± 2.7	0.0 ± 5.7
48	92.0 ± 2.3	3.5 ± 0.0
51	33.7 ± 15.1	7.2 ± 0.0
59	96.3 ± 1.3	3.1 ± 0.0

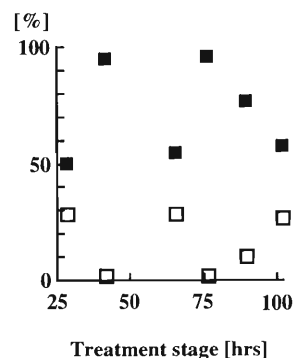


Fig. 1. Effects of embryo treatment with N-ion beams within a dose range of 10 Gy at different developmental stages on frequency of morphologically abnormal plants (□) and germination percentage (■).

quencies of abnormal plants were approximately 30% (Fig. 1). The sensitivity of these organs decreased in the following order: embryos during fertilization cycle, imbibition seeds, dry seeds.

### References

- 1) T. Abe et al.: RIKEN Accel. Prog. Rep. **33**, 140 (2000).
- 2) T. Abe et al.: RIKEN Accel. Prog. Rep. **30**, 127 (1997).

\* Faculty of Science Technology, Tokyo University of Science

## Isolation of sterile mutants of *Verbena hybrida* using heavy-ion beam irradiation

K. Suzuki,\*<sup>1</sup> Y. Yomo,\*<sup>2</sup> T. Abe, Y. Katsumoto,\*<sup>1</sup> K. Miyazaki,\*<sup>2</sup> S. Yoshida, and T. Kusumi\*<sup>2</sup>

Long blooming period and a large number of flowers are the important characteristics of floricultural crops. Plants belonging to the genus *Verbena* (Verbenaceae) are one of the most commercially used major bedding plants. Suntory Ltd. (Osaka, Japan) has developed a new cultivar of the verbena 'Temari' series (*Verbena hybrida*), which has many characteristics superior to those of common verbena cultivars. Because most Temari cultivars continuously bloom with a large number of flower clusters from spring until autumn in temperate areas, 'Coral Pink' of the Temari series sometimes shows a decrease in the number of flower clusters compared to other varieties. Coral Pink of the Temari series was also observed to produce self-seeds autonomously at a high frequency. We hypothesized that the number of flower clusters would be increased by the repression of autonomous self-seed setting, and isolated sterile mutants of Coral Pink of the Temari series using heavy-ion beam irradiation.

We have successfully isolated the flower color mutant of *Petunia altiplana* by irradiation of fertilized egg cells under *in vivo* conditions.<sup>1)</sup> In this report, because we expect that the characteristics of the host plant and its mutant are identical except for sterility, *in vitro* plant materials maintained on MS solid medium were used for all irradiation experiments. The results of preliminary irradiation of several organs from several *in vitro* plant materials including *Verbena* suggested that irradiation of a nodal culture with an <sup>14</sup>N heavy-ion beam at a dose of less than 10 Gy is effective in mutational breeding of sterile plants without undesirable mutations such as dwarfing, leaf curling and slow growth. Sixty-four single nodes containing two lateral meristems at each base of two opposite leaves of Coral Pink of the Temari series were cultured in one plastic dish and irradiated with 0, 1, 2, 5 and 10 Gy of the <sup>14</sup>N heavy-ion beam at 135 MeV/u. All shoots that developed from the lateral meristems after irradiation were planted in soil and grown in a greenhouse. About 80% shoot formation was observed for all doses of irradiations, and most of the shoots showed normal morphology. The sterile-mutant phenotype of each flower in clusters after open pollination was easily detected, as shown by an unenlarged ovary. Clusters with different frequencies of sterile flowers were observed. Some branches of clusters whose flowers are all sterile were selected, and were propagated several times by cutting. These plants were grown to flowering and the next selection was carried out by the same methods.

Repeats of this selection system could concentrate the sterile phenotype, removing the fertile one from probable chimerical plants that developed from the irradiated meristems harboring mass proliferative cells. Finally, four mutant lines with stable sterility were successfully selected (Table 1).

In order to determine the effect of seed setting on flowering characteristics, field trials of both the host plant and its sterile mutants were carried out from spring until autumn. The sterile mutants continuously grew well compared to the host plant, and in particular, at the end of the blooming season, autumn, the host plant started senescence probably due to a continuous reproductive state of seed setting. It was observed three times in the three-month pot experiment that the sterile mutants had a larger number of flower clusters than the host plant. In the field trials, it was observed that the sterile mutants of Coral Pink of the Temari series produced a small number of seeds, which has not been observed completely under the greenhouse condition due to lack of pollinators. This seed setting at low frequency and the observation of almost no effect on growth are similar to those found in other Temari series, indicating self-incompatibility; thus, it is assumed that the pollination with genetically heterogeneous combinations between the pollen and the pistil as a male and female, respectively, can only produce seeds. A cross-pollination test indicated that the sterile mutants of Coral Pink of the Temari series also exhibit self-incompatibility. It is noted that the characteristics of the host plant and its mutants are identical except for sterility. Finally, we conclude that heavy-ion beam irradiation is an excellent tool for mutational breeding of sterile mutants at a high frequency. Moreover the mutation which causes fertile plants to produce sterile mutants leads to an increase in the number of flower clusters and good growth.

Table 1. Summary data for isolation of sterile mutants of Coral Pink of the Temari series.

Dose of irradiation	No. of materials	No. of meristems cultured	No. of shoots developed	No. of sterile plants
0 Gy	15	30	25	0
1 Gy	64	128	115	0
2 Gy	64	128	88	0
5 Gy	64	128	115	1
10 Gy	64	128	108	3

### References

- 1) K. Suzuki et al.: RIKEN Accel. Prog. Rep. **32**, 146 (1999).

\*<sup>1</sup> Institute for Fundamental Research, Suntory Ltd.

\*<sup>2</sup> Flower Division, Suntory Ltd.

## Isolation of variegated mutants of *Petunia hybrida* using heavy-ion beam irradiation

K. Miyazaki,\*<sup>1</sup> K. Suzuki,\*<sup>2</sup> T. Abe, Y. Katsumoto,\*<sup>2</sup> S. Yoshida, and T. Kusumi\*<sup>2</sup>

Variation with various patterns in yellow, white or red, at a particular part of the leaf, regularly or irregularly, is a special and historical characteristic of many ornamental plants in horticulture. *Petunia* is one of the most important bedding plants in the world. Fifteen varieties of Surfinia (*Petunia hybrida*), propagated by vegetative cuttings, were developed and commercialized by Suntory Ltd. and Keisei Rose Nursery Ltd. Due to substantial propagation by vegetative cuttings, variegated plants were found by chance, though the frequency was quite low. We investigated how we could efficiently isolate those variegated plants of Surfinia, using heavy-ion beam irradiation to induce an artificial mutation.

In the first step, we irradiated *in vitro* nodal cuttings, containing lateral meristems cultured in MS medium, of 10 varieties of Surfinia with <sup>14</sup>N (135 MeV/u) at a dose of 5, 10, and 20 Gy, or <sup>20</sup>Ne (135 MeV/u) at a dose of 1, 5, and 10 Gy. We selected variegated mutants among *in vitro* shoots developed from irradiated lateral meristems. Other normal shoots were acclimated and grown, and were screened under greenhouse conditions. From the several variegated mutants isolated, some showed chimerical phenotypes containing both variegated and normal leaves in one plant, however they lost the variegations due to the dominance of normal leaves which were vigorous. We isolated independently two mutants by *in vitro* selection, and two mutants by greenhouse selection.

In order to rescue such chimerical mutants, we developed an alternative modified selection method using an *in vitro* regeneration technique. We again irradiated *in vitro* nodal cuttings of 12 varieties of Surfinia with <sup>12</sup>C 5 Gy, <sup>14</sup>N 5 Gy, and <sup>20</sup>Ne 1 Gy. The frequencies of variegated mutants including pale green leaves



Fig. 1. Variegated mutant from surfinia 'Blue Vein.'

by the first *in vitro* selection were 18.9%, 26.8% and 10.8% isolated by <sup>12</sup>C, <sup>14</sup>N, <sup>20</sup>Ne irradiations, respectively. We obtained many regenerated shoots from leaf disks of these variegated leaves in MS medium with 1 mg/l BA and 0.1 mg/l NAA. It was observed that most of the regenerated shoots showed normal or albino leaves, but some of them showed un-chimerical variegated leaves with quite a low frequency. As a result, we successfully isolated one and four mutants (Fig. 1) of variegated plants from *in vitro* and *in vitro* regeneration selections, respectively.

These results indicate that heavy-ion beam irradiation and its related selection system using *in vitro* tissue culture techniques are powerful tools for the isolation of variegated *Petunia*.

\*<sup>1</sup> Flower Division, Suntory Ltd.

\*<sup>2</sup> Institute for Fundamental Research, Suntory Ltd.

## Induction of mutation in *Sandersonia aurantiaca* Hook. by heavy-ion beam irradiation

M. Horita,\* K. Sakamoto, T. Abe, and S. Yoshida

*Sandersonia* (*Sandersonia aurantiaca* Hook.) belongs to the *Liliaceae* family, and is the only species in its genus, however, less intra-specific variations can be found in this species. Thus, there is no variety in the *Sandersonia* currently available on the market. Inter-specific hybrids of the genus can not be made. *Sandersonia* is only available in orange. Mutation breeding is considered to be an effective method to develop new varieties in such cases. We applied the heavy-ion beam irradiation method which has been reported to be an effective mutagen in many plant species.

Dry seeds of *Sandersonia* were irradiated with  $^{14}\text{N}$ -ion beams at doses rates of 20, 50, and 100 Gy, respectively. Embryos were excised from irradiated dry seeds, and cultured on a modified Murashige & Skoog medium at 22°C. The embryos germinated within one month and grew in culture vessels up to the two-leaf stage. Then, they were transferred to potted soil and grown in a green house. The influence of irradiation on the germination rate of embryos and the induction of mutation of M1 plants was evaluated.

The germination rate of embryos was not influenced at a dosage rate of 20 Gy. A dosage rate of 50 Gy slightly decreased the germination frequency of embryos and a rate of 100 Gy decreased the germination severely (Table 1). Mutation characteristics were observed in 9 out of 432 plants with 20 Gy irradiation, which was 2.1% of the mutant appearance frequency. Among 9 plants, some albino plants could be seen in the culture vessels. Although 50 Gy irradiation was slightly inferior to that of 20 Gy in terms of the fre-

quency of induction of mutants, 6 mutants out of 346 plants were obtained. A dosage rate of 100 Gy irradiation produced only one mutant from 109 plants. These results suggest that dosage rates of 20 Gy or less are suitable for the induction of mutant plants in the case of dry seed treatment of *Sandersonia*. Mutation characteristics observed in the M1 generation were albino, striped leaf, dwarf and deformed leaf (Fig. 1). These results show that heavy-ion beam irradiation is effective for the induction of mutations in *Sandersonia*, at least in the leaf stage. Flowering was not observed in M1 plants, therefore mutation in flower color remains to be evaluated. However, these mutant plants, among other plants, formed tubers.

We are now investigating the appearance of mutant plants particularly in terms of flower color in the M2 generation.



Fig. 1. Mutated plants of *Sandersonia* induced by  $^{14}\text{N}$  heavy-ion beam irradiation. Albino plant (left) and plant with striped leaves (right).

Table 1. Effects of  $^{14}\text{N}$  heavy-ion beam irradiation on *Sandersonia*.

Irradiation dose (Gy)	No. of cultured embryos	No. of germinated embryos (%)	No. of albino plants	No. of stripe-leaf plants	Others*
20	720	432 (60.0)	5	2	2
50	784	346 (44.1)	5	1	0
100	791	109 (13.8)	0	1	0
Cont.**	56	33 (58.9)	0	0	0

\* Dwarfed plant and plant with deformed leaves

\*\* Untreated embryo

\* Hokkaido Green-Bio Institute

## Mutation induction in human cells after low-dose exposure to heavy ions

S. Morimoto, T. Kato, M. Honma,\* M. Kase, F. Hanaoka, and F. Yatagai

It is very difficult to detect biological effects of low-dose ionizing radiation, particularly those of heavy-ion radiation. However, it is highly desired to obtain such information not only for estimation of radiation risk to human body but also for basic understanding of cellular responses.

Our previous studies have revealed unique characteristics of cellular responses and genetic changes in the human lymphoblastoid cell line TK6, after a relatively high-dose heavy-ion exposure. For example, mutation induction in the *hypoxanthine phosphoribosyl transferase (HPRT)* gene,<sup>1)</sup> p53 induction,<sup>2)</sup> and cell cycle arrest<sup>3)</sup> were extensively examined using this cell line. We extended this line of work to low-dose radiation exposure such as 10 cGy exposure and determined out that the number of p53-induced cells depends on the kind of heavy ion.<sup>4)</sup>

In this study, we applied loss-of-heterozygosity (LOH) analysis<sup>5)</sup> to the mutants at the heterozygous thymidine kinase (*TK*) locus to elucidate the genetic effects of low-dose radiation exposure in more detail. We considered this analysis very attractive because the type of LOH provides information about the LOH induction pathway, homologous recombination or DNA nonhomologous end-joining, through which DNA double-strand breaks (DSBs) can be repaired (Fig. 1).

TK6-20C cells were irradiated with 10 cGy of X-rays or C ions and the observed mutation frequencies (MF) at the *TK* locus are summarized in Table 1. The LOH analysis demonstrated an increase in the relative por-

tion of hemizygous LOH among all the number of TK mutants, *i.e.*, 10 to 42% by X-ray exposure (Fig. 2), although there was no significant increase in MF (Table 1). Furthermore, C-ion exposure enhanced such proportion to 58% (Fig. 2), resulting in more than twofold increase in MF (Table 1).

These results indicate that radiation-specific induction of hemizygous LOH is more efficient after exposure to C ions than the X-ray exposure. This finding suggests that DSBs are more frequently produced by 22 keV/ $\mu$ m C-ion exposure than by X-ray exposure.<sup>6)</sup> This assumption is consistent with our previous result that the number of p53-induced cells after 10 cGy of 22 keV/ $\mu$ m C-ion exposure is higher than that after X-ray exposure.<sup>4)</sup> Alternatively, DSBs produced by C-ion exposure are more complicated than by X-ray exposure and the difficulty in repairing such complicated DSBs might produce hemizygous LOH more efficiently. At present, we are analyzing the LOH pattern in more detail using the satellite marker on chromosome 17 to further clarify the radiation exposure effects.

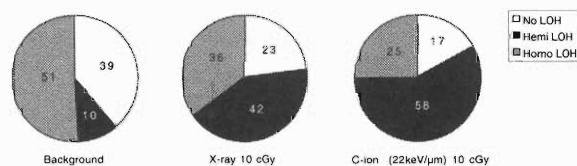


Fig. 2. Population of non-, hemizygous, and homozygous LOH mutants after X-ray or C-ion (22 keV/ $\mu$ m) exposure. 110 mutants were determined for Background, 92 for X-ray, and 67 for C-ion exposure.

Table 1. *TK* Mutation frequencies induced by 10 cGy of X-ray or C-ion exposure.

Treatment	Mutation Frequency <sup>a</sup> ( $\times 10^{-6}$ , mean $\pm$ SD)
Background	5.7 $\pm$ 1.3
X-ray	6.9 $\pm$ 2.8
C-ion (22 keV/ $\mu$ m)	17.9 $\pm$ 8.9

a) Obtained from three independent experiments

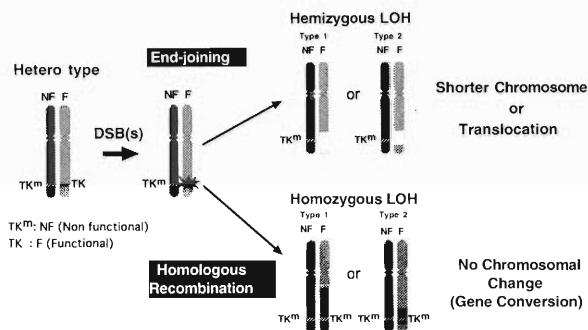


Fig. 1. A model of expected loss of heterozygosity (LOH), which is induced by double-strand breaks (DSBs). DSB repair through end-joining could produce hemizygous LOH, while that through homologous rejoining could produce homozygous LOH. Both types of LOH have no functional allele.

\* Division of Genetic Mutagenesis, National Institute of Health Sciences

### References

- 1) Y. Kagawa et al.: *Mutagenesis* **14**, 199 (1999).
- 2) A. Gordon et al.: *RIKEN Accel. Prog. Rep.* **33**, 131 (2000).
- 3) S. Goto et al.: *RIKEN Accel. Prog. Rep.* **34**, 176 (2001).
- 4) S. Morimoto et al.: *RIKEN Accel. Prog. Rep.* **34**, 177 (2001).
- 5) M. Honma et al.: *Mol. Carcinog.* **28**, 203 (2000).
- 6) T. Fujisaki et al.: *HIMAC Rep.* 110 (2000).

## Delayed cell-cycle progression following exposure to heavy ions

S. Goto,\* S. Morimoto, M. Kase, and F. Yatagai

High-LET (linear energy transfer) radiation is one of the tools for tumor treatment, but it is not as popular as X-ray irradiation. Compared to X-ray irradiation, the basic mechanisms responsible for such cellular effects are still not well understood. For better understanding of cellular effect, cellular responses after exposure of human lymphoblastoid cell TK6 to 3 Gy of C ions (22 keV/ $\mu\text{m}$ ) or Fe ions (1000 keV/ $\mu\text{m}$ ) were examined in this study.

Cell-cycle progression after exposure was determined by laser scanning cytometry (LSC). G2/M-phase cells accumulated in all cases of irradiation. Compared to X-ray irradiation, the number of accumulated cells was less in the G2/M-phase after Fe ion irradiation (Fig. 1(A)). This measurement did not confirm the following possibilities that a) the cell-cycle progression irradiated cells was arrested in the S-phase and did not proceed to the G2/M-phase, and that b) they were not accumulated in the G2/M-phase during a certain period. Therefore, we prelabeled S-phase cells with BrdU before the exposure, and monitored the cell-cycle progression of these labeled cells. By LSC analysis, we could visualize the pattern (Fig. 1(B)) that indicates the position of the labeled cells in the cell-cycle. Moreover, the rate of progression of the labeled cells from the S-phase to the G2/M-phase can be calculated as shown in Fig. 1(C). The S-phase cells

exposed to Fe ions showed delayed progression to the G2/M-phase (Fig. 1(B) and (C)). Such delay is probably due to the difficulty in repairing the so-called clus-

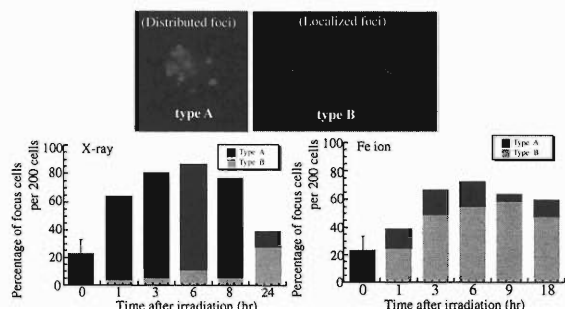


Fig. 2. Different patterns of Rad51 focus distribution between X-ray and Fe ion irradiation. At the indicated post-irradiation time, the cells were stained with the Rad51 rabbit polyclonal antibody. The Rad51-foci-formation pattern was determined by fluorescence microscopy. The photographs show examples of two different types of focus formation pattern (Type A and B). Type A is the localized formation pattern and type B is the uniformly distributed formation pattern. The histogram is expressed as a percentage of cells forming Rad51 foci. Each column in the histogram consists of types A and B focus formation patterns.

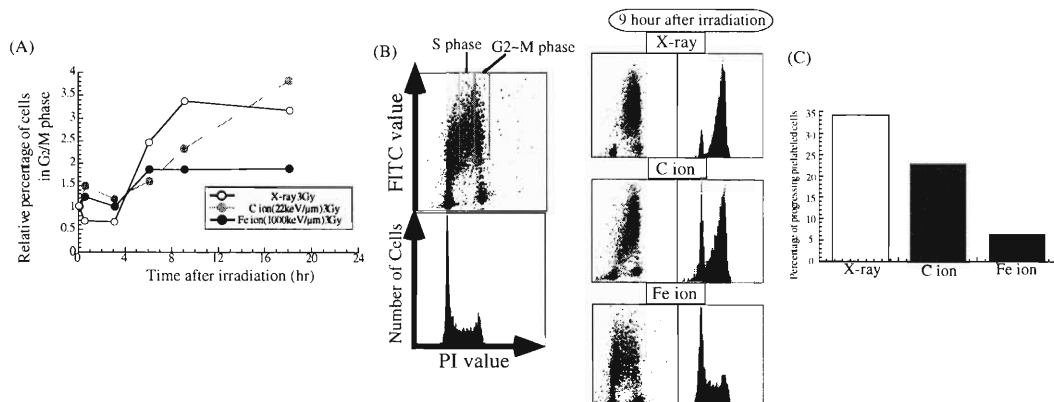


Fig. 1. (A) Cell-cycle progression in TK6 after irradiation with X-ray, C ions (22 keV/ $\mu\text{m}$ ), and Fe ions (1000 keV/ $\mu\text{m}$ ). Following the irradiation, cells were fixed with ice-cold methanol at each postirradiation time and the nuclear region of the cells was stained with propidium iodide (PI). Cell-cycle distributions were analyzed by laser scanning cytometry (LSC). The population of cells in the G2/M-phase is expressed as a relative percentage with respect to that in the G2/M-phase of the unirradiated sample. (B) Cell-cycle progression of prelabeled S-phase cells after irradiation with X-ray, C ions (22 keV/ $\mu\text{m}$ ), and Fe ions (1000 keV/ $\mu\text{m}$ ). Before irradiation, S-phase cells were prelabeled with BrdU for 15 min. Nine hours after irradiation, the position of the labeled S-phase cells in the cell cycle was determined by LSC. (C) The proportion of cells that progressed from the S-phase to the G2/M-phase 9 hours after irradiation was calculated from the results of LSC analysis.

\* Department of Health Science, School of Pharmaceutical Science, Nagasaki University

tered DNA damage<sup>1,2)</sup> caused by exposure to high-LET heavy ions. We also examined the *in situ* distribution of the Rad51 protein, which localizes at sites of the DNA double-strand breaks and repairs the breaks by DNA homologous recombination. The localization of Rad51 was visualized as a focus using the antibody against Rad51. The majority of Rad51 foci formed after Fe ions irradiation showed a localized formation pattern (Fig. 2, Type B), in contrast to those induced mainly by X-ray irradiation that showed a uniformly distributed formation pattern (Fig. 2, Type A). Furthermore, the proportion of Rad51-foci-formed cells was maintained at the induced level even 18 hours af-

ter the exposure. In contrast, such proportion after X-ray irradiation returned to the unirradiated level.

These results obtained from the cell-staining experiments also support the possibility that the DNA damage induced by Fe ion irradiation is clustered. Such damage might provide a delay in the cell-cycle progression due to the difficulty in repairing the clustered DNA damage as mentioned above.

#### References

- 1) B. Rydberg: Rad. Res. **145**, 200 (1996).
- 2) W. R. Holley and A. Chatterjee: Rad. Res. **145**, 188 (1996).

## 5. Instrumentation



## Development of the in-flight separator CRIB

Y. Yanagisawa, T. Teranishi,<sup>\*1</sup> S. Kubono,<sup>\*1</sup> S. Michimasa,<sup>\*1</sup> M. Notani,<sup>\*1</sup> Y. Ohshiro,<sup>\*1</sup> S. Shimoura,<sup>\*1</sup> K. Ue,<sup>\*1</sup> S. Watanabe,<sup>\*1</sup> N. Yamazaki,<sup>\*1</sup> S. Kato,<sup>\*2</sup> T. Morikawa,<sup>\*3</sup> Y. Mizoi, T. Kishida, H. Iwasaki,<sup>\*1</sup> H. Baba,<sup>\*4</sup> A. Saito,<sup>\*4</sup> Y. Satou,<sup>\*1</sup> M. Kurokawa,<sup>\*1</sup> and M. Kase

We reported the installation of an in-flight low-energy radioisotope (RI)-beam separator CRIB last year.<sup>1)</sup> In this report, the results of test experiments for the production of the RI beam and beam devices installed for measuring the beams are described.

CRIB consists of seven magnets and two focal planes with the configuration of F0-Q1-M1-D1-Q2-F1-D2-M2-Q3, where F0 is the production target position. The principle of RI beam separation is based on magnetic rigidity analysis and the energy loss of fragments. RI beams produced at F0 are analyzed with their momenta and transported to the dispersive focus plane F1. A degrader is placed at F1 to generate the energy loss. Next, RI beams are reanalyzed and collected at achromatic focal plane F2. With the in-flight separation method, the wedge-shaped degrader has been widely used at the dispersive focal plane. In the case of CRIB at low energies of a few MeV/nucleon, a suitable thickness for the degrader was a few mg/cm<sup>2</sup>, in view of multiple scattering and energy straggling. Such a wedge degrader is too thin to fabricate. We have used a homogeneous degrader, an aluminized mylar foil with a thickness of 1.7 mg/cm<sup>2</sup>, for RI beam separation. The effect of the degrader is described by Ue *et al.* elsewhere in this report.<sup>2)</sup>

We have installed a beam diagnosis device at each focal plane. The profile of a primary beam at the production-target position (F0) is measured with a single-wire profile monitor and a ZnS beam viewer. The beam profile of a secondary beam is measured at F1 and F2 using delay-line parallel plate avalanche counters (PPAC) with segmented horizontal and vertical cathodes. The PPAC at F1 is used for the momentum measurement, and the one at F2 is for monitoring the isotopic separation and tuning beam profile at

the secondary target position. The particle identification for secondary beams realized by a combination of time-of-flight (TOF) and energy loss ( $\Delta E$  or  $E$ ) measurements. The TOF is measured between RF signals from the AVF cyclotron and the timing signal of the PPAC. Silicon detectors are placed at F1 and F2 to measure energy losses.

The first test experiment was performed for producing a <sup>12</sup>N beam for the experiment of <sup>12</sup>N + p elastic scattering.<sup>3)</sup> A primary beam of <sup>10</sup>B at 7.8 MeV/nucleon with an intensity of 200 pA bombarded a <sup>3</sup>He gas target with 0.25 mg/cm<sup>2</sup>. The <sup>12</sup>N beam was produced via the (<sup>3</sup>He,n) reaction in inverse

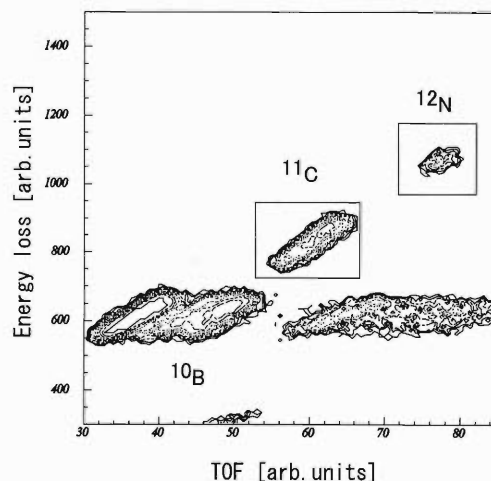


Fig. 1. Particle identification spectrum for the result of production of <sup>12</sup>N. The  $x$ -axis represents a TOF between RF and PPAC signals and the  $y$ -axis represents an energy loss of particles in the silicon detector.

Table 1. Summary of RI beams obtained by CRIB. Here, primary beam intensity was 200 pA.

RI beam	<sup>10</sup> C	<sup>11</sup> C	<sup>12</sup> N	<sup>14</sup> O
Primary beam	<sup>10</sup> B <sup>4+</sup>	<sup>10</sup> B <sup>4+</sup>	<sup>10</sup> B <sup>4+</sup>	<sup>14</sup> N <sup>6+</sup>
Energy (per nucleon)	7.8 MeV	7.8 MeV	7.8 MeV	8.4 MeV
Reaction	(p,n)	( <sup>3</sup> He,pn)	( <sup>3</sup> He,n)	(p,n)
Target	CH <sub>4</sub>	<sup>3</sup> He	<sup>3</sup> He	CH <sub>4</sub>
	1.3 mg/cm <sup>2</sup>	0.25 mg/cm <sup>2</sup>	0.25 mg/cm <sup>2</sup>	1.3 mg/cm <sup>2</sup>
Intensity (cps)	$1.6 \times 10^5$	$1.6 \times 10^4$	$2.5 \times 10^3$	$8 \times 10^5$
Energy (per nucleon)	6.1 MeV	3.4 MeV	3.9 MeV	6.7 MeV

<sup>\*1</sup> Center for Nuclear Study, University of Tokyo

<sup>\*2</sup> Yamagata University

<sup>\*3</sup> Kyushu University

<sup>\*4</sup> Rikkyo University

kinematics. The RI beams produced were separated and transported to F2. Figure 1 shows a particle identification spectrum for the  $^{12}\text{N}$  beam. Particles were identified using the technique of TOF measurement between RF and the timing signal of the PPAC and the energy loss signals from the silicon detector. The  $^{12}\text{N}$  beam of 2500 cps was obtained. The purity of  $^{12}\text{N}$  beams was about 3%. The main contamination of the beam was a scattered primary beam from the wall of the first dipole magnet. We have also performed experiments for producing the RI beams  $^{11}\text{C}$ ,  $^{10}\text{C}$  and  $^{14}\text{O}$ . The RI beams obtained are summarized in Table 1. The development of a Wien filter installed after F2

and a windowless gas target<sup>4)</sup> for a production target is now in progress, being essential for the production of high-intensity RI-beams with high purity.

#### References

- 1) Y. Yanagisawa et al.: RIKEN Accel. Prog. Rep. **34**, 183 (2001).
- 2) K. Ue et al.: RIKEN Accel. Prog. Rep. **35**, 137 (2002).
- 3) T. Teranishi et al.: RIKEN Accel. Prog. Rep. **35**, 60 (2002).
- 4) T. Kishida et al.: Nucl. Instrum. Methods Phys. Res. A **438**, 70 (1999).

## Test of low-energy RI beam production with CRIB

K. Ue,<sup>\*1</sup> S. Kubono,<sup>\*1</sup> T. Teranishi,<sup>\*1</sup> S. Shimoura,<sup>\*1</sup> M. Notani,<sup>\*1</sup> Y. Yanagisawa, S. Michimasa,<sup>\*1</sup>  
 H. Iwasaki,<sup>\*1</sup> M. Kurokawa,<sup>\*1</sup> Y. Satou,<sup>\*1</sup> T. Morikawa,<sup>\*2</sup> A. Saito,<sup>\*3</sup> H. Baba,<sup>\*3</sup>  
 Y. Ohshiro,<sup>\*1</sup> N. Yamazaki,<sup>\*1</sup> S. Watanabe,<sup>\*1</sup> and M. Kase

To establish a technique of producing a low-energy RI beam by means of the in-flight method, we have conducted a test experiment to produce an  $^{14}\text{O}$  beam at low energy (6.6 A MeV) using a homogeneously thin degrader for isotope separation. We studied the achromaticity of the RI beam at the exit of CRIB separator.<sup>1)</sup>

A wedge-shaped energy degrader with the thickness of 100–1000 mg/cm<sup>2</sup> has been widely used for the in-flight method at intermediate energies. The use of a wedge-shaped degrader allows one to achieve achromaticity easily. However, the suitable thickness is 1–10 mg/cm<sup>2</sup> for such a low beam energy. Because it is difficult to construct a wedge-shaped degrader with such a small thickness, we tested a method using a homogeneously thin degrader. The use of a homogeneous degrader breaks the achromaticity. We treated the effect of particle energy-loss in the degrader in the framework of the ion-optical transfer matrix and adjusted the optics of CRIB, so that the achromaticity could be restored.<sup>2)</sup>

A primary beam of  $^{14}\text{N}$  at 8.4 A MeV bombarded a gas target of 1.5 mg/cm<sup>2</sup> CH<sub>4</sub>. The target gas was confined in a small cell with entrance and exit windows made of Havar foils (2.4  $\mu\text{m}$  thick). An  $^{14}\text{O}$  beam produced by the  $^{14}\text{N}(p,n)^{14}\text{O}$  reaction in inverse kinematics was separated from other particles by CRIB. We installed an aluminized mylar foil with thickness 1.7 mg/cm<sup>2</sup> as the homogeneous degrader at the dispersive focal plane (F1) of CRIB. At the achromatic focus (F2), particle identification was performed using timing information from two parallel plate avalanche counters (PPAC)<sup>3)</sup> and energy information (E) from a silicon detector. The beam profile and position at F2 were measured using the PPACs.

The beam purity of  $^{14}\text{O}$  at F2 was about 60% without the degrader and about 80% with the degrader. The main background was  $^{14}\text{N}$  scattered from the wall of the first dipole magnet of CRIB, the beam pipe and the target cell.

To verify the achromaticity, the horizontal centroid position of the  $^{14}\text{O}$  beam was measured at F2 as a function of its momentum. The momentum was selected at F1 by using an aperture of 2 mm, which corresponds to the momentum spread of 0.13%. The aperture position was moved from 0 to 50 mm. Figure 1 shows the centroid position at F2 ( $x_2$ ) as a function of aperture position at F1 ( $x_1$ ).

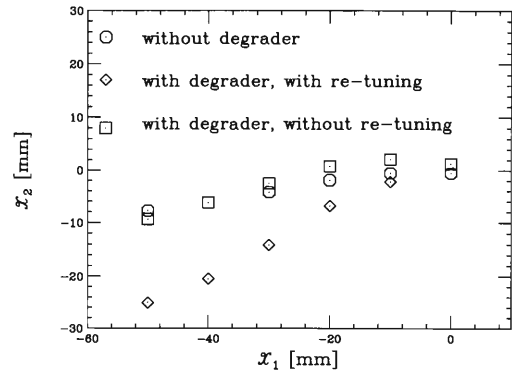


Fig. 1. Vertical and horizontal axes show the horizontal centroid position of the beam spot at F2 ( $x_2$ ) and of the aperture at F1 ( $x_1$ ), respectively. The positions  $x_1 = 0, -10, -20, -30, -40,$  and  $-50$  mm correspond to 0,  $-0.63, -1.3, -1.9, -2.5,$  and  $-3.2\%$ , respectively, in deviation from the central momentum.

Table 1. Properties of  $^{14}\text{O}$  beam produced by using  $\text{H}(^{14}\text{N}, ^{14}\text{O})\text{n}$  reaction at 8.4 A MeV. The intensity of the  $^{14}\text{N}$  beam was 500 p nA.

Energy	6.6 A MeV
Intensity	$2 \times 10^6$ pps
Momentum spread	5%
Purity	80%
Spot size (FWHM)	$\phi$ 14 mm

tion at F1 ( $x_1$ ). When the degrader was not used, the shift of  $x_2$  was measured to be 8 mm at  $x_1 = -50$  mm. When the degrader was used and the optics was adjusted, the shift was 9 mm at  $x_1 = -50$  mm. Both values of shift were significantly smaller than  $x_2 = 25$  mm at  $x_1 = -50$  mm with the degrader and without the adjustment. Therefore, the adjustment of the separator system is important for the use of the homogeneously thin degrader. The properties of the  $^{14}\text{O}$  beam are summarized in Table 1. The spot size with the degrader was wider by 5 mm than that without the degrader. This is mainly due to a large energy straggling in the degrader.

### References

- 1) Y. Yanagisawa et al.: RIKEN Accel. Prog. Rep. **34**, 183 (2001).
- 2) S. Mitsuoka et al.: Nucl. Instrum. Methods Phys. Res. A **372**, 489 (1996).
- 3) S. Kumagai et al.: Nucl. Instrum. Methods Phys. Res. A **470**, 562 (2001).

<sup>\*1</sup> Center for Nuclear Study, University of Tokyo

<sup>\*2</sup> Kyushu University

<sup>\*3</sup> Rikkyo University

## The first observation of slow muon beam at the RIKEN-RAL Muon Facility

Y. Matsuda, P. Bakule, Y. Miyake,\* K. Shimomura,\* S. Makimura,\* P. Strasser,  
T. Matsuzaki, K. Ishida, I. Watanabe, and K. Nagamine

We have been constructing a slow muon beam line at the RIKEN Muon Facility at the Rutherford Appleton Laboratory,<sup>1)</sup> adopting the resonant ionization method. The advantage of a slow muon beam over conventional muon beam is enormous. The energy of slow muons can be varied from a few eV to a few tens of keV, while the energy spread when they are generated is on the order of a few eV. On the other hand, the currently available muon beam (surface muon beam) has a fixed momentum of approximately 27 MeV/c (energy 3.5 MeV) and its momentum spread is as large as 10%. The nature of the slow muon beam will extend the application of  $\mu$ SR studies to thin films, surfaces and interfaces which have been impossible to be investigated with  $\mu$ SR technique. The time resolution will also be much improved compared to that of the current beam available at the RIKEN Muon Facility, thanks to the narrow time width of the laser beam which is used to generate the slow muon beam.

The resonant ionization method was developed at the Meson Science Laboratory of the High Energy Accelerator Research Organization.<sup>2)</sup> The surface muon beam is injected into a thin tungsten foil, which is heated to approximately 2500 K. Muonium atoms with thermal kinetic energy are evaporated from the surface after its formation following electron capture at the surface of the foil. Then the electrons of the muonium atoms are removed by irradiation with VUV laser to produce very slow muons. This process is illustrated in Fig. 1. Generated slow muons are extracted and accelerated by SOA lenses and transported to a microchannel plate (MCP) detector, with which they are detected.

We ionized muonium through a series of two transitions,  $1s \rightarrow 2p$  and  $2p \rightarrow \text{unbound}$ . A sophisticated laser system has been developed to generate an intense Lyman- $\alpha$  VUV light which matches the energy difference between the  $1s$  and  $2p$  states, which corresponds to the wavelength of 122.09 nm in the case of muonium. Another 355 nm of photons from a frequency-tripled Nd:YAG laser were used to remove electrons through transition from the  $2p$  state to an unbound state. The scheme is illustrated in Fig. 2. A detailed explanation of the laser system is given in the previous report.<sup>1)</sup>

We carried out the experiment in the summer of 2001 for 5 days in the Port 3 experimental area at the RIKEN Muon Facility. The first slow muon beam was successfully observed at the beam line. An observed

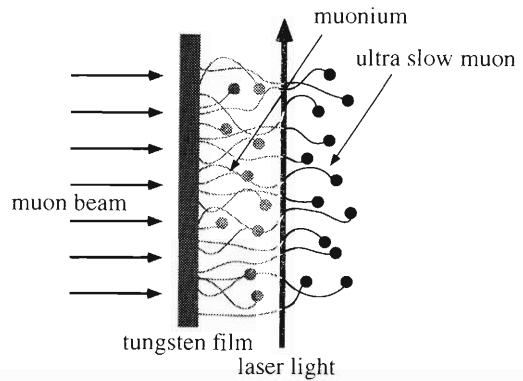


Fig. 1. Schematic diagram of the laser ionization method for generating slow muons.

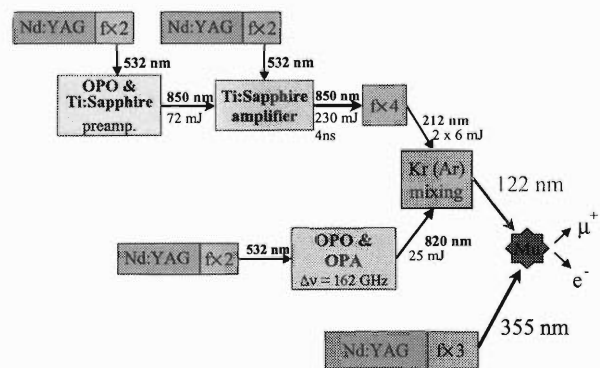


Fig. 2. Schematic diagram of the laser system which has been developed for the resonant ionization of muonium atom.

time-of-flight (TOF) spectrum is shown in Fig. 3.

It is noted that the laser system is operating with a 25 Hz repetition rate, whereas the pulsed muon beam has a 50 Hz repetition rate. We observed a clear peak only when VUV light was introduced to the production region. The signal was confirmed to be caused by slow muon from the measurement of the bending magnet field in the beam transport line, and by agreement of the TOF difference between laser irradiation and signal arrival time according to acceleration voltage. In order to change the wavelength of the VUV light, the frequency of a tunable OPO laser was scanned. Figure 4 shows that the yield of slow muon peaked at 820.4 nm, which corresponds to the matching frequency of the  $1s \rightarrow 2p$  transition of muonium atoms.

It was observed that the yield almost linearly de-

\* Institute for Materials Structure Science, High Energy Accelerator Research Organization (KEK)

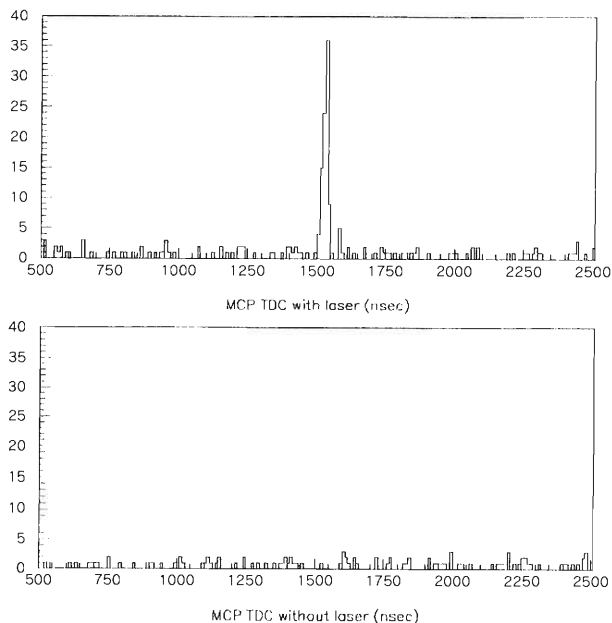


Fig. 3. Typical slow muon signal is shown. The upper graph shows the TOF spectrum of the MCP detector when laser lights are introduced in to the production region, and the lower graph shows the spectrum when laser lights are not introduced.

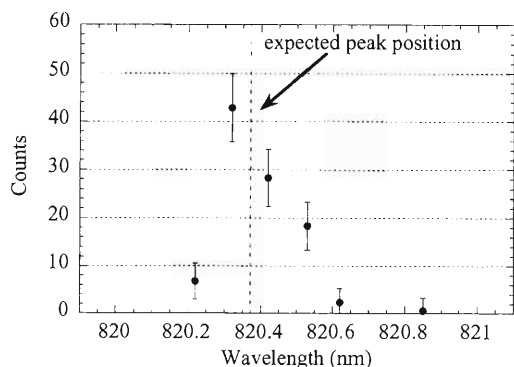


Fig. 4. Yield of slow muons are plotted against frequency of tunable OPO laser. The wavelength was calibrated by He-Ne laser and by observing hydrogen ionization signal at 844.8 nm.

depends on both VUV laser power and 355 nm laser power, suggesting that laser power was not saturated

in the production region.

The obtained count rate of slow muon was about 0.03 slow muons/sec, which is about 30 times smaller than expected. We believe that this is largely due to the smallness of the power of the VUV light and 355 nm light which ionize the muonium atoms. We monitored the strength of the VUV light by observing an ionization signal from NO gas which is filled in a chamber located at the end of the laser path. The signal during the beam time was less than 10% of what we obtained during the commissioning period in Japan. The 355 nm laser was operating at approximately one third of its maximum power because of a fault in its power supply. The vacuum around the target was about  $5 \times 10^{-8}$  mbar, which is also poorer than that in our design due to the short period of baking time. although this level of vacuum will not disturb the slow muon trajectory markedly, it will deteriorate the cleanness of the surface of the target, which will affect the efficiency of muonium production.

We are currently working to improve laser performance. It has been indicated that a lower intensity of VUV light was caused by the strong focusing of laser beams in the Kr chamber, which causes saturation of VUV generation. By slightly defocusing the laser beams to obtain a larger generation area, we expect to obtain significantly stronger VUV light. In the last beam experiment, we split the 212 nm laser into two, and used only one of them to avoid damage on a BBO crystal in the laser system. We are planning to use the second 212 nm laser light with a new BBO crystal to introduce another VUV light to the chamber. The power supply of the 355 nm laser has been fixed to yield maximum power. Improvement of the vacuum system is also under way, including installation of a cryopump, which was not available last summer.

With these improvements, we expect to obtain at least 100 times more slow muons, which will be sufficient for  $\mu$ SR study of some samples. We are planning to install a  $\mu$ SR spectrometer in 2002.

#### References

- 1) Y. Matsuda et al.: RIKEN Accel. Prog. Rep. **33**, 263 (2000).
- 2) K. Nagamine et al.: Phys. Rev. Lett. **74**, 4811 (1995).

## Design of a spin polarized positron beam and a spin rotator

F. Saito, N. Suzuki, Y. Itoh, A. Goto, Y. Nagashima,\*<sup>1</sup> T. Kurihara,\*<sup>2</sup> and T. Hyodo\*<sup>1</sup>

A high-intensity spin polarized slow positron beam is developed in RIKEN for the researches of surface and of interface magnetism. A high-intensity beam can be attained by using an electrodeposited  $^{18}\text{F}$  (produced by the AVF cyclotron) positron source<sup>1)</sup> and a high-efficiency tungsten mesh moderator.<sup>2)</sup>

The specifications of the beam transferring system was already reported:<sup>3)</sup> the positron spin is rotated by using a spin rotator. A polarimeter is used to measure the positron spin polarization of the beam. The previous design,<sup>3)</sup> however, requires some improvements. In this paper, the simulation of beam transfer of a new designed apparatus as well as a magnetic field and an electric field of the spin rotator are reported. The electric and magnetic fields of the spin rotator were optimized by means of OPERA-3d/TOSCA (Vector Field, Ltd.). The beam transfer efficiency was simulated by means of Simion (Idaho N. E. Lab.).

A Wien filter is used as a spin rotator which has a static electric field ( $\mathbf{E}$ ) and a magnetic field ( $\mathbf{B}$ ) perpendicular to the beam axis and to each other. When the beam passes through the magnetic field, the spin rotates in the magnetic field direction due to the Larmor precession. The transverse motion of the positron is restrained by the electric field when the Wien condition  $e(\mathbf{E} + \mathbf{v} \times \mathbf{B}) = 0$  is satisfied. Thus, the adjustment of the magnetic field and the electric field is of vital importance for the beam transfer efficiency. The dimensions of the designed spin rotator are 50 mm length along the beam axis, 20 mm gap between magnetic pole pieces and 16 mm gap between electrodes. The diameter of the beam passing the rotator is about 10 mm. The schema of the spin rotator is shown in Fig. 1. The deviation of the magnetic field and the electric field along the transverse direction ( $x$ -axis) at the center ( $z = 0$ ) of the spin rotator is shown in Fig. 2. The electric field produced by the curved surface electrodes corresponds better to the magnetic field

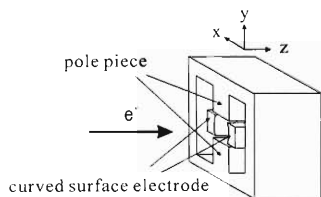


Fig. 1. Schema of spin rotator. The origin of the coordinates is the center of the spin rotator.

\*<sup>1</sup> Department of Basic Sciences, Graduate School of Arts and Science, University of Tokyo

\*<sup>2</sup> Institute of Materials Structure Science, High Energy Accelerator Research Organization (KEK)

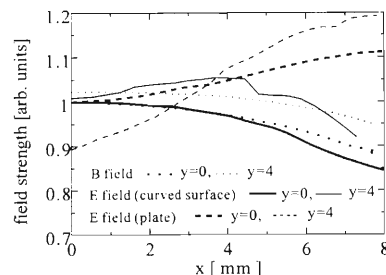


Fig. 2. Deviation of electric fields and magnetic fields, each normalized by the value at  $(x, y) = (0, 0)$ .

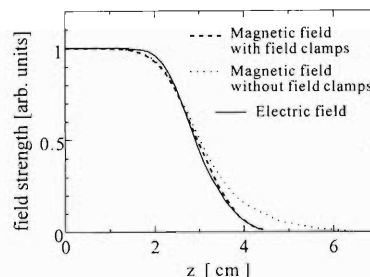


Fig. 3. Fringing magnetic field and electric fields, each normalized by the value at the center of the rotator. The end of the rotator and the field clamp are situated at 2.5 and 4 cm from the center, respectively.

than that produced by the plate electrodes at positions along the  $x$ -axis with  $y = 0$  and  $y = 4$ .

Figure 3 shows the simulation of the magnetic fields with and without field clamps and the electric field along the beam axis. The width of the fringe magnetic field at the entrance and the exit of the rotator can be reduced and adjusted to that of the electric field by employing field clamps.

The simulation of the beam transfer efficiency shows all the positrons emitted from a circular area (dia. 6 mm) with an energy of 1-3 eV and an angle of 0-80 degrees to the beam axis can be transported to the target sample.

In conclusion, the design of the spin-polarized slow positron beam apparatus has been completed and the simulation shows that this apparatus exhibits high beam transfer efficiency.

### References

- 1) F. Saito et al.: Nucl. Instrum. Methods Phys. Res. A **450**, 491 (2000).
- 2) Y. Nagashima et al.: Jpn. J. Appl. Phys. **39**, 5356 (2000).
- 3) J. H. Kim et al.: Rad. Phys. Chem. **52**, 759 (2000).

## On-line collection of $^8\text{Li}$ ions from the projectile fragment separator using an rf-ion guide system

M. Wada, Y. Ishida, T. Nakamura, Y. Nakai, T. M. Kojima, Y. Kanai, N. Ohshima, H. Ohyama, T. Kambara, Y. Yamazaki, A. Yoshida, T. Kubo, Y. Matsuo, Y. Fukuyama, K. Okada,\*<sup>1</sup> T. Sonoda,\*<sup>2</sup> K. Noda,\*<sup>3</sup> H. Kawakami,\*<sup>4</sup> S. Ohtani,\*<sup>5</sup> and I. Katayama\*<sup>4</sup>

The projectile fragment separator (RIPS) at the RIKEN accelerator facility (RARF) provides a wide variety of energetic radioactive beams. However, it is not adequate for low-energy beam experiments such as precision spectroscopy of trapped ions. Aiming at efficient deceleration and cooling of the energetic radioactive ions, the development of an rf-ion guide system comprising a large He gas cell and an rf funnel structure in the cell is in progress.<sup>1-5)</sup> Energetic ion beams from the fragment separator are stopped in the gas cell after passing through an energy degrader. In the conventional ion guide, the transport of ions in the cell is carried out only by the gas flow which limits the possible size of the cell. In the rf-ion guide, on the other hand, the ions in the cell are under the control of the applied dc and rf fields, which enables us to use a large cell. The dc field transports the ions toward the exit aperture, while the rf gradient field at the wall of the cell repels the ions.

A proof of the principle (pop) machine has been successfully tested on-line for the collection of 70 MeV/u  $^8\text{Li}$  ions. The setup used in the test experiment is

shown in Fig. 1. A compact gas cell of 70 cm in length and 10 cm in diameter with a He gas pressure of 30 Torr was placed after a newly developed wedge shaped energy degrader. The degrader is made of water packed between thin aluminium windows connected by bellows. This arrangement is capable of varying both the wedge angle and the thickness. A photograph of the wedge degrader is shown in Fig. 2.

The ions stopped in the gas were extracted orthogonally to the beam axis by the dc field penetrating through the rf funnel structure. The ions follow the lines of electric force toward the surface of the electrode, although they do not hit the electrode due to the presence of the rf barrier field. In this way the ions move slightly above the surface of the funnel structure toward the exit aperture of 0.5 mm in diameter.

The transported  $^8\text{Li}$  ions were collected on a silicon detector and delayed- $\alpha$  decay was observed for their detection. The overall efficiency of the pop system was  $\sim 10^{-4}$  as depicted in Fig. 3. The radial acceptance of the cell for the extended beam after the degrader was measured to be 30% using a collimated beam. The stopping capability of the 30 Torr gas cell was 0.43% which was deduced from a range calculation by using the TRIM code, the measured energy distribution after the energy degrader, and the radial acceptance. Thus the overall efficiency can be separated into the gas stopping efficiency of 0.43% and the ion-guide efficiency of 2.4%. The former is limited by the geometry of the cell and the pressure of the He gas. The latter is due to the present rf voltage limitation of 40 V. Both components have the potential to be increased up to the 10% range by employing a larger cell, higher pressure, and higher rf voltage, which would yield an

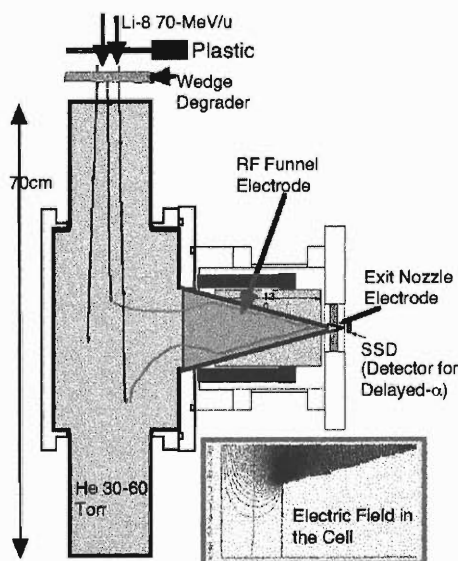


Fig. 1. Diagram of the rf ion guide on-line test setup.

\*1 Department of Physics, Sophia University

\*2 Cyclotron RI Center, Tohoku University

\*3 National Institute for Radiological Science

\*4 Institute of Particle and Nuclear Studies, High Energy Accelerator Research Organization (KEK)

\*5 Institute for Laser Science, University of Electro-Communications



Fig. 2. Wedge shaped energy degrader of variable angle and thickness.

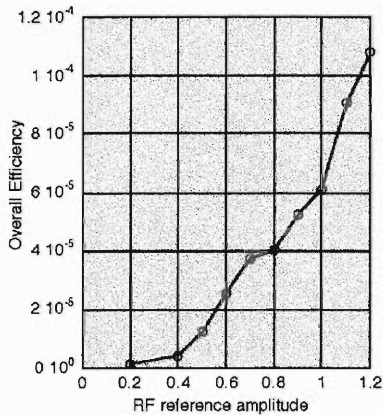


Fig. 3. Overall efficiency (= detected  $\alpha$ /RIPS output) plotted as a function of applied rf voltage. The reference value of 1.0 corresponds to about 40 V.

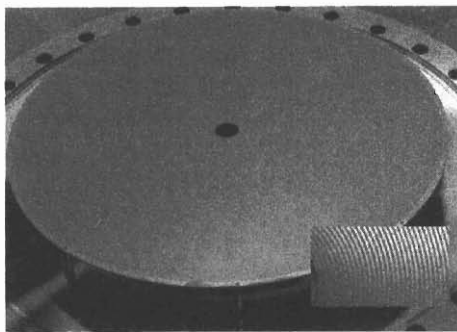


Fig. 4. New rf electrode assembly made of planar PCB. Part of the electrode is enlarged at the bottom right. An additional small central electrode will be attached at the center.

expected overall efficiency of 1%.

With this in mind a new large cell of 40 cm in diameter and 2 m in length has recently been installed. In this new cell, the rf funnel structure was replaced by a planar Printed Circuit Board (PCB) disk with fine ring electrodes (Fig. 4). The spatial period of the ring electrodes is 0.5 mm and the disk is 260 mm in diameter. In the first on-line test of the new setup, the overall efficiency already exceeded  $10^{-3}$ , although there was a vacuum leak in the cell which resulted in a poor background pressure of  $10^{-5}$  Torr. A typical experimental result is shown in Fig. 5. The overall efficiency is plotted versus the applied dc gradient field

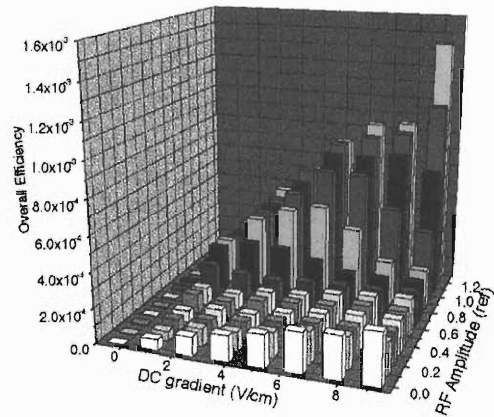


Fig. 5. Overall efficiency of the new setup plotted versus the applied dc gradient field and the rf amplitude.

and the rf amplitude. Since at the time of the first test a central part of the electrode assembly was not installed, we could observe some transported  $^8\text{Li}$  ions even when the rf field was turned off. In this case a fraction of ions stopped in the cell can be transported by the dc field only, since the central aperture is 14 mm in diameter. The additional central part of the electrode made of a plane PCB of 0.2 mm thick with a fine electrode structure and a small exit aperture of 0.5 mm in diameter is under fabrication.

Two types of downstream experimental instruments are also in preparation. One is a linear rf trap for precision spectroscopy of the hyperfine structure of  $^{11}\text{Be}$  ions.<sup>6)</sup> The other is a multireflection time-of-flight mass spectrometer.<sup>7)</sup> They will be connected to the present rf ion guide system for future on-line experiments with unstable nuclear beams.

#### References

- 1) M. Wada et al.: Presented in Int. Workshop on Ion Guide Isotope Separator On-Line (IGISOL-6), Dubna 1997, unpublished.
- 2) I. Katayama et al.: *Hyperfine Interact.* **115**, 165 (1998).
- 3) M. Wada et al.: *RIKEN Accel. Prog. Rep.* **33**, 180 (2000).
- 4) M. Wada et al.: *RIKEN Rev.*, No. 31, 56 (2000).
- 5) M. Wada et al.: *AIP Conf. Proc.* **606**, 625 (2002).
- 6) T. Nakamura et al.: *RIKEN Accel. Prog. Rep.* **35**, 99 (2002).
- 7) Y. Ishida et al.: *RIKEN Accel. Prog. Rep.* **35**, 157 (2002).

## Development of RI atomic beam device with a Laval-type nozzle

H. Miyoshi,<sup>\*1</sup> H. Ueno, K. Asahi, H. Ogawa,<sup>\*2</sup> J. Murata, K. Sakai,<sup>\*1</sup> D. Kameda,<sup>\*1</sup> Y. Kobayashi, W. Sato,  
A. Yoshimi, H. Watanabe, K. Yoneda, N. Imai,<sup>\*3</sup> J. Kaihara,<sup>\*1</sup> K. Shimada,<sup>\*1</sup> and T. Koike<sup>\*1</sup>

A number of nuclear moments have been measured at the RIKEN Ring Cyclotron during the last decade, using spin-polarized beams from the fragmentation reaction combined with nuclear magnetic resonance via change in the angular distribution of  $\beta$  rays ( $\beta$ -NMR method). This approach, however, requires that several conditions be fulfilled.

To avoid the difficulties forecast for certain requirements when the measurement is extended to the heavier mass region, we have attempted to develop a method which involves a low-energy spin-polarized radioactive isotope (RI) beam, which we call the *RI atomic-beam method* (RIAB). The advantage of this method is that no special host material or  $\beta$ -ray asymmetry is required, since the magnetic resonance is performed in-flight and the resonance is detected simply by counting the radiations of the transmitted RI. A schematic view of the total setup is shown in Ref. 1.

A hexapole magnet is installed to converge the beam from the nozzle of the cell. In order to choose the field strength of the magnet, we need to determine the range of velocities at which the RI atoms emerge from the nozzle. As the first step toward this goal, we performed an experiment to measure the total spout efficiency (*i.e.*, stopping efficiency  $\times$  spout efficiency).

The experiment was carried out at RIPS. A  $^{17}\text{N}$  beam was produced from the fragmentation of  $^{18}\text{O}$  projectiles on a  $1.48\text{ g/cm}^2$  thick  $^9\text{Be}$  target at an energy of  $E/A = 100\text{ MeV/u}$ .

First, the  $^{17}\text{N}$  atoms must be stopped by a noble gas in a cell. We chose Ar for the stopping gas material. The temperature of the gas was kept as low as 150 K. From our simulation, velocity ranges below 400 m/s are favorable for the RIAB technique. The major factors determining this are the vacuum system performance and the field strengths realizable with the hexapole magnet. The RI atoms are ejected from the cell together with the Ar carrier gas into vacuum. A nozzle<sup>2)</sup> was mounted on the exit of the cell so that the gas spouts out at forward angles. A schematic view of the setup including this *Laval-type nozzle* is shown in Fig. 1.

In this experiment, we measured the counting rate of  $\beta$  rays from  $^{17}\text{N}$  with a plastic counter telescope. The experiment was performed under two different conditions: the  $\beta$  particles were counted with and without

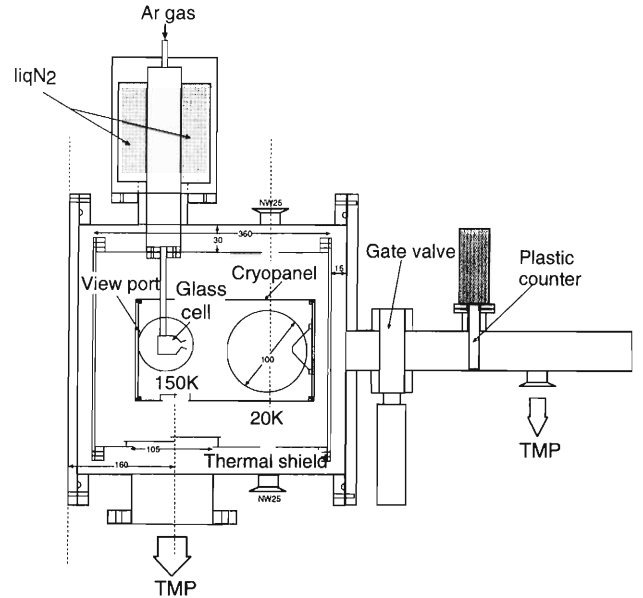


Fig. 1. Schematic view of the setup. The  $^{17}\text{N}$  beam is incident at the cell from the direction perpendicular to the figure, and a fraction of atoms in the beam are stopped in a gas in the cell. **TMP**: Turbomolecular pump.

Table 1. Result of the experiment.

status	BaF <sub>2</sub> (counts)	Plastic (counts)	$R (= \frac{\text{Plastic}}{\text{BaF}_2})$
Ar Flow	15923159	19385	$1.217 \times 10^{-3}$
No Flow	13163251	15347	$1.166 \times 10^{-3}$

the Ar carrier gas flow. From the difference in the  $\beta$ -counting rates between the two conditions, we ascertained the  $^{17}\text{N}$  atoms to indeed be extracted from the cell by the carrier gas. The experimental result is shown in Table 1.

The BaF<sub>2</sub> counter which counts scattering particles such as  $\gamma$  rays and neutrons was used as a  $^{17}\text{N}$  beam monitor. The counter was located far from the RIAB setup. From Table 1, a definite difference is observed between the beam-normalized  $\beta$ -counting rates  $R$  for the gas flowing and non-flowing conditions. The difference, however, is not as large as expected, presumably because of a large background consisting of  $\beta$  rays and neutrons which were emitted from  $^{17}\text{N}$  activities stopped in the cell wall. The rate of  $^{17}\text{N}$  particles incident at the cell was counted with a beam counter (a plastic scintillator). From the observed difference in

<sup>\*1</sup> Tokyo Institute of Technology

<sup>\*2</sup> National Institute of Advanced Industrial Science and Technology

<sup>\*3</sup> University of Tokyo

$\beta$  countings, divided by the beam rate (normalized by the BaF<sub>2</sub> counts) and corrected for the  $\beta$ -solid angles, we obtain a total spout efficiency (= number of extracted <sup>17</sup>N atoms / number of incident <sup>17</sup>N atoms) of about  $3.95 \times 10^{-7}$ . Since the momentum distribution of the <sup>17</sup>N beam was rather sharply cut at the RIPS momentum slit at the F1 focal plane ( $\pm 3\%$  at momentum peak), we could estimate the fraction of the incident <sup>17</sup>N particles that are stopped by a gas in the cell. The net spout efficiency, defined as the ratio of the number

of extracted <sup>17</sup>N atoms to that of stopped <sup>17</sup>N in the gas, is estimated to be 0.4%. Modification of the system (the shape of the cell, temperature, *etc.*) is under way in order to improve efficiency.

#### References

- 1) H. Miyoshi et al.: RIKEN Accel. Prog. Rep. **34**, 181 (2001).
- 2) W. J. Hiller and W.-D. Schmidt-Ott: Nucl. Instrum. Methods **139**, 331 (1976).

## Development of a detector system for transient magnetic field experiments

H. Ueno, W. Sato, H. Ogawa,<sup>\*1</sup> Y. Kobayashi, D. Kameda,<sup>\*2</sup> H. Miyoshi,<sup>\*2</sup> J. Kaihara,<sup>\*2</sup> N. Imai,<sup>\*3</sup>  
H. Watanabe, A. Yoshimi, K. Yoneda, and K. Asahi

For the  $g$ -factor measurement of short-lived ( $\tau \sim$  ps) excited states of unstable nuclei, we are preparing transient field experiments<sup>1)</sup> using radioactive nuclear beams. In this report, the annealing of thick ferromagnetic targets and development of a detector system for the transient field<sup>2)</sup> using a  $^{22}\text{Ne}$  beam are described.

For the preparation of ferromagnetic material, annealing of self-supported Gd foils with thicknesses of  $t = 25$  and  $100 \mu\text{m}$  were employed. After being placed in the quartz-tube furnace, the foils were heated at 1100 K for 10 minutes at a pressure of  $1 \times 10^{-6}$  Torr. The heating power was then reduced slowly and the foils were cooled to room temperature. Although hexagonal Gd shows magnetic anisotropy between the easy direction of magnetization and the crystallographic  $c$ -axis depending on the temperature, it has been reported that well-annealed polycrystalline foils show almost the same magnetization as the single crystal.<sup>3)</sup> Magnetization of the Gd foils was measured with a SQUID magnetometer as a function of the polarizing field  $B_{\text{ext}}$  at  $T = 77$  K. The measured magnetization as a function of temperature is shown in Fig. 1. The obtained magnetizations of 4.5 and 4.1 in units of  $\mu_{\text{B}}/\text{atom}$  for the samples with  $t = 25$  and  $100 \mu\text{m}$  at  $B_{\text{ext}} \sim 0.03$  T, at which the magnetization should be saturated if the sample is well-annealed, were found to be inadequate compared with the reported value of  $6.2 \mu_{\text{B}}/\text{atom}$  for  $t = 2\text{--}4 \text{ mg}/\text{cm}^2$  thin foils.<sup>3)</sup> This is due to difficulties in the annealing of thick samples. Thick foils, however, are needed for RI-beam experiments, so that development of another method of annealing is in progress.

The performance of the detector system, whose design is described in the previous report,<sup>1)</sup> was tested using a  $^{22}\text{Ne}$  beam, in order to detect the particle- $\gamma$  coincidence. The  $J^\pi = 2^+$  first excited state of  $^{22}\text{Ne}$  at  $E_x = 1.275$  MeV, whose magnetic moment and lifetime are known to be  $\mu = +0.65(2)\mu_{\text{N}}$  and  $\tau = 3.63(5)$  ps, respectively, was populated by the scattering from a  $50 \text{ mg}/\text{cm}^2$  thick Pb target. The average energy of the  $^{22}\text{Ne}$  beam was  $E = 12.9 \text{ MeV}/\text{nucleon}$ , which corresponds to a beam velocity of  $v = 22.9v_0$ , where  $v_0$  is the Bohr velocity. Although the velocity might be excessive for the transient field experiment, the detector system was tested in this situation, taking into account the fact that RI beams produced by the projectile frag-

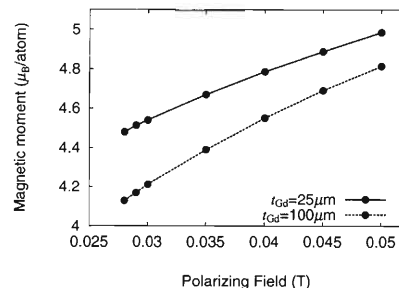


Fig. 1. Measured magnetization of Gd foils with thicknesses of  $t = 25$  and  $100 \mu\text{m}$  at a temperature  $T = 77$  K as a function of the polarizing magnetic field.

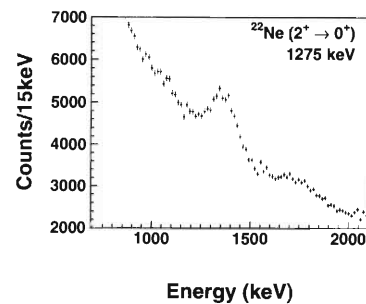


Fig. 2. A  $\gamma$ -ray spectrum obtained for the de-excitation from the  $2^+$  first excited state of  $^{22}\text{Ne}$  after the Coulomb excitation.

mentation reaction have very high velocities compared to the Bohr velocity. In the experiment de-excitation  $\gamma$  rays from the  $2^+$  first excited state after the Coulomb excitation were identified as a peak in the obtained  $\gamma$  spectrum as shown in Fig. 2.

The observed large background, however, interferes seriously with the determination of the photo-peak area in the experiment with RI beams. To reduce the background, we are improving the detector system.

### References

- 1) H. Ueno et al.: RIKEN Accel. Prog. Rep. **33**, 190 (2000).
- 2) R. R. Borchers, B. Herskind, J. D. Bronson, L. Grondzins, R. Kalish, and D. E. Murnick: Phys. Rev. Lett. **20**, 424 (1968).
- 3) O. Häusser, H. R. Andrews, D. Ward, N. Rud, P. Taras, R. Nicole, J. Keinonen, P. Skensved, and C. V. Stager: Nucl. Phys. A **406**, 339 (1983).

<sup>\*1</sup> National Institute of Advanced Industrial Science and Technology

<sup>\*2</sup> Tokyo Institute of Technology

<sup>\*3</sup> University of Tokyo

## Gas cell RI beam stopper with electric transportation system

J. Kaihara,\*<sup>1</sup> K. Asahi, N. Imai,\*<sup>2</sup> D. Kameda,\*<sup>1</sup> Y. Kobayashi, T. Koike,\*<sup>1</sup> H. Miyoshi,\*<sup>1</sup> J. Murata, H. Ogawa,\*<sup>3</sup> K. Sakai,\*<sup>1</sup> W. Sato, K. Shimada,\*<sup>1</sup> H. Ueno, H. Watanabe, K. Yoneda, and A. Yoshimi

As part of the plan for building a radioactive atomic beam apparatus (RIAB) with the goal of producing highly polarized radioactive nuclei,<sup>1)</sup> we performed R&D of an ion-stopping gas cell, for the purpose of stopping the RI beam produced by the projectile fragmentation reaction and separated by the RIPS (**RIKEN Projectile-Fragment Separator**) at RIKEN. In order to use the RI beam as an ion beam incident to the RIAB, the beam momentum must be degraded, and also electrically neutralized. In the year 2000, we confirmed by a simulation study that the RIAB has extensive potential for studies using polarized RI and will be able to obtain nearly 100% polarization, which gives us precise measurements of nuclear moments in a wide range of the nuclear chart, application to surface materials science, and also a test of fundamental symmetries such as time-reversal invariance.

The most challenging technical part of the RIAB is the ion stopper. A low-pressure gas cell ion stopper (LPGS) is located immediately in front of the RIAB magnets, providing supersonic cold ion flows with a Laval-type nozzle.<sup>2)</sup> Because of its very low pressure of around 1 Torr, we cannot expect sufficient stopping power and resultant transportation efficiency. The goal of the present study is to build another high-pressure gas cell stopper (HPGS) located immediately in front of the low-pressure gas cell in order to increase the efficiency. The incident ions are stopped inside the gas volume (He gas, 730 Torr), and then transported outside the gas cell through a small hole by an electric field. We applied a unique electric field, which can lead the charged ions through a very localized output hole with small loss. By utilizing electric transportation, we can solve the problem of severe contamination of the carrier gas downstream. Also, the sufficiently fast transportation time allows us to use short-lived radioactive nuclei.

We built the first prototype chamber apparatus of the HPGS after a simulation study, and it is shown in Fig. 1. The field pattern was optimized to achieve maximum transportation efficiency. In order to obtain a strong focusing force at the end point, a one-order-higher field was applied there. A test using a radioactive source must be carried out as a first step. However, because of the difficulties in achieving an ion-emitting source and detecting the low-energy ions, we performed a test experiment, using an ion beam at RIKEN in October 2001. We used  $^{17}\text{N}$  ions produced by projectile

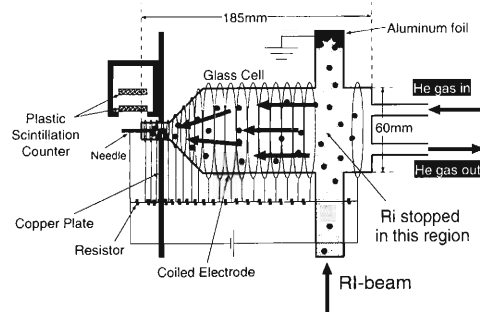


Fig. 1. Schematic view of the setup. (The copper plates are the shield for  $\beta$ )

fragmentation reaction of a 100 MeV/u  $^{18}\text{O}$  beam on a 1.48 ng/cm<sup>2</sup>  $^{9}\text{Be}$  target, separated by RIPS at the E6 beam line of RIKEN Ring Cyclotron. The incident beam energy at the HPGS is about 500 keV/u after degrading.

The transported ions are counted by two plastic scintillation counters, which detect  $\beta$  particles emitted from  $\beta$ -unstable ions. By observing the field strength dependence on the  $\beta$  counting rate, we can estimate the transportation rate. Unfortunately, no clear evidence of the transportation was obtained in the first test experiment.  $^{17}\text{N}$  was not clearly observed. Possible reasons for this are ion neutralization due to gas impurity, a low beam-stopping rate, a nonoptimal electric field, and charge-up of the glass cell.

Considering our experience with the test experiment, we are now attempting to change the design drastically. For example, we will place electrodes inside a large gas volume instead of surrounding the glass cell with electrodes. As a result, the apparatus can achieve a high vacuum level, therefore, the gas impurity problem should be significantly reduced. As regards the test procedure, a test without using an ion beam should be performed for simplicity. Production and detection of the helium ions using a mass separator can advance our R&D.

Our efforts to modify the current HPGS system must succeed within one year. The R&D of the LPGS and the design for the magnets are successfully under way, therefore, we can expect to see the first polarized radioactive atomic beam in the near future.

### References

- 1) H. Miyoshi et al.: RIKEN Accel. Prog. Rep. **34**, 181 (2001).
- 2) H. Miyoshi et al.: RIKEN Accel. Prog. Rep. **35**, 143 (2002).

\*<sup>1</sup> Tokyo Institute of Technology

\*<sup>2</sup> University of Tokyo

\*<sup>3</sup> National Institute of Advanced Industrial Science and Technology

## RF deflector system for proton-rich RI beams (II)

K. Yamada,\* I. Tanihata, and T. Motobayashi\*

The construction of the RF deflector system reported previously<sup>1)</sup> is continuing to make progress. The system is expected to be installed in the RIPS<sup>2)</sup> beam line to obtain high-purity proton-rich RI beams. The secondary beam in the second stage of RIPS passes through a vertically arranged parallel-electrode, to which a high voltage with half the frequency of the cyclotron RF signal is applied. The particles in the beam are deflected depending on their arrival time at the position of the electrodes, and are filtered by a two-dimensional slit placed at the focal point.

The deflector system is shown in Fig. 1. It consists of an electrode part, a two-dimensional slit system (2D slit), a main amplifier, a DC power supply, and a low-level control system. The parallel-electrodes are set in a main vacuum chamber, and are connected electronically to a cavity resonator.

The high voltage is in the sinusoidal form with a frequency of 12–18 MHz. The maximum peak-to-peak voltage is slightly higher than 100 kV, depending on the frequency. To generate the voltage, a coaxial cavity resonator with cylindrical shape is adopted. The structure with a fixed-length cavity and two tuners attached on the sides to change the resonance frequency enables a shorter cavity length compared with a commonly adopted design with a variable-length cavity. The cavity is 2250 mm long and 700 mm in diameter, and the inner shaft with 120 mm in diameter is water cooled and is directly connected to the upper electrode. Each deflector electrode is made of copper, and

is 120 mm wide and 700 mm long. The electrode gap is fixed to be 40 mm. The deflector body can be moved aside from the beam line with the help of a rail stage when it is not being used. The main amplifier with 20 kW output power is placed beside the cavity and directly coupled to the feeder. The total power input of about 70 kVA and water flow of 55 lit/min are required. The two-dimensional slit system is made of 25-mm-thick copper plates and the slit aperture is remote controlled to within  $\pm 100$  mm. The deflector will be installed between the Q9 lens and the F2 focal plane of RIPS by replacing the switching magnet. The slit chamber will be placed upstream of the Q10 lens. The distance between the center of the electrode and the slit is about 1.8 m.

The performance of the deflector is evaluated according to first-order beam optics. It is assumed that the beam is focused on the F2 slit in the horizontal direction and on the new slit in the vertical direction. In the case of the  $^{54}\text{Ni}$  secondary beam produced from  $^{58}\text{Ni}$  with the energy of 57 A MeV, its purity in the total secondary beam was about  $10^{-4}$ . With the use of the present RF deflector, the purity is expected to increase by approximately 100 times.

### References

- 1) K. Yamada et al.: RIKEN Accel. Prog. Rep. **34**, 201 (2001).
- 2) T. Kubo et al.: Nucl. Instrum. Methods. Phys. Res. B **70**, 309 (1992).

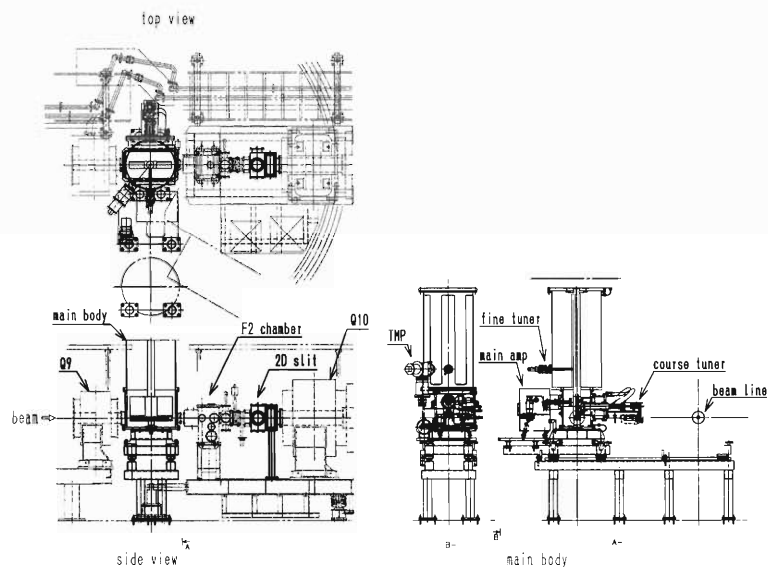


Fig. 1. The general plan for RF deflector system.

\* Department of Physics, Rikkyo University

## Liquid hydrogen target for SMART experiments

T. Uesaka,<sup>\*1</sup> K. Suda,<sup>\*1</sup> M. Hatano,<sup>\*2</sup> K. Sekiguchi,<sup>\*2</sup> A. Tamii,<sup>\*2</sup> N. Sakamoto, T. Ohnishi, K. Yako,<sup>\*2</sup> S. Sakoda,<sup>\*2</sup> T. Saito,<sup>\*2</sup> N. Uchigashima,<sup>\*2</sup> H. Okamura,<sup>\*1</sup> and H. Sakai<sup>\*2</sup>

Polarization transfer observables are sensitive to specific spin-dependent transition amplitudes and can be a powerful tool for probing the fundamental interactions relevant to the reaction. This is also the case in the investigation of three-nucleon (3N) force effects in the  $d+p$  scattering. A theoretical calculation predicts that the effects of the 3N force, which are by nature spin dependent, manifest themselves most clearly in polarization transfer coefficients  $K_{yy}^y$ ,  $K_{xx}^y$ , and  $K_{xz}^y$  at backward angles.<sup>1)</sup> We have developed a liquid hydrogen target for the polarization transfer measurement<sup>2)</sup> of the  $d+p$  elastic scattering at SMART.

An overview of the target system is shown in Fig. 1. The target volume is  $20\text{ mm}\phi \times 2\text{ mm}^t$  and is sealed by  $6\text{-}\mu\text{m}$ -thick Havar foils on both sides. The target cell is attached to the second stage ( $\sim 4\text{ K}$ ) of a commercial refrigerator and is surrounded by a radiation shield. The radiation shield is mounted on the first stage of the refrigerator whose temperature is approximately  $50\text{ K}$ . A thin heater inserted between the refrigerator and the target cell is used to maintain the target temperature at approximately  $17\text{ K}$ . A silicon diode sensor on the target cell continuously monitors the temperature of the target. We employ no feedback system for controlling the target temperature since the temperature is found to be stable within the range of  $\pm 0.1\text{ K}$  when extra heat load is absent. The temperature increases by only  $0.3\text{ K}$  when a  $270\text{ MeV}$  deuteron beam of  $50\text{ nA}$  is incident on the target, where the heat load is  $\sim 100\text{ mW}$ .

Hydrogen gas is fed to the target cell through a reservoir of a  $35\text{ l}$  volume as shown in Fig. 2. In the course of a measurement, all the valves A–F are closed and the inner pressure of the target, being about  $1\text{ atm}$  throughout the measurement, is continuously monitored by a Baratron gauge. To prevent the inner pres-

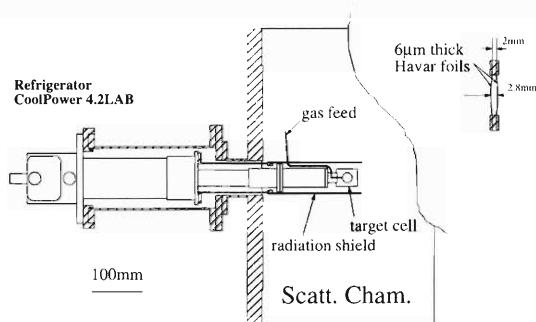


Fig. 1. View of liquid hydrogen target.

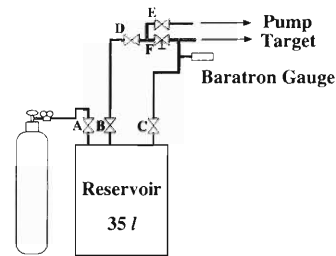


Fig. 2. Gas feeding system.

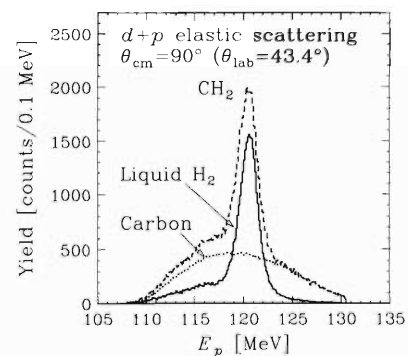


Fig. 3. Proton energy spectra of the  $d+p$  elastic scattering from polyethylene (broken line) and from liquid hydrogen target (solid line). Spectrum for a carbon target (dotted line) under the same experimental conditions is also shown.

sure of the target from becoming too high, an electric valve C opens in the case that the readout pressure of the Baratron gauge exceeds  $2\text{ atm}$ .

Figure 3 shows a proton energy spectrum for the  $d+p$  elastic scattering at  $E_d = 270\text{ MeV}$  and  $\theta_{\text{cm}} = 90^\circ$ . The solid line represents the spectrum obtained with the liquid hydrogen target. A shoulder at the lower energies is due to deuteron breakup from a hydrogen target. For comparison, spectra obtained with a polyethylene target (broken line) and a carbon target (dotted line) under the same experimental conditions are shown in the figure. With the known cross-section<sup>3)</sup> of the  $d+p$  elastic scattering, we obtained the effective thickness of the target to be  $2.8\text{ mm}$  ( $20\text{ mg/cm}^2$ ). This indicates that the Havar foil on each side swells by  $0.4\text{ mm}$ .

### References

- 1) H. Kamada et al.: personal communications.
- 2) K. Sekiguchi et al.: RIKEN Accel. Prog. Rep. **35**, 44 (2002).
- 3) H. Sakai et al.: Phys. Rev. Lett. **84**, 5288 (2000).

<sup>\*1</sup> Saitama University

<sup>\*2</sup> University of Tokyo

## Development of polarized proton target for RI beam experiment

T. Wakui, M. Hatauo,\*<sup>1</sup> H. Sakai,\*<sup>1</sup> T. Uesaka,\*<sup>2</sup> and A. Tamii\*<sup>1</sup>

A polarized solid proton target is being developed for experiments with RI beams. The target will be used for the structural study of unstable nuclei through experiments involving inverse kinematics. In such experiments, low-energy recoiled protons (typically less than 10 MeV) must be detected. A conventional polarized proton target system is not suitable for such experiments because it requires a high magnetic field ( $\geq 2.5$  T) and a very low temperature ( $\leq 1$  K). These conditions will create difficulties in the detection of recoiled protons. Therefore, a polarized proton target that can be operated in a lower magnetic field ( $\leq 0.3$  T) at a higher temperature ( $\geq 77$  K) is desirable for RI beam experiments. The goal of this study is to attain a polarization of more than 60% in a target with a diameter of 20 mm and a thickness of 2 mm.

Protons in a crystal of aromatic molecules such as naphthalene or *p*-terphenyl doped with pentacene are polarized by means of a microwave-induced optical nuclear polarization technique combined with the integrated solid effect (ISE) method.<sup>1)</sup> In this method, pentacene molecules are excited to the lowest triplet state by laser irradiation. A population difference appears in the Zeeman sublevels of the triplet state due to the angular momentum selection rule; the electron

alignment occurs spontaneously. The obtained population difference, 73%, is independent of the magnetic field strength and the temperature. Then, the population difference is efficiently transferred to proton polarization even in a magnetic field of 0.3 T by the ISE method. The polarization procedure is described in Ref. 2.

The crystals are produced by the Bridgman technique after purification of materials by the zone-melting method. A purification system and a crystallization system were constructed last year.<sup>3)</sup> A proton polarizing system was also assembled and test experiments to polarize protons have been started.<sup>4)</sup>

Figure 1 shows a schematic of the proton polarizing system. A target crystal, whose typical size is  $4 \times 5 \times 3$  mm<sup>3</sup>, is placed in a microwave cavity mounted in the center of a C-type magnet. The laser used in this study is a continuous wave Ar<sup>+</sup> laser having a maximum power of 5 W. In order to obtain a large population difference in the triplet state, the laser beam is pulsed by an optical chopper and the resulting power is 40 mW. The pulsed microwave irradiates the target crystal before pentacene molecules in the triplet state decay to the ground state. The frequency and power of the microwave are 9.1 GHz and 2.5 W, respectively.

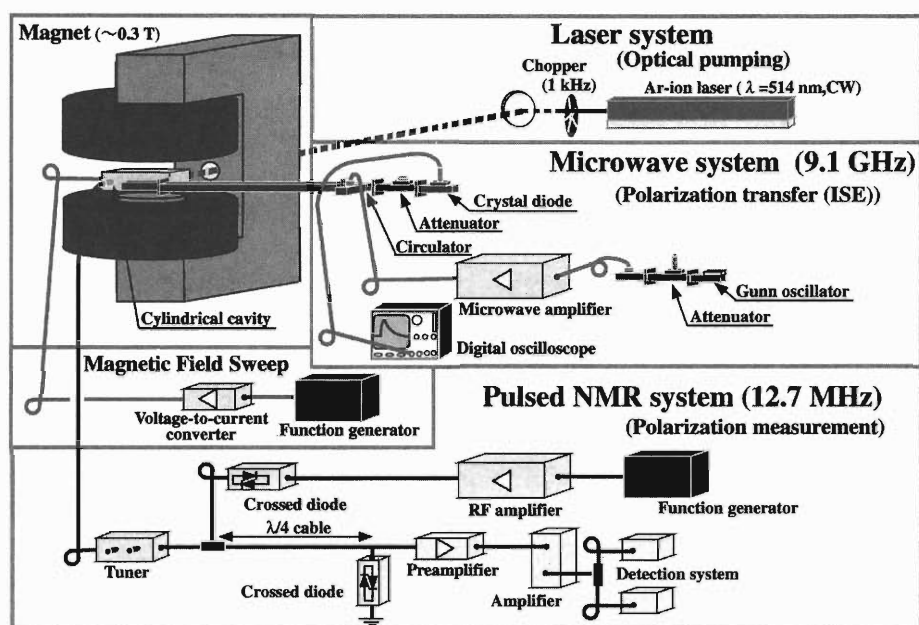


Fig. 1. Schematic of the proton polarizing system. The system consists of a magnet, a laser system for optical pumping, a microwave system and a magnetic field sweep system for polarization transfer, and a pulsed NMR system for polarization measurement.

\*<sup>1</sup> University of Tokyo

\*<sup>2</sup> Saitama University

During the microwave irradiation, the magnetic field is swept by applying a triangular wave current of 53 A (peak-to-peak) to a set of coils placed in the microwave cavity. This current produces the maximum magnetic field of  $\pm 35$  Gauss. The proton polarization is measured with a pulsed NMR system, whose frequency is 12.7 MHz.

Figure 2 shows a result obtained with a crystal of *p*-terphenyl doped with pentacene in 0.3 T at room temperature. The measured buildup time was  $8.2 \pm 0.5$  minutes, and the extrapolated maximum proton polarization was  $0.38 \pm 0.02\%$ . The polarization was enhanced by a factor of 4000 compared to that at thermal equilibrium under the same conditions. The relaxation time was  $17.5 \pm 1.3$  minutes.

Recently, we have succeeded in polarizing protons up to  $18.4 \pm 3.9\%$  in 0.3 T at 100 K. Figures 3 and 4 show the proton polarization as a function of time in the buildup and relaxation processes, respectively. The crystal was naphthalene doped with 0.01 mol% pentacene. The measured buildup time was  $1.7 \pm 0.2$  hours and the relaxation time was  $21 \pm 3$  hours.

The proton polarization can be improved by using a higher power laser for the optical pumping. This is because a single laser pulse can excite only 0.1% of pentacene to the lowest triplet state. Therefore, we will upgrade the laser to one with a maximum power of 25 W with which proton polarization higher than

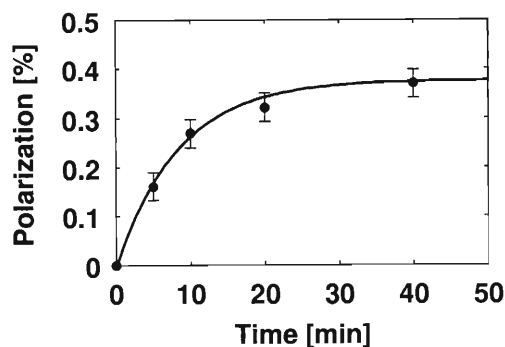


Fig. 2. Proton polarization as a function of time in the buildup process in 0.3 T at room temperature. The target crystal is *p*-terphenyl doped with pentacene. The buildup time is about  $8.2 \pm 0.5$  minutes and the extrapolated maximum proton polarization is  $0.38 \pm 0.02\%$ .

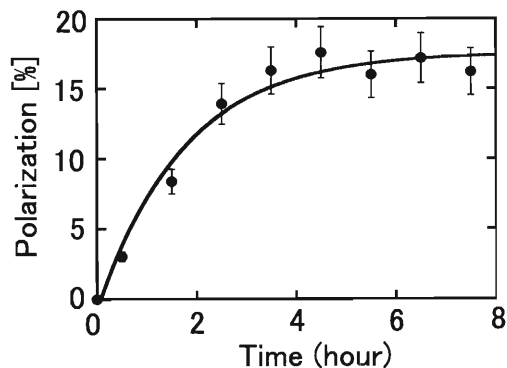


Fig. 3. Proton polarization as a function of time in the buildup process in 0.3 T at 100 K. The target crystal is naphthalene doped with pentacene. The proton polarization is  $18.4 \pm 3.9\%$ .

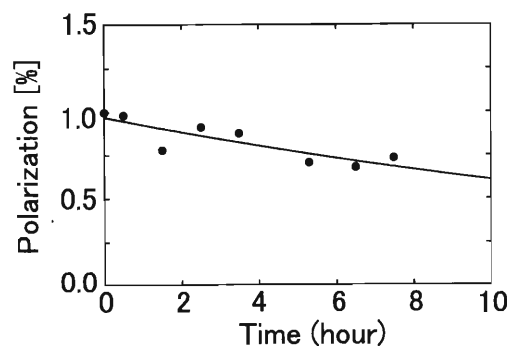


Fig. 4. Proton polarization in the relaxation process in 0.3 T at 100 K. The relaxation time is  $21 \pm 3$  hours.

40% is expected.

We are also planning further improvement of the system: an increase of the repetition rate of the laser pulse and an enlargement of the crystal size.

#### References

- 1) A. Henstra et al.: Phys. Lett. A **134**, 134 (1988).
- 2) M. Hatano et al.: RIKEN Accel. Prog. Rep. **33**, 182 (2000).
- 3) M. Hatano et al.: RIKEN Accel. Prog. Rep. **34**, 196 (2001).
- 4) T. Wakui et al.: RIKEN Accel. Prog. Rep. **34**, 194 (2001).

# Continuous spin precession of noble gas nuclei with active feedback system

A. Yoshimi, K. Asahi, and T. Koike\*

We report on the study of continuous spin precession of noble gas nuclei<sup>1,2)</sup> where the spin-polarized nuclei continue to precess beyond their intrinsic transverse relaxation time with the help of a feedback system. The aim of this study is to realize a high-precision measurement of spin precession frequency for fundamental physics experiments. We have constructed the optical detection system for nuclear spin precession of  $^{129}\text{Xe}$  instead of using a pick-up coil.<sup>2,3)</sup> This method can realize the observation of continuous nuclear spin precession at a very low spin density ( $< 1$  torr) and low frequencies ( $< 100$  Hz), and thus can be applied to a heavier noble gas Rn and a neutrons, which are important for fundamental symmetry studies.

The experimental apparatus is shown in Fig. 1. A sample cell which contains  $^{129}\text{Xe}$  gas and a small amount of Rb vapor is located in a magnetic shield.  $^{129}\text{Xe}$  nuclear spins, which are polarized through spin exchange interaction with optically pumped Rb atoms, precess around a static field  $B_0 = 28.3$  mG ( $\nu_0 = 33.5$  Hz) produced by a solenoid coil. The nuclear precession at such a low frequency produces a small sinusoidal variation in the transverse polarization of Rb atoms via the spin exchange. A probe laser beam from a narrow-frequency-bandwidth ( $< 1$  nm) diode laser, which has a wavelength of the Rb D1-absorption line (794.7 nm) and is modulated in circular polarization by a photoelastic modulator (PEM), passes through the cell in the precession plane. Thus the nuclear precession of  $^{129}\text{Xe}$  is detected by observing the change in the intensity of the transmitted probe laser beam. In order to preserve the nuclear precession, a feedback field  $B_{\text{FB}}$  is applied to the cell by applying a current into a pair

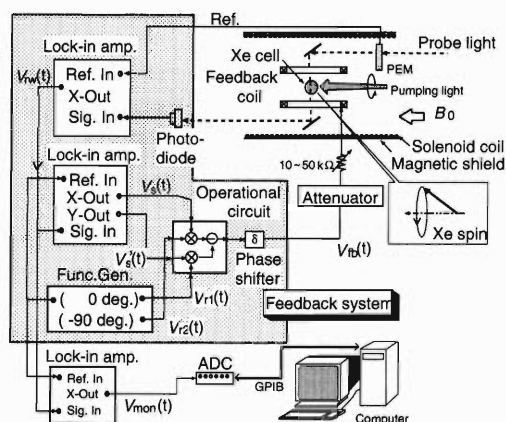


Fig. 1. Experimental apparatus.

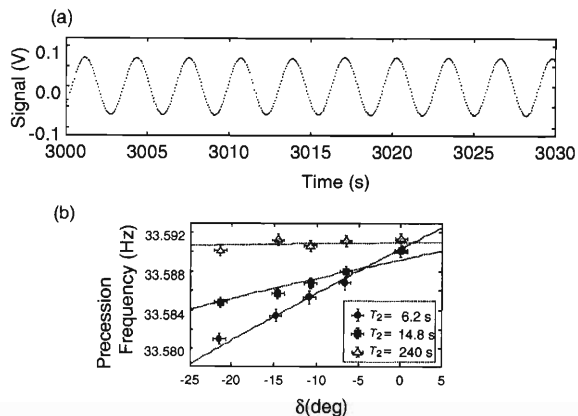


Fig. 2. (a) Observed continuous precession signal. (b) Observed frequency shift to phase error  $\delta$  of feedback signal.

of coils around the cell. The phase and amplitude of the feedback current are tuned such that the  $B_{\text{FB}}$  field is kept perpendicular to the transverse component of the spin polarization vector. The current fulfilling such conditions is synthesized from the phase-sensitively detected signal  $V_s(t)$  ( $\sim 0.3$  Hz) and the reference signals for lock-in detection  $V_{r1}(t)$  and  $V_{r2}(t)$  ( $\sim 33.2$  Hz). This method of producing the  $B_{\text{FB}}(t)$  can considerably decrease ( $\sim 10^{-3}$ ) the noise component in the raw signal  $V_{\text{rw}}(t)$  ( $\sim 33.5$  Hz).<sup>2)</sup>

A continuous precession signal was observed after turning on the feedback system as shown in Fig. 2 (a). The observed signal  $V_{\text{mon}}(t)$  was phase-sensitively detected by the reference signal of 33.2 Hz and thus had the frequency of 0.3 Hz. We investigated the response of the precession frequency to a phase detuning  $\delta$  of  $B_{\text{FB}}$  using a phase shifter, because the sensitivity of the oscillation frequency to  $\delta$ , if it is high, might be a serious source of error in a high-precision experiment. As shown in Fig. 2 (b), the frequency shift due to  $\delta$  is smaller for longer transverse relaxation time  $T_2$ .

We are currently attempting to use a smaller density  $^{129}\text{Xe}$  in this experiment. Thus far we have confirmed that the  $^{129}\text{Xe}$  spins of a 10 torr gas pressure can realize the continuous precession. An improvement in the frequency stability is also being prepared.

## References

- 1) A. Yoshimi et al.: RIKEN Accel. Prog. Rep. **34**, 215 (2001).
- 2) A. Yoshimi et al.: AIP Conf. Proc. **570**, 353 (2001).
- 3) R. E. Stoner et al.: Phys. Rev. Lett. **77**, 3971 (1996).

\* Tokyo Institute of Technology

## Rotating target system for the Big-RIPS separator

A. Yoshida, T. Kubo, Y. Takahashi, and I. Tanihata

A rotating target system for the projectile fragment separator (Big-RIPS) in the RI Beam Factory (RIBF) has been developed. It was reported<sup>1)</sup> that a test experiment was performed using an  $^{40}\text{Ar}^{9+}$  beam at 24 A MeV and 1.9 pμA. Simulation studies were carried out to explain the data and to estimate the beam spot temperature under future Big-RIPS operating conditions.

A thermal dynamics calculation code, ANSYS (Copyright.c, ANSYS, Inc.), was used for the simulation. A carbon target disk, 2 mm in thickness and 260 mm in diameter and sandwiched by aluminum cooling plates, which was used in the experimental setup, was modeled. A schematic view of the disk was shown in our previous report.<sup>1)</sup> Precise meshing was required around the beam spot because the heat deposited by the beam is very much localized to a circular area of approximately 3 mm in diameter. A Gaussian shape beam intensity distribution was assumed at the beam spot and an energy loss function of  $^{40}\text{Ar}$  beam in carbon material was applied. The boundary temperature for the cooling water inside the aluminum plate was fixed at 25°C. A surface emission option was considered for the thermal radiation effect and a measured emissivity value of 0.84 was used. Nonlinear analysis was carried out using the temperature-dependent heat conductivity and specific heat of the materials used.<sup>2)</sup> This code can control the rotation of a disk by means of a mass transport option and a transitional analysis. Because the model size is large and complex, it takes a few hours of CPU time for one rotation, although we checked that the beam spot temperature becomes constant after several times of rotation. On the other hand, if there is no water cooling, the beam spot temperature does not change considerably but the temperatures of the other parts increase very slowly to reach a few hundreds °C. This indicates that the water cooling does not affect significantly the beam spot but affects other parts of the target system and helps the system works safely.

The results of the simulation are indicated in Fig. 1. Because there was an ambiguity for measuring the actual beam spot size in the experiment, a series of calculations were carried out for various spot sizes. The measured beam spot size was approximately 3 mm in diameter using a ZnS foil. The simulations also supported the same beam spot size. In the low-rotation-speed region, the measured temperature is lower than the simulated one. This may be because of the position resolution of an infrared radiation thermoviewer used for this measurement. Its specific resolution, 0.6 mm/pixel and 0.1°C in digital image, was good enough, but there was a slight vibration observed during the rotation. It was ±1 mm in the radial direction

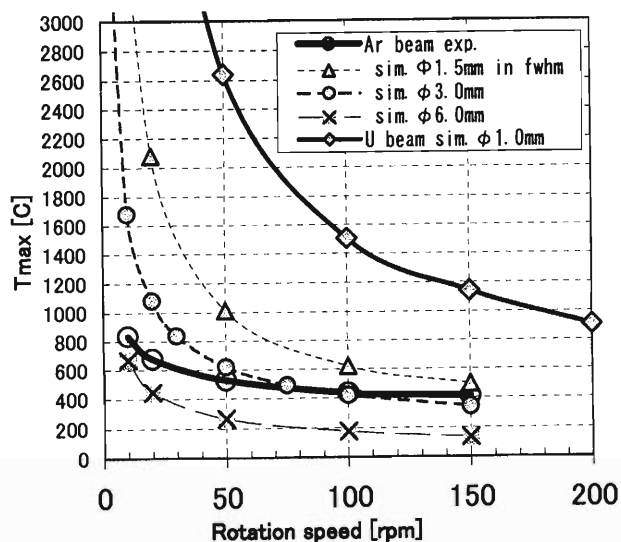


Fig. 1. Maximum temperature of the beam spot at various rotation speeds of the carbon target disk. Experimental data (thick straight line) and simulation results for various beam spot sizes (dotted lines) are shown for the  $^{40}\text{Ar}$  beam test experiment. The estimation for  $^{238}\text{U}$  beam (thick dotted line) is also indicated.

of the target disk, whereas the temperature gradient at 10 rpm near the beam spot was too steep, approximately 25°C/mm. This may cause the broadening of the beam spot temperature distribution.

The estimated beam spot temperature under the severest operating conditions of the future Big-RIPS, namely, a  $^{238}\text{U}$  primary beam at 400 A MeV with 1 pμA intensity onto the carbon target of 5.3 mm thickness, is also indicated in Fig. 1. The assumed beam spot size of  $\phi$  1 mm in FWHM and a total heat loss of 22 kW give an energy density of 5.1 kW/mm<sup>3</sup>. A typical simulation result for the rotation speed of 100 rpm is shown in Fig. 2. The temperature at the beam spot exceeds 1300°C, whereas that near the aluminum plates is approximately 150°C, because the cooling water diffuses the heat effectively.

Based on the simulation result shown in Fig. 1, if the rotation speed is higher than 200 rpm, the beam spot temperature is maintained sufficiently low compared to the melting point temperature of 3500°C of carbon. A rotation faster than 1 krpm is mechanically possible; thus, we can make the disk size more compact while maintaining the velocity of the beam spot in the tangential direction. This is important in the design of the target remote handling system. More simulation studies and R&D experiments are under way to optimize the disk size and to check the possibilities of

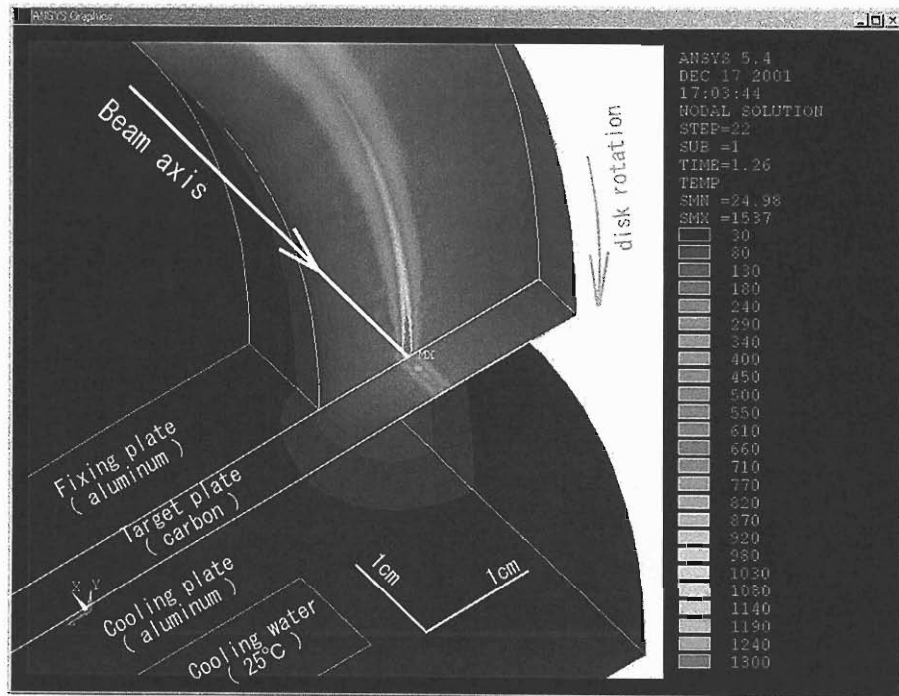


Fig. 2. Cross-sectional view of the temperature distribution in the target disk near the  $^{238}\text{U}$  beam spot.

using other metal targets such as Be and Ta.

#### References

- 1) A. Yoshida et al.: RIKEN Accel. Prog. Rep. **34**, 188 (2001).
- 2) National Astronomical Observatory: Chronological Scientific Tables (in Japanese) (Maruzen, Tokyo, 2001); A Catalogue for Aluminum and Carbon (Ibideu Co., Ogaki, 2001).

## Performance of a new gas-filled recoil separator GARIS at RILAC facility measured using $^{208}\text{Pb}$ and $^{209}\text{Bi}$ recoils

K. Morita, K. Morimoto, D. Kaji,\* A. Yoneda, Y.-L. Zhao, T. Suda, A. Yoshida, K. Katori, and I. Tanihata

Last year, we transferred a gas-filled recoil separator (GARIS)<sup>1)</sup> from the E1-experimental hall of the RIKEN Ring Cyclotron facility to the experimental hall of the RILAC facility.<sup>2)</sup> The separator was designed for fast (in-flight) and effective collection of nuclear reaction products, separating them from an intense primary beam. The GARIS will be used in the search for new isotopes of the heaviest elements whose production cross sections are extremely small.

Along with this relocation, we have made some improvements to the GARIS, as described in Ref. 2. The original GARIS consisted of three magnets in a D1-Q1-Q2 configuration, where D denotes the dipole magnet and Q denotes the quadrupole magnet, as described in Ref. 1. The distance between Q1 and Q2 was 330 mm. This distance has now been increased to 520 mm. When we designed the Q-magnet, the effect of the large bore radius (150 mm) was not suitably taken into account. As a consequence, the focusing power of Q2 was lacking at the highest  $B\rho$  value of the D-magnet. By changing only the distance between Q1 and Q2, the focusing power is expected to be recovered without changing the power supply to the Q-magnet.

Another improvement was carried out by installing a new D-magnet (D2) between Q2 and the focal plane. In the experiment, incident beams are stopped by a graphite wall in the D1-magnet where a large number of light-charged particles are emitted. Although the  $B\rho$  values of these light-charged particles differ greatly from the values of the reaction products of interest, because their source points are not the same as those of the reaction products, they reach the focal plane by passing through the Q-magnets. These light-charged particles enter the focal plane detectors and create a main background signal in our detection system. The additional D-magnet sweeps such light-charged particles from the focal point. Thus, we expect to realize a low background condition at the highest beam intensity.

This year, we performed testing experiments for measuring the characteristics of the new GARIS system. The ion-optical acceptance (solid angle) of the GARIS and transmissions for low-energy stable ions ( $^{208}\text{Pb}$  (0.26 MeV/nucleon),  $^{209}\text{Bi}$  (0.11 MeV/nucleon)) were measured. Equilibrium charge states of these ions in helium gas were deduced. One important characteristic that we wanted to study is background reduction, in order to determine the effect of the newly installed D2-magnet. However, the experiment could not be carried out this year due to a radiation safety

problem that must be resolved as soon as possible.

The ion-optical acceptance of the GARIS was measured using an  $^{241}\text{Am}$   $\alpha$ -source. The source was set at the target position of the separator. The  $\alpha$ -particles were detected in the focal plane using a position sensitive silicon detector (PSD) whose effective area was 60 mm  $\times$  60 mm. The intensity of the source was calibrated separately. A helium buffer gas was not used to fill the chamber in this measurement. The measured value of the acceptance was 12.2 msr. The value corresponds to an average angular acceptance of  $\pm 62$  mrad ( $\pm 3.6$  deg.). The effect of a change in distance between Q1 and Q2 magnets mentioned above on ion optics was confirmed by this measurement. The system obtained a double focusing condition in the focal plane at the highest  $B\rho$  value of the D1 magnet.

Transmissions of the GARIS for low-energy ions of  $^{208}\text{Pb}$  and  $^{209}\text{Bi}$  were measured. Target recoils, which correspond to near 180 deg. elastic scattering of the  $^{40}\text{Ar}$  incident beam from the RILAC, were used as low-energy ions. The target recoils were detected in the focal plane of the GARIS with the above-mentioned detector. At the same time,  $^{40}\text{Ar}$  ions elastically scattered by the target were measured by a silicon PIN photodiode (SSD) set at 45 deg. with respect to the beam direction in the target chamber. Under the present experimental conditions, the interaction energies were well below the Coulomb barriers of the reactions. Therefore, cross sections of both reactions are described purely by Rutherford scatterings for all scattering angles. The change in the Rutherford cross section with a scatter angle near 180 deg. is very small. For example, the difference between those for 180 deg. and 170 deg. in the center of mass frame, corresponding to target recoils for 0 deg. and 5 deg. in the laboratory frame, is only 1.5%. Thus, we can consider an angular distribution of the recoil is uniform in our acceptance angle. From these experimental conditions, the ratio of the number of recoils going into acceptable solid angles of the GARIS to the number of scattered incident particles detected by the SSD, in the same run is determined only by a geometrical factor. This means that the ratio does not depend on beam intensity, target thickness, or beam energy. Then, we can determine the absolute transmissions of the GARIS by comparing the number of detected recoils in the focal plane to the number of scattered  $^{40}\text{Ar}$  in the target chamber in the same run.

The beam energy from the accelerator was 114 MeV. A  $^{208}\text{Pb}$  metal target material was evaporated on 100  $\mu\text{g}/\text{cm}^2$  carbon foil. The thickness of the tar-

\* Niigata University

get was  $640 \mu\text{g}/\text{cm}^2$ . The target was irradiated from the carbon side by the incident beam. The incident beam energy at the half-depth of the target was 109 MeV. In the Bismuth case the metal target material was evaporated on a  $3.9 \text{ mg}/\text{cm}^2$  aluminum foil that was used as an energy degrader for an incident beam as well as a mechanical support. The thickness of  $^{209}\text{Bi}$  target was  $300 \mu\text{g}/\text{cm}^2$ . The incident beam energy at the half-depth of the target was 52 MeV. The central values of the kinetic energies of the  $^{208}\text{Pb}$  ion and the  $^{209}\text{Bi}$  ion just downstream of the targets were estimated to be 54.5 MeV (0.26 MeV/nucleon) and 22.5 MeV (0.11 MeV/nucleon), respectively. Typical energy spectra measured by the PSD are shown in Fig. 1. The central values of energy in the figure are lower than those mentioned above. The difference is explained by taking into account the following factors; the energy loss of the ions in helium gas, that of the  $1 \mu\text{m}$  Mylar foil set in front of the detector, and the detector response for heavy ions. The foil was used for separating the vacuum region where the detector was set from the gas region.

The obtained transmissions were 0.85 for  $^{208}\text{Pb}$  (0.26 MeV/nucleon) and 0.33 for  $^{209}\text{Bi}$  (0.11 MeV/nucleon). Positional distributions of ions detected by the PSD in the horizontal axis are depicted in Fig. 2

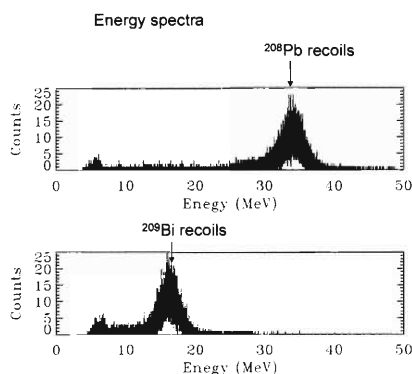


Fig. 1. Typical energy spectra of ions measured by a PSD set at the focal plane of GARIS.

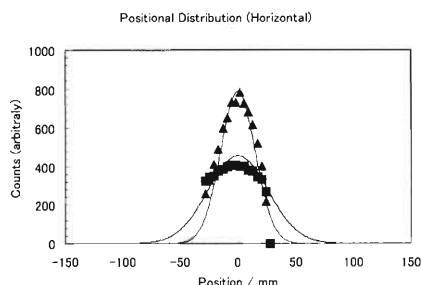


Fig. 2. Positional distribution of ions in the horizontal axis at the focal plane of the GARIS. Experimental ones are shown in symbols: triangle  $^{208}\text{Pb}$  (0.26 MeV/nucleon), square  $^{209}\text{Bi}$  (0.11 MeV/nucleon). Curves are those produced by simulation.

by symbols (triangle:  $^{208}\text{Pb}$ , square:  $^{209}\text{Bi}$ ) together with the result of a simulation, shown by curves. The PSD is divided into 16 strips in the horizontal axis. The experimental distribution was obtained by counting the number of ions detected in each strip. Relative intensities are normalized using the transmissions obtained experimentally as the ratio of the total number of  $^{208}\text{Pb}$  detected by the PSD to that of  $^{208}\text{Bi}$  to become 0.85/0.33. The simulation was carried out assuming that the ions change direction only due to Rutherford scattering with helium nuclei of the buffer gas. The simulation reproduces the relative intensities as well as the shape of the positional distribution well.

The equilibrium charge states of the ions in helium gas were deduced from the estimated velocities of the ions at the center of the D1 magnet and magnetic flux densities of the D1 magnet which gave the maximum yields at the detector. The deduced values are 8.3 for  $^{208}\text{Pb}$  of 0.26 MeV/nucleon and 5.4 for  $^{209}\text{Bi}$  of 0.11 MeV/nucleon. The values agree with those calculated using an empirical formula given by Ghiorso *et al.*<sup>3)</sup> with 10% accuracy. Knowledge of this quantity is important for setting the appropriate magnetic field strength of the magnets, particularly for experiments involving a search for unknown elements. We will continue measurements of the equilibrium charge states in helium gas for heavier ions using known fusion evaporation reactions next year in order to make a precise extrapolation of them possible for the heaviest system.

We can estimate a possible event rate for an experiment searching for a new element, for example nucleus  $^{278}[113]$  of the 113th element which is expected to be produced via  $^{209}\text{Bi}(^{70}\text{Zn},n)$  reaction, using the numbers obtained in the present results.  $3 \times 10^{-37}$  (0.3 pbarn) as an expected production cross section,  $3 \times 10^{13}/\text{s}$  (5 particle  $-\mu\text{A}$ ) as a beam intensity,  $6 \times 10^{17}/\text{cm}^2$  ( $200 \mu\text{g}/\text{cm}^2$ ) as a target thickness, and 0.37 as an overall efficiency estimated by the simulation. Using these numbers we obtain an event rate of  $2.0 \times 10^{-6}/\text{s} = 1.2/\text{week}$ . This event rate shows that the experiment is feasible.

In the next experimental period (from January to March 2002), experiments to measure the equilibrium charge states in helium gas for the 100th (Fm) and 102nd (No) elements are scheduled.

We will continue measurements of the quantities for greater atomic numbers up to 112 in 2002. We foresee starting the experiments regarding the search for a new element at the end of 2002.

## References

- 1) K. Morita *et al.*: Nucl. Instrum. Methods Phys. Res. B **70**, 220 (1992).
- 2) K. Morita *et al.*: RIKEN Accel. Prog. Rep. **34**, 184 (2001).
- 3) A. Ghiorso *et al.*: Nucl. Instrum. Methods Phys. Res. A **269**, 192 (1996).

# Installation of a high-resolution magnetic spectrograph PA

N. Yamazaki,\* T. Teranishi,\* S. Michimasa,\* Y. Mizoi, M. Notani,\* Y. Ohshiro,\* S. Shimoura,\*  
K. Ue,\* S. Watanabe,\* Y. Yanagisawa, and S. Kubono\*

A high-resolution magnetic spectrograph, called PA, has been installed as one of the CNS major facilities in the E2 experimental hall at the RIKEN Accelerator Research Facility. It was originally designed and constructed at the Institute for Nuclear Study at the Tanashi Campus of the University of Tokyo.<sup>1)</sup> It was frequently used for high-precision spectroscopic measurements of nuclear structures and nuclear astrophysics studies, and it will now be used primarily for high resolution spectroscopy at low energies.

Figure 1 shows a plane view of the PA spectrograph. The spectrograph has the following features. It has a QDD configuration, and has double focusing at the focal plane. Although it has a high resolving power, it is very convenient to use; the DC current is provided in a series for D1 and D2, and the Q-magnet current is set automatically following the current for the Dipole magnets. A spectrum at the focal plane can be obtained simply by moving the focal plane detector, since the focal plane position depends on the reaction kinematics. The specifications of the spectrograph are summarized in Table 1.

When the spectrograph was transferred from Tanashi to RIKEN, several modifications were applied to the system as follows:

(1) The platform at the focal plane area was rebuilt to extend the area with a high rigidity for future development of the detector system.

(2) The gate valve at the entrance of the spectrograph was renewed.

(3) The entire controls system has been renewed using a sequencer and touch panels, which controls the target and the turn-table in the scattering chamber,

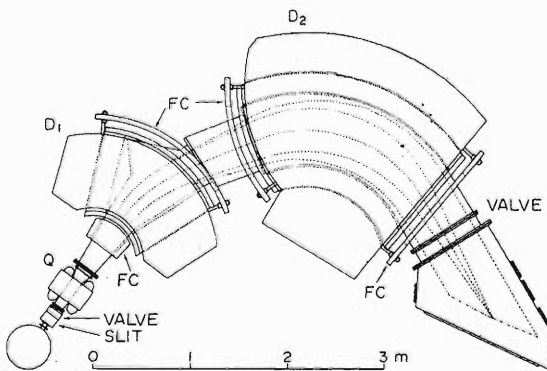


Fig. 1. Plane view of the high-resolution magnetic spectrograph PA.

Table 1. Specifications of PA.

Dispersion	2.79
Magnification:	
Horizontal	-0.37
Vertical	4.44
Orbit radius	130-150 cm
Maximum energy	150 Q <sup>2</sup> /A MeV
Angular range	-20 - +136 deg.
Momentum resolution	1/10000
Energy range	30%
Maximum solid angle:	6.4 msr
Focal plane:	
Length	100 cm
Tilted angle	55 deg.
Radius of curvature	600 cm
Maximum field strength:	
Dipole magnet	11.9 kG
Quadrupole magnet	0.896 kG/cm
Total weight	55 t

the spectrograph angle, and the focal plane positioning. It also controls the vacuum system, including the section of the beam line just before the scattering chamber.

(4) All of the control systems of the DC power supplies were renewed as they were too old and had some instability. The oil condenser was also changed to a dry condenser for safety reasons.

(5) The maximum angle available for measurements is now limited to about 136 degrees, by the new triplet Q magnets on the beam line.

The setting precision was measured before moving the spectrograph from the Tanashi Campus. Some parameters, particularly around the target chamber, were misaligned by nearly 2 mm. This problem was considered to come partly from a structural weakness at the central target region, because the scattering chamber was sitting on a structure to avoid the water pipes for the magnets. This problem has been rectified by changing the water pipe system. All of the alignments have been made with precision of 0.2 mm.

The spectrograph will be ready for experiments in the spring of 2002. The focal plane detectors available are explained in Refs. 2 and 3.

## References

- 1) S. Kato, M. H. Tanaka, and T. Hasegawa: Nucl. Instrum. Methods **154**, 19 (1978).
- 2) M. H. Tanaka, S. Kubono, and S. Kato: Nucl. Instrum. Methods **195**, 509 (1982).
- 3) X. Liu et al.: Nucl. Phys. A **432**, 66 (1999).

\* Center for Nuclear Study, University of Tokyo

## Development of a multiple-reflection TOF mass spectrometer

Y. Ishida, M. Wada, Y. Matsuo, I. Tanihata, A. Casares,\* and H. Wollnik\*

The masses of stable and long-lived nuclei are known with good accuracy, while information is scarce in the regions far from  $\beta$ -stability. However, particularly the masses of nuclei in such regions are interesting because they play an important role in astrophysical processes, and because the predictions of various mass models differ from each other greatly.

We plan to measure the masses of very short-lived nuclei far from stability using a multiple-reflection time-of-flight mass spectrometer (MR-TOF). Via projectile fragmentation, a large variety of exotic nuclei can be produced and separated in flight by the RIKEN projectile fragment separator (RIPS) or Big RIPS in the RIKEN RI-Beam Factory project. Subsequently, energetic ions are injected into an RF ion-guide system,<sup>1)</sup> and thermalized in it. The ions are extracted from this system and guided to the MR-TOF for mass spectrometry.

If the width of the flight-time distribution cannot be reduced, one must increase the overall flight time in order to increase the mass-resolving power of a time-of-flight mass spectrometer. To achieve such an increased flight time, ions are repeatedly reflected between two pulsed grid-free ion mirrors. In such a system the mass resolving power  $m/\Delta m$  is expected to increase linearly with the number of reflections.

The MR-TOF has been built as a coaxial system with two pulsed grid-free ion mirrors. The main body of the MR-TOF is shown in Fig. 1. The total length is about 40 cm. There are 15 gold-coated aluminum ring-electrodes inside a plastic tube. These electrodes act as two ion mirrors and two einzel lenses. We coaxially placed an electron impact ion source on one side and microchannel plates on another side for an off-line test. The ions produced in the ion source are accelerated to an energy of 1.5 keV, and extracted into the MR-TOF at 1 kHz repetition frequency. With switching the electric voltages of the ion mirrors on and off, the ions can move back and forth between the ion mirrors repeatedly. The more energetic ions penetrate deeper into the repeller fields of the ion mirrors, thus the system can become energy-isochronous, that is, the flight times of ions do not depend on the ion energies although they vary with the ion masses.<sup>2)</sup> The system can operate in a low-resolution linear mode, *i.e.*, without reflections. In this case, a complete mass spectrum is recorded. To achieve a higher mass-resolving power, the MR-TOF can be operated in the multiple-reflection mode. Even in this mode, the measuring time is less than 1 ms. This means that the MR-TOF can be applied to very short-lived nuclei.

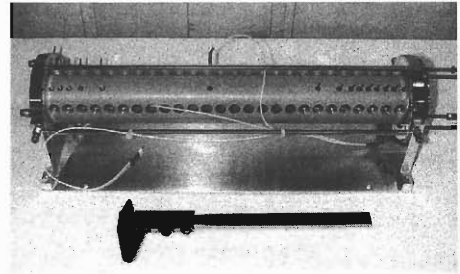


Fig. 1. Main body of the MR-TOF. Inside a plastic tube there are 15 gold-coated aluminum ring-electrodes as ion mirrors and lenses.

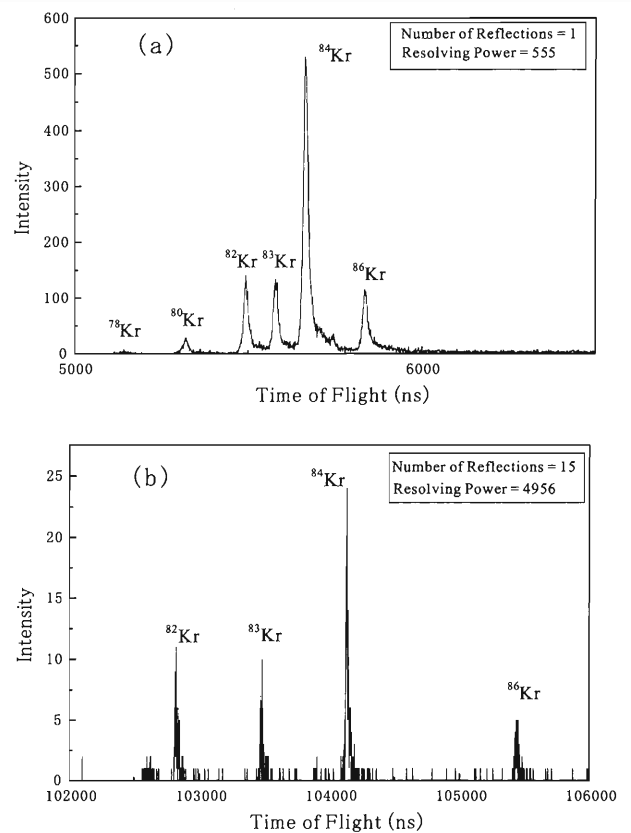


Fig. 2. Measured mass spectra of the krypton isotopes with natural abundance (a) in the linear mode and (b) after 15 reflections. Peaks of the isotopes are labeled with isotopic symbols. The mass-resolving powers of  $m/\Delta m \approx 555$  and 4956 are achieved for the linear and 15-reflection modes, respectively.

In the linear mode, without reflections, the mass spectrum for the krypton isotopes with natural abundance is shown in Fig. 2 (a). The flight-time difference

\* Oak Ridge National Laboratory, USA

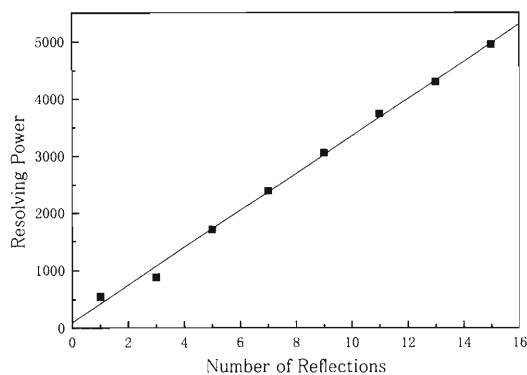


Fig. 3. Mass-resolving power as a function of the number of reflections.

between  $^{83}\text{Kr}$  and  $^{84}\text{Kr}$  and the FWHM of the peak are 86 ns and 13 ns, respectively. We have achieved a base resolving power of  $m/\Delta m \approx 555$ . Using the multi-reflection mode after 15 reflections, the flight-time difference increases to 649 ns, while the FWHM is as narrow as in the linear mode. As seen in Fig. 2 (b), the mass-resolving power of  $m/\Delta m \approx 4956$  has been achieved.

Figure 3 indicates that the mass-resolving power in-

creases almost linearly with the number of reflections. In other words, the MR-TOF satisfies the energy-isochronous conditions for any number of reflections chosen, thus the increase of the mass-resolving power depends only on the overall flight time of the ions.

The results are consistent with those obtained at the Max-Planck Institute for space applications.<sup>3)</sup> It is possible to make the mass resolving power increase up to  $2 \times 10^4$  with more than 100 reflections. In order to reach a higher resolution, it is necessary to elongate the MR-TOF because the resolving power of the MR-TOF is mainly limited by the stability of the power supply for the electrodes.<sup>4)</sup> For on-line measurements using RIPS or Big RIPS, an ion-bunching device to operate between an RF ion-guide system and the MR-TOF must be developed.

#### References

- 1) M. Wada et al.: RIKEN Accel. Prog. Rep. **34**, 202 (2001).
- 2) H. Wollnik and M. Przewłoka: Int. J. Mass Spectrom. Ion Processes **96**, 267 (1990).
- 3) A. Casares et al.: Proc. 48th ASMS Conf. on Mass Spectrometry, Long Beach, USA, (2000) p. WPA010.
- 4) A. Casares, A. Kholomeev, and H. Wollnik: Int. J. Mass Spectrom. **206**, 267 (2001).

## Improving neutron detection efficiency by using passive converters

T. Baumann,<sup>\*1</sup> H. Ikeda, M. Kurokawa,<sup>\*2</sup> M. Miura,<sup>\*2</sup> T. Nakamura,<sup>\*2</sup> Y. Nishi, S. Nishimura, A. Ozawa, T. Sugimoto,<sup>\*2</sup> I. Tanihata, and M. Thoennessen<sup>\*1</sup>

Rare isotope beam facilities that use projectile fragmentation and in-flight separation to produce neutron-rich nuclei require neutron detection systems with a high detection efficiency at energies of approximately 50 to 400 MeV for the measurement of neutrons from breakup reactions. Although liquid or plastic scintillators are usually well suited for large-area detectors, the interaction length of neutrons in these materials requires a large detector volume in order to achieve high detection efficiencies. A possible means to boost neutron detection efficiency, particularly for higher neutron energies, is to use passive converter materials that have a much shorter interaction length for neutrons.

Here we report on measurements of relative detection efficiencies for a combination of iron converter and plastic scintillator compared to those for a pure plastic scintillator detector for neutrons of 20–140 MeV. The experiment was performed at the RIKEN Accelerator Research Facility. Elements of the NEUT neutron detector array (see, *e.g.*, Ref. 1) were used for this measurement. Neutrons of a broad energy range were produced using a 100 MeV/nucleon beam of  $^{13}\text{C}$  from the RIKEN Ring Cyclotron impinging on a 2-cm-thick aluminum target. The primary beam was stopped in the target, so that only lighter fragments and neutrons could reach the detector setup. A thin plastic start detector was placed 10 cm in front of the production target, while the neutron detectors were mounted at a distance of about 5 m behind the target.

The neutron detector setup consisted of two sets which were placed symmetrically with respect to the beam axis. This assured the same neutron flux through both detector sets. Each set contained 3 blocks of  $6 \times 6 \times 108 \text{ cm}^3$  BC-408 plastic scintillators stacked vertically. The front of each set was covered by plastic veto detectors of 5 mm thickness in order to discriminate charged reaction products. Iron converters of 2 cm and 3 cm thickness were added to one of the two detector sets, enabling a direct comparison of the number of detected neutrons in each of the two detector sets. The iron converter was placed between the veto detectors and the neutron detectors. In order to account for the asymmetries of the setup, a measurement without an iron converter was also performed. Separation of beam-related gamma rays and neutrons was achieved by time-of-flight measurement.

The results of these measurements are presented as detection efficiency ratios dependent on neutron en-

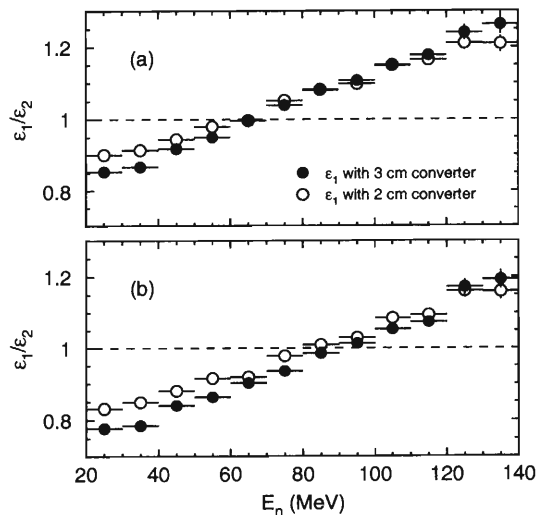


Fig. 1. Measured efficiency ratios. Open symbols correspond to the 2 cm, solid symbols to the 3 cm converter. Results for a 2 MeV (a) and a 5 MeV (electron equivalent) cutoff threshold (b) are plotted.

ergy. The efficiency ratios were calculated by dividing the number of neutrons per energy bin that were detected with the converter-equipped detector set by the number of neutrons that the pure plastic scintillator detected. Accordingly, an efficiency ratio above one would indicate an enhancement of the detection efficiency by the passive converter. Figure 1 shows the results for two different cutoff thresholds that were applied to data from the same measurement.

This measurement corroborates our results from simulations showing that passive iron converters can be effectively used to enhance the neutron detection efficiency at energies below 200 MeV. We found experimental evidence for a 10–20% increase in detection efficiency at neutron energies between 100 and 140 MeV for the combination of a 2 cm or 3 cm iron converter and a 6 cm plastic scintillator. A more detailed discussion can be found in Ref. 2.

This work was supported by the U. S. National Science Foundation under grant PHY 95-28844.

### References

- 1) T. Nakamura et al.: Phys. Lett. B **331**, 296 (1994).
- 2) T. Baumann et al.: accepted for Nucl. Instrum. Methods Phys. Res. B (2002).

<sup>\*1</sup> National Superconducting Cyclotron Laboratory, Michigan State University, USA

<sup>\*2</sup> Tokyo Institute of Technology

## High-efficiency positron moderator using electropolished tungsten meshes

F. Saito, Y. Nagashima,<sup>\*1</sup> L. Wei,<sup>\*2</sup> Y. Itoh,<sup>\*3</sup> A. Goto, and T. Hyodo<sup>\*1</sup>

A high moderation efficiency and long-term stability of positron moderators have been important factors in the development of variable energy positron beams. The moderation efficiency is defined as the ratio of the number of extracted slow positrons to the number of positrons emitted in the radioactive source per unit time.

Recently, we reported that a six-overlapping tungsten mesh moderator has a high moderation efficiency.<sup>1,2)</sup> Since the meshes have a large surface area for the volume, high efficiency is expected when they overlap. By reducing the diameter of the wires in the meshes, it is thought that even greater moderation efficiencies may be obtained for an optimal combination of meshes.

In the present paper, we report high-efficiency positron moderators with stacks of electropolished tungsten meshes.

The meshes, as received, originally exhibited 85% transmission with 20  $\mu\text{m}$  wires. They were held in an acrylic frame, 20 mm  $\times$  20 mm in size, and electropolished in NaOH solution of 0.5 N at room temperature. First, a current of 500 mA was passed for 60 s, then, 100 mA for 15 s, and 50 mA for 5 s. Through this process, the wires of the meshes were thinned to a diameter of about 10  $\mu\text{m}$ .

The meshes were cut into rectangles, 7 mm  $\times$  18 mm in size, and then annealed in vacuum ( $\sim 6 \times 10^{-7}$  torr) by passing an electric current through tungsten foils enclosing them. The temperature was raised and maintained at 2000°C for 2 min. After annealing, the meshes were quickly transported in air and installed in the moderator assembly of the beam apparatus.

The moderator was placed 1 mm away from the window of a  $^{22}\text{Na}$  positron source of activity  $1.38 \times 10^8 \text{Bq}$  (3.73mCi). The moderator was held at an electrostatic potential of +350 V with respect to the chamber walls and 9 V below the source potential.

The experimental system used to measure the efficiency of the moderator was a magnetically guided positron beam system with a trochoidal  $E \times B$  filter. The beam intensity was measured by counting 511 keV  $\gamma$ -rays using a high-purity Ge detector.

The beam intensities for 6 to 24 overlapping mesh moderators are shown in Fig. 1. The moderation efficiencies determined from the beam intensities are also shown in Fig. 1.

Although the efficiency is expected to increase with

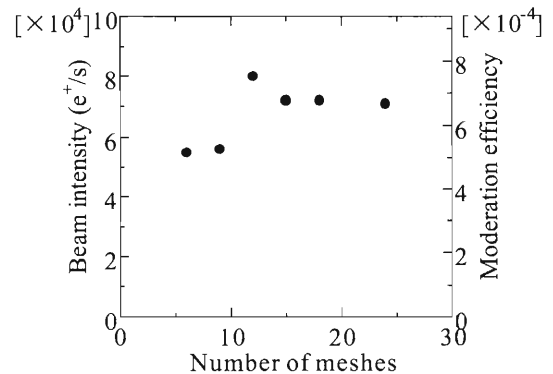


Fig. 1. Slow positron beam intensity plotted versus number of overlapping tungsten meshes of the moderators. The activity of the  $^{22}\text{Na}$  source is  $1.38 \times 10^8 \text{Bq}$  (3.73mCi). The scale on the right side indicates the moderation efficiency.

the number of overlapping meshes, the value is saturated when the number of the meshes exceeds 12. This is probably due to the increase in the fraction of the slow positrons trapped by the wire surfaces of the meshes.

The highest value of moderation efficiency is  $7.5 \times 10^{-4}$  for 12 overlapping meshes. This value is higher than that of the tungsten mesh moderator with 20  $\mu\text{m}$  wires reported previously.<sup>1,2)</sup> This value is also higher than that obtained using a transmission moderator with a tungsten single-crystal foil.<sup>3)</sup> Although the value is lower than that of solid rare-gas moderators,<sup>4-6)</sup> the tungsten mesh moderator has the following advantages: the treatment is easier, the cost is lower, and the long-term stability is higher.

We thank the members of the Division of Research Instruments Development at RIKEN, in particular, S. Nioka for expert technical assistance.

### References

- 1) Y. Nagashima et al.: Jpn. J. Appl. Phys. **39**, 5356 (2000).
- 2) Y. Nagashima et al.: RIKEN Accel. Prog. Rep. **34**, 115 (2001).
- 3) E. Gramsch et al.: Appl. Phys. Lett. **51**, 1862 (1987).
- 4) A. P. Mills, Jr. et al.: Appl. Phys. Lett. **49**, 1121 (1986).
- 5) R. G. Greaves et al.: Can. J. Phys. **74**, 445 (1996).
- 6) N. Oshima et al.: RIKEN Accel. Prog. Rep. **34**, 114 (2001).

<sup>\*1</sup> University of Tokyo

<sup>\*2</sup> Institute of High Energy Physics, China

<sup>\*3</sup> Advanced Research Institute for Science and Engineering

## Development of a time-of-flight detector with streak camera II

K. Morimoto, T. Ohnishi, F. Tokanai,\* and I. Tanihata

The high-resolution time-of-flight (ToF) detector using a streak camera is under development for the high-resolution particle identification system.<sup>1,2)</sup> It is expected to be useful for experiments using high-energy radio isotope (RI) beams at the RI Beam Factory.

The configuration of this ToF detector is shown in Fig. 1. This detector consists of two identical sets of streak cameras. These systems are tilted at 45 degrees with respect to the beam path. A thin target foil is mounted at the center of each system to emit secondary electrons. A 300-Å-thick Au layer evaporated on both sides of a 1.5- $\mu\text{m}$ -thick mylar foil is used for the target. Acceleration meshes are mounted on both sides of the foil at a distance of 2.7 mm. At the streak-image detector part, the secondary electrons from the meshes are accelerated by the electric field and focused by an electric lens. These electrons are swept by applying a 100 MHz sine wave voltage to the vertical and horizontal diffraction plates. These swept electrons impinge on a position-sensitive detector. In constant, at the center-image detector part, the secondary electrons are also accelerated, focused by an electric lens, and directly impinge on the position-sensitive detector. In a previous system, a phosphor screen (P-43) and an image intensifier (II) with CCD were used for the position-sensitive detectors. In order to improve the event acquisition rate, the II with CCD as replaced with a MCP with a Wedge-and-Strip anode detector that has a capability of 20 kHz event rate and 50  $\mu\text{m}$

FWHM of position resolution.

The performance test of the system was carried out using  $^{20}\text{Ne}$  beams of 135 A MeV energy at the RIKEN Ring Cyclotron E1 beam course. In this experiment, the basic operation of the system was investigated; for example phase-lock of sweeping electric fields between systems 1 and 2, in particular detection efficiency was measured. The test revealed that the detection efficiency was about 50% at each MCP with the Wedge-and-Strip assembly compared with the trigger signal made by a plastic scintillator installed immediately after the streak ToF detector. This low detection efficiency was due to low secondary electron emission from the thin foil with evaporated Au. Although the detection efficiency was measured with a target foil evaporated with Al, the detection efficiency was almost the same as that of an Au target. In order to improve the detection efficiency, we are preparing a target that is evaporated with CsI. It is expected to increase the number of second electron emissions.<sup>3)</sup>

### References

- 1) F. Tokanai et al.: IEEE Trans. Nucl. Sci. **47**, 1753 (2000).
- 2) F. Tokanai et al.: RIKEN Accel. Prog. Rep. **33**, 159 (2000).
- 3) H. L. Seifert et al: Nucl. Instrum. Methods Phys. Res. A **292**, 533 (1990).

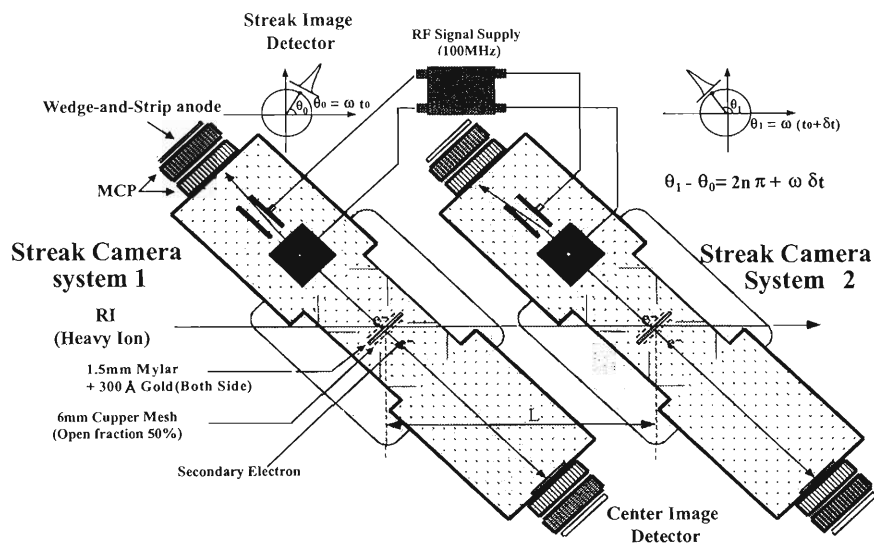


Fig. 1. Schematic of the ToF detector system.

\* Yamagata University

## Study of scintillator radiation hardness

S. Nishimura, M. Kurata-Nishimura, K. Morimoto, Y. Nishi, and I. Tanihata

The RI beam factory (RIBF),<sup>1)</sup> which is under the construction at RIKEN, has the capability to explore new isotopes for the astrophysics r-process as well as detailed studies of nuclear structures, a skin and a halo. Its maximum accelerator performance can be achieved by using a high-resolution time-of-flight (TOF) detector with a timing resolution of below 30 ps to separate the produced secondary nuclei, particularly for the heavy-mass region above 130 a.u. We have reported an ultrahigh-resolution TOF scintillation detector with a timing resolution below 10 ps by optimizing the detectors.<sup>2)</sup> Our studies suggest the importance of a larger number of photoelectrons for high-resolution TOF scintillation detectors. It is known that a reduction of scintillation light is expected after irradiation of charged particles.<sup>3,4)</sup> Reduction of the number of photoelectron caused by such radiation damage is a critical issue in relation to timing resolution. In this report, we focus on the timing resolution of an ultrafast scintillation detector as a function of the total radiation dose in order to evaluate the radiation resistance of the heavy-ion beam.

The test experiment was performed in the E1b beam line at the RIKEN Ring Cyclotron (RRC), where the primary beam of  $^{40}\text{Ar}$  was extracted at an energy of 95 MeV per nucleon. Figure 1 shows a schematic of our experimental setup. Two identical scintillation detectors (S0 and S1) were installed in the beam line. Each scintillation detector consists of a piece of plastic scintillator (Bicron BC422Q) and two identical PMTs (Hamamatsu R2083). The scintillators were wrapped with aluminum foil, so that the light was transmitted mainly by total internal reflection. For the operation of the scintillation detector with high beam in-

tensity, we have added booster HVs to the last three dynodes of the PMTs to supply sufficient current in the tubes. The current of the last dynode of PMT increased up to 2.5 mA at the beam intensity of  $3 \times 10^6$ . The integrated number of counts on detector S0 was recorded by a scaler. The ratio of double-beam events to one-beam events in one RF cycle is estimated to be below 10% under the high-beam-intensity condition. The size of the beam spot on the scintillator was estimated to be less than  $4 \times 2 \text{ mm}^2$ . Strong reduction of pulse heights for both scintillation detectors was observed as the total dose increased. After a total hits of  $1.03 \times 10^{11}$ , the pulse height was reduced by a factor of 1/5. Figure 2 (a) shows the time-of-flight (TOF) spectrum under the primary condition. Because detectors S0 and S1 are identical, the intrinsic timing

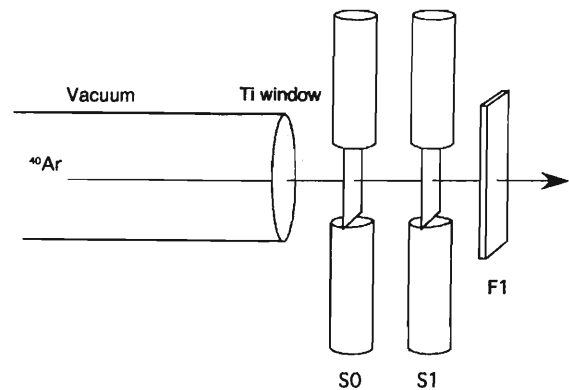


Fig. 1. Experimental setup for study of radiation hardness of scintillation detector.

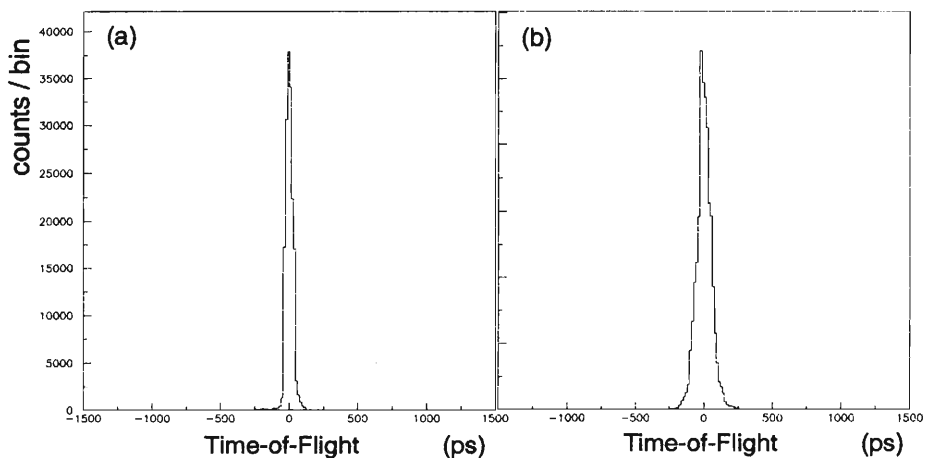


Fig. 2. Time-of-flight (TOF) spectra between S0 and S1 (a) before and (b) after the radiation dose.

resolution was extracted by assuming equivalent timing resolutions. As previously reported,<sup>2)</sup> the intrinsic timing resolution for the nonirradiated detector was estimated to be 13 ps. Figure 2(b) shows the TOF spectrum after the radiation damage. The broadening of the TOF spectrum is observed with radiation damage, where the intrinsic timing resolution was approximately 38 ps. An additional improvement in timing resolution is expected with the pulse height cor-

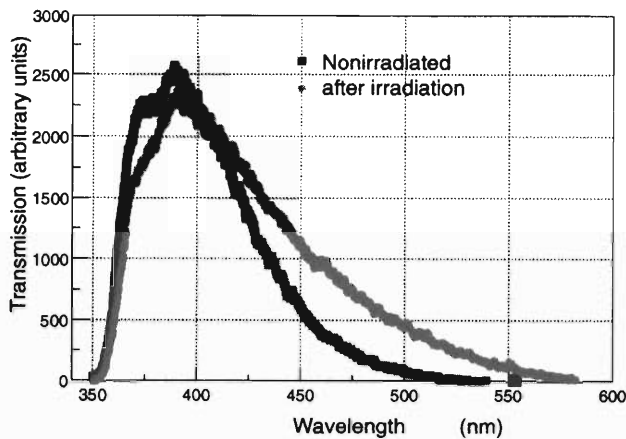


Fig. 3. Emission spectra for nonirradiated and irradiated scintillators.

rection, together with the position correction using an additional position sensitive detector near the scintillation detector. In order to investigate the characteristics of the scintillator itself, the wavelength of scintillation light was measured using a monochromatic illuminator. The results of the emission spectra for nonirradiated and irradiated scintillators are presented in Fig. 3. The results show a greater decrease of emission intensity in the black region relative to the longer wavelength as was observed.<sup>3,4)</sup>

We have observed the reduction of pulse height as well as a wider TOF spectrum after the irradiation with the heavy-ion beam. The poorer timing resolution after radiation damage can be explained by the reduction of pulse height based on the statistical explanation of the number of photoelectrons.<sup>5)</sup>

#### References

- 1) I. Tanihata: *J. Phys. G: Nucl. Part. Phys.* **24**, 1311 (1998).
- 2) S. Nishimura et al.: *RIKEN Accel. Prog. Rep.* **34**, 209 (2001).
- 3) S. Majewski et al.: *Nucl. Instrum. Methods Phys. Res. A* **281**, 500 (1989).
- 4) M. M. Hamada et al.: *Nucl. Instrum. Methods Phys. Res. A* **422**, 148 (1999).
- 5) M. Kurata et al.: *Nucl. Instrum. Methods Phys. Res. A* **349**, 447 (1994).

## Development of fast timing beam line scintillator for RIPS with PMTs operated in vacuum

R. Kanungo, I. Tanihata, M. Chiba, and T. Suda

The present day focus of nuclear physics experiments is concentrated primarily on studies involving unstable nuclei. These nuclei are produced as secondary beams. The technique for such production at RIKEN is projectile fragmentation which introduces a large momentum spread in the secondary beams. It is therefore, essential to be able to measure the momentum of these secondary beams with high precision in order to perform further experiments with them.

The plastic scintillator detector is one of the simplest devices which can be used for momentum measurement using the time-of-flight (TOF) between two such detectors. The RIKEN Projectile fragment separator (RIPS) beam line scintillator detectors have a time resolution  $\sim 100$ – $200$  ps. This requires upgrading for high-precision experiments. During the last two years we have constructed ultra-fast timing scintillator detectors, with the time resolution of 30 ps (with  $^{40}\text{Ar}$  beam), to meet this requirement, and they have been used for several experiments at RIPS.

The scintillators are large in size ( $70\text{ mm} \times 70\text{ mm}$  and  $150\text{ mm} \times 100\text{ mm}$ ) to meet secondary beam requirements and are coupled to Hamamatsu 1 inch photomultiplier tube (PMT) with the help of a light guide. The scintillator was in vacuum while the PMT had to be operated in air. The light guide was thus used to break the vacuum. This makes the installation of such detectors quite cumbersome.

It was thus important to develop a compact detector with the PMT being operated in vacuum. In addition to solving the problem of the installation of such detectors, it is necessary to have such an arrangement in order to directly couple the scintillator to the PMT without any light guide. Such coupling is found to yield a better time resolution.

The primary problem associated with operating the hybrid PMT assembly, designed by Hamamatsu, in vacuum was the outgassing from the PMT. To avoid this, we used the Hamamatsu R4998 PMT and designed and prepared the booster circuit and its coupling to the PMT in such a way as to make it suitable for use in vacuum. The booster circuit designed is also expected to have a high rate stability,  $\sim 10^7$  cps, however, at present we have only made a preliminary test upto  $10^4$  cps.

We used a  $70\text{ mm} \times 70\text{ mm}$  scintillator coupled to the prepared PMTs at both ends with a light guide, and the entire assembly was put in vacuum. In order to compare its timing performance with our previously used hybrid PMT assembly, we coupled same PMTs,

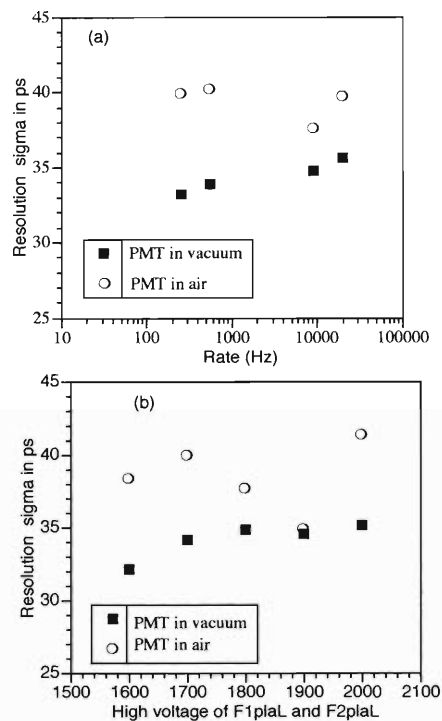


Fig. 1. Intrinsic time resolution comparison of PMT developed for use in vacuum and PMT used in air, (a) as a function of counting rate, and (b) as a function of PMT high voltage.

but booster designed by Hamamatsu, with the same size scintillator and operated it in air.

The test was performed at the E1c beam line of RRC using a  $70\text{ A MeV }^{18}\text{O}$  beam. The detector could be successfully operated in vacuum  $\sim 10^{-6}$  torr for a period of 24 hours. No change of the vacuum condition or fluctuation of the pulse height of the detector was observed. The results of a comparison between the intrinsic time resolution of the newly fabricated detector operated in vacuum and the one operated in air are shown in Fig. 1. The time resolution of the newly fabricated detector appears to be marginally improved compared to the usual one.

Since the successful test of this detector, we have fabricated similar scintillator detectors for use at RIBLL, Lanzhou, China for RIKEN-China collaboration experiments. This detector is expected to be very useful for the future RI Beam factory where we may expect to achieve much better time resolution using scintillators directly coupled to PMT.

## Development of plastic scintillators as possible energy detectors for proton scattering at RIBF

R. Kanungo, H. Sakaguchi,\* I. Tanihata, T. Onishi, T. Suda, H. Takeda,\*  
T. Murakami,\* S. Ota,\* and S. Terashima\*

Proton scattering at intermediate energies at the RI Beam Factory, RIKEN requires the development of high-energy-resolution detectors. NaI(Tl) satisfies this required criteria. However, it has some inconveniences, some of the primary ones are as follows:

- (1) Due to its extremely hygroscopic nature it becomes difficult to store the crystal, particularly very large crystals, for a long period of time and retaining its original performance.
- (2) The temperature of the crystal must be maintained at a constant level during very long experiments.
- (3) The reaction of protons in NaI(Tl) decreases detection efficiency and introduces complexities in analysis.
- (4) Extremely large crystals are quite expensive.

To overcome or minimize some of these difficulties we considered an alternative method of energy measurement of the recoil protons. This method is based on the time of flight between two plastic scintillators. To test its feasibility, we performed a very preliminary test experiment using a 12 MeV primary beam of protons available from the tandem accelerator, at Kyoto University. After scattering on a Au target the beam was incident on the scintillator detectors.

The first test had two primary objectives:

1. To determine the best time resolution we can obtain with low-energy protons.
2. To observe the effect of using a light guide on time resolution with large scintillators.

To achieve objective 1, we used small scintillators 20 mm wide and 70 mm long which were directly coupled to the photomultiplier tubes (PMT), with a photocathode 20 mm in diameter. Two PMTs were coupled on two sides of the scintillator. Two types of scintillator materials with thicknesses of, 2 mm (small sc-1) and 3 mm (small sc-2) were used. The protons were stopped in these detectors. The intrinsic time resolution of such a detector can be estimated from a Gaussian fit to the time difference between the left and the right PMTs after correction for position dependence, *i.e.*, intrinsic time resolution =  $\sigma$  (Tl-Tr)/sqrt(2).

In a simple estimate, if we have two identical detectors and assume that each PMT used has the same time resolution, then it can be easily shown that the time-of-flight (TOF) resolution between such detectors is equal to the intrinsic time resolution of each detector. Since the time difference between the two ends of

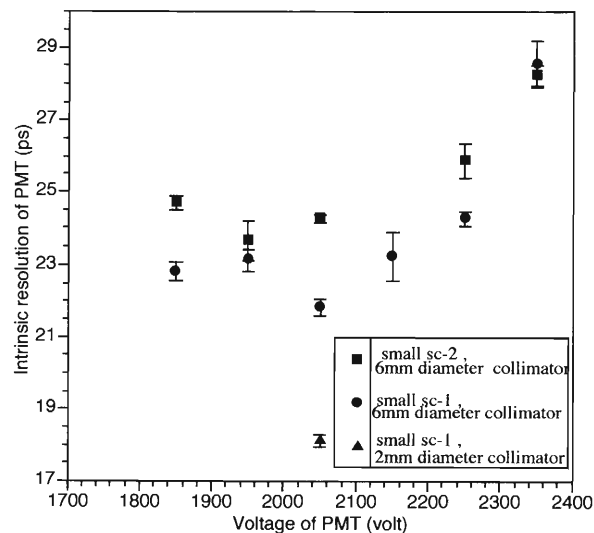


Fig. 1. Intrinsic time resolution of PMT directly coupled to small scintillator.

a scintillator is strongly dependent on the position of the incident particle, we need to correct for the position dependence in order to obtain the true time resolution. In the absence of position-sensitive detectors for the present test, we collimated the incident protons using a 6-mm-diameter circular collimator and also a 2-mm-diameter one. The latter was found to improve the time resolution more than the former. The estimated position resolution from the present data is about 1.24 mm in sigma. There is a small difference in time resolution between the two different types of scintillator materials tested and the small sc-2 type appears to be better (Fig. 1). The results show that an intrinsic time resolution of 18 ps can be achieved with the use of this scintillator. With a flight path of 1.6 m the energy resolution of full-width at half maximum (FWHM) is 62 keV for 20 MeV protons and 1.06 MeV for 120 MeV protons.

We also used large scintillators (70 × 70 mm) coupled to the PMT by twisted a light guide for achieving objective 2 of our test. Figure 2 shows the intrinsic time resolution obtained with such scintillators which is clearly worse than the ones without a light guide.

In conclusion, the results of the time resolution of plastic scintillator detectors with 12 MeV proton beam shows extremely good timing response for small-width scintillators coupled directly to the PMT, down to 18 ps in sigma. Translating this to proton energy res-

\* Graduate School of Physics, Kyoto University

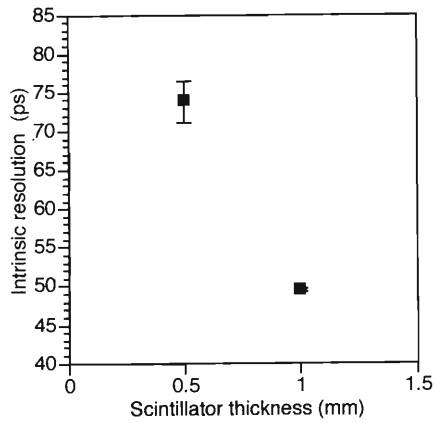


Fig. 2. Intrinsic time resolution of PMT coupled to large scintillator by a light guide.

olution, 62 keV in FWHM with 20 MeV protons can be expected given a flight path of 1.6 m. This resolution is much better than that of NaI(Tl), 280 keV, FWHM. However, NaI(Tl) yields a better result at higher proton energies such as 680 keV (FWHM) for 120 MeV protons as compared to 1.02 MeV (FWHM) as estimated from TOF.

Additional tests with longer and wider scintillators coupled to wider PMTs, are being planned in order to ascertain finally the feasibility of using this detector for proton energy measurement.

## Development of segmented Ge array

M. Kurokawa,\*<sup>1</sup> S. Shimoura,\*<sup>1</sup> H. Iwasaki,\*<sup>1</sup> H. Murakami,\*<sup>2</sup> and H. Sakai\*<sup>1</sup>

An array of Ge detectors is being developed at CNS for the detection of  $\gamma$  rays emitted from fast recoiling nuclei ( $\beta = 0.3-0.5$ ). To perform accurate correction of the energy for such Doppler-shifted  $\gamma$  rays, the emitted polar angle must be measured as accurately as possible using position sensitivity of the detector.

In the array, a ninefold-segmented Ge detector as shown in Fig. 1 will be employed for this purpose. The detector manufactured by Eurisys Mesures has a planar-type structure and is cylindrical with a diameter of 3.5 cm for the crystal itself and 3.0 cm for the effective area, in which a parallel electric field along the depth of the detector is expected. The thickness of the detector is 2.0 cm. The size of a segment is determined by the absorption length of 1 MeV  $\gamma$  rays to avoid multihit in a segment, which will deteriorate the timing signal from the segment and the position resolution of the detector. This segmented surface is grounded and the opposite surface has a high voltage of 2000 V.

For a small dead space when the array is aligned, two crystals are encapsulated in one cryostat so that their high-voltage surfaces face each other. At present, 18 clusters of such a pair of crystals are considered to be used for the array. To subtend the solid angle as large as possible, the detectors should be aligned at a polar angle of 90 degrees and as close as possible to the target position. As one example fulfilling such requirements, three units of six clusters are placed at 70, 90, and 110 degrees, and the distance between the target and the center of the detectors is approximately 10 cm. The side surface of the detector faces the target in order to extract an emitted angle of  $\gamma$  rays based on the position sensitivity along the depth direction. When

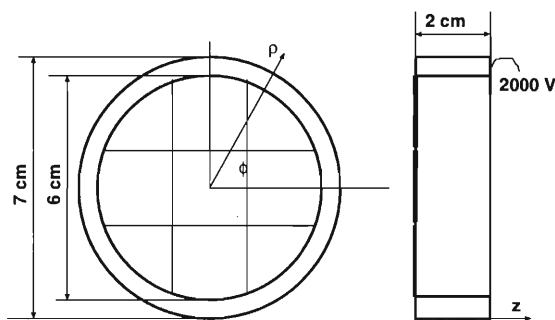


Fig. 1. Illustration of a segmented Ge detector manufactured by Eurisys Mesures. Its coordinate system is also presented.

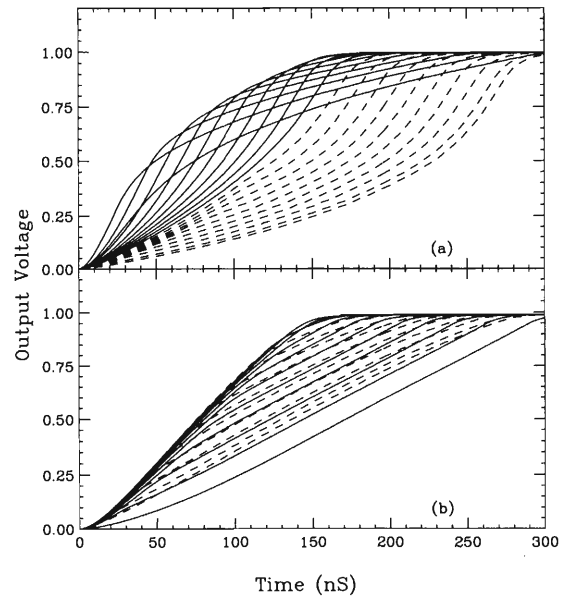


Fig. 2. Calculated results for the output signals from the preamplifier, when the interaction occurs at the position of  $\rho = 0.9$  cm and  $\phi = 0.0^\circ$  in a cylindrical coordinate system of the detector shown in Fig. 1. The interaction depth  $z$  is varied from 0.0 to 2.0 cm in a 0.1 cm step. The corresponding interaction depth for each line is explained in the text. (a) Output signals which are connected to the segment including the interaction points. (b) Total output signals from the detector, which is equivalent to the summation of signals from nine preamplifiers.

the recoiling velocity  $\beta$  is 0.3, the detection efficiency for 1.0 MeV  $\gamma$  rays is estimated to be more than 5% using the Monte-Carlo simulation code GEANT-4<sup>1)</sup> for the above alignment.

A position sensitivity of better than the segment size will be provided by pulse shape analysis of output signals from preamplifiers. Examples of simulated output signals are shown in Fig. 2, where the interaction depth  $z$  is varied from 0.0 to 2.0 cm in a 0.1 cm step, and the radius and the azimuthal angle are fixed to be 0.9 cm and  $0^\circ$ , respectively, in a cylindrical coordinate system. The calculation method for the signals was described in Ref. 2. For events with  $z$  smaller than 0.9 cm, dashed lines are used to represent the response. Their rise times, which are determined by the drifting time for both electrons and holes to reach their relevant electrodes, distribute between 150 ns and 300 ns. Among them, the line with the longest rise time is related to the event with  $z$  of 0.0 cm, and that with the shortest rise time is seen when the interaction occurs

\*<sup>1</sup> Center for Nuclear Study, University of Tokyo

\*<sup>2</sup> Department of Physics, Rikkyo University

at  $z$  of 0.9 cm or almost at half the depth of the detector. Because both electrons and holes drift at almost constant velocities under the present condition of electric field, a similar explanation can be applied to the events with  $z$  from 1.0 to 2.0 cm, which are indicated by solid lines, and to the symmetric characteristics of rise times particularly seen in the total output (Fig. 2 (b)). The deviation between Fig. 2 (a) for the segment and Fig. 2 (b) is due to the partial charge induced by electrons, or holes can be collected in one segment depending on the charge carrier position. Hence, to obtain the interaction position, pulse shaping has to be performed to distinguish two signals with the same rise time but different shapes.

As one of the methods of pulse shaping, zero cross timings are investigated for signals obtained by differentiating twice and integrating four times with a time constant of  $50 \mu\text{s}$  ( $\text{CR}^2\text{-RC}^4$  shaping). The results are shown in Fig. 3. The interaction points are shown

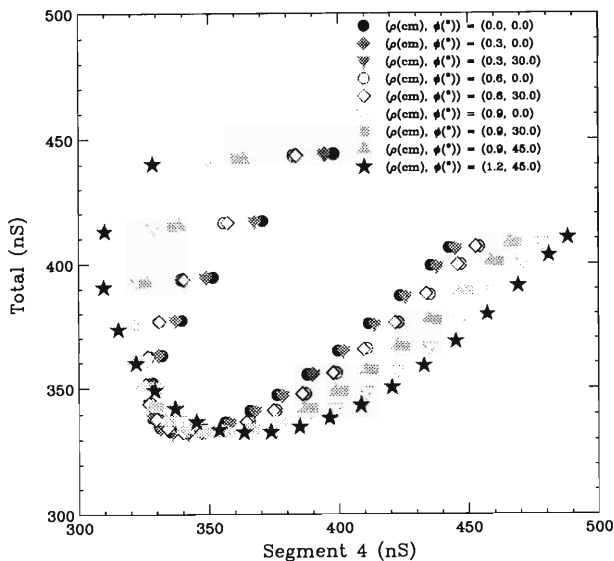


Fig. 3. Zero cross timings for  $\text{CR}^2\text{-RC}^4$ -shaped signals, where a signal is generated from the preamplifier including the interaction points and the other originates from the summation of output signals produced by nine preamplifiers. Interaction points are shown in the cylindrical coordinate system for their radius  $\rho$  and their azimuthal angle  $\phi$ . The interaction depth  $z$  distributes from 0 cm to 2.0 cm in a 0.1 cm step, and corresponding points are located counterclockwise.

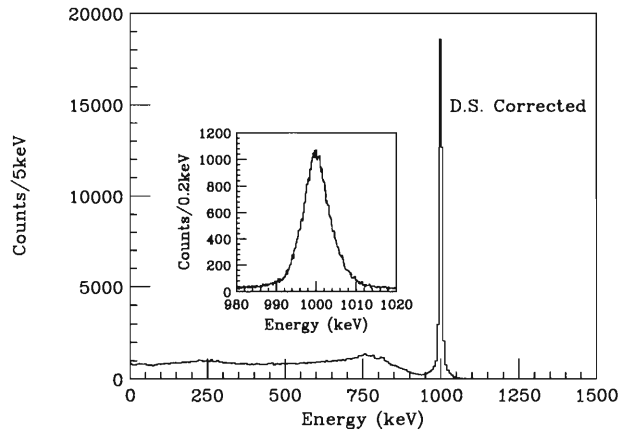


Fig. 4. Doppler-corrected energy spectrum for  $\gamma$  rays emitted from recoiling nuclei with  $\beta$  of 0.3.

in the figure for their radius  $\rho$  and azimuthal angle  $\phi$ . The interaction depth  $z$  distributes from 0 cm to 2.0 cm in a 0.1 cm step, and corresponding points are located counterclockwise. For events with the same  $\rho$  and  $\phi$ , the shortest distance between the points corresponds to about 3 ns. The information on  $\rho$  and  $\phi$  will be obtained from the transient signals generated in neighboring segments. For example, deviation from the center position of a segment in a horizontal direction is expected to be evaluated from the amplitude ratio between signals from the left and right neighboring segments. Therefore, a position resolution of 1 mm will be achieved along the  $z$  direction.

Under the assumption that the position resolution is 1 mm along the  $z$  direction, the effect of Doppler correction is simulated for previously described alignment of detectors using the code GEANT-4. Figure 4 shows the obtained Doppler-corrected energy spectrum for  $\gamma$  rays emitted from recoiling nuclei with  $\beta$  of 0.3. The simulated energy resolution is about 8.0 keV in FWHM. In the simulation, the effect of multihits is not completely taken into account yet. Experimental confirmation of the simulation including the multihit effect is now in progress.

#### References

- 1) GEANT4: *Detector Simulation Toolkit* (CERN, Geneva, 2000).
- 2) M. Kurokawa et al.: *CNS Ann. Rep.* **2000**, 70.

## A hybrid array for charged-particle and $\gamma$ detection

H. Hasegawa,<sup>\*1</sup> T. Motobayashi,<sup>\*1</sup> S. Takeuchi,<sup>\*1</sup> H. Kawasaki,<sup>\*1</sup> K. Demichi,<sup>\*1</sup>  
H. Murakami,<sup>\*1</sup> A. Saito,<sup>\*1</sup> and S. Shimoura<sup>\*2</sup>

Recent development of radioactive beams has allowed extensive nuclear structure studies of unstable nuclei. We plan to construct a hybrid array for charged-particle and  $\gamma$ -ray detection to be used in the RI beam factory (RIBF) which will produce a wider range of nuclei far from stability, than those produced by the present facility.

One method of studying structures of unstable nuclei is to measure  $\gamma$ -rays from fast-moving residual nuclei, with velocities of 30–50% of the speed of light. It allows one to determine the transition probability excitation energy, and level scheme of the nuclei. However, due to the high beam velocities, the  $\gamma$ -ray energy is Doppler-shifted depending on the emission angle with respect to the direction of the residual nuclei, and experiments are performed using a very-low-intensity beam to study very unstable nuclei. In such a case, high angular resolution and efficient detection of  $\gamma$ -rays are strongly desired.

For particle transfer reactions in reversed kinematics, the angular distribution of light recoil particles provides important information on the specific reaction process.

Thus, a system including  $\gamma$ -ray and charged-particle detectors has been designed to be applied to experiments in RIBF. The  $\gamma$ -detector is a granular array of 160 NaI(Tl) scintillators which is capable of high angular resolution and efficiency. The charged-particle detector is an array of CsI(Tl) scintillators which can provide good particle identification of  $^1,2,3\text{H}$ ,  $^3,4\text{He}$ , heavy ions and  $\gamma$ -rays. Figures 1 and 2 show schematics of the detectors. These systems can be combined according to the purpose of the measurement.

The complete setup of the NaI(Tl) array consists of 160 NaI(Tl) scintillators surrounding the target. Each scintillator is of a rectangular shape with a size of  $40 \times 80 \times 160 \text{ mm}^3$ , coupled to a 38 mm- $\phi$  photomultiplier tube. Eighteen layers, each of which consists of 4–12 scintillators, are arranged coaxially with respect to the beam axis, and are closely packed to cover the angular range of 14–166°. The distance from the target is 40 cm for the layer at 90°. The total length of the system along the beam axis is about 90 cm. The angular resolution of  $\gamma$ -ray detection is about 6° at 90°, where the Doppler effect is at a maximum. The efficiency and the  $\gamma$ -ray energy resolution were simulated by means of the GEANT code.<sup>1)</sup> Figure 3 shows the energy dependence of the photo peak efficiency and the energy resolution (FWHM) from residual nuclei

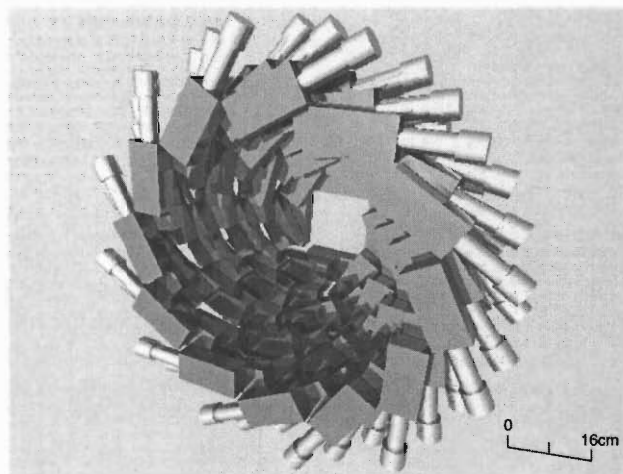


Fig. 1. Schematic of half of the NaI(Tl) array which consists of 80 crystals.

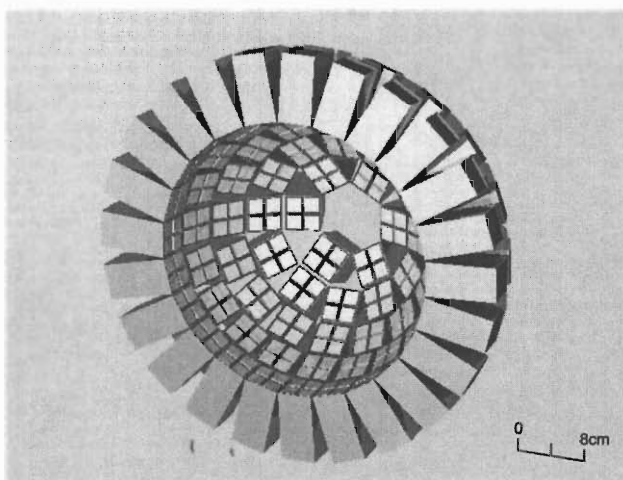


Fig. 2. Schematic of the CsI(Tl) array which consists of 312 crystals.

moving with  $v/c = 0.4$ . The performance is enhanced compared with the previous NaI(Tl) array consisting of 68 NaI(Tl) scintillators, whose efficiency and resolution are about 20% and 100 keV at  $E_\gamma = 1 \text{ MeV}$ , respectively.

The criteria for designing for the CsI(Tl) ball are good charged-particle identification capability, high angular resolution, and compact geometry. The CsI(Tl) scintillator is effective for light-particle identification,<sup>2,3)</sup> and its light can be collected by a silicon photodiode that provides minimal mass compared

<sup>\*1</sup> Rikkyo University

<sup>\*2</sup> Center for Nuclear Study, University of Tokyo

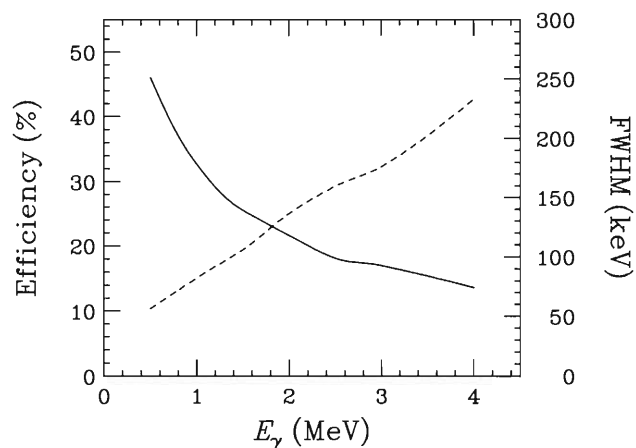


Fig. 3. Calculated efficiency (solid curve) and FWHM (dashed curve) of the NaI(Tl) array as functions of the  $\gamma$ -ray energy  $E_\gamma$  from residual nuclei moving with  $v/c = 0.4$ .

with a photo multiplier. The CsI(Tl) ball consists of 312 crystals, each of which is of a rectangular shape with a size of  $16 \times 16 \times 50 \text{ mm}^3$ , directly coupled to a  $10 \times 10 \text{ mm}^2$  silicon photodiode. Assemblies, each of which is composed of four individual CsI(Tl) crys-

tals, form a hemisphere with the target at its center. The radius of the CsI(Tl) ball is 15 cm at the center of the crystal and 21 cm at the outer diameter including the photodiode. The high angular resolution of  $5^\circ$  in full width allows for precise determination of the angular distribution of recoil particle nuclei resulting from a reaction. Furthermore, due to its compactness, one can install the CsI(Tl) ball in a vacuum chamber. Particle identification is accomplished by pulse shape discrimination based on the ballistic deficit method and/or zero-crossing method.<sup>2)</sup> The good charged-particle identification capability of the CsI(Tl) ball will enable selection of exit channels for detailed spectroscopy.

The construction of the hybrid array will be carried out during the year 2002 in collaboration with ATOMKI (Nuclear Research Institute of Hungarian Academy of Science).

#### References

- 1) GEANT3: *Detector Description and Simulation Tool* (CERN, Geneva, 1993).
- 2) J. Gétraz et al.: Nucl. Instrum. Methods Phys. Res. A **399**, 407 (1997).
- 3) D. G. Sarantites et al.: Nucl. Instrum. Methods Phys. Res. A **381**, 418 (1996).

## Development of reaction-suppressed total-energy detector

T. Suda, M. Chiba, D. Courallet,\* R. Kanungo, T. Kato, A. Ozawa, I. Tanihata, T. Yamaguchi, and T. Zheng

We report here on

- (1) the responses of several inorganic scintillators, such as NaI(Tl), CsI(Tl) and GSO, to an energetic ion beam of a 70A MeV  $^{18}\text{O}$ , and
- (2) the development of a “nuclear-reaction-suppressed” detector to reduce the contribution of nuclear reaction inside inorganic scintillators.

A total-energy detector, which has a good energy resolution and small contribution of nuclear reaction inside the detector, is very important for particle identification, for example, by the conventional  $\Delta E$ - $E$  method, in reactions involving heavy ions. The total kinetic energy of radioactive isotope beams provided by the present RIPS facility normally exceeds a couple of GeV, consequently the light output from, for example, the NaI(Tl) crystal is high enough to achieve an energy resolution of better than 1%. Indeed, as shown in Fig. 1, a NaI(Tl) detector is shown to have an excellent total-energy resolution of 0.7% (FWHM) for a  $^{22}\text{Ne}$  beam of 110A MeV measured at RIKEN.

A serious problem in particle identification using such crystals is, however, background due to nuclear reaction inside the crystal, which generates a long tail towards the low-energy side (and a small tail on ‘high-energy’ side) in the pulse height spectrum, as clearly observed in Fig. 1. In the case of the 110A MeV  $^{22}\text{Ne}$  beam, about 7% of the events suffer from the nuclear reaction inside the NaI(Tl) detector.

One way to eliminate such a nuclear reaction contribution is to divide the crystal into several layers in

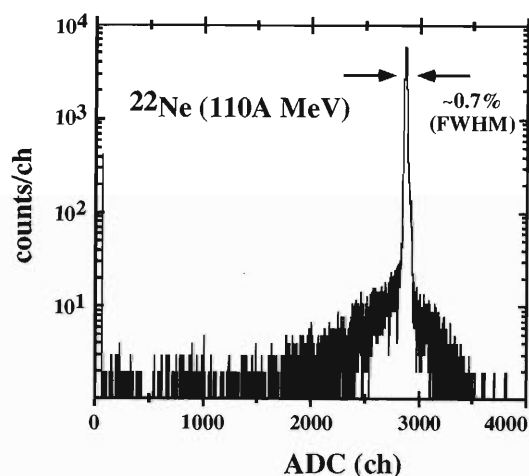


Fig. 1. Pulse height spectrum of the NaI(Tl) detector for  $^{22}\text{Ne}$  beam of 110A MeV.

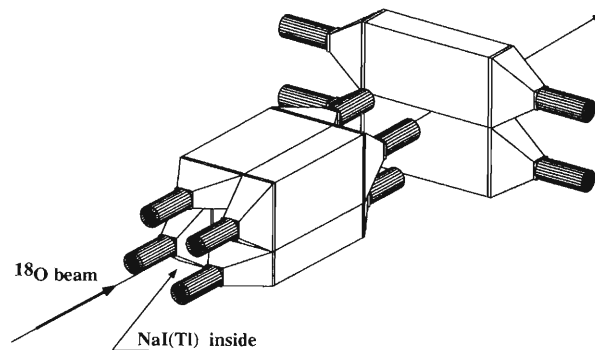


Fig. 2. Schematic view of the reaction suppressor. The total E detector is placed inside the suppressor.

order to check the energy loss in each layer. This is based on the fact that the energy loss in one layer where the nuclear reaction takes place may be different from the expected energy loss. It is, however, difficult to construct such a detector at the RIPS experiments, since the range is normally quite short (less than  $\sim$  a few cm) and a crystal such as NaI(Tl) is (very) hygroscopic.

The method we take to eliminate the nuclear-reaction contribution inside the crystal is to detect escaping particles from the crystal in order to tag the nuclear reaction. Since some of the beam energy become invisible in a pulse height spectrum, neutral particles and/or light ions are supposed to be emitted from the crystal.

For this purpose, a “nuclear-reaction suppressor” was constructed; the schematic drawing is shown in Fig. 2. It consists of six plastic scintillator bars ( $10 \times 20 \times 40 \text{ cm}^3$ ), each of which is viewed by two phototubes at both ends. The NaI(Tl) detector was placed inside the suppressor; the suppressor covers about 96% of  $4\pi$  geometrically. In order to keep the detection efficiency for neutrons as high as possible, the detection threshold was set to be lower than 100 keVee (electron energy equivalent).

We carried out a measurement of the “nuclear-reaction suppression” capability of the suppressor using an  $^{18}\text{O}$  beam of 70A MeV at the E1C beam course of RIKEN. In addition to the NaI(Tl) crystal, we also employed CsI(Tl) and GSO crystals as the total-energy detectors to measure their response to an energetic ion beam, and the suppression efficiency of the suppressor. The dimensions of NaI(Tl) and CsI(Tl) crystals are  $3''\phi \times 6 \text{ cm}$ , and those of GSO are  $4 \times 4 \times 4 \text{ cm}^3$ , respectively. All crystals were optically coupled to  $3''$  phototubes (HAMAMATSU R6091).

The energy resolution and the nuclear reaction rate

\* Ecole des Mines de Nantes, France

of each crystal for the  $^{18}\text{O}$  beam are summarized in Table 1. The energy resolutions of CsI(Tl) and GSO relative to NaI(Tl) are found to be consistent with the relative light output of these crystals. (Strictly speak-

Table 1. Energy resolution, nuclear reaction rate inside crystals and the nuclear suppression efficiency of the NaI(Tl), CsI(Tl) and GSO detectors for the 70A MeV  $^{18}\text{O}$  beam. The threshold of the suppressor is set to be 100 keVee.

crystal	density ( $\text{g}/\text{cm}^3$ )	$\Delta E/E$ (% (FWHM))	tail (%)	rejection (%)
NaI(Tl)	3.67	0.95	6	64
CsI(Tl)	4.53	1.5	5.2	59
GSO	7.13	1.8	4.4	81

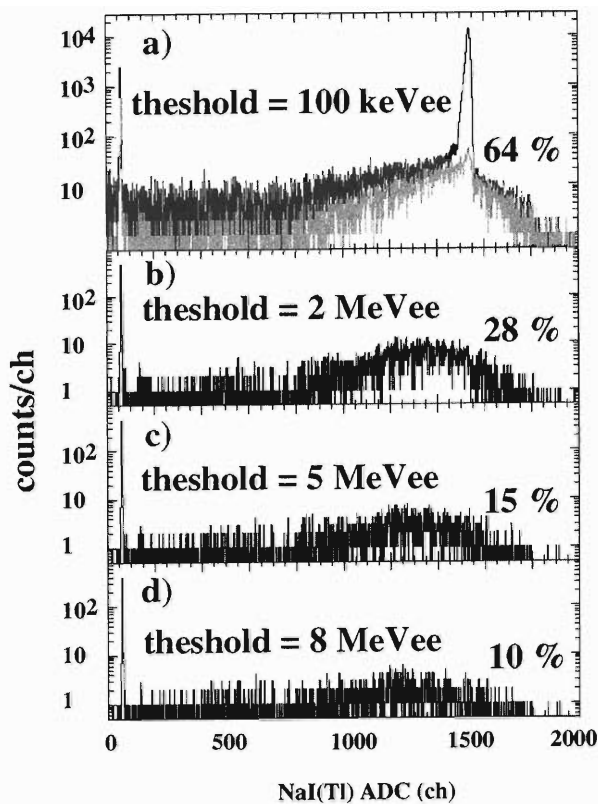


Fig. 3. NaI(Tl) pulse height spectra gated by the suppressor with different thresholds.

ing, it is the peak width relative to the peak position, and not the energy resolution. This is because the linear relationship between the pulse height and total energy is not yet confirmed. It is, however, sufficient for our purpose of particle identification.)

Figure 3 a) shows the NaI(Tl) pulse height spectrum for the  $^{18}\text{O}$  beam, where the sharp peak at around 1500 channels corresponds to total energy deposit. In the same figure, the NaI(Tl) spectrum gated by the suppressor, whose threshold is set to be 100 keVee, is also plotted together. Here, at least one scintillator bar of the suppressor is requested to be fired. The reaction suppressor is quite effective, and about 64% of the nuclear reaction events distributed in the tails of the pulse height spectrum can be eliminated. Figure 3 b), c), and d) show the NaI(Tl) spectra gated by the suppressor with different thresholds as indicated in the figures.

As seen in Fig. 3, the rejection efficiencies rapidly decrease with higher thresholds becomes rapidly small, which may indicate the emission of low-energy particles including neutrons. Setting a lower threshold is essential for achieving high rejection efficiency.

Finally, let us briefly discuss the experimental results for the GSO detector. The nuclear reaction rate of GSO is found to be lower (4.4%) than those of the other crystals, probably due to the higher average atomic weight, which gives a smaller number of nuclei in a fixed range. In addition, the suppression rate of the GSO detector measured under the same conditions is found to be more than 80%. The facts that GSO has very fast response ( $\sim 60$  ns), relatively high light output ( $\sim 30\%$  of NaI(Tl) light output), absence of hygroscopicity and much greater radiation hardness ( $10^9$  rad) than, for example, NaI(Tl) ( $10^3$  rad),<sup>1)</sup> make the GSO crystal be a good candidate for a total-energy detector in future radioactive beam facilities.

We plan to modify the suppressor in order to identify the emitted charge, and then, to examine the responses of these crystals and the reaction suppressor using a higher-energy ion beam available at NIRS (National Institute of Radiological Sciences).

#### References

- 1) V. V. Avdeichikov et al.: Nucl. Instrum. Method Phys. Res. A **349**, 216 (1994).

## Development of a beam loss monitor

Y. Uwamino, S. Ito, K. Matsuno,\*<sup>1</sup> and T. Hirota\*<sup>2</sup>

The beam loss at IRC, SRC and the beam lines of the RI beam factory (RIBF) must be precisely controlled, because an excessive loss may cause an excessive level of radiation in and around the facility. Conventional radiation monitors are working at the present Nishina building, and one or two devices are placed in each experimental room and the cyclotron vault. Similar monitors will be placed outside the bulk shielding of the RIBF, but a number of monitors will be necessary inside the shielding to directly measure the radiation produced by the beam loss. A conventional monitor is accurate for the measurement of effective dose, but it is expensive and not radiation-resistant. We need an inexpensive and radiation-resistant device for the RIBF.

A simple plastic scintillator can be used as a beam loss monitor, because it is sensitive to high-energy neutrons, which are the dominant source component for thick shielding. A prototype of the monitor was fabricated, and its response was measured at the E1 room of the Nishina building. The scintillator used was 2.5 cm in diameter and 2.5 cm in length; the count rate of the discriminator and the anode current can be read for low-level and high-level radiation fields, respectively.

The test neutron fields were created by the 135-MeV/u  $^4\text{He}$  and the 135-MeV/u  $^{14}\text{N}$  beams which bombarded a 2.5-cm-thick copper target. The scintillator was placed at several angles from the beam line and the distance from the target was about 1 m. A neutron rem counter (Aloka TPS-451S) was placed behind the scintillator for comparison and another rem counter placed at a stationary position was also used for the beam current reference. The beam current was dynamically changed at each angle, and the response to the beam current was measured.

Figure 1 shows the response of the anode current to the He beam. The ordinate is the voltage which is converted from the anode current. The voltage is fairly proportional to the current, and has a dynamic range of more than three decades. Figure 2 shows the proportional factors for He and N beams. Since the high-energy neutrons have a strong forwardness, the angular dependence of these factors shows steep curves. The dynamic range of this monitor can be expanded when the discriminated count is also read.

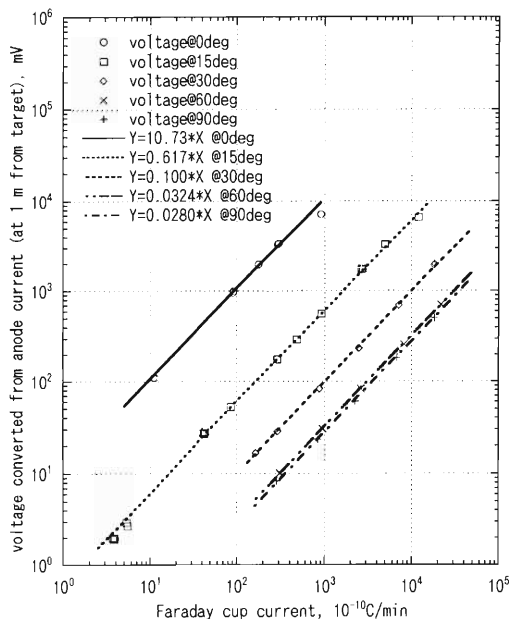


Fig. 1. Anode current response to the He beam current. The monitor was placed 1 m from the target, and the anode current was converted to voltage.

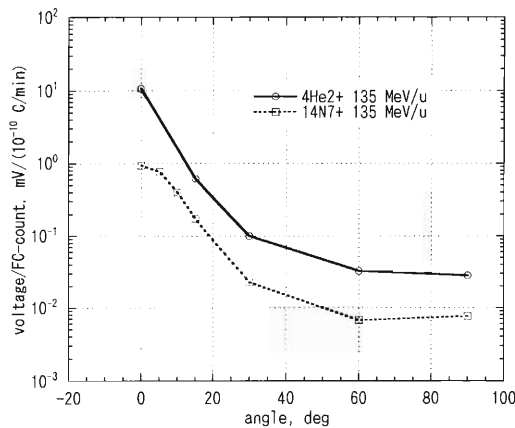


Fig. 2. Ratio of the voltage (mV) to the beam current ( $10^{-10}$  C/min) at various angles from the He and N beams.

\*<sup>1</sup> Fuji Electric Systems Co., Ltd.

\*<sup>2</sup> Yanagawa Engineering Co.

## Absolute calibration of deuteron beam polarization at intermediate energies via $^{12}\text{C}(\vec{d}, \alpha)^{10}\text{B}[2^+]$ reaction

K. Suda,<sup>\*1</sup> H. Okamura,<sup>\*1</sup> T. Uesaka,<sup>\*1</sup> H. Kumasaka,<sup>\*1</sup> R. Suzuki,<sup>\*1</sup> H. Sakai,<sup>\*2</sup> A. Tamii,<sup>\*2</sup> K. Sekiguchi,<sup>\*2</sup>  
K. Yako,<sup>\*2</sup> M. Hatanaka,<sup>\*2</sup> Y. Maeda,<sup>\*2</sup> T. Saito,<sup>\*2</sup> T. Ishida,<sup>\*2</sup> N. Sakamoto, Y. Satou,<sup>\*3</sup>  
K. Hatanaka,<sup>\*4</sup> T. Wakasa,<sup>\*4</sup> and J. Kamiya<sup>\*4</sup>

At the RIKEN Accelerator Research Facility (RARF), the beam polarization of the intermediate energy deuteron is measured using a polarimeter (high-energy polarimeter), which applies the  $d$ - $p$  elastic scattering as a polarimetry.<sup>1)</sup> We have reported the calibration of the analyzing powers for the  $d$ - $p$  elastic scattering at 270 and 140 MeV using the  $^{12}\text{C}(\vec{d}, \alpha)^{10}\text{B}[2^+]$  reaction.<sup>2)</sup> Since the analyzing power  $A_{zz}$  of  $^{12}\text{C}(\vec{d}, \alpha)^{10}\text{B}[2^+]$  is unity at  $0^\circ$ , the ambiguity of the beam polarization can be minimized. The results were compared with the calibration data obtained using the  $^{12}\text{C}(\vec{d}, p)^{13}\text{C}$  reaction<sup>1)</sup> or  $^3\text{He}(\vec{d}, p)^4\text{He}$  reaction<sup>3)</sup> at low energy. Although the agreement is good, we need more angular points to compare the angular distributions. Thus, we calibrated the  $d$ - $p$  elastic scattering at six angles at  $E_d = 270, 200,$  and  $140$  MeV as shown in Table 1. We usually measure the beam polarization at  $\theta_{c.m.} = 86.5^\circ, 82.5^\circ,$  and  $110.0^\circ$  for  $E_d = 270, 200,$  and  $140$  MeV, respectively. A few other points are selected to measure the angular distribution of the  $d$ - $p$  elastic scattering. Also the angle  $\theta_{c.m.} \simeq 120^\circ$  is selected, because the tensor analyzing power  $T_{20} (= -(A_{xx} + A_{yy})/\sqrt{2})$  takes nearly the maximum value irrespective of the energy measured. Since the cross section of the  $(d, \alpha)$  reaction is hundreds of times smaller than that for the  $d$ - $p$  elastic scattering, it takes several hours to obtain sufficient statistics of the beam polarization, even with a beam intensity of 100 nA. Thus, in this calibration, we measured the  $d$ - $p$  elastic scattering at six angles by one shot. In the beam polarization measurement, we detect both deuterons and protons in kinematical coincidence. We usually use a relatively large solid angle of the plastic scintillation counters in order to obtain sufficient statistics within a relatively short time with small accidental events. However, the counters cover four degrees of the scattering angle in the laboratory system. It is too large for the purpose of this cali-

bration to measure the precise angular distribution of the  $d$ - $p$  elastic scattering. Thus, we constructed new counters. For scattered deuterons, as the scattering angle measured is contracted in a narrow forward region and a higher count rate is expected, one scintillation counter is used as a  $\Delta E$  counter for all of the angles except for  $\theta_{c.m.} = 120^\circ$ . For recoil protons, six separate counters are used, and the solid angles are determined by protons. The angular spread of each proton counter is set to  $\Delta\theta_{lab} = 1.0^\circ$ . One of the proton counters is set at  $\theta_{lab} \simeq 30^\circ$  in order to detect both deuterons and protons scattered to  $\theta_{c.m.} \simeq 120^\circ$ . Four sets of these seven counters are set around the beam axis in the directions of Left, Right, Up, and Down.

We used three polarization modes,  $(p_Z, p_{ZZ}) = (0, 0), (1/3, -1),$  and  $(1/3, +1)$ . The spin axis is directed perpendicular to the horizontal plane, which is parallel to the magnetic field of cyclotrons. These three modes are switched every few seconds in order to reduce short-term fluctuation of the polarization. The actual values of the beam polarization were about 70% during the measurement.

The  $^{12}\text{C}(\vec{d}, \alpha)^{10}\text{B}[2^+]$  reaction is measured using the SMART spectrograph. A self-supporting natural carbon foil with a thickness of  $8.79 \text{ mg/cm}^2$  is used for  $E_d = 270$  and  $200$  MeV, and a polyethylene film with a thickness of  $5.8 \text{ mg/cm}^2$  is used as a carbon target for  $E_d = 140$  MeV. The beam intensity was 100 nA for all energies. The detector setup is the same as that in Ref. 1. The analyzing power of this reaction is  $A_{zz} = 1$  at  $0^\circ$  due to parity conservation. Thus the tensor polarization  $p_{ZZ}$  can be determined with less systematic uncertainty. However, since this relation is valid only at exactly  $0^\circ$ , it is necessary to measure the angular distributions and extrapolate them to  $0^\circ$ . The extrapolation result for  $E_d = 270$  MeV is shown in Fig. 1. The magnitude of the vector polarization  $p_Z$  can be deduced multiplying tensor polarization by one third. This relation is fairly robust since it is not affected by the efficiency of the RF transition at the polarized ion source. The  $d$ - $p$  elastic scattering is measured using the high-energy polarimeter. A thin polyethylene film with a thickness of  $30 \mu\text{m}$  is used as a hydrogen target. The measurement is performed using the same beam at the same with the  $(d, \alpha)$  measurement. Thus, the long-term stability of the beam polarization has no influence on the result.

When the beam axis is vertical as in the  $(d, \alpha)$  measurement, there is no sensitivity to  $A_{xz}$ . Therefore,

Table 1. Measured angles for  $d$ - $p$  elastic scattering.

$E_d$ (MeV)	$\theta_{c.m.}$ (deg)
270	80.6, 83.6, 86.6, 89.6, 92.6, 117.7
200	76.6, 79.5, 82.5, 85.5, 88.5, 117.4
140	82.0, 88.0, 94.0, 100.0, 110.0, 119.0

<sup>\*1</sup> Department of Physics, Saitama University

<sup>\*2</sup> Department of Physics, University of Tokyo

<sup>\*3</sup> Center for Nuclear Study, University of Tokyo

<sup>\*4</sup> Research Center for Nuclear Physics, Osaka University

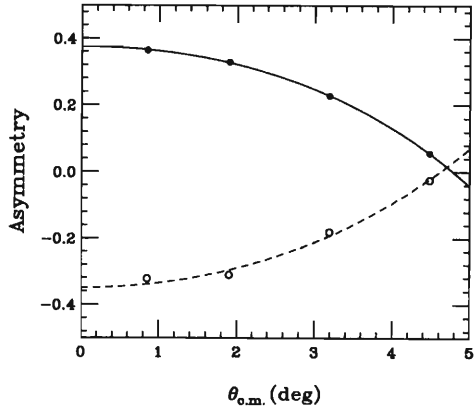


Fig. 1. Angular distribution of the asymmetry of the  $^{12}\text{C}(\vec{d}, \alpha)^{10}\text{B}[2^+]$  reaction. The closed and open circles represent the second and the third polarization modes, respectively (see text). This asymmetry agrees with  $p_{zz}A_{zz}$  at  $0^\circ$ . The results of the polynomial fit are shown as solid and dashed lines. The fitted function is (asymmetry) =  $a_0 + a_2\theta^2 + a_4\theta^4$ .

we also calibrated  $A_{xz}$  after the measurement of the  $(d, \alpha)$  reaction at each energy. In order to precess the spin axis, we employed the swinger dipole magnet of the SMART spectrograph, rotated to  $90^\circ$ . When the spin axis is perpendicular to the magnetic field of the swinger, the spin axis precesses by  $\Delta\beta \simeq -15^\circ$  at the exit of the swinger, depending on the deuteron energy. Since this precession angle is accurately calculated, the uncertainty for  $A_{xz}$  is reduced. The  $d$ - $p$  elastic scattering is measured simultaneously using the same beam before and after the swinger with two polarimeters, the high-energy polarimeter and the swinger polarimeter. The measured angles are  $\theta_{c.m.} = 86.5^\circ, 82.5^\circ,$  and  $110.0^\circ$  for  $E_d = 270, 200,$  and  $140$  MeV, respectively. The advantage of this method is that the spin axis  $(\beta, \phi)$  before the precession can be determined even without any information on the analyzing powers. The result indicates that the spin axis of the deuteron beam from the cyclotron is inclined by 7–10 degrees for all measured energies.

The spin axis  $(\beta, \phi)$  is necessary in order to extract the polarization  $(p_Z, p_{ZZ})$  from the  $(d, \alpha)$  reaction. We deduced the spin axis by fitting the data of  $d$ - $p$  elastic scattering measured simultaneously with the  $(d, \alpha)$  reaction, with the constraints that the ratios between  $A_{xx}, A_{yy},$  and  $A_{xz}$  obtained from  $A_{xz}$  measurement are conserved. With the obtained polarization and the asymmetry of the  $d$ - $p$  elastic scattering, all of the analyzing powers  $A_y, A_{yy}, A_{xx},$  and  $A_{xz}$  for the  $d$ - $p$  elastic scattering are deduced. The results for  $E_d = 270$  MeV are shown in Fig. 2. The errors shown are statistical

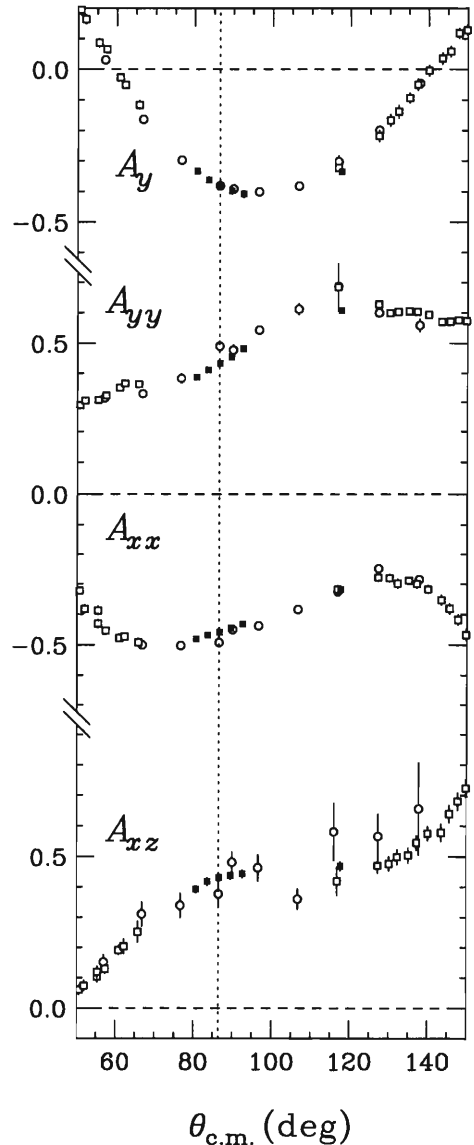


Fig. 2. Analyzing powers for the  $d$ - $p$  elastic scattering at  $E_d = 270$  MeV. The present results are indicated by closed squares. The data indicated by open circles are taken from Ref. 1 and those indicated by open squares are from Ref. 4. The errors are statistical ones only.

ones only. Further analysis for  $E_d = 200$  and  $140$  MeV is in progress.

#### References

- 1) N. Sakamoto et al.: Phys. Lett. B **367**, 60 (1996).
- 2) K. Suda et al.: RIKEN Accel. Prog. Rep. **34**, 186 (2001).
- 3) T. Uesaka et al.: RIKEN Accel. Prog. Rep. **33**, 153 (2000).
- 4) H. Sakai et al.: Phys. Rev. Lett. B **84**, 5288 (2000).

## Advanced network for RIKEN Accelerator Research Facility

T. Ichihara, Y. Watanabe, A. Yoshida, and K. Yoshida

The security of the computer network is a very important issue at the RIKEN Accelerator Research Facility (RARF). Recently, many personal computers in RARF are connected to the Internet *via* the RIKEN Local Area Network (LAN). But it is not easy to maintain the security of each personal computer at a certain level, when they are managed by individual users. Many security holes have been discovered one after another for various operating systems (OS) and it has been necessary to update the OS or apply patches to close the security holes each time.

The network Intrusion Detecting System (IDS) has been installed at the boundary of the RARF LAN and RIKEN LAN in order to monitor unauthorized access. The IDS consists of the free software SNORT,<sup>1)</sup> MySQL,<sup>2)</sup> ACID<sup>3)</sup> and RedHat 7.1 Linux pc. The IDS detects IP packets of the unauthorized access to the RARF LAN and logs them through the MySQL database. The IDS is very helpful in improving the security of RARF LAN, however, security is still not sufficient. The IDS records security-related events but it does not prevent unauthorized access itself.

Under these circumstances, we decided to introduce a new advanced network to the RARF, where the security of the computers is maintained at a sufficient level with minimum effort.

Figure 1 shows the configuration of the RARF advanced LAN.

The RARF Advanced LAN consists of two components, RARF private LAN as shown in the lower part of the figure and the RARF global LAN as shown in the upper part.

All the computers connected to the RARF private LAN are assigned private addresses statically or dynamically. To access the Internet, these private addresses are translated dynamically to the global address by a firewall machine (PIX 535). There is no

way to access the private LAN directly *via* the Internet and therefore the security of the computers connected to the private LAN is maintained at a higher level. We assume that most of the personal computers managed by individuals are connected to the private LAN. Also all the printers are connected to the private LAN. These private LANs are divided into several groups (subnets) categorized by the buildings and laboratories. The routing of the IP and AppleTalk protocols between these subnets is carried out for convenience.

All the computers connected to the global LAN are assigned global addresses. We assume that the server computers such as those with Web servers are connected to the global LAN. No address translation is carried out when accessing the Internet. However, the global LAN is connected to the Internet *via* the firewall machine (PIX 535). At the firewall, the access limitation rules are applied to all the computers which can be identified by port number and network address bases one by one. By the default setting, no access into the computers from the Internet is allowed. This minimizes the ability of unauthorized access to the computers connected to global LAN from the Internet.

In order to prevent virus infections *via* E-mail, a virus detecting and eliminating system has been installed to the central mail server (RARFEXP) of the RARF in the summer of 2001. This system detects and eliminates viruses contained in incoming, outgoing and local E-mails.

The migration of the current LAN to the new advanced LAN was started in November 2001 and has been completed in February 2002.

### References

- 1) <http://www.snort.org/>
- 2) <http://www.mysql.org/>
- 3) <http://www.cert.org/kb/acid/>

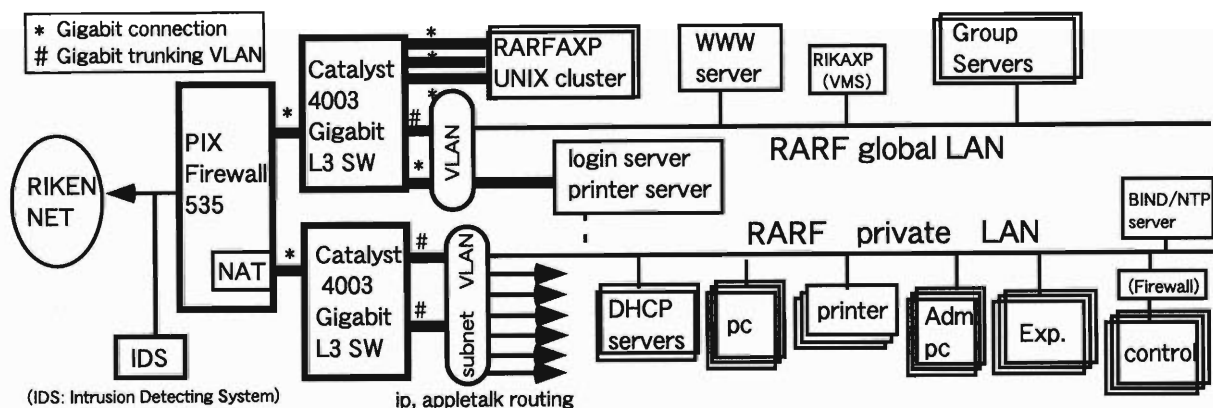


Fig. 1. Configuration of the RARF Advanced LAN.

## RIPS control system with EPICS

K. Yoshida, M. Kobayashi-Komiyama, M. Sugimoto,\* and T. Kubo

The computer control system of RIPS has been upgraded to one based on the Experimental Physics and Industrial Control System (EPICS).<sup>1)</sup> The recent change of the control system of the RIKEN Ring Cyclotron<sup>2)</sup> has rendered the existing RIPS control system<sup>3)</sup> obsolete since they shared the same control computer. To ensure the compatibility of their respective software, a new control system of RIPS was developed with EPICS same as that of the RIKEN Ring Cyclotron.

Most parts of the control software for magnets, slits and actuators are taken from those developed for the cyclotron. Specially developed is the  $B\rho$ -scaling mode for all beam-line magnets in RIPS. Since RIPS is the secondary beam separator, the setting of the magnets of RIPS is often carried out by  $B\rho$ -scaling from the primary beam to the desired secondary beam. Therefore, a convenient method is required for the scaling. This is carried out with the support of the EPICS database program and the EPICS sequencer. In the database program, the required currents of magnets are calculated from the given  $B\rho$  value and the excitation function of the magnets and then they are set

into the magnet power supply. The sequencer sets the given  $B\rho$  value in the control program for each magnet. Parallel processing is taken into account whenever hardware permits. This reduces the setting time of the magnet currents greatly in comparison with the old control system.

The user interface is created by using the DM2K display program. The program runs in the server machine and we access it through the X-terminal machine. Figure 1 shows the control windows appeared in a terminal. Most controls are made by setting the numerical value in a value field and pressing the set button next to the field. More stable operation is accomplished by using EPICS.

### References

- 1) <http://www.aps.anl.gov/epics/>
- 2) M. Komiyama, I. Yokoyama, M. Nagase, E. Ikezawa, M. Fujimaki, R. Abe, T. Tanabe, and M. Kase: Proc. 13th Symp. on Accelerator Science and Technology, Suita, 2001-10, in press.
- 3) N. Inabe et al.: RIKEN Accel. Prog. Rep. 24, 100 (1991).

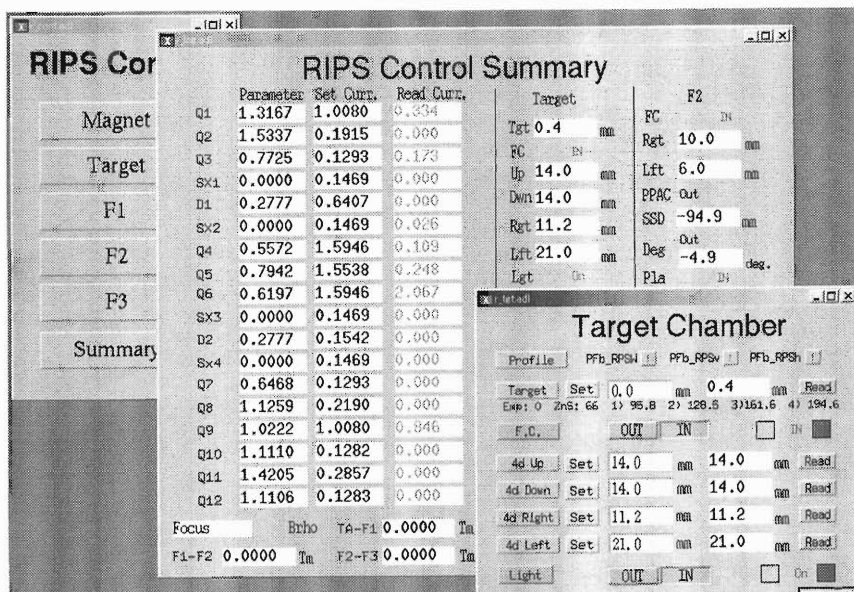


Fig. 1. Control windows appearing in the terminal.

\* Mitsubishi Electric Control Software Corporation

## Trial of RTLinux for embedded control and measuring system

J. Fujita

Ethernet is about to become as necessary standard interface as RS-232C or GP-IB is usually furnished in control and measuring tools. Adapter units that convert these ordinary standard interfaces directly to Ethernet are already being sold as attachments to these tools, and if the product specifications are within the range of our purpose, this combination is sufficient to be embedded in the system. However, actual requests are often out of range of the specifications of manufacturer's products. The conditions for the control and measuring tools to be embedded within an electric apparatus are as follows.

- (1) The size is as compact as possible.
- (2) Ethernet is the on-board standard port.
- (3) The operating system can treat real-time events.
- (4) Expansion of function is free and easy.
- (5) It is easy to obtain hard and soft elements in view of cost and time.

Many plans have been proposed for the embedded control system but the Silicon-Linux (Si-Linux) project<sup>1)</sup> seems to satisfy the above conditions and be easy to access. A Real-Time Linux (RTLinux)<sup>2)</sup> program runs on a small single board computer (SBC) in this project. The RTLinux system operating directly on the PCM-5820 SBC (Advantech) is offered from the project in the form of compressed file called Si-Linux. The board is small in size (145 mm × 102 mm) and has as many interfaces as an ordinary PC/AT computer, including the Ethernet interface. It also provides industry standard architecture (ISA) expansion bus for PC/104 standard and a socket for a compact flash card on the board. The use of the compact flash card is outstanding and makes fabrication of the system very simple. The kernel and modules of the RTLinux are developed and written into a blank flash card in a note book or desktop personal computer (PC) other than the SBC. The flash card is inserted into the socket on the SBC and when the SBC is turned on, the RTLinux operating system is booted from the flash card and starts its tasks. Since the content of the flash card is not deleted by the sudden cutoff of power, the flash card system is more reliable and stable than the hard disk system. Application programs are developed in the form of Linux module in the note book or desktop PC and copied to the flash card in the SBC by the Ethernet LAN.

The environment for development of the Si-Linux was built using the following procedure. Here, the following systems are used: the PCM-5820 SBC, the 420CDT note book PC (Toshiba) and an ordi-

nary desktop PC with motherboard of SV-119 ATX (ACER). A compact flash card has the capacity of 16 MB with a fully compatible IDE interface.

First, debian GNU Linux Ver. 2.2 is installed in each PC. PCMCIA card service must be set on the note book PC so that the compact flash card can be recognized as an IDE fixed disk. In the case of the desktop PC, the compact flash card is connected to the secondary IDE port through an IDE cable, the end of which has been modified for direct insertion of the card, and is also recognized as a secondary disk without the PCMCIA card service. Since the compact flash card has much less storage capacity than a hard disk, some directories and files must be compressed for conservation of storage capacity. Therefore, the option of file compression must be enabled when the kernel is configured. Server functions for LAN, telnet, ftp and nfs are required in both PCs for networking with the SBC. When installing the Si-Linux, the archived file of Si-Linux must be decompressed to a directory in the PC. Since the file size of this system is larger than that of the compact flash card, other directories, except for directories `/`, `/dev` and `/boot`, are compressed as mentioned above, and this modified file system is written into the flash card.

Since the minimum amount of software of RTLinux is installed in the SBC, the RTLinux system with the same configuration as the SBC must be introduced in the PCs for program development. The RTLinux system is distributed by the RTLinux project as a patch file for the conventional Linux kernel. We applied the RTLinux patch to the kernel version 2.2.14 of Linux and reconfigured the kernel to match the SBC.

Two test programs that use API of RTLinux including time scheduling were developed and successfully run on the SBC. One generates square wave signal of a 30  $\mu$ sec period in the parallel port, that is, the printer port of the SBC. The other outputs pulses on the PCM-3724 digital I/O board (Advantech) that is connected to the PC/104 standard bus in the SBC. The API of hardware interrupt has not been tested yet, but the RTLinux on the target and developed systems works accurately, as expected.

If an A/D converter board with the same PC/104 standard is added, this board system will become a more usable tool as a small remote embedded control system in the Ethernet LAN.

### References

- 1) <http://www.si-linux.org/>
- 2) <http://www.rtlinux.org/>

## Simulation of imaging using Compton camera

Q. Y. Pan,<sup>\*1,\*2</sup> Y. Gono,<sup>\*1</sup> S. Motomura,<sup>\*1</sup> T. Sasaki,<sup>\*1</sup> Y. F. Yang,<sup>\*2</sup> M. Hirasawa, S. Enomoto, Y. Yano, and K. Asahi

In comparison with the other  $\gamma$ -ray cameras (*e.g.*, SPECT and PET) used for source imaging, the novel Compton camera produces images using the kinematics of Compton scattering. Its potential advantages are increased efficiency and multiple angular views of the source distribution from a single position due to the absence of the lead collimator. Three-dimensional images can also be obtained using the Compton camera without moving detectors. If Compton cameras are used for clinical diagnosis, these advantages may reduce the radiation dose administered to the patient in order to produce a useful image. First, the increased sensitivity of the Compton camera will allow the use of isotopes with lower activity levels and/or shorter half-lives. Secondly, the reduced angular motion of the detectors will result in less time wasted between angular stops.

Compton cameras have been used in many applications in the fields of X-ray and  $\gamma$ -ray astronomy,<sup>1)</sup> and the nuclear energy industry for site and environmental surveys. The source imaging research with HPGe detectors has been carried out by us. In this report, we present the simulation method and the results of the use of the first HPGe camera in our laboratory. This  $\gamma$ -camera consists of two separate HPGe detectors.<sup>2)</sup> The active volume of each detector is  $50 \times 50 \times 20 \text{ mm}^3$ , which is segmented into 25 units with an equal size of  $10 \times 10 \times 20 \text{ mm}^3$ . The first HPGe detector is called the "scatter detector." Its functions are to promote and detect the position of interactions. The second detector is referred to as the "absorption detector" and its function is to absorb scattered  $\gamma$ -rays. Both of the detectors are used to measure the  $\gamma$ -ray hitting position and deposited energy. The position of the interactions, including the scatter angle, limits the photon's possible source location to a cone surface whose axis is in line with the positions of the two interactions and whose opening angle is equal to the scatter angle; however, with multiple photons, the cone surfaces will only cross at the true source position. The intersection of this cone with an image plane generates an ellipse with parameters which can be determined directly by the measured energy deposited on each detector and the interaction positions. A succession of the detected Compton scattered events will generate a number of ellipses. If a single point source is considered, these ellipses cross a common point, thereby defining the image point as shown in Fig. 1. In our previous work, the entire ellipse was used to produce the image. Actually,

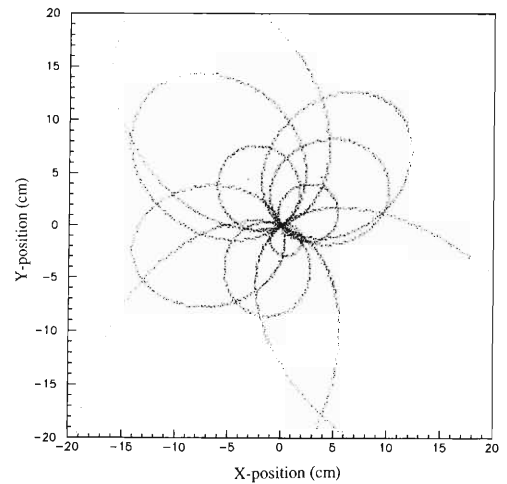


Fig. 1. Ellipses generated from the intersection of the Compton scatter cone with an image plane for a point source.

only one point of each ellipse is useful for the data reconstruction. Here, we choose the common point of ellipses for producing images. This new method can improve the resolution and background suppression of images greatly. The image reconstruction for a continuous-distribution source can be obtained by direct summation of all the common points of the produced ellipses. The detected sufficient scattered events

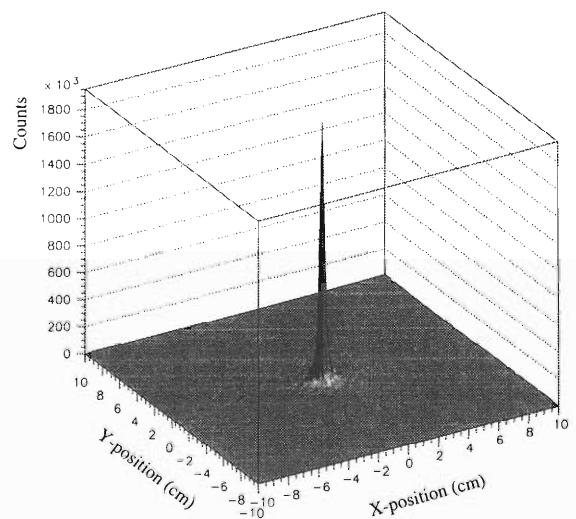


Fig. 2. X-Y plot for the center point source. A  $200 \times 200 \text{ mm}^2$  image plane with 2 mm pixels was used for the reconstructions, with 1000 Compton scatter events. The resolution (FWHM) is 4 mm in the X- and Y-directions.

\*1 Department of Physics, Kyushu University

\*2 Institute of Modern Physics, Chinese Academy of Sciences, China

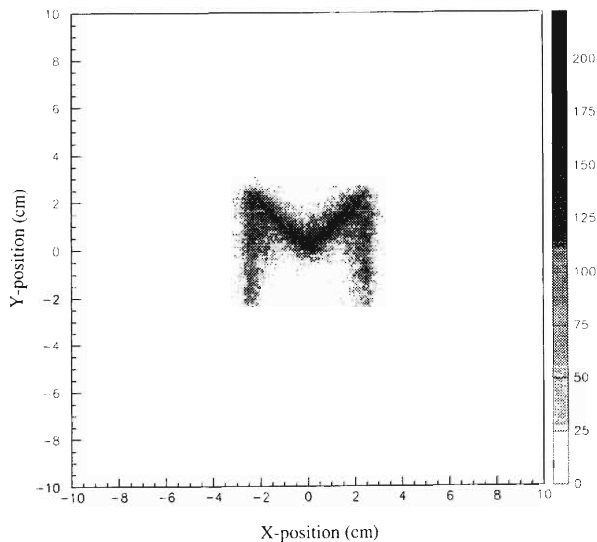


Fig. 3.  $X$ - $Y$  plot for a uniformly distributed volume source in the form of the letter M. The size of the M is  $50 \times 50 \text{ mm}^2$ . Six thousand events were used for the image.

will produce a statistically stable image.

Monte-Carlo simulations of our HPGe camera using the simulation tool GEANT 3.21<sup>3)</sup> were performed. Results of the simulations are presented in Figs. 2 and

3 for images of a point source and a uniformly distributed volume source in the form of the letter M, respectively. It is evident in Fig. 2 that this new method is able to produce point images with the correct position in all three dimensions, and that the images are symmetric around all three axes. The point source image has a FWHM of  $\leq 4 \text{ mm}$  in  $X$ - and  $Y$ -directions. For the continuous source image, the source position can also be reproduced correctly. The only distortion in the simulation is that the relative intensity cannot be reproduced precisely as shown in Fig. 3. The intensities along the two legs of the M-source are slightly weak compared with the other parts. This shortage will be expected to be overcome by the calibration of the detector efficiency with spatial position in the future work. Although some distortions take place, the general success of the reconstruction method is apparent. More images will be produced soon.

#### References

- 1) V. Schonfelder, A. Hirner, and K. Schneider: Nucl. Instrum Methods Phys. Res. **107**, 385 (1973).
- 2) Y. F. Yang, Y. Gono, S. Motomura, S. Enomoto, and Y. Yano: IEEE Trans. Nucl. Sci. **48**, 656 (2001).
- 3) R. Brun et al.: GEANT3 Users' Guide, DD/EE/84-1, (CERN, Geneva, 1987).

## 6. Material Analysis



# Mechanical properties of polyimide films implanted with metals

T. Kobayashi, A. Nakao, and M. Iwaki

Recently, metal-doped diamond-like carbons (Me-DLC) have received attention due to their favorable characteristics, such as a low friction coefficient. One method of producing Me-DLCs is metallic ion implantation into polymers. Polyimide (PI) is very attractive not only for its mechanical and chemical stability and high glass transition temperature, but also for its ability to easily change its structure into amorphous carbon by cross-linking due to ion implantation.

In this study, we chose the tungsten ion to form compounds with carbon. We used a MEVVA-type ion source without a mass separation system to obtain a high-flux tungsten ion beam. The average energy of ions is 190 keV. The chemical states of the implanted atoms were investigated by X-ray photoelectron spectroscopy (XPS) and the cross-sectional structure of the implanted region was observed by transmission electron spectroscopy (TEM). Friction coefficient measurements were performed using a pin-on-disk method with an alumina ball.

The shift in XPS spectra due to the charging-up effect was corrected using the deviation of the C 1s peak from that originating from the polyimide standard sample observation (285 eV). We estimated the chemical state of W implanted in PI to be WC, compared with standard sample observations of W metal and the WC compound. A small number of WO bonds exist at the surface of the specimen implanted at  $5 \times 10^{17} \text{ cm}^{-2}$ .

Cross-sectional TEM micrographs of the specimens implanted at  $1 \times 10^{16} \text{ cm}^{-2}$  and  $1 \times 10^{17} \text{ cm}^{-2}$  showed that the cracks in the brittle implanted region were introduced by the microtoming process. In the case of Ag, Cu and Pd implantation into PI, we reported that the formation of nanosized crystalline colloids of metal due to diffusion of the implanted atoms during implantation was observed. In contrast, in the case of W implantation, no aggregation of W atoms around the projected range was observed. The formation of WC bonds seems to suppress the migration of W atoms.

Figure 1 shows two sets of results for the friction coefficient measurement in a pin-on-disk sliding test with a load of 5 N. The friction coefficient of the specimens implanted at less than  $1 \times 10^{16} \text{ cm}^{-2}$  increased from that at the beginning of the observation. On the other hand, in the case of specimens implanted at more than  $1 \times 10^{17} \text{ cm}^{-2}$ , it initially decreased. We assume that the difference is due to products related to tungsten in the shallow region because no morphological change due to implantation was observed in the surface by SEM. The friction coefficient of the unimplanted specimen varied from 0.4 to 0.8 and reproducibility was poor.

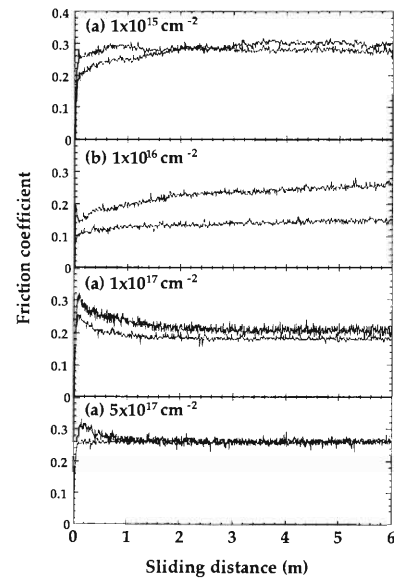


Fig. 1. The results of friction coefficient measurement in the pin-on-disk sliding test with an alumina counterface at a load of 5 N.

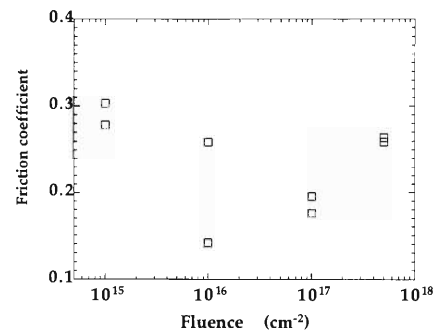


Fig. 2. The friction coefficient of the specimens implanted with W at a sliding distance of 6 m.

The friction coefficient at a sliding distance of 6 m is plotted in Fig. 2. It will be minimized at a fluence of between  $10^{16} \text{ cm}^{-2}$  and  $10^{17} \text{ cm}^{-2}$ . While it is affected by the thickness of the PI film, the minimum value of the friction coefficient obtained in the present study was 0.14 in a specimen implanted at  $1 \times 10^{16} \text{ cm}^{-2}$ , which is comparable to that of DLC produced on a metal substrate by a plasma processing method. The reason for the variation in the results is still being inspected; we assume that it will be due to the nonuniformity of the fluence particularly in the outer region of the implantation area. The role of W-C bonds in reducing the friction coefficient is still not clear. However, it is shown that tungsten implantation at a fluence of between  $10^{16} \text{ cm}^{-2}$  and  $10^{17} \text{ cm}^{-2}$  can result in low friction and a wear-resistant surface on the PI film.

## Development of a highly sensitive high-resolution in-air particle-induced X-ray emission (PIXE) system: II

K. Maeda, K. Hasegawa,<sup>\*1</sup> H. Hamanaka,<sup>\*1</sup> M. Maeda,<sup>\*2</sup> S. Yabuki, and K. Ogiwara

Particle-induced X-ray emission (PIXE) analysis of high energy-resolution is one of the most effective tools for direct investigation of chemical bonding states of atoms in target materials. Recently, we constructed a compact crystal spectrometer system equipped with a position-sensitive proportional counter (PSPC) for high-resolution PIXE measurements in air.<sup>1)</sup> The utility of the system for direct chemical state analysis was demonstrated by measuring  $K\alpha$ <sup>2)</sup> and  $K\beta$ <sup>3)</sup> spectra of third period elements.

As the next step, we have developed a large-window PSPC in order to increase the X-ray detection efficiency of the spectrometer system by one order of magnitude. A prototype of the large-window PSPC (multinode type) was reported previously.<sup>4)</sup> An improved and practical version of the large-window PSPC, a stacked-type assembly, has now been accomplished.<sup>5)</sup> We installed a mechanism for time-resolved spectrum measurements in the new spectrometer system.

The experimental setup is the same as that reported in a previous paper<sup>6)</sup> with the exception of the PSPC. A target sample is placed in air and bombarded with a 2.1 MeV proton beam of 3 mm diameter. X-rays emitted from the target are analyzed with a flat single crystal, and detected using a large-window PSPC assembly.

The newly developed detector comprises a stacked assembly of five PSPCs with a  $512 \times 5$  channel analyzer. Each PSPC employs a  $7\text{-}\mu\text{m}$ -diameter carbon fiber as the anode. The position-to-channel conversion gains ( $\sim 0.106$  mm/channel) of the five PSPCs agree within  $\pm 1\%$ . The sensitive width of each PSPC is 27 mm. The total sensitive height is  $7.4 \times 5 = 37$  mm, *i.e.* about five times larger than that of the previous single-anode PSPC.<sup>1)</sup> Usually, we use a mixed gas of Ar+CH<sub>4</sub> (9:1) as the counter gas under a gas pressure of 1 bar. When we use Kr+CH<sub>4</sub> or Kr+CO<sub>2</sub>, the detection efficiency is much improved, *e.g.* a factor of two in cases of P and S  $K\alpha$  X-rays. Thus, the sensitivity of the present spectrometer system is improved by five to ten times compared to the previous one.<sup>1)</sup>

The ability of the system for carrying out rapid chemical state analysis was examined by measuring the chemical shift of P  $K\alpha_{1,2}$  line. Figure 1(a) shows two-dimensional data of P  $K\alpha$  spectra obtained from a disc of  $\text{Ca}(\text{H}_2\text{PO}_4)_2 \cdot \text{H}_2\text{O}$  powder. The proton beam current was 50 nA and the measurement time was 6 s. After correcting the offset channel of each spectrum, five spectra were summed and recorded on the lowest frame. Prior to the rapid measurements, the offset

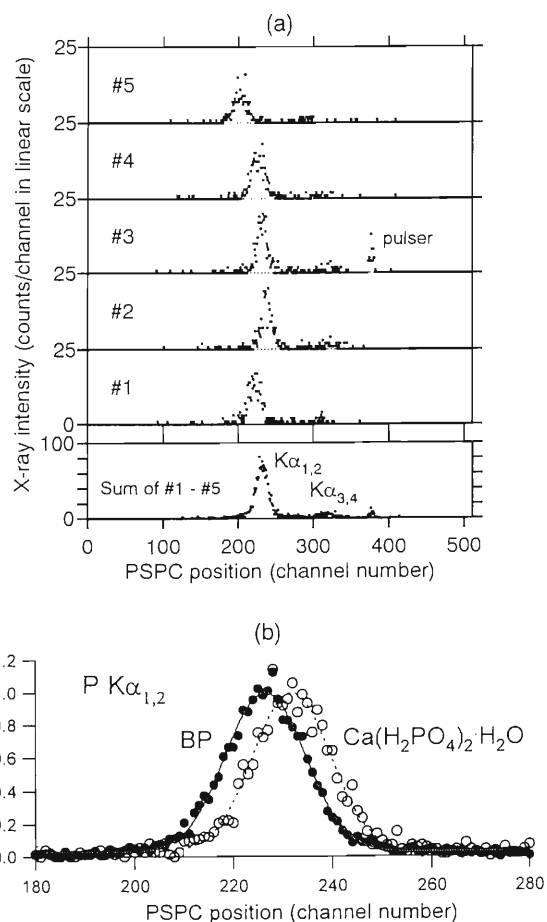


Fig. 1. P  $K\alpha$  spectra: (a) measured and summed spectra of  $\text{Ca}(\text{H}_2\text{PO}_4)_2 \cdot \text{H}_2\text{O}$ , (b) summed P  $K\alpha_{1,2}$  spectrum of  $\text{Ca}(\text{H}_2\text{PO}_4)_2 \cdot \text{H}_2\text{O}$  compared with that of BP (maximum counts/channel: BP, 241;  $\text{Ca}(\text{H}_2\text{PO}_4)_2 \cdot \text{H}_2\text{O}$ , 82). Analyzing crystal; Ge (111): 0.158 eV/channel.

channel values from the center PSPC were determined with a long measurement time (200 s) using a BP powder disc as a reference material. The summed P  $K\alpha_{1,2}$  spectrum of  $\text{Ca}(\text{H}_2\text{PO}_4)_2 \cdot \text{H}_2\text{O}$  is compared with that of BP in Fig. 1(b). The spectrum of BP shown here was also obtained with a measurement time of 6 s. The rapid measurements were repeatedly carried out, changing the target from the sample one to the reference one alternatively. The shift of the P  $K\alpha_{1,2}$  centroid in the spectrum of  $\text{Ca}(\text{H}_2\text{PO}_4)_2 \cdot \text{H}_2\text{O}$  with respect to that of BP was determined to be 5.2 channels with a standard deviation (S.D.) (reproducibility,  $n = 5$ ) of  $\pm 0.3$  channels, corresponding to an energy shift of  $0.82 \pm 0.05$  eV. The reproducibility of 0.05 eV obtained

<sup>\*1</sup> Faculty of Engineering, Hosei University

<sup>\*2</sup> Tokyo University of Fisheries

here is sufficient to estimate chemical bonding states.

Since it was ascertained that the rapid chemical shift measurement was sufficient to distinguish chemical species, we installed a mechanism to measure the time variation of PIXE spectra due to chemical reactions. Up to twenty measurements can be carried out repeatedly and successively. Data of (512 ch  $\times$  5 anodes)  $\times$  20 recorded on a computer are converted to 20 summed-up time-resolved spectra by software. Figure 2 shows examples of time-resolved spectra of

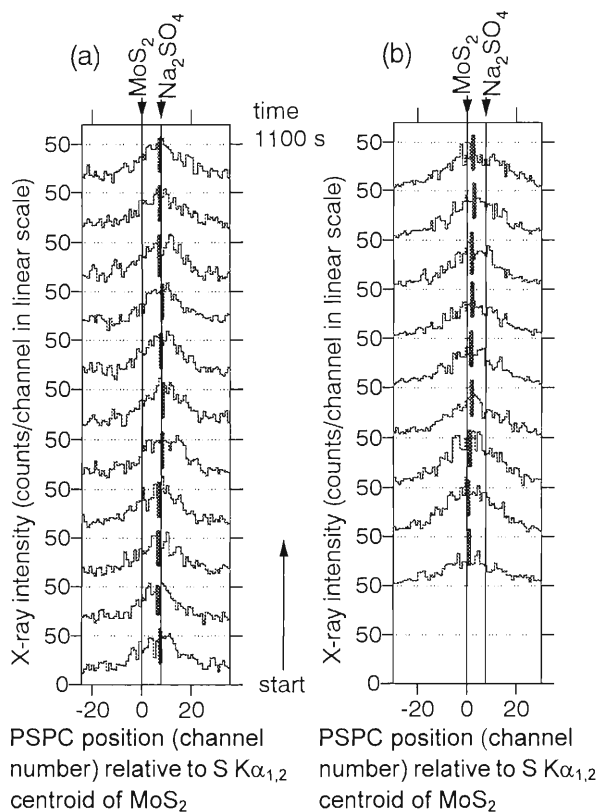


Fig. 2. Time-resolved S  $K\alpha_{1,2}$  spectra of (a) aerosol (S concentration = 4 weight%) and (b) marine sediment (S concentration = 2 weight%) samples. Short and thick bars indicate the centroid of each spectrum. Long vertical bars indicate the centroid positions of S  $K\alpha_{1,2}$  line of  $\text{MoS}_2$  and  $\text{Na}_2\text{SO}_4$ . Proton bombardment began at time = 0. Analyzing crystal;  $\text{NaCl}$  (200): 0.164 eV/channel.

S  $K\alpha_{1,2}$ . The targets are (a) aerosol and (b) marine sediment samples. The aerosol sample was collected on a Polyflon filter for 3 weeks in May 2000 at Wako-shi. Using a core sampler, the marine sediment sample was obtained from Tokyo bay at a water depth of 20 m in November 2000. The core sample was cut into 1-cm-thick slices and kept frozen until the PIXE measurement: a portion of the defrosted sediments was deposited on a Millipore filter. The filters loaded with samples were used as PIXE targets without any pre-treatment.

$\text{MoS}_2$  was used as the reference material for S  $K\alpha_{1,2}$ . The proton beam current was 30–40 nA. The measurement time of each spectrum was 100 s. The sample targets were repeatedly moved by a programmable stage controller in order to reduce sample damage due to proton bombardment. Along with the centroid position of S  $K\alpha_{1,2}$  from  $\text{MoS}_2$  ( $\text{S}^{2-}$ ), that from  $\text{Na}_2\text{SO}_4$  ( $\text{S}^{6+}$ ) is shown in Fig. 2. As seen from Fig. 2 (a), the S  $K\alpha_{1,2}$  centroid positions of the aerosol sample were almost constant during the 1100 s measurement. The figure indicates that S in this aerosol sample is in a stable oxidation state of 6+. On the other hand, the S  $K\alpha_{1,2}$  centroid positions of the marine sediment sample varied gradually over time to the higher energy side, *i.e.* to a higher oxidation number due to oxidation by air. From extrapolation of the centroid positions, the S  $K\alpha_{1,2}$  line shift of the marine sediment sample at time = 0 referring to  $\text{MoS}_2$  was estimated to be +0.44 (S.D.  $\pm 0.23$ ) channels, indicating that S in this sample was originally present as 2- to 0 oxidation state. To our knowledge, this is the first experiment wherein the time variations of chemical shifts of X-rays emitted from practical samples were directly determined.

#### References

- 1) K. Maeda et al.: Nucl. Instrum. Methods Phys. Res. B **134**, 418 (1998).
- 2) K. Maeda et al.: Nucl. Instrum. Methods Phys. Res. B **150**, 124 (1999).
- 3) K. Maeda et al.: Nucl. Instrum. Methods Phys. Res. B **136–138**, 994 (1998).
- 4) K. Hasegawa et al.: Int. J. PIXE **8**, 47 (1998); K. Maeda et al.: RIKEN Accel. Prog. Rep. **33**, 183 (2000).
- 5) K. Maeda et al.: Nucl. Instrum. Methods Phys. Res. B in press.
- 6) K. Maeda et al.: Int. J. PIXE **10**, 47 (2000).



## 7. RIKEN-BNL Collaboration on Spin Physics Program



# Polarized gluon distribution for light hadron pair productions in semi-inclusive pol-DIS

Y.-B. Dong,<sup>\*1</sup> T. Morii,<sup>\*2</sup> and T. Yamanishi<sup>\*3</sup>

To solve the so-called proton spin puzzle, it is crucially important to know how the gluon polarizes in a proton. However, knowledge of the polarized gluon distribution  $\Delta g$  is still very limited because it is difficult to directly extract its information from existing data.

Here, we propose a new formula for clearly extracting the polarized gluon distribution from the light hadron pair production in pol-DIS. In general, a large- $p_T$  hadron pair is produced via photon-gluon fusion (PGF) and QCD Compton at the lowest order of QCD. The PGF gives us direct information on the polarized gluon distribution in the nucleon, while QCD Compton becomes background to the signal process for extracting the polarized gluon distribution.<sup>1,2)</sup> The cross section of the hadron pair production for semi-inclusive process, can be calculated based on the parton model with various fragmentation functions. Then, by using symmetry relations among fragmentation functions and taking an appropriate combination of various hadron pair production processes, we can possibly remove the contribution of QCD Compton components from the cross section and thus, get clear information of the polarized gluon distribution from the remaining PGF components.<sup>3,4)</sup>

Let us consider the process  $l + N \rightarrow l' + h_1 + h_2 + X$  in polarized lepton scattering off polarized nucleon targets, where  $h_1$  and  $h_2$  denote light hadrons in a pair. We consider the following 4 pairs of produced hadrons  $h_1$  with  $z_1$  and  $h_2$  with  $z_2$ ,

- (i)  $(\pi^+, \pi^-)$ ,      (ii)  $(\pi^-, \pi^+)$ ,  
 (iii)  $(\pi^+, \pi^+)$ ,      (iv)  $(\pi^-, \pi^-)$ .

From these pair productions, we can make an interesting combination of cross sections which contains only the PGF contribution as follows;

$$\begin{aligned} & d\Delta\sigma^{\pi^+\pi^-} + d\Delta\sigma^{\pi^-\pi^+} - d\Delta\sigma^{\pi^+\pi^+} - d\Delta\sigma^{\pi^-\pi^-} \\ & \sim \frac{10}{9} \Delta g(\eta, Q^2) d\Delta\hat{\sigma}_{PGF} \\ & \times \left\{ D(z_1, Q^2)D(z_2, Q^2) + \tilde{D}(z_1, Q^2)\tilde{D}(z_2, Q^2) \right. \\ & \left. - D(z_1, Q^2)\tilde{D}(z_2, Q^2) - \tilde{D}(z_1, Q^2)D(z_2, Q^2) \right\}. \end{aligned}$$

Furthermore, the double spin asymmetry  $A_{LL}$  of this combination is defined by

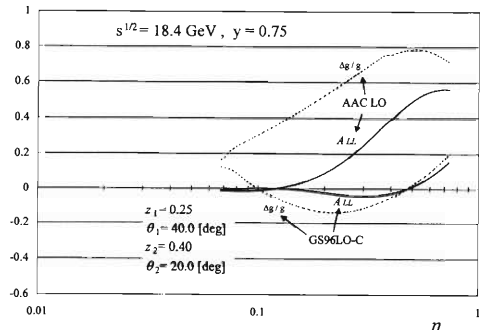


Fig. 1. Calculated results of the double spin asymmetry for the process proposed here and  $\Delta g/g$  as a function of  $\eta$ .

$$\begin{aligned} A_{LL} &= \frac{d\Delta\sigma^{\pi^+\pi^-} + d\Delta\sigma^{\pi^-\pi^+} - d\Delta\sigma^{\pi^+\pi^+} - d\Delta\sigma^{\pi^-\pi^-}}{d\sigma^{\pi^+\pi^-} + d\sigma^{\pi^-\pi^+} - d\sigma^{\pi^+\pi^+} - d\sigma^{\pi^-\pi^-}} \\ &= \frac{\Delta g(\eta, Q^2)}{g(\eta, Q^2)} \cdot \frac{d\Delta\hat{\sigma}_{PGF}}{d\hat{\sigma}_{PGF}}. \end{aligned} \quad (1)$$

We calculate the double spin asymmetry of Eq. (1) at the energy of COMPASS experiments by using the AAC<sup>5)</sup> and GS96<sup>6)</sup> parametrizations at LO QCD as polarized parton distribution functions and GRV98<sup>7)</sup> and MRST98<sup>8)</sup> as unpolarized ones. At  $\sqrt{s} = 18.4$  GeV,  $y = 0.75$ ,  $Q^2 \geq 1$  GeV<sup>2</sup> and  $W^2 \geq 10$  GeV<sup>2</sup> with  $z_1 = 0.25$ ,  $\theta_1 = 40^\circ$ ,  $z_2 = 0.40$  and  $\theta_2 = 20^\circ$  for the produced pion pair, the calculated  $A_{LL}$  are shown as a function of  $\eta$  in Fig. 1. From Fig. 1, one can see a big difference in the behavior of  $A_{LL}$  depending on the models of  $\Delta g/g$  and hence, we can extract the behavior of  $\Delta g$  rather clearly from this analysis.

## References

- 1) A. Bravar, D. von Harrach, and A. Kotzinian: Phys. Lett. B **421**, 349 (1998).
- 2) A. De Roeck, A. Deshpande, V. W. Hughes, J. Lichtenstadt, and G. Rädcl: Eur. Phys. J. C **6**, 121 (1999).
- 3) G. Grigopoulos, A. P. Contogouris, and G. Veropoulos: Phys. Rev. D **62**, 014023 (2000).
- 4) Y.-B. Dong, T. Morii, and T. Yamanishi: Phys. Lett. B **520**, 99 (2001).
- 5) Asymmetry Analysis Collaboration, Y. Goto et al.: Phys. Rev. D **62**, 034017 (2000).
- 6) T. Gehrmann and W. J. Stirling: Phys. Rev. D **53**, 6100 (1996).
- 7) M. Glück, E. Reya, and A. Vogt: Eur. Phys. J. C **5**, 461 (1998).
- 8) A. D. Martin, R. G. Roberts, W. J. Stirling, and R. S. Thorne: Eur. Phys. J. C **4**, 463 (1998).

<sup>\*1</sup> Institute of High Energy Physics, Academia Sinica, China

<sup>\*2</sup> Faculty of Human Development, Kobe University

<sup>\*3</sup> Department of Management Science, Fukui University of Technology

# Polarized $s$ -Quark distribution in charmed hadron production

K. Sudoh\*

Proton spin puzzle is currently one of the most interesting and challenging topics in high-energy spin physics. The polarized parton distribution function plays an important role on deep understandings of the spin structure of proton. However, the polarized sea quark distribution functions remain still poorly clarified.

Recently, the HERMES group has reported<sup>1)</sup> that direct measurements of the strange sea are required to explain the violation of the Ellis-Jaffe sum rule. However, we do not have sufficient knowledge to determine the polarized sea quark distribution. Here, I focus on the polarized  $s$  and  $\bar{s}$  quark distribution.

In order to extract the polarized  $s/\bar{s}$  quark density, I studied semi-inclusive  $D^{*+}/D^{*-}$  production in charged current DIS,  $e^+ + \bar{p} \rightarrow \bar{\nu}_e + D^{*+} + X$  and  $e^- + \bar{p} \rightarrow \nu_e + D^{*-} + X$ , in unpolarized electron-polarized proton collisions which might be observed in the forthcoming experiments at THERA or  $e$ -RHIC, where the incident proton is longitudinally polarized. In naive quark model,  $D^{*+}/D^{*-}$  is dominantly produced by the fragmentation of  $c/\bar{c}$  quark which is produced by  $s/\bar{s}$  quark through the  $t$ -channel  $W$  exchange in the leading order. Hence we can expect that measurement of the spin correlation will provide information about the polarized  $s$  quark distribution in proton.

In these processes, I calculated the single spin asymmetry  $A_L$  defined by

$$A_L(p_T) \equiv \frac{[d\sigma_+ - d\sigma_-]/dp_T}{[d\sigma_+ + d\sigma_-]/dp_T} = \frac{d\Delta\sigma/dp_T}{d\sigma/dp_T}.$$

For instance, in the  $D^{*+}$  production, the spin-dependent differential cross section generally has a form,

$$d\Delta\sigma(D^{*+}) = \{U_{cs}^2 \Delta s(x) + U_{cd}^2 \Delta d(x)\} dx \\ \times \left( \frac{d\Delta\hat{\sigma}}{d\hat{t}} \right) d\hat{t} D_c^{D^{*+}}(z) dz,$$

where  $\Delta s(x)$  and  $\Delta d(x)$  are polarized  $s$  quark and  $d$  quark distribution functions, respectively. Here, I adopted the AAC<sup>2)</sup> and GRSV01<sup>3)</sup> ("standard scenario") parameterizations for the polarized parton distribution.  $D_c^{D^{*+}}(z)$  denotes the unpolarized fragmentation function and I used the Peterson model.<sup>4)</sup>

The  $p_T$  distribution of  $A_L$  in the  $D^{*+}$  production and the  $D^{*-}$  production at center-of-mass energy  $\sqrt{s} = 300$  GeV are shown in Figs. 1 and 2, respectively. As shown in the figures,  $A_L$  in the  $D^{*-}$  production largely depends on the model of the polarized parton distribution function, and significant differences can be

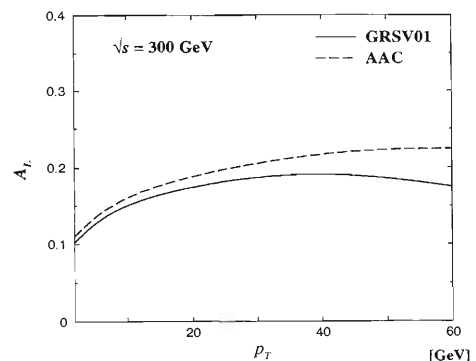


Fig. 1. Single spin asymmetry in  $e^+ + \bar{p} \rightarrow \bar{\nu}_e + D^{*+} + X$  as a function of  $p_T$  at  $\sqrt{s} = 300$  GeV. The solid and dashed curves represent the "standard scenario" of GRSV01 and AAC parametrization, respectively.

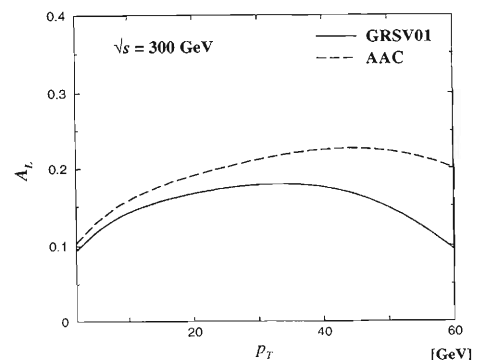


Fig. 2. Single spin asymmetry in  $e^- + \bar{p} \rightarrow \nu_e + D^{*-} + X$  as a function of  $p_T$  at  $\sqrt{s} = 300$  GeV. The curves indicate the same cases as in Fig. 1.

observed in larger  $p_T$  regions. Therefore, I conclude that measuring the single spin asymmetry in this process is quite effective not only for testing the model of the parton distribution function but also for extracting the polarized strange sea distribution directly. On the other hand, for  $D^{*+}$  production we cannot determine the  $s$  quark distribution clearly, since the contribution from the valence  $d$  quark is large.

## References

- 1) HERMES Collaboration: Phys. Lett. B **464**, 123 (1999).
- 2) Asymmetry Analysis Collaboration, Y. Goto et al.: Phys. Rev. D **62**, 034017 (2000).
- 3) M. Glück et al.: Phys. Rev. D **63**, 094005 (2001).
- 4) C. Peterson et al.: Phys. Rev. D **27**, 105 (1983).

\* Graduate School of Science and Technology, Kobe University

# Charmed hadron production and polarized gluon distribution

K. Ohkuma,<sup>\*1</sup> T. Morii,<sup>\*2</sup> and S. Oyama<sup>\*1</sup>

The so-called proton spin puzzle is still one of the most challenging topics in nuclear and particle physics. As is well-known, a proton is not an elementary but compound particle composed of quarks and gluons. Therefore, to understand the proton's spin structure, it is very important to know how quarks and gluons polarize in the proton.

Many experimental and theoretical studies have been done so far to extract information about polarized distributions of quarks and gluons, and now we have rather good knowledge of the polarized distributions of valence quarks. However, knowledge of the polarized gluon distribution  $\Delta g$  is still very limited because it is quite difficult to directly extract its information from existing experimental data. To extract its information, various processes depending on gluon interactions must be studied.

Here we propose another process,  $p\bar{p} \rightarrow \bar{\Lambda}_c^+ X$ , to study the polarized gluon distribution in a proton. The lowest order diagram for this process is gluon-gluon fusion and thus, its cross section is directly proportional to the gluon distribution in the proton. To get information of  $\Delta g$ , we study the two-spin correlation of the target proton and produced  $\Lambda_c^+$  baryon,<sup>1)</sup> which is defined as,

$$A_{LL} = \frac{d\sigma_{++} - d\sigma_{+-} + d\sigma_{--} - d\sigma_{-+}}{d\sigma_{++} + d\sigma_{+-} + d\sigma_{--} + d\sigma_{-+}} \quad (1)$$

$$\equiv \frac{d\Delta\sigma/d\eta}{d\sigma/d\eta},$$

where  $d\sigma_{+-}$ , for example, denotes the spin-dependent differential cross section with the positive helicity of the target proton and the negative helicity of the produced  $\Lambda_c^+$  baryon.  $\eta$  means pseudo-rapidity.  $A_{LL}$  for this process will be measured by the forthcoming BNL-RHIC experiment. Here, we are interested in the sensitivity of the observable defined by Eq. (1).

To numerically estimate  $A_{LL}$ , we take the GRSV01<sup>2)</sup> and AAC<sup>3)</sup> parameterization models for the polarized gluon distribution function and GRV98<sup>4)</sup> for the unpolarized one. Though both of GRSV01 and AAC models excellently reproduce the experimental data on the polarized structure function of nucleons  $g_1(x)$ , the polarized gluon distributions for those models are quite different. In other words, the data on polarized structure function of nucleons  $g_1(x)$  are not enough to distinguish the model of gluon distributions. Since the process is semi-inclusive, the fragmentation function

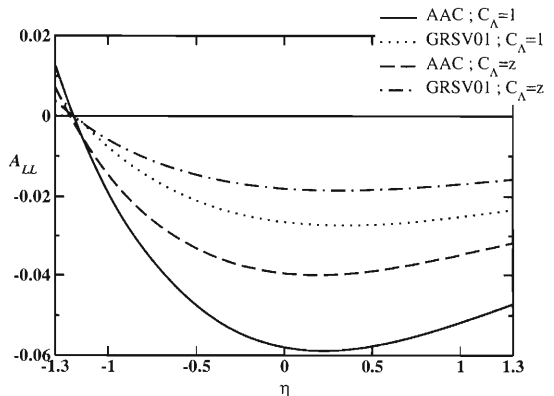


Fig. 1. Spin correlation Asymmetry  $A_{LL}$  as a function of  $\eta$  at  $\sqrt{s} = 500$  GeV.

of a charm quark to  $\Lambda_c^+$  is necessary to do numerical calculations. Then, for the unpolarized fragmentation function, we use Peterson fragmentation function,<sup>5)</sup>  $D_{c \rightarrow \Lambda_c^+}(z)$ .<sup>a)</sup> In addition, since we have no data, at present, about the polarized fragmentation function for the polarized  $\Lambda_c^+$  production, we take the following ansatz:

$$\Delta D_{\bar{c} \rightarrow \bar{\Lambda}_c^+}(z) = C_{c \rightarrow \Lambda_c^+} D_{c \rightarrow \Lambda_c^+},$$

where  $C_{c \rightarrow \Lambda_c^+}$  is scale-independent spin transfer coefficient. In this analysis, we study two cases: (1)  $C_{c \rightarrow \Lambda_c^+} = 1$  (non-relativistic quark model) and (2)  $C_{c \rightarrow \Lambda_c^+} = z$  (Jet fragmentation model<sup>6)</sup>).

Numerical results of  $A_{LL}$  are shown in Fig. 1. As shown in Fig. 1,  $A_{LL}$  is rather sensitive to the model of the polarized gluon distribution functions. Therefore, the process discussed here could provide good information about the distribution of the polarized gluons in a nucleon.

To get better knowledge of  $\Delta g$ , we need more detailed information about the spin-dependent fragmentation function of a charm quark to  $\Lambda_c^+$ .

## References

- 1) K. Ohkuma et al.: Phys. Lett. B **491**, 117 (2000).
- 2) M. Glück et al.: Phys. Rev. D **63**, 094005 (2001).
- 3) Y. Goto et al.: Phys. Rev. D **62**, 034017 (2001).
- 4) M. Glück et al.: Eur. Phys. J. C **5**, 461 (1998).
- 5) C. Peterson et al.: Phys. Rev. D **27**, 105 (1983).
- 6) A. Bartl et al.: Z Phys. C **6**, 335 (1980).

<sup>\*1</sup> Graduate School of Science and Technology, Kobe University

<sup>\*2</sup> Faculty of Human Development, Kobe University

<sup>a)</sup>  $z$  denotes the momentum fraction from charm quark to  $\Lambda_c^+$  baryon.

## Uncertainty of polarized gluon distribution at RHIC

Y. Goto, M. Hirai, T. Horaguchi,<sup>\*1</sup> H. Kobayashi, S. Kumano,<sup>\*2</sup> M. Miyama,<sup>\*3</sup> N. Saito, and T.-A. Shibata<sup>\*1</sup>

In order to investigate nucleon spin structure, we have parametrized polarized parton distribution functions (Pol-PDFs) by using polarized deep inelastic scattering (Pol-DIS) experimental data.<sup>1)</sup> As a next step, we investigate Pol-PDF uncertainty, which is important to provide more reliable information for predicted physical quantities. It is difficult to estimate precise uncertainty of a nonlinear function in multi-dimensional parameter space. However, we could use a Hessian method for the uncertainty estimation when the function  $\chi^2(a_i)$  of the parameter  $a_i$  is approximated to a parabolic function. The Hessian is obtained as the second derivative term in the expansion of  $\chi^2(a_i)$  around the minimum point. Then, an error matrix is given by the inverse matrix of the Hessian. Parameter errors are obtained by the square roots of diagonal elements, and non-diagonal elements have correlation effects with other parameters. In this way, uncertainty of a distribution function  $F(x)$  is given by

$$[\delta F(x)]^2 = \sum_{ij} \frac{\partial F(x)}{\partial a_i} \varepsilon_{ij} \frac{\partial F(x)}{\partial a_j},$$

where  $\varepsilon_{ij}$  is an error matrix and  $a_i$  denotes a parameter. In the parametrization, the following functional form is used as initial parton distributions at  $Q^2 = 1 \text{ GeV}^2$ :

$$\Delta f_i(x) = [\delta_i x^{\nu_i} - \kappa_i (x^{\nu_i} - x^{\mu_i})] f_i(x),$$

where  $i$  denotes  $u_v$ ,  $d_v$ ,  $\bar{q}$ , or *gluon*,  $f_i(x)$  is the corresponding unpolarized parton distribution, and  $\delta_i$ ,  $\nu_i$ ,  $\kappa_i$ ,  $\mu_i$  are free parameters. These parameters are constrained by the positivity condition and flavor SU(3) symmetry, and they are optimized by a  $\chi^2$  analysis. A Fortran program library of our Pol-PDFs is available from the AAC home page.<sup>2)</sup>

In order to use the Hessian method, the  $\chi^2(a_i)$  function needs to satisfy the parabolic approximation. In our analysis, most  $\chi^2(a_i)$  curves can be approximated by quadratic functions. However, some parameters are stopped at a limit which is given by the positivity condition. These parameters control the asymptotic behavior of the Pol-PDFs in the  $x \rightarrow 1$  (or 0) limit, where experimental data do not exist. Because these parameters cannot be determined by the Pol-DIS data, we should fix them to obtain a proper error matrix.

According to our estimation, the polarized valence quark distributions have small uncertainty, so that these distributions are determined well by the present experimental data. On the other hand, the polarized

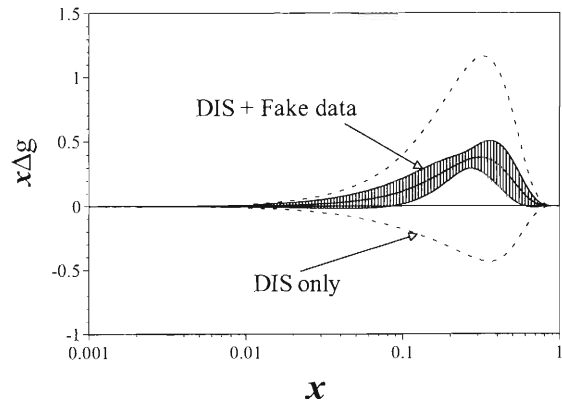


Fig. 1. Uncertainty of the polarized gluon distribution at  $Q^2 = 1 \text{ GeV}^2$ . The solid curves are obtained by including fake gluon data, and the dotted curves are obtained only by the DIS data.

antiquark distribution  $\Delta\bar{q}(x)$  has large uncertainty in the small  $x$  region. Its small- $x$  behavior seriously affects the quark spin content  $\Delta\Sigma$ . The polarized gluon distribution  $\Delta g(x)$  has large uncertainty even in the NLO analysis. These results indicate that it is difficult to determine  $\Delta\bar{q}(x)$  and  $\Delta g(x)$  by the Pol-DIS data. This fact suggests that we should improve our analysis by including other measurements from SMC, HERMES, COMPASS, and RHIC.

In particular, prompt photon production at RHIC is expected to play an important role in determining the polarized gluon distribution. The spin asymmetry  $A_{LL}^\gamma$  is dominated by the contribution from the gluon Compton process. The statistical error of  $A_{LL}^\gamma$  is inversely proportional to the square root of the total number of photon. The statistic error can be estimated by the event generator PYTHIA under the geometrical acceptance at RHIC. We assume that  $\Delta g(x)$  is measured near AAC NLO-1, gluon fake data with statistical error are created at  $\sqrt{s} = 200, 500 \text{ GeV}$  by full luminosity for 1 year at RHIC. The gluon uncertainty is estimated again by including these data. Figure 1 shows the uncertainty of the AAC (NLO-1) gluon distribution and the one with the fake gluon data. The uncertainty becomes small if the fake gluon data are included. We can expect to reduce polarized gluon uncertainty by the prompt photon measurements.

### References

- 1) Y. Goto et al.: Phys. Rev. D **62**, 034017 (2000).
- 2) <http://spin.riken.bnl.gov/aac/>

<sup>\*1</sup> Tokyo Institute of Technology

<sup>\*2</sup> Saga University

<sup>\*3</sup> Tokyo Metropolitan University

# Single-spin asymmetries and soft-gluon poles

Y. Koike\*

The interest in the single transverse spin asymmetry  $A_N$  in the pion production,  $N(P, S_\perp) + N(P') \rightarrow \pi(\ell_T) + X$ , and the hyperon (typically  $\Lambda$ ) polarization  $P_\Lambda$  in the unpolarized  $NN$  collision,  $N(P) + N(P') \rightarrow \Lambda(\ell_T, S_\perp) + X$ , resides in the fact that they probe quark-gluon correlation in the hadrons (higher twist effect) which is not included in the parton model.

In this note, I will discuss  $A_N$  and  $P_\Lambda$  in the framework of the collinear factorization. According to the generalized QCD factorization theorem, the cross section for  $A_N$  typically consists of three kinds of twist-3 cross sections,

$$(A) \quad G_a(x_1, x_2) \otimes q_b(x') \otimes \hat{q}_{c \rightarrow \pi}(z) \otimes \hat{\sigma}_{ab \rightarrow c}^1, \quad (1)$$

$$(B) \quad \delta q_a(x) \otimes \mathbf{E}_b(\mathbf{x}'_1, \mathbf{x}'_2) \otimes \hat{q}_{c \rightarrow \pi}(z) \otimes \hat{\sigma}_{ab \rightarrow c}^2, \quad (2)$$

$$(C) \quad \delta q_a(x) \otimes q_b(x') \otimes \hat{E}_{c \rightarrow \pi}(z_1, z_2) \otimes \hat{\sigma}_{ab \rightarrow c}^3, \quad (3)$$

and  $P_\Lambda$  likewise receives two contributions,

$$(A') \quad E_a(x_1, x_2) \otimes q_b(x') \otimes \delta \hat{q}_{c \rightarrow \Lambda}(z) \otimes \hat{\sigma}_{ab \rightarrow c}^4, \quad (4)$$

$$(C') \quad q_a(x) \otimes q_b(x') \otimes \hat{G}_{c \rightarrow \Lambda}(z_1, z_2) \otimes \hat{\sigma}_{ab \rightarrow c}^5. \quad (5)$$

Here the functions with two variables (momentum fractions)  $G_a(x_1, x_2)$ ,  $E_a(x_1, x_2)$ ,  $\hat{E}_{c \rightarrow \pi}(z_1, z_2)$ ,  $\hat{G}_{c \rightarrow \Lambda}(z_1, z_2)$  are twist-3 quantities:  $G_a$  and  $E_a$  are, respectively, the transversely polarized distribution and the unpolarized distribution functions in the nucleon. The functions with a hat,  $\hat{E}_{c \rightarrow \pi}$  and  $\hat{G}_{c \rightarrow \Lambda}$  are, respectively, the unpolarized fragmentation function for the pion and the transversely polarized fragmentation function for  $\Lambda$ .  $a, b$  and  $c$  stand for the parton's species.

The twist-3 fragmentation functions are defined from

$$\begin{aligned} \widehat{M}_{Fij}^\alpha(z_1, z_2) &= \sum_X \int \frac{d\lambda}{2\pi} \int \frac{d\mu}{2\pi} e^{-i\lambda/z_1} e^{-i\mu(1/z_2 - 1/z_1)} \\ &\quad \times \langle 0 | \psi_i(0) | HX \rangle \langle HX | g F^{\alpha\beta}(\mu n) n_\beta \bar{\psi}_j(\lambda n) | 0 \rangle. \end{aligned} \quad (6)$$

$\widehat{M}_F^\alpha(z_1, z_2)$  is decomposed to define twist-3 fragmentation functions as

$$\begin{aligned} \widehat{M}_F^\alpha(z_1, z_2) &= M/4 \not{p} \epsilon^{\alpha p n S_\perp} \hat{G}_F(z_1, z_2)/z_2 \\ &\quad - iM/4 \not{p} \gamma_5 S_\perp^\alpha \hat{G}_F^5(z_1, z_2)/z_2 \\ &\quad - iM(S \cdot n)/4 \gamma_5 (\not{p}^\alpha \not{p} \not{p} - \gamma^\alpha \not{p}) \hat{H}_F(z_1, z_2)/z_2 \\ &\quad + M/4 \gamma_5 \not{p} \gamma_\nu \epsilon^{\nu \alpha n p} \hat{E}_F(z_1, z_2)/z_2 + \dots, \end{aligned} \quad (7)$$

where  $\dots$  stands for the twist higher than 3. In Eq. (6), if one shifts the gluon field strength  $g F^{\alpha\beta}(\mu n) n_\beta$  into

the matrix element with  $\psi(0)$  and call it  $\widehat{M}_{FR}^\alpha(z_1, z_2)$ , similar decomposition of  $\widehat{M}_{FR}^\alpha$  defines another fragmentation functions ( $\hat{G}_{FR}$ ,  $\hat{G}_{FR}^5$ ,  $\hat{H}_{FR}$ ,  $\hat{E}_{FR}$ ). But these functions are related to ( $\hat{G}_F$ ,  $\hat{G}_F^5$ ,  $\hat{H}_F$ ,  $\hat{E}_F$ ) by the hermiticity. In addition if we assume naive time reversal invariance, these functions become real and obey the relation  $\hat{G}_{FR}(z_1, z_2) = \hat{G}_F(z_2, z_1)$ ,  $\hat{E}_{FR}(z_1, z_2) = \hat{E}_F(z_2, z_1)$ ,  $\hat{G}_{FR}^5(z_1, z_2) = -\hat{G}_F^5(z_2, z_1)$ ,  $\hat{H}_{FR}(z_1, z_2) = -\hat{H}_F(z_2, z_1)$ . We assume this symmetry property in our analysis.

With the complete set of the distribution and fragmentation functions up to twist-3, one can derive the cross section formula corresponding to Eqs. (1)–(5). We follow the previous analyses Refs. 1–4 and employ the *valence-quark soft-gluon* approximation to analyze the cross section. In this approximation we keep only the terms with the derivative of the twist-3 functions such as  $dE_F(x, x)/dx$  and  $d\hat{E}_F(z, z)/dz$ . This approximation should be valid at large  $x_F \rightarrow 1$ , which probe the region with large  $x$ , small  $x'$  and large  $z$  in Eqs. (1)–(5) where the relations such as  $|dE_F(x, x)/dx| \gg E_F(x, x)$  and  $|d\hat{E}_F(z, z)/dz| \gg \hat{E}_F(z, z)$  hold. The (B) term for  $A_N$  may cause enhancement in the asymmetry at  $x_F \rightarrow -1$ , but it turns out that it is negligible in all kinematic region because of the smallness of the hard cross section  $\hat{\sigma}^2$  (Ref. 3).

To get a rough idea on the behavior of (C) and (C') contribution to  $A_N$  and  $P_\Lambda$ , we have performed a numerical estimate of each term. We have used the same distribution and fragmentation functions used in Refs. 3 and 4. For the twist-3 functions, we make an extension of the ansatz taken in Refs. 1–4,  $G_F^a(x, x) = K_a q^a(x)$ ,  $E_F^a(x, x) = K'_a \delta q^a(x)$ ,  $\hat{G}_F^a(x, x) = \tilde{K}_a \hat{q}^a(x)$ ,  $\hat{E}_F^a(x, x) = \tilde{K}'_a \hat{q}^a(x)$ , and set  $K_u = -K_d = 0.07$ ,  $K'_u = \tilde{K}_u = K_a$  ( $a = u, d$ ), and  $\tilde{K}'_u = -0.11$ ,  $\tilde{K}'_d = -0.19$ . This choice of  $\tilde{K}'_a$  is simply motivated to reproduce  $A_N$  approximately at large  $x_F$ . The result shows<sup>5)</sup> that the (C) term alone can give equally good fit to the E704 data as the (A) term studied in Ref. 1. The (C') contribution also gives rise the rising behavior of  $P_\Lambda$  at large  $x_F$ .<sup>5)</sup>

## References

- 1) J. Qiu and G. Sterman: Phys. Rev. D **59**, 014004 (1999).
- 2) Y. Kanazawa and Y. Koike: Phys. Lett. B **478**, 121 (2000).
- 3) Y. Kanazawa and Y. Koike: Phys. Lett. B **490**, 99 (2000).
- 4) Y. Kanazawa and Y. Koike: Phys. Rev. D **64**, 034019 (2001).
- 5) Y. Koike: hep-ph/0106260, Proc. DIS 2001, Bologna, Italy, 2001-4, to be published.

\* Department of Physics, Niigata University

# Partons and QCD in high-energy $pp$ collisions

W. Vogelsang

Current and future dedicated high-energy spin experiments will provide much new information on the nucleon's spin-dependent parton distributions. The question arises of how to consistently determine the various densities from the measurements. Such a "global analysis" of the data makes use of a  $\chi^2$  minimization and will usually require thousands of theory computations of the cross section for every data point. The computing time required for a fit easily becomes excessive, in particular if the partonic hard-scattering is treated at higher-orders in perturbation theory. Here we propose a way<sup>1)</sup> of implementing efficiently, and without approximations, higher-order expressions for any cross section into the fitting procedure.

A general spin-dependent cross section in longitudinally polarized  $pp$  collisions, differential in a certain observable  $O$  and integrated over experimental bins in other kinematical variables  $T$ , can be written as

$$\frac{d\Delta\sigma^H}{dO} = \sum_{a,b} \int_{bin} dT \int dx_a \int dx_b \Delta f_a(x_a, \mu) \times \Delta f_b(x_b, \mu) \frac{d\Delta\hat{\sigma}_{ab}^H}{dO dT}(x_a P_A, x_b P_B, P_H, T, \mu), \quad (1)$$

where the  $\Delta f_i$  are the spin-dependent parton distributions and  $\mu$  the factorization/renormalization scale. The sum is over all partonic channels  $ab \rightarrow HX$  with their spin-dependent partonic cross section  $d\Delta\hat{\sigma}_{ab}^H$ .

We now express the  $\Delta f_i$  by their Mellin inverses,

$$\Delta f_i(x, \mu) = \frac{1}{2\pi i} \int_{\mathcal{C}_n} dn x^{-n} \Delta f_i^n(\mu). \quad (2)$$

One subsequently interchanges integrations and finds

$$\frac{d\Delta\sigma^H}{dO} \equiv \sum_{a,b} \int_{\mathcal{C}_n} dn \int_{\mathcal{C}_m} dm \Delta f_a^n(\mu) \Delta f_b^m(\mu) \times \Delta\tilde{\sigma}_{ab}^H(n, m, O, \mu), \quad (3)$$

where the  $\Delta\tilde{\sigma}_{ab}^H(n, m, O, \mu)$  do not depend on the parton distribution functions and can be pre-calculated *prior* to the fit for a specific set of the two Mellin variables  $n$  and  $m$ . They contain all the tedious and time-consuming integrations. The double inverse Mellin transformation which finally links the parton distributions with the pre-calculated  $\Delta\tilde{\sigma}_{ab}^H(n, m, O, \mu)$  of course still needs to be performed in each step of the fitting procedure, but becomes extremely fast by choosing the values for  $n, m$  on the contours  $\mathcal{C}_n, \mathcal{C}_m$  simply as the supports for a Gaussian integration.

As a specific example, we consider prompt photon production,  $\vec{p}\vec{p} \rightarrow \gamma X$ , at RHIC. We use  $\sqrt{S} = 200$  GeV and consider five values of  $p_T$  which will be accessible experimentally. We average over  $|\eta| < 0.35$  in

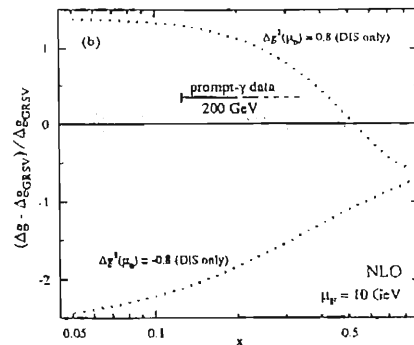


Fig. 1. Variations of the polarized gluon densities obtained in the combined fits, with respect to  $\Delta g$  of Ref. 3. See Ref. 1 for further details.

pseudorapidity and choose  $\mu = p_T$ . The crucial asset of our method is the speed at which one can calculate the full hadronic cross section, once the  $\Delta\tilde{\sigma}_{ab}^\gamma(n, m, p_T, \mu)$  have been pre-calculated. We found that 1000 evaluations of the full NLO prompt photon cross section take only about 10–15 seconds on a standard workstation.

Figure 1 shows the results for the gluon density found in a "toy" global analysis,<sup>1)</sup> of the available data on polarized deep-inelastic scattering<sup>2)</sup> and of *fictitious* data on prompt photon production at RHIC, which we project by simply calculating  $A_{LL}^\gamma$  to NLO using the set of polarized parton distributions of Ref. 3. Ideally, thanks to the strong sensitivity of the prompt photon reaction to  $\Delta g$ , the gluon density in such a fit should return close to the function we assumed when calculating the fictitious prompt photon "data," in the region of  $x$  mainly probed. Indeed, as shown in Fig. 1, this happens. The shaded band illustrates the deviations of the gluon densities obtained in a large number of global fits, from the "reference  $\Delta g$ "<sup>3)</sup> used in generating the pseudo-data. As is expected, the gluon density is rather tightly constrained in the  $x$ -region dominantly probed by the prompt photon data. This is true in particular at  $x \approx 0.15$ , as a result of our most precise "data point" for  $A_{LL}^\gamma$  at  $p_T = 12.5$  GeV. Our analysis clearly underlines the potential and importance of upcoming measurements of  $A_{LL}^\gamma$  at RHIC for determining  $\Delta g$ .

## References

- 1) M. Stratmann and W. Vogelsang: Phys. Rev. D **64**, 114007 (2001).
- 2) for a recent review of the data on polarized deep-inelastic scattering, see: E. Hughes and R. Voss: Annu. Rev. Nucl. Part. Sci. **49**, 303 (1999).
- 3) M. Glück, E. Reya, M. Stratmann, and W. Vogelsang: Phys. Rev. D **63**, 094005 (2001).

## Gluon saturation from small- $x$ evolution equation

E. Iancu,<sup>\*1</sup> K. Itakura, and L. McLerran<sup>\*2</sup>

There has been significant progress in recent years towards understanding the hadron structure in the regime of high parton density at small  $x$ , which is the regime relevant for high-energy scattering. As one goes to smaller  $x$  with the transverse resolution scale  $Q^2$  being fixed, the number of gluons per unit transverse plane increases rapidly. This is described by a linear evolution equation such as the BFKL or DLA (double log approximation) equations. However, at some point, gluons start to overlap with each other and the “gluon recombination” is expected to occur. Obviously this annihilation of gluons leads to slower increase of the gluon density. This is the phenomenon called “gluon saturation.” This regime is governed by a non-linear evolution equation. The same thing can happen when we go down to lower transverse momentum scale with  $x$  being fixed. The transverse momentum scale  $Q_s(x)$  when the gluons are piled up on the transverse plane is called the *saturation scale*.

Study of the saturated gluons is very important for determining the initial condition of the heavy-ion collisions. To describe physics in the saturation regime, an effective theory was proposed based on the recognition that the matter can be in a new state, the “Color Glass Condensate.”<sup>1,2)</sup> Let us consider a hadron or a nucleus moving at the speed of light. We separate the degrees of freedom of this system into two: the large  $x$  and small  $x$  partons. The large- $x$  partons (valence particles) are treated as a color source  $\rho_a(x_\perp)$  which is *randomly* distributed on a two dimensional transverse plane. Its randomness is governed by a weight function  $W[\rho]$ . For example, in the very original formulation,<sup>1)</sup> it was taken to be Gaussian,

$$W[\rho] = \exp \left\{ -\frac{1}{2} \int d^2x_\perp \frac{\rho_a^2(x_\perp)}{\mu^2} \right\},$$

where  $\mu$  is the average value of the color charge. On the other hand, small  $x$  gluons are considered as classical fields originated from the color source. This is the basic picture of the Color Glass Condensate.

“Evolution equation” describes the change of this effective theory under the variation of the energy of the system. It turned out that within the leading  $\alpha_s \ln x$ , the change can be represented as the change of the weight function  $W[\rho]$ .

$$\frac{\partial W_\tau[\alpha]}{\partial \tau} = \int d^2x_\perp d^2y_\perp \frac{\delta}{\delta \alpha^a(x_\perp)} \left[ \chi_{x_\perp, y_\perp}^{ab}[\alpha] \frac{\delta W_\tau[\alpha]}{\delta \alpha^b(y_\perp)} \right],$$

where  $\tau = \ln 1/x$ ,  $\alpha$  is a gluon field and  $\chi_{x_\perp, y_\perp}^{ab}$  is a complicated function of  $\alpha$ . Since the gluon field is

determined by the source  $\rho$ , the argument of  $W$  has been changed into  $\alpha$ . This is the renormalization group equation which describes the quantum evolution of the Color Glass Condensate.

In order to know how the system evolves as we go to higher energy, we have to solve this non-linear, functional differential equation. With the complicated  $\chi[\alpha]$ , we are forced to perform approximations which make the structure simple.<sup>3,4)</sup> We tried two approximations. One is the mean field approximation (MFA) in which we replace  $\chi[\alpha]$  by its “expectation value”

$$\chi[\alpha] \rightarrow \chi^{\text{MFA}} = \langle \chi[\alpha] \rangle_\tau \equiv \int \mathcal{D}\alpha \chi[\alpha] W_\tau[\alpha],$$

and the other is the random phase approximation (RPA) where we ignore the  $\alpha$  dependence of  $\chi$  (which is a function of Wilson lines of  $\alpha$ ). In both cases, the weight function becomes Gaussian. Once we determine it, we can compute the evolution of any physical quantity  $O[\alpha]$  such as the gluon density ( $O[\alpha] = F_a^{+i} F_a^{+i}$ )

$$\frac{\partial}{\partial \tau} \langle O[\alpha] \rangle_\tau = \chi^{\text{MFA, RPA}} \left\langle \frac{\delta^2 O[\alpha]}{\delta \alpha^2} \right\rangle_\tau.$$

MFA leads to a non-linear evolution equation for the gluon density, which reproduces the linear DLA equation at high transverse momentum. Therefore, MFA is expected to work well at high transverse momentum. In this region, the gluon number density is proportional to  $1/k_\perp^2$ . By considering the case when non-linear effects becomes non-negligible, we can define the saturation scale  $Q_s^2(\tau) = e^{c\bar{\alpha}_s\tau}$  with  $c$  being a constant and  $\bar{\alpha}_s = \alpha_s N_c / \pi$ . On the other hand, RPA works well at low transverse momentum where non-linear effect in the evolution equation is really important. We found that the gluon number density is proportional to  $\alpha_s^{-1} \ln Q_s^2(\tau) / k_\perp^2$ . This implies that as a result of the non-linear evolution, the increase of gluon density becomes slower in low momentum than in high momentum. Therefore, we have shown that the Color Glass Condensate really derives the gluon saturation at lower transverse momentum less than the saturation scale, where the transverse size of the gluon is large and gluons overlap with each other.

### References

- 1) L. McLerran and R. Venugopalan: Phys. Rev. D **49**, 2233 (1994); Phys. Rev. D **49**, 3352 (1994); Phys. Rev. D **50**, 2225 (1994).
- 2) E. Iancu, A. Leonidov, and L. McLerran: Nucl. Phys. A **692**, 583 (2001); E. Ferreiro, E. Iancu, A. Leonidov, and L. McLerran: hep-ph/0109115.
- 3) E. Iancu and L. McLerran: Phys. Lett. B **510**, 145 (2001).
- 4) E. Iancu, K. Itakura, and L. McLerran: in preparation.

<sup>\*1</sup> Service de Physique Théorique, CE Saclay, France

<sup>\*2</sup> Brookhaven National Laboratory, USA

# Structural change of Cooper pairs in color superconductivity

H. Abuki,\* T. Hatsuda,\* and K. Itakura

Because of the asymptotic freedom and the Debye screening in QCD, deconfined quark matter is expected to be realized at very high density. This state is not a usual Fermi liquid but a superconducting state due to the presence of attractive quark-quark interaction. Many studies have been done so far on this “color superconductivity” and we have observed that QCD phase diagram has richer structure than the naive phase structure with a single quark-hadron transition. Our knowledge about the color superconductivity is divided into two different approaches. One is the QCD-based analysis that works well at very high density, and the other is somewhat phenomenological description for lower densities based on effective theories with four Fermi interactions. It has not been clear how the weak-coupling QCD description at very high density changes into the effective description at lower density.

We have studied the two-flavor color superconductivity with an emphasis on the *spatial*-momentum dependence of the gap and on the *spatial*-structure of Cooper pairs.<sup>1)</sup> The gap function has the following structure  $\langle qq \rangle = (\lambda_2 \tau_2)(C i \gamma_5) \Delta$  where  $C$  is the charge conjugation,  $\tau_2$  is the Pauli matrix in the flavor space,  $\lambda_2$  is an anti-symmetric Gell-Mann matrix. Our model includes (i) medium effects of the gluon propagators (Landau damping and Debye screening), (ii) momentum-dependent vertex, and (iii) antiquark-pole contribution. The property (iii) is introduced so that we can go to lower densities, otherwise the coupling constant blows up at low momentum scale, which invalidates the calculation. Our model derives the perturbative QCD gap equation at very high density, while it reproduces the chiral symmetry breaking at lower density. Therefore, our model can be applied to a very wide region of the density.

By solving the non-linear equation for the gap function numerically, we found the following results. The gap at extremely high density has a sharp peak near the Fermi surface due to the weak-coupling nature of QCD. This is consistent with the usual BCS picture in metals. On the other hand, the gap is a smooth function of the momentum at lower densities due to strong color magnetic and electric interactions. Density dependence of the gap function is shown in Fig. 1. The structural change of Cooper pairs can be seen in quantities such as quark correlations in the color superconductor. Especially, we have found that the size of the Cooper pair becomes comparable to the averaged inter-quark distance at low densities, while the ratio

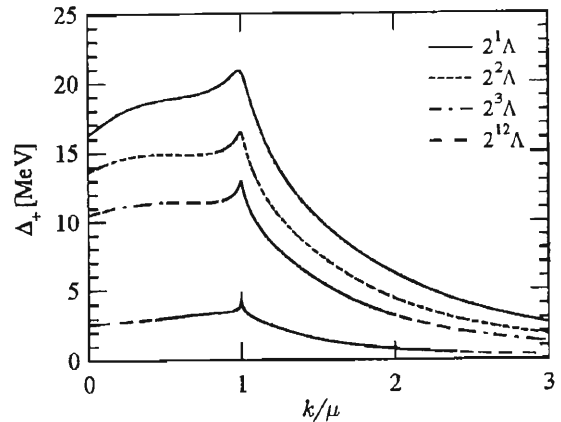


Fig. 1.  $\Delta_+(k)$  as a function of momentum (in unit of the Fermi momentum  $k_F = \mu$ ) at various densities  $\mu = 2^n \Lambda$  with  $n = 1, 2, 3, 12$  and  $\Lambda = 400$  MeV.

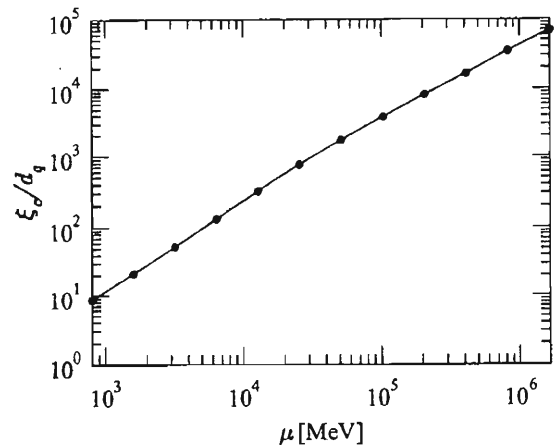


Fig. 2. Ratio of the Cooper pair size  $\xi_c$  and the average inter quark distance  $d_q$  as a function of the chemical potential  $\mu$ .

is very large at high density (Fig. 2). These features are highly contrasted to the standard BCS superconductivity in metals. They rather suggest that quark matter at lower density could be a “strong coupling” superconductivity where Bose-Einstein condensate will be a more suitable description.

## References

- 1) H. Abuki, T. Hatsuda, and K. Itakura: hep-ph/0109013; Phys. Rev. D, to be published.

\* Department of Physics, University of Tokyo

# Light Goldstone boson and domain walls in the $K^0$ -condensed phase of high density quark matter

D. T. Son\*

Recently, many authors<sup>1-3)</sup> emphasize the likelihood of kaon condensation in matter at high baryon densities. The crucial observation is that kaons have small masses<sup>4)</sup> in the color-flavor locked phase (CFL)<sup>5)</sup> of high-density QCD. A relatively small strangeness chemical potential is thus sufficient to drive kaon condensation. Moreover, it was argued that the mass of the strange quark also works in favor of kaon condensation.<sup>2)</sup>

In contrast to the conventional charged kaon condensation in nuclear matter,<sup>6)</sup> in the CFL phase it is the neutral kaons which are more likely to condense. This is due to the inverse mass ordering<sup>4)</sup> of mesons in the CFL phase, which makes the neutral kaons lighter than the charged kaons, at least at very high densities. The fact that neutral kaons rather than charged kaons condense might have important astrophysical consequences, since it implies that the kaon-condensed phase does not require electrons to be electrically neutral, which is one of the properties of the pure CFL phase without kaon condensation.<sup>7)</sup>

In a recent paper<sup>8)</sup> we show that the  $K^0$ -condensed phase possesses another distinct feature: it has in its spectrum an extremely light bosonic particle, whose presence implies the existence of non-topological metastable domain walls.

This feature can be understood easily from symmetry arguments. Like most Bose-Einstein condensates, the  $K^0$  condensate spontaneously breaks a global  $U(1)$  symmetry: the strangeness. From Goldstone's theorem, one expects a Goldstone boson to appear in the spectrum. This boson is the  $U(1)_S$  phase of the condensate, which will be denoted as  $\varphi$ . It might appear that the  $K^0$ -condensed phase is a two-component superfluid, the dynamics of which is determined by two  $U(1)$  phases.

A closer examination reveals that the particle arising from the  $U(1)_S$  breaking is in fact only a *pseudo*-Goldstone boson. Although strangeness is an exact symmetry of QCD, it is violated by weak processes, hence the would-be Goldstone boson acquires a mass. Since symmetry breaking is due entirely to weak interactions, the mass must be a small value proportional to  $G_F^{1/2}$ .

The existence of a light Goldstone boson in the spectrum leads to the appearance of metastable domain walls. Indeed, at very low energies, the effective Lagrangian for  $\varphi$  must have the form

$$L = \frac{f^2}{2} [(\partial_0\varphi)^2 - u^2(\partial_i\varphi)^2] - V(\varphi), \quad (1)$$

where  $f$  is the decay constant of the boson (which of order  $\mu$ ),  $u$  is its velocity, and  $V(\varphi)$  comes entirely from the explicit violation of strangeness by weak interactions. Due to the nature of  $\varphi$  as a phase variable,  $V(\varphi)$  is required to be a periodic function of  $\varphi$ . Moreover, to leading order in  $G_F$ ,  $V(\varphi) \sim \cos\varphi$ . The simplest way to see that is to express the superfluid ground state with a definite value of  $\varphi$  as a superposition of states with definite values of strangeness,

$$|\varphi\rangle = \sum_S e^{iS\varphi} |S\rangle. \quad (2)$$

To leading order in perturbation theory, the energy shift of the state  $|\varphi\rangle$  caused by an interaction Hamiltonian  $H_{\text{int}}$  is  $\langle\varphi|H_{\text{int}}|\varphi\rangle$ . To order  $G_F$ , the effective Hamiltonian of weak interactions has only  $\Delta B = 1$  matrix elements, so  $V(\varphi)$  is proportional to  $\cos\varphi$ . The Lagrangian (1) is that of the sine-Gordon theory, which possesses domain wall solutions interpolating between  $\varphi = 0$  and  $\varphi = 2\pi$ .

If baryon number is violated, the superfluid Goldstone mode also acquires a mass. Since the superfluid order parameter is a dibaryon, the mass square of the superfluid Goldstone boson is proportional to the amplitudes of the  $\Delta B = 2$  transitions, but not the  $\Delta B = 1$  ones. Using the experimental bound on  $n\bar{n}$  oscillations,  $\tau_{n\leftrightarrow\bar{n}} > 10^8$  s, we find  $m < 10^{-7}$  eV. The thickness of the corresponding domain wall is larger than about 1 m, and still might be less than the radius of neutron stars. However, unless the neutron star under consideration rotates very slowly, a domain wall that thick is unlikely to exist because of the high density of vortices, which are separated by distances of order  $10^{-2}$  cm.

## References

- 1) T. Schäfer: Phys. Rev. Lett. **85**, 5531 (2000).
- 2) P. F. Bedaque and T. Schäfer: hep-ph/0105150.
- 3) D. B. Kaplan and S. Reddy: hep-ph/0107265.
- 4) D. T. Son and M. A. Stephanov: Phys. Rev. D **61**, 074012 (2000); Phys. Rev. D **62**, 059902(E) (2000).
- 5) D. B. Kaplan and A. E. Nelson: Phys. Lett. B **175**, 57 (1986).
- 6) K. Rajagopal and F. Wilczek: Phys. Rev. Lett. **86**, 3492 (2001).
- 7) K. Rajagopal and F. Wilczek: Phys. Rev. Lett. **86**, 3492 (2001).
- 8) D. T. Son: hep-ph/0108260.

\* Columbia University, USA

# Non-perturbative renormalization of pion exchange<sup>†</sup>

U. van Kolck\*

For the last few years Effective Field Theory (EFT) has emerged as a useful framework in which to describe few-nucleon dynamics consistently with QCD. The most general Lagrangian involving low-energy degrees of freedom (such as low-momentum nucleons) and the symmetries of QCD (in particular, chiral symmetry) is constructed, and interactions are ordered according to an expansion in powers of momenta.

A critical issue has been<sup>1)</sup> the power counting of pion interactions in the EFT for momenta  $Q \sim m_\pi \ll M_{QCD} \sim m_\rho$ . Naive dimensional analysis suggests that one-pion exchange should be iterated to all orders in the nuclear amplitudes together with two momentum-independent contact interactions. However, arguments from perturbation theory apparently indicate that this procedure introduces spurious cutoff dependence, which could be avoided only by treating pion interactions as perturbative corrections to short-range effects. On the other hand, it has been recently discovered that the renormalization of a non-perturbative problem can be dramatically different from the renormalization of its perturbative series.<sup>2)</sup>

In the chiral limit ( $m_\pi \rightarrow 0$ ), the relevant interaction is the  $1/r^3$  tensor potential, so the problem boils down to the old, unresolved issue of the renormalization of

singular potentials. Using EFT techniques, we have recently shown that a central  $1/r^n$  potential can indeed be renormalized by a short-range interaction containing a single parameter.<sup>3)</sup> The extension to the relevant case of pion interactions in the  $^1S_0$  and  $^3S_1$ - $^3D_1$  two-nucleon channels has also been carried out.<sup>4)</sup> We were able to show that the two momentum-independent contact parameters can be varied in such a way that the remaining cutoff dependence can be taken care of by smaller, higher-order operators. Away from the chiral limit, we confirmed perturbative results that implied that explicit chiral-symmetry-breaking terms should, and can, be treated in perturbation theory.<sup>4)</sup> Other channels are currently under investigation.

## References

- 1) U. van Kolck: Proc. 3rd Int. Conf. on Perspectives in Hadronic Physics, Nucl. Phys. A, to be published.
- 2) P. F. Bedaque, H. W. Hammer, and U. van Kolck: Nucl. Phys. A **646**, 444 (1999).
- 3) S. R. Beane, P. F. Bedaque, L. Childress, A. Kryjevski, J. McGuire, and U. van Kolck: Phys. Rev. A **64**, 042103 (2001).
- 4) S. R. Beane, P. F. Bedaque, M. J. Savage, and U. van Kolck: Nucl. Phys. A **700**, 377 (2002).

---

<sup>†</sup> This research was supported in part by a DOE OJI Award.

\* University of Arizona, USA

# The flow of colored glass in heavy ion collisions

R. Venugopalan\*

At high energies, parton densities in nuclei saturate at a value  $n \sim 1/\alpha_S(\Lambda_s) \gg 1$ , where  $\Lambda_s (\gg \Lambda_{QCD})$  is the saturation scale.<sup>1)</sup> Matter in this state, in a manner analogous to a spin glass, forms a Color Glass Condensate<sup>2)</sup> (CGC). In a heavy ion collision, the CGC melts producing a large number of partons. Since the occupation number of partons is large, classical methods can be used to study the initial conditions for particle production in heavy ion collisions.<sup>3)</sup> Krasnitz and I have developed non-perturbative numerical (lattice) techniques to study the real time gluodynamics of matter produced in heavy ion collisions.<sup>4)</sup> Our results depend on two external parameters; these are the saturation scale  $\Lambda_s$  and the radius  $R$  of the nucleus. All dimensionful quantities can therefore be expressed in terms of appropriate powers of the saturation scale times a non-perturbative function of the dimensionless product  $\Lambda_s R$ .

We have applied these non-perturbative techniques to compute several quantities of interest in heavy ion collisions. These include the energy and number distributions of produced gluons,<sup>5)</sup> the topological charge generated by fluctuations<sup>6)</sup> and the momentum anisotropy (usually characterized by the elliptic flow parameter  $v_2$ ) generated in non-central collisions.<sup>7)</sup> These results were made possible by a couple of important technical developments in the last year. The first of these was the extension of the SU(2) gauge theory results to the physical SU(3) case.<sup>5)</sup> The second was the replacement of the periodic boundary conditions used previously with open boundary conditions.<sup>7)</sup> The latter is essential in computing elliptic and radial flow. Both of these technical improvements were accomplished in collaboration with Yasushi Nara of the RIKEN-BNL Research Center.

We now describe our results.

- We find that gluon number distributions can be fit by the form  $1/\pi R^2 dN/d\eta/d^2k_t = f_n(k_t/\Lambda_s)/g^2$ . For  $k_t/\Lambda_s < 3$ , we find that the form is  $f_n = a_1[\exp(\sqrt{k_t^2 + m^2}/T_{eff}) - 1]^{-1}$ , namely, a massive Bose-Einstein distribution in two dimensions. For  $k_t/\Lambda_s > 3$ ,  $f_n = a_2\Lambda_s^4/k_t^4 \ln(4\pi k_t/\Lambda_s)$ , which is the result one expects from perturbative QCD. We have argued that this scaling of the number distributions (which manifests itself as  $m_t$  scaling for hadrons) is seen in the RHIC data.<sup>8)</sup>
- The Yang-Mills equations at high energies are boost invariant. Note that rapidity distributions in high energy collisions (including RHIC) are

known to be boost invariant. We have demonstrated that the boost invariance of the Yang-Mills equations forbids sphaleron transitions.<sup>6)</sup> Chern-Simons number and topological charge can be generated only by fluctuations. We have computed this contribution to the topological charge. It is small-one unit of topological charge for two units of rapidity at RHIC and one unit of topological charge per unit of rapidity at LHC.

- We have very recently computed the second Fourier component of the momentum anisotropy, the elliptic flow parameter  $v_2$  and studied its dependence on impact parameter as well as its momentum dependence  $v_2(p_t)$ . Our conclusion is that elliptic flow is generated very early in the collision and that a significant contribution to this flow is from edge effects. At late times, the sum of the two transverse components of the pressure equals the energy density confirming that the system has achieved free streaming.<sup>7)</sup>

A systematic study of the RHIC data within the model is still lacking. For instance, it would be very interesting to study two particle (Hanbury-Brown Twiss) correlations since the RHIC data on these disagree with most models. Further technical improvements such as fully three dimensional simulations are also feasible. An interesting problem to investigate further is the matching of the classical field computations to transport theory in the late stages of the collision.

## References

- 1) L. V. Gribov, E. M. Levin, and M. G. Ryskin: Phys. Rep. **100**, 1 (1983).
- 2) L. D. McLerran and R. Venugopalan: Phys. Rev. D **49**, 2233 (1994); E. Iancu, A. Leonidov, and L. D. McLerran; Phys. Lett. B **510**, 133 (2001).
- 3) A. Kovner, L. D. McLerran, and H. Weigert: Phys. Rev. D **52**, 6231 (1995); Phys. Rev. D **52**, 3809 (1995).
- 4) A. Krasnitz and R. Venugopalan: Phys. Rev. Lett. **86**, 1717 (2001); Phys. Rev. Lett. **84**, 4309 (2000); Nucl. Phys. B **557**, 237 (1999).
- 5) A. Krasnitz, Y. Nara, and R. Venugopalan: Phys. Rev. Lett. **87**, 192302 (2001).
- 6) D. Kharzeev, A. Krasnitz, and R. Venugopalan: arXiv:hep-ph/0109253; submitted to Phys. Lett. B.
- 7) A. Krasnitz, Y. Nara, and R. Venugopalan: to be submitted to Phys. Rev. Lett.
- 8) J. Schaffner-Bielich, D. Kharzeev, L. D. McLerran, and R. Venugopalan: arXiv:nucl-th/0108048; submitted to Phys. Lett. B.

\* Brookhaven National Laboratory, USA

## Soft gluon dynamics at non-zero baryon density

D. Bödeker and M. Laine\*

The properties of QCD at a finite temperature  $T$  and chemical potential  $\mu$  play an important role for the physics of the early universe, heavy ion collision experiments, and neutron stars. Despite the presence of a potentially large scale, say  $T \gg \Lambda_{\text{QCD}}$ , QCD however remains sensitive to non-perturbative infrared physics. Various effective theories may be derived in perturbation theory, but the rich phenomena encoded in them may have to be addressed non-perturbatively.

Quite generically, effective theories tend to possess extra symmetries, only broken by higher dimensional operators. A familiar example is weak interaction induced strangeness violation in zero temperature QCD.

Similar phenomena take place also in high temperature physics. For instance, the dimensionally reduced effective field theory describing the thermodynamics of the electroweak sector of the Standard Model has extra symmetries: parity (P) and charge conjugation (C) are only broken by higher dimensional operators.<sup>1)</sup>

In QCD, perturbative interactions break neither P nor C, but the latter can be broken by the thermal ensemble, if there is a finite baryon density ( $\mu \neq 0$ ). Indeed, in the dimensionally reduced effective field theory for the thermodynamics of QCD, there is again a new C-odd operator, of higher order than the leading C even operator.<sup>2)</sup>

Here we will discuss the same phenomenon for dynamical quantities, that is in real time. We show that a purely gluonic C-odd operator is induced by quark loops. Thus C-odd observables may be directly sensitive to non-perturbative bosonic dynamics.

The environment in which we may envisage our results to have significance is mainly that of heavy ion collision experiments. Precision studies of dimensional reduction show that effective theories of the type considered may be quantitatively accurate down to  $T \sim 2T_c$ . At the same time, the infrared dynamics described by the effective theories is completely non-perturbative at any reasonable temperature. Direct four-dimensional (4d) lattice simulations are not available either for real time quantities (for a review, see Ref. 3). Thus effective theories appear presently to be the only way of studying quantitatively some interesting non-perturbative processes for phenomenologically relevant temperatures.

We have calculated the 1-loop contribution of hard ( $p \sim T$ ) quarks to the effective action for soft gluons to all orders in the gluon field and to first subleading order in the high temperature expansion,<sup>4)</sup>

$$\Gamma_{\text{C-odd}} = -\frac{1}{2\pi^2} g^3 \mu N_f \int d^4x \int_{\mathbf{v}}$$

$$\text{Tr} \left( \frac{1}{v \cdot D} v^\alpha F_{\alpha\mu} \right) \left( \frac{1}{v \cdot D} v^\beta F_{\beta\mu} \right) \left( \frac{1}{v \cdot D} D^\sigma \frac{1}{v \cdot D} v^\gamma F_{\gamma\sigma} \right). \quad (1)$$

Here  $F_{\mu\nu} = F_{\mu\nu}^a T^a$  is the gluon field strength tensor,  $D_\mu$  is the covariant derivative, and  $v^\mu = (1, \mathbf{v})$ . The integral is over the orientations of the unit vector  $\mathbf{v}$  which represents the 3-velocity of hard quarks.

Now consider the kinetic equations

$$v \cdot \partial \bar{f} = g v^\mu F_{\mu i}^a \frac{\partial f^a}{\partial p^i},$$

$$(v \cdot D)^{ab} f^b = \frac{g}{2} g^{abc} v^\mu F_{\mu i}^b \frac{\partial f^c}{\partial p^i} + \frac{g}{2N} v^\mu F_{\mu i}^a \frac{\partial \bar{f}}{\partial p^i}. \quad (2)$$

These are solved in expansion in  $|\mathbf{k}|/T$  where  $\mathbf{k}$  is a typical wave vector of the gauge fields. At lowest order  $\bar{f}(p) = N n_{\text{Fermi}}(p \pm \mu)$  for quarks and antiquarks, respectively. Then the equation  $j = \delta\Gamma/\delta A$  is integrated for the current

$$j_\mu^a = -\sum_i g_i \int \frac{d^3p}{(2\pi)^3} v_\mu f^{a(i)}, \quad (3)$$

where the sum runs over all quark species  $i$ . At first non-trivial order one obtains the well known hard thermal loop effective action. We found that at the next order  $\Gamma$  is indeed equal to  $\Gamma_{\text{C-odd}}$  in Eq. (1). This opens the possibility to use Eq. (2) for simulating the soft gauge field dynamics to account for C-odd effects (for lattice simulations of the hard thermal loop effective theory see Ref. 5).

As a further check that Eq. (2) reproduces the physics of the soft gauge fields we have considered the static field limit of Eq. (1). This is non-trivial considering the non-local nature of  $\Gamma_{\text{C-odd}}$ . One finds

$$(S_{\text{C-odd}})_{\text{static}} = -\mu \frac{g^3 N_f}{3\pi^2} \text{Tr} A_0^3. \quad (4)$$

This is precisely the leading C-odd contribution in dimensionally reduced action.<sup>2)</sup> A word of caution is in order, however. Very recently it was found that at the next order in the high temperature expansion Eq. (2) does not give the correct static limit.<sup>6)</sup>

### References

- 1) K. Kajantie, M. Laine, K. Rummukainen, and M. Shaposhnikov: Phys. Lett. B **423**, 137 (1998).
- 2) A. Hart, M. Laine, and O. Philipsen: Nucl. Phys. B **586**, 443 (2000).
- 3) D. Bödeker: Nucl. Phys. B (Proc. Suppl.) **94**, 61 (2001).
- 4) D. Bödeker and M. Laine: J. High Energy Phys. **0109**, 029 (2001).
- 5) D. Bödeker, G. D. Moore, and K. Rummukainen: Phys. Rev. D **61**, 056003 (2000).
- 6) M. Laine and C. Manuel: arXiv:hep-ph/0111113.

\* CERN Theory Division, Switzerland

# Neutrino cross sections and future observations of ultrahigh-energy cosmic rays

A. Kusenko\*

Detection of ultrahigh-energy (UHE) neutrinos is one of the important challenges of the next generation of cosmic ray detectors. Their discovery will mark the advent of UHE neutrino astronomy, allowing the mapping on the sky of the most energetic, and most distant, sources in the Universe. In addition, detection of UHE neutrinos may help resolve the puzzle of cosmic rays with energies beyond the Greisen-Zatsepin-Kuzmin cutoff<sup>1)</sup> by validating Z-bursts,<sup>2)</sup> topological defects,<sup>3)</sup> superheavy relic particles,<sup>4)</sup> *etc.*

Several approved and proposed experiments have adopted a strategy for detection of UHE neutrinos by observation of the nearly horizontal air showers (HAS) in the Earth's atmosphere resulting from  $\nu$ -air interactions. The expected rates are proportional to the neutrino cross section. Calculations of this cross section at  $10^{20}$  eV necessarily use an extrapolation of parton distribution functions and Standard Model (SM) parameters far beyond the reach of experimental data. The uncertainty in the cross section allows for smaller values of the neutrino-nucleon cross section. The corresponding rates of HAS are proportional to this cross section and may also be lower. Hence, a lower value of the cross section could compromise the main detection signal that has been proposed for UHE neutrino experiments.

It was shown, however, that regardless of possible theoretical uncertainties in the cross section, the future experiments can observe the UHE neutrinos if they adopt a new strategy.<sup>5)</sup> In fact, a smaller cross section, for which the rate of HAS is low, would offer a double advantage for the planned experiments because, in addition to doing neutrino astronomy, future detectors can also measure the neutrino cross section at energies far beyond those achievable in collider experiments. This study was motivated in part by a recent analysis of upward events by Feng *et al.*<sup>6)</sup>

In addition to HAS, proposed cosmic ray experiments can also observe up-going charged muon and tau leptons (UCL) produced by neutrinos interacting just below the surface of the Earth, and the up-going air showers (UAS) initiated by these leptons. A smaller value of this cross section reduces the shadowing of UHE neutrinos by the Earth. Therefore, the neutrino angles with respect to horizon need not be so "skimming." More importantly, the expected rate of UCLs and UASs may (1) be larger, and (2) depend on the cross section.

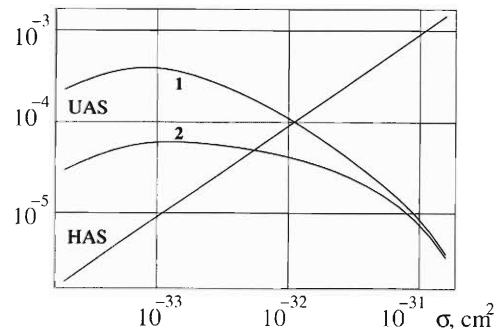


Fig. 1. The air shower probability per incident tau neutrino as a function of the neutrino cross section. The energy threshold for detection of UAS was assumed  $E_{th} = 10^{18}$  eV for curve 1 and  $10^{19}$  eV for curve 2.

The relative rates of horizontal and up-going events are shown in Fig. 1.

In addition, the neutrino cross section may be determinable from the angular distribution of UCL events alone, independent of the neutrino flux. One expects the angular distribution of UCL to peak near  $\cos\theta_{peak} \sim \lambda_\nu/2R_\oplus$ , where  $\lambda_\nu$  is the mean free path of neutrino in the Earth. This implies  $\sigma_{\nu N} \sim (2\langle\rho\rangle R_\oplus \cos\theta_{peak})^{-1}$ .

## References

- 1) K. Greisen: Phys. Rev. Lett. **16**, 748 (1966); G. T. Zatsepin and V. A. Kuzmin: Pisma Zh. Eksp. Teor. Fiz. **4**, 114 (1966).
- 2) T. Weiler: Phys. Rev. Lett. **49**, 234 (1982); Astropart. Phys. **11**, 303 (1999).
- 3) For reviews, see, e.g., A. Vilenkin and E. P. S. Shellard: *Cosmic Strings and Other Topological Defects* (Cambridge University Press, Cambridge, 1994); M. B. Hindmarsh and T. W. B. Kibble: Rep. Prog. Phys. **58**, 477 (1995); V. A. Kuzmin and I. I. Tkachev: Phys. Rept. **320**, 199 (1999).
- 4) V. Berezhinsky, M. Kachelriess, and A. Vilenkin: Phys. Rev. Lett. **79**, 4302 (1997); V. A. Kuzmin and V. A. Rubakov: Phys. Atom. Nucl. **61**, 1028 (1998); M. Birkel and S. Sarkar: Astropart. Phys. **9**, 297 (1998); P. Blasi: Phys. Rev. D **60**, 023514 (1999); S. Sarkar: hep-ph/0005256.
- 5) A. Kusenko and T. Weiler: arXiv:hep-ph/0106071.
- 6) J. L. Feng, P. Fisher, F. Wilczek, and T. M. Yu: arXiv:hep-ph/0105067.

\* Department of Physics and Astronomy, University of California, Los Angeles, USA

## Scaling relations for the transverse mass spectra and the color glass condensate

J. Schaffner-Bielich,<sup>\*1</sup> D. Kharzeev,<sup>\*2</sup> L. McLerran,<sup>\*2</sup> and R. Venugopalan<sup>\*2</sup>

In recent works,<sup>1,2)</sup> we demonstrated that the transverse mass distribution of produced hadrons as recently measured at the Relativistic Heavy-Ion Collider (RHIC)<sup>3)</sup> can be described by generalized scaling relations. These relations are motivated from scaling properties of the color glass condensate, the initial saturated gluon state which scales as<sup>4)</sup>

$$\frac{1}{\sigma} \frac{dN_g}{d\eta d^2p_t} = \frac{1}{\alpha_s(Q_s^2)} f_g \left( \frac{p_t^2}{Q_s^2} \right). \quad (1)$$

Here,  $f_g$  is a universal, dimensionless function for the produced gluons which depends only on the ratio of the transverse momentum  $p_t$  and the saturation momentum  $Q_s$ . Different energies or scales are described by the same function with a correspondingly changed saturation momentum. This picture has been successfully applied for the charged multiplicity data at RHIC.<sup>5)</sup>

Therefore, we argue that a corresponding relation of the form

$$\frac{1}{\sigma} \frac{dN_h}{dy d^2m_t} = \frac{1}{\alpha_s(p_s)} \kappa_h \cdot f \left( \frac{m_t}{p_s} \right), \quad (2)$$

holds for the recently measured transverse mass spectra at RHIC. Here, the function  $f$  stands for an universal, dimensionless function. The parameters are  $\sigma$  for the transverse area, and  $p_s$  for the hadronic saturation momentum which are changing according to centrality, system size and bombarding energy. The saturation momentum  $p_s$  should follow the same dependence as one expects for the corresponding saturation momentum for gluons,  $Q_s$ .

The predictions of the above relation are twofold: first, it predicts that the transverse mass spectra can be described by one universal function which depends only on the transverse mass  $m_t$  and the saturation momentum  $p_s$ . Corrections to that behavior are due to the parameter  $\kappa_h$  which controls the particle abundance for high  $p_t$  and is of order one. Indeed, we have checked that this generalized scaling works for describing the recent preliminary data from RHIC<sup>2)</sup> (see Fig. 1). Second, the relation predicts that the transverse mass spectra for different centralities can be rescaled into one universal curve by properly readjusting the transverse area and the saturation momentum  $p_s$ . Also this remarkable feature was confirmed by us using the recent preliminary data from RHIC<sup>2)</sup> (see Fig. 2).

We extracted the parameters  $\sigma/\alpha_s$  and  $p_s$  from the data as a function of centrality. It turns out that

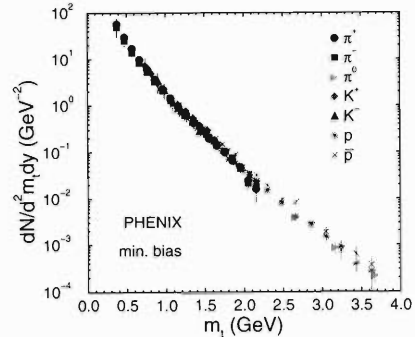


Fig. 1. Minimum bias data rescaled as a function of transverse mass (preliminary data taken from PHENIX collaboration<sup>3)</sup>).

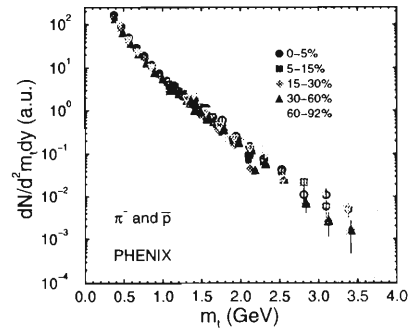


Fig. 2. Spectra for different centralities rescaled as a function of transverse mass (preliminary data taken from PHENIX collaboration<sup>3)</sup>).

both parameters are changing as expected,  $\sigma/\alpha_s(p_s) \sim N_{\text{part}}^{2/3} \ln p_s/\mu$  and  $p_s^2 \sim c + c' \cdot N_{\text{part}}^{1/3}$ . For comparison, the saturation momentum for gluons is expected to change as  $Q_s^2 \sim N_{\text{part}}^{1/3}$ . The additional constant  $c$  in the centrality dependence of  $p_s$  stands for the finite mean transverse momentum as measured in  $pp$  and  $p\bar{p}$  collisions.

### References

- 1) L. McLerran and J. Schaffner-Bielich: Phys. Lett. B **514**, 29 (2001).
- 2) J. Schaffner-Bielich, D. Kharzeev, L. McLerran, and R. Venugopalan: nucl-th/0108048.
- 3) J. Velkovska, PHENIX Collaboration: nucl-ex/0105012; W. A. Zajc et al., PHENIX Collaboration: nucl-ex/0106001.
- 4) A. Krasnitz and R. Venugopalan: Phys. Rev. Lett. **86**, 1717 (2001); Phys. Rev. Lett. **84**, 4309 (2000).
- 5) D. Kharzeev and M. Nardi: Phys. Lett. B **507**, 121 (2001); D. Kharzeev and E. Levin: nucl-th/0108006.

<sup>\*1</sup> Columbia University, USA

<sup>\*2</sup> Brookhaven National Laboratory, USA

## Hadronic signals of QGP

S. Jeon\*

At temperatures exceeding  $\Lambda_{\text{QCD}}$ , the quarks and gluons bound inside hadrons are supposed to be freed and form a Quark-Gluon Plasma (QGP). This ‘new’ state of matter was in existence briefly in the very early universe, but few microseconds after big-bang, the temperature became low enough to bind them into ordinary hadrons we see today.

One of the expressed goals of the heavy ion collision experiments is to re-create this state of matter and study it. At the Relativistic Heavy Ion Collider, we are quite certain that the collision energy is high enough to produce such a state. The question is then, once created, how do we observe it? The answer is not simple because even though we create liberated quarks and gluons, ultimately what we observe in our detectors are the ordinary mesons and baryons. If a QGP was indeed created, it must leave foot-marks in the properties of the hadronic system created from the QGP. In this brief report, I report my research on answering this question, namely, how to see the QGP in the fluctuations of hadrons.

One of the distinguishing properties about quarks from hadrons is that the quarks carry fractional charges. This difference clearly shows up in the charge fluctuation per charged degree of freedom

$$\mathcal{D} = \frac{\langle \Delta Q^2 \rangle}{\langle N_{\text{ch}} \rangle}. \quad (1)$$

In a pion gas, the charge fluctuation simply equals the pion number fluctuation since the pions carry unit charges. If one assumes a thermal equilibrium, then the number fluctuation in turn is approximately the same as the average number. Hence in this case  $\mathcal{D} \approx 1$ . In a QGP, a  $u$  quark carries a charge of  $2/3$  and a  $d$  quark carries a charge of  $-1/3$ . Hence the charge fluctuation is  $(1/3)^2 + (2/3)^2 = 5/9$  of the quark number fluctuation. This alone would reduce the charge fluctuation by almost a factor of 2 compared to the pion case. Furthermore, the final state charged degree of freedom include contribution from the neutral gluons. Combining the two effects, we can conclude that if a QGP is formed, then the hadronic system arising from it should have  $\mathcal{D}_{\text{QGP}} = 1/3 - 1/4$  which is a factor of 3 to 4 smaller compared to that of the pion gas.<sup>1)</sup>

When the system created by a collision is small, such as the one created in a peripheral collision, the concept

of grand-canonical ensemble is not applicable. Rather, one should apply the concept of micro-canonical ensemble where the conserved quantities (except the energy and momentum) are fixed absolutely instead of on average. As the system size gets larger, this difference disappears. However, for small systems, the two ensembles give a markedly different results. In a paper written by V. Koch, K. Redlich, X.-N. Wang and the present author,<sup>2)</sup> we derived a master equation for production of particle pairs under a strict conservation law. An important result is that by measuring the second factorial moment of such pairs, for instance kaons, we can determine if the system started out with an over-population or under-population.

While V. Koch and the author advocated the charge fluctuation as the QGP signal, Scott Pratt has advocated the changes in the balance functions as the signal. Recently, Scott and the author joined forces and clarified the relationship between these two approaches.<sup>3)</sup> In terms of correlation functions, a charge balance function can be defined in the following way:

$$B(\Delta y|Y) = \frac{1}{2} \left\{ \frac{dn_+}{dy} C_{++}(\Delta y) + \frac{dn_-}{dy} C_{--}(\Delta y) - \left( \frac{dn_+}{dy} + \frac{dn_-}{dy} \right) C_{+-}(\Delta y) \right\}, \quad (2)$$

where  $C_{ij}$  is the correlation of the species  $i$  and  $j$  as a function of rapidity differences.  $Y$  is the size of the rapidity bin in which the balance function is being calculated. The relationship between the charge fluctuation and the balance function is simply

$$\frac{\langle \Delta Q^2 \rangle}{\langle N_{\text{ch}} \rangle} = 1 - \int_0^Y d\Delta y B(\Delta y|Y), \quad (3)$$

in the limit  $\langle N_{\text{ch}} \rangle \gg \langle Q \rangle$ . The information coded in the balance function is therefore more local whereas the charge fluctuation encodes more global information.

### References

- 1) S. Jeon and V. Koch: Phys. Rev. Lett. **85**, 2076 (2000).
- 2) S. Jeon, V. Koch, K. Redlich, and X. N. Wang: Nucl. Phys. A **697**, 546 (2002).
- 3) S. Jeon and S. Pratt: arXiv:hep-ph/0110043, to be published in Phys. Rev. C.

\* McGill University, USA

## Kaon condensation in QCD

T. Schäfer\*

Quark matter at very high baryon density is expected to behave as a color superconductor.<sup>1,2)</sup> Color superconductivity implies that the local gauge symmetry is broken by a Higgs mechanism. There is a gap in the fermion excitation spectrum and gauge fields are screened by the Meissner effect. In addition to that, color superconductivity can lead to the breakdown of global symmetries, such as the  $U(1)$  of baryon number or the  $SU(N_f)_L \times SU(N_f)_R$  chiral symmetry. The symmetry breaking pattern depends on the number of colors  $N_c$ , the number of flavors  $N_f$ , and the quark masses.

A particularly symmetric phase is the color-flavor-locked (CFL) phase of three flavor quark matter. This phase is believed to be the true ground state of strange quark matter at very large density. The CFL phase is characterized by the order parameter

$$\langle q_{L,i}^a C q_{L,j}^b \rangle = -\langle q_{R,i}^a C q_{R,j}^b \rangle = \phi (\delta_i^a \delta_j^b - \delta_i^b \delta_j^a).$$

In the CFL phase the chiral  $SU(3)_L \times SU(3)_R$  symmetry is broken to  $SU(3)_V$ , which is identical to the chiral symmetry breaking pattern of QCD at zero baryon density.

At baryon densities relevant to astrophysical objects distortions of the pure CFL state due to non-zero quark

masses cannot be neglected. We have studied this problem using the effective chiral theory of the CFL phase.<sup>3)</sup> The ground state and its low energy excitations can be described by a chiral field  $\Sigma = XY^\dagger$  which depends on the relative flavor direction of the left and right handed diquark condensates  $X$  and  $Y$ . If the quark masses are equal we find that the ground state corresponds to  $\Sigma = 1$ . However, if the strange quark mass  $m_s$  exceeds some critical value then it becomes energetically favorable to rotate  $\Sigma$  in the neutral or charged kaon direction. At very large baryon density the critical  $m_s$  can be computed in perturbative QCD. We find  $m_s|_{crit} = 3.03 \cdot m_d^{1/3} \Delta^{2/3}$ . This result suggests that for values of the strange quark mass and the gap that are relevant to compact stars CFL matter is likely to support a kaon condensate.

### References

- 1) D. Bailin and A. Love: Phys. Rep. **107**, 325 (1984).
- 2) R. Rapp, T. Schäfer, E. V. Shuryak, and M. Velkovsky: Phys. Rev. Lett. **81**, 53 (1998); M. Alford, K. Rajagopal, and F. Wilczek; Phys. Lett. B **422**, 247 (1998).
- 3) P. F. Bedaque and T. Schäfer: hep-ph/0105150.

---

\* Department of Physics, State University of New York, Stony Brook, USA

# Novel phenomena in high-density QCD

M. A. Stephanov\*

This paper is a summary of Refs. 1 and 2. The aim of this work is to understand the physics of QCD at large baryon density. This regime is of relevance primarily to the neutron star physics, but may also shed light on properties of high-density QCD relevant to heavy-ion collision experiments. Theoretically, the regime of very, asymptotically, large baryon chemical potential  $\mu$  is attractive because the asymptotic freedom of QCD allows controllable calculations.

In this work we describe the physics of the lowest excitations of the high density QCD. The number of light quark flavors  $N_f$  turns out to play a crucial role. The simplest case is  $N_f = 2$  where up and down quarks are massless and other quarks are neglected. This model is a rather good approximation to realistic quark matter at moderate densities, such as in the neutron star interiors. The ground state of this model at high baryon densities is the two-flavor color-superconducting (2SC) state, characterized by the condensation of diquark Cooper pairs. These pairs are antisymmetric in spin  $(\alpha, \beta)$ , flavor  $(i, j)$  and color  $(a, b)$  indices:

$$\begin{aligned} \langle q_{L\alpha}^{ia} q_{L\beta}^{jb} \rangle^* &= \epsilon_{\alpha\beta} \epsilon^{ij} \epsilon^{abc} X^c, \\ \langle q_{R\alpha}^{ia} q_{R\beta}^{jb} \rangle^* &= \epsilon_{\alpha\beta} \epsilon^{ij} \epsilon^{abc} Y^c. \end{aligned}$$

The condensates  $X^c$  and  $Y^c$  are complex color 3-vectors. In the ground state,  $X^c$  and  $Y^c$  are aligned along the same direction in the color space, and they break the color  $SU(3)_c$  group down to  $SU(2)_c$ . Thus, five of the original eight QCD gluons acquire “masses” by the Meissner effect, similar to the Higgs mechanism. The remaining three gluons are massless (perturbatively). Due to the pairing, the spectrum of quarks carrying  $SU(2)$  color charge has a gap  $\Delta$

$$\Delta = b\mu g^{-5} e^{-c/g(\mu)} \ll \mu, \quad c = 3\pi^2/\sqrt{2},$$

where  $g(\mu)$  is the gauge coupling at the scale  $\mu$ , and  $b$  is some numerical constant.

In order to understand the physics below the energy scale  $\Delta$  we must examine the pure gluodynamics in the remaining unbroken  $SU(2)$  sector. We find that the process of high-density “deconfinement” is quite nontrivial in this case: the quarks are *always* confined (assuming that  $SU(2)$  Yang-Mills theory confines), but, the confinement radius,  $R_c \equiv 1/\Lambda'_{\text{QCD}}$  grows *exponentially* with increasing density:

$$\Lambda'_{\text{QCD}} \sim \Delta e^{-2\pi/(\beta_0 \alpha'_s)} \sim \Delta \exp\left[-\frac{2\sqrt{2}\pi}{11} \frac{\mu}{g\Delta}\right].$$

We term this phenomenon *asymptotic deconfinement*.

We also find that, at scales much shorter than the confinement radius, the dynamics of the  $SU(2)$  gluons is similar to electrodynamics in a dielectric medium with a large refraction index

$$\epsilon = 1 + \frac{g^2 \mu^2}{18\pi^2 \Delta^2}.$$

This can be interpreted as a consequence of the fact that the Cooper pairs have large size (of order  $1/\Delta$ ) and so are easy to polarize.

In perturbation theory, there is a degeneracy of the ground state with respect to the relative  $U(1)$  phase between  $X^a$  and  $Y^a$ . This is due to the  $U(1)_A$  symmetry of the QCD Lagrangian at the classical level. The  $U(1)_A$  symmetry is spontaneously broken by the color-superconducting condensate. Since this is a global symmetry, its breaking gives rise to a Goldstone boson — pseudoscalar  $\eta$ . Due to the well-known anomalous breaking of the  $U(1)_A$  symmetry the  $\eta$  boson acquires a small mass, which is much smaller than  $\Delta$ .

$$m_\eta = 2\pi\sqrt{a}\Delta \ll \Delta,$$

where

$$a = 5 \times 10^4 \left( \ln \frac{\mu}{\Lambda_{\text{QCD}}} \right)^7 \left( \frac{\Lambda_{\text{QCD}}}{\mu} \right)^{29/3}.$$

The effective action for the  $\eta$  field admits a classical configuration corresponding to a domain wall with the width of the order of  $1/m_\eta$ . The tension of the domain wall is

$$\sigma = (4/\pi)\sqrt{a/3}\mu^2\Delta.$$

This wall is metastable. The decay proceeds through nucleation of a critical hole in the wall, similarly to the decay of a false vacuum. A more detailed and quantitative discussion of the wall’s decay can be found in Ref. 2. Here we note that the wall’s lifetime is exponentially large at large  $\mu$ .

Although we discussed 2-flavor QCD, a light pseudoscalar and domain walls also occur in QCD with 3 light flavors. These phenomena as well as asymptotic deconfinement are present in QCD at finite isospin density, a theory which can be studied by a lattice Monte Carlo simulation at any value of isospin chemical potential.

## References

- 1) D. H. Rischke, D. T. Son, and M. A. Stephanov: Phys. Rev. Lett. **87**, 062001 (2001).
- 2) D. T. Son, M. A. Stephanov, and A. R. Zhitnitsky: Phys. Rev. Lett. **86**, 3955 (2001).

\* University of Illinois at Chicago, USA

# Hydrodynamic analysis of elliptic flow at RHIC<sup>†</sup>

T. Hirano\*

Nucleus-nucleus collisions at the Relativistic Heavy Ion Collider (RHIC) give us an opportunity to study a new state of deconfined nuclear matter, the quark-gluon plasma (QGP). The main goals in the physics of relativistic heavy-ion collisions are not only the discovery of the QGP, but also the investigation of thermodynamical aspects of its new phase, *i.e.*, the equation of state (EOS), the order of phase transition between the QGP phase and the hadron phase, or the critical temperature. It is very important to check whether the thermalization of the nuclear matter produced at the very early stage of collisions is really achieved, before discussing the thermodynamics of the QGP. Elliptic flow in non-central collisions is suited for this purpose.<sup>1)</sup> If produced particles frequently rescatter with each other, we naively expect that thermalization of the system is achieved and that the large pressure is built in the reaction zone. The pressure produces the momentum anisotropy of observed particles from the spatial deformation in the transverse plane. The coefficients of second harmonics in the azimuthal distribution, not only its magnitude  $v_2$  but also its transverse momentum dependence  $v_2(p_t)$  and its centrality dependence  $v_2(b)$ , seem to be good indicators for thermalization of nuclear matter. Hydrodynamic simulations, in which full local thermalization is assumed, give us excellent agreement with the first result of  $v_2(p_t)$  from Au+Au 130 A GeV collisions at the RHIC up to  $p_t \sim 1.5$  GeV/ $c$  near midrapidity.<sup>2)</sup> Their results are based on a (2+1)-dimensional hydrodynamic model with the Bjorken's scaling solution. One cannot, however, discuss the rapidity dependence of observables by exploiting the Bjorken's model. Since this model is assumed to give a good description of space-time evolution of nuclear matter near the midrapidity region, the agreement between the model calculation and experimental data means that early thermalization at the RHIC is achieved at least only at midrapidity. We investigate how far from midrapidity thermalization in the early stage is achieved through comparison of the pseudorapidity dependence of elliptic flow from a genuine three-dimensional hydrodynamic model<sup>3)</sup> with

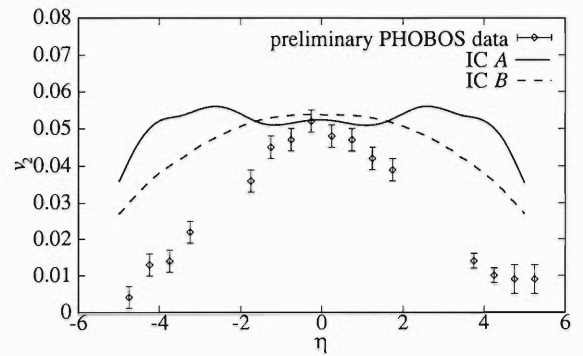


Fig. 1. Pseudorapidity dependence of elliptic flow  $v_2(\eta)$ .

experimental data recently measured by the PHOBOS Collaboration.<sup>4)</sup>

Figure 1 shows the pseudorapidity dependence of elliptic flow  $v_2(\eta)$  for charged particles. Preliminary experimental data is obtained by the PHOBOS Collaboration.<sup>4)</sup> Two lines correspond to two different parametrization for initial energy density which have already been so tuned as to reproduce single particle spectra of hadrons, such as pseudorapidity distribution and transverse momentum distribution in Au + Au 130 A GeV collisions.<sup>3)</sup> Although we reproduce the pseudorapidity distribution of charged particles in whole rapidity region, our results for  $v_2(\eta)$  are consistent with the experimental data only near mid(pseudo)rapidity. This suggests thermalization of the system produced in Au + Au collisions at RHIC is achieved only near midrapidity. On the other hand, only partial thermalization is achieved in forward and backward rapidity regions.

## References

- 1) J.-Y. Ollitrault: Phys. Rev. D **46**, 229 (1992).
- 2) P. F. Kolb, P. Huovinen, U. Heinz, and H. Heiselberg: Phys. Lett. B **500**, 232 (2001).
- 3) T. Hirano: Phys. Rev. C **65**, 011901 (2002).
- 4) PHOBOS Collaboration, I. Park et al.: Nucl. Phys. A **698**, 564 (2002).

<sup>†</sup> Condensed from the article in Phys. Rev. C **65**, 011901 (2002).

\* Physics Department, University of Tokyo

# Initial coherent gluon production from the color glass condensate in relativistic nuclear collisions

A. Krasnitz,<sup>\*1</sup> Y. Nara,<sup>\*2</sup> and R. Venugopalan<sup>\*2</sup>

The Relativistic Heavy Ion Collider (RHIC) is currently colliding beams of gold nuclei at the highest center of mass energies per nucleon,  $\sqrt{s_{NN}} = 200$  GeV. The goal of these experiments is to explore strongly interacting matter, in particular the quark gluon plasma (QGP) predicted by lattice QCD.

The possible formation and dynamics of the QGP depends crucially on the initial conditions, namely, the distribution of partons in each of the nuclei *before* the collision. At high energies and for large nuclei, parton distributions saturate and form a color glass condensate (CGC).<sup>1)</sup>

The early stages of a relativistic heavy-ion collision are examined in the framework of an effective classical Yang-Mills theory in the transverse plane. We compute the initial energy and number distributions, per unit rapidity, at mid-rapidity, of gluons produced in high energy heavy ion collisions.<sup>2-4)</sup> In the theory, the scale  $\Lambda_s$  and the size of the nucleus  $R$  are the only physically relevant dimensional parameters.<sup>2-4)</sup> In Fig. 1, we plot the normalized gluon transverse momentum distributions versus  $k_T/\Lambda_s$  with the value  $\Lambda_s R = 83.7$ , together with SU(2) result. Clearly, we see that the normalized result for SU(3) is suppressed relative to the SU(2) result in the low momentum region. At large transverse momentum, we see that the distributions scale exactly as  $N_c^2 - 1$ , the number of color degrees of freedom. This is as expected since at large trans-

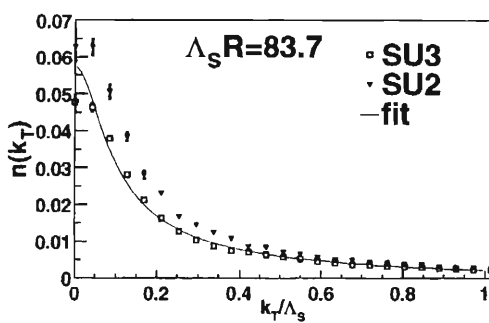


Fig. 1. Transverse momentum distribution of gluons per unit area, normalized to the color degrees of freedom,  $n(k_T) = dn/d^2k_t/(N_c^2 - 1)$  as a function of  $\Lambda_s R$  for SU(3) (squares) and SU(2) (diamonds). Solid lines correspond to the fit with the Bose-Einstein form.

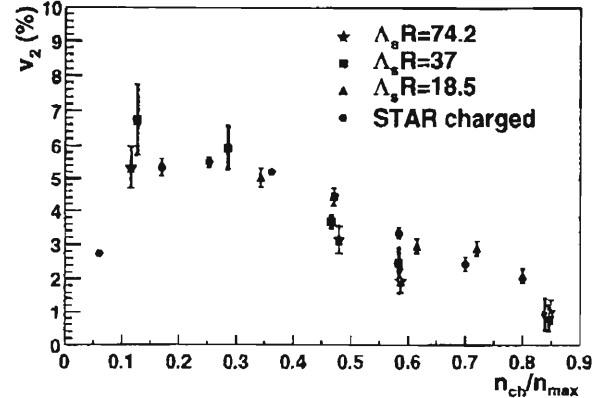


Fig. 2. Calculated results with  $\Lambda_s R = 74$  (diamonds), 37 (triangles), and 18.5 (squares) are compared to the STAR data<sup>6)</sup> (circles) on the centrality dependence of the elliptic flow parameter  $v_2$  defined by the second Fourier coefficient.

verse momentum, the modes are nearly those of non-interacting harmonic oscillators. At smaller momenta, the suppression is due to non-linearities, whose effects, we have confirmed, are greater for larger values of the effective coupling  $\Lambda_s R$ .

We calculate anisotropy in momentum space in Fig. 2 by solving classical SU(2) Yang-Mills equations of motion on the lattice. It is shown that initial gluons are produced with anisotropy in momentum space in the typical time scale  $\tau \sim 0.3$  fm/c.<sup>5)</sup> This anisotropy in the momentum flow originates from the spatial anisotropy of the strongly interacting gauge field in the almond-shape overlap region of a collision.

## References

- 1) L. McLerran and R. Venugopalan: Phys. Rev. D **49**, 2233 (1994); Phys. Rev. D **49**, 3352 (1994); Phys. Rev. D **50**, 2225 (1994).
- 2) A. Krasnitz and R. Venugopalan: Phys. Rev. Lett. **84**, 4309 (2000).
- 3) A. Krasnitz and R. Venugopalan: Phys. Rev. Lett. **86**, 1717 (2001).
- 4) A. Krasnitz, Y. Nara, and R. Venugopalan: Phys. Rev. Lett. **87**, 192302 (2001).
- 5) A. Krasnitz, Y. Nara, and R. Venugopalan: in preparation.
- 6) STAR Collaboration: Phys. Rev. Lett. **86**, 402 (2000).

<sup>\*1</sup> CENTRA and Faculdade de Ciências e Tecnologia, Universidade do Algarve, Campus de Gambelas, Portugal

<sup>\*2</sup> Physics Department, Brookhaven National Laboratory, USA

# Probing the QGP equation of state with two-particle interferometry

S. A. Bass,<sup>\*1</sup> S. Soff,<sup>\*1</sup> D. H. Hardtke,<sup>\*2</sup> and S. Y. Panitkin<sup>\*2</sup>

Bose-Einstein correlations in multiparticle production processes<sup>1)</sup> provide valuable information on the space-time dynamics of fundamental interactions.<sup>2)</sup> In particular, lattice QCD calculations predict the occurrence of a phase transition at high temperature. A first order phase transition leads to a prolonged hadronization time as compared to a cross-over or ideal hadron gas with no phase transition, and has been related to unusually large Hanbury-Brown-Twiss (HBT) radii.<sup>3)</sup> The phase of coexisting hadrons and QGP reduces the “explosivity” of the high-density matter before hadronization, extending the emission duration of pions.<sup>3)</sup> This phenomenon should then depend on the hadronization (critical) temperature  $T_c$  and the latent heat of the transition.

In our study, we have calculated the Gaussian radius parameters of the pion-emitting source in high energy heavy ion collisions,<sup>4)</sup> assuming a first order phase transition from a thermalized Quark-Gluon-Plasma (QGP) to a gas of hadrons. Our calculations have been performed in the framework of a hybrid macro/micro transport approach, utilizing hydrodynamics for the early, dense, QGP phase of the reaction and microscopic transport theory for the later, dilute, hadronic reaction phase.<sup>5)</sup> Such a model leads to a very long-lived dissipative *hadronic* rescattering phase which dominates the properties of the two-pion correlation functions. Figure 1 shows that if the dissipative hadronic phase is taken into account, the radii as well as the  $R_{out}/R_{side}$  ratio are found to depend only weakly on the thermalization time  $\tau_i$ , the critical temperature  $T_c$  (and thus the latent heat), and the specific entropy of the QGP. The dissipative hadronic stage enforces large variations of the pion emission times

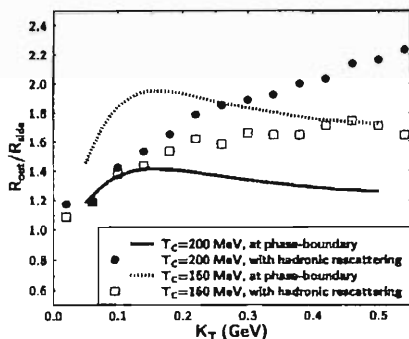


Fig. 1.  $R_{out}/R_{side}$  for pions at RHIC initial conditions, as a function of  $K_T$  at freeze-out (symbols) and at hadronization (lines).

<sup>\*1</sup> Lawrence Berkeley National Laboratory, USA

<sup>\*2</sup> Brookhaven National Laboratory, USA

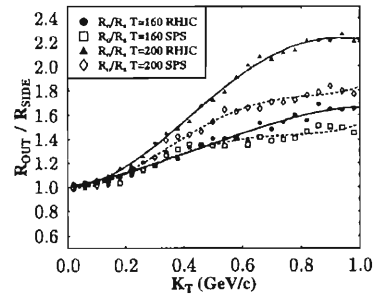


Fig. 2.  $R_{out}/R_{side}$  for kaons at RHIC (full symbols) and at SPS (open symbols), as a function of  $K_T$  for critical temperatures  $T_c \simeq 160$  MeV and  $T_c \simeq 200$  MeV, respectively. The lines are to guide the eye.

around the mean. Therefore, the model calculations suggest a rapid increase of  $R_{out}/R_{side}$  as a function of  $K_T$  if a thermalized QGP were formed.

Extending our analysis from pions to kaons<sup>6)</sup> we find that the kaon radii as well depend only weakly on the thermalization time  $\tau_i$ , the critical temperature  $T_c$  (and thus the latent heat), and the specific entropy of the QGP. However, kaons are less distorted by decays of (long-living) resonances. The predicted increase in the  $R_{out}/R_{side}$  ratio with  $K_T$  is rather moderate compared to pions.

At high transverse momenta  $K_T \sim 1$  GeV/c, however, direct emission from the phase boundary becomes important (approx. 30% of the kaons are then emitted directly from the phase-boundary). The emission duration signal, *i.e.*, the  $R_{out}/R_{side}$  ratio, and its sensitivity to  $T_c$  (and thus to the latent heat of the phase transition) are enlarged (see Fig. 2). Moreover, the QGP + hadronic rescattering transport model calculations do not yield unusual large radii ( $3 \leq R_i \leq 9$  fm). Finite momentum resolution effects have a strong impact on the extracted HBT parameters ( $R_i$  and  $\lambda$ ) as well as on the ratio  $R_{out}/R_{side}$ .

## References

- 1) G. Goldhaber, S. Goldhaber, W. Lee, and A. Pais: Phys. Rev. **120**, 300 (1960).
- 2) E. Shuryak: Phys. Lett. B **44**, 387 (1973).
- 3) S. Pratt: Phys. Rev. D **33**, 1314 (1986).
- 4) S. Soff, S. A. Bass, and A. Dumitru: Phys. Rev. Lett. **86**, 3981 (2001).
- 5) S. A. Bass and A. Dumitru: Phys. Rev. C **61**, 064909 (2000).
- 6) S. Soff, S. A. Bass, D. H. Hardtke, and S. Y. Panitkin: e-Print archive, nucl-th/0109055.

# Hadron spectrum for quenched domain-wall fermions with an improved gauge action<sup>†</sup>

Y. Aoki

Numerical simulation with use of lattice gauge theory is a powerful tool to analyze QCD nonperturbatively. It provides method to calculate quantities from the first principle. However, in the restricted amount of computational resources there are always systematic uncertainties to be carefully considered.

To define the lattice field theory, one needs as much symmetries as the continuum theory has. While it is expected that the all symmetries are recovered in the continuum limit, breaking the symmetries in the finite lattice generally could give rise the scaling violation, which becomes the major source of the systematic error.

Domain-wall fermion (DWF) action provides the good control of the chiral symmetry and has exact flavor symmetry, which conventional fermion actions do not have. It is useful for the calculation where the chiral symmetry is important. Moreover the scaling properties appear to be excellent, which could be understood by the good symmetries it has. Contrary to these good properties, there is a problem of increasing amount of computation from the existence of the extra-dimensional degree of freedom.

Studies<sup>2,3)</sup> for quenched DWF have shown that if the lattice spacing is small  $a < 0.1$  fm the breaking of chiral symmetry is small  $m_{res} \simeq m_{u,d}$  with modest size of fifth dimension  $L_s$  with Wilson gauge action. And if one employs a renormalization-group improved gauge action of Iwasaki,<sup>4)</sup>  $m_{res}$  gets 1/10 times smaller than that for Wilson. However, these studies also have shown that for  $a > 0.1$  GeV, in order to get the small  $m_{res}$  as for  $a \simeq 0.1$  GeV one needs extremely large  $L_s$ , which makes people avoid using it for application.

Motivated by the success of the improved gauge action, we have investigated further improvement of gauge action. We found that the DBW2 action,<sup>5)</sup> which is a non-perturbative version of Iwasaki action, provides a better chiral symmetry for the DWF.<sup>6)</sup>

The measure of goodness of chiral symmetry is residual quark mass  $m_{res}$  which is the additive renormalization to the quark mass, defined through the chiral Ward-Takahashi identity. The residual quark mass vanishes in the limit of  $L_s \rightarrow \infty$ , realizing exact chiral symmetry. We obtain for  $L_s = 16$

$$m_{res} \simeq 0.7 \text{ MeV}; a \simeq 0.15 \text{ fm}, \quad (1)$$

$$m_{res} \simeq 0.03 \text{ MeV}^6); a \simeq 0.1 \text{ fm}. \quad (2)$$

$m_{res}$  for the DBW2 action at  $a \simeq 0.1$  fm is about 1/10

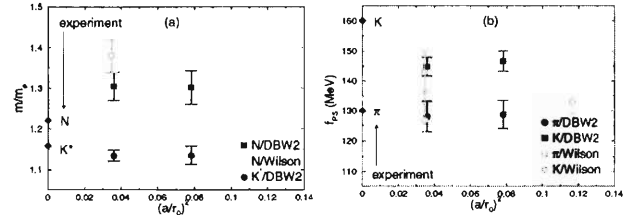


Fig. 1. Nucleon and  $K^*$ -to-rho mass ratios (a) and decay constants (b) as functions of lattice spacing squared.

of that for the Iwasaki action at the same lattice spacing. We note that  $m_{res}$  for the DBW2 action even at  $a \simeq 0.15$  fm is smaller than that for Wilson gauge action at  $a \simeq 0.1$  fm. This is a great advantage of using the DBW2 action, as one can do the precise calculation at  $a \simeq 0.15$  fm, where the simulation is much cheaper than the finer lattice and the other action do not give such a small  $m_{res}$ .

The next step is to test DBW2 gauge action whether the basic physical spectrum is obtained without any peculiarity. The main interest is how good the scaling property is for the spectrum. Figure 1 (a) shows the nucleon-to-rho mass ratio and the  $K^*$ -to-rho mass ratio as functions of lattice spacing  $a$  normalized by conventional scale parameter  $r_0$  calculated from the heavy quark potential.

Both nucleon and  $K^*$  masses show good scaling and nucleon mass for DBW2 is fairly consistent with that for DWF/Wilson gauge data.<sup>3)</sup> Figure 1 (b) shows the scaling of pseudoscalar decay constant. Both  $f_\pi$  and  $f_K$  show the good scaling.  $f_\pi$  is consistent with the experimental value but  $f_K$  is not, which is expected from the quenched chiral perturbation theory.<sup>7)</sup>

In summary, the combination of quenched DWF and DBW2 gauge action make chiral symmetry breaking sufficiently small even for a coarse lattice  $a \simeq 0.15$  fm. The hadron masses and decay constants show good scaling. These indicate that one can use results obtained at  $a \simeq 0.15$  fm for the reliable continuum extrapolation.

## References

- 1) Y. Aoki, RBC-Collaboration: hep-lat/0110143.
- 2) CP-PACS Collaboration, A. Ali Khan et al.: Phys. Rev. D **63**, 114504 (2001).
- 3) T. Blum et al.: hep-lat/0007038.
- 4) Y. Iwasaki: UTHEP-118 (1983).
- 5) T. Takaishi: Phys. Rev. D **54**, 1050 (1996).
- 6) K. Orginos: RIKEN Accel. Prog. Rep. **35**, 212 (2002); hep-lat/0110074.
- 7) C. Bernard and M. Golterman: Phys. Rev. D **46**, 853 (1992).

<sup>†</sup> This work has been done in the RBC Collaboration. See Ref. 1 for the more detailed article

# Calculation of $K \rightarrow \pi\pi$ decay in quenched domain-wall QCD

J. Noaki

One of the long-standing issue in lattice QCD is quantitative understanding of the  $K \rightarrow \pi\pi$  decay including the  $\Delta I = 1/2$  rule and the value of  $\varepsilon'/\varepsilon$ . This article is a summary of our calculation of these decay amplitudes.<sup>1)</sup> We used the relations between the  $K \rightarrow \pi\pi$  and  $K \rightarrow \pi$  matrix elements derived in chiral perturbation theory at the lowest order.<sup>2)</sup> This method avoids the serious problem in the direct calculation of  $K \rightarrow \pi\pi$ , but requires the chiral symmetry on the lattice.

Our numerical simulations were carried out in quenched QCD with the domain-wall fermion action and the renormalization group improved gluon action. This choice is known to have advantage in the point of chiral properties,<sup>3)</sup> compared to the other conventional actions. In this calculation, the gauge coupling corresponds to the scale  $1/a = 1.94$  GeV. We used the domain wall height  $M = 1.8$  and the fifth dimensional size  $N_s = 16$ . Gauge configurations are generated *independently* for each value of the degenerate  $u$ - $d$  and  $s$  quark mass,  $m_f$ . Our statistics are summarized in Table 1 for the two lattice volumes and  $m_f$  used in the calculation. The numerical task is to calculate the  $K \rightarrow \pi$  and  $K \rightarrow 0$  matrix elements of the local 4-quark operators that appear in the effective weak Hamiltonian. Each operator is divided into the contributions to  $\Delta I = 1/2$  and  $3/2$  channels. After checking the required chiral properties of the  $K \rightarrow \pi$  matrix elements, we estimated physical quantities in the following way:

- (1) We construct the  $K \rightarrow \pi\pi$  decay amplitudes from the  $K \rightarrow \pi$  and  $K \rightarrow 0$  matrix elements.
- (2) Renormalization of these matrix elements is made perturbatively at one-loop level<sup>4)</sup> at the scale  $1/a$ .
- (3) The renormalization group running to  $m_c$  ( $= 1.3$  GeV) is carried out for the  $N_f = 3$ .<sup>5)</sup>
- (4) Combining these results with the Wilson coefficients, we obtain the decay amplitudes  $A_I$ , where  $I = 0, 2$  is the isospin of final state.

In Fig. 1, we present the ratio  $\omega^{-1} = \text{Re } A_0/\text{Re } A_2$  as a function of squared pion mass on the lattice,  $m_M^2$ . We observe that the data from the volumes  $16^3$  (open symbols) and  $24^3$  (filled symbols) are consistent. Lines drawn are the fit curves with the quadratic function (solid) in  $m_M^2$  or a form including chiral logarithm

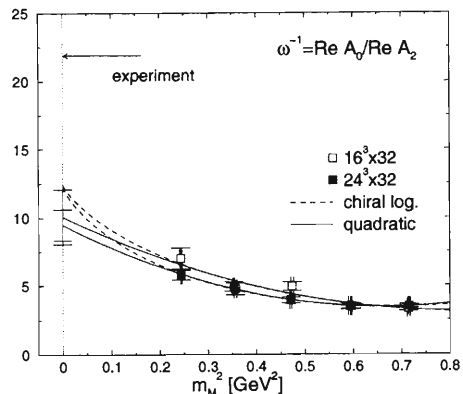


Fig. 1. The ratio  $\omega^{-1} = \text{Re } A_0/\text{Re } A_2$  as a function of  $m_M^2$  [GeV<sup>2</sup>]. See the text for the explanation.

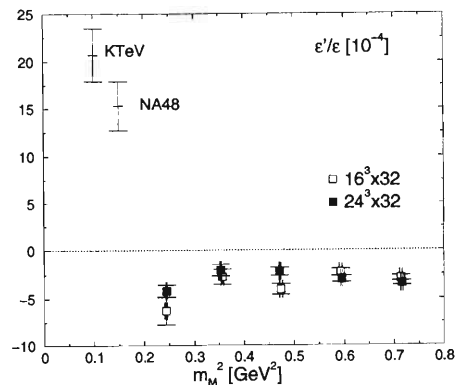


Fig. 2.  $\varepsilon'/\varepsilon$ , with symbols meaning same as in Fig. 1.

(dashed). The  $\Delta I = 1/2$  rule, *i.e.*,  $\omega^{-1} \approx 22$ , is reproduced only by about 50% in the chiral limit. This situation comes from the fact that whereas the  $I = 2$  amplitude is reasonably consistent with experiment, the  $I = 0$  amplitude is sizably smaller.

Using our results for only  $\text{Im } A_{0,2}$ , we obtain the values of  $\varepsilon'/\varepsilon$  seen in Fig. 2. In contrast to the experiments, our results are negative because the contributions from  $I = 0$  are smaller than those from  $I = 2$ .

These insufficient results come from the poor enhancement of  $\Delta I = 1/2$  channel that are regarded as a pathology of this method.

## References

- 1) CP-PACS Collaboration, J. Noaki et al.: hep-lat/0108013.
- 2) C. Bernard et al.: Phys. Rev. D **32**, 2343 (1985).
- 3) CP-PACS Collaboration, A. Ali Khan et al.: Phys. Rev. D **63**, 114504 (2001).
- 4) S. Aoki et al.: Phys. Rev. D **60**, 114504 (1999).
- 5) A. J. Buras et al.: Rev. Mod. Phys. **68**, 1125 (1996).

Table 1. Numbers of configurations generated in our calculation for each combination of  $m_f$  and volume.

$m_f$	0.02	0.03	0.04	0.05	0.06
$16^3 \times 32$	407	406	406	432	435
$24^3 \times 32$	432	200	200	200	200

# CP violation in K decay from lattice QCD<sup>†</sup>

T. Blum

Last year we reported on progress towards the determination of matrix elements of the effective weak Hamiltonian describing strangeness changing non-leptonic weak decays of kaons from first principles using lattice QCD.<sup>1)</sup> This year we summarize the complete results of that calculation.<sup>2)</sup> Such matrix elements are necessary to determine the ratio of  $CP$  violation parameters  $\epsilon'/\epsilon$  in the Standard Model (see Fig. 1) which have been measured in experiments at Fermilab and CERN. We have also computed the real parts of these  $K \rightarrow \pi\pi$  decay amplitudes which yield the  $\Delta I = 1/2$  rule for kaon decays. The enhancement observed in the isospin zero decay channel has been a long standing theoretical puzzle in particle physics. Our results are summarized in Table 1.

Defining decay amplitudes as

$$\begin{aligned} A(K^0 \rightarrow \pi\pi(I)) &= A_I e^{i\delta_I}, \\ A(\bar{K}^0 \rightarrow \pi\pi(I)) &= -A_I^* e^{i\delta_I}, \end{aligned} \quad (1)$$

where  $I = 0, 2$  is the isospin of the final state pions and  $\delta_I$  the corresponding  $s$ -wave phase shift, it can be shown that

$$\frac{\epsilon'}{\epsilon} = \frac{i e^{-i(\delta_0 - \delta_2)} \text{Re } A_2}{\sqrt{2} \epsilon} \left( \frac{\text{Im } A_2}{\text{Re } A_2} - \frac{\text{Im } A_0}{\text{Re } A_0} \right), \quad (2)$$

where we have neglected isospin breaking effects (these are expected to decrease the value of  $\epsilon'$ ). The factors outside of the parentheses are well known experimen-

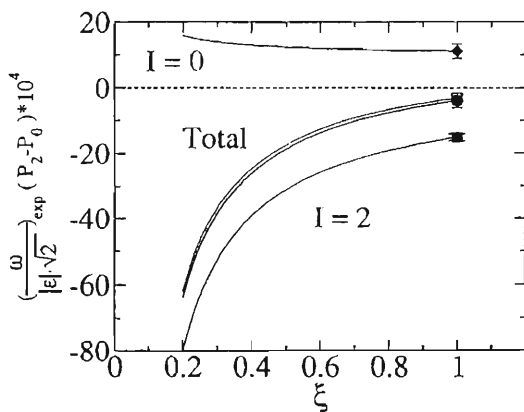


Fig. 1. The ratio of  $CP$  violation parameters  $\epsilon'/\epsilon$ . Totals are shown for lowest order (upper) and one-loop (lower) chiral perturbation theory. The  $I = 0$  and 2 contributions are shown for the one-loop case only.

Table 1. Summary of the calculation and comparison with experiment. The amplitudes are in units of GeV. The experimental results for  $\epsilon'/\epsilon$  are from the NA48 (first entry) and KTEV experiments.

Quantity	Experiment	This calculation
Re $A_0$	$3.33 \times 10^{-7}$	$2.96(17) \times 10^{-7}$
Re $A_2$	$1.50 \times 10^{-8}$	$1.172(53) \times 10^{-8}$
$\omega^{-1}$	22.2	25.3(18)
Re ( $\epsilon'/\epsilon$ )	$15.3(26) \times 10^{-4}$	$-4.0(23) \times 10^{-4}$
	$20.7(28) \times 10^{-4}$	

tally, so we quote values of  $\epsilon'/\epsilon$  using these known values. Thus, the calculation of  $\epsilon'/\epsilon$  boils down to determining the difference of ratios  $P_I \equiv \text{Im } A_I / \text{Re } A_I$ . The  $\Delta I = 1/2$  rule is simply given by the ratio of the real parts of the  $I = 0$  and 2 amplitudes,  $\omega^{-1} \equiv \text{Re } A_0 / \text{Re } A_2$ .

In Fig. 1 we show  $\epsilon'/\epsilon$  as a function of a fictitious mass parameter  $((m_\pi^2, m_K^2) \rightarrow \xi \times (m_\pi^2, m_K^2))$  in  $A_{0,2}$  which allows us to study the chiral behavior of our result. At the physical point  $\xi = 1$  our result is small and slightly negative in contrast to the experimental one. This happened because of a nearly complete cancellation between the two channels which are dominated by the QCD penguin operators  $Q_6$  and  $Q_4$  and the electroweak penguin  $Q_8$ , respectively. On the other-hand, our result for the  $\Delta I = 1/2$  rule is consistent with experiment. At the renormalization scales used in our study, we find a large enhancement of the  $I = 0$  matrix element of the progenitor weak operator  $Q_2$  over the  $I = 2$  one which along with the perturbative enhancement of roughly a factor of two is enough to explain most of the  $\Delta I = 1/2$  rule. The contributions from the QCD penguin operators are small.

Our calculation which represents a significant milestone in the calculation of non-leptonic kaon decays has significant approximations including quenching, use of perturbation theory below  $m_{\text{charm}}$ , and incomplete next-to-leading order calculations in chiral perturbation theory which will be addressed in future calculations. The road ahead will be interesting, especially if we must turn away from the Standard Model.

## References

- 1) T. Blum: RIKEN Accel. Prog. Rep. **34**, 277 (2001).
- 2) T. Blum, et al.: (RBC), hep-lat/0110075; J-I. Noaki, et al.: (CP-PACS), hep-lat/0108013.

<sup>†</sup> This work was done in collaboration with N. Christ, C. Cristian, C. Dawson, G. Fleming, X. Liao, G. Liu, S. Ohta, A. Soni, P. Vranas, R. Mawhinney, M. Wingate, L. Wu, and Y. Zhestkov. We thank RIKEN, Brookhaven National Laboratory and the U. S. Department of Energy for providing the facilities essential for this work.

# Chirality and localisation of domain wall fermion eigenvectors<sup>†</sup>

C. Dawson, for the RBC Collaboration

The spectrum of a Euclidean-space, anti-hermitian, chirally symmetric Dirac operator,  $D$ , may be split up into either zero-modes with eigenvector chirality  $\pm 1$  or paired modes,  $\psi_{\pm i\lambda}$ , with imaginary eigenvalues  $\pm i\lambda$ ,  $\gamma_5 \psi_{i\lambda} = \psi_{-i\lambda}$  and zero chirality. Lattice QCD provides a technique to study both the eigenvalue spectrum and the structure of the corresponding eigenvectors.

In particular while the global chirality of the paired modes must be zero the mechanism behind this is of interest. One possibility is that locally the eigenvectors have a definite  $\pm 1$  chirality (*cf.* Instanton Liquid Model) which adds to zero over all space-time, or the local chirality could be random, averaging to zero over a much smaller volume. Since being introduced in the context of Wilson fermions in Ref. 1 which favoured the latter picture this question has been addressed by many groups.<sup>2-5)</sup> Here we will summarise the results of our study<sup>6)</sup> using domain wall fermions (DWF).<sup>7)</sup> This fermion action has, at the expense of introducing a fifth dimension, chiral properties at finite lattice spacing that are greatly improved over standard actions and so is well suited to this problem.

To study this question we solved for the low-lying eigenvectors of the hermitian DWF Dirac operator

$$\gamma_5 R D_{\text{DWF}}$$

where  $D_{\text{DWF}}$  is the DWF Dirac operator using the conventions given in Ref. 8 and  $R$  is reflection about the middle of the fifth dimension. From these we construct 4d vectors,  $\Psi_{4d}$ , by summing the left-hand half of the 5th dimension to form the left-hand part of the 4d eigenvector and similarly with the right-hand piece. As we are only looking at the low-lying modes, which are very well localised to the domain wall,<sup>6,8)</sup> this should be a good representation of eigenvectors of a hermitian 4d Dirac operator  $\gamma_5(D + m)$ , with a finite mass arising from both the bare input mass and residual chiral symmetry breaking effects from DWF. For our study the mass will be very small, and for simplicity it will be neglected in the following. See Ref. 6 for a treatment of these corrections.

We studied a quenched gauge field ensemble of 55 configurations generated using the Iwasaki gauge action with a  $16^4$  lattice volume and an inverse lattice spacing of approximately 2 GeV. For each configura-

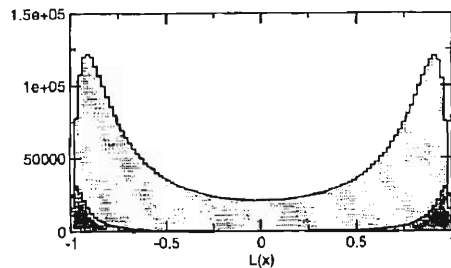


Fig. 1.  $L(x)$  for the Iwasaki ensemble.

tion we solved for the lowest 18 eigenvalues and the corresponding eigenvectors using a fifth dimension of size 16 and a bare quark masses of  $5 \times 10^{-4}$ .

To study the localisation of chirality we first separate the eigenvectors into paired and non-paired by making a cut on the absolute value of the global chirality with anything above 0.8 being considered a zero-mode. We then construct the local norm of each vector  $\Omega_H(x) = \Psi_{4d}^\dagger(x)\Psi_{4d}(x)$  and the local chirality  $X_H(x) = \Psi_{4d}^\dagger(x)\gamma_5\Psi_{4d}(x)$ . We pick out the points in the lattice that contribute most by making cuts  $\Omega_H > \Omega_{\min}$  and for the admitted points we histogram the local chirality,

$$L(x) = X_H(x)/\Omega_H(x).$$

If the eigenvectors are locally chiral this will cluster around  $\pm 1$ , whereas a flat distribution would be expected if the chirality were random. Figure 1 shows this histogram for  $\Omega_{\min} > 3 \cdot 10^5$  and  $\Omega_{\min} > 8 \cdot 10^5$ . This corresponds to admission of 6% and 29% of the total norm respectively. As can be seen it is clear that using DWF the paired modes of the low-lying eigenvectors are locally chiral.

## References

- 1) I. Horvath et al.: hep-lat/0102003.
- 2) I. Hip et al.: hep-lat/0105001.
- 3) C. Gattringer et al.: hep-lat/0107016.
- 4) R. G. Edwards and U. M. Heller: hep-lat/0105004.
- 5) T. DeGrand and A. Hasenfratz: hep-lat/0103002.
- 6) T. Blum et al.: hep-lat/0105006.
- 7) Y. Shamir: Nucl. Phys. B **406**, 90 (1993).
- 8) T. Blum et al.: hep-lat/0007038.

<sup>†</sup> This work was done in collaboration with T. Blum, N. Christ, C. Cristian, G. Liu, R. Mawhinney, L. Wu, and Y. Zhestkov. We thank RIKEN, Brookhaven National Laboratory and the U. S. Department of Energy for providing the facilities essential for this work.

## QCDOC project<sup>†</sup>

P. A. Boyle,<sup>\*1,\*2</sup> D. Chen,<sup>\*3</sup> N. H. Christ,<sup>\*2</sup> C. Cristian,<sup>\*2</sup> Z. Dong,<sup>\*2</sup> A. Gara,<sup>\*3</sup> B. Joó,<sup>\*1,\*2</sup> C. Kim,<sup>\*2</sup>  
L. Levkova,<sup>\*2</sup> X. Liao,<sup>\*2</sup> R. D. Mawhinney,<sup>\*2</sup> S. Ohta,<sup>\*4</sup> T. Wettig,<sup>\*5</sup> and A. Yamaguchi<sup>\*2</sup>

The QCDOC (QCD On a Chip) project started in 1999 as a joint effort of RIKEN, Columbia University and IBM Research to design a massively parallel computer optimized for lattice quantum chromodynamics (QCD). The architecture combines state-of-the-art system-on-a-chip technology with custom-designed logic specially optimized for lattice QCD calculations to provide computing power in the tens of TFlops range at a price/performance ratio of 1 US\$ per sustained MFlops.<sup>1)</sup> The British UKQCD collaboration and the US lattice gauge theory community later endorsed the project.

For physically relevant lattice QCD numerical calculations to be completed within a reasonable amount of time, it is essential to distribute the total volume onto as many nodes as possible. This implies small local lattice volumes, as small as  $2^4$ , and hence requires communications between neighboring nodes with extremely low latencies that cannot be achieved using off-the-shelf networking components used in PC clusters such as Myrinet. Massively parallel machines with custom-designed communications hardware (with latencies 10-100 times smaller than in the case of Myrinet) appear to be the only viable alternative.

The QCDOC architecture is capable of delivering computing power in the tens of TFlops range at a price/performance ratio of 1 US\$ per sustained MFlops. QCDOC is a multiple-instruction, multiple-data (MIMD) machine with distributed memory. Nowadays it is possible to integrate the components that make up a single processing node on a single chip, creating an application-specific integrated circuit (ASIC). The QCDOC chip is such an ASIC, consisting of (a) a 500 MHz, 32-bit PowerPC 440 processor core, (b) a 64-bit, 1 GFlops floating-point unit, (c) 4 MBytes embedded-DRAM memory, (d) controllers for embedded and external memory, (e) nearest-neighbor serial communications unit (SCU) with latencies of 120 ns (300 ns) for send (receive), overlapped between the 12 independent directions and an aggregate bandwidth of 12 Gbit/s, and (f) other components such as Ethernet controller, *etc.* The power consumption of the chip will be in the range of 1-2 W. Two such ASICs will be mounted on a daughterboard, together with two

industry-standard double data rate (DDR) SDRAM modules (one per ASIC). 32 daughterboards will be mounted on a motherboard, and 8 motherboards in a crate with a single backplane. The final machine consists of a certain number of such crates.

There are two separate networks: the physics network and an Ethernet-based auxiliary network. The physics network consists of high-speed serial links between nearest neighbors with a bandwidth of  $2 \times 500$  Mbits/s per link. The nodes are arranged in a 6-dimensional torus which allows for an efficient partitioning of the machine in software. The SCU in the ASIC provides direct memory access, single-bit error detection with automatic resend, and a low-latency store-and-forward mode for global operations. The Ethernet-based 100 Mbit/s auxiliary network is used for booting, diagnostics, and I/O over Ethernet, with an Ethernet controller integrated on the ASIC. Hubs or switches on the motherboard will provide a bandwidth of 1.6 Gbit/s off a motherboard to commercial switches and the host workstation.

The ASIC functional design is nearly finished. Single-node physics code is running on the VHDL simulator, and from these simulations we obtained the performance figures of about 50% efficiency maintained for lattice QCD calculations. In another test environment two nodes have successfully communicated in the VHDL simulator over their Ethernet interfaces and/or the HSSLs. The operating system is being developed on a system with seven PowerPC boards, five Ethernet-JTAG boards, and a RISCWatch probe. The current design has been successfully synthesized, and an analysis net list has been provided to IBM for floorplanning purposes. Anticipating a few iterations to satisfy timing constraints the complete design should be transferred to IBM by the end of 2001. Production of the chip can start after that.

### References

- 1) D. Chen et al.: Lattice 2000, Bangalore, India, 2000-8; hep-lat/0011004, Nucl. Phys. B (Proc. Suppl.) **94**, 825 (2001); P. A. Boyle et al.: Lattice 2001, Berlin, Germany, 2001-8; hep-lat/0110124, Nucl. Phys. B (Proc. Suppl.) **106**, 177 (2002).

<sup>†</sup> We thank RIKEN and the US Department of Energy

<sup>\*1</sup> University of Edinburgh, UK

<sup>\*2</sup> Columbia University, USA

<sup>\*3</sup> IBM Research, USA

<sup>\*4</sup> Institute for Particle and Nuclear Studies, High-Energy Accelerator Research Organization (KEK)

<sup>\*5</sup> Yale University, USA

## QCD phase structure with many flavors

S. Kim<sup>\*1</sup> and S. Ohta<sup>\*2</sup>

In the perturbative expansion of Callan-Symanzik  $\beta$ -function of quantum chromodynamics (QCD),

$$\beta(g) = \mu \frac{\partial g}{\partial \mu} = b_0 g^3 + b_1 g^5 + \mathcal{O}(g^7),$$

the first two coefficients,  $b_0$  and  $b_1$ , are dependent on the number of light flavors,  $N_f$ . Since they change signs at different  $N_f$ , a non-trivial zero may develop in  $\beta(g)$ . It was argued that such a zero may change the long or short distance behavior of QCD.<sup>1)</sup> Within this perturbation analysis this can only happen for  $N_f > 8$ , and the zero resides in a region in the coupling where the perturbation cannot be valid. Hence this interesting problem is left to be investigated non-perturbatively. Indeed there have been several lattice studies with multi-flavored QCD<sup>2-4)</sup> which suggest such rich phase structures.

For eight light staggered quark flavors, there is a strong first order phase transition which separates the strong coupling region from the weak coupling region. For a given lattice spatial volume, this transition appears to be  $N_t$ -independent bulk transition where  $N_t$  is the number of sites along the time direction. The weak coupling phase is divided into two region: in one region of weak coupling space chiral condensates shows linear behavior in quark mass, and in the other region they show non-linearity.<sup>3)</sup> It has been speculated that there may be a normal finite temperature phase transition between these two different weak coupling phases. On the other hand, using simulation results with Wilson quark formulation in the strong coupling limit, the authors of Ref. 4 argue that lattice QCD for  $N_f \geq 7$  has an interesting limit without quark confinement. Even if the color confinement and the spontaneous chiral symmetry breaking is rigorously proven in the infinite coupling limit (in quenched approximation to QCD), it is claimed that copious addition of light quark flavors modifies the string-like vacuum structure of a theory with gluon only.

Although the existence of a strong first order bulk phase transition which separates the strong coupling region and the weak coupling one is well established,

the continuum limit of lattice theories for multi-flavor QCD is much less clear. For staggered quark simulations, investigation of the weak coupling phase by use of hadron spectroscopy calculation was hampered by small spatial lattice volumes.<sup>3)</sup> Simulation result with Wilson dynamical quark in the strong coupling limit is difficult to make a contact with the continuum limit. Further study in the weak coupling phases of multi-flavor QCD using light dynamical quarks is needed. Here, we would like to endeavor toward this direction. Our efforts will be concentrated on various susceptibilities such as chiral susceptibility and finite size scaling of them.<sup>5)</sup>

We use the R-algorithm<sup>6)</sup> to simulate QCD with arbitrary number of quark flavors and employ staggered fermion method for the dynamical quarks. Target platform for our project is the 128-node Fujitsu VPP-700 at RIKEN. As a first step, the weak coupling phases with  $N_f = 6$  and 8 are investigated. There exist a linear relation between the chiral condensate and the light dynamical quark mass, which is in agreement with the earlier results. For the planned more detailed investigation of the weak coupling phase, several aspects of the current lattice calculation need to be refined: First, we need to test whether the systematic error arising from finite step size of the current algorithm is small enough. Second, we need to add more observables: various susceptibilities such as chiral susceptibility calculation and specific heat calculation are currently being implemented.

### References

- 1) T. Banks and A. Zaks: Nucl. Phys. B **196**, 173 (1982).
- 2) J. B. Kogut et al.: Phys. Rev. Lett. **54**, 1475 (1985); M. Fukugita, et al.: Phys. Rev. Lett. **60**, 178 (1988).
- 3) F. R. Brown et al.: Phys. Rev. D **46**, 5655 (1992).
- 4) Y. Iwasaki et al.: Prog. Theor. Phys. Suppl. **131**, 415 (1998); Nucl. Phys. B (Proc. Suppl.) **42**, 502 (1995); Nucl. Phys. B (Proc. Suppl.) **53**, 449 (1997); Phys. Rev. Lett. **69**, 21 (1992).
- 5) S. Kim and S. Ohta: Lattice 2001, hep-lat/0111040, Nucl. Phys. B (Proc. Suppl.) **106**, 873 (2002).
- 6) S. Gottlieb et al.: Phys. Rev. D **35**, 2531 (1987).

---

<sup>\*1</sup> Sejong University, Korea

<sup>\*2</sup> Institute for Particle and Nuclear Studies, High-Energy Accelerator Research Organization (KEK)

# Nucleon axial charge on the lattice

T. Blum, S. Ohta,\*<sup>1</sup> K. Orginos, and S. Sasaki\*<sup>2</sup>

The domain-wall fermion (DWF) method in lattice quantum chromodynamics (QCD), practical use of which has been pioneered by the RIKEN-BNL-Columbia-KEK QCD collaboration, preserves the important chiral symmetry almost exactly<sup>1)</sup> the violation is exponentially suppressed by adjusting parameters associated with the extra fifth lattice dimension. The nucleon (iso-vector) axial charge  $g_A$  poses an interesting challenge for this method. From neutron  $\beta$  decay we know its experimental value  $g_A = 1.2670(35)$  in units of the conserved vector charge,  $g_V = \cos \theta_{\text{Cabibbo}}$ . Deviation of the ratio  $g_A/g_V$  from unity, in contrast to the conservation of the vector charge,  $g_V$  itself, reflects the fact that the axial current is only partially conserved in the strong interaction because of the spontaneous breakdown of the chiral symmetry. Thus, the calculation of  $g_A$  is an especially relevant test of the chiral properties of the DWF method in the baryon sector. It is also an important first step in studying polarized nucleon structure functions. An important advantage of the DWF method, in contrast to the conventional methods, is that we can maintain a relation  $Z_A = Z_V$  between the lattice renormalizations of the axial and vector currents so that the lattice value  $(g_A/g_V)^{\text{lattice}}$  directly yields the continuum value  $(g_A/g_V)^{\text{con}}$ . Our first DWF calculation with Wilson's single-plaquette gauge action found the ratio  $g_A/g_V$  with a strong quark-mass dependence, and a simple linear extrapolation to the chiral limit yielded a value about a factor of two smaller than the experiment. This deviation might be caused by such systematic effects as finite lattice volume and quenching (for example quenched chiral logarithms, zero modes, and the absence of the full pion cloud). In the present work we focus on the former: while the first calculation employed a rather small physical volume of about  $(1.6 \text{ fm})^3$ , the present work employs about  $(2.4 \text{ fm})^3$ . Given the current capabilities of the QCDSF supercomputer, this large volume would result in an unacceptably large chiral symmetry breaking if we kept using the Wilson's gauge action because one would be forced to use coarser lattices. Fortunately, however, recent studies from the RBCK collaboration<sup>2)</sup> have shown that renormalization-group inspired improved gauge actions, such as the DBW2 action,<sup>3)</sup> suppresses

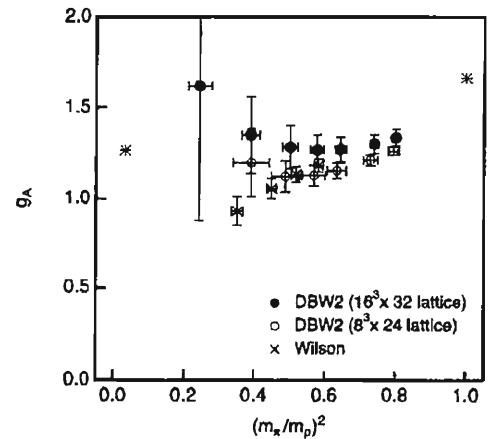


Fig. 1.  $g_A/g_V$  plotted against pion mass squared, scaled with  $\rho$ -meson mass squared. DBW2 (filled and open circles) and Wilson (cross) actions.

the symmetry breaking by two orders of magnitude, enabling the current study. As shown in Fig. 1, our preliminary results using DBW2 gauge action represented by filled (larger volume of  $\sim (2.4 \text{ fm})^3$ ) and open (smaller volume of  $\sim (1.2 \text{ fm})^3$ ) circles, prove a clear finite volume effect, which seems to become large in the lighter quark mass region. In addition, the larger volume results have a milder quark mass dependence except for the two lightest points, which still have large statistical errors. On the other hand, the smaller volume results seem to be in rough agreement with our previous results using the Wilson gauge action ( $\times$ ) with the strong mass dependence.

## References

- 1) RBCK Collaboration, T. Blum et al.: hep-lat/0007038, to appear in Phys. Rev. D; hep-lat/0102005, submitted for publication in Phys. Rev. D; hep-lat/0110075, submitted for publication in Phys. Rev. D; T. Blum, S. Ohta, and S. Sasaki: Lattice 2000, Nucl. Phys. B (Proc. Suppl.) **94**, 295 (2001); and references cited in these works.
- 2) RBCK Collaboration, K. Orginos et al., in preparation; RBCK Collaboration, Y. Aoki et al., in preparation.
- 3) QCD-TARO Collaboration: Nucl. Phys. B **577**, 263 (2000).

\*<sup>1</sup> Institute for Particle and Nuclear Studies, The High-Energy Accelerator Research Organization (KEK)

\*<sup>2</sup> Department of Physics, University of Tokyo

# Gauge actions and chiral symmetry of domain wall fermions

K. Orginos, and RBC Collaboration

We report here our results from our studies of the residual chiral symmetry breaking of domain wall fermions for the 1-loop Symanzik, Iwasaki,<sup>1)</sup> and DBW2 actions. The DBW2 action was introduced in Ref. 2 and it was shown by QCD-TARO in Ref. 3 that it is a good approximation of the RG flow on the two dimensional plane of the plaquette and rectangle couplings.

All the above gauge actions can be written as

$$S_G = \frac{\beta}{3} \left( c_0 \sum_{x:\mu<\nu} P_{\mu\nu} + c_1 \sum_{x:\mu\neq\nu} R_{\mu\nu} + c_2 \sum_{x:\mu<\nu<\sigma} C_{\mu\nu\sigma} \right),$$

where  $P_{\mu\nu}$  is the standard plaquette in the  $\mu, \nu$  plane, and  $R_{\mu\nu}$  and  $C_{\mu\nu\sigma}$  denote the real part of the trace of the ordered product of SU(3) link matrices along  $1 \times 2$  rectangles and  $1 \times 1 \times 1$  paths, respectively. For the 1-loop Symanzik action the coefficients  $c_0$ ,  $c_1$ , and  $c_2$  are computed in tadpole improved one loop perturbation theory.<sup>4)</sup> While  $c_2 = 0$  and  $c_0 = 1 - 8c_1$  for both Iwasaki and DBW2,  $c_1 = -0.331$  and  $-1.4069$  respectively.

As a measure of the chiral symmetry breaking we use the so called residual mass,

$$m_{res} = \frac{\langle J_q^5(0) J^5(t) \rangle}{\langle J^5(0) J^5(t) \rangle} \Big|_{t \geq t_{min}},$$

where  $J_q^5$  is the mid-point chiral symmetry breaking term which appears in the axial Ward identity of domain wall fermions, and  $t_{min}$  is sufficiently large to avoid short-distance lattice artifacts.

We present the simulation parameters we used in Table 1. In Fig. 1 we show the  $L_s$  dependence of the residual mass. All data are for  $a^{-1} \sim 2$  GeV and bare quark mass  $m_q = 0.02$ . The value of  $\frac{M_\pi}{M_\rho}$  is within 10% of .55. Since we are interested in differences by factors of ten, and since we know that the  $m_{res}$  depends mildly on the quark mass,<sup>5,6)</sup> the data can be directly compared as is. For completeness we also present the CP-PACS residual mass results.<sup>6)</sup> We have confirmed their results for  $L_s = 16$  (diamond in Fig. 1). For the Symanzik action we ran at  $L_s = 16$  only; the residual mass turns out to be smaller by a factor of three than the Wilson residual mass at the same  $L_s$ , and it is larger by a factor of two than that of the Iwasaki action. The DBW2 action not only gives the smallest residual mass, but also has the steepest decrease as a function of  $L_s$ . Since we have only three points, we cannot claim that we know the asymptotic behav-

Table 1. The simulation parameters for all the actions.

Action	$\beta$	$M_\rho$	$M_5$	$L_s$
Wilson <sup>5)</sup>	6.00	0.404(8)	1.8	12-24
Symanzik	8.40	0.411(14)	1.8	16
Iwasaki	2.60	0.415(13)	1.8	16
DBW2	1.04	0.399(11)	1.7	8-16

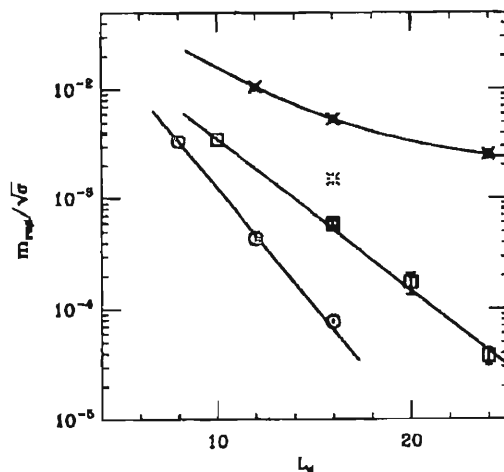


Fig. 1.  $L_s$  dependence of  $m_{res}$  at  $a^{-1} \sim 2$  GeV. The octagons correspond to the DBW2 action, the squares (CP-PACS<sup>6)</sup>) and diamond (RBC) to Iwasaki, the burst to Symanzik, and the fancy squares to Wilson.

ior; it is interesting to note however, that a simple fit gives us  $m_{res}(s) \sim q^s$  with  $q \sim 0.6$ . Shamir's one loop perturbative result<sup>7)</sup> is  $q = 0.5$ .

Using the DBW2 action, we have essentially eliminated the problem of residual chiral symmetry breaking for domain wall fermions at 2 GeV with  $L_s = 16$ . Assuming a 440 MeV string tension, the bare DBW2 residual mass is about 30 KeV. Our results also suggest that the DBW2 action should also be useful for overlap fermions, since it probably makes the approximation to the sign function converge faster by eliminating the small eigenvalues of the Hermitian Wilson Dirac operator.

## References

- 1) Y. Iwasaki: unpublished UTHEP-118 (1983).
- 2) T. Takaishi: Phys. Rev. D **54**, 1050 (1996).
- 3) P. de Forcrand et al.: Nucl. Phys. B **577**, 263 (2000).
- 4) M. G. Alford et al.: Phys. Lett. B **361**, 87 (1995).
- 5) T. Blum et al.: hep-lat/0007038 (2000).
- 6) A. Ali Khan et al.: Phys. Rev. D **63**, 114504 (2001)
- 7) Y. Shamir: Phys. Rev. D **62**, 054513 (2000).

# Scalar glueball mass reduction at finite temperature in SU(3) anisotropic lattice QCD

N. Ishii, H. Suganuma,<sup>\*1</sup> and H. Matsufuru<sup>\*2</sup>

Finite temperature QCD is one of the most interesting subjects in the quark hadron physics. At high temperature, QCD undergoes the deconfinement and/or chiral phase transition at the critical temperature  $T_c$  to the quark gluon plasma (QGP) phase, and significant changes are expected such as the existence of isolated quarks and gluons. However, even below  $T_c$ , a lot of phenomenological effective models predict changes in the hadronic properties. Although the lattice QCD Monte Carlo simulation provides a model independent method to study the nonperturbative natures of QCD, the lattice QCD studies of the thermal hadron properties had been inadequate until quite recent. This is due to the difficulty in measuring hadronic two-point correlators on the lattice at finite temperature. At finite temperature, owing to the shrink of the physical temporal size of the lattice and the consequent reduction of the number of lattice points in the temporal direction, the accurate mass measurement from the temporal correlations is quite difficult. Hence, the finite temperature mass shift had been studied through the spatial correlations, *i.e.*, the screening mass, which, however, is afflicted with the mixture of the large Matsubara frequencies.<sup>1)</sup> Recently, the use of the anisotropic lattice has been established,<sup>2)</sup> which makes it possible to study the mass shift directly from the temporal correlations. Here, we report the thermal glueball properties below  $T_c$  using quenched SU(3) lattice QCD.<sup>3-5)</sup>

To study the thermal glueball properties, at finite temperature, we need the smearing method<sup>6)</sup> in addition to the anisotropic lattice. The smearing method is a method to enhance the ground state contribution in the two-point correlator. The simplest interpolating field for the glueball is the plaquette operator  $\phi$ , which, however, has only a weak overlap with the ground state glueball, *i.e.*,  $|\langle G|\phi|0\rangle|^2$  is rather small. Instead, the correlator receives sizable contributions from excited states, which makes the accurate mass measurement difficult, especially at high temperature where the physical temporal size of the lattice is limited. It is known that this is due to the fact that the “size” of the plaquette operator is  $O(a)$ , which is much smaller than the physical size of the glueball.<sup>6)</sup> The smearing method is used to generate the spatially extended operator with a definite “size” very systematically. By choosing the smearing parameters so that the extended operator has the same “size” as the physical size of the glueball, we can maximize the ground state overlap, which is the original usage of

the smearing method.<sup>6)</sup> However, it can be also used to give a rough estimate of the glueball size by numerically seeking for the best smearing parameters to achieve the maximum ground state overlap. The physical size of the glueball is then estimated by the “size” of the corresponding extended glueball operator.<sup>3,4)</sup> In this way, we can simultaneously study both the mass and the size of the glueball at finite temperature based on the two-point correlators in quenched SU(3) lattice QCD. In Fig. 1, thus obtained thermal glueball masses are plotted against the temperature.<sup>4)</sup> The solid circle denotes the  $0^{++}$  glueball mass, and the open circle the  $2^{++}$  glueball mass for reference. We see that, at low temperature ( $T = 126$  MeV), we have  $m_G \simeq 1.54$  GeV for the  $0^{++}$  glueball, which is consistent with  $m_G \simeq 1.5 \sim 1.7$  GeV.<sup>7,8)</sup> In comparison to this, we observe about 20% mass reduction of the  $0^{++}$  glueball mass at higher temperature ( $0.8T_c < T < T_c$ ) as  $m_G(T) \simeq 1.25 \pm 0.1$  GeV. As for the glueball size, we find no significant change for the  $0^{++}$  glueball, and the estimated  $0^{++}$  glueball size is  $R \simeq 0.5 \sim 0.6$  fm both at low and high temperature.

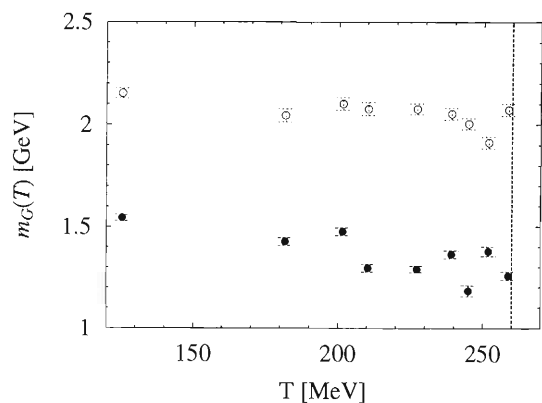


Fig. 1. The thermal glueball masses plotted against temperature. The solid circle denotes the  $0^{++}$  glueball mass, and the open circle the  $2^{++}$  glueball mass. The vertical dotted line indicates the critical temperature  $T_c \simeq 260$  MeV for the deconfinement transition.

## References

- 1) C. DeTar and J. B. Kogut: Phys. Rev. Lett. **59**, 399 (1987).
- 2) T. R. Klassen: Nucl. Phys. B **533**, 557 (1988).
- 3) N. Ishii, H. Suganuma, and H. Matsufuru: hep-lat/0109011.
- 4) N. Ishii, H. Suganuma, and H. Matsufuru: Proc. LEP-top Scattering, Hadrons and QCD, Adelaide, Australia,

<sup>\*1</sup> Faculty of Science, Tokyo Institute of Technology

<sup>\*2</sup> Yukawa Institute of Theoretical Physics, Kyoto University

- 2001-3 (World Scientific, 2001), p. 252.
- 5) N. Ishii, H. Suganuma, and H. Matsufuru: Proc. Lattice 2001, Berlin, Germany, 2001-8, Nucl. Phys. B (Proc. Suppl.), **106-107**, 516 (2002).
  - 6) APE Collaboration: Phys. Lett. B **192**, 163 (1987).
  - 7) C. J. Morningstar and M. Peardon: Phys. Rev. D **60**, 034509 (1999).
  - 8) J. Sexton, A. Vaccarino, and D. Weingarten: Phys. Rev. Lett. **75**, 4563 (1995).

# Calorons and localization of Dirac eigenvectors in lattice QCD

T. Wettig\*

One of the many interesting features of QCD is the finite-temperature chiral phase transition,  $\langle \bar{\psi}\psi \rangle \rightarrow 0$  as  $T \rightarrow T_c$ . It can be understood in terms of the eigenvalue spectrum of the QCD Dirac operator, since  $\langle \bar{\psi}\psi \rangle = -\pi\rho(0)/V$ , where  $\rho(\lambda)$  is the eigenvalue density. In the instanton liquid model, the nonvanishing value of  $\rho(0)/V$  originates from the quasi-zero modes that result from the shift of the exact zero modes of noninteracting instantons to values of order  $\mathcal{O}(1/V)$  after interactions are turned on. As  $T \rightarrow T_c$ , instantons and anti-instantons combine to form molecules, and the associated eigenvalues are no longer of order  $1/V$  so that  $\langle \bar{\psi}\psi \rangle \rightarrow 0$ .

We are interested in relating this picture to the localization properties of the Dirac eigenfunctions. If chiral symmetry is broken, they must be extended. (Proof by contradiction: Because of the fermion determinant and the Jacobian resulting from diagonalization, the eigenvalues are repelled from the origin. The mechanism to compensate for this and to ensure that  $\rho(0)/V \neq 0$  is repulsion between the eigenvalues. However, if the eigenfunctions were localized, the eigenvalues would be uncorrelated so that there is no eigenvalue repulsion, hence  $\langle \bar{\psi}\psi \rangle = 0$ .) The question now is whether the chiral phase transition is reflected in a change of the localization properties of the Dirac eigenfunctions.

In the quenched case, attention must be paid to the phase of the Polyakov loop which clusters around  $\theta_P = 0, \pm 2\pi/3$  because of a  $Z_3$  symmetry of the gauge action. For  $T > 0$ , the classical solutions of the field equations are called calorons, which are periodic instanton configurations that are localized in space but not in time. We find that the corresponding zero modes fall off like

$$|\psi|^2 \sim e^{-2(\pi-|\theta_P|)rT}/r^2 \quad \text{for large } r,$$

*i.e.* the localization length depends on the  $Z_3$  sector. As a measure of localization, we define the gauge-invariant probability density  $p_\lambda(x) = \sum_{\alpha=1}^{N_c} |\psi_\lambda^\alpha(x)|^2$  and the  $\langle \gamma_5 \rangle$ -density  $\langle \gamma_5 \rangle(x) = \sum_{\alpha=1}^{N_c} \psi_\lambda^\alpha(x)^\dagger \gamma_5 \psi_\lambda^\alpha(x)$ . These quantities were computed in lattice simulations using staggered fermions and the Wilson<sup>1)</sup> as well as the Lüscher-Weisz<sup>2)</sup> gauge action. We expect, and indeed find in the lattice simulations, characteristic differences in the localization patterns between the  $Z_3$  sectors if (and only if)  $T > T_c$ . Only the real sector ( $\theta_P \approx 0$ ) shows localization in space, which means that the eigenstates must be extended in time since a localized state would be unaffected by a  $Z_3$  transformation.

To see whether the difference in the localization properties is due to the presence of calorons, we test

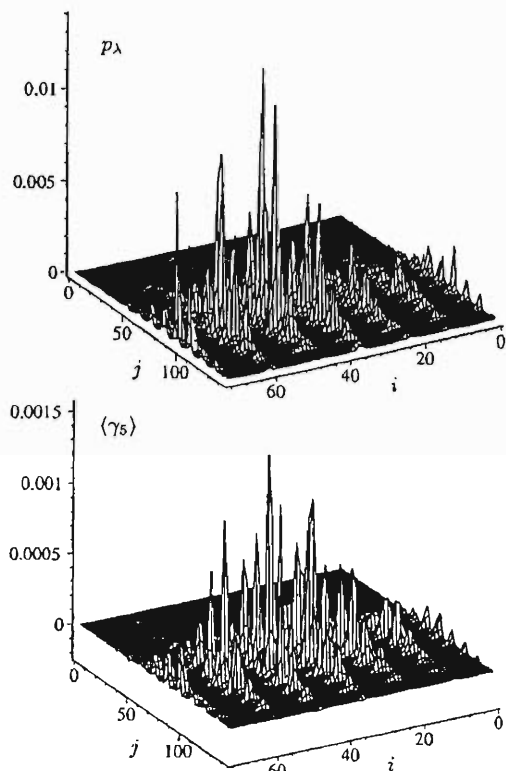


Fig. 1. A “caloron” state on a  $12^3 \times 6$  lattice for  $\beta = 6.1$  in the  $\theta_P \approx 0$  sector. The gauge-invariant density is plotted above, the expectation value of  $\gamma_5$  below. Both show localization in space but not in time.

the localization pattern in 4-d on a  $12^3 \times 6$  lattice by defining

$$\begin{aligned} i &= x + 12t & \text{with } x, y, z &= 0, \dots, 11 \\ j &= y + 12z & t &= 0, \dots, 5. \end{aligned}$$

The quantities  $p_\lambda(x)$  and  $\langle \gamma_5 \rangle(x)$  are plotted in Fig. 1 for a mode corresponding to a very small eigenvalue. This mode is also an approximate chiral eigenstate within the limitations of staggered fermions.

The advantage of our method is that it allows us to characterize the semiclassical properties of the gauge field without any cooling. For  $T > T_c$  we find isolated modes with definite handedness that are localized in space but not in time and thus show essential properties of quark states associated with calorons.

I would like to thank M. Göckeler, P. E. L. Rakow, A. Schäfer, and W. Söldner for fruitful collaborations.

## References

- 1) M. Göckeler et al.: Phys. Rev. Lett. **87**, 042001 (2001).
- 2) M. Göckeler et al.: hep-lat/0110182.

\* Yale University, USA

## Overview of RIKEN/RBRC activities for RHIC spin physics 2001

H. En'yo and G. Bunce\*

We succeeded in storing and accelerating polarized proton beams for the first time at RHIC last year.<sup>1)</sup> We are going to start a physics run this year using polarized proton-proton collisions at  $\sqrt{s} = 200$  GeV. The goal of the machine commissioning is to provide beam polarization of 50% or more and luminosity of  $5 \times 10^{30} \text{ cm}^{-2} \text{ sec}^{-1}$ . If these goals are met, we should be able to carry out significant measurements of single transverse-spin asymmetries  $\mathcal{A}_N$  and double longitudinal-spin asymmetries  $\mathcal{A}_{LL}$  for hadron and lepton production at the highest energy ever achieved.

The RHIC has achieved its designed values in energy ( $= \sqrt{s_{NN}} = 200$  GeV) and luminosity ( $= 2 \times 10^{26} \text{ cm}^{-2} \text{ sec}^{-1}$ ). The PHENIX experiment has accumulated  $42 \mu\text{b}^{-1}$  on tape, which is about 10 times the integrated luminosity of last year. We have just started to inject polarized proton beams to RHIC rings at the injection energy of 24.5 GeV/c. Both RHIC rings have a proton-carbon CNI polarimeter<sup>2)</sup> and complete sets of snake magnets thus we should be able to accelerate polarized proton beams to 100 GeV, where we observed zero polarization with single snake operation<sup>1)</sup> last year. The beam polarization will be determined using the final results from AGS E-950.<sup>3)</sup> This year we are going to use a newly made waveform digitizer to manage the pile-up of events<sup>2)</sup> due to the anticipated high beam currents. The analysis code has been developed based on the results from detailed analysis of last year's data.<sup>4)</sup>

For PHENIX, we have significantly extended the active volume this year with an additional read-out electronics for the electromagnetic calorimeter, and with completion of the South Muon Arm.<sup>5,6)</sup> The Muon Identifier has been operated successfully in the highest-energy gold-gold collisions<sup>7)</sup> and its performance has been greatly improved by shielding the area close to the beam pipe with steel blocks.<sup>8)</sup> For the polarized  $pp$  run, which is to start soon, we have added a normalization trigger counter, trigger boards for EMCal and RICH and a T0 counter for trigger-bias studies. The expected reaction rate with this year's luminosity ( $\mathcal{L} = 5 \times 10^{30} \text{ cm}^{-2} \text{ sec}^{-1}$ ) is 250 kHz. Possible bottlenecks this year are event builder data processing ( $\sim 1.2$  kHz) and the total bandwidth ( $\sim 30$  Mbytes/sec  $\sim 700$  Hz). Extensive studies on trigger performance are ongoing and will be fully ready for the physics run. For example, a sample of hadron with large transverse momentum, which is sensitive to gluonic contributions such as gluon polarization  $\Delta g(x)$ , can be enhanced by both level-1 and level-2 triggers.<sup>9)</sup>

In calculating the asymmetries, which are actually

asymmetries in reaction cross sections, stable luminosity and polarization monitoring are irreducible. Since we are searching for asymmetries of the order of  $\sim 1\%$ , the luminosity monitoring must be precise and stable. Towards this end, scaler boards for 120 bunches have been developed and commissioned in gold-gold collisions. This special monitoring program<sup>10)</sup> has been developed especially to show zero asymmetry measurements using gold beams.

In addition, we are preparing for the exploratory measurements at the 12 o'clock intersection to search for nonzero  $\mathcal{A}_N$  in inclusive photon production in the extremely forward direction, where sizable asymmetry is predicted based on the large asymmetries observed in the Fermi lab. If  $\mathcal{A}_N$  is nonzero, we can use it to commission the operation of the spin rotators, which are to be fully installed next year. With spin rotators, the spin direction at collision points is going to be completely transparent to the rest of the rings. We should be able to confirm full longitudinal polarization by observing the nonexistence of transverse asymmetry,  $\mathcal{A}_N$ .

The data analyses are in progress at the RHIC Computing Facility (RCF) and the PHENIX Computing Center in Japan (CC-J).<sup>11)</sup> A database management system has been carefully chosen to ensure identical references of calibration constants at both RCF and CC-J.<sup>12)</sup> Duplication facilities for the data tapes are well established at RCF, and weekly shipments of data tapes have been arranged. Detailed descriptions of the progress of CC-J and the results from both RCF and CC-J can be found in this volume.

Towards more precise knowledge of the hadron reactions using perturbative quantum chromodynamics, we have been continuing global analysis of data from polarized lepton scattering especially in the area of error estimation for the obtained parton distributions.<sup>13)</sup> We also started an involvement in BELLE collaboration in KEK to determine any spin dependence in quark fragmentation functions.

### References

- 1) M. Ishihara and G. Bunce: RIKEN Accel. Prog. Rep. **34**, 227 (2001).
- 2) K. Kurita et al.: RIKEN Accel. Prog. Rep. **35**, 226 (2002).
- 3) J. Tojo et al.: RIKEN Accel. Prog. Rep. **35**, 221 (2002).
- 4) O. Jinnouchi et al.: RIKEN Accel. Prog. Rep. **35**, 228 (2002).
- 5) D. E. Fields: RIKEN Accel. Prog. Rep. **35**, 229 (2002).
- 6) H. Kobayashi et al.: RIKEN Accel. Prog. Rep. **35**, 232 (2002).
- 7) A. Taketani et al.: RIKEN Accel. Prog. Rep. **35**, 224 (2002).

\* Brookhaven National Laboratory, USA

- 
- 8) H. D. Sato et al.: RIKEN Accel. Prog. Rep. **35**, 225 (2002).
  - 9) K. Okada et al.: RIKEN Accel. Prog. Rep. **35**, 222 (2002).
  - 10) Y. Goto et al.: RIKEN Accel. Prog. Rep. **35**, 220 (2002).
  - 11) T. Ichihara et al.: RIKEN Accel. Prog. Rep. **35**, 236 (2002).
  - 12) S. Yokkaichi et al.: RIKEN Accel. Prog. Rep. **35**, 238 (2002).
  - 13) Y. Goto et al.: RIKEN Accel. Prog. Rep. **35**, 188 (2002).

# Measurement of neutral pion transverse momentum distributions at $\sqrt{s_{NN}} = 130$ GeV Au+Au collisions

H. Torii,\* A. Bazilevsky, H. En'yo, Y. Goto, K. Imai,\* and N. Saito, for the PHENIX Collaboration

One of the proposed QGP signatures is the jet-quenching effect.<sup>1)</sup> In the Quantum Chromo Dynamic (QCD) calculation, the scattered partons arising from collisions are predicted to lose greater energy in the QGP matter than in the hadron matter. The hard  $\pi^0$  fragmented from the jet can be used as a probe to detect the energy loss in the QGP matter. Below, we present the result of  $\pi^0$  measurement at  $\sqrt{s_{NN}} = 130$  GeV Au+Au collisions.

The PHENIX<sup>2)</sup> experiment is one of four experiments being conducted at RHIC. In 2000, RHIC produced collisions of gold ions at beam energies of up to 65 GeV per nucleon with  $5 \times 10^{25} \text{ cm}^{-2} \text{ sec}^{-1}$  luminosity. The two photons decayed from  $\pi^0$  were measured by the PHENIX EMCAL<sup>3)</sup> with  $-0.35$  to  $0.35$  rapidity coverage. To identify photons, we applied time-of-flight and shower profile cuts, which helped reduce the nonphoton background by a factor of 2 to 20 depending on the energy region. After combinatorial background subtraction, and acceptance and efficiency corrections,<sup>4)</sup> the  $\pi^0$  yields were obtained in different centrality collisions.

Figure 1 shows the yield per event as a function of  $p_T$  for 60–80% and 0–10% centrality event data. In the

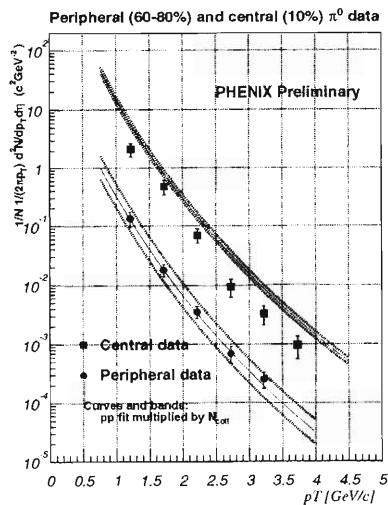


Fig. 1. The yields per collision for  $\pi^0$  as a function of  $p_T$  for 60–80% (lower squares) and 0–10% (upper squares) centrality event samples with references (line) to the yield per collision in N+N collisions of  $\pi^0$  scaled up by  $\langle N_{binary} \rangle$ . The error bars indicate the quadrature sums of systematic and statistical errors, and bands of reference indicate the uncertainty in the N+N reference and in the determination of  $\langle N_{binary} \rangle$ .

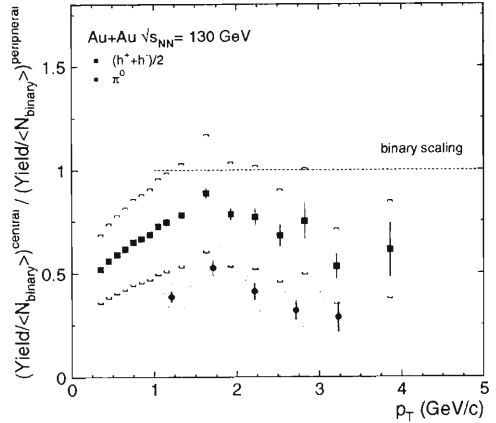


Fig. 2.  $\pi^0$  (square) and  $(h^+ + h^-)/2$  (circle) ratio of yield per event in the central to that in the peripheral Au+Au collisions as a function of  $p_T$ , with divided by  $\langle N_{binary} \rangle$  for that class. The surrounding bands (shaded for  $\pi^0$ 's, brackets for  $(h^+ + h^-)/2$ ) are the quadrature sums of (i) the parts of the systematic errors on the spectra that do not cancel in the ratio, and (ii) the uncertainty in  $\langle N_{binary} \rangle$ .

peripheral, the data shows consistency with the  $p + p$  data scaled by the number of binary collisions ( $= 20$ ), which is determined using the Glauber model. Figure 2 shows the ratio of yield per collision in the central to that in the peripheral, each divided by  $\langle N_{binary} \rangle$ . The ratio in the  $p_T$  lower than 2 GeV, which is dominated by soft  $\pi^0$ , obeys  $\langle N_{participant} \rangle$  scaling, so that the ratio is obviously smaller than 1. In higher  $p_T$ , the  $\pi^0$  ratio shows a significant suppression from  $\langle N_{binary} \rangle$  scaling. The square shown in the figure is the ratio for charged hadrons<sup>5)</sup> which also indicates suppression.

In conclusion, we observed a significant suppression of the  $\pi^0$  yield in central collisions relative to out expectation from binary scaling in higher  $p_T$ , where the hard  $\pi^0$  from the jet dominates.

## References

- 1) X. N. Wang and M. Gyulassy: Phys. Rev. D **44**, 3501 (1991).
- 2) G. P. Morrison et al.: Nucl. Phys. A **638**, 565c (1998).
- 3) E. Kistenev et al.: Proc. 5th Int. Conf. Calorimetry in High Energy Physics, New York, USA, 1994-9 ~ 10 (World Scientific, 1994), p. 211; H. Torii et al.: RIKEN Accel. Prog. Rep. **33**, 168 (2000); H. Torii et al.: RIKEN Accel. Prog. Rep. **35**, 243 (2002).
- 4) T. Sakaguchi et al.: RIKEN Accel. Prog. Rep. **34**, 261 (2001).
- 5) K. Adcox et al.: nucl-ex/0109003, accepted to Phys. Rev. Lett. **88**, 022301 (2002); G. David et al.: nucl-ex/0105014.

\* Kyoto University

# Measurement of the transverse energy distributions in Au+Au collisions at $\sqrt{s_{NN}} = 130$ GeV

A. Bazilevsky, for the PHENIX Collaboration

The PHENIX detector<sup>1)</sup> at the Relativistic Heavy Ion Collider (RHIC) at Brookhaven National Laboratory, is designed to measure the properties of nuclear matter at very high temperatures and energy densities and to search for new phenomena. Many interesting results were obtained from PHENIX experiment in the first RHIC run with Au-Au collisions at  $\sqrt{s_{NN}} = 130$  GeV.<sup>2)</sup>

Transverse energy ( $E_T$ ) measurements enable excellent characterization of the nuclear geometry of a reaction on an event-by-event basis and are sensitive to the underlying reaction dynamics.<sup>3)</sup>

The present measurements of  $E_T$  are made using a part of the electromagnetic lead/scintillating tile calorimeter<sup>4)</sup> (EMCal). For  $E_T$  measurements at mid-rapidity in the collider, the EMCal acts as a thin but effective hadronic calorimeter. For example, charged pions with  $p_T \leq 0.35$  GeV/c, kaons ( $p_T \leq 0.64$  GeV/c) and protons ( $p_T \leq 0.94$  GeV/c)— $p_T$  values which are near or above  $\langle p_T \rangle$  for all 3 cases—stop (*i.e.*, deposit all their kinetic energy) in the EMCal.

The raw spectrum of measured transverse energy,  $E_{T\text{EMC}}$ , in the fiducial aperture of the PHENIX EMCal for Au+Au collisions at  $\sqrt{s_{NN}} = 130$  GeV is shown in Fig. 1 (upper scale). The lower scale cor-

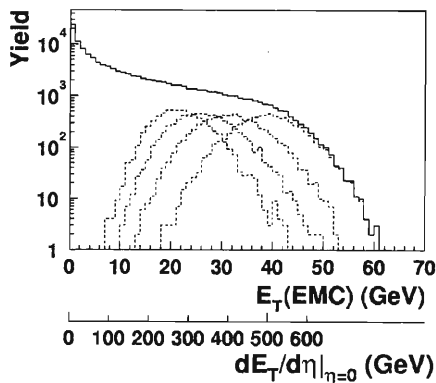


Fig. 1. The raw  $E_{T\text{EMC}}$  distribution (upper scale) and total hadronic  $dE_T/d\eta|_{\eta=0}$  (lower scale). The solid line is the minimum bias distribution; the dashed lines correspond to the distributions for the four centermost bins,<sup>6)</sup> 0–5% to 15–20%.

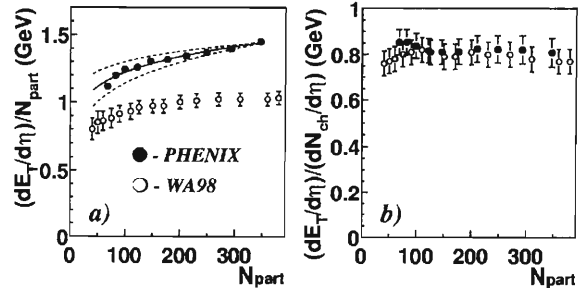


Fig. 2. (a) Transverse energy density per participant  $dE_T/d\eta|_{\eta=0}/N_{\text{part}}$  for Au+Au collisions at  $\sqrt{s_{NN}} = 130$  GeV as a function of  $N_{\text{part}}$ , the number of participants, compared to data from WA98<sup>7)</sup> for Pb+Pb collisions at  $\sqrt{s_{NN}} = 17.2$  GeV. (b) PHENIX  $dE_T/d\eta|_{\eta=0}/dN_{ch}/d\eta|_{\eta=0}$  versus  $N_{\text{part}}$ , compared to WA98.

responds to the hadronic  $dE_T/d\eta|_{\eta=0}$  in the full azimuth.<sup>5)</sup> For the most central 5% of the inelastic cross section  $\langle dE_T/d\eta|_{\eta=0} \rangle = 503 \pm 23$  GeV.

Figure 2(a) shows the transverse energy density per participating nucleon. It grows faster with the number of participants  $N_{\text{part}}$ <sup>6)</sup> than at SPS<sup>7)</sup> keeping  $\langle E_T \rangle / \langle N_{ch} \rangle$  at a constant value of approximately 0.8 GeV (Fig. 2(b)). This indicates that the additional energy density is achieved mainly by an increase in particle production rather than by an increase in transverse energy per particle.

## References

- 1) D. Morrison for the PHENIX Collaboration: Nucl. Phys. A **638**, 565 (1998).
- 2) W. A. Zajc et al.: nucl-ex/0106001; Nucl. Phys. A **698**, 39 (2002).
- 3) For example, Proc. Quark Matter 1984, edited by K. Kajantie (Springer, Berlin 1985); Proc. Quark Matter 1987, edited by H. Satz, H. J. Specht, and R. Stock.
- 4) G. David et al.: IEEE Trans. Nucl. Sci. **43**, 1491 (1996); IEEE Trans. Nucl. Sci. **45**, 692 (1998).
- 5) PHENIX Collaboration, K. Adcox et al.: Phys. Rev. Lett. **87**, 052301 (2001).
- 6) PHENIX Collaboration, K. Adcox et al.: Phys. Rev. Lett. **86**, 3500 (2001).
- 7) WA98 Collaboration, M. M. Aggarwal et al.: Eur. Phys. J. C **18**, 651 (2001).

## Spin monitoring for first polarized proton collisions

Y. Goto, A. Bazilevsky, G. Bunce, H. En'yo, M. Grosse Perdekamp, O. Jinnouchi, H. Kobayashi, K. Kurita, N. Saito, H. D. Sato,\* A. Taketani, J. Tojo,\* and S. Yokkaichi

In 2001 we start asymmetry measurements with polarized proton collisions at RHIC. By using transversely polarized beams, the left-right asymmetry (single transverse-spin asymmetry),  $A_N = (\sigma_L - \sigma_R) / (\sigma_L + \sigma_R)$ , is measured, and by using longitudinally polarized beams, the asymmetry of parallel and anti-parallel cross sections (double longitudinal-spin asymmetry),  $A_{LL} = (\sigma_{++} - \sigma_{+-}) / (\sigma_{++} + \sigma_{+-})$ , is measured. Although one advantage of the asymmetry measurements is the cancellation of the detector and beam asymmetry, this leaves systematic uncertainty in final error evaluation.

In the RHIC polarized proton collider, each bunch in the RHIC rings is filled independently so that the pattern of polarization direction for the bunches can be arranged to yield all possible spin combinations for the colliding bunches. This enables successive measurements of parallel and anti-parallel cross sections in the  $A_{LL}$  measurement, and of angular distribution in the  $A_N$  measurement. It greatly reduces time-dependent uncertainty.

In these measurements, bunch-by-bunch monitoring of beam conditions and crossing-by-crossing monitoring of collisions are indispensable. This is a new development which is not required in the heavy-ion collisions. First, by determining the bunch number of each bunch, we can compare bunch-by-bunch information provided by the RHIC accelerator and the RHIC polarimeter.<sup>1)</sup> Polarization information from the polarimeter is one of the most primitive elements of the asymmetry measurements. The polarization direction must be confirmed by comparing the intended polarization pattern provided by the accelerator and the polarization values from the polarimeter. Another one of the most primitive elements is the luminosity information. One method of the luminosity measurement is given as a product of the bunch currents of two rings,

the blue ring and the yellow ring, provided by the accelerator. This is an appropriate reference to compare with the crossing-by-crossing scalers for the luminosity measurement implemented on the global trigger board ("GL1-P board") of the PHENIX detector.

The GL1-P scalers are four types of 32-bit scalers for each of the 120 crossings. The beam-beam counter, the normalization trigger counter, the zero degree calorimeter, and the electromagnetic calorimeter are planned to be used for these four types of scalers. For the luminosity measurement, these scalers should not have asymmetry, because they are used to normalize the number of events for the asymmetry measurement. To confirm that these scalers have no asymmetry, or to determine the upper limit of the asymmetry, it is necessary to compare four types of scalers with each other.

In the luminosity measurement, we investigate the GL1-P scalers, level-1 and level-2 trigger<sup>2)</sup> rates, bunch current products, and the ratios of these values. All of these are monitored crossing-by-crossing, and their time evolutions are tracked. We need to investigate their stability, and define their acceptable range. One useful data for these purposes is the crossing vertex distribution.

All of these monitoring functions are implemented in the PHENIX-standard on-line monitor program. It checks whether all necessary information is ready, that all of the functions are consistent, and how stable they are, in order to maximize the given beam time of the RHIC polarized proton collisions.

### References

- 1) K. Kurita et al.: RIKEN Accel. Prog. Rep. **34**, 229 (2001); RIKEN Accel. Prog. Rep. **34**, 234 (2001).
- 2) K. Okada et al.: RIKEN Accel. Prog. Rep. **35**, 222 (2002).

---

\* Kyoto University

## Final result of analyzing power measurement of proton-carbon elastic scattering in CNI region at 22 GeV/c

J. Tojo,<sup>\*1</sup> I. Alekseev,<sup>\*2</sup> M. Bai,<sup>\*3</sup> B. Bassalleck,<sup>\*4</sup> G. Bunce,<sup>\*3</sup> A. Deshpande, J. Doskow,<sup>\*5</sup> S. Eilerts,<sup>\*4</sup> D. E. Fields,<sup>\*4</sup> Y. Goto, H. Huang,<sup>\*3</sup> V. Hughes,<sup>\*6</sup> K. Imai,<sup>\*1</sup> M. Ishihara, V. Kanavets,<sup>\*2</sup> K. Kurita, K. Kwiatkowski,<sup>\*5</sup> B. Lewis,<sup>\*4</sup> W. Lozowski,<sup>\*5</sup> Y. Makdisi,<sup>\*3</sup> H.-O. Meyer,<sup>\*5</sup> B. V. Morozov,<sup>\*2</sup> M. Nakanura,<sup>\*1</sup> B. Przewoski,<sup>\*5</sup> T. Rinkel,<sup>\*5</sup> T. Roser,<sup>\*3</sup> A. Rusek,<sup>\*3</sup> N. Saito, B. Smith,<sup>\*4</sup> D. N. Svirida,<sup>\*2</sup> M. Syphers,<sup>\*3</sup> A. Taketani, T. L. Thomas,<sup>\*4</sup> D. Underwood,<sup>\*7</sup> D. Wolfe,<sup>\*4</sup> K. Yamamoto,<sup>\*1</sup> and L. Zhu<sup>\*1</sup>

Analyzing power,  $\mathcal{A}_N$ , for hadronic elastic scattering in the coulomb-nuclear interference (CNI) region has been studied in order to probe the hadronic spin-flip amplitude  $r_5$ .<sup>1)</sup> Recent theoretical developments in  $r_5$ <sup>2)</sup> and requirements for high-energy proton polarimetry at BNL-RHIC<sup>3)</sup> motivated us to measure the  $\mathcal{A}_N$  for proton-carbon ( $pC$ ) elastic scattering in the CNI region at 22 GeV/c. We carried out the experiment BNL-AGS E950 in March 1999. The preliminary result is presented in Ref. 4. In this article, we report the final result of the  $\mathcal{A}_N$  measurement.

Our method of identifying  $pC$  elastic scattering in the CNI region detects only recoil carbons which have a very low energy ranging from 100 keV to a few MeV. We developed the detector system consisting of two symmetric left and right arms to measure the energy and the time-of-flight (TOF) of recoil carbons. Each detector arm consisted of a silicon strip detector (SSD) and a microchannel plate (MCP) assembly with a thin carbon foil. Details of the detector system, its performance and the experimental conditions are described in Ref. 5.

Recoil carbon events detected using the SSD were identified by the mass reconstructed from both the energy and the TOF. Recoil carbon events were selected with the 2.5- $\sigma$  mass resolution cut dependent on momentum transfer to determine the analyzing power. Momentum transfer  $t$  (GeV/c)<sup>2</sup> was determined from both the energy and the TOF, taking into account the weights of detector resolutions. The backgrounds of a prompt event, target fragment and excited states in the selected recoil carbon sample were estimated to be 1–13% dependent on momentum transfer. We recorded  $2.2 \times 10^7$  events of  $pC$  elastic scattering in  $0.009 < -t < 0.041$  (GeV/c)<sup>2</sup> to determine the  $\mathcal{A}_N$ .

Beam polarization was independently measured with the polarimeter of the experiment BNL-AGS E925,<sup>6)</sup> based on the analyzing power of  $pp$  elastic scattering at momentum transfer  $-t = 0.15$  (GeV/c)<sup>2</sup>,  $\mathcal{A}_N^{pp} = 0.0400 \pm 0.0048$  (sys). The  $pp$  elastic scatter-

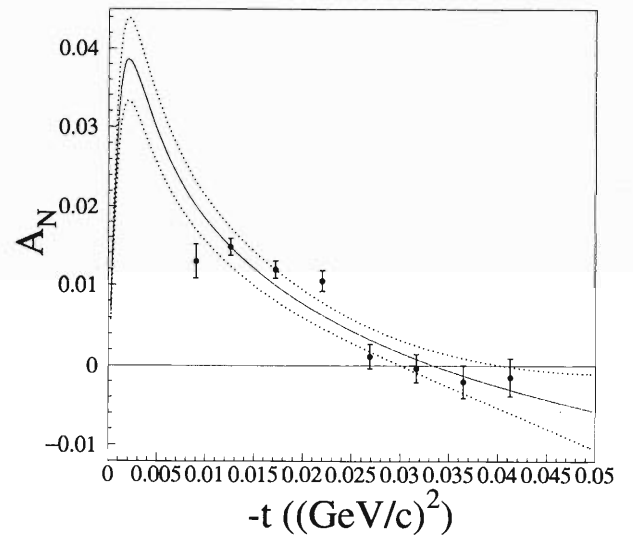


Fig. 1. Analyzing power for  $pC$  elastic scattering in the CNI region at 22 GeV/c. Bars indicate statistical errors only.

ing was identified by detecting both scattered protons and recoil protons. The beam polarization during the experiment was  $\mathcal{P}_B = 0.407 \pm 0.036$  (stat)  $\pm 0.049$  (sys).

The  $\mathcal{A}_N$  was determined as a function of  $t$ , using the “square-root formula.” The final result with the theoretically fitted curve<sup>2)</sup> is shown in Fig. 1. The solid curve represents the fitted result including the statistical and systematic errors. The dotted curves indicate the 1-sigma error band of the fitted result.

In summary, the  $\mathcal{A}_N$  for  $pC$  elastic scattering in the CNI region at 22 GeV/c was measured successfully. We established the principle of the polarimetry at RHIC using the CNI.

### References

- 1) N. H. Buttimore et al.: Phys. Rev. D **59**, 114010 (1999).
- 2) B. Z. Kopeliovich and T. L. Trueman: Phys. Rev. D **64**, 34004 (2000).
- 3) Proc. Workshop on Hadron Spin-Flip at RHIC Energies, Vol. 3, edited by T. D. Lee (RIKEN BNL Research Center, New York, 1997).
- 4) J. Tojo et al.: RIKEN Accel. Prog. Rep. **34**, 236 (2001)., J. Tojo et al.: AIP Conf. Proc. **570**, 790 (2001).
- 5) I. Alekseev et al.: RIKEN Accel. Prog. Rep. **33**, 170 (2000).
- 6) K. Krueger et al.: Phys. Lett. B **459**, 412 (1999); C. E. Allgower et al.: submitted to Phys. Rev. D.

\*1 Department of Physics, Kyoto University

\*2 Institute of Theoretical and Experimental Physics, Russia

\*3 Brookhaven National Laboratory, USA

\*4 Department of Physics and Astronomy, University of New Mexico, USA

\*5 Indiana University Cyclotron Facility, USA

\*6 Department of Physics, Yale University, USA

\*7 Argonne National Laboratory, USA

# Asymmetry measurement of charged hadrons at PHENIX

K. Okada, Y. Goto, N. Saito, H. En'yo, M. Grosse Perdekamp, K. Barish,\* W. Xie,\* and B. K. Nandi,\*

The first collisions of polarized proton beams will occur at RHIC in December 2001. Using these collisions, longitudinal spin asymmetry,  $A_{LL}$ , of charged hadrons will be measured in order to investigate gluon polarization. As shown in Fig. 1,  $A_{LL}$  is expected to be non-zero in the high-transverse-momentum region.<sup>1)</sup> This report describes the trigger scheme of the PHENIX detector system for selecting charged hadrons.

There are two levels of trigger, level-1 and level-2, in the PHENIX detector system. The level-1 trigger comprises signals of “fast” detectors which have fast response. The charged hadron trigger uses signals of an electromagnetic calorimeter (EMCal). Due to the requirement of a certain threshold value of deposit energy in the EMCal, not only charged hadrons but also electrons, photons, and anti-neutrons are selected. The level-2 trigger<sup>2)</sup> analyzes events in the event builder, and select events by using both “fast” and “slow” detectors. One of the functions of the level-2 trigger is analyzing the drift chamber (DC) data. Low-momentum charged particles which have a large curved trajectory and neutral particles ( $\gamma$ ,  $\bar{n}$ ) are rejected.

By assuming a beam luminosity of  $5 \times 10^{30} \text{ cm}^{-2} \text{ sec}^{-1}$ , the proton-proton collision rate is 250 kHz for a total cross section of 50 mb. According to the experience of heavy-ion collisions, the bandwidth of the event builder in the proton collisions will be limited to 3 kHz by performance of the sub-event buffer (SEB). Since we expect that a 1 kHz bandwidth will be allocated to charged-hadron events, a rejection power of 250 needs to be achieved in the level-1 trigger. From a detector simulation based on GEANT<sup>3)</sup> with a PYTHIA<sup>4)</sup>

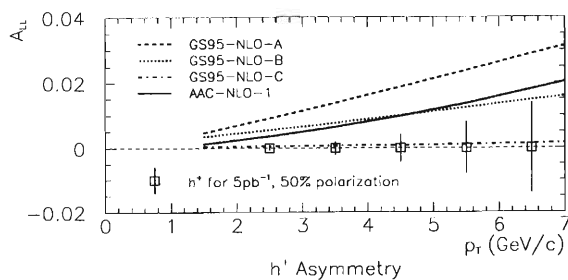


Fig. 1. Asymmetry of charged hadrons estimated by the use of various gluon polarization models. Statistical errors are shown by assuming an integrated luminosity of  $5 \text{ pb}^{-1}$  and a polarization of 50%.

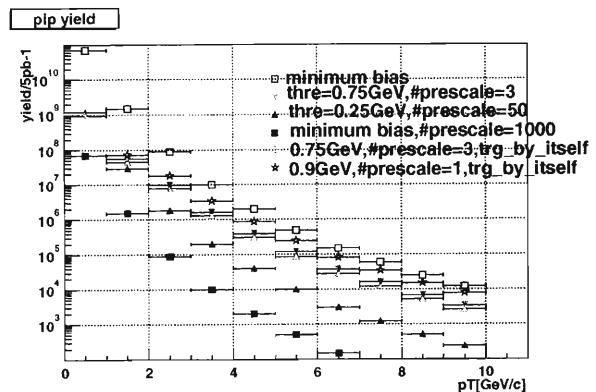


Fig. 2. Transverse momentum ( $p_T$ ) spectrum of  $\pi^+$  yield in this period of polarized-proton collisions. Stars indicate final-number evaluation of  $\pi^+$ .

event generator, the rejection powers of the level-1 trigger are estimated to be 189, 89, and 5 by requiring deposit energies in the EMCal of 0.9, 0.75 and 0.25 GeV, respectively. A rejection power of 250 will be achieved by setting the threshold value at slightly higher than 0.9 GeV. The next hurdle comes from the speed of data strage which is limited to 800 Hz. The level-2 trigger is required to decrease the event rate to 200 Hz as an allocation of charged-hadron events. The required rejection power is 5. This is estimated by simulation with single muons. For the events that survived the level-1 trigger with a threshold value of 0.9 GeV, the rejection power is 5.9, which satisfies the requirement of the level-2 trigger.

Figure 2 shows yield estimation of  $\pi^+$ 's in this period of polarized-proton collisions, where “trg\_by\_itself” means further event selection by off-line analysis to remove trigger bias after the trigger selection described above. These show a final-number evaluation of  $\pi^+$  in this period. Statistical errors in Fig. 1 reflect the final numbers. Many sufficiently charged hadrons should be collected to distinguish various models of the gluon polarization with  $5 \text{ pb}^{-1}$  total luminosity.

## References

- 1) A. Bazilevsky et al.: RIKEN Accel. Prog. Rep. 34, 243 (2001).
- 2) PHENIX Collaboration: submitted to Nucl. Instrum. Methods Phys. Res.
- 3) CERN Program Library Long Writeup W5013 (1993).
- 4) T. Sjöstrand: Comput. Phys. Commun. 82, 74 (1994).

\* University of California, USA

# Parity violation at RHIC in jet production

J. Murata

The author developed a simulation tool POLBY as a plug-in program for PYTHIA in the year 2000, aiming at studies of parity violation via new interaction beyond the standard model.<sup>1,2)</sup> Using PYTHIA + POLBY, the Drell-Yan process was studied as a first step. Although the Drell-Yan process is simple and clean, we need to examine the jet production process, which has a large production cross-section because of the small yield in the Drell-Yan process. In case of the Drell-Yan process, all the interactions we need to consider are the standard model  $\gamma^*/Z^0$ , the contact interaction, and their interference terms. In contrast, we need to take into consideration QCD,  $\gamma^*$ ,  $Z^0$ ,  $W^\pm$ , the contact interaction, and their complex interference terms for the jet production process. In PYTHIA, above processes must be generated as independent subprocesses. This restriction causes a severe problem when we consider the interference terms between different subprocesses in PYTHIA because interference effects cannot exist if we distinguish the subprocesses. In case of the Drell-Yan process, we can use single subprocess, therefore, the interference effects can be automatically included.

Recently, POLBY was modified in order to restore quantum mechanics in the PYTHIA simulation for the jet production. In the modified POLBY, a hadronic spin asymmetry,  $A$ , is estimated using event-by-event asymmetry weight factor  $W(A)$ ;  $A = \frac{\sum_{i=event} W^i(A)}{\sum_{i=event} 1}$ . Here, the “events” are generated by PYTHIA subprocesses. The “interference correction” can be performed by  $W^i(A) \rightarrow W^i(A) \times \frac{\sum_{process=QCD,Weak,EM,CT} \sigma^{process}}{\sigma^{QCD}}$ . Then, if we use pure QCD subprocesses for the PYTHIA event generation, contributions from other processes on the asymmetry can be taken into account by summing up all of the processes. The mean value of the  $W(A)$  distribution gives us the final hadronic spin asymmetry. Due to the correction, the  $W(A)$  distribution is distorted and we can obtain the corrected asymmetry from the distorted distribution. As an example, parity violation around the Jacobean peak is examined. In Fig. 1, we can confirm the large contribution from the interference term on the parity violation around the Jacobean peak. The subprocess-separated plot in Fig. 1 shows that the  $q\bar{q}' \rightarrow q\bar{q}'$  subprocess dominates the parity violation at the W peak.

The simulation results can be compared with theoretical calculations (Fig. 2). The results from the present study and those of Virey<sup>1,3)</sup> are roughly in agreement with each other. The small differences can be understood by the difference in the choice of the polarized PDFs. Regarding the disagreement at the Jacobean peak, it can be under-

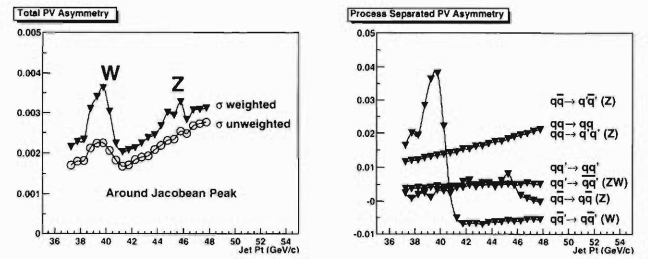


Fig. 1. Fine structure of the Jacobean peak on parity violating spin asymmetries.

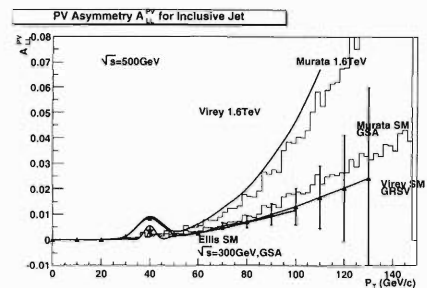


Fig. 2. Comparison with other theoretical calculations.

stood to be a binning effect. Virey estimated the asymmetry as  $A_{LL}^{PV}(Et = 40 \text{ GeV})$ , while we estimate it as  $\int_{40 \text{ GeV}}^{40 \text{ GeV} + \Delta} A_{LL}^{PV}(x) dx / \int_{40 \text{ GeV}}^{40 \text{ GeV} + \Delta} dx$ , where  $\Delta = 2 \text{ GeV}$ . There can also be a difference regarding the treatment of the interference terms. If we compare the present results and Ellis’ NLO calculation ( $\sqrt{s} = 300 \text{ GeV}$ ),<sup>4)</sup> we find that they show similar results at the Jacobean peak. Ellis uses the same GSA pol-PDF as that used the present study.

In order to use PYTHIA + POLBY as a standard model reference, the NLO calculation is indispensable. The NLO effect is difficult to take into account in an event generator. The situation is similar to the treatment of the interference. One large assumption for the interference correction is that, pure QCD process (generated events) and other processes must have the same final states. In principle, NLO correction using similar cross-section correction should be applicable. Theoretical calculations in NLO are now under way.<sup>4)</sup> We should and will be ready to examine experimental data from RHIC in the near future.

## References

- 1) J. Murata: RIKEN Accel. Prog. Rep. **34**, 246 (2001) and references therein.
- 2) J. Murata: in press in Czech. J. Phys. **52**, Suppl. A (2002); hep-ex/0110069.
- 3) P. Taxil and J.-M. Virey: hep-ph/0109094.
- 4) J. Ellis, S. Moretti, and D. A. Ross: hep-ph/0102340.

## Operation of the PHENIX muon identifier

A. Taketani, V. Cianciolo,<sup>\*1</sup> H. En'yo, G. Gogiberidze,<sup>\*2</sup> A. Glenn,<sup>\*2</sup> K. Imai,<sup>\*3</sup> M. Ishihara,  
L. Kotchenda,<sup>\*4</sup> Y. Mao,<sup>\*5</sup> J. Newby,<sup>\*2</sup> K. Read,<sup>\*1,\*2</sup> N. Saito, H. D. Sato,<sup>\*3</sup>  
S. Sorensen,<sup>\*2</sup> L. Villatte,<sup>\*2</sup> G. Young,<sup>\*1</sup> for the PHENIX Collaboration

The muon identifier (MuID) of the PHENIX experiment has been installed.<sup>1)</sup> We commissioned a part of the south MuID in 2000.<sup>2)</sup> The full south muon arm has been commissioned with Au-Au  $\sqrt{s_{NN}} = 200$  GeV as well as other PHENIX subsystems. This article describes the gas system and high-voltage (HV) system operations. We have been correcting data from the south arm which consists of the MuID and the Muon Tracking detector.

The muon arm is expected to measure the gluon polarization by identifying  $J/\Psi$  as a part of this year's RHIC spin program.<sup>3)</sup> The major role of the MuID detector is to identify the muon in the trigger and reconstruction programs.<sup>4)</sup> The MuID covers 10 to 35 degrees in  $\theta$  and 360 degrees in  $\phi$  at 7 meters from the interaction point with the sandwiching of five absorber steel plates and proportional tubes.<sup>5)</sup> The detectors are located in the forward and backward regions, so-called south and north arms.

Each chamber of the MuID panels is separated into two gas volumes.<sup>1)</sup> One is the primary volume that include anode wires. The  $\text{CO}_2/i\text{-C}_4\text{H}_{10}$  (92.5/7.5 percent) gas flows into it. The south arm has a volume of  $25\text{ m}^3$  as the primary volume. The flow rate is one exchange volume per day and half of the gas is recirculated after being checked for the  $\text{O}_2$  and  $\text{H}_2\text{O}$  contamination. The another volume is the secondary volume which surrounds the primary volume. It is filled with the  $\text{N}_2$  to keep the electronics clean and dry. Also, it is useful to dilute the flammable gas component in the case of leakage from the primary volume. The  $\text{N}_2$  flow rate is 40 l/minute for the south arm. No  $\text{N}_2$  are flowed into the north arm secondary volume. The north arm primary volume has been flowed with  $\text{N}_2$  to maintain the chamber in good condition during this year. The flow rate, recirculation rate, chamber head pressure and outlet pressure are monitored by a computer controlled system. If a readout value exceeds a certain threshold, appropriate action(s) will be initiated automatically, as well as warning issued to the PHENIX shift crews. For example, if the chamber head pressure is too high, then the gas flow into the primary volume will be shut off. The gas system is checked by the shift crew every four hours. The gas system has been in the stable operation since May 2001. A few parts have failed during the operation, but they were

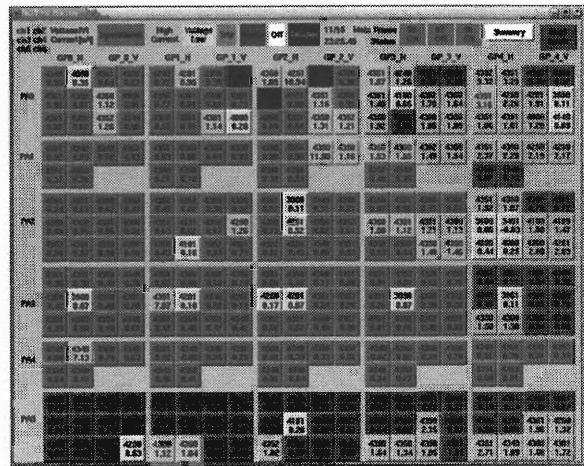


Fig. 1. Monitor display.

replaced or recalibrated within the minimum shutdown period. All readout values are logged in the database, which is useful for monitoring and diagnostic.

There are 300 HV channels for the south arm. Each channel can be controlled individually. Parameters to be controlled are target voltage, trip current limit, and ramp up/down rate. It is difficult to control these 300 HV channels manually, therefore we use a semi-automatic control system. The system consists of a GUI part and a control program part which receives the setting parameters from the GUI and communicates with the HV power supply. Also, the GUI part contains the status of the each channels, and displays them. Figure 1 shows the monitor display. Each square box corresponds to an individual HV channel and indicates the measured voltage and current by values and state such as stable, trip, ramp, and high current by color. The control program has five major functions. (1) Turn on/off the power supply. (2) Recover from trip. (3) Log HV status for offline study. (4) Protect from frequent trips and sparks. (5) Protect from steady high current due to the beam condition. Functions (4) and (5) can be adjusted according to the data from (3) for stable operation. The HV system has been operated since July 2001.

### References

- 1) A. Taketani et al.: RIKEN Accel. Prog. Rep. **33**, 166 (2000).
- 2) A. Taketani et al.: RIKEN Accel. Prog. Rep. **34**, 230 (2001).
- 3) H. D. Sato et al.: RIKEN Accel. Prog. Rep. **34**, 244 (2001).
- 4) Y. Mao et al.: RIKEN Accel. Prog. Rep. **34**, 242 (2001).
- 5) Y. Mao et al.: RIKEN Accel. Prog. Rep. **30**, 36 (1997).

<sup>\*1</sup> Oak Ridge National Laboratory, USA

<sup>\*2</sup> University of Tennessee, USA

<sup>\*3</sup> Kyoto University

<sup>\*4</sup> State InterPhysica, Russia

<sup>\*5</sup> Beijing University, China

## Performance of the PHENIX muon identifier

H. D. Sato,<sup>\*1</sup> V. Cianciolo,<sup>\*2</sup> H. En'yo, A. Glenn,<sup>\*3</sup> G. Gogiberidze,<sup>\*3</sup> T. Ichihara, K. Imai,<sup>\*1</sup> K. Kurita, Y. Mao,<sup>\*4</sup> J. Newby,<sup>\*3</sup> K. Read,<sup>\*2,\*3</sup> N. Saito, S. Sorensen,<sup>\*3</sup> A. Taketani, L. Villatte,<sup>\*3</sup> Y. Watanabe, S. Yokkaichi, and G. Young,<sup>\*2</sup> for the PHENIX Collaboration

A part of the South Muon Identifier (MuID) in the PHENIX Muon Spectrometer<sup>1)</sup> was operated last year.<sup>2)</sup> This year the entire South MuID has been operated successfully for Au + Au nucleus collisions at  $\sqrt{s_{NN}} = 200$  GeV.<sup>3)</sup>

We have implemented the so-called NIM-logic-trigger<sup>4)</sup> to obtain cosmic ray data for calibration purposes. Using the cosmic ray data, the chamber efficiency was found to be approximately 95% for each plane. HV excitation curves for efficiencies were measured and good plateaus were found between 4300 V to 4500 V, in which range the actual operation voltages are set. Discriminator-threshold curves were also measured which show no threshold dependence for efficiencies between 70 mV and 120 mV. The operation threshold is set to 90 mV. Below 70 mV, noise becomes significant. Using cosmic rays, we have also confirmed that the chamber geometry is as we expected, by considering the residual distributions for all channels.

The entire South MuID has successfully been operated for Au + Au collisions at  $\sqrt{s_{NN}} = 200$  GeV since July 2001. There have been no major problems in the gas system, high-voltage supplies or online-monitor software.<sup>5)</sup> Figure 1 shows the correlation between the number of hits in MuID and the charge sum in the

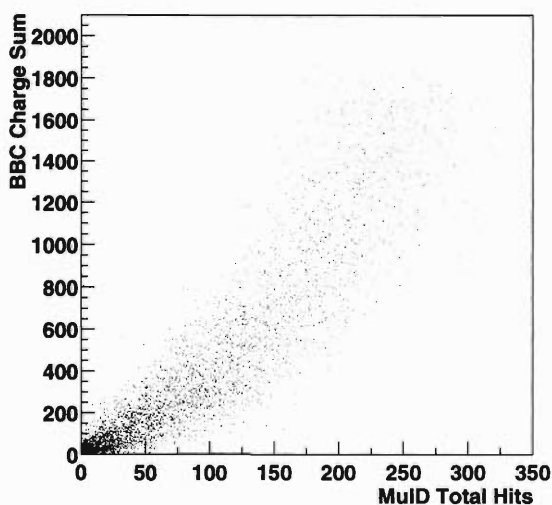


Fig. 1. Correlation between the total number of hits in MuID and the charge sum in the beam-beam counter (BBC).

beam-beam counter which covers  $3.1 < |\eta| < 4$ , where  $\eta$  is the pseudo-rapidity of a charged particle. This good correlation indicates that MuID is finding collisions.

Figure 2 shows the comparison of hit rates for each channel on the one-panel plane between real data and the simulation. A part of the simulation data was produced using the large LINUX farm in the RIKEN Computer Center in Japan (CCJ). They agree reasonably well. The numbers of reconstructed roads were also compared and again real data and the simulation agree well, which indicates that we understand the detector satisfactory and there is no major concern regarding either hardware or software.

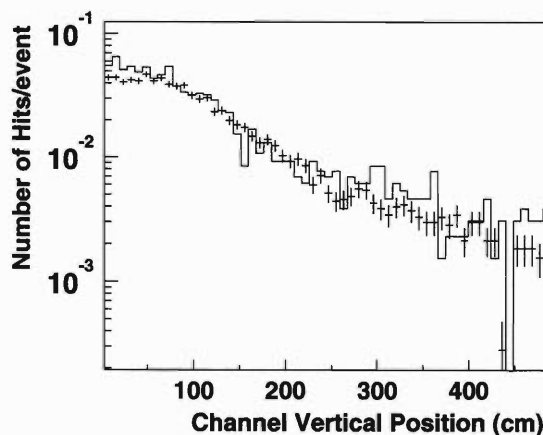


Fig. 2. Number of hits per event for each channel on the 4th horizontal plane, upper West panel. Lines indicate simulation and points indicate real data with statistical errors.

### References

- 1) <http://www.phenix.bnl.gov/>
- 2) A. Taketani et al.: RIKEN Accel. Prog. Rep. **34**, 230 (2001).
- 3) H. D. Sato for the PHENIX Collaboration: 1st Joint Meet. of the Nuclear Physics Divisions of APS and JPS, Hawaii, USA, Oct. (2001).
- 4) K. Read for the PHENIX Collaboration: 1st Joint Meet. of the Nuclear Physics Divisions of APS and JPS, Hawaii, USA, Oct. (2001).
- 5) Detailed description of MuID infrastructure can be found in A. Taketani et al.: RIKEN Accel. Prog. Rep. **35**, 224 (2002).

\*1 Kyoto University

\*2 Oak Ridge National Laboratory, USA

\*3 University of Tennessee, USA

\*4 China Institute of Atomic Energy, China

## RHIC pC CNI polarimeter readout

K. Kurita, H. Spinka,<sup>\*1</sup> D. Underwood,<sup>\*1</sup> H. Huang,<sup>\*2</sup> Z. Li,<sup>\*2</sup> W. MacKay,<sup>\*2</sup> G. Mahler,<sup>\*2</sup> Y. Makdisi,<sup>\*2</sup> W. McGahern,<sup>\*2</sup> S. Rescia,<sup>\*2</sup> T. Roser,<sup>\*2</sup> G. Bunce,<sup>\*2</sup> G. Igo,<sup>\*3</sup> W. Lozowski,<sup>\*4</sup> I. Alekseev,<sup>\*5</sup> V. Kanavets,<sup>\*5</sup> D. N. Svirida,<sup>\*5</sup> H. En'yo, K. Imai,<sup>\*6</sup> J. Tojo,<sup>\*6</sup> N. Saito, D. E. Fields,<sup>\*7</sup> S. Dhawan,<sup>\*8</sup> and V. Hughes<sup>\*8</sup>

Polarized proton acceleration commissioning is under way at the Relativistic Heavy Ion Collider (RHIC) in Brookhaven National Laboratory. Polarimetry was one of the biggest issues in polarized acceleration since no technique was available when the polarized proton collision was planned at RHIC. We have led an R&D effort to achieve polarimetry and established a technique of monitoring the RHIC proton beams utilizing proton carbon elastic scattering in the Coulomb Nuclear Interference (CNI) region.<sup>1)</sup>

The CNI polarimeter determines the left-right asymmetry of the number of carbons scattered from an ultrathin microribbon carbon target<sup>2)</sup> by the proton beam. This target allows low-energy recoil carbons (as low as 100 keV) to come out of it and also minimizes the increase in beam emittance during the measurement. Although our target is the thinnest available, the carbon counting rate estimated for the full luminosity of the RHIC proton beam is of the order of 10 MHz. The CAMAC FERA-based data acquisition system that was used to confirm the feasibility of the CNI polarimeter in the RHIC ring with a much reduced number of beam bunches and intensity is not applicable since the dead time of the system is excessive and the system takes too long to accumulate sufficient statistics. To be able to measure the polarization at full luminosity without disturbing the beam, a new readout scheme is necessary. The statistics we need for one polarization measurement typically comprises twenty million events.

The requirements of the RHIC pC CNI polarimeter readout are the following.

- dead-time-less system operating at a 10 MHz event rate
- capability either to store or process 20 M events per measurement
- capability to reject overlapping events which may give rise to false asymmetry

It was found that the 8 bit and 420 MHz waveform digitizer developed at Yale University satisfies all the above requirements. Therefore, a prototype was fabricated for the last polarized proton commissioning and the functionality of the waveform digitizing part was

<sup>\*1</sup> Argonne National Laboratory, USA  
<sup>\*2</sup> Brookhaven National Laboratory, USA  
<sup>\*3</sup> University of California, Los Angeles, USA  
<sup>\*4</sup> Indiana University, USA  
<sup>\*5</sup> Institute for Theoretical and Experimental Physics, Russia  
<sup>\*6</sup> Kyoto University  
<sup>\*7</sup> University of New Mexico, USA  
<sup>\*8</sup> Yale University, USA

successfully confirmed using actual CNI recoil carbon signals. Figure 1 shows a typical waveform from the carbons.

The next step is how to deal with the huge amount of data flow in the order of 100 MB/sec. We have been developing two ways to deal with this issue. One way is to select carbons using memory look up table created to cut out the carbon kinematics (pulse height and the arrival time with respect to the RHIC RF clock) realized on Xilinx Vertex100 FPGA. During the last commissioning, we found that we can extract background-free carbons by applying only kinematic constraint. After the carbon identification is carried out, the number of carbons is counted with appropriate scalers programmed in the FPGA. WFD works as a selective scaler, thus it is not necessary to store large amounts of data (waveforms). The schematic diagram of the FPGA program is shown in Fig. 2. It is an elegant way to handle large amounts of data, but systematic errors must be evaluated using other methods.

The other way to deal with the data flow is to store all waveforms utilizing on-board random access memory (RAM). Xilinx provides a RAM driver library with a FPGA chip and the same software tools can be used to configure it. In the new version of the WFD, 128 MB DRAM is implemented on each module which takes care of four channels. Each waveform takes approximately 25 bytes and 20 million events with a total of 12 WFD modules (48 Si channels), which correspond to a total of 500 MB and approximately 40 MB per WFD board. Therefore, 128 MB DRAM on each module is more than sufficient for our application. We take advantage of the fact that the event rate is very high but the total amount of data to be buffered per measurement is sufficiently small to handle with the current RAM technology. This is the only method which

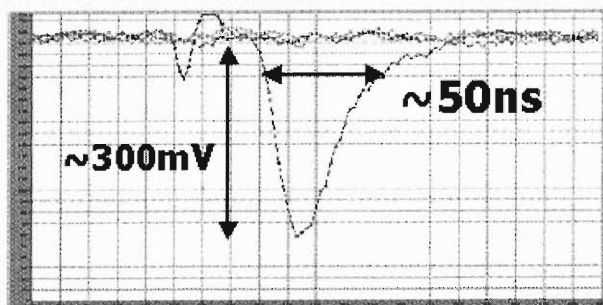


Fig. 1. A typical waveform from CNI recoil carbons.

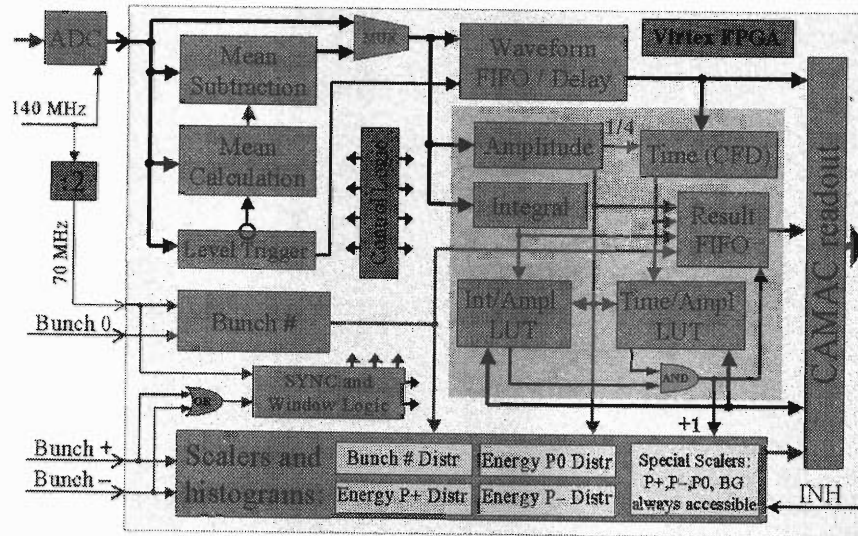


Fig. 2. Schematic diagram of the FPGA program.

allows us to analyze the waveforms and extract the asymmetry from them offline.

Thus far, the online processing FPGA program has been run and confirmed to extract the correct amplitude and the timing from waveforms. A memory look-up table will be created and tested at the beginning of the commissioning which will start in December, 2001. On the other hand, the RAM is incorporated in the current WFD hardware design but is still to be configured softwarewise. Therefore, we plan to debug the FPGA program with a limited number of waveforms which are available in the FPGA buffer. We can perform all necessary checking of the system except extraction of asymmetry directly from the full data set

(waveforms) offline.

The commissioning of the full-configuration RHIC-polarized proton acceleration starts from December, 2001 and the WFD performance will be thoroughly investigated. Upon successful commissioning, the first polarized proton collider experiments will be started at RHIC.

#### References

- 1) K. Kurita et al.: RIKEN Accel. Prog. Rep. **34**, 229 (2001).
- 2) W. R. Lozowski and J. D. Hudson: Nucl. Instrum. Methods Phys. Res. A **303**, 34 (1991).

## Results from RHIC polarimeter commissioning run 2000

O. Jinnouchi, K. Kurita, J. Tojo,<sup>\*1</sup> N. Saito, I. Alekseev,<sup>\*2</sup> D. N. Svirida,<sup>\*2</sup> D. E. Fields,<sup>\*3</sup> G. Bunce,<sup>\*4</sup> T. Roser,<sup>\*4</sup> H. Huang,<sup>\*4</sup> W. Glenn,<sup>\*4</sup> H. Spinka,<sup>\*5</sup> Z. Li,<sup>\*4</sup> W. Mackay,<sup>\*4</sup> G. Mahler,<sup>\*4</sup> Y. Makdisi,<sup>\*4</sup> W. McGahern,<sup>\*4</sup> S. Rescia,<sup>\*4</sup> T. Russo,<sup>\*4</sup> G. Igo,<sup>\*6</sup> W. Lozowski,<sup>\*7</sup> V. Kanavets,<sup>\*2</sup> D. Koehler,<sup>\*3</sup> D. Brown,<sup>\*8</sup> S. Dhawan,<sup>\*9</sup> V. Hughes,<sup>\*9</sup> R. Krisst,<sup>\*9</sup> H. En'yo, K. Imai,<sup>\*1</sup> A. Deshpande, Y. Goto, M. Ishihara, T. Ichihara, A. Taketani, and Y. Watanabe

In September 2000, spin commissioning using the polarized proton beam was carried out at the Relativistic Heavy Ion Collider (RHIC).<sup>1)</sup> The aim of this commissioning was to assess the feasibility of polarized proton acceleration and its polarization measurement for the p-p runs which are going to start from this year.

In order to accelerate the polarized proton, one set of helical dipole magnets called Siberian snakes<sup>2)</sup> was installed in the RHIC blue ring. In this case, the stable spin direction would be horizontal when a single snake turned on adiabatically after injection. The pC CNI polarimeter<sup>3)</sup> was also installed in the same ring (at the 12 o'clock position). A very thin carbon target was placed at the beam position. The recoiled carbons from pC elastic scatterings can be identified by the relation between their energies and the time of flight (TOF). Four Si detectors each equipped with 8 strips were installed obliquely, 15 cm from the target.

The fast analysis yielded the following results.

- (1) A vertical spin direction was observed with the snake off, with significant size.
- (2) A horizontal spin direction was observed when the snake was turned on.
- (3) Horizontal spin rotation was observed through the acceleration from injection energy.
- (4) No asymmetry at  $G\gamma \geq 61.3$  was observed.

In the upcoming spin run, the quick polarization measurement is required. The fast data acquisition with a scaler (counter) is our solution. It is realized with the wave form digitizer (WFD) which counts the selected carbon signals on board. Developing on the accurate and reliable algorithm for asymmetry calculation is urgent and indispensable, therefore further detailed analysis of the commissioning data is strongly needed.

Our analysis is based on mass particle identification. The simultaneous kinematic fit to  $\alpha$  and carbon loci in the ADC vs TOF distribution yields energy scale and T0 parameters for each Si strip. Carbon and  $\alpha$  masses, slewing effect, the distance between the target and the Si, and the dead layer depth on the Si surface have

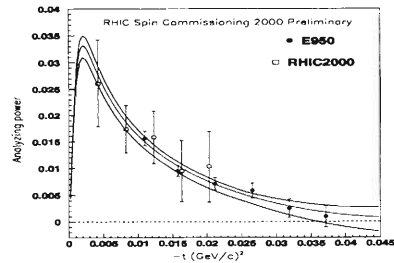


Fig. 1.  $-t$  dependence of the asymmetries, being normalized with the analyzing power from E950 result.

been measured and constrained. The energy and TOF values are converted into the mass. Mass distribution shows a clear separation of carbon from  $\alpha$  implying that extremely small  $\alpha$  contamination is expected.

It is also important to confirm that the measured carbons are elastically scattered-off. We investigate this from two aspects. The first is to see the slope parameter of the differential cross section as a function of the transferred momentum squared,  $-t$ . The obtained value is consistent with the elastic value from the other experiments. The second is to observe the energy dependencies of the recoiled carbon angles. The energy vs angle distribution well fits with the kinematic curve of the elastic one; inelastic scattering (4.4 MeV excitation state) has been clearly excluded. From the detector resolution study, the energy resolution is at most 10% for the whole energy range, so that it is reasonable to define the  $-t$  value only from energy. This is a profitable discovery as the WFD defines the asymmetry as a function of the energy this year. The raw asymmetry is obtained as a function of  $-t$  (Fig. 1). With the analyzing power determined from the E950 result,<sup>4)</sup> the polarization during the spin commissioning is extracted. The preliminary result using the typical run set yields  $P = A(t)/A_N(t) = 0.181 \pm 0.029$ , which has been depolarized after the AGS extraction ( $P = 33\%$ ).

From these experiences and results, we are sure to be successful in the upcoming spin run this year.

<sup>\*1</sup> Kyoto University  
<sup>\*2</sup> Institute of Theoretical and Experimental Physics, Russia  
<sup>\*3</sup> University of New Mexico, USA  
<sup>\*4</sup> Brookhaven National Laboratory, USA  
<sup>\*5</sup> Argonne National Laboratory, USA  
<sup>\*6</sup> University of California, USA  
<sup>\*7</sup> Indiana University, USA  
<sup>\*8</sup> New Mexico State University, USA  
<sup>\*9</sup> Yale University, USA

### References

- 1) K. Kurita et al.: RIKEN Accel. Prog. Rep. **34**, 229 (2001).
- 2) W. W. Mackay et al.: DESY-PROC-1999-03, p. 163.
- 3) K. Kurita et al.: RIKEN Accel. Prog. Rep. **34**, 234 (2001).
- 4) J. Tojo et al.: RIKEN Accel. Prog. Rep. **34**, 236 (2001).

## PHENIX muon tracker: Construction, year-2 operation and preliminary data analysis

D. E. Fields\*

The design of the PHENIX detectors has been optimized for a broad dynamic range from central A-A collisions (focusing on the generation, detection, and subsequent characterization of the quark-gluon plasma (QGP)) to  $\bar{p}$ - $\bar{p}$  collisions (measuring the helicity distributions of flavor-separated quarks and antiquarks, as well as the first *direct* measurement of the gluon polarization in the nucleon). In particular, the experiment will be able to identify exclusive leptons, photons, and high- $p_T$  hadrons with good momentum and energy resolution, as well as very accurate particle identification. In A-A collisions, rare probes are particularly intriguing, since they address some of the most pressing questions in heavy-ion physics, such as charmonium production and suppression and direct photon production. More details and current information on the PHENIX experiment can be found in Ref. 1, and a concise recent summary of the planned RHIC spin program can be found in Ref. 2.

Muons are an important probe of the physics for both the heavy ion and the spin program. The most interesting muons originate from the following sources: vector meson ( $J/\Psi$ ,  $\Upsilon$ , etc.) decays, Drell-Yan decays,  $W$ -decay, and heavy flavor (c and b) meson decays.

The muon tracking system (see Fig. 1) will enable measurement of the momentum and direction of flight of muons. This information will be used to reconstruct the invariant mass of dimuon pairs originating from the vertex. Mass resolution for the decay pairs from the Upsilon dictates a position measurement precision of 100 microns at each tracking station. In order to achieve this, cathode strip chambers (CSCs) with a honeycomb structure were chosen as the baseline design for the PHENIX muon tracker stations 1 and 3. Because of lower scattering length restrictions at station 2, the honeycomb structure was replaced by mylar foils, held taut by aluminum frames. The basic mechanical structure of a CSC is that of a conventional proportional wire chamber. However, rather than reading out the anode wires to obtain position resolution, a precise position coordinate is determined from the induced signal on cathode strips perpendicular to the anode wires. A detailed description of the final chamber design can be found in Ref. 3.

The South Muon tracking chambers were completed in the spring of 2000. Figure 2 shows the completed station one detectors being surveyed on a test wall after completion. The chambers were installed into the magnet successfully, integrated into the entire PHENIX system and are operating well as the first 200 GeV

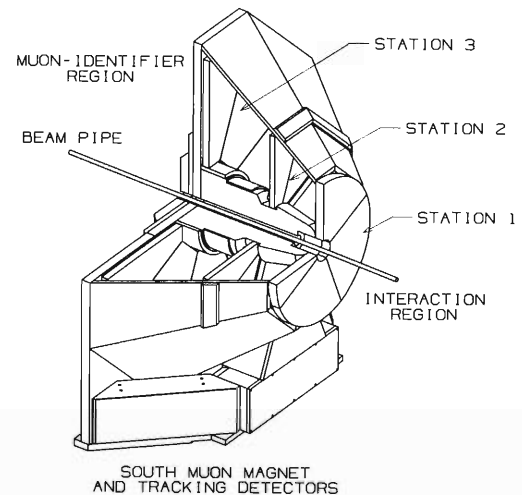


Fig. 1. The South Muon ARM tracking spectrometer. Muons from the intersection region, to the right, intercept the station 1, 2, and 3 detectors and proceed to the muon identifier detectors to the left (not shown).

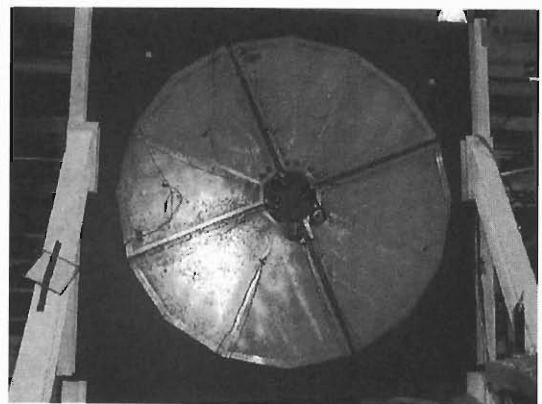


Fig. 2. Station 1 is built in four quadrants but is electrically divided into octants to match the octants of stations 2 and 3.

Au-Au data are being recorded. The operation of the detectors includes monitoring of the gas system, the high voltage systems, the low voltage system (for the front-end electronics (FEE)), the alignment system (for precise positioning) and finally the gain and pedestal calibrations, taken and recorded on a daily basis. This complex task including the monitoring of the performance of over 20,000 cathode readout channels has been developed in phases to achieve the smooth-running operation mode now in place.

Early test results from the chambers are very en-

\* University of New Mexico, USA

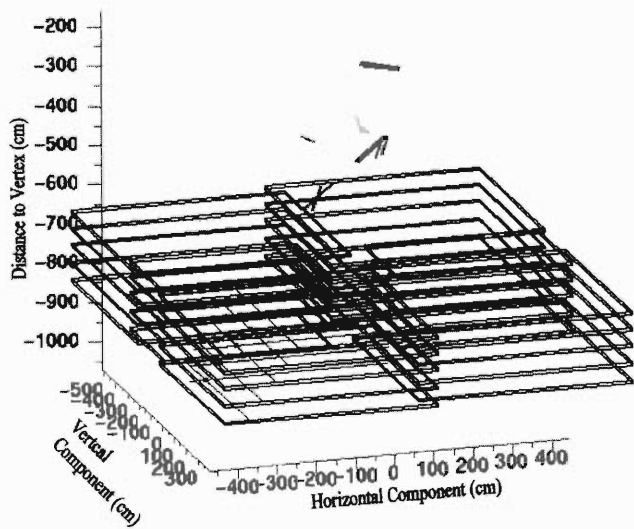


Fig. 3. Cosmic ray track in the South Muon Arm.

couraging. Fully instrumented station 2 octants were tested prior to installation using cosmic rays, and were found to achieve the desired position resolution. Real-data studies from the current 200 GeV Au+Au run have shown that resolutions very close to nominal have already been achieved. Figure 3 shows a track from cosmic triggers that is found in the tracker and matched to the muon identifier.

The North Muon Spectrometer is mechanically complete and is awaiting the next RHIC shutdown and delivery of the FEE system for installation and operation. This second arm will more than double the acceptance for high transverse momentum muon pairs.

#### References

- 1) <http://www.phenix.bnl.gov>
- 2) G. Bunce et al.: hep-ph/0007218.
- 3) PHENIX NIM, to be published.

## Geometry alignment of PHENIX Muon tracker

N. Kamihara,<sup>\*1</sup> H. Kobayashi, S. Batsouli,<sup>\*2</sup> M. L. Brooks,<sup>\*3</sup> N. Bruner,<sup>\*4</sup> D. E. Fields,<sup>\*4</sup> D. M. Lee,<sup>\*3</sup>  
M. X. Liu,<sup>\*3</sup> J. Murata, N. Saito, T.-A. Shibata,<sup>\*1</sup> W. Sondheim,<sup>\*3</sup> and A. Taketani

The PHENIX Muon arm has an important role in both spin and heavy-ion physics at RHIC. We can measure several features of the proton spin structure using the muon probe. For example, gluon polarization can be measured by the  $J/\psi$  and open heavy flavor decay. Quark polarization can be measured by the Drell-Yan process and W boson production. The Muon arm has capabilities to identify muons and measure their momentum. It covers the forward and backward region, which is  $1.1 \leq |\eta| \leq 2.4$ , the so-called south and north arm.

The PHENIX Muon consists of muon a identifier (MuID), muon magnets and a muon tracker (MuTr). A MuTr detector is located on the muon magnet. The muon magnet has a radial field and the incident charged particle bends on the plane which is perpendicular to the beam pipe. The MuTr detector consists of a cathode strip chamber. There are three layers of chambers which are separated 116 cm and 163 cm along the beam. Thus good alignment of each chamber position is essential for obtaining proper momentum resolution as well as calibration of each cathode strip.

One of the major goals of muon arm physics is to identify the quarkonium decaying into the  $\mu^+\mu^-$ , such as  $J/\psi$  and  $\Upsilon$ . Particularly for  $\Upsilon$ , it is interesting to distinguish between the different mass states ( $\Upsilon(1S)$  (9.46 GeV) from  $\Upsilon(2S+3S)$  (10.36 GeV)) to investigate Quark-Gluon Plasma. Thus, the required momentum resolution is 1 percent. The typical muon momentum from  $\Upsilon$  is 10 GeV. The displacement of the muon track in the middle layer in the MuTr detector due to the magnetic field is 1 cm. Thus, we need  $100 \mu\text{m}$  positioning accuracy relative to the other MuTr layers. Multiple scattering dominates the mass resolution of the  $J/\psi$ . The required position resolution is  $300 \mu\text{m}$  for separating  $J/\psi$  from  $\psi'$ .

MuTr mechanical installation in the PHENIX experimental hall was completed by the end of last year.<sup>1)</sup> The accuracy of the mechanical installation between stations is of 1 mm order. Alignment is important for high position resolution. Test chamber resolution using a prototype front-end electronics (FEE) at LANL in 1999 was  $\sigma = 165 \mu\text{m}$ ; the position resolution was determined by a simple center-of-gravity method.<sup>1,2)</sup>

An Optical Alignment System (OASys) monitors the second-layer position relative to the first and third layers every hour.<sup>3)</sup> The relative accuracy of the The OASys is about  $20 \mu\text{m}$ . The OASys can be used for short-term correction. The straight-track method will give us the reference alignment based on the tracking information.

We obtained many zero-magnetic field run data in beam collision time. Tracks of the charged particles are expected to be straight lines. The straight line is fitted to hits in single layers which have four to six cathode planes depending on the layer. The width of the residual distribution reflects the chamber spatial resolution of each hit and the average value corresponds to the geometrical accuracy of each layer construction. After obtaining a straight track segment in each layer, three segments are fitted in one track. The average of the fit residual reflects the relative position of the layers. Calibration and analysis are under way and a position resolution of  $100 \mu\text{m}$  is expected for the chamber.

### References

- 1) J. Murata et al.: RIKEN Accel. Prog. Rep. **34**, 237 (2001).
- 2) J. Murata et al.: RIKEN Accel. Prog. Rep. **33**, 165 (2000).
- 3) H. Kobayashi et al.: RIKEN Accel. Prog. Rep. **35**, 232 (2002).

---

<sup>\*1</sup> Tokyo Institute of Technology

<sup>\*2</sup> Columbia University, USA

<sup>\*3</sup> Los Alamos National Laboratory, USA

<sup>\*4</sup> University of New Mexico, USA

## First commissioning of the PHENIX south muon tracker: The gas system and the optical alignment system

H. Kobayashi, M. L. Brooks,<sup>\*1</sup> D. S. Brown,<sup>\*2</sup> N. Bruner,<sup>\*3</sup> D. E. Fields,<sup>\*3</sup> A. Hoover,<sup>\*2</sup> N. Kamihara,<sup>\*4</sup>  
D. Kim,<sup>\*5</sup> D. M. Lee,<sup>\*1</sup> M. Leitch,<sup>\*1</sup> M. X. Liu,<sup>\*1</sup> S. Pate,<sup>\*2</sup> N. Saito, T.-A. Shibata,<sup>\*4</sup>  
W. Sondheim,<sup>\*1</sup> J. Murata, R. Towell,<sup>\*1</sup> and K. Yongil<sup>\*5</sup>

The PHENIX south muon tracker is a subsystem in the south muon arm which consists of a muon identifier and a muon tracker. The muon tracker consists of three stations of cathode strip chambers aligned in the radial field magnet.

Following the mechanical installation of the chambers and electronics support structures, which was finalized in December 2000, the installation of the front-end electronics and the high-voltage system was carried out. Finally, in May 2001 the south muon magnet was installed in the interaction region of the PHENIX experimental hall. Figure 1 shows a picture taken when the south muon tracker was installed in the interaction region with full integration of chambers and electronics for the first time. The RIKEN team has taken responsibility for the design and construction of the chamber gas supply system and the optical alignment system. Both systems were installed during the period when the electronics were installed.

The muon tracker gas system uses a nonflammable gas mixture,  $\text{Ar} : \text{CO}_2 : \text{CF}_4 = 50 : 30 : 20$ , with recirculation of the return gas. The requirements and structure of the gas system are described in a previous ar-

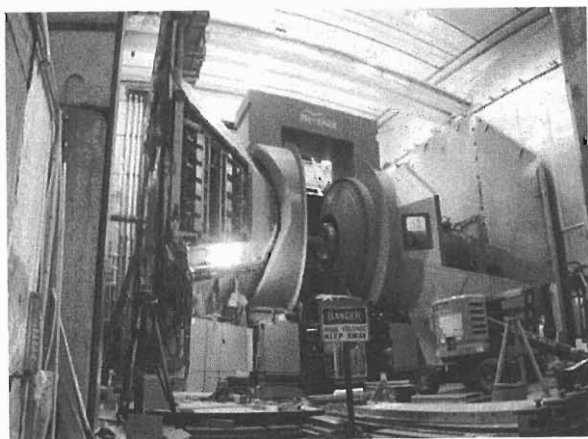


Fig. 1. Three stations of cathode strip chambers and their front-end electronics for the south muon tracker have been installed in the south muon magnet (left in the picture). The north muon tracker (right) will be installed in the summer of 2001.

ticle.<sup>1)</sup> The electronic read-out system of pressure and flow measurements was constructed using the ADAM 5000 system. This system is used for an alarm system and the values are collected by a Windows-based server and logged to the database. Oxygen contamination in the supply gas is monitored by an oxygen analyzer and proved to be less than 300 ppm in the non-recirculation mode, while it is at a maximum of 5 ppm in the fresh gas. There was a minor problem in the compressor which was used for the recirculation of the return gas. The compressor was replaced with a new one which has a smaller volume than the original. Since the replacement, the gas system has been running very stably.

The optical alignment system was designed<sup>1)</sup> for the purpose of real-time monitoring of the relative alignment between the three stations. Each optical alignment system unit consists of an optical fiber as a light source at station 1, a convex lens at station 2 and a video camera at station 3. A metal halide high-intensity discharge lamp was chosen for the base light source to meet the requirements for high-intensity white light, low infrared intensity and long lifetime of more than 6000 hours. There are 56 optical alignment system units mounted in the south muon tracker. Images from each CCD camera are captured once per hour, processed online and saved in a database. Figure 2 shows a three day history of focal image position measured by the optical alignment system. We observed a  $60 \mu\text{m}$  shift when the magnetic field of the spectrometer was switched on. Systematic analysis to clarify the alignment change detected in all 56 cameras is under way.

Deviation of the initial geometry alignment from the design value was expected to be less than a millimeter, because each chamber is constructed within a  $25 \mu\text{m}$  tolerance and the survey data after installation shows less than 1 mm of misalignment between stations. The correction of the misalignment can be achieved using straight tracks taken by field-off collision runs or field-off cosmic runs. The correction of the misalignment between the three stations is under way<sup>2)</sup> using the muon tracker reconstruction software.

We have been recording Au-Au collision data with the muon tracker since July 2001. Figure 3 shows the coincidence between the multiplicity of clusters in muon tracker station 1 and the total charge detected in the beam-beam counter measured for the Au-Au collisions at  $\sqrt{s_{NN}} = 200 \text{ GeV}$ . There is a clear positive

<sup>\*1</sup> Los Alamos National Laboratory, USA

<sup>\*2</sup> New Mexico State University, USA

<sup>\*3</sup> University of New Mexico, USA

<sup>\*4</sup> Tokyo Institute of Technology

<sup>\*5</sup> Yonsei University, Korea

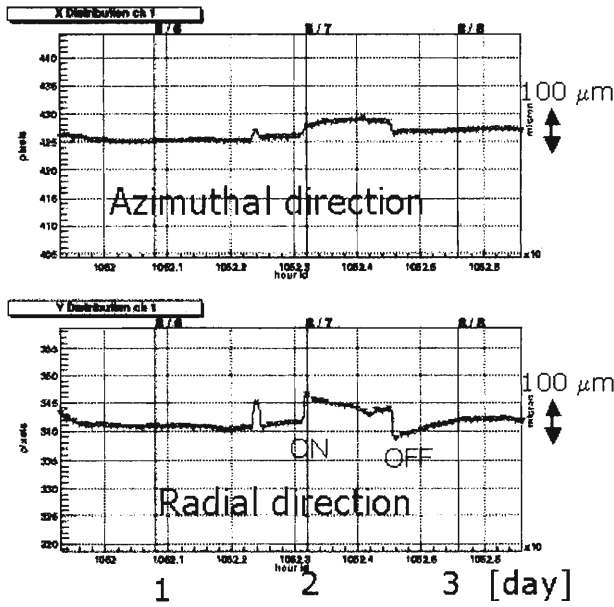


Fig. 2. History of focal image position for azimuthal direction (upper) and radial direction (lower). In the middle of the measured period in the plot, a  $60\ \mu\text{m}$  position shift caused by the spectrometer magnet ON/OFF was detected.

correlation as expected since the beam-beam counter covers the rapidity range of  $3 < |\eta| < 4$  while the muon tracker covers  $1.1 < |\eta| < 2.4$ .

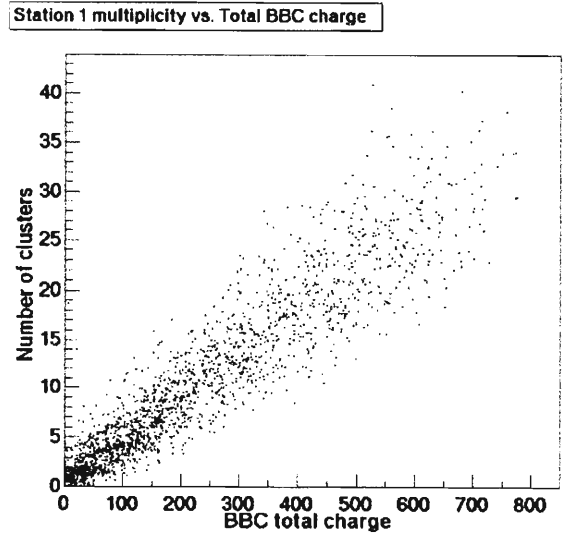


Fig. 3. Coincidence between multiplicity of clusters in muon tracker station 1 and total charge detected in the beam-beam counter measured in the Au-Au collisions at  $\sqrt{s_{NN}} = 200\ \text{GeV}$ .

#### References

- 1) J. Murata et al.: RIKEN Accel. Prog. Rep. **34**, 237 (2001).
- 2) N. Kamihara et al.: RIKEN Accel. Prog. Rep. **35**, 231 (2002).

# Analytical field calculation of helical magnets with an axially symmetric iron yoke

T. Tominaka,\* M. Okamura, and T. Katayama

The contribution of an axially symmetric iron yoke to the helical magnets is studied, as a basic study of the helical dipoles for the Relativistic Heavy Ion Collider (RHIC), with consideration of the analytical expressions of the magnetic fields due to a single helical current.<sup>1)</sup> In order to obtain rigorous expressions for the contribution of an axially symmetric iron yoke without saturation to the interior field of helical magnets, a three-dimensional potential problem is solved.<sup>2,3)</sup> Then, the calculation of the interior field of the helical dipole magnet is compared with other numerical calculations.<sup>4)</sup>

In this paper, SI (MKS) units are used. The magnetic induction  $B$ , the magnetic scalar potential  $\phi_m$  and the vector potential  $A$  are defined as follows,

$$B = -\mu\nabla\phi_m = \nabla \times A. \quad (1)$$

Similarly, the relation between the magnetic induction  $B$  and the magnetic field intensity  $H$  is defined as follows,

$$B = \mu_0(H + M) = \mu_0(1 + \chi_m)H = \mu_0\kappa_m H = \mu H, \quad (2)$$

where  $\mu$  is the absolute permeability,  $\chi_m$  is the magnetic susceptibility, and  $\kappa_m$  is the relative permeability.

In the case that a single helical current carrying conductor is located at a point ( $r = b$ ,  $\theta = 0$ ) in the  $z = 0$  plane placed inside a cylindrical hole in iron of  $\mu_2 = \kappa_m\mu_0$ , as shown in Figs. 1 and 2, the general form for the magnetic scalar potential  $\phi_1$  of region 1 ( $r < a$ ) is expressed as a sum of the contribution  $\phi_{1,coil}$  of a single helical current conductor and the contribution  $\phi_{1,iron}$  of an axially symmetric iron yoke. Since the terms of the modified Bessel function of the second kind,  $K_n(nkr)$ , are excluded by the condition that the origin be a regular point for the contribution of iron, the general solutions at  $z = 0$  for the magnetic scalar potential  $\phi_1$  and  $\phi_2$  of both regions can be written in the following forms with the unknown constants of  $A_n$ ,  $B_0$ , and  $B_n$ .

for  $b < r < a$ ,

$$\begin{aligned} \phi_1(r, \theta, z = 0) &= -\frac{I}{2\pi}\theta - \frac{I}{\pi}kb \sum_{n=1}^{\infty} I'_n(nkb)K_n(nkr) \sin n\theta \\ &\quad - \frac{I}{\pi} \sum_{n=1}^{\infty} A_n I_n(nkr) \sin n\theta. \end{aligned} \quad (3)$$

Similarly, for  $r > a$ ,

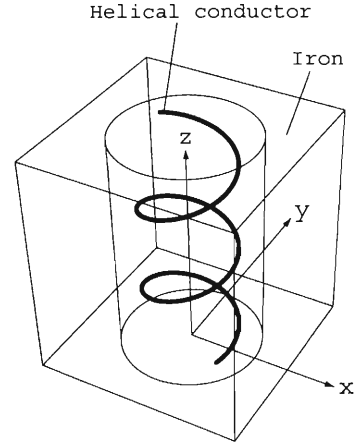


Fig. 1. Schematic view of a single helical coil placed inside a cylindrical hole in iron.

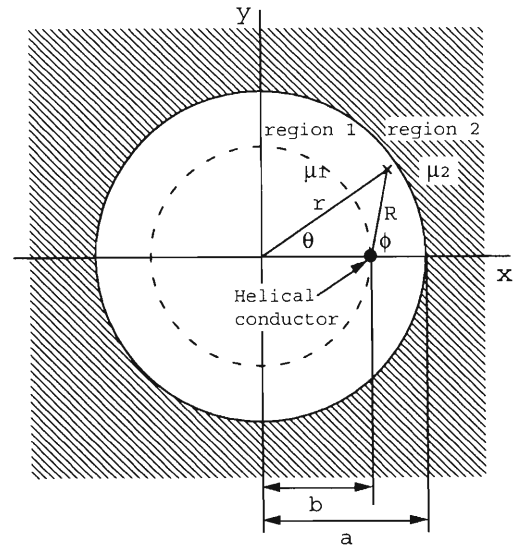


Fig. 2. Cross section of a single helical coil placed inside a cylindrical hole in iron ( $z = 0$ ).

$$\begin{aligned} \phi_2(r, \theta, z = 0) &= -\frac{I}{2\pi}B_0\theta - \frac{I}{\pi} \sum_{n=1}^{\infty} B_n K_n(nkr) \sin n\theta. \end{aligned} \quad (4)$$

The constants may be determined by the use of the boundary conditions at the interface,  $r = a$ , between regions 1, ( $r < a$ ) and 2, ( $r > a$ ).

As a result, for the general case that a single helical current carrying conductor is located at a point ( $r = b$ ,  $\theta = \varphi$ ) on the  $z = 0$  plane, the magnetic scalar

\* Hitachi, Ltd.

potential  $\phi_{1,iron}$  due to an axially symmetric iron yoke in region 1 is expressed as follows,

$$\begin{aligned} & \phi_{1,iron}(r, \theta, z) \\ &= \frac{I}{\pi} \sum_{n=1}^{\infty} \left\{ \frac{\kappa_m - 1}{\kappa_m - I'_n(nka)K_n(nka)/I_n(nka)K'_n(nka)} \right\} \\ & \times \frac{K_n(nka)}{I_n(nka)} kb I'_n(nkb) I_n(nkr) \sin\{n(\theta - \varphi - kz)\}. \end{aligned} \quad (5)$$

For the simple case that a single helical current carrying conductor with radius  $b = 0.2$  m, angle of helical line current at the  $z = 0$  plane,  $\varphi = 0$ , current,  $I = 10^5$  A, pitch length,  $L = 2$  m, and  $k = 2\pi/L = \pi$  rad/m, is placed inside a cylindrical hole with radius  $a = 0.3$  m, in iron of relative permeability,  $\kappa_m = 10^3$ , as shown in Fig. 3, the above-mentioned analytical calculation is compared with a numerical calculation by TOSCA.<sup>5)</sup>

In TOSCA calculation, the cross-section of the helical conductor is set to be small ( $\approx 1$  mm<sup>2</sup>) so that the conductor can be treated as a helical thin line current. In addition, the length of the conductor is finite as shown in Fig. 3, and the partial thin layer of the yoke is replaced with the reduced potential region defined by means of TOSCA analysis. The periodic boundary condition is utilized so that the length of iron can be treated as infinity.

On the other hand, for simplicity, in this analytical calculation, the iron is treated with the approximation of infinite permeability ( $\kappa = \infty$ ). The comparisons between the analytical and numerical calculations for the distributions of  $B_x(z)$ ,  $B_y(z)$ , and  $B_z(z)$  of the magnetic field due to only iron along a line of  $x = 0.15$  m are shown in Fig. 4. The calculated results based on the analytical expressions up to  $n = 20$  in Eq. (5) are shown by the solid lines, and the numerically calculated results by TOSCA are shown by dots. As a result, the good agreement between the analytical and numerical calculations is obtained. It seems that this difference of two calculated results comes from the coarseness of the elements of finite element method in TOSCA. Therefore, it is expected that the analytical calculation can be utilized to check the soundness of the numerical calculation.

For the fundamental field calculation for the helical magnets with an axially symmetric iron yoke, the analytical expression of the magnetic field is obtained as a rigorous solution of the three-dimensional potential

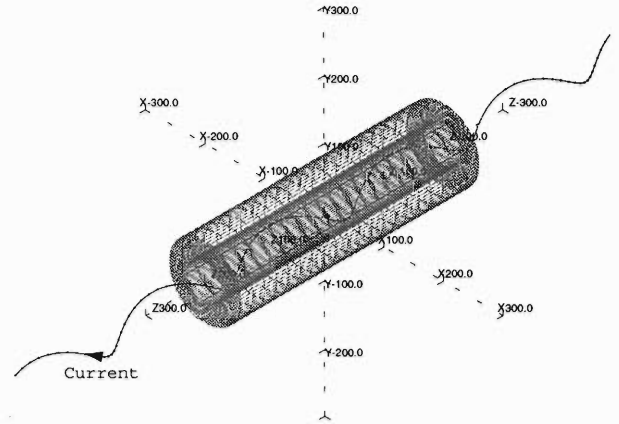


Fig. 3. Schematic drawing in the case of a single helical coil placed inside a cylindrical hole in iron.

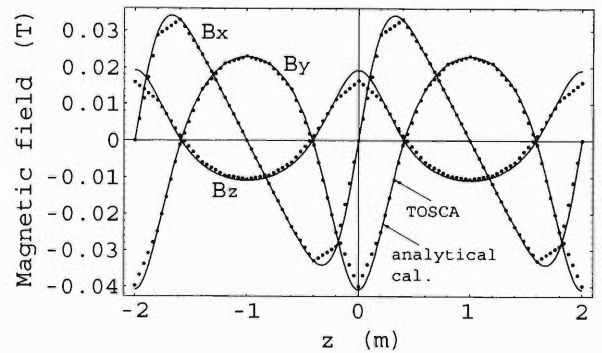


Fig. 4.  $B_x(z)$ ,  $B_y(z)$ , and  $B_z(z)$  due to iron, along a line of  $x = 0.15$  m and  $y = 0$ .

problem for the case that a single helical current carrying conductor is placed inside a cylindrical hole in iron. In addition, this analytical expression is compared with a numerical calculation by TOSCA with good agreement.

#### References

- 1) T. Tominaka et al.: Nucl. Instrum. Methods, Phys. Res. A **459**, 398 (2001).
- 2) T. Tominaka et al.: BNL Internal Report C-A/AP/55 (2001).
- 3) T. Tominaka et al.: Nucl. Instrum. Methods, Phys. Res. A to be published.
- 4) T. Tominaka et al.: IEEE Trans. Appl. Supercond., to be published.
- 5) OPERA-3d/TOSCA, Vector Field, Ltd., Oxford, UK.

## Computing center in Japan for RHIC physics (CC-J)

T. Ichihara, Y. Watanabe, S. Yokkaichi, N. Hayashi, O. Jinnouchi, Y. Goto, S. Sawada,\*1 N. Saito, H. En'yo, H. Hamagaki,\*2 and M. Ishihara

The RIKEN CC-J,<sup>1)</sup> which serves as the computing center in Japan for RHIC physics, started operation in June 2000. The CC-J is aimed at being the principal site of computing for PHENIX<sup>2)</sup> simulation, a regional PHENIX Asian computing center, and a center for the analysis of RHIC<sup>3)</sup> spin physics. The size of the CC-J almost reached 80% of the planned full scale in November 2001.

The first PHENIX experiment at RHIC for Au + Au collision was carried out in the summer of 2000. The raw data of approximately 1 TB was transferred from the RHIC Computing Facility (RCF) at BNL to the CC-J over the Wide Area Network (WAN). The official Data Summary Tapes (DST) were produced at the CC-J and they were used by all PHENIX Collaborators. The Quark Mater 2001 conference was held in January 2001 at BNL. Among 33 PHENIX contributed papers, 21 papers were using the DST produced at the CC-J. The other applications for the CC-J are described in detail elsewhere.<sup>4-8)</sup> The year-2 experiment at RHIC PHENIX started in August 2001. The DST production for the year-2 experiment is now in preparation at the RCF.

The following table shows the size of the components of the CC-J system.

	2000	2001	2002
CPU (SPECint95 <sup>9)</sup> )	5900	13000	18000
Tape Storage (TB)	110	110	1400
Disk Storage (TB)	9	21	21
Tape I/O (MB/s)	45	45	300

Figure 1 shows the configuration of the current CC-J system. The main components of the CC-J are (1) a High-Performance Storage System (HPSS), (2) data servers and (3) CPU farms. Since the CC-J handles approximately 250 TB of data per year, the HPSS was adopted as a hierarchical storage system.<sup>10)</sup>

Figure 2 shows the photograph of the CPU farms. In 2001, the number of CPUs was increased from 160 to 224. Current CPU farms consist of 14 boxes of the Alta cluster. The current CPUs are Pentium III 700–1000 MHz. The linux kernel was updated from 2.2.14 to 2.2.19. Evaluation for the Pentium 4 of 2 GHz has begun. Load Sharing Facility (LSF 4.1) is used for the batch queuing system.

Four sets of 1 TB Fiber Channel (FC) Redundant Arrays of Independent Disks (RAID) were added to the HPSS server as cache disks. The total file transfer rate of 100 MB/s was observed between the HPSS servers and Linux CPU farms, which is close to the limit of

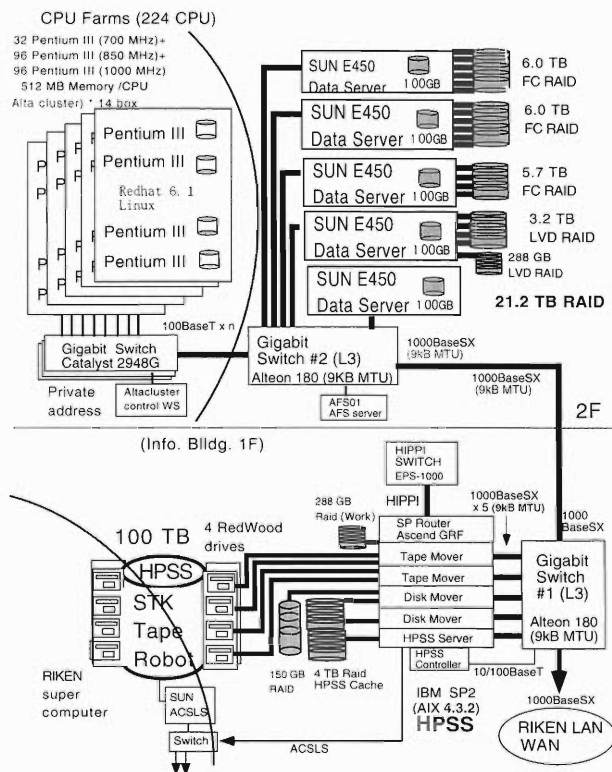


Fig. 1. Configuration of the CC-J system.

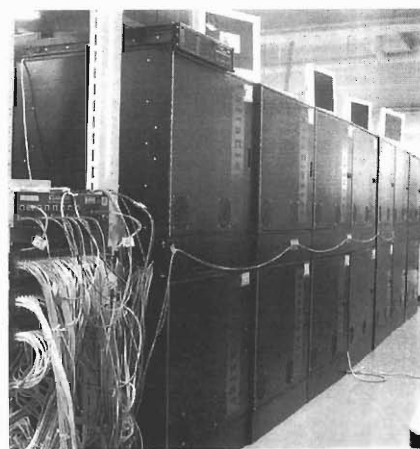


Fig. 2. Linux CPU farms.

line speed (1 Gbps) of the current Local Area Network (LAN). An upgrade plan for the LAN is now under consideration.

Two SUN Enterprise 450 servers and 12 sets of FC RAID of 1 TB (total 12 TB RAID) were added as data servers. A Bonnie benchmark test showed that the

\*1 High Energy Accelerator Research Organization (KEK)

\*2 Center for Nuclear Study, University of Tokyo

read and write performance for one FC RAID for the 2 GB file is 45 MB/s. The total transfer rate for these new 12 TB RAID is approximately 540 MB/s.

We are currently using half of the StorageTek PowderHorn silo and four units of the SD-3 Redwood tape drives for the tape library system as a part of HPSS. The capacity of the SD-3 tape cartridge is 50 GB per volume and the transfer rate of the Redwood drive is 11 MB/s. The current total capacity of the tape library for the CC-J is 110 TB, while the expected data amount for the nominal year at the CC-J is 250 TB. Therefore, we decided to install a new tape silo, which can store 5000 tape cartridges.

We are also planning to upgrade the tape drives from Redwood to 9950B in 2002, which is expected to have the capacity of 200 GB per volume using the same size of tape cartridge. As a result, the total tape-storage capacity is estimated to be 1400 TB (1.4 Peta Byte) in 2002.

The objectivity/DB had been adopted and commonly used for the detector calibration databases for PHENIX. The daily mirroring scripts for the objectivity/DB were developed to synchronize the DB at CC-J and RCF.<sup>10)</sup>

To optimize data access at the HPSS, data carousel software<sup>11)</sup> was installed at the CC-J, which was originally developed at the Oak Ridge National Laboratory (ORNL) and modified at the BNL for the RHIC experiment.

Regarding the WAN connectivity between RIKEN and BNL, the bandwidth of the RIKEN connection to the internet was increased from 15 Mbps to 50 Mbps

in January 2001. The bandwidth of the APAN<sup>12)</sup> US-Japan link was also upgraded from 120 Mbps to 1.2 Gbps in October 2001. We are considering a possible entire data transfer by the Network in the near future. The spin experiment at RHIC is scheduled to start in December 2002, and we are planning to transfer the entire data from BNL to CCJ for extensive analyses.

The authors are grateful to Professor Bruce Gibbard and the staff of the RCF for their earnest cooperation and discussions.

#### References

- 1) T. Ichihara et al.: RIKEN Accel. Prog. Rep. **34**, 252 (2001), see also <http://ccjsun.riken.go.jp/ccj/>
- 2) <http://www.rhic.bnl.gov/phenix/>
- 3) <http://www.rhic.bnl.gov/>
- 4) T. Hachiya et al.: RIKEN Accel. Prog. Rep. **35**, 241 (2002).
- 5) S. Kametani et al.: RIKEN Accel. Prog. Rep. **35**, 242 (2002).
- 6) H. Torii et al.: RIKEN Accel. Prog. Rep. **35**, 243 (2002).
- 7) A. Kiyomichi et al.: RIKEN Accel. Prog. Rep. **35**, 244 (2002).
- 8) M. Naruki et al.: RIKEN Accel. Prog. Rep. **35**, 245 (2002).
- 9) <http://www.spec.org/>
- 10) S. Yokkaichi et al.: RIKEN Accel. Prog. Rep. **35**, 238 (2002).
- 11) O. Jinnouchi et al.: RIKEN Accel. Prog. Rep. **35**, 240 (2002).
- 12) <http://www.jp.apan.net/>

## Operation of Objectivity/DB system at CCJ

S. Yokkaichi, H. En'yo, Y. Goto, H. Hamagaki,\*<sup>1</sup> O. Jinnouchi, N. Hayashi,  
T. Ichihara, S. Sawada,\*<sup>2</sup> and Y. Watanabe

Objectivity/DB<sup>1)</sup> is a commercial Object-Oriented Database Management System (ODBMS) and is widely tested and used in the field of high energy/nuclear physics. It has been studied through the CERN RD45 project<sup>2)</sup> and the ATLAS experiment. It was used in the Zeus experiment for the tag DB in offline analysis. In the Babar experiment, it was used for online data storage and DST (data summary tapes) storage. However, in some experiments, such as the STAR experiment, gave up to use Objectivity/DB, due to difficulty in maintaining the system.

In the PHENIX experiment, we also use Objectivity/DB as a calibration DB and a run DB in online/offline computing. Single Federation DB (FDB) is being operated on a dedicated Linux machine in the PHENIX counting house. FDB in Objectivity means a set of database files managed under a single namespace. Almost all online programs in the counting house and almost all offline analysis programs on the machines in RCF (RHIC Computing Facility at BNL) access the single FDB.

In RIKEN CCJ,<sup>3)</sup> we also require the data in Objectivity/DB to run the PHENIX analysis program, particularly for the 'reconstruction' process in the data analysis flow. In this process, the raw data and simulation data are converted to the DST, which has 'reconstructed' particle track information, shower cluster information in calorimeters, Čerenkov ring image in RICH and so on. Then we have to access and read the PHENIX official FDB. Some methods were discussed and we now operate a 'snap-shot' copy method<sup>4)</sup> to duplicate the official FDB and deploy it in CCJ. Using the copied FDB, official PHENIX DST production for the data taken in 2000 was performed at CCJ last December and about 40% of the available raw data is processed in CCJ. The remainder was processed at RCF.

For such production, the calibration DB can be used with fixed — 'snap-shot' — data which is copied by hand at the appropriate time. However, during preproduction, calibration works are ongoing and there are frequent updates of the official DB. In this case, frequent updating of the DB in CCJ is also expected. The automatic daily copying is now being tested for two month. Current size of the PHENIX FDB is about 2.4 GB. The two main causes of failure of automatic duplicate processes were as follows.

(1) Failure of the DB backup process in RCF using built-in command 'oobackup.' This is caused by the

remaining DB locking, mainly from some dead or forgotten processes. (2) Network failure between RIKEN and BNL. Instability of WAN broke or delayed the file transfer using the 'scp' command. These two facts convinced us that the 'replication' function of Objectivity/DB, which is a real-time data duplication method via a network which we did not adopt, could cause many problems in the operation of the official FDB in our current network environment.

A dedicated Linux host for DB in CCJ has dual 1 GHz Pentium III CPUs, 1 GB memory and a 16 GB SCSI local disk. 1000Base-SX ethernet connects the DB host machine to the 1000Base-SX/100Base-T ethernet switches. Linux machines as CPU farms on which the reconstruction jobs run are connected with the switches using 100Base-T. In fact the DB host is one of the farm machines but the network interface has been upgraded. SUN E450 as NFS servers with Fibre Channel RAID disks are also connected with the switches using 1000Base-SX. The RAID disks are served to both the DB host and CPU farm hosts. These configurations are shown in Fig. 1. In this environment, the network bandwidth was measured using a benchmark program 'netperf.'<sup>5)</sup> Over 100 MB/s was achieved using multiple sessions from the DB host to 30 CPU farm nodes, while 12 MB/s was achieved from the DB host to typical single CPU farm node. The DISK I/O bandwidth of the DB host was 26 MB/s for

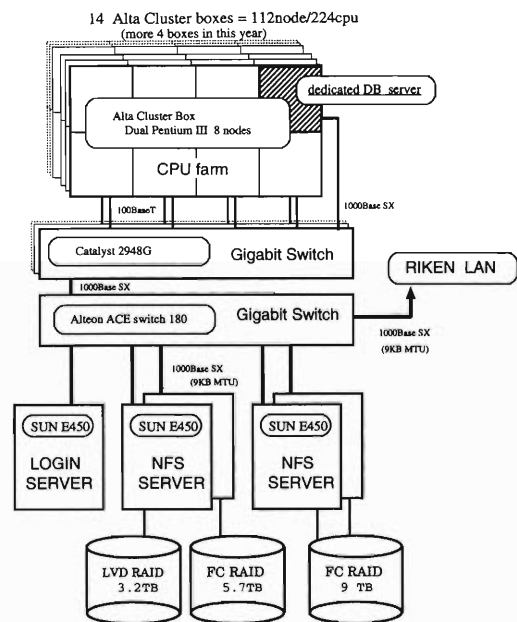


Fig. 1. Current CCJ system configurations.

\*<sup>1</sup> Center for Nuclear Study, University of Tokyo

\*<sup>2</sup> High Energy Accelerator Research Organization (KEK)

block read, which was measured using a benchmark program 'bonnie.'<sup>6)</sup>

We measured the data reading performance of the Objectivity/DB using the PHENIX reconstruction program for 2001 data (Oct. 28 version). This program reads about 300 MB of calibration data and run-information data from the DB at the initialization stage. Multiple jobs running on multiple CPU farm nodes read the Objectivity/DB data simultaneously (differences in starting times of jobs are less than 60 seconds). Two read methods are tested. One uses the Objectivity Advanced Multi Thread Server (AMS). AMS runs on the DB host, reading the DB data from the local disk and transferring it to the client processes. The other uses ordinary NFS. Client processes read the data from the NFS disk on which the DB data is placed. In both cases, the Objectivity Lock Server also runs on the DB host and processes the read lock of DB.

In the AMS case, about 4 MB/s was achieved for a single job, 40 MB/s for 10 jobs, 35 MB/s for 100 jobs and 28 MB/s for 200 jobs. The saturation effect was observed. CPU usage was 95% for over 40 jobs. Local disk I/O does not seem to limit the performance. A cache effect may be effective for such multiple access to the same data at the same time. These were measured using the UNIX command 'netstat -i.' The number of the AMS thread had no clear effect between 8 (default), 4 and 16 with respect to the data output flow.

In the NFS case, about 50 MB/s was achieved for 200 jobs, for the DB data placed on the SUN NFS server. This was measured using SNMP (simple network monitoring protocol) at a port of the ethernet switch connected with the NFS server. CPU usage of the NFS server host was about 50% for kernel and 50% was idle.

It seems that the latter is more efficient than the former. However, the NFS method with the Linux disk will be compared with the AMS method on Linux, because the SUN NFS server is more expensive and may not be available in such dedicated way.

We would like to thank our collaborators at PHENIX. Dr M. Purschke advised us regarding a kernel configuration of the DB host machine. Dr T. Chujo and A. Kiyonichi explained the behavior of AMS from their experience of production job management at RCF.

#### References

- 1) <http://www.objectivity.com/>
- 2) <http://wwwinfo.cern.ch/asd/rd45/index.html>
- 3) T. Ichihara et al.: RIKEN Accel. Prog. Rep. **35**, 236 (2002); RIKEN Accel. Prog. Rep. **34**, 252 (2001).
- 4) S. Yokkaichi et al.: RIKEN Accel. Prog. Rep. **34**, 256 (2000).
- 5) <http://www.netperf.org/netperf/NetperfPage.html>
- 6) <http://www.textuality.com/bonnie/>

## Data Carousel/ORNL batch system for HPSS at CCJ

O. Jinnouchi, T. Ichihara, Y. Watanabe, S. Yokkaichi, Y. Goto, N. Saito, M. Ishihara, H. Hamagaki,<sup>\*1</sup>  
S. Sawada,<sup>\*2</sup> J. Lauret,<sup>\*3</sup> T. G. Throwe,<sup>\*4</sup> and H. En'yo

The huge amount of data (of petaByte order) from the PHENIX experiment<sup>1)</sup> at the Brookhaven National Laboratory (BNL)<sup>2)</sup> is stored in the HPSS (High Performance Storage System).<sup>3)</sup> which consists of a large tape library system.

As the PHENIX experiment being the large group collaboration, a large number of simultaneous data retrieval requests from different users and at different submission times are expected. In order to deal with such conditions and to achieve the optimum file transferring performance, the Data Carousel/ORNL batch system has been introduced at the RHIC Computing Facility (RCF).<sup>4)</sup>

In RIKEN CCJ,<sup>5)</sup> the complete data summary tape (DST) and raw data produced by the PHENIX detector are stored in HPSS in exactly the same manner as in RCF. Therefore, in order to provide a high-performance data retrieval facility to regional users, it is necessary to install the Data Carousel/ORNL system at CCJ as well.

This system consists of two parts, namely, the ORNL batch system and the Data Carousel. The ORNL batch system was designed such that HPSS could receive file-list oriented requests rather than requiring a per file restoration basis. This feature was believed to have eliminated the inefficiency which exists due to the fact that HPSS itself physically consists of tapes and not of disks. However, the ORNL batch system alone could not solve this problem because of the characteristics of the means of requesting the data. Data requests were carried out in the following, (1) multiple users and different groups are not aware of each other's activities. (2) The users submit the file-list at the time when the data is required for their analysis. Thus, requests are received intermittently rather than consecutively. To optimize these overlapping requests by multiple users, there should be one layer on the top of the ORNL batch system; this is the Data Carousel.

Figure 1 shows how the ORNL/Data Carousel works. The Data Carousel consists of a server and a client base system. The user only interacts with the client side of the carousel using the script `/usr/local/carousel/hpss-user.pl`, either from ccjsun or from linux nodes. A detailed description has been given by the author who designed this scripts.<sup>6)</sup> For a new user at CCJ, a simple usage guide for this script can be found on the web.<sup>7)</sup>

<sup>\*1</sup> Center for Nuclear Study, University of Tokyo  
<sup>\*2</sup> High Energy Accelerator Research Organization (KEK)  
<sup>\*3</sup> Dept. Chem., State University of New York, USA  
<sup>\*4</sup> Brookhaven National Laboratory, USA

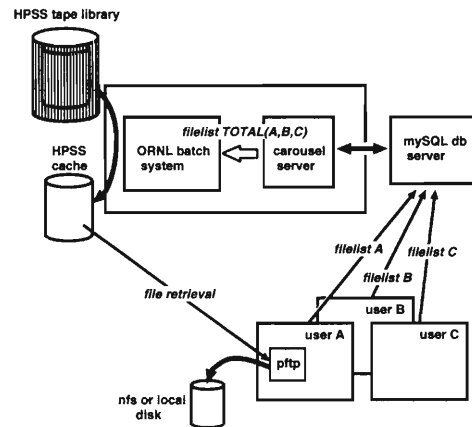


Fig. 1. Schematic diagram of the ORNL/Data Carousel function.

The file lists from several users are gathered in the MySQL database<sup>8)</sup> which resides in ccjsun.

On the server end, the Data Carousel inspects the MySQL database and generates comprehensive file lists using the script `hpss_server.pl`. Then the file lists are submitted to the ORNL batch system. This script is currently invoked every twelve minutes by a cron job. HPSS then stages the files on cache disks, and issues data transfer to local disks through the `pftp` command. Users are also able to check the current status of requests through MySQL queries.

The latest version of the Data Carousel currently used in RCF has several new features. One is a group account with which users are categorized according to their sub-detectors, the physics working group they belong to, and so on. The other is a facility for real time queries through web browsing. CCJ also plans to upgrade the carousel scripts in order to realize these features.

The data carousel/ORNL batch system will surely contribute to the RIKEN Spin Physics project which is going to produce a huge amount of data from this year onwards.

### References

- 1) <http://www.phenix.bnl.gov>
- 2) <http://www.bnl.gov>
- 3) <http://www.sdsc.edu/hpss/>
- 4) <http://www.rhic.bnl.gov/RCF/>
- 5) <http://www.ccjsun.riken.go.jp/ccj/>
- 6) <http://nucwww.chem.sunysb.edu/pad/offline/carousel/carousel.html>
- 7) [http://www.ccjsun.riken.go.jp/ccj/doc/carousel/carousel\\_uguide.html](http://www.ccjsun.riken.go.jp/ccj/doc/carousel/carousel_uguide.html)
- 8) for more information see, <http://www.mysql.com/documentation/index.html>

# Measurement of electron and photon at RHIC-PHENIX

T. Hachiya<sup>\*1</sup> and Y. Akiba,<sup>\*2</sup> for the PHENIX Collaboration

One of the unique characteristics of the PHENIX<sup>1)</sup> experiment among all the RHIC experiments is its ability to identify and to measure electrons and electron pairs at central rapidity region. During the first physics run of RHIC in 2000, PHENIX recorded more than five million Au+Au collisions at  $\sqrt{s_{NN}} = 130$  GeV.

Electron measurement is important in studying all stages of time-space evolution of heavy ion collisions. There are many interesting processes such as open charm semi-leptonic decays, thermal radiation, and dilepton decay of vector mesons, while background electron sources include Dalitz decays and photon conversions in the detector.

Photon measurement is also important in investigating the characteristics of hot and dense matter created in heavy ion collisions. Photons can be measured by  $e^+e^-$  pairs from internal and external conversions. The conversion method is a powerful tool in the low  $P_t$  region because the method provides a clean measurement of identified photons from the collision vertex with a better momentum resolution than the calorimeter method.

For the electron measurement,<sup>2)</sup> charged particle tracks are reconstructed by a tracking device (the DC and the PC) and are confirmed by an associated hit in EMCal. We use the number of hits and the shape of the Čerenkov ring measured in the RICH, and the  $E/p$  ratio in order to select electron tracks. Energy ( $E$ ) and momentum ( $p$ ) are measured by the EMCal and the DC, respectively. Electron detection efficiency is estimated by using a PHENIX detector simulator (PISA) based on GEANT. The detector's response in the PISA is well tuned so that real data can be reproduced.

For the photon measurement<sup>3)</sup> by the conversion method, similar  $e^+$  ( $e^-$ ) selection criterion is applied. After the selection, the invariant mass of  $e^+$  and  $e^-$  is calculated. Then, we select the pairs with mass less than 80 MeV as conversion photon. The photon detection efficiency is also estimated by using PISA with  $\pi^0$  as the photon source.

Figures 1 and 2 show the transverse momentum spectra of inclusive  $e^+$ ,  $e^-$  and photon with minimum bias Au+Au collisions. Those spectra are corrected for the electron and photon detection efficiencies, respectively. The work to determine which particles are the source of electron and photon is in progress.

We used the PHENIX Computing Center in Japan (RIKEN CC-J)<sup>4)</sup> for the electron and photon analysis. The large computing power of the facility was very

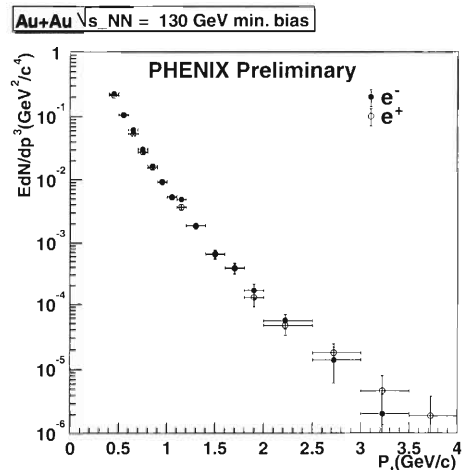


Fig. 1. Transverse momentum spectra of inclusive electron (black) and positron (white).

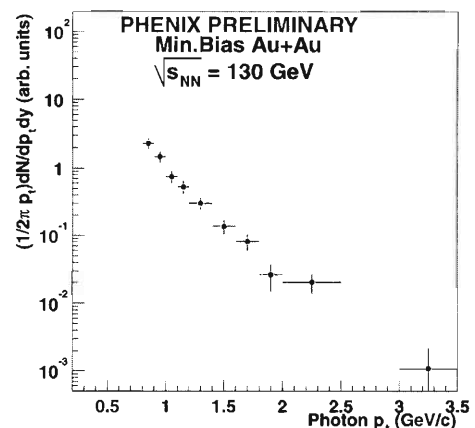


Fig. 2. Transverse momentum spectrum of inclusive photon.

helpful in the simulation and the efficiency study. We would like to thank the members of the Radiation Laboratory for their support of our project.

## References

- 1) PHENIX Conceptual Design Report, BNL (1993) (unpublished).
- 2) Y. Akiba et al.: PHENIX Analysis Note No. 90 (2001).
- 3) Y. Akiba for the PHENIX Collaboration: Nucl. Phys. A **698**, 269c (2002).
- 4) T. Ichihara et al.: RIKEN Accel. Prog. Rep. **34**, 252 (2000).

<sup>\*1</sup> Hiroshima University

<sup>\*2</sup> High Energy Accelerator Research Organization (KEK)

## Performance of PHENIX RICH for RHIC first year run

S. Kametani,\*<sup>1</sup> H. Hamagaki,\*<sup>1</sup> K. Ozawa,\*<sup>1</sup> T. Sakaguchi,\*<sup>1</sup> K. Oyama,\*<sup>1</sup>  
T. Matsumoto,\*<sup>1</sup> J. Kikuchi,\*<sup>2</sup> M. Hibino,\*<sup>2</sup> and M. Tamai\*<sup>2</sup>

To investigate the properties of hadrons and QCD physics in hot and dense matter, electrons are useful because they have no strong interaction with matter. In PHENIX experiment,<sup>1)</sup> electron identification is performed by a Ring Image Cherenkov (RICH) detector.<sup>2)</sup> In RICH, electrons are identified by Cherenkov lights which are generated in the gas volume of RICH and focused on PMTs with a mirror.

RICH detector provides  $e/\pi$  discrimination below the  $\pi$  Cherenkov threshold, which is set at about  $4\text{ GeV}/c$ . In combination with the electromagnetic calorimeter (EMCAL) in each PHENIX arm and the time expansion chamber (TEC) in one arm, the goal is to limit the false identification of hadrons as  $e^+$  and  $e^-$  to less than 1 per  $10^4$ , for momenta below the Cherenkov threshold. The EMCAL is capable of rejecting about 90% of hadrons at momenta  $> 1\text{ GeV}/c$ , and the TEC (present in only one arm of PHENIX) enables  $dE/dx$  separation of electrons from pions for momenta below about  $1\text{ GeV}/c$ .

The PHENIX RICH detector was successfully operated in the first RHIC run, designated run 1, which took place in 2000. The results have been used to evaluate the performance of the RICH.

The occupancy of the RICH was low, only about 3.4% even for the most central Au + Au collisions, due to the very high granularity of the detector. The mean number of photo electrons per ring is  $\sim 10.8$ , which agrees very well with simulation results and the design goal. Figure 1 shows a contour plot of RICH hits associated with tracks. The ring can be clearly observed.

Figure 2 illustrates electron identification using the RICH detector. In this figure, the ratio of the energy (measured by the calorimeter) and the momentum of the charged tracks in the transverse momentum range of  $1.1 < p_T < 1.2\text{ GeV}/c$  is plotted.

For all charged tracks, the  $E/p$  ratio has a nip peak at  $E/p \sim 0.3$  superimposed on a broad distribution caused by hadronic interactions. When RICH hits are required, a clear peak appears at  $E/p = 1.0$ , which is the electron signal. The background due to random associations of RICH hits and tracks is estimated, and also is shown in Fig 2.

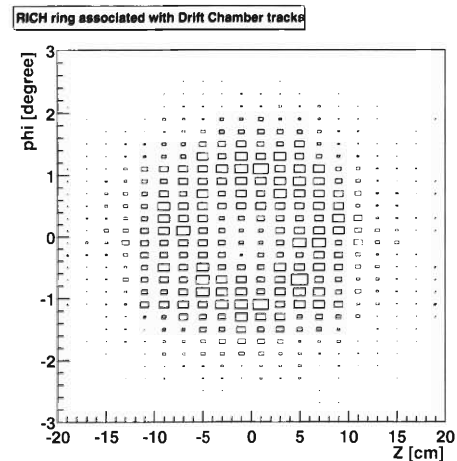


Fig. 1. Contour plot of RICH hits relative to the projected ring centroid from tracking, summed over many tracks.

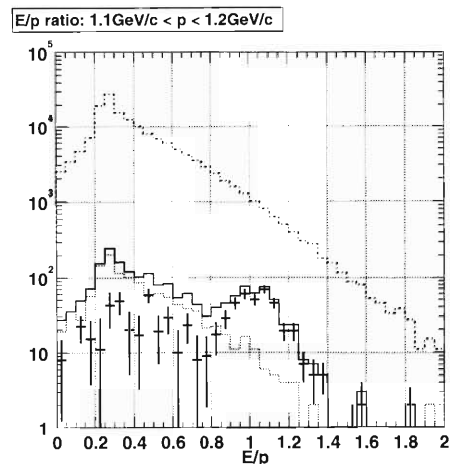


Fig. 2. Ratio of energy and momentum for all Drift Chamber (DC) tracks.

### References

- 1) Y. Akiba et al.: Nucl. Instrum. Methods Phys. Res. A **453**, 279 (2000).
- 2) T. Sakaguchi et al.: Nucl. Instrum. Methods Phys. Res. A **453**, 382 (2000).

\*<sup>1</sup> Center for Nuclear Study, Graduate School of Science, University of Tokyo

\*<sup>2</sup> Advanced Research Institute for Science and Engineering, Waseda University

## Performance of the PHENIX EMCalorimeter

H. Torii,\* A. Bazilevsky, H. En'yo, Y. Goto, K. Imai,\* and N. Saito, for the PHENIX Collaboration

In the early summer of 2000, the PHENIX experiment for heavy-ion physics at RHIC began, and that for spin physics was started in 2001. In this experiment, the electromagnetic calorimeter (EMCal) plays an important role in detecting photons and electrons/positrons. In order to cover topics in both areas of physics, *e.g.*, thermal photon measurements in heavy-ion physics, and prompt photon,  $\pi^0$  and weak boson measurements in spin physics, the EMCal must cover a wide energy range from a few hundred MeV to 80 GeV. Spin physics also requires the energy measurement to be within 2% accuracy for measuring cross sections of prompt photons and  $\pi^0$  production with 10% errors, because the cross sections have steep transverse momentum ( $p_T$ ) slopes. The PHENIX EMCal consists of a lead scintillator (PbSc) and lead glass (PbGl). In this paper, we will report only the performance of the PbSc and the achievement of 2% accuracy.

The PbSc is a Shashlik-type sampling calorimeter made of alternating tiles of lead and scintillator. The basic block is a module consisting of four towers which are optically isolated and are read out individually.<sup>1)</sup> The module has a  $5.52 \times 5.52 \text{ cm}^2$  cross section and 37.5 cm length. From several beam tests at BNL<sup>2)</sup> and CERN,<sup>3,4)</sup> the PbSc was found to have a nominal energy resolution of  $\sigma_E/E = 2.1\% \oplus 8.1\%/\sqrt{E}$  from 0.5 GeV/c to 80 GeV/c, where  $\oplus$  represents the quadratic sum.

Figure 1 depicts the comparison of energy deposits by 1.0 GeV/c  $\pi^+$  at the BNL beam test and 0.9–1.1 GeV/c  $\pi^+$  at PHENIX Au+Au collision  $\sqrt{s_{NN}} = 130 \text{ GeV}$  with a 0.27 GeV minimum ionization peak.

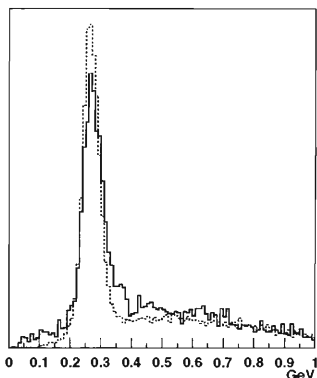


Fig. 1. Comparison of 1.0 GeV/c  $\pi^+$  energy spectrum (dotted line) at AGS beam test and 0.9–1.1 GeV/c  $\pi^+$  energy spectrum (line) at PHENIX Au+Au collision  $\sqrt{s} = 130 \text{ A GeV}$ .

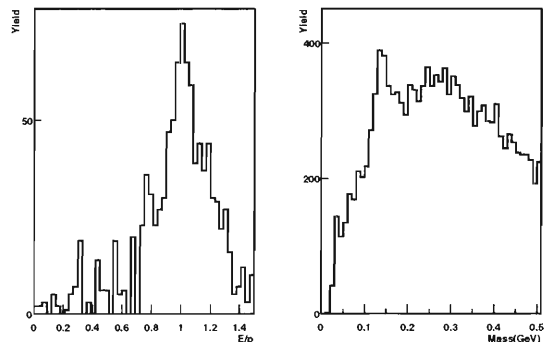


Fig. 2. (Left) Ratio of measured energy and momentum for electron sample at PHENIX Au+Au Collision  $\sqrt{s_{NN}} = 130 \text{ GeV}$ . (Right) Two-photon invariant mass spectrum at PHENIX Au+Au Collision  $\sqrt{s_{NN}} = 130 \text{ GeV}$ .

The  $\pi^+$  is identified by the momentum measured by the tracking system and the time of flight measured by the EMCal itself. The relative energy scale<sup>5)</sup> for all towers during Au+Au collision is already calibrated using the minimum ionization energy of a cosmic muon traversing laterally and that of a charged  $\pi$  traversing lengthwise. The minimum ionization peak of 1.1 GeV/c (0.9 GeV/c)  $\pi^+$  is predicted to be higher (lower) than that of 1.0 GeV/c  $\pi^+$  by 2%. The above comparisons are consistent within 2% accuracy.

Figure 2 shows the  $E/p$  spectrum for the electron sample, which has a peak at 1.02, and the two-photon invariant-mass spectrum with a  $\pi^0$  peak. The electron sample required a hit in Ring Image Čerenkov counter (RICH). The background in the  $E/p$  spectrum is already subtracted. Because of the 2% error in the momentum measurement of the tracking system, the  $E/p$  spectrum indicates that the energy measurement has a  $1.02 \pm 0.02$  accuracy. The  $\pi^0$  mass is evaluated after background subtraction by the event mixing method and is consistent with a nominal  $\pi^0$  mass within a 2% statistical error.

From these three independent measurements, 1.0 GeV/c  $\pi^+$  minimum ionization peak,  $E/p$  spectrum, and  $\pi^0$  mass, we can conclude that the absolute energy scale has 2% accuracy and our physics requirement is satisfied.

### References

- 1) G. David et al.: IEEE Trans. Nucl. Sci. **42**, 306 (1995).
- 2) E. Kistenev et al.: Proc. 5th Int. Conf. Calorimetry in High Energy Physics, New York, USA, 1994-9 ~ 10 (World Scientific, 1994), p. 211.
- 3) Y. Goto et al.: RIKEN Accel. Prog. Rep. **32**, 47 (1999).
- 4) H. Torii et al.: RIKEN Accel. Prog. Rep. **33**, 168 (2000).
- 5) H. Torii et al.: RIKEN Accel. Prog. Rep. **34**, 238 (2001).

\* Kyoto University

## Hadron measurement at RHIC/PHENIX

A. Kiyomichi,<sup>\*1</sup> T. Chujo,<sup>\*2</sup> A. Danmura,<sup>\*1</sup> S. Esumi,<sup>\*1</sup> S. Kato,<sup>\*1</sup> Y. Kuroki,<sup>\*1</sup> H. Masui,<sup>\*1</sup> Y. Miake,<sup>\*1</sup>  
H. Ohnishi,<sup>\*2</sup> M. Ono,<sup>\*1</sup> S. Sakai,<sup>\*1</sup> S. Sato,<sup>\*2,\*3</sup> M. Suzuki-Nara,<sup>\*1</sup> and H. Tsuruoka<sup>\*1</sup>

Heavy ion collisions at relativistic energy offer the possibility of producing highly compressed strongly interacting matter, which may form the quark gluon plasma (QGP). The production of hadrons is one of the important probes of the QGP, since hadrons contain basic information about collision dynamics. Hadron momentum spectra and rapidity densities are affected by thermal freeze-out and collective flow. The particle ratios are sensitive to the chemical properties of the system and particle production mechanism. These measurements will be a first step in investigating whether the QGP is formed or not.

The highest energy heavy ion collisions at  $\sqrt{s_{NN}} = 130$  GeV began in the summer of 2000 at the relativistic heavy-ion collider (RHIC) at BNL. PHENIX is one of the major experiments at RHIC to measure a variety of signals from the heavy-ion collisions. Particle identification for charged hadrons is performed by time-of-flight measurement using the beam-beam counters (BBC) and the time-of-flight counters (TOF), while the drift chamber (DC) and pad chamber 1 (PC1) provide the momentum measurement. The designed time-of-flight resolution is about 100 ps. This allows us to achieve a PID capability for high-momentum particles, a  $4\sigma$   $\pi$ /K separation at momenta up to 2.4 GeV/c and a K/proton separation up to 4.0 GeV/c.

Figure 1 shows a contour plot of the time-of-flight versus the inverse momentum multiplied with the sign of the charge. The time-of-flight is measured as the TOF minus collision time zero given by BBC in minimum bias Au+Au collisions at the energy of  $\sqrt{s_{NN}} = 130$  GeV. A clear separation between particles is seen in the figure. This clearly demonstrates the particle identification capability using the TOF in the year 2000 run period.

The detector calibration of both BBC and TOF set performed at CC-J. The calibration of TOF was performed after track reconstruction and momentum calculation. By selecting high momentum pion, the timing offsets for each of the counters are adjusted. The time-of-flight resolution of 96 ps is achieved at central Au + Au collisions (Fig. 2).

In the summer of 2001, RHIC achieved the full energy collision, and the second year data are collected until the end of 2001 with Au+Au ions at  $\sqrt{s_{NN}} =$

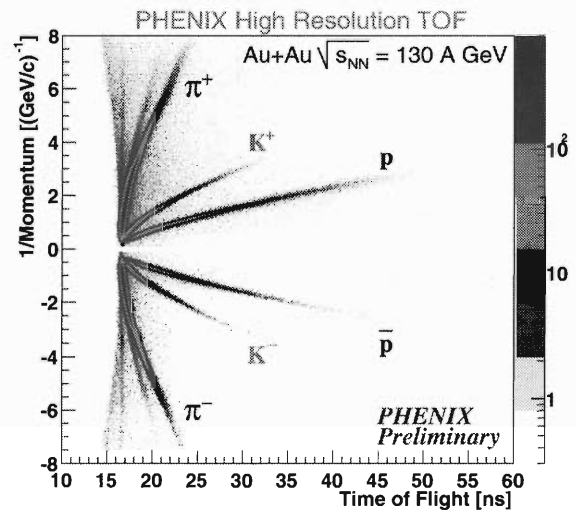


Fig. 1. Contour plot of the time-of-flight versus inverse momentum.

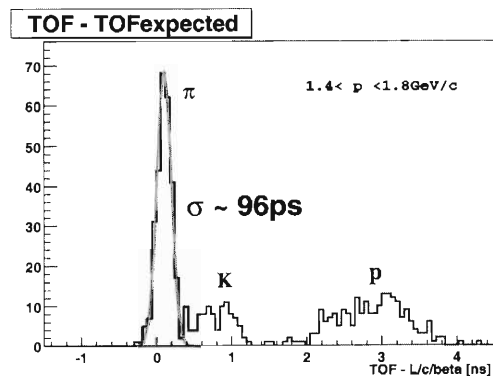


Fig. 2. The time-of-flight distribution in the momentum is  $1.4 < p < 1.8$  GeV/c for positively charged pions. The overall time-of-flight resolution of less than 100 ps is achieved.

200 GeV. The detector calibration for the second year run will be performed at CC-J.

We would like to thank the members of the Radiation Laboratory for their support of our project, especially Dr. T. Ichihara, Dr. Y. Watanabe, Dr. S. Yokkaichi, and other CC-J staffs.

<sup>\*1</sup> University of Tsukuba

<sup>\*2</sup> Brookhaven National Laboratory, USA

<sup>\*3</sup> Japan Society for the Promotion of Science

# Analysis of experiment KEK PS-E325, for the measurement of $\omega/\phi$ meson decays in nuclear matter

M. Naruki,<sup>\*1</sup> J. Chiba,<sup>\*2</sup> H. En'yo, H. Funahashi,<sup>\*1</sup> H. Hamagaki, M. Iciri,<sup>\*2</sup> M. Ishino,<sup>\*3</sup> H. Kanda,<sup>\*4</sup> M. Kitaguchi, S. Mihara,<sup>\*3</sup> T. Miyashita,<sup>\*5</sup> T. Murakami, R. Muto,<sup>\*1</sup> M. Nomachi,<sup>\*6</sup> K. Ozawa,<sup>\*7</sup> F. Sakuma, O. Sasaki,<sup>\*2</sup> H. D. Sato, M. Sekimoto, T. Tabaru, K. H. Tanaka,<sup>\*2</sup> S. Yadama,<sup>\*1</sup> S. Yokkaichi, and Y. Yoshimura<sup>\*8</sup>

It is generally believed that 99% of hadron mass is generated due to the spontaneous breaking of the symmetry in the strong force. However, only few experimental evidences exist to support this idea. Since the modification of hadron mass and decay width in a nuclear medium is theoretically predicted as a consequence of the restoration of the broken symmetry, experimental observation of such phenomena has become one of the most interesting topics in hadron physics today.

We are currently performing an experiment at the KEK proton synchrotron to observe the decay of  $\phi$  meson from nuclear targets, to inspect the modification of hadron properties at normal nuclear density. The experiment is to measure the invariant mass spectra of  $\phi \rightarrow e^+e^-$  and  $\phi \rightarrow K^+K^-$  decay modes simultaneously. We also measure branching ratios in the two decay modes, which are sensitive to the mass shift of  $\phi$  mesons and kaons.

In the analysis of the 1998–1999 data, we have ob-

served the significant enhancement below the  $\omega$  mass peak of  $e^+e^-$  pairs for the copper target, which is attributed to the mass modification effect in nuclear matter (Fig. 1).<sup>1)</sup> The  $\phi$  meson peak is also visible in the  $e^+e^-$  spectra, but further analysis is indispensable to confirm the modification of  $\phi$ .

In year 2000, we newly installed a forward lead glass calorimeter and a vertex chamber to improve the tracking and the particle identification performance for the further study of such modification of meson property.

To expedite the analysis, we have recently started to use CC-J at RIKEN. Thanks to the excellent cpu power of CC-J, our most time-consuming step, the track reconstruction, can be achieved 10 times faster simply by using the surplus time of CC-J. The statistics of our results will thus be improved very soon.

## References

- 1) K. Ozawa et al.: Phys. Rev. Lett. **86**, 22 (2001).

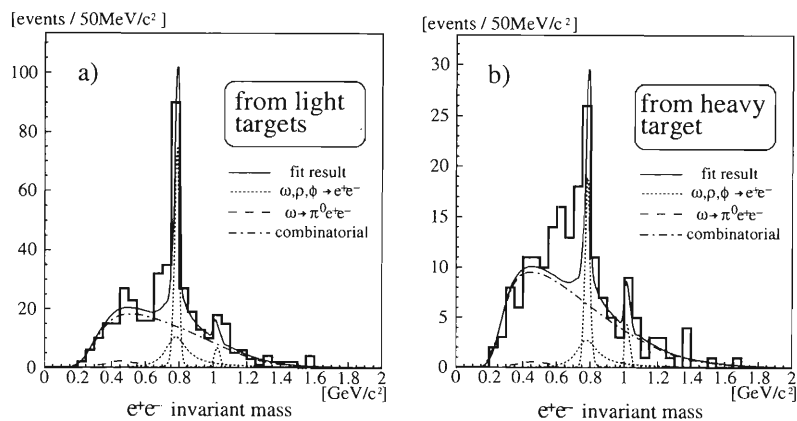


Fig. 1. Invariant mass spectrum of 1998  $e^+e^-$  data.

<sup>\*1</sup> Kyoto University  
<sup>\*2</sup> Institute for Particle and Nuclear Studies, High Energy Accelerator Research Organization (KEK)  
<sup>\*3</sup> International Center for Elementary Particle Physics, University of Tokyo  
<sup>\*4</sup> Tohoku University  
<sup>\*5</sup> Fujitsu Corporation  
<sup>\*6</sup> Research Center for Nuclear Physics, Osaka University  
<sup>\*7</sup> Center for Nuclear Study, University of Tokyo  
<sup>\*8</sup> Xaxon Corporation



## 8. Miscellaneous



## Development of new analytical system using the electron cyclotron resonance ion source and heavy ion linear accelerator

M. Kidera, T. Nakagawa, S. Enomoto, K. Takahashi, H. Baba,<sup>\*1</sup> R. Hirunuma, T. Ohyama,<sup>\*2</sup> K. Igarashi,<sup>\*3</sup>  
M. Fujimaki, E. Ikezawa, O. Kamigaito, M. Kase, A. Goto, and Y. Yano

As an extension of accelerator mass spectrometry (AMS) for detecting trace elements in various materials and for overcoming the disadvantages of the present AMS, we propose a novel method using the ECRIS and heavy ion linear accelerator<sup>1)</sup> (ECRIS-AMS). The production of positive ions in ECR plasma does not have problems such as the difficulty in production of negative ions, which is because of the electron affinity, because the electrons in ECR plasma have a high kinetic energy and easily ionize any atom. Furthermore, when using this system, the acceleration as well as transport depends only on the mass-to-charge ratio ( $A/q$ ) of heavy ions. This indicates that many trace elements can be analyzed simultaneously. Thus, this method allows us to analyze about 80% of the elements when choosing only ions of  $A/q = 3, 4,$  and  $5$ . It is possible to carry out a very low background experiment, because the effect of molecules will be minimized using the accelerator. Part of the results and method are described in Refs. 2 and 3.

To ionize the trace elements in a sample, we inserted it directly into the plasma of the ion source. For example, a solid rod is inserted into the plasma and then heated to obtain sufficient vapor pressure. For production of intense beams of highly charged ions with  $A/q = 3, 4,$  and  $5$ , we need a high-performance ion source. For this purpose, we used the RIKEN 18 GHz-ECRIS which is highly suitable for producing intense beams of highly charged heavy ions. The performance of this ECRIS is described in Ref. 4.

To demonstrate the sensitivity of the method, we analyzed a  $\text{Al}_2\text{O}_3$  rod which is difficult to analyze in conventional AMS. The  $\text{Al}_2\text{O}_3$  rod was inserted into the plasma and heated to obtain sufficient vapor pressure. The particles with  $A/q = 5$  as analyzed using the first analyzer magnet were accelerated to 2.0 MeV/u with RILAC and the RFQ linear accelerator. For beam tuning, the parameters of each of the magnets were fixed to  $A/q = 5$  for beam transport after the acceleration. The elements with same  $A/q = 5$  were selected using two dipole magnets for analysis. We detected elements with mass numbers which were multiples of 5.

Figure 1 shows the absolute concentrations of trace elements in the  $\text{Al}_2\text{O}_3$  rod (purity of 99.5%). Open and closed circles are the results obtained by using inductive coupled plasma-atomic emission spectrometry (ICP-AES) and ECRIS-AMS. For obtaining the ab-

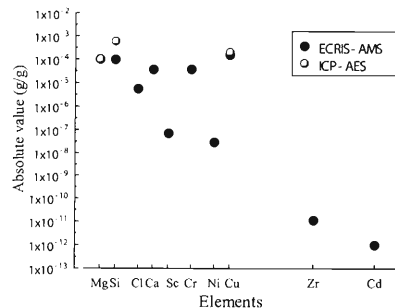


Fig. 1. Relative abundances of trace elements for  $\text{Al}_2\text{O}_3$  rod of 99.5% purity are compared in results of ECRIS-AMS with ICP-AES.

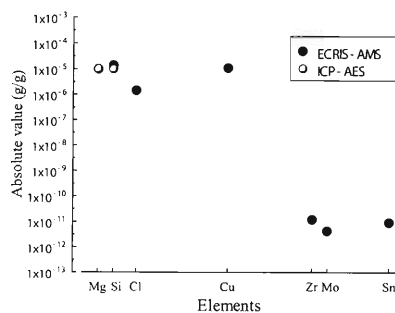


Fig. 2. Relative abundances of trace elements for  $\text{Al}_2\text{O}_3$  rod of 99.99% purity are compared in results of ECRIS-AMS with ICP-AES.

solute value of the concentration in the case of using ECRIS-AMS, the relative concentration of trace elements was normalized using the value of Mg, which was obtained by ICP-AES. In Fig. 1, it is clearly seen that 10 trace elements could be detected and identified by ECRIS-AMS with a short term experiment (about 20 minutes). In particular, the detection limit of the element in the mass region of  $\sim 100$  was  $10^{-12}$  in this experiment. The consumption rate of the sample was less than 1 mg/h. Figure 2 shows the same tendency as Fig. 1 for the  $\text{Al}_2\text{O}_3$  rod (purity of 99.99%)

### References

- 1) M. Odera et al.: Nucl. Instrum. Methods Phys. Res. **227**, 187 (1984).
- 2) T. Nakagawa and M. Kidera: J. Mass Spectrom. Soc. Jpn. **48**, 169 (2000).
- 3) M. Kidera et al.: Nucl. Instrum. Methods Phys. Res. B **172**, 316 (2000).
- 4) T. Nakagawa et al.: Nucl. Instrum. Methods Phys. Res. A **396**, 9 (1997).

\*1 Rikkyo University

\*2 Shizuoka University

\*3 Showa Women's University



## **IV. NUCLEAR DATA**



## New method for calculating aggregate fission-product decay heat with full use of macroscopic-measurement data

K. Oyamatsu,\*<sup>1</sup> H. Takeuchi,\*<sup>2</sup> M. Sagisaka,\*<sup>3</sup> and J. Katakura\*<sup>4</sup>

We propose a new “hybrid” method for calculating the aggregate decay heat from fission product nuclides after a fission burst.<sup>1)</sup> The decay heat should be evaluated not only in the operation of nuclear reactors but also in the reprocessing, transportation and disposal of radioactive materials produced in the reactors. It should be noted that the evaluations should not be limited to fissile nuclides in the initial inventory since other fissile nuclides are produced through transmutation processes in nuclear reactors.

In the present method, the decay heat from a given fissioning system is expressed as a linear combination of macroscopic-measurement data for other fissioning systems with a small residual term. This method is based on the linearity of the decay heat to the fission yield. The coefficients in the linear combination are obtained from fitting the fission yield of the given fissioning system with a linear combination of fission yields of other fissioning systems.

To demonstrate usefulness of this method, it is applied to examining the consistency among measured decay heat powers of five fast and three thermal neutron induced fissions. The hybrid-method calculations agree well with the measurements and conventional summation calculations at cooling times of less than 4000 s, except for a  $\gamma$  component measurement of the  $^{235}\text{U}$  thermal fission at about 2000 s (see Fig. 1).

These results indicate the consistency and reliability of the decay heat evaluation for these systems, with the above exception. Furthermore, they also imply usefulness of the present method in predicting the decay heat of other fissioning systems, for which no measurements have been performed so far.

Lastly, it is remarked that the present method could

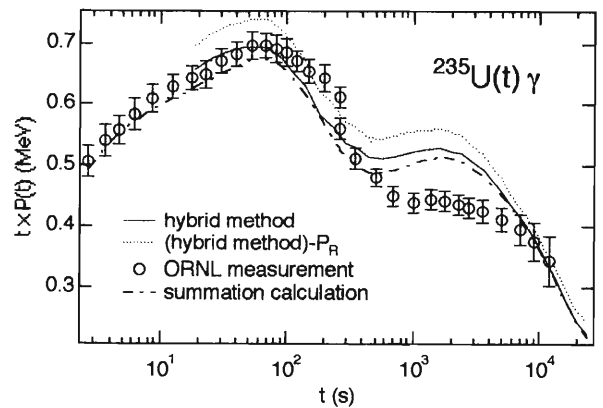


Fig. 1. Decay heat power from a pulse thermal fission of  $^{235}\text{U}$ . The solid (dotted) line shows the decay heat power calculated using the hybrid method with (without) a correction term. Also shown for comparison are the results of ORNL measurements (open circles with error bars) and summation calculations with ENDF/B-VI (dash-dotted line).

also be used to identify incorrect decay data values of individual fission product nuclides, which deteriorate the decay heat evaluation. For these values, precise experimental determination can be realized easily in the RI Beam Factory due to its capability of supplying a high-purity intense RI beam.

### References

- 1) K. Oyamatsu et al.: J. Nucl. Sci. Technol. **38**, 477 (2001).

\*1 Aichi Shukutoku University

\*2 Nihon Unisys, Ltd.

\*3 Nuclear Fuel Industries, Ltd.

\*4 Japan Atomic Energy Research Institute



## **V. DEVELOPMENT OF ACCELERATOR FACILITIES**



# Effect of plasma electrode position on the beam intensity of heavy ions from RIKEN 18 GHz ECRIS

Y. Higurashi,\*<sup>1</sup> T. Nakagawa, M. Kidera, T. Aihara,\*<sup>2</sup> M. Kase, and Y. Yano

To investigate the effect of plasma electrode position on beam intensity, we measured the beam intensity of Ar ions with various charge states as a function of the electrode position. In this experiment, we observed that the beam intensity of highly charged Ar ions is strongly dependent on the electrode position and that there is an optimum position for maximizing the beam intensity. The optimum position varies with the charge state of the ions. A beam intensity of 1.3 mA for Ar<sup>8+</sup> was obtained at the optimum plasma electrode position. In the last decade, we have applied various kinds of techniques to improve the performance of ECR ion sources.<sup>1)</sup> Through a series of improvements, we have obtained the essential points for effective beam production from ECRISs in hand. That is, we need to increase the magnetic field and the microwave frequency of ECRIS, and to optimize the boundary conditions of ECR plasma, i.e., for the Al cylinder method,<sup>2)</sup> and the negatively biased electrode method<sup>3)</sup> and so forth. Obviously, the cylinder and electrode form part of the boundary of ECR plasma, and consequently they affect its condition. Therefore, it is not far from reality that the beam intensity would be enhanced if we could find the most suitable condition of ECR plasma. From this point of view, we performed experiments involving changing the position of the plasma electrode for each charge state to find the correlation between the electrode position and the beam intensity. In this paper, we report the experimental results of Ar ions produced from RIKEN 18 GHz ECRIS when we change the electrode position, and discuss the role of the electrode.

Figure 1 shows the cross-sectional view of RIKEN 18 GHz ECRIS and its plasma chamber. An Al cylinder covered the inner wall of the plasma chamber. The thickness of the Al cylinder was 1 mm. We also used the negatively biased electrode method to increase the beam intensity. Further details of the design and performance of the RIKEN 18 GHz ECRIS are described in Ref. 3.

We have chosen three positions of the plasma electrode (positions A, B and C) to investigate the effect of its position on the beam intensity. Other parameters (gas pressure, magnetic field, microwave power and negative voltage of the biased electrode) were set so as to maximize the beam intensity at each position. Figure 2 shows the beam intensities of Ar<sup>8+</sup> as a function of extraction voltage. The open and closed circles are the results obtained at electrode positions A and B, respectively. It is clearly evident that the beam inten-

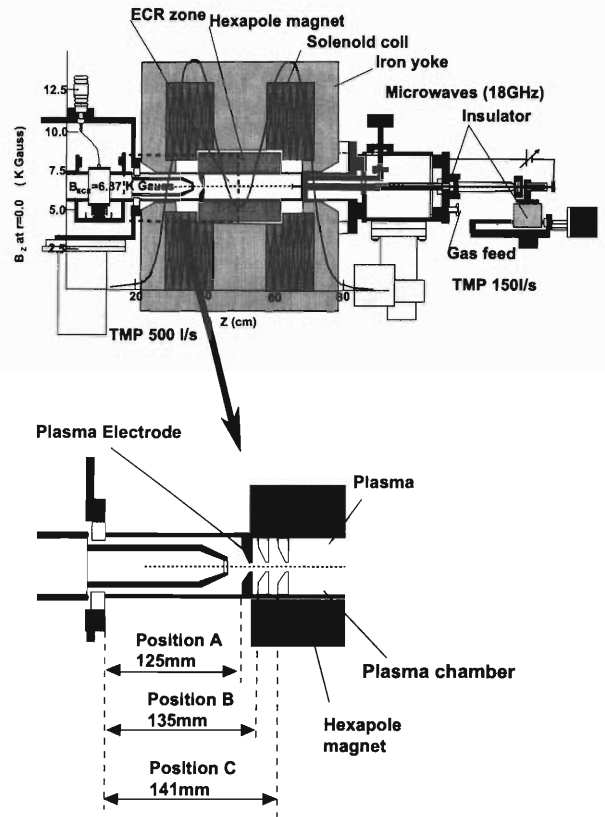


Fig. 1. Cross-sectional view of RIKEN 18 GHz ECRIS and its plasma chamber.

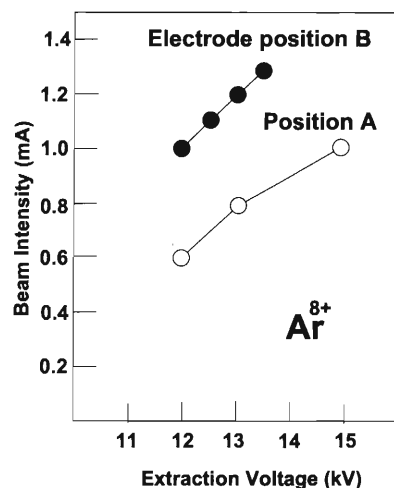


Fig. 2. Beam intensity of Ar<sup>8+</sup> as a function of extraction voltage at electrode positions A and B.

\*<sup>1</sup> Rikkyo University

\*<sup>2</sup> SHI Accelerator Service, Ltd.

sity increases with increasing extraction voltage. At electrode position A, the best result of 1 mA was obtained at an extraction voltage of 15 kV. On the other hand, at electrode position B, we obtained 1.3 mA at an extraction voltage of 13.5 kV. At position B, we could obtain a higher beam current at a lower extraction voltage compared to that at position A. At the same extraction voltage, the beam intensity of  $\text{Ar}^{8+}$  at position B is almost 50% higher than that at position A.

Figure 3 shows the beam intensity of Ar ions as a function of the plasma electrode position. It is clearly evident that the beam intensity is strongly dependent on the position. The maximum beam intensity of  $\text{Ar}^{8+}$  is obtained at position C. In the case of  $9+$ , however, the beam intensity gradually increases and becomes almost maximum at position B, and then decreases with movement of the electrode toward the ECR zone, which is the same tendency as described in Refs. 4 and 5. From these experimental results, it seems that the optimum electrode position for maximizing the beam intensity of multicharged Ar ions exists, and that this position varies with the charge state. The plasma electrode placed near the ECR zone is suitable for producing lower charge state Ar ions ( $8+$ ,  $7+$ ). At the edge of the hexapole magnet, the beam intensity of higher charge state Ar ions ( $11+$ ) is strongly enhanced.

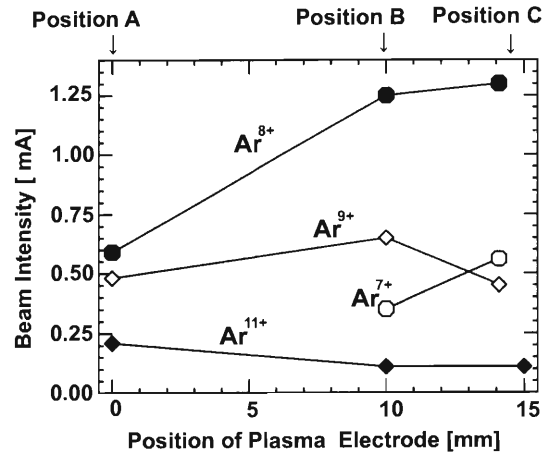


Fig. 3. Beam intensity of various charge states of Ar ions as a function of plasma electrode position.

#### References

- 1) R. Geller: *Electron Cyclotron Resonance Ion Sources and ECR Plasma* (IOP, Bristol, 1996) and references therein.
- 2) T. Nakagawa et al.: *Jpn. J. Appl. Phys.* **35**, 4077 (1996).
- 3) For example, S. Biri et al.: *Nucl. Instrum. Methods Phys. Res. B* **152**, 386 (1999).
- 4) P. Yuan et al.: *Proc. 15th Int. Conf. on Cyclotrons and Their Applications* (IOP, Bristol, 1999), p. 402.
- 5) Private communication with D. Hitz.

# Effect of plasma chamber surface on production of highly charged ions from ECRIS

Y. Higurashi,\*<sup>1</sup> M. Kidera, T. Nakagawa, T. Aihara,\*<sup>2</sup> M. Kase, and Y. Yano

To increase the beam intensity of highly charged heavy ions from ECRIS, it is important not only to increase the magnetic field and microwave frequency, but also to optimize the boundary condition of ECR plasma. Since we observed the strong enhancement of highly charged heavy ion beam intensity after coating  $\text{Al}_2\text{O}_3$  on the surface of the plasma chamber,<sup>1)</sup> many laboratories have used it to increase the beam intensities of highly charged heavy ions. Recently it was reported that the emissive dielectric layer on the surface of the plasma chamber helps to increase the beam intensity of highly charged Ar ions.<sup>2)</sup> All of these experiments suggest that the surface of plasma chamber is quite important to optimize the ECRIS performance.

To investigate the effect of the  $\text{Al}_2\text{O}_3$  surface directly, we plated with the  $\text{Al}_2\text{O}_3$  on the surface of Al cylinder ( $\text{Al}_2\text{O}_3$  plating method) and compared the beam intensity when using the  $\text{Al}_2\text{O}_3$  plating method and Al cylinder. As the surface of cylinder become completely  $\text{Al}_2\text{O}_3$  when using  $\text{Al}_2\text{O}_3$  plating method, we can check its effect clearly.

For investigating the effect of  $\text{Al}_2\text{O}_3$ , we used two different cylinders; 1 mm-thick Al cylinder, and an Al cylinder of 1 mm thickness plated with  $\text{Al}_2\text{O}_3$  of about  $20\ \mu\text{m}$  thickness. New plating cylinder was fabricated by DIPSOL CHEMICALS Co., Ltd. These cylinders were inserted into the plasma chamber and covered the inner wall of the plasma chamber of RIKEN 18 GHz ECRIS.

Figure 1 shows the beam intensity of  $\text{Ar}^{11+}$  as a function of RF power at the extraction voltage of 13 kV when using the Al cylinder (open circles) and

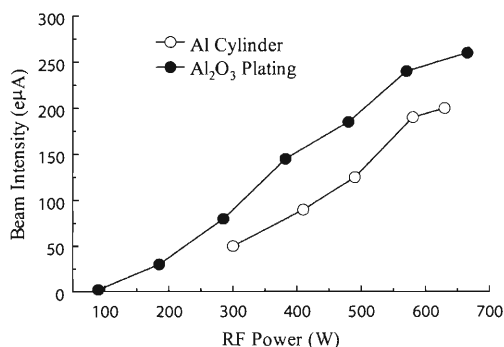


Fig. 1. Beam intensity of  $\text{Ar}^{11+}$  as a function of RF power. Open and closed circles are the results by using Al cylinder method and  $\text{Al}_2\text{O}_3$  plating method, respectively.

\*<sup>1</sup> Rikkyo University

\*<sup>2</sup> SHI Accelerator Service, Ltd.

the  $\text{Al}_2\text{O}_3$ -plated cylinder (closed circles). The beam intensity increased with increasing RF power up to 700 W. The beam intensity of  $\text{Ar}^{11+}$  for  $\text{Al}_2\text{O}_3$ -plated cylinder was always higher than that by using the Al cylinder. It should be stressed that the beam intensity was not saturated and we may obtain higher intensity at higher RF power.

Figure 2 shows the beam intensity of Ar ions as a function of extraction voltage. For both cases ( $\text{Al}_2\text{O}_3$ -plated cylinder and Al cylinder), the beam intensity increased with increasing extraction voltage. The beam intensity for the  $\text{Al}_2\text{O}_3$ -plated cylinder was always higher than that for the Al cylinder. The beam intensity when using  $\text{Al}_2\text{O}_3$  plating method was almost 50% higher. The best result of  $290\ \text{e}\mu\text{A}$  was obtained at an extraction voltage of 13 kV in this test experiment.

To investigate the effect above in the case of  $\text{Al}_2\text{O}_3$  plating method for RIKEN 18 GHz ECRIS, we carefully measured the beam intensity of  $\text{Ar}^{11+}$  with and without using gas mixing method. At the extraction voltage of 12 kV, we obtained  $200\ \text{e}\mu\text{A}$  of  $\text{Ar}^{11+}$  without using the gas mixing method. At the same extraction voltage, the best result of  $250\ \text{e}\mu\text{A}$  was obtained using gas mixing method (we used  $\text{O}_2$  gas as a mixing gas). When using the  $\text{Al}_2\text{O}_3$  plating method, gas mixing is still effective to increase the beam intensity in the case of RIKEN 18 GHz ECRIS.

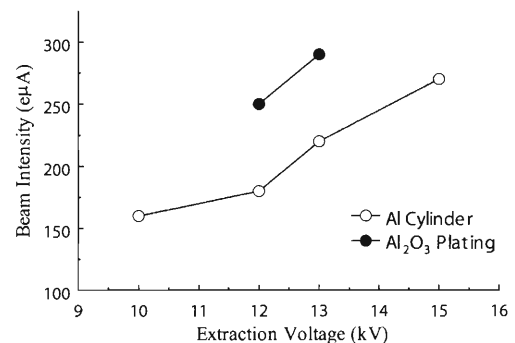


Fig. 2. Beam intensity of  $\text{Ar}^{11+}$  as a function of extraction voltage. Open and closed circles are the results by using Al cylinder method and  $\text{Al}_2\text{O}_3$  plating method, respectively.

## References

- 1) T. Nakagawa et al.: Jpn. J. Appl. Phys. **30**, L930 (1991).
- 2) L. E. Stiebing et al.: Rev. Sci. Instrum. **71**, 918 (2000).

## Liquid-He-free SC-ECRIS at RIKEN

T. Nakagawa, M. Kidera, Y. Higurashi,\*<sup>1</sup> T. Kageyama, T. Aihara,\*<sup>2</sup> M. Kase, and Y. Yano

Since 1998, we have constructed a new superconducting ECR ion source (SC-ECRIS) as an external ion source for the AVF cyclotron. The main purpose is to increase the beam intensity of highly charged heavy ions (*e.g.*, Ar<sup>11+</sup> and Kr<sup>20+</sup> ions) extracted from the AVF cyclotron.

The main feature of the ECRIS is to use the small refrigerator for cooling the solenoid coils to 4.2 K. Figure 1 shows the cross-sectional view of this ECR ion source. The solenoid coils are cooled by a small Gifford-McMahon refrigerator. The refrigerator maintains the superconductivity of the solenoid coils without using liquid He. The hexapole magnet consists of 24 segments of permanent magnet. The maximum strength of the mirror magnetic field are 2 and 3 T at the beam extraction and microwave injection side, respectively. The minimum magnetic field strength of mirror magnetic field ( $B_{\min}$ ) is approximately 0.3 T. The maximum magnetic field strength at the inner surface of the plasma chamber is 1.2 T. The injected microwave frequency is 18 GHz. The maximum power of microwave is 1.5 kW. The plasma chamber length and diameter are 35 and 7.2 cm, respectively. Details of the structure of this ECIS are described in Ref. 1.

This past summer, we successfully produced the first beam from this ECRIS. Figure 2 shows the beam intensities for various charge states of Kr ions. The typical magnetic field configuration is shown in Fig. 3. The

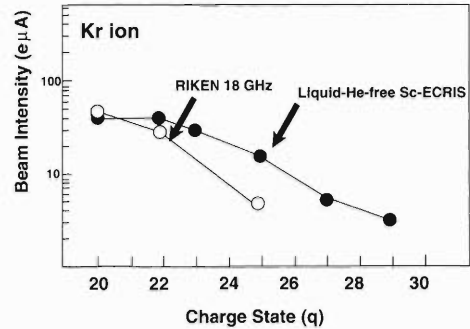


Fig. 2. Beam intensities of highly charged Kr ions. Closed and open circles are the beam intensities produced from SC-ECRIS and RIKEN 18 GHz ECRIS, respectively.

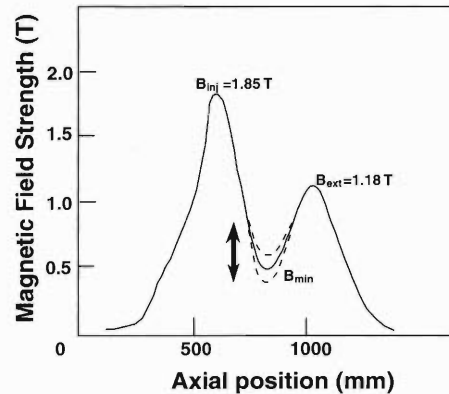


Fig. 3. Typical magnetic configuration for producing the Kr ions.

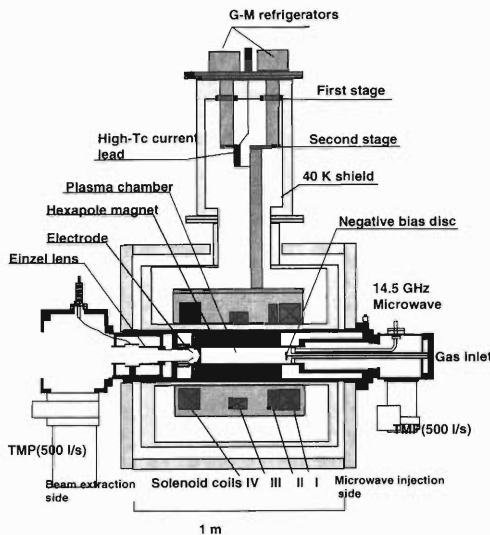


Fig. 1. Cross-sectional view of liquid-He-free SC-ECRIS at RIKEN.

\*1 Rikkyo University  
 \*2 SHI Accelerator Service, Ltd.

typical power of the microwave was about 600 W. The gas pressure of the plasma chamber was  $4 \times 10^{-7}$  Torr. The extraction voltage was 12 kV.

To evaluate the performance of this ECRIS, we compared our results with the beam intensities of Kr ions produced from RIKEN 18 GHz ECRIS (open circles in Fig. 2). It is clearly evident that the beam intensity of highly charged Kr ions produced from liquid-He-free SC-ECRIS is much higher than that of ions produced from RIKEN 18 GHz ECRIS. For producing these ions, the typical magnetic field strength of RIKEN 18 GHz ECRIS is about 1.4 T. The plasma chamber length is about 25 cm. As described in Ref. 2, the ion confinement time is  $\tau_{\text{cof}} = B_{\text{max}}/B_{\text{min}}(L/v_i)$ , where  $B_{\text{min}}$  and  $B_{\text{max}}$  are the minimum and maximum magnetic field strengths of the mirror magnetic field.  $L$  and  $v_i$  are the length of plasma and velocity of ions in plasma, respectively. This equation shows that the longer plasma chamber and stronger magnetic field

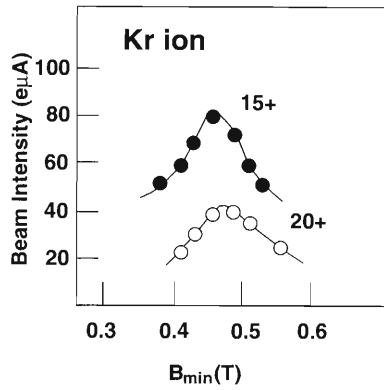


Fig. 4. Beam intensities of Kr ions as a function of  $B_{\min}$ .

cause better ion confinement. This is one of the rea-

sons why the liquid-He-free SC-ECRIS can produce the higher intensity of highly charged Kr ions compared to that produced from RIKEN 18 GHz ECRIS.

To test the effect of  $B_{\min}$  on the beam intensity of highly charged Kr ions, we only changed the  $B_{\min}$  without changing  $B_{\text{inj}}$  and  $B_{\text{ext}}$ . Figure 4 shows the beam intensities of Kr ions as a function of  $B_{\min}$ . The beam intensities gradually increase up to 0.5 T and then gradually decrease. We found that the optimized magnetic field of  $B_{\min}$  is not dependent on charge state of Kr ions under this experimental condition.

#### References

- 1) T. Kurita et al.: *Rev. Sci. Instrum.* **71**, 909 (2000).
- 2) R. Geller: *Electron Cyclotron Resonance Ion Source and ECR Plasma* (IPO, Bristol, 1996).

## Development of ECR ion sources for high-intensity heavy ion beams

Y. Ohshiro,\* S. Watanabe,\* T. Kageyama, T. Nakagawa, M. Kidera, M. Kase, S. Kubono, and T. Katayama

A CRIB separator<sup>1)</sup> was installed in the RIKEN accelerator facility and used for nuclear experiments in 2000–2001. Ion beams produced by the K70 AVF cyclotron with the RIKEN 10 GHz ECR ion source were delivered to the CRIB separator. Because the users of this separator have requested intense beams of highly charged heavy ions, we have made two developments: a method of feeding solid materials into the ECR ion source and a new beam transport system for installation of a 14 GHz ECR ion source (named a Hyper ECR ion source).

A beam of metallic ions such as  $^{10}\text{B}^{4+}$  was used for the first experiment with the CRIB separator. The ion beams were produced by two methods: rod insertion for feeding the vapor from a natural boron crystal into the ECR plasma and introduction of the  $\text{BF}_3$  gas containing enriched  $^{10}\text{B}$  atoms. Thus far, the beam intensities extracted from the ECR ion source and those of ions from the AVF cyclotron are about  $1\mu\text{A}$  and  $100\text{enA}$  for the boron crystal, and  $5\mu\text{A}$  and  $1\mu\text{A}$  for the  $\text{BF}_3$  gas, respectively. To produce more intense beams of  $^{10}\text{B}^{4+}$ , we have prepared a volatile material of  $\text{B}_{10}\text{H}_{14}$  for the MIVOC technique.<sup>2)</sup>

A new beam transport system has been installed at the RIKEN AVF cyclotron in order to utilize the Hyper ECR ion source as a second external multicharge ion source in addition to the conventional 10 GHz ion source. Because the Hyper ECR ion source works with a higher microwave frequency and stronger magnetic field than the conventional ECR ion source, the production of more intense beams of highly charged ion beams was expected.

We installed the Hyper ECR ion source in the ion source room of the AVF cyclotron in 2001. This source had been previously developed, and was used for atomic physics experiments at CNS Tanashi until 1998. We succeeded in producing intense beams of highly charged ion beams (*e.g.*,  $300\text{e}\mu\text{A}$  of  $^{14}\text{N}^{5+}$  and  $60\text{e}\mu\text{A}$  of  $^{14}\text{N}^{6+}$ ) from this source. The source was designed to operate at 14.25 GHz microwave frequency. The axial confinement of plasma was obtained with two solenoid coils that provide the magnetic mirror field. The solenoid coils are fully enclosed with an ion yoke to reduce the coil current. Electrical power consumption is nearly 60 kW. The mirror ratio is about 2.6 ( $B_{\text{max}} \sim 11\text{ kG}$  and  $B_{\text{min}} \sim 4.2\text{ kG}$ ). To confine the plasma radially, we used a sextuple magnet constructed using Nd-Fe-B permanent magnets. The

field strength at the surface of the magnets was about 11 kG. Details of the design of the Hyper ECR ion source have already been described.<sup>3)</sup>

The beam transport system of the Hyper ECR ion source were designed and placed in the ion source room in 2000–2001. The system consists of four elements: one pair of quadrupole magnets for optical matching between the source and the beam line, a double-focusing analyzer with the bending angle of  $90^\circ$  and the bending radius of 50 cm, a solenoid magnet for focusing, and a rotatable  $90^\circ$  bending magnet for switching the two ECR sources. A schematic drawing of the final setup is shown in Fig. 1 and a list of the elements with their specifications is given in Table 1.

A rotatable bending magnet has been installed upstream of the axial injection line of the cyclotron. This magnet is used to deflect the beams by  $90^\circ$  from the horizontal line to the vertical axial injection line. It can rotate the beam direction with respect to the center axis of the cyclotron and the entrance side can be connected to each ECR beam transport line. The magnet has been used with good transmission efficiency of the 10 GHz ECR ion beam.

To reduce the losses of the beams transported from the ion source to the cyclotron, we have made three improvements in this system, as follows. (1) To increase the beam extraction voltage of the source to 20 kV, the new transport system was designed with a maximum magnet rigidity of approximately 118.5 kGcm. (2) The source was set close to the beam analyzer by putting

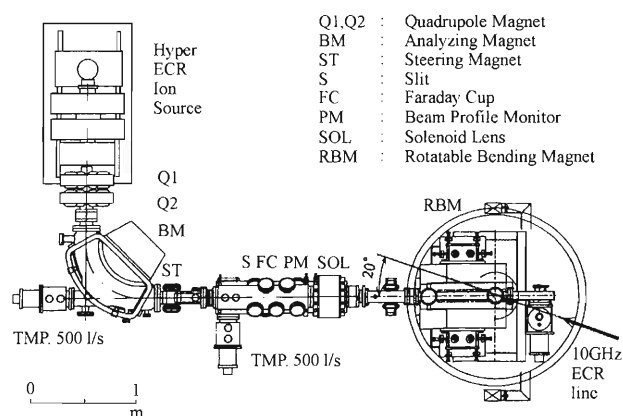


Fig. 1. Top view of the Hyper ECR ion source and the beam transport line to the rotatable bending magnet. The beam line was set to have a  $20^\circ$  deviation angle from that of the conventional ECR.

\* Center for Nuclear Study, Graduate School of Science, University of Tokyo

Table 1. Summary of beam analysis system and beam transport elements.

Drift to analyzing magnet	108.5 cm
Quadrupole magnets	$G = 0.24 \text{ kG/cm}$ ( $I = 20 \text{ A}$ ) pole length = 10 cm pole gap = 12.1 cm
Analyzing magnet	bending angle = $90^\circ$ radius = 50 cm gap = 8 cm $B_{\text{max}} = 2.37 \text{ kG}$ ( $I = 220 \text{ A}$ ) edge angle = $29.6^\circ$ both entrance and exit magnification = 1
Drift to image slits	108.5 cm
Solenoid	length = 20 cm bore radius = 12.4 cm $B_{\text{max}} = 2.5 \text{ kG}$ ( $I = 100 \text{ A}$ )
Bending magnet	bending angle = $90^\circ$ radius = 50 cm gap = 8 cm $B_{\text{max}} = 1.5 \text{ kG}$ ( $I = 102 \text{ A}$ ) edge angle = $29.6^\circ$ both entrance and exit magnification = 1

together the extraction point of the source and the object point of the analyzer. (3) A pair of quadruple magnets was set between the source and the analyzer to focus emitted beams from the source. In addition, another coil was attached to each pole of the quadruple magnet to correct the beam deflection caused by the uncontrollable leakage field from the cyclotron main magnet.

The design parameters of the beam injection line of the cyclotron were optimized by using the emittance matching calculations for the beam injection through the axial hole (hole lens) to the inflector entrance. The assumed beam emittance was  $138 \pi \text{ mmmrad}$  in the horizontal plane and  $91 \pi \text{ mmmrad}$  in the vertical plane. This emittance was the measured value with the beams from the Hyper ECR ion source at CNS Tanashi. Figure 2 shows the envelopes of the

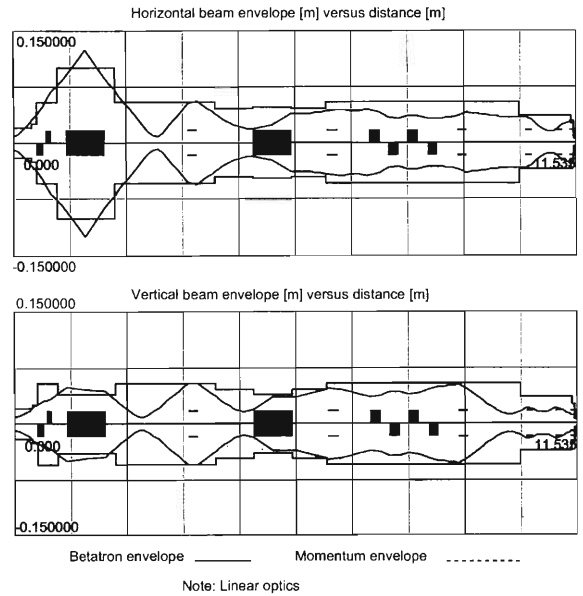


Fig. 2. First-order beam envelope along the injection line calculated for the  $^{14}\text{N}^{5+}$  beam:  $B\rho = 30 \text{ kGcm}$ .

beam in both transverse planes calculated with the WINAGIL.<sup>4)</sup>

We have installed the Hyper ECR ion source and the beam transport system at the RIKEN AVF cyclotron. We can deliver a beam of highly charged ions to the cyclotron by operating two ECR ion sources. When one source supplies the beam to the cyclotron, the other may be used to test the next beam shift and develop a new beam in order to enhance the beam intensities of highly charged heavy ion beams. The beam test of the new system is under way.

#### References

- 1) Y. Yanagisawa et al.: CNS Ann. Rep. **2000**, 11 (2001).
- 2) H. Koivisto et al.: Nucl. Instrum. Methods Phys. Res. B **94**, 291 (1994).
- 3) Y. Yamashita et al.: Proc. 8th Symp. Accelerator Science and Technology, Wako (1991), p. 84.
- 4) P. Bryant, AC Division, CERN: private communication.

## Laser plasma for direct plasma injection to RFQ Linac on RIKEN laser ion source

S. Ozawa, T. Takeuchi,\*<sup>1</sup> T. Katayama, T. Nakagawa, M. Okamura, K. Yano, S. Kondrashev,\*<sup>2</sup>  
N. Mescheryakov,\*<sup>2</sup> and B. Sharkov\*<sup>2</sup>

Recently, through a CNS-RIKEN-TIT collaboration, a new type of heavy-ion source that consists of a laser plasma source and a radio-frequency quadrupole Linac (RFQ Linac) have been developed. In order to determine the parameters of the ion beams injected into the RFQ Linac by the direct plasma injection method, measurement of the laser plasma properties was carried out at the RIKEN laser ion source (RIKEN LIS).<sup>1)</sup>

A schematic view of the experimental setup is shown in Fig. 1. A 4 J TEA CO<sub>2</sub> laser with 100 ns pulse duration was used to produce the ablation plasma. The feed gas mixture ratio was CO<sub>2</sub>:N<sub>2</sub>:He = 2:1:4. As shown in the figure, the laser beam was transported by two plain mirrors and injected into the target chamber that was designed and fabricated at the ITEP.<sup>2)</sup> A NaCl window was used to create a vacuum in the chamber, typically  $7 \times 10^{-4}$  Pa. The laser light was reflected by another plain mirror which was placed in front of the target. The reflected light was focused onto the surface of the target using a focusing mirror. Subsequently, induced plasma passed through the openings of the mirrors to the beam line. The target itself was a bulk of carbon material which could be rotated by a ratchet which coincided with the shot-by-shot operation of the laser. The target chamber was grounded and the produced plasma had very slow velocity. The plasma in the target chamber expanded through a drift space to the electric analyzer system (see Fig. 2). At the entrance to the analyzer, ions were extracted and guided to a detector. This electrostatic analyzer was fabricated at the ITEP and was installed

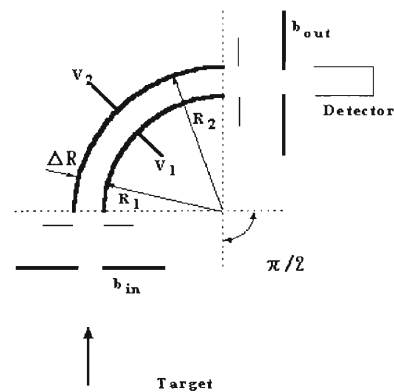


Fig. 2. Structure of the electric analyzer.

Table 1. Design parameters of the electric analyzer.

Geometry of plates:	cylindrical
Deflection angle:	90 deg.
Mean radius of the plates, R <sub>0</sub> :	100 mm
Gap between the plates, R <sub>0</sub> :	5 mm
Geometric factor of the analyzer:	$k = \frac{R_0}{2DR} = 10$
Maximum potential of electrodes:	$U = \pm 20$ kV
Energy dynamic range:	$\frac{E_{\max}}{E_{\min}} = 4 \times 10^4$
Input slit: accuracy of control:	$Db_{\text{in}} = 2.5$ mm
width range:	$b_{\text{in}} = 5$ mm
Output slit: accuracy of control:	$Db_{\text{out}} = 2.5$ mm
width range:	$b_{\text{out}} = 5$ mm
Detector (electron multiplier):	Ceratron
coefficient of multiplication:	up to $10^8$
applied voltage:	up to 4 kV

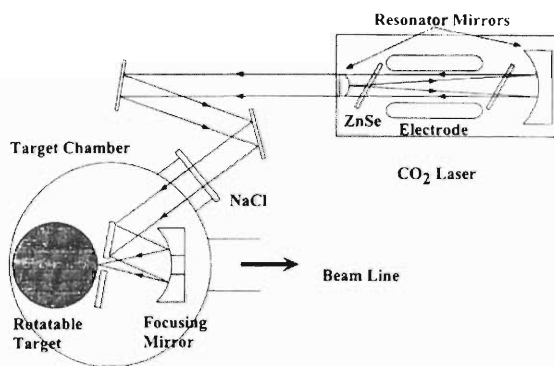


Fig. 1. Experimental setup.

\*<sup>1</sup> Center for Nuclear Study, University of Tokyo

\*<sup>2</sup> Institute of Theoretical and Experimental Physics, Russia

in the RIKEN LIS. The main parameters of the analyzer are summarized in Table 1. The analyzed ions were detected by Ceratron, EMT-6081B.

The current amplification coefficient of the Ceratron detector is reported to be  $10^8$  at bias voltage = 4 kV. Unfortunately, the reference gave no data for the electron amplification to low-energy carbon ions in each charge state. Therefore, we had to determine the dependence of the secondary electron emission coefficient of carbon ions on energy and charge states. We carried out the calibration measurement using a Faraday cup. The Faraday cup had an aperture of 50 mm diameter and a length of 250 mm, and was located at a distance of 2.92 m from the target. From the measured current signal and the Ceratron signal under the same experimental conditions, the ratio of the calibrated value (CR/FC value) to the real current was obtained.

A typical spectrum measured with Ceratron at a distance of 4.43 m from the carbon target is shown in Fig. 3. To clearly separate the peaks for each charge state, the flight distance was set at 4.43 m. The signal shape was averaged for 32 shots. The potentials of the electrodes were set to  $\pm 8$  V.

We can determine the velocities and beam energies of the ions corresponding to each peak. Then, using the ratio of the calibration value to the current value, we can obtain the charge distribution and time variation of the ions contained in the laser plasma at a distance of 264 mm from the target to the entrance of the RFQ Linac, as described in Fig. 4. The fraction of the current value for each charge state of the ions is shown in Table 2.

The absolute values of the beam currents were estimated from the total current. In this measurement, a Faraday cup, with an aperture of 10 mm diameter located at a distance of 1.25 m from the target, detected a current of 6.45 mA. Using the formula  $j \propto \left(\frac{L_0}{L}\right)^3$ , we can estimate the total carbon ion current under the conditions of the direct plasma injection method (a dis-

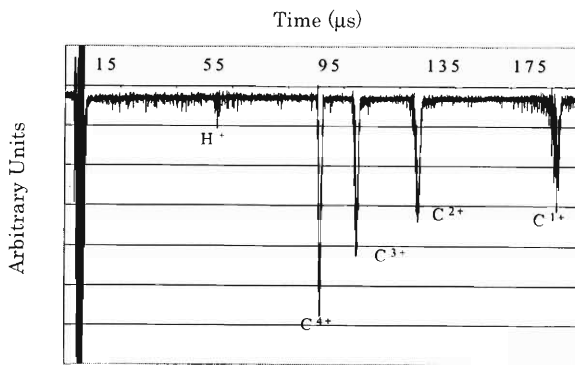


Fig. 3. Typical Ceratron signal.

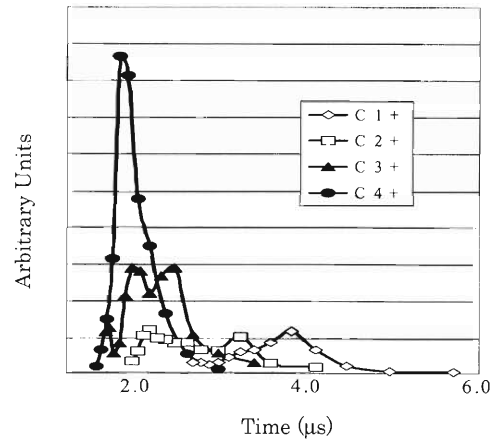


Fig. 4. Pulse time structure for each charge state of the carbon ions.

Table 2. Fraction in laser plasma and the current for each charge state of the carbon ions.

	C <sup>4+</sup>	C <sup>3+</sup>	C <sup>2+</sup>	C <sup>1+</sup>
Fraction	47%	31%	14%	8%
Estimated Current	44.1 mA	29.1 mA	13.1 mA	7.5 mA

tance of 264 mm from the target, 4 mm aperture slit).  $L$  and  $L_0$  are the distances between the target and the detector with estimated current and measured current, respectively. Estimated current values are summarized in Table 2.

#### References

- 1) T. Takeuchi et al.: Proc. EPAC2000 (2000), p. 1622.
- 2) S. Kondrashev: RIKEN-AF-AC-15 (1999).
- 3) B. Sharkov et al.: Proc. EPAC96 (1996), p. 1550.

# Carbon beam acceleration using direct injection method

M. Okamura, T. Takeuchi,\*<sup>1</sup> T. Hattori,\*<sup>2</sup> R. A. Jameson, and T. Katayama

For MUSES<sup>1)</sup> the project at RIKEN, we studied the RFQ linac to determine its ability to accept beams from a laser ion source.<sup>2)</sup> Generally, this type of pulsed ion source can provide high-intensity heavy-ion beams with highly charged states and is well suited for injection to synchrotrons. However, the beams from the laser ion source have a broad energy spread, strong space charge effect, and time variation of current, which consists of various charge states. Also, the beam profile changes dynamically.<sup>3)</sup> Due to the complex features mentioned above, it is extremely complicated to design a low-energy transport line between the source and the first-stage accelerator which usually consists of an extraction system and specially fabricated focusing devices.<sup>4)</sup> In order for the RFQ linac to accept pulsed intense beams from the laser ion source, special attention should be paid to the design of the injection scheme of the RFQ.<sup>5)</sup> In this paper, a completely new injection method will be introduced and the results of the verification experiment will also be reported.

Using a 4 J TEA CO<sub>2</sub> laser with 70 ns pulse duration, the basic parameters of an expanding plasma have been measured. The irradiated power density was estimated to be 10<sup>11</sup> W/cm<sup>2</sup> and the measured divergence of an expanding ablation plasma was less than 20 degrees.<sup>6)</sup> In the case of a carbon target, we obtained several tens mA of C<sup>4+</sup> beam at a distance of 3 m from the target. An efficient method of injecting a high-current beam into an RFQ must be investigated.

The beam emittance from the laser source is mainly determined by emittance growth due to the strong space charge effect. If we consider only the expanding shape of plasma which has a 0.3 mm radius laser spot on the target and 20 degrees of divergence, the normalized beam emittance of ions in the plasma would be only about 0.057 $\pi$  mm mrad.

In order to reduce the space charge effect in the initial beam from the source, a direct injection method has been proposed. A schematic view of the injection system is shown in Fig. 1. The laser target is located in a vacuum chamber which is directly connected to an RFQ but electrically isolated. After the laser hits the target, ablated plasma expands in the target vacuum chamber under the high-voltage power supply, and the plasma enters directly the RFQ channel. At the entrance of the RFQ, the electrons in the plasma will be deflected and only the ion beams will be trapped by the RFQ focusing force. Finally, the injected intense beam will be accelerated to the designed energy.

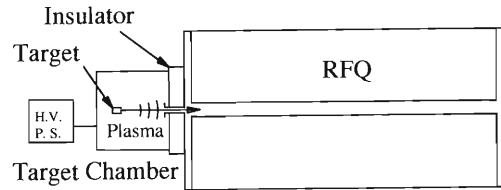


Fig. 1. Schematic view of the direct injection method.

In order to verify the feasibility of this scheme, an acceleration test was carried out using TITech RFQ.<sup>7)</sup> This heavy-ion RFQ was originally designed for medium-current beams and is not appropriate for accommodating the intense beam from the laser source. In this experiment, it was utilized in order to prove the principle of the direct injection method. The main design parameters of the RFQ are listed in Table 1.

A conceptual layout of the experimental set up is indicated in Fig. 2. The laser beam, emitted from the TEA CO<sub>2</sub> cavity, was guided by two planer mirrors and then focused onto the carbon target by a concave

Table 1. Main parameters of the TITech RFQ.

Designed Values	
Charge-to-mass ratio	$\geq 1/16$
Operating frequency (MHz)	80
Input energy (keV/amu)	5
Output energy (keV/amu)	214
Normalized emittance (100%) (cm · mrad)	0.05 $\pi$
Vane length (cm)	422
Total number of cells	273
Characteristic bore radius, $r_0$ (cm)	0.466
Synchronous phase, $\phi_s$	$-90^\circ \rightarrow -20^\circ$
Transmission for $q/A = 1/16$ beam 10 mA input	<b>6.84 mA</b>

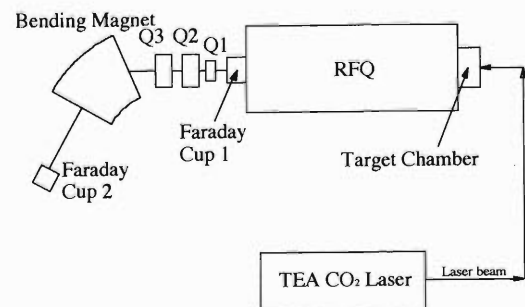


Fig. 2. Layout of the experimental setup.

\*<sup>1</sup> Graduate School of Science, University of Tokyo

\*<sup>2</sup> Research Laboratory for Nuclear Reactors, Tokyo Institute of Technology

donut-shaped mirror, which is installed between the target and the RFQ cavity. The ablation plasma is induced from the target surface and expands, passing through the hole of the concave mirror and then a small slit. This slit,  $\phi = 4$  mm, is aimed at scraping the excess plasma that cannot fit into the beam channel of the RFQ, and is placed very close, 6 mm from the electrodes, to the RFQ. Only a small portion of the ablated plasma, estimated to be about several hundreds mA of the beam current, can enter the RFQ. In order to adjust the velocity of the carbon ions to the designed value of the RFQ, high voltage was supplied to the target chamber.

The accelerated carbon beam was observed successfully at the Faraday cup located next to the RFQ. The measured peak current reached 25 mA, as shown in Fig. 3. The observed ion current clearly reflects the bunch structure of the accelerated beam due to the short distance between the RFQ and the Faraday Cup. This means that the beam current shape shown in Fig. 3 represents the envelope of the peaks which appear at RF cycles of 80 MHz. The observed peak current of 25 mA can be converted into the averaged peak current of 8 mA. For this measurement, the target was at 20 kV. It is expected that the current measured at Faraday cup (FC) 1 contains  $C^{3+}$ ,  $C^{4+}$ , and  $C^{5+}$  which have injection ion velocities greater than the design value. The analyzed beam current at FC 2 is shown in Fig. 4.

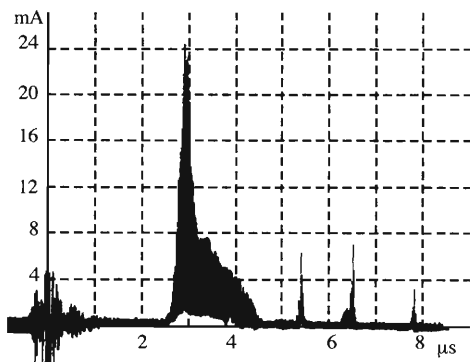


Fig. 3. Measured current at at FC 1.

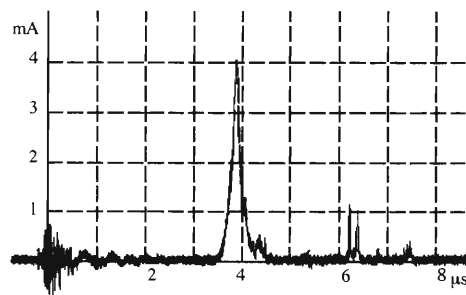


Fig. 4. Analyzed  $C^{4+}$  beam.

The triplet of quadrupole magnets was optimized to obtain the highest current. The distance between the FC 2 and the RFQ is sufficient to de bunch the beam. The effect of the bunch structure on the current is not necessary to take into account. The measured peak currents were 3.9 mA and 1.6 mA for  $C^{4+}$  and  $C^{3+}$ , respectively. The TITech RFQ was optimized to get 6.8 mA of a  $q/A = 1/16$  beam. In the case of  $C^{4+}$ ,  $q/A = 4/12$ , the space charge effect was behave more than twenty times stronger. The numerically predicted value was 1.85 mA, which is much lower than the experimentally achieved current of 3.9 mA. It was found that the direct injection method is effective for the laser ion source.

In order to capture the intense ion beams from a laser ion source, the direct injection method has been proposed. The first accelerated carbon beam was successfully observed and the obtained current was much higher than expected. This method is useful for utilizing the intense beam from a laser ion source.

#### References

- 1) T. Katayama et al.: Proc. EPAC2000 (2000), p. 68.
- 2) B. Wolf: in *Handbook of Ion Source* (CRC Press, Boca Raton, 1995), p. 147.
- 3) P. Fournier et al.: Rev. Sci. Instrum. **71**, 924 (2000).
- 4) P. Fournier et al.: Proc. Particle Accelerator Conf., New York, USA, 1999-3 (1999), p. 103.
- 5) M. Okamura et al.: Proc. EPAC2000 (2000), p. 848.
- 6) T. Takeuchi et al.: Proc. EPAC2000 (2000), p. 1622.
- 7) M. Okamura et al.: Nucl. Instrum. Methods Phys. Res. B **99**, 694 (1995).

## Development of long-lived carbon foil for charge stripper in RILAC

H. Hasebe,\*<sup>1</sup> I. Sugai,\*<sup>2</sup> H. Akiyoshi, and M. Kase

Carbon foils (C-foils) are extensively used as charge strippers for heavy-ion beams. However, C-foils have the serious disadvantage of having a short lifetime with a high-intensity heavy-ion beam. The C-foil lifetime is very short in the RIKEN RI Beam Factory (RIBF). Therefore, the production of long-lived C-foils is urgently required for the RIBF project. A large amount of progress has been made in developing long-lived C-foil production techniques. We are planning to produce a self-sufficient number of long-lived C-foils according to the techniques presented in Ref. 1.

C-foils with a thickness of  $10 \mu\text{g}/\text{cm}^2$  were produced by the arc discharge evaporation method. The arc discharges were generated by AC voltage as well as by DC voltage. Figure 1 shows the interior view of the

vacuum chamber. The AC and DC arc discharge evaporation sources are placed in the middle of the vacuum chamber. The angle between the direction of the arc discharge and the horizontal plane was varied from 0 to 45 degrees. The discharge currents used were 300 A, 350 A, 400 A, 450 A, and 500 A. The thickness of the C-foil was continuously measured by a quartz crystal thickness gauge. The gauge was calibrated by measuring the mass and the area of the C-foil. Two resistance-heated sources for releasing the agent were placed in both sides of the vacuum chamber. A substrate rotation mechanism was used in order to make the film thickness uniform. The angle between the substrates and the horizontal plane was varied according to the position of the evaporation source.

The durability of C-foils under beam irradiation was

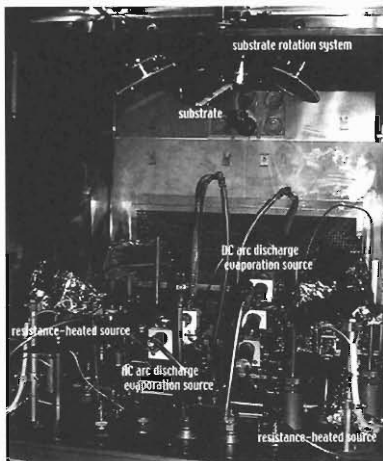


Fig. 1. Interior of the vacuum chamber.

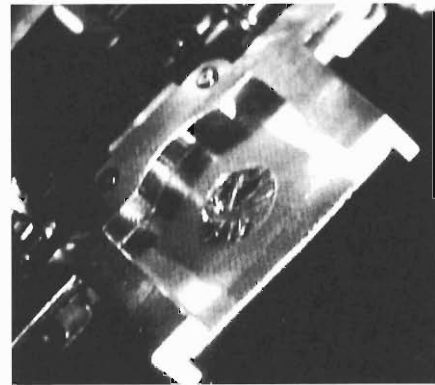


Fig. 2. Photograph of C-foil folder in vacuum chamber. A  $10 \mu\text{g}/\text{cm}^2$  C-foil was mounted on the folder.

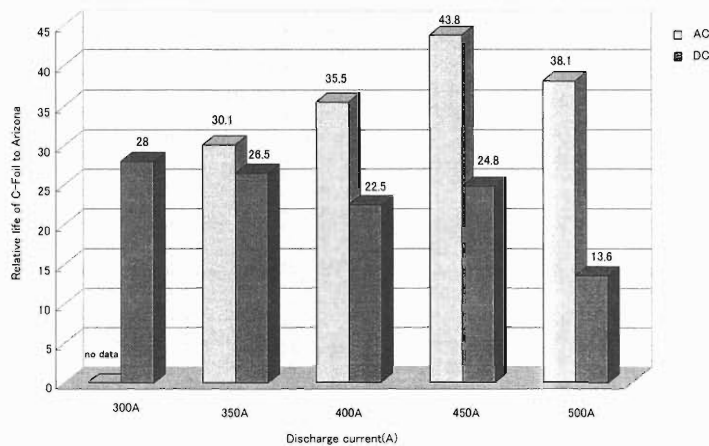


Fig. 3. Dependence of C-foil lifetime on the discharge current.

\*<sup>1</sup> SHI Accelerator Service, Ltd.

\*<sup>2</sup> High Energy Accelerator Research Organization (KEK)

measured. A 32 keV/u  $^{136}\text{Xe}^{9+}$  beam with an intensity of 1.1 pμA from a 500 kV terminal was focused on a C-foil. The beam spot is rectangular with a size of 5 mm × 5 mm. The beam spot was carefully made to form a uniform beam. The break of the C-foil was detected by the beam current measured downstream of the foil and also by observing the foil using a TV camera. Figure 2 shows a C-foil mounted on an aluminum folder in the vacuum chamber. This chamber was set on the beam line. The C-Foil folders of 40 sheets moved within the chamber automatically. The lifetime of commercially available C-foils (Arizona Carbon Foil Co.) with the same thickness was measured to be 60 s on average. This lifetime is taken as the standard in this work.

Figure 3 shows the dependence of the C- foil lifetime on the discharge current. The longest lifetimes were measured when the current was 450 A in the case of the AC discharge, and 300 A in the case of the DC

discharge. We successfully produced a C-foil whose lifetime was 40 times longer than the commercial foil when the discharge current was AC 450 A, there was 0 degrees between the direction of the arc discharge and the horizontal plane, and OT-5200N(S) graphite rods and a releasing agent of NiCl<sub>2</sub> were used.

The conditions for production of a long-lived C-foil have been determined. The preparation of C-foils with an increased thickness of 80 μg/cm<sup>2</sup> is now in progress. We will soon test this C-foil with a few Mev/u intense heavy-ion beam in the realistic case for the RIBF project.

#### References

- 1) I. Sugai, M. Oyaizu, H. Kawakami, C. Ohmori, T. Hattori, K. Kawasaki, M. J. Borden, and R. J. Macek: Nucl. Instrum. Methods Phys. Res. A **362**, 70 (1995).

## Low-energy beam test of liquid film charge stripper

H. Akiyoshi, T. Chiba, H. Hasebe,\* M. Kase, and Y. Yano

A charge stripper plays an essential role in heavy ion accelerators. With the higher intensity and high-mass beams of the RIKEN RI Beam Factory (RIBF), commonly used carbon stripper foils are expected to break within short lifetimes. In order to overcome the stripper foil lifetime problem, a charge stripper system using a thin oil film has been developed.

A liquid film with a large area was produced by a rotating disc touching the surface of silicone oil, as described in the last report.<sup>1)</sup> The motor of a turbomolecular pump which rotated the disc was replaced by an AC servo motor which was placed outside the vacuum chamber. The motor rotates the disc through a ferrofluid sealed rotary motion feedthrough. The replacement of the motor allowed beams to pass through, enabling us to perform the beam test. Figure 1 shows a photograph of the liquid film. The slanting dim white line from the middle to the upper left of the photograph shows the upper edge of the liquid film.

A low-energy beam test of the liquid film stripper was performed using a Cockcroft-Walton injector of the RIKEN heavy ion linac (RILAC).

Figure 2 shows a schematic layout of the experimental setup.  ${}^4\text{He}^+$  ions at 500 keV were focused on the thinnest area of a liquid film by observing the fluorescent image of the beam on a quartz plate in front of the liquid film. The thickness distribution of the liquid film was observed by means of an optical interference pattern of visible rays. The beam spot had a nearly



Fig. 1. Photograph of liquid film.

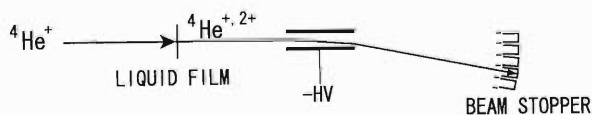


Fig. 2. Schematic layout of experimental setup.

\* SHI Accelerator Service, Ltd.

<sup>1)</sup> ACF-Metals, The Arizona Carbon Foil Co., Inc.

round shape, and the diameter was about 6 mm. A blue fluorescent image of the beam was also observed on the liquid film itself when a high-intensity beam was bombarded. It is probable that a certain number of  ${}^4\text{He}^+$  ions pass by the liquid film because the beam was focused nearly on the upper edge of the film. When beam intensity was increased, the upper edge of the film was broken like a waterfall into which a log was thrust. This increases the numbers of helium ions which pass by the liquid film. Some of the helium ions are likely to be charge-exchanged by oil mist or other residual gases without passing through the liquid film. The energy of these helium ions is 500 keV, the same as that of incident helium ions, while the energy of the helium ions which passed through the liquid film is somewhat lower than 500 keV because of the energy loss in the liquid film. Therefore, roughly speaking,  ${}^4\text{He}^+$  and  ${}^4\text{He}^{2+}$  ions with two energies emerge from the stripper system.

The helium ions that emerged from the stripper were injected into a parallel-plate electrostatic deflector, and split according to their energy and charge state. A beam stopper was placed behind the electrostatic deflector. The beam stopper was divided into nine blocks in each two degree as plotted in Fig. 2, and the current of incident helium ions on each block was extracted separately. The currents were measured by varying the voltage of the deflector.

Figure 3 shows the differences in the deflector volt-

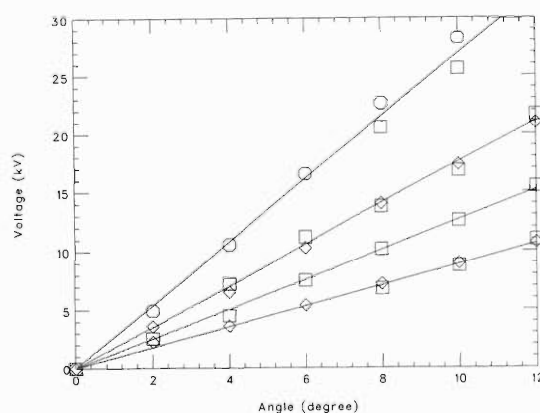


Fig. 3. Sorted helium ions by electrostatic deflector according to their energy and charge states. The horizontal axis indicates the deflection angle, and the vertical axis indicates the voltage of the deflector. Squares and diamonds indicate the data measured with a liquid film produced by 1600 rpm disc rotation and a  $80 \mu\text{g}/\text{cm}^2$  carbon foil,<sup>a</sup> respectively. Circles indicate the data obtained without any stripper.

ages according to the energy and the charge states of the helium ions coming to each block of the beam stopper. The data points roughly form four lines. It is probable that these lines correspond to, from the upper line to the lower line, the  ${}^4\text{He}^+$  ions which passed by the liquid film (first line), the  ${}^4\text{He}^+$  ions which passed through the liquid film (second line), the  ${}^4\text{He}^{2+}$  ions which passed by the liquid film (third line), and the  ${}^4\text{He}^{2+}$  ions which passed through the liquid film (fourth line). Therefore, one can estimate the thickness of the liquid film at the beam position from the difference between the first and second lines. The interpretation of the lines was checked by observing the data points of  $80\ \mu\text{g}/\text{cm}^2$  carbon foil<sup>a</sup> that lay closely on the second and fourth lines which had been fitted to the data points of the liquid film produced by 1600 rpm disc rotation.

The thickness of the liquid film varies as a function of the rotating frequency of the disc. Derived thicknesses are plotted in Fig. 4 as a function of the rotating frequency of the disc. When the disc is rotated at 1500–1800 rpm, the thickness of the liquid film at the thinnest area is such that it is suitable for use as a charge stripper for ions with energies of about 4–6 MeV/nucleon.<sup>2)</sup>

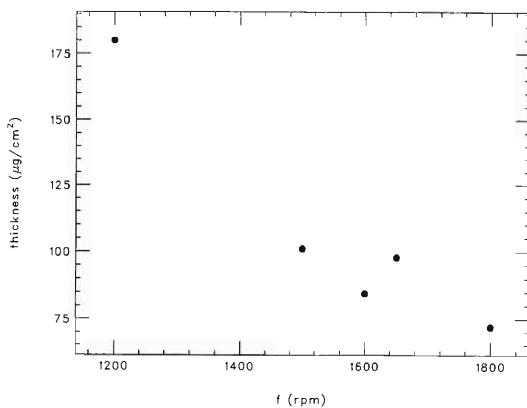


Fig. 4. Thickness of the liquid film as a function of rotating frequency of the disc.

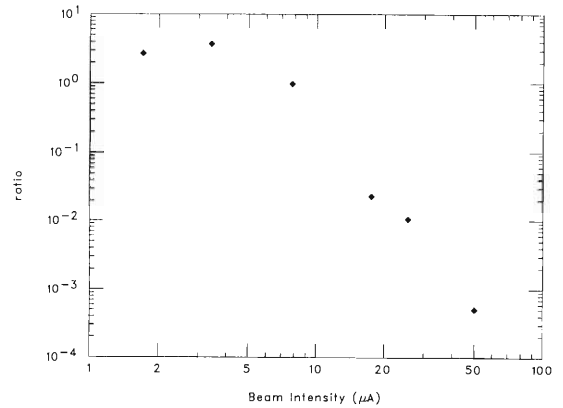


Fig. 5. The current of  ${}^4\text{He}^{2+}$  ions which passed through the liquid film divided by the current of  ${}^4\text{He}^+$  ions which passed by the liquid film as a function of beam intensity measured by a Faraday cup placed upstream of the stripper. The disc was rotated at 1500 rpm.

Figure 5 shows ratios of the current of the  ${}^4\text{He}^{2+}$  ions which passed through the liquid film to the current of the  ${}^4\text{He}^+$  ions which passed by the liquid film in the case of 1500 rpm disc rotation. As beam intensity was increased, the upper edge of the film was broken. This significantly decreases the ratio as is seen in Fig. 5. The limit of beam intensity is estimated preliminarily to be about  $10\ \mu\text{A}$ , which corresponds to a power density of  $8\ \text{W}/\text{cm}^2$ . If a  $5.85\ \text{MeV}/\text{nucleon}$   ${}^{136}\text{Xe}$  beam has the same beam spot size, this limit value corresponds to the beam current of  $300\ \text{pA}$ . In the case of  $0.9\ \text{MeV}/\text{nucleon}$   ${}^{238}\text{U}$ , the limit value corresponds to  $200\ \text{pA}$ .

We are presently preparing for a higher energy beam test at RILAC in order to measure the equilibrium charge state distribution and obtain more practical information about durability against high-intensity heavy ion beams.

#### References

- 1) H. Akiyoshi, T. Chiba, M. Kase, and Y. Yano: RIKEN Accel. Prog. Rep. **34**, 315 (2001).
- 2) E. Baron: IEEE Trans. Nucl. Sci. **26**, 2411 (1979).

## Control system for RRC, AVF and RILAC

M. Kobayashi-Komiyama, I. Yokoyama, M. Nagase, E. Ikezawa, M. Fujimaki, R. Abe,\*  
T. Tanabe, and M. Kase

The control system of the RIKEN Ring Cyclotron (RRC) and one of its injectors, AVF Cyclotron, has been replaced in the new system using the Experimental Physics and Industrial Control System (EPICS)<sup>1)</sup> and has been used since April, 2001. The details of this project and the system development are shown in Ref. 2. By this system renewing, the M60/AR Mitsubishi minicomputer, which was a host computer in the previous system, has been used no longer for the beam operation. However, the previous system has another M60 minicomputer for the operation of the RIKEN Heavy Ion Linac (RILAC), the other injector of the RRC, which also needs to be replaced.

The M60/500 used for the RILAC operation controls the CAMAC-CIM/DIM system<sup>3)</sup> and the GP-IB system. The CAMAC-CIM/DIM system controls some magnet power supplies and some beam diagnostic devices. It is able to control the CAMAC-CIM/DIM system only by adding the operational data into the existing Oracle database. On the other hand, GP-IB, which is a new device of our EPICS for RRC and AVF control, controls some power supplies for the magnets and for the RF system from the first tank to the fourth tank of the RILAC. Thus, we need to develop another

device support for GP-IB. There are no significant differences in the construction of the EPICS database between a CAMAC-CIM/DIM system and a GP-IB system. Therefore, the device support for the GP-IB device was developed in the same way as the device supports for the CIM/DIM. Their operation was tested using the same kind of GUIs as the CAMAC system and it was succeeded last summer. We are to replace the M60/500 system in the EPICS within this year.

Furthermore, a part of the new introduced system of the RILAC facility has also been controlled by EPICS since April, 2001. The project on energy upgrading of RILAC has started several years before, and the beam transport system of the RILAC facility has been replaced in the new system in summer of 2000.<sup>4)</sup> In this system, a network I/O (NIO) system<sup>5)</sup> was introduced to control the new power supplies. The device supports for NIO were also developed by ourselves.

Figure 1 shows the structure of the control system of the RIKEN Accelerator Research Facility (RARF) using EPICS. In our control system, one HP-UX 11.0 machine works as a server and several PCs work as clients. This server machine was introduced to our

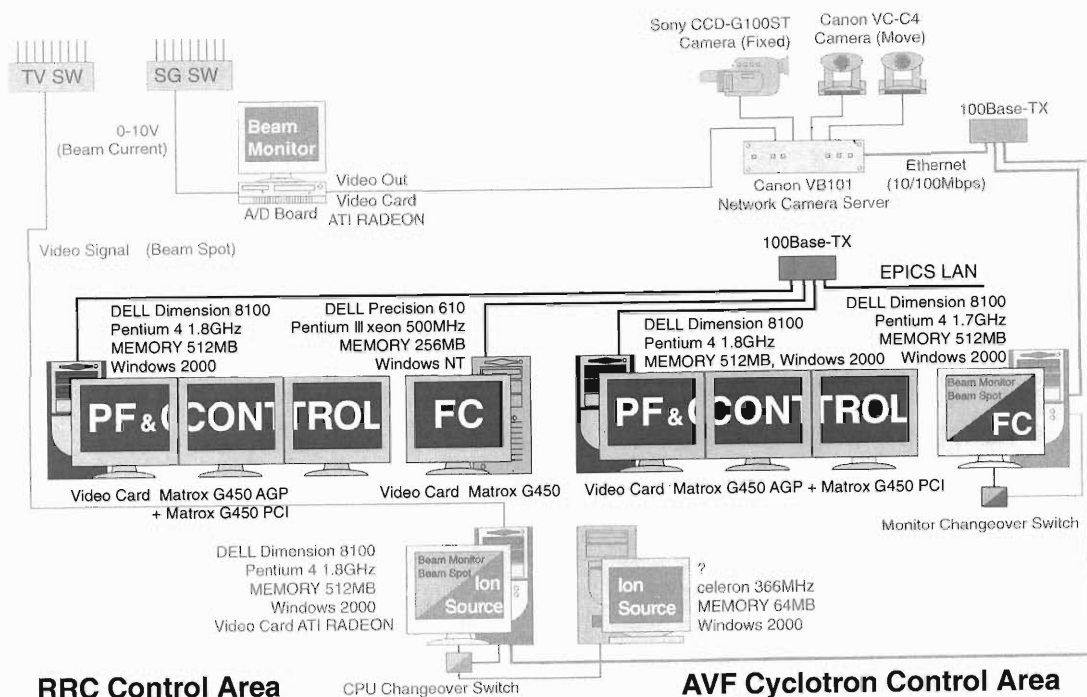


Fig. 1. Structure of the RARF control system using EPICS.

\* SHI Accelerator Service, Ltd.

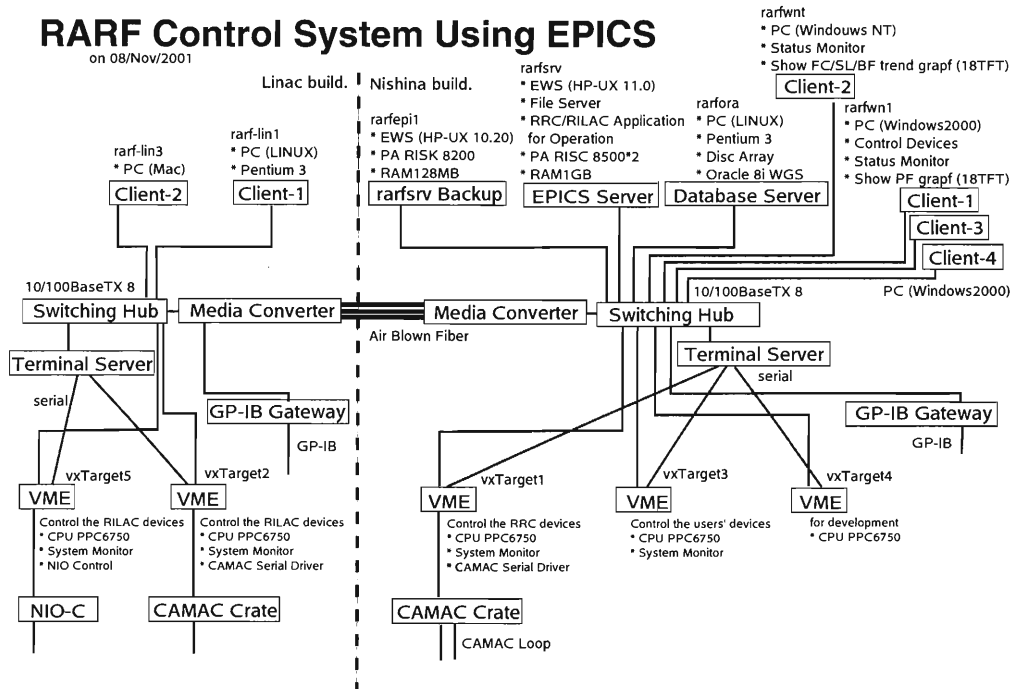


Fig. 2. Client PC configuration for EPICS at the RRC control room.

system last October instead of the HP-UX 10.20 workstation to make the control system more stable. All EPICS databases and EPICS sequencers, which are written in the state notation language for sequential operations, are loaded on several VME computers from the server computer. An operator connects his PC to the HP-UX server machine, and controls accelerator devices by communication with objected EPICS records on the VME computer. There are five VME computers in our system as shown in Fig. 1. The vxTarget1 controls all CAMAC-CIM/DIM devices in the AVF and the RRC system. The vxTarget2 controls all CAMAC-CIM/DIM devices and GP-IB devices in the RILAC system. The vxTarget3 controls the RRC users' system, SMART (E4) and RIPS (E6), and the vxTarget5 controls all the magnet power supplies controlled by NIO in the RILAC system. The vxTarget4 is used only for the system development. Currently, there are more than 20,000 EPICS records on the vxTarget1. This number is too big. However, it is difficult to separate these records into two and to load them to plural VME computers, because it is difficult to divide the CAMAC control loop in two. Therefore, we are using the VME CPU module which mounts 128 MByte memory for vxTarget1 for operation without resource troubles. Approximately 50% of the memory is used in constant, and we can continue beam operation smoothly. The vxTarget1 and the vxTarget2 have CPU modules which mount 128 MByte memory, and the others have

CPU modules which mount 64 MByte memory. Since the amounts of EPICS records in the vxTarget2, vxTarget3, vxTarget4 and vxTarget5 are smaller than that in the vxTarget1, our system has sufficient capacity.

Figure 2 shows the client PC configuration for EPICS at the control room in the Nishina building. At the present, almost all RRC devices connected to the CAMAC-CIM/DIM system can be controlled by EPICS. Beam operation is carried out by using each GUI and the condition of the magnet power supplies is monitored every 10 s using one of the standard EPICS host tools, Alarm Handler (ALH). It tells us unexpected malfunctioning of the power supplies by beeping. Furthermore, the beam intensity is measured by a Faraday cup every 200 ms and always shown on the trend graph on PC at the control desk.

We are to control all beam devices which compose the RRC and the RILAC system using EPICS in the near future.

#### References

- 1) <http://www.aps.anl.gov/epics/>
- 2) M. Kobayashi-Komiyama et al.: RIKEN Accel. Prog. Rep. **34**, 318 (2001).
- 3) T. Wada et al.: Sci. Papers I.P.C.R. **79**, 28 (1985).
- 4) E. Ikezawa et al.: Proc. 13th Symp. Accelerator Science and Technology, Suita (2001), p. 169.
- 5) <http://elc.aska.or.jp/denshi/system/kasokuki/>

## Measurement of an open-loop transfer function of a feedback control system of cavity voltage

Y. Chiba, O. Kanigaito, and N. Sakamoto

An open-loop transfer function of rf-amplitude modulation was measured for an rf system of the booster linac in the charge-state multiplier (CSM),<sup>1)</sup> using a network analyzer along with a simple circuit based on a conventional op-amp. The measurement, which was performed under the high-power operation in cw mode, has shown that the feedback control system meets the requirements of the stability condition over a wide range of gap voltage.

Figure 1 shows a simplified block diagram of the feedback control system of the cavity voltage. The voltage is detected by a pickup electrode and transferred to a level controller through a 50-ohm cable. The level controller first demodulates the pickup signal, and then compares it with a reference voltage of the cavity. The resultant error voltage passes through a loop amplifier. The rf signal from the signal generator is attenuated according to the amplified error, and transmitted to the cavity through the rf-amplifier chain. This loop is represented by a solid line in Fig. 1.

There are two main components that characterize the open-loop transfer function; the cavity and the loop amplifiers. The cavity response to the amplitude modulation has the property of a simple low-pass filter. Using the loaded Q-value  $Q_L$ , it is written in the following form;

$$G_{cav}(f) \propto \frac{1}{1 + 2jQLf/f_c}, \quad (1)$$

where  $f$  and  $f_c$  are the modulation frequency and the

rf frequency, respectively. The loop amplifiers are designed to stabilize the cavity voltage as much as possible while keeping the feedback loop in a stable condition. In the level controllers of the CSM, two loop amplifiers, denoted by Loop Amplifier-1 and -2 in Fig. 1, are dominant in the low modulation frequencies. The former is based on a low-pass filter with phase lag compensations, as shown in Fig. 2. The latter is a single-pole low-pass filter whose time constant is 10  $\mu$ s.

In the real system, however, other factors such as the characteristics of the modulator, demodulator and the op-amps used in the level controller contribute the feedback performance, particularly at the high modulation frequencies. These effects cannot be estimated easily, since they are sometimes dependent on the cavity voltage and the circuit environments. Therefore, it is important to measure the transfer function directly during cavity operation.

The method we used in the measurement is illustrated in Fig. 1. A measurement circuit is inserted into the feedback loop. Through this circuit, amplitude modulation of frequency  $f$  is added with a network analyzer (Hewlett-Packard HP4195A) to the rf signal. The network analyzer also detects the signals on the loop at two points, denoted in Fig. 1 by T and R, respectively. It finally calculates the ratio of the signals, yielding the open-loop transfer function  $G(f)$  by  $G(f) = R(f)/T(f)$ , where  $T(f)$  and  $R(f)$  are the transferred and the detected amplitudes, respectively.

Figure 3 shows the measurement circuit in detail. It is based on a conventional op-amp (National Semiconductor TL082). The voltage gain from the positive input to the output is chosen to be 1.0, while that from the negative input to the output is  $-0.1$ . The input impedance of the positive input is adjusted to that of

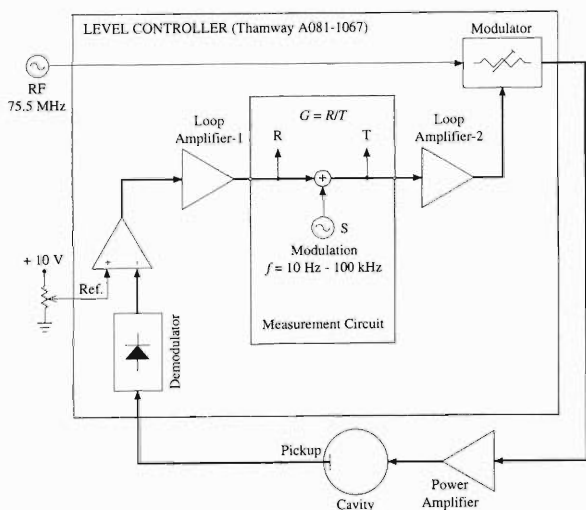


Fig. 1. Simplified block diagram of the feedback control system of cavity voltage of the CSM.

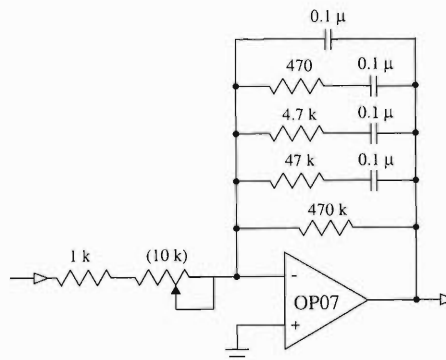


Fig. 2. Schematic drawing of a loop amplifier in the CSM level controller,<sup>2)</sup> denoted by Loop Amplifier-1 in Fig. 1.

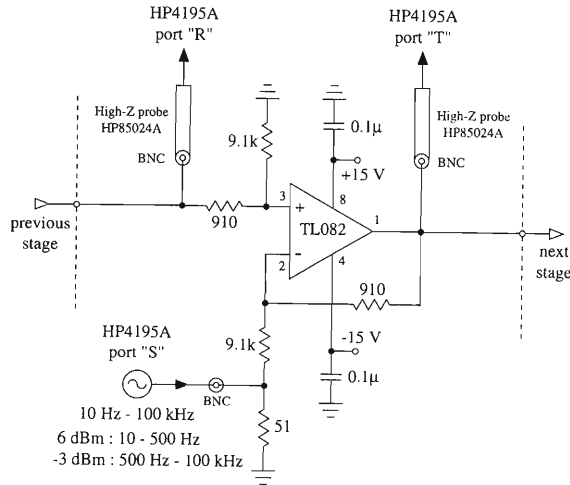


Fig. 3. Schematic drawing of the measurement circuit.

the following op-amp in order not to change the feedback loop with the insertion.

The frequency range of the measurements is set to be 10 Hz to 100 kHz; 10 Hz is the lowest frequency available with the network analyzer. First, it was confirmed that the amplitude and the phase of the voltage gains of the measurement circuit are constant within 0.01 dB and 1 degree, respectively, in this frequency range.

The measurement was performed in the A3 cavity of the CSM booster whose resonant frequency is 75.5 MHz, at three voltage levels; 140, 180 and 300 kV. The measured transfer functions are given in Fig. 4. Although they are affected by noise in the low-frequency region, almost the same curves have been obtained for the three voltage levels. It is also remarkable to see that the values of the phase margin remain around 30 degrees, which means that the stability conditions are well satisfied.

In Fig. 4, the calculated transfer function is also illustrated, which was obtained by multiplying the cavity response (1) and the transfer functions of the two loop amplifiers shown in Fig. 1. In the calculation of the gain, a constant factor has been introduced so that the calculated value can fit the measured results at the lowest frequency (10 Hz). The predicted value reproduces the phase and the slope of the gain in the low-frequency region well. The differences in the high-frequency region can be attributed to various factors, some of which are mentioned above.

The procedure described above is applicable to all

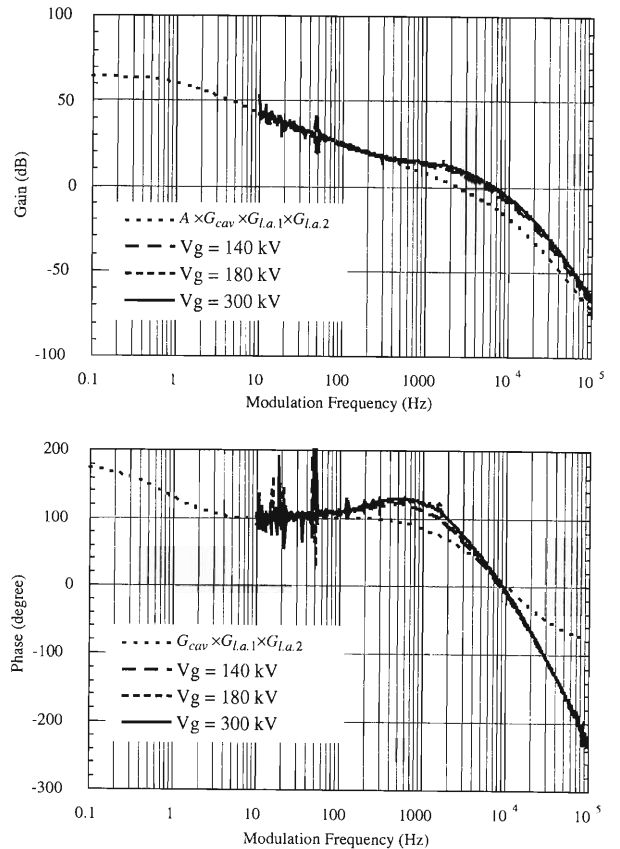


Fig. 4. Bode diagrams of the open-loop transfer functions of the rf-amplitude modulation. Solid and dashed curves are the measured ones. The dotted curve is the calculated transfer function, which is given by the cavity and the two loop amplifiers in Fig. 1. In the calculation, the loaded Q-value of the cavity response was set for the measured value of 12,500.

rf-control systems of this kind. It provides real transfer functions directly during high-power operation. If an rf-control system is equipped with the above circuit for a small expense, it would be useful for the optimization of the feedback performance as well as for the diagnostics of the system.

#### References

- 1) O. Kamigaito et al.: Proc. 13th Symp. on Accelerator Science and Technology, Suita (2001), p. 229.
- 2) Thamway Co., Ltd.: Circuit Drawing, No. T20C99A-30182A, April 2001.

## Development of multi-injection system for the AVF cyclotron

T. Kageyama, Y. Ohshiro,\* M. Kidera, T. Nakagawa, and M. Kase

The AVF cyclotron was constructed for use in experiments using a beam with a few MeV/u of energy or as an injector of the ring cyclotron (RRC) in 1988.<sup>1)</sup> Through collaboration between RIKEN and the Center for Nuclear Study (CNS) of University of Tokyo, the Hyper ECRIS<sup>2)</sup> of CNS was installed in an injection room for the AVF cyclotron in 2001. Three ion sources, Hyper ECRIS, RIKEN 10 GHz ECRIS and RIKEN polarized ion source (PIS), could be used as the injection source for the AVF cyclotron. The new multi-injection system was constructed to allow compatibility between the development of a new ion beam and easy operation for operator.

The old system, consisting of two 45° bending magnets and three quadrupole singlets, is achromatic and bends the beam vertically down to the AVF cyclotron. The new system consists of a dipole magnet, a steering magnet and a beam monitoring chamber. This system

can be rotated 290° to give vertical axis of the cyclotron in order to bend two beams injected from the 10 GHz ECRIS and Hyper ECRIS. The performance of

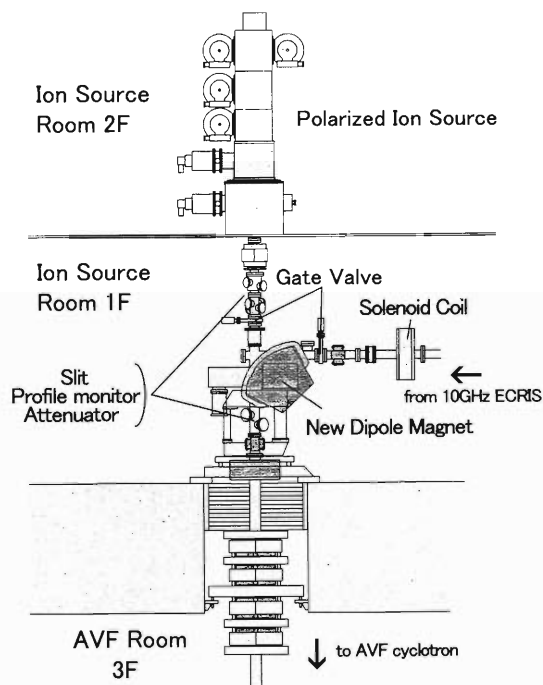


Table 1. Performance and parameters of the dipole magnet.

Rotation angle of magnet	290°
Max. magnetic field	0.15 T
Radius of curvature	500 mm
Bending angle	90°
Width of coil gap	80 mm
Max. operation current	102.2 A
Number of coil turns	112

Fig. 2. Side view of the multi-injection system and polarized ion source (PIS).

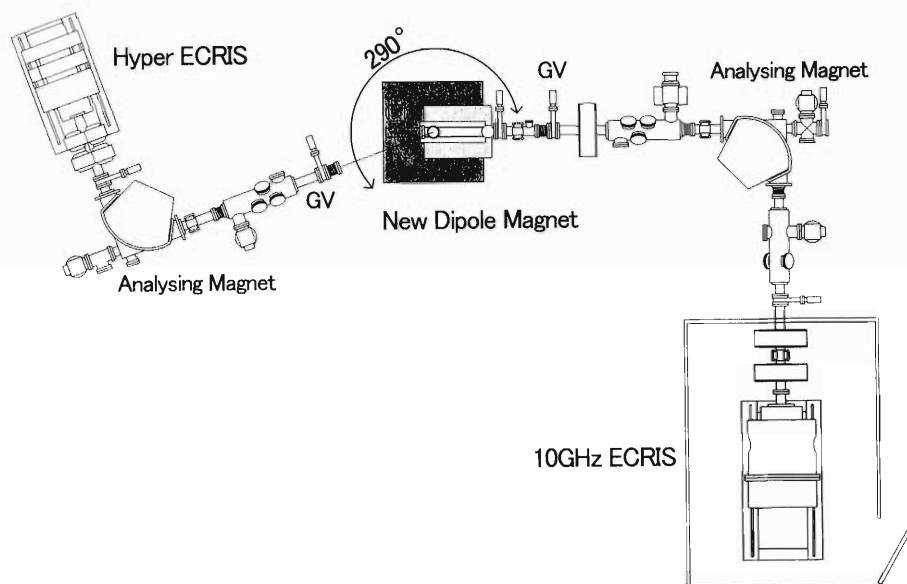


Fig. 1. Plan view of the RIKEN 10 GHz ECRIS, Hyper ECRIS and multi-injection system.

\* Center for Nuclear Study, University of Tokyo

the dipole magnet is shown in Table 1. Figure 1 shows the plan view of Hyper ECRIS, RIKEN 10 GHz ECRIS and the new multi-injection system. The two ECRISs each have a beam monitoring chamber, and they are used for the development of a new ion beam. Figure 2 shows the side view of the PIS and the multi-injection system. The new system can be rotated without breaking the vacuum in the vacuum chamber of the dipole

magnet and the monitoring chamber.

#### References

- 1) A. Goto et al.: RIKEN Accel. Prog. Rep. **22**, 202 (1989).
- 2) Y. Yamashita et al.: Proc. 8th Symp. on Accelerator Science and Technology, Wako (1991), p. 84.

## Construction of the flat-top acceleration system in the RIKEN AVF Cyclotron

S. Kohara, A. Goto, O. Kamigaito, M. Kase, N. Sakamoto, S. Watanabe,\* T. Katayama, and Y. Yano

The flat-top acceleration system in the RIKEN AVF Cyclotron was constructed and installed in August 2001 in order to improve the extraction efficiency and energy spread of the beam.<sup>1)</sup> The flat-top accelerating voltage is generated by a superposition of the fundamental and 3rd-harmonic frequencies. The fundamental-frequency range is from 12 to 24 MHz, the 3rd-harmonic-frequency range is from 36 to 72 MHz.

Fifth harmonics instead of 3rd harmonics can also be used for this purpose. However, we decided to adopt the 3rd-harmonics mode instead of the 5th-harmonics one for the following reason. In general, the power loss can be less for the 5th-harmonics than for the 3rd-harmonics, since the required amplitude of the 5th-harmonics for flat topping is about 1/25 of the fundamental frequency, while that of the 3rd-harmonics is about 1/9 of the fundamental frequency. Thus a cold model test using superposition of the 5th harmonics was carried out three years ago.<sup>2)</sup> Generation of flat-top voltage over the entire frequency range was confirmed but the power loss of the resonator was not measured at that time. Prior to designing the real system, we again measured the rf characteristics in detail using the model and found that the power loss for the 3rd harmonics was actually less than that for the 5th harmonics.

Cross-sectional views of the system are shown in Fig. 1. The newly added flat-top resonator is coupled to the original main resonator with a coupling

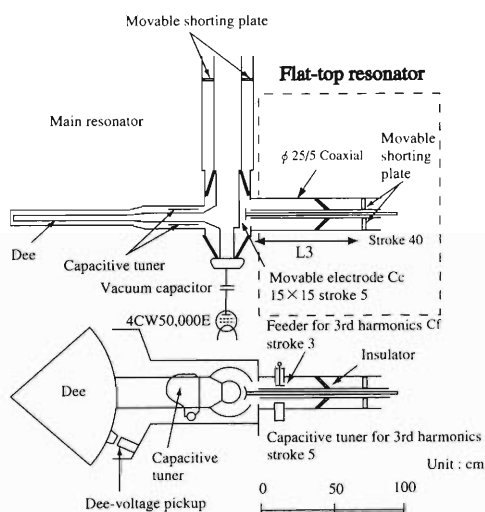


Fig. 1. Cross-sectional view of the flat-top acceleration system for the RIKEN AVF Cyclotron.

\* Center for Nuclear Study, Graduate School of Science, University of Tokyo

capacitor ( $C_c$ ). It makes the combined system resonate at both fundamental and 3rd-harmonic frequencies simultaneously.<sup>3)</sup> Rf power of the 3rd harmonics is fed through a variable capacitor ( $C_f$ ), which matches the input impedance of the flat-top resonator to the impedance of the feeder ( $50\ \Omega$ ). The amplitude and phase of the 3rd harmonics are adjusted to produce a voltage proportional to  $\cos(\omega t) - 1/9 \cos(3\omega t)$  across the dee gap. Tuning for the fundamental frequency is performed in the main resonator and then that for the 3rd harmonics is carried out with both a shorting plate ( $L_3$ ) and coupling capacitor ( $C_c$ ). These tunings interfere with each other. The resonance of the 3rd harmonics is kept constant automatically with a capacitive tuner of the 3rd harmonics by detecting the incident and reflected waves on the feeder line. The stroke of the capacitive tuner is 50 mm. A ceramics insulator is used for support of the inner conductor of the coaxial resonator as well as for achieving a vacuum seal. The flow rate of cooling water for each of the two flat-top resonators is 9 l/min. A photograph of the flat-top resonator installed on the existing main resonator is shown in Fig. 2.

Positions of the tuning elements that satisfy simultaneous resonance are measured with a network analyzer for each resonant frequency. The measured positions of the movable shorting plate and the movable coupling capacitor of the flat-top resonator are shown in Fig. 3 as a function of the 3rd-harmonic frequency. The optimum values for a combination of these two parameters were researched in such a way that the transmission efficiency (the ratio  $\alpha$  mentioned below) became the largest. It was found that the 3rd-harmonic resonance was limited below 63.3 MHz and did not reach the required highest frequency. For the frequencies higher than 63.3 MHz, we plan to retest with a reduction in the size of the coupling capacitor ( $C_c$ ). Let  $v_f$  be the

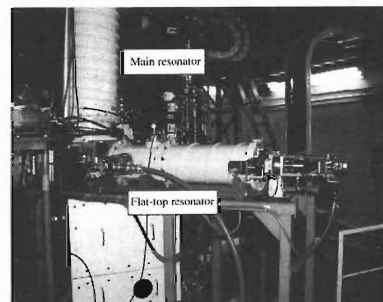


Fig. 2. Photograph of the flat-top resonator installed on the existing main resonator.

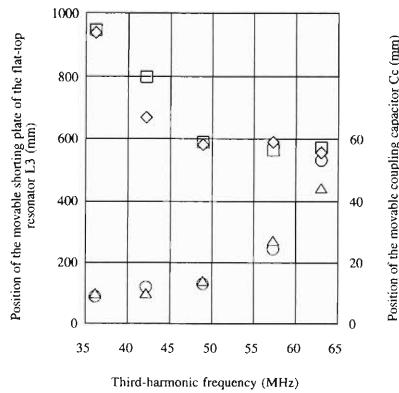


Fig. 3. Positions of the movable shorting plate and the coupling capacitor of the flat-top resonator as a function of the 3rd-harmonics frequency. Squares and circles represent the positions of the shorting plate and the coupling capacitor of the No. 1 resonator, respectively. Diamonds and triangles represent the positions of the shorting plate and the coupling capacitor of the No. 2 resonator, respectively.

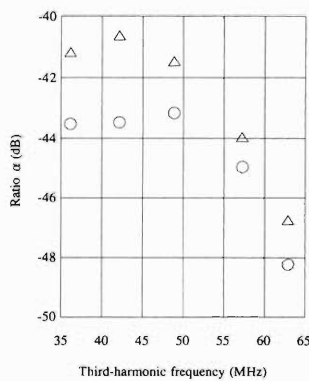


Fig. 4. Ratio of the amplitude at the dee voltage pickup to that at the feeder of the flat-top resonator. Circles represent the ratio of the No. 1 resonator and triangles represent that of the No. 2 resonator.

voltage on the feeder of the flat-top resonator and  $v_m$  be the output voltage of the dee voltage pickup. The ratio  $\alpha = v_m/v_f$  is measured at the 3rd-harmonic frequency in simultaneous resonance. If impedance matching at the feeder is made correctly, the necessary power of the 3rd harmonics for a dee voltage Pd is given by  $(k \cdot v_d)^2 / (2 \cdot z_o \cdot \alpha^2)$ ; here,  $v_d$ : peak voltage of the 3rd harmonics,  $k = v_m/v_d$ : pre-calibrated dividing factor of the dee voltage pickup, and  $z_o$ : characteristic impedance of the feeder. Figure 4 shows the measured ratio  $\alpha$ . The estimated powers for the required maximum voltages of the 3rd harmonics are shown in Fig. 5. The required voltage of the 3rd harmonics is defined as 1/9 of the required maximum fundamental acceleration voltage, which is determined mainly by the condition of the coupled operation with the ring cyclotron (RRC). The measured  $\alpha$  and thus the required power

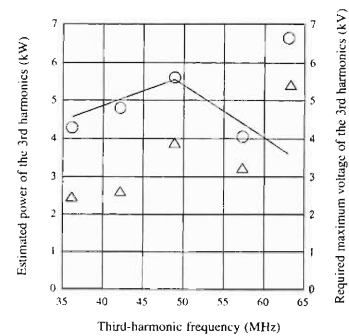


Fig. 5. Estimated power and the required maximum voltage of the 3rd harmonics. Circles represent the estimated power of the No. 1 resonator and triangles represent that of the No. 2 resonator. Solid line represents 1/9 of the required maximum fundamental acceleration voltage.

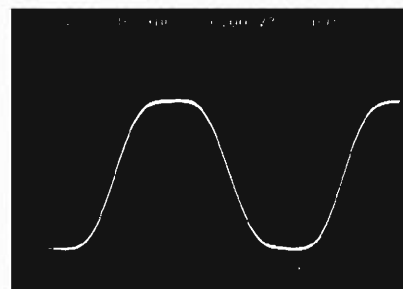


Fig. 6. Typical waveform of the flat-top voltage measured by the dee-voltage pickup. The fundamental frequency was 16.3 MHz and the 3rd-harmonic frequency was 48.9 MHz. The fundamental voltage was 50 kV.

are different for the No. 1 and No. 2 resonators; the causes of this difference are under investigation. The measured frequency change covered by the capacitive tuner of the 3rd harmonics was about 1%. The frequency change of the fundamentals was negligible in this measurement.

The power test was carried out to generate a flat-top voltage on the dee. Each power of the fundamental and the 3rd-harmonic frequencies were fed into the resonator at the same time. The parameters of the flat-top resonator were set at their own optimum positions as shown in Fig. 3. A typical waveform of the flat-top voltage of the No. 2 resonator is shown in Fig. 6.

A beam test using the flat-top acceleration system will be performed in the near future.

#### References

- 1) S. Kohara et al.: Proc. 13th Symp. on Accelerator Science and Technology, Suita (2001), p. 235.
- 2) S. Kohara et al.: Proc. 12th Symp. on Accelerator Science and Technology, Wako (1999), p. 227.
- 3) J. L. Conradie et al.: Proc. 14th Int. Conf. on Cyclotrons and Their Applications, Cape Town, South Africa (1995), p. 249.

## AVF-PA beam transport system

N. Fukunishi, M. Nagase, M. Kase, Y. Yano, T. Teranishi,\* N. Yamazaki,\* S. Watanabe,\* and S. Kubono\*

A high-resolution magnetic spectrograph, called PA, has been installed in the E2 experimental vault as a major facility of the Center for Nuclear Study (CNS) at the RIKEN Accelerator Research Facility (RARF). It was moved from CNS in the Tanashi campus where it was frequently used for high-precision spectroscopic measurements of nuclear structure and nuclear astrophysics studies. The spectrograph will be ready for experiments by the fall of 2001. Construction of the AVF-PA beam transport system has started to provide the beams accelerated by the K-70 MeV AVF cyclotron to PA. The schematic layout is provided in Fig. 1. The beam transport system will be used as a momentum analyzer of AVF beams. Its use in the dispersion-matching mode is also planned. The maximum magnetic rigidity is 1.2 Tm. Last year, the first section of the AVF-PA beam line, which is shown with bold lines in Fig. 1, was constructed. The first section mainly consists of two dipole magnets and five sets of quadrupole magnets. This section shifts beams down by 4 meters to match the level of the AVF beam line to PA and also shifts beams horizontally by 8.3 meters to avoid interference with the RIKEN Ring Cyclotron (RRC). The unique feature of the section from the QD-ST0 to the QD-A21 is that the section is a skew beam line, which means that the horizontal beam shifting section is rotated by 25.73 degrees in a vertical direction. The original horizontal beam shifting section consists of two dipole magnets and four sets of quadrupole magnets, which form a doubly achromatic and doubly telescopic section with negative unity magnifications. Hence, we are free from complicated coupling between the horizontal and vertical motions when we rotate the beam lines vertically.

Specifications of the newly fabricated magnets are

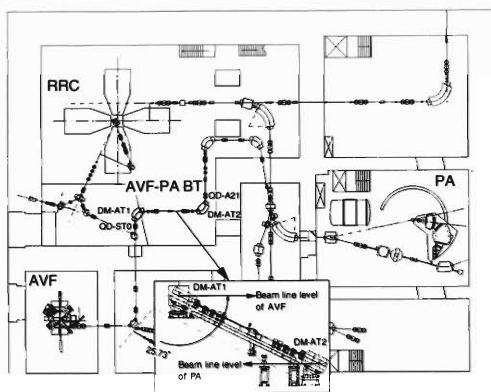


Fig. 1. Layout of AVF-PA beam line. A vertical view of the skew beam line is shown in the rectangular box.

summarized in Tables 1 and 2. The shape of the quadrupole magnet is the same as that used in RARF (Q170 type). The dipole magnets are newly designed based on magnetic-field calculations with OPERA-2D and OPERA-3D. The cross-sectional shape and the radial distribution of magnetic fields are shown in Fig. 2. We find that the uniformity of radial field distributions is very good. These magnets are fabricated by Sumitomo Heavy Industry. In addition, steering magnets, power supplies for the magnets, vacuum system and chambers for beam-monitoring devices were also fabricated. The construction of the first section was finished within the last fiscal year and we will proceed with the construction of the remaining section.

Table 1. Specifications of dipole magnets.

Type	DM90
Deflection angle (degree)	90
Curvature radius (m)	0.8
Maximum field (T)	1.5
Pole gap (mm)	60
Pole face rotation (degree)	25/25
Size of hollow conductor (mm)	□13.5-φ8
Total number of coil windings	280
Maximum excitation current (A)	300
Maximum voltage (V)	47.7

Table 2. Specifications of quadrupole magnets.

Type	Q170
Aperture (mm)	70
Length (mm)	170
Effective length (mm)	200
Maximum field gradient (T/m)	15.5
Size of hollow conductor (mm)	□6-φ3
Number of coil windings (/pole)	30
Maximum excitation current (A)	260
Maximum voltage (V)	17.3

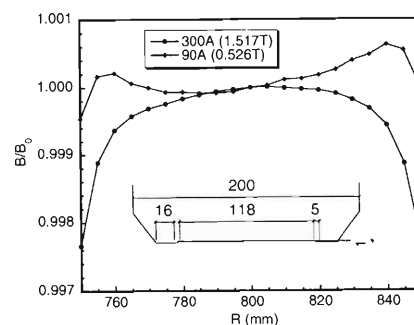


Fig. 2. Cross-sectional view of the dipole magnet and the radial distributions of magnetic fields are shown.

\* Center for Nuclear Study, University of Tokyo

## Beam transport line from AVF to CRIB-F0 target

S. Watanabe,\* T. Teranishi,\* Y. Yanagisawa, S. Michimasa,\* M. Notani,\* K. Ue,\* S. Kubono,\* Y. Ohshiro,\* N. Yamazaki,\* T. Katayama, and M. Kase

A new beam line has been constructed in the experimental hall 7, called E7, of the RIKEN Accelerator Research Facility (RARF) for a low-energy secondary beam separator, the CRIB.<sup>1)</sup> The newly constructed beam line is downstream of the vertical bending magnet, called DM7C, as shown in Fig. 1. The designed beam optics and constructed system are summarized in the literature.<sup>2,3)</sup> An overview of the E7 beam line from the AVF cyclotron to the CRIB target is presented in this report.

Table 1 shows a list of magnets in the E7 beam line. Components are listed in order along the beam line from the AVF cyclotron to the CRIB target chamber, called F0. In Table 1, the magnet name refers to the abbreviation listed in the control table of the K70-AVF cyclotron. Steering magnets are located at each straight section. The Q-doublet, called QDC11,

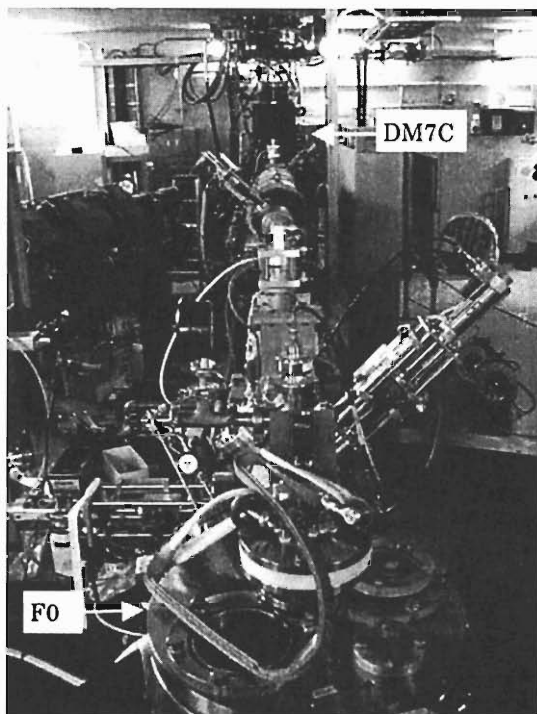


Fig. 1. The E7 beam line. The K70-AVF cyclotron beam is transmitted from the upper floor and is bent by DM7C in the E7. The quartet-Q magnets and CRIB-F0 target are seen in front sight. Vacuum isolation between the E7 beam line and the K70-AVF cyclotron can be realized with a rotary shutter RC-CE7 with the gate valve function.

Table 1. List of magnets in the AVF-E7 BT.

Mag. Name	Gap or Bore	EFB
QTC01a	70 $\phi$	0.25 m
QTC01b	70 $\phi$	0.45 m
QTC01c	70 $\phi$	0.25 m
QTC02a	70 $\phi$	0.20 m
QTC02b	70 $\phi$	0.20 m
DM7C	60 h	1.256 m
QDC11a <sup>*1</sup>	70 $\phi$	0.20 m
QDC11b <sup>*1</sup>	70 $\phi$	0.20 m
DM7C <sup>*2</sup>	60 h	1.256 m
QT7A1a	90 $\phi$	0.23 m
QT7A1b	90 $\phi$	0.23 m
QT7A1c	90 $\phi$	0.23 m
QT7A1d	90 $\phi$	0.23 m

\*1 Rotation angle is set at +10 degrees (right) when the CRIB beam line is selected.

\*2 Rotation angle is fixed at +10 degrees in x-y coordinates when the CRIB beam line is selected. The measured EFB of a steering magnet equipped in the E7 beam line is 0.18 m.

in the vertical beam line is equipped with a rotatable supporting frame. The vertical bending magnet, called DM7C, is also equipped with a rotatable supporting frame. The DM7C utilizes the different beam courses in the E7. The DM7C has been rotated by 10 degrees in the clockwise direction to guide the beam to the CRIB. The upstream QDC11 can generate a skew component in order to compensate for a beam rotation down stream of the DM7C. A quartet-Q (QT7A) is located in the E7 to focus the pin-spot beam on the CRIB-F0 target.

The magnet power supplies for the E7 beam line are summarized in Table 2, and the newly constructed ones are indicated. All of the power supplies are controlled by the RARF computer control system. The interface system named DIM is used to communicate with the upstream control system. The interlock system is also monitored by the same control system.

Four sets of beam profile monitors are equipped in the E7 beam line. The first, called PF8, and the third, called PF9, of the beam profile monitors using 3-wire sensors are located at the exit of the vertical bending magnet (DM7C) and immediately in front of the CRIB-F0 target, respectively. The second, a hybrid-beam profile monitor named HBPFM, has been installed.<sup>4)</sup> The HBPFM provide the both sensors, the 3-wire tungsten sensor and a fluorescence screen. The fluorescence screen is made of  $\text{Al}_2\text{O}_3+\text{Cr}$ . It is located downstream of the quartet-quadrupole magnets named

\* Center for Nuclear Study, Graduate School of Science, University of Tokyo

Table 2. List of magnet power supplies.

Mag. Name	$V_p$ (V coil)	Current
QTC01a	15 V	150 A
QTC01b	22 V	150 A
QTC01c	15 V	150 A
QTC02a	16 V	260 A
QTC02b	16 V	260 A
DMC1	76 V	300 A
QDC11a* <sup>1</sup>	18 (16.4) V	400 A
QDC11b* <sup>1</sup>	18 (16.4) V	400 A
DM7C	76 V	300 A
QT7A1a* <sup>2</sup>	40 (29.32) V	40 A
QT7A1b* <sup>2</sup>	30 (21.99) V	30 A
QT7A1c* <sup>2</sup>	30 (21.99) V	30 A
QT7A1d* <sup>2</sup>	40 (29.32) V	40 A

\*<sup>1</sup> Moved from the Tanashi SF-Cyclotron facility.

\*<sup>2</sup> Newly constructed by IDX Corp. Ltd.

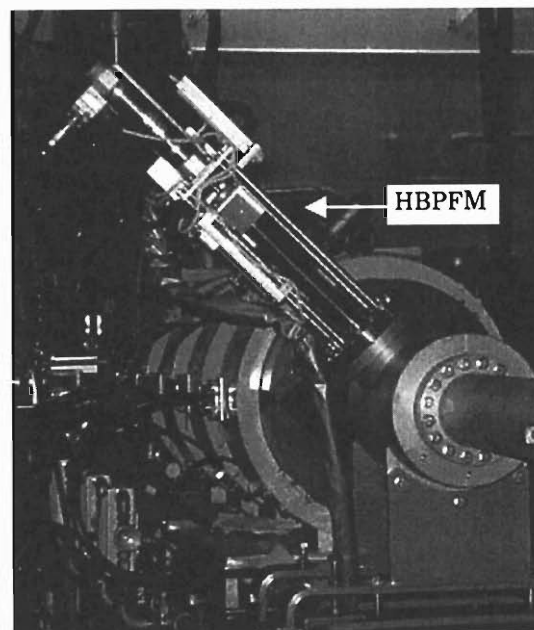


Fig. 2. The HBPFM located downstream of the QT7A1d. The fluorescence screen is monitored by a TV camera through the glass window located at the opposite side of the HBPFM.

QT7A as shown in Fig. 2. The fourth, a fluorescence screen coated with ZnS, is installed in the CRIB-F0 target chamber.

The Faraday cup monitor, called C01, is equipped at the exit of AVF. Identical monitors, called 7A0 and 7A1, are equipped downstream of the DM7C, respectively. The CRIB-F0 target chamber provides the Faraday cup monitor behind the nuclear target.

A test of the E7 beam line has been carried using the primary beam of 7 MeV/nucleon  $^{14}\text{N}^{5+}$ . The test of the beam line aims to confirm the beam sizes, transmission efficiency, and the center of the beam line. In this beam test, acquired beam properties were confirmed by comparing the findings with the calculated beam optics, taking into account the assumed emittances and momentum spread at the exit of the AVF cyclotron. The twice parameters  $\beta_x$ ,  $\alpha_x$ ,  $\beta_z$ ,  $\alpha_z$ ,  $\eta_x$ , and full-momentum spread are assumed 4.56 m, -2.97, 0.985 m, -2.98, 0.859 m, and 0.1%, respectively. The measured beam properties agree well with the calculated results. The obtained transmission efficiency is 88% at the CRIB-F0 target.

A beam alignment system in the E7 horizontal beam line has been constructed to align the beam center along the centerline of the F0 target. The details of the beam alignment system using the HBPFM are de-

scribed in the elsewhere.<sup>5)</sup>

The AVF-E7 beam transport line was constructed to guide the beam to the CRIB. A first beam of 7 MeV/nucleon  $^{14}\text{N}^{5+}$  was transported to the CRIB-F0 target on Nov. 25, 2000. The constructed beam transport line has worked as designed.

The authors express their thanks to the RIKEN accelerator group for their support in constructing the developed system as well as in the operation of the AVF cyclotron and beam transport line.

#### References

- 1) T. Teranishi et al.: CNS-REP-39, Oct. (2001).
- 2) S. Watanabe et al.: CNS Ann. Rep. **1999**, 44.
- 3) S. Watanabe et al.: CNS Ann. Rep. **2000**, 9.
- 4) S. Watanabe: CNS Ann. Rep. **2000**, 58.
- 5) S. Watanabe et al.: CNS Ann. Rep. **2000**, 60.

# Conceptual design of the fixed-frequency ring cyclotron

T. Mitsumoto,\* A. Goto, N. Sakamoto, K. Uno,\* and Y. Yano

A fixed-frequency ring cyclotron (fRC) is proposed for the RIKEN RI Beam Factory Project.<sup>1)</sup> The fRC is used between the Riken Ring Cyclotron (RRC) and the Intermediate-stage ring cyclotron (IRC).<sup>2)</sup> The fRC will enable us to obtain a 350 MeV/nucleon uranium beam at the exit of the Superconducting Ring Cyclotron (SRC).

The main parameters of the fRC are listed in Table 1. The fRC will be installed in an experimental room of the existing Riken Accelerator Research Facility (RARF).<sup>3)</sup> The size of the fRC is restricted by the size of the room. One of the more severe conditions for the sector magnet is the limited height. The position of the beam line is 1.7 m above the floor level. Thus, the height of the sector magnet must be less than 3.4 m. This height is about 65% of the height of the RRC, which is almost the same size as the fRC in terms of the k-value of 540. Even under this condition, the distance between the top of the magnet and the bottom of the crane gutter of the room is 1.5 m. We should pay attention to this distance when the magnets will be assembled in the room.

The fRC is a fixed-frequency cyclotron, so the injection and extraction energies are fixed. The major ions to be accelerated are  $^{238}\text{U}^{72+}$  and  $^{136}\text{Xe}^{48+}$ . Table 2 shows the field parameters for the ions.

Because of the different field levels among the ions, a conventional structure of the sector magnet does not realize isochronous conditions for all ions in spite of there being the same energy conditions. Figure 1 shows

Table 1. Main parameters of the fRC.

K-b value	510 MeV	
Number of sectors	4	
Harmonics	8	
Mean radius	Injection	1.58 m
	extraction	3.16 m
Injection energy	10.95 MeV/nucleon	
Extraction energy	46.28 MeV/nucleon	
Velocity gain factor	2.0	
Number of cavities	2	
RF frequency	36.66 MHz	

Table 2. Field parameters for the ions.

	$^{238}\text{U}^{72+}$	$^{136}\text{Xe}^{48+}$	$^{16}\text{O}^{8+}$
q/A	0.303	0.353	0.5
Mean field			
Injection	0.998 T	0.855 T	0.604 T
Extraction	1.035 T	0.887 T	0.626 T

\* Sumitomo Heavy Industries, Ltd.

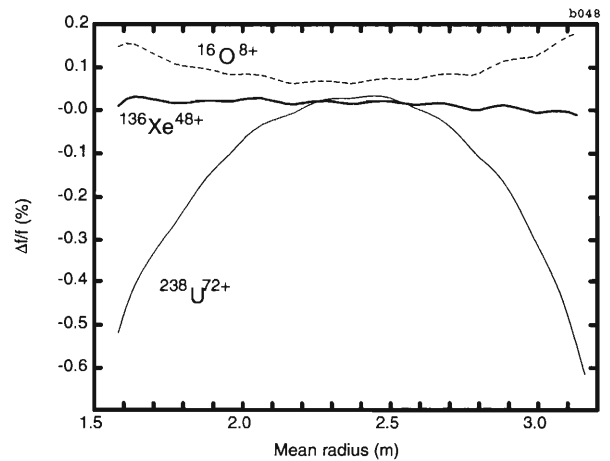


Fig. 1. Isochronism of three ions for a conventional sector magnets.

the isochronism of each of the ions for the conventional sector magnet. The pole shape of the magnet is optimized for  $^{136}\text{Xe}^{48+}$ . Errors in the isochronism of  $^{238}\text{U}^{72+}$  ions reach 0.5%. The errors originate from iron saturation of the magnet.

In order to compensate the errors, it is common to use trimcoils. This method is straightforward and flexible. However, by adopting trimcoils, the structure of the magnet becomes very complicated and numbers of power supplies are required. Another method of compensation is pole shape optimization. This method uses that the lack of the iron inside the pole affects the field distribution at a high field level. Figure 2 shows a schematic of the method. At the side of the pole, an intentional lack was created. This method can reduce the error in isochronism for both ions  $^{238}\text{U}^{72+}$  and  $^{136}\text{Xe}^{48+}$  to less than 0.05%.

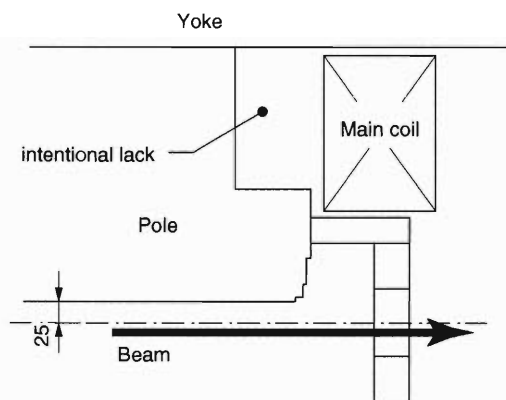


Fig. 2. Schematic cross-sectional view of the pole.

Figure 3 shows the conceptual plane view of the sector magnet. The sector magnets, resonators, injection and extraction devices are shown. The main components of the cyclotron are installed in an area 9.6 m square. The total weight of the cyclotron is approximately 1300 tons.

Table 3 shows the main parameters of the sector

Table 3. Main parameters of the sector magnets.

Pole gap	50 mm
Sector angle	58.4 degree
Total height	3.34 m
Weight	300 ton/sector
Maximum magnetic field	1.65 T
Main coil	
Maximum current	600 A
Maximum excitation current	84 kA/sector
Power consumption	50 kW/sector

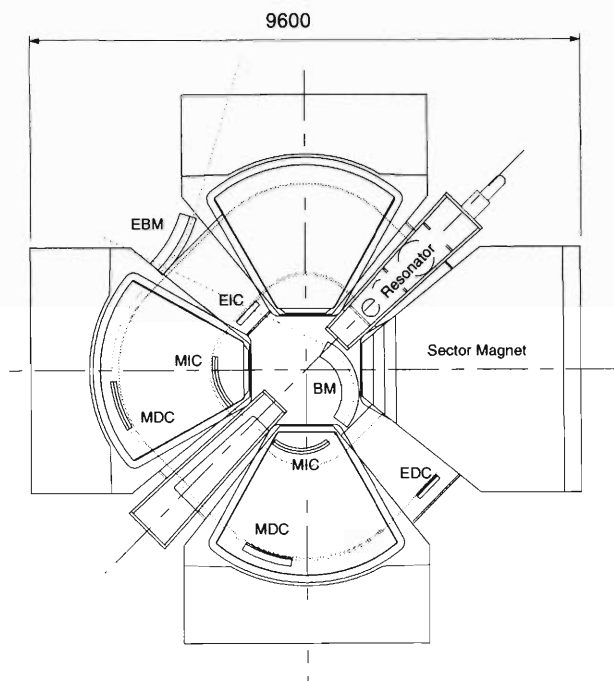


Fig. 3. Conceptual plan view of the fRC.

magnets. The sector angle is chosen to be as large as possible such that the sector field becomes low. Otherwise the design of the injection devices become more difficult. Even in the present design, the magnetic field in the MIC is 2.1 Tesla, including the sector field of 1.6 Tesla. The MIC for the fRC should create 0.5 Tesla at maximum, which is twice the value of the MIC for the IRC.

Further optimization of the design of the fRC is being carried out. The RF system of the fRC is being studied in order to obtain high efficiency in the total system of the RI beam factory, *i.e.*, its phase stability, the requirement of bunchers, the possibility of flat top resonators, and so on.

#### References

- 1) Y. Yano et al.: RIKEN Accel. Prog. Rep. **34**, 301 (2001).
- 2) T. Mitsumoto et al.: RIKEN Accel. Prog. Rep. **34**, 331 (2001).
- 3) <http://www.rarf.riken.go.jp/>

## Magnetic field measurement of the IRC sector magnets

J. Ohnishi, T. Mitsumoto,\* A. Goto, and Y. Yano

All elements of the intermediate-stage ring cyclotron (IRC) were completed at Niihama factory, Sumitomo Heavy Industries, Ltd., in spring 2001. Some of their magnetic elements such as four sector magnets were assembled at the factory and excitation tests and magnetic measurements were carried out. Following the measurement of the E-sector magnet performed in 2000, the magnetic field mapping measurements of all four sector magnets (E, N, W, and S sectors) were performed. These sector magnets were arranged as shown in Fig. 1. Due to space limitation in the factory building, two sets of the sector magnets were separated, unlike their actual arrangement. The measuring apparatus of the magnetic field mapping were designed and fabricated exclusively for the IRC sector magnets.<sup>1)</sup>

The mapping measurements were performed at magnetic field levels of 0.6, 1.0, 1.4, 1.6, 1.7, 1.8 and 1.9 T. The number of measurement points is about 34000 in the region of 180 degrees for two sector magnets, and the measurements took about 15 hours including 3 hours for setting the magnetic field. Figure 2 shows the magnetic field distributions along the sector centerline of the four sector magnets at 1.6 T. The difference of the magnetic field among the four sectors was largest at this magnetic field level. The difference is about 70 gauss at a maximum and the difference of the field slope in the radial direction is about 20 gauss. These differences will be corrected by adjusting the main and the trim coil currents among the sector magnets in order to reduce the first-harmonic field.

Each sector magnet has 20 pairs of the trim coils wound by one turn on the upper and the lower pole faces. Each pair of trim coils was excited with an individual power supply and the magnetic fields were measured. An example of the magnetic field distributions produced by the trim coils is shown in Fig. 3.

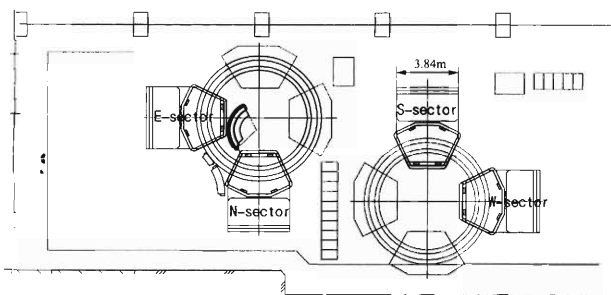


Fig. 1. Arrangement of the IRC sector magnets when the magnetic field measurements were carried out at Niihama factory.

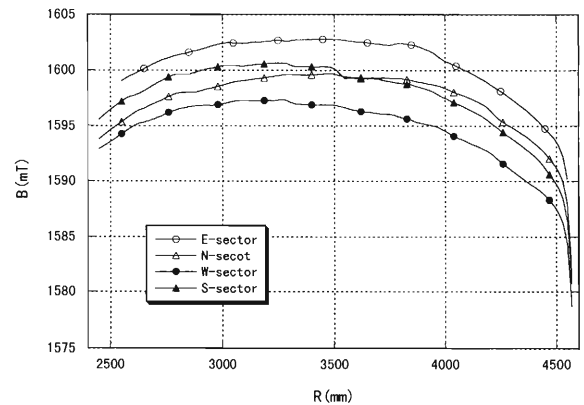


Fig. 2. Difference of the magnetic field distributions among four sector magnets at the main coil current of 290 A.

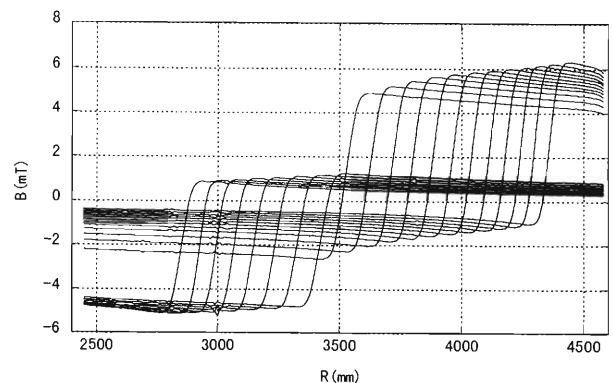


Fig. 3. Trim coil field distributions along the sector centerline at the base field of 1.6 T. The current values are  $-200$  A for the inner 8 coils and  $250$  A for the outer 12 coils, which are half of the nominal currents. The minus sign of the current indicates that the current direction is the reverse of that of the main coil.

Since these magnetic field distributions depend on the magnetic field strength, they were measured at five magnetic field levels. By using these magnetic field data, the current values of the main and the trim coils can be calculated to generate the isochronous magnetic fields required for beam acceleration.<sup>2)</sup>

Poles of the sector magnets consist of two pieces of pure iron plate with a thickness of 26 cm. When the beam chambers are evacuated, atmospheric pressure is applied to one piece of the iron plate and deforms it. The influence of the deformation was measured. Seven Hall probes were placed in a pipe inserted along the sector centerline and the beam chamber was evacuated. Figure 4 shows the change of the magnetic field

\* Sumitomo Heavy Industries, Ltd.

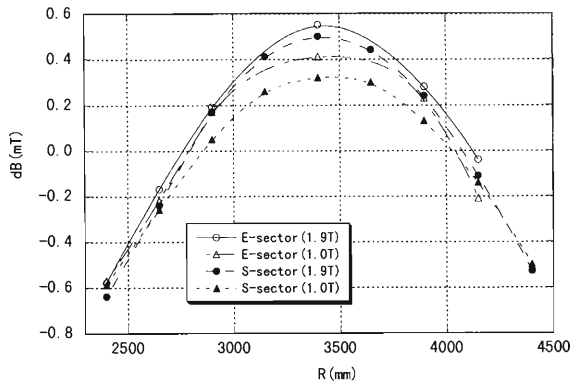


Fig. 4. Change of the magnetic fields along the sector centerline when the beam chamber was evacuated.

before and after evacuation. The maximum change is about  $\pm 6$  gauss, which corresponds to the deformation of about  $35 \mu\text{m}$ . This effect is not negligibly small and

must be corrected in the calculation to generate the isochronous field.

The MIC1 and the MDC1, the magnetic elements for beam injection and extraction,<sup>3)</sup> were installed into the W-sector and the S-sector, respectively, and their magnetic fields were measured. In the future, we plan to make the magnetic field measurements of all the injection and extraction elements (MIC2, MDC2, BM1, EBM1, and EBM2) and obtain the magnetic field data necessary for cyclotron operation. Thus, the magnetic field measurements will be performed for a short period after assembling the IRC at RIKEN.

#### References

- 1) J. Ohnishi et al.: RIKEN Accel. Prog. Rep. **34**, 333 (2001).
- 2) J. Ohnishi et al.: Proc. 16th Int. Conf. Cyclotrons and Their Applications (2001), p. 351.
- 3) T. Mitsumoto et al.: RIKEN Accel. Prog. Rep. **33**, 208 (2000).

## Electric field measurement of the acceleration resonator for the Intermediate-stage Ring Cyclotron (IRC)

N. Sakamoto, O. Kamigaito, T. Mitsunoto, Y. Miyazawa, S. Kohara, H. Okuno, A. Goto, and Y. Yano

We carried out an electric field measurement of the single-gap acceleration resonator for the IRC whose operational frequency range is 18–40.5 MHz.<sup>1)</sup> The strength of the electric field was measured by a perturbation method. A schematic view of the setup of the measurement is shown in Fig. 1. The phase variation of the signal from pickup A was measured moving a perturber from  $x_1$  to  $x_{17}$  along the beam orbit step-by-step (Fig. 2). The measured  $\Delta\phi$  was less than 45 degrees. The perturber used was a spherical one made of  $\text{TiO}_3$  ( $\epsilon^* = 31$ ) with a diameter of 30 mm. The radial distribution of gap voltage  $V(R)$  was obtained from the phase variation as

$$V(R_n) \propto \sum_{i=1}^{17} \sqrt{\tan \Delta\phi(x_i)} \text{ [arb.units]}$$

$R_n$ : Radial position ( $n = 1 \sim 10$ ),

for the frequencies of 18, 28, 36, and 41 MHz (Fig. 3).

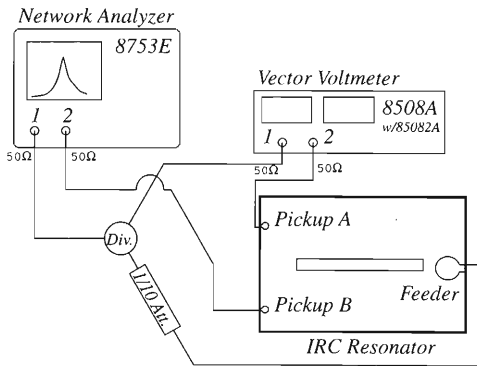


Fig. 1. Schematic view of an electric field measurement by a perturbation method.

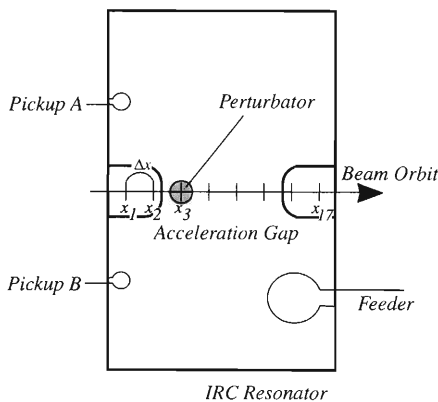


Fig. 2. Setup of the phase-shift measurement.

The parallel shunt resistance ( $R_s$ ) were also evaluated as

$$R_s = \frac{(\epsilon^* + 2)}{3(\epsilon^* - 1)} \cdot \frac{36000}{\Delta V} \left( \sum_{i=1}^{17} \sqrt{\frac{\tan \Delta\phi(x_i)}{2 \cdot f_0}} \Delta x \right)^2 \text{ [M}\Omega\text{]}$$

$\Delta V$ : Volume of the perturber [ $\text{m}^3$ ]

$f_0$ : Resonant frequency [Hz],

and shown in Fig. 4 with unloaded Q values. The

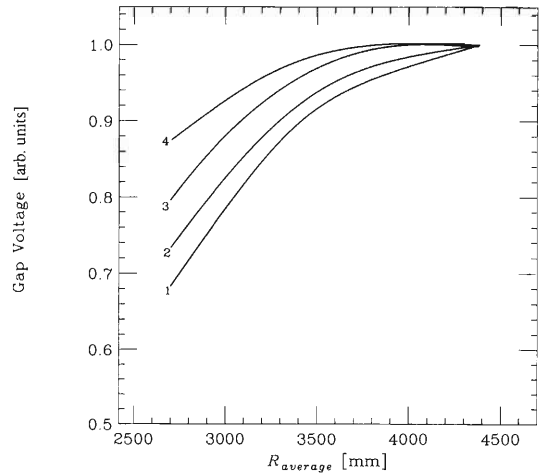


Fig. 3. Voltage distributions as a function of averaged radius of the beam orbit for (1) 18 MHz, (2) 28 MHz, (3) 36 MHz, and (4) 41 MHz. The gap voltage is maximum at the extraction radius.

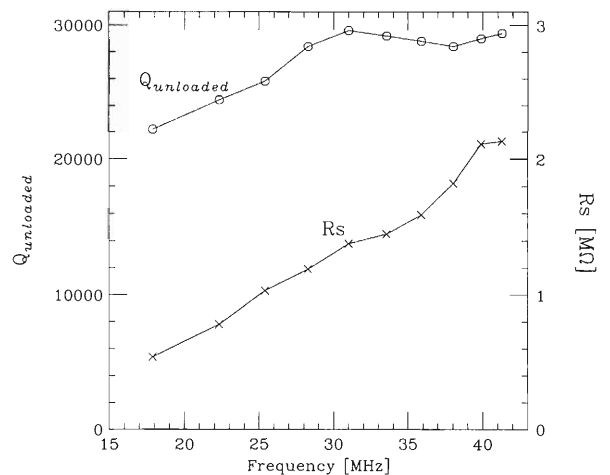


Fig. 4.  $R_s$  and unloaded Q-values as a function of frequency.

measured  $R_s$  values are as large as about 75% of the calculated values using the MAFIA code. Q-values are also 74-79% of the calculated ones. At the frequency of the 38 MHz, 400 MeV/nucleon acceleration, the required peak voltage of 600 kV is expected to be obtained with 100 kW rf power while the maximum

output power of the final amplifier is 150 kW.

#### References

- 1) N. Sakamoto et al.: Proc. 16th Int. Conf on Cyclotrons and Their Applications, East Lansing, USA, 2001-5 (American Institute of Physics, 2001), p. 306.

## Design study on beam transport system from IRC to RARF

N. Fukunishi, M. Kase, and Y. Yano

In the RIKEN RI Beam Factory (RIBF) project, a two-stage acceleration scheme and simultaneous utilization of heavy-ion beams in both the existing RIKEN Accelerator Research Facility (RARF) and the RIBF facility were proposed.<sup>1)</sup> A cascade of two cyclotrons, a  $K = 980$ -MeV Intermediate-Stage Ring Cyclotron (IRC) and a  $K = 2500$ -MeV Superconducting Ring Cyclotron (SRC) were chosen to be the post-accelerators of the existing RIKEN Ring Cyclotron (RRC). A part of the IRC beam will be transferred back to the existing facility. Recently, insertion of a  $K = 510$ -MeV fixed rf-frequency Ring Cyclotron (fRC) between RRC and IRC was proposed.<sup>2)</sup> The new cyclotron cascade is designed to accelerate a uranium beam up to 350 MeV/nucleon in order to produce RI beams efficiently via the projectile-fission reaction. In the new scheme, IRC is capable of producing heavy-ion beams with an energy of more than 100 MeV/nucleon over the entire range of atomic masses. The beams accelerated by IRC have sufficient energy to produce RI beams and the ranges in materials for IRC beams are shorter than those for SRC beams. Hence, unique experiments with IRC beams in RARF have been proposed. One example is to use RI beams as a probe to investigate the properties of materials.

In simultaneous utilization of both the existing facility and the RIBF, it is important to determine how to share an IRC beam. Many users of RARF seriously discussed this problem and two schemes were proposed. One is the conventional time-sharing method in which a pulsing magnet is used. This is a very simple method but DC beams are not obtainable. The other is to use a charge stripper. A part of an IRC beam will be charge-stripped and the charge-stripped beam will be transferred back to the existing facility. By this method, DC beams are obtainable but a sizeable beam loss is predicted for ions with  $Z > 60$ . Moreover, a complex system consisting of one analyzing magnet and two additional bending magnets is necessary. The analyzing magnet will separate the beam into two parts by utilizing the difference in magnetic rigidity. The additional two bending magnets are necessary to match the trajectories of various ions to the beam line from IRC to RARF. The time-sharing method was finally adopted to avoid the use of a complex system. The maximum magnetic rigidity was chosen to be 4.2 Tm. It is based on the estimation<sup>3)</sup> of the magnetic rigidity of the beams with  $Z < 80$ . For heavier ions, separation of RI beams is difficult with the existing RIKEN Projectile-Fragment Separator (RIPS).

The new beam transport system from IRC to RARF was designed to perform RI-beam experiments using the RIPS. The beam transport system is illustrated in

Fig. 1. The beams accelerated by IRC will be doubly achromatic at P1 shown in Fig. 1. The section from P1 to P2 will shift the beams upwards by 3 meters. Doubly achromatic transformation will occur for the section from P2 to P3. The quadrupole quartet between P3 and P4 is introduced to obtain an erect ellipse at P4. The section from P4 to P5 is doubly achromatic and telescopic. The beam will be expanded once and strongly focused by the quadrupole doublet placed below the RIPS target.

All magnets and power supplies will be newly fabricated except for the power supply of the pulsing magnet. We plan to use the existing power supply developed by Kouzu *et al.*<sup>4)</sup> for the pulsing magnet, which was designed by Kusaka *et al.*<sup>5)</sup> The specifications of the dipole magnets are summarized in Table 1. The newly designed dipole magnets will be compact and are designed to have wide regions where magnetic fields are

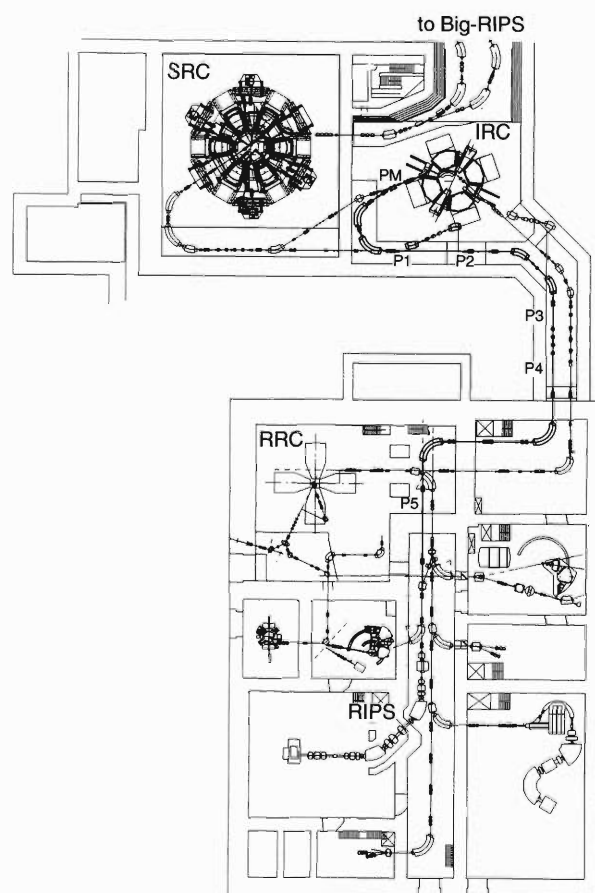


Fig. 1. The beam line from IRC to RARF is shown in bold. The PM indicates the pulsing magnet introduced for the time-sharing of beams.

Table 1. Parameters of dipole magnets.

Type	DM90	DM72	DM45	DM25
Deflection angle (degree)	90	72.5	45	25
Curvature radius (m)	2.7	2.7	2.7	2.7
Maximum field (T)	1.56	1.56	1.56	1.56
Pole gap (mm)	60	60	60	60
Pole face rotation (degree)	25/25	25/25	15/15	12.5/12.5
Size of hollow conductor (mm)	□13.5-φ8	□13.5-φ8	□13.5-φ8	□13.5-φ8
Total number of coil windings	288	288	288	288
Maximum excitation current (A)	330	330	330	330
Maximum voltage (V)	133.7	108.2	70.4	45.1
Number of magnets	2	2	2	2

uniform. The quadrupole magnets will have the same shape as those developed for the beam transport system of the RIBF.<sup>6)</sup> Construction of the magnets and power supplies has already started and will be finished in March 2002.

#### References

- 1) Y. Yano et al.: Proc. 1997 Particle Accelerator Conf., Vol. 1, Vancouver, Canada (1997), p. 930.
- 2) Y. Yano et al.: Proc. 16th Int. Conf. on Cyclotrons and Their Applications, 2001-5, East Lansing, USA (2001), p. 161.
- 3) H. Ueno et al.: private communication.
- 4) H. Kouzu et al.: RIKEN Accel. Prog. Rep. **34**, 355 (2001).
- 5) K. Kusaka et al.: RIKEN Accel. Prog. Rep. **35**, 297 (2002).
- 6) N. Fukunishi et al.: RIKEN Accel. Prog. Rep. **34**, 329 (2001).

## Status of the SRC for the RIKEN RI Beam Factory

A. Goto, H. Okuno, J. Ohnishi, N. Fukunishi, S. Fujishima,\*<sup>1</sup> T. Tominaka,\*<sup>2</sup> K. Ikegami, N. Sakamoto, Y. Miyazawa, T. Mitsumoto,\*<sup>3</sup> O. Kanigaito, S. Yokouchi, H. Akiyoshi, T. Morikawa, M. Kase, and Y. Yano

In this report, we give a general description of the status of construction of the Superconducting Ring Cyclotron (SRC); detailed reports on the main components are given elsewhere in this Progress Report.

One of the tasks on which we have concentrated our efforts for the sector magnet is a detailed structural analysis of the superconducting main and trim coil vessels, pole, yoke, cryostat vacuum chamber and beam chamber, *etc.* Detailed design explorations examining how to electrically insulate and fix the indirectly cooled superconducting trim coils in their coil vessel were also carried out. To confirm the design, the heat-transfer coefficient and strength and voltage resistance of the epoxy resin that is to be used for insulation were measured. Detailed quench analyses to protect the superconducting main and trim coils have been carried out.<sup>1)</sup> At present the specifications of the power supplies for the superconducting main and trim coils and the normal-conducting trim coils are being finalized. The design of the cryogenic cooling system and arrangement of its components such as the refrigerator and the compressors in their respective rooms is also being finalized. Both Hitachi and Mitsubishi are fabricating the sector magnets. The first vessel of the main coil before winding has already been machined at each factory, and the winding is scheduled to start in mid-December, 2001. Details of the design of the sector magnet are given in Ref. 2.

The superconducting bending magnet (SBM), which is uniquely superconducting among the injection and extraction elements, is halfway to its completion;<sup>3)</sup> winding of the superconducting coils around the pole has been completed. Fundamental and mechanical designs of the other injection and extraction magnetic elements, which are normal-conducting and similar to those of the RIKEN Ring Cyclotron (RRC) and the Intermediate-stage Ring Cyclotron (IRC), are being made.<sup>4)</sup> Design mechanisms for installing and fixing the magnetic channels and electrostatic channels in the complicated structure of the beam chambers and the valley chamber, respectively, have been finalized.

The mechanical design of the main rf resonators, which are of a similar type to those of the IRC, has already been completed,<sup>5)</sup> that of the flat-top resonator is currently being made. Amplifiers are designed to be set immediately outside the magnetic shield of the sector magnet on the same level as the resonators. As of November 2001, the outer boxes of two out of the four

main resonators have been fabricated. The amplifier systems for the four main resonators have already been completed.

The fundamental design of the vacuum system has been finalized as reported in Ref. 6. The mechanical design of the rf resonators and valley chambers with respect to how and where the cryopumps should be set has been made. The effect of oscillation of a cryopump on the rf characteristics is being investigated.

Beam diagnostic devices are designed to be similar to those of the IRC. They consist mainly of a main differential radial probe, two differential radial probes in the extraction region and twenty pairs of phase probes. The main differential radial probe, which is too long

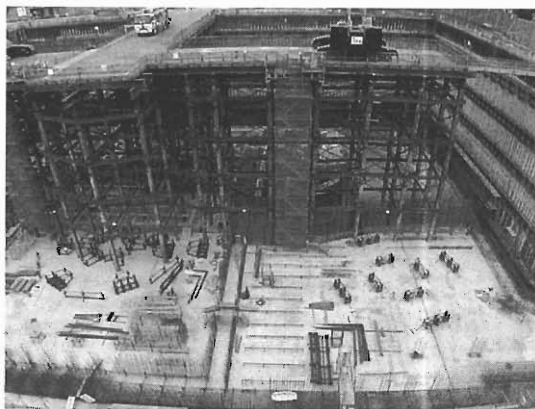


Fig. 1. Photograph of the SRC vault along with the IRC vault in April 2001. The bases for the sector magnets of both cyclotrons can be seen.



Fig. 2. Photograph of the SRC vault in April 2001. The bases for the sector magnets can be clearly seen.

\*<sup>1</sup> Ishikawajima-Harima Heavy Industries Co., Ltd.

\*<sup>2</sup> Hitachi, Ltd.

\*<sup>3</sup> Sumitomo Heavy Industries, Ltd.

to be set inside the magnetic shield, has been designed so as to penetrate the side door of the magnetic shield.

The design of the plumbing of the helium transfer tubes and emergency He-discharge line has almost been finalized, while that of the water cooling pipes for the cyclotron itself and its power supplies is being made.

Construction of the building including the SRC vault is proceeding according to schedule. As for the SRC vault, cranes are scheduled to be installed at the end of 2001 and ceiling concrete slabs to be set at the beginning of 2002. Figure 1 shows the SRC vault along with the IRC vault, and Fig. 2 shows a close-up of the SRC vault; both photographs were taken in April 2001.

#### References

- 1) T. Tominaka et al.: Proc. 17th Int. Conf. on Magnet Technology, Geneve, 2001-9, to be published.
- 2) A. Goto et al.: Proc. 16th Int. Conf. on Cyclotrons and Their Applications, East Lansing, 2001-5 (2001), p. 319.
- 3) H. Okuno et al.: Proc. 17th Int. Conf. on Magnet Technology, Geneve, 2001-9, to be published.
- 4) S. Fujishima et al.: Proc. 17th Int. Conf. on Magnet Technology, Geneve, 2001-9, to be published.
- 5) N. Sakamoto et al.: Proc. 16th Int. Conf. on Cyclotrons and Their Applications, East Lansing, 2001-5 (2001), p. 306.
- 6) K. Sugii et al.: RIKEN Accel Prog. Rep. **33**, 226 (2000).

## Effect of $\nu_r + \nu_z = 2$ resonance in the SRC

T. Mitsumoto,\* A. Goto, N. Fukunishi, and Y. Yano

The SRC for the RIKEN RI-Beam factory project<sup>1)</sup> is designed to accelerate various kinds of heavy ions up to 400 MeV/nucleon. In the case of an ion with an extraction energy of 400 MeV/nucleon and  $A/q = 2$ , betatron frequencies lie very near a resonance line of  $\nu_r + \nu_z = 2$ . In this report, the effect of the resonance is studied.

Resonances in coupled oscillations in a cyclotron were studied by Joho.<sup>2)</sup> A Hamiltonian and the equations of motion in  $(x, y)$  cartesian coordinate are:

$$\begin{aligned} H &= H_0 + H_1, \\ H_0 &= \frac{1}{2}(p_x^2 + \nu_x^2 x^2 + p_y^2 + \nu_y^2 y^2), \\ H_1 &= a_p x^n y^m \cos p(\theta - \theta_0), \end{aligned}$$

and

$$\begin{aligned} x'' + \nu_x^2 x &= -n a_p x^{n-1} y^m \cos p(\theta - \theta_0), \\ y'' + \nu_y^2 y &= -m a_p x^n y^{m-1} \cos p(\theta - \theta_0). \end{aligned}$$

The resonance condition is satisfied if

$$n\nu_x \pm m\nu_y - p \approx 0.$$

In this report, for simplicity, we do not consider the effect of the radius of the cyclotron.

Employing a canonical transformation and neglecting the fast oscillating part, the final Hamiltonian  $K(\rho_x, \Phi)$  and the equations of motion are given by:

$$K = -\kappa q \rho_x - \kappa \rho_x^{\frac{n}{2}} \rho_y^{\frac{m}{2}} \cos \Phi,$$

and

$$\begin{aligned} \rho_x' &= -\kappa \rho_x^{\frac{n}{2}} \rho_y^{\frac{m}{2}} \sin \Phi, \\ \Phi' &= -\kappa q - \frac{\kappa}{2} \left( n \rho_x^{\frac{n-2}{2}} \rho_y^{\frac{m}{2}} \pm n \rho_x^{\frac{n}{2}} \rho_y^{\frac{m-2}{2}} \right) \cos \Phi, \end{aligned} \quad (1) \quad (2)$$

where

$$\begin{aligned} J_0 &= J_y \mp m \tilde{J}_x = \frac{H_{0y}}{\nu_x} \pm \frac{m H_{0x}}{n \nu_x} = \text{const}, \\ \rho_x &\equiv \frac{m \tilde{J}_x}{J_0} = \frac{m J_x}{n |J_0|} = \frac{m \nu_x}{2n |J_0|} x_0^2, \end{aligned} \quad (3)$$

$$\rho_y \equiv \frac{J_y}{|J_0|} = \frac{\nu_y}{2 |J_0|} y_0^2, \quad (4)$$

$$q \equiv \frac{\Delta \nu}{\kappa},$$

$$\Delta \nu \equiv n \nu_x \pm m \nu_y - p,$$

$$\kappa = m a_p^* \left( \frac{n}{2m \nu_x} \right)^{\frac{n}{2}} \frac{1}{(2 \nu_y)^{\frac{m}{2}}} |J_0|^{\frac{m+m-2}{2}}. \quad (5)$$

In Eqs. (3) and (4),  $x_0$  and  $y_0$  represent the amplitudes of betatron oscillation.

For the SRC, we focus on the  $\nu_r + \nu_z = 2$  resonance, *i.e.*,  $n = m = 1$ ,  $p = 2$ . The equations of motion (1), (2) and (5) become:

$$\rho_x' = -\kappa \rho_x^{\frac{1}{2}} (\rho_x - 1)^{\frac{1}{2}} \sin \Phi, \quad (6)$$

$$\Phi' = -q \kappa - \frac{\kappa}{2} \left[ \left( \frac{\rho_x - 1}{\rho_x} \right)^{\frac{1}{2}} + \left( \frac{\rho_x}{\rho_x - 1} \right)^{\frac{1}{2}} \right] \cos \Phi, \quad (7)$$

where

$$\kappa = \frac{a_2^*}{2} \left( \frac{1}{\nu_x \nu_y} \right)^{\frac{1}{2}}, \quad (8)$$

$$a_2^* = a_2.$$

We assume that  $x$  represents radial motion and  $y$  represents axial motion. Under normal acceleration conditions in a cyclotron, radial motion should have some amplitude of the oscillation around an equilibrium orbit. Axial motion, however, ideally has no oscillation. We can apply the dominating  $x$ -oscillation condition of the sum-resonance defined by Joho.

$$J_x - J_y = -J_0 \quad (J_0 < 0), \quad (9)$$

$$\rho_y = \rho_x - 1 \quad (\rho_x \geq 1). \quad (10)$$

Under the condition that the axial oscillation is much smaller than the radial oscillation,  $\rho_x$  is nearly 1.

We can roughly estimate the maximum growth rate analytically from the equations of motion (6) and (3).

$$\begin{aligned} \rho_x' &= -\kappa \rho_x^{\frac{1}{2}} (\rho_x - 1)^{\frac{1}{2}} \sin \Phi \leq \kappa \rho_x, \\ \rho_x' &= \frac{2}{x_0} \frac{dx_0}{d\theta} < \kappa. \end{aligned} \quad (11)$$

Thus, the growth rate of the radial amplitude of the oscillation  $x_0$  per turn ( $2\pi$ ) is:

$$\frac{2\pi}{x_0} \frac{dx_0}{d\theta} < \pi \kappa. \quad (12)$$

Using Eqs. (3), (4) and (10), we can determine the axial amplitude of oscillation  $y_0$  from  $x_0$

$$y_0^2 = \frac{\nu_x}{\nu_y} x_0^2 - \frac{2|J_0|}{\nu_y}. \quad (13)$$

Using a numerical integration method, we can obtain precise information from the equation of motion. Figure 1 shows results obtained by numerical integration of the equations of motion (6) and (7) with the Runge-Kutta algorithm. Consecutive points are plotted at intervals of  $\Delta\theta = 2\pi$ . In this figure, polar coordinates  $\sqrt{\rho_x}$  and  $\Phi$  are used, since  $\sqrt{\rho_x}$  is proportional to the amplitude  $x_0$ . If the beam is above the threshold of resonance, *i.e.*,  $|q| > 1$ , the equations of motion

\* Sumitomo Heavy Industries, Ltd.

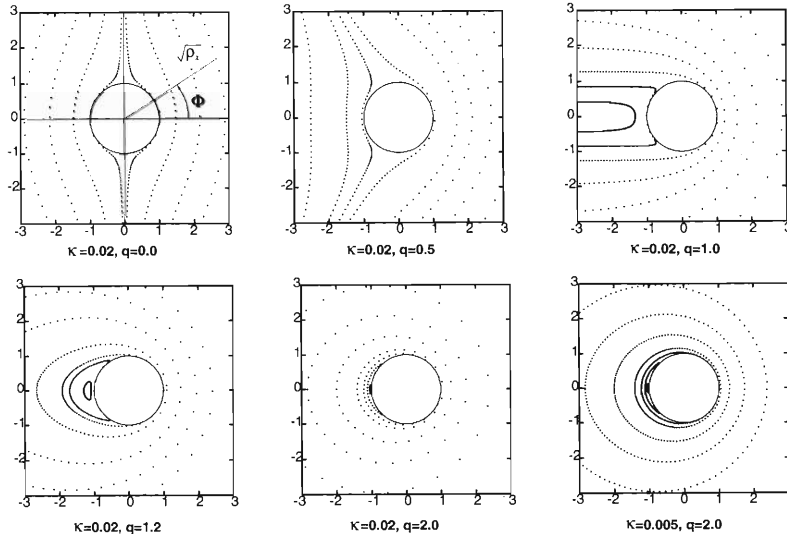


Fig. 1. Phase-space plots for the  $\nu_r + \nu_z = 2$  resonance with polar coordinates  $\sqrt{\rho_x}$  and  $\Phi$ . Consecutive points are plotted at intervals of  $\Delta\theta = 2\pi$ . If  $|q| > 1$ , the equations of motion have oscillating solutions.

have oscillating solutions.

When we consider the construction and installation of the sector magnets of the SRC, the tilt angle around azimuthal axis can be easily suppressed by less than 1 mrad. In this case, the value of  $a_2$  in Eq. (8) is approximately  $1 \times 10^{-3}$ . Thus the maximum of  $\kappa$  is  $5 \times 10^{-4}$  from Eq. (8). Using Eq. (12), we can calculate turn number  $n$  when the radial amplitude increases by 10%.

$$n = 0.1 \frac{2\pi}{x_0} \frac{dx_0}{d\theta} > 0.1/\pi\kappa \approx 60. \quad (14)$$

We assume that the radial amplitude is 6 mm, which is the case when large off-centering is introduced for acceleration, and the axial amplitude is almost zero. The increase of 10% radial amplitude corresponds to 0.6 mm, while the vertical amplitude is calculated to be 4 mm from Eq. (13).

From these studies, we can estimate the effect of the  $\nu_r + \nu_z = 2$  resonance in the SRC. Figure 2 shows the calculated  $\nu_r + \nu_z$  value of the SRC for an ion with an extraction energy of 400 MeV/nucleon and  $A/q = 2$ . One dot corresponds to 4 or 5 turns. If  $\kappa = 5 \times 10^{-4}$ , the resonance band is  $1 \times 10^{-3}$  ( $2\kappa$ ). When the beam crosses the resonance during acceleration, the amplitude of oscillation may increase at the outside of the bandwidth. Taking the safety factor of 2, we obtain a the bandwidth of  $2 \times 10^{-3}$  ( $4\kappa$ ). Even in this case, the turn number inside the band is about 30. This number is a half-turn number estimated by Eq. (14). Therefore, the effect of the resonance is not fatal for the SRC.

In conclusion, we consider the following points as being effective in minimizing the effect of the resonance.

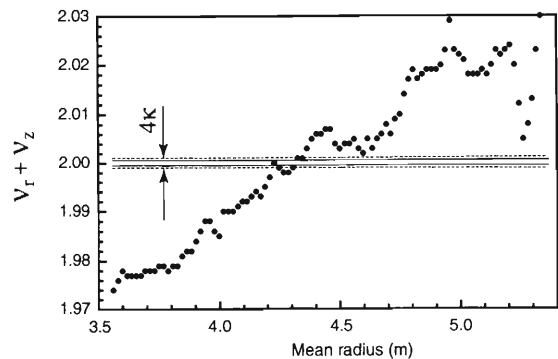


Fig. 2. Dots represent calculated  $\nu_r + \nu_z$  values for the SRC with an ion of 400 MeV/nucleon and  $A/q = 2$ . One dot corresponds to 4 or 5 turns. The area between the solid lines shows resonance band ( $2\kappa$ ). The area between the dashed lines is the area where the amplitude of oscillation may increase due to the resonance ( $4\kappa$ ).

- First, the coupling factor should be small which means that good alignment is important.
- In the initial condition of the beam, the axial oscillation should be small. If the axial oscillation is zero, growth of the amplitude due to resonance does not appear.
- The radial oscillation of the beam should be small. In this sense, large off-centering is not favorable when the effect of the resonance is considered.

#### References

- 1) Y. Yano et al.: RIKEN Accel. Prog. Rep. **34**, 301 (2001).
- 2) W. Joho: SIN-Report TM-11-8, Appendix (1970).

# Superconducting bending magnet for the injection system of the RIKEN SRC

H. Okuno, S. Fujishima,<sup>\*1</sup> T. Tominaka,<sup>\*2</sup> A. Goto, and Y. Yano

A bending magnet for the beam injection system of the SRC<sup>1,2)</sup> should be superconducting since the required fields are about 4 T and the curvature of the coils is about 1.2 m. The design of the bending magnet was finalized for real production based on successful results of the R&D coils.<sup>3)</sup> In this paper the final design will be described, along with the status of the fabrication.

Figure 1 shows a cross section and plan view of the superconducting bending magnet (SBM). The two flat coils, the iron poles and the yokes generate the required fields. The yoke is divided into two parts: cold yoke and warm yoke. The cold yoke, which about half the flux passes through, is H-type. This configuration makes the shifting forces and unbalanced forces on the cold mass small, while the weight of the cold mass is not too large (about 3 ton). C-type is adopted for the warm yoke because the available space for the warm yoke in the side of the sector magnet is very narrow. A warm duct is installed for the ion beams. Iron shims and water-cooled baffle slits are attached to the duct.

Two-dimensional analysis was carried out to optimize the geometry of the coils, yokes and iron shims. The results are summarized in Table 1. The overall current density must be about 150 A/mm<sup>2</sup> to achieve the required field. The value of current density is selected on the basis of the results of the test coil described in the next section. Magnetic forces on the cold mass were calculated for the mechanical designs. The geometry of the yokes is optimized so that the shifting forces and unbalanced forces on the cold mass are minimized.

Three-dimensional field analysis was carried out to

study the maximum fields at the coil end and the effective field lengths. Coupling of the field of the SBM with fields from the sector magnets is studied using a model that includes the SBM and two sector magnets. The generated field of the SBM decreases by 5% compared to the stand alone excitation. Shifting forces on the cold mass are estimated to be less than about 4 kN. This force is comparable with but has the opposite sign to that from the two dimensional analysis. These results indicate that the cold mass is well shielded from the sector magnet system by the warm yoke of the SBM.

Rectangular monolithic NbTi wire of 0.8 mm × 2.4 mm in size was adopted so as to be wound with

Table 1. Summary of the magnetic design.

2D analysis	
Field (overall current density)	4.1 T (155.5 A/mm <sup>2</sup> )
Forces on coil (Horizontal) (Vertical)	731.9 kN/m (expansive) 75.9 kN/m (repulsive)
Shifting forces on the cold mass	4.23 kN/m
Unbalanced force (Horizontal) (Vertical)	5 kN/mm 6 kN/mm
3D analysis	
BL value (overall current density)	3.47 Tm 150 A/mm <sup>2</sup>
Field at plateau	4.0 T
Effective length	1.74 m

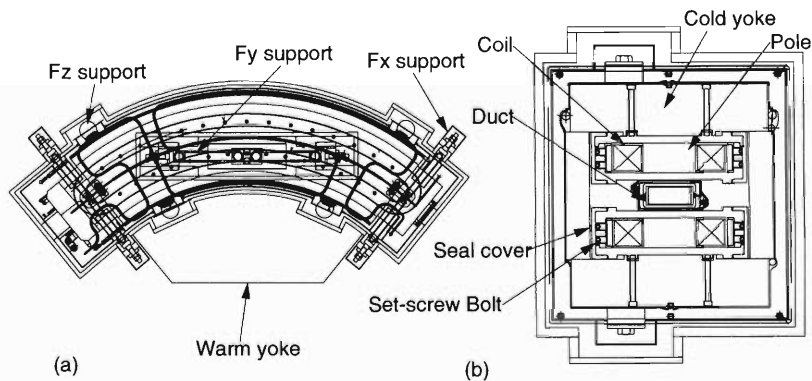


Fig. 1. (a) Plan view and (b) cross-sectional view of the SBM.

<sup>\*1</sup> Ishikawajima-Harima Heavy Industries Co., Ltd.

<sup>\*2</sup> Hitachi Ltd.

good alignment. The conductor was coated with polyimide of  $50\ \mu\text{m}$  in thickness for electrical insulation. Polyimide was adopted because of its strength against radiation. The operation point is less than 30% of the critical current.

Coil winding is one of the key issues in SBM production because the coils of the SBM have negative curvature, and thus cannot be wound with any tension. The following method was adopted. In the first step the coil is wound with tension to a shape which has no negative curvature. The circumference of the coil should be the same as that of the final shape of the SBM coil. After winding of a few layers, the layers are pushed to the mandrel to form the coil into its proper shape. The merit of the method is that the time for winding can be reduced without a decrease in performance. This method was successfully applied to the real coil. After completion of the winding, the coil is impregnated in the vacuum vessel. Figure 1 shows the cross section of the coil casing. The radial and vertical pre-compressions required to maintain the coil compression when the magnet is excited are provided by set-screw bolts and vertical bolts, respectively. This support structure was successfully applied to the test coil. Iron, which shrinks less from 300 K to 4.5 K than stainless steel, will be used for the inner mandrel of the center coil to decrease the degradation of the stress of the coil. The coil casing is partially covered by seal covers for He tightness. The two coil casings are attached to the cold yoke.

The cold mass of the SBM is installed in the vacuum vessel made of structural iron of 20 mm thickness. It functions as a part of the yoke which makes shifting forces and unbalanced forces small. The duct for the beam bore is connected to the vessel at its ends. The

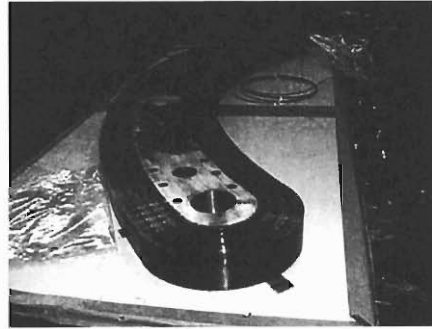


Fig. 2. A coil after vacuum impregnation.

cold mass was supported by three types of thermal insulating supports from room temperature as shown in Fig. 1. They are designed to support the cold mass stably against the shifting and unbalanced forces as well as against large earthquakes (1 g and 0.5 g in the horizontal and vertical directions, respectively).

The fabrication of the SBM has started. Two coils are successfully wound and impregnated as shown in Fig. 2. The difference of the real coil shape from the designed one is less than 1 mm, which is acceptable for maintain the flatness of the field along the trajectory. The fabrication of the SBM will be completed by March of 2002.

#### References

- 1) Y. Yano et al.: Proc. 16th Int. Conf. on Cyclotrons and Their Applications, Michigan (2001) p. 161.
- 2) A. Goto et al.: Proc. 16th Int. Conf. on Cyclotrons and Their Applications, Michigan (2001) p. 319.
- 3) H. Okuno et al.: Proc. 16th Int. Conf. on Magnet Technology, Tallahassee, USA, 1999-10 (2000), p. 228.

## Superconducting sector magnet for the RIKEN SRC

H. Okuno, J. Ohnishi, N. Fukunishi, T. Mitsumoto,\*<sup>1</sup> S. Fujishima,\*<sup>2</sup> T. Tominaka,\*<sup>3</sup>  
K. Ikegami, Y. Miyazawa, A. Goto, and Y. Yano

In previous reports, the significant changes to the design of the sector magnets of the SRC<sup>1,2)</sup> were described. In this report, we will describe the details of the design which we are concentrating on finalizing in 2002.

Cross-sectional and plan views of the designed sector magnet are shown in Fig. 1, excluding the magnetic shields. The sector magnet is 7.2 m long and 6 m high. The weight is about 800 tons each. The sector angle is 25 deg. The maximum sector field is 3.8 T, which is required to accelerate 350 MeV/nucleon  $U^{88+}$  ions. The main components of the sector magnet are: a pair of superconducting main coils, four sets of superconducting trim coils and, their cryostats, thermal insulation support links, twenty-two pairs of normal conducting trim coils, warm-poles and a yoke.

The superconductor for the sector magnet has a rectangular shape consisting of a Rutherford-type NbTi cable located at the center of the conductor and a stabilizer housing.<sup>3)</sup> The conductors' cross-sectional area measures 8 mm by 15 mm. The stabilizer material is aluminum alloy with 1000 ppm Ni, which gives a high 0.2%-yield strength of approximately 60 MPa at

room temperature, keeping the residual resistivity ratio greater than 800. The total length of the conductors for the six sector magnets is 51 km.

For the main coils, 396 ( $22 \times 18$ ) turns are wound, giving the maximum magneto-motive force per sector of 3.96 MA. The maximum current is 5000 A. A solenoid winding is adopted for the main coil with cooling gaps of 0.8 mm and 1.5 mm horizontally and vertically, respectively. Spacers made of FRP (fiber reinforced plastic) are placed in both gaps between the conductors; about 50% of the vertical conductor surface is exposed to liquid helium, while the horizontal surface is not exposed. The main coil is designed based on Maddock's partial stabilization criterion. The main coil vessel, made of stainless steel of 50 or 60 mm thick covers the cross section of the main coil block ( $208 \text{ mm} \times 284 \text{ mm}$ ). It was designed to be sufficiently rigid to support the electromagnetic force on the coil. The horizontal electromagnetic force of about 260 ton/m is exerted on the long section of the vessel covering the beam area. In order to support this force, a pair of connecting plates is attached to both sides of this section. The plate is 1 m in width and 25 mm in thickness. One of these plates crosses through the rectangular hole (1.5 m in width and 160 mm in height) of the warm iron pole.

Two types of trim coils are used to help generate different isochronous fields for various kinds of ions: superconducting trim coils and normal-conducting trim coils. Superconducting trim coils which consist of four sets are attached to the main coil vessels and the connecting plates. A double-pancake winding of the same conductor as that for the main coil is adopted, in which the coils are indirectly cooled by forcing two-phase helium through tubes engraved on the coil case made of aluminum alloy plates of 18 mm thickness. The four sets of trim coils consist of 2 (layers)  $\times$  4 (turns)  $\times$  2 (blocks),  $2 \times 5 \times 5$ ,  $2 \times 7 \times 2$  and  $2 \times 8 \times 2$ , respectively. The maximum current is 3,000 A. Twenty-two pairs of normal-conducting trim coils are attached to the surface of the beam chamber that is part of the cryostat, as shown in Fig. 1. The maximum current is 600 A.

The side walls of the cryostat are made of stainless steel. The upper and lower walls, which constitute part of the yoke, are made of steel. The upper warm pole is welded to the upper wall, forming a part of the cryostat chamber. The lower pole is welded to the lower wall in the same way. The side walls and the upper and lower walls are welded to each other. The gap distance between the connecting plate and the surface of the hole of the warm pole is 70 mm. These gaps are sufficiently wide to incorporate 70 K thermal radi-

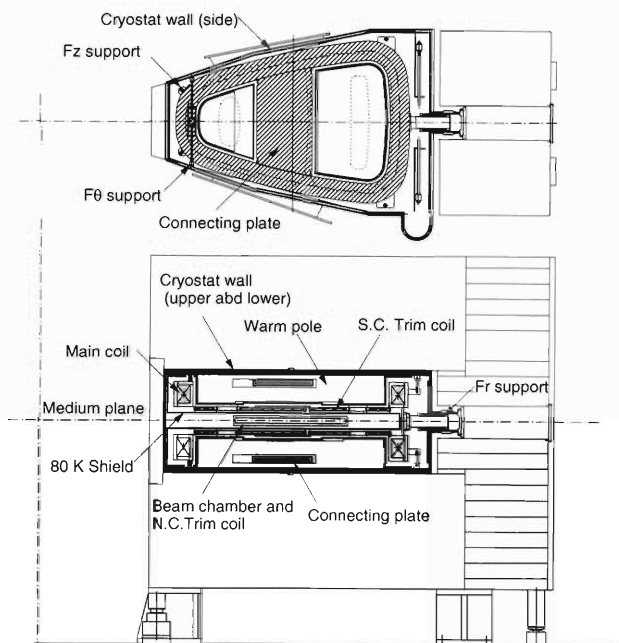


Fig. 1. Cross-sectional and plan views of the SRC sector magnet.

\*1 Sumitomo Heavy Industries, Ltd.

\*2 Ishikawajima-Harima Heavy Industries Co., Ltd.

\*3 Hitachi, Ltd.

ation shields. The area of the radiation shields is about  $85\text{ m}^2$ . The thickness of the beam chamber wall made of stainless steel is 45 mm, and the gap of the chamber, to which the injection and extraction elements are placed, is 90 mm.

The cold mass is supported with a total of 17 thermal-insulation support links. A multicylinder type of support link is used for the radial support. The multicylinder, made of stainless steel with an outermost diameter of 320 mm and a length of 850 mm, is designed to sustain the radial shifting force of 90 ton. It is fixed onto the surface of the back yoke. The vertical support is achieved with four support links at the inner-radius part and four at the outer-radius part. The azimuthal support is also achieved with four support links at the inner-radius part and four at the outer-radius part. The support links are made of titanium-alloy rod and are designed to have a spring constant larger than 140/190 (100/85) kN/mm to sustain the vertical (azimuthal) unbalanced force. The vertical support links are fixed at the upper and lower yokes. The azimuthal links are fixed onto the surface of the upper and lower walls of the cryostat. The entire system of support links is designed to sustain additional forces due to an earthquake of  $980\text{ cm/s}^2$  and  $490\text{ cm/s}^2$  in the horizontal and vertical directions, respectively.

The pole is divided into two pieces in order to generate a hole that allows the connecting plate of the main coil vessel to cross through it. These poles, together with the upper and lower walls of the cryostat chamber, are fixed onto the surface of the upper/lower yoke with long screws through the yoke, because a total force of 760 ton due to electromagnetic force and atmospheric pressure is exerted on the pair of poles toward the median plane. The slabs of the upper and lower yokes are stacked in the horizontal direction in order to keep the deformation due to electromagnetic forces as small as possible.

In order to protect the superconducting main and

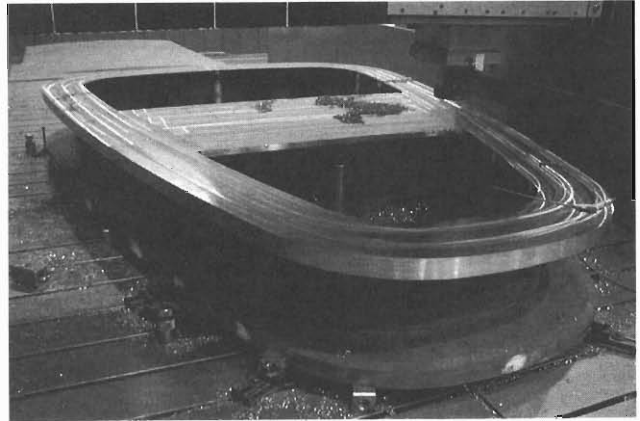


Fig. 2. Photograph of machining a main coil vessel.

trim coils, the quench characteristics were simulated with respect to current decay, temperature rise, and voltage development. The simulation shows that the optimal resistance of the dump resistor should be  $0.3\ \Omega$  and  $0.1\ \Omega$  for the main coil and the trim coil, respectively. The temperature of the main coil rises to about 140 K with this dump resistor. The maximum voltage generated between the main coil and the coil vessel can be up to half of 1,500 V, by taking the earth at the middle point of the dump resistor.

The first two vessels of the main coils are being machined as shown in Fig. 2. The winding will start in mid-Dec. 2001. The fabrication of all of the parts will be completed at the end of March 2002.

#### References

- 1) Y. Yano et al.: Proc. 16th Int. Conf. on Cyclotrons and Their Applications, East Lansing (2001), p. 161.
- 2) A. Goto et al.: Proc. 16th Int. Conf. on Cyclotrons and Their Applications, East Lansing (2001), p. 319.
- 3) M. Sugimoto et al.: Proc. 2000 Meet. of the Cryogenic Society of Japan, Tsukuba (2000).

## Design of the extraction bending magnet for the RIKEN SRC

S. Fujishima,\*<sup>1</sup> H. Okuno, N. Fukunishi, T. Tominaka,\*<sup>2</sup> A. Goto, and Y. Yano

The RIKEN Superconducting Ring Cyclotron (SRC)<sup>1)</sup> is one of the main accelerators for the RIKEN RI Beam Factory.<sup>2)</sup> The basic design of the injection and extraction systems for the SRC has been completed.<sup>3)</sup>

Figure 1 shows a schematic layout of the injection and extraction elements, and shows the trajectory of the beam.

The extraction system consists of one electrostatic deflection channel (EDC), three normal-conducting magnetic deflection channels (MDC1, MDC2 and MDC3), and one normal-conducting extraction bending magnet (EBM). Maximum magnetic rigidity of the extraction beams is 7.94 Tm.

Table 1 lists the design conditions of EBM. The design magnetic fields of EBM include the margin of 5%.

Figure 2 shows the cross-sectional plan of EBM. The turn separation at the entrance of EBM is about 350 mm. EBM is placed in the background stray fields from the sector magnets, and the stray fields rise to the order of  $-450$  Gauss at the maximum excitation. The iron of EBM gathers and disturbs the magnetic field in the acceleration region of the SRC, thus compensation coils are indispensable to suppress the field disturbance. The required field uniformity in the central region of EBM is in the order of  $10^{-3}$ . Built-in vertical and horizontal steerers are also required to generate additional steering fields of 200 Gauss and 600

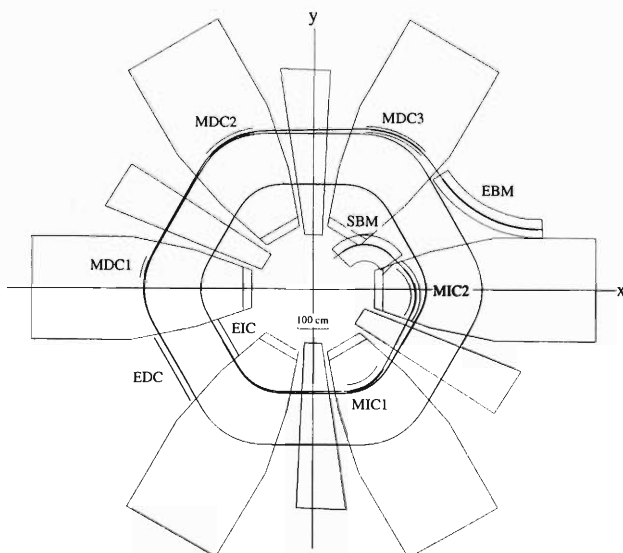


Fig. 1. Schematic layout of the injection and extraction elements and trajectory of the beam.

\*<sup>1</sup> Ishikawajima-Harima Heavy Industries Co., Ltd.

\*<sup>2</sup> Hitachi, Ltd.

Table 1. Design conditions of EBM.

Design magnetic field	from $-1.26$ to $-2.14$ T
Background magnetic field	from $+0.005$ to $-0.045$ T
Bending radius	3800 mm
Bending angle	55.0 deg.
Arc length	3648 mm
Iron pole gap	46 mm
Bore of beam pipe	$\phi 40$ mm

Table 2. Hollow conductors used in EBM.

Coil	Function	Size [mm]	Current [A]
A	main coil	$13 \times 13$	690
C	compensation coil	$9 \times 14$	$-960$
H	horizontal steerer	$13 \times 13$	$\pm 1000$
V	vertical steerer	$6 \times 6$	$\pm 640$

Gauss, respectively. The spaces on both the up-and downstream sides of EBM are small, and thus both end-structures of EBM should be compact.

Table 2 lists the hollow conductors used in EBM. Coil-A and Coil-C are wound flatly without bending up at the ends, to shorten the end-parts. Coil-H consists of one set of bipolar coils. The arc length of Coil-H is one-half of the arc of EBM, and Coil-H is built into the downstream side of EBM. Coil-V consists of two sets of independent-current bipolar coils. The arc length of each Coil-V is one-third of the arc of EBM, and each Coil-V is built into the both up-and downstream sides of EBM.

The quantity of the iron yoke should be the minimum necessary, because the iron gathers and disturbs the magnetic field in the acceleration region of the SRC. Outer-arc side return yoke is necessary to restrain coil-C from decreasing the magnetic field in the central region of EBM. The iron poles were tapered to concentrate magnetic flux into the central region of EBM, and the shapes of the pole faces were optimized to maintain good field uniformity for all excitation levels. Figure 3 shows the field uniformity in the central region. With the bore of  $\phi 40$  mm, field uniformity is about  $2 \times 10^{-3}$ .

The efficiency of field generation with respect to the magnetomotive force of coil-A is estimated to be 82%. Total power consumption of coil-A and coil-C is estimated roughly 175 kW at the maximum excitation.

The basic design of the extraction bending magnet for the SRC has been studied. The detail design is in progress in consideration of the fabrication process.

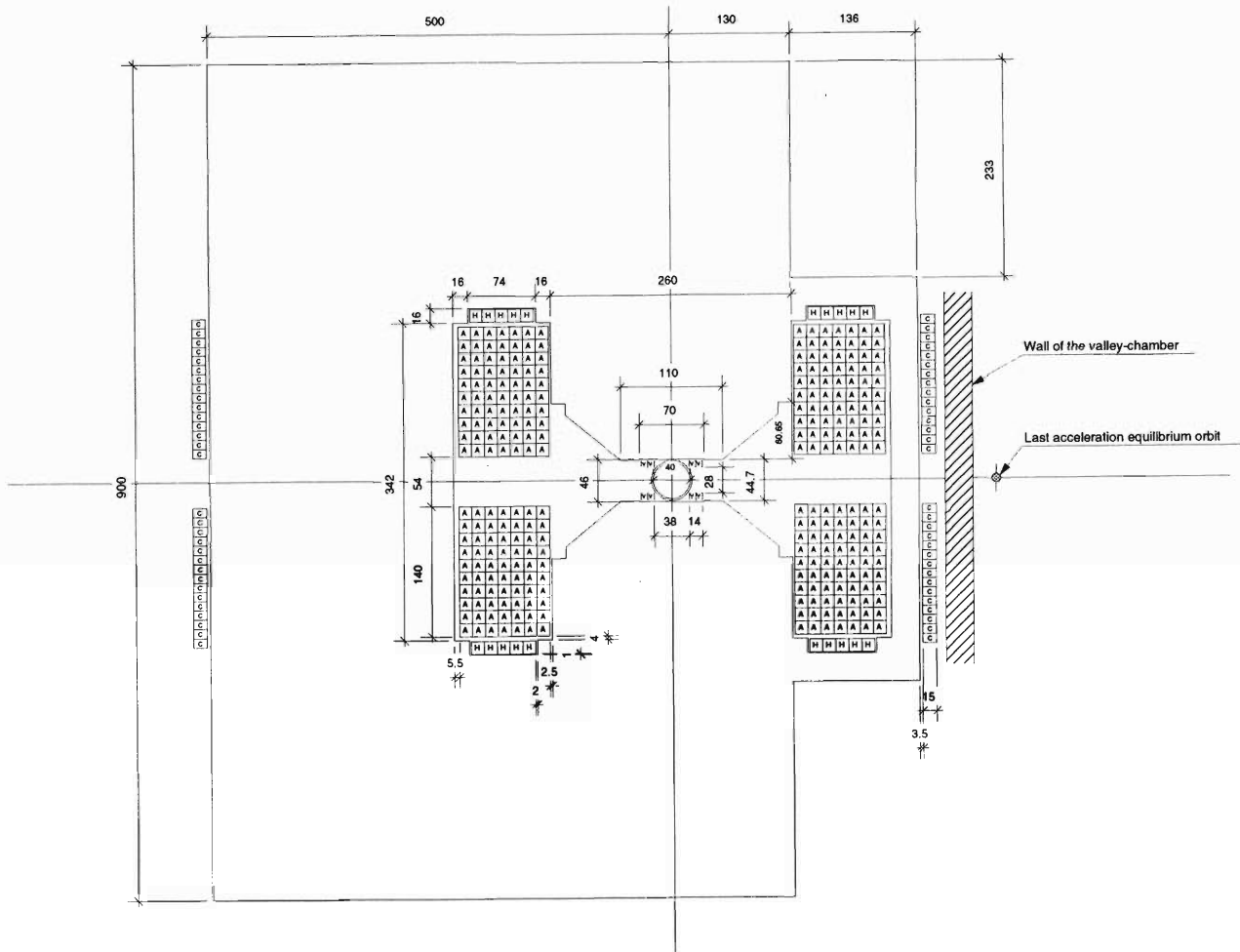


Fig. 2. Cross-sectional plan of EBM.

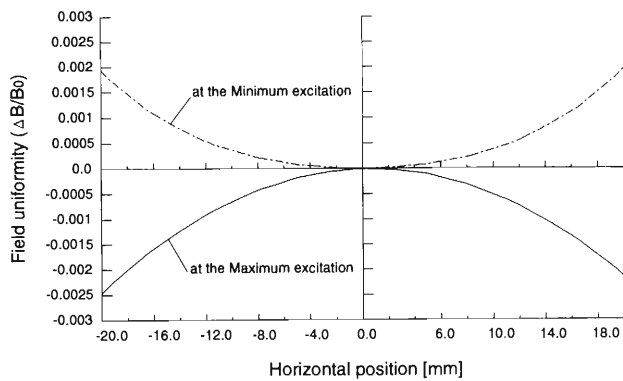


Fig. 3. Field uniformity in the central region.

#### References

- 1) H. Okuno et al.: Proc. 13th Symp. on Accelerator Science and Technology, Suita (2001) p. 65.
- 2) Y. Yano et al.: Proc. 13th Symp. on Accelerator Science and Technology, Suita (2001), p. 20.
- 3) S. Fujishima et al.: Proc. 16th Int. Conf. on Cyclotrons and Their Applications, East Lansing, USA (2001), p. 449.

# Quench protection of RIKEN Superconducting Ring Cyclotron

T. Tominaka,\* J. Ohnishi, H. Okuno, N. Fukunishi, A. Goto, and Y. Yano

For the design of the protection system of the superconducting main coils of the RIKEN Superconducting Ring Cyclotron (SRC),<sup>1)</sup> the quench characteristics are calculated with respect to various parameters, such as current decay, temperature rise, and voltage development, using the computer program “QUENCH-M”.<sup>2)</sup> The AC losses and pressure rise pertaining to the quench are also estimated.

The principal circuit diagram for the superconducting main coils of all six sectors of the SRC is shown in Fig. 1. There are subsidiary power supplies with dump resistors for use in the adjustment of the magnetic field of each sector. As the effects of the subsidiary power supplies and the dump resistors are minor, the quench analysis is performed for the simplified principal circuit diagram shown in Fig. 1.

The calculated results for two cases for the dump resistor,  $R_m$  of 0.3 and 0.4  $\Omega$  with different quench velocities and different switching off times of the power supply, are listed in Table 1. The quench velocity of 4.1 m/s is estimated under the adiabatic condition. In order to confirm the calculations with program “QUENCH-M,” the calculated results for the low quench velocity of 0.04 m/s are compared with those of the hot-spot temperature.<sup>3)</sup> It was found that they agree with each other.

According to the calculation of the voltage development pertaining to the quench detection, the switching off of the power supply can be made about 1 s after a quench. In addition, the effect of the delay time from 1 to 2 s is not large for the maximum temperature after a quench due to the long current decay time.

We chose the value of 0.3  $\Omega$  as the dump resistance,  $R_m$ , considering the following requirements: (1) the maximum temperature must not exceed 300 K (room temperature) even in the case of very low quench velocity which is the worst possible case; (2) in the case of normal quench velocity, the maximum temperature

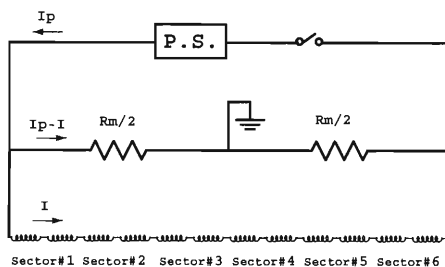


Fig. 1. Principal electric circuit for all superconducting main coils of all six sectors of SRC.

must be approximately 100 K, which is the allowable temperature for thermal expansion; and (3) the maximum voltage must be lower than 1.5 kV to facilitate coil fabrication.

Current decay, temperature rise and voltage development of the superconducting main coil of SRC during a quench in the case of  $R_m = 0.3 \Omega$  (Run# 1 in Table 1) are plotted in Fig. 2. As shown in Fig. 2 as well as in Table 1, the main coils of SRC are well protected against the quench.

For the estimation of eddy current effects, the AC loss is calculated during the quench, as well as during the charge and discharge processes of the main coils. Analytical expressions<sup>4,5)</sup> were used for the calculation of hysteresis and coupling losses, while the ELEKTRA<sup>a</sup> code was used for that of AC loss in the

Table 1. Results calculated by “QUENCH-M” program.

Run #	$R_m$ ( $\Omega$ )	$V_{ad.i}$ (m/s)	$T_{max}$ (K)	$V_{max}$ (kV)	$V_L$ (V)	$E_{in}$ (MJ)	$t_{sw}$ (s)
1	0.3	4.1	131	1.5	25	37	1.0
2	0.3	0.04	185	1.5	11	0	1.0
3	0.3	4.1	136	1.5	28	40	2.0
4	0.4	4.1	98	2.0	15	18	1.0
5	0.4	0.04	109	2.0	15	0	1.0
6	0.4	4.1	102	2.0	15	20	2.0

$I$ : Operating current, 5000 A

$L$ : Inductance, 18.8 H

$R_m$ : Dump resistance of main coil

$V_{ad.i}$ : Initial (adiabatic) quench velocity

$T_{max}$ : Maximum temperature

$V_{max}$ : Maximum voltage in the circuit

$V_L$ : Maximum voltage between layers

$E_m$ : Initial stored energy of 6 sectors, 235 MJ

$E_{in}$ : Dissipated energy in the superconducting coils

$t_{sw}$ : Time of switching-off of power supply

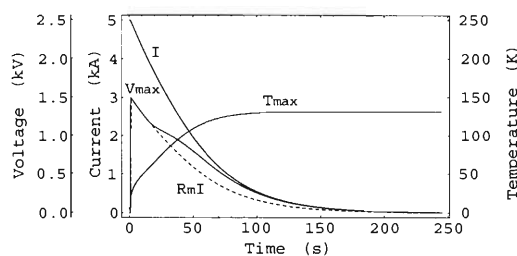


Fig. 2. Current,  $I$ , maximum temperature,  $T_{max}$ , the maximum voltage difference inside the coil,  $V_{max}$  and voltage drop across the dump resistor,  $R_m I$  of the superconducting main coil of SRC during quench, in the case of  $R_m = 0.3 \Omega$  (Run#1 in Table 1).

\* Hitachi, Ltd.

<sup>a</sup> ELEKTRA, Vector Field, Ltd., Oxford, UK

Al casing of trim coils. We adopted 100 s as a typical time of the current decay during the quench, as shown in Fig. 1, and 3600 s as a typical time of the charge or discharge. The calculated results of AC loss of one-half sector (upper or lower unit within one sector) for the charge or discharge process as well as for the quench process are listed in Table 2, in which the AC losses in different parts of the sector magnet are given as well as in the entire magnet.

Figure 3 shows the distribution of the eddy current for only one-half of the Al-alloy trim coil casing which has a total thickness of 48 mm. In the contour plot of Fig. 3, the white region in the peripheral part of the casing corresponds to the high-density of the induced eddy current, while the dark region of the central part corresponds to the low-density. It seems that this distribution of the eddy current results from the fact that the magnetic field component perpendicular ( $z$  direction) to the Al casing has a rather uniform distribution.

The total AC loss for the coil parts at 4.5 K during the quench is about 1% of the stored energy (235 MJ). In addition, there are AC losses in the iron pole and yoke at room temperature, which are not yet determined at present. The calculation of the quench protection was carried out on the assumption that all stored energy is consumed by joule heating in the coil

Table 2. AC loss for the coil parts at 4.5 K of one-half sector.

Charge or discharge time	3600 (s)	100 (s)
1) Loss in coil	1.8	3.6
Hysteresis loss	1.7	1.7
Coupling loss within strand	0.0017	0.061
Coupling loss in cable	0.011	0.39
Loss in Al matrix	0.039	1.4
2) Loss in vessel of main coil	1.8	64
3) Loss in casing of trim coils	4.3	160
Total Loss per half sector	7.9	230
Total Loss of all six sectors	95	2700

Unit: kJ

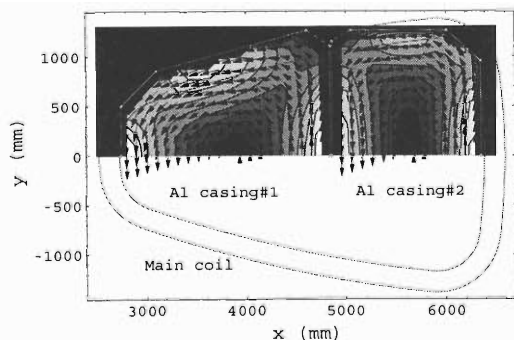


Fig. 3. Contour of  $|j|$  and vector plots of  $(j_x, j_y)$  for eddy current density in the Al casing of trim coils.

or dump resistor, neglecting the eddy current effect. However, it is expected that the maximum temperature is slightly bit lower than the calculated value shown in Table 1 or Fig. 2, due to the eddy current effect. The cooling scheme with two-phase helium for the Al trim coil casing is designed on the basis of the heat input due to AC loss during the charge or discharge process, the radiation, *etc.*<sup>1)</sup> Currently, a slow discharge with the small dump resistance ( $0.015 \Omega$ ) for some accidents without quench is being planned, in order to reduce the eddy current losses.

Following a quench, approximately 24 kg ( $0.2 \text{ m}^3$ ) of helium is expelled from the coil vessel through an exhaust pipe of 70 mm diameter and 10 m length. The maximum pressure induced during a quench must be estimated to ensure the structural integrity. The pressure rise and the mass flow from the vessel are calculated utilizing the Benedict-Webb-Rubin equation of state. The calculations are carried out for the worst case, in which it is assumed that the state of the helium released is gaseous. Figure 4 shows the results in which the pressure rise and the residual He mass in the coil vessel and the mass flow rate in the pipe after a quench are plotted as functions of elapsed time. On the other hand, if the state of the helium released is liquid, the pressure drop along the exhaust pipe is expected to decrease to about one tenth that in the case of gas. It is expected that the maximum pressure within the He vessel will not reach the maximum permissible pressure, 4 atm, because the actual helium released is a mixture of liquid and gas.

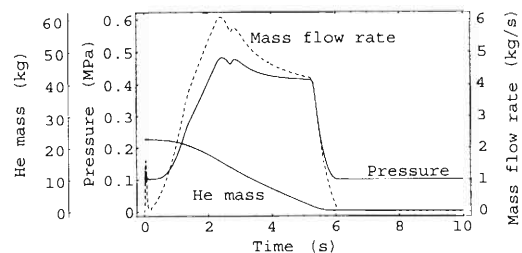


Fig. 4. Pressure rise and residual He mass in the coil vessel, and mass flow rate in pipe after a quench.

#### References

- 1) A. Goto et al.: Proc. 16th Int. Conf. on Cyclotrons and Their Applications (Cyclotrons'01, 2001), to be published.
- 2) T. Tominaka et al.: IEEE Trans. Magn. **28**, 727 (1992).
- 3) T. Tominaka et al.: Proc. 17th Int. Conf. on Magnet Technology (MT-17, 2001); IEEE Trans. Magn., to be published.
- 4) Y. Iwasa: in *Case Studies in Superconducting Magnets* (Plenum Press, New York, 1994), p. 264.
- 5) K. Mess et al.: in *Superconducting Accelerator Magnets* (World Scientific, Singapore, 1996), p. 104.

## Design study of beam transport lines from SRC to Big RIPS

K. Kusaka, T. Kubo, and Y. Mizoi

In the RI-Beam Factory (RIBF) project, energetic heavy-ion beams from SRC will be delivered to projectile fragment separators, called Big RIPS,<sup>1)</sup> to produce RI beams. Two Big RIPS separators will be constructed, so that two different RI-beam experiments can be conducted at the same time. Big RIPS I is characterized by large-aperture superconducting quadrupoles. Even projectile fragments produced by in-flight fission of uranium beams can be collected efficiently. On the other hand, Big RIPS II consists of normal conducting magnets whose apertures are similar to those of the present RIPS. These two separators share primary beams from SRC by means of time sharing so that users of two separators can control beam intensity independently. A design study of beam transport lines from SRC to two Big RIPS's has been carried out, taking the constraints of building layout and design of magnets into account.

In this design study, we consider a fast pulsing magnet (PM) system with a ramping time of about 10 ms for time sharing between Big RIPS I and II. The PM will be operated in both DC and pulsing modes. An example of the pulsing operation pattern for time sharing between Big RIPS I and Big RIPS II is shown in Fig. 1.

A layout of beam lines, together with SRC and Big RIPS separators, is schematically shown in Fig. 2. A primary beam extracted from SRC by EBM, together with other extraction elements, is transferred from the SRC room to the IRC room by the quadrupole quartet (QQ). The dipole magnet D1 changes the direction of the beam by 20° and directs the beam to the PM together with the quadrupole multiplet TQ and DQ. While the PM is turned off, an unkicked beam is transported to the beam line to target T1 for Big RIPS I. The beam line for Big RIPS I consists of two 50° dipole magnets (R1-D1 and R1-D2), a quadrupole doublet (R1-DQ), and two quadrupole triplets (R1-TQ1 and R1-TQ2), as shown in Fig. 2. The dipoles R1-D1 and R1-D2 are a 2-Tesla normal conducting bending magnet (2TBM).<sup>2)</sup> While the PM is excited, on the other hand, the beam is delivered to a branch line to target T2 for Big RIPS II, which consists of four bending magnets, a quadrupole doublet (R2-QD), and two quadrupole triplets (R2-TQ1 and R2-TQ2). The bending magnets are a 17°-C-type Dipole magnet (R2-D1), a 50° 2TBM (R2-D2) and two 30°-2TBMs (R2-D3 and R2-D4). We should note that the aperture of the last quadrupole triplets, R1-TQ2 and R2-TQ2, must be large in order to focus the beam to targets T1 and T2 with small spot sizes. The bore radius of the quadrupoles, except for R1-TQ2 and R2-TQ2, is 35 mm and the maximum field gradient is 22 T/m.

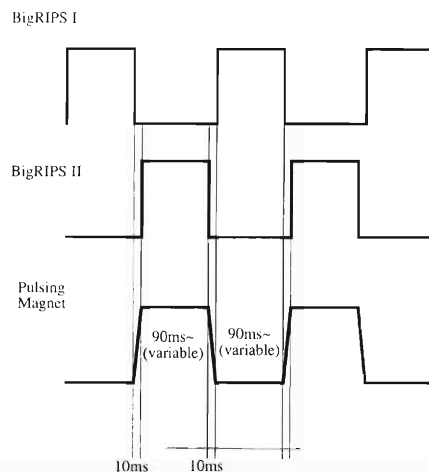


Fig. 1. Operation pattern of the pulsing mode.

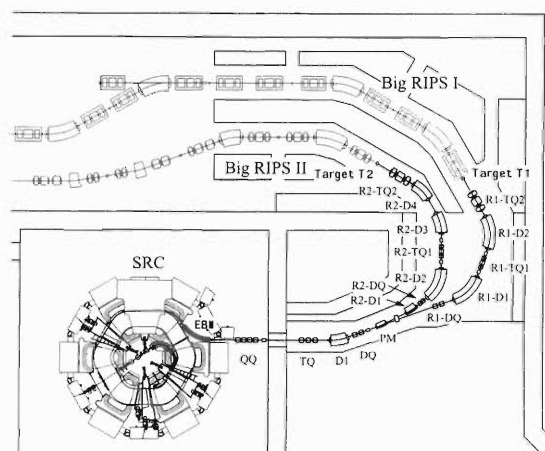


Fig. 2. Schematic layout of the beam transport line from SRC to Big RIPS separators.

On the other hand, the bore radius and the maximum field gradient of R1-TQ2 and R2-TQ2 are 55 mm and 17.5 T/m, respectively.<sup>3)</sup> Specifications of the bending magnets are listed in Table 1.

The pulsing magnet power supply has been fabricated and tested for R & D studies.<sup>4)</sup> The circuit of the power supply consists of two parts. One is a forcing circuit which quickly energizes and de-energizes the magnet with a high voltage. The other is the main circuit to control the excitation current using a transistor dropper. The maximum output current is 1600 A. The maximum output voltage in the pulse mode is 2170 V and that in the DC mode is 65 V. The designed switching time was shorter than 50 ms with a load magnet having inductance and resistance of 25.9 mH and

Table 1. Specifications of the bending magnets.

Symbol	Type	Bending Angle [deg]	Bending Radius [mm]	Full Gap [mm]	Maximum Field [T]
D1	H	20	5000	60	1.6
R1-D1	H	50	4020	60	2.0
R1-D2	H	50	4020	60	2.0
PM	C	7	9000	60	0.89
R2-D1	C	13	5300	60	1.51
R2-D2	H	50	4020	60	2.0
R2-D3	H	30	4020	60	2.0
R2-D4	H	30	4020	60	2.0

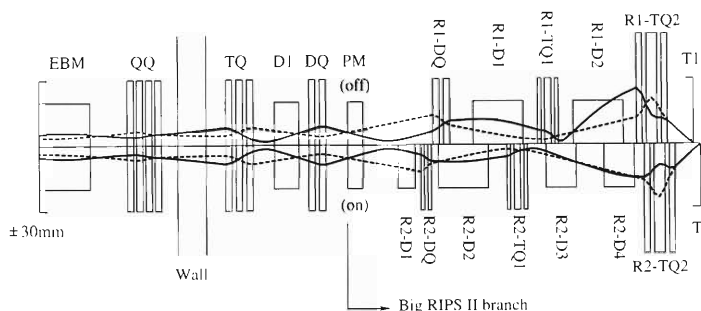


Fig. 3. First-order beam envelopes for the beam line from SRC to BigRIPS I and II. Solid (dashed) lines represent the horizontal (vertical) envelopes.

33.3 m $\Omega$ , respectively. The rise time of 35 ms and the descending time of 17 ms are achieved in test operations with a test load.

We are aiming at a switching time of  $\sim 10$  ms with small modifications of the power supply by changing the parameters of the load PM. The PM in the design is a C-type dipole magnet with a bending angle of  $7^\circ$  and an orbit radius of 9 m. Design values of its inductance and resistance are 6.94 mH and 15.7 m $\Omega$ , respectively. With these PM parameters, the expected voltage drop for a 5 msec rise time is 1675 V, which is sufficiently smaller than the maximum output voltage of the power supply. Precise timing control of gate turn-off thyristors that switch the forcing circuit on and/or off and modification of the dropper transistor control are planned to improve the power supply for  $\sim 10$  ms switching.

The same PM system is planned to be used in the beam transport line from IRC, which is a pre-accelerator for SRC. The beam extracted from IRC is delivered simultaneously to both SRC and an existing experimental room in the RIKEN Accelerator Research Facility (RARF).<sup>5)</sup> Two PM's under consideration are designed such that the same power supply can be used in common. The PM for the beam line from IRC is now being fabricated by Toshiba.

Figure 3 shows an example of calculated first-order beam envelopes of the beam lines from EBM to T1 and T2. The assumed beam is  $^{238}\text{U}^{88+}$  with an energy

of 350 MeV/u, which has the highest magnetic rigidity of 7.94 [Tm]. The beam shape at EBM is based on calculated beam trajectories traced in SRC.<sup>6)</sup> The emittance of  $\epsilon_x = \epsilon_y = 3\pi$  mm mrad and momentum spread of  $\Delta p/p = \pm 0.05\%$  are assumed. We have made the ion-optical design so that the beam spot size on the target T1 and T2 is 1 mm and the beam lines for BigRIPS I and II are ion-optically identical, in other words, their transfer matrices are identical. The maximum value of the quadrupole-filling factor is designed to be 50%. The beams on T1 and T2 are achromatized by tuning the quadrupole triplets R1-TQ1 and R2-TQ1. Further optimization of the layout and magnet design is now in progress.

#### References

- 1) T. Kubo et al.: RIKEN Accel. Prog. Rep. **35**, 301 (2002).
- 2) T. Nagafuchi et al.: RIKEN Accel. Prog. Rep. **33**, 234 (2000); Y. Mizoi et al.: RIKEN Accel. Prog. Rep. **35**, 305 (2002).
- 3) Y. Mizoi et al.: RIKEN Accel. Prog. Rep. **35**, 299 (2002).
- 4) H. Kouzu et al.: RIKEN Accel. Prog. Rep. **34**, 355 (2001).
- 5) N. Fukunishi et al.: RIKEN Accel. Prog. Rep. **35**, 283 (2002).
- 6) S. Fujishima et al.: RIKEN Accel. Prog. Rep. **35**, 293 (2002).

# Design study of quadrupole magnets for the beam-transport line and BigRIPS separator

Y. Mizoi, K. Kusaka, and T. Kubo

We designed 3 normal-conducting quadrupole magnets with high magnetic field gradients and large Bore radii for the beam-transport line and normal-conducting BigRIPS separator.<sup>1)</sup>

Their types and specifications are summarized in Ta-

ble 1.

In order to obtain the excitation function of the field gradient with a reasonably small saturation, and good uniformity of the field gradient, we designed the magnets using OPERA-2d and -3d, for the 2- and 3-

Table 1. Specifications of the quadrupole magnets. Currents and power consumptions are the typical values at the maximum field gradients.

Magnet name	Q110	Q160	Q200
Field gradient (T/m)	17.5	12.5	9.0
Bore radius (mm $\phi$ )	110	160	200
Pole length (mm)	400, 800	800	800
Current (A)	325, 290	485	406
Power consumption (kW)	20, 23	53	49
Hollow conductor	9 $\times$ 9 mm <sup>2</sup> - $\phi$ 6 mm	10 $\times$ 10 mm <sup>2</sup> - $\phi$ 7 mm	10 $\times$ 10 mm <sup>2</sup> - $\phi$ 7 mm
Turn number	84	76	100
Water-circuit number	4/pole	4/pole	4/pole

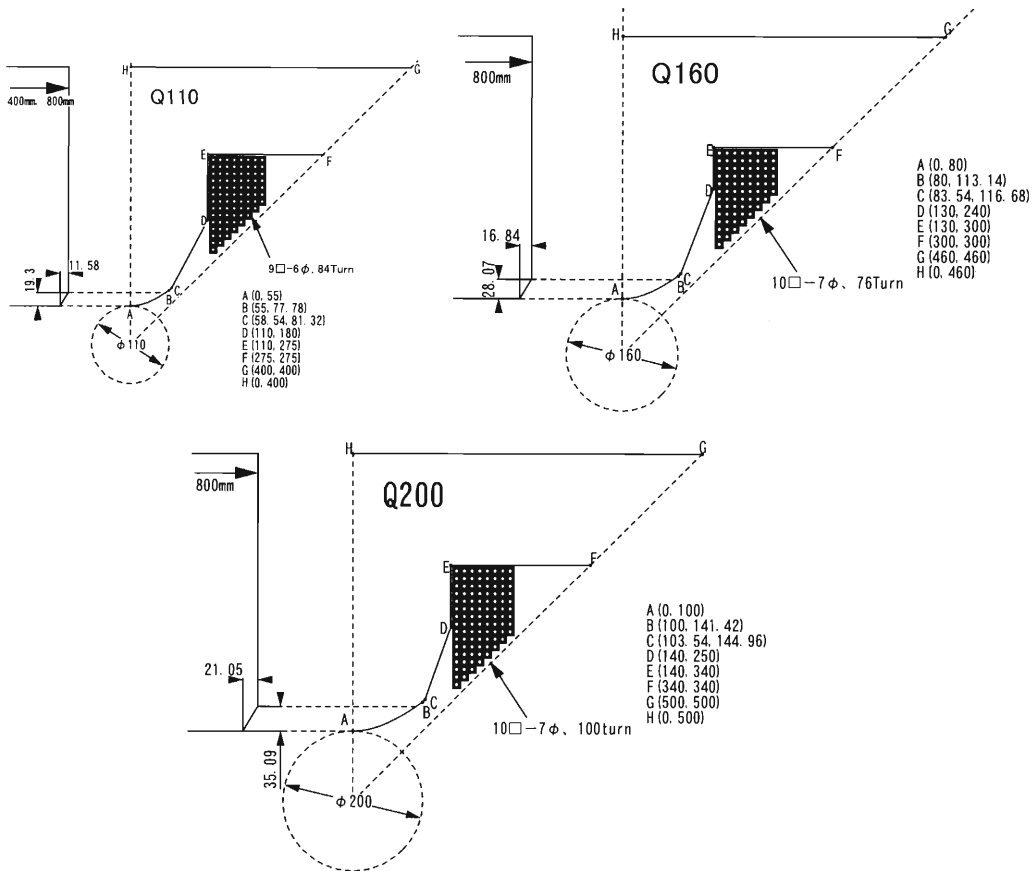


Fig. 1. Cross-sectional view of the quadrupole magnets, Q110, Q160 and Q200. Half of the poles and the coils are drawn. Letters correspond to the points on the Cartesian coordinates located at the origin in the center of the Bore radius. The shapes of pole end are also drawn.

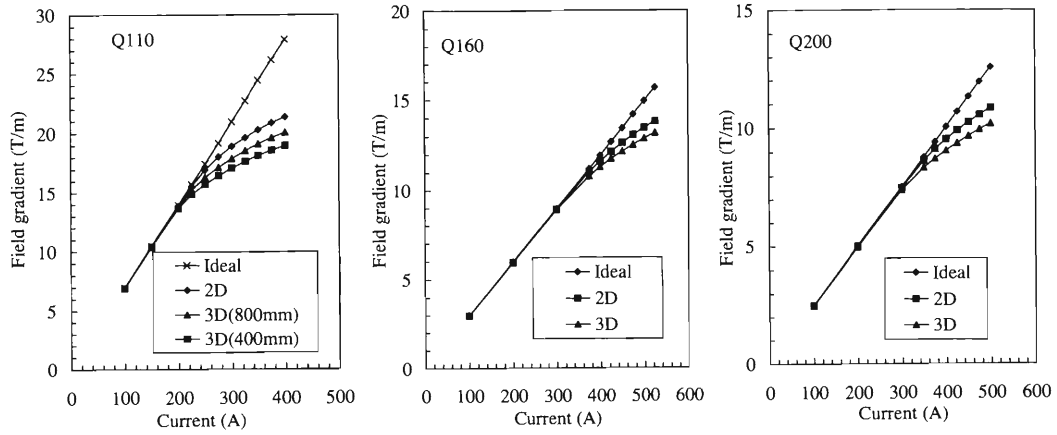


Fig. 2. Excitation curve of the field gradient for Q110, Q160 and Q200. Q110 has two pole lengths, 400 mm and 800 mm.

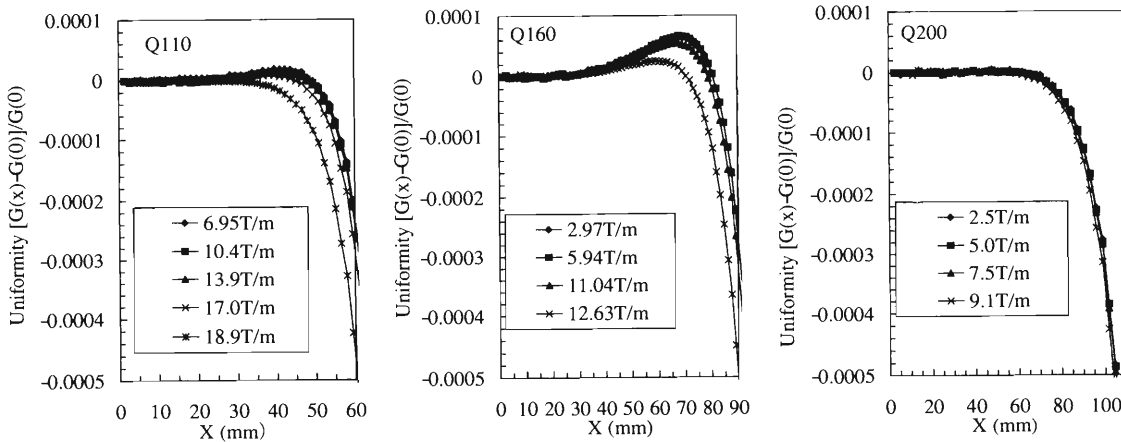


Fig. 3. Uniformity of the field gradient for Q110, Q160 and Q200. The horizontal axis indicates the distance from the center of the Bore radius.

dimensional field calculations. We used the B-H curve of SUYP0 in the present calculations.

The cross-sectional view of the magnets are shown in Fig. 1.

Figure 2 shows their excitation curves. The results of 2-dimensional and 3-dimensional calculations are shown, and in addition, the ideal excitation curves are also depicted. Although 3-dimensional effects of saturation are observed, comparing the calculated values with the ideal ones reveals that the saturation of the excitation curve is reasonably small in the region of

interest. Figure 3 shows the uniformities of the field gradients of the magnets. The uniformity is very good within the Bore radius.

We obtained a reasonable design of quadrupole magnets. In future studies, we will perform a multipole analysis of these magnet.

#### References

- 1) T. Kubo et al.: RIKEN Accel. Prog. Rep. **33**, 236 (2000).

# Projectile fragment separator BigRIPS for the RI-Beam Factory project

T. Kubo, Y. Mizoi, and K. Kusaka

In this report we outline the projectile fragment separator BigRIPS, which is to be used for the production of RI beams in the RIKEN RI Beam Factory project.

In the project, heavy-ion beams can be accelerated up to 400 MeV/nucleon in the case of relatively light elements and 350 MeV/nucleon in the case of heavy elements.<sup>1)</sup> The maximum beam intensity is expected to be as high as 1  $\mu$ A, even for very heavy elements such as uranium. Such high performance encourages us to use in-flight fission of uranium beams as a production reaction, in addition to the projectile fragmentation reaction that has been commonly used to date. The in-flight fission of uranium beams is very powerful for the production of neutron-rich RI beams with medium-heavy mass, because it has much a larger production cross section for this mass region. The BigRIPS separator has been designed taking into consideration the use of in-flight fission, so that intensity of RI beams can be significantly increased. The design goal of the separator was that it could produce RI beams with as high an intensity as possible and that it could produce RI beams as far from the stability line as possible.

We plan to build two projectile fragment separators, which are named BigRIPS I and BigRIPS II. Figure 1 shows a schematic layout of the system. The SRC is followed by a beam transport line,<sup>2)</sup> and then by the two BigRIPS separators. These two separators can share primary heavy-ion beams from the SRC by means of time sharing, which is achieved by placing a pulsing magnet (PM) in the beam transport line.<sup>2)</sup> This scheme allows us to conduct two different RI-beam experiments simultaneously.

The BigRIPS separators have been designed to be

what we call a tandem fragment separator or a cascade of two fragment separators. Each stage of the tandem fragment separator forms an achromatic spectrometer with intermediate focuses. The first stage serves to produce and separate RI beams, while the second stage serves to identify RI-beam species as well as to measure their momentum in an event-by-event mode. This scheme allows us to deliver tagged RI beams to experimental setups placed downstream. RI-beam experiments would be significantly facilitated by this scheme as emittance and purity of RI beams are expected to be poor in our energy domain.

The main parameters of BigRIPS separators are listed in Table 1. The BigRIPS I separator has been designed taking into consideration the use of in-flight

Table 1. BigRIPS parameters.

	BigRIPS I	BigRIPS II
Quadrupoles	Super	Normal
Angular acceptance [mr]		
Horizontal	80	20
Vertical	100	30
Momentum acceptance [%]	6	3
Maximum magnetic rigidity [Tm]	9	9
Total length [m]	77	54
Momentum dispersion [cm/%]		
First stage	-2.31 (F1)	-2.1 (F1)
Second stage	3.30 (F5)	0.57 (F3)
Momentum resolution*		
First stage	1300 (F1)	2000 (F1)
Second stage	3300 (F5)	600 (F3)

\* First-order momentum resolution, for which object size is assumed to be 1 mm.

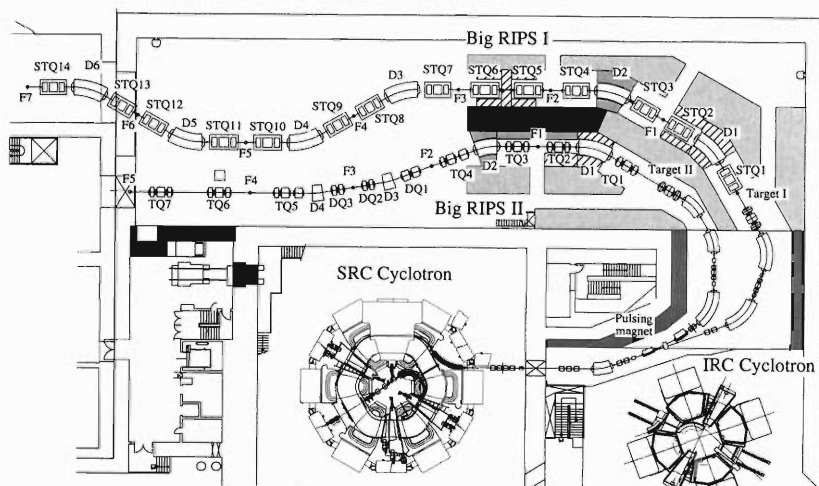


Fig. 1. A schematic layout of the BigRIPS separator. Quadrupole magnets are indicated by STQ<sub>n</sub>, TQ<sub>n</sub> and DQ<sub>n</sub>, while dipole magnets are indicated by D<sub>n</sub>. F<sub>n</sub> denotes focuses.

fission of uranium beams. According to their reaction kinematics at 350 MeV/nucleon, angular and momentum spreads of fission fragments amount to approximately 100 mrad and 10%, respectively, when symmetric fission is assumed. The BigRIPS I separator has large acceptances comparable to these values, so that it can collect as many fission fragments as possible. Superconducting quadrupoles with large apertures and high fields are to be used for the BigRIPS I separator to achieve the high acceptances. The dipoles to be used also have a large gap, although they are normal conducting magnets. In the case of using projectile fragmentation reactions, the large acceptances can increase the intensity of RI beams significantly, if the RI beams are very far from the projectile or if the RI beams are light isotopes. In these cases, the angular and momentum spreads of fragments are expected to become larger, according to the reaction kinematics of projectile fragmentation reactions.

On the other hand, the BigRIPS II separator has been designed to have relatively small acceptances. The acceptances were determined taking into consideration only the use of projectile fragmentation reactions of medium-heavy projectiles, in which the angular and momentum spreads of projectile fragments are much smaller than those of the fission fragments. Normal-conducting quadrupoles with a small aperture are to be used in this case. Dipoles are also normal conducting magnets. The acceptances of the BigRIPS II separator are sufficiently large to produce medium-heavy and heavy RI beams using projectile fragmentation reactions.

The BigRIPS I separator is to be mainly used for experiments using RI beams very far from the stability line, a subject which has never been studied before and is of great interest. Such experiments may be called frontier experiments. On the other hand, the BigRIPS II separator is to be mainly used for what we call factory experiments, in which systematic studies are conducted by using a long beam-time.

As shown in Fig. 1, the first stage of the BigRIPS I separator forms a two-bend achromatic spectrometer, consisting of four superconducting quadrupole triplets (STQ1 to STQ4).<sup>3)</sup> each of which is installed in a single cryostat, and two dipoles with a 30-degree bend (D1 and D2). An energy degrader is placed at the intermediate focus F1 for isotope separation. A telescopic system consisting of two quadrupole triplets (STQ5 and STQ6) placed after focus F2 transport RI beams to the second stage. Thick concrete shielding surrounds the first stage to prevent neutron radiation. The second stage, starting from focus F3, forms a four-bend achromatic spectrometer, which consists of eight su-

perconducting quadrupole triplets (STQ7 to STQ14) and four dipoles with a 30-degree bend (D3 to D6). The four bends allow a higher momentum resolution in this stage, where the tagging of RI beams is achieved. Tagging detectors are to be placed at focuses such as F3, F5 and F7 to measure angles, positions, energy loss, and time-of-flight of RI beams. The BigRIPS II separator has a relatively simple configuration because of the constraints of the building layout. Both stages are designed to form a two-bend achromatic spectrometer. The bends in the first stage are not symmetric: 30 degrees and 20 degrees. The momentum resolution in the second stage is poor because of a small bending angle (10 degrees). Tagging of RI beams may not be very useful in the case of the BigRIPS II separator.

The superconducting quadrupole triplets in the concrete shielding (STQ1 to STQ5) are to be cooled by a large refrigeration system through a liquid-helium transfer line. Its cooling capacity is around 250 W at 4.5 K. This is because the quadrupole triplets, particularly the first two triplets, are exposed to high neutron radiation which causes significant heat loads on the cryostat. The heat loads from the neutron radiation are estimated to be around 100 W.<sup>4)</sup> On the other hand the superconducting quadrupole triplets downstream (STQ6 to STQ14) are cooled by a small refrigeration system whose details are reported elsewhere.<sup>5)</sup> The small refrigeration system is mounted on the cryostat of each quadrupole triplet. We adopted this scheme because the neutron radiation is expected to be low in the second stage. This scheme reduces the fabrication cost significantly.

Each BigRIPS separator is to be followed by RI-beam delivery lines, which transport the tagged RI beams to different experimental setups placed downstream. The building is to be extended at the left-hand side shown in Fig. 1 to accommodate the RI-beam delivery lines and the experimental setups.

The fabrication of the BigRIPS separators begins next year.

## References

- 1) Y. Yano: RIKEN Accel. Prog. Rep. **34**, 301 (2001).
- 2) K. Kusaka et al.: RIKEN Accel. Prog. Rep. **35**, 297 (2002).
- 3) T. Hiramachi et al.: IEEE Trans. Appl. Supercond. **10**, 236 (2000); T. Kubo et al.: RIKEN Accel. Prog. Rep. **33**, 238 (2000); H. Kouzu et al.: RIKEN Accel. Prog. Rep. **34**, 350 (2001); T. Tominaka et al.: RIKEN Accel. Prog. Rep. **34**, 353 (2001).
- 4) T. Mukhopadhyay et al.: RIKEN Accel. Prog. Rep. **33**, 241 (2000).
- 5) K. Kusaka et al.: RIKEN Accel. Prog. Rep. **35**, 303 (2002).

# Superconducting quadrupole magnet with small refrigerators

K. Kusaka, T. Kubo, T. Tominaka,<sup>\*1</sup> Y. Mizoi, Y. Yano,  
N. Kakutani,<sup>\*2</sup> T. Tsuchihashi,<sup>\*2</sup> and O. Ohsaki<sup>\*2</sup>

Superconducting quadrupole magnets are to be used for the BigRIPS separator in order to efficiently produce RI beams.<sup>1,2)</sup> Two types of cryogenic system for the quadrupoles are planned.

The cryogenic system for the quadrupoles located close to the production targets and beam dumps is an integrated system with a large cooling capacity, in which a single refrigerator supplies liquid He (LHe) to a number of magnets through transfer lines. Since the magnets are exposed to high neutron radiation, a large cooling power for the refrigerator system is required due to large heat load of neutron radiation.

Another system is a stand-alone-type superconducting magnet equipped with small refrigerators on its cryostat. The stand-alone type magnet is financially preferable, since no big cryogenic plant is necessary. The stand-alone-type magnets are to be used in the analyzing section of the BigRIPS where the possible radiation level is reasonably low. In this report, we summarize the design of a superconducting quadrupole magnet with small refrigerators.

A prototype of the superferric quadrupole triplet has been fabricated and tested for R&D studies.<sup>1,2)</sup> The main parameters of the magnet are listed in Table 1. The magnets are installed in a dewar-type cryostat and cooled by the LHe bath cooling method. We designed a new cryostat with small refrigerators based on the prototype cryostat by reducing heat load as much as possible. A cross-sectional view of the cryostat with small refrigerators is shown in Fig. 1.

We show, in Table 2, the estimated values of the heat loss of the superconducting quadrupole magnet with

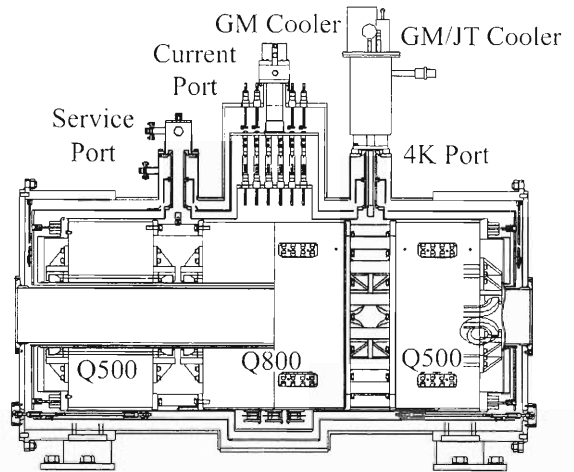


Fig. 1. Quadrupole triplet with small refrigerators.

small refrigerators. Those of the prototype cryostat are also listed for comparison. A key to reducing heat loss in the He vessel is new current leads. The number of the current leads for three quadrupole magnets is reduced from 6 to 4 and a high- $T_c$  superconducting material is used to reduce Joule heat.

A Gifford-McMahon/Joule-Thomson (GM/JT) cooler, mounted on the 4 K port, is used to cool the He vessel. It liquifies He gas that evaporates in the He vessel with the recondensing heat exchanger unit. The cooling capacity of the GM/JT cooler is 2.5 W at 4.3 K. When the magnets are operated under a constant current, the margin of cooling capacity over the heat load is expected to be 0.58 W.

A Gifford-McMahon (GM) cooler is mounted on the current port of the cryostat. It cools the 80 K shield and the high- $T_c$  superconducting current leads (HTCL) by heat conduction. The cooling capacity of the GM cooler is 90 W at 80 K and is sufficient to cool HTCL and the 80 K shield at all times. Both refrigerators operate using separate water-cooled compressors.

Since the cold mass of the magnet is too large for small refrigerators to cool from room temperature to 4 K, precooling with liquid  $N_2$  and LHe is necessary. The service port is used to transfer LHe and liquid  $N_2$  from an external storage. A pressure release valve (0.05 MPa), a bursting disk (0.1 MPa), and terminals for sensors are also installed on the service port.

The excitation circuit for the quadrupole triplet is shown in Fig. 2. If an abnormal voltage drop of HTCL is detected or HTCL is broken, the current lead protection switch cuts the power supply output and the

Table 1. Main parameters of Q500 and Q800 quadrupoles.

	Q500	Q800
Effective magnetic length [m]	~0.54	~0.84
Pole tip radius [mm]	170	170
Warm clear bore radius [mm]	140	140
Max field gradient [T/m]	14.1	14.1
Winding of coil	orderly	orderly
Nominal current per pole [kA]	199	190
Nominal current [A]	142	136
Nominal current density [A/mm <sup>2</sup> ]	115	110
Straight length of coil [mm]	440	740
Total length of coil [mm]	640	940
Length of iron [mm]	440	740
Outer radius of yoke [mm]	480	480
Inductance [H]	12 ~ 20	18 ~ 28
Stored energy [MJ]	0.13	0.19

<sup>\*1</sup> Hitachi, Ltd.

<sup>\*2</sup> Toshiba Corporation

Table 2. Expected heat loss (unit [W]) of two cryostats.

			with small refrigerators			prototype cryostat (dewar type)		
			magnet status			magnet status		
	Parts	Type of Heat Load	(de-)energizing	energized	de-energized	(de-)energizing	energized	de-energized
He Vessel	Thermal Shield	Radiation	0.18	←	←	0.18	←	←
	Support	Conduction	0.65	←	←	0.65	←	←
	Current Lead	Conduction+Joule heat	0.49/4P	←	0.2/4P	0.97/6P	←	0.49/6P
	Gas He Port	Conduction	0.58	←	←	0.69	←	←
	Bellows	Conduction	0.17	←	←	0.82	←	←
	Coil (Triplet)	AC loss (1 A/s ramp.)	11.4	0	←	11.4	0	←
		Total		13.32	1.92	1.82	14.75	3.35
			GM/JT capacity 2.5 W at 4.3 K					
80 K Shield	Vacuum Vessel	Radiation	7.11	←	←	7.11	←	←
		Residual Gas	0.55	←	←	0.55	←	←
	Support	Conduction	12.34	←	←	12.34	←	←
	Current Lead	Conduction+Joule heat	28.9/4P	←	18.4/4P	N/A	←	←
	Gas He Port	Conduction	N/A	←	←	4.71	←	←
	Bellows	Conduction	1.31	←	←	5.13	←	←
		Total		50.21	←	39.71	29.84	←
			GM capacity 90 W at 80 K					

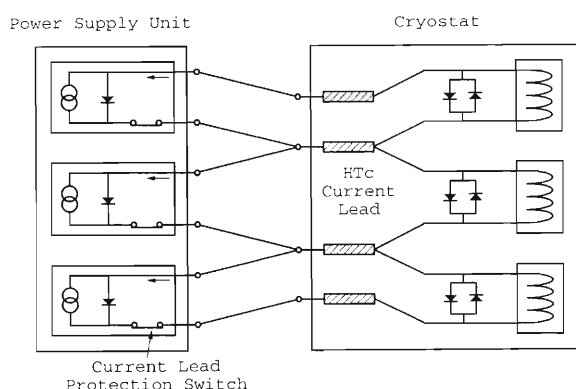


Fig. 2. Excitation circuit of the quadrupole triplet.

stored energy of the magnet is dissipated in the diodes in the He vessel. On the other hand, if quenching of a coil occurs, the power supply is switched off due to the output overvoltage, so that the current is discharged through the diode in the power supply unit and the stored energy is dissipated in the coil. In other abnormal cases, *e.g.*, a failure of a refrigerator, the stored energy is transferred outside of the cryostat and is dissipated by the diode in the power supply. The current is discharged with the speed of 1 A/s in this case.

Since the heat loss of the He vessel exceeds the capacity of the GM/JT cooler when the power supply sweeps the excitation current, we estimated the pressure increase. If the He vessel is fully filled with  $\sim 600$  L of LHe, the pressure of the He vessel reaches its relief pressure after 8.5 minutes of continuous change of the current at a rate of 1 A/s. If the magnets are

kept energized (de-energized), the excess cooling capacity of the GM/JT cooler reduces the pressure from its limit to atmospheric pressure within 1.7 hours (1.4 hours). In a standard operation of the fragment separator, the current ramping rate is expected to be  $\sim 0.3$  A/s, when the current is changed to a large extent. Although a rapid change (close to 1 A/s) may be required for fine adjustments, the period is expected to be several seconds in this case. We thus expect that the pressure of the He vessel seldom exceeds its relief pressure.

If water and/or electric supply is suspended for a long time, LHe in the He vessel will evaporate and will then be lost as a relief gas. About 84 L of LHe will be lost if the refrigerator stops functioning for 24 hours. The entire amount of LHe ( $\sim 600$  L) in the He vessel will be lost if the refrigerator stops functioning for 3 days. A backup for the electric and water supplies of the refrigerators is important.

To test the cryogenic system of the superconducting quadrupole magnet with small refrigerators, a new cryostat is currently being fabricated in Toshiba. The cryostat of the prototype has been disassembled and the magnets in it are ready for reinstallation in the new cryostat. Cooling and excitation tests will be performed in the near future.

#### References

- 1) T. Hiramachi et al.: IEEE Trans. Appl. Supercond. **10**, 238 (2000).
- 2) H. Kouzu et al.: RIKEN Accel. Prog. Rep. **34**, 350 (2001); T. Tominaka et al.: RIKEN Accel. Prog. Rep. **34**, 353 (2001).

## Design study of 2 Tesla dipole magnet by three-dimensional calculation

Y. Mizoi, N. Kakutani,\* K. Kusaka, and T. Kubo

We are studying the design of a 2 T dipole magnet (2 T) with normal-conducting coils for the beam-transport line from SRC<sup>1)</sup> to BigRIPS<sup>2)</sup> separators. Two-dimensional magnetic-field calculations were performed by Nagafuchi *et al.*<sup>3)</sup> and the 2 T cross section was determined. In order to estimate the three-dimensional effects, we are performing three-dimensional calculations by means of OPERA-3d.

Figure 1 shows the schematic view of 2 T. Although the radius of 2 T presented by Nagafuchi *et al.*<sup>3)</sup> was 3.75 m, the present radius is 4 m, because the magnetic rigidity of SRC has been upgraded. In addition, the bending angles of 2 T are also changed to 30 and 50 degrees from 30 and 70 degrees, respectively, according to the results of a beam-optics study. Figure 2 shows

the cross-sectional view of 2 T, which is the same as the previous one.

In the present calculations, we use the B-H curve of SUYP0, and the ends of the poles are cut with C30 for the first trial. Figure 3 shows the excitation function of 2 T in the case of a bending angle of 30 degrees. Compared with the ideal excitation curve, the 2 T saturation is sufficiently small for satisfactory operation. Figure 4 shows the uniformity of the magnetic field at the center of 2 T. The uniformity of the magnetic field is reasonably good in the region of  $\pm 50$  mm within  $10^{-4}$ . This is consistent with the results of two-dimensional calculations.<sup>3)</sup> The present specifications of 2 T are summarized in Table 1.

For subsequent trials, we will perform multipole

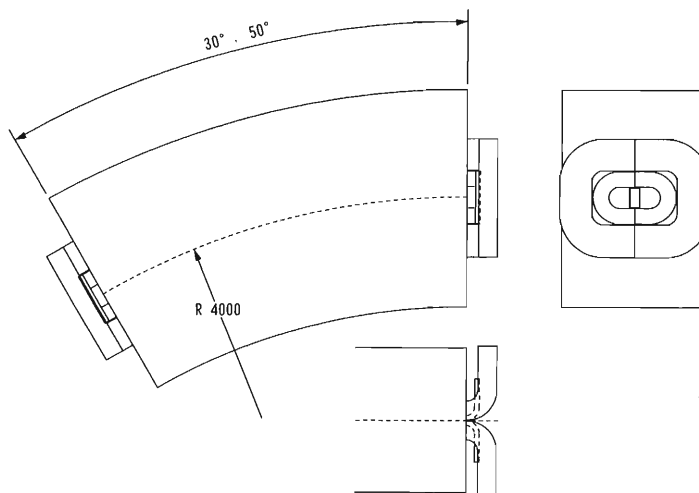


Fig. 1. Schematic view of 2 T.

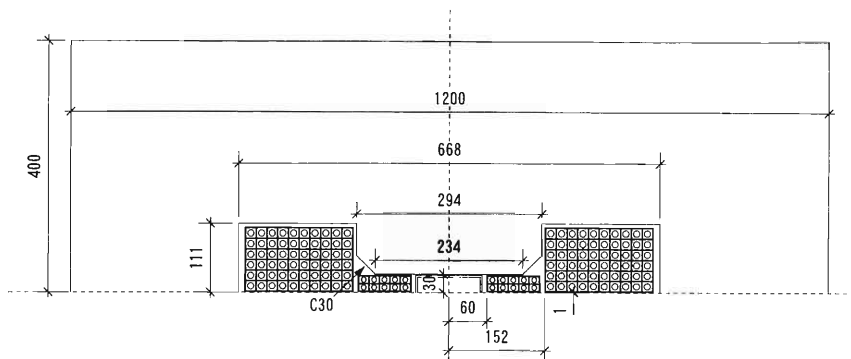


Fig. 2. Cross-sectional view of 2 T.

\* Toshiba Corporation

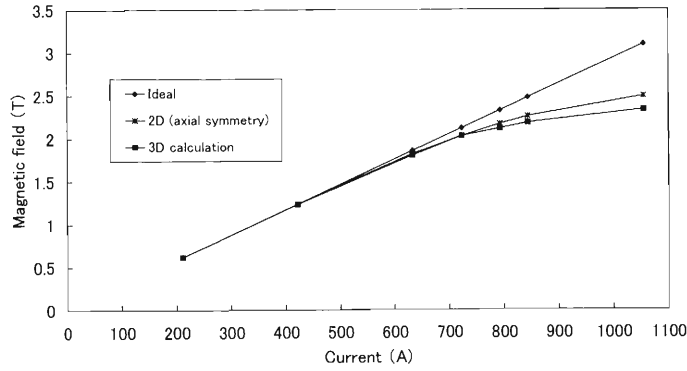


Fig. 3. Excitation curves of the magnetic field by the 3D calculation. The ideal excitation curve and the results of 2D calculation are also plotted.

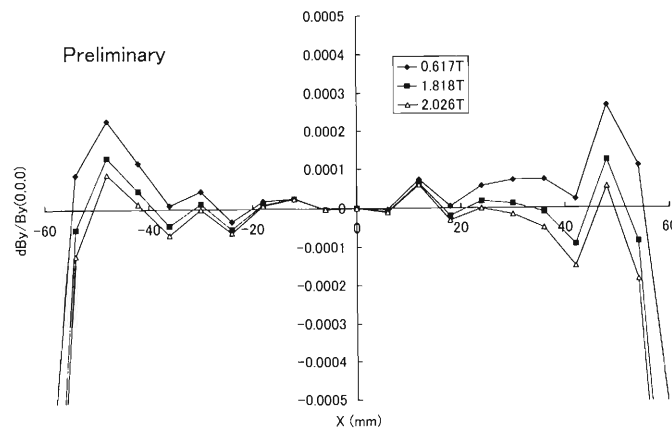


Fig. 4. Uniformity of the magnetic field.

Table 1. Specifications of 2 T.

Main parameter	
Magnetic rigidity	8.0 Tm
Bending radius	4.0 m
Bending angle	30, 50 degrees
Field strength	up to 2.0 T
Pole gap	60 mm
Good field region	$\pm 50$ mm within $10^{-4}$
Nominal current at 2 T	723 A
Nominal power consumption at 2 T	66 kW for 30 degrees, 95 kW for 50 degrees
Coil parameter	
Turn number	70/pole, (inner 10 + outer 60)
Hollow conductor of inner coil	W15.5 mm (W) $\times$ H11.5 mm - $\phi$ 8 mm W2 turn $\times$ H5 turn
Hollow conductor of outer coil	W16 mm $\times$ H16 mm - $\phi$ 10 mm W10 turn $\times$ H6 turn
Water-cooling-circuit number	8/pole (inner 2 + outer 6)

analysis around the pole ends with Rogowski shape.

#### References

- 1) Y. Yano et al.: Proc. 15th Int. Conf. on Cyclotrons and Their Applications, Caen, France (1998), p. 696.
- 2) T. Kubo et al.: RIKEN Accel. Prog. Rep. **33**, 236 (2000).
- 3) T. Nagafuchi et al.: RIKEN Accel. Prog. Rep. **33**, 234 (2000).

## Studies on MUSES control system using RT-CORBA

T. Tanabe, T. Masuoka, M. Takano, and T. Katayama

Common Object Request Broker Architecture (CORBA)<sup>1)</sup> is the standard distributed object architecture for an open software bus, which allows programs created by different operating systems (OSs) and languages to communicate with each other. In our previous R&D efforts,<sup>2)</sup> we confirmed interoperability through IIOP among different ORBs. It has also been shown that the performance degradation compared to that of pure socket communication is insignificant.

The recent introduction of RT-CORBA specifications allows us to utilize the full capability of RTOS such as VxWorks.<sup>3)</sup> RT-CORBA augments the shortcomings of regular CORBA 2.x specs, namely, the lack of quality of service (QoS) controls, real-time programming features and performance optimizations. Among the various features of RT-CORBA, we have mainly examined processor resources control such as thread pools, priority mechanism and intra-process mutexes. VisiBroker 4.1a for Tornado<sup>4)</sup> and ORBexpress-RT 2.3.2<sup>5)</sup> were chosen for comparison.

RT-CORBA mutex operations would conceal the difference in the thread-synchronizing mechanism in the underlying OS. We have compared the elapsed times of *lock()/unlock()* operations that are repeated 1000 times for (a) VxWorks native *semTake()*, *semGive()*, (b) *rtMutex -> lock()*, *rtMutex -> unlock()* for VisiBroker, (c) the same for ORBexpress. The elapsed time was measured by “WindView” tool.<sup>3)</sup> The results (average time for 1000 operations in msec and standard deviation) are shown in Table 1. It appears that the latency caused by RT-CORBA abstraction is less than 1  $\mu$ sec and considered to be negligible for most accelerator applications.

Thread pools can be defined and associated using the Portable Object Adaptor in an RT-CORBA server. They can have both a fixed number of static threads, and dynamic threads whose maximum number should be specified. With a proper priority mapping, RT-CORBA priorities can also conceal the variations of native priority mechanism of RTOSs. For example, VxWorks has the highest priority of 0 and pSOSystem has 255 as its highest. The highest RT-CORBA priority is always 32767. There are two types of Priority Model policies, “server declared” and “client propagated.” We have set ORB’s priority at 25 and that of VxWorks at 155, and measured the connection time for both

Table 1. Comparison between VxWorks semaphore and *rtMutex*.

	Semaphore	VisiBroker	ORBexpress
Ave. (ms)	2.092	2.334	2.742
St. Dev.	0.00625	0.00833	0.005

the server-declared model and the client-propagated model. For both static and dynamic threads, two threads can be created in the test program. Since ORBexpress-RT 2.3.2 lacks *create\_threadpool()* API, this test was conducted only in VisiBroker.

First, with the help of WindView, it was confirmed that VxWorks tasks could be switched based on CORBA priorities. Then, the time required to establish the connection between a client and a servant for the server-declared model was measured (Table 2). For dynamic threads, the default timeout to destroy them is 300 seconds. Measurement was carried out for both cases, one with existing threads and one after their disappearance. The same type of measurement was done for the client-propagated model and the results are summarized in Table 3.

The results indicate that the initial connection always takes longer because the POA manager has to be activated. However, from the second time and thereafter, there is not much difference among the various cases we tested. Even though there are still more functionalities to be tested in RT-CORBA, the processor resource controls appear to be satisfactory.

Table 2. Connection time for server-declared model.

Static Thread			
	Init. Connection	From 2 <sup>nd</sup> Connection	
Ave (ms)	4.623	3.308	
St. Dev.	0.008	0.143	
Dynamic Thread			
	Init. Conn.	From 2 <sup>nd</sup> w. threads	From 2 <sup>nd</sup> w.o.threads
Ave (ms)	4.800	3.326	3.581
St. Dev.	0.012	0.125	0.152

Table 3. Connection time for client-propagated model.

Static Thread			
	Init. Connection	From 2 <sup>nd</sup> Connection	
Ave (ms)	4.621	3.491	
St. Dev.	0.016	0.175	
Dynamic Thread			
	Init. Conn.	From 2 <sup>nd</sup> w. threads	From 2 <sup>nd</sup> w.o.threads
Ave (ms)	4.801	3.545	3.801
St. Dev.	0.010	0.190	0.195

### References

- 1) <http://www.omg.org/>
- 2) <http://accelconf.web.cern.ch/accelconf/e00/PAPERS/TUP4B15.pdf>
- 3) <http://www.windriver.com/>
- 4) <http://www.borland.com/>
- 5) <http://www.ois.com/>

## Update of MUSES ACR lattice design

H. Tsutsui,\* K. Ohtomo,\* and T. Katayama

After two of the authors had completed the design for the lattice of the Accumulator Cooler Ring (ACR) of Multi-Use Experimental Storage rings (MUSES) last year,<sup>1)</sup> the required transition gamma  $\gamma_T$  for the cooling mode was lowered<sup>2)</sup> ( $\gamma_T = 2.6 \rightarrow 1.6-1.7$ ) in order to optimize the longitudinal stochastic cooling efficiency by the notch filter technique. Consequently, this report describes a new ACR lattice design study with lower transition gamma.

Theoretically, in order to decrease  $\gamma_T$  one should increase the horizontal dispersion function  $D_x$  in bending magnets (BMs) and/or decrease the circumference  $C$ :

$$\frac{1}{\gamma_T^2} \equiv \alpha_c \equiv \frac{1}{C} \oint ds \frac{D_x}{\rho} = \frac{2\pi \langle D_x \rangle_{BM}}{C}, \quad (1)$$

where  $\alpha_c$ ,  $\rho$ ,  $\langle D_x \rangle_{BM}$  are the momentum compaction factor, the curvature radius of the reference orbit, and the average of the dispersion function in BMs, respectively. Since the circumference should be sufficiently long to incorporate all accelerator elements, we chose  $C = 134.8$  m, which is four times the extraction orbit length of the Superconducting Ring Cyclotron (SRC). By applying Eq. (1), the average of the dispersion function should be  $\langle D_x \rangle_{BM} = 8.4$  m. Another requirement is that the dispersion function should be free in the cooling section, thus, the maximum dispersion function in the arc section should be around 20 m or more, which results in a large horizontal beam size in the middle of the arc section.

We used two methods to decrease  $\gamma_T$  without greatly increasing the maximum  $D_x$ . First, we replaced the low dispersion arc (B-arc) with a high dispersion arc (A-arc). In the case of the lattice in the previous report, the replacement changed  $\gamma_T$  from 2.56 to 1.95.

Second, we moved a portion of the BMs to a higher dispersion function region. In the previous report, the ratio of the BMs in the low dispersion region to those in the high dispersion region was 2:2, and the total number of BMs was  $(2+2) \times 4 = 16$ , as shown in Table 1. We tried 1:3 and 2:3 schemes, and adopted the 2:3 scheme because in the 1:3 scheme only one BM in the low dispersion region could not generate a large dispersion function in the high dispersion region. The ratio 1:2 or 2:4 may be another solution. However, the bending angle in the 1:2 scheme is  $30^\circ$  which may be too large to fabricate a BM, and we require many BMs in the 2:4 scheme, which results in a larger circumference.

In order to cool the beam efficiently by Stochastic Cooling (SC), there are two other requirements for the lattice; that the local transition gamma from the

Table 1. Lattice parameters of the ACR.

	prev. report <sup>1)</sup>	this report
$C$ (m)	134.8	134.8
Ring size (m)	50.7/29.8	53.7/25.4
Max. $B\rho$ (T m)	8	8
Tune $Q_{x,y}$	3.23/2.58	2.27/3.81
Max. $\beta_{x,y}$ (m)	28.6/31.6	74.0/31.3
Max. $D_x$ (m)	15.3	20.0
Natural $\xi_{x,y}$	-3.1/ - 3.0	-4.0/2.0
$\gamma_T$	2.562	1.611
$\gamma_{pk}, \gamma_{kp}$	1.688/5.489	1.342/1.841
$\Delta Q_{(x,y),pk}$	0.75/0.75	0.75/1.75
$\beta_{x,y}$ at SC (m)	15/10	25.2/14.8
$L_{SC}$ (m)	6	6
$\beta_{x,y}$ at EC (m)	4.0/14.3	3.3/29.9
$L_{EC}$ (m)	9.5	10
$\beta_{x,y}$ at inj. pt. (m)	12.5/5.0	5.8/7.0
$\alpha_{x,y}$ at inj. pt. (m)	0.0/0.0	-1.3/ - 0.11
$D_x$ at inj. pt. (m)	4.4	3.2
$D'_x$ at inj. pt. (m)	0.0	-0.99
No. of BMs	16	20
ratio of BMs*	2:2	2:3
No. of Quadrupoles	33	38
No. of Sextupoles	16	20

\*) Ratio of the bending magnets in the low dispersion function region to those in the high dispersion function region.

pickup to the kicker  $\gamma_{pk}$  which is defined as

$$\frac{1}{\gamma_{pk}^2} \equiv \frac{1}{L_{pk}} \int_{pickup}^{kicker} ds \frac{D_x}{\rho} = \frac{\pi \langle D_x \rangle_{BM}}{L_{pk}}, \quad (2)$$

where  $L_{pk}$  is the orbit length from the pickup to the kicker, should be small, and that the horizontal and vertical betatron phase advances from the pickup to the kicker  $\Delta Q_{x,pk}$ ,  $\Delta Q_{y,pk}$ , should be quarter of odd integers. From Eq. (2),  $L_{pk}$  should be small.

We used MAD8<sup>3)</sup> and WinAGILE<sup>4)</sup> to find a lattice which satisfies the above requirements. The resultant layout and Twiss parameters of an updated ACR are shown in Fig. 1 and Fig. 2, respectively. One finds large rises and falls of the beta functions in the arc section, which may be inevitable in this type of extremely low  $\gamma_T$  lattice with long dispersion-free regions.

We estimated the dynamic aperture and injection efficiency for the present low  $\gamma_T$  lattice. After the horizontal and the vertical chromaticities were corrected by applying the sextupole fields, the dynamic aperture was calculated as shown in Fig. 3. It indicates that the dynamic aperture is sufficiently large compared to the beam acceptance. The multiturn injection efficiency was calculated as a function of the injection turn number for various injection beam sizes and septum thick-

\* Sumitomo Heavy Industries, Ltd.

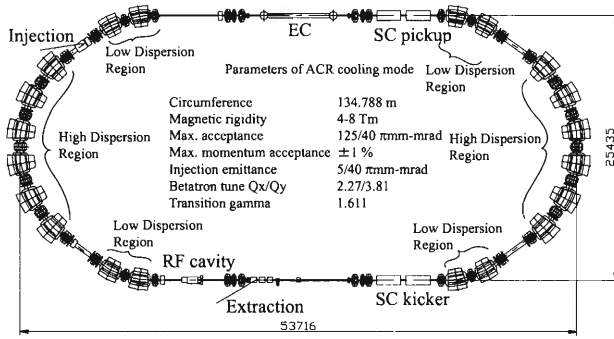


Fig. 1. Layout of updated ACR.

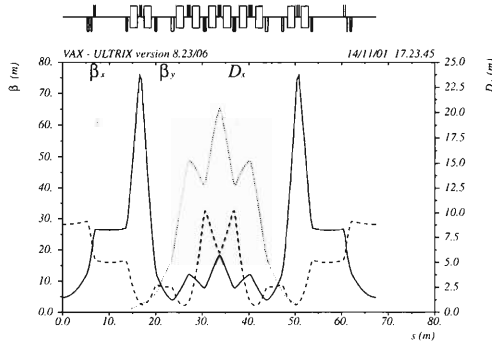


Fig. 2. Twiss parameters of the ACR.

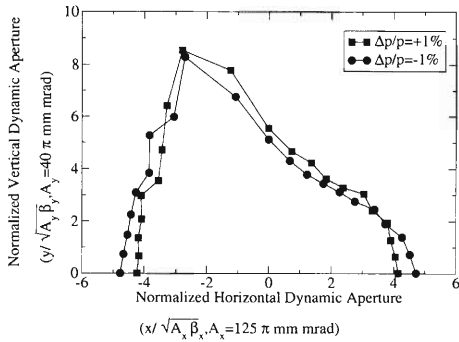


Fig. 3. Dynamic aperture of the ACR at the center of the electron cooling (EC) section with  $\Delta p/p = \pm 1\%$ . The particles were tracked by MAD8<sup>3)</sup> for various initial transverse positions  $(x, y)$  normalized by the beam size.

nesses, as shown in Fig. 4. In the calculation, the bump fields decay linearly during injection. Emittances and the momentum spread of the beam from the Big-RIPS are assumed to be 5 (horizontal)/40 (vertical)  $\pi$ mm-mrad and 0.15%,<sup>5)</sup> respectively. The efficiency reached around 1000% using a thin septum. The lower efficiency than in the previous report may be due to lower  $\beta_x$  at the injection point.

Another possible way to decrease  $\gamma_T$  is to use in-

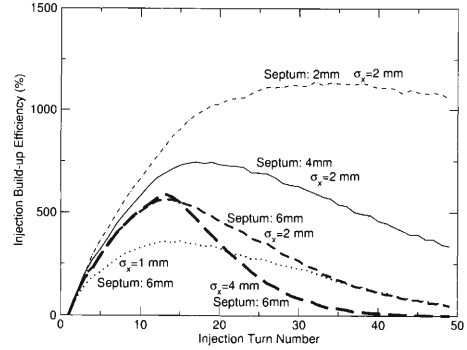


Fig. 4. Multiturn injection efficiency of the ACR for several septum thicknesses (2 mm, 4 mm, 6 mm) and horizontal sizes of the injection beam ( $\sigma_x = 1$  mm, 2 mm, 4 mm).

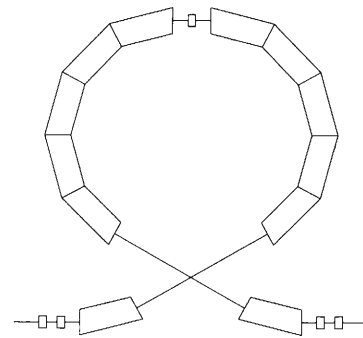


Fig. 5. The concept of an insertion device to lower the transition gamma.

sersion devices.<sup>6)</sup> Direct application of the method shown in the reference to our case is not efficient because the dispersion function has a large amplitude variation in the device. In our case, an insertion device of the kind shown in Fig. 5 may be more efficient. By using a device of  $\gamma_{T,ins}$ , the new  $\gamma_T$  will be  $1/\gamma_{T,new}^2 = (C/\gamma_T^2 + L/\gamma_{T,ins}^2)/(C+L)$ , where  $L$  is the orbit length of the device. This may be studied in the future.

The RF stacking process should be simulated, and the isochronous mode operation should also be studied carefully in the future.

## References

- 1) K. Ohtomo et al.: RIKEN Accel. Prog. Rep. **34**, 357 (2001).
- 2) M. Wakasugi: private communication.
- 3) H. Grote and F. C. Iselin: CERN/SL/90-13 (AP) Rev. 5 (1996).
- 4) P. J. Bryant: Proc. European Particle Accelerator Conf. 2000 (2000), p. 1357.
- 5) C. C. Yung: 138th MUSES Meet. (Beam Physics and Engineering Laboratory, RIKEN), Wako, Sep. (2001).
- 6) M. Giovannozzi et al.: Proc. European Particle Accelerator Conf. 2000 (2000), p. 1030.

## Design of MUSES electron cooler at RIKEN

M. Nishiura, T. Tanabe, T. Katayama, E. Syresin,<sup>\*1</sup> and I. Watanabe<sup>\*2</sup>

The Radioisotope Beam Factory (RIBF) is under construction at RIKEN.<sup>1)</sup> In the RIBF, multi-use experimental storage rings (MUSES)<sup>2)</sup> consists of an accumulator cooler ring (ACR) and an electron-RI beam collider (e-RI Collider). The ACR is equipped with an electron cooler (EC).

The design of the EC for the ACR has recently been proposed and discussed.<sup>3)</sup> It was found that it is not necessary to use the high magnetic field of a few Tesla in the gun section,<sup>4)</sup> because the ion lifetime is reduced due to the fast recombination of ions with low-temperature electrons. Moreover, the reduction of the electron transverse temperature from the cathode temperature of  $T_{cath} = 100$  meV to  $T_e = 5$  meV produced by the magnetic expansion of the electron beam does not provide a significant advantage in terms of cooling time during the injection. Syresin *et al.*<sup>5)</sup> reported that the magnetic expansion factor  $B_i/B_{cool}$  from 1 to 8 is sufficient to cool the  $^{92}\text{U}_{238}$  coasting beam with  $E = 100$  MeV/u,  $\Delta p/p = \pm 1.5 \times 10^{-3}$ , and  $\varepsilon_v = 40\pi$ -mm-mrad. Here  $B_i$  and  $B_{cool}$  are the magnetic field in the gun and in the cooling section, respectively.

On the basis of the previous ACR-EC design,<sup>3)</sup> we refined the design of the electron gun, the collector and the magnetic field strength with the help of the computer simulation codes SAM<sup>6)</sup> and EGUN.<sup>7)</sup> In Table 1 the new parameters of the ACR-EC are listed; the maximum  $B_i$  is reduced from 4T to 4kG, and therefore the ratio of  $B_i/B_{cool}$  is decreased to be 2.5 times smaller than the previous one.

The electron gun proposed for the ACR-EC consists of three electrodes: a flat cathode, a Pierce electrode, and an anode. The electron beam is finally acceler-

ated up to 220 keV, and introduced into the cooling section through a toroidal section. For simplicity, the toroidal section is assumed to be a linear section in this simulation.

The magnetic field on the beam axis is calculated in  $r$ - $z$  coordinates. The input parameters used here are shown in Table 2. Figure 1 shows the dependence of the transverse temperature  $E_{tra}$  on  $B_{cool}$  calculated by SAM and EGUN. The transverse temperature calculated by SAM tends to be lower than that calculated by EGUN at the beam edge. In both cases  $E_{tra}$  becomes less than 1 eV at the beam edge, and less than 100 meV at  $r = 5.436$  mm, and depends on the cathode temperature at the center of the electron beams.

It is desirable that electron beams for an EC have a low transverse temperature. Since the initial velocity of electrons emitted from the cathode determines the final transverse temperature, the electric field in front of the cathode should be vertical to the cathode surface. Two anode shapes are proposed as shown in Fig. 2 for the comparisons of the transverse temperature. Figure 3 shows the dependence of the transverse temperature in the cases of A1 (previous anode shape)

Table 1. ACR parameters.<sup>4)</sup>

Circumference, m	134.788
Ion energy, MeV/u	60-400
Beam acceptance, $\varepsilon_{acep}$ , $\pi$ -mm-mm	125/40
Maximum momentum spread, %	$\pm 1$
Emittance of injected beam, $\varepsilon_{inj}$ , $\pi$ -mm-mm	5/40
Initial momentum spread, %	$\pm 0.15$
Beta function in cooler (hor./vert.), m	4/14.34
Length of EC solenoid, m	3.6
Magnetic field in cooling section, kG	0.5-2
Magnetic field in gun section, kG	2-4
Magnetic expansion factor	1-8
Electron beam current, A	4
Electron energy, keV	30-250

\*1 JINR, Russia

\*2 Toshiba Corporation

Table 2. Input parameters for EGUN.

Electron beam current, A	4
Electron energy, keV	220
Cathode-anode voltage, kV	30
Cathode diameter, cm	2.57
Magnetic field in gun section, kG	4
Magnetic field in cooling section, kG	0.5-2

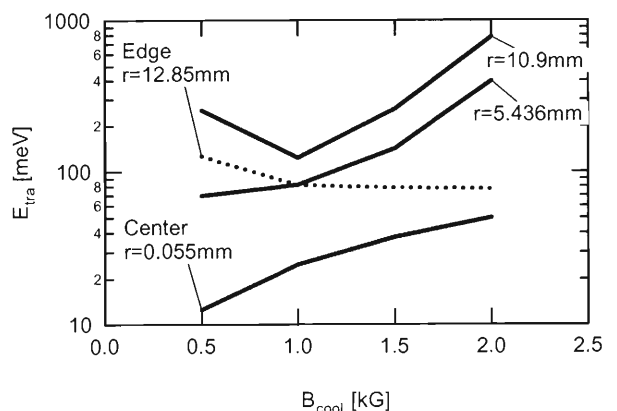


Fig. 1. Transverse electron temperature in the cooling section calculated by SAM (dotted lines) and EGUN (solid lines). The value of  $r$  indicates the radial beam position at the dispenser cathode.

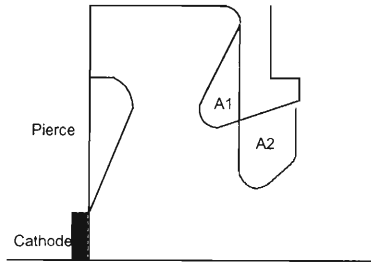


Fig. 2. Cross-sectional view of previous anode shape (A1) and modified anode shape (A2).

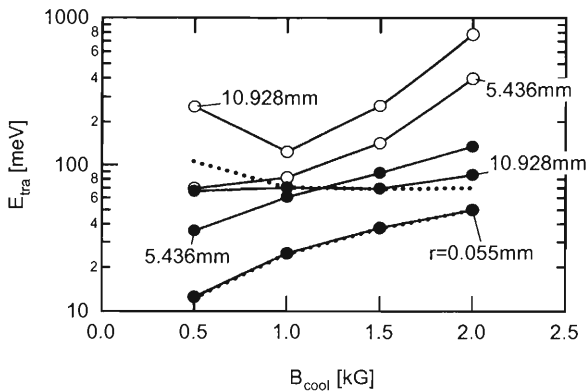


Fig. 3. Dependence of the transverse temperature on the magnetic field in the cooling section. Open and solid circles indicate the cases of A1 and A2, respectively. Dotted lines for  $E_{tra}$  show the results calculated by SAM in the case of A2.

and A2 (proposed anode shape). The electron beams in the case of the new A2 shape have a lower transverse temperature than those in the case of the previous one, and yield a 20% improvement of  $E_{tra}$  by SAM and a 50–90% improvement by EGUN near the beam edge. A higher uniformity of  $E_{tra}$  is also achieved.

In the collector section of the ACR-EC, the beam trajectory calculations have been carried out. The initial beam parameters are taken from the final beam parameters calculated above in the case of  $B_i/B_{cool} = 4 \text{ kG}/(2-0.5 \text{ kG})$ . When the expansion factor is higher, the beam radius is very close to the deceleration tube radius. In order to prevent beams from hitting the wall and the electrodes, the focus lens should be placed in front of the entrance of the collector.

The feasibility study on triode and cooling sections for the ACR-EC will be carried out using a three-dimensional simulation code.

#### References

- 1) Y. Yano et al.: Proc. PAC '97 (1998), p. 930.
- 2) T. Katayama et al.: Proc. EPAC '98 (1998), p. 529.
- 3) T. Tanabe et al.: Nucl. Instrum. Methods Phys. Res. A **441**, 104 (2000).
- 4) T. Tanabe et al.: to be published in Proc. Cooling Workshop 2001, Germany.
- 5) E. Syresin et al.: to be published in Proc. Cooling Workshop 2001, Germany.
- 6) M. Tiunov, B. Fomel, and V. Yakovlev: Preprint Budker Institute of Nuclear Physics 1, 159 (1985).
- 7) W. H. Herrmannsfeldt: SLAC-226, 1 (1979).

## Instability during electron-cooling bunching, predicted from a simulation

M. Takanaka

The Radioisotope Beam Factory (RIBF)<sup>1)</sup> will have an electron-RI beam collider (e-RI Collider). In previous works, using a multiparticle tracking simulation where the three-dimensional space-charge force is taken into account, we studied ion-beam electron-cooling bunching to prepare the required ion beam at the e-RI collider, and described the characteristics of the bunched beam.<sup>2)</sup> Here we review only the instability of the beam.

In order to simulate the electron-cooling bunching of an ion beam, we have used a model where the following sources of forces acting on ions are taken into account:

- Longitudinal monopole space-charge impedance on the assumption of a transverse Gaussian beam-charge distribution and a cylindrical vacuum chamber.
- Transverse space-charge field including the influence of the chamber wall, calculated from a transverse charge distribution.
- Transverse dipole broad-band impedance based on the broad-band impedance model, corresponding to a horizontal broad-band impedance  $\frac{Z_{\perp}^{\parallel}}{p}$  of  $50 \Omega$ .
- Electron-cooling (EC) force.
- Solenoid field  $B_0$  at the EC section.
- Beam twist due to the toroid field at both ends of the EC section.
- A constantly focusing section and a drift EC section which the ring lattice is let to consist of.
- RF field for beam bunching.

Using 40,000 macroparticles, we simulated the EC bunching of  $^{238}\text{U}^{92+}$  ion beams of 4 mA, or of  $5.4 \times 10^6$  ions per bunch at 150 MeV/u.

One of the simulation results is the time evolution shown in Fig. 1. First, the coasting beam is cooled to the sixfold-rms momentum spread of  $5 \times 10^{-4}$ . Then, the fundamental RF voltage is increased in such a way that the momentum spread at the EC section is maintained at  $5 \times 10^{-4}$ . The RF voltage increase stops when the sixfold-rms bunch length reaches 1 m. When the momentum spread reaches  $1.9 \times 10^{-4}$  or most of the beam stays within the one-third bunch spacing, the third-harmonic RF voltage is increased to 290 kV while maintaining the momentum spread.

Around 30 ms, the increase in the beam line density due to bunch shortening turns the transverse emittances to increase in spite of the EC. At 33 ms, the beam starts a transverse coherent oscillation with an instantaneous current at the bunch center of 80 mA. It meets a transverse instability with increases in the transverse-coherent-oscillation amplitude and the

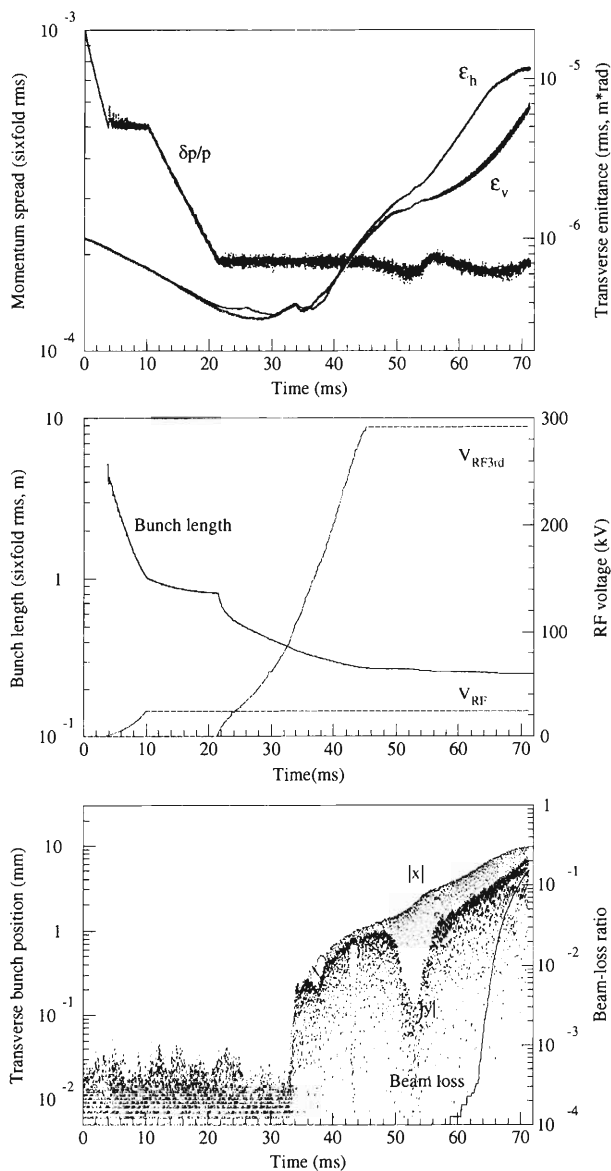


Fig. 1. Time evolution of the EC bunching of a  $^{238}\text{U}^{92+}$  ion beam of 4 mA at 150 MeV/u.

transverse emittances, while the bunch shortening stops at 45 ms. After 45 ms, the instantaneous current becomes about 120 mA. Beam loss due to hitting the chamber wall starts at 60 ms.

The transverse phase-space distribution of the unstable beam at 49 ms shown in Fig. 2 indicates that a dipole mode of transverse instability starts at the bunch center.

If we neglect the beam twist due to the toroid field

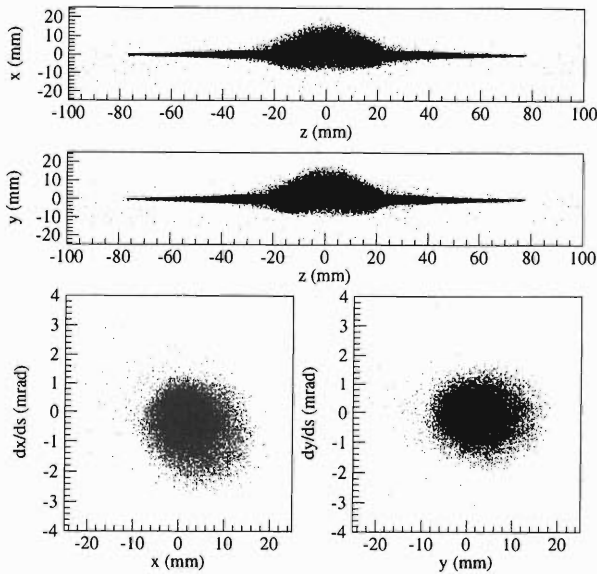


Fig. 2. Transverse phase-space distribution of the unstable bunched beam at 49 ms.

in the simulation, we obtain another result wherein the beam is very stable and the transverse rms emittances remain about  $3 \times 10^{-7}$  m  $\times$  rad under the third-harmonic RF voltage of 290 kV.

For the case where an EC device is aligned horizontally, the toroid section is shown in Fig. 3 where the toroid structure is idealized for calculation of the field. The horizontal field integrated along the  $s$  axis which ions experience in the toroid section is approximately described by

$$B_0 x_t (\log r_t - \log x_t) + B_0 x.$$

The first term expresses the effect of bending beams vertically and the second term the effect of twisting the beams. We can describe the thin-lens approximation of the twist force as a kicker of a delta function in terms of a Fourier series of azimuthal functions. The ion equation of motion due to the twist force is

$$\frac{d^2 y}{d\theta^2} + \nu_v^2 y = \sum_i \epsilon_i x_0 \cos \nu_h \theta \cos i\theta,$$

$$2\epsilon_0 = \epsilon_i \quad (i \neq 0),$$

where  $i$  is 0 or a positive integer. The equation means that there are an emittance-increasing resonance at  $\nu_h + \nu_v = i$  and an emittance-beating resonance at  $\nu_h - \nu_v = \pm i$ . This holds true, as well, when we con-

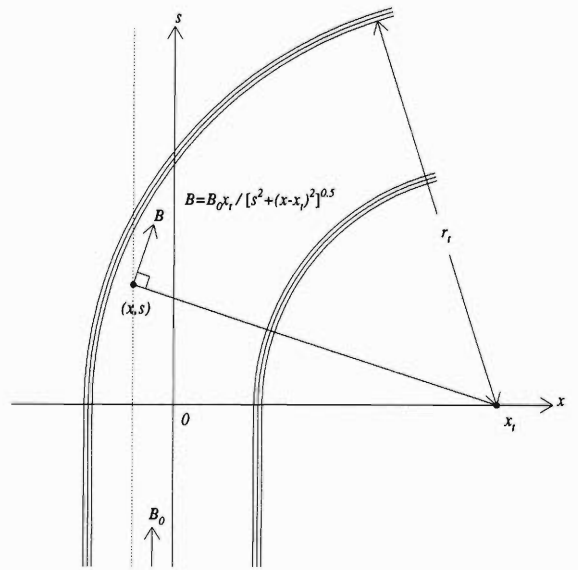


Fig. 3. Toroid structure idealized for calculation of the field.

sider twist forces at both ends of the EC section. In the current case, the emittance-increasing resonances have half a resonance width  $\Delta i$  of 0.01 near the operation point. Even if ions are trapped in the resonances, they can not stay within the resonance widths because the increases in the betatron amplitudes make the betatron tunes shift upwards. After the EC decreases the amplitudes, the ions are trapped in the resonances again. The repetition of the increases and decreases in the amplitudes eventually produces the coherent oscillation and the instability described above when the instantaneous beam current is beyond a threshold which depends on the strength of EC, the operation point, and the beam energy.

Since the instability is not induced through any real part of beam coupling impedance, it is not controlled by adjusting the chromaticities; it can be cured using a transverse feedback system.

In conclusion, we predict from the simulation analysis that the source of the transverse instability during EC bunching is the toroid field that twists the beam.

#### References

- 1) Y. Yano et al.: Proc. PAC2001, ROPA007 (2001).
- 2) M. Takanaka: Proc. PAC2001, FPAH093 (2001); M. Takanaka: RIKEN-AF-AC-29 (2001); M. Takanaka: Proc. 13th Symp. on Accelerator Science and Technology (2001), p. 89.

## Design of highly-sensitive current monitor with HTS SQUID and HTS magnetic shield

T. Watanabe, S. Watanabe, T. Ikeda, M. Kase, and T. Katayama

A high-temperature superconducting (HTS) magnetic shield based on  $\text{Bi(Pb)}_2\text{-Sr}_2\text{-Ca}_2\text{-Cu}_3\text{-O}_x$  (Bi-2223) was fabricated by plasma spraying for the purpose of observing a somatosensory-evoked magnetic field generated from the human brain.<sup>1)</sup> Recently, a Bi-2223 cylindrical magnetic shield was developed by dip-coating on a 99.9% MgO ceramic substrate. A highly-sensitive current monitor using this HTS magnetic shield in combination with a HTS Superconducting QUantum Interference Device (SQUID) is being developed in the RIKEN RI beam factory for high-accuracy nondestructive measurement of faint beams such as a radioisotope beam.

A DC current transformer (DCCT) based on the second-harmonic modulator-demodulator has been used in a circular ring, the sensitivity of which is about  $1\ \mu\text{A}$ .<sup>2)</sup> In order to measure a beam intensity less than  $0.1\ \mu\text{A}$ , current transformers using the principle of a low temperature superconducting (LTS) cryogenic current comparator (CCC) had been developed.<sup>3,4)</sup> On the other hand, a prototype HTS CCC with an HTS gradiometer SQUID has been successfully demonstrated as a means of nondestructive sensing of argon beams in the current range of  $1\text{--}20\ \mu\text{A}$ .<sup>5)</sup> The HTS technology enables us to develop a system equipped with a highly-sensitive current monitor with HTS SQUID and a HTS magnetic shield in the range of  $1\ \text{nA}\text{--}10\ \mu\text{A}$ .

The principle of superconductive CCC is based on the property of the Meissner effect of superconducting materials. A schematic drawing of the superconductive CCC that we are designing is shown in Fig. 1 (a). The MgO ceramic tube as a substrate of the HTS magnetic shield is coated on both sides, inside and outside, with a thin HTS material. The sketch (Fig. 1 (b)) represents the structure of the SQUID gradiometer and the magnetic core near the bridge. When the charged particle (ion or electron) beam is being passed along the axis of a HTS tube, a shielding current produced by the Meissner effect flows in the opposite direction along the wall of the HTS tube so as to screen the magnetic field generated by the beam. Since the outer surface is designed to have a bridge circuit (Fig. 1), the current generated by the charged particle beam concentrates on the bridge circuit and forms an azimuthal magnetic field  $\Phi$  around the bridge circuit. Moreover, the HTS SQUID is close to the bridge circuit and the HTS SQUID can detect the azimuthal magnetic field with a high  $S/N$  ratio. In particular, since the SQUID gradiometer has two pickup coils that are wound in opposite directions and connected in series, the signal level is expected to

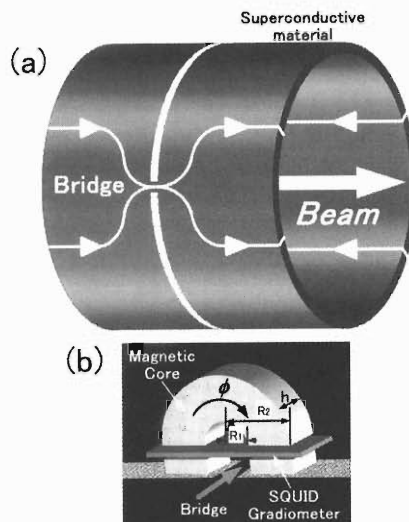


Fig. 1. (a) Schematic drawing of the superconductive CCC that we are designing. (b) Structure of the SQUID gradiometer and the magnetic core near the bridge.

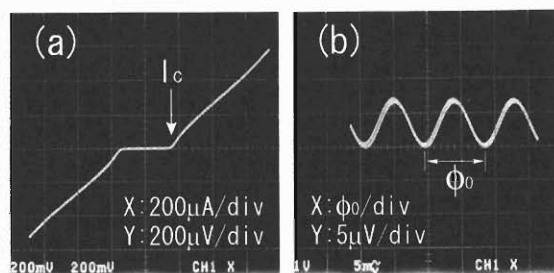


Fig. 2. Characteristics of SQUID; (a) current ( $x$ -axis) vs. voltage ( $y$ -axis) appears across the Josephson junctions of HTS SQUID, (b) relationship of the magnetic field  $B$  ( $x$ -axis) at the input coil with voltage ( $y$ -axis).

be improved by a factor 2, while a background noise can then be greatly reduced. Furthermore, to obtain a higher coupling efficiency, we consider the possibility of introducing the high-permeability magnetic core in the HTS CCC.

Figure 2 shows the characteristics of HTS SQUID; (a) current ( $x$ -axis) vs. voltage ( $y$ -axis) appears across the Josephson junctions of the HTS SQUID, (b) the relationship of the magnetic field  $B$  ( $x$ -axis) at the input coil with voltage ( $y$ -axis). A flux-locked loop method is usually used in the HTS SQUID circuit because a wide dynamic range and a high resolution of the flux sensitivity are required. Figure 3 shows the circuit diagram of the HTS SQUID and flux-locked loop. The magnetic flux density  $B$  induced by the charged particle

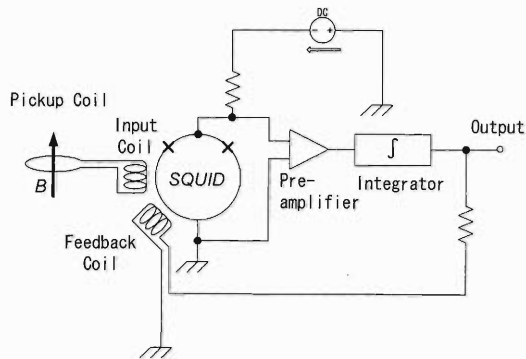


Fig. 3. Circuit diagram of a SQUID and flux-locked loop.

beam is transferred to the HTS SQUID with the aid of the pickup coil and the input coil, which are built-in in the HTS SQUID itself. The flux-locked loop can make a linear operation with respect to the HTS SQUID circuit because it cancels the external magnetic flux density  $B$ , with the aid of the bias current flowing in the feedback coil as shown in Fig. 3. The voltage appearing in the resistance, if it appears in the figure, is measured in order to obtain the calibrated shield current, namely, the beam current passing through the HTS tube.

The development of HTS CCC is currently in progress. In particular, the examination of the HTS magnetic shield coated on the MgO substrate is proceeding step by step. The critical current ( $I_c$ ) and critical temperature ( $T_c$ ) of the Bi-2223 cylindrical HTS shield should be confirmed to obtain a stable HTS CCC. In order to confirm the  $I_c$  and  $T_c$ , the DC four-probe method has been examined using a small piece of Bi-2223. X-ray diffraction analysis has been used to identify the formation of the Bi-2223 phase. After the above-mentioned tests, we intend to test the model of the HTS CCC. This is a combination of two cylindrical HTS shields that are reinforced by a mu-metal shield and HTS CCC. The diameters ( $D$ ) are 148 mm and 98 mm, and the length ( $L$ ) is 250 mm for both shields. We are afraid that the unexpected external magnetic field appeared on the associated measurement device. The attenuation of the external magnetic field is calculated using the following equation;

$$S = \frac{B_0}{B} = \exp\left(-\alpha \frac{L}{D}\right),$$

where  $S$ ,  $B$ ,  $B_0$  and  $\alpha$  are the attenuation factor, the external magnetic field density, the attenuated magnetic field density measured at the center of the inside of the HTS shield and the shielding coefficient, respectively.

In order to measure the field distribution inside the HTS magnetic shield and to obtain the attenuation factor  $S$ , we constructed the X-Y stage; which is moved by four stepping motors in the X-Y plane (Fig. 4).

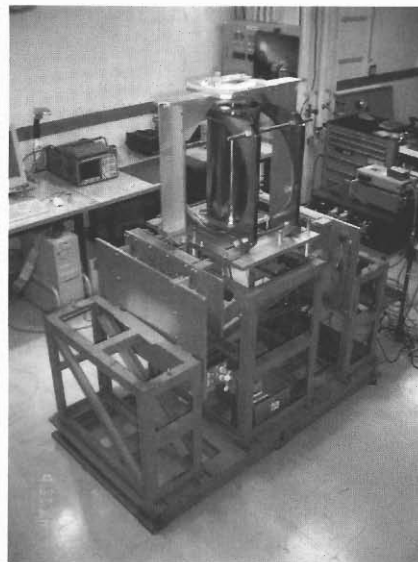


Fig. 4. The X-Z stage which is moved by four stepping motors in the X-Y plane. The X-Y stage is remotely controlled by a personal computer (PC). The X-Y stage is equipped with a Helmholtz coil, which can produce a uniform magnetic field of 1 mT.

The X-Y stage is remotely controlled by a personal computer (PC). The X-Y stage is equipped with a Helmholtz coil, which can produce a uniform magnetic field of 1 mT. Furthermore, we have scheduled the following measurements in the domain of time and frequency:

- (1) Noise level and stability of the HTS SQUID system,
- (2) Signal level of HTS SQUID using a simulated signal,
- (3) Noise level caused by trapped an environmental magnetic field in the HTS SQUID.

We have a plan to construct a prototype of highly-sensitive current monitor with a HTS SQUID and a HTS magnetic shield aimed of measuring the beam current in the beam transport line of the RIKEN Ring Cyclotron (RRC) by the end of the fiscal year of 2001.

#### References

- 1) H. Ohta et al.: IEEE Trans. Appl. Supercond. **9**, 4073 (1999).
- 2) T. Watanabe, S. Watanabe, and A. Iatano: Proc. 6th Symp. on Accelerator and Technology, Tokyo, 1987-10, (IONICS Publishing, 1987), p. 216.
- 3) A. Peters et al.: Proc. 5th European Particle Accelerator Conf., Barcelona, Spain, 1996-6, (Institute of Physics Publishing, 1996), p. 1627.
- 4) T. Tanabe et al.: Proc. 6th European Particle Accelerator Conf., Stockholm, Sweden, 1998-6, (Institute of Physics Publishing, 1998), p. 1610.
- 5) L. Hao et al.: IEEE Trans. Appl. Supercond. **11**, 635 (2001).

## Development of the kicker magnet for MUSES (II)

T. Ohkawa,\* Y. Chiba, M. Wakasugi, and T. Katayama

In the MUSES project, kicker magnets are used for ion-beam injection and fast extraction. The injection kicker field must fall from approximately 99% to 10% of full strength and the extraction kicker field must rise from approximately 10% to 99% of full strength during the time interval between bunches. The high performance of the kicker magnet is important for the efficiency of beam injection and extraction. In this paper, the development of kicker magnets for MUSES is presented.

We have designed, fabricated and tested the kicker magnet and the power supply.<sup>1)</sup> The design parameters of the kicker magnet are listed in Table 1. The kicker magnet and the power supply are connected by a transmission cable. In order to minimize the loss in the cable, the length of the cable should be as short as possible. Thus, the length of the cable was set at 7 m.

A single-turn long search coil is used for the measurement of the magnetic field. Output voltages are measured with a high-voltage probe and digital oscilloscope. The waveform of the magnetic field is obtained by integrating the induced voltage at the ends of the search coil. Here the effective length of the magnet is assumed to be 240 mm for the calculation.

Figure 1 shows the waveforms of induced voltage and magnetic field in the core gap at 100 kV and Fig. 2 shows the waveform of magnetic field at the flat-top. The rise time of the waveform is approximately 206 ns, the flat-top (field stability is  $\pm 1\%$ ) time is 774 ns. The rise time of the field is longer than the design value (95 ns). This is due to the mismatch of impedance between the kicker magnet and feedthrough. Therefore, matching capacitors were inserted between the kicker magnet and feedthrough to improve matching. We use a high-voltage probe in the measurement. When this probe tip is connected to the search coil, additional re-

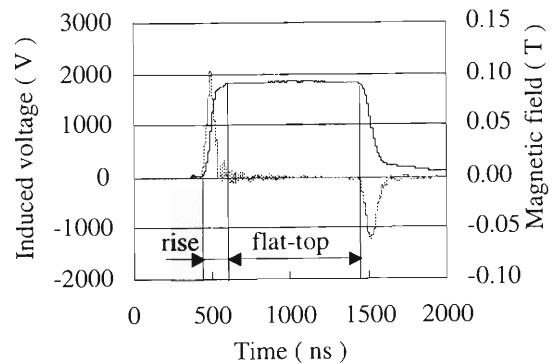


Fig. 1. Magnetic field and induced voltage.

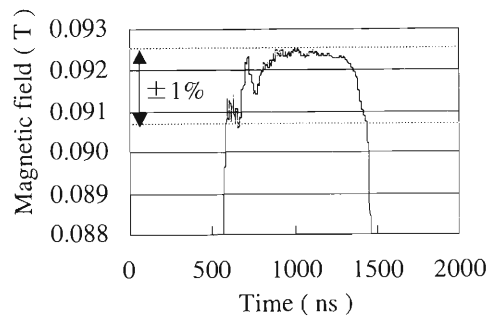


Fig. 2. Magnetic field at the flat-top.

Table 1. Parameters of the kicker magnet.

ITEM	DESIGN VALUE
Gap height	30 mm
Gap width	130 mm
Total core length	225 mm
Cell number	9
Inductance of unit cell	0.136 $\mu$ H
Capacitance of unit cell	108.9 pF
Characteristic impedance	25 $\Omega$
Gap field	0.084 T
Coil current	2000 A
PFN voltage	100 kV
Field rise time	95 ns

\* Mitsubishi Heavy Industries, Ltd.

sistance, capacitance, and inductance are introduced into the measurement circuit and this is expected to result in a resonant circuit. This circuit causes parasitic ringing visible within the bandwidth of the oscilloscope. The error of the measurement with a high-voltage probe is too large to accurately estimate the field stability. Therefore, to avoid the parasitic ringing, we have decided to use attenuators with a coaxial structure whose characteristic impedance is 50  $\Omega$  instead of a high-voltage probe. Because the maximum induced voltage at the ends of the search coil is larger than the allowable input voltage of the attenuator, we change the width of the search coil from 5 mm to 2 mm in order to reduce it. In order to improve the signal to noise ratio of the measured voltage, two signals measured by switching the polarity of the search coil are averaged upon changing the sign.

Figures 3 and 4 show the improved waveforms at 100 kV. The optimum values of the capacitance are 122 pF at the inlet and 295 pF at the outlet of the kicker magnet. The rise time of the waveform is approximately 83 ns, while the flat-top time is 888 ns. These results satisfy the specifications.

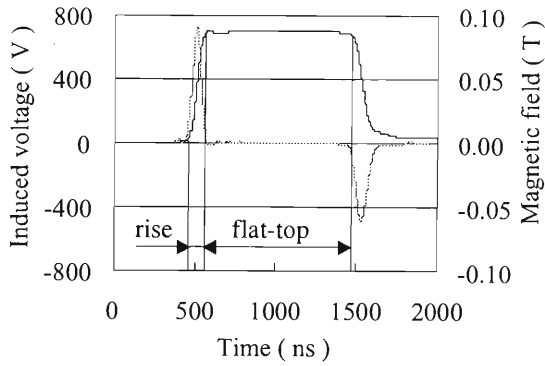


Fig. 3. Magnetic field and induced voltage with the capacitors.

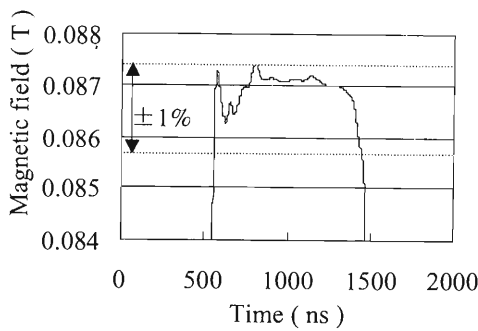


Fig. 4. Magnetic field at the flat-top with the capacitors.

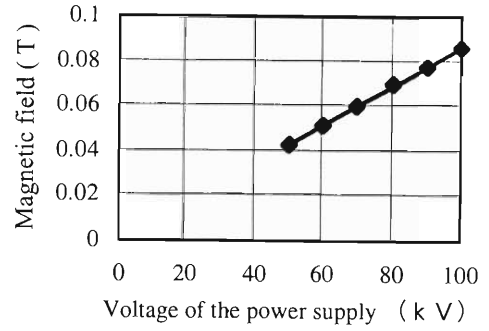


Fig. 5. Dependence of the magnetic field strength on the voltage of the power supply.

We have also measured the absolute value of the magnetic field with a short search coil. The result of the measurement shows that the effective length of the long search coil is 242 mm. The dependence of the magnetic field at the flat-top on the voltage of the power supply is shown in Fig. 5. The measurement is in good agreement with the calculation within  $\pm 1\%$ .

We intend to perform further tests to study the field distribution.

#### References

- 1) T. Ohkawa et al.: Proc. EPA2000, Vienna, Austria, 2000-6 (The European Physical Society Interdivisional Group on Accelerators, 2000), p. 2113.



## **VI. RADIATION MONITORING**



## Routine work for radiation safety in the Ring Cyclotron Facility

Y. Uwamino, S. Fujita, S. Ito, H. Sakamoto,\*<sup>1</sup> N. Hirao,\*<sup>2</sup> T. Nakamura,\*<sup>2</sup> and M. Kase

We report here on the residual radioactivity and leakage radiation level at the Ring Cyclotron Facility.

Residual radioactivities in the Ring Cyclotron Facility were measured at various locations using ionization-chamber survey meters.

The measurements were performed after almost every beam experiment as well as during the routine overhaul period. The routine overhaul started immediately after the experiment which was carried out with the  $^{10}\text{B}$  beam of 7.8 MeV/nucleon in the E7 experimental vault from Aug. 6 to 11, 2001. The dose rates at the deflectors in the injector AVF cyclotron and the Ring Cyclotron were found to be 0.85 mSv/h on Aug. 22, 2001 and 14 mSv/h on Aug. 24, 2001, respectively, during the overhaul period.

In addition to the above routine measurement, dose rates inside the injector AVF cyclotron were measured when its acceleration chamber was opened on Mar. 13, 2001 because of an insulation failure of the deflector. The dose rate at the AVF cyclotron deflector was 1.3 mSv/h. The Ring Cyclotron was opened as well on Jun. 1, 2001 for the same reason and the dose rate at

the Ring Cyclotron deflector was 30 mSv/h.

During the period from Oct. 1, 2000 to Sept. 30, 2001, dose rates were measured along the beam lines. The spots **a–y**, marked by bullets in Fig. 1, are the places where the dose rates exceeded  $10\ \mu\text{Sv/h}$ . Table 1 summarizes the observed dose rates and gives the dates when the measurements were performed. The maximum dose rate was found to be 3.5 mSv/h ( $3500\ \mu\text{Sv/h}$ ) at the target chambers in the E3 and the E4 experimental vaults denoted by **u** and **y** in Fig. 1, respectively. Whenever we observed a high dose rate, we roped off the area and posted a sign warning that it was dangerous to remain for a long time in that place.

We also continuously monitor the leakage radiation from the Ring Cyclotron Facility.

Having analyzed the collected data of leakage neutrons, we found that the radiation levels in the controlled area were much lower than the allowable dose limit. The leakage of  $\gamma$ -rays and neutrons was below the detection limit of the environmental monitors. We evaluated the radiation level at the boundary of the accelerator facility using the monitor which was installed

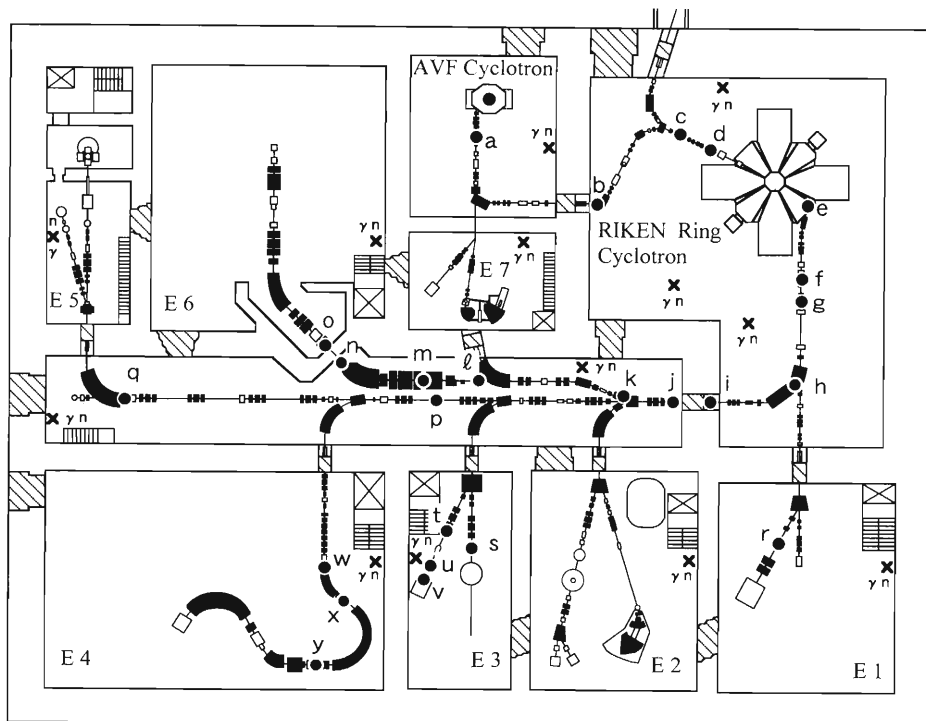


Fig. 1. Layout of the RIKEN Ring Cyclotron Facility as of 2001. Measured locations of residual radioactivities along the beam lines are shown by bullets **a–y**.

\*<sup>1</sup> SHI Accelerator Service, Ltd.

\*<sup>2</sup> Faculty of Science, Tokyo University of Science

Table 1. Summary of the dose rates measured along the beam lines with ionization-chamber survey meters. The detection points **a-y** indicate the measured locations shown in Fig. 1.

Detection point	Measured dose rate ( $\mu\text{Sv/h}$ )	Date	Particle	Energy (MeV/u)	Intensity (enA)	Period (days)
<b>a</b>	60	Apr 2, '01	Fe-56	90	1	3
<b>b</b>	90	Dec 18, '00	C-12	117	1	1
<b>c</b>	35	Dec 18, '00	C-12	117	1	1
<b>d</b>	45	Dec 18, '00	C-12	117	1	1
<b>e</b>	650	Apr 20, '01	p	210	10	1
<b>f</b>	500	Dec 18, '00	C-12	117	1	1
<b>g</b>	500	Aug 6, '01	N-14	135	800	5
<b>h</b>	55	Dec 18, '00	C-12	117	1	1
<b>i</b>	250	Aug 6, '01	N-14	135	800	5
<b>j</b>	200	Jun 13, '01	p	210	100	3
<b>k</b>	250	Nov 14, '00	Ar-40	95	1200	1
<b>l</b>	1400	Nov 14, '00	Ar-40	95	1200	1
<b>m</b>	2000	Dec 18, '00	C-12	117	1	1
<b>n</b>	80	Jun 13, '01	p	210	100	3
<b>o</b>	30	Apr 25, '01	C-12	135	1000	1
<b>p</b>	25	Aug 6, '01	N-14	135	800	5
<b>q</b>	17	Dec 18, '00	C-12	117	1	1
<b>r</b>	35	Jul 11, '01	O-18	70	1350	1
<b>s</b>	19	Feb 15, '01	p	150	1	1
<b>t</b>	70	Aug 6, '01	N-14	135	800	5
<b>u</b>	3500	Aug 6, '01	N-14	135	800	5
<b>v</b>	3200	Aug 6, '01	N-14	135	800	5
<b>w</b>	120	Jun 8, '01	d	140	100	2
<b>x</b>	150	Dec 12, '00	d	270	70	1
<b>y</b>	3500	Dec 12, '00	d	270	70	1

in the computer room on the ground floor immediately above a bending magnet which guided the beams from the ring cyclotron vault to the distribution corridor. As

a result, we obtained a radiation level of approximately  $5 \mu\text{Sv/year}$  which was much lower than the allowable dose limit ( $1 \text{ mSv/year}$ ).

## Shielding calculation for the CSM installation at RILAC

Y. Uwamino, S. Ito, S. Fujita, and N. Fukunishi

The Charge State Multiplier (CSM) was installed after the RIKEN Linear Accelerator (RILAC), and the maximum energy was nominally upgraded to 6.5 MeV/nucleon for all elements. Since the building of RILAC had been designed to meet the maximum energy of 4 MeV/nucleon, some local shielding became necessary. Here we briefly report the shielding calculations and their results.

Shin *et al.*<sup>1)</sup> measured the thick-target neutron yield for charged particles, and the results were fitted by using the moving-source model. The fitted data of 6.25-MeV/nucleon  $^{12}\text{C}$  beam bombardment on copper are given in their paper,<sup>1)</sup> and the spectra are shown in Fig. 1. The ANISN<sup>2)</sup> transport code was used for shielding calculations, along with their source data and the HILO86R group constants.<sup>3)</sup>

The results for the 90-deg bending magnet, whose yoke is made of 17-cm-thick iron, are shown in Fig. 2. The calculation geometry is a multilayer slab (17-cm-thick iron and 183-cm-thick ordinary concrete) which is normally irradiated by the neutrons of Fig. 1. The ordinate is  $r^2H$ , where  $r$  [cm] is the distance from the loss point and  $H$  [Sv/h] is the dose rate due to the neutrons and the secondary gammas. Calculations of similar geometries with 30-cm-thick iron and without iron were also performed, and the attenuation curves in the concrete part were fitted by the following exponential formula:

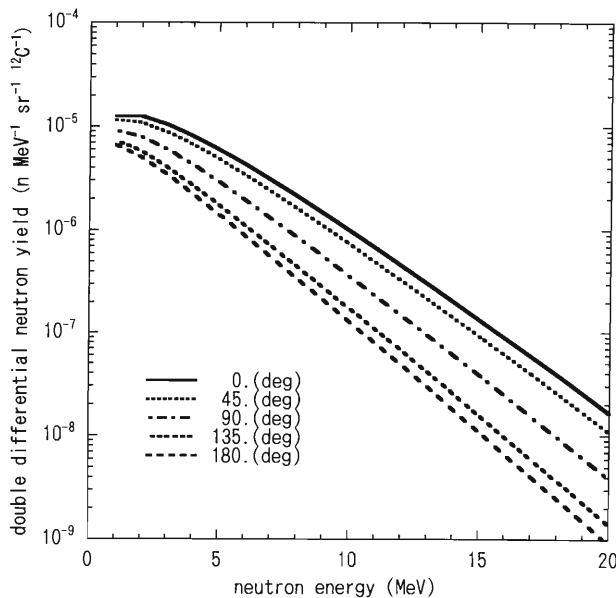


Fig. 1. Neutron spectra of 6.25-MeV/nucleon  $^{12}\text{C}$  beam bombardment on a full-stop copper target.

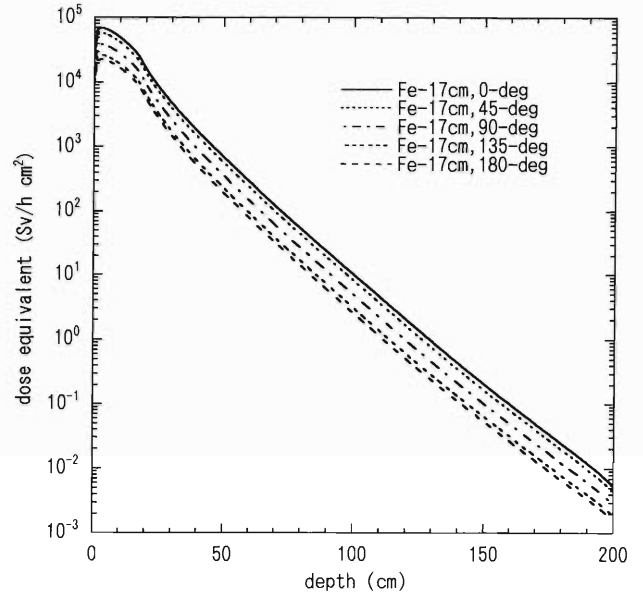


Fig. 2. Dose equivalent distribution in a 17-cm-thick-iron+183-cm-thick-ordinary-concrete slab. The irradiating neutrons are produced by 6.25-MeV/nucleon  $^{12}\text{C}$  beam bombardment on copper.

$$r^2H = H_0 \exp(-x/\lambda) \quad [\text{Sv/h cm}^2], \quad (1)$$

where  $x$  [cm] is the shield thickness including the iron slab, and  $\lambda$  [cm] is the attenuation length. The  $H_0$  values can be fitted by the following formula:

$$H_0 = A \exp(B \cos \theta), \quad (2)$$

where  $A$  and  $B$  are the fitting parameters, and they are listed in Table 1 with the attenuation lengths.

The additional local shield is necessary for the 90-deg bending magnet and the GARIS magnet. The effect of the polyethylene local shield for the 90-deg magnet is shown in Fig. 3, that is, 10-cm- to 70-cm-thick polyethylene shields are inserted behind the 17-cm iron slab. Polyethylene is an efficient moderator for neutrons making the thermal neutron flux high, but almost ineffective for capture gammas. The penetrative iron-capture gammas of 7.6 MeV raise the dose rate in the concrete part particularly in the case of thick

Table 1.  $\lambda$ ,  $A$  and  $B$  values in Eqs. (1) and (2) for 6.5-MeV/nucleon 10-pμA  $^{12}\text{C}$  beam.

iron slab thickness	0 cm	17 cm	30 cm
$\lambda$ [cm]	0.079	0.079	0.077
$A$ [Sv/h cm <sup>2</sup> ]	25800	8200	5720
$B$	0.619	0.660	0.592

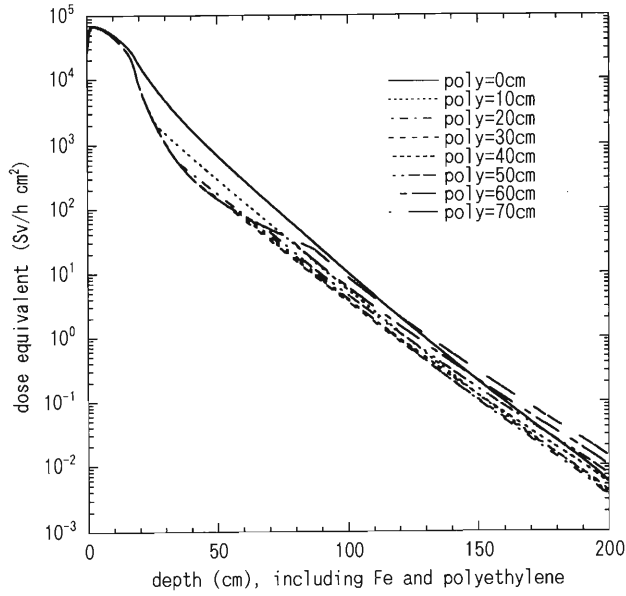


Fig. 3. Dose equivalent distribution in a 17-cm-thick-iron+polyethylene+ordinary-concrete slab. The irradiating neutrons are produced by 6.25-MeV/nucleon  $^{12}\text{C}$  beam bombardment on copper.

polyethylene. It was on the basis of these data that the local shielding at RILAC was designed.

#### References

- 1) K. Shin et al.: Nucl. Sci. Eng. **120**, 40 (1995).
- 2) W. W. Engle, Jr.: K-1963, Oak Ridge Gaseous Diffusion Plant, Oak Ridge (1967).
- 3) H. Kotegawa et al.: JAERI-M 93-020 (1993).

## Improvement of radiation safety system for RIKEN Ring Cyclotron

Y. Uwamino, S. Fujita, S. Ito, H. Sakamoto,\*<sup>1</sup> N. Hirao,\*<sup>2</sup> T. Nakamura,\*<sup>1</sup> and M. Kase

The first radiation safety system for the Nishina Building which started operation in 1986 was replaced by the second network dispersed system<sup>1)</sup> in 1999. Now the RI Beam Factory (RIBF) project is in progress and its accelerator building is under construction next to the Nishina Building. As a part of the RIBF project, a charge state multiplier was installed at the RIKEN Linear Accelerator (RILAC), and the maximum energy was upgraded to approximately 6 MeV/nucleon. Experiments on radioisotope production can be performed with this upgraded beam. At the same time, the classification of the radiation controlled area in the RILAC facility has been changed from 2nd grade (contamination free) to 1st grade (contamination possible). To compensate for these changes, the radiation safety system was upgraded as follows.

(1) Installation of a third hand-foot-clothes monitor at the Nishina Building

Because the RIBF accelerator facility will be accessed through the Nishina Building for the time being, a new hand-foot-clothes monitor, which can be seen on the extreme right in Fig. 1, was installed in the Nishina contamination control room. Three hand-foot-clothes monitors are presently connected to the host computer, and the box-type monitor seen in the middle of Fig. 1 is a spare unit. Another monitor will be installed in the future to cope with the expected increase of workers accessing the facilities.

(2) Expansion of the radiation monitoring system to cover all of the facilities including RILAC

The radiation monitoring system, which forms a part



Fig. 1. The hand-foot-clothes monitors installed in the contamination test room of the Nishina Building.

of the Nishina Building's radiation safety system, consists of a central supervisory console and radiation monitors. This monitoring system was recently expanded to cover a larger area including RILAC, with the installation of new neutron and gamma-ray monitor sets (4 sets for RILAC and 8 sets for the Nishina Building). Most sets are of the conventional stationary type, but several sets are of the movable-head type, shown in Fig. 2 (the round case on the left is the movable detector head that is connected to the controller — the box on the right — with a 20-m-long cable). All of the monitors are connected to the radiation safety system of the Nishina Building, and the data can also be accessed from the RILAC control room.

(3) Improvement of the access control system at the RILAC facility

With the classification of the RILAC radiation control area being changed to 1st grade, the access control at the contamination control room was tightened. Two hand-foot-clothes monitors were introduced, the previous door was replaced by an automatic one with an electric locking system, and a barcode reader was installed so that workers entering or leaving the facility could be identified from their dosimeter barcodes. The automatic door and the barcode reader are shown in Fig. 3. A central supervisory console that is described in the next section controls these instruments.

(4) Installation of a central supervisory console at RILAC

A central supervisory console for the radiation safety system was installed in the RILAC control room to centralize all of the data from the radiation monitors, the entry and exit control system and the interlock control system. Because this console is connected to all

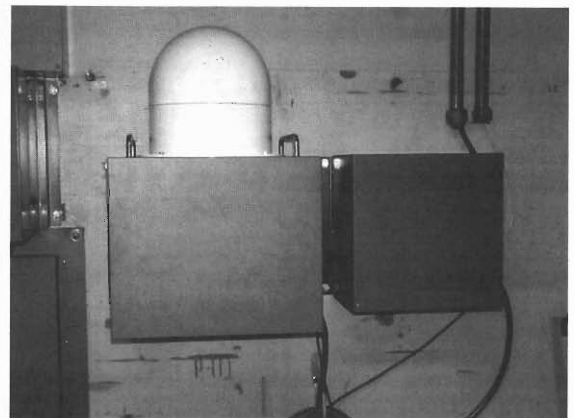


Fig. 2. The movable-head type radiation monitor in the 2nd basement corridor of the Nishina Building.

\*<sup>1</sup> SHI Accelerator Service, Ltd.

\*<sup>2</sup> Faculty of Science, Tokyo University of Science

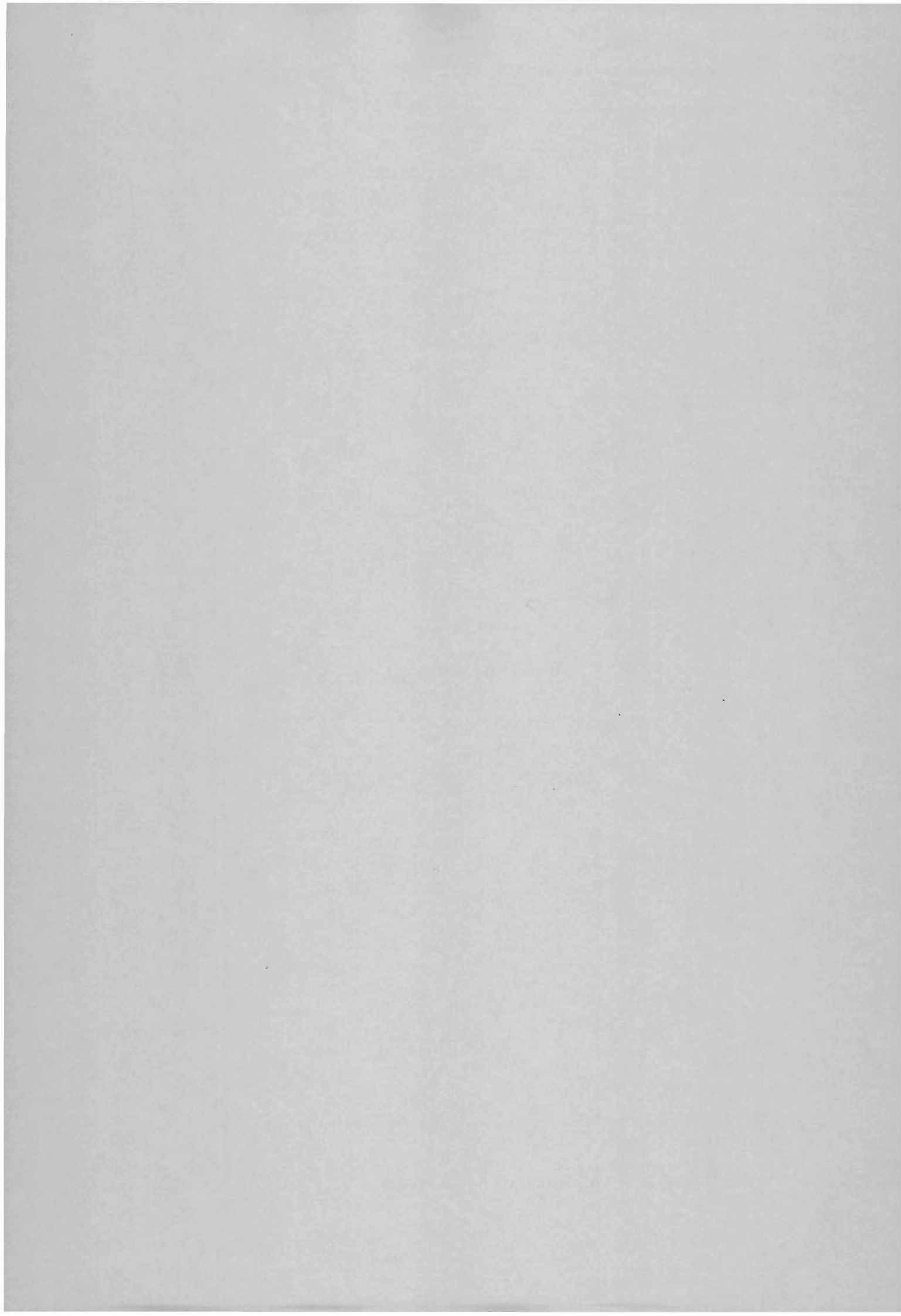


Fig. 3. The automatic door and the barcode reader in the RILAC contamination test room. The door on the left with a glass window is the automatic door, and the barcode reader is to the left of the door.

of the radiation monitors, the hand-foot-clothes monitors, the automatic door and the barcode reader at RILAC, it allows us to access and monitor all data concerning radiation levels and workers entering or leaving the controlled area. The same data can be accessed in the Radiation Safety Office of the Nishina Building.

#### References

- 1) S. Fujita, S. Nakajima, S. Ito, H. Sakamoto, A. Fujiwara, A. Uchiyama, M. Kase, and Y. Uwamino: RIKEN Accel. Prog. Rep. **33**, 265 (2000).





## VII. LIST OF PUBLICATIONS

- Accelerator development and accelerator physics

T. Tanabe, T. Rizawa, K. Ohtomo, T. Katayama, A. Yamashita, E. Syresin, and I. Meshkov: “Design of an electron cooling device for the Accumulator Cooler Ring in MUSES project”, Nucl. Instrum. Methods Phys. Res. A **441**, 104–109 (2000).

T. Tominaka: “Two-dimensional magnetic fields of polygonal conductors”, Nucl. Instrum. Methods Phys. Res. A **458**, 619–626 (2001).

T. Nunomiya, N. Nakao, P. Wright, S. Nakamura, E. Kim, T. Kurosawa, S. Taniguchi, M. Sasaki, H. Iwase, Y. Uwamino, T. Shibata, S. Ito, and D. Perry: “Measurement of deep penetration of neutrons produced by 800-MeV proton beam through concrete and iron at ISIS”, Nucl. Instrum. Methods Phys. Res. B **179**, 89–102 (2001).

Y. Yano, A. Goto, M. Kase, and T. Katayama: “Progress report of RIKEN RI Beam Factory”, Proc. 13th Symp. on Accelerator Science and Technology, Suita, 2001–10, RCNP, Osaka University, Osaka, pp. 20–24 (2001).

O. Kamigaito, N. Sakamoto, M. Kase, E. Ikezawa, S. Kohara, Y. Miyazawa, T. Chiba, M. Hemmi, Y. Chiba, A. Goto, and Y. Yano: “Rf cavities of the RIKEN charge-state multiplier”, Proc. 13th Symp. on Accelerator Science and Technology, Osaka, 2001–10, RCNP, Osaka University, Osaka, pp. 229–231 (2001).

H. Akiyoshi, T. Chiba, H. Hasebe, M. Kase, and Y. Yano: “Liquid film stripper for RIKEN RI Beam Factory”, Proc. 13th Symp. on Accelerator Science and Technology, Suita, 2001–10, RCNP, Osaka University, Osaka, pp. 331–333 (2001).

Y. Yano, T. Katayama, A. Goto, and M. Kase: “RIKEN RI Beam Factory Project”, Proc. 16th Int. Conf. on Application of Accelerators in Research and Industry, Texas, USA, 2000–11, edited by J. L. Duggan and I. L. Morgan, AIP, New York, pp. 679–682 (2001).

O. Kamigaito, M. Kase, E. Ikezawa, M. Fujimaki, S. Kohara, N. Fukunishi, N. Sakamoto, M. Hemmi, Y. Miyazawa, Y. Chiba, T. Chiba, A. Goto, and Y. Yano: “Upgrade of RIKEN heavy-ion linac for nuclear physics experiments”, Proc. 26th Linear Accelerator Meet. in Japan, Tsukuba, 2001–8, KEK, Tsukuba, pp. 43–45 (2001).
- Nuclear physics and nuclear instrumentation

H. Izumi, K. Asahi, H. Ueno, H. Okuno, H. Sato, K. Nagata, Y. Hori, M. Adachi, N. Aoi, A. Yoshida, G. Liu, N. Fukunishi, and M. Ishihara: “Electric quadrupole moments of neutron-rich nuclei  $^{14}\text{B}$  and  $^{15}\text{B}$ ”, Phys. Lett. B **366**, 51–55 (1996).

Y. Mizoi, T. Miyachi, Y. Matsuyama, T. Fukuda, Y. Watanabe, N. Fukuda, N. Aoi, M. Notani, Y. Watanabe, A. Yoshida, and H. Sakurai: “Study of the  $^{6,7}\text{Li}(\alpha, n)^{6,7}\text{B}$  reaction by using new MUSIC detector”, Inst. Nucl. Study, Univ. Tokyo, Ann. Rept. **1996**, 36–37 (1997).

T. Kishida: “RI Beam Factory Project at RIKEN”, Proc. 3rd Japan-Italy Joint Symp. '97 on Perspectives in Heavy Ion Physics, Padova, Italy, 1997–10, edited by C. Signorini, F. Soramel, and T. Kishida, World Scientific, Singapore, pp. 274–281 (1997).

T. Suzuki and T. Otsuka: “Effects of halo on the Coulomb displacement energy of the isobaric analog state of  $^{11}\text{Li}$ ”, Nucl. Phys. A **635**, 86–96 (1998).

K. Asahi, A. Yoshimi, K. Sakai, H. Ogawa, T. Suzuki, and M. Nagakura: “Fundamental physics with polarized nuclear spins: Spin maser for the neutron EDM measurements”, Czech. J. Phys. **50**, Suppl. 1, pp. 176–186 (2000).

T. Kurosawa, N. Nakao, T. Nakamura, H. Iwase, H. Sato, Y. Uwamino, and A. Fukumura: “Neutron yields from thick C, Al, Cu, and Pb targets bombarded by 400 MeV/nucleon Ar, Fe, Xe and 800 MeV/nucleon Si ions”, Phys. Rev. C **62**, 044615-1–044615-11 (2000).

H. Kurasawa and T. Suzuki: “Role of the Dirac sea in relativistic nuclear models”, Soryushiron Kenkyu **102**, A110–A115 (2000).

T. Fujita, K. Sagara, K. Shigenaga, K. Tsuruta, T. Yagita, T. Nakashima, N. Nishimori, H. Nakamura, and H. Akiyoshi: “Difference between  $nd A_y$  and  $pd A_y$  below 16 MeV”, AIP Conf. Proc. **570**, 709–713 (2001).

K. Sekiguchi, H. Sakai, H. Okamura, N. Sakamoto, A. Tamii, T. Uesaka, T. Wakasa, Y. Sato, T. Ohnishi, K. Yakou, K. Suda, S. Sakoda, H. Kato, Y. Maeda, M. Hatano, and J. Nishikawa: “Measurement of cross section and analyzing powers for  $dp$  scattering at intermediate energies and three-nucleon force effect”, AIP Conf. Proc. **570**, 714–718 (2001).

Y. Mochizuki and T. Izuyama: “New phase of theories for pulsar glitches: Relation between nuclear structure and superfluidity inside neutron stars”, J. Phys. Soc. Jpn. **56**, 316–325 (2001).

T. Kato, T. Doke, J. Kikuchi, F. Nishikido, H. Okada, I. Tanihata, and K. Morimoto: “Time and energy responses of liquid-xenon scintillation chamber for  $^{20}\text{Ne}$  ion beam at 135 A MeV”, Jpn. J. Appl. Phys. **40**, 3377–3381 (2001).

N. Nakao, T. Kurosawa, S. Nakamura, and Y. Uwamino: “Absolute measurements of the response function of an NE213 organic liquid scintillator for the neutron energy range up to 206 MeV”, Nucl. Instrum. Methods Phys. Res. A **463**, 275–287 (2001).

- M. Takada, S. Taniguchi, S. Nakamura, N. Nakao, Y. Uwamino, T. Shibata, and K. Fujitaka: “Neutron spectrometry in a mixed field of neutrons and protons with a phoswich neutron detector: Part 1: response functions for photons and neutrons of the phoswich neutron detector”, *Nucl. Instrum. Methods Phys. Res. A* **465**, 498–511 (2001).
- H. Kumagai, A. Ozawa, N. Fukuda, K. Summerer, and I. Tanihata: “Delay-line PPAC for high-energy light ions”, *Nucl. Instrum. Methods Phys. Res. A* **470**, 562–570 (2001).
- K. Yasuda, T. Hotta, M. Kato, M. Kawabata, Y. Maeda, N. Matsuoka, T. Matsuzuka, Y. Mizuno, M. Nomachi, T. Noro, Y. Sugaya, K. Takahisa, K. Tamura, H. Yoshida, M. Yoshimura, Y. Yokota, Y. Yuasa, K. Imai, T. Murakami, J. Murata, I. Nakagawa, T. Tamae, H. Tsubota, and H. Akiyoshi: “Measurement of proton-proton bremsstrahlung at 389 MeV”, *Nucl. Phys. A* **684**, 400–402 (2001).
- K. Sekiguchi, H. Sakai, H. Okamura, N. Sakamoto, A. Tamii, T. Uesaka, Y. Sato, T. Ohnishi, T. Wakasa, K. Yakou, K. Suda, S. Sakoda, H. Kato, Y. Maeda, M. Hatano, and J. Nishikawa: “Measurement of cross sections and analyzing powers for the  $d$ - $p$  elastic scattering at intermediate energies”, *Nucl. Phys. A* **684**, 574c–576c (2001).
- N. Dinh Dang: “Description of single- and multiple-phonon giant dipole resonances within the phonon damping model”, *Nucl. Phys. A* **687**, 253c–261c (2001).
- Y. Mochizuki: “ $^{44}\text{Ti}$ : its initial abundance in Cas A and its detection possibility in SN 1987A with INTEGRAL”, *Nucl. Phys. A* **688**, 58c–61c (2001).
- T. Yamazaki: “Strangeness nuclear physics toward the new millennium: A personal summary of HYP2000”, *Nucl. Phys. A* **691**, 515c–530c (2001).
- A. Ozawa, T. Suzuki, and I. Tanihata: “Nuclear size and related topics”, *Nucl. Phys. A* **693**, 32–62 (2001).
- T. Kato: “The response of scintillation light produced by heavy ion beams in liquid xenon and its application to particle identification”, *Nucl. Study* **46**, No. 3, pp. 51–59 (2001).
- K. Yoneda, H. Sakurai, T. Gomi, T. Motobayashi, N. Aoi, N. Fukuda, U. Futakami, Z. Gacsi, Y. Higurashi, N. Imai, N. Iwasa, H. Iwasaki, T. Kubo, M. Kunibu, M. Kurokawa, Z. Liu, T. Minemura, A. Saito, M. Serata, S. Shimoura, S. Takeuchi, Y. Watanabe, K. Yamada, Y. Yanagisawa, K. Yogo, A. Yoshida, and M. Ishihara: “Deformation of  $^{34}\text{Mg}$  studied via in-beam  $\gamma$ -ray spectroscopy using radioactive-ion projectile fragmentation”, *Phys. Lett. B* **499**, 233–237 (2001).
- A. Toyoda, K. Ishida, K. Shinomura, Y. Matsuda, W. Higemoto, S. Nakamura, T. Matsuzaki, and K. Nagamine: “Measurements of an ortho-para effect in muon-catalyzed fusion in solid deuterium”, *Phys. Lett. B* **509**, 30–36 (2001).
- P. Kienle and T. Yamazaki: “Empirical deduction of a medium-modified quark condensate from  $1s \pi^-$  states in heavy nuclei”, *Phys. Lett. B* **514**, 1–6 (2001).
- A. Ansari, N. Dinh Dang, and A. Arima: “Thermal shape and orientation fluctuation corrections for the hot giant dipole resonance within the static path approximation”, *Phys. Rev. C* **63**, 024310-1–024310-5 (2001).
- N. Dinh Dang, V. Kim Au, T. Suzuki, and A. Arima: “Pygmy and giant dipole resonances in neutron-rich nuclei within quasiparticle representation of phonon damping model”, *Phys. Rev. C* **63**, 044302-1–044302-10 (2001).
- H. Akiyoshi, K. Sagara, S. Ueno, N. Nishimori, T. Fujita, K. Maeda, H. Nakamura, and T. Nakashima: “Measurement of analyzing powers of the  $^1(d, ^3\text{He})\gamma$  reaction at 17.5 MeV”, *Phys. Rev. C* **64**, 034001-1–034001-6 (2001).
- A. Arima and N. Dinh Dang: “Phonon damping model using random-phase-approximation operators”, *Phys. Rev. C* **64**, 024302-1–024302-4 (2001).
- H. Sato, T. Kurosawa, H. Iwase, S. Nakamura, Y. Uwamino, and N. Nakao: “Measurements of double differential neutron production cross sections by 135 MeV/nucleon He, C, Ne and 95 MeV/nucleon Ar ions”, *Phys. Rev. C* **64**, 034607-1–034607-12 (2001).
- T. Suzuki, N. Dinh Dang, and A. Arima: “Description of the Gamow-Teller resonance within the phonon damping model”, *Phys. Rev. C* **64**, 027303-1–027303-3 (2001).
- A. Krasnitz, Y. Nara, and R. Venugopalan: “Coherent gluon production in very-high-energy heavy-ion collisions”, *Phys. Rev. Lett.* **87**, 192302-1–192302-4 (2001).
- K. Iida, G. Watanabe, and K. Sato: “Formation of nuclear ‘Pasta’ in cold neutron star matter”, *Prog. Theor. Phys.* **106**, 551–559 (2001).
- K. Asahi, H. Ogawa, H. Ueno, D. Kameda, H. Miyoshi, Y. Kobayashi, A. Yoshimi, K. Yogo, A. Goto, T. Suga, K. Sakai, N. Imai, Y. Watanabe, K. Yoneda, N. Fukuda, N. Aoi, A. Yoshida, T. Kubo, M. Ishihara, W. Schmidt-Ott, G. Neyens, and S. Teughels: “Quadrupole moments and magnetic moments in exotic nuclei”, *RIKEN Rev. No.* 39, pp. 142–147 (2001).
- A. Kohama, R. Seki, A. Arima, and S. Yamaji: “Feasibility of determining surface of matter density distributions of nuclei at RIBF”, *RIKEN Rev. No.* 39, pp. 155–160 (2001).

### 3. Atomic and solid-state physics

- M. Takekawa and Y. Itikawa: “Theoretical study of electron collision by OCS molecule: elastic process”, *At. Collision Res. Jpn. No.* 26, pp. 12–13 (2000).

- D. Murakoshi, N. Okabayashi, Y. Iwai, H. Torii, Y. Morishita, K. Nishio, H. Masuda, K. Komaki, and Y. Yamazaki: "Charge state and scattering angle measurements of 800 eV/q Xe<sup>9+</sup> ions transmitted through Ni-microcapillaries for multiple electron transfer study", *At. Collision Res. Jpn. No. 26*, pp. 14–15 (2000).
- M. Hoshino, M. Kitajima, H. Tanaka, Y. Nakai, Y. Kanai, and Y. Yamazaki: "Angular distribution measurements of double electron capture processes in very slow C<sup>4+</sup>-He collision", *At. Collision Res. Jpn. No. 26*, pp. 32–33 (2000).
- A. Itoh, T. Majima, H. Tsuchida, Y. Nakai, and T. Kambara: "Anomalous q-dependence of fragment ions from C<sub>60</sub> bombarded by 30 MeV Ne<sup>9+</sup> ions", *At. Collision Res. Jpn. No. 26*, p. 44 (2000).
- Y. Iwai, S. Thuriiez, Y. Kanai, H. Oyama, K. Ando, R. Hutton, H. Masuda, K. Nishio, K. Komaki, and Y. Yamazaki: "High-resolution soft X-ray spectroscopy of 2.3 keV/u Ne<sup>9+</sup> ions through Ni microcapillary target", *At. Collision Res. Jpn. No. 26*, pp. 50–51 (2000).
- T. Ikeda, Y. Iwai, T. Oku, C. Otani, H. Kato, K. Kawai, H. Sato, H. Shimizu, Y. Takizawa, Y. Nakai, H. Miyasaka, Y. Morishita, H. Watanabe, and Y. Yamazaki: "X-ray spectroscopy of highly charged ions using superconducting tunnel junctions", *At. Collision Res. Jpn. No. 26*, pp. 62–63 (2000).
- D. Dumitriu, Y. Kanai, Y. Iwai, Y. Morishita, H. Oyama, and Y. Yamazaki: "Charge state distribution of highly charged ions passing through microcapillaries", *At. Collision Res. Jpn. No. 26*, pp. 64–65 (2000).
- T. Kambara, Y. Kanai, T. Kojima, Y. Nakai, A. Yoneda, Y. Yamazaki, and K. Kageyama: "Short ultrasonic pulse from fast heavy-ion impact on metals", *At. Collision Res. Jpn. No. 26*, pp. 103–105 (2000).
- M. Wada, I. Katayama, S. Okada, Y. Ishida, T. Nakamura, T. Sonoda, T. Oshima, Y. Nakai, T. Kojima, Y. Kanai, T. Kambara, Y. Yamazaki, A. Yoshida, T. Kubo, K. Okada, K. Noda, H. Kawakami, and S. Ohtani: "RF ion-guide system for trapping energetic radioactive nuclear ions", *At. Collision Res. Jpn. No. 26*, pp. 106–108 (2000).
- N. Oshima, T. Kojima, D. Dumitriu, A. Mohri, H. Oyama, T. Kambara, Y. Kanai, Y. Nakai, M. Wada, and Y. Yamazaki: "Development of a slow-positron source", *At. Collision Res. Jpn. No. 26*, pp. 109–110 (2000).
- E. Yagi: "The study on the state of hydrogen dissolved in metals by means of the channeling method", *Corros. Eng.* **49**, 417–426 (2000).
- Y. Kobayashi, Y. Yoshida, A. Yoshida, Y. Watanabe, K. Hayakawa, K. Yukihira, F. Shimura, and F. Ambe: "In-beam Mössbauer study of <sup>57</sup>Mn/<sup>57</sup>Fe in Si following projectile fragmentation and implantation", *Hyperfine Interact.* **126**, 417–420 (2000).
- T. Maruyama, H. Yamada, T. Mochizuki, K. Akimoto, and E. Yagi: "Quenching mechanism of luminescence in Sm-doped ZnS", *J. Cryst. Growth* **214/215**, 954–957 (2000).
- N. Kuroda, N. Ishikawa, Y. Chimi, A. Iwase, S. Okayasu, H. Ikeda, R. Yoshizaki, and T. Kambara: "Effect of damage morphology on the pinning and vortex dynamics in Bi<sub>2</sub>Sr<sub>2</sub>CaCu<sub>2</sub>O<sub>8+δ</sub> irradiated with GeV heavy ions", *Physica B* **284/288**, 847–848 (2000).
- H. Ikeda, N. Kuroda, T. Kambara, K. Yoshikawa, and R. Yoshizaki: "Heavy-ion irradiation effects in Ag-Cu alloy sheathed Bi-2223 tapes", *Physica B* **284/288**, 871–872 (2000).
- T. Kambara, Y. Kanai, T. Kojima, Y. Nakai, A. Yoneda, Y. Yamazaki, and K. Kageyama: "Ultrasonic pulse from fast heavy-ion irradiation on solids", 16th Int. Conf. on Application of Accelerators in Research and Industry, Denton, USA, 2000–11, edited by J. L. Duggan and I. L. Morgan, American Institute of Physics, New York, pp. 1040–1043 (2001).
- C. Zhu, Y. Teranishi, and H. Nakamura: "Nonadiabatic transitions due to curve crossings: Complete solutions of the Landau-Zener-Stueckelberg problems and their applications", *Adv. Chem. Phys.* **117**, 127–233 (2001).
- Y. Teranishi, K. Nagaya, and H. Nakamura: "New way of controlling molecular processes by lasers", *Advances in Multi-Photon Processes and Spectroscopy*, Honolulu, USA, 1999–12, edited by R. J. Gordon and Y. Fujimura, World Scientific, Singapore, pp. 215–227 (2001).
- F. Saito, Y. Nagashima, T. Kurihara, N. Suzuki, J. Kim, L. Wei, Y. Ito, A. Goto, and T. Hyoudo: "Recovery of <sup>18</sup>F from [<sup>18</sup>O] water by electrochemical method", *Appl. Radiat. Isot.* **55**, 755–758 (2001).
- T. Nakatsukasa and K. Yabana: "Photoabsorption spectra in the continuum of molecules and atomic clusters", *J. Chem. Phys.* **114**, 2550–2561 (2001).
- S. Kitazawa, H. Ida, N. Matsui, T. Takayanagi, K. Wakiya, K. Iemura, S. Ohtani, H. Suzuki, Y. Kanai, and U. Safronova: "Electron spectra from singlet and triplet states of Ne<sup>6+\*</sup> produced by low energy Ne<sup>8+</sup> + He, Ne and Ar collisions", *J. Phys. B* **34**, 3205–3220 (2001).
- L. Wei, N. Suzuki, J. Kim, F. Saito, Y. Ito, A. Goto, T. Kurihara, Y. Nagashima, and T. Hyoudo: "Slow positron yields from some porous materials", *Mater. Sci. Forum* **363/365**, 643–645 (2001).
- F. Saito, N. Suzuki, J. Kim, L. Wei, Y. Ito, A. Goto, T. Kurihara, Y. Nagashima, and T. Hyoudo: "<sup>18</sup>F source for a slow positron beam", *Mater. Sci. Forum* **363/365**, 679–681 (2001).
- M. Hasegawa and E. Yagi: "Positron annihilation and ion channelling methods", *Met. Technol.* **71**, 962–

- 967 (2001).
- F. Saito, T. Hyoudo, Y. Nagashima, T. Kurihara, N. Suzuki, Y. Ito, and A. Goto: "Intense radioisotope sources for spin polarized positron beams", *New Directions in Antimatter Chemistry and Physics*, edited by C. M. Surko and F. A. Gianturco, Kluwer Academic Publishers, Amsterdam, pp. 35–45 (2001).
- M. Tachikawa, I. Shimamura, R. Buenker, and M. Kimura: "Bound states of positron with molecules", *New Directions in Antimatter Chemistry and Physics*, edited by C. M. Surko and F. A. Gianturco, Kluwer Academic Publishers, Dordrecht, pp. 437–450 (2001).
- Y. Kanai, K. Ando, T. Azuma, R. Hutton, K. Ishii, T. Ikeda, Y. Iwai, K. Komaki, T. Kuroki, H. Masuda, Y. Morishita, K. Nishio, H. Oyama, M. Sekiguchi, and Y. Yamazaki: "Metastable states produced with beam-capillary interaction", *Nucl. Instrum. Methods Phys. Res. B* **182**, 174–179 (2001).
- Y. Nakai, T. Kambara, A. Ito, H. Tsuchida, and Y. Yamazaki: "Production of singly charged fullerene-like fragment ions a fast  $\text{He}^{2+}$ - $\text{C}_{60}$  collision", *Phys. Rev. A* **64**, 043205-1–043205-6 (2001).
- R. Whitehead, J. McCann, and I. Shimamura: "Laser-assisted formation of antihydrogen", *Phys. Rev. A* **64**, 023401-1–023401-6 (2001).
- N. Suzuki, Y. Nagai, Y. Itoh, A. Goto, Y. Yano, and T. Hyodo: "Vacancy formation energy for indium determined by a positron annihilation technique", *Phys. Rev. B* **63**, 180101-1–180101-3 (2001).
- N. Kuroda, N. Ishikawa, Y. Chimi, A. Iwase, H. Ikeda, R. Yoshizaki, and T. Kambara: "Effect of defect morphology on the properties of the vortex system in  $\text{Bi}_2\text{Sr}_2\text{CaCu}_2\text{O}_{8+\sigma}$  irradiated with heavy ions", *Phys. Rev. B* **63**, 224502-1–224502-5 (2001).
- M. Hori, J. Eades, R. S. Hayano, T. Ishikawa, J. Sakaguchi, E. Widmann, H. A. Torii, B. Juhasz, D. Hoevath, and T. Yamazaki: "Sub-ppm laser spectroscopy of antiprotonic helium and a CPT-violation limit on the antiprotonic charge and mass", *Phys. Rev. Lett.* **87**, 093401-1–093401-4 (2001).
- T. Aziuna, T. Ito, Y. Takabayashi, K. Komaki, Y. Yamazaki, E. Takada, and K. Murakami: "Resonant coherent excitation of hydrogen-like Ar ions to the  $n = 3$  states", *Phys. Scr. T* **92**, 61–64 (2001).
- A. Ito, T. Majima, H. Tsuchida, Y. Nakai, and T. Kambara: "Charge-state dependence of  $\text{C}_{60}$ -multi-fragmentation in collisions of 30 MeV  $\text{Ne}^{2-9+}$  ions", *Phys. Scr. T* **92**, 176–178 (2001).
- Y. Zou, R. Hutton, S. Huldt, K. Ando, and H. Oyama: "Effects of foil aging properties on the intensities of atomic transition lines following ion-foil interaction", *Phys. Scr. T* **92**, 253–255 (2001).
- R. Hutton, Y. Zou, S. Huldt, K. Ando, and H. Oyama: "The spectroscopy of high spin states for highly charged Mg-like ions", *Phys. Scr. T* **92**, 325–326 (2001).
- M. Hoshino, M. Kitajima, Y. Kanai, Y. Nakai, H. Tauaka, and Y. Yamazaki: "Angular resolved energy gain spectroscopy to study double electron-capture processes in very slow  $e^{4+}$ -He collisions", *Phys. Scr. T* **92**, 339–340 (2001).
- Y. Kanai, D. Dumitriu, Y. Iwai, T. Kambara, T. Kojima, A. Mouri, Y. Morishita, Y. Nakai, H. Oyama, N. Ohshima, and Y. Yamazaki: "Slow highly charged ion facility at RIKEN", *Phys. Scr. T* **92**, 467–470 (2001).
- H. Ikeda, N. Ishikawa, A. Iwase, T. Kambara, K. Yoshikawa, and R. Yoshizaki: "Flux pinning potential in Bi-2223 tapes irradiated by Xe ion", *Physica C* **357/360**, 494–496 (2001).
- S. Okayasu, M. Sasase, N. Kuroda, A. Iwase, Y. Kazumata, and T. Kambara: "Pinning properties of quenched and melt growth method-YBCO bulk samples", *Physica C* **357/360**, 501–504 (2001).
- T. Nakatsukasa and K. Yabana: "Real-space calculation of the continuum response: Photoabsorption in molecules", *Proc. 3rd Japan-Korea Joint Workshop on 1st-Principles Electronic Structure Calculations*, (NRIM), Tsukuba, 2000–10–11, edited by T. Ohno, NRIM, Tsukuba, pp. 112–115 (2001).
- S. Kaneko, Y. Ono, N. Nishida, and T. Kambara: "Columnar defect-induced strain and superconductivity in  $\text{Bi}_2\text{Sr}_2\text{CaCu}_2\text{O}_x$  observed by LT-STs/STM", *Surf. Sci.* **493**, 692–696 (2001).
- #### 4. Radiochemistry, radiation chemistry, and radiation biology
- S. Enomoto: "Development of the multitracer technique by using RIKEN Ring Cyclotron", *Proc. 12th Symp. on Accelerator Science and Technology*, Wako, 1999–10, Wako, pp. 130–131 (1999).
- R. Hirunuma and S. Enomoto: "Behavior of various elements in selenium-deficient rats using the multitracer technique", *Proc. 12th Symp. on Accelerator Science and Technology*, Wako, 1999–10, Wako, pp. 358–360 (1999).
- T. Yanagiya, N. Imura, S. Enomoto, and S. Himeno: "Screening for metals exhibiting altered accumulation in Cd-resistant metallothionein null cells using a multitracer technique", *Proc. 12th Symp. on Accelerator Science and Technology*, Wako, 1999–10, Wako, pp. 361–363 (1999).
- R. Hirunuma, S. Enomoto, F. Ambe, and H. Sakurai: "Behavior of various trace elements in Se-deficient rats", *Proc. 16th Symp. on Trace Nutrients Research*, Japan Trace Nutrients Research Society, No. 16, pp. 17–24 (1999).
- T. Ozaki, S. Enomoto, Y. Minai, S. Ambe, and Y. Makide: "A survey of trace elements in pteridophytes", *Biol. Trace Elem. Res.* **74**, 259–273 (2000).
- H. Sakurai, H. Yasui, T. Takino, A. Tamura, Y. Kojima, K. Kawabe, S. Enomoto, and R. Hirunuma:

- “Treatment of diabetes by vanadium”, Biomed. Res. Trace Elements **11**, 311–312 (2000).
- K. Matsumoto, R. Hirunuma, S. Enomoto, and K. Endo: “Contents and uptake rates of bio-trace elements in Se-deficient rat liver cell fractions”, Biomed. Res. Trace Elements **11**, 403–404 (2000).
- S. Enomoto, R. Hirunuma, and H. Tamano: “Transport and accumulation of trace elements in the pregnant rats - fetus”, Biomed. Res. Trace Elements **11**, 439–440 (2000).
- F. Yatagai, S. Morimoto, A. Gordon, T. Nohmi, M. Kusakabe, N. Fukunishi, T. Kurobe, T. Kato, T. Mizuno, F. Hanaoka, and Y. Yano: “Biological effect of p53 after heavy-ion exposure”, Exploring Future Research Strategies in Space Radiation Sciences: Proc. 2nd Int. Space Workshop 2000, (NIRS, NASDA), Chiba, 2000–2, edited by H. J. Majima and K. Fujitaka, Iryokagakusha, Chiba, pp. 92–98 (2000).
- T. Ozaki, S. Enomoto, Y. Minai, S. Ambe, F. Ambe, and Y. Makide: “Beneficial effect of rare earth elements on the growth of *Dryopteris erythrosora*”, J. Plant Physiol. **156**, 330–334 (2000).
- Y. Furusawa, K. Fukutsu, M. Aoki, H. Itsukaichi, K. Eguchi-Kasai, H. Ohara, F. Yatagai, T. Kanai, and K. Ando: “Inactivation of aerobic and hypoxic cells from three different cell lines by accelerated  $^3\text{He}$ -,  $^{12}\text{C}$ - and  $^{20}\text{Ne}$ -ion beams”, Radiat. Res. **154**, 485–496 (2000).
- S. Enomoto: “Trace elements in man and animals”, SCIAS **66**, 86–90 (2000).
- R. Hirunuma, S. Enomoto, S. Ambe, and F. Ambe: “Distribution of selenium, arsenic, iron, and scandium in selenium-deficient rats using the multitracer technique”, Trace Elements in Man and Animals 10, edited by A. M. Roussel, R. A. Anderson, and A. E. Favier, Kluwer Academic/Plenum Publishers, New York, pp. 1099–1102 (2000).
- S. Morimoto, A. Gordon, N. Fukunishi, and F. Yatagai: “Cellular responses by exposure to heavy-ions”, Adv. Space Res. **27**, 401–409 (2001).
- K. Matsumoto, T. Inagaki, R. Hirunuma, S. Enomoto, and K. Endo: “Contents and uptake rates of Mn, Fe, Co, Zn, and Se in Se-deficient rat liver cell fractions”, Anal. Sci. **17**, 587–591 (2001).
- C. Bae, T. Abe, T. Matsuyama, N. Fukunishi, N. Nagata, T. Nakano, Y. Kaneko, K. Miyoshi, H. Matsushima, and S. Yoshida: “Regulation of chloroplast gene expression is affected *in ali*, a novel tobacco albino mutant”, Ann. Bot. **88**, 545–553 (2001).
- K. Ishioka, M. Hase, M. Kitajima, and K. Ushida: “Ultrafast carrier and phonon dynamics in ion-irradiated graphite”, Appl. Phys. Lett. **78**, 3965–3967 (2001).
- S. Enomoto: “The multitracer technique: Manufacturing and application on the bio-trace elemental research”, Biomed. Res. Trace Elements **12**, 71–84 (2001).
- H. Tamano, B. Liu, S. Enomoto, and A. Takeda: “Tumor accumulation of radioactive trace elements: A multitracer study”, Biomed. Res. Trace Elements **12**, 96–101 (2001).
- P. Mehnati, F. Yatagai, T. Tsuzuki, F. Hanaoka, and H. Sasaki: “Judgement on “hit or non-hit” of CHO cells exposed to accelerated heavy-ions (Fe- or Ar-ions) using division delay and CR-39 plastics as an indicator”, Fukuoka Acta Medica **92**, No. 3, pp. 46–58 (2001).
- Y. F. Yang, Y. Gono, S. Motomura, S. Enomoto, and Y. Yano: “A Compton camera for multitracer imaging”, IEEE Trans. Nucl. Sci. **48**, 656–661 (2001).
- R. Amano and S. Enomoto: “Brain regional uptake of radioactive Sc, Mn, Zn, Se, Rb and Zr tracers into normal mice during aging”, J. Radioanal. Nucl. Chem. **247**, 507–511 (2001).
- T. Abe and S. Yoshida: “New method of plant mutagenesis using the RIKEN Ring Cyclotron”, Radiat. Chem. **71**, 28–32 (2001).
- S. Ambe, T. Ozaki, R. Weginwar, S. Enomoto, and F. Ambe: “Simultaneous production of  $^{28}\text{Mg}$  and  $^{47}\text{Ca}$  by high-energy heavy-ion irradiation for applications in biology”, Radiochim. Acta **89**, 63–66 (2001).
- H. Wang, S. Ambe, N. Takematsu, and F. Ambe: “Multitracer studies on the effects of model acid rain on the adsorption of trace elements on soils”, Radiochim. Acta **89**, 101–107 (2001).
- K. Matsumoto, R. Hirunuma, S. Enomoto, and K. Endo: “Evaluation of *in vivo* oxidative stress in liver of selenium-deficient rat”, RIKEN Rev. No. 35, pp. 14–18 (2001).
- S. Enomoto and R. Hirunuma: “Fetoplacental transport of various trace elements in pregnant rat using the multitracer technique”, RIKEN Rev. No. 35, pp. 31–34 (2001).
- R. Hirunuma, K. Endo, S. Enomoto, and F. Ambe: “Study on the distribution of radioactive trace elements in vitamin D-overloaded and deficient rats using the multitracer technique”, RIKEN Rev. No. 35, pp. 35–39 (2001).
- R. Hirunuma, T. Ozaki, K. Endo, H. Yasui, H. Sakurai, and S. Enomoto: “Uptake of various elements in selenium-deficient rats: Application of the multitracer technique”, RIKEN Rev. No. 35, pp. 40–44 (2001).
- H. Yasui, T. Takino, J. Fugono, R. Hirunuma, S. Enomoto, and H. Sakurai: “Effect of vanadium treatment on tissue distribution of biotrace elements in normal and streptozotocin-induced diabetic rats: Simultaneous analysis of V and Zn using radioactive multitracer”, RIKEN Rev. No. 35, pp. 45–47 (2001).
- A. Nakayama, H. Yasui, R. Hirunuma, S. Enomoto, and H. Sakurai: “Distribution of biotrace elements in partially hepatectomized rats”, RIKEN Rev.

- No. 35, pp. 48–49 (2001).
- K. Igarashi, A. Sasaki, Y. Yoda, H. Inage, Y. Nakakoshi, T. Yanagiya, R. Hirunuma, S. Enomoto, and S. Kimura: “Effect of sodium iron ethylenediaminetetraacetic acid on the absorption of various trace elements in anemic rats”. RIKEN Rev. No. 35, pp. 50–54 (2001).
- T. Ohyama, T. Yoshida, H. Maetsu, M. Noguchi, H. Suganuma, R. Hirunuma, S. Enomoto, M. Yanaga, and T. Omori: “Specific cobalt metabolism under Zn-deficient condition”, RIKEN Rev. No. 35, pp. 55–56 (2001).
- H. Tamano, S. Enomoto, R. Hirunuma, and A. Takeda: “Uptake of radioactive elements in rats brain tumor”, RIKEN Rev. No. 35, pp. 57–58 (2001).
- T. Tarohda, Y. Yabushita, Y. Kanayama, R. Amano, and S. Enomoto: “Elemental concentrations and tracer uptake behavior of manganese, zinc, and selenium in brain of normal mice during development”, RIKEN Rev. No. 35, pp. 61–63 (2001).
- Y. Yabushita, Y. Kanayama, T. Tarohda, K. Washiyama, R. Amano, and S. Enomoto: “Element-element interrelationship in brain under deficient and excessive states of an essential trace element”, RIKEN Rev. No. 35, pp. 64–66 (2001).
- S. Yoshida, M. Masuda, M. Nakayama, M. Yamasaki, H. Morikawa, R. Hirunuma, and S. Enomoto: “Study on the absorption site of divalent cations in the intestinal loop, using the multitracer technique”, RIKEN Rev. No. 35, pp. 67–68 (2001).
- T. Nabekura, T. Minami, R. Hirunuma, S. Enomoto, and Y. Ito: “Uptake of trace elements in adult and suckling rat lenses”, RIKEN Rev. No. 35, pp. 69–70 (2001).
- T. Yanagiya, N. Imura, S. Enomoto, Y. Kondo, and S. Himeno: “Reduction of cadmium cytotoxicity by manganese”, RIKEN Rev. No. 35, pp. 71–72 (2001).
- Y. Oura, S. Enomoto, and H. Nakahara: “Application of prompt gamma ray analysis to biological samples”, RIKEN Rev. No. 35, pp. 73–75 (2001).
- J. Furukawa, R. Hirunuma, S. Enomoto, and T. Nakanishi: “Measurement of binding affinity of various metal elements to plant apoplast protein in root tips”, RIKEN Rev. No. 35, pp. 78–79 (2001).
- H. Suzuki, H. Kumagai, F. Mori, K. Sakamoto, K. Inubushi, and S. Enomoto: “Influence of lanthanum on the uptake of various elements by marigold”, RIKEN Rev. No. 35, pp. 80–81 (2001).
- T. Ozaki and S. Enomoto: “Uptake of rare earth elements by *Dryopteris erythrosora* (autumn fern)”, RIKEN Rev. No. 35, pp. 84–87 (2001).
- R. Amano, T. Tsuji, K. Washiyama, S. Enomoto, K. Tagami, and S. Uchida: “Isolation and purification of  $^{95m}\text{Tc}$  and  $^{96}\text{Tc}$  from Ag target irradiated with heavy ion beams”, RIKEN Rev. No. 35, pp. 94–95 (2001).
- C. Egawa, Y. Takahashi, S. Enomoto, R. Hirunuma, and H. Shimizu: “Multitracer study on the diffusion behavior of various ions through the porewater of granite”, RIKEN Rev. No. 35, pp. 96–97 (2001).
- S. Shibata, S. Enomoto, and R. Hirunuma: “Preliminary study of amalgam extracting method for production of multitracer”, RIKEN Rev. No. 35, p. 115 (2001).
- S. Motomura, Y. Yang, Y. Gono, S. Enomoto, Y. Yano, and K. Asahi: “MT-GEI: A new detection system for multitracer”, RIKEN Rev. No. 35, pp. 116–117 (2001).
- H. Suzuki, H. Kumagai, K. Oohashi, K. Sakamoto, K. Inubushi, and S. Enomoto: “Transport of trace elements through the hyphae of an arbuscular mycorrhizal fungus into marigold determined by the multitracer technique”, Soil Sci. Plant Nutr. **47**, 131–137 (2001).
- T. Nabekura, T. Minami, R. Hirunuma, S. Enomoto, R. Hori, and Y. Ito: “Comparative uptake behavior of trace elements in adult and suckling rat lens”, Toxicology **163**, 101–105 (2001).

## 5. Material analysis

- M. Tanaka and K. Takahashi: “Determination of the changes of the basic structures of silica species in dependence on the concentration of sodium chloride by FAB-MS”, Fresenius J. Anal. Chem. **368**, 786–790 (2000).
- K. Maeda, T. Hasegawa, H. Hamanaka, K. Hasegawa, and M. Maeda: “Direct speciation of sulfur in marine sediment by high-resolution PIXE”, Int. J. PIXE **10**, 47–56 (2000).
- T. Sugimura, J. Kawai, K. Maeda, A. Fukushima, S. Shin, M. Motoyama, and T. Nakajima: “F K-edge soft X-ray absorption spectroscopy”, Adv. X-Ray Chem. Anal. Jpn. **32**, 161–172 (2001).
- K. Maeda, K. Hasegawa, and H. Hamanaka: “Chemical specification by high-resolution PIXE”, Proc. 1st Seminar on Application of Accelerator Radiation, (National Tsing Hua University), Hsinchu, Taiwan, 2000–12, edited by T.-C. Chu, National Tsing Hua University, Hsinchu, pp. 263–273 (2001).

## 6. RIKEN-BNL Collaboration on Spin Physics Program

- R. Jaffe and N. Saito: “QCD selection rules in polarized hadron collisions”, Phys. Lett. B **382**, 165–172 (1996).
- N. Saito and PHENIX Collaboration: “Spin physics with the PHENIX detector system”, Nucl. Phys. A **638**, 575c–578c (1998).
- H. Hamagaki and N. Saito: “The PHENIX experiment and PHENIX-J activities”, Nucl. Phys. News **8**, No. 4, pp. 26–30 (1998).
- N. Saito: “High Energy Spin Physics and RIKEN BNL Research Center”, Parity **13**, No. 12, pp. 108–109

- (1998).
- N. Hayashi, Y. Goto, and N. Saito: “RHIC spin physics”, Proc. 6th Int. Workshop on Deep Inelastic Scattering and QCD: DIS98, Brussels, Belgium, 1998–4, edited by G. H. Coremans and R. Roosen, World Scientific, Singapore, pp. 675–679 (1998).
- G. Bunce, N. Saito, J. Soffer, and W. Vogelsang: “Prospects for spin physics at RHIC”, Ann. Rev. Nucl. Part. Sci. **50**, 525–575 (2000).
- B. A. Berg, H. Markun, R. Pullirsch, and T. Wettig: “Spectrum of the U(1) staggered Dirac operator in four dimensions”, Phys. Rev. D **63**, 014504-1–014504-4 (2000).
- E. Laenen, G. Serman, and W. Vogelsang: “Higher-order QCD corrections in prompt photon production”, Phys. Rev. Lett. **84**, 4296–4299 (2000).
- T. Tominaka, M. Okamura, and T. Katayama: “Analytical field calculation of helical coils”, Nucl. Instrum. Methods Phys. Res. A **459**, 398–411 (2001).
- N. Ishii: “Goldberger-Treiman relation and  $g_{\pi NN}$  from the three quark BS/Faddeev approach in the NJL model”, Nucl. Phys. A **689**, 793–845 (2001).
- A. Ali Khan, S. Aoki, Y. Aoki, R. Burkhalter, S. Ejiri, M. Fukugita, S. Hashimoto, N. Ishizuka, Y. Iwasaki, T. Izubuchi, K. Kanaya, T. Kaneko, Y. Kuramashi, T. Manke, K. Nagai, J. Naoki, M. Okawa, H. P. Shanahan, Y. Taniguchi, A. Ukawa, and T. Yoshié: “Calculation of  $K \rightarrow \pi$  matrix elements in quenched domain-wall QCD”, Nucl. Phys. B (Proc. Suppl.) **94**, 283–286 (2001).
- A. Ali Khan, S. Aoki, Y. Aoki, R. Burkhalter, S. Ejiri, M. Fukugita, S. Hashimoto, N. Ishizuka, Y. Iwasaki, T. Izubuchi, K. Kanaya, T. Kaneko, Y. Kuramashi, K. Nagai, J. Naoki, M. Okawa, H. P. Shanahan, Y. Taniguchi, A. Ukawa, and T. Yoshié: “Kaon B-parameter from quenched domain-wall QCD”, Nucl. Phys. B (Proc. Suppl.) **94**, 287–290 (2001).
- A. Ali Khan, S. Aoki, Y. Aoki, R. Burkhalter, S. Ejiri, M. Fukugita, S. Hashimoto, N. Ishizuka, Y. Iwasaki, T. Izubuchi, K. Kanaya, T. Kaneko, Y. Kuramashi, T. Manke, K. I. Nagai, J. Naoki, M. Okawa, H. P. Shanahan, Y. Taniguchi, A. Ukawa, and T. Yoshié: “Eigenvalues of the hermitian Wilson-Dirac operator and chiral properties of the domain-wall fermion”, Nucl. Phys. B (Proc. Suppl.) **94**, 725–728 (2001).
- R. Baier, A. Mueller, D. Schiff, and D. Son: “Bottom-up thermalization in heavy ion collisions”, Phys. Lett. B **502**, 51–58 (2001).
- K. Kurita and E-802 Collaboration: “Systematics of midrapidity transverse energy distributions in limited apertures from  $p$ +Be to Au+Au collisions at relativistic energies”, Phys. Rev. C **63**, 064602-1–064602-25 (2001).
- M. Glueck, E. Reya, M. Stratmann, and W. Vogelsang: “Models for the polarized parton distributions of the nucleon”, Phys. Rev. D **63**, 094005-1–094005-12 (2001).
- M. Wingate and S. Ohta: “Deconfinement transition and string tensions in SU(4) Yang-Mills theory”, Phys. Rev. D **63**, 094502-1–094502-9 (2001).
- A. Ali Khan, S. Aoki, Y. Aoki, R. Burkhalter, S. Ejiri, M. Fukugita, S. Hashimoto, N. Ishizuka, Y. Iwasaki, T. Izubuchi, K. Kanaya, T. Kaneko, Y. Kuramashi, T. Manke, I. K. Nagai, J. Naoaki, M. Okawa, P. H. Shanahan, Y. Taniguchi, A. Ukawa, and T. Yoshié: “Chiral properties of domain-wall quarks in quenched QCD”, Phys. Rev. D **63**, 114504-1–114504-19 (2001).
- M. Stratmann and W. Vogelsang: “Towards a global analysis of polarized parton distributions”, Phys. Rev. D **64**, 114007-1–114007-10 (2001).
- A. Ali Khan, S. Aoki, Y. Aoki, R. Burkhalter, S. Ejiri, M. Fukugita, S. Hashimoto, N. Ishizuka, Y. Iwasaki, T. Izubuchi, K. Kanaya, T. Kaneko, Y. Kuramashi, T. Manke, K. Nagai, J. Naoki, M. Okawa, H. P. Shanahan, Y. Taniguchi, A. Ukawa, and T. Yoshié: “Kaon  $B$  parameter from quenched domain-wall QCD”, Phys. Rev. D **64**, 114506-1–114506-21 (2001).
- A. Bazilevsky, G. M. Bunce, A. Deshpande, H. En’yo, Y. Goto, M. G. Perdekamp, N. Hayashi, T. Ichihara, K. Imai, M. Ishihara, B. V. Jacak, K. Kurita, Z. Li, Y. Mao, J. Murata, F. Sakuma, H. Sato, T. Shibata, M. Sugioka, A. Taketani, E. Taniguchi, J. Tojo, H. Torii, Y. Watanabe, S. Yokkaichi, and PHENIX Collaboration: “Centrality dependence of charged particle multiplicity in Au-Au collisions at  $\sqrt{s_{NN}} = 130$  GeV”, Phys. Rev. Lett. **86**, 3500–3505 (2001).
- D. Son, M. Stephanov, and A. Zhitnisky: “Domain wall of high density QCD”, Phys. Rev. Lett. **86**, 3955–3958 (2001).
- A. Bazilevsky, G. M. Bunce, A. Deshpande, H. En’yo, Y. Goto, P. M. Gross, N. Hayashi, T. Ichihara, K. Imai, M. Ishihara, K. Kurita, Y. Mao, J. Murata, N. Saito, F. Sakuma, H. Sato, T. Shibata, A. Taketani, J. Toljo, H. Torii, Y. Watanabe, S. Yokkaichi, and PHENIX Collaboration: “Measurement of the midrapidity transverse energy distribution from  $\sqrt{s_{NN}} = 130$  GeV Au + Au collisions at RHIC”, Phys. Rev. Lett. **87**, 05230-1–05230-6 (2001).
- V. W. Hughes, M. G. Perdekamp, D. Kawall, W. Liu, K. Jungmann, and G. zuPutlitz: “Test of  $CPT$  and Lorentz invariance from muonium spectroscopy”, Phys. Rev. Lett. **87**, 11804-1–11804-4 (2001).
- M. Göckeler, P. E. L. Rakow, A. Schäfer, W. Söldner, and T. Wettig: “Calorons and localization of quark eigenvectors in lattice QCD”, Phys. Rev. Lett. **87**, 042001-1–042001-4 (2001).
- D. Rischke, D. Son, and M. Stephanov: “Asyptonic deconfinement in high-density QCD”, Phys. Rev. Lett. **87**, 062001-1–062001-4 (2001).
- A. Kusenko and P. J. Steinhardt: “Q-ball candidates for self-interacting dark matter”, Phys. Rev. Lett.

- 87**, 141301-1–141301-4 (2001).
- N. Ishii, H. Suganuma, and H. Matsufuru: “Gluon properties in anisotropic SU(3) lattice QCD with an improved action”, Proc. of the Workshop on Lepton Scattering, Hadrons and QCD, (The Special Research Center for the Subatomic Structure of Matter, National Institute for Theoretical Physics), Adelaide, Australia, 2001-3~4, edited by W. Melnitchouk, A. W. Schreiber, A. W. Thomas, and P. C. Tandy, World Scientific, Singapore, pp. 252–259 (2001).
- K. Itakura and S. Maedan: “Light-front realization of chiral symmetry breaking”, Prog. Theor. Phys. **105**, 537–571 (2001).
- M. Göckeler, H. Hehl, P. E. L. Rakow, A. Schäfer, and T. Wettig: “Spectrum of the SU(3) Dirac operator on the lattice: Transition from random matrix theory to chiral perturbation theory”, Phys. Rev. D **65**, 034503-1–034503-10 (2002).
- A. Bazilevsky, G. M. Bunce, A. Deshpande, H. En'yo, M. G. Perdekamp, N. Hayashi, T. Ichihara, K. Imai, M. Ishihara, B. V. Jacak, K. Kurita, Z. Li, Y. Mao, J. Murata, N. Saito, F. Sakuma, H. Sato, T. Shibata, M. Sugioka, A. Taketani, E. Taniguchi, J. Tojo, H. Torii, Y. Watanabe, S. Yokkaichi, and PHENIX Collaboration: “Suppression of Hadrons with large transverse momentum in central Au + Au collisions at  $\sqrt{s_{NN}} = 130$  GeV”, Phys. Rev. Lett. **88**, 022301-1–022301-6 (2002).

## VIII. LIST OF PREPRINTS

2001

RIKEN-AF-NP

- 381 N. Dinh. Dang, V. K. Au, T. Suzuki, and A. Arima: “E1 resonances in neutron-rich nuclei within phonon damping model”
- 382 Y. Mochizuki: “ $^{44}\text{Ti}$ : Its initial abundance in Cas A and its detection possibility in SN 1987A with INTEGRAL”
- 383 T. Kato, T. Doko, J. Kikuchi, F. Nishikido, H. Okada, K. Morimoto, and I. Tanihata: “Time and energy resonances of liquid-xenon scintillation chamber for  $^{20}\text{Ne}$  ion beam at 135A MeV”
- 384 A. Ozawa, T. Suzuki, and I. Tanihata: “Nuclear size and related topics”
- 385 Y. X. Watanabe, A. Yoshida, T. Fukuda, T. Sekine, Y. Watanabe, H. Ikezoe, Y. Nagame, T. Ikuta, I. Nishinaka, Y. Mizoi, J. Nakano, M. Hirai, H. Sakurai, H. Kobinata, Y. Pu, K. Kimura, and M. Ishihara: “Measurement of fusion excitation functions of  $^{27,29,31}\text{Al}+^{197}\text{Au}$ ”
- 386 N. Itagaki, S. Okabe, K. Ikeda, and I. Tanihata: “Molecular-orbital structure in neutron-rich C isotopes”
- 387 H. Sagawa and K. Asahi: “ $N/Z$  dependence of core polarization charges and quadrupole moments of B-isotopes”
- 388 P. Kienle and T. Yamazaki: “Empirical deduction of a medium-modified quark condensate from  $1s \pi^-$  states in heavy nuclei”
- 389 H. Geissel, H. Gilg, A. Gillitzer, R. S. Hayano, S. Hirenzaki, K. Itahashi, M. Iwasaki, P. Kienle, M. Münch, G. Münzenberg, W. Schott, K. Suzuki, D. Tomono, H. Weick, T. Yamazaki, and T. Yoneyama: “Deeply bound  $1s$  and  $2p$  pionic states in  $^{205}\text{Pb}$  and determination of the  $s$ -wave part of the pion-nucleus interaction”
- 390 M. Hori, J. Eades, R. S. Hauyano, T. Ishikawa, J. Sakaguchi, E. Widmann, H. Yamaguchi, H. A. Torii, B. Juhász, D. Horváth, and T. Yamazaki: “Sub-ppm laser spectroscopy of antiprotonic helium and a CPT-violation limit on the antiprotonic charge and mass”
- 391 T. Yamazaki: “Antiprotonic helium - An exotic hydrogenic atom”
- 392 Y. Akaishi and T. Yamazaki: “Deeply-bound kaonic nuclear states”
- 393 T. Yamazaki: “Strangeness nuclear physics toward the new millenium - A personal summary of HYP2000”
- 394 H. Koura, M. Uno, T. Tachibana, and M. Yamada: “Table of atomic masses and related quantities calculated by the mass formula of Koura, Uno, Tachibana, and Yamada”
- 395 M. Petrascu, I. Tanihata, K. Kobayashi, M. Giurgiu, K. Morimoto, K. Katori, I. Crucearu, A. Isbasescu, H. Petrascu, R. Ruscu, M. Chiba, Y. Nishi, S. Nishimura, A. Ozawa, T. Suda, K. Yoshida, A. Constantinescu, C. Bordeanu, and A. Tudorica: “Neutron pair pre-emission in the fusion of  $^{11}\text{Li}$  halo nuclei with Si targets”
- 396 M. Terasawa, K. Sumiyoshi, T. Kajino, G. J. Mathews, and I. Tanihata: “New nuclear reaction flow during r-process nucleosynthesis in supernovae: Critical role of light neutron-rich nuclei”
- 397 S. Takeuchi, S. Shimoura, T. Motobayashi, H. Akiyoshi, Y. Ando, N. Aoi, Zs. Fülöp, T. Gomi, Y. Higurashi, M. Hirai, N. Iwasa, H. Iwasaki, Y. Iwata, H. Kobayashi, M. Kurokawa, Z. Liu, T. Minemura, S. Ozawa, H. Sakurai, M. Serata, T. Teranishi, K. Yamada, Y. Yanagisawa, and M. Ishihara: “Isobaric analog of  $^{14}\text{Be}$ ”

- 398 T. Motobayashi: “Indirect measurements of the solar-neutrino production reaction  ${}^7\text{Be}(p,\gamma){}^8\text{B}$ ”
- 399 H. Kurasawa and T. Suzuki: “Electron scattering in relativistic nuclear models”
- 400 R. Kanungo, I. Tanihata, and A. Ozawa: “Possibility of enlarged core structure of  $N=15$  neutron-rich nuclei”
- 401 R. Kanungo, I. Tanihata, and A. Ozawa: “Observation of new neutron and proton magic numbers”
- 402 M. Hirai, S. Kumano, and M. Miyama: “Parton distribution functions in nuclei”
- 403 K. Sugawara-Tanabe, S. Yamaji, and A. Arima: “Pseudospin symmetry and spin symmetry in the relativistic mean-field with deformed potential”
- 404 T. Motobayashi: “Spectroscopy of nuclei around  $N = 20$  with direct reactions”
- 405 Y. Akaishi and T. Yamazaki: “Nuclear  $\bar{K}$  bound states in light nuclei”
- 406 T. Yamazaki, N. Morita, R. S. Hayano, E. Widmann, and J. Eades: “Antiprotonic helium”
- 407 N. Dinh. Dang and V. Zelevinsky: “Improved treatment of ground-state correlations: Modified random phase approximation”
- 408 N. Itagaki, S. Hirose, T. Otsuka, and K. Ikeda: “Triaxial deformation in  ${}^{10}\text{Be}$ ”
- 409 H. Iwasaki, T. Motobayashi, H. Sakurai, K. Yoneda, T. Gomi, N. Aoi, N. Fukuda, Zs. Fülöp, U. Futakami, Z. Gacsi, Y. Higurashi, N. Imai, N. Iwasa, T. Kubo, M. Kunibu, M. Kurokawa, Z. Liu, T. Minemura, A. Saito, M. Serata, S. Shinoura, S. Takeuchi, Y. X. Watanabe, K. Yamada, Y. Yanagisawa, and M. Ishihara: “Large collectivity of  ${}^{34}\text{Mg}$ ”
- 410 Y. Satou, S. Ishida, H. Sakai, H. Okamura, H. Otsu, N. Sakamoto, T. Uesaka, T. Wakasa, T. Ohnishi, K. Sekiguchi, K. Yako, T. Ichihara, T. Niizeki, K. S. Itoh, and N. Nishimori: “Measurement of single and double spin-flip probabilities in inelastic deuteron scattering on  ${}^{12}\text{C}$  at 270 MeV”
- 411 N. Dinh. Dang: “Strength of the double-phonon state within an exactly solvable model”
- 412 T. Yamazaki: “Quasi-stable exotic atoms/nuclei as resonances states”
- 413 A. Kohama, R. Seki, A. Arima, and S. Yamaji: “Determination of matter surface distribution of unstable nuclei”

#### RIKEN-AF-AC

- 26 A. Bolshakov, P. Zenkevich, and T. Katayama: “Code for calculation of dynamical aperture with account of the space charge effect and its application to ACR storage Ring”
- 27 V. Alexandrov, N. Kazarinov, V. Mironov, V. Shevtsov, G. Shirkov, Y. Yano, and T. Nakagawa: “Optimization of ion beam line from ECRIS to RFQ at RIKEN”
- 28 G. Shirkov: “Different modes of laser ion loading into ECR ion source”
- 29 M. Takanaka: “Characteristics of electron-cooled bunched beams predicted by a simulation”
- 30 C. C. Yun: “The simulation of emittance growth by Ray-tracing method”

- 31 A. Skrinsky, I. Meshkov, V. Alexandrov, V. Shevtsov, and G. Shirkov: "Selected reports of the ISTC-RIKEN Japan workshop on Russia/CIS accelerator technologies"
- 32 N. Nagaoka: "Evaluation of some properties of the electron ring for MUSES"

## IX. PAPERS PRESENTED AT MEETINGS

### 1. Accelerator development and accelerator physics

- T. Tominaka, M. Okamura, and T. Katayama: "Rotation angle of a helical dipole", 1999 Particle Accelerator Conf. (PAC '99), (Brookhaven National Laboratory), New York, USA, Mar.-Apr. (1999).
- A. Goto: "RIKEN RI Beam Factory", Seminar on Accelerator Technology and Its Applications, Yogyakarta, Indonesia, Sept. (2000).
- Y. Yano, T. Katayama, A. Goto, and M. Kase: "RIKEN RI Beam Factory Project", 16th Int. Conf. on Application of Accelerators in Research and Industry, Denton, USA, Nov. (2000).
- T. Mitsumoto, A. Goto, M. Kase, J. Ohnishi, O. Kamigaito, N. Sakamoto, K. Ikegami, H. Okuno, Y. Miyazawa, Y. Yano, T. Hiasa, and Y. Kumata: "Construction of the RIKEN IRC", 16th Int. Conf. on Cyclotrons and Their Applications, East Lansing, USA, May (2001).
- A. Goto, H. Okuno, J. Ohnishi, N. Fukunishi, T. Mitsumoto, S. Fujishima, T. Tominaka, K. Ikegami, Y. Miyazawa, and Y. Yano: "Progress on the sector magnets for the RIKEN SRC", 16th Int. Conf. on Cyclotrons and Their Applications, East Lansing, USA, May (2001).
- S. Vorozhtsov, A. Vorozhtsov, A. Goto, T. Mitsumoto, N. Fukunishi, and Y. Yano: "Space charge effects in RIKEN Cyclotrons", 16th Int. Conf. on Cyclotrons and Their Applications, East Lansing, USA, May (2001).
- J. Ohnishi, T. Mitsumoto, A. Goto, and Y. Yano: "Magnetic field measurement of RIKEN IRC sector magnets", 16th Int. Conf. on Cyclotrons and Their Applications, East Lansing, USA, May (2001).
- T. Tanabe, M. Nishiura, I. Watanabe, T. Katayama, E. Syresin, and I. Meshikov: "MUSES-ACR electron coolers", Workshop on Beam Cooling and Related Topics 2001, (Forschungszentrum Julich), Bad Honnef, Germany, May (2001).
- M. Kidera, T. Nakagawa, S. Enomoto, K. Takahashi, H. Baba, R. Hirunuma, T. Ohyama, K. Igarashi, M. Fujimaki, E. Ikezawa, O. Kamigaito, M. Kase, A. Goto, and Y. Yano: "Development of new analytical system using the electron cyclotron resonance ion source and heavy ion linear accelerator", Int. Congr. on Analytical Sciences 2001 (ICAS 2001), (The Japan Society for Analytical Chemistry), Tokyo, Aug. (2001).
- O. Kamigaito, M. Kase, E. Ikezawa, M. Fujimaki, S. Kohara, N. Fukunishi, N. Sakamoto, M. Hemmi, Y. Miyazawa, Y. Chiba, T. Chiba, A. Goto, and Y. Yano: "Upgrade of RIKEN heavy-ion linac for nuclear physics experiments", 26th Linear Accelerator Meet. in Japan, (KEK), Tsukuba, Aug. (2001).

- M. Kidera, T. Nakagawa, Y. Higurashi, M. Kase, and Y. Yano: "Effect of plasma chamber surface for production of highly charged ions from ECRIS", 9th Int. Conf. on Ion Sources, (Lawrence Berkeley National Laboratory), Oakland, USA, Sept. (2001).
- Y. Higurashi, T. Nakagawa, M. Kidera, T. Aihara, M. Kase, and Y. Yano: "Effect of plasma electrode position on the beam intensity of heavy ions from RIKEN 18 GHz ECRIS", 9th Int. Conf. on Ion Sources, (Lawrence Berkeley National Laboratory), Oakland, USA, Sept. (2001).
- T. Nakagawa, M. Kidera, T. Kurita, Y. Higurashi, T. Kageyama, M. Kase, and Y. Yano: "Intense beam production from RIKEN 18 GHz ECRIS and liquid He free SC-ECRIS", 9th Int. Conf. on Ion Sources, (Lawrence Berkeley National Laboratory), Oakland, USA, Sept. (2001).
- Y. Yano: "Progress report on RI Beam Factory Project at RIKEN (Invited)", 2nd Asian Particle Accelerator Conf. (APAC'01), (Institute of High Energy Physics of the Chinese Academy of Sciences), Beijing, China, Sept. (2001).
- M. Takanaka: "Characteristics of electron-cooled bunched beams predicted by a simulation", 13th Symp. on Accelerator Science and Technology, (RCNP and ISIR, Osaka University), Suita, Oct. (2001).
- M. Nishiura, T. Tanabe, T. Katayama, I. Watanabe, and E. Syresin: "Development of MUSES electron cooler at RIKEN", 13th Symp. on Accelerator Science and Technology, (RCNP and ISIR, Osaka University), Suita, Oct. (2001).
- O. Kamigaito, N. Sakamoto, M. Kase, E. Ikezawa, S. Kohara, Y. Miyazawa, T. Chiba, M. Hemmi, Y. Chiba, A. Goto, and Y. Yano: "Rf cavities of the RIKEN charge-state multiplier", 13th Symp. on Accelerator Science and Technology, (RCNP and ISIR, Osaka University), Suita, Oct. (2001).
- T. Masuoka, M. Takano, and T. Katayama: "Preliminary design of MUSES control system based on RT-CORBA and java", 8th Int. Conf. on Accelerator and Large Experimental Physics Control Systems (ICALEPCS 2001), (SLAC), San Jose, USA, Nov. (2001).

### 2. Nuclear physics and nuclear instrumentation

- H. Ogawa, K. Sakai, T. Suzuki, M. Nagakura, H. Miyoshi, K. Asahi, K. Yogo, A. Goto, T. Suga, T. Honda, A. Yoshimi, H. Ueno, N. Imai, Y. Watanabe, K. Yoneda, N. Fukuda, N. Aoi, Y. Kobayashi, W. Schmidt-Ott, G. Neyens, S. Teughels, A. Yoshida, T. Kubo, and M. Ishihara: "Electric quadrupole moment of  $^{17}\text{B}$  and magnetic moment of  $^{15}\text{C}$  measured with polarized radioactive beams", Int. RIKEN

- Symp. on Shell Model 2000, Wako, Mar. (2000).
- K. Asahi, K. Sakai, H. Ogawa, H. Miyoshi, K. Yogo, A. Goto, T. Suga, H. Ueno, Y. Kobayashi, A. Yoshida, T. Kubo, Y. Watanabe, N. Imai, K. Yoneda, N. Fukuda, N. Aoi, M. Ishihara, W. Schmidt-Ott, G. Neyens, and S. Teughels: “Electromagnetic moments of neutron-rich nuclei measured with polarized radioactive ion beams”, Int. RIKEN Symp. on Shell Model 2000, Wako, Mar. (2000).
- K. Asahi: “Nuclear spin maser, and an attempt at new masing scheme”, Int. Symp. on Strong Correlations in Many-body Systems, (University of Tokyo), Nikko, June (2000).
- J. Kim, F. Saito, N. Suzuki, L. Wei, T. Kurihara, Y. Nagashima, M. Okamura, Y. Itoh, A. Goto, T. Hyodo, and F. Saito: “A design of spin rotator for polarized slow positron beam at RIKEN”, 12th Int. Conf. on Positron Annihilation (ICPA-12), München, Germany, Aug. (2000).
- H. Ogawa, K. Asahi, H. Ueno, T. Suzuki, M. Nagakura, A. Goto, T. Suga, K. Yogo, H. Miyoshi, T. Honda, K. Sakai, A. Yoshimi, Y. Watanabe, N. Imai, K. Yoneda, N. Aoi, N. Fukuda, Y. Kobayashi, A. Yoshida, T. Kubo, W. Schmidt-Ott, G. Neyens, and S. Teughels: “Electromagnetic moment of neutron-rich nuclei”, CNS/RIKEN Symp. on Physics of RI-Beam at Low Energy, Wako, Aug. (2000).
- K. Asahi: “RIKEN radioactive beam facility and polarized radioactive beams”, Int. School of Nuclear Physics, 22nd Course Radioactive Beams for Nuclear and Astro Physics, (Deutsche Forschungsgemeinschaft), Erice, Italy, Sept. (2000).
- K. Morimoto, K. Morita, I. Tanihata, N. Iwasa, R. Kanungo, T. Kato, K. Katori, H. Kudo, T. Suda, I. Sugai, S. Takeuchi, F. Tokanai, K. Uchiyama, Y. Wakasaya, T. Yamaguchi, A. Yeremin, A. Yoneda, and A. Yoshida: “Search for a  $Z = 118$  super-heavy nucleus in the reaction of Kr with Pb target at RIKEN”, Tours Symp. on Nuclear Physics IV (TOURS 2000), Tours, France, Sept. (2000).
- H. Ogawa, K. Sakai, H. Ueno, M. Nagakura, K. Asahi, H. Miyoshi, T. Suzuki, K. Yogo, A. Goto, T. Suga, T. Honda, N. Imai, Y. Watanabe, K. Yoneda, A. Yoshimi, N. Fukuda, N. Aoi, Y. Kobayashi, W. Schmidt-Ott, G. Neyens, S. Teughels, A. Yoshida, T. Kubo, and M. Ishihara: “Effective charge anomaly in neutron-rich nuclei revealed from spin-polarized RI beam experiments”, 14th Int. Spin Physics Symp. (SPIN 2000), (RCNP and ISIR, Osaka University), Suita, Oct. (2000).
- K. Asahi, K. Sakai, H. Ogawa, H. Ueno, Y. Kobayashi, A. Yoshimi, H. Miyoshi, K. Yogo, A. Goto, T. Suga, N. Imai, Y. Watanabe, K. Yoneda, N. Fukuda, N. Aoi, W. Schmidt-Ott, G. Neyens, S. Teughels, A. Yoshida, T. Kubo, and M. Ishihara: “Nuclear moment studies with polarized radioactive nuclear beams”, 14th Int. Spin Physics Symp. (SPIN 2000), (RCNP and ISIR, Osaka University), Suita, Oct. (2000).
- H. Ueno, H. Miyatake, Y. Yamamoto, M. Sasaki, N. Aoi, Y. Mizoi, T. Shimoda, A. Ozawa, K. Yoneda, H. Izumi, H. Ogawa, M. Notani, K. Asahi, S. Tanimoto, E. Ideguchi, T. Kubo, T. Kishida, S. Mitsuoka, T. Shirakura, N. Takahashi, and M. Ishihara: “Beta-delayed neutron spectroscopy using a spin-polarized  $^{17}\text{B}$  beam”, Int. Symp. on Perspectives in Physics with Radioactive Isotope Beams 2000 (RIB00), (RIKEN and Center for Nuclear Study, University of Tokyo), Hayama, Nov. (2000).
- S. Takeuchi, S. Shimoura, T. Motobayashi, H. Akiyoshi, Y. Ando, N. Aoi, Z. Fülöp, T. Gomi, Y. Higurashi, M. Hirai, N. Iwasa, H. Iwasaki, Y. Iwata, H. Kobayashi, M. Kurokawa, T. Minemura, S. Ozawa, H. Sakurai, M. Serata, T. Teranishi, K. Yamada, Y. Yanagisawa, L. Zhong, and M. Ishihara: “Isobaric analog state of  $^{14}\text{Be}$ ”, Int. Symp. on Perspectives in Physics with Radioactive Isotope Beams 2000 (RIB00), (RIKEN and Center for Nuclear Study, University of Tokyo), Hayama, Nov. (2000).
- K. Yoneda, H. Sakurai, T. Gomi, T. Motobayashi, N. Aoi, N. Fukuda, U. Futakami, Z. Gacsi, Y. Higurashi, N. Imai, N. Iwasa, H. Iwasaki, T. Kubo, M. Kunibu, M. Kurokawa, Z. Liu, T. Minemura, A. Saito, M. Serata, S. Shimoura, S. Takeuchi, Y. Watanabe, K. Yamada, Y. Yanagisawa, K. Yogo, A. Yoshida, and M. Ishihara: “Very large deformation of the neutron-rich isotope  $^{34}\text{Mg}$  from in-beam gamma-ray spectroscopy with RI beam fragmentation”, Int. Symp. on Perspectives in Physics with Radioactive Isotope Beams 2000 (RIB00), (RIKEN and Center for Nuclear Study, University of Tokyo), Hayama, Nov. (2000).
- H. Ogawa, K. Asahi, K. Sakai, H. Ueno, T. Suzuki, H. Miyoshi, M. Nagakura, K. Yogo, A. Goto, T. Suga, T. Honda, N. Imai, Y. Watanabe, K. Yoneda, N. Fukuda, A. Yoshimi, N. Aoi, Y. Kobayashi, W. Schmidt-Ott, G. Neyens, S. Teughels, A. Yoshida, T. Kubo, and M. Ishihara: “Quenching of neutron E2 effective charge in neutron-rich nuclei”, Int. Symp. on Perspectives in Physics with Radioactive Isotope Beams 2000 (RIB00), (RIKEN and Center for Nuclear Study, University of Tokyo), Hayama, Nov. (2000).
- H. Miyoshi, K. Asahi, H. Ogawa, H. Ueno, D. Kameda, K. Yoneda, T. Suga, A. Goto, A. Yoshimi, H. Watanabe, W. Sato, and T. Shinozuka: “Development of low energy polarized radioactive isotope beams”, Shingata Saikurotoron Kyoudou Riyou Purojekuto Kentoukai, (Tohoku University), Sendai, Nov. (2000).
- K. Yoneda, H. Sakurai, T. Gomi, T. Motobayashi, N. Aoi, N. Fukuda, U. Futakami, Z. Gacsi, Y. Higurashi, N. Imai, N. Iwasa, H. Iwasaki, T. Kubo,

- M. Kunibu, M. Kurokawa, Z. Liu, T. Minemura, A. Saito, M. Serata, S. Shimoura, S. Takeuchi, Y. Watanabe, K. Yamada, Y. Yanagisawa, K. Yogo, A. Yoshida, and M. Ishihara: "In-beam gamma-ray spectroscopy with RI projectile fragmentation", Workshop on Direct Reactions with Radioactive Isotope Beams, (Rikkyo University), Tokyo, Nov. (2000).
- S. Takeuchi, S. Shimoura, T. Motobayashi, H. Akiyoshi, Y. Ando, N. Aoi, Z. Fülöp, T. Gomi, Y. Higurashi, M. Hirai, N. Iwasa, H. Iwasaki, Y. Iwata, H. Kobayashi, M. Kurokawa, T. Minemura, S. Ozawa, H. Sakurai, M. Serata, T. Teranishi, K. Yamada, Y. Yanagisawa, L. Zhong, and M. Ishihara: "Isobaric analog state of  $^{14}\text{Be}$ ", Workshop on Direct Reactions with Radioactive Isotope Beams, (Rikkyo University), Tokyo, Nov. (2000).
- T. Nakatsukasa: "Theoretical introduction to nuclear collective motion", 11th RIKEN Winter School on In-beam Gamma-ray Spectroscopy with RI Beams, Tsunan-cho, Jan. (2001).
- T. Nakatsukasa: "Linear response in the continuum spectral region", Mean-field Approaches to Structure of Unstable Nuclei, Wako, Jan. (2001).
- K. Ishida: "Simulation of pion and muon production at a carbon target with 3 GeV proton beam", Muon Science 2001 Symp. for KEK-JEARI Joint Project, (KEK, JEARI), Tsukuba, Jan. (2001).
- Y. Mochizuki: "Magic numbers related to the r-process nucleosynthesis and RI-Beam Factory Project", Workshop on the Origin of the Elements and the Evolution of the Universe, (Sophia University), Tokyo, Jan. (2001).
- S. Fujii: "Shell-model calculations for  $^{17}\text{O}$  using microscopic  $\Lambda\text{N}$  and  $\Sigma\text{N}$  effective interactions", Int. Symp. on Hadrons and Nuclei, (Yonsei University), Seoul, Korea, Feb. (2001).
- A. Ozawa: "Measurements of total reaction cross sections", Int. Workshop Reaction Mechanisms with Exotic Nuclei, (ECT\*), Trento, Italy, Feb. (2001).
- T. Nakatsukasa and K. Yabana: "3D real space calculations of the continuum response", RIKEN Symp. on Physics at Drip Lines, Wako, Feb. (2001).
- K. Asahi, H. Ogawa, H. Ueno, H. Miyoshi, D. Kameda, Y. Kobayashi, A. Yoshimi, K. Yogo, A. Goto, T. Suga, K. Sakai, N. Imai, Y. Watanabe, K. Yoneda, N. Fukuda, N. Aoi, A. Yoshida, T. Kubo, M. Ishihara, W. Schmidt-Ott, G. Neyens, and S. Teughels: "Quadrupole moments and magnetic moments in exotic nuclei", RIKEN Symp. on Physics at Drip Lines, Wako, Feb. (2001).
- T. Nakatsukasa: "Local harmonic approaches to nuclear collective dynamics", Workshop on Nuclear Structure of Unstable Nuclei, (Kyoto University), Kyoto, Feb. (2001).
- D. Kameda, K. Asahi, H. Ogawa, H. Ueno, H. Miyoshi, K. Yoneda, H. Watanabe, N. Imai, T. Suga, K. Oono, W. Sato, A. Yoshimi, K. Yogo, K. Sakai, Y. Kobayashi, A. Yoshida, T. Kubo, and M. Ishihara: "Development of an adiabatic field rotation method for the polarization measurement of a fragment beam", 56th Ann. Meet. of Physical Soc. of Japan, Hachioji, Mar. (2001).
- K. Ishida, K. Nagamine, T. Matsuzaki, S. Nakamura, N. Kawamura, Y. Matsuda, S. Sakamoto, M. Tanase, M. Kato, H. Sugai, K. Kudoh, N. Takeda, and G. Eaton: "Muon catalyzed fusion experiment in D-T system at RIKEN-RAL Muon Facility: Non-equilibrium effect", 56th Ann. Meet. of Physical Soc. of Japan, Hachioji, Mar. (2001).
- A. Kohama, S. Yamaji, R. Seki, and A. Arima: "Systematic error in analysis of one-body density distributions with a Gaussian-basis expansion", 56th Ann. Meet. of Physical Soc. of Japan, Hachioji, Mar. (2001).
- Y. Mochizuki: "Video presentation "The quest for the origin of the elements" and beyond (invited)", 56th Ann. Meet. of Physical Soc. of Japan, Hachioji, Mar. (2001).
- T. Matsuzaki, K. Nagamine, K. Ishida, N. Kawamura, Y. Matsuda, S. Nakamura, M. Tanase, M. Kato, H. Sugai, K. Kudoh, N. Takeda, and G. Eaton: "t-t muon catalyzed fusion experiment at RIKEN-RAL Muon Facility: Fusion neutron energy distribution", 56th Ann. Meet. of Physical Soc. of Japan, Hachioji, Mar. (2001).
- Y. Mochizuki: "Retarded beta-decay of  $^{44}\text{Ti}$  in supernova remnants and its importance", ISAS High-Energy Astrophysics Branch Seminar, (The Institute of Space and Astronautical Science), Sagami-hara, Apr. (2001).
- M. Kato, H. Sugai, M. Tanase, T. Matsuzaki, K. Ishida, and K. Nagamine: "Development of compact tritium gas recycling system", Int. RIKEN Conf. on Muon Catalyzed Fusion and Related Exotic Atoms ( $\mu\text{CF01}$ ), Shimoda, Apr. (2001).
- K. Ishida, K. Nagamine, T. Matsuzaki, N. Kawamura, S. Nakamura, Y. Matsuda, M. Kato, H. Sugai, M. Tanase, K. Kudo, N. Takeda, and G. H. Eaton: "Measurement of fusion protons and X-rays in muon catalyzed d-t fusion at RIKEN-RAL", Int. RIKEN Conf. on Muon Catalyzed Fusion and Related Exotic Atoms ( $\mu\text{CF01}$ ), Shimoda, Apr. (2001).
- T. Matsuzaki, K. Nagamine, K. Ishida, N. Kawamura, S. Nakamura, Y. Matsuda, M. Kato, H. Sugai, M. Tanase, K. Kudoh, N. Takeda, and G. Eaton: "Recent results on muon catalyzed t-t fusion at RIKEN-RAL", Int. RIKEN Conf. on Muon Catalyzed Fusion and Related Exotic Atoms ( $\mu\text{CF01}$ ), Shimoda, Apr. (2001).
- T. Nakatsukasa and K. Yabana: "Resonance and continuum states in weakly bound systems", 7th Int. Spring Seminar on Nuclear Physics, 'Challenges of Nuclear Structure', (INFN, University of Naples).

- Maiori, Italy, May (2001).
- A. Ozawa: “New Magic Number,  $N = 16$ , near the neutron magic number”, Int. Conf. on Nuclear Physics at Border Lines, (Messina University, Fondazione Bonino-Pulejo Messina), Lipari, Italy, May (2001).
- Y. Mochizuki: “Element genesis: Solving the mystery (video presentation and interpretation) (invited)”, Int. Symp. on Nuclear Astrophysics (NAP 2001), Darmstadt, Germany, May (2001).
- S. Fujii: “YN interactions and spin-orbit splittings in  $\Lambda$  hypernuclei”, KEK Theory Seminar, Tsukuba, May (2001).
- S. Fujii: “A study of  $\Lambda$  hypernuclear structure with unitary-model-operator approach”, Nuclear Theory Seminar at University of Tsukuba, Tsukuba, May (2001).
- Y. Mochizuki: “Element genesis: Solving the mystery (video presentation and interpretation)”, Seminar at Max-Planck-Institut fuer Astronomie, Heidelberg, Germany, May (2001).
- N. Shimizu: “Quadrupole collective states in the Monte Carlo shell model”, NATO Advanced Research Workshop on the Nuclear Many-Body Problem 2001, Pula, Croatia, June (2001).
- Y. Mochizuki: “Microscopic nuclear rod model for the origin of neutron star glitches”, Nuclear Physics Seminar at RCNP of Osaka University, Osaka, June (2001).
- S. Fujii: “YN interactions and spin-orbit splittings in  $\Lambda$  hypernuclei”, Nuclear Physics Seminar at Tokyo Institute of Technology, Tokyo, June (2001).
- H. Sakai, T. Wakui, M. Hatano, A. Tamii, and T. Uesaka: “Spin polarized solid proton target for experiments by the radio-isotope beam”, 3rd Int. Conf. on Exotic Nuclei and Atomic Masses (enam 2001), (University of Jyvaskyla), Hameenlinna, Finland, July–Aug. (2001).
- H. Sakai, K. Sekiguchi, Y. Maeda, W. Glockle, M. B. Greenfield, K. Hatanaka, M. Hatano, D. Hirooka, H. Kamada, J. Kamiya, H. Kato, T. Ohnishi, H. Okamura, J. Rapaport, T. Saito, N. Sakamoto, S. Sakoda, Y. Sato, K. Suda, A. Tamii, N. Uchigashima, T. Uesaka, T. Wakasa, H. Witala, and K. Yakou: “Clear signature of three-nucleon force effects via the precise measurements of  $\vec{d}p$  and  $\vec{n}d$  scatterings”, Int. Nuclear Physics Conf. (INPC2001), (Berkeley National Laboratory), Berkeley, USA, July Aug. (2001).
- Y. Mochizuki: “Electron capture beta-decay under ultra-high pressures”, Nuclear Physics Seminar at Kyushu University, Fukuoka, July (2001).
- S. Fujii: “Unitary-model-operator approach to  $\Lambda$  hypernuclei”, Nuclear Theory Seminar at University of Tokyo, Tokyo, July (2001).
- Y. Mochizuki: “Microscopic nuclear rod model for the origin of neutron star glitches”, Nuclear and Statistics Physics Seminar at Nihon University, Tokyo, July (2001).
- Y. Mochizuki: “The origin of elements and life in the universe (invited)”, Atomic Collision Soc. of Japan, Tokyo, Aug. (2001).
- A. Ozawa: “Nuclear size and related topics”, Beijing Int. Summer School on Subatomic Physics, (Beijing University), Beijing, China, Aug. (2001).
- H. Sakai, T. Wakui, M. Hatano, A. Tamii, and T. Uesaka: “Development of a spin polarized solid proton target for experiments by the radio-isotope beam”, 9th Workshop on High Energy Spin Physics (Spin-01): Joint Inst. for Nucl. Res. Int. Committee for Energy Spin Physics Symp., Dubna, Russia, Aug. (2001).
- H. Sakai: “Search for a three-nucleon force effects via the polarization measurements on  $\vec{d}p$  and  $\vec{n}d$  scattering”, 9th Workshop on High Energy Spin Physics (Spin-01): Joint Inst. for Nucl. Res. Int. Committee for Energy Spin Physics Symp., Dubna, Russia, Aug. (2001).
- K. Iida: “Color superconductivity: Approach from weak coupling”, Thermal quantum field theories and their application, (Yukawa Institute for Theoretical Physics, Kyoto University), Kyoto, Aug. (2001).
- K. Ishida: “Measurement of X-rays from muon-to-alpha sticking in muon catalyzed fusion”, Meet. on Basic Science using Muons and Muon Catalyzed Fusion, (Meson Science Users Association), Tsukuba, Sept. (2001).
- A. Kohama: “RIKEN efforts on proton scattering with unstable nuclei”, Workshop on Relativistic Description of Proton-Nucleus Scattering, (PCNP, Osaka University), Osaka, Sept. (2001).
- H. Sakai: “Clear evidence of three-nucleon force effects in  $Nd$  scattering”, 1st Joint Meet. of the Nuclear Physics Divisions of APS and JPS Hawaii 2001 (HAW01), Maui, USA, Oct. (2001).
- Y. Mochizuki, I. Tanihata, Y. Yano, and R. N. Boyd: “Element genesis: Solving the mystery (video presentation) (invited)”, 1st Joint Meet. of the Nuclear Physics Divisions of APS and JPS Hawaii 2001 (HAW01), Maui, USA, Oct. (2001).
- H. En’yo: “Measurements of in-medium decay of vector mesons at KEK-PS”, 1st Joint Meet. of the Nuclear Physics Divisions of APS and JPS Hawaii 2001 (HAW01), Maui, USA, Oct. (2001).
- K. Ishida, K. Nagamine, T. Matsuzaki, Y. Matsuda, N. Kawamura, S. Nakamura, M. Kato, H. Sugai, M. Tanase, K. Kudo, N. Takeda, and G. H. Eaton: “Muon-catalyzed fusion experiments at RIKEN-RAL muon facility”, 1st Joint Meet. of the Nuclear Physics Divisions of APS and JPS Hawaii 2001 (HAW01), Maui, USA, Oct. (2001).
- K. Sekiguchi, H. Sakai, A. Tamii, K. Yakou, S. Sakoda, H. Kato, Y. Maeda, M. Hatano, T. Saito, N. Uchigashima, H. Okamura, T. Uesaka, K. Suda, J.

- Nishikawa, N. Sakamoto, T. Ohnishi, T. Wakasa, Y. Sato, N. Kalantar-Nayestanaki, and K. Ermisch: "Search for three nucleon force effect via deuteron-proton scattering", 1st Joint Meet. of the Nuclear Physics Divisions of APS and JPS Hawaii 2001 (HAW01), Maui, USA, Oct. (2001).
- H. Koura, T. Tachibana, and T. Yoshida: "Estimation of alpha-decay half lives and fission barriers from the viewpoint of a new mass formula", Int. Conf. on Nuclear Data for Science and Technology, (JAERI), Tsukuba, Oct. (2001).
- T. Matsuzaki, K. Nagamine, K. Ishida, M. Kato, H. Sugai, M. Tanase, and G. H. Eaton: "An in-situ tritium-deuterium gas-purification system for muon catalyzed fusion experiments at the RIKEN-RAL Muon Facility", 6th Int. Conf. on Tritium Science and Technology (TRITIUM 2001), (JAERI), Tsukuba, Nov. (2001).
- M. Kato, T. Itoh, H. Sugai, K. Yoshinori, H. Takumi, N. Masataka, M. Tanase, T. Matsuzaki, K. Ishida, and K. Nagamine: "Development of a compact tritium gas recycling system", 6th Int. Conf. on Tritium Science and Technology (TRITIUM 2001), (JAERI), Tsukuba, Nov. (2001).
- A. Saito, S. Shimoura, S. Takeuchi, T. Motobayashi, H. Akiyoshi, Y. Ando, N. Aoi, Z. Fulop, T. Gomi, Y. Higurashi, M. Hirai, N. Iwasa, H. Iwasaki, Y. Iwata, H. Kobayashi, M. Uesaka, Z. Liu, T. Minemura, S. Ozawa, H. Sakurai, M. Serata, T. Teranishi, K. Yamada, Y. Yanagisawa, and M. Ishihara: "Molecular states in neutron-rich beryllium isotopes", Int. Symp. on Clustering Aspects of Quantum Many-body Systems, (Yukawa Institute for Theoretical Physics, Kyoto University), Kyoto, Nov. (2001).
- K. Iida: "Phenomenology and sum rules in color superconducting quark matter", 6th APCTP Winter School/2nd Dense Matter School, Pohang, Korea, Nov. (2001).
- K. Iida, G. Watanabe, and K. Sato: "Formation of nuclear "pasta" in cold neutron star matter", Yukawa Int. Seminar 2001 (YKIS01): Physics of Unstable Nuclei, (Yukawa Institute for Theoretical Physics, Kyoto University), Kyoto, Nov. (2001).
- A. Kohama, R. Seki, A. Arima, and S. Yamaji: "Model-independent determination of surface density distribution of unstable nuclei at radioactive beam facilities", Yukawa Int. Seminar 2001 (YKIS01): Physics of Unstable Nuclei, (Yukawa Institute for Theoretical Physics, Kyoto University), Kyoto, Nov. (2001).
- A. Saito, S. Shimoura, S. Takeuchi, T. Motobayashi, H. Akiyoshi, Y. Ando, N. Aoi, Z. Fulop, T. Gomi, Y. Higurashi, M. Hirai, N. Iwasa, H. Iwasaki, Y. Iwata, H. Kobayashi, M. Uesaka, Z. Liu, T. Minemura, S. Ozawa, H. Sakurai, M. Serata, T. Teranishi, K. Yamada, Y. Yanagisawa, and M. Ishihara: "Molecular states in neutron-rich beryllium isotopes", Yukawa Int. Seminar 2001 (YKIS01): Physics of Unstable Nuclei, (Yukawa Institute for Theoretical Physics, Kyoto University), Kyoto, Nov. (2001).
- Y. Mochizuki: "Intersection between meteorites and nucleosynthesis studies", Earth and Planet Science Seminar at University of Tokyo, Tokyo, Dec. (2001).
- S. Fujii: "Shell-model calculations for  ${}^{17}_{\Lambda}\text{O}$  and  ${}^{16}_{\Lambda}\text{O}$  using microscopic effective interactions with degrees of freedom of  $\Sigma$ ", YITP Workshop on New Topics for Strangeness Nuclear Physics, (Yukawa Institute for Theoretical Physics, Kyoto University), Kyoto, Dec. (2001).

### 3. Atomic and solid-state physics

- Y. Yoshida, Y. Kobayashi, F. Ambe, E. Yagi, X. Diao, J. Nakamura, H. Hasslein, A. Feinauer, T. Grund, A. Rock, and A. Seeger: "Direct observation of self-interstitial motion in pure iron by  ${}^{56}\text{Fe}(\text{d},\text{p}){}^{57}\text{Fe}$  in-beam Mössbauer spectroscopy", Int. Symp. of Diffusion in Materials 2000 (DIMAT2000), Paris, France, July (2000).
- Y. Yoshida, Y. Kobayashi, K. Hayakawa, K. Yukihiro, F. Shimura, A. Yoshida, X. Diao, H. Ogawa, Y. Yano, and F. Ambe: "In-beam Mössbauer study on interstitial and substitutional  ${}^{57}\text{Mn}/{}^{57}\text{Fe}$  jumps in Si", Int. Symp. of Diffusion in Materials 2000 (DIMAT2000), Paris, France, July (2000).
- Y. Kanai, Y. Iwai, D. Dumitriu, H. Masuda, Y. Morishita, D. Murakoshi, and Y. Yamazaki: "Excited states produced by beam-capillary interaction", 13th Int. Workshop on Inelastic Ion-Surface Collisions, (Instituto Balseiro and Centro Atomico Bariloche), San Carlos de Bariloche, Argentina, Nov. (2000).
- T. Hasegawa, A. Iwase, S. Ishino, Y. Chimi, N. Ishikawa, T. Tobita, M. Suzuki, and T. Kambara: "Hardness of FeCu alloys irradiated with GeV heavy ions", Kyoto Daigaku Genshiro Jikkenjo Kenkyukai, Kumatori, Jan. (2001).
- T. Matsuzaki: "Pion target at ISIS facility", Muon Science 2001 Symp. for KEK-JEARI Joint Project, Tsukuba, Jan. (2001).
- T. Ikeda: "Application to atomic physics", RIKEN Symp. on Development and Application of Superconductor Radiation Detectors, Wako, Jan. (2001).
- M. Wada: "Test experiment on the ion transport in gas cell by RF ion-guide", Workshop on Physics Applications of Medical Use Particle Accelerator, (National Institute Radiological Sciences), Chiba, Jan. (2001).
- M. Wada: "Precision hyperfine structure spectroscopy of unstable nuclei", RIKEN Symp. on Studies on Condensed Matter Physics, Atomic Physics, Hyperfine Interactions and Biomedical Sciences Using RIKEN Accelerators, Wako, Feb. (2001).
- Y. Nakai: "TOF analysis of fragment ion of  $\text{C}_{60}$  by

- fast ion impact”, RIKEN Symp. on Studies on Condensed Matter Physics, Atomic Physics, Hyperfine Interactions and Biomedical Sciences Using RIKEN Accelerators, Wako, Feb. (2001).
- N. Ishikawa, Y. Chimi, A. Iwase, O. Michikami, H. Wakana, T. Hashimoto, R. Neumann, and T. Kambara: “Defect production process in oxide superconductors irradiated with high energy ions”, 56th Ann. Meet. of Physical Soc. of Japan, Hachioji, Mar. (2001).
- N. Oshima, T. Kojima, D. Dumitriu, A. Mohri, H. Oyama, Y. Kanai, T. Kambara, Y. Nakai, M. Wada, M. Niigaki, and Y. Yamazaki: “Development of a slow positron beam using a rare gas solid moderator (III)”, 56th Ann. Meet. of Physical Soc. of Japan, Hachioji, Mar. (2001).
- Y. Nakai, T. Kambara, A. Itoh, H. Tsuchida, and Y. Yamazaki: “Ionization and fragmentation of  $C_{60}$  by fast ion impact: Analysis of TOF spectrum profile of fullerene-like fragment ions (II)”, 56th Ann. Meet. of Physical Soc. of Japan, Hachioji, Mar. (2001).
- D. Murakoshi, N. Okabayashi, Y. Iwai, Y. Morishita, Y. Nakai, Y. Kanai, H. Torii, K. Nishio, H. Masuda, K. Komaki, and Y. Yamazaki: “Measurement of charge state distribution of  $N^{q+}$  transmitted through micro-capillaries”, 56th Ann. Meet. of Physical Soc. of Japan, Hachioji, Mar. (2001).
- A. Endo, H. Torii, K. Yoshiki Franzen, K. Komaki, and Y. Yamazaki: “The development of a mini-EBIS using high- $T_c$  superconductors (III)”, 56th Ann. Meet. of Physical Soc. of Japan, Hachioji, Mar. (2001).
- T. Ikeda, Y. Iwai, T. Oku, N. Oshima, C. Otani, H. Oyama, H. Kato, Y. Kanai, K. Kawai, H. Sato, H. Shimizu, Y. Takizawa, Y. Nakai, K. Nishio, H. Masuda, H. Miyasaka, Y. Morishita, H. Watanabe, and Y. Yamazaki: “X-ray spectroscopy of highly charged ions using superconducting tunnel junctions (II)”, 56th Ann. Meet. of Physical Soc. of Japan, Hachioji, Mar. (2001).
- Y. Iwai, R. Hutton, Y. Kanai, H. Oyama, K. Ando, H. Masuda, K. Nishio, K. Komaki, and Y. Yamazaki: “High resolution soft X-ray spectroscopy of highly charged ions through Au microcapillary target”, 56th Ann. Meet. of Physical Soc. of Japan, Hachioji, Mar. (2001).
- E. Yagi: “The analysis of the state of hydrogen dissolved in crystals by means of the nuclear reaction channelling method”, Symp. on the Role of Hydrogen in the Embrittlement of Structural Materials in the Environmental Atmosphere, (The Iron and Steel Institute of Japan), Tokyo, Mar. (2001).
- T. Ikeda, Y. Nakai, C. Ohtani, H. Sato, Y. Kanai, H. Oyama, Y. Takizawa, Y. Iwai, Y. Morishita, N. Oshima, T. Oku, H. Shimizu, H. Watanabe, H. Miyasaka, H. Kato, K. Kawai, Y. Yamazaki, H. Akoh, M. Aoyagi, H. Nakagawa, S. Takada, and T. Taino: “X-ray spectroscopy of highly charged ions using superconducting tunnel junctions”, 8th Int. Surperconductive Electronics Conf., Osaka, June (2001).
- Y. Yamazaki: “Soft x-rays emitted in HCI-microcapillary interactions”, 17th Int. Symp. on Ion-Atom Collisions (ISIAC XVII), (Centro de Ciencias Fisicas), Baja California, Mexico, July (2001).
- Y. Yamazaki: “A micro-capillary target as a metastable hollow ion source”, 19th Int. Conf. on Atomic Collisions in Solids, Paris, France, July–Aug. (2001).
- T. Kambara, K. Kageyama, Y. Kanai, T. Kojima, Y. Nakai, A. Yoneda, and Y. Yamazaki: “Elastic wave from fast heavy-ion irradiation on solids”, 19th Int. Conf. on Atomic Collisions in Solids, Paris, France, July–Aug. (2001).
- Y. Iwai, Y. Kanai, H. Oyama, K. Ando, H. Masuda, K. Nishio, M. Nakao, T. Tamamura, K. Komaki, and Y. Yamazaki: “High-resolution soft x-ray spectroscopy of 2.3 keV/u  $N^{7+}$  ions through a microcapillary target”, 19th Int. Conf. on Atomic Collisions in Solids, Paris, France, July–Aug. (2001).
- T. Ikeda, Y. Nakai, C. Ohtani, H. Sato, H. Oyama, Y. Kanai, Y. Iwai, Y. Morishita, N. Oshima, H. Shimizu, and Y. Yamazaki: “X-ray detection using superconducting tunnel junctions in slow highly charged ion collision with surface”, 19th Int. Conf. on Atomic Collisions in Solids, Paris, France, July–Aug. (2001).
- M. Wada: “Development of an RF ion guide for trapping energetic radioactive nuclear ions”, 2001 Workshop on Non-Neutral Plasmas, San Diego, USA, July–Aug. (2001).
- A. Mohri, T. Kojima, N. Ohshima, M. Niigaki, and Y. Yamazaki: “System of slow highly charged ion beam generation using a cold positron plasma trap at RIKEN”. 2001 Workshop on Non-Neutral Plasmas, San Diego, USA, July–Aug. (2001).
- M. Takekawa, Y. Itikawa, and I. Shimamura: “Elastic scattering of electrons from carbonyl sulfide”, 22nd Int. Conf. on Photonic, Electronic and Atomic Collisions (XXII ICPEAC), (IUPAP and others), Santa Fe, USA, July (2001).
- M. Niigaki, N. Ohshima, T. Kojima, and Y. Yamazaki: “Extraction system for ultra-slow highly-charged ions from a trap in a strong magnetic field”, 22nd Int. Conf. on Photonic, Electronic and Atomic Collisions (XXII ICPEAC), (IUPAP and others), Santa Fe, USA, July (2001).
- H. Shimada, Y. Nakai, T. Kambara, K. Ando, H. Oyama, and Y. Yamazaki: “Momentum distributions of highly charged noble gas ions produced by intense laser light”, 22nd Int. Conf. on Photonic, Electronic and Atomic Collisions (XXII ICPEAC), (IUPAP and others), Santa Fe, USA, July (2001).
- Y. Nakai: “Production of heavy fragment ions ( $C_{60-2n}^{1+,2+,3+}$ ) in collisions of  $C_{60}$  with fast ions”,

- 22nd Int. Conf. on Photonic, Electronic and Atomic Collisions (XXII ICPEAC), (IUPAP and others), Santa Fe, USA, July (2001).
- S. Sakaguti, K. Ohtsuki, and T. Watanabe: "Theoretical calculation of double electron transfer processes in collisions of  $\text{He}^{2+}$  with Mg", 22nd Int. Conf. on Photonic, Electronic and Atomic Collisions (XXII ICPEAC), (IUPAP and others), Santa Fe, USA, July (2001).
- Y. Iwai, Y. Kanai, H. Oyama, K. Ando, H. Masuda, K. Nishio, M. Nakao, T. Tamamura, K. Komaki, and Y. Yamazaki: "X-ray measurement for 2.3 keV/u  $^{15}\text{N}^{7+}$  ions passing through Au and Ni microcapillary targets", 22nd Int. Conf. on Photonic, Electronic and Atomic Collisions (XXII ICPEAC), (IUPAP and others), Santa Fe, USA, July (2001).
- T. Ikeda, Y. Nakai, C. Ohtani, H. Sato, H. Oyama, Y. Kanai, Y. Iwai, Y. Morishita, N. Oshima, H. Shimizu, and Y. Yamazaki: "X-ray spectroscopy of highly charged ions using superconducting tunnel junctions", 22nd Int. Conf. on Photonic, Electronic and Atomic Collisions (XXII ICPEAC), (IUPAP and others), Santa Fe, USA, July (2001).
- Y. Nagashima, Y. Ito, A. Goto, and T. Hyoudo: "Detection of positron annihilation induced characteristic X-rays", 38th Ann. Meet. on Radioisotopes and Radiation in the Physical Sciences and Industries, (Japan Radioisotope Association), Tokyo, July (2001).
- N. Oshima, T. Kojima, A. Mohri, M. Niigaki, T. Kambara, Y. Kanai, Y. Nakai, H. Oyama, M. Wada, and Y. Yamazaki: "Study of a slow HCl production technique using a positron cooling method", 38th Ann. Meet. on Radioisotopes and Radiation in the Physical Sciences and Industries, (Japan Radioisotope Association), Tokyo, July (2001).
- F. Saito, Y. Nagashima, T. Kurihara, Y. Ito, A. Goto, and T. Hyoudo: "Tungsten mesh moderator for slow positron beams", 38th Ann. Meet. on Radioisotopes and Radiation in the Physical Sciences and Industries, (Japan Radioisotope Association), Tokyo, July (2001).
- I. Shimamura: "Bound states of positron with molecules", 11th Workshop on Low Energy Positron and Positronium Physics, (ICPEAC), Santa Fe, USA, Aug. (2001).
- S. Sakaguti, K. Otsuki, and T. Watanabe: "Calculation of double electron transfer processes in collisions of  $\text{He}^{2+}$  with Mg", 26th Ann. Meet. of the Soc. for Atomic Collision Research, Tokyo, Aug. (2001).
- M. Takekawa, Y. Itikawa, and I. Shimamura: "Elastic scattering of electrons from carbonyl sulfide", 26th Ann. Meet. of the Soc. for Atomic Collision Research, Tokyo, Aug. (2001).
- M. Hoshiino, M. Kitajima, Y. Kanai, Y. Nakai, H. Tanaka, and Y. Yamazaki: "Experimental studies for highly-charged-ion and atom collisions with crossed-beam technique", 26th Ann. Meet. of the Soc. for Atomic Collision Research, Tokyo, Aug. (2001).
- T. Ikeda: "X-ray detection using superconducting tunnel junctions", 26th Ann. Meet. of the Soc. for Atomic Collision Research, Tokyo, Aug. (2001).
- T. Ikeda, Y. Nakai, C. Ohtani, H. Sato, H. Oyama, Y. Kanai, Y. Takizawa, Y. Iwai, Y. Morishita, T. Oku, N. Ohshima, H. Watanabe, H. Miyasaka, K. Kawai, H. Kato, Y. Yamazaki, and H. Shimizu: "X-ray spectroscopy in atomic collision experiment using superconducting tunnel junctions", 5th European Conf. on Applied Superconductivity (EUCAS 2001), (DEFU and others), Copenhagen, Denmark, Aug. (2001).
- K. Ishioka, M. Hase, K. Ushida, and M. Kitajima: "Coherent acoustic phonon-defect scattering in graphite", 10th Int. Conf. on Phonon Scattering in Condensed Matter, Hanover, USA, Aug. (2001).
- N. Ohshima, T. Kojima, A. Mohri, M. Niigaki, H. Oyama, Y. Kanai, T. Kambara, Y. Nakai, M. Wada, K. Komaki, and Y. Yamazaki: "Development of a slow positron source for cooling highly charged ions", 2001 Fall Meet. of the Physical Soc. of Japan, Tokushima, Sept. (2001).
- A. Mohri, T. Kojima, N. Ohshima, M. Niigaki, and Y. Yamazaki: "Dynamics during positron beam injection into an electron plasma", 2001 Fall Meet. of the Physical Soc. of Japan, Tokushima, Sept. (2001).
- T. Kambara, K. Kageyama, Y. Kanai, T. Kojima, Y. Nakai, A. Yoneda, and Y. Yamazaki: "Elastic wave generation in solid by irradiation of fast heavy ions", 2001 Fall Meet. of the Physical Soc. of Japan, Tokushima, Sept. (2001).
- Y. Iwai, Y. Kanai, H. Oyama, K. Ando, H. Masuda, K. Nishio, M. Nakao, T. Tamamura, K. Komaki, and Y. Yamazaki: "High resolution soft X-ray spectroscopy of highly charged ions through Au microcapillary target II", 2001 Fall Meet. of the Physical Soc. of Japan, Tokushima, Sept. (2001).
- T. Kojima, N. Ohshima, M. Niigaki, A. Mohri, and Y. Yamazaki: "RIKEN positron-MCI trap II: confinement of electrons positrons", 2001 Fall Meet. of the Physical Soc. of Japan, Tokushima, Sept. (2001).
- M. Wada: "Slow and trapped RNB from a projectile fragment separator and their applications", 4th Italy-Japan Symp. on Heavy Ion Physics, Wako, Sept. (2001).
- F. Saito, Y. Nagashima, L. Wei, Y. Ito, A. Goto, and T. Hyoudo: "High-efficiency positron moderator with electro-polished tungsten meshes", 9th Int. Workshop on Positron Beam Techniques for Solids and Surfaces, Dresden, Germany, Sept. (2001).
- F. Saito, N. Suzuki, Y. Ito, A. Goto, T. Kurihara, Y. Nagashima, and T. Hyoudo: "Development and application of spin polarized positron beams", Specialist Research Meet. on Positron Beam Techniques

- and Their Applications, Kumatori, Oct. (2001).
- Y. Nagashima, T. Hyoudo, Y. Ito, and A. Goto: "Search for positron annihilation induced characteristic X-rays", Specialist Research Meet. on Positron Beam Techniques and Their Applications, Osaka, Oct. (2001).
- M. Hase, K. Ishioka, K. Ushida, and M. Kitajima: "Dephasing of coherent THz phonons in bismuth studied by femtosecond pump-probe technique", 6th Int. Conf. on Laser Ablation (COLA '01), Tsukuba, Oct. (2001).
- K. Ishioka, M. Hase, K. Ushida, and M. Kitajima: "Femtosecond carrier and phonon dynamics in defective graphite and GaAs", 6th Int. Conf. on Laser Ablation (COLA '01), Tsukuba, Oct. (2001).
4. Radiochemistry, radiation chemistry, and radiation biology
- S. Enomoto: "Dynamics of various trace elements in the body: Approach of physiological metabolism using multitracer technique", 49th Symp. on Coordination Chemistry of Japan, Sapporo, Sept. (1999).
- Y. Oura, S. Enomoto, and H. Nakahara: "Application of prompt  $\gamma$  ray analysis to rats", 43rd Meet. of Radiation Chemical Soc. of Japan, (The Japan Society of Nuclear and Radiochemical Sciences), Tsukuba, Oct. (1999).
- K. Matsumoto, S. Ueda, H. Urata, K. Endo, R. Hirunuma, S. Enomoto, S. Ambe, and F. Ambe: "Distribution of elements in cell fraction of the liver of Se-deficient rats", 43rd Meet. of Radiation Chemical Soc. of Japan, (The Japan Society of Nuclear and Radiochemical Sciences), Tsukuba, Oct. (1999).
- T. Ozaki, Y. Kawamura, S. Ambe, S. Enomoto, Y. Minai, and Y. Makide: "Study on the antagonism between elements and uptake of various elements in plants", 43rd Meet. of Radiation Chemical Soc. of Japan, (The Japan Society of Nuclear and Radiochemical Sciences), Tsukuba, Oct. (1999).
- T. Ohyama, T. Yoshida, M. Iwama, M. Yanaga, M. Noguchi, T. Omori, R. Hirunuma, and S. Enomoto: "Uptake of trace elements in Zn-deficient mice", 43rd Meet. of Radiation Chemical Soc. of Japan, (The Japan Society of Nuclear and Radiochemical Sciences), Tsukuba, Oct. (1999).
- T. Taroda, R. Amano, H. Sakamoto, and S. Enomoto: "Bio-behavior of multitracer in the young mice", 43rd Meet. of Radiation Chemical Soc. of Japan, (The Japan Society of Nuclear and Radiochemical Sciences), Tsukuba, Oct. (1999).
- S. Enomoto, Y. Kawamura, Y. Komatsu, and R. Amano: "Separation of metal ions for multitracer products", 16th Int. Symp. on Separation Chemistry, (National Institute of Research in Inorganic Materials), Tsukuba, Nov. (1999).
- S. Yoshida, M. Masuda, M. Nakayama, M. Yamasaki, S. Enomoto, and H. Morikawa: "Study on the absorption of mineral in the digestive organs", 19th Ann. Meet. Japanese Society of Magnesium Research, Hiroshima, Nov. (1999).
- S. Enomoto and R. Hirunuma: "Fetoplacental transport and metabolism of various trace elements: development of the multitracer technique", RIKEN Symp. on Bio-Trace Elements '99.12, Wako, Dec. (1999).
- T. Taroda, R. Amano, H. Sakamoto, and S. Enomoto: "Biobehavior of multitracers in the brain of young mice", RIKEN Symp. on Bio-Trace Elements '99.12, Wako, Dec. (1999).
- K. Matsumoto, S. Ueda, H. Urata, K. Endo, R. Hirunuma, and S. Enomoto: "Distribution of trace elements in cell fraction of selenium-deficient rat liver", RIKEN Symp. on Bio-Trace Elements '99.12, Wako, Dec. (1999).
- K. Igarashi, Y. Nakanishi, S. Kimura, R. Hirunuma, and S. Enomoto: "Effect of NaFeEDTA on the biodistribution of trace elements in rats", RIKEN Symp. on Bio-Trace Elements '99.12, Wako, Dec. (1999).
- Y. Shiobara, Y. Ogura, K. Suzuki, R. Hirunuma, and S. Enomoto: "Effect of dietary selenium species and dose on the organ distribution of multitracer", RIKEN Symp. on Bio-Trace Elements '99.12, Wako, Dec. (1999).
- H. Suzuki, H. Kumagaya, K. Oohashi, and S. Enomoto: "Influence of Arbuscular mycorrhizal hyphae on absorption of trace elements in plants", RIKEN Symp. on Bio-Trace Elements '99.12, Wako, Dec. (1999).
- Y. Kawamura, T. Ozaki, S. Enomoto, and R. Amano: "Synthesis of organometallic complex using the multitracer technique", RIKEN Symp. on Bio-Trace Elements '99.12, Wako, Dec. (1999).
- T. Yanagiya, S. Enomoto, N. Imura, S. Himeno, and Y. Kondo: "The role of transport system for manganese in cadmium resistance", RIKEN Symp. on Bio-Trace Elements '99.12, Wako, Dec. (1999).
- T. Ohyama, T. Yoshida, H. Maetsu, M. Iwama, M. Yanaga, M. Noguchi, T. Omori, R. Hirunuma, and S. Enomoto: "Uptake of trace elements in Zn-deficient mice", RIKEN Symp. on Bio-Trace Elements '99.12, Wako, Dec. (1999).
- H. Tamano, S. Enomoto, E. Igasaki, N. Oku, N. Itoh, K. Tanaka, and A. Takeda: "Study on hepatic zinc-metallothionein elevated after subcutaneous injection of tumor cells", 120th Ann. Meet. of the Pharmaceutical Soc. of Japan, Gifu, Mar. (2000).
- T. Yanagiya, N. Imura, S. Enomoto, Y. Kondo, and S. Himeno: "Suppression of Mn transport system in Cd-resistant cell line", 120th Ann. Meet. of the Pharmaceutical Soc. of Japan, Gifu, Mar. (2000).
- R. Hirunuma, H. Tamano, Y. Kawamura, Y. Yano, and S. Enomoto: "Transfer of various elements from

- the placenta to the fetus by using the multitracer technique", 120th Ann. Meet. of the Pharmaceutical Soc. of Japan, Gifu, Mar. (2000).
- K. Matsumoto, S. Ueda, H. Urata, K. Endo, R. Hirunuma, and S. Enomoto: "Behavior of trace elements in the liver of Se-deficient rats", 120th Ann. Meet. of the Pharmaceutical Soc. of Japan, Gifu, Mar. (2000).
- S. Yoshida, M. Masuda, M. Nakayama, M. Yamasaki, S. Enomoto, and H. Morikawa: "Study on the intestinal absorption of mineral", 52h Ann. Meet. of Japan Soc. of Obstetrics and Gynecology, Tokushima, Apr. (2000).
- R. Hirunuma, K. Matsumoto, S. Enomoto, and K. Endo: "Behavior of metals in cell fraction of selenium-deficient rat liver", 10th Symp. on the Role of Metals in Biological Reaction, Biology, and Medicine, (The Pharmaceutical Society of Japan), Tokyo, May (2000).
- S. Enomoto, R. Hirunuma, H. Tamano, Y. Kawamura, and Y. Yano: "Biological transport of the various trace elements in the pregnant rats and fetus", 6th Int. Symp. on Metal Ions in Biology and Medicine, (Armed Forces Institute of Pathology), Puerto Rico, USA, May (2000).
- H. Sakurai, H. Yasui, T. Takino, S. Enomoto, and R. Hirunuma: "Treatment of diabetes by vanadium", 11th Ann. Meet. of the Japan Soc. for Biomedical Research on Trace Elements, Nagoya, June (2000).
- S. Enomoto, F. Ambe, and Y. Yano: "Advancement of manufacture technology of multitracer and applied research of multitracer", 13th Seminar on Ion Exchange, (The Japan Society on Ion Exchange), Tokyo, July (2000).
- T. Abe, T. Matsuyama, N. Fukunishi, S. Sekido, and S. Yoshida: "An effective mutation method for plants using heavy-ion beams (II)", 18th Ann. Meet. and Symp. of Japanese Soc. for Plant Cell and Molecular Biology, Shizuoka, July (2000).
- S. Yoshida, M. Masuda, M. Nakayama, M. Yamasaki, S. Enomoto, and H. Morikawa: "Study on the intestinal absorption of divalent cations", 24th Ann. Meet. of the Japan Soc. of Women's Nutrition and Metabolism, Nagoya, Aug. (2000).
- T. Ohyama, M. Yanaga, T. Yoshida, H. Maetsu, M. Noguchi, H. Suganuma, T. Omori, R. Hirunuma, and S. Enomoto: "Characteristic behavior of metals in Zn-deficient mice", 44th Symp. on Radiochemistry, (The Japan Society of Nuclear and Radiochemical Sciences), Kobe, Sept. (2000).
- T. Taroda, Y. Yabushita, R. Amano, T. Nakanishi, and S. Enomoto: "Concentration and uptake-behavior of trace elements in the brain of young mice using instrumental neutron activation analysis and multitracer technique", 44th Symp. on Radiochemistry, (The Japan Society of Nuclear and Radiochemical Sciences), Kobe, Sept. (2000).
- S. Shibata, S. Enomoto, and R. Hirunuma: "Preliminary study of amalgam extracting method of multitracer production", 44th Symp. on Radiochemistry, (The Japan Society of Nuclear and Radiochemical Sciences), Kobe, Sept. (2000).
- Y. Yabushita, Y. Kanayama, T. Kimura, T. Taroda, K. Washiyama, R. Amano, and S. Enomoto: "Element-element interaction in mouse brain under deficient and excessive state of an essential trace element using multitracer technique", 44th Symp. on Radiochemistry, (The Japan Society of Nuclear and Radiochemical Sciences), Kobe, Sept. (2000).
- S. Yoshida, M. Masuda, M. Yamasaki, M. Nakayama, H. Morikawa, R. Hirunuma, and S. Enomoto: "Study on the absorption of divalent cations in the digestive organs", 9th Int. Magnesium Symp. (MAG2000), (The International Society for the Development of Research on Magnesium), Vichy, France, Sept. (2000).
- Y. Gono, Y. Yang, S. Motomura, S. Enomoto, and Y. Yano: "Position identification of gamma-ray sources", Nuclear Science Symp. and Medical Imaging Conf., (IEEE), Lyon, France, Oct. (2000).
- Y. Kobayashi, Y. Yoshida, A. Yoshida, K. Kubo, Y. Yamada, K. Hayakawa, K. Yukihiro, H. Ogawa, H. Ueno, K. Asahi, and F. Ambe: "In-beam Mössbauer study of  $^{57}\text{Fe}$  using a secondary  $^{57}\text{Mn}$  beam and ion implantation", Int. Symp. on Perspectives in Physics with Radioactive Isotope Beams 2000 (RIB00), (RIKEN and Center for Nuclear Study, University of Tokyo), Hayama, Nov. (2000).
- S. Yoshida, M. Masuda, M. Nakayama, M. Yamasaki, S. Enomoto, and H. Morikawa: "Study on the intestinal absorption of divalent cations in the digestive organs", 37th Ann. Meet. of Japanese Society of Applied Physiology, Nara, Nov. (2000).
- S. Enomoto: "Biological transport of the various trace elements in pregnant rats and tetuses", Int. Chemical Congr. of Pacific Basin Soc. (PACIFICHEM 2000), Honolulu, USA, Dec. (2000).
- K. Matsumoto, R. Hirunuma, S. Enomoto, and K. Endo: "Contents and uptakes of Mn, Fe, Co, Zn, and Se in Se-deficient rat liver cell-fractions by instrumental neutron activation analysis and multitracer technique", Int. Chemical Congr. of Pacific Basin Soc. (PACIFICHEM 2000), Honolulu, USA, Dec. (2000).
- T. Ohyama, T. Yoshida, M. Yanaga, M. Noguchi, H. Suganuma, T. Omori, R. Hirunuma, and S. Enomoto: "Effects of Zn-deficiency to uptakes of trace elements", Int. Chemical Congr. of Pacific Basin Soc. (PACIFICHEM 2000), Honolulu, USA, Dec. (2000).
- Y. Kobayashi, K. Kubo, Y. Yamada, A. Yoshida, H. Ogawa, K. Asahi, and F. Ambe: "In-beam Mössbauer studies of  $^{57}\text{Fe}$  ions arising from  $^{57}\text{Mn}$  implanted into  $\text{KMnO}_4$ ", Int. Chemical Congr. of

- Pacific Basin Soc. (PACIFICHEM 2000), Honolulu, USA, Dec. (2000).
- K. Matsumoto, N. Sotogaku, R. Hirunuma, S. Enomoto, S. Ambe, and F. Anibe: "Multitracer study on complex formation of lanthanide ions with bovine serum albumin and transferrin", Int. Chemical Congr. of Pacific Basin Soc. (PACIFICHEM 2000), Honolulu, USA, Dec. (2000).
- Y. Kawamura, S. Komatsu, S. Umetani, S. Tsurubou, A. Hokura, S. Enomoto, and R. Amano: "Separation of alkaline earth metal ions by solvent extraction method combined with inorganic ion-exchange system", Int. Chemical Congr. of Pacific Basin Soc. (PACIFICHEM 2000), Honolulu, USA, Dec. (2000).
- A. Nakayama, H. Yasui, R. Hirunuma, S. Enomoto, and H. Sakurai: "Distribution of multitracer elements in rats partially hepatectomized", RIKEN Symp. on Bio-Trace Elements 2000, Wako, Dec. (2000).
- Y. Yabushita, Y. Kanayama, T. Taroda, K. Washiyama, R. Amano, and S. Enomoto: "Element-element interaction in mouse brain under deficient and excessive state of an essential trace element", RIKEN Symp. on Bio-Trace Elements 2000, Wako, Dec. (2000).
- T. Taroda, Y. Yabushita, Y. Kanayama, R. Amano, and S. Enomoto: "Elemental concentration and tracer uptake behavior of manganese, zinc and selenium in the brain of normal mice during development", RIKEN Symp. on Bio-Trace Elements 2000, Wako, Dec. (2000).
- S. Enomoto and R. Hirunuma: "Fetoplacental transport of the various trace elements in the pregnant rat by using the multitracer technique", RIKEN Symp. on Bio-Trace Elements 2000, Wako, Dec. (2000).
- J. Furukawa, R. Hirunuma, S. Enomoto, and T. Nakanishi: "Measurement of the affinity for binding of various metal elements with plant apoplast protein in root tip", RIKEN Symp. on Bio-Trace Elements 2000, Wako, Dec. (2000).
- S. Shibata, S. Enomoto, and R. Hirunuma: "Preliminary study of amalgam extracting method for production of multitracer", RIKEN Symp. on Bio-Trace Elements 2000, Wako, Dec. (2000).
- T. Yanagiya, N. Imura, S. Enomoto, Y. Kondo, and S. Himeno: "Reduction of cadmium toxicity by manganese", RIKEN Symp. on Bio-Trace Elements 2000, Wako, Dec. (2000).
- T. Ohyama, T. Yoshida, H. Maetsu, M. Noguchi, H. Suganuma, R. Hirunuma, S. Enomoto, M. Yanaga, and T. Omori: "Specific cobalt metabolism under Zn-deficient state", RIKEN Symp. on Bio-Trace Elements 2000, Wako, Dec. (2000).
- S. Yoshida, M. Masuda, M. Yamasaki, M. Nakayama, H. Morikawa, R. Hirunuma, and S. Enomoto: "Study on the absorption of divalent cations in the digestive organs", RIKEN Symp. on Bio-Trace Elements 2000, Wako, Dec. (2000).
- T. Nabekura, T. Minami, R. Hirunuma, S. Enomoto, and Y. Ito: "Uptake of trace elements in adult and suckling rat lens", RIKEN Symp. on Bio-Trace Elements 2000, Wako, Dec. (2000).
- Y. Oura, S. Enomoto, and H. Nakahara: "Application of prompt gamma ray analysis to biological samples", RIKEN Symp. on Bio-Trace Elements 2000, Wako, Dec. (2000).
- R. Hirunuma and S. Enomoto: "Application of the multitracer technique: Effect of selenium on the distribution of trace elements in rat", RIKEN Symp. on Bio-Trace Elements 2000, Wako, Dec. (2000).
- K. Igarashi, A. Sasaki, Y. Yoda, H. Image, Y. Nakanishi, R. Hirunuma, S. Enomoto, and S. Kimura: "Effect of sodium iron EDTA on the absorption and the distribution of trace elements in anemic rats", RIKEN Symp. on Bio-Trace Elements 2000, Wako, Dec. (2000).
- K. Matsumoto, R. Hirunuma, S. Enomoto, and K. Endo: "Evaluation of in vivo oxidative stress in liver of selenium-deficient rat", RIKEN Symp. on Bio-Trace Elements 2000, Wako, Dec. (2000).
- H. Suzuki, H. Kumagaya, F. Mori, K. Sakamoto, K. Inubushi, and S. Enomoto: "Influence of lanthanum on the uptake of various elements by marigold", RIKEN Symp. on Bio-Trace Elements 2000, Wako, Dec. (2000).
- R. Amano, T. Tsuji, T. Taroda, K. Washiyama, and S. Enomoto: "Isolation and purification of  $^{95m}\text{Tc}$  and  $^{96}\text{Tc}$  in the distilled waste fraction during chemical separation of multitracer from Ag target", RIKEN Symp. on Bio-Trace Elements 2000, Wako, Dec. (2000).
- C. Egawa, Y. Takahashi, S. Enomoto, R. Hirunuma, and H. Shimizu: "Multitracer study on the diffusion of various ions through the porewater of granite", RIKEN Symp. on Bio-Trace Elements 2000, Wako, Dec. (2000).
- H. Tamano, S. Enomoto, R. Hirunuma, and A. Takeda: "Uptake of radioactive elements in rat brain tumor", RIKEN Symp. on Bio-Trace Elements 2000, Wako, Dec. (2000).
- F. Yatagai, T. Nohmi, and M. Kusakabe: "Mutation induction by heavy-ion of gpt $\Delta$  transgenic mice: effect of p53 gene knockout", 17th Symp. on Space Utilization Research, (The Institute of Space and Astronautical Science), Sagamihara, Jan. (2001).
- R. Hirunuma and S. Enomoto: "Analysis of metals in various organs of Se-deficient rats", 9th Symp. on Research Center for Nuclear Science and Technology in University of Tokyo, Tokyo, Jan. (2001).
- Y. Kobayashi: "Applications of  $^{57}\text{Mn}/^{57}\text{Fe}$  Mössbauer spectroscopy to chemistry", RIKEN Symp. on Studies on Condensed Matter Physics, Atomic Physics, Hyperfine Interactions and Biomedical Sciences Using RIKEN Accelerators, Wako, Feb. (2001).

- T. Matsuyama, T. Abe, R. Kiuchi, T. Nakano, T. Asami, and S. Yoshida: "Profiling of RLGS patterns using DNA sequences in Arabidopsis genomes", 2001 Ann. Meet. of Japan Soc. for Bioscience: Biotechnology and Agrochemistry, Kyoto, Mar. (2001).
- Y. Konomi, T. Abe, K. Sekino, H. Koyanagi, Y. Yamada, F. Sugawara, and S. Yoshida: "Benzobicyclon resistance using heavy ion-beam mutagenesis", 26th Ann. Meet. of Pesticide Science Soc. of Japan, Sakai, Mar. (2001).
- M. Hase, K. Ishioka, M. Kitajima, and K. Ushida: "Effect of lattice defects on generation and relaxation of coherent phonons in n-GaAs", 56th Ann. Meet. of Physical Soc. of Japan, Hachioji, Mar. (2001).
- K. Ishioka, M. Hase, M. Kitajima, and K. Ushida: "Effect of defects on carrier and phonon dynamics in graphite", 56th Ann. Meet. of Physical Soc. of Japan, Hachioji, Mar. (2001).
- Y. Yoshida, A. Saeki, T. Kozawa, S. Seki, K. Ushida, and S. Tagawa: "Geminate ion recombination in liquid alkane studied by subpicosecond pulse radiolysis", 79th Natl. Meet. of the Chemical Soc. of Japan, Kobe, Mar. (2001).
- K. Takahashi, S. Enomoto, T. Minami, T. Nakagawa, M. Kidera, and Y. Yano: "Chemical and mineralogical studies on natural cinnabar ore and the samples from ancient tomb", RIKEN Symp. on Research for Cinnabar from Ancient Tomb, Wako, Mar. (2001).
- M. Kidera, T. Nakagawa, S. Enomoto, K. Takahashi, T. Minami, M. Fujimaki, E. Ikezawa, O. Kanigaito, M. Kase, A. Goto, and Y. Yano: "Trace elements analysis and isotope search using the electron cyclotron resonance ion source", RIKEN Symp. on Research for Cinnabar from Ancient Tomb, Wako, Mar. (2001).
- H. Tamano, M. Hirate, R. Hirunuma, S. Enomoto, N. Oku, and A. Takeda: "Behavior of bio-trace elements in El (epilepsy) rat brain", 121st Ann. Meet. of the Pharmaceutical Soc. of Japan, Sapporo, Mar. (2001).
- T. Nabekura, T. Minami, R. Hirunuma, S. Enomoto, and Y. Ito: "Behavior of uptake of bio-trace elements in adult and suckling rat lenses", 121st Ann. Meet. of the Pharmaceutical Soc. of Japan, Sapporo, Mar. (2001).
- H. Tamano, M. Hirate, R. Hirunuma, S. Enomoto, N. Oku, and A. Takeda: "Distribution of trace elements in the brain of El (epilepsy) mice", 121st Ann. Meet. of the Pharmaceutical Soc. of Japan, Sapporo, Mar. (2001).
- R. Hirunuma and S. Enomoto: "Study of the uptake of trace elements in Se-excessive rats using the multitracer technique", 121st Ann. Meet. of the Pharmaceutical Soc. of Japan, Sapporo, Mar. (2001).
- K. Matsumoto, I. Ui, R. Hirunuma, S. Enomoto, and K. Endo: "In vivo evaluation of behavior of bio-trace elements in rats using the multitracer technique", 121st Ann. Meet. of the Pharmaceutical Soc. of Japan, Sapporo, Mar. (2001).
- M. Kitajima, M. Hase, K. Ishioka, and K. Ushida: "Coherent phonons and the effect of lattice defects in solids", 48th Spring Meet. 2001 of The Japan Soc. of Applied Physics and Related Soc., Tokyo, Mar. (2001).
- Y. Kobayashi: "Exotic valence states of  $^{57}\text{Fe}$  arising from  $^{57}\text{Mn}$ ", Workshop on Science with Low-Energy Short-lived Nuclear Beam, (KEK), Tsukuba, Mar. (2001).
- M. Hamatani, T. Abe, K. Miyoshi, M. Yamamoto, and S. Yoshida: "Flower mutants of dahlia (*Dahlia pinnata* Cav.) induced by heavy-ion beams", 99th Congr. of the Breeding Soc. of Japan, Fujisawa, Apr. (2001).
- S. Morimoto, S. Goto, T. Kato, M. Izumi, M. Komiyama, N. Fukunishi, M. Honma, F. Hanaoka, and F. Yatagai: "Cellular responses to low dose heavy-ion exposure in human cell", 13th Symp. on Microdosimetry (MICROS 2001), (INFN-Laboratori Nazionali di Legnaro and Sezione INFN di Milano), Stresa, Italy, May-June (2001).
- F. Yatagai, S. Morimoto, S. Goto, T. Kato, M. Honma, and F. Hanaoka: "Mutation induction in human cell after low-dose X-ray exposure", 13th Symp. on Microdosimetry (MICROS 2001), (INFN-Laboratori Nazionali di Legnaro and Sezione INFN di Milano), Stresa, Italy, May-June (2001).
- S. Enomoto: "Research proposal for RIBF Project from viewpoint of Multitrace Technology", Nuclear Crossover Research: 2001 Workshop on Radiation Damage Repair and Multitracer Application, Kanazawa, May (2001).
- F. Yatagai: "Research proposal for RIBF Project from viewpoint of Radiation Biology Effects", Nuclear Crossover Research: 2001 Workshop on Radiation Damage Repair and Multitracer Application, Kanazawa, May (2001).
- R. Hirunuma and S. Enomoto: "Study of the uptake of bio-trace elements in Se-excessive rats", 18th Symp. of Trace Nutrients Research, Kyoto, May (2001).
- K. Ishioka, M. Hase, K. Ushida, and M. Kitajima: "Coherent acoustic phonon in ion-irradiated graphite", 10th Int. Conf. on Time-resolved Vibrational Spectroscopy, Okazaki, May (2001).
- T. Abe, K. Sekino, T. Matsuyama, Y. Konomi, H. Koyanagi, Y. Yamada, F. Sugawara, and S. Yoshida: "Heavy ion-beam mutagenesis for benzobicyclon resistant plants", 17th Int. Conf. on Plant Growth Substances (IPGSA 2001), (Mendel University of Agriculture and Forestry), Brno, Czech Republic, June (2001).
- F. Yatagai, S. Morimoto, T. Kato, M. Honma, and F. Hanaoka: "Change in pattern of LOH on chromosome 17q after 10 cGy of X-ray exposure", DOE/NASA Radiation Investigators' Work-

- shop, Washington, D.C., USA, June (2001).
- K. Suzuki, Y. Yomo, T. Abe, Y. Katsumoto, S. Yoshida, and T. Kusumi: "Isolation of sterile mutants of *Verbena hybrida* using heavy-ion beams irradiation", 19th Ann. Meet. and Symp. of Japanese Soc. for Plant Cell and Molecular Biology, Tokyo, July (2001).
- K. Miyazaki, K. Suzuki, T. Abe, S. Yoshida, and T. Kusumi: "Isolation of variegated mutants of *Petunia hybrida* using heavy-ion beams irradiation", 19th Ann. Meet. and Symp. of Japanese Soc. for Plant Cell and Molecular Biology, Tokyo, July (2001).
- T. Abe, T. Matsuyama, S. Yoshida, N. Fukunishi, and Y. Yano: "New method of plant mutagenesis using heavy-ion beams", 19th Ann. Meet. and Symp. of Japanese Soc. for Plant Cell and Molecular Biology, Tokyo, July (2001).
- T. Matsuyama, T. Abe, K. Koike, T. Ebisuzaki, and S. Yoshida: "Analysis of mutants induced by radiation using RLGS-simulation pattern", 19th Ann. Meet. and Symp. of Japanese Soc. of Plant Cell and Molecular Biology, Tokyo, July (2001).
- T. Abe and N. Fukunishi: "Ion-beam mutagenesis research in RARF", 40th Gamma Field Symp., Tsukuba, July (2001).
- S. Goto, S. Morimoto, T. Kurobe, M. Izumi, N. Fukunishi, M. Watanabe, and F. Yatagai: "Delayed cell-cycle arrest following heavy-ion exposure", Int. Symp. on Radiation and Homeostasis, (Health Research Foundation), Kyoto, July (2001).
- T. Ohyama, H. Maetsu, M. Noguchi, H. Suganuma, R. Hirunuma, S. Enomoto, M. Yanaga, and T. Omori: "Abnormal metabolisms in trace elements under the Zn-deficient condition", 12th Ann. Meet. of the Japan Soc. for Biomedical Research on Trace Elements, Tokyo, July (2001).
- S. Enomoto, T. Yanagiya, R. Hirunuma, and R. Amano: "Multitracer gamma-ray emission imaging (MT-GEI): A new detection system for multitracer", 12th Ann. Meet. of the Japan Soc. for Biomedical Research on Trace Elements, Tokyo, July (2001).
- R. Hirunuma and S. Enomoto: "Study on development of new trace elements analytical system using the electron cyclotron resonance ion source and heavy ion linear accelerator", 12th Ann. Meet. of the Japan Soc. for Biomedical Research on Trace Elements, Tokyo, July (2001).
- H. Tamano, A. Takeda, N. Oku, S. Enomoto, and R. Hirunuma: "Uptake of various elements in rat brain tumor", 12th Ann. Meet. of the Japan Soc. for Biomedical Research on Trace Elements, Tokyo, July (2001).
- J. Furukawa, R. Hirunuma, S. Enomoto, and T. Nakanishi: "A study of multitracer to measure the binding affinity to an apoplast protein of the root in the presence of Al", IUPAC Int. Congr. on Analytical Sciences 2001, (Japan Society for Analytical Chemistry), Tokyo, Aug. (2001).
- Y. Takahashi, Y. Minai, and S. Enomoto: "Application of multitracer technique for environmental and geochemical studies", IUPAC Int. Congr. on Analytical Sciences 2001, (Japan Society for Analytical Chemistry), Tokyo, Aug. (2001).
- R. Hirunuma and S. Enomoto: "Application of the multitracer technique: Metabolic study of various elements in Se-deficient and Se-excessive rats", IUPAC Int. Congr. on Analytical Sciences 2001, (Japan Society for Analytical Chemistry), Tokyo, Aug. (2001).
- K. Matsumoto, R. Hirunuma, S. Enomoto, and K. Endo: "In vivo detection of dynamics elements in a living rat using multitracer technique", IUPAC Int. Congr. on Analytical Sciences 2001, (Japan Society for Analytical Chemistry), Tokyo, Aug. (2001).
- S. Enomoto: "The multitracer technique: Manufacturing and application to bio-trace elemental research", IUPAC Int. Congr. on Analytical Sciences 2001, (Japan Society for Analytical Chemistry), Tokyo, Aug. (2001).
- T. Ohyama, M. Kidera, T. Nakagawa, K. Takahashi, K. Igarashi, R. Hirunuma, and S. Enomoto: "Accelerator mass spectrometry using electron cyclotron resonance ion source (Application study for analysis of trace elements)", 12th Chalk Talk (Meet. for Organism and Trace Elements), (University of Shizuoka), Shizuoka, Aug. (2001).
- T. Abe, T. Matsuyama, and S. Yoshida: "Genome Analysis of plant mutants induced by ion-beam irradiation using RLGS profiles", 8th Seminar of Accelerator and Related Technology for Application, Tokyo, Sept. (2001).
- Y. Kobayashi, K. Kubo, Y. Yamada, T. Saito, A. Yoshida, H. Ogawa, H. Ueno, and K. Asahi: "In-beam Mössbauer study of  $^{57}\text{Fe}$  species arising from  $^{57}\text{Mn}$  implanted into  $\text{KMnO}_4$ ", Int. Conf. on the Applications of the Mössbauer Effect (ICAME2001), Oxford, UK, Sept. (2001).
- F. Yatagai, S. Goto, S. Morimoto, and T. Kato: "Estimation for biological effects of heavy-ion exposure in space", 15th Ann. Meet. of Japanese Soc. for Biological Sciences in Space, Tokyo, Sept. (2001).
- T. Takanami, H. Takahashi, T. Abe, S. Yoshida, and A. Higashitani: "Repair systems for DNA damage by heavy-ion irradiation in meiotic cells", 15th Ann. Meet. of Japanese Soc. for Biological Sciences in Space, Tokyo, Sept. (2001).
- H. Nagase, F. Ike, N. Hiraiwa, and A. Yoshiki: "An attempt to screen cancer susceptibility loci by introducing germline mutation using heavy ion beams", 60th Ann. Meet. of the Japanese Cancer Association, Yokohama, Sept. (2001).
- H. Tsujimoto, M. Kishii, T. Yamada, and T. Abe: "Molecular cytogenetic analysis of chromosome breakage in wheat induced by heavy ion-beam irradiation", 73rd Ann. Meet. of the Genetics Soc. of

- Japan, Tokyo, Sept. (2001).
- T. Matsuyama: "RLGS analysis in plant mutants induced by physical mutagens and virtual RLGS profiling", 100th Congr. of the Breeding Soc. of Japan, Fukuoka, Oct.–Nov. (2001).
- K. Matsumoto, H. Nagashima, R. Hirunuma, S. Enomoto, and K. Endo: "Affinity of various bio-trace elements to lipid membrane: *In vitro* study using multitracer", 2001 Asia-Pacific Symp. on Radiochemistry and Ann. Meet. of the Japan Soc. of Nuclear and Radiochemical Sciences (APSORC 2001 and 45th SORC), Fukuoka, Oct.–Nov. (2001).
- T. Saito, Y. Kobayashi, K. Kubo, and Y. Yamada: "Development and application of Parallel-Plate Avalanche Counter for in-beam Mössbauer spectroscopy", 2001 Asia-Pacific Symp. on Radiochemistry and Ann. Meet. of the Japan Soc. of Nuclear and Radiochemical Sciences (APSORC 2001 and 45th SORC), Fukuoka, Oct. Nov. (2001).
- Y. Kobayashi, K. Kubo, Y. Sakai, Y. Yamada, T. Saito, H. Shoji, C. Yonezawa, and H. Matsue: "In-beam Mössbauer spectroscopic studies of chemical effects associated with the  $^{56}\text{Fe}(n,\gamma)^{57}\text{Fe}$  reaction", 2001 Asia-Pacific Symp. on Radiochemistry and Ann. Meet. of the Japan Soc. of Nuclear and Radiochemical Sciences (APSORC 2001 and 45th SORC), Fukuoka, Oct.–Nov. (2001).
- Y. Yabushita, Y. Kanayama, T. Tarohda, R. Amano, and S. Enomoto: "Multitracer and neutron activation screening: Brain regional concentration and tracer uptake behavior in mice bred under controlled diets", 2001 Asia-Pacific Symp. on Radiochemistry and Ann. Meet. of the Japan Soc. of Nuclear and Radiochemical Sciences (APSORC 2001 and 45th SORC), Fukuoka, Oct.–Nov. (2001).
- T. Ohyama, M. Yanaga, H. Maetsu, M. Noguuchi, H. Saganuma, K. Ishikawa, M. Kidera, T. Nakagawa, R. Hirunuma, S. Enomoto, and T. Omori: "The abnormal metabolism of trace elements in mouse induced by Zn deficiency during the growing period", 2001 Asia-Pacific Symp. on Radiochemistry and Ann. Meet. of the Japan Soc. of Nuclear and Radiochemical Sciences (APSORC 2001 and 45th SORC), Fukuoka, Oct.–Nov. (2001).
- Y. Kobayashi, K. Kubo, T. Saito, H. Ueno, H. Miyoshi, K. Yoneda, W. Sato, and Y. Yamada: "Valence states of  $^{57}\text{Fe}$  decayed from  $^{57}\text{Mn}$  implanted into  $\text{KMnO}_4$ ", 2001 Asia-Pacific Symp. on Radiochemistry and Ann. Meet. of the Japan Soc. of Nuclear and Radiochemical Sciences (APSORC 2001 and 45th SORC), Fukuoka, Oct.–Nov. (2001).
- K. Matsumoto, I. Ui, R. Hirunuma, S. Enomoto, and K. Endo: "*In vivo* assessment of dynamics of various elements living rat using multitracer", 2001 Asia-Pacific Symp. on Radiochemistry and Ann. Meet. of the Japan Soc. of Nuclear and Radiochemical Sciences (APSORC 2001 and 45th SORC), Fukuoka, Oct.–Nov. (2001).
- S. Morimoto, T. Kato, M. Honma, S. Goto, M. Izumi, F. Hanaoka, and F. Yatagai: "Analysis of *tk* mutation induced by low dose ionizing radiation in human cells", 44th Ann. Meet. of the Japan Radiation Research Society, Osaka, Oct. (2001).
- F. Yatagai, S. Goto, S. Morimoto, T. Kato, F. Hanaoka, and Y. Yano: "Cellular responses after heavy-ion exposure", 44th Ann. Meet. of the Japan Radiation Research Society, Osaka, Oct. (2001).
- M. Hoshino, K. Masumura, F. Yatagai, M. Ochiai, O. Ueda, H. Suzuki, H. Nakagama, M. Fukuoka, and T. Nomi: "X-ray-induced mutations in the brain and the spleen of *gpt* delta transgenic mouse", 8th Int. Conf. on Environmental Mutagens, Shizuoka, Oct. (2001).
- Y. Kobayashi: "Valence states of  $^{57}\text{Fe}$  atoms arising from  $^{57}\text{Mn}$  implanted into  $\text{KMnO}_4$ ", Specialist Research Meet. on Positron Beam Techniques and Condensed Matter. (Research Reactor Institute, Kyoto University), Kumatori, Oct. (2001).
- T. Abe: "A new method for mutation induction by heavy-ion irradiation on plants", 100th Meet. of the Japanese Society of Breeding, Fukuoka, Oct. (2001).
- Y. Konomi, T. Abe, K. Sekino, H. Koyanagi, Y. Yamada, F. Sugawara, and S. Yoshida: "Benzobicyclon resistant tobacco using heavy ion-beam mutagenesis", 36th Ann. Meet. of the Japanese Society for the Chemical Regulation of Plants, Toyama, Oct. (2001).
- T. Matsuyama, K. Koike, T. Ebisuzaki, T. Abe, and S. Yoshida: "A DNA polymorphism detection system by computer simulation using the Arabidopsis genome sequences—a virtual imaging restriction landmark genomic scanning", 10th DNA Polymorphism, Okayama, Nov. (2001).
- S. Morimoto, S. Goto, T. Kato, M. Honma, F. Hanaoka, and F. Yatagai: "Genetic Alteration in human cell after low-dose IR exposure", 18th Radiation Biology Center Int. Symp. on Bioregulation of Radiation Response: Damage Recognition, Processing and Cellular Response, (Radiation Biology Center, Kyoto University), Kyoto, Nov. (2001).
- T. Abe, T. Matsuyama, and S. Yoshida: "Induction of mutation in plants using ion-beam irradiation", 9th Radiation Process Symp., Tokyo, Dec. (2001).

## 5. Material analysis

- K. Maeda, K. Hasegawa, and H. Hamanaka: "Chemical specification by high-resolution PIXE", 1st Sino-Japanese Seminar on Application of Acceleration Radiation, (National Science Council Taiwan), Hsinchu, Taiwan, Dec. (2000).
- K. Maeda, K. Hasegawa, H. Hamanaka, M. Maeda, S. Yabuki, and K. Ogiwara: "Rapid chemical state analysis by a highly sensitive high-resolution PIXE

- system”, 15th Int. Conf. on Ion Beam Analysis, (The Australian National University), Cairns, Australia, July (2001).
- J. Kawai, Y. Fukuda, J. Kawamura, and K. Maeda: “PK $\beta$  X-ray fluorescence spectrum of B<sub>13</sub>P<sub>2</sub>”, 50th Ann. Meet. of the Japan Soc. for Analytical Chemistry, Kumamoto, Nov. (2001).
- H. Hamanaka, K. Maeda, K. Hasegawa, and S. Yumoto: “Chemical state analysis of Al compounds using a crystal spectrometer in PIXE measurements (sample positioning using a laser displacement sensor)”, 18th PIXE Symp., (The Japan Society for Particle Induced X-ray Emission (PIXE) Research), Chiba, Nov. (2001).
- K. Maeda, K. Hasegawa, H. Hamanaka, and M. Maeda: “Improvement in the sensitivity of in-air high-resolution PIXE”, 18th PIXE Symp., (The Japan Society for Particle Induced X-ray Emission (PIXE) Research), Chiba, Nov. (2001).
- H. Hamanaka, K. Hasegawa, and K. Maeda: “Sample positioning using a laser displacement sensor in high-resolution PIXE with a position sensitive crystal spectrometer”, 20th Symp. on Materials Science and Engineering, (Research Center of Ion Beam Technology, Hosei University), Koganei, Dec. (2001).
- ## 6. RIKEN-BNL Collaboration on Spin Physics Program
- W. Vogelsang: “Current issues in prompt photon production”, 8th Int. Workshop on Deep-Inelastic Scattering (DIS 2000), Liverpool, UK, Apr. (2000).
- W. Vogelsang: “Prompt photon production in polarized hadron collisions”, 8th Int. Workshop on Deep-Inelastic Scattering (DIS 2000), Liverpool, UK, Apr. (2000).
- W. Vogelsang: “Spin asymmetries in polarized hadron collisions and the polarized gluon density”, 7th Conf. on Intersections of Particle and Nuclear Physics (CIPANP2000), Québec, Canada, May (2000).
- E. Laenen, G. Sterman, and W. Vogelsang: “Combined recoil and threshold resummation for hard scattering cross sections”, 30th Int. Conf. on High Energy Physics (ICHEP 2000), Osaka, July-Aug. (2000).
- E. Laenen, G. Sterman, and W. Vogelsang: “Power corrections in eikonal cross sections”, 30th Int. Conf. on High Energy Physics (ICHEP 2000), Osaka, July-Aug. (2000).
- D. Son: “Hydrodynamics of relativistic systems with broken continuous symmetries”, Meet. of the Division of Particle and Fields of the Am. Phys. Soc. (DPF2000), (APS), Columbus, USA, Aug. (2000).
- J. Murata, N. Saito, T. Shibata, and M. Sugioka: “Construction of the PHENIX south arm muon tracking chamber”, 55th Ann. Meet. of Physical Soc. of Japan, Niigata, Sept. (2000).
- S. Yokkaichi, T. Ichihara, H. En’yo, Y. Goto, S. Sawada, A. Taketani, N. Hayashi, H. Hamagaki, and Y. Watanabe: “PHENIX computing center in Japan (CC-J): Open and operating status”, 55th Ann. Meet. of Physical Soc. of Japan, Niigata, Sept. (2000).
- W. Vogelsang: “Nucleon spin structure functions”, 14th Int. Spin Physics Symp. (SPIN 2000), (RCNP, Osaka University), Suita, Oct. (2000).
- D. Son: “Electroweak matter”, 2000 Fall Meet. of the Division of Nuclear Physics, (ADS), Williamsburg, USA, Oct. (2000).
- H. Kobayashi: “Polarized parton distributions with estimate of uncertainties”, Int. Workshop on Polarized Partons at High Q<sup>2</sup> Region, Kyoto, Oct. (2000).
- J. Murata: “Beyond standard model at RHIC”, Int. Workshop on Polarized Partons at High Q<sup>2</sup> Region, (Yukawa Institute for Theoretical Physics, Kyoto University), Kyoto, Oct. (2000).
- W. Vogelsang: “Soft-gluon effects in prompt-photon production”, RSC Meet., Kyoto, Oct. (2000).
- K. Itakura: “Gluon saturation from non-linear evolution equation at small x”, Kenkyukai “Ba no Ryoshiron no Kisoteki Shomondai to Oyo”, (Yukawa Institute for Theoretical Physics, Kyoto University), Kyoto, Dec. (2000).
- Y. Watanabe: “Regional computing center in Japan for RHIC/PHENIX Experiment”, ICEPP Seminar 2001, (International Elementary Particle Physics, University of Tokyo), Tokyo, Jan. (2001).
- N. Ishii, H. Suganuma, and H. Matsufuru: “Glueball properties in anisotropic SU(3) lattice QCD with an improved action”, Workshop on Lepton Scattering, Hadrons and QCD, (The Special Research Center for the Subatomic Structure of Matter and the National Institute for Theoretical Physics), Adelaide, Australia, Mar.-Apr. (2001).
- M. Hirai: “Determination of polarized parton distribution at RHIC”, RCNP Workshop on Hadron Structure and Reaction by Non-Perturbative QCD Approach, (RCNP and ISIR, Osaka University), Osaka, July (2001).
- N. Ishii, H. Suganuma, and H. Matsufuru: “Glueball properties at finite temperature”, RCNP Workshop on Hadron Structure and Reaction by Non-Perturbative QCD Approach, (RCNP and ISIR, Osaka University), Osaka, July (2001).
- N. Ishii, H. Suganuma, and H. Matsufuru: “Glueball properties at finite temperature”, LATTICE2001: 19th Int. Symp. on Lattice Field Theory, (DESY Zeuthen), Berlin, Germany, Aug. (2001).
- S. Yokkaichi, T. Ichihara, Y. Watanabe, N. Hayashi, S. Sawada, Y. Goto, O. Jinnouchi, H. Hamagaki, and H. En’yo: “The RIKEN CCJ (computing center in Japan) for RHIC physics”, Int. Conf. on Computing in High Energy and Nuclear Physics (CHEP 2001), Beijing, China, Sept. (2001).

H. Kobayashi: "Alignment and calibration of the PHENIX muon tracker", 1st Joint Meet. of the Nuclear Physics Divisions of APS and JPS Hawaii 2001 (HAW01), (American Physical Society), Maui, USA, Oct. (2001).

N. Ishii, H. Sugauma, and H. Matsufuru: "Glueball properties at finite temperature", 1st Joint Meet.

of the Nuclear Physics Divisions of APS and JPS Hawaii 2001 (HAW01), Maui, USA, Oct. (2001).

M. Hirai: "Uncertainty of polarized parton distributions", 3rd Circum-Pan-Pacific Symp. on High Energy Spin Physics, (Peking University), Beijing, China, Oct. (2001).

## X. LIST OF SYMPOSIA

(Jan.–Dec. 2001)

- 1) 11th RIKEN Winter School on In-beam Gamma-ray Spectroscopy with RI Beams  
8–13 Jan., Niigata, RI Beam Science Lab., RIKEN
- 2) RIKEN Workshop on Approaches to the Structure of Unstable Nuclei in the Mean Field Models  
17–19 Jan., Wako, RI Beam Science Lab., RIKEN
- 3) RIKEN Symp. on Physics at Drip Lines  
13–16 Feb., Wako, RI Beam Science Lab., RIKEN
- 4) RBRC Workshop on RHIC Spin Physics V  
21 Feb., New York, USA, RBRC, RIKEN
- 5) Int. Workshop on Radiation Damage 2001: Repair, Mutagenesis, and Visualization  
14–16 Mar., Tokyo, Radioisotope Technology Div., Cellular Physiology Lab., RIKEN and Promotion Committee on Nuclear Cross-Over Research
- 6) RIKEN Workshop on Towards Physics of Unstable Nuclei  
24–26 Mar., Wako, RI Beam Science Lab., RIKEN
- 7) Muon Catalyzed Fusion and Related Exotic Atoms  
22–26 Apr., Shimoda, Muon Science Lab., RIKEN
- 8) RIKEN Workshop on Alpha-particle Condensation and Two-neutron Condensation in the Neutron-rich Nuclei ( $N \gg Z$ )  
1–3 May, Wako, RI Beam Science Lab., RIKEN
- 9) RBRC Workshop on Spin Physics at RHIC in Year-1 and Beyond  
14–18 May, New York, USA, RBRC, RIKEN
- 10) RBRC Workshop on High Energy QCD: Beyond the Pomeron  
21–25 May, New York, USA, RBRC, RIKEN
- 11) RIKEN Workshop on Cluster Physics and Unstable Nuclei  
30 Aug.–1 Sept., Wako, RI Beam Science Lab., RIKEN
- 12) 4th Italy-Japan Symp. on Heavy Ion Physics  
26–29 Sept., Wako, Tokyo, RI Beam Science Lab., RIKEN
- 13)  $\mu$ SR Studies at RIKEN-RAL  
1 Oct., Wako, Muon Science Lab., RIKEN
- 14) RBRC Workshop on RHIC Spin Physics VI  
1 Oct., New York, USA, RBRC, RIKEN
- 15) RIBF Nuclear Astrophysics Workshop (I) on Pigmy Resonances and the r-Process  
6 Oct., Wako, RI Beam Science Lab., RIKEN
- 16) Workshop on Cyclotron Mutagenesis  
8 Oct., Fukuoka, Plant Functions Lab., RIKEN and Japanese Society of Breeding
- 17) RBRC Workshop on RHIC Spin Physics VI Part-2  
15 Nov., New York, USA, RBRC, RIKEN

- 18) Physics with Primary Beams of 400 MeV/u at RIBF  
28-29 Nov., Wako, RI Beam Science Lab., RIKEN
- 19) RIBF Nuclear Astrophysics Workshop (II) on Stellar Electron Capture and Supernovae  
10-11 Dec., Wako, RI Beam Science Lab., RIKEN
- 20) Int. Workshop on Developments of Ge Detector Array and Frontiers of Gamma-ray Spectroscopy  
11-13 Dec., Wako and Tokyo, RI Beam Science Lab., RIKEN, CNS, and Rikkyo University
- 21) Development and Application of the Multitracer Technique  
21 Dec., Wako, Cyclotron Center, RIKEN

## XI. LIST OF SEMINARS

(Jan.–Dec. 2001)

Radiation Lab., RI Beam Science Lab., Applied Nuclear Physics Lab., and Beam Technology Div.

- 1) T.-L. Khoo, Argonne National Laboratory (USA), 15 Jan.  
“At the limits of nuclear charge, spin and energy with heavy shell-stabilized nuclei”
- 2) G. Bunce, BNL/RBRC (USA), 14 Feb.  
“Precise measurement of the positive muon anomalous magnetic moment”
- 3) K. Hikasa, Tohoku University (Sendai), 14 Feb.  
“Old and new physics vs  $(g-2)_\mu$ ”
- 4) G. D. Dang, Laboratoire de Physique Theorique Universite de Paris-Sud (France), 9 Mar.  
“Dissipation of a slow motion by a complex system: A random matrix approach”
- 5) V. Zagrebaev, JINR (Russia), 13 Mar.  
“Exploration of multi-neutron halos in  $^{6,8}\text{He}$  induced low-energy transfer reactions”
- 6) P. Schuck, Université Joseph Fourier (France), 26 Apr.  
“Proton-neutron pairing in low density symmetric and asymmetric nuclear matter”
- 7) G. Roepke, Universität Rostock (Germany), 26 Apr.  
“Correlations in dense matter”
- 8) G. Duchêne, Institut de Recherches Subatomiques (France), 4 June  
“First results with EUROBALL IV and hints in the future of  $\gamma$ -spectroscopy”
- 9) K. Iida, RIKEN (Wako), 26 June  
“Superfluid phases of quark matter: Ginzburg-Landau theory and color neutrality”
- 10) K. Varga, Oak Ridge National Laboratory (USA), 16 July  
“From nuclei to quantum dots: Large scale variational calculations”
- 11) G. Kosenko, Omsk State University (Russia), 27 Aug.  
“Stochastic-statistical approach for fusion-fission reactions”
- 12) N. Shimizu, RIKEN (Wako), 28 Aug.  
“Quadrupole collective states in the Monte-Carlo shell model”
- 13) K. Arai, Université Libre de Bruxelles (Belgium), 3 Sept.  
“Low-energy  $^6\text{He}+p$  reaction in a microscopic multicluster model”
- 14) C. Shen, China Institute of Atomic Energy (China), 17 Sept.  
“Dynamical calculation of residue cross section for superheavy elements”
- 15) O. Klepper, GSI Darmstadt (Germany), 21 Sept.  
“Measurements of nuclear masses and half-lives in the cooler-storage ring ESR”
- 16) A. Bulgac, University of Washington (USA), 24 Oct.  
“Local density approximation for systems with pairing correlations”
- 17) J. Gal, ATOMKI (Hungary), 6 Nov.  
“The electronics of the EUROBALL’s CsI particle detector array. (Processing of CsI detector signals for determination of the type and the energy of the particles)”
- 18) G. Kalinka, ATOMKI (Hungary), 6 Nov.  
“Construction of high quality CsI(Tl) scintillation detectors for charged particle spectroscopy”
- 19) G. Lalazisis, Aristotle University of Thessaloniki (Greece), 12 Nov.  
“Relativistic Hartree-Bogoliubov (RHB) description”
- 20) A. Volya, Michigan State University (USA), 13 Nov.  
“Towards better understanding of nuclear pairing and its interplay with other residual interactions”
- 21) U. D. Pramanik, GSI (Germany), 16 Nov.  
“The study of properties of unstable nuclei at GSI”
- 22) V. Y. Denisov, GSI (Germany), 16 Nov.  
“Formation of superheavy elements in fusion reactions: Interaction potential well between very heavy ions”
- 23) Z. Ren, Nanjing University (China), 19 Nov.  
“Neutron halo and proton halo in light exotic nuclei”

- 24) N. Sandulescu, Institute for Physics and Nuclear Engineering (Romania), 26 Nov.  
“Pairing correlations and continuum effects in drip line nuclei”
- 25) S. M. Lukyanov, JINR (Russia), 29 Nov.  
“Fusion enhancement above the barrier for the  $6\text{He} + 209\text{Bi}$ -reaction”
- 26) Yu. E. Penionzhkevich, JINR (Russia), 29 Nov.  
“Radioactive ion beams in Dubna: The DRIBs project”

#### RI Beam Science Lab.

- 1) T. Suzuki, Fukui University (Fukui)/RIKEN (Wako), 24 May  
“Nuclear surface”
- 2) B. Sherrill, Michigan State University (USA), 14 June  
“Coupled cyclotron facility at MSU”
- 3) Y. Oganessseian, JINR (Russia), 14 June  
“The properties of superheavy nuclei with  $Z = 114$ - $116$  and their synthesis in fusion reactions with  $^{48}\text{Ca}$  ions”
- 4) K. Oyamatsu, Aichi Shukutoku University (Nagakute), 23 July  
“The equation of state of asymmetric nuclear matter”
- 5) Y. En'yo, KEK (Tsukuba), 18 Sept.  
“Neutron and proton densities in light unstable nuclei studied with AMD”
- 6) M. Smith, Oak Ridge National Laboratory (USA), 4 Oct.  
“Radioactive beam experiments & theoretical models of stellar explosions”
- 7) A. Schaefer, Regensburg University (Germany), 30 Oct.  
“Topological modes in lattice QCD”
- 8) W. von Oertzen, Freie Universität Berlin/Hahn-Meitner-Institut (Germany), 31 Oct.  
“Covalently bound molecular structures in light nuclei”
- 9) K. Langanke, Aarhus University (Denmark), 11 Dec.  
“Supernova and nuclear physics”

#### Applied Nuclear Physics Lab.

- 1) Y. Hsia, Nanjing University (China), 26 Oct.

“Brownian motion and anchor effect”

- 2) R. H. Herber, The Hebrew University of Jerusalem (Israel), 26 Oct.  
“Metal atom dynamics and vibrational anisotropy in iron organometallics”

#### Atomic Physics Lab.

- 1) R. Neumann, GSI (Germany), 27 Feb.  
“Survey of materials research at GSI”
- 2) J. Horacek, Charles University (Czech Republic), 9 Mar.  
“Recent progress in dissociative attachment”
- 3) D. Gotta, University Juelich (Germany), 20 Apr.  
“Strong-interaction effects in light antiprotonic atoms”
- 4) H. Tsuchida, Nara Women's University (Nara), 26 Apr.  
“Elastic deformation of metal foils by ion beam irradiation”
- 5) P. Nordlander, Rice University (USA), 18 May  
“Interaction of Rydberg atoms with metal surfaces”
- 6) V. Varentsov, V. G. Khlopin Radium Institute (Russia), 8 June  
“A new approach to the extraction system design and a cooler for intense low-energy ion beams”
- 7) H. O. Lutz, Bielefeld University (Germany), 15 June  
“How molecules and clusters explode”
- 8) T. Nishimura, University Rome (Italy), 10 Aug.  
“Low-energy positron dynamics in polyatomic gases”
- 9) H. Suno, Kansas State University (USA), 10 Aug.  
“Rydberg atoms in parallel electromagnetic field”
- 10) B. DePaola, Kansas State University (USA), 16 Aug.  
“Low-energy alkali collisions with ground and excited state Rb, investigated using MOTRIMS”
- 11) K. D. A. Wendt, Johannes Gutenberg-Universität (Germany), 16 Aug.  
“Ultra trace isotope determination in environmental, bio-medical and fundamental research by high resolution laser-mass spectrometry”
- 12) A. Casares, Oak Ridge National Laboratory

(USA), 26 Oct.

“Multi reflection time of flight mass spectrometer”

- 13) W. Heiland, Osnabrück University (Germany), 19 Nov.  
“Electronic surface corrugation evaluated from surface channeling experiments”
- 14) R. Hutton, Lund University (Sweden), 26 Nov.  
“Atomic physics in the home”
- 15) H. A. Schuessler, Texas A&M University (USA), 4 Dec.  
“Endohedral secrets”
- 16) F. B. Rosmej, GSI (Germany), 11 Dec.  
“Direct observation of space resolved charge state distribution of fast ions inside matter”

#### Cellular Physiology Lab.

- 1) H. Matsumoto, Fukui Medical Univ. (Fukui), 16 Feb.  
“Bystander effects by NO radical”
- 2) E. Drobetsky, Maisonneuve-Rosemont Hospital (Canada), 12 Mar.  
“The role of the p53/p21/pRb pathway in nucleotide excision repair”
- 3) E. Sage, Institut Curie (France), 19 Oct.  
“Roles of RAD30 and REV3 genes in solar UV mutagenesis in *Saccharomyces cerevisiae*”

#### RIBF Project Office, Beam Physics and Engineering Lab., Beam Dynamics Div., and Beam Technology Div.

- 1) G. Shirkov, JINR (Russia), 9 May  
“Laser ion loading into ECR source”
- 2) Y. Mori and S. Machida, KEK (Tsukuba), 8 June  
“FFAG Accelerator (I): Aiming at acceleration of the short-lived particles”
- 3) N. Ohuchi, KEK (Tsukuba), 22 June  
“Magnetic field measurement system for superconducting magnets at KEK”
- 4) M. Yoshii, KEK (Tsukuba), 16 July  
“Longitudinal barrier bucket”
- 5) K. Sato, RCNP, Osaka University (Suita), 17 July  
“Longitudinal-transverse coupling motion with second-order term of energy deviation in circular accelerators”

- 6) R. Nagaoka, ESRF (France), 3 Sept.  
“Overview of transverse beam instability studies made at the ESRF”
- 7) D. Bazin, Michigan State University (USA), 11 Sept.  
“The S800 spectrograph at NSCL: Presentation and some results”
- 8) M. D. Giacomo, GANIL (France), 12 Sept.  
“Introduction to the GANIL RF systems”
- 9) R. Nagaoka, ESRF (France), 17 Sept.  
“Work carried out at the ESRF to characterize and correct the coupling”
- 10) I. N. Meshkov, JINR (Russia), 5 Oct.  
“Recent progress of electron cooling at Julich”
- 11) B. Sharkov, ITEP (Russia), 5 Oct.  
“Status of laser ion source for LHC-CERN”

- 12) M. Shiho, JAERI (Tokai), 19 Nov.  
“Studies of induction linacs at the JAERI”

#### Computational Science Div.

- 1) K. Isao, Universite de Sherbrooke (Canada), 19 Apr.  
“Electron wave packet dynamics with a dual transformation technique”
- 2) H. Shinkai, RIKEN (Wako), 10 May  
“Introduction to numerical relativity”
- 3) T. Yamamoto, RIKEN (Wako), 14 June  
“First principles calculations of minerals”
- 4) T. Iitaka, RIKEN (Wako), 30 Aug.  
“First principles calculation of elastic properties of solid argon at high pressures”
- 5) T. Morishita, RIKEN (Wako), 11 Oct.  
“Liquid-liquid phase transitions of phosphorus via constant-pressure first-principles molecular dynamics simulations”

#### RIKEN BNL Research Center

- 1) M. Burkhardt, New Mexico State University (USA), 9 Jan.  
“Physics of off-forward parton distributions”
- 2) A. Ogawa, Pennsylvania State University (USA), 6 Feb.  
“Azimuthal asymmetries in hadron production at  $e^+e^-$  colliders and chiral-odd fragmentation functions”

- 3) R. Bellwied, Wayne State University (USA), 27 Feb.  
“Transverse polarization of the Lambda measured in Au-Au collisions”
- 4) S. Gupta, Tata Institute for Fundamental Physics (India), 13 Mar.  
“Longitudinally polarised parton densities”
- 5) Y. Koike, Niigata Univ., 27 Mar.  
“Single spin asymmetries at RHIC”
- 6) P. Nadolsky, Michigan State University (USA), 3 Apr.  
“Resummation in polarized W-Boson production: Lepton-level results”
- 7) K. Orginos, RBRC (USA), 17 Apr.  
“Nucleon matrix elements with lattice QCD”
- 8) V. Rykov, Wayne State University (USA), 21 May  
“CP-violating higgs at RHIC spin and at the future linear  $e^+e^-$  collider”
- 9) J.-C. Peng, Los Alamos National Laboratory (USA), 12 June  
“pA physics opportunities at PHENIX ?”
- 10) A. Deshpande, RBRC (USA), 19 June  
“The physics and status of EIC (I)”
- 11) J. Murata, RIKEN (Wako)/RBRC (USA), 3 July  
“Simulation formalism for parity violation via SM and contact interaction”
- 12) Y. Shestakov, BINP (Russia), 10 July  
“High density polarized deuterium gas targets”
- 13) J. Qiu, Iowa State University (USA), 14 Aug.  
“Single transverse spin asymmetries in drell-yan lepton’s angular distribution”
- 14) E. Predazzi, INFN (Italy), 15 Aug.  
“Diffractive contribution to spin flip and polarization prediction at RHIC”
- 15) S. Sasaki, University of Tokyo (Tokyo), 15 Aug.  
“Spin on lattice”
- 16) P. Haegler, Universität Regensburg (Germany), 14 Sept.  
“Parton orbital angular momentum”
- 17) A. Freund, Universität Regensburg (Germany), 18 Sept.  
“DVCS in next-to-leading order”
- 18) J. Tojo, Kyoto University (Kyoto), 21 Sept.  
“E950 data”
- 19) B. Kopeliovich, L. Trueman, Max-Planck-Institute (Germany)/BNL (USA), 21 Sept.  
“Polarimetry at RHIC: Present status and perspectives”
- 20) H. Huang, BNL (USA), 16 Oct.  
“Tutorial of polarized proton acceleration”
- 21) G. Xu, BNL (USA), 23 Oct.  
“A possible test to T-violation and its mechanisms”
- 22) D. Boer, Vrije University (The Netherlands), 30 Oct.  
“Transversely polarized Lambda production”
- 23) W. Mackay, BNL (USA), 6 Nov.  
“Preparation for first polarized proton collisions: Update on accelerator preparation”
- 24) K. Kurita, RBRC (USA), 6 Nov.  
“Preparation for first polarized proton collisions: Update on polarimetry”
- 25) Y. Goto, RBRC (USA), 6 Nov.  
“Preparation for first polarized proton collisions: Spin monitoring”

## XII. LIST OF PERSONNEL

### RARF/RIBF Project Head Office

INOUE Yorinao 井上 頼直 (Director)  
ISHIHARA Masayasu 石原 正泰 (Project Advisor)

### Cyclotron Group

YANO Yasushige 矢野 安重 \*1

### Beam Dynamics Team

FUJIMAKI Masaki 藤 卷 正 樹  
GOTO Akira 後 藤 彰 \*2  
INABE Naohito 稲 辺 尚 人  
KAGEYAMA Tadashi 影 山 正  
NAGASE Makoto 長 瀬 誠  
OHTAKE Masao 大 竹 政 雄  
SAKAMOTO Naruhiko 坂 本 成 彦  
WAKASUGI Masanori 若 杉 昌 徳

FUKUNISHI Nobuhisa 福 西 暢 尚  
IKEGAMI Kumio 池 上 九 三 男  
ITO Sachiko 伊 藤 祥 子  
KAMIGAITO Osamu 上 垣 外 修 一  
OHNISHI Jun-ichi 大 西 純 一  
OKUNO Hiroki 奥 野 広 樹  
TANABE Toshiya 田 辺 敏 也

### Beam Technology Team

FUJIMAKI Masaki 藤 卷 正 樹 (兼)  
FUJITA Shin 藤 田 新  
INABE Naohito 稲 辺 尚 人 (兼)  
KAGEYAMA Tadashi 影 山 正 (兼)  
KOHARA Shigeo 小 原 重 夫  
NAGASE Makoto 長 瀬 誠 (兼)  
OGIWARA Kiyoshi 荻 原 清

FUJITA Jiro 藤 田 二 郎  
IKEZAWA Eiji 池 沢 英 二  
ITO Sachiko 伊 藤 祥 子 (兼)  
KASE Masayuki 加 瀬 昌 之 \*2  
MORITA Kosuke 森 田 浩 介  
NAKAGAWA Takahide 中 川 孝 秀  
TANABE Toshiya 田 辺 敏 也 (兼)

### Experimental Rings Group

KATAYAMA Takeshi 片 山 武 司 \*1

### Accumulator Cooler Ring Team

INABE Naohito 稲 辺 尚 人 (兼)  
NAKAMURA Masato 中 村 仁 音  
TANABE Toshiya 田 辺 敏 也 (兼)  
WATANABE Tamaki 渡 邊 環

KATAYAMA Takeshi 片 山 武 司 (兼) \*2  
OKAMURA Masahiro 岡 村 昌 宏  
WAKASUGI Masanori 若 杉 昌 徳 (兼)

### Collider Ring Team

INABE Naohito 稲 辺 尚 人 (兼)  
OKAMURA Masahiro 岡 村 昌 宏 (兼)  
WATANABE Tamaki 渡 邊 環 (兼)

KATAYAMA Takeshi 片 山 武 司 (兼) \*2  
WAKASUGI Masanori 若 杉 昌 徳 (兼)

### Experimental System Group

TANIHATA Isao 谷 畑 勇 夫 \*1

### Nuclear Reaction Team

KORSHENINNIKOV Alexei A.  
MORIMOTO Kouji 森 本 幸 司  
OZAWA Akira 小 沢 顕  
TANIHATA Isao 谷 畑 勇 夫 (兼) \*2  
YOSHIDA Koichi 吉 田 光 一

KUBO Toshiyuki 久 保 敏 幸  
NISHIMURA Shunji 西 村 俊 二  
SUDA Toshimi 須 田 利 美  
WATANABE Yasushi 渡 邊 康  
YOSHIDA Atsushi 吉 田 敦

### Low Energy Team

ASAHI Koichiro 旭 耕一郎 \*2  
KOBAYASHI Yoshio 小林義男  
UENO Hideki 上野秀樹

KISHIDA Takashi 岸田 隆  
SHIMIZU Hirohiko 清水裕彦

### Atomic and Other Science Team

ABE Tomoko 阿部知子  
IKEDA Tokihiro 池田時浩  
KANAI Yasuyuki 金井保之  
KOJIMA Takao 小島隆夫  
NAKAI Yoichi 中井陽一  
WADA Michiharu 和田道治

ENOMOTO Shuichi 榎本秀一  
KAMBARA Tadashi 神原 正  
KOBAYASHI Yoshio 小林義男 (兼)  
MATSUO Yukari 松尾由賀利  
OYAMA Hitoshi 大山 等  
YAMAZAKI Yasunori 山崎泰規 \*2

### Experiment Support Team

ICHIHARA Takashi 市原 卓  
KANAI Yasuyuki 金井保之 (兼)  
MORITA Kosuke 森田浩介 (兼)  
YATAGAI Fumio 谷田貝文夫

KAMBARA Tadashi 神原 正 (兼) \*2  
MATSUZAKI Teiichiro 松崎禎市郎  
WATANABE Yasushi 渡邊 康 (兼)

### Planning and Coordination Group

MANABE Tadashi 真鍋 烈 \*1

### Planning and Coordination Office

EMOTO Takashi 江本 隆  
NAKAMURA Toshiko 中村とし子  
OKAZOE Hiromu 岡添 弘 \*3  
TASHIRO Satoshi 田代 聡  
UWAMINO Yoshitomo 上 蓑義朋

KOGURE Mieko 小暮美恵子  
NUMATA Shigeo 沼田茂男  
SATO Kenji 佐藤研治  
TOKUOKA Haruhiro 徳岡治洋

### Steering Committee

ASAHI Koichiro 旭 耕一郎  
EN'YO Hideto 延與秀人  
KAMBARA Tadashi 神原 正  
KATAYAMA Takeshi 片山武司  
NAGAMINE Kanetada 永嶺謙忠  
TANIHATA Isao 谷畑勇夫  
YANO Yasushige 矢野安重  
YOSHIDA Shigeo 吉田茂男

GOTO Akira 後藤 彰  
ICHIHARA Takashi 市原 卓  
KASE Masayuki 加瀬昌之  
MATSUZAKI Teiichiro 松崎禎市郎  
SAWA Hiroshi 澤 宏  
YAMAZAKI Yasunori 山崎泰規  
YATAGAI Fumio 谷田貝文夫

---

\*1 Group Director, \*2 Team Leader, \*3 Head

\*\*\*\*\*  
 Members (included Special Postdoctoral Researcher,  
 RIKEN Fellow, and Contract Researcher)  
 \*\*\*\*\*

## Cosmic Radiation Laboratory

### Members

KATO Hiroshi 加藤 博 MIYASAKA Hiromasa 宮坂浩正  
 YOSHIDA Atsumasa 吉田篤正

### Visiting Members

GOKA Tateo 五家建夫 (NASDA)  
 KOSHIISHI Hideki 越石英樹 (NASDA)  
 MATSUMOTO Haruhisa 松本晴久 (NASDA)

## Radiation Laboratory

### Head

EN'YO Hideto 延與秀人

### Members

HIRAI Masanori 平井正紀	ICHIHARA Takashi 市原 卓
ISHII Noriyoshi 石井理修	JINNOUCHI Osamu 陣内 修
KISHIDA Takashi 岸田 隆	MIZOI Yutaka 溝井 浩
MURATA Jiro 村田次郎	NAITO Kenichi 内藤謙一
OKADA Kensuke 岡田謙介	SAITO Naohito 齊藤直人
TABARU Tsuguchika 田原司睦	TAKETANI Atsushi 竹谷 篤
TANIDA Kiyoshi 谷田 聖	WATANABE Yasushi 渡邊 康
WATANABE Yutaka 渡辺 裕	YASUI Yoshiaki 安井良彰
YOKKAICHI Satoshi 四日市 悟	

### Visiting Members

AKIBA Yasuyuki 秋葉康之 (KEK)  
 ALEKSEEV Igor (Phys. Dept., BNL, USA)  
 ANDO Yoshiaki 安藤嘉章 (Coll. Sci., Rikkyo Univ.)  
 AOI Nori 青井 考 (Dept. Phys., Grad. Sch. Sci., Univ. Tokyo)  
 ASAI Masato 浅井雅人 (JAERI)  
 ASAMI Hiroyasu 浅海弘保 (KEK)  
 ASAKAWA Masayuki 浅川正之 (Fac. Sci., Kyoto Univ.)  
 BAUMANN Thomas (Natl. Puperconducting Cycl. Lab., Michigan State Univ., USA)  
 BAZIN Daniel (Natl. Puperconducting Cycl. Lab., Michigan State Univ., USA)  
 BECK F. A. (CRN, France)  
 BENTZ Wolfgang (Dept. Phys., Grad. Sch. Sci., Univ. Tokyo)  
 BHANG Hyong Chan (Dept. Phys., Seoul Natl. Univ., Korea)  
 BROGLIA R. (Univ. Milano, Italy)  
 BROOKS Melynda (LANL, USA)  
 BURWARD-HOY Muriel Jane (Dept. Phys., State University New York, Stony Brook, USA)  
 CASTEN Rick (Phys. Dept., BNL, USA)  
 CHUJO Tatsuya 中條達也 (Phys. Dept., BNL, USA)  
 COLO Gianluca (Univ. Milano, Italy)  
 CRIST Norman (Columbia Univ., USA)  
 DOMBRADI Zsolt (Inst. Nucl. Res. Hung. Acad. Sci., Hungary)  
 DOOI Makoto 堂井 真 (Inst. Phys., Univ. Tsukuba)  
 ELEKES Zoltan (Inst. Nucl. Res. Hung. Acad. Sci., Hungary)  
 FLOCARD Hubert (Div. Phys. Theor., Inst. Phys. Nucl., France)  
 FUCHI Yoshihide 渕 好秀 (KEK)  
 FUJII Hirotsugu 藤井宏次 (Grad. Sch. Arts Sci., Univ. Tokyo)  
 FUJIKAWA Kazuo 藤川和男 (Fac. Sci., Univ. Tokyo)  
 FUKUDA Mitsunori 福田光順 (Grad. Sch. Sci., Osaka Univ.)

FUKUDA Tomokazu 福田共和 (KEK)  
 FÜLÖP Zsolt (Inst. Nucl. Res. Hung. Acad. Sci., Hungary)  
 FURUTAKA Kazuyoshi 古高和禎 (JAERI)  
 GAL Janos (Inst. Nucl. Res. Hung. Acad. Sci., Hungary)  
 GELBERG Adrian (Koln Univ., Germany)  
 GONO Yasuyuki 郷農靖之 (Fac. Sci., Kyushu Univ.)  
 HAMAMOTO Ikuko 浜本育子 (Lund Inst. Technol., Univ. Lund, Sweden)  
 HATSUDA Tetsuo 初田哲男 (Fac. Sci., Kyoto Univ.)  
 HAYASHI Naoki 林直樹 (JAERI)  
 HAYASHIGAKI Arata 林垣新 (Dept. Phys., Grad. Sch. Sci., Univ. Tokyo)  
 HIKASA Kenichi 日笠健一 (Grad. Sch. Sci., Tohoku Univ.)  
 HIRANO Tetsufumi 平野哲文 (Dept. Phys., Grad. Sch. Sci., Univ. Tokyo)  
 HOMMA Kensuke 本間謙輔 (Fac. Sci., Hiroshima Univ.)  
 HORIUCHI Hisashi 堀内昶 (Fac. Integr. Human Studies, Dept. Fund. Sci., Kyoto Univ.)  
 HOTTA Tomohiro 堀田智洋 (Grad. Sch. Arts Sci., Univ. Tokyo)  
 ICHIMURA Munetake 市村宗武 (Grad. Sch. Arts Sci., Univ. Tokyo)  
 IEKI Kazuo 家城和夫 (Coll. Sci., Rikkyo Univ.)  
 IMAI Kenichi 今井憲一 (Fac. Sci., Kyoto Univ.)  
 IMOTO Michiko 井本道子 (Coll. Sci. Technol., Nihon Univ.)  
 ISHII Tetsuro 石井哲朗 (JAERI)  
 ITABASHI Kenta 板橋健太 (Tokyo Inst. Technol.)  
 IWASAKI Masahiko 岩崎雅彦 (Tokyo Inst. Technol.)  
 IZUMI Hideaki 出水秀明 (Grad. Sch. Sci., Osaka Univ.)  
 JIN Genming 靳根明 (Inst. Mod. Phys., Chin. Acad. Sci., China)  
 KAKI Kaori 嘉規香織 (Fac. Sci., Shizuoka Univ.)  
 KALINKA Gabor (Inst. Nucl. Res. Hung. Acad. Sci., Hungary)  
 KASAGI Jirota 笠木治郎太 (Lab. Nucl. Sci., Tohoku Univ.)  
 KATO Seigo 加藤静吾 (Fac. Ed., Yamagata Univ.)  
 KIM Jong Chan 金鐘贊 (Dept. Phys., Seoul Natl. Univ., Korea)  
 KISTENEV Edouard (Phys. Dept., BNL, USA)  
 KIYO Yuichiro 清裕一郎 (Grad. Sch. Sci., Tohoku Univ.)  
 KODAIRA Jirou 小平治郎 (Fac. Sci., Hiroshima Univ.)  
 KOIKE Yuji 小池裕司 (Fac. Sci., Niigata Univ.)  
 KUMANO Shunzo 熊野俊三 (Fac. Sci. Eng., Saga Univ.)  
 KUNIHICO Teiji 國弘悌二 (Yukawa Inst. Theor. Phys., Kyoto Univ.)  
 KUSAKARI Hideshige 草刈英榮 (Fac. Ed., Chiba Univ.)  
 LIU Guanhua 劉冠華 (Inst. Mod. Phys., Chin. Acad. Sci., USA)  
 LIU Zhong (Inst. Mod. Phys., Chin. Acad. Sci., China)  
 LOMON Earle (Massachusetts Inst. Technol., USA)  
 LOUKIANOV Serguei (Flerov Lab. Nucl. React., Joint Inst. Nucl. Res., Russia)  
 LUCCIO Alfredo (Phys. Dept., BNL, USA)  
 MAO Yajun (Inst. Mod. Phys., Chin. Acad. Sci., China)  
 MATSUDA Satoshi 松田哲 (Dept. Fund. Sci., Fac. Integr. Human Studies, Kyoto Univ.)  
 MATSUI Tetsuo 松井哲男 (Grad. Sch. Arts Sci., Univ. Tokyo)  
 MATSUYANAGI Kenichi 松柳研一 (Fac. Sci., Kyoto Univ.)  
 MENGONI Alberto (Phys. Div., ENEA, Italy)  
 MIAKE Yasuo 三明康郎 (Inst. Phys., Univ. Tsukuba)  
 MIDORIKAWA Shoichi 緑川章一 (Fac. Eng., Aomori Univ.)  
 MIN Byung-Joo 閔丙珠 (Korea At. Energy Res. Inst., Korea)  
 MITARAI Shiro 御手洗志郎 (Fac. Sci., Kyushu Univ.)  
 MIYAMA Masanori 深山正紀 (Fac. Sci., Tokyo Metrop. Univ.)  
 MIYATAKE Hiroari 宮武宇也 (KEK)  
 MOLLER Peter (LANL, USA)  
 MORII Toshiyuki 森井俊行 (Fac. Human Develop., Kobe Univ.)  
 MORIKAWA Tsuneyasu 森川恒安 (Fac. Sci., Kyushu Univ.)  
 MORINOBU Shunpei 森信俊平 (Fac. Sci., Kyushu Univ.)  
 MOTOBAYASHI Tohru 本林透 (Coll. Sci., Rikkyo Univ.)

MOTTELSON Ben R. (Nordita, Denmark)  
 MUELLER Ludwig (Phys. Dept., Univ. Padova, Italy)  
 MURAKAMI Takeshi 村上 健 (Natl. Inst. Radiol. Sci.)  
 MURAKAMI Hiroyuki 村上 浩之 (Coll. Sci., Rikkyo Univ.)  
 NAGAE Tomofumi 永江 知文 (KEK)  
 NAGAI Yasuki 永井 泰樹 (RCNP, Osaka Univ.)  
 NAGAMIYA Shoji 永宮 正治 (KEK)  
 NAKAJIMA Mitsuo 中島 充夫 (Grad. Sch. Nagatsuta, Tokyo Inst. Technol.)  
 NAKAMURA Shogo 中村 正吾 (Fac. Ed., Yokohama Natl. Univ.)  
 NAKAMURA Takashi 中村 隆司 (Tokyo Inst. Technol.)  
 NAKAMURA Masanobu 中村 正信 (Fac. Sci., Kyoto Univ.)  
 NAKAYAMA Shiintaro 中山 信太郎 (Fac. Integr. Arts Sci., Univ. Tokushima)  
 NIIZEKI Takashi 新関 隆 (Tokyo Kasei Univ.)  
 NISHIMURA Jun 西村 淳 (Cen. Integr. Res. Sci. Eng., Nagoya Univ.)  
 NONAKA Chiho 野中 千穂 (Fac. Sci., Hiroshima Univ.)  
 NORO Tetsuo 野呂 哲夫 (RCNP, Osaka Univ.)  
 ODAHARA Atsuko 小田原厚子 (Nishinippon Inst. Technol.)  
 OGAWA Masao 小川 雅生 (Tokyo Inst. Technol.)  
 OGAWA Akio 小川 暁生 (Phys. Dept., BNL, USA)  
 OHSIMA Kazuto 大嶋 一人 (Gunma Natl. Coll. Technol.)  
 OKAMURA Hiroyuki 岡村 弘之 (Fac. Sci., Saitama Univ.)  
 ONISHI Hiroaki 大西 宏明 (Phys. Dept., BNL, USA)  
 OOISHI Ryutarō 大石 竜太郎 (Inst. Phys., Univ. Tsukuba)  
 ORIHARA Hikonojo 織原 彦之丞 (Cycl. Radioisot. Cen., Tohoku Univ.)  
 OSHIMA Masumi 大島 真澄 (JAERI)  
 OUTA Haruhiko 応田 治彦 (KEK)  
 PAN Qiangyan 潘 強岩 (Inst. Mod. Phys., Chin. Acad. Sci., China)  
 PASCUZZI Edward (Phys. Dept., BNL, USA)  
 PENIONZHKEVICH Iouri (Flerov Lab. Nucl. React., Joint Inst. Nucl. Res., Russia)  
 PIERROUTSAKOU Dimitra (Sezione Napoli (INFN), Italy)  
 REN Zhongzhou 任 中洲 (Nanjing Univ., China)  
 SAITO Koichi 斎藤 晃一 (Tohoku Pharm. Univ.)  
 SAKAGUCHI Harutaka 坂口 治隆 (Fac. Sci., Kyoto Univ.)  
 SAKURAGI Hiroyuki 櫻木 弘之 (Fac. Sci., Osaka City Univ.)  
 SAKURAI Hiroyoshi 櫻井 博儀 (Dept. Phys., Grad. Sch. Sci., Univ. Tokyo)  
 SASAKI Shoichi 佐々木 勝一 (Dept. Phys., Grad. Sch. Sci., Univ. Tokyo)  
 SATO Hikaru 佐藤 皓 (KEK)  
 SATO Susumu 佐藤 進 (Inst. Phys., Univ. Tsukuba)  
 SAWADA Shinya 澤田 真也 (KEK)  
 SCHAEFER Markus (Phys. Inst., Univ. Goettingen, Germany)  
 SCHAFER Andreas (Inst. Theor. Phys., Univ. Regensburg, Germany)  
 SCHMIDT-OTT Wolf-Dieter (Phys. Inst., Univ. Goettingen, Germany)  
 SEDERWALL Bo (Royal Inst. Technol., Sweden)  
 SEKIMOTO Michiko 関本 美知子 (KEK)  
 SHIBATA Toshiaki 柴田 利明 (Tokyo Inst. Technol.)  
 SHIGAKI Kenta 志垣 賢太 (KEK)  
 SHIMIZU Hajime 清水 肇 (Fac. Ed., Yamagata Univ.)  
 SHIMIZU Yoshifumi 清水 良文 (Fac. Sci., Kyushu Univ.)  
 SHIMODA Tadashi 下田 正 (Grad. Sch. Sci., Osaka Univ.)  
 SIGNORINI Cosimo (Phys. Dept., Univ. Padova, Italy)  
 STROE Lucian (Phys. Dept., Univ. Padova, Italy)  
 SUGAWARA Masahiko 菅原 昌彦 (Chiba Inst. Technol.)  
 SUGITATE Toru 杉立 徹 (Fac. Sci., Hiroshima Univ.)  
 SUN Zuxun (China Inst. At. Energy, China)  
 SUZUKI Yasuyuki 鈴木 宜之 (Fac. Sci., Niigata Univ.)  
 SUZUKI Katsuhiko 鈴木 克彦 (Dept. Phys., Grad. Sch. Sci., Univ. Tokyo)  
 SUZUKI Toshio 鈴木 敏男 (Fac. Eng., Fukui Univ.)

TAJIMA Yasuhisa 田島靖久 (Cycl. Radioisot. Cen., Tohoku Univ.)  
 TAKADA Eiichi 高田栄一 (Natl. Inst. Radiol. Sci.)  
 TAKAHASHI Tadayuki 高橋忠幸 (Inst. Space Astronaut. Sci.)  
 TAKEMOTO Hiroki 竹本宏輝 (JAERI)  
 TAKIGAWA Noboru 滝川昇 (Grad. Sch. Sci., Tohoku Univ.)  
 TAKIZAWA Makoto 瀧澤誠 (Showa Coll. Pharm. Sci.)  
 TAMII Atsushi 民井淳 (Fac. Sci., Univ. Tokyo)  
 TANAKA Masahiko 田中雅彦 (KEK)  
 TANOKURA Atsushi 田野倉敦 (Fac. Sci. Technol., Sophia Univ.)  
 TERAOKA Atsuki 寺川貴樹 (Cycl. Radioisot. Cen., Tohoku Univ.)  
 TOYAMA Takeshi 外山毅 (KEK)  
 TOYOKAWA Hidenori 豊川秀訓 (JASRI)  
 UEMATSU Tsuneo 植松恒夫 (Dept. Fund. Sci., Fac. Integr. Human Studies, Kyoto Univ.)  
 UENO Hideki 上野秀樹 (Lab. Nucl. Studies, Fac. Sci., Osaka Univ.)  
 UNO Masahiro 宇野正宏 (Min. Ed., Culture, Sports Sci. Technol.)  
 WAKAMATSU Masashi 若松正志 (Lab. Nucl. Studies, Fac. Sci., Osaka Univ.)  
 WAKASA Tomotsugu 若狭智嗣 (RCNP, Osaka Univ.)  
 WHITE Sebastian (Phys. Dept., BNL, USA)  
 XU Shuwei 徐樹威 (Inst. Mod. Phys., Chin. Acad. Sci., China)  
 YAMANISHI Teruya 山西輝也 (Fac. Eng., Fukui Univ. Technol.)  
 YAMASHITA Yoshiki 山下芳樹 (Hirosaki Univ.)  
 YAZAKI Koichi 矢崎紘一 (Tokyo Women's Chr. Univ.)  
 YOSHIMURA Koji 吉村浩司 (Int. Cen. Element. Part. Phys., Univ. Tokyo)  
 YOSHINAGA Naotaka 吉永尚孝 (Fac. Sci., Saitama Univ.)  
 YOSOI Masaru 與曾井優 (Fac. Sci., Kyoto Univ.)  
 ZHANG Yu-Hu 張玉虎 (Inst. Mod. Phys., Chin. Acad. Sci., China)  
 ZHOU Xiaohong 周小紅 (Inst. Mod. Phys., Chin. Acad. Sci., China)  
 ZHU Lihua (China Inst. At. Energy, China)

#### *Trainees*

ADACHI Yusuke 足立雄哉 (Dept. Phys., Grad. Sch. Sci., Univ. Tokyo)  
 BABA Hidetada 馬場秀忠 (Coll. Sci., Rikkyo Univ.)  
 DEMICHI Kimihiko 出道仁彦 (Coll. Sci., Rikkyo Univ.)  
 ENOKIZONO Akitomo 榎園昭智 (Fac. Sci., Hiroshima Univ.)  
 FUKAO Yoshinori 深尾祥紀 (Fac. Sci., Kyoto Univ.)  
 FUKUCHI Tomonori 福地知則 (Fac. Sci., Kyushu Univ.)  
 GOMI Tomoko 五味朋子 (Coll. Sci., Rikkyo Univ.)  
 HACHIYA Takashi 蜂谷崇 (Fac. Sci., Hiroshima Univ.)  
 HASEGAWA Hirokazu 長谷川浩一 (Coll. Sci., Rikkyo Univ.)  
 HAYASHI Takeshi 林剛史 (Tokyo Inst. Technol.)  
 HIRAI Kazuyoshi 平井一賢 (Tokyo Inst. Technol.)  
 HIRAMATSU Takashi 平松尚志 (Dept. Phys., Grad. Sch. Sci., Univ. Tokyo)  
 IKEDA Hiroshi 池田宙 (Tokyo Inst. Technol.)  
 INOUE Masaki 井上正樹 (Fac. Sci., Kyushu Univ.)  
 ISHIDA Tomoyuki 石田智之 (Dept. Phys., Grad. Sch. Sci., Univ. Tokyo)  
 KAJIHARA Fukutaro 梶原福太郎 (Dept. Phys., Grad. Sch. Sci., Univ. Tokyo)  
 KAMIHARA Nobuyuki 神原信幸 (Tokyo Inst. Technol.)  
 KANEKO Emi 金子恵美 (Coll. Sci., Rikkyo Univ.)  
 KANG Byonghwi (Dept. Phys., Seoul Natl. Univ., Korea)  
 KANNO Shouko 菅野祥子 (Coll. Sci., Rikkyo Univ.)  
 KATAYAMA Takeshi 片山武士 (Tokyo Inst. Technol.)  
 KAWASAKI Hiroaki 河崎洋章 (Coll. Sci., Rikkyo Univ.)  
 KIM Jungho (Dept. Phys., Seoul Natl. Univ., Korea)  
 KIYOMICHI Akio 清道明男 (Inst. Phys., Univ. Tsukuba)  
 KOMIYAMA Takeshi 小宮山武士 (Dept. Phys., Grad. Sch. Sci., Univ. Tokyo)  
 KONDO Yosuke 近藤洋介 (Tokyo Inst. Technol.)  
 KUBOKI Hironori 久保木浩功 (Dept. Phys., Grad. Sch. Sci., Univ. Tokyo)

KUROKI Yoshiaki 黒木善昭 (Inst. Phys., Univ. Tsukuba)  
 LIM Heejoong (Dept. Phys., Seoul Natl. Univ., Korea)  
 MAEDA Yukie 前田幸重 (Dept. Phys., Grad. Sch. Sci., Univ. Tokyo)  
 MATSUYAMA Yuuichi 松山裕一 (Coll. Sci., Rikkyo Univ.)  
 MIURA Motooki 三浦元隆 (Tokyo Inst. Technol.)  
 MIYAJIMA Akari 宮島明里 (Tokyo Inst. Technol.)  
 MOTOMURA Shinji 本村信治 (Fac. Sci., Kyushu Univ.)  
 MUTO Ryotaro 武藤亮太郎 (Fac. Sci., Kyoto Univ.)  
 NAKAMURA Tomoaki 中村智昭 (Fac. Sci., Hiroshima Univ.)  
 NARUKI Megumi 成木 恵 (Fac. Sci., Kyoto Univ.)  
 NARUSHIMA Koichi 成嶋功一 (Coll. Sci., Rikkyo Univ.)  
 OHKUMA Kazumasa 大熊一正 (Fac. Human Dev., Kobe Univ.)  
 OKADA Shinji 岡田信二 (Tokyo Inst. Technol.)  
 ONG Hooi Jin (Dept. Phys., Grad. Sch. Sci., Univ. Tokyo)  
 ONISHI Takeo 大西健夫 (Dept. Phys., Grad. Sch. Sci., Univ. Tokyo)  
 ONO Masaya 小野雅也 (Inst. Phys., Univ. Tsukuba)  
 OYAMA Satoshi 大山 聡 (Dept. Phys., Grad. Sch. Sci., Univ. Tokyo)  
 SAITO Takaaki 斎藤孝明 (Dept. Phys., Grad. Sch. Sci., Univ. Tokyo)  
 SAITOU Akito 斎藤明登 (Coll. Sci., Rikkyo Univ.)  
 SAKUMA Fuminori 佐久間史典 (Fac. Sci., Kyoto Univ.)  
 SASAKI Takafumi 佐々木隆文 (Fac. Sci., Kyushu Univ.)  
 SATO Hiroki 佐藤博紀 (Fac. Sci., Kyoto Univ.)  
 SATO Masaharu 佐藤将春 (Tokyo Inst. Technol.)  
 SUDOH Kazutaka 須藤和敬 (Fac. Human Dev., Kobe Univ.)  
 SUGIMOTO Takashi 杉本 崇 (Tokyo Inst. Technol.)  
 SUGITA Noriyuki 杉田宣之 (Fac. Sci., Hiroshima Univ.)  
 SUZUKI Miwako 鈴木美和子 (Inst. Phys., Univ. Tsukuba)  
 SUZUKI Takatoshi 鈴木隆敏 (Dept. Phys., Grad. Sch. Sci., Univ. Tokyo)  
 TAKESHITA Eri 竹下英理 (Coll. Sci., Rikkyo Univ.)  
 TANAKA Shuichi 田中周一 (Fac. Sci., Kyushu Univ.)  
 TOGAWA Manabu 外川 学 (Fac. Sci., Kyoto Univ.)  
 TOJO Junji 東城順治 (Fac. Sci., Kyoto Univ.)  
 TORII Hisayuki 鳥井久行 (Fac. Sci., Kyoto Univ.)  
 TSURUOKA Hiroshi 鶴岡裕士 (Inst. Phys., Univ. Tsukuba)  
 UCHIGASHIMA Nobuyuki 内ヶ島暢之 (Dept. Phys., Grad. Sch. Sci., Univ. Tokyo)  
 WAKABAYASHI Yasuo 若林泰生 (Fac. Sci., Kyushu Univ.)  
 YAKO Kentaro 矢向謙太郎 (Dept. Phys., Grad. Sch. Sci., Univ. Tokyo)  
 YONEYAMA Tetsu 米山 哲 (Tokyo Inst. Technol.)

## RI Beam Science Laboratory

### Head

TANIHATA Isao 谷畑勇夫

### Members

FANG Deging	FUKUYAMA Yoshimitsu 福山祥光
IDEUCHI Eiji 井手口栄治	IIDA Kei 飯田 圭
ISHIDA Yoshihisa 石田佳久	KANUNGO Rituparna
KOHAMA Akihisa 小濱洋央	KORSHENINNIKOV Alexei A.
KUSAKA Kensuke 日下健祐	MATSUO Yukari 松尾由賀利
MOCHIZUKI Yuko 望月優子	MORIMOTO Kouji 森本幸司
NAKATSUKASA Takashi 中務 孝	NISHI Yuji 西 勇二
NISHIMURA Shunji 西村俊二	NISHIMURA Mizuki 西村美月
OZAWA Akira 小沢 顕	ONISHI Takashi 大西 崇
OHNISHI Tetsuya 大西哲也	SUDA Toshimi 須田利美
WAKUI Takashi 涌井宗志	YAMAGUCHI Takayuki 山口貴之
YAMAZAKI Toshimitsu 山崎敏光	YOSHIDA Atsushi 吉田 敦

YOSHIDA Koichi 吉田光一

*Visiting Members*

ABE Yasuhisa 阿部恭久 (Yukawa Inst. Theor. Phys., Kyoto Univ.)  
ADACHI Shizuko 安達静子 (ICFD)  
AHMADY Mohammad (Western Ontario Univ., Canada)  
AOKI Yasuo 青木保夫 (Fac. Sci., Univ. Tsukuba)  
AOYAMA Shigeyoshi 青山茂義 (Kitami Inst. Tech.)  
ARITOMO Yoshihiro 有友嘉浩 (J.I.N.R., Russia)  
BOLBOT Michael (Notre Dame Univ., USA)  
BOYD Richard (Ohio Univ., USA)  
BROCKMANN Roff (Inst. Phys., Univ. Mainz, Germany)  
CASARES Antonio (Oak Ridge Lab., USA)  
CRUCCERU Ilie (Horia Inst. Eng., Romania)  
DATAR Vivek (Bhabha At. Res. Cen., India)  
DAVID Dean J. (CALTEC, USA)  
DEMYANOVA Alla S. (Kurchatov Inst. At. Energy, Russia)  
DOKE Tadayoshi 道家忠義 (Adv. Res. Inst. Sci. Eng., Waseda Univ.)  
ENYO Yoshiko 延與佳子 (Cen. Nucl. Study, Univ. Tokyo)  
FAMIANO Michael (Ohio State Univ., USA)  
FOMITCHEV Andrei (JNRF, Russia)  
FUJIWARA Mamoru 藤原守 (RCNP, Osaka Univ.)  
FÜLÖP Zsolt (ATOMKI, Hungary)  
GACSI Zoltan (ATOMKI, Hungary)  
GEISSEL Hans (GSI, Germany)  
GIURGIU Mircea (Horia Inst. Nucl. Eng., Romania)  
GOLOVKOV Mkheil S. (Kurchatov Inst., Russia)  
GONCHAROV Sergei A. (Kurchatov Inst., Russia)  
GORIELY Stephanoe (Inst. Astron., Belgium)  
GORINE Alexander (IHEO, Russia.)  
GOSWAMI Ranjana (Variable Energy Cycl. Cen. Calcutta, India)  
GUNJI Shuichi 郡司修一 (Fac. Sci., Yamagata Univ.)  
HARADA Toru 原田融 (Fac. Sci. Inf., Sapporo Gakuin Univ.)  
HASEBE Nobuyuki 長谷部伸行 (Fac. Sci. Eng., Waseda Univ.)  
HIEN Nguyen Thuc (Hanoi Univ., Vietnam.)  
HIRENZAKI Satoru 比連崎悟 (Fac. Sci., Nara Women's Univ.)  
HONMA Michio 本間通雄 (Univ. Aizu)  
HORIBATA Takatoshi 堀端孝俊 (Fac. Eng., Aomori Univ.)  
HORIGUCHI Masakatu 堀口正勝 (Horiguchi Ironworks)  
HORIUCHI Hisashi 堀内昶 (Fac. Sci., Kyoto Univ.)  
IKEDA Akitsu 池田秋津 (Shizuoka Inst. Sci. Tech.)  
IKEDA Kiyomi 池田清美  
ISHIMOTO Shigeru 石元茂 (KEK)  
ITAGAKI Naoyuki 板垣直之 (Fac. Sci., Univ. Tokyo)  
ITAHASHI Kenta 板橋健太 (Fac. Sci., Tokyo Inst. Technol.)  
IWAMOTO Akira 岩本昭 (Tokai Res. Estab., JAERI)  
IWASA Naohito 岩佐直仁 (Fac. Sci., Tohoku Univ.)  
IWASAKI Aiichi 岩崎愛一 (Nishogakusya Univ.)  
IZUMIKAWA Takuji 泉川卓司 (Fac. Sci., Niigata Univ.)  
IZUYAMA Takeo 伊豆山健夫 (Fac. Sci., Toho Univ.)  
KAMIMURA Masayasu 上村正康 (Fac. Sci., Kyushu Univ.)  
KANEKO Kazuya 金子和也 (Kyushu Sangyo Univ.)  
KATO Kiyoshi 加藤幾芳 (Fac. Sci., Hokkaido Univ.)  
KATORI Kenji 鹿取謙二  
KIKUCHI Jun 菊池順 (Sci. Eng. Res. Lab., Waseda Univ.)  
KIMURA Kikuo 木村喜久雄 (Fac. Eng., Nagasaki Inst. Appl. Sci.)  
KOBAYASHI Toshio 小林俊雄 (Fac. Sci., Tohoku Univ.)

KOLATA James (Notre Dame Univ., USA)  
 KOSENKO Grigori (OMSK State Univ., Russia)  
 KOURA Hiroyuki 小浦寛之 (Fac. Sci. Eng., Waseda Univ.)  
 KOUZMINE Evgueni (Kurchatov Inst., Russia)  
 KRASZNAHORKAY Attila (ATOMKI, Hungary)  
 KUMAGAI Hidekazu 熊谷秀和  
 KUMARU Suresh (Bhabha At. Res. Cen., India)  
 LE HONG Khiem (Inst. Phys., Natl. Cen. Sci. Technol., Vietnam)  
 LU Hongfeng (Peking Univ., China)  
 MIZUSAKI Takahiro 水崎高浩 (Fac. Sci., Univ. Tokyo)  
 MARUYAMA Koichi 丸山浩一 (Inst. Nucl. Study., Univ. Tokyo)  
 MARUYAMA Tomoyuki 丸山智幸 (Nihon Univ.)  
 MATSUOKA Nobuyuki 松岡伸行 (RCNP, Osaka Univ.)  
 MATSUTA Kensaku 松多健策 (Fac. Sci., Osaka Univ.)  
 MATSUYANAGI Kenichi 松柳研一 (Grad. Sch. Sci., Kyoto Univ.)  
 MATSUZAKI Masayuki 松崎昌之 (Fac. Ed., Fukuoka Univ. Ed.)  
 MATSUYAMA Yoshitaka 松山芳孝 (Inst. Nucl. Study., Univ. Tokyo)  
 MENG Jie (Peking Univ., China)  
 MIDORIKAWA Shouichi 緑川章一 (Fac. Eng., Aomori Univ.)  
 MINAMISONO Kei 南園啓 (Fac. Sci., Osaka Univ.)  
 MINAMISONO Tadanori 南園忠則 (Fac. Sci., Osaka Univ.)  
 MITTING M. (GANIL, France)  
 MIHARA Mototugu 三原基嗣 (Fac. Sci., Osaka Univ.)  
 MIRGULE Ekanath Tanu (Bhabha At. Res. Cen., India)  
 MIYAKE Yasuo 三明康朗 (Fac. Sci., Univ. Tsukuba)  
 MIYAMURA Osamu 宮村修 (Fac. Sci., Hiroshima Univ.)  
 MIYACHI Takashi 宮地孝 (Fac. Sci. Eng., Waseda Univ.)  
 MOMOTA Sadao 百田佐多生 (Kochi Univ. Technol.)  
 MORITA Hiroaki 森田弘明 (Horiguchi Ironworks)  
 MURAOKA Mitsuo 村岡光男 (Fac. Eng., Aomori Univ.)  
 MUTA Atsushi 牟田淳 (Inst. Phys., Univ. Tsukuba)  
 MUTO Kazuo 武藤一雄 (Inst. Sci., Tokyo Inst. Technol.)  
 NAKADA Hitoshi 中田仁 (Fac. Sci., Chiba Univ.)  
 NOJIRI Yoichi 野尻洋一 (Kochi Univ. Technol.)  
 NOMURA Izumi 野村和泉 (NIFS)  
 OGAWA Kengo 小川健吾 (Fac. Sci., Chiba Univ.)  
 OGAWA Yoko 小川洋子 (Fac. Sci., Osaka Univ.)  
 OGLOBLIN Alexei A. (Kurchatov. Inst., Russia)  
 OHTA Masahisa 太田雅久 (Fac. Sci., Konan Univ.)  
 OHTSU Hideaki 大津秀暁 (Fac. Sci., Tohoku Univ.)  
 OHTSUBO Takashi 大坪隆 (Fac. Sci., Niigata Univ.)  
 OMATA Kazuo 小俣和夫 (Inst. Nucl. Study, Univ. Tokyo)  
 ONISHI Naoki 大西直毅 (Fac. Eng., Yamanashi Univ.)  
 ONO Akira 小野章 (Fac. Sci., Tohoku Univ.)  
 OKUDA Takashi 奥田貴志 (Fac. Sci., Tohoku Univ.)  
 OOI Makito 大井万紀人 (Dep. Phys., Sch. Sci., Univ. Tokyo)  
 ORYU Shinsho 尾立晋祥 (Fac. Sci. Technol., Tokyo Univ. Sci.)  
 OTSUKA Takaharu 大塚孝治 (Fac. Sci., Univ. Tokyo.)  
 OYAMATSU Kazuhiro 親松和浩 (Aichi Shukutoku Univ.)  
 OZEKI Takashi 大関和貴 (Fac. Sci., Tohoku Univ.)  
 PETRASCU Horia (Horia Inst. Phys. Nucl. Eng., Romania)  
 PETRASCU Marius (Horia Inst. Phys. Nucl. Eng., Romania)  
 POLLACCO Emmanuel (EAC, France)  
 REN Zhang Zhou (Nanjing Univ., China)  
 ROUSSEL-CHAMAZ P. (GANIL, France)  
 SAGAWA Hiroyuki 佐川弘幸 (Cen. Math. Sci., Univ. Aizu)  
 SAKAGUCHI Harutaka 坂口治隆 (Grad. Sch., Kyoto Univ.)

SAKAI Hideyuki 酒井英行 (Fac. Sci., Univ. Tokyo)  
 SAKURAI Hirohisa 櫻井敬久 (Fac. Sci., Yamagata Univ.)  
 SAMANTA Chhanda (Sala Inst. Nucl. Phys., Calcutta, India)  
 SARHAN Badawy (Cairo Univ., Egypt)  
 SASA Hiromasa 佐々博政 (Horiguchi Ironworks)  
 SATO Hiroshi 佐藤 紘 (Seikei Univ.)  
 SATO Kazuhiro 佐藤和洋 (Tokyo Fire Dept.)  
 SATO Kenichi 佐藤憲一 (Dept. Phys., Tohoku Coll. Pharm.)  
 SAVAJOLS H. (GANIL, France)  
 SCHROEDER Lee S. (Laurence Berkeley Lab., USA)  
 SEKI Ryoichi 関 亮一 (California Univ., USA)  
 SERRA Milena (Tech. Munich Univ., Germany)  
 SHERRIL Bradley M. (Michigan State Univ., USA)  
 SHEN Caiwan (Dept. Nucl. Phys., China Inst. At. Energy, China)  
 SHIBATA Mitihiko 柴田理尋 (Dept. Energy Eng. Sci., Nagoya Univ.)  
 SHIBATA Toru 柴田 徹 (Sci. Eng., Aoyama Gakuin Univ.)  
 SIGNORINI Cosimo (INFN, Italy)  
 SMITH Michael (Inst. Oak Ridge, USA)  
 SUGANUMA Hideo 菅沼秀夫 (RCNP, Osaka Univ.)  
 SUGAWARA Masahiko 菅原昌彦 (Fund. Sci., Chiba Inst. Technol.)  
 SUMIYOSHI Kohsuke 住吉光介 (Numazu College Technol.)  
 SÜMMERER Klaus (GSI, Germany)  
 SUZUKI Akihiro 鈴木昭弘 (Shinshu Univ.)  
 SUZUKI Hideyuki 鈴木英行 (KEK)  
 SUZUKI Takeshi 鈴木 健 (Fac. Sci., Niigata Univ.)  
 SUZUKI Tsuneo 鈴木恒雄 (Fac. Sci., Kanazawa Univ.)  
 SUZUKI Toshio 鈴木俊夫 (Coll. Hum. Sci., Nihon Univ.)  
 SUZUKI Toshio 鈴木敏男 (Sci. Eng., Fukui Univ.)  
 SUZUKI Yasuyuki 鈴木宣之 (Fac. Sci., Niigata Univ.)  
 TACHIBANA Takahiro 橋 高博 (Sen. High Sch., Waseda Univ.)  
 TAKAHASHI Yoshiyuki 高橋義幸 (Alabama Univ., USA)  
 TAKAHASHI Yutaka 高橋 豊 (Fac. Sci., Osaka Univ.)  
 TAKANO Masatoshi 鷹野正利 (Fac. Sci. Eng., Waseda Univ.)  
 TAKEMASA Tadashi 武政尹士 (Kyoto Univ. Ed.)  
 TAKIGAWA Noboru 滝川 昇 (Fac. Sci., Tohoku Univ.)  
 TAJIMA Naoki 田嶋直樹 (Fac. Sci., Fukui Univ.)  
 TANABE Kazuko 田辺和子 (Otsuna Women's Univ.)  
 TANAKA Kazuhiro 田中和広 (Med. Dept., Juntendo Univ.)  
 TANAKA Takaya 田中孝哉 (Fac. Sci., Saitama Univ.)  
 TERASAWA Kazuhiro 寺沢和洋 (Fac. Sci. Eng., Waseda Univ.)  
 TER-AKOPIAN G. (Dubna, Russia)  
 TEZUKA Hirokazu 手塚洋一 (Dept. Liberal Arts. Fac. Literature, Toyo Univ.)  
 THIROLF P. (Univ. Munchen, Germany)  
 TOHYAMA Mitsuru 遠山 満 (Kyorin Univ.)  
 TOKANAI Fuyuki 門叶冬樹 (Fac. Sci., Yamagata Univ.)  
 TOKI Hiroshi 土岐 博 (RCNP, Osaka Univ.)  
 TOMODA Toshiaki 友田敏章 (Fac. Sci., Aomori Univ.)  
 TORBJOEN Baeck (Stockholm Univ., Sweden)  
 TOSTEVIN Jeffrey A. (Univ. Surry, India)  
 UCHIHORI Yukio 内掘幸夫 (Inst. Rad. Sci.)  
 UTSUNO Yutaka 宇津野 穰 (Tokai Res. Estab., JAERI)  
 UTSUNOMIYA Hiroaki 宇都宮弘章 (Fac. Sci., Konan Univ.)  
 VARGA Kalman (Inst. Oak Ridge, USA)  
 WADA Takahiro 和田隆宏 (Fac. Sci., Konan Univ.)  
 WAKAI Masamiti 若井正道 (Grad. Sch. Sci., Osaka Univ.)  
 WINKLER Martin (GSI, Germany)  
 WOLLNIK Hermann (Oak Ridge Lab., USA)

YABANA Kazuhiro (Fac. Sci., Univ. Tsukuba)  
 YAGI Hirosuke 八木浩輔 (Fac. Sci., Univ. Tsukuba)  
 YAMADA Shoichi 山田章一 (Fac. Sci., Univ. Tokyo)  
 YAMAGUCHI Yoshio 山口嘉夫 (Inst. Nucl. Study., Univ. Tokyo)  
 YORANN Alhassid (Yale Univ., USA)  
 YOSHIDA Nobuaki 吉田宣章 (Fac. Inf., Kansai Univ.)  
 YOSHINAGA Naotaka 吉永尚孝 (Fac. Sci., Saitama Univ.)  
 YUZUKI Akira 柚木 彰 (Toshiba Corp.)  
 ZAHAR Mohamed (Dept. Phys., Notre Dam Univ., USA)  
 ZHENG Tao (Fac. Sci. Technol., Sci. Univ. Tokyo)  
 ZHOU Shan-Gi (Peking Univ., China)

*Trainees*

CHIBA Masami 千葉将充 (Fac. Sci., Tohoku Univ.)  
 COURALLET Delphine (Ecole Mines Nantes, France)  
 FUZIMURA Takeshi 藤村 岳 (Sci. Eng., Aoyama Gakuin Univ.)  
 HARA Kenichiro 原 健一朗 (Fac. Sci. Eng., Waseda Univ.)  
 HARUKI Masamichi 春木正道 (Fac. Sci. Eng., Waseda Univ.)  
 HASHIMOTO Izumi 橋本和泉 (Fac. Sci., Osaka Univ.)  
 HASHIZUME Kazuaki 橋詰和明 (Fac. Sci., Konan Univ.)  
 HIBINO Masaru 日比野 優 (Fac. Sci. Eng., Waseda Univ.)  
 IHARA Akifumi 井原亜紀史 (Fac. Sci. Eng., Waseda Univ.)  
 ITO Hiroshi 伊藤浩巳 (Fac. Sci. Eng., Waseda Univ.)  
 KATO Tomomi 加藤智美 (Fac. Sci., Niigata Univ.)  
 KATO Toshiyuki 加藤俊幸 (Fac. Sci. Eng., Waseda Univ.)  
 KAWA Tadahisa 河 忠久 (Fac. Sci., Osaka Univ.)  
 KAWAMURA Yoshie 川村淑恵 (Fac. Sci., Niigata Univ.)  
 KIHIRA Eiichi 吉平栄一 (Fac. Sci. Eng., Waseda Univ.)  
 KITANI Takao 木谷貴雄 (Fac. Sci. Eng., Waseda Univ.)  
 KIYAMU Atushi 喜谷武篤史 (Fac. Sci. Eng., Ibaraki Univ.)  
 KOBAYASHI Shingo 小林進吾 (Fac. Sci. Eng., Waseda Univ.)  
 KOIKE Takayuki 小池貴之 (Fac. Sci. Eng., Waseda Univ.)  
 KUDO Syuichi 工藤修一 (Fac. Sci., Osaka Univ.)  
 KURIYAMA Koji 栗山幸治 (Sci. Eng., Aoyama Gakuin Univ.)  
 MASUMURA Takahiro 増村考洋 (Fac. Sci. Eng., Waseda Univ.)  
 MIYAKE Toru 三宅 徹 (Fac. Sci., Osaka Univ.)  
 MUTO Nobuo 武藤信雄 (Fac. Eng., Aoyama Gakuin Univ.)  
 NAGATOMO Kiyoshi 長友 傑 (Fac. Sci., Osaka Univ.)  
 NISHIKIDO Humihiko 錦戸文彦 (Fac. Sci. Eng., Waseda Univ.)  
 OGURA Masako 小倉昌子 (Fac. Sci., Osaka Univ.)  
 OHZEKI Kazuki 大関和貴 (Fac. Sci., Tohoku Univ.)  
 OKA Akihiro 岡 晃弘 (Fac. Sci. Eng., Waseda Univ.)  
 OKUDA Takashi 奥田貴志 (Fac. Sci., Tohoku Univ.)  
 OKUDAIRA Osamu 奥平 修 (Fac. Sci. Eng., Waseda Univ.)  
 OZAKI Kiminori 尾崎公教 (Fac. Sci. Eng., Waseda Univ.)  
 SAKAGUCHI Takao 坂口貴男 (Fac. Sci. Eng., Waseda Univ.)  
 SASAKI Makoto 佐々木 誠 (Fac. Sci., Osaka Univ.)  
 SATO Kazunori 佐藤和則 (Fac. Sci., Osaka Univ.)  
 SEKIGUCHI Masatugu 関口昌嗣 (Fac. Sci., Tohoku Univ.)  
 SHIMIZU Noritaka 清水則孝 (Fac. Sci., Univ. Tokyo)  
 SOURI Hirofumi 惣宇利啓史 (Fac. Sci. Eng., Waseda Univ.)  
 SUGIMOTO Satoshi 杉本 聡 (RCNP, Osaka Univ.)  
 TAKEMURA Atsushi 竹村 淳 (Fac. Sci., Osaka Univ.)  
 TAKEMURA Haruyuki 竹村春礼 (Fac. Sci. Eng., Waseda Univ.)  
 TAKENAKA Sunao 竹中 直 (Fac. Sci. Eng., Waseda Univ.)  
 TAKENOUCHI Masatoshi 竹之内正俊 (Fac. Sci. Eng., Waseda Univ.)  
 TAKEUCHI Satoshi 武内 聡 (Fac. Sci., Rikkyo Univ.)

TANAKA Motoyuki 田中基之 (Fac. Sci., Waseda Univ.)  
 TAZAWA Shinya 田沢伸也 (Fac. Sci., Tohoku Univ.)  
 TERASAWA Mariko 寺澤真理子 (Fac. Sci., Univ. Tokyo.)  
 TERUHI Shigeru 照日 繁 (Fac. Sci. Eng., Waseda Univ.)  
 UMEMURA Tomohiro 梅村朋弘 (Fac. Sci. Eng., Waseda Univ.)  
 UZIIIE Toru 氏家 徹 (Fac. Sci., Tohoku Univ.)  
 WATANABE Kiwamu 渡辺極之 (Fac. Sci., Tohoku Univ.)  
 WATANABE Shigeo 渡邊茂夫 (Fac. Sci., Niigata Univ.)  
 YAKUSHIJI Takashi 薬師寺 嵩 (Fac. Sci., Tohoku Univ.)  
 YAMADA Kazunari 山田一成 (Fac. Sci., Rikkyo Univ.)  
 YAMAGUCHI Yoshitaka 山口由高 (Fac. Sci., Niigata Univ.)  
 YAMASHITA Masaki 山下雅樹 (Adv. Res. Inst. Sci. Eng., Waseda Univ.)  
 YAMASHITA Naoyuki 山下直之 (Fac. Sci. Eng., Waseda Univ.)  
 YASHIRO Junichi 矢代淳一 (Fac. Sci. Eng., Waseda Univ.)  
 YOSHIOKA Hideki 吉岡秀樹 (Fac. Sci. Eng., Waseda Univ.)

### Applied Nuclear Physics Laboratory

#### Head

ASAHI Koichiro 旭 耕一郎

#### Members

KOBAYASHI Yoshio 小林義男	UENO Hideki 上野秀樹
MURATA Jiro 村田次郎	SATO Wataru 佐藤 渉
YONEDA Kenichiro 米田健一郎	YOSHIMI Akihiro 吉見彰洋
WATANABE Hiroshi 渡邊 寛	

#### Visiting Members

EINAGA Yasuaki 栄長泰明 (Fac. Sci., Univ. Tokyo)  
 IMAI Nobuaki 今井伸明 (Dept. Phys., Grad. Sch. Sci., Univ. Tokyo)  
 KUBO Kenya 久保謙哉 (Fac. Sci., Univ. Tokyo)  
 MIYOSHI Hisanori 三好永哲 (Grad. Sch. Sci. Eng., Tokyo Inst. Technol.)  
 OGAWA Hiroshi 小川博嗣 (Fac. Sci., Tokyo Inst. Technol.)  
 OKADA Takuya 岡田卓也 (Fac. Sci., Gakushuin Univ.)  
 SAKAI Kenji 酒井健二 (Fac. Sci., Tokyo Inst. Technol.)  
 YAMADA Yasuhiro 山田康洋 (Fac. Sci., Tokyo Univ. Sci.)

#### Trainees

HORI Kentaro 堀 健太郎 (Fac. Sci., Tokyo Univ. Sci.)  
 KATSUMATA Keiichi 勝又啓一 (Fac. Sci., Tokyo Univ. Sci.)  
 MIYAZAKI Jun 宮崎 淳 (Fac. Sci., Tokyo Univ. Sci.)  
 SAITO Takashi 齋藤 崇 (Fac. Sci., Tokyo Univ. Sci.)  
 KAMEDA Daisuke 亀田大輔 (Fac. Sci., Tokyo Inst. Technol.)  
 KAIHARA Jou 貝原星宇 (Fac. Sci., Tokyo Inst. Technol.)  
 OGAWA Shigeru 小川 茂 (Fac. Sci., Shizuoka Inst. Sci. Tech.)  
 ONO Yuuki 小野祐樹 (Fac. Sci., Tokyo Univ. Sci.)  
 SHIMAZAKI Hideo 島崎秀生 (Fac. Sci., Tokyo Univ. Sci.)  
 ISHIKAWA Yumiko 石川由美子 (Fac. Sci., Tokyo Univ. Sci.)  
 SHIMIZU Yasunori 清水康功 (Fac. Sci., Shizuoka Inst. Sci. Tech.)

### Atomic Physics Laboratory

#### Head

YAMAZAKI Yasunori 山崎泰規

#### Members

IKEDA Tokihiro 池田時浩	KAMBARA Tadashi 神原 正
---------------------	----------------------

KANAI Yasuyuki 金井保之  
MORISHITA Yuichiro 森下雄一郎  
NAKAMURA Takashi 中村貴志  
OURA Masaki 大浦正樹  
SHIMAMURA Isao 島村 勲  
TERANISHI Yoshiaki 寺西慶哲

KOJIMA Takao M. 小島隆夫  
NAKAI Yoichi 中井陽一  
NISHIDA Masami 西田雅美  
OYAMA Hitoshi 大山 等  
TAKEKAWA Michiya 竹川道也  
WADA Michiharu 和田道治

*Visiting Members*

ANDO Kozo 安藤剛三  
AWAYA Yohko 粟屋容子 (Coll. Art Design Gen. Ed., Musashino Art Univ.)  
AZUMA Toshiyuki 東 俊行 (Dept. Phys., Tokyo Metrop. Univ.)  
CHIMI Yasuhiro 知見康弘 (Tokai Res. Estab., JAERI)  
DEPAOLA Brett (Dept. Phys., Kansas State Univ., USA)  
DUMITRIU Dana (Natl. Inst. Phys. Nucl. Eng., Romania)  
EICHLER Jörg (Hahn-Meitner Inst. Berlin, Germany)  
ENDO Atsumi 遠藤厚身 (Dept. Phys., Grad. Sch. Sci., Univ. Tokyo)  
FAIFMAN Mark (Russ. Res. Cen., Kurchatov Inst., Russia)  
FUJIMA Kazumi 藤間一美 (Fac. Eng., Yamanashi Univ.)  
HARA Shunsuke 原 俊介 (Dept. Gen. Ed., Tsukuba Coll. Technol.)  
HAYAKAWA Kazuo 早川一生 (Shizuoka Inst. Sci. Technol.)  
HINO Ken-ichi 日野健一 (Inst. Appl. Phys., Univ. Tsukuba)  
HITACHI Akira 月出 章 (Kochi Med. Sch.)  
HORACEK Jiri (Charles Univ., Czech Republic)  
HOSHINO Masamitsu 星野正光 (Grad. Sch. Sci. Eng., Sophia Univ.)  
HUTTON Roger (Dept. Phys., Lund Univ., Sweden)  
ICHIMURA Atsushi 市村 淳 (Inst. Space Astr. Sci.)  
IGARASHI Akinori 五十嵐明則 (Fac. Eng., Miyazaki Univ.)  
IKEDA Hiroshi 池田 博 (Univ. Tsukuba)  
INOKUTI Mitio 井口道生 (Argonne Natl. Lab., USA)  
ISHII Keishi 石井慶之 (Fac. Sci. Eng., Ritsumeikan Univ.)  
ISHIKAWA Norito 石川法人 (Tokai Res. Estab., JAERI)  
ITO Takaomi 伊藤高臣 (Grad. Sch. Arts Sci., Univ. Tokyo)  
ITOH Akio 伊藤秋男 (Fac. Eng., Kyoto Univ.)  
ITOYOH Yoh 伊藤 陽 (Fac. Sci., Josai Univ.)  
IWAI Yoshio 岩井良夫 (Dept. Phys., Grad. Sch. Sci., Univ. Tokyo)  
IWASE Akihiro 岩瀬彰宏 (Tokai Res. Estab., JAERI)  
KAGEYAMA Kensuke 蔭山健介 (Fac. Eng., Saitama Univ.)  
KAWATSURA Kiyoshi 川面 澄 (Fac. Eng. Design, Kyoto Inst. Technol.)  
KIMURA Kenji 木村健二 (Fac. Eng., Kyoto Univ.)  
KIMURA Mineo 季村峯生 (Fac. Eng., Yamaguchi Univ.)  
KITAJIMA Masashi 北島昌史 (Fac. Sci. Technol., Sophia Univ.)  
KOBAYASHI Nobuo 小林信夫 (Dept. Phys., Tokyo Metrop. Univ.)  
KOIKE Fumihito 小池文博 (Sch. Med., Kitasato Univ.)  
KOIZUMI Tetsuo 小泉哲夫 (Dept. Phys., Rikkyo Univ.)  
KOMAKI Ken-ichiro 小牧研一郎 (Grad. Sch. Arts Sci., Univ. Tokyo)  
KOWARI Kenichi 小割健一 (Dept. Appl. Phys. Chem., Univ. Electro-Commun.)  
KUROKI Kenro 黒木健郎 (Natl. Res. Inst. Police Sci.)  
MATSUNAMI Noriaki 松波紀明 (Sch. Eng., Nagoya Univ.)  
MATSUO Takashi 松尾 崇 (Dept. Pathol., Tokyo Med. Dent. Univ.)  
MATSUZAWA Michio 松澤通生 (Dept. Appl. Phys. Chem., Univ. Electro-Commun.)  
MITSUKE Koichiro 見附孝一郎 (Inst. Mol. Sci.)  
MIZOGAWA Tatsumi 溝川辰巳 (Wakayama Natl. Coll. Technol.)  
MOHRI Akihiro 毛利明博  
MUKOYAMA Takeshi 向山 毅 (Kansai Gaidai Univ.)  
NIIGAKI Megumi 新垣 恵 (Dept. Phys., Grad. Sch. Sci., Univ. Tokyo)  
NISHIMURA Tamio 西村民男 (Univ. Rome, Italy)  
OHTANI Shunsuke 大谷俊介 (Dept. Appl. Phys. Chem., Univ. Electro-Commun.)

OSHIMA Nagayasu 大島永康 (Grad. Sch. Arts Sci., Univ. Tokyo)  
 OKABAYASHI Norio 岡林則夫 (Grad. Sch. Arts Sci., Univ. Tokyo)  
 OKADA Kunihiro 岡田邦宏 (Fac. Sci. Technol., Sophia Univ.)  
 OKAYASU Satoru 岡安悟 (Tokai Res. Estab., JAERI)  
 OKUNO Kazuhiko 奥野和彦 (Dept. Phys., Tokyo Metrop. Univ.)  
 ONO Fumihisa 小野文久 (Dept. Phys., Okayama Univ.)  
 PICHL Lukáš (Dept. Comput. Software, Univ. Aizu)  
 QU Yi-Zhi 屈一至 (Univ. Sci. Technol. China, China)  
 ROSMEJ Frank B. (GSI, Germany)  
 SAKAI Akio 坂井昭夫 (Vacuum Products Co.)  
 SATO Hiroshi 佐藤浩史 (Fac. Sci., Ochanomizu Univ.)  
 SCHUCH Reinhold H. (Stockholm Univ., Sweden)  
 SCHUESSLER Hans A. (Texas A & M Univ., USA)  
 SHIMA Kunihiro 島邦博 (Tandem Accel. Cen., Univ. Tsukuba)  
 SHIMAKURA Noriyuki 島倉紀之 (Fac. Sci., Niigata Univ.)  
 TONUMA Tadao 戸沼正雄 (Adv. Res. Inst. Sci. Eng., Waseda Univ.)  
 TORII Hiroyuki 鳥居寛之 (Grad. Sch. Arts Sci., Univ. Tokyo)  
 TOSHIMA Nobuyuki 戸嶋信幸 (Inst. Appl. Phys., Univ. Tsukuba)  
 TSUCHIDA Hidetsugu 土田秀次 (Fac. Sci., Nara Women's Univ.)  
 UEDA Kiyoshi 上田潔 (Inst. Multidiscip. Res. Adv. Mater., Tohoku Univ.)  
 WATANABE Shinichi 渡辺信一 (Dept. Appl. Phys. Chem., Univ. Electro-Commun.)  
 YAGISHITA Akira 柳下明 (KEK)  
 YOSHIDA Yutaka 吉田豊 (Shizuoka Inst. Sci. Technol.)  
 YOSHIKI FRANZÉN Ken (Grad. Sch. Arts Sci., Univ. Tokyo)  
 ZOU Yaming (Shanghai Jiao Tong Univ., China)

#### *Trainees*

ARIKAWA Kazuhiro 有川和宏 (Grad. Sch. Sci., Shizuoka Inst. Sci. Technol.)  
 CHEN Fanfu 陳帆夫 (Dept. Phys., Grad. Sch. Sci., Rikkyo Univ.)  
 GHADA H. Machtoub (Dept. Appl. Phys. Chem., Univ. Electro-Commun.)  
 HAMATANI Yuutarou 濱谷祐多郎 (Dept. Phys., Okayama Univ.)  
 KANEKO Manabu 兼子学 (Grad. Sch. Sci., Shizuoka Inst. Sci. Technol.)  
 KURODA Naofumi 黒田直史 (Dept. Phys., Grad. Sch. Sci., Univ. Tokyo)  
 MAJIMA Takuya 間嶋拓也 (Grad. Sch. Eng., Kyoto Univ.)  
 MIZOGUCHI Satoshi 溝口智 (Grad. Sch. Sci. Eng., Sophia Univ.)  
 OGAWA Shigeru 小川茂 (Grad. Sch. Sci., Shizuoka Inst. Sci. Technol.)  
 SAKAGUTI Syuiti 坂口修一 (Grad. Sch. Sci. Eng., Saitama Univ.)  
 SATO Hiroyuki 佐藤浩行 (Fac. Eng., Iwate Univ.)  
 SATO Yasuhiro 佐藤裕広 (Dept. Phys., Grad. Sch. Sci., Univ. Tokyo)  
 SHIMADA Hiroyuki 島田紘行 (Dept. Phys., Grad. Sch. Sci., Univ. Tokyo)  
 SONODA Tetsu 園田哲 (Grad. Sch. Sci., Tohoku Univ.)  
 TAKABAYASHI Yuichi 高林雄一 (Dept. Phys., Grad. Sch. Sci., Univ. Tokyo)  
 WATANABE Satoko 渡邊聡子 (Grad. Sch. Sci. Eng., Saitama Univ.)

### **Muon Science Laboratory**

#### *Head*

NAGAMINE Kanetada 永嶺謙忠

#### *Members*

ISHIDA Katsuhiko 石田勝彦	KOYAMA Akio 小山昭雄
MATSUDA Yasuyuki 松田恭幸	MATSUZAKI Teiichiro 松崎禎市郎
OKAMOTO Toshifumi 岡本敏史	STRASSER Patrick
WATANABE Isao 渡邊功雄	YAMASE Hiroyuki 山瀬博之

#### *Visiting Members*

ADACHI Tadashi 足立匠 (Fac. Eng., Tohoku Univ.)

ADROJA Devashibhai (Fac. Sci., Hiroshima Univ.)  
 AJIRO Yoshitami 網代芳民 (Fac. Sci., Kyushu Univ.)  
 AKIMITSU Jun 秋光 純 (Coll. Sci. Eng., Aoyama Gakuin Univ.)  
 AKOSHIMA Megumi 阿子島めぐみ (Fac. Eng., Tohoku Univ.)  
 ARAI Juichiro 新井重一郎 (Tokyo Univ. Sci.)  
 AWAGA Kunio 阿波賀邦夫 (Grad. Sch. Arts Sci., Univ. Tokyo)  
 BAKULE Pavel (Rutherford Appleton Lab., UK)  
 BOGDANOVA N. Ludmila (Inst. Theor. Exp. Phys., Russia)  
 BRIERRE Tina M. (KEK)  
 DAS Prasad Tara (Dept. Phys., State Univ. New York, Albany, USA)  
 FLEMING D. (TRIUMF, Canada)  
 FUJII Yutaka 藤井 裕 (Fac. Eng., Fukui Univ.)  
 FUJITA Masaki 藤田全基 (Inst. Chem. Res., Kyoto Univ.)  
 FUKAYA Atsuko 深谷敦子 (Columbia Univ., USA)  
 FUKUSHIMA Kenji 福島謙二  
 HAGIWARA Makoto 萩原 亮 (Fac. Eng. Design, Kyoto Inst. Technol.)  
 HIGEMOTO Wataru 髭本 亘 (KEK)  
 HONDA Morihito 本田守広 (Inst. Cosmic Ray Res., Univ. Tokyo)  
 HIYAMA Emiko 肥山詠美子 (KEK)  
 IKEDA Susumu 池田 進 (KEK)  
 ITO Atsuko 伊藤厚子  
 IWASAKI Masahiko 岩崎雅彦 (Dept. Phys., Tokyo Inst. Technol.)  
 KADONO Ryosuke 門野良典 (KEK)  
 KAMIMURA Masayasu 上村正康 (Fac. Sci., Kyushu Univ.)  
 KATO Mineo 加藤岑生 (Tokai Res. Estab., JAERI)  
 KAWAMURA Naritoshi 河村成肇 (KEK)  
 KINO Yasushi 木野康志 (Fac. Sci., Tohoku Univ.)  
 KOIKE Takahisa 小池貴久 (KEK)  
 KOIKE Youji 小池洋二 (Fac. Eng., Tohoku Univ.)  
 KRAVTSOV Andrey (Russ. Fed. Nucl. Cen., Russia)  
 KUNO Yoshitaka 久野良孝 (KEK)  
 MACRAE Roderick M. (Notre Dame Radiat. Lab., USA)  
 MAKIMURA Syunsuke 牧村俊助 (KEK)  
 MARUTA Goro 丸田悟朗 (KEK)  
 MEKATA Mamoru 目方 守 (Fac. Eng., Fukui Univ.)  
 MIKHAILOV A. (Petersburg Nucl. Phys. Inst., Russia)  
 MINAMISONO Tadanori 南園忠則 (Fac. Sci., Osaka Univ.)  
 MIYAKE Yasuhiro 三宅康博 (KEK)  
 MIYAKO Yoshihito 都 福仁 (Fac. Sci., Osaka Univ.)  
 MOCHIKU Takashi 茂筑高士 (Natl. Res. Inst. Metals)  
 NAKAMURA Satoshi N. 中村 哲 (Fac. Sci., Tohoku Univ.)  
 NAKANO Takehito 中野岳仁 (Fac. Sci., Osaka Univ.)  
 NISHIDA Nobuhiko 西田信彦 (Fac. Sci., Tokyo Inst. Technol.)  
 NISHIYAMA Kusuo 西山樟生 (KEK)  
 NOZUE Yasuo 野末泰夫 (Fac. Sci., Osaka Univ.)  
 PEREVOZCHIKOV V. V. (Inst. Theor. Exp. Phys., Russia)  
 PONOMAREV Leonid I. (Kurchatov Inst., Russia)  
 PRATT Francis L. (Rutherford Appleton Lab., UK)  
 SAKAMOTO Shinichi 坂元真一 (KEK)  
 SATO Kazuhiko 佐藤一彦 (Fac. Sci., Saitama Univ.)  
 SHIMOMURA Koichiro 下村浩一郎 (KEK)  
 SOLOVJEV E. (Univ. Skopja, Russia)  
 STORCHAK Vyacheslav G. (Kurchatov Inst., Russia)  
 SUGAI Hiroyuki 須貝宏行 (Tokai Res. Estab., JAERI)  
 TAKABATAKE Toshiro 高畠敏郎 (Grad. Sch. Adv. Sci. Matter, Hiroshima Univ.)  
 TAKEDA Keiji 武田啓司 (Hokkaido Univ.)  
 TAKIGAWA Masashi 瀧川 仁 (Inst. Solid State Phys.)

TANASE Masakazu 棚瀬正和 (Tokai Res. Estab., JAERI)  
 TOLSTIKHINE O. (Kurchatov Inst., Russia)  
 TORIKAI Eiko 鳥養映子 (Fac. Eng., Yamanashi Univ.)  
 TOYODA Akihisa 豊田晃久 (KEK)  
 UEDA Kazuo 上田和夫 (Inst. Solid State Phys.)  
 UMEO Kazunori 梅尾和則 (Fac. Sci., Hiroshima Univ.)  
 WADA Nobuo 和田信雄 (Grad. Sch. Arts Sci., Univ. Tokyo)  
 WATANABE Tsutomu 渡部力 (Int. Chr. Univ.)  
 YAGI Eiichi 八木栄一  
 YAMADA Kazuyoshi 山田和芳 (Inst. Chem. Res., Kyoto Univ.)  
 YUKHIMCHUK A. A. (Russ. Fed. Nucl. Cen., Russia)

*Trainees*

MIYADERA Haruo 宮寺晴夫 (Grad. Sch., Univ. Tokyo)  
 TANAKA Hiroyuki 田中宏幸 (Grad. Sch., Nagoya Univ.)

**Beam Physics and Engineering Laboratory**

*Head*

KATAYAMA Takeshi 片山武司

*Members*

FUKUDA Naoki 福田直樹	HAMAGAKI Manabu 浜垣 学
KOSEKI Tadashi 小関 忠	KUMAGAI Keiko 熊谷桂子
NAKAMURA Masato 中村仁音	NISHIURA Naoki 西浦正樹
OKAMURA Masahiro 岡村昌宏	OZAWA Shuichi 小澤修一
SAKUMI Akira 作美 明	TAKANAKA Masao 高仲政雄
TAMBA Moritake 丹波護武	WATANABE Tamaki 渡邊環
YANAGISAWA Yoshiyuki 柳澤善行	YOKKAICHI Satoshi 四日市 悟
YUN Chong-Cheoul 尹 鍾哲	

*Visiting Members*

AMEMIYA Hiroshi 雨宮 宏  
 CHIBA Yoshiaki 千葉好明  
 DIKANSKI Nikolai (Budka Inst. Nucl. Phys., Russia)  
 HARA Tamio 原 民夫 (Toyota Technol. Inst.)  
 HASHIMOTO Yuichi 橋本雄一 (Canon Inc.)  
 HATTORI Toshiyuki 服部俊幸 (Res. Lab. Nucl. React., Tokyo Inst. Technol.)  
 JAMESON Robert (Univ. Colorado, USA)  
 KAMETANI Souichiro 亀谷聡一郎 (CNS, Univ. Tokyo)  
 KATO Shigeki 加藤茂樹 (KEK)  
 MATSUMOTO Takashi 松元貴志 (CNS, Univ. Tokyo)  
 MICHIMASA Shin'ichiro 道正新一郎 (CNS, Univ. Tokyo)  
 MIYAZAKI Hirofumi 宮崎洋文 (Sumitomo Heavy Ind., Ltd.)  
 OGAWA Masao 小川雅生 (Tokyo Inst. Technol.)  
 OGURI Yoshiyuki 小栗慶之 (Res. Lab. Nucl. React., Tokyo Inst. Technol.)  
 OKAZAKI Kiyohiko 岡崎清比古  
 SAKAKIBARA Takeshi 榊原 剛 (Chuo Univ.)  
 SAKAMOTO Yuichi 坂本雄一 (Nichimen Co.)  
 SERATA Masaki 世良田真来 (Coll. Sci., Rikkyo Univ.)  
 SIDORIN Anatoly (J.I.N.R., Russia)  
 SUGII Kazuo 杉井一生 (Osaka Vacuum, Ltd.)  
 SYRESIN Evgeny (J.I.N.R., Russia)  
 TAKANO Motonobu 高野元信  
 TAKEUCHI Takeshi 竹内 猛 (CNS, Univ. Tokyo)  
 TSUTSUI Hiroshi 筒井裕士 (Sumitomo Heavy Ind., Ltd.)  
 TUCHIYA Masao 土屋将夫 (Ishikawajima-Harima Heavy Ind., Ltd.)

YAMAKAWA Koji 山川晃司 (Irie Koken Co. Ltd.)  
YANO Katsuki 矢野勝喜  
YUKITAKE Mitsuteru 雪竹光輝 (Hitachi, Ltd)  
XIAO Meiqin 肖美琴 (Fermi Natl. Accel. Lab., USA)  
FUCHI Yoshihide 淵好秀 (KEK)  
FÜLÖP Zsolt (ATOMKI, Hungary)  
GALSTER Wilfried (CNS, Univ. Tokyo)  
HAMAGAKI Hideki 浜垣秀樹 (CNS, Univ. Tokyo)  
HIRANO Midori 平野みどり (CNS, Univ. Tokyo)  
IWASAKI Hironori 岩崎弘典 (CNS, Univ. Tokyo)  
KATO Seigo 加藤静吾 (Yamagata Univ.)  
KOHNO Kiyoji 河野清次 (CNS, Univ. Tokyo)  
KUBONO Shigeru 久保野茂 (CNS, Univ. Tokyo)  
KUBOTA Shogo 久保田昌吾 (CNS, Univ. Tokyo)  
MIYACHI Takashi 宮地孝 (CNS, Univ. Tokyo)  
NAKANO Joe 中野譲 (CNS, Univ. Tokyo)  
NOTANI Masahiro 野谷将広 (CNS, Univ. Tokyo)  
OHSHIRO Yukimitsu 大城幸光 (CNS, Univ. Tokyo)  
OYAMA Ken 大山健 (CNS, Univ. Tokyo)  
OZAWA Kyoichiro 小沢恭一郎 (CNS, Univ. Tokyo)  
SAKAGUCHI Takao 坂口貴男 (CNS, Univ. Tokyo)  
SATO Yoshiteru 佐藤義輝 (CNS, Univ. Tokyo)  
SHIMOKOSHI Fumio 霜越文夫 (CNS, Univ. Tokyo)  
SHIMOURA Susumu 下浦享 (CNS, Univ. Tokyo)  
TAKAKU Seisaku 高久清作 (CNS, Univ. Tokyo)  
TANAKA Masahiko 田中雅彦 (KEK)  
TERANISHI Takashi 寺西高 (CNS, Univ. Tokyo)  
UESAKA Meiko 上坂明子 (CNS, Univ. Tokyo)  
WATANABE Shin-ichi 渡辺伸一 (CNS, Univ. Tokyo)  
YAMAZAKI Norio 山崎則夫 (CNS, Univ. Tokyo)

*Trainees*

NISHIMOTO Takeshi 西本武史 (Res. Lab. Nucl. React., Tokyo Inst. Technol.)  
ISOBE Tadaaki 磯部忠昭 (Waseda Univ.)  
KATO Koichi 加藤公一 (Waseda Univ.)  
LEE Ju Hahn 李柱漢 (Chung-Ang Univ., Korea)  
NANJYO Hajime 南條創 (Univ. Tokyo)  
OTA Shinsuke 大田晋輔 (Kyoto Univ.)  
TAMAI Munetaka 玉井宗孝 (Waseda Univ.)  
UE Koji 上浩二 (CNS, Univ. Tokyo)

**Cellular & Molecular Biology Laboratory**

*Head*

SHIBATA Takehiko 柴田武彦

*Members*

LING Feng 凌楓

**Cellular Physiology Laboratory**

*Head*

HANAOKA Fumio 花岡文雄

*Members*

YATAGAI Fumio 谷田貝文夫

### Visiting Members

ANDO Koichi 安藤興一 (Natl. Inst. Radiol. Sci.)  
FURUSAWA Yoshiya 古澤佳也 (Natl. Inst. Radiol. Sci.)  
HAMA Yoshimasa 浜 義昌 (Sci. Eng. Res. Lab., Waseda Univ.)  
HASE Yoshihiro 長谷純宏 (Takasaki Rad. Chem. Res. Estab., JAERI)  
HOSHINO Kazuo 星野一雄 (Natl. Inst. Radiol. Sci.)  
ITO Hisao 伊東久夫 (Sch. Med., Chiba Univ.)  
ITSUKAICHI Hiromi 五日市ひろみ (Natl. Inst. Radiol. Sci.)  
KANAI Tatsuaki 金井達明 (Natl. Inst. Radiol. Sci.)  
KASAI Kiyomi 笠井清美 (Natl. Inst. Radiol. Sci.)  
KAWACHI Kiyomitsu 河内清光 (Natl. Inst. Radiol. Sci.)  
KOBAYASHI Yasuhiko 小林泰彦 (Takasaki Rad. Chem. Res. Estab., JAERI)  
MATSUFUJI Naruhiro 松藤成弘 (Natl. Inst. Radiol. Sci.)  
MINOHARA Shinichi 箕原伸一 (Natl. Inst. Radiol. Sci.)  
MURAKAMI Masahiro 村上正弘 (Natl. Inst. Radiol. Sci.)  
SAITO Mizuho 齊藤瑞穂 (Natl. Inst. Radiol. Sci.)  
SASAKI Hiroshi 佐々木 弘 (Fac. Med., Kyushu Univ.)  
SHIKAZONO Naoya 鹿園直哉 (Takasaki Rad. Chem. Res. Estab., JAERI)  
SOGA Fuminori 曾我文宣 (Inst. Nucl. Study, Univ. Tokyo)  
TANAKA Atsushi 田中 淳 (Takasaki Rad. Chem. Res. Estab., JAERI)  
TOMURA Hiromi 外村浩美 (Natl. Inst. Radiol. Sci.)  
WATANABE Masami 渡辺正己 (Fac. Pharm., Nagasaki Univ.)  
YAMASHITA Shoji 山下昌次 (Natl. Saitama Hospital)

### Trainees

LI Ryonpha 李 玲華 (Natl. Inst. Radiol. Sci.)

## Plant Functions Laboratory

### Head

YOSHIDA Shigeo 吉田茂男

### Members

ABE Tomoko 阿部知子  
SAKAMOTO Koichi 坂本浩一  
MIYAZAWA Yutaka 宮沢 豊  
MATSUYAMA Tomoki 松山知樹  
FUJIWARA Makoto 藤原 誠

### Visiting Members

CHIN Chee-kok (Dept. Plant Sci., Rutgers Univ., USA)  
FURUKAWA Koji 古川浩二 (Mukoyama Orchids Ltd.)  
HAMATANI Misako 浜谷美佐子 (Hiroshima City Agr. Forest. Promot. Cen.)  
HARA Yasuhide 原 靖英 (Kanagawa Inst. Agr. Sci.)  
HONDA Ichiro 本多一郎 (Natl. Agr. Res. Cen., Min. Agr. Forest. Fish.)  
HORITA Mitsugu 堀田 貢 (Hokkaido Green-bio Inst.)  
KITAURA Takeo 北浦健生 (Kanagawa Inst. Agr. Sci.)  
LILL Ross Edward (Crop & Food Research, New Zealand)  
MIYOSHI Kazumitsu 三吉一光 (Fac. Bioresour. Sci., Akita Pref. Univ.)  
SUZUKI Kenichi 鈴木賢一 (Suntory Ltd.)  
TOKUHARA Ken 徳原 憲 (Dogashima Orchid Cen.)  
YOSHIDA Takuji 吉田拓司 (Takii Seed Co., Ltd.)  
TSUJIMOTO Hisashi 辻本 壽 (Kihara Biol. Res. Inst., Yokohama City Univ.)

### Trainees

KONAMI Yuki 許斐佑紀 (Fac. Sci. Tech., Tokyo Univ. Sci.)  
SAITO Hiroyuki 齊藤宏之 (Dep. Agr., Grad. Sch. Sci. Technol., Niigata Univ.)

## Microbial Toxicology Laboratory

### Head

YAMAGUCHI Isamu 山口 勇

### Members

MOTOYAMA Takayuki 本山高之

## CYCLOTRON CENTER

### Chief Scientist

YANO Yasushige 矢野安重

## RIBF Project Office

### Head

YANO Yasushige 矢野安重

### Members

DINH DANG Nguyen

INABE Naohito 稲辺 尚人

KUBO Toshiyuki 久保敏幸

MINEMURA Toshiyuki 峯村俊行

WAKASUGI Masanori 若杉昌徳

FUJII Shinichiro 藤井新一郎

KIM Ka-hae 金 佳恵

MADOKORO Hideki 間所秀樹

TAKEICHI Hiroshige 竹市博臣

YAMAJI Shuhei 山路修平

### Visiting Members

ARAKAWA Kazuo 荒川和夫 (Takasaki Rad. Chem. Res. Estab., JAERI)

BANDYOPADHYAN Arup (Var. Ener. Cycl. Cen., India)

CHAKRABARTI Alok (Var. Ener. Cycl. Cen., India)

CHATTOPADHYAY Subrata (Var. Ener. Cycl. Cen., India)

FUJINAWA Tadashi 藤縄 雅 (Mitsubishi Electric Co., Ltd.)

FUJISHIMA Shiro 藤島史郎 (Ishikawajima-Harima Heavy Ind. Co., Ltd.)

FUKUDA Mitsuhiro 福田光宏 (Takasaki Res. Estab., JAERI)

HIASA Toshikazu 日朝俊一 (Sumitomo Heavy Ind., Ltd.)

HIRUMACHI Tamiko 蛭町多美子 (Toshiba Corp.)

HONMA Toshihiro 本間寿広 (Natl. Inst. Radiol. Sci.)

KAKUTANI Nobukazu 角谷暢一 (Toshiba Corp.)

KIDO Syuuichi 木戸修一 (Hitachi Ltd.)

KOZU Hideo 神津秀雄 (Toshiba Corp.)

KUMADA Masayuki 熊田雅之 (Natl. Inst. Radiol. Sci.)

KUNO Kazuo 久野和雄 (Mitsubishi Electric Co., Ltd.)

MASUNO Shin-ichi 益野真一 (Mitsubishi Electric Co., Ltd.)

MASUOKA Toshikatu 益岡俊勝 (Hitachi Zosen Corp.)

MATSUI Ju-Mei 松井重明 (Mitsubishi Electric Co., Ltd.)

MIRONOV Vladmir (J.I.N.R., Russia)

MITSUMOTO Toshinori 密本俊典 (Sumitomo Heavy Ind., Ltd.)

MORIKAWA Tetsuya 森川鐵也

MOTONAGA Shoushichi 元永昭七

NAKAZAWA Taro 中沢太郎

OHKAWA Tomohiro 大川智宏 (Mitsubishi Res. Inst. Inc.)

OHTOMO Kiyotaka 大友清隆 (Sumitomo Heavy Ind., Ltd.)

SASAKI Mutsuko 佐々木睦子

SHEN Caiwan (Inst. Theor. Phys., China)

SIDORIN Anatoly (J.I.N.R., Russia)

TOMINAKA Toshiharu 冨中利治 (Hitachi Ltd.)

## Beam Dynamics Division

### Head

GOTO Akira 後藤 彰

### Members

FUKUNISHI Nobuhisa 福西暢尚

KAMIGAITO Osamu 上垣外修一

OHNISHI Jun-ichi 大西純一

OKUNO Hiroki 奥野広樹

SAKAMOTO Naruhiko 坂本成彦

SUZUKI Naoki 鈴木直毅

### Visiting Members

FUJISAWA Takashi 藤沢高志 (Natl. Inst. Radiol. Sci.)

FUJIWARA Ichiro 藤原一郎 (Dept. Econ., Otomon Gakuin Univ.)

HYODO Toshio 兵頭俊夫 (Grad. Sch. Arts Sci., Univ. Tokyo)

ITOH Yoshiko 伊東芳子 (Adv. Res. Inst. Sci. Eng., Waseda Univ.)

ITOH Kazuya 伊藤和也 (Tandem Accel. Cen., Univ. Tsukuba)

IWATA Ren 岩田 錬 (Cycl. Radioisot. Cen., Tohoku Univ.)

KAWAZU Akira 河津 璋 (Techno Riken Co., Ltd.)

KURIHARA Toshikazu 栗原俊一 (KEK)

MACHIDA Shinji 町田慎二 (KEK)

MATSUO Junko 松尾純子 (Yuuai Corp.)

MORI Yoshiharu 森 義治 (KEK)

NAGASHIMA Yasuyuki 長嶋泰之 (Grad. Sch. Arts Sci., Univ. Tokyo)

NOZAKI Tadashi 野崎 正 (Purex Co.)

OKAMURA Hiroyuki 岡村弘之 (Dept. Phys., Saitama Univ.)

SAITO Fuminori 斉藤文修

SAITO Katsuhiko 斉藤勝彦 (Sumitomo Heavy Ind., Ltd.)

UESAKA Tomohiro 上坂友洋 (Dept. Phys., Saitama Univ.)

VOROJTSOV Serguei (J.I.N.R., Russia)

### Trainees

IKEDA Takuichiro 池田拓一郎 (Dept. Phys., Saitama Univ.)

ISHIKAWA Kazuhiro 石川和宏 (Dept. Phys., Saitama Univ.)

ITOH Keisuke 伊藤圭介 (Dept. Phys., Saitama Univ.)

ITOKAWA Sakutarō 糸川咲太郎 (Dept. Phys., Saitama Univ.)

KAMIYA Junichiro 神谷潤一郎 (Grad. Sch. Sci., Osaka Univ.)

KUDO Takashi 工藤 隆 (Dept. Phys., Saitama Univ.)

KUMASAKA Hirokazu 熊坂弘一 (Dept. Phys., Saitama Univ.)

NISHIKAWA Jun 西川 純 (Dept. Phys., Saitama Univ.)

SEKIGUCHI Kimiko 関口仁子 (Dept. Phys., Sch. Sci., Univ. Tokyo)

SUDA Kenji 須田健嗣 (Dept. Phys., Saitama Univ.)

SUZUKI Ryoko 鈴木涼子 (Dept. Phys., Saitama Univ.)

YAMADA Hiroshi 山田 洋 (Dept. Phys., Saitama Univ.)

## Beam Technology Division

### Head

KASE Masayuki 加瀬昌之

### Members

AKIYOSHI Hiromichi 秋吉啓充

BHATTACHARJEE Sudeep

FUJIMAKI Masaki 藤巻正樹

FUJITA Jiro 藤田二郎

FUJITA Shin 藤田 新

IKEZAWA Eiji 池沢英二

ITO Sachiko 伊藤祥子

KAGEYAMA Tadashi 影山 正

KIDERA Masanori 木寺正憲

KIMURA Kazuie 木村一宇

KOHARA Shigco 小原重夫

KOMIYAMA Misaki 込山美咲

MASUDA Akiko 益田晶子

MORITA Kosuke 森田浩介

NAGASE Makoto 長瀬 誠

NAKAGAWA Takahide 中川孝秀

OGIWARA Kiyoshi 荻原 清  
USHIDA Kiminori 丑田公規  
YONEDA Akira 米田 晃

TANABE Toshiya 田辺敏也  
YOKOUCHI Tadashi 横内 正

*Visiting Members*

ABURAYA Takashi 油谷崇志 (NASDA)  
ANZAWA Osamu 安沢 修 (NASDA)  
AOYAMA Kazuhiro 青山和広 (NASDA)  
ARAI Nobuaki 荒井修亮 (Grad. Sch. Inf., Kyoto Univ.)  
BABA Shinji 馬場信次 (NASDA)  
BIRI Sandor (ATOMKI, Hungary)  
CHIBA Toshiya 千葉利哉  
DEGUCHI Yasushi 出口 泰 (NASDA)  
EFREMOV Andrei (J.I.N.R., Russia)  
FURUSE Kaoru 古瀬 馨 (NASDA)  
FUTAMI Yasuyuki 二見康之 (Natl. Inst. Radiol. Sci.)  
GOKA Tateo 五家建夫 (NASDA)  
HATANAKA Kichiji 畑中吉治 (RCNP, Osaka Univ.)  
HATSUKAWA Yuichi 初川雄一 (Tokai Res. Estab., JAERI)  
HAYANO Ryugo S. 早野龍五 (Fac. Sci., Univ. Tokyo)  
HEMMI Masatake 逸見政武  
HIEDA Kohtaro 檜枝光太郎 (Coll. Sci., Rikkyo Univ.)  
HIROSE Takayuki 広瀬孝幸 (NASDA)  
HIROTA Teruo 廣田輝夫 (Toyo Denshi Keisoku Co., Ltd)  
IDESAWA Masanori 出澤正徳 (Univ. Electro-Commun.)  
IIDE Yoshiya 飯出芳弥 (NASDA)  
IIO Seiji 飯尾晴二 (Sumitomo Heavy Ind., Ltd.)  
IKEZOE Hiroshi 池添 博 (Tokai Res. Estab., JAERI)  
INAMUARA Takashi 稲村 卓 (Warsaw Univ., Poland)  
ISHIZUKA Takeo 石塚武男 (Dept. Phys., Saitama Univ.)  
IWAI Satoshi 岩井 敏 (Nucl. Dev. Co., Ltd)  
JEONG S. C. (KEK)  
KANAMORI Takashi 金森 崇 (NASDA)  
KATAYAMA Ichiro 片山一郎 (KEK)  
KATSURAGAWA Hidetsugu 桂川秀嗣 (Fac. Sci., Toho Univ.)  
KAWAI Jyun 河合 潤 (Grad. Sch. Eng., Kyoto Univ.)  
KUBOYAMA Satoshi 久保山智司 (NASDA)  
KUDO Hisaaki 工藤久昭 (Fac. Sci., Niigata Univ.)  
KUROSAWA Tadahiro 黒澤忠弘 (Electrotechn. Lab., Agency Ind. Sci. Tech.)  
LEE San-mu 李 相茂 (Inst. Phys., Univ. Tsukuba)  
MAKIHARA Akiko 榎原亜紀子 (NASDA)  
MATSUDA Sumio 松田純夫 (NASDA)  
MATSUNAMI Noriaki 松波紀明 (Sch. Eng. Nagoya Univ.)  
MATSUNO Kiyoshi 松野 清 (Fujiden Eng. Co., Ltd)  
MATSUSE Takehiro 松瀬丈浩 (Fac. Textile Sci. Tech., Shinshu Univ.)  
MECHTCHRIAKOV Nikolai (Inst. Theor. Phys., China)  
MINAMISONO Tadanori 南園忠則 (Grad. Sch. Sci., Osaka Univ.)  
MIYATAKE Hiroari 宮武宇也 (KEK)  
MIYAZAWA Yoshitoshi 宮沢佳敏  
MURAKAMI Tetsuya 村上哲也 (Grad. Sch. Sci., Kyoto Univ.)  
NAGAI Yuki 永井由紀 (NASDA)  
NAKAMURA Takashi 中村尚司 (Cycl. Radioisot. Cen., Tohoku Univ.)  
NAKAO Noriaki 中尾徳晶 (KEK)  
NEMOTO Norio 根本規生 (NASDA)  
NOMURA Toru 野村 亨 (KEK)  
OHIRA Hideharu 大平秀春 (NASDA)  
OHTSUKI Tsutomu 大槻 勤 (Lab. Nucl. Sci., Tohoku Univ.)

OHYA Jiro 大矢次郎 (NASDA)  
 OHZONO Hironobu 大園浩之 (NASDA)  
 OISHI Koji 大石晃嗣 (Shimizu Construction Co., Ltd)  
 OOTOMO Hiromitsu 大友洋光 (NASDA)  
 SAGARA Kenshi 相良建至 (Fac. Sci., Kyushu Univ.)  
 SAKAI Hideyuki 酒井英行 (Dept. Phys., Sch. Sci., Univ. Tokyo)  
 SAKURAI Yutaka 桜井裕 (Jyoho System Kenkyusho)  
 SATO Osamu 佐藤理 (Mitsubishi Res. Inst. Inc.)  
 SEKINE Toshiaki 関根俊明 (Takasaki Rad. Chem. Res. Estab., JAERI)  
 SHEN W.-Q. (Shanghai Inst. Nucl. Res., China)  
 SHIBAMURA Eido 柴村英道 (NASDA)  
 SHIMADA Osamu 島田修 (NASDA)  
 SHINDO Hiroyuki 新藤浩之 (NASDA)  
 SHINOZUKA Tsutomu 篠塚勉 (Cycl. Radioisot. Cen., Tohoku Univ.)  
 SHIRKOV Grigori (J.I.N.R., Russia)  
 SOMEKAWA Shuji 染河秀治 (NASDA)  
 SUEKI Keisuke 末木啓介 (Fac. Sci., Tokyo Metrop. Univ.)  
 SUGAI Isao 菅井勲 (KEK)  
 SUGIYAMA Hiroki 杉山大樹 (NASDA)  
 SUZUKI Masami 鈴木正美 (Irie Koken Co. Ltd.)  
 TAGISHI Yoshihiro 田岸義宏 (Inst. Phys., Univ. Tsukuba)  
 TAKADA Norio 高田憲生 (NASDA)  
 TAKAGI Syunji 高木俊治 (Mitsubishi Res. Inst. Inc.)  
 TOYOKAWA Hiroyuki 豊川弘之 (Electrotechn. Lab., Agency Ind. Sci. Tech.)  
 TSUBAKI Noriyuki 椿則幸 (NASDA)  
 UEHARA Takashi 上原丘 (Nuclear Development Co., Ltd)  
 URITANI Akira 瓜谷章 (Dept. Phys., Grad. Sch. Sci., Nagoya Univ.)  
 UTSUNOMIYA Hiroaki 宇都宮弘章 (Fac. Sci., Konan Univ.)  
 WADA Ryoichi 和田良一 (Texas A&M Univ., USA)  
 WASHIO Masakazu 鷺尾方一 (Adv. Res. Inst. Sci. Eng., Waseda Univ.)  
 YAMAKI Tsutomu 八巻務  
 YAMAZAKI Hirohito 山崎寛仁 (Lab. Nucl. Sci., Tohoku Univ.)  
 YOKOYAMA Ichiro 横山一郎  
 YOSHIOKA Yasuhiro 吉岡康弘 (NASDA)

#### *Trainees*

FUJIMOTO Rintaro 藤本林太郎 (Dept. Phys., Sch. Sci., Univ. Tokyo)  
 GOMI Tomoko 五味朋子 (Coll. Sci., Rikkyo Univ.)  
 HIGURASHI Yoshihide 日暮祥英 (Coll. Sci., Rikkyo Univ.)  
 IWASE Hiroshi 岩瀬広 (Fac. Sci., Tohoku Univ.)  
 KAJI Daiya 加治大哉 (Fac. Sci., Niigata Univ.)  
 KOBAYASHI Masataka 小林雅貴 (Adv. Res. Inst. Sci. Eng., Waseda Univ.)  
 KOSHIMIZU Masanori 越水正典 (Dept. Eng., Grad. Sch. Eng., Univ. Tokyo)  
 MATSUYAMA Tadayoshi 松山正佳 (Fac. Sci., Tohoku Univ.)  
 MIYAKE Norio 三宅範夫 (Grad. Sch. Eng., Univ. Tokyo)  
 MORI Masakazu 森雅和 (Adv. Res. Inst. Sci. Eng., Waseda Univ.)  
 NOMURA Masayoshi 野村匡芳 (Grad. Sch. Eng., Univ. Tokyo)  
 SASAKI Michiya 佐々木道也 (Grad. Sch. Sci., Tohoku Univ.)  
 UMEBAYASHI Rei 梅林励 (Dept. Eng., Grad. Sch. Eng., Univ. Tokyo)  
 YONAI Shunsuke 米内俊祐 (Fac. Sci., Tohoku Univ.)

### **Radioisotope Technology Division**

#### *Head*

YATAGAI Fumio 谷田貝文夫

### Members

ENOMOTO Shuichi 榎本秀一  
TSUKADA Teruyo 塚田晃代  
HIRUNUMA Rieko 蛭沼利江子  
TAKAHASHI Kazuya 高橋和也  
YANAGIYA Takahiro 柳谷隆宏

### Visiting Members

DING Wenjun 丁文軍 (Inst. High Energy Phys., Chin. Acad. Sci., China)  
GORDON Alasdair  
HABA Hiromitsu 羽場宏光 (Adv. Sci. Res. Cen., JAERI)  
KAGAWA Yasuhiro 香川康浩 (Toray Res. Cen. Inc.)  
KATO Takesi 加藤武司  
KAWABE Kenji 川辺賢司 (Kyoto Pharm. Univ.)  
KAWATA Tetsuya 川田哲也 (Sch. Med., Chiba Univ.)  
MAEZAWA Hiroshi 前澤博 (Fac. Med. Technol., Univ. Tokushima)  
MORIMOTO Shigeko 森本茂子  
NAGAME Yuichiro 永目諭一郎 (Adv. Sci. Res. Cen., JAERI)  
NAKANISI Tomoko 中西友子 (Grad. Sch. Agr. Life Sci., Univ. Tokyo)  
OGURA Koichi 小倉紘一 (Coll. Ind. Technol., Nihon Univ.)  
PAN Qiangyan 潘強岩 (Inst. Mod. Phys., Chin. Acad. Sci., China)  
AMANO Ryohei 天野良平 (Fac. Med., Kanazawa Univ.)  
HIMENO Seiichiro 姫野誠一郎 (Sch. Pharm. Sci., Kitasato Univ.)  
INAGE Hiroko 稲毛寛子 (Showa Women's Univ.)  
MATSUMOTO Ken-ichiro 松本謙一郎 (Showa Pharm. Univ.)  
MINAI Yoshitaka 葉袋佳孝 (Cen. Art. Sci., Musashi Univ.)  
MINAMI Takeshi 南武志 (Dept. Living Sci., Kinki Univ., Toyooka Jr. Coll.)  
NABEKURA Tomohiro 鍋倉智弘 (Fac. Pharm. Sci., Kinki Univ.)  
NAKANISHI Yukiko 中西由季子 (Showa Women's Univ.)  
OGURA Yasumitsu 小椋康光 (Fac. Pharm. Sci., Chiba Univ.)  
SAKURAI Hiromu 桜井弘 (Kyoto Pharm. Univ.)  
SHIBATA Sadao 柴田貞夫 (Natl. Inst. Radiol. Sci.)  
SHINOHARA Atsushi 篠原厚 (Dept. Chem., Grad. Sch. Sci., Osaka Univ.)  
SUZUKI Hiroyuki 鈴木弘行 (RI Res. Cen., Chiba Univ.)  
SUZUKI Kazuo 鈴木和夫 (Fac. Pharm. Sci., Chiba Univ.)  
TAGAMI Keiko 田上恵子 (Natl. Inst. Radiol. Sci.)  
TAKAHASHI Masaaki 高橋正昭 (Coll. Agr., Osaka Pref. Univ.)  
TAKAHASHI Yoshio 高橋嘉夫 (Fac. Sci., Hiroshima Univ.)  
TAKEDA Atsushi 武田厚司 (Sch. Pharm. Sci., Shizuoka Univ.)  
TAMANO Haruna 玉野春南 (Sch. Pharm. Sci., Shizuoka Univ.)  
UCHIDA Shigeo 内田滋夫 (Natl. Inst. Radiol. Sci.)  
YAMASAKI Mineo 山崎峰夫 (Nara Med. Univ.)  
YANAGA Makoto 矢永誠人 (Fac. Sci., Shizuoka Univ.)  
YANG Yongfeng 楊永峰 (Inst. Mod. Phys., Chin. Acad. Sci., China)  
YASUI Hiroyuki 安井裕之 (Kyoto Pharm. Univ.)  
ZHAO Yuliang 趙宇亮 (Inst. High Energy Phys., Chin. Acad. Sci., China)

### Trainees

FUGONO Jun 畚野純 (Kyoto Pharm. Univ.)  
FURUKAWA Jun 古川純 (Grad. Sch. Agr. Life Sci., Univ. Tokyo)  
GOTO Sachiko 後藤佐智子 (Fac. Pharm. Sci., Nagasaki Univ.)  
IGARASHI Kaori 五十嵐香織 (Showa Women's Univ.)  
IKEGAMI Hiromu 池上拓 (Fac. Sci. Eng., Waseda Univ.)  
KANAYAMA Yousuke 金山洋介 (Fac. Med., Kanazawa Univ.)  
KAWAMOTO Yumi 川本有美 (Fac. Sci., Shizuoka Univ.)  
KOIKE Mariko 小池真理子 (Fac. Sci., Shizuoka Univ.)  
MAETSU Hitomi 前津仁美 (Fac. Sci., Shizuoka Univ.)  
MATSUO Tsutomu 松尾力 (Fac. Sci. Eng., Waseda Univ.)  
NAKAYAMA Akihiro 中山明弘 (Kyoto Pharm. Univ.)

OGI Takanori 小木 貴憲  
OHYAMA Takuya 大山 拓也 (Fac. Sci., Shizuoka Univ.)  
OIDA Takashi 笈田多加史 (Fac. Sci., Shizuoka Univ.)  
OKA Toshitaka 岡 壽崇 (Fac. Sci. Eng., Waseda Univ.)  
SHIOBARA Yamato 塩原大和 (Fac. Pharm. Sci., Chiba Univ.)  
TSUJI Takae 辻 孝枝 (Fac. Med., Kanazawa Univ.)  
UCHIYAMA Junichi 内山潤一 (Fac. Sci. Eng., Waseda Univ.)  
YABUSHITA Yuko 藪下裕子 (Fac. Med., Kanazawa Univ.)  
YOSHIDA Shozo 吉田昭三 (Nara Med. Univ.)

## Liquid Helium Service Division

### Head

YANO Yasushige 矢野安重

### Members

IKEGAMI Kumio 池上九三男

OTAKE Masao 大竹政雄

### Visiting Members

KATO Kenichi 加藤賢一

NAKANO Kazushiro 中野和城

## ADVANCED ENGINEERING CENTER

### Research Instruments Development Division

#### Head

SENOO Katsumi 妹尾克己

#### Members

IKEGAMI Yuji 池上祐司

NOMIYA Yoshio 野宮芳雄

SHIMODA Susumu 霜田進

SUGAHARA Seigo 菅原正吾

URAI Teruo 浦井輝夫

YAMADA Shogo 山田正吾

KITSUNAI Tokuji 橘内徳司

SHIGA Tsunenobu 志賀常信

SHIRAIISHI Akira 白石明

TAJIMA Norio 田島典夫

WATANABE Tokuji 渡辺徳治

YAMADA Yutaka 山田豊

#### Contracting Members

KANEKO Naoe 金子直恵

KUBO Ushizo 久保丑蔵

MATSUMOTO Akira 松本昭

NIIOKA Yuzo 新岡勇三

SASAMOTO Tetsuji 笹本哲司

TAKAHASHI Kiyoji 高橋清二

TOKIWA Saburo 常盤三郎

YAMAMOTO Sumio 山本澄雄

## CHARACTERIZATION CENTER

### Surface Characterization Division

#### Head

IWAKI Masaya 岩木正哉

#### Members

KOBAYASHI Tomohiro 小林知洋

WATANABE Kowashi 渡辺剛

NAKAO Aiko 中尾愛子

## ADVANCED COMPUTING CENTER

### Computational Science Division

#### Head

EBISUZAKI Toshikazu 戎崎俊一

#### Members

IITAKA Toshiaki 飯高敏晃

SHINKAI Hisaaki 真貝寿明

YAMAMOTO Tomoyuki 山本知之

MORISHITA Tetsuya 森下徹也

### Image Information Division

#### Head

SHIMIZU Hirohiko 清水裕彦

#### Members

OTANI Chiko 大谷知行

OKU Takayuki 奥隆之

WATANABE Hiroshi 渡辺博

ADACHI Tomohiro 安達智宏

SHIKI Shigetomo 志岐成友

SAKAKI Naoto 榊直人

SATO Hiromi 佐藤広海

TAKIZAWA Yoshiyuki 滝澤慶之

KAWASAKI Yoshiya 川崎賀也

IKEDA Kazuaki 池田一昭

MORISHIMA Takahiro 森嶋隆裕

SUZUKI Shun 鈴木春

#### Visiting Members

KURAKADO Masahiko 倉門雅彦

SAKAI Kenji 酒井健二

## RIKEN BIORESOURCE CENTER

### Experimental Animal Division

#### Head

Obata Yuichi 小幡裕一

#### Members

HIRAIWA Noriko 平岩典子

YOSHIDA-NORO Chikako 野呂知加子

IKE Fumio 池郁生

YOSHIKI Atsushi 吉木淳

### RIKEN BNL Research Center

#### Head

LEE Tsung-Dao\*<sup>1</sup>

SAMIOS Nicholas P.\*<sup>2</sup>

EN'YO Hideto 延與秀人\*<sup>3</sup>

---

\*<sup>1</sup> Director, \*<sup>2</sup> Deputy Director, \*<sup>3</sup> Associate Director

### Experimental

#### Group Leader

EN'YO Hideto 延與秀人

#### Deputy Group Leader

BUNCE Gerry M.

#### Members

BAZILEVSKY Alexander

FIELDS Douglas Edward

GOTO Yuji 後藤雄二

DESHPANDE Abhay

FOX Brendan

GROSS PERDEKAMP Matthias

ICHIHARA Takashi 市原 卓  
KURITA Kazuyoshi 栗田和好  
SAITO Naohito 齊藤直人  
WATANABE Yasushi 渡邊 康

KOBAYASHI Hideyuki 小林秀幸  
MURATA Jiro 村田次郎  
TAKETANI Atsushi 竹谷 篤  
YOKKAICHI Satoshi 四日市 悟

*Visiting Members*

LANGE Jens Soren (BNL, USA)

**Theory**

*Group Leader*

LEE Tsung-Dao

*Deputy Group Leader*

BALTZ Anthony J.

*Members*

AOKI Yasumichi 青木保道  
BOER Daniel  
ITAKURA Kazunori 板倉数記  
NEMOTO Yukio 根本幸雄  
ORIGINOS Konstantinos  
VOGELSANG Werner

BLUM Thomas  
DAWSON Christopher  
NARA Yasushi 奈良 寧  
NOAKI Jun-ichi 野秋淳一  
SCHAFFNER-BEILICH Jurgen

*Visiting Members*

BASS Steffen A. (Duke Univ., USA)  
BODEKER Dietrich (Niels Bohr Inst., Denmark)  
GYULASSY Miklos (Columbia Univ., USA)  
JAFFE Robert L. (Massachusetts Inst. Technol., USA)  
JEON Sangyong (McGill Univ., Canada)  
KUSENKO Alexander (Univ. California, Los Angeles, USA)  
MAWHINNEY Robert (Columbia Univ., USA)  
SCHAEFER Thomas (State Univ. New York, Stony Brook, USA)  
SHURYAK Edward (State Univ. New York, Stony Brook, USA)  
SON Dam Thanh (Columbia Univ., USA)  
STEPHANOV Mikhail A. (Univ. Illinois, Chicago, USA)  
VAN KOLCK Ubirajara (Univ. Arizona, USA)  
VENUGOPALAN Rajagopal (BNL, USA)  
WETTIG Tilo (Yale Univ., USA)

*Administration*

ESPOSITO Pamela  
GREENBERG Rae  
HEINZ Tammy Anne  
ITO Taeko 伊藤 妙子

*Administrative Manager*

NODA Toshihito 野田 淑人

*Deputy Administrative Manager*

HORIE Hironori 堀江 博憲

**RIKEN PLANT SCIENCE CENTER**

**Laboratory for Remediation Research**

*Head*

YAMAGUCHI Isamu 山口 勇

*Members*

SOSHI Takayuki 曾 雌 隆 行

**Safety Center**

*Head*

SAWA Hiroshi 澤 宏

*Members*

FUKAZAWA Kunio 深 沢 国 雄

KAGAYA Satoru 加 賀 屋 悟

KOBAYASHI Hiroshi 小 林 博

SHIMAGAKI Masayuki 嶋 垣 正 之

UWAMINO Yoshitomo 上 養 義 朋

YOSHIKI Hajime 吉 識 肇

HARASAWA Kaoru 原 沢 薫

KATO Hiroko 加 藤 博 子

MIYAGAWA Makoto 宮 川 真 言

SHINOHARA Shigemi 篠 原 茂 己

YAMAGISHI Nobuyasu 山 岸 信 康





- ERMISCH Karsten 44  
 ESUMI Shinichi 江角晋一 244  
 FÜLÖP Zsolt 49, 55, 56, 58, 59, 60, 62, 63, 69, 70, 73, 74  
 FAMIANO Michael A. 32, 80  
 FIELDS Douglas E. 221, 226, 228, 229, 231, 232  
 FORTIER Simone 52  
 FUJII Shinichiro 藤井新一郎 36  
 FUJIMAKI Masaki 藤巻正樹 3, 5, 247, 266  
 FUJIMOTO Rintaro 藤本林太郎 11  
 FUJISHIMA Shiro 藤島史郎 285, 289, 291, 293  
 FUJITA Jiro 藤田二郎 178  
 FUJITA Shin 藤田 新 319, 321, 323  
 FUKUCHI Tomonori 福地知則 41  
 FUKUDA Naoki 福田直樹 43, 49, 52, 57, 71, 72, 73, 74  
 FUKUNISHI Nobuhisa 福西暢尚 3, 5, 274, 283, 285,  
 287, 291, 293, 295,  
 321  
 FUKUYAMA Yoshimitsu 福山祥光 101, 141  
 FULTON Brian 80  
 FUNAHASHI Haruhiko 舟橋春彦 245  
 FURUKAWA Jun 古川 純 118  
 FUTAKAMI Udai 二上宇内 69, 70, 73, 74, 75, 76  
 GACSI Zoltan 73  
 GARA Alan 209  
 GEISSEL Hans 82  
 GELBERG Adrian 49  
 GILG Hansjoerg 82  
 GILLITZER Albrecht 82  
 GLENN Andrew 224, 225  
 GLENN Woody 228  
 GOGIBERIDZE George 224, 225  
 GOMI Tomoko 五味朋子 49, 53, 54, 55, 56, 57, 58, 59,  
 61, 62, 63, 69, 70, 71, 72, 73,  
 74, 75, 76  
 GONO Yasuyuki 郷農靖之 41, 77, 116, 179  
 GOTO Akira 後藤 彰 3, 5, 102, 103, 140, 160, 247,  
 272, 277, 279, 281, 285, 287,  
 289, 291, 293, 295  
 GOTO Sachiko 後藤佐智子 133  
 GOTO Yuji 後藤雄二 188, 218, 220, 221, 222, 228,  
 236, 238, 240, 243  
 GROSSE PERDEKAMP Matthias 220, 222  
 HABA Hiromitsu 羽場宏光 123  
 HACHIYA Takashi 蜂谷 崇 241  
 HAMAGAKI Hideki 浜垣秀樹 78, 236, 238, 240, 242,  
 245  
 HAMANAKA Hiromi 浜中廣見 182  
 HAMATANI Yutaro 濱谷祐多朗 89  
 HANAOKA Fumio 花岡文雄 132  
 HARDTKE David H. 204  
 HASEBE Hiroo 長谷部裕雄 3, 262, 264  
 HASEGAWA Hirokazu 長谷川浩一 49, 69, 70, 71, 72,  
 75, 76, 169  
 HASEGAWA Kenichi 長谷川賢一 182  
 HASEGAWA Koichi 長谷川浩一 57  
 HASHIZUME Kazuaki 橋詰和明 28  
 HATANAKA Kichiji 畑中吉治 174  
 HATANO Michio 波田野道夫 44, 45, 46, 148, 149, 174  
 HATSUDA Tetsuo 初田哲夫 192  
 HATTORI Toshiyuki 服部俊幸 260  
 HAYANO Ryugo S. 早野龍五 82, 106  
 HAYASHI Naoki 林 直樹 236, 238  
 HAYASHI Takeshi 林 剛史 43  
 HIBINO Masaru 日々野 優 242  
 HIGURASHI Yoshihide 日暮祥英 53, 54, 55, 56, 58,  
 59, 61, 62, 63, 69,  
 70, 71, 73, 74, 75,  
 76, 251, 253, 254  
 HIMENO Seiichiro 姫野誠一郎 117  
 HIRAI Kazuyoshi 平井一賢 43  
 HIRAI Masaaki 平井正明 55, 56, 58, 59, 62  
 HIRAI Masanori 平井正紀 52, 188  
 HIRANO Tetsufumi 平野哲文 202  
 HIRAO Norie 平尾法恵 319, 323  
 HIRAOKA Nozomu 平岡 望 103  
 HIRASAWA Masahiko 平澤雅彦 179  
 HIRENZAKI Satoru 比連崎 悟 82  
 HIROSE Shun-ichi 広瀬俊亮 18  
 HIROTA Teruo 広田輝夫 173  
 HIRUNUMA Rieko 蛭沼利江子 108, 109, 114, 115,  
 116, 118, 121, 123,  
 247  
 HONMA Masamitsu 本間正充 132  
 HONMA Michio 本間道雄 9, 10, 11, 12  
 HOOVER Andrew 232  
 HORAGUCHI Takuma 洞口拓磨 188  
 HORI Masaki 堀 雅樹 106  
 HORITA Mitsugu 堀田 貢 131  
 HORVÁTH Deszo 106  
 HOSHINO Masamitsu 星野正光 97  
 HUANG Haixin 黄 海新 221, 226, 228  
 HUGHES Vernon 221, 226, 228  
 HUI Qin 101  
 HUTTON Roger 96  
 HYODO Toshio 兵頭俊夫 102, 103, 140, 160  
 IANCU Edmond 191  
 ICHIHARA Takashi 市原 卓 48, 176, 225, 228, 236,  
 238, 240

- IDEGUCHI Eiji 井手口栄治 41 59, 60, 61, 62, 63, 69, 70,  
 IEIRI Masaharu 家入正治 245 71, 72, 73, 74, 75, 76,  
 IEKI Kazuo 家城和夫 53, 54, 61, 62, 69, 70, 74, 75, 76 135, 137, 167  
 IGARASHI Kaori 五十嵐香織 115, 247  
 IGO George 226, 228  
 IIDA Kei 飯田 圭 31  
 IKEDA Hiroshi 池田 宙 43, 75, 76, 159  
 IKEDA Kiyomi 池田清美 13, 14, 18, 19  
 IKEDA Tokihiro 池田時浩 314  
 IKEGAMI Kumio 池上九三男 285, 291  
 IKEZAWA Eiji 池沢英二 3, 5, 247, 266  
 IMAI Ken'ichi 今井憲一 218, 221, 224, 225, 226, 228,  
 243  
 IMAI Nobuaki 今井伸明 49, 52, 53, 54, 57, 58, 59, 61,  
 62, 63, 65, 69, 70, 71, 73, 75,  
 76, 91, 107, 143, 145, 146  
 IMURA Nobumasa 井村伸正 117  
 INOUE Koji 井上耕治 102, 103  
 INUBUSHI Kazuyuki 犬伏和之 119  
 ISHIDA Katsuhiko 石田勝彦 39, 138  
 ISHIDA Satoru 石田 悟 48  
 ISHIDA Tomoyuki 石田智之 174  
 ISHIDA Yoshihisa 石田佳久 141, 157  
 ISHIHARA Masayasu 石原正泰 41, 49, 52, 54, 55, 56,  
 57, 58, 59, 62, 63, 69,  
 70, 72, 73, 74, 75, 76,  
 221, 224, 228, 236,  
 240  
 ISHII Noriyoshi 石井理修 213  
 ISHIKAWA Katsutoshi 石川勝利 109  
 ISHIKAWA Norito 石川法人 89  
 ISHIKAWA Takashi 石川 隆 106  
 ISHINO Masaya 石野雅也 245  
 ISSHIKI Hiroshi 一色 博 5  
 ISUPOV Alexandre Yurievich 45, 46  
 ITAGAKI Naoyuki 板垣直之 18, 19  
 ITAHASHI Kenta 板橋健太 43, 82  
 ITAKURA Kazunori 板倉数記 191, 192  
 ITO Sachiko 伊藤祥子 173, 319, 321, 323  
 ITOH Akio 伊藤秋男 93  
 ITOH Kazuya S. 伊藤和也 48  
 ITOH Yoshiko 伊東芳子 102, 103, 140, 160  
 ITOU Masayoshi 伊藤真義 103  
 IWAI Yoshio 岩井良夫 95  
 IWAKI Masaya 岩木正哉 181  
 IWASA Naohito 岩佐直仁 53, 54, 55, 56, 58, 59, 61,  
 62, 63, 67, 68, 69, 70, 71,  
 72, 73, 74, 75, 76  
 IWASAKI Hironori 岩崎弘典 49, 52, 53, 54, 55, 56, 58,  
 59, 60, 61, 62, 63, 69, 70,  
 71, 72, 73, 74, 75, 76,  
 135, 137, 167  
 IWASAKI Masahiko 岩崎雅彦 43, 82  
 IWASE Akihiro 岩瀬彰宏 89  
 IWATA Yoshiyuki 岩田佳之 55, 56, 58, 59, 62, 63  
 IZUMIKAWA Takuji 泉川卓司 42, 66  
 JAMESON Robert A. 260  
 JEON Sangyong 199  
 JINNOUCHI Osamu 陣内 修 220, 228, 236, 238, 240  
 JOO Balint 209  
 JUHÁSZ Berti 106  
 KAGEYAMA Kensuke 蔭山健介 88  
 KAGEYAMA Tadashi 影山 正 5, 254, 256, 270  
 KAIHARA Jou 貝原星宇 65, 143, 145, 146  
 KAJI Daiya 加治大哉 154  
 KAJINO Toshitaka 梶野敏貴 33, 34  
 KAKUTANI Nobukazu 角谷暢一 303, 305  
 KAMBARA Tadashi 神原 正 88, 89, 93, 125, 141  
 KAMEDA Daisuke 亀田大輔 65, 77, 91, 107, 143, 145,  
 146  
 KAMETANI Soichiro 亀谷聡一朗 78, 242  
 KAMIGAITO Osamu 上垣外修一 3, 5, 247, 268, 272,  
 281, 285  
 KAMIHARA Nobuyuki 神原信幸 231, 232  
 KAMIYA Junichiro 神谷潤一郎 174  
 KANAI Yasuyuki 金井保之 88, 95, 96, 97, 141  
 KANAVETS Vadim 221, 226, 228  
 KANAYAMA Yousuke 金山洋介 110, 111, 112, 113  
 KANBARA Akemi 神原朱美 114  
 KANDA Hiroki 神田浩樹 245  
 KANEKO Emi 金子恵美 49  
 KANG Byoung Hwi 43  
 KANNO Shouko 菅野祥子 49, 53, 54, 61, 69, 70, 71,  
 72, 75, 76  
 KANUNGO Rituparna 24, 25, 42, 50, 64, 66, 67, 68,  
 164, 165, 171  
 KASE Masayuki 加瀬昌之 3, 5, 125, 132, 133, 135,  
 137, 247, 251, 253, 254,  
 256, 262, 264, 266, 270,  
 272, 274, 275, 283, 285,  
 314, 319, 323  
 KASHIYAMA Osamu 樫山 修 41  
 KATAKURA Jun-ichi 片倉純一 249  
 KATAYAMA Ichiro 片山一郎 99, 100, 141  
 KATAYAMA Takeshi 片山武司 38, 92, 234, 256, 258,  
 260, 272, 275, 307,  
 308, 310, 314, 316  
 KATAYAMA Takeshi 片山武士 43

- KATO Hiromitsu 加藤裕充 44, 45, 46  
 KATO Mineo 加藤岑生 39  
 KATO Seigo 加藤静吾 40, 135  
 KATO Sumio 加藤純雄 244  
 KATO Takeshi 加藤武司 132  
 KATO Tomomi 加藤智美 66  
 KATO Toshiyuki 加藤俊幸 42, 64, 171  
 KATORI Kenji 鹿取謙二 64, 154  
 KATSUMOTO Yukihisa 勝元幸久 129, 130  
 KAWABE Kenji 川辺賢司 108  
 KAWAKAMI Hirokane 川上宏金 141  
 KAWAMURA Naritoshi 河村成肇 39  
 KAWAMURA Yoshie 川村淑恵 66  
 KAWASAKI Hiroaki 河崎洋章 49, 169  
 KHARZEEV Dima 198  
 KIDERA Masanori 木寺正憲 3, 5, 247, 251, 253, 254,  
 256, 270  
 KIENLE Paul 82  
 KIKUCHI Jun 菊池 順 78, 242  
 KIM Changhoan 209  
 KIM DongJo 232  
 KIM JungHo 43  
 KIM Ka-Hae 金 佳恵 16  
 KIM Seyong 金 世容 210  
 KIMURA Kazuie 木村一字 125  
 KIMURA Kikuo 木村喜久雄 66  
 KIMURA Mineo 季村峯生 83, 105  
 KIMURA Shuichi 木村修一 115  
 KINUGAWA Hiroto 衣川裕人 74  
 KISHIDA Takashi 岸田 隆 41, 49, 77, 135  
 KITAGUCHI Masaaki 北口雅暁 245  
 KITAJIMA Masashi 北島昌史 97  
 KIYOMICHI Akio 清道明男 244  
 KOBAYAKAWA Akira 小早川 彰 75, 76  
 KOBAYASHI Hideyuki 小林秀幸 188, 220, 231, 232  
 KOBAYASHI Hiroshi 小林 寛 55, 56, 58, 59, 62, 63  
 KOBAYASHI Kiyoshi 小林清志 5  
 KOBAYASHI Tomohiro 小林知洋 7, 181  
 KOBAYASHI Toshio 小林俊雄 57  
 KOBAYASHI Yoshio 小林義男 65, 77, 90, 91, 107, 143,  
 145, 146  
 KOBAYASHI-KOMIYAMA Misaki 小林-込山美咲 3, 5,  
 177,  
 266  
 KOEHLER Daniel 228  
 KOHAMA Akihisa 小濱洋央 23  
 KOHARA Shigeo 小原重夫 3, 5, 272, 281  
 KOIKE Shigetoshi 小池茂年 94  
 KOIKE Takaaki 小池孝明 65, 143, 146, 151  
 KOIKE Yoji 小池洋二 104  
 KOIKE Yuji 小池裕司 189  
 KOJIMA Takao M. 小島隆夫 88, 98, 141  
 KOMAKI Ken-ichiro 小牧研一郎 95, 96  
 KOMATSU Yu 小松 優 122  
 KONDO Yousuke 近藤洋介 49, 57  
 KONDRASHEV Sergei 258  
 KONOMI Yuki 許斐佑紀 128  
 KOSENKO Grigory 29  
 KOTCHENDA Leonid 224  
 KOURA Hiroyuki 小浦寛之 26, 27  
 KOWARI Ken-ichi 小割健一 87  
 KRASNITZ Alex 203  
 KRISST Ray 228  
 KUBO Kenya M. 久保謙哉 107  
 KUBO Toshiyuki 久保敏幸 41, 49, 52, 57, 69, 70, 73,  
 74, 75, 76, 141, 152, 177,  
 297, 299, 301, 303, 305  
 KUBONO Shigeru 久保野 茂 53, 54, 60, 61, 69, 70,  
 74, 135, 137, 156, 256,  
 274, 275  
 KUDO Katsuhisa 工藤勝久 39  
 KUMAGAI Hidekazu 熊谷秀和 52, 74  
 KUMAGAI Hiroshi 熊谷 宏 119  
 KUMANO Shunzo 熊野俊三 188  
 KUMAR Suresh 50  
 KUMASAKA Hirokazu 熊坂弘一 45, 46, 174  
 KUNIBU Makoto 國分 誠 53, 54, 61, 69, 70, 71, 72,  
 73, 74, 75, 76  
 KURATA-NISHIMURA Mizuki 倉田-西村美月 80, 162  
 KURIHARA Toshikazu 栗原俊一 140  
 KURITA Kazuyoshi 栗田和好 220, 221, 225, 226, 228  
 KUROKAWA Meiko 黒川明子 55, 56, 58, 59, 60, 62,  
 63, 71, 72, 73, 135,  
 137, 167  
 KUROKAWA Minako 黒川三奈子 75, 76, 159  
 KUROKI Yoshiaki 黒木善昭 244  
 KUSAKA Kensuke 日下健祐 50, 297, 299, 301, 303, 305  
 KUSAKABE Toshio 日下部俊男 105  
 KUSENKO Alexander 197  
 KUSUMI Takaaki 久住高章 129, 130  
 KWIATKOWSKI Kris 221  
 LADYGIN Vladimir Petrovich 45, 46  
 LADYGINA Nadezhda Borisovna 45, 46  
 LAINE Mikko 196  
 LAURENT Henri 52  
 LAURET Jerome 240  
 LEE David M. 231, 232  
 LEITCH Mike 232

- LEVKOVA Ludmila 209 72, 74, 75, 76,  
 LEWIS Benji 221 135, 137, 156,  
 LI Zheng 226, 228 275  
 LIAO Xiadong 209  
 LIM Heejoong 43  
 LIU Ming X. 231, 232  
 LIU Zhong 刘忠 55, 56, 58, 59, 62, 63, 73, 75, 76  
 LOZOWSKI William 221, 226, 228  
 LUKYANOV Serguei M. 52  
 MÜNCH Matthias 82  
 MÜNZENBERG Gottfried 82  
 MACKAY William 226, 228  
 MADOKORO Hideki 間所秀樹 15  
 MAEDA Kuniko 前田邦子 182  
 MAEDA Masaru 前田 勝 182  
 MAEDA Yukie 前田幸重 44, 45, 46, 174  
 MAETSU Hitomi 前津仁美 109  
 MAHLER George 226, 228  
 MAIE Takeshi 真家武士 5  
 MAISON Jean-Marie 52  
 MAKDISI Yousef 221, 226, 228  
 MAKIMURA Shunsuke 牧村俊助 138  
 MALAKHOV Alexandre Ivanovich 45, 46  
 MAO Yajun 冒 亜軍 224, 225  
 MARUYAMA Koichi 丸山浩一 40  
 MASUDA Hideki 益田秀樹 95, 96  
 MASUI Hiroshi 益井 宙 244  
 MASUOKA Toshikatsu 益岡俊勝 307  
 MATHEWS Grant 33, 34  
 MATSUDA Yasuyuki 松田恭幸 39, 138  
 MATSUFURU Hideo 松古栄夫 213  
 MATSUMOTO Takashi 松元貴志 78, 242  
 MATSUMOTO Takehiko 松本武彦 94  
 MATSUNO Kiyoshi 松野 清 173  
 MATSUO Yukari 松尾由賀利 101, 141, 157  
 MATSUURA Taeko 松浦妙子 75, 76  
 MATSUYAMA Yuuichi U. 松山裕一 53, 54, 61, 69, 70,  
 71, 75, 76  
 MATSUZAKI Masayuki 松崎昌之 15  
 MATSUZAKI Teiichiro 松崎禎市郎 39, 138  
 MAWHINNEY Robert D. 209  
 McGAHERN William 226, 228  
 McLERRAN Larry 191, 198  
 MENGONI Alberto 52  
 MESCHERYAKOV Nickolay 258  
 MEYER Hans-Otto 221  
 MIAKE Yasuo 三明康郎 244  
 MICHIMASA Shin'ichiro 道正新一郎 49, 53, 54, 60,  
 61, 69, 70, 71,  
 MIFUNE Tomoharu 三船倫治 121  
 MIHARA Satoshi 三原 智 245  
 MINEMURA Toshiyuki 峯村俊行 49, 53, 54, 55, 56,  
 58, 59, 61, 62, 63,  
 69, 70, 71, 73, 74,  
 75, 76  
 MIRGULE Ekanath Tanu 50  
 MITSUMOTO Toshinori 密本俊典 277, 279, 281, 285,  
 287, 291  
 MIURA Motooki 三浦元隆 43, 49, 57, 75, 76, 159  
 MIYAJIMA Akari 宮島明里 43  
 MIYAKE Yasuhiro 三宅康博 138  
 MIYAMA Masanori 深山正紀 188  
 MIYASHITA Takuya 宮下卓也 245  
 MIYAZAKI Kiyoshi 宮崎 潔 129, 130  
 MIYAZAWA Yoshitoshi 宮沢佳敏 281, 285, 291  
 MIYOSHI Hisanori 三好永哲 65, 77, 91, 107, 143, 145,  
 146  
 MIZOI Yutaka 溝井 浩 72, 135, 156, 297, 299, 301,  
 303, 305  
 MIZUSAKI Takahiro 水崎高浩 9, 10, 11, 12  
 MOCHIZUKI Yuko 望月優子 30  
 MOHRI Akihiro 毛利明博 98  
 MOMOTA Sadao 百田佐多生 66  
 MORI Fumiko 森 史子 119  
 MORII Toshiyuki 森井俊行 185, 187  
 MORIKAWA Tetsuya 森川鐵也 285  
 MORIKAWA Tsuneyasu 森川恒安 41, 60, 135, 137  
 MORIMOTO Kouji 森本幸司 50, 64, 154, 161, 162  
 MORIMOTO Shigeko 森本茂子 132, 133  
 MORISHITA Yuichiro 森下雄一郎 96  
 MORITA Kosuke 森田浩介 154  
 MOROZOV Boris V. 221  
 MOTOBAYASHI Tohru 本林 透 49, 51, 52, 53, 54,  
 55, 56, 57, 58, 59,  
 61, 62, 63, 69, 70,  
 71, 72, 73, 74, 75,  
 76, 147, 169  
 MOTOMURA Shinji 本村信治 41, 116, 179  
 MOTOSHIMIZU Yosuke 元清水陽介 89  
 MUKUMOTO Yoshinori 椋本佳範 89  
 MURAKAMI Hiroyuki 村上浩之 53, 58, 59, 62, 69, 70,  
 74, 75, 76, 167, 169  
 MURAKAMI Tetsuya 村上哲也 165, 245  
 MURATA Jiro 村田次郎 65, 143, 146, 223, 231, 232  
 MURPHY Alexander 80

MUTO Ryotaro 武藤亮太郎 245  
NAGAE Tomofumi 永江知文 43  
NAGAME Yuichiro 永目諭一郎 123  
NAGAMINE Kanetada 永嶺謙忠 39, 104, 138  
NAGASE Makoto 長瀬 誠 3, 5, 266, 274  
NAGASHIMA Yasuyuki 長嶋泰之 140, 160  
NAKAGAWA Takahide 中川孝秀 3, 5, 247, 251, 253,  
254, 256, 258, 270  
NAKAI Yoichi 中井陽一 88, 93, 97, 141  
NAKAMURA Masanobu 中村正信 221  
NAKAMURA Satoshi N. 中村 哲 39  
NAKAMURA Takashi 中村貴志 99, 100, 141  
NAKAMURA Takashi 中村隆司 43, 49, 52, 53, 54, 57,  
61, 69, 70, 71, 72, 75,  
76, 159  
NAKAMURA Takeshi 仲村武志 319, 323  
NAKANISHI Tomoko M. 中西友子 118  
NAKANISHI Yukiko 中西由季子 115  
NAKAO Aiko 中尾愛子 181  
NAKAO Masashi 中尾正史 95  
NAKATSUKASA Takashi 中務 孝 17  
NAKAYAMA Akihiro 中山明弘 108  
NANDI Basanta K. 222  
NARA Yasushi 奈良 寧 203  
NARUKI Megumi 成木 恵 245  
NAYESTANAKI Nasser-Kalatar 44  
NEWBY Jason 224, 225  
NIIGAKI Megumi 新垣 恵 98  
NIIZEKI Takashi 新関 隆 48  
NISHI Yuji 西 勇二 32, 80, 159, 162  
NISHIDA Minoru 西田 稔 5  
NISHIKAWA Jun 西川 純 44, 45, 46  
NISHIMORI Nobuyuki 西森信行 48  
NISHIMOTO Takeshi 西本武史 92  
NISHIMURA Shunji 西村俊二 32, 67, 68, 80, 159, 162  
NISHIO Kazuyuki 西尾和之 95  
NISHIURA Masaki 西浦正樹 310  
NOAKI Jun-ichi 野秋淳一 206  
NODA Koji 野田耕司 141  
NOGUCHI Motoko 野口基子 109  
NOMACHI Masaharu 能町正治 245  
NOTANI Masahiro 野谷将広 49, 60, 71, 72, 75, 76,  
135, 137, 156, 275  
NUMATA Shigeo 沼田茂男 5  
ODAHARA Atsuko 小田原厚子 41, 77  
OGAWA Hiroshi 小川博嗣 65, 91, 107, 143, 145, 146  
OGAWA Shigeru 小川 茂 90  
OGIWARA Kiyoshi 荻原 清 7, 94, 182  
OGURI Yoshiyuki 小栗慶之 92  
OHKAWA Tomohiro 大川智宏 316  
OHKI Tomonori 大木智則 3  
OHKUMA Kazumasa 大熊一正 187  
OHNISHI Hiroaki 大西宏明 244  
OHNISHI Jun-ichi 大西純一 279, 285, 291, 295  
OHNISHI Takeo 大西建夫 49  
OHNISHI Tetsuya 大西哲哉 44, 45, 46, 48, 64, 148,  
161, 165  
OHNUMA Hajime 大沼 甫 52  
OHSAKI Osamu 大崎 治 303  
OHSHIMA Nagayasu 大島永康 141  
OHSHIRO Yukimitsu 大城幸光 135, 137, 156, 256,  
270, 275  
OHTA Masahisa 太田雅久 28  
OHTA Ryuichi 太田隆一 5  
OHTA Shigemi 太田滋生 209, 210, 211  
OHTANI Shunsuke 大谷俊介 99, 100, 141  
OHTOMO Kiyotaka 大友清隆 308  
OHYAMA Hitoshi 大山 均 141  
OHYAMA Takuya 大山拓也 109, 247  
OKABE Shigeto 岡部成玄 18, 19  
OKADA Kensuke 岡田謙介 222  
OKADA Kunihiro 岡田邦宏 99, 100, 141  
OKADA Shinji 岡田信二 43  
OKAMOTO Ryoji 岡本良治 36  
OKAMURA Hiroyuki 岡村弘之 44, 45, 46, 48, 148, 174  
OKAMURA Masahiro 岡村昌宏 234, 258, 260  
OKUNO Hiroki 奥野広樹 281, 285, 289, 291, 293, 295  
OMORI Takashi 大森 魏 109  
ONG Hooi Jin 王 惠仁 49  
ONISHI Takashi 大西 崇 66  
ONO Fumihisa 小野文久 89  
ONO Masaya 小野雅也 244  
ORGINOS Konstantinos 212  
ORGINOS Kostas 211  
OSHIMA Nagayasu 大島永康 98  
OTA Shinsuke 大田晋輔 165  
OTSU Hideaki 大津秀暁 48  
OTSUKA Takaharu 大塚孝治 9, 10, 11, 12, 16, 18, 19  
OUTA Haruhiko 応田治彦 43  
OYAMA Hitoshi 大山 等 95  
OYAMA Ken 大山 健 78, 242  
OYAMA Satoshi 大山 聡 187  
OYAMATSU Kazuhiro 親松和浩 249  
OZAWA Akira 小沢 顕 24, 25, 42, 50, 64, 66, 67, 68,  
159, 171  
OZAWA Kyoichiro 小沢恭一郎 78, 242, 245  
OZAWA Shuichi 小澤修一 55, 56, 58, 59, 62, 63, 258  
PAN Qiangyan 潘 強岩 75, 76, 179

- PANITKIN Sergei Y. 204  
 PATE Stephen 232  
 PITA Santiago 52  
 POUTISSOU Jean-Michel 80  
 POUTISSOU Renee 80  
 PRZEWOSKI Barbara 221  
 READ Ken 224, 225  
 RESCIA Sergio 226, 228  
 REZNIKOV Serguei Grigorievich 45, 46  
 RINCKEL Tom 221  
 ROSER Thomas 221, 226, 228  
 RUSEK Adam 221  
 RUSSO Thomas 228  
 SAGISAKA Mitsuyuki 匂坂充行 249  
 SAHIN Latife 80  
 SAITO Akito 齋藤明登 49, 53, 54, 55, 57, 60, 61, 69,  
 70, 71, 72, 73, 74, 75, 76, 135,  
 137, 169  
 SAITO Fuminori 齋藤文修 140, 160  
 SAITO Naohito 齋藤直人 188, 218, 220, 221, 222, 224,  
 225, 226, 228, 231, 232, 236,  
 240, 243  
 SAITO Takaaki 齋藤孝明 44, 45, 46, 148, 174  
 SAITO Takashi 齋藤 崇 107  
 SAITOH Kohji 齋藤浩司 41  
 SAKAGUCHI Harutaka 坂口治隆 165  
 SAKAGUCHI Jun 坂口 淳 106  
 SAKAGUCHI Takao 坂口貴男 78, 242  
 SAKAI Hideyuki 酒井英行 44, 45, 46, 48, 148, 149,  
 167, 174  
 SAKAI Kenji 酒井健二 143, 146  
 SAKAI Shingo 坂井真吾 244  
 SAKAMOTO Hisao 坂本久雄 319, 323  
 SAKAMOTO Kazunori 坂本一憲 119  
 SAKAMOTO Koichi 阪本浩一 131  
 SAKAMOTO Naruhiko 坂本成彦 44, 45, 46, 48, 148,  
 174, 268, 272, 277,  
 281, 285  
 SAKODA Seitaro 迫田誠太郎 44, 45, 46, 148  
 SAKUMA Fuminori 佐久間史典 245  
 SAKUMI Akira 作美 明 92  
 SAKURAI Hiromu 桜井 弘 108  
 SAKURAI Hiroyoshi 櫻井博儀 49, 52, 53, 54, 55, 56,  
 57, 58, 59, 61, 62, 63,  
 69, 70, 71, 72, 73, 74,  
 75, 76  
 SAKURAI Yoshiharu 櫻井吉晴 103  
 SAMANTA Chhanda 67, 68  
 SANETO Ryuji 実藤竜二 101  
 SASAKI Osamu 佐々木 修 245  
 SASAKI Shoichi 佐々木勝一 211  
 SASAKI Takafumi 佐々木隆文 179  
 SATO Hiroki D. 佐藤博紀 220, 224, 225, 245  
 SATO Katsuhiko 佐藤勝彦 31  
 SATO Masaharu 佐藤将春 43  
 SATO Susumu 佐藤 進 244  
 SATO Wataru 佐藤 涉 65, 77, 91, 107, 143, 145, 146  
 SATOU Yoshiteru 佐藤義輝 44, 45, 46, 48, 60, 135,  
 137, 174  
 SAWADA Shin'ya 澤田真也 236, 238, 240  
 SCHAFFNER-BIELICH Jürgen 198  
 SCHOTT Wolfgang 82  
 SCHUESSLER Hans A. 99  
 SCHÄFER Thomas 200  
 SEKI Ryoichi 関 亮一 23  
 SEKIGUCHI Kimiko 関口仁子 44, 45, 46, 48, 148, 174  
 SEKIMOTO Michiko 関本美知子 245  
 SERATA Masaki 世良田真来 53, 54, 55, 56, 58, 59, 61,  
 62, 63, 69, 70, 71, 73, 75,  
 76  
 SHARKOV Boris 258  
 SHEN Caiwan 沈 彩万 29  
 SHIBATA Masataka 柴田雅隆 41  
 SHIBATA Toshi-Aki 柴田利明 188, 231, 232  
 SHIMADA Kenji 島田健司 65, 143, 146  
 SHIMAMURA Isao 島村 勲 83, 84, 85, 105  
 SHIMIZU Noritaka 清水則孝 9  
 SHIMOMURA Koichiro 下村浩一郎 138  
 SHIMOURA Susumu 下浦 享 49, 53, 54, 55, 56, 58,  
 59, 60, 61, 62, 63, 69,  
 70, 71, 72, 73, 74, 75,  
 76, 135, 137, 156, 167,  
 169  
 SHINOHARA Atsushi 篠原 厚 123  
 SMITH Braunen 221  
 SOFF Sven 204  
 SON Dam T. 193  
 SONDHEIM Walter 231, 232  
 SONODA Tetsu 園田 哲 141  
 SORENSEN Soren 224, 225  
 SOSHI Takayuki 曾雌隆行 127  
 SPINKA Harold 226, 228  
 STEPHANOV Mikhail 201  
 STRASSER Patrick 138  
 SUDA Kenji 須田健嗣 44, 45, 46, 148, 174  
 SUDA Toshimi 須田利美 40, 42, 64, 66, 67, 68, 154,  
 164, 165, 171  
 SUDOH Kazutaka 須藤和敬 186

- SUGAI Hiroyuki 須貝宏行 39  
 SUGAI Isao 菅井 勲 262  
 SUGANUMA Hideo 菅沼英夫 109  
 SUGANUMA Hideo 菅沼秀夫 213  
 SUGAWARA Fumio 菅原二三男 128  
 SUGIMOTO Makoto 杉本 誠 177  
 SUGIMOTO Satoru 杉本 聡 13, 14  
 SUGIMOTO Takashi 杉本 崇 43, 49, 57, 69, 70, 71, 72, 75, 76, 159  
 SUMIYOSHI Kohsuke 住吉光介 33, 34, 35  
 SUZUKI Hideyuki 鈴木英之 33, 35  
 SUZUKI Hiroyuki 鈴木弘行 119  
 SUZUKI Ken-ichi 鈴木賢一 129, 130  
 SUZUKI Kenji 鈴木賢二 36  
 SUZUKI Ken 鈴木 謙 82  
 SUZUKI Naoki 鈴木直毅 102, 103, 140  
 SUZUKI Ryoko 鈴木涼子 45, 46, 174  
 SUZUKI Takatoshi 鈴木隆敏 43  
 SUZUKI Takeshi 鈴木 健 42, 66, 67, 68  
 SUZUKI Toshio 鈴木俊夫 20  
 SUZUKI-NARA Miwako 奈良(鈴木)美和子 244  
 SVIRIDA Dmitry N. 221, 226, 228  
 SYPHERS Michael 221  
 SYRESIN Evgeny 310  
 TABARU Tsuguchika 田原司睦 245  
 TACHIBANA Takahiro 橘 孝博 27  
 TACHIKAWA Masanori 立川仁典 83  
 TAJIMA Norio 田島典夫 94  
 TAKAHASHI Katsuhiko 高橋克彦 5  
 TAKAHASHI Kazuya 高橋和也 247  
 TAKAHASHI Kenichiro 高橋健一郎 104  
 TAKAHASHI Yoshio 高橋嘉夫 121  
 TAKAHASHI Yutaka 高橋 豊 152  
 TAKANAKA Masao 高仲政雄 312  
 TAKANO Motonobu 高野元信 307  
 TAKEDA Hiroyuki 竹田浩之 165  
 TAKEDA Naoto 武田直人 39  
 TAKESHITA Eri 竹下英里 53, 54, 61, 69, 70, 71, 72, 75, 76  
 TAKETANI Atsushi 竹谷 篤 220, 221, 224, 225, 228, 231  
 TAKEUCHI Hiroki 竹内弘樹 249  
 TAKEUCHI Satoshi 武内 聡 49, 53, 54, 55, 56, 58, 59, 61, 62, 63, 69, 70, 71, 73, 74, 75, 76, 169  
 TAKEUCHI Takeshi 竹内 猛 258, 260  
 TAMAI Munetaka 玉井宗孝 78, 242  
 TAMAMURA Toshiaki 玉村敏昭 95  
 TAMII Atsushi 民井 淳 44, 45, 46, 148, 149, 174  
 TANABE Toshiya 田辺敏也 38, 266, 307, 310  
 TANAKA Hiroshi 田中 大 97  
 TANAKA Kazuhiro H. 田中万博 245  
 TANAKA Yoshito 田中義人 78  
 TANASE Masakazu 棚瀬正和 39  
 TANIHATA Isao 谷畑勇夫 24, 25, 32, 40, 42, 50, 64, 66, 67, 68, 80, 101, 147, 152, 154, 157, 159, 161, 162, 164, 165, 171  
 TAROHDA Tohru 太郎田 融 110, 111  
 TERANISHI Takashi 寺西 高 52, 53, 54, 55, 56, 58, 59, 60, 61, 62, 63, 135, 137, 156, 274, 275  
 TERANISHI Yoshiaki 寺西慶哲 84, 85  
 TERASAWA Mariko 寺澤真理子 33, 34  
 TERASHIMA Satoru 寺嶋 知 165  
 THOENNESSEN Michael 159  
 THOMAS Timothy L. 221  
 THROWE Thomas G. 240  
 TOJO Junji 東城順治 220, 221, 226, 228  
 TOKANAI Fuyuki 門叶冬樹 50, 161  
 TOKI Hiroshi 土岐 博 13, 14, 35  
 TOMINAKA Toshiharu 富中利治 234, 285, 289, 291, 293, 295, 303  
 TOMONO Dai 友野 大 43, 82  
 TORII Hiroyuki A. 鳥居寛之 96, 106  
 TORII Hisayuki 鳥井久行 218, 243  
 TOWELL Rusty 232  
 TSUCHIDA Hideo 土田英夫 41  
 TSUCHIDA Hidetsugu 土田秀次 93  
 TSUCHIHASHI Takahiro 土橋隆博 303  
 TSUJI Takae 辻 孝枝 112, 114  
 TSUKIORI Noritoshi 月居憲俊 5  
 TSURUOKA Hiroshi 鶴岡祐士 244  
 TSUTSUI Hiroshi 筒井裕士 308  
 TSUTSUMI Tsuyoshi 堤 剛志 41  
 UCHIGASHIMA Nobuyuki 内ヶ島暢之 44, 45, 46, 148  
 UCHIYAMA Akito 内山暁仁 3  
 UE Koji 上 浩二 53, 54, 60, 61, 69, 70, 71, 72, 75, 76, 135, 137, 156, 275  
 UENO Hideki 上野秀樹 65, 77, 91, 107, 143, 145, 146  
 UESAKA Tomohiro 上坂友洋 44, 45, 46, 48, 148, 149, 174  
 UMETANI Shigeo 梅谷重夫 122  
 UNDERWOOD David 221, 226  
 UNO Kōichi 宇野浩一 277  
 URAI Teruo 浦井輝夫 7, 94  
 UTSUNO Yutaka 宇都野 穰 10, 11  
 UWAMINO Yoshitomo 上養義朋 173, 319, 321, 323

- van KOLCK Ubirajara 194  
 VENUGOPALAN Raju 195, 198, 203  
 VILLATTE Laurence 224, 225  
 VOGELSSANG Werner 190  
 WADA Michiharu 和田道治 99, 100, 141, 157  
 WAKASA Tomotsugu 若狭智嗣 44, 48, 174  
 WAKASUGI Masanori 若杉昌徳 316  
 WAKUI Takashi 涌井崇志 149  
 WALDEN Patric 80  
 WATANABE Gentaro 渡辺元太郎 31  
 WATANABE Hiroshi 渡邊 寛 41, 49, 65, 77, 91, 107,  
 143, 145, 146  
 WATANABE Ikuo 渡辺郁男 310  
 WATANABE Isao 渡邊功雄 104, 138  
 WATANABE Kiwamu 渡辺極之 57  
 WATANABE Shin-ichi 渡辺伸一 135, 137, 156, 256,  
 272, 274, 275, 314  
 WATANABE Tamaki 渡邊 環 314  
 WATANABE Yasushi 渡邊 康 176, 225, 228, 236,  
 238, 240  
 WATANABE Yutaka X. 渡辺 裕 57, 73  
 WEI Long 魏 龍 160  
 WEICK Hermut 82  
 WETTIG Tilo 209, 215  
 WIDMANN Eberhard 106  
 WOLFE David 221  
 WOLLNIK Hermann 157  
 XIE Wei 222  
 YABANA Kazuhiro 矢花一浩 17  
 YABUKI Sadayo 矢吹貞代 182  
 YABUSHITA Yuko 藪下裕子 110, 111, 113  
 YAGI Eiichi 八木栄一 94  
 YAIRI Satoshi 矢入 聡 104  
 YAKO Kentaro 矢向謙太郎 44, 45, 46, 48, 148, 174  
 YAKUSHIJI Takashi 薬師寺 崇 57  
 YAMADA Hirohisa 山田裕久 122  
 YAMADA Kazunari 山田一成 53, 54, 55, 56, 58, 59,  
 61, 62, 63, 69, 70, 71,  
 73, 75, 76, 147  
 YAMADA Masami 山田勝美 27  
 YAMADA Satoru 山田 悟 245  
 YAMADA Shoichi 山田章一 33, 35  
 YAMADA Yasuhiro 山田康洋 107  
 YAMAGUCHI Azusa 山口あづさ 209  
 YAMAGUCHI Hidetoshi 山口英敏 106  
 YAMAGUCHI Isamu 山口 勇 127  
 YAMAGUCHI Takayuki 山口貴之 42, 64, 66, 67, 68, 171  
 YAMAGUCHI Yoshitaka 山口由高 64, 66  
 YAMAJI Shuhei 山路修平 23  
 YAMAMOTO Kazuhiro 山本和弘 221  
 YAMAMOTO Sukeyasu 山本祐靖 41  
 YAMAMOTO Tomoyuki 山本知之 86  
 YAMANISHI Teruya 山西輝也 185  
 YAMAUCHI Hiromoto 山内啓資 3  
 YAMAZAKI Norio 山崎則夫 135, 137, 156, 274, 275  
 YAMAZAKI Toshimitsu 山崎敏光 37, 82, 106  
 YAMAZAKI Yasunori 山崎泰規 88, 93, 95, 96, 97, 98,  
 141  
 YANAGA Makoto 矢永誠人 109  
 YANAGISAWA Yoshiyuki 柳澤善行 53, 54, 55, 56, 57,  
 58, 59, 60, 61, 62,  
 63, 69, 70, 71, 72,  
 73, 74, 75, 76,  
 135, 137, 156,  
 275  
 YANAGIYA Takahiro 柳谷隆宏 117  
 YANG Yongfeng 楊 永峰 41, 179  
 YANO Katsuki 矢野勝喜 258  
 YANO Yasushige 矢野安重 3, 5, 179, 247, 251, 253,  
 254, 264, 272, 274, 277,  
 279, 281, 283, 285, 287,  
 289, 291, 293, 295, 303  
 YASUI Hiroyuki 安井裕之 108  
 YATAGAI Fumio 谷田貝文夫 132, 133  
 YOKKAICHI Satoshi 四日市 悟 220, 225, 236, 238,  
 240, 245  
 YOKOUCHI Shigeru 横内 茂 285  
 YOKOYAMA Ichiro 横山一郎 3, 5, 266  
 YOMO Yasunori 四方康範 129  
 YONEDA Akira 米田 晃 5, 88, 154  
 YONEDA Ken-ichiro 米田健一郎 49, 52, 57, 65, 69, 70,  
 71, 73, 74, 75, 76, 91,  
 107, 143, 145, 146  
 YONEYAMA Tetsu 米山 哲 43, 82  
 YONGIL Kwon 232  
 YOSHIDA Atsushi 吉田 敦 64, 69, 70, 90, 141, 152,  
 154, 176  
 YOSHIDA Koichi 吉田光一 50, 58, 59, 62, 63, 64, 66,  
 176, 177  
 YOSHIDA Shigeo 吉田茂男 128, 129, 130, 131  
 YOSHIDA Yutaka 吉田 豊 90  
 YOSHIMI Akihiro 吉見彰洋 65, 77, 91, 143, 145, 146,  
 151  
 YOSHIMURA Yoshio 吉村善郎 245  
 YOUNG Glenn 224, 225  
 ZELEVINSKY Vladimir 22  
 ZHANG Yuho 張 玉虎 41  
 ZHAO Yu-Liang 趙 宇亮 154

ZHENG Tao 鄭 濤 42, 64, 66, 67, 68, 171  
ZHOU Xiaohong 周 小紅 41, 75, 76  
ZHU Lihua 221

## **RIKEN Accelerator Progress Report Vol. 35**

理化学研究所加速器年次報告 第35卷 (2002)

---

印刷 平成14年(2002)3月20日

発行 平成14年(2002)3月29日

発行者 理化学研究所

代表者 小林 俊 一

〒351-0198 埼玉県和光市広沢2番1号

電話 (048) 462-1111

編集者 理化学研究所加速器研究施設

運営委員会

印刷所 三美印刷株式会社

〒116-0013 東京都荒川区西日暮里5-9-8

---

定価5,000円

(消費税別)



理化学研究所

埼玉県 和光市 広沢